13th Annual Review of Progress in

APPLIED

COMPUTATIONAL

ELECTROMAGNETICS

at the

Naval Postgraduate School

Monterey, CA

March 17-21, 1997

CONFERENCE PROCEEDINGS

CONFERENCE PROCEEDINGS

VOLUME I

13th Annual Review of Progress in

APPLIED

COMPUTATIONAL

ELECTROMAGNETICS

at the

Naval Postgraduate School

Monterey, CA

March 17-21, 1997

TECHNICAL PROGRAM CHAIRMAN

Eric C. Michielssen

Sponsored by

The Applied Computational Electromagnetics Society

Naval Postgraduate School, DOE/LLNL, University of Illinois, University of Kentucky,

USAF, DOD AND DOE IN COOPERATION WITH IEEE, URSI, ASEE, SIAM AND AMTA

THE NAVAL POSTGRADUATE SCHOOL

VOLUME I

SESSION 1: VISUALIZATION
        Chair: Janice L. Karty

SESSION 2: ADVANCED TIME-DOMAIN METHODS
        Chair: Steve Gedney

II

III

IV

VI

THE APPLIED COMPUTATIONAL ELECTROMAGNETIC SOCIETY

CALL FOR PAPERS

The 14th Annual Review of Progress
in Applied Computational Electromagnetics

16-20 March, 1998

Naval Postgraduate School, Monterey, California

Share your knowledge and expertise with your colleagues

The Annual ACES Symposium is an ideal opportunity to participate in a large gathering of EM analysis enthusiasts. The purpose of the Symposium is to bring analysts together to share information and experience about the practical application of EM analysis using computational methods. The symposium offerings include technical presentations, demonstrations, vendor booths and short courses. All aspects of electromagnetic computational analysis are represented. Contact Jianming Jin for details.

The ACES Symposium is a highly influential outlet for promoting awareness of recent technical contributions to the advancement of computational electromagnetics. Attendance and professional program paper participation from non-ACES members and from outside North America are encouraged and welcome.

Technical Program Chairman
Jianming Jin
ECE Department
University of Illinois
1406 W. Green Street
Urbana, IL 61801-2991
Phone: (217) 244-0756
FAX: (217) 333-5962
Email:j-jin1@uiuc.edu

Symposium Administrator
Richard W. Adler
ECE Dept/Code EC/AB
Naval Postgraduate School
833 Dyer Road, Room 437
Monterey, CA 93943-5121
Phone: (408) 646-1111
FAX: (408) 649-0300
Email:rwa@ibm.net

Symposium Co-Chairman
Michael A. Jensen
ECE Dept., 459 CB
Brigham Young University
Provo, UT 84602
Phone: (801) 378-5736
FAX: (801) 378-6586
Email:jensen@ee.byu.edu

THE APPLIED COMPUTATIONAL ELECTROMAGNETIC SOCIETY

CALL FOR PAPERS

The 14th Annual Review of Progress
in Applied Computational Electromagnetics

Papers may address general issues in applied computational electromagnetics, or may focus on specific applications, techniques, codes, or computational issues of potential interest to the Applied Computational Electromagnetics Society membership. Area and topics include:

* Code validation
* Code performance analysis
* Computational studies of basic physics
* Examples of practical code application
* New codes, algorithms, code enhancements, and code fixes
* Computer Hardware Issues
* Partial list of applications:

antennas	wave propagation
radar imaging	radar cross section
shielding	bioelectromagnetics
EMP, EMI/EMC	visualization
dielectric & magnetic materials	inverse scattering
microwave components	MIMIC technology
fiberoptics	remote sensing & geophysics
communications systems	propagation through plasmas
eddy currents	non-destructive evaluation

* Partial list of techniques:

frequency-domain & time-domain techniques
integral equation & differential equation techniques
finite difference & finite element analysis

diffraction theories	physical optics
modal expansions	perturbation methods
hybrid methods	moment methods

INSTRUCTIONS FOR AUTHORS AND TIMETABLE

For both summary and final paper, please supply the following data for the principal author: name, address, Email address, FAX, and phone numbers for both work and home.

October 26, 1997: Submission deadline. Submit four copies of a 300-500 word summary to the Technical Program Chairman.

November 25, 1997: Authors notified of acceptance

January 10, 1998: Submission deadline for camera-ready copy. The papers should not be more than 8 pages long including figures.

REGISTRATION FEE

Registration fee per person for the Symposium will be approximately $255 for ACES Members; $295 for non-members, $115 for Student, Retired and Unemployed, does not include conference proceedings; or $150 for Student/Unemployed/retired, which includes proceedings. The exact fee will be announced later. All Conference participants are required to register for the Conference and to pay the indicated registration fee.

SHORT COURSES

Short courses will be offered in conjunction with the Symposium covering numerical techniques, computational methods, surveys of EM analysis and code usage instruction. It is anticipated that short courses will be conducted principally on Monday March 16 and Friday March 20. Fee for a short course is expected to be approximately $90 per person for a half-day course and $140 for a full-day course, if booked before March 3, 1998. Full details of 1998 Symposium will be available by November 1997. Short Course Attendance is not covered by the Symposium Registration Fee!

EXHIBITS

Vendor booths and demonstrations will feature commercial products, computer hardware and software demonstrations, and small company capabilities.

1997 Symposium Program Committee

for the

13th Annual Review of Progress in

APPLIED COMPUTATIONAL ELECTROMAGNETICS

at the
Naval Postgraduate School
Monterey, CA

Technical Program Chairman:

Eric Michielssen
ECE Department
Univ. of Illinois
1406 West Green Street
Urbana, IL 61801-2991
Phone: (217) 333-3803
FAX: (217) 333-5962
Email:michiels@decwa.ece.edu

Co-Chair:

Jiaming Jin
ECE Department
University of Illinois
1406 West Green Street
Urbana, IL 61801-2991
Phone: (217) 333-3801
FAX: (217) 333-5962
Email:j-jin1@uiuc.edu

Co-Chair:

Keith Whites
EE Department
Univ. of Kentucky
453 Anderson Hall
Lexington, KY 40506-0046
Phone: (606) 257-1768
Fax: (606) 257-3092
Email:whites@engr.uky.edu

Symposium Administrator

Richard W. Adler
ECE Department, Code EC/AB
Naval Postgraduate School
833 Dyer Road, Room 437
Monterey, CA 93943-5121
Phone: (408) 646-1111
FAX: (408) 649-0300
Email:rwa@ibm.net

Short Course Chairman:

Keith Whites
EE Department
Univ. of Kentucky
453 Anderson Hall
Lexington, KY 40506-0046
Phone: (606) 257-1768
Fax: (606) 257-3092
Email:whites@engr.uky.edu

Conference Secretary:

Mrs. Pat Adler

Advisory Committee:

Richard W. Adler, Naval Postgraduate School
Duncan C. Baker, University of Pretoria
Robert Bevensee, Consultant
Pat Foster, Microwave & Antenna Systems
Todd Hubing, University of Missouri-Rolla
Adalbert Konrad, University of Toronto
John Brauer, Ansoft Corp.
Edmund K. Miller
Andrew Peterson, Georgia Institute of Tech.
Harold Sabbagh, Sabbagh Assoc. Inc.
W. Perry Wheless, Jr., University of Alabama

PREFACE
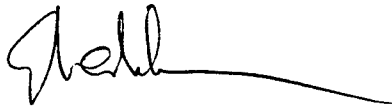
On behalf of the ACES Technical Program Committee, I welcome you to "The 13th Annual Review of Progress in Applied Computational Electromagnetics". The Symposium spans the five day period from Monday, March 17 through Friday, March 21, 1997, and takes place at the Naval Postgraduate School (NPS) in Monterey, California. The Symposium is sponsored by the Applied Computational Electromagnetics Society, NPS, the University of Illinois at Urbana-Champaign, and the University of Kentucky.

Monday, March 17 and Friday, March 21 are devoted uniquely to Short Courses. A total of 10 Short Courses will be offered. Technical sessions will take place Tuesday, March 18 through Thursday, March 20, with an Interactive Session and Vendor Exhibits scheduled for Tuesday afternoon. This year's Symposium features a total of 25 technical sessions containing well over 220 presentations! For the first time, the ACES Symposium will feature a Student Paper Contest.

The organization of the Symposium would not have been possible without the cooperation of my colleagues Professor Jianming Jin, who edited the conference proceedings, and Professor Keith Whites, who organized short courses, vendor exhibits, and conference advertising. Dr. Bob Bevensee was the driving force behind the organization of the Student Paper Contest. I would especially like to thank Professor Richard Adler for providing access to the NPS facilities and his unending dedication to the annual ACES conferences. Pat Adler and Shirley Dipert assisted in the compilation of the author database and the printing of the proceedings. Finally, I would like to thank Professor Mike Jensen and Randy Haupt for their commitment to organizing next year's Symposium.

Enjoy the 13th Annual Review, and your stay in Monterey.

Eric Michielssen
Technical Program Chair
1997 ACES Conference

ACES PRESIDENT'S STATEMENT

Welcome to the 13th Annual Review of Progress in Applied Computational Electromagnetics. It is not always easy to predict the weather in Monterey in March, but we can always predict that the ACES Conference will be bright, warm (perhaps heated at times), and responsive to your needs. This year, for the first time, we will feature a student paper competition. Technical Program Chairman, Eric Michielssen, and his co-chairmen, Jianming Jin and Keith W. Whites, deserve our congratulations for organizing what should be another outstanding conference.

We hope that you will attend one or more of our collateral events, such as a short course, and our awards banquet. You will also want to visit some of the sites in Monterey, such as the aquarium, while you are here.

Remember that, as a society of volunteers ACES looks to you, its members, for support. If you have time and spirit to give to ACES, please let me know. We're looking for you.

Enjoy the 13th Annual Review.

Harold A. Sabbagh
Sabbagh Associates, Inc.
4635 Morningside Drive
Bloomington, IN 47408
(812)339-8273
(812)339-8292 FAX
email: has@sabbagh.com

ACES 1997 SHORT COURSES

MONDAY MARCH 17	FULL-DAY COURSES

0830-1630 "Finite Elements for Electromagnetics," by Dr. John Brauer and Dr. Zoltan Cendes, Ansoft Corp.

0830-1630 "Ray-Tracing Techniques for the Prediction of Propagation Parameters in Mobile Communications. Application to Microcells and Picocells." Prof. Felipe Catedra, University of Cantabria, Spain.

0830-1630 "Transmission Line Matrix (TLM) Modeling of Electromagnetic Fields in Space and Time," Prof. Wolfgang J.R. Hoefer, University of Victoria, Canada.

0830-1630 "Practical EMI/EMC Design and Modeling," Prof. Todd Hubing, University of Missouri-Rolla.

MONDAY MARCH 17 **HALF-DAY COURSES**

0830-1200 "Numerical Optimization in Electromagnetics: Genetic Algorithms," Dr. Randy L. Haupt, United States Air Force Academy.

FRIDAY MARCH 21 **FULL-DAY COURSES**

0830-1630 "Finite Difference Time Domain Modeling and Applications," Prof. Stephen Gedney, University of Kentucky and Dr. James Maloney, Georgia Tech. Research Institute.

0830-1630 "Introduction to RADAR via Physical Wavelets," Dr. Gerald Kaiser, Prof. of Mathematical Sciences at U-Mass-Lowell.

0830-1630 "Mathematical Software for Computational Electromagnetics," Dr. Jovan Lebaric, Naval Postgraduate School,

FRIDAY MARCH 21 **HALF-DAY COURSES**

0830-1200 "Radiation Physics," Dr. E.K. Miller

1300-1630 "Introduction to FEKO: A Hybrid Method of Moments/Physical Optics (MoM/PO) Code," Dr. F.J.C. Meyer, EM Software and Systems, South Africa, and Dr. U. Jakobus, Univ. of Stuttgart, Germany.

FINAL AGENDA

The Thirteenth Annual Review of Progress in Applied Computational Electromagnetics

NAVAL POSTGRADUATE SCHOOL
17-21 MARCH 1997

Eric Michielssen, Technical Program Chairman

Jianming Jin, Conference Co-Chair

Keith Whites, Short Course and Vendor Chairman

Robert Bevensee, Assistant Conference Co-Chair

Richard W. Adler, Conference Facilitator

MONDAY MORNING 17 MARCH 1997

0730-0820	**SHORT COURSE REGISTRATION**	Glasgow 103
0830-1630	**SHORT COURSE (FULL-DAY)** "Finite Elements for Electromagnetics", John Brauer & Zoltan Cendes, Ansoft Corp.	Glasgow 102
0830-1630	**"SHORT COURSE (FULL-DAY)** "Ray-Tracing Techniques for the Prediction of Propagation Parameters in Mobile Communications. to Applications Microcells and Picocells" , Felipe Catedra, University of Cantabria	Ingersoll 122
0830-1630	**SHORT COURSE (FULL-DAY)** "Transmission Line Matrix (TLM) Modeling of Electromagnetic Fields in Space and Time" Wolfgang J.R. Hoefer, University of Victoria	Engr. Auditorium
0830-1630	**SHORT COURSE (FULL-DAY)** "Practical EMI/EMC Design and Modeling", Todd Hubing, University of Missouri-Rolla	Spanagel 101A
0900-1200	**CONFERENCE REGISTRATION**	Glasgow 103
0830-1200	**SHORT COURSE (HALF-DAY)** "Numerical Optimization in Electromagnetics: Genetic Algorithms", Randy L. Haupt, USAF Academy	Glasgow 109
1200-2000	**CONFERENCE REGISTRATION**	Glasgow 103

MONDAY EVENING

1900	**PUBLICATIONS DINNER**	**Chef Lee's Mandarin House**

TUESDAY MORNING 18 MARCH 1997

0700-0745	**CONTINENTAL BREAKFAST**	**Glasgow Courtyard**
0745	**WELCOME** Eric Michielssen	**Glasgow 102**
SESSION 1:	**VISUALIZATION** (Parallel with Sessions 2, 3, & 4) Chair Janice L. Karty (Organizer)	**Glasgow 102**

0840	"Visualization: A Powerful Tool for Understanding Electromagnetics"	E.K. Miller
0900	"Computational Diagnostic Techniques for Electromagnetic Scattering Analytical Imaging, Near Fields, and Surface Currents"	K.W. Hom, N.A. Talcott, Jr., J. Shaeffer
0920	"Interferometric 3D Imaging"	C.A. Au
0940	"Modern Graphics Applications for Visualization of Electromagnetic Radiation and Scattering"	C.L. Yu, R. Kipp, D.J. Andersh, S.W. Lee
1000	**BREAK**	
1020	"A Versatile Geometry Tool for Computational Electromagnetics (CEM): MrPatches"	D.D. Car & J M. Roedder
1040	"Visualisation Issues for Time Domain Integral Equation Modelling"	S.J. Dodson & S.P. Walker
1100	"An Antenna Training Aid Using Electromagnetic Visualisation"	A. Nott & D. Singh
1120	The Fieldinspector: A Graphic Field Representation System"	P. Leuchtmann & A. Witzig
1140	"A Data Compression Techniques for Antenna Pattern Storage and Retrieval"	A. Nott
1200	**LUNCH**	

TUESDAY MORNING 18 MARCH 1997

SESSION 2:   **ADVANCED TIME-DOMAIN METHODS (Parallel with Sessions 1, 3, & 4)**   Ingersoll 122
                        Chair Steve Gedney (Organizer)

0840   "Solution of Boundary Value Problems in Time Domain Using Multiresolution Analysis"   L.P.B. Katehi & J. Harvey

0900   "High Resolution Schemes for Maxwell Equation in the Time Domain"   J.S. Shang

0920   "FDTD M24 Dispersion and Stability in Three Dimensions"   G. Haussmann & M. Piket-May

0940   "Transparent Absorbing Boundary (TAB): Truncation of Computational Domain without Reflections"   J. Peng & C.A. Balanis

1000   **BREAK**

1020   "The Design of Maxwellian Smart Skins"   R.W. Ziolkowski, F. Auzanneau

1040   "Numerical Analysis of Periodic Structures Using the Split-Field Update Algorithm"   P.H. Harms, J.A. Roden, J.G. Maloney, M.P. Kesler, E.J. Kuster & S.D Gedney

1100   "Modeling Dispersive Soil for FDTD Computation by Fitting Conductivity Parameters"   C.M. Rappaport & S. Winton

1120   "A Hybrid Analysis Using FDTD and FETD for Locally Arbitrary Shaped Structures"   D. Koh, H.-B Lee, B. Houshmand, & T. Itoh

1140   "A Simple Method for Distributed Parallel Processing with a Cartesian Coordinate System Based Finite-Difference Time-Domain Code"   E.A. Baca, J.T. MacGillivray, D. Dietz, C.E. Davis, S.A. Blocher & C.E. Davis

1200   **LUNCH**

SESSION 3:   **MODEL REDUCTION METHODS FOR COMPUTATIONAL ELECTROMAGNETICS**   Engr Auditorium
                        Chair Jin-Fa Lee (Organizer), Co-Chair Din-Kow Sun
                        (Parallel with Sessions 1, 2, & 4)

0840   "Computation of Transient Electromagnetic Wavefields in Inhomogeneous Media Using a Modified Lanczos Algorithm"   R.F. Remis, P.M. van den Berg

0900   "S-Parameters of Microwave Resonators Computed by Direct Frequency and Modal Frequency Finite Element Analysis"   J. Brauer & A. Frenkel

0920   "Reduced-Order Modeling of Electromagnetic Systems with Pade via Lanczos Approximations"   A.C. Cangellaris & L. Zhao

0940   "Integrating Data Obtained from Electromagnetic Field Analysis into Circuit Simulations"   W.T. Beyene. J.E. Schutt-Aine

1000   **BREAK**

1020   "Application of AWE Method to the Spectral Responses of 3D TVFEM Modeling of Passive Microwave Devices"   X. Zhang, J-F Lee. R. Dyczij-Edlinger

1040   "Solution of EM Problems Using Reduced-order Models by Complex Frequency Hopping"   M.A. Kolbedhari, R. Achar, M. Nakhla, R. Achar, M. Srinivasan

1100   "Transient Analysis via Electromagnetic Fast-Sweep Methods and Circuit Models"   E. Bracken & Z. Cendes

SESSION 4:   **COMPUTER SIMULATION OF ANTENNAS**   Ingersoll 361
                        Chair Jim Breakall, Co-Chair Boris Tomasic
                        (Parallel with Sessions 1, 2, & 3)

0840   "Application of Computational Electromagnetics to Shipboard HFDF System Simulation"   J.B. Knorr

0900   "Calculation of the Near Fields of a Large Complex Antenna Structure and Comparison with *In Situ* Measurements"   C. Selcher, E. Kennedy, E. Kennedy, P. Elliot

0920   "Theoretical Studies on the Effect of Waveguide Geometry on the Radiating Slot"   V.V.S. Prakash, N. Balakrishnan, S. Christopher

0940   "Computed and Measured Radiation Patterns of Antennas with Aerodynamic Radomes"   D.C. Jenn & S.M. Herzog

1000   **BREAK**

1020   "SAF Analysis Codes for Computing Shipboard Antenna Pattern Performance, Antenna Coupling, and RADHAZ"   B.J. Cown & J.P. Estrada

1040   "Far Field Patterns of Combined TE/TM Aperture Distributions"   R.A. Speciale

1100   "Calculation of Equivalent Generator Voltage and Generator Internal Impedance for Cylindrical Antennas in the Receiving Mode"   C.-C. Su

1120   "Arrays of Sleeved Monopoles - Computer Codes"   B. Tomasic, E. Cohen, K. Sivaprasad

TUESDAY MORNING 18 MARCH 1997

1145   **BOARD OF DIRECTORS MEETING/LUNCHEON**   **Terrace Room, Herrmann Hall**

1200   **LUNCH**

TUESDAY AFTERNOON 18 MARCH 1997

SESSION 5:   **RADIATION PHYSICS (Parallel with Sessions 6, 7, & 8)**   **Glasgow 102**
                Chair Ed Miller (Organizer), Co-Chair Bob Bevensee

1320   "An Exploration of Radiation Physics in Electromagnetics"   E.K. Miller

1340   "Formulae for Total Energy and Time-Average Power Radiated from Charge-Current   R.M. Bevensee
        Distributions"

1400   "An Overview of Antenna Radiation Basic Principles"   W.P. Wheless, Jr. & L.T. Wurtz

SESSION 6:   **COMPUTATIONAL METHODS FOR INVERSE SCATTERING**   **Ingersoll 122**
                Chair Bill Weedon (Organizer), Co-Chair Gregory Newman
                (Parallel with Sessions 5, 7, & 8)

1320   "Application of Kaczmarz's Method to Nonlinear Inverse Scattering"   W.H. Weedon

1340   "Statistical Characteristics of Reflection and Scattering of Electromagnetic Radar Pulses   Y. Miyazaki, K. Takahashi,
        by Rough Surface and Buried Objects"   S. Knedlik

1400   "Nondestructive Materials Measurement of Electrical Parameters with Readily Made   T.R. Holzheimer
        Coaxial Probes"   C.V. Smith, Jr.

1420   "A Volume-Integral Code for Electromagnetic Nondestructive Evaluation"   R. Murphy, H.A. Sabbagh,
                                                  A. Chan, & E.H. Sabbagh

SESSION 7:   **WAVELETS AND FRACTALS (Parallel with Sessions 5, 6, & 8)**   **Engr Auditorium**
                Chair Randy Haupt, Co-Chair Doug Werner (Co-Organizers)

1320   "Application of Coifman Wavelets to the Solution of Integral Equations"   M. Toupikov & G. Pan

1340   "Fast Array Factor Calculations for Fractal Arrays"   R.L. Haupt & D.H. Werner

1400   "NEC2 Modeling of Fractal-Element Antennas (FEA)"   N. Cohen

1420   "Genetic Antenna Optimization with Fractal Chromosomes"   N. Cohen

SESSION 8:   **FDTD AND FVTD I (Parallel with Sessions 5, 6, & 7)**   **Ingersoll 361**
                Chair Melinda Picket-May

1320   "An FDTD/FVTD 2D-Algorithm to Solve Maxwell's Equations for a Thinly Coated Cylinder"   J.S. Chen & K.S. Yee

1340   "Improved Computational Efficiency by Using Sub-Regions in FDTD   E.A. Jones & W.T. Joines
        Simulations"   **STUDENT PAPER CONTEST**

1400   "Finite Difference Time Domain Electromagnetic Code Validation Using an Infrared Measurement   C. Reuter & M. Seifert,
        Technique"   T. Karle

1420   "PML-FDTD Simulation for Dispersive, Inhomogeneous, and Conductive Earth"   W.C. Chew, M. Oristaglio,
                                                  T. Wang

1440   "Study of Absorbing Boundary Conditions in the Context of the Hybrid Ray-FDTD Moving   Y. Pemper, E. Heyman,
        Window Solution"   R. Kastner, R.W. Ziolkowski

INTERACTIVE TECHNICAL SESSION 9   **Ballroom, Herrmann Hall**
1520 - 1740

VENDOR EXHIBITS   **Ballroom, Herrmann Hall**
1300 - 1800

WINE AND CHEESE BUFFET   **Ballroom, Herrmann Hall**
1630 - 1800

SESSION 9A: **FDTD AND FVTD II**   **Ballroom, Herrmann Hall**

        "A Generalized Finite-Volume Time-Domain Algorithm for a Microwave Heating Problem on   H. Zhao & I. Turner
        Arbitrary Irregular Grids"

        "A Parallel FVTD Maxwell Solver Using 3D Unstructured Meshes"   J.-P. Cioni, L. Fezoui,
                                                    L. Anne & F. Poupaud

        "Adapting an Algorithm of Computational Fluid Dynamics for Computational   T.E. Hodgetts & C.C. Lytton
        Electromagnetics"

        "Application of a Finite-Volume Time-Domain Technique to Three-Dimensional Objects"   F.G. Harmon & A.J. Terzuoli

        "Comparison of Equations for the FDTD Solution in Anisotropic and Dispersive Media"   G.J. Burke & D.J. Steich

        "A Near-Field to Near-Field Transformation for Steady-State FDTD"   K.A. Lysiak & D.H. Werner

TUESDAY AFTERNOON 18 MARCH 1997

SESSION 9B: INTEGRATED CIRCUITS AND PHOTONICS   **Ballroom, Herrmann Hall**

"Transient Simulation of Breakdown Characteristics of a Miniaturized MOSFET based on a Non-Isothermal Non-Equilibrium Transport Model"   W.-C. Choi, H. Kawashima, R. Dang

"Numerical Simulation of Electro-thermal Characteristics of Semiconductor Devices "Taking Account of Chip Self-heating and In-chip Thermal Interdependence"   H. Kawashima, C. Moglestue, M. Schlechtweg & R. Dang

"Applications of Photonic Band Gap Materials"   M.M. Sigalas, R. Biswas, Q. Li, K.-M. Ho, C.M. Souloulis, D.D. Crouch

SESSION 9C: SIGNAL PROCESSING TECHNIQUES FOR CEM   **Ballroom, Herrmann Hall**

"Investigating the Use of Model-Based Parameter Estimation for Electromagnetic-Data Phase Recovery"   E.K. Miller

"Real Time Adaptive Forward Error Correction Scheme"   S. Veluswamy

"A Novel Spatial Modulation Spread-Spectrum Technique"   S.A. Pradels, N. Marshall, N. Aery, O.R. Baiocchi

"Time Frequency and Time Scale Analysis for Electromagnetics Spectrograms, Wavelets and More"   C.J. McCormack

SESSION 9D: ANTENNA APPLICATIONS   **Ballroom, Herrmann Hall**

"Antenna Array Factors for Dipole Antennas Above an Imperfectly Conducting Half-Space"   J.W. Williams

"Energy Transfer from Free Space Transient Waveforms Through HF Antennas to Arbitrary Loads"   M.J. Packer

"A 12 Beam Cylindrical Array Antenna for AMPS and PCS Applications"   G.A. Martek & J.T. Elson

"A Hybrid-Method Synthesis of a Radiometric Antenna for Near-Field Sensing"   E.Di Giampaolo & F. Bardati

"An Evaluation of Software Packages Based on Moment Methods for TV Antenna Design"   I.F. Anitzine, C. Jaureguibeitia, J.A. Romo

SESSION 9E: SCATTERING AND DIFFRACTION   **Ballroom, Herrmann Hall**

"Algorithm for Prediction of Scattering from Thin Cylindrical Conductors Using Field Decomposition"   P.K. Bishop, J.R. James, R.T. Biggs

"Numerically Exact Algorithm for the H and E-Wave Scattering from a Resistive Flat-Strip Periodic Grating"   T. Zinenko, A.I. Nosich, Y.Okuno, & A. Matsushima

SESSION 9F: NUMERICAL METHODS   **Ballroom, Herrmann Hall**

"Numerical Convergence and Richardson Extrapolation"   R.C. Booton, Jr.

"Powerful Recursive Algorithm for the Exhaustive Resolution of a Nonlinear Eigenvalue Problem"   Ph. Riondet, D. Bajon, H. Baudrand

"A Dense Out-of-Core Solver for Workstation Environments"   C.E. Lee & R.M. Zazworsky

"Mathematical Representation of Multiport Resonator Test Data"   R.A. Speciale

SESSION 9G: SIMULATION   **Ballroom, Herrmann Hall**

"A Comparison of Analytical and Numerical Solutions for Induction in a Sphere with Equatorially Varying Conductivity by Low-Frequency Uniform Magnetic Fields of Arbitrary Orientation"   T.W. Dawson & M.A. Stuchly

"Modeling of Laminated Cores by Homogeneous Anisotropic Cores for Magnetics Simulation"   J.E. Kiwitt, A. Dietermann, K. Reiss

"Barring Characteristic of an Ion Shutter"   B.M. Cramer & D.A. Mlynski

Stability Analysis of Re-Entrant Multi-Turn Toroidal/Helical Electron Orbits in Strong-Focusing Alternating-Gradient Magnetic Fields"   R.A. Speciale

TUESDAY EVENING 18 MARCH 1997

1830   **NO HOST BAR**   **Ballroom, Herrmann Hall**

1930   **AWARDS BANQUET**   **Ballroom, Herrmann Hall**

WEDNESDAY MORNING 19 MARCH 1997

0700-0745	**CONTINENTAL BREAKFAST**	**Glasgow Courtyard**
0730	**ACES BUSINESS MEETING** President Hal Sabbagh	**Glasgow 102**
SESSION 10:	**FINITE ELEMENT ANALYSIS (Parallel with Sessions 11, 12, & 13)** Chair John Brauer (Organizer), Co-Chair Zoltan Cendes	**Glasgow 102**
0840	"Finite-Element and Method-Of-Moments Analyses of an Ultra-wide Bandwidth TEM Horn"	M.H. Vogel
0900	"A Modified Mei Method for Solving Scattering Problems with the Finite Element Method"	Y. Li & Z. Cendes
0920	"Investigation of the Limitations of Perfectly-Matched Absorber Boundaries in Antenna Applications"	J.F. DeFord
0940	"The Spectral Lanczos Decomposition Method for Solving Axisymmetric Low-Frequency Electromagnetic Diffusion by the Finite-Element Method"	M. Zunoubi, J.-M. Jin, W.C. Chew & D. Kennedy
1000	**BREAK**	
1020	"Duality Between Finite Elements and Hodge Operator in Three Dimensions"	A. de La Bourdonnaye & S. Lala
1040	"A Generalized Method for Including Two Port Networks in Microwave Circuits Using the Finite Element Method"	E. Yasan, J.-F. Yook, L.P.B. Katehi
1100	"Projecting Between Complementary Vector Basis Functions" **STUDENT PAPER CONTEST**	J. Scott Savage A.F. Peterson

SESSION 11:	**ADVANCES IN TRANSMISSION LINE MATRIX (TLM) MODELING I** Chair Wolfgang Hoefer (Organizer), Co-Chair Fred German **(Parallel with Sessions 10, 12, & 13)**	**Ingersoll 122**
0840	"Modelling of Ferrite Tiles as Frequency Dependent Boundaries in General Time- Domain TLM Schemes"	V. Trenkic, J. Paul,. I. Argyri, C. Christopoulos
0900	"The Use of Sources for TLM Modeling of Complex Materials"	J. Represa, A.C.L. Cabeceira, I. Barba
0920	"Electromagnetic Fields Generated by Current Transients on Protection Structures Using TLM - A FD-TD Comparison"	G.P. Caixeta & J.P. Pissolato
0940	"Towards a TLM Description of an Open-Boundary Condition"	D. de Cogan & Z. Chen
1000	**BREAK**	
1020	"A Modified 3D-TLM Variable Node for the Berenger's Perfectly Matched Layer Implementation"	J.L. Dubard & D. Pompei
1040	"Electromagnetic Field Computations by a Generalized Network Formulation"	L.B. Felsen, M. Mongiardo, P. Russer
1100	"A Comparative Study of Dispersion Errors and Performance of Absorbing Boundary Conditions in SCN-TLM and FDTD"	L. De Menezes, C. Eswarappa, W.J.R. Hoefer
1120	"Analysis of Planar Structure on General Anisotropic Material: Unified TLM Modelin Frequency- and Time-Domain and Experimental Verification"	K. Wu, Q. Zhang, & J. Huang
1140	"A Digital Filter Technique for Electromagnetic Modelling of Thin Composite Layers in TLM"	J.A. Cole, J.F. Dawson, S.J. Porter

SESSION 12:	**HYBRID TECHNIQUES FOR LARGE BODY PROBLEMS** Chair Donald Pflug, Co-Chair Robert Burkholder (Co-Organizers) **(Parallel with Sessions 10, 11, & 13)**	**Engr Auditorium**
0840	"Hybrid MoM/SBR Method to Compute Scattering from a Slot Array Antenna in a Complex Geometry"	A.D. Greenwood & J. Jin
0900	"Use of Near-Field Predictions in the Hybrid Approach"	J.L. Karty, J.M. Putnam, J.M. Roedder, & L. Yu
0920	"A Hybrid Surface Integral Equation and Partial Differential Equation Method"	J. Putnam, M. Axe D.S. Wang
0940	"Improved Hybrid Finite Element-Integral Equation Methods"	S. Bindiganavale, J. Gong, Y. Erdemli, & J. Volakis
1000	**BREAK**	
1020	"A Hybrid Approach for Simulation of Log Periodic Antennas on an Aircraft"	B.E. Gray & J.J. Kim
1040	"Duct RCS Computation Using a Hybrid Finite Element Integral Equation Approach"	Y.C. Ma, R. McClary, M. Sancer, & G. Antilla
1100	"Validation Studies of the GEMACS Computational Electromagnetics Code Using Measurement Data from the Transformable Scale Aircraft-Like Model (TSAM)"	D.R. Pflug & T.W. Blocher

SESSION 12:   HYBRID TECHNIQUES FOR LARGE BODY PROBLEMS (cont)

1120	"A Combination of Current- and Ray-Based Techniques for the Efficient Analysis of Electrically Large Scattering Problems"	U. Jakobus & F.M. Landstorfer
1140	"Field Computation for Large Dielectric Bodies by the PPP Method"	M.S. Abrishamian, N.J. McEwan, R.A. Sadeghzadeh
1200	**LUNCH**	

SESSION 13:   COMPOSITE MATERIALS   (Parallel with Sessions 10,11, & 12)   Glasgow 109
Chair Keith Whites (Organizer), Co-Chair Rodolfo E. Diaz

0840	"Application of the Analytic Theory of Materials to the Modeling of Composites in Electromagnetic Engineering"	R.E. Diaz
0900	"Scattering from Inhomogeneous Chiral Cylindrical Composites Using Axial Beltrami Fields and the Fast Multipole Method"	B. Shanker, E. Michielssen, W.C. Chew
0920	"Diaz-Fitzgerald Time Domain Method Applied to Electric and Magnetic Debye Material"	F. De Flaviis, M. Noro, R. E. Diaz, & N.G. Alexopoulos
0940	"Numerical Multipole Modelling of Bianisotropic and Complex Composite Materials"	L.R. Arnaut
1000	**BREAK**	
1020	"Experimental Confirmation of a Numerical Constitutive Parameters Extraction Methodology for Uniaxial Bianisotropic Chiral Materials"	K.W. Whites & C.Y. Chung
1040	"A Frequency Domain Dispersion and Absorption Model for Numerically Extracting the Constitutive Parameters of an Isotropic Chiral Slab from Measured Reflection and Transmission Coefficients"	M. Bingle, I.P. Theron J.H. Cloete

WEDNESDAY AFTERNOON 18 MARCH 1997

SESSION 14:   NEC AND COMPUTER CODES FOR COMPUTATIONAL ELECTROMAGNETICS   Glasgow 102
Chair Pat Foster, Co-Chair Richard Adler
(Parallel with Sessions 15, 16, 17 & 18)

1320	"IONEC: Mesh Generation and Data Entry for NEC"	S.P. Walker
1340	"Experiments with NEC3 and NEC4 - Simulation of Helicopter HF Antennas"	S.J. Kubina, C.W. Trueman, D. Gaudine
1400	"Building Models for NEC2 and NEC-BSC"	U. Lidvall
1420	"Recent Enhancements to ALDAS V3.00"	P.R. Foster
1440	"Simulation of Portable UHF Antennas in the Presence of Certain Dielectric Structures Using the Numerical Electromagnetics Code"	R.J. DeGroot, A.A. Efanov, E. Krenz, & J.P. Phillips
1500	**BREAK**	
1520	"SCATTMAT: A Mode Matching and Generalized Scattering Matrix Code for Personal Computers in a Windows Environment"	A. Liberal, C. del Rio, R. Gonzalo, & M. Sorolla
1540	"Evaluation of Near Field Electromagnetic Scattering Codes for Airborne Application"	J.M. Taylor, Jr., & A.J. Terzuoli
1600	"FASANT: Fast Computer Code for the Analysis of Antennas on Board Complex Structures"	M.P. Catedra, J. Perez, F.S. de Adana
1620	"FASPRO: Fast Computer Tool for the Analysis of Propagation in Personal Communication Network"	M.F. Catedra & J. Perez

SESSION 15:   PML: THEORETICAL AND NUMERICAL IMPLEMENTATION ISSUES   Ingersoll 122
Chair Andreas Cangellaris, Co-Chair Peter Petropoulos (Co-Organizers)
(Parallel with Sessions 14, 16, 17 & 18)

1320	"On the Construction and Analysis of Absorbing Layers in CEM"	S. Abarbanel & D. Gottlieb
1340	"The Application of PML ABCs in High-Order FD-TD Schemes	P.G. Petropoulos
1400	"Efficient Implementation of the Uniaxial PML Absorbing Media for the Finite-Difference Time-Domain Method"	S.D. Gedney
1420	"Generalization of PML to Cylindrical Geometries"	J. Maloney, M. Kesler, G. Smith
1440	"Complex Coordinate System as a Generalized Absorbing Boundary Condition"	W.C. Chew, J.M. Jin, E. Michielssen
1500	**BREAK**	

WEDNESDAY AFTERNOON 18 MARCH 1997

SESSION 15:   **PML: THEORETICAL AND NUMERICAL IMPLEMENTATION ISSUES (cont)**

1520	"Using PML in 3D FEM Formulations for Electromagnetic Field Problems"	J.-F. Lee, R. Dyczij-Edlinger, G. Peng
1540	"The Design of Maxwellian Absorbing Materials for Numerical Absorbing Boundary Conditions"	R.W. Ziolkowski
1600	"A New Artificial Medium Using Unsplit Anisotropic PML for Mesh Truncation in FDTD Analysis"	Y. Chen, M.-s Tong, M. Kuzuoglu, & R. Mittra
1620	"On the Use of PML ABC's in Spectral Time-Domain Simulations of Electromagnetic Scattering"	B. Yang, D. Gottlieb, J.S. Hesthaven
1640	"FVTD Schemes Using Conformal Hybrid Meshes and a PML Medium Technique"	F. Bonnet, J.P. Cioni L. Fezoui & F. Poupaud
1700	"PML Study of FEM Modeling of Antennas and Microwave Circuits"	Y. Botros, J. Gong, J.L. Volakis

SESSION 16:   **FAST SOLVERS FOR ELECTROMAGNETIC SCATTERING PROBLEMS**   **Engr Auditorium**
Chair Eric Michielssen (Organizer), Co-Chair Weng Chew
(Parallel with Sessions 14, 15, 17 & 18)

1320	"Least -Squares Based Far-Field Expansion in the Adaptive Integral Method (AIM)"	E. Bleszynski, M. Bleszynski, T. Jaroszewicz
1340	"Scattering of Electromagnetic Waves in Large-Scale Rough Surface Problems Based on the Sparse-Matrix Canonical-Grid Method"	K. Pak, L. Tsang, C.H. Chan, J. Johnson, & Q. Li
1400	"Planar Structures Analysis with the Adaptive Integral Method (AIM)""	S.S. Bindiganavale, H. Anastassiu, & J. Volakis
1420	"Fast Illinois Solver Code (FISC)"	J.M. Song, C.C. Lu, W.C. Chew, & S.W. Lee
1440	"A Hybrid Fast Steepest Descent - Multipole Algorithm for Analyzing 3-D Scattering from Rough Surfaces"	V. Jandhyala, E. Michielssen, W.C Chew
1500	**BREAK**	
1520	"Fast Wavelet Packet Algorithm for the CombinedField Integral Equation"	W. Golik, G. Welland, D.S. Wang
1540	"Matrix Assembly in MOM/FMM Codes"	E. Yip & Benjamin Dembart
1600	"A Near-Resonance Decoupling Approach (NRDA) for Scattering Solution of Near Resonant Structures"	C.C. Lu & W.C. Chew
1620	"Solution of Maxwell Equations Using Krylov Subspace from Inverse Powers of Stiffness Matrix"	V. Druskin, L. Knizhnerman, P. Lee

SESSION 17:   **WAVE PROPAGATION**   (Parallel with Sessions 14, 15, 16, & 18)   **Ingersoll 361**
Chair Bill Weedon

1320	"Wave Propagation on Two Dimensional Slow-Wave Structures with Square Lattice"	R.A. Speciale
1340	"Wave Propagation on Two Dimensional Slow-Wave Structures with Hexagonal Lattice"	R.A. Speciale
1400	"Wave Propagation on Two-Level Twin-Stacked-Honeycomb Structures"	R.A. Speciale
1420	"Adiabatic Modes of Curved EM Waveguides of Arbitrary Cross Section"	V.A. Baranov & A.V. Popov
1440	"Ground Conductivity Evaluation Method based on Measurements of Radio Wave Path Loss"	I. P. Zolotarev, A.V. Popov, V.P. Romanuk
1500	**BREAK**	
1520	"Two-Scale Asymptotic Description of Radar Pulse Propagation in Lossy Subsurface Medium" **STUDENT PAPER CONTEST**	V.A. Vinogradov, V.A. Baranov A.V. Popov

SESSION 18:   **EMI/EMC**   (Parallel with Sessions 14, 15, 16, & 17)   **Spanagel 117**
Chair Todd Hubing (Organizer), and Co-Chair Jim Drewniak

1320	"Modeling of EMI Emissions from Microstrip Structures with Imperfect Reference Planes"	B. Archambeault
1340	"Pre-Construction Modeling of Open Area Test Sites (OATS)"	B. Archambeault
1400	"Reducing EMI Through Shielding Enclosure Perforations Employing Lossy Material: FDTD Modeling and Experiments"	M. Li, S. Radu, J. Nuebel, J.L. Drewniak, T.H. Hubing, T.P. VanDoren
1420	"Statistical Description of Cable Current Response Inside a Leaky Enclosure"	R. Holland & R. St. John
1440	"Coupling into Non-Rectangular Cavities: Simulation and Experiments"	J.L. Drewniak, T.H. Hubing, J.v. Hagen, D. Lecointe, J.-L. Lasserre & W. Tabbara

WEDNESDAY AFTERNOON 18 MARCH 1997

SESSION 18:	**EMI/EMC (cont)**	**Spanagel 117**

1500 **BREAK**

1520 "A Simple Computational Electromagnetic Analysis Example of Electromagnetic Coupling to Pyro Circuits" — R. Perez

1540 "TRAK_RF - Simulation of Electromagnetic Fields and Particle Trajectories in High-power RF Devices" — S. Humphries, Jr. & D. Rees

THURSDAY MORNING 20 MARCH 1997

0700-0745 **CONTINENTAL BREAKFAST** — **Glasgow Courtyard**

SESSION 19: **CEM ANALYSIS: THE APPROACH OF THE FUTURE** — **Glasgow 102**
Chair Kenneth Siarkiewicz (Organizer), Co-Chair Andrew Drozd
(Parallel with Sessions 20, 21, & 22)

0840 "Application of the Research and Engineering Framework (REF) to Antenna Design at Raytheon" — B. Hantman, J. LaBelle, Y. Chang, & R. Abrams

0900 "An Algorithm for Solving Coupled Thermal and Electromagnetic Problems" — H. Sabbagh, L.W. Woo, X.Yang

0920 "Computational Electromagnetics' Future Database Architecture" — G.T. Capraro & K. Siarkiewicz

0940 "An Expert System Tool to Aid CEM Model Generation" — A. L.S. Drozd, T.W. Blocher, K.R. Siarkiewicz. V.K.C. Choo

1000 **BREAK**

1020 "Web-Based High Performance Computational Electromagnetics Servers" — D.M. Leskiw, G.S. Ingersoll, T.J. Vidoni, G.C. Fox, K. Dincer

1040 "Graphical User Interface for Computational Electromagnetic Software" — B. Joseph, A. Paboojian, S. Woolf, & E. Cohen

SESSION 20: **FDTD APPLICATIONS** **(Parallel with Sessions 19, 21, & 22)** — **Ingersoll 102**
Chair John H. Beggs (Organizer), Co-Chair Sydney Blocher

0840 "Implementation of a Two Dimensional Plane Wave FDTD Using One Dimensional FDTD on the Lattice Edges — S.C. Winton & C.M. Rappaport

0900 "Numerical Modeling of Light-Trapping in Solar Cells" — T. Marshall & M. Piket-May

0920 "Numerical Modeling of a Clock Distribution Network for a Superconducting Multichip Module" — P. Vichot, M. Piket-May, J. Mix, Z. Schoenborn, & J. Dunn

0940 "Computational Evaluation of an Optical Sensor Using the Finite Difference TimeDomain Method" — R.R. DeLyser

1000 **BREAK**

1020 "Applications of the Hybrid Dynamic-Static Finite Difference Approach on 3D-MMIC Structures" — S. Lindenmeier, P. Russer W. Heinrich

1040 "Application of FD-TD Methods to Planetary and Geological Remote Surface Sensing" — J.E. Baron, G.L. Tyler, R.A. Simpson

1100 "Incorporation of Active Devices Using Digital Networks in FDTD Method" — C.-N. Kuo & T. Itoh

1120 "FDTD Calculations of Energy Absorption in an Anatomically Realistic Model of the Human Body" — P.J Dimbylow

1200 **LUNCH**

SESSION 21: **PLANAR ANTENNAS AND CIRCUITS** **(Parallel with Sessions 10, 20, & 22)** — **Engr. Auditorium**
Chair Guy Vandenbosch (Organizer), Co-Chair Niels Fache

0840 "Planar Antennas: Overview of the Modeling Efforts in Europe" — G.A.E. Vandenbosch

0900 "Microstrip Patch Antenna Research Activities at the Technical University of Lisbon" — C. Peixeiro

0920 "A Full-Wave Electromagnetic Simulation Technology for the Analysis of Planar Circuits" — N. Fache

0940 "Analysis of Metal Patches, Strips and Corrugations Inside Cylindrical Multilayer Structures by Using G1DMULTc" — Z. Sipus, P.-S. Kildal, S. Raffaelli

1000 **BREAK**

1020 "A Numerical Algorithm G1DMULT for Computing Green's Function of Multilayer Objects" — P.-S. Kildal, M. Johansson, Z. Sipus

1040 "Fast Moment Method Algorithm for Electromagnetic Scattering by Finite Strip Array on Dielectric Slab" — B. Popovski, B. Spasenovski, J. Bartolic

XXVIII

THURSDAY MORNING 20 MARCH 1997

SESSION 21: **PLANAR ANTENNAS AND CIRCUITS** **(Parallel with Sessions 20, 21, & 23) (cont)**

1100   "Optimization of Various Printed Antennas Using Genetic Algorithm: Applications and Examples"   M. Himdi & J.P. Daniel

1120   "Characterization of Asymmetric Microstrip Transmission Lines on Multilayers with FR-4 Composite Overlay"   M. El-Shenawee & H.-Y. Lee

SESSION 22: **SCATTERING (Parallel with Sessions 19, 20, & 21)**   **Glasgow 109**
     Chair Jianming Jin, Co-Chair Atef Elsherbeni

0840   "RCS and Antenna Modeling with MOM Using Hybrid Meshes"   J. M. Putnam & J. D. Kotulski

0900   "Application of Moment Method Solutions to RCS Measurement Error Mitigation"   J. Stach

0920   "Scattering from Arbitrarily Shaped Cylindrical Objects Characteristic Modes"   G. Amendola, G. Angiulli, G. Di Massa

0940   "A High Order Solver for Problems of Scattering by Heterogeneous Bodies"   O.P. Bruno & A. Sei

1000   **BREAK**

1020   "Electromagnetic Scattering from Eccentric Cylinders at Oblique Incidence"   H.A. Yousif & A.Z. Elsherbeni

1040   "Iterative Technique for Scattering and Propagation Over Arbitrary Environments"   O.M. Conde & M.F. Catedra

1100   "A New Approach for Solving Scattering Problems in Stratified Conductive Media in Time Domain"   M. Weber & K. Reiss

1120   "Effects of Multiple Scattering in Photon Correlation Spectroscopy"   V.I. Ovod, D.W. Mackowski, D.F. Nicoli & R. Finsy

1140   "Fictitious Domain Method for Calculating the Radar Cross Section"   F. Millot & F. Collino

THURSDAY AFTERNOON 20 MARCH 1997

SESSION 23: **OPTIMIZATION TECHNIQUES FOR ELECTROMAGNETICS**   **Glasgow 102**
     Chair John Volakis (Organizer), Co-Chair Eric Michielssen
     (Parallel with Sessions 24 & 25)

1320   "Optimisation of Wire Antennas Using Genetic Algorithms and Simulated Annealing"   B. Kemp, S.J. Porter, J.F. Dawson

1340   "Automated Electromagnetic Optimization of Microwave Circuits"   J.W. Bandler, R.M. Biernacki, S.H. Chen

1400   "Design Optimization of Patch Antennas Using the Sequential Quadratic Programming Method"   Z. Li, P. Papalambros, J. Volakis

1420   "A Novel Integration of Genetic Algorithms and Method of Moments (GA/MoM) for Antenna Design"   J. M. Johnson Y. Rahmat-Samii

1440   "The Application of Novel Genetic Algorithms to Electromagnetic Problems"   D. Treyer, D.S. Weile, E. Michielssen,

1500   **BREAK**

1520   "Continuous Parameter vs. Binary Genetic Algorithms"   R.L. Haupt & S.E. Haupt

1540   "Complex Plane Array Pattern Control Using a Genetic Algorithm"   R.J. Mitchell, B. Chambers, A.P. Anderson

1600   Design, Analysis and Optimisation of Quadrifilar Helix Antennas on the European Met Op Space Craft   G.A.J. van Dooren & R. Cahill

SESSION 24: **ADVANCES IN TRANSMISSION LINE MATRIX (TLM) MODELING II**   **Ingersoll 122**
     Chair Wolfgang J.R. Hoefer (Organizer), Co-Chair Peter Russer
     (Parallel with Sessions 23 & 25)

1320   "Characteristics of the Optimization Problem for Analysis of Time Series Obtained from TLM or 2D-FDTD Homogeneous Waveguide Simulations"   U. Mueller, M.M. Rodriguez, M. Walter, & A. Beyer

1340   "Comparison of 3D TLM Meshing Techniques for Modeling Microwave Components"   J.L. Herring & W.J.R. Hoefer

1400   "A Comparison of Commercially Available Transmission Line Modeling (TLM) and Finite Element Method (FEM) 3-D Field Solvers"   F.J. German & J.A. Svigelj

1420   "Validation of Transmission Line Matrix, Finite-Integration Technique, and Finite-Difference Time-Domain Simulations of a Multi-Segment Dielectric Resonator Antenna"   N.R.S. Simons, A. Petosa, M. Cuhaci, A. Ittipiboon, R. Siushansian, J.Lo Vetri, S. Gutschling

1440   "Microstrip Antenna Characterization Using TLM and Berenger's Perfectly Matched Layers (PML)"   J.L. Dubard & D. Pompei

1500   **BREAK**

THURSDAY AFTERNOON 20 MARCH 1997

SESSION 24:   ADVANCES IN TRANSMISSION LINE MATRIX (TLM) MODELING II (cont)

1520	"Parallelization of a 3D-TLM-Algorithm on a Workstation Cluster"	C. Fuchs, P. Fischer, A.J. Schwab
1540	"A Comparison of the TLM and Finite-Difference Excitation Schemes for Diffusion-and Wave-Equations"	C. Kenny, R. Harvey, D. de Cogan
1600	"Drift-Diffusion Using Transmission Line Matrix Modelling"	A. Chakrabarti & D. de Cogan
1620	"Full Wave Characteristics of a Two Conductor Multilayer Microstrip Transmission Line .Using the Method of Lines"	M. El-Shenawee, A.Z. Elsherbeni
1640	"Sources of Error within Lattice Gas Automata Simulation of Electromagnetic Field Problems"	N. Simons, G. Bridges, D. Cule, M. Zhang, & M. Cuhaci

SESSION 25:   PLANAR AND CONFORMAL ANTENNAS AND CIRCUITS)   **Engr Auditorium**
                  Chair Giuseppe Vecchi (Organizer)
                  (Parallel with Sessions 23 & 24

1320	"Transmission Line Approach for the Study of Planar Periodic Structures"	R. Orta, P. Savi, R. Tascone, R. Zich
1340	"Analysis of Arrays of Elements over Surfaces which can be Conformed to a Body of Revolution"	S. Piedra, J. Basterrechea, M.F. Catedra
1400	"Computational Aspects of Finite and Curved Frequency Selective Surfaces"	J. Vardaxoglou
1420	"Computationally Efficient MoM and Its Applications"	L. Alatan, N. Kinayman, M.I. Aksun, K. Leblebicioglu, M.T. Birand
1440	"Analysis and Synthesis of Conformal Microstrip Antennas with a Fast and Accurate Algorithm Using New Symbolic Objects"	J.-P Damiano, J.-M. Ribero, M. Scotto
1500	**BREAK**	
1520	"Space/Time Adaptive Meshing Using the Multiresolution Time Domain Method (MRTD)"	E.I Tentzeris, A. Cangellaris, L.P.B. Katehi
1540	"Static Extraction, "Static" Basis Functions and Regularization in the Analysis of Printed Antennas"	G. Vecchi, P. Pirinoli, L. Matekovits, & M. Orefice
1600	"Wavelet-Based Modeling of Wired Antennas and Scatterers"	K.F. Sabet & L.P.B. Katehi, K. Sarabandi

FRIDAY MORNING 21 MARCH 1997

0830-1630	**SHORT COURSE (FULL-DAY)** "Finite Difference Time Domain Modeling and Applications" Stephen Gedney, University of Kentucky and James Maloney, Georgia Tech Res. Institute	**Glasgow 102**
0830-1630	**SHORT COURSE (FULL-DAY)** "Introduction to Radar via Physical Wavelets", Gerald Kaiser, U Mass-Lowell	**Ingersoll 122**
0830-1630	**SHORT COURSE (FULL-DAY)** "Mathematical Software for Computational Electromagnetics", Jovan Lebaric, Naval Postgraduate School	**Spanagel 419**
0830-1200	**SHORT COURSE (HALF-DAY)** "Radiation Physics", Edmund K. Miller	**Engr. Auditorium**

FRIDAY AFTERNOON

1300-1630	**SHORT COURSE (HALF-DAY)** "Introduction to FEKO: A Hybrid Method of Moments/Physical Optics (MoM/PO) Code" J.F.C. Meyer, EM Software	**Engr. Auditorium**

SESSION 1:

VISUALIZATION

Chair: Janice L. Karty

VISUALIZATION: A POWERFUL TOOL FOR UNDERSTANDING ELECTROMAGNETICS

E. K. Miller
3225 Calle Celestial, Santa Fe, NM 87501-9613
505-820-7371, emiller@esa.lanl.gov

0.0 ABSTRACT
Computer-based visualization has grown remarkably in capability since the first pen and carriage plotters made an appearance in the early 1960s. Scientific visualization has come to be an accepted and expected accompaniment for analysis, measurement and computation, and has even made possible new fields of research. Indeed, such topics as fractals and chaos theory could hardly have been developed without the possibility of displaying visual images of what their abstract mathematical descriptions actually represent. Few other physics and engineering disciplines share with electromagnetics (EM) the combination of a complex mathematical foundation that describes physical phenomena that are for the most part nonvisible. Both of these aspects of EM, its complex mathematics and physical non visibility, make computer-based visualization an especially powerful and useful tool for a variety of applications.

The use of visualization in EM, or visual electromagnetics (VEM), serves at least two distinct applications purposes: 1) to display a problem's physical characteristics, and its corresponding numerical representation or model; and 2) to display EM quantities associated with that model. In either case, the resulting visual display provides a more understandable and interpretable way for the user to access the underlying numerical data, vastly increasing the "bandwidth" of that interaction. VEM can also be a great value in the development of computer models such as NEC, FDTD and the like. Most uses of VEM deal with 2) since there is infinitely more variability provided by responses obtained as a function of frequency or time, etc. than the static physical model on which such responses are based. Nevertheless, 1) is of comparable importance, since unless a valid problem representation begins the process, subsequent responses obtained therefrom will hardly be useful. VEM can also be invaluable in code development, a use that may be transparent to most modelers, but which is also illustrated below. Examples from these various perspectives are included here, emphasizing the benefits of visualization from the viewpoint of its practical utility in identifying numerical errors and improving physical understanding.

1.0 INTRODUCTION
"I understand what an equation means if I have a way of figuring out the characteristics of its solution without actually solving it," is attributed to P. A. M. Dirac (of the Dirac delta function). Einstein is said to have visualized the effects of relativity theory before he actually developed the mathematics to describe it. Both would certainly have been fascinated with what computers and computer visualization are now contributing to the solution process. Computers are revolutionizing how we: (1) think about, (2) formulate, (3) solve, and (4) interpret problems in all of science and engineering. This is especially true of electromagnetics because of its abstract mathematical nature and the general "non visibility" of most electromagnetic phenomena to human senses. Graphics is not new, of course, but the computer is providing unprecedented capabilities to:

> Create and acquire modeling and measurement data;
> Manipulate, process and transform that data;
> Present and display that data using static and dynamic formats.

To regard the computer as just a fast calculating machine really misses the point. Just as the internal combustion engine made possible faster travel over land, it also soon led to the new dimension of con-

trolled travel through the air. That was a revolution for transportation no more profound than that for the intellect made possible by the computer and computer visualization..

However, to be really useful, our use of visual electromagnetics (VEM) must not become so preoccupied with the "pretty-picture" novelty of being able to produce color graphics and movies that we fail to productively exploit the benefits that VEM can provide. In other words, the medium is not the message, and while color, sound and motion can be invaluable in discovering hidden facets of electromagnetic physics, their inappropriate use might obscure important phenomena or otherwise mislead the observer about what is being graphically displayed. The goal of achieving better solutions and improved understanding of electromagnetic physics should be foremost in the practice of VEM.

2.0 USING VEM IN CODE DEVELOPMENT

VEM has been found invaluable over the years in the development of NEC, for which two examples are included here, both of which deal with the Sommerfeld integrals that arise when modeling objects located near a planar interface. As anyone who has encountered the Sommerfeld integrals has discovered, their numerical evaluation is non-trivial, even when supercomputers are available. An approach that was found invaluable in the early stages of NEC development was motivated by a dawning recognition that the fields these integrals describe are much less complex than the mathematically complicated integrals that describe them make it appear. This recognition originated from developing some plots of the spatial variation of the Sommerfeld fields, an example of which is shown in Fig. 1. It can be seen that the fields vary relatively smoothly, showing not only the field's spatial simplicity but suggesting the possibility of modeling them using curve-fitting techniques This was done initially using low-order polynomials [Miller et al. (1977)], but was later generalized to the current NEC treatment that uses model-based parameter estimation [Burke et al. (1981)].
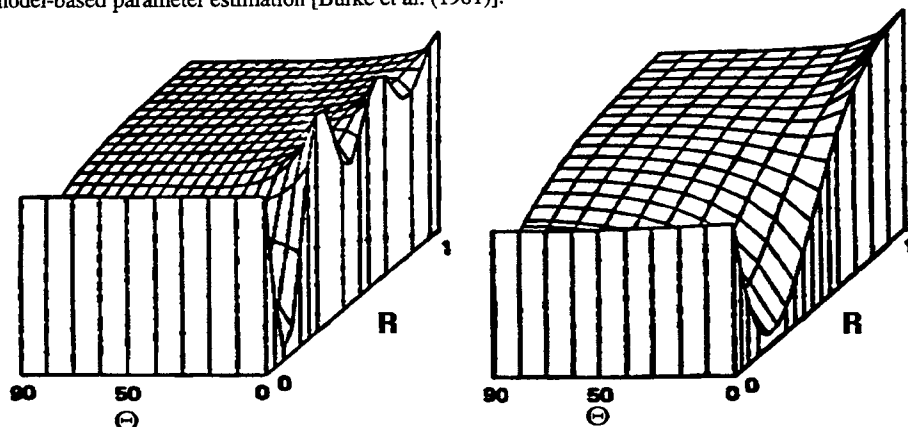
Figure 1. A typical result for the field near an interface [Burke et al. (1981)]. The source in this case is a horizontal electric Hertzian element above a half space of relative dielectric constant equal to 4 and zero conductivity (left), and 16 and 0.001 mhos/m (right). Distance $R = (\sqrt{r^2 + (z + z')^2}$, elevation angle $\Theta = \tan^{-1}[(z + z')/r]$, with observation and source elevations above the interface indicated by primed and unprimed coordinates, respectively, and r the radial distance between them. These fields are smooth enough to be accurately approximated by simple interpolation functions, thus circumventing the need to compute Sommerfeld integrals when filling a NEC impedance matrix. The surface wave that exists along the interface for the zero-conductivity case is seen to disappear when loss is introduced.

Also very early in NEC development, we decided to examine the impedance matrices generated by an electric-field, integral-equation (EFIE) model by plotting them graphically. At the time, computer graphics was in its infancy, and so we made printouts on standard 15-inch-wide, tractor-feed paper whose entries were the numerical values of the matrix-coefficients exponents printed in a regular grid.

3

Even for a small structure, this required about a 8 x 8 foot square of paper, which was displayed by tacking paper from floor to ceiling and several strips wide along a wall. Although these were crude "plots," patterns could be seen but little resolution was discernible. Many years later, we revisited this exercise, but with the new hardware and software that had become available, much better results were obtained, examples of which may be seen in Miller (1995). An unanticipated benefit of making such plots is demonstrated in Fig. 2, where the impedance matrix for a wire near an interface is shown [Burke (1985)]. A problem in the Sommerfeld-integral evaluation can be seen as a noise-like pattern in part of this matrix, at a level several orders of magnitude below the peak. It is extremely unlikely that this effect would have been discovered had a visual display of the matrix not been generated.
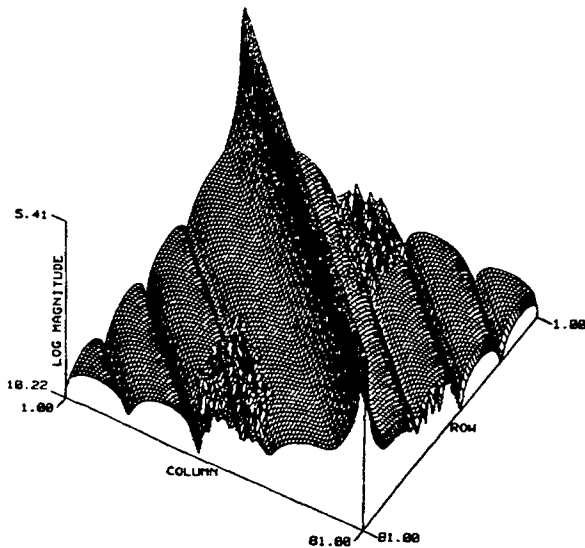
Figure 2. A surface plot of the NEC impedance matrix for a wire located near a half space [Burke (1985)]. The effect of a numerical problem in evaluating the Sommerfeld fields causes the "noise" seen in part of the matrix.

3.0 USING VEM FOR CODE VALIDATION

The potential uses of VEM in the actual process of modeling are virtually unlimited. Current and charge, near and far fields, shown as a function of time, frequency, angle and space, and in contour, surface, density and vector plots are a few of the possibilities. Two quite different applications, but by no means the only ones, are for validation purposes and displaying the physics of EM fields in different ways as shown here and in the next section.

An example of the former is given in Fig. 3, where a comparison is made of two models for the Poynting's vector of the fields propagating in a waveguide excited by a plane wave incident at an angle of 30 deg from the waveguide axis [Ling et al. (1987)]. Although a numerical measure of their difference might provide a more quantitative indication of the ray model's accuracy relative to a rigorous solution, a visual comparison like this can highlight limitations the approximate simplified approach.

4.0 USING VEM FOR ILLUSTRATING BASIC PHYSICS

An example of using VEM to illustrate EM physics is shown in Fig. 4, where far-field, space-time contour plots are shown for a Gaussian-pulse- and time-harmonically-excited, center-fed dipole antenna [Miller et al. (1981)]. For the former, the field contours are seen to be centered on the feed point (the outer circle) and the ends, demonstrating that the far-field radiation originates from these two points. Were a longer time window to be used, there would be a succession of nested radiation circles centered on the ends as the current-charge pulses propagation back-and-forth along the dipole. The time-harmonic case, by contrast, exhibits no clear-cut source of radiation, although we know that its radiation also is dominated by end and, depending on its length, center contributions.

Space-time contour plots of the current excited by a Gaussian voltage source at the center of a straight dipole and a conical spiral, both 1-m in length, are presented in Fig. 5 [Miller and Landt (1980)]. The dispersivity caused by the curvature of the spiral is readily apparent when compared with the result obtained for the dipole. A "data image" representation of the scattered field from a long, metal rod is

shown in Fig. 6, as a different way to more effectively display a large volume of scattering data. Such data images might provide an alternative to range-profile displays as a way to visualize a target

(a)

(b)
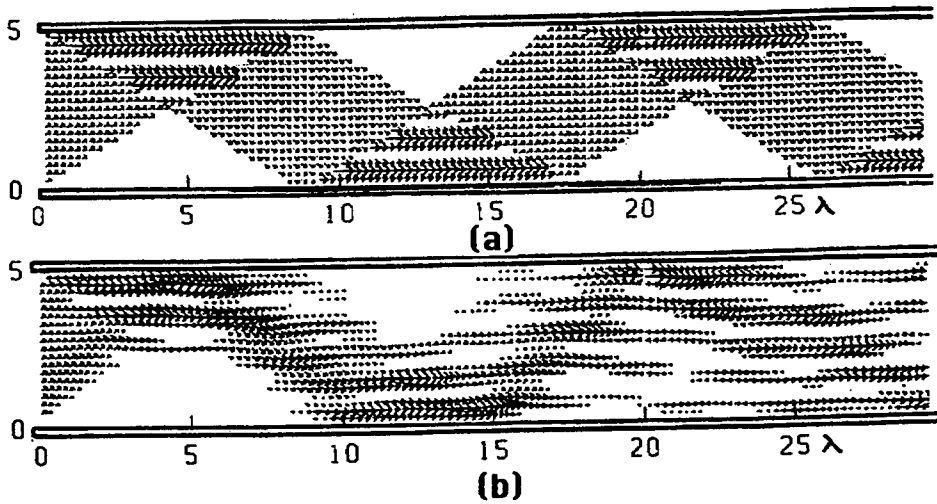
Figure 3. Graphical comparison of the time-average Poynting's vector as a function of length in a waveguide as obtained from a ray-optics representation (a) and a rigorous solution (b) [Ling et al. (1987)]. A visual comparison of the two results provides a semi-quantitative indication of how valid the ray approximation is for a guide only five wavelengths wide.
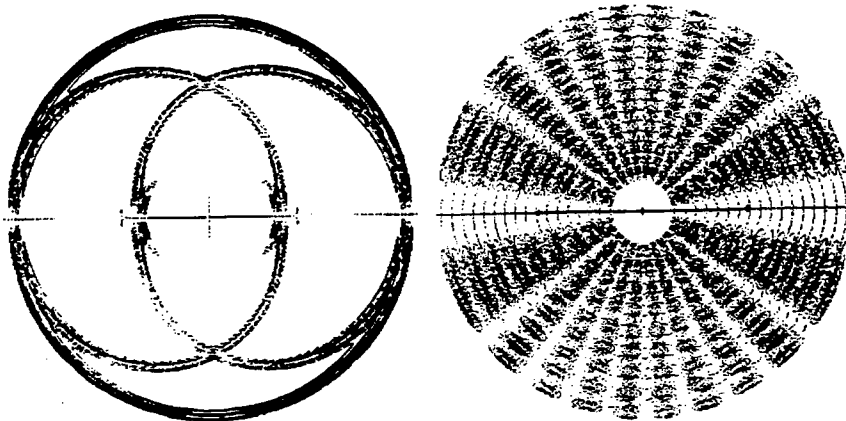
Figure 4. Far-field space-time contour plots for a Gaussian-pulse excitation (left) and for time-harmonic excitation (right) of a center-fed dipole [Miller et al. (1981)]. For pulse excitation, the dipole is about 10 times as long as the space width of the Gaussian pulse, while for the time-harmonic case, the wire is 10 wavelengths long. In each case, the time delay to the far field is removed, and the dipole lengths are to scale. It's clear in the pulse-excited case that the radiation comes form the center and ends of the dipole while this is not at all clear for the time-harmonic case.

The result of Fig. 7 was developed to determine whether a current wave propagating on a wire grid exhibits any directional anisotropy in propagation speed. A vertical, wire monocone, located at the grid's

center, was excited with a Gaussian voltage pulse and the combination modeled using the TWTD (Thin-Wire Time Domain) code [Miller et al. (1981)]. Contours of constant values of peak current times radial distance (to remove the spreading effect) are plotted at successive time steps. This result indicates that that the propagation speed is not direction-dependent.
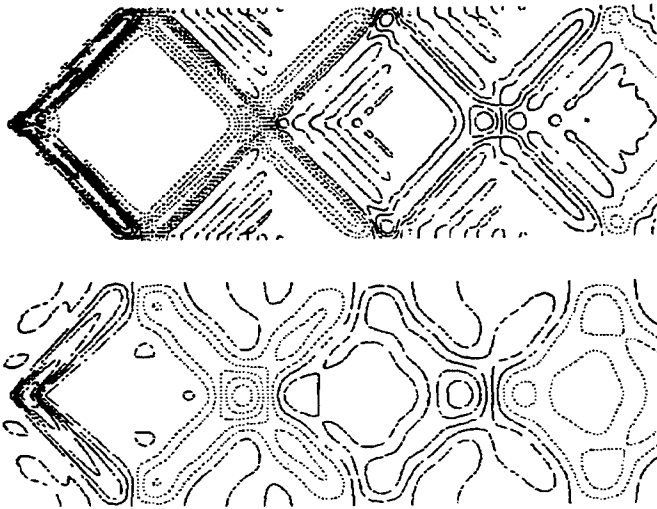
Figure 5. Space-time contour plots of the current excited by a Gaussian pulse at the center of a straight wire (top) and a conical spiral (bottom) where both wires have the same length [adapted from Miller and Landt (1980)]. The pulse propagating on the straight wire exhibits relatively little dispersion compared with the spiral, where it widens and decays in amplitude with distance.

In Fig. 8 is shown the time-average Poynting's vector for a current source located near a penetrable half space. Even though quite near the interface, the power flow close to, and on either side of it are in close accord with Snell's Law, a possibly unexpected result.

Figure 6. A frequency, aspect-angle contour plot (or "data image") of the radar cross section of a long, metal rod as obtained from a FDTD computer model [Trueman et al. (1992), Trueman (1992)]. This kind of data presentation provides an "image" different from the usual range-profile images, yet contains all the available scattering information over the frequency range covered in the plot. Such plots could be useful in developing quantitative measures for a "similarity/dissimilarity" index of targets for which a radar is intended to provide a discrimination or recognition capability.

Look angle [degrees]
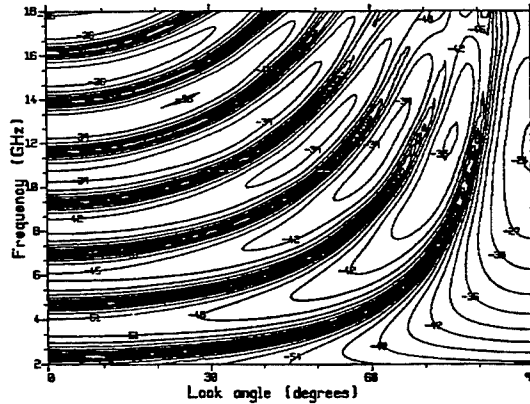
5.0 CONCLUDING REMARKS

It should be self-evident that Visual ElectroMagnetics (VEM) represents a tool essential for electromagnetics, in general, and for computational electromagnetics, in particular. The amount of data that can be generated by present-day models and computers, as well as measurements, to say nothing of future expectations in this regard, can be overwhelming. Were it not for the possibility of examining such data visually, as opposed to tabular numerics, it's likely that many important features of the results would be missed. However, it's important to emphasize that the beguiling attraction of simply developing eye-catching visual displays must not displace the greater value of VEM for helping to validate CEM models and their results while also providing access to the physical phenomena being displayed.

6
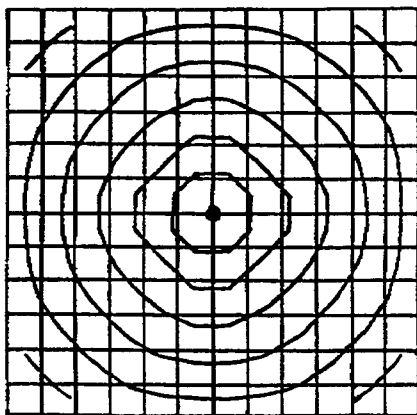
Figure 7. Contours of constant values of peak current times radial distance at successive time steps for a wire grid excited by a wire monocone antenna at the grid's center [Miller et al. (1981)]. These results indicate that a short distance from the source, the current propagates at an angle-independent speed.
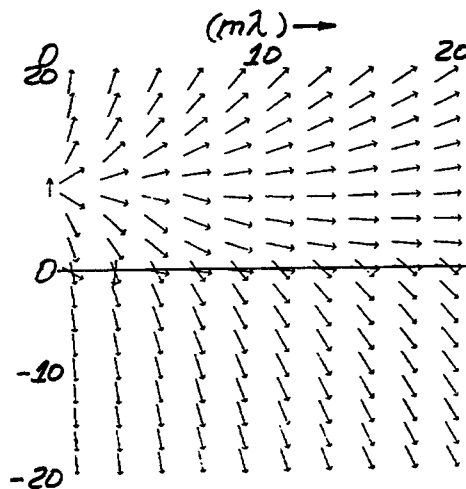
Figure 8. Time average Poynting's-vector plots for a vertical, electric Hertzian dipole located 0.0875 wavelengths above a halfspace (vertical arrow) having a relative dielectric constant of 9 at a frequency of 3 MHz [Lytle et al. (1976)]. Near the interface, shown by the horizontal line, the vectors refract downwards toward the vertical axis, as would be expected, although their respective angles don't precisely satisfy Snell's Law which is rigorously applicable to plane waves only.

REFERENCES

Burke, G. J. (1985), Private Communication.

Burke, G. J., E. K. Miller, J. N. Brittingham, D. L. Lager, R. J. Lytle (1981), "Computer Modeling of Antennas Near the Ground", *Electromagnetics*, **1**, pp. 29-49.

Business Week, December 23, 1996, Cover Story, "Video Game--Surprise! This Product Might Actually Help Your Children Learn.

Ling, H., R. Chou and S. W. Lee (1987), "Rays Versus Modes: Pictorial Display of Energy Flow in an Open-Ended Waveguide," *IEEE Trans. Antennas Propagat.*, **AP-35**, pp. 605-607.

Lytle, R. J., D. L. Lager and E. K. Miller (1976), "Poynting-Vector Behavior in Lossy Media and Near a Half Space", *Radio Science*, **11**, pp. 875-883.

Miller, E. K., J. N. Brittingham, and J. T. Okada (1977), "Bivariate- Interpolation Approach for Efficiently and Accurately Modeling Antennas Near a Half Space", *Electronics Letters*, **13**, pp. 690-69

Miller, E. K. and J. A. Landt (1980), "Direct Time-Domain Techniques for Transient Radiation and Scattering from Wires", Invited Paper in *Proceedings of the IEEE*, **68**, pp. 1396-1423.1.

Miller, E. K., F. J. Deadrick, G. J. Burke and J. A. Landt (1981), "Computer-Graphics Applications in Electromagnetic Computer Modeling, *Electromagnetics*, **1**, pp. 135-153.

E. K. Miller (1995), "Model-Based Parameter Estimation in Electromagnetics: III--Applications to EM Integral Equations, "Applied Computational Electromagnetics Society Journal, 10 (3), pp. 9-29.

Trueman, C. W. (1992), Private Communication.

Trueman, C. W., S. J. Kubina, R. J. Luebbers, K. S. Kunz, S. R. Mishra and C. Larose (1992), "RCS of Cubes, Strips, Rods and Cylinders by FDTD," in 8th Annual Review of Progress in Applied Computational Electromagnetics, Naval Postgraduate School, Monterey, CA, pp. 487-494.

Computational Diagnostic Techniques for Electromagnetic Scattering: Analytical Imaging, Near Fields, and Surface Currents

Kam W. Hom, Noel A. Talcott, Jr.
NASA Langley Research Center
Hampton, Virginia 23665

John Shaeffer
Marietta Scientific, Inc.
376 Powder Springs St., Suite 240A
Marietta, Georgia 30064
(770) 425-9760

ABSTRACT

This paper presents three techniques and the graphics implementations which can be used as diagnostic aides in the design and understanding of scattering structures: Imaging, near fields, and surface current displays. The imaging analysis is a new bistatic k space approach which has potential for much greater information than standard experimental approaches. The near field and current analysis are implementations of standard theory while the diagnostic graphics displays are implementations exploiting recent computer engineering work station graphics libraries.

INTRODUCTION

The goals and motivation of this work are to provide insight and guidance into the design of scattering structures. Analytical/computer codes have historically been conceived only to provide predictions of experimentally measured quantities, i.e., backscatter RCS versus angle. In principle, an analytical code should be able to provide a much greater insight into the scattering process if we just ask the proper questions. Our inspiration is similar to efforts in computational fluid dynamics where we are attempting to better understand the interaction of an EM wave with a structure, the nature of the scattering process, and ultimately better design.

BISTATIC IMAGE ANALYSIS USING k SPACE CONCEPTS

The experimental development of microwave images has been a powerful tool to understand scattering from various geometries. Imaging may be in one dimension, i.e., down range; or in two dimensions, i.e., down and cross range. This capability allows one to understand the scattering process in

terms of specific scattering centers and mechanisms. Image development has been mostly experimental. While one could apply the same methods to predictive scattering algorithms, the computation burden has always been considered to great. This occurs because, experimentally, down range information is obtained by illuminating the target over a bandwidth of frequencies typically numbering 16, 32, 64, 128 or even 512. To do this with a method of moments analysis, one would have to recompute and solve the system matrix for each frequency. This computation burden is so great that the swept frequency approach is seldom pursued analytically.

B. A. Cooper developed a new approach that requires only one computation of induced currents and therefore only one MOM matrix computation for down range images. A formal bistatic k space image theory was then developed, reference 1. This formulation is not limited by the small angle focus requirement. Cross range images are computed without smearing. The bistatic k space analytical image technique does not require a MOM code matrix solution for each frequency. Only one current distribution (matrix computation) is computed at the frequency of interest. The image is the Fourier transform of the k space bistatic scattered radiation for values of $\mathbf{k}^{scat}$ that correspond to downrange and cross range. The natural Fourier transform variables are wave number $\mathbf{k}$ and spatial position $\mathbf{R}$. If we compute a bistatic field as a function of $\mathbf{k}^{scat} = (k^{downrange}, k^{cross\ range})$ then the Fourier transform of the scattered field is naturally a function of the transformed spatial coordinates, $\mathbf{R}^{scat} = (R^{downrange}, R^{cross\ range})$. The computation of the scattered field in k space is a generalization of the standard bistatic radiation integral. The difference is that E^{scat} is computed in term of $\mathbf{k}^{scat}$ for down and/or down/cross range rather than in terms of the usual bistatic angles (θ, ϕ). Body currents are computed only once at the user specified incident angle and polarization.

Bistatic k space image technique features are: 1) Resolution up to $\lambda/2$ unlimited by the usual experimental frequency and angle extent bandwidth concerns; 2) Image focus / smear does not occur due to the formulation of the approach; 3) Images computed at the frequency and angle of body excitation. The body currents are computed only for this $\mathbf{k}^{inc}$. In contrast to the experimental approach, the currents do not change with changes in the bistatic $\mathbf{k}^{scat}$ vector sweep; 4) One, two, or three dimensional images may be obtained. The limiting feature for obtaining 3D images is the display of the solution since multidimensional FFT algorithms are available; 5) The scattering body is imaged in a bistatic sense from the same direction as the excitation, i.e., a backscatter image. However, a more general bistatic approach is entirely possible since the center of $\mathbf{k}^{scat}$ is not required to be the negative of $\mathbf{k}^{inc}$; and 6) A co or cross polarized image may be computed.

This list shows that *the bistatic analytical approach to imaging can potentially yield substantially more information than experimental images. The bistatic image approach can be applied to any predictive algorithm for electromagnetic scattering or antenna radiation, e.g., Physical Optics or Method of Moments.*

Briefly, the theory for this analytical imaging technique can be developed as follows. A current distribution is computed for a given angle of excitation and polarization. A scattered field is computed using the far field radiation integral as a function of down and cross range bistatic k directions,

$$E^{\alpha,\beta}(\bar{k}^{inc},\bar{k}^{scat}) = \int \{ \hat{n}^{\alpha} \bullet \bar{J}^{\beta}(\bar{k}^{inc}) \} e^{j\bar{k}^{scat} \bullet \bar{R}} \, dS \qquad\qquad 1$$

where α and β are the polarization of the scattered and incident field, $\mathbf{k}^{inc}$ is the direction of the incident excitation, and $\mathbf{k}^{scat}$ is the k space direction for the scattered field. This equation is the usual radiation integral as written before specifying $\mathbf{k}^{scat}$ as a function of look angle (θ,ϕ). We compute E as a function of $\mathbf{k}^{scat} = \mathbf{k}^{downrange} + \mathbf{k}^{crossrange}$. The downrange k is centered on the free space absolute value of $\mathbf{k}^{inc}$

$$k_r = \frac{2\pi}{\lambda_0} \pm \Delta k \qquad\qquad 2$$

The Fourier transform of this E field, computed in down and cross range k space, is our desired image,

$$E^{\alpha,\beta}(r_{down}, r_{cross}) = \int \left\{ \int W(\bar{k}^s) \, E^{\alpha,\beta}(\bar{k}^{inc}, \bar{k}^{scat}) \, e^{j\bar{k}_{down} \bullet \bar{R}} \, dk_{down}^{scat} \right\} e^{j\bar{k}_{cross} \bullet \bar{R}} \, dk_{cross}^{scat}$$

$$3$$

where W is a weight function and the square magnitude of E is our down/cross range image. It is noted that the computational cost of this process is *cheap* compared to the effort in a MOM code to compute **J**.

NEAR FIELDS and CURRENTS

The computation of near fields must resort back to the fundamental definition for fields rather than the simpler far field expression. The currents **J** are, of course, computed by a MOM code as part of the solution. The near fields are specified in terms of the vector and scalar potentials in terms of the current distribution:

$$\bar{E}^{scat}(\bar{r}_f) = -jk\eta \int \left\{ \bar{J} - (\nabla_s \cdot \bar{J})(1 + jkR)(\bar{r}_f - \bar{r}_s) / (kR)^2 \right\} g \, dS$$

$$4$$

where the integral is over the source currents and g is the Greens' function.

The currents **J** and fields **E** are time varying vector quantities. We may choose to display the two time quadrature values, the real and imaginary parts, which correspond to 0 and -90 degrees phase, or to display the time animation of these vectors as

$$\bar{E}(\bar{r}, \omega t) = \Re\{\bar{E}(\bar{r})\}\cos(\omega t) - \Im\{\bar{E}(\bar{r})\}\sin(\omega t) \qquad\qquad 5$$

by letting ωt vary from 0 to 2π, or to compute a time average root mean square

$$E_{rms} = \frac{(\vec{E} \cdot \vec{E}^*)^{1/2}}{\sqrt{2}} \qquad\qquad 6$$

For the E field quantities, we can display the scattered field, or the total field (sum of incident plus scattered), or just the incident field (not very interesting).

DIAGNOSTIC GRAPHICS DISPLAYS

Continued development of very fast engineering workstations has enabled the everyday use of graphics to visually display the EM vector and scalar quantities for fields, currents, and images. Visual display of the data includes color coded contour maps of the surface current magnitudes and the total and scattered electric field magnitudes for both RMS averages and time harmonic animation. The current and electric field vectors can be overlaid on this mapping or displayed separately to show field orientation and direction. The graphics program presently is capable of displaying and animating up to 50 planar cuts of a 100 x 100 field point matrix either simultaneously or individually. In addition, the program can display the triangle element mesh (up to 10,000 elements) which contains the surface current information. FORTRAN graphics routines have been developed for Silicon Graphics series workstations.

EXAMPLE

The techniques described herein have been incorporated into the MOM code of reference 2 which was used for the 3λ aircraft like geometry shown in Figure 1. The traditional backscatter computation is shown in Figure 2 for horizontal and vertical polarization.

Bistatic k-space images for the scattering centers when viewed nose on is shown in Figure 3 for both polarization's. Scattering centers at this angle are the engine pods, wing roots, and leading and trailing edges.

Surface currents for nose on horizontal polarization illumination is shown in Figure 4. The high current regions are the sides of the fuselage, the leading edges of the wing and horizontal fin, and the wing root region.

Near total electric fields about the target is shown in Figure 5 for nose on horizontal polarization illumination.

WHAT WE CAN LEARN

Imaging yields great insight into the scattering mechanism process, i.e., specular scattering, end region contribution, leading and trailing edge diffraction, traveling wave, creeping wave, edge wave scattering, etc. This new technique allows us to utilize imaging with computational MOM codes with little additional computational cost. In addition, we have the potential to do three dimensional images, bistatic imaging, and cross polarized imaging (even for circular polarization). Resolutions approaching $\lambda/2$ are possible. In fact, early efforts used resolutions less than $\lambda/2$ so that images of the MOM code basis functions were observed. Because the analytical approach is different from the swept frequency experimental approach, we have seen some differences in images, particularly for traveling wave scattering mechanisms where this new approach shows radiation as emanating from an extended region over which a reflected surface wave is propagating.

Current display diagnostics allow us to highlight regions of high and low current flow over a body. Low current regions could then be noted for possible addition of secondary structures such as vents, doors, or avionics sensors such that they would have minimum impact on scattering. In addition, one could gauge the design success of resistive treatments along edges and at tips by examining residual current levels and the taper function.

Near field plots have potential to examine the over all influence of the body structure on the field incident on secondary structures such as inlets and exhaust cavities. Since the main body influences the field, the polarization incident on secondary structure may not be that of the incident free space illumination.

As with any set of new tools, we do not fully know the potential benefit of all that is now possible. Clearly, images are of great value. Current and field knowledge help in our understanding of the scattering mechanisms, but we may have to be creative in how we use these diagnostics to exploit their full potential.

REFERENCES

1. J. F. Shaeffer, Kam W. Hom, R. Craig Baucke, Brett A. Cooper, and Noel A. Talcott, Jr., "Bistatic k-Space Imaging for Electromagnetic Prediction Codes for Scattering and Antennas," NASA Technical Paper 3569, July 1996.

2. J. F. Shaeffer, "MOM3D Method of Moments Code Theory Manual," NASA CR-189594, NAS1-18603, March 1992.

12

Figure 1 - Three wavelength aircraft geometry.

Horizontal Polarization

Vertical Polarization
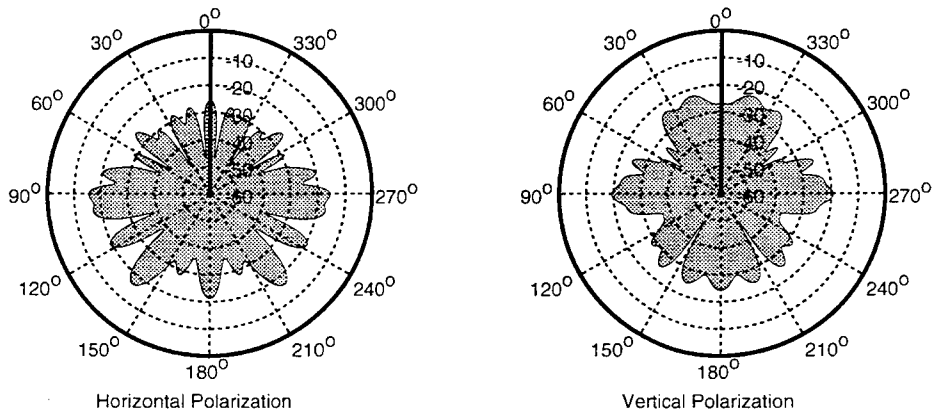
Figure 2 - Backscatter RCS plots of three wavelength aircraft geometry, horizontal and vertical polariztion, 0° elevation.

Horizontal Polarization

Vertical Polarization
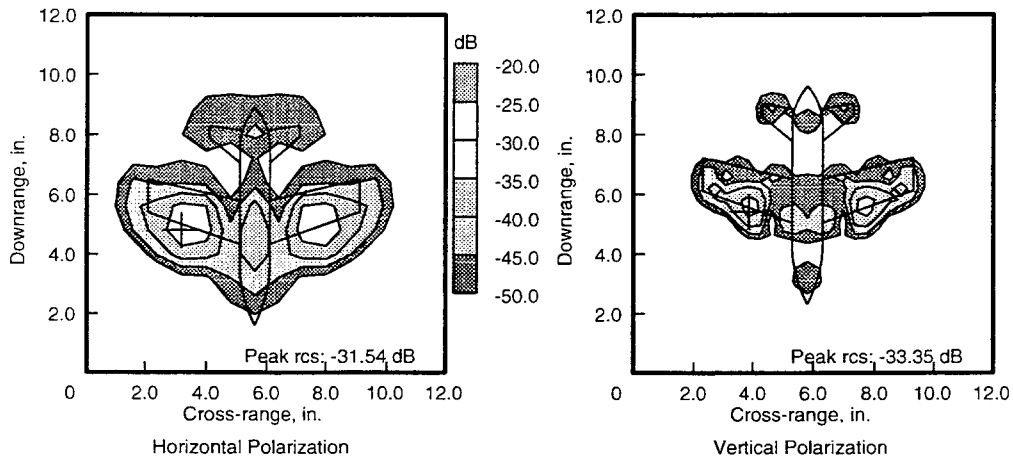
Figure 3 - Bistatic images of three wavelength aircraft geometry, horizontal and vertical polarization, 0° elevation, 0° azimuth.

13
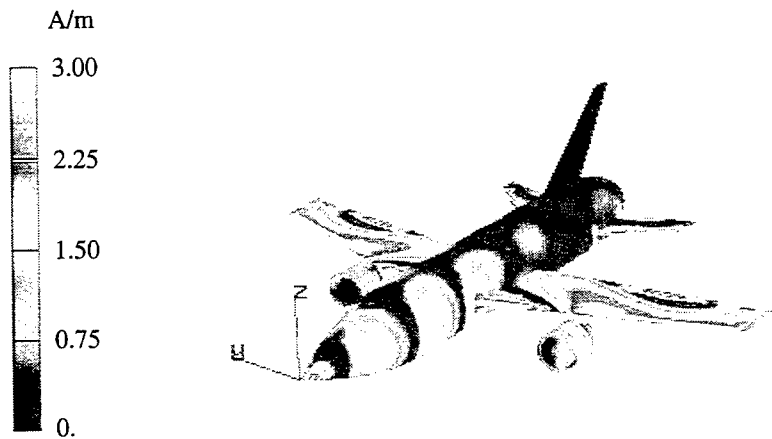
Figure 4 – Surface currents on three wavelength aircraft geometry, horizontal polarization, 0° elevation, 0° azimuth.
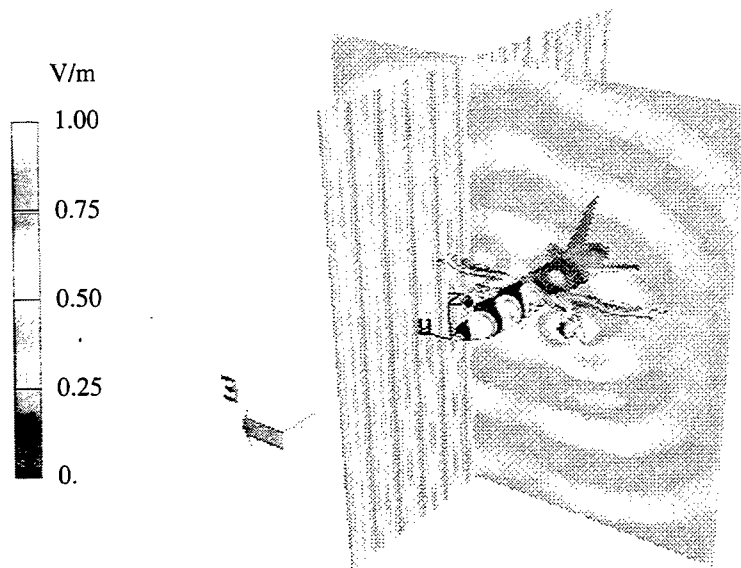
Figure 5 – Total electric field about three wavelength aircraft geometry, horizontal polarization, 0° elevation, 0° azimuth.

14

INTERFEROMETRIC 3D IMAGING
C. A. Au
McDonnell Douglas Corporation
P.O. Box 516
Mail Code S0642263
St. Louis, MO 63166

1. Introduction

Radar cross section (RCS) measurements can be displayed in three dimensions (3D) to allow more faithful visualization of the scattering mechanisms of targets. Additionally, visualization along the vertical dimension may provide a means to gate out undesired effects such as scattering from the target support structure.

RCS data is most commonly acquired using Inverse Synthetic Aperture Radar (ISAR) techniques. ISAR measurements require finely sampled data along the frequency and azimuth axis to compute the down range and cross range location of scatterers. Traditional methods of computing 3D images extend the 2D ISAR process by finely sampling along a third elevation axis. Such measurements yield high resolution 3D RCS images. Unfortunately, the acquisition time and memory required to collect 3D ISAR data can be prohibitively large. This is especially true when measuring aircraft-sized targets. For example, the time and memory required to collect 3D ISAR data can easily exceed by 50 times, that required for 2D images.

Ohio State University (OSU) has demonstrated a novel approach to 3D imaging of RCS data [1]. The technique "interferometric" imaging provides an efficient means to visualize the scattering from a complex target in 3D. Unlike 3D ISAR measurements, interferometric imaging requires only two images measured at slightly different elevation angles. By comparing the down range change of an image measured at a different elevation angle, the vertical location of each scatterer can be computed. This approach is analogous to the way the brain transforms information from the left and right eye to perceive depth. Information about the displacement or binocular disparity of the eye required to focus on objects at differing distances is processed by the nerve cells in the visual cortex to give an impression of distance [2].

McDonnell Douglas Corporation (MDC) has extended OSU's interferometric imaging technique to handle more general non-point scattering mechanisms. By processing the images as a series of cross range slices, we are able, for example, to map the vertical locations of leading and trailing edge scatterers.

2. Basic Principle

Changes to the measurement elevation angle will result in only changes to the down range location of each scatterer in an image. Furthermore, the amount of this down range displacement is a function of the vertical height of the scatterer. There should be no cross range displacement between elevation angle changes. This assumes that there is no multibounce scattering mechanism present. This concept is illustrated in Figure 1.
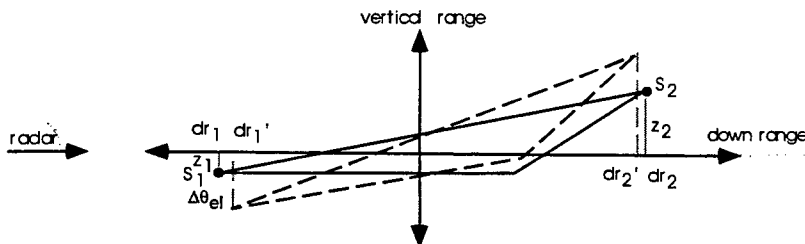
Figure 1. Down range Displacement of Scatterers at Differing Elevation Angles

In Figure 1 is shown a dart target similar in shape to one we measure. As the elevation angle of the dart rotates counterclockwise, the nose tip scatterer S_1 moves farther from the radar. In contrast, the rear tip scatterer S_2 moves closer to the radar. The amount of this down range change is a function of the height and down range location of the scatterer. By accurately measuring this change, we can compute the scatterers vertical location. For the setup shown in Figure 1, the height of each scatterer z_i can be computed using the geometrically derived equation:

$$z_i = \frac{\Delta dr_i - dr_i * \sin^2(\Delta\theta_{el})}{\sin(\Delta\theta_{el})}$$

(Eq. 1)

$$\text{where } \Delta dr_i = dr_i - dr_i{}^{'}.$$

The expression $\Delta\theta_{el}$ is equal to the change in elevation angle between measurements.

3. Registration of Scatterers Between Images

The most difficult part of interferometric imaging is the "registration" or identification of which scatterer in the "reference" image corresponds to a scatterer in a "matching" image. By viewing a 2D image as a series of cross range slices (Figure 2), what appears to be a 2D registration process can be simplified into a 1D problem. Since the changes between the images measured at different elevation angles is strictly along the down range axis, we can dramatically simplify the registration of the two images.
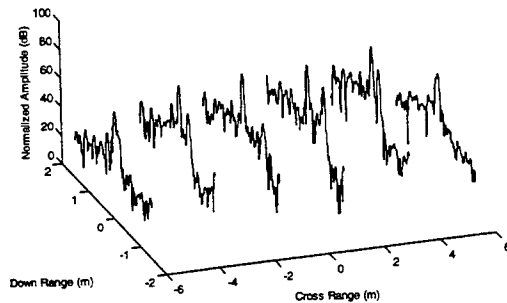
Figure 2. Displayed are 6 of 256 Cross Range Slices from a 2D Image

The first step in registering images is to identify the scatterers of an image. Scatterers are located by examining the cross range slices of the image. At this point in development, scatterer identification is limited to those scatterers demonstrating a peak response. This will eventually be broadened to include scatterers demonstrating a relatively flat down range response that is well above the noise floor. To eliminate the effects of processing sidelobes which can be as great as -30 dB, identified scatterers must have amplitudes within 30 dB of the peak amplitude of the image. This dramatically reduces the occurrences of misregistration of scatterers between two images.

Once all scatterers have been identified, we begin correlating the scatterers between the reference and matching images. Ohio State University's peak matching criteria based on the proximity and amplitude of the scatterer produces good image registration. The first criteria is that the change in down range location of correlated scatterers, Δdr_i, is within a certain distance. This distance is based on the highest and lowest vertical dimension of the target. The down range criteria assumes that the scattering mechanism (i.e. physical optics, traveling wave, etc...) remains the same for both images.

16

The second criteria is that the amplitude remains within 9 dB of each other. In order to satisfy this last criteria, only small changes in the elevation angle between the images should be used. Figure 3 illustrates the registration process by comparing slices from the same cross range location of two images measured at slightly different elevation angles. It is clear to see that two peaks are successfully matched to each other.
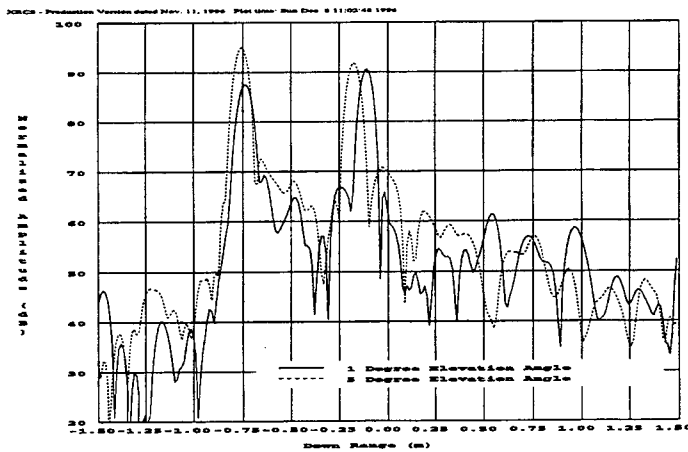
Figure 3. Cross Range Slices from 1° and 5° Images

Once scatterers have been correlated between images, the height of the scatterer can be computed using Eq. 1 and the data placed into a 3D data file. There are numerous other registration techniques using cross correlation functions that also merit consideration.

4. Improved Resolution

By examining Eq. 1, the vertical resolution is dependent upon the down range resolution by a factor of $1/\sin\theta_{el}$. Since the down range location of each pixel of an ISAR image is derived from the Fast Fourier Transform (FFT) of the measured RCS data, zero padding of the down range data can be used to improve vertical resolution [3]. Any amount of zero padding can be applied but I have chosen sufficient padding to yield a vertical resolution equivalent to the down range resolution.

5. Results

Interferometric imaging has been successfully demonstrated on ISAR data of a dart shaped target measured at MDC's Near Field Test Facility. The measurement setup is illustrated in Figure 4. Two broadside images of the dart were measured at 1° and 5° elevation angles. Broadside images were specifically chosen to highlight the interferometric imaging technique's ability to discriminate scatterers along the vertical dimension.
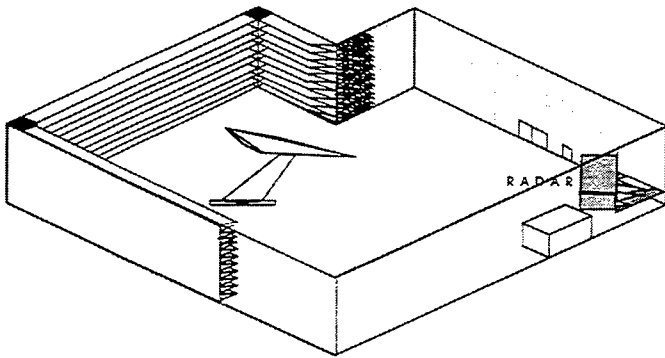
Figure 4. Measurement Setup

To date, we have been able to display the 3D interferometric image using projected 2D images along the three major planes (Figure 5). An overlay is superimposed on the data to illustrate how well interferometric imaging has located scatterers in the vertical dimension. Vertical range resolutions on the order of down range resolutions have been successfully achieved with the use of zero padding interpolation.
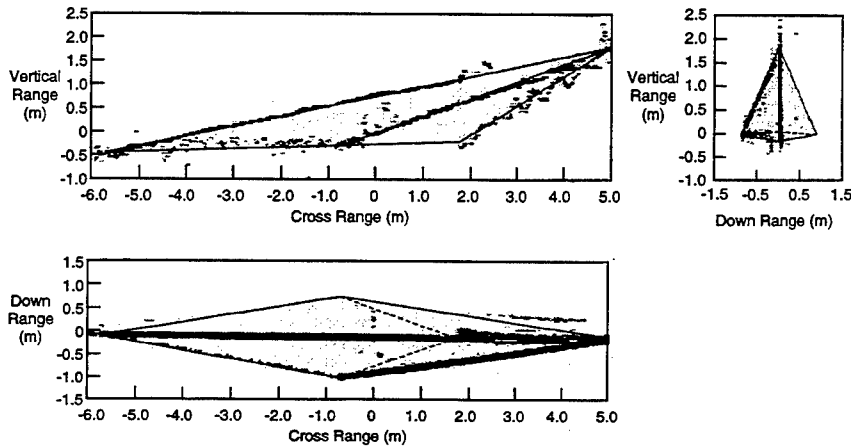
Figure 5. Using 2D Projected Planes to Display of 3D Interferometric Data

While successfully displayed using projected 2D planes, a 3D representation of the interferometric data eliminates the need to mentally piece together the data. To achieve this 3D representation, we have used the commercially available Spyglass™ software. Unfortunately, a black and white 2D print out of this file shown in Figure 6 does not fully illustrate the added dimensionality provided by color amplitude coding. Visualization in 3D is also enhanced with shading and the ability to view the data from a variety of angles.
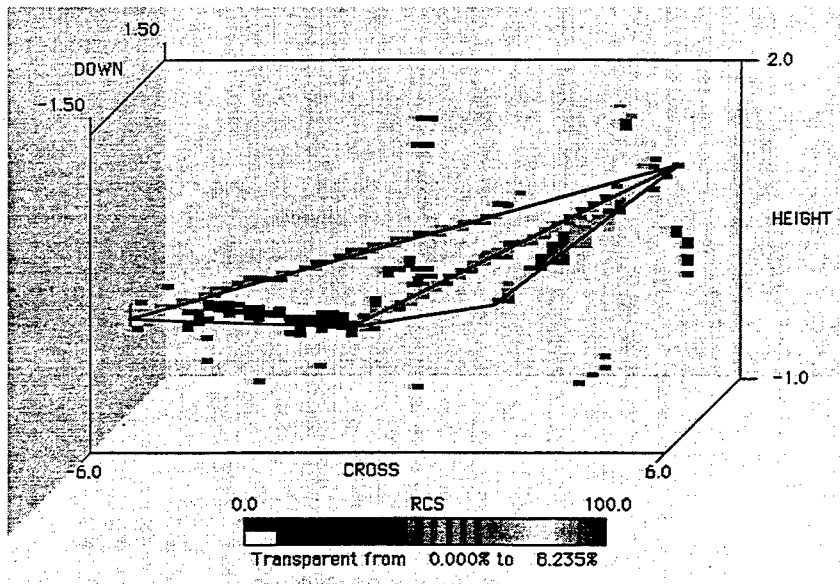
Figure 6. Using Spyglass[TM] to Display 3D Interferometric Data

6. Conclusion

We have successfully demonstrated how well interferometric imaging produces a 3D rendering of the RCS scattering from a target. This added visualization is obtained by a time efficient technique requiring virtually no additional measurements. Further improvements can be achieved by using a third matching image during the registration process. This reduces the effects of misregistration of scatterers by providing additional matching criteria.

7. References

[1]   L. C. Chang and W. D. Burnside, "Removal of Undesired Scattering Centers using a Radar Image Technique, " The Ohio State University ElectroScience Laboratory, Columbus OH, 1993.

[2]   Erich Krestel, "Imaging Systems for Medical Diagnostics," Berlin and Munich: Siemens Aktiengesellschaft, 1990, p.41.

[3]   E. Oran Brigham, "The Fast Fourier Transform and its Applications," Prentice Hall, New Jersey, 1988, p. 198-199.

MODERN GRAPHICS APPLICATIONS FOR VISUALIZATION OF ELECTROMAGNETIC RADIATION AND SCATTERING

C. Long Yu*
Naval Air Warfare Center Weapons Division
Point Mugu, CA 93042-5001

R. Kipp, D. J. Andersh and S. W. Lee
DEMACO Inc.
Champaign IL 61820

ABSTRACT

As modern computer and graphics technologies continue to advance, there is a growing demand for effective means of graphical representation of electromagnetic phenomena and their associated data visualization. In fact, a great challenge to the test and evaluation (T&E) community of radar-guided weapons systems is how to describe the electromagnetic scattering characteristics of complex test targets and their associated scattering centers with graphical visualization in a total system testing environment. This includes radar scenarios from far-field tracking to near-field end-game encounter.

The objective of this paper is to discuss various electromagnetic visualization tools developed in modern RF digital-simulation models to characterize and simulate the radar-scattering of complex platforms including airborne targets, terrain and urban sites. The techniques used in the visualization tools include three dimensional computer-aided design models, ray tracing methods and terrain rendering. EM simulation models which combine high-frequency techniques and these visualization tools provides sophisticated, user-friendly engineering tools for predicting the radar-signature of a complex radar target on a modern powerful workstation. The tools are especially useful in radar-signature diagnostics study, ambiguity resolution and radar scattering "cause and effect" analysis. Examples will be given to illustrate practical applications of these integrated tools in radar-target characterization, mission planning, and wireless communication.

1.0 INTRODUCTION

As modern computer and graphics technologies advance, visualization of data and information becomes a vital research and applications frontier shared by a variety of science, medical, engineering, business, and entertainment fields. In fact, a great challenge to the test and evaluation (T&E) community of radar-guided weapons systems is how to describe the electromagnetic (EM) scattering characteristics of complex test targets and their associated surrounding environment with graphical visualization in a total system testing environment. The test scenarios include radar applications from far-field detection and tracking, mid-course guidance, to near-field end-game engagement. The complexity of airborne weapon testing thus creates a great demand for effective means of graphical representation of electromagnetic phenomena and their associated data visualization for radiation and scattering problems.

An effective way to present the high-frequency EM phenomena is via computer simulation using computer-aided design (CAD) graphics packages and the shooting and bounce rays (SBR) method [1] on a graphical workstation. This approach offers T&E engineers an excellent capability to interpret and visualize complex EM radiation and radar scattering on a computer-graphics display. For example,

the locations of radar scattering centers of a complex platform can be easily and accurately determined via ray tracing and radar imagining techniques. Multiple bounce phenomena and mutual shadow problems often encountered in electromagnetic scattering testing of complex radar targets can also be easily visualized and identified by graphical ray tracing. This paper introduces three high-frequency electromagnetic codes and their associated graphical display capabilities as promising tools for radar-guided weapons systems test and evaluation applications.

The three EM packages are **Xpatch**, a far-field radar cross section (RCS) code [2], **Npatch**, a near-field RCS code [3] and **Apatch**, an antenna/platform radiation code [4]. These codes, developed by DEMACO, Inc., employ the SBR method for radiation and radar scattering analysis of airborne platforms (such as aircraft and missiles) and surface targets. With user-friendly, graphical user interfaces (GUI) and visualization software, these packages provide sophisticated tools for effectively pinpointing graphically the "cause and effect" of EM scattering in many diversified practical problems. The following sections present their modeling methodologies for EM radiation and scattering analysis and simulation. Examples of their application to practical problems such as radar-target characterization, airborne weapon engagement, and airborne antennas are also illustrated.

2.0 EM MODELING:

In radar-guided weapon/target engagements, it is well known that electromagnetic scattering phenomena play a critical role in determining the radar signature (far- and near-field) of the target encountered and the fuzing of warhead detonation. In a typical encounter as shown in Fig. 1, the missile passes from the far-field scattering zone, through the intermediate-zone and into the near-zone of the target. Most radar scattering predictors assume that the target is in the far-field of the radar. The far-field assumption is that the wavefront incident at the target has uniform magnitude and phase, and the scattered wave arrives back at the radar antenna from a single direction, as seen in Figure 1. In the end-game missile encounters, however, the missile and target are in close proximity and the transmitting and receiving antennas on the missile are generally located in the near-field zone of the scattered field from the target. An EM wavefront of nonuniform magnitude and phase dictates the complete scattering phenomena in this region. So, far-field assumptions lead to gross errors under near-field conditions. Additionally, radar return computation in the near-field is complicated by the partial target illumination, nonuniform antenna patterns, target material coatings, and engine inlet returns. Figure 1 illustrates the important differences between near-field and far-field missile/target encounter situations. This is why a near-field capability is essential for end-game applications. Consequently, **Npatch** was recently developed to handle the complex near-field RCS prediction of end-game simulation while **Xpatch,** developed over many years already, is primarily used for far-field RCS computation for missile guidance applications.

As discussed earlier, **Xpatch, Npatch** and **Apatch** employ the SBR method as the core computational engine for EM modeling. SBR provides not only an excellent tool for EM analysis but also graphic visualization via ray tracing. SBR uses geometrical optics (GO) ray tracing 3-D CAD models to implement physical optics (PO) [3] and is suitable for missile/target end-game scenarios which include the effects of the missile antenna pattern, multiple reflections, complex-shape shadowing, and material coatings. The sophisticated 3-D CAD models represent realistic, complex radar targets required for accurate EM modeling. Target CAD models are typically composed of 10,000 - 200,000 facets (triangular surfaces), or 10,000 to 50,000 bi-cubic patches, depending on the target level of detail. Effective SBR techniques require a fast ray tracer to track the 10,000 - 10 million rays needed to fully interrogate complex geometries. The ray tracer currently used in these models was developed by DEMACO, Inc. and supports CAD models described in facet (ACAD), bi-cubic (IGES-114) and NURB (IGES-128) formats.
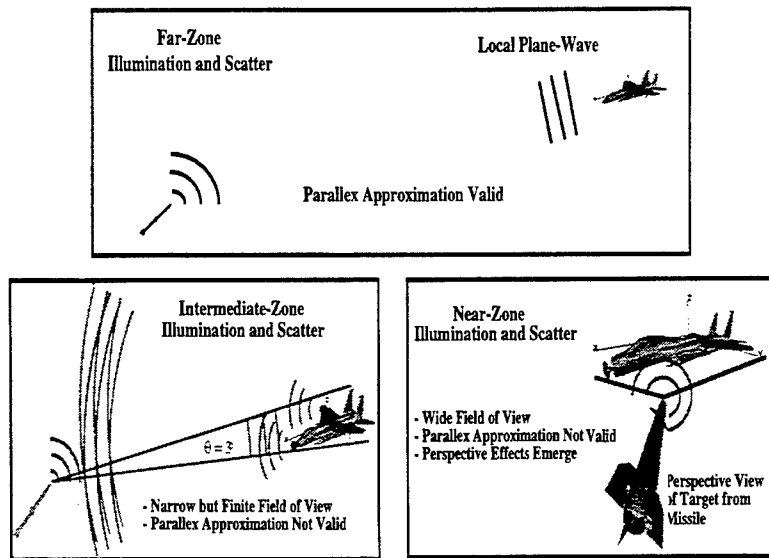
Figure 1. Definition of far-zone, intermediate-zone, and near-zone for a missile encounter with a target.

Since the EM modeling process of **Xpatch** and **Apatch** models have been well documented and can be found in Ref. [1,2], they will not be discussed here. Instead, the near-field modeling process of the **Npatch** model will be presented to illustrate the implementation of the SBR approach. Figure 2 shows a missile/target engagement scenario where a missile located at point R_m with an instantaneous velocity v_m is engaging its target located at point R_t with velocity v_t. The missile antenna illuminates the target, which scatters energy in all directions. Some of that energy scatters back toward the missile and is partially absorbed by the antenna. The quantity of interest is the near-field RCS, the ratio of the received power to the transmitted power P_r/P_t at the antenna terminals including the phase shift, as a function of frequency.

The SBR method is applied to compute this quantity in the following manner. The target is illuminated by thousands of rays weighted by the radiation pattern $A(\theta_m,\phi_m)$ of a mounted missile antenna (located at R_a) as if emanating from a point source toward the target (see Fig. 2). A CAD ray-tracer is then used to determine which target surfaces are lit and which surfaces are shadowed. The illuminating rays are treated as ray tubes, which cast "footprints" on the target body. Using PO principles, the induced surface currents over the domain of each footprint are computed. The computed surface currents, which depend on the material attribute of the surface at each ray hit point, then re-radiate EM energy in all directions. Using free-space Green's function, one computes the scattered energy at the point R_a from each footprint. Only a fraction of this energy will be absorbed by the missile antenna depending on the direction of arrival. Hence, in computing P_r/P_t, one weights the scattered energy at R_a by the receiving cross-section of the missile antenna at the arrival angle.

The rays which illuminate target surfaces are specularly reflected from their hit points. The ray tracer continues to trace these rays until they escape. Some will escape after the first bounce, and they

produce no further contributions at the receiver. This process produces the 1st-bounce contribution. Others will become multi-bounce rays, also shown in Figure 2. These rays continue to induce further currents on the target surface, which are then radiated back to the missile antenna in the same manner as described above. As a result, they also contribute to the radar received power. In this sense, SBR is a multi-bounce implementation of physical optics for complex target interactions. The advantage of this approach is that the target can be very complicated and realistic and SBR can produce much more accurate near-field scattering results than other available near-field predictors.
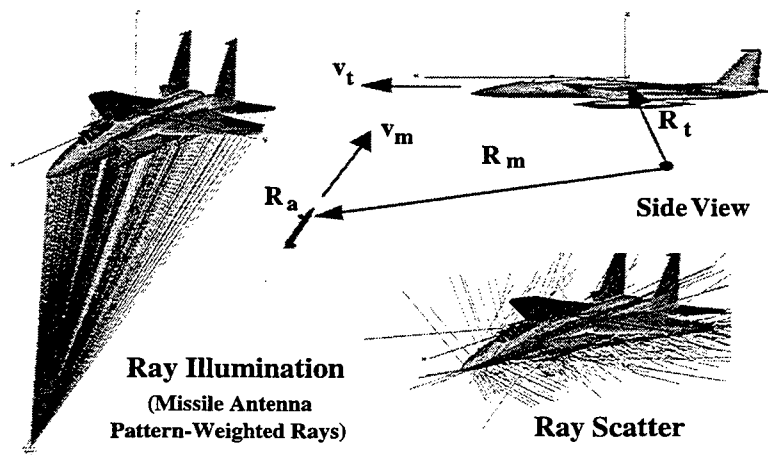
Figure 2. End-game encounter: Antenna pattern-weighted rays are launched from missile and scatter off of the target, leaving surface currents that radiate back to the missile.

3.0 SIMULATION RESULTS:

To demonstrate the EM analysis and visualization display capabilities of these models, the following graphical examples of RF problems, which involve a variety of complex 3-D targets, are depicted in Fig. 3-6. Case 1 illustrates the **Xpatch** results of a VFY 218 aircraft model for RCS study as a function of frequency and aspect angle. Case 1 also presents graphical display of ray hit points on the VFY 218 model for multiple-interaction scattering effects. Case 2 presents the **Apatch** results of antenna pattern analysis on a P-3 aircraft model for optimal pattern coverage and antenna installation. The antenna in this case is a blade antenna operating in UHF frequency band. Case 3 involves a MIG-29 model shown in Figure 5 in a missile/target end-game encounter simulation predicted by the **Npatch**. In this case, **Npatch** is directed to trace rays up to 50 bounces for multi-bounce computation. The radar frequency for this prediction is 10 GHz, and the antenna pattern is a 14-element array whose main beam points 10° forward of broadside. The aircraft surfaces are assumed to be perfectly conducting.

Finally, Case 4 illustrates four color frames (as seen in Fig. 6) of a missile end-game encounter against a F-15 model in a time-sequence display. These frames were produced by **Npatch** in a full-motion 3-D end-game encounter display. This full-motion display package is devoted specifically to provide visual simulation of the encounter scenario for missile performance assessment and diagnostic analysis. This tool shows the time-stepped end-game encounter in 3-D, with full rendering of the target and missile from their 3-D CAD models. A unique feature is the target surfaces color-coding according to the

strength of the target surface scattering contribution back toward the missile. The missile is displayed flying past the target, with overlays of scattering regions sweeping across the target.

1-bounce: green
2-bounce: blue
3-bounce: white
4 or more: yellow
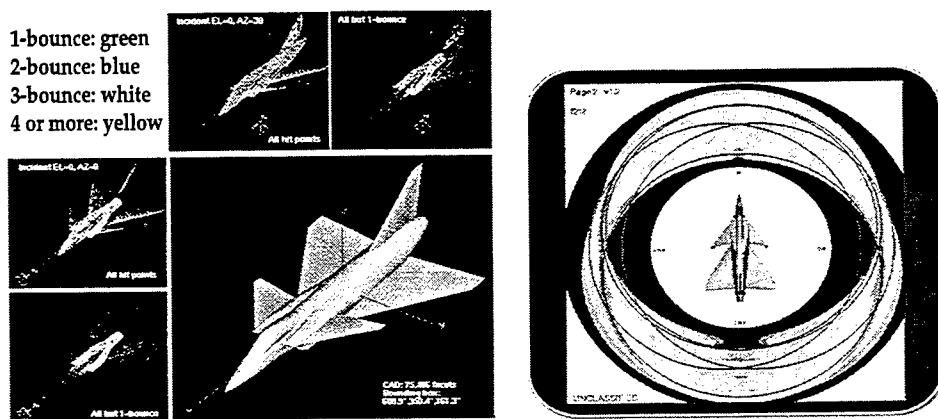
Figure 3. Ray hit points on a VFY 218 model from multi-bounce contributions and a 2D RCS pattern display as a function of aspect angle and frequency.
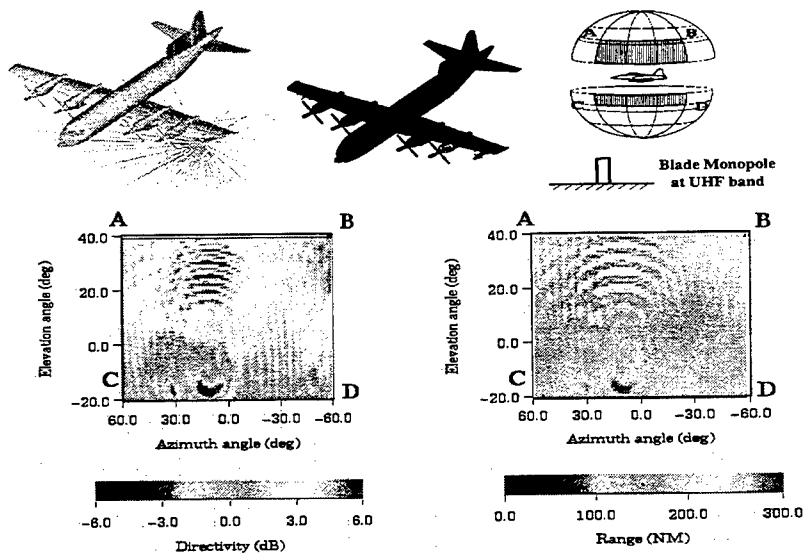
Figure 4. Displays of ray picture and ray hit points on a P-3 aircraft model for a wing-tip mounted isotropic antenna; and volumetric antenna patterns and range coverage patterns of a blade antenna mounted on top of the fuselage.

24
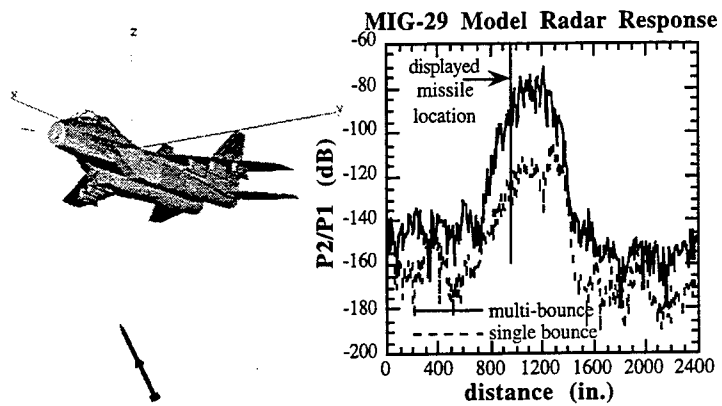
Figure 5. Significance of multi-bounce in MIG-29 model scattering return predicted by Npatch.
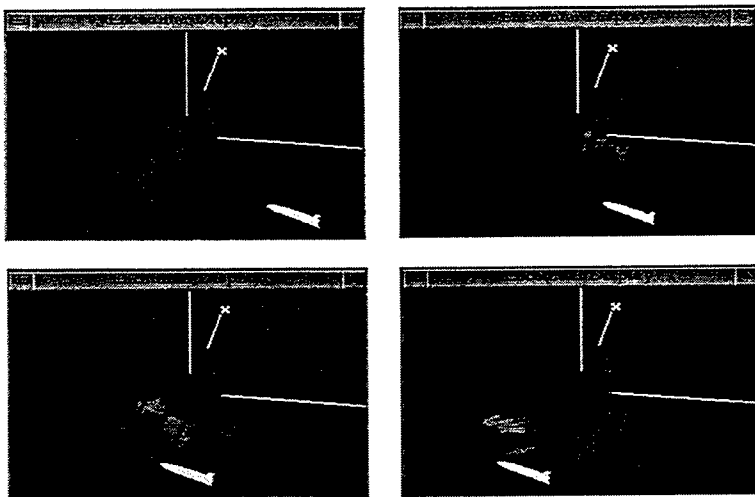
Figure 6. Full-motion 3-D encounter hot-spots display of a F-15 model predicted by Npatch.

4.0 CONCLUSION:

Three visualization and diagnostic tools for test and evaluation of radar-guided weapons systems simulation were presented. These software tools incorporated a computer-aided design (CAD) graphic package and the shooting and bouncing ray (SBR) approach to provide both graphical visualization and electromagnetic radiation and scattering computation of complex platforms. As shown from the

examples presented, the SBR method provides not only the ray paths for physical insight of EM scattering mechanisms but also the ray hit points for scattering center identification. It is well-suited for analyzing multiple-reflection phenomena and mutual shadow problems encountered in electromagnetic scattering on complex platforms. The graphical representation of the radar target and ray-paths is particularly helpful in understanding the EM scattering phenomena by visually pinpointing its "cause and effect". The unique visualization capability of these EM models is presently adequate and significant for many antenna and radar problems. Applications of this capability have also been extended to many areas such as mission planning, RF chamber design, wireless communication, etc. which will be discussed in the coming oral presentation. However, further improvements and enhancements are needed and will be continued in order to meet the challenges imposed by the test and evaluation requirements of radar-guided weapons systems.

5.0 **REFERENCES**:

[1] H. Ling, R. Chou, and S. W. Lee, "Shooting and bouncing rays: calculating the RCS of an arbitrarily shaped cavity," *IEEE Trans. Antennas Propagat.*, vol. 37, 1988, pp. 194-205.

[2] D.J. Andersh, S.W. Lee, *et al.*, "XPATCH: a high frequency electromagnetic scattering prediction code and environment for complex three-dimensional objects," *IEEE Antennas and Propagation Magazine*, vol. 36, no. 1, Feb. 1994, pp. 65 - 69.

[3] R. A. Kipp, Near-Field Radar Signature Modeling For EW/End-Game, SBIR Phase I Final Report, DEMACO, Inc., Champaign, IL, 1996.

[4] T. Ozdemir, M. W. Nurnberger, J. L. Volakis, R. Kipp, and J. Berrie, " A hybridization of finite-element and high-frequency methods for pattern prediction for antennas on aircraft structures," IEEE Antennas Propagat. Mag., vol. 38, pp.28-38, June 1996.

A Versatile Geometry Tool for Computational Electromagnetics (CEM): MrPatches

D. D. Car and J. M. Roedder
McDonnell Douglas Corporation
Mail Code S064 2263
PO Box 516
St. Louis, MO 63166

Abstract

High accuracy in radar cross section (RCS) simulations increasingly requires that CAD descriptions of targets incorporate great detail and fidelity. MrPatches is an enabling tool used at McDonnell Douglas Corporation (MDC) to achieve rapid, reliable, first time quality results for complex CEM problems. This paper describes the key elements of the architecture of the code, its major features, the geometry/CAD protocols it supports, its platform portability, and its link to other CEM software tools. Finally, specific examples drawn from various applications illustrate the versatility of this code.

1. Background

By way of introduction, we begin with a brief history of MrPatches. The idea of a graphical geometry code directed at the particular needs of the RF engineer originated with Mr. Mike Caddy (Naval Air Warfare Center - Weapon Division - Patuxent River, MD) and Mr. Denny Elking (MDA). In 1990 Mr. Caddy was funding a Graphical User Interface (GUI) for the CADDSCAT RCS analysis code [Ref. 1]. MrPatches was developed with MDC funds as a companion code to that GUI. It was first used in 1991. GEOMPACK was used for the framework of MrPatches since it was the geometry kernel of CADDSCAT at the time. GEOMPACK had an IGES processor, a ray tracer, routines to support diffracting edge analysis, and a gap space curve capability [Ref. 1].

The first release of MrPatches was written entirely in Silicon Graphics GL including the user interface. However, the use of GL made portability of the code to other systems difficult. With the advent of HP workstations it became necessary to use more portable graphics. The use of Motif and strictly X-Windows for the user interface began in 1993.

The MDC CFD (Computational Fluid Dynamics) group developed the MDGL (McDonnell Douglas Graphics Library) package [Ref. 2] to support its graphical tools on a wide array of graphics devices. This package allows the same graphical subroutine calls to access 'native' drawing routines on many operating systems. By adopting this package for MrPatches in 1994, it is possible to draw geometry in 'native mode' on the SGI, IBM RISC (also using GL), and HP workstations. X-Window drawing capability is available on a host of systems, including the Sun Solaris and Intel Paragon systems.

MrPatches has been used as a pre/post-processor with the method of moments based CARLOS code and the infrared radiation analysis IRIMAGE code. Recent efforts involve support for more intuitive input features: the spaceball and arrow keys can be used for geometry viewing in addition to translation/rotation/zoom sliders.

2. Architecture

A key component of MrPatches is GEOMPACK. The structure of GEOMPACK supports facet and curved surface entities in an efficient manner. Curved surfaces can be rational as well as polynomial of degree 3 or higher. Second order IGES curved surfaces [Ref. 3] are always internally converted to parametric bi-cubic (PBC) form. GEOMPACK has an option to convert surfaces that are higher order than cubic to PBC form for editing and ray tracing. For efficient RCS computation of curved surfaces, CADDSCAT requires PBCs but can compute physical optics of any IGES surface that GEOMPACK supports.

GEOMPACK allows support for the processing of numerous facet file formats. These facet files fall into two categories. The first category is the MISCAT-type format which defines facet vertex information for each surface independent of other surfaces. The other category is an ACAD-like format which first specifies the vertices for the entire model and then defines the facets in terms of how the vertices are connected. This second format utilizes computer memory more efficiently by allocating memory only once for a vertex common to several facets.

```
COMMENT  ----------------
COMMENT  pylons (mirrored)
/home/roedder/c17/geometry/pylon_inbd_rh.iges+x
/home/roedder/c17/geometry/pylon_outbd_rh.iges+x

COMMENT  ----------------
COMMENT  outboard engine (mirrored)
/home/roedder/c17/geometry/engine_outbd_rh.iges+x

COMMENT  ----------------
COMMENT  translate engine to inboard station and
COMMENT  mirror for other side
TRANSLATE 255.8901 -138.1309 12.2062
/home/roedder/c17/geometry/engine_outbd_rh.iges+x

COMMENT  ----------------
COMMENT  wings and  tails
/home/roedder/c17/geometry/wing_fairing_flap_rh.iges+x
/home/roedder/c17/geometry/wing_rh.iges+x
/home/roedder/c17/geometry/vert_cap_horiz_rh.iges+x

COMMENT  ----------------
COMMENT  radomes: do not mirror these
/home/roedder/c17/geometry/radome_fwd.iges
/home/roedder/c17/geometry/radome_aft.iges

COMMENT  ----------------
COMMENT  fuselage:
/home/roedder/c17/geometry/fus_fillet_wing_rh.iges+x
/home/roedder/c17/geometry/fus_fwd_rh.iges+x
/home/roedder/c17/geometry/fus_whlpod_rh.iges+x
COMMENT  ----------------
COMMENT  aft fuselage and doors
/home/roedder/c17/geometry/fus_aft.iges
/home/roedder/c17/geometry/fus_aft_doors.iges
/home/roedder/c17/geometry/cargo_door.iges
COMMENT  ----------------

END FILE INPUT
```

Figure 1. Example GEOMPACK Component File

GEOMPACK consists of approximately 50K lines of POSIX C code. Core routines are FORTRAN, C, and C++ callable. The C code accommodates systems which require a trailing underscore (i.e. "_") for function declarations in order to link with FORTRAN, as well as those which do not. Memory for entities is dynamically allocated. GEOMPACK has been tested with 'Sentinel Memory Advisor' to ensure there are no memory leaks. When used in a 'virtual machine' consisting of many workstations, such as when CADDSCAT is configured for a multi-processor run, GEOMPACK reads geometry files on a single processor and uses MPI (Message Passing Interface) to communicate the geometry to other nodes. Considerable memory savings are possible for models that are reflected about a cardinal plane. This is accomplished by deriving a reflected surface matrix from the 'parent' on the fly.

Since 1989, GEOMPACK allows processing of multiple geometry files. Presently, GEOMPACK accommodates up to 150 files. The GEOMPACK 'component file' is used to supply geometry file names and processing directives. A keyword driven format enables file translation, rotation, subdivision, triangulation, mirroring, etc. Figure 1 shows an

actual component file for a C17 model. The example shows mirroring (+x extension to file name), translation ('TRANSLATE' keyword), and comments ('COMMENT' keyword).

GEOMPACK supports a number of surface geometry formats. On input: IGES curved parametric entities (114, 128) as well as finite element mesh entities (134, 136); Patran Neutral File curved surface (entity 33); ACAD, CARLOS, IRIMAGE IAG, and MISCAT facet files; and height fields [Ref 1]. On output: IGES entity 114 and all facet formats except ACAD. It is very easy to add other geometry formats as either inputs or outputs.

Another module of MrPatches is MDGL. This package is written in ANSI C and has been ported to most UNIX platforms. Current implementations support HP, SG, IBM RISC, SUN, Motorola, DEC, Cray, and Paragon systems. Preliminary versions exist for Microsoft Windows, Borland BGI, and Macintosh. Numerous hardcopy devices are supported. Like GEOMPACK, graphics calls support C and FORTRAN.

MDGL features include 2D and 3D orthographic and perspective projections, viewports, double buffering, z-buffering, and most other standard graphics calls. Double buffering provided by MDGL for X-Window devices is a unique feature not directly supported under X. When opening a window, MDGL queries the device being used. If the system does not support a native graphics language, the X-Window graphics protocol is used.

3. Basic Features

MrPatches editing capabilities allow surface normal direction correction, creation or deletion of surfaces, and merging or separation of geometry. Areas on the geometry can be flagged for treatment schemes. By picking with the mouse, detailed geometrical information about specific locations can be obtained. Color shading and radius of curvature plots aid the analyst in verifying the integrity of the model prior to EM analysis. Additional capabilities exist to display the diffracting door gaps and edges processed by CADDSCAT. To assist in understanding multi-bounce scattering problems, MrPatches interactively performs ray tracing of the geometry.

MrPatches displays and modifies triangular grids such as used by the MDC CARLOS code. MrPatches can automatically collapse points, adjust symmetry edges, and split long triangle edges. Output from CARLOS can be input to MrPatches to graphically pinpoint geometry trouble spots and apply corrections. MrPatches displays CARLOS currents, images, and current vectors.

We now present a detailed discussion of four representative features of MrPatches. These are the edge abutment display, the gap geometry modeling, the visualization of multi-bounce effects, and various editing options useful with CARLOS.

4. Edge Abutment Display

The GEOMPACK 'Edge Abutment Table' (or just 'Edge Table') is used for several purposes:
- defining diffracting edges (CADDSCAT)
- tracking surface waves (Enhanced CADDSCAT, [Ref. 4])
- evaluating surfaced model quality by displaying the wedge angle between abutting surfaces.

The 'edge table' is automatically created by GEOMPACK using a graduated tolerance approach. The algorithm starts with very tight tolerances, gradually loosening the tolerances as more difficult abutments are sought. The abutment detection algorithm is sophisticated. It can find abutments of partial borders, even for curved parametric surfaces such as in Figure 2 and Figure 3. In the most general case, the mapping of the surface parametric variables across a border is a non-linear function. Figure 2 shows the diffracting edge configuration for fixture56.iges. Figure 3 zooms in on an area of 'non one-for-one' patching in Fixture 56. Figure 11 of [Ref. 4] shows the surface wave tracking on another numerical fixture.
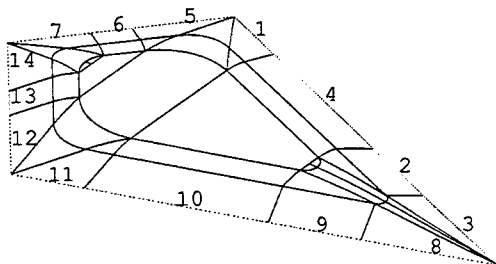
Figure 2. Diffracting Edge Configuration for Fixture 56
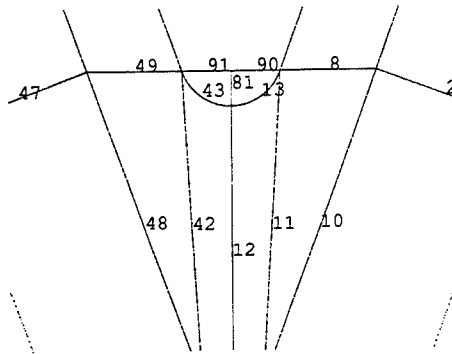
Figure 3. Non One-For-One Abutments Identified

5. Gap Geometry Modeling

Because gaps can be a major scattering contributor for low observable platforms, MDC has employed a hybrid gap analysis capability since 1989 [Ref. 1]. In practical applications, a user friendly visual interface for checking the gap geometry is required. For example, there are hundreds of gap segments on a typical aircraft such as the F/A-18. The approach to RF modeling of gaps at MDA is similar to that for moldline geometry modeling. CADDSCAT and CAVERN [Ref. 5] use the designer's moldline definition *exactly* via IGES files (i.e. without facetization). IGES geometry developed by the configuration designer is used directly in the RF analysis. A similar approach is used for gaps. Thus the designer defines the door gaps as IGES space curves which are the direct input to CADDSCAT. Allowed IGES entities are 112 (spline curve) and 126 (B-spline curve). B-spline curves are allowed to be rational. Note that gap geometry is modelled only as space curves in the high frequency asymptotic code. The gap geometry is analyzed in a psuedo-3D manner using CARLOS and the scattering characteristics in the gap principal plane are input to CADDSCAT.

RF gap processing must have the moldline normal available at every point along the gap. GEOMPACK develops a description of the surface normal parameterized as a function of the gap parameter. Any gaps not satisfying the input gap tolerance are displayed in red in MrPatches indicating re-work is required, - i.e., the gap space curve is not close enough to the surface. Figure 4 shows a gap layout with the sampled normal (the short lines) on fixture56.iges.
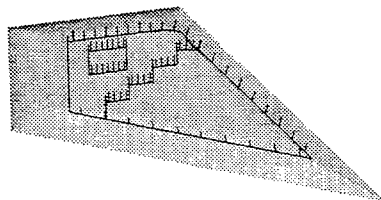
Figure 4. Gap Configuration for Fixture 56 (The 'whiskers' are the gap normals.)

6. Visualization of Multi-Bounce Effects

The standard MDC practice is to compute first bounce and multi-bounce scattering effects separately to gain more insight into subtleties of each target being analyzed. In 1994, MDA CEM analysts performed a signature analysis of the forward swept wing configuration of Figure 5. No significant multi-bounce effects had been anticipated for this target. However a multi-bounce condition was found at 0 elevation and 135 degree azimuth.
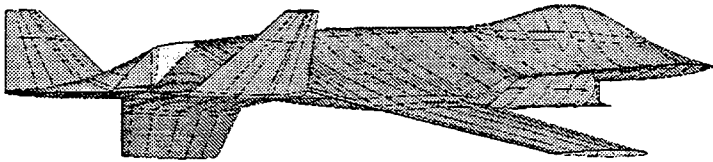
Figure 5. Forward Swept Wing Model

Since the usual ISAR imaging techniques do not map multi-bounce RCS directly onto the scatterer, identifying multi-bounce scattering sources can be challenging. MrPatches is used to help resolve these nuances. To do this, CADDSCAT provides the coherent higher-bounce RCS contributions from each surface at the aspect of interest. (Note, a range of aspects is not used.) These outputs are displayed in MrPatches as a 'PATCH DATA' file. It is advisable to utilize the GEOMPACK 'EQUALSIZE' component file keyword to subdivide the geometry into surfaces of roughly similar size. This causes the color coding of surfaces to be more meaningful, since the RCS of each surface is dependent on size.

Using this technique, we obtained the plot of Figure 6 which clearly located the last bounce on the canopy. Using the MrPatches interactive ray tracing feature, the actual ray paths were identified. MrPatches also supports the ray tracing of 'star bursts' for visualizing near field multi-bounce situations [Ref. 6]. Figure 7 shows a ray star burst, which hypothetically originates from an antenna illuminating a Harpoon missile.
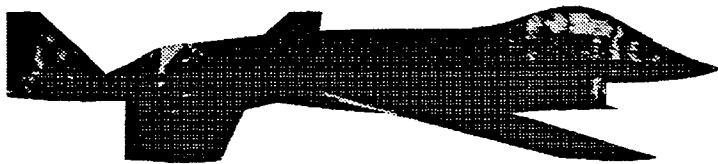
Figure 6. Multibounce Image for Forward Swept Wing Model
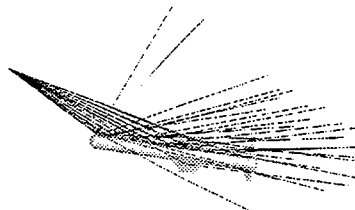
Figure 7. Ray Star Burst on Harpoon Missile

31

7. Editing Options and CARLOS Applications

One of the features of MrPatches is its ability to edit geometry. Options are available to translate, scale, and rotate geometry as well as creating or deleting surfaces. When several geometry files have been read in and modified, the files can be written back out keeping the original file groupings. This feature is used heavily where different geometry files are assigned as treatment regions in CARLOS [Ref. 7]. Modified files stored in the IGES format can be imported back into the original CAD modeling system.

To modify specific surfaces, the user selects them by picking them with the mouse. Users can select groups of surfaces by using a screen box, by specifying a geometry file, by picking all surfaces of a B-surface, or by keying in surface identifiers. Each surface selected changes color. If the wrong surface was selected, picking the surface again will de-select it. Surfaces can be selected at any time while the model is being rotated with arrow keys, dials, sliders, or spaceball. Once the desired surfaces are selected any operation can be performed.

MrPatches is not intended for gridding an entire model from start to finish. Another MDC tool, ZONI3G is used to perform the bulk of the gridding operations. ZONI3G creates triangular or quad meshes. MrPatches is used to make the fine corrections in these grids. Often problems arise with the mesh that are difficult to spot due to the large quantity of triangles. CARLOS has a feature to write a file that MrPatches uses to identify mesh problems. The problems CARLOS detects are color coded to indicate free edges, degenerate triangles, duplicate surfaces, and multiple edge abutment. MrPatches can display the CARLOS currents or images on the geometry model. Figure 8 shows a current image for an F18C model.
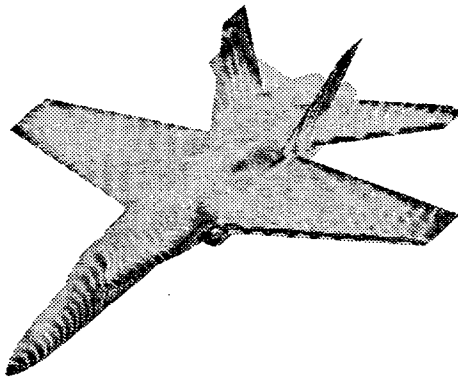
Figure 8. F18C CARLOS Image at 500 MHz, 149636 Facets

Special options in MrPatches are helpful in editing CARLOS triangular facet files. After entering a user defined tolerance, points within this tolerance can be snapped together. Points within a tolerance of a symmetry plane can be snapped to that plane. Triangles that become degenerate are deleted and the user has the option to delete surfaces that lie entirely in a symmetry plane. Triangles with edges greater than a specified length can be split while maintaining one-for-one edge integrity. MrPatches can create three or four sided facets. Vertex points can be keyed in, however, they can also be picked with the mouse. Picking options allow the mouse to select an arbitrary point, a point on an edge, or a surface vertex. When a large gap exists, two rows of points can be chosen and zippered together to seam the gap.

8. Conclusions

MrPatches is built on two standard MDA software packages: MDGL and GEOMPACK. The McDonnell Douglas Graphics Library (MDGL) allows graphics applications to port seamlessly to all major workstations and employs the native graphics language on each system. The MDA geometry package GEOMPACK, supports a variety of geometry formats, including IGES and several facet formats. It forms the backbone of several MDA CEM codes such as CADDSCAT. MrPatches geometry outputs can be provided in a variety of faceted or curved surface formats. PostScript (PS), Extended PostScript (EPS), and TIFF format files are also available outputs.

MrPatches is an excellent tool for developing the geometry and providing pre/post processing for such high fidelity RCS codes as CADDSCAT, CAVERN, and CARLOS. In addition, although not discussed here, MrPatches also supports IR analysis at MDA [Ref. 8]. Because MrPatches supports the exact same set of geometry processing options as the RF codes, there is a 100% compatibility of this tool with the CEM analysis engines. The use of existing code building blocks (i.e. GEOMPACK and MDGL) has expedited the development of this computer code.

MrPatches is normally distributed to users as part of the CADDSCAT High Frequency RCS analysis/design package. This package is available to qualified government requesters. Contact Jim Roedder at (314)232-7083.

9. Acknowledgments

10. References

[1] D.M. Elking, J.M. Roedder, D.D. Car, S.D. Alspach, "A Review of High Frequency Radar Cross Section Analysis Capabilities at McDonnell Douglas Corporation", IEEE A&P Magazine, Vol 37, No. 5, Oct 1995.

[2] J.A. Johnson, "McDonnell Douglas Graphics Library (MDGL) Programmers Reference Manual", Copyright Unpublished 1992, 1993, 1994.

[3] "Initial Graphics Exchange Specification", Version 4.0, available from National Institute of Standards and Technology.

[4] S.D. Alspach, D.M. Elking, K.E. Castle, "High Frequency Surface Current Based Approach for Computing Edge and Tip Diffraction", HAVE FORUM 1994 Symposium Proceeding, Vol 1, WL-TR-95-6003.

[5] J.L. Karty, J.M. Roedder, S.D. Alspach, "CAVERN: A prediction Code for Cavity Electromagnetic Analysis", IEEE A&P Magazine, Vol 37, No. 3, June 1995.

[6] J.L. Karty, J.M. Putnam, J.M. Roedder, C.L. Yu, "Use of Near-Field Predictions in the Hybrid Approach", ACES Symposium Proceeding Monterey, CA, March 1997.

[7] J.M. Putnam, M.B. Gedera, "CARLOS-3D: A General Purpose Three Dimensional Method of Moments Scattering Code", IEEE A&P Magazine, Vol 35, No. 2, Apr 1993.

[8] D.W. Walter, A.R. Tucker, "A Reverse Monte Carlo Full Vehicle IR Signature Code", IRIS Targets Backgrounds and Discrimination Conference Proceeding, Monterey, CA, February 1994.

Visualisation issues for time domain integral equation modelling

S J Dodson, S P Walker

Imperial College of Science, Technology and Medicine, London, UK

Abstract

The use of large, sophisticated computer aided design software is very widespread in 'mechanical' applications such as automotive and aerospace design. The application of such tools in electromagnetics, and in particular high frequency electromagnetics, is much less ubiquitous.

In this paper we describe the use of the MSC/PATRAN CAD suite, developed primarily for solid mechanics applications, as the geometry entry, meshing, post-processing and display tool for the Zeus CEM analysis code. Difficulties which arise in such an implementation, including topics more peculiar to scattering analysis such as near field calculation and display are discussed.

1. Introduction

Improvements in CEM techniques and the use of larger computers to solve these problems has resulted in larger and more complex targets being analysed. This has brought the issues of geometry entry, mesh generation and result visualisation to prominence. Big CEM problems now demand just the same capabilities and sophistication in these areas as do say solid mechanics analyses.

The need in solid mechanics applications arose rather before that in CEM, and there now exists a considerable body of commercially available CAD, meshing and visualisation software developed for such purposes. The mode of use typically starts with the entry / generation of the geometry, in the form of a 'solid model'. The volume or surface of this is then discretised, generally by its division into finite elements, and this discretised geometry is then used in the analysis code. Results so generated are then fed back into the CAD package for postprocessing and display. In many commercial packages the stages of solid modelling, meshing, running of the analysis codes, post processing of results (and even data and tool preparation for manufacture) are linked via a seamless graphical user interface.

In this paper we describe the development and operation of schemes to allow the use of such software as the meshing and visualisation tool for a time domain integral equation CEM suite, denoted Zeus. This is an implicit integral equation time domain code[1]. The basic formulation is based on the time domain MFIE for a perfectly conducting scatterer surrounded by dielectric[2,3].

$$2\pi\, \mathbf{H}(\mathbf{r},t) = 4\pi\, \mathbf{H}_{inc}(\mathbf{r},t) + \int_{\partial\Omega} \left(\mathbf{n}' \times \mathbf{H}(\mathbf{r}',t^*)\right) \times \frac{\hat{\mathbf{R}}}{R^2} + \left(\mathbf{n}' \times \frac{\partial \mathbf{H}}{\partial t'}(\mathbf{r}',t^*)\right) \times \frac{\hat{\mathbf{R}}}{R}\, ds'$$

where $\mathbf{H}$ is the magnetic field, $\mathbf{n}'$ is the normal vector at $\mathbf{r}'$, c is the speed of wave propagation and t^* is the retarded time. The integration is carried out over the surface of the scatterer s'.

The spatial discretisation of the MFIE is achieved by dividing the surface into M disjoint, generally curved elements. The time dependence is modelled using quadratic lagrangian basis functions (T_β) with

34

nodal separation (timestep) Δt. Using the isoparametric approach we obtain a discrete equation for the unknowns $\mathbf{H}_i^k$, the H-field at the ith node and kth time step.

$$2\pi\mathbf{H}_i^k = 4\pi\mathbf{H}_{inc,i}^k + \sum_{m=1}^{M}\iint_{\xi\eta}\sum_{\alpha}S_{\alpha}\sum_{\beta}\left(\frac{T_{\beta}(\tau(\xi,\eta))}{R^3} + \frac{\dot{T}_{\beta}(\tau(\xi,\eta))}{\Delta t R^2}\right)\left[(\mathbf{n}'\times\mathbf{H}_j^{k'})\times\mathbf{R}\right]|\mathbf{J}|d\xi d\eta$$

In the above $\mathbf{J}$ is the Jacobian. The functions S_{α} and T_{β} are the quadratic spatial and temporal shape functions respectively, with spatial intrinsic co-ordinates (ξ,η) and intrinsic time τ.

The element types used correspond to surface element types available in commercial meshing packages. Although a whole library of different element types could be employed (akin to finite elements) the code currently supports eight or nine noded quadrilateral elements and six noded triangular elements. Any combination of these element types can be used in meshing a solid model. Fuller details of all of this can be found in the references cited[2,3].

The use of the meshing package allows for local refinement of the mesh in areas of high curvature or complex geometry. If the time dependence is treated explicitly the timestep must be smaller than the smallest spatial nodal separation. These methods are also prone to instabilities[4,5]. Therefore, an implicit treatment is employed where the timestep is based on the largest nodal separation. These packages generally also allow use of tools to easily determine element distortion or curvature.

2. Mesh/Analysis Code Interface

This section details the methods used to create an interface between the CAD software, the meshing package and the Zeus analysis code. The meshing package we mostly use is MSC/PATRAN although a similar interface has been developed successfully for SDRC Ideas. Normally a solid model is created using PATRAN's geometry modeller, although alternatively we can import solid models from other CAD packages into PATRAN. As the analysis is a boundary element method, we only need to discretise the surface of the solid model. This is achieved by meshing the surface of the solid model using the range of meshing tools available in the package. These include for example, non-uniform seeding of the mesh in areas of high curvature, mapped or free meshing and automatic refinement of the mesh in geometrically complex areas, along with practical aids such as zoom and rotate.

The next stage is to convert the mesh information into a format that can be used as input to the Zeus code. The mesh and control information required by the Zeus code is supplied in the form of an ASCII file containing information 'datasets'. An example of a dataset is the list of nodal co-ordinates. These datasets have start and end delimiters and have a specified format for the data contained between the delimiters. The mesh information required by the Zeus code is a dataset containing the nodal co-ordinates and a dataset containing the element types and connectivities.

PATRAN and Ideas both have the facility to export an ASCII file containing the mesh information as 'datasets'. In the case of PATRAN this file is called a 'PATRAN neutral file'. The datasets in the neutral file are not in the same format as the datasets in the input file to the Zeus code. Therefore, a simple format converter code (named p_PREP) is used to create the Zeus code datasets from the PATRAN neutral file. This procedure is summarised in figure 1.

The next step is to add to the file containing the Zeus code mesh datasets such control information datasets as are required. These typically might consist of the incident wave data, the timestep size and the order of quadrature to be used. The Zeus code can then be run and will output a result file containing surface current values at nodal locations and at all timesteps.

3. Post Processing and Display; Surface Fields

Once a result file for a particular mesh has been generated, the results can then be read into PATRAN or Ideas. The results can then be displayed on the same representation of the body as was used to create the mesh, and surface currents at nodal locations visualised.

PATRAN has a facility whereby the user can add additional menu options and preferences to tailor PATRAN to the user's application. This involves writing programs in PCL (PATRAN Command Language) which can be linked into the main PATRAN code when the user starts up PATRAN. This has provided a method to integrate the reading of Zeus code results directly into PATRAN. A different scheme was adopted for Ideas, which is less welcoming in this respect; the Zeus code result file was converted into an 'Ideas universal file' using a format conversion program, and the resulting universal file imported into Ideas.

The procedure for reading the results into PATRAN is as follows. The user opens the database containing the mesh information supplied to the Zeus code. Using the additional PATRAN menu option created for the Zeus code, the user can select the result file to read in. As the result file contains surface currents at all nodes and at all timesteps it can be rather large. For example, a mesh of a NASA almond consisting of 2450 nodes (sufficient to model it as a ~6 wavelength long body), run for 200 timesteps, generates in a result file totalling approximately 25 Mb. To circumvent this difficulty, the user can select a range of timesteps to read in, which may be a small subset of the total.

Once the results have been read in, the wide variety of display tools available in the meshing package can be used. The results can be displayed as a vector plot or as a scalar fringe plot, where the scalar values are based on the magnitude of the surface field or the magnitude of a vector component. The results can also be animated and areas of interest magnified or shown in isolation. (figure 5)

4. Post Processing and Display; Near Fields

Once the surface field is known the far field and near field values can be calculated (this procedure is summarised in figure 2). The near field values represent the behaviour of the scattered field close to the target. A near field value is calculated at all timesteps by integrating from the point in space where we wish to know the near field value over the surface fields at the appropriate retarded times. Calculating the near field values for a set of field points allows us to build up an image of how the field is scattered close to the target.

A separate code (m_NEARFIELD) is used to calculate the near field values. Input to this code is the same as the input to the original Zeus code with an additional dataset containing the co-ordinates of the near field points and a dataset containing the surface field results.

Typically we are interested in the near field values on a 'cutting plane' through the target. We can easily create a set of points on such a plane in PATRAN. First, we create a cutting plane surface on the solid model geometry. This can then be meshed to create a set of nodal locations on the cutting plane. Using the same procedure used in converting the original mesh data to Zeus code datasets, the near field locations can be converted to a dataset for input to m_NEARFIELD.

Running m_NEARFIELD results in a result file containing the field values at all the points on the cutting plane at all timesteps. These results can then be read into PATRAN using exactly the same method as described section 2. The near field results can then be displayed as vectors or scalars in a same way as the original surface results. (see figure 6)

5. Integration Issues

The above sections describe how the Zeus code is used with a commercial CAD and meshing package such as PATRAN.

We have developed a seamless graphical interface, written in PCL, to allow all of the above manipulations to be performed from within PATRAN. However, as described, the Zeus code is not wholly

36

embedded into PATRAN. Rather, as indicated in the vaious figures, the user must create the solid model and mesh in PATRAN, then export the mesh data before running the Zeus code externally. The result file is then read into PATRAN for display. This method is convenient for developers as the user has a direct interface with the code they are developing. Also, due to the size of the problems solved the Zeus code is often run on external machines where PATRAN is not available, such as the 512 processor T3D at Edinburgh. A degree of separation of the visualisation and analysis aspects is thus in practice convenient.

6. Conclusions

We have here described the use of a CAD suite, developed primarily for solid mechanics applications, as the geometry entry, meshing and post-processing and display tool for a CEM analysis code. The combination works well, allowing all the features and sophistication of the CAD suite, developed for and at the expense of the much larger solid mechanics applications market, to be made available to the CEM analyst.

Acknowledgements

References

1. S.P. Walker, M.J. Bluck, M.D. Pocock, C.Y. Leung and S.J. Dodson, Curvilinear, isoparametric modelling for rcs prediction, using time domain integral equations, *12th Annual Rev Prog Appl Comp.Electromagnetics* 1, 196-204 (1996).

2. Poggio, A.J. and Miller, E.K. Integral Equation Methods of Three-Dimensional Scattering Problems. In: *Computer Techniques for Electromagnetics*, edited by Mittra, R. Oxford: Pergamon Press, 1973, p. 159-265.

3. M.J. Bluck and S.P. Walker, Time Domain BIE Analysis of Large Three Dimensional Electromagnetic Scattering Problems, *IEEE Transactions on Antennas and Propagation* (submitted), (1995).

4. S.J. Dodson, S.P. Walker and M.J. Bluck, Implicitness and stability of time domain integral equation scattering analyses, *IEEE Transactions on Antennas and Propagation* (submitted), (1996).

5. B.P. Rynne, Instabilities in time marching methods for scattering problems, *Electromagnetics* 6, 129-144 (1986).
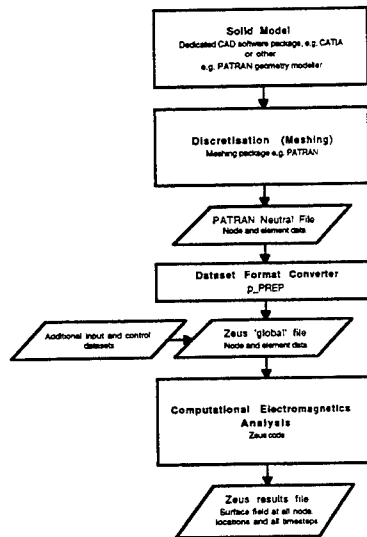
Figure 1: Schematic of PATRAN mesh/Zeus code interface
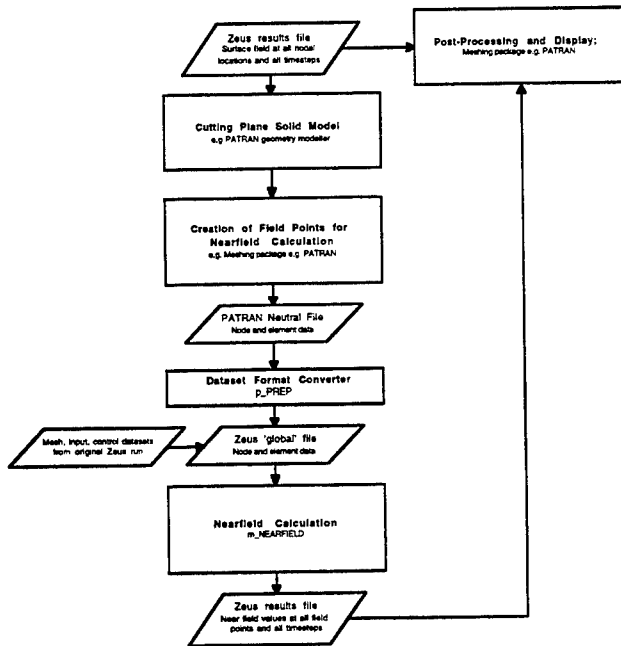
Figure 2: Schematic of near field calculation and results display procedure
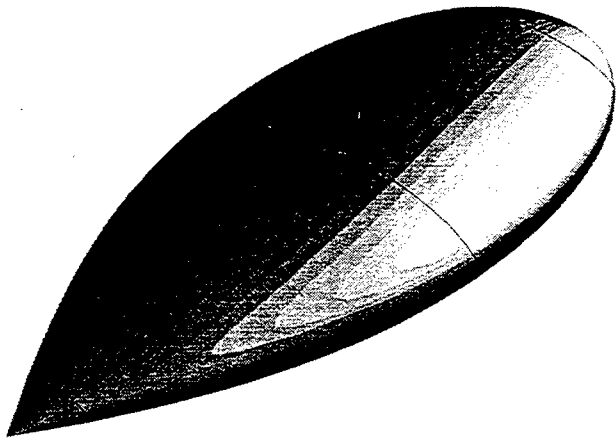
Figure 3: Solid Model of NASA Almond
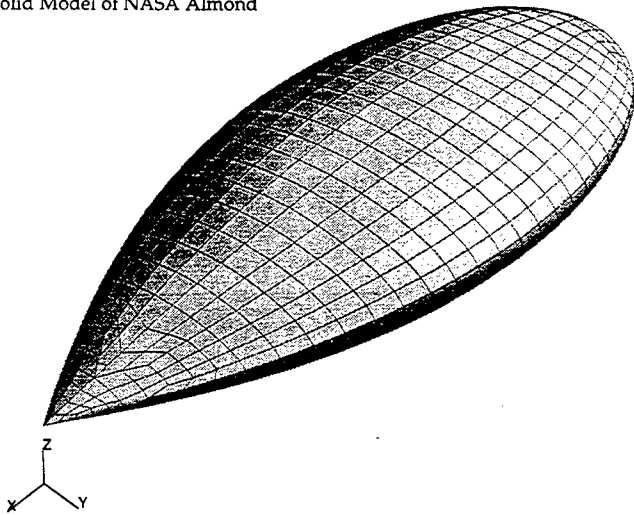
Figure 4: 2450 Node mesh of NASA Almond

1.723
1.609
1.494
1.380
1.266
1.151
1.037
.9224
.8080
.6936
.5792
.4648
.3504
.2360
.1216
.007204

Figure 5: 2450 NASA Almond at 7GHz. Harmonic wave, propagating in -x, VV polarisation. Main picture: magnitude of H field. Inset: vector plot of H field at selected nodal locations.

FRINGE PLOT LC=2.49 RES=1.1(VEC-MAG) MSC/PATRAN R-5.1 EMsolver 10-Jan-97 15:29:55

2.423
2.262
2.100
1.939
1.777
1.615
1.454
1.292
1.131
.9693
.8077
.6462
.4846
.3231
.1615
-.0000001490
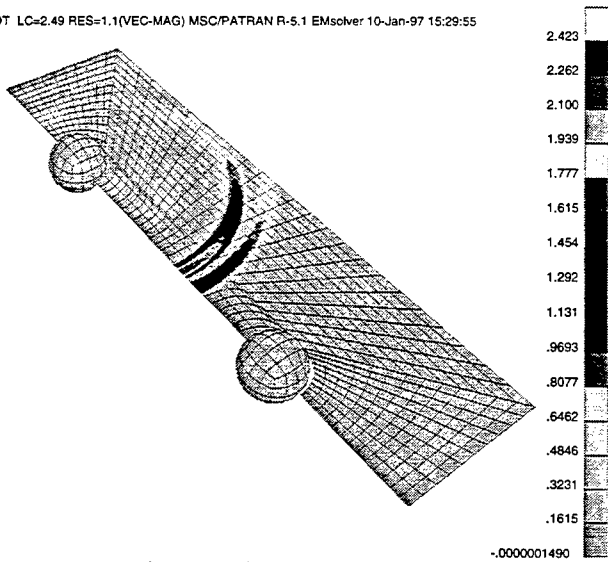
Figure 6: Near field H in region surrounding two spheres. Solution for two spheres obtained using Gauss pulse excitation propagating along a line passing through the spheres (left to right) E polarised in the plane shown.

An Antenna Training Aid Using Electromagnetic Visualisation.

Alan Nott, BEE, CEng, MIEE
Senior Electromagnetics and Software Engineer
and
Deepak Singh BEng (Elec), Project Engineer
Army Technology and Engineering Agency (ATEA)
Department of Defence, Australia.
email: nott@atea.mat.army.defence.gov.au

Abstract.
Antenna radiation patterns can be represented as three-dimensional surfaces in space, gain being specified with respect to two angles theta and phi, or in azimuth and elevation. Graphical methods have been the traditional means of conveying information on the pattern shapes. Using the rendering and animation package 3D Studio®, three dimensional images can be produced that dramatically convey pattern characteristics that would otherwise require a multitude of graphs to convey. This paper describes in some detail a method of production of such images and their application to a computer based aid training being developed for signals personnel of the Australian Army.

Background.
Both the Australian Army and Navy make significant use of high frequency (HF) communications for a variety of scenarios. While the prevailing ionospheric conditions play a vital part in the success or otherwise of HF communications to locations over the horizon, without adequate knowledge of the radiation patterns of antennas at both ends of the transmission path, all but trivial communications may not be established. Education of the communicator is vital - particularly when he is dropped into an unfamiliar location and expected to have his HF link up and running within ten minutes. Some have developed an 'antenna intuition' from years of experience. The less experienced have to rely on whatever training they have been given. Any improvement in the training can be expected to provide a corresponding improvement in communications availability. For this reason the Australian Army Technology and Engineering Agency (ATEA) is developing a series of computer based interactive training aids to convey the nature of radiation patterns in a fast but memorable way. Up to 50000 images of antenna radiation patterns are stored on a compact disk (CD), which can be viewed with a purpose-written viewer.

The images are created with ATEA's AutoNEC capability (refererence 1), which was originally conceived as a useful interface to the Lawrence Livermore Laboratory's Numerical Electromagnetics Code (NEC). AutoCAD® was customised to provide a model creation environment for NEC, as well as a means of creating three dimensional drawings of antenna radiation pattern data from the results of the modelling, and makes extensive use of AutoLISP® procedures. This capability has been extended with interfaces to the rendering and animation program 3D Studio. Still and animated 3D images of radiation patterns can be readily produced which provide a far greater perception of radiation pattern characteristics that the multitude of graphs that would otherwise be needed.

Range of antennas and configurations.
The training aids are primarily designed to support the RAVEN HF single channel radio equipment in service with the Australian Army. Apart from a range of vehicle installations and manpack configurations, each with its specific antenna types, the RAVEN antenna suite consists of a range of wire antenna kits which can be configured into a wide variety of tuned and untuned antennas. These can be erected at varying heights above ground, with and without reflectors and counterpoises, and will be used over a variety of soil types ranging from very poor sands to rich moist and highly mineralised soils. The number of generic antenna types in the RAVEN suite is fourteen, each of which will be modelled over three soil types loosely described as poor, average and good. The range of heights at which an antenna can be erected will depend on its type, and as a minimum, three will be considered for each antenna.

® 3D Studio, AutoCAD and AutoLISP are registered trademarks of Autodesk Inc.

Description of the Training Aid.
The training aid consists of CD for each antenna type. The CD contains sets of image files for the antenna, together with a viewer and auxiliary files. An viewer allows the user to view the images in a meaningful order under mouse and keyboard control, allowing interactive viewing of the effects on the pattern of frequency, ground type, height above ground and other factors. The user can adjust his viewpoint in azimuth and elevation, thus enhancing his perception of the three-dimensional characteristics of the pattern. The radiation pattern is displayed over an image of the ground appropriate to the soil type. This not only reminds the user of the soil type, but provides natural reference points for antenna and pattern orientation. Other sections of the display show textual data such as the antenna name, configuration, height, frequency, and soil type. A line drawing of the antenna is also shown, viewed from the same viewpoint as the antenna pattern. Viewpoint azimuth and elevation are also shown.

Generation of antenna data.
The RAVEN broad band antennas have fixed geometry across the HF band. Models of the antennas are created as AutoCAD line drawings and have diameter, excitation, loading, and other data appended as extended entity data. A procedure written in AutoLISP, runs within AutoCAD to create a NEC-like geometry file, together with an auxiliary file containing excitation, loading, network and other data. A further procedure written in TurboPascal performs some error checking on the model, assigns wire diameters where not specified, and assigns wire segmentation as a function of frequency. It then merges the auxiliary data file to create a series of NEC input files, one per frequency, complete with control 'cards'. A batch file is created to run the job. The use of separate files for each frequency allows different segmentation for different frequencies, thus maintaining optimum segment lengths. It also reduces the problems associated with recovery after a power failure while running NEC, as the data from frequencies already processed is not lost.

The tuned antennas have wire element lengths which are changed by the user to suit the particular frequency. This information is supplied in a table supplied with the antenna kit. The antenna is drawn in AutoCAD in the usual way and a single frequency NEC input file generated. Using this as a prototype, together with data from the antenna geometry table, a purpose-written program is created which produces a series of NEC input files over the required frequency range, and a batch file to run the job.

After the NEC runs are completed successfully, the radiation pattern data across the band is extracted and written to a single file. This file contains one table of antenna gains for each frequency, the antenna data being for one antenna configuration, soil type and height. The file also contains an audit trail showing the processing to that time.

Experience has shown that five degree increments in azimuth and elevation (or theta and phi) provides sufficient angular resolution for most antennas, and this resolution has been used almost exclusively for this work. As the antennas concerned are ground-based, antenna pattern data is only obtained for the upper hemisphere. This gives a total antenna gain dataset of 1368 points per frequency.

Creation of antenna pattern surfaces.
Using another AutoLISP procedure, the radiation pattern file is read into AutoCAD to create a series of three-dimensional surfaces with their origins at (0,0,0). Each surface consists of 1368 3D Faces and is on its own layer, corresponding to the data for one particular frequency. The sequence of layer names 'RP02' to 'RP30' has been used to cover the HF band, corresponding for the frequencies from 2 to 30 MHz. The vertex creation order of these faces should be such that they have an outwards-facing normal - *i.e.* the vertices are created in an anti-clockwise order when viewed from outside the pattern. This ensures proper rendering in 3D Studio, without having to force 2-sided rendering, which significantly increases processing time. The face creation order is unimportant, except that it must be the same for each surface.

The same procedure then produces a .DXF (drawing exchange format) file which is used to transfer the radiation pattern surfaces to 3D Studio. It has been found that a number of AutoCAD commands involving entity selection have the potential to change the order of entities in the AutoCAD database and must be avoided. While having no visual effect on the image either in AutoCAD or 3D Studio, morphing in 3D Studio breaks down dramatically due to the different connectivity of the faces in the morphed objects. Thus although the .DXF file will be larger, it

should be written without using entity selection, and preferably immediately after creation of the pattern surfaces. Although Version 13 of AutoCAD can directly produce 3D Studio (.3DS) files, a procedure is being written that will convert the NEC output files directly into a .DXF file, reducing the handling and the potential for errors.

Use of 3D Studio
Successful creation of images in 3D Studio is not a trivial task, requiring a significant amount of user interaction and understanding of the various processes. A knowledge of lighting and camera techniques is essential, together with the ability to think and draft in three dimensions. A sense of the theatrical is probably another prerequisite if the dramatic potentials of this package are to be completely realised.

3D Studio consists of a number of editors which are briefly described in reference 2. Those mentioned in this paper are the 2D Editor, the Lofter, the 3D Editor, the Keyframer, the Materials Editor and the Keyframer. A full description of each is also available in the 3D Studio handbooks.

To create the images, the .DXF (or .3DS) file is loaded into 3D Studio. This will create a series of objects in the 3D editor corresponding to the gain surfaces in AutoCAD. If the AutoCAD layer names have been chosen ending with a 2 digit numeric string, they will be transferred directly to 3D Studio. Their origins will be at (0,0,0).

Once loading is complete, all but one surface - RP02 - is hidden by the user. A suitable material is then attached to this object. Of the 180 or more standard materials that come with 3D Studio, blue marble has proved the most useful for depicting radiation patterns. It has dark striations, and although not having any significance in the radiation pattern context, these enhance the perception of shape. As the material is textured, mapping must also be applied to the object. Spherical mapping is used, with its axis passing vertically through (0,0,0).

If the patterns are to be displayed above a representation of the ground, a ground object should be added at this time. Section of a sphere is used as its curvature enhances the perception of distance in the final images. A sphere of appropriate size is created at (0,0,0) in the 3D Editor and excess faces deleted. It is then repositioned with its upper surface just below the radiation pattern object RP02. Hills and valleys can be created by judicious manipulation of the vertices of this object. An aerial photograph of the required ground is then attached to this surface. Before this can be done a material referencing the image file must first be created in the Materials Editor.

If an illustration of the antenna is to be included, it can be created using the tools available in the 3D editor, or imported from AutoCAD (using another DXF or 3DS file) if a suitable drawing available. Note that AutoCAD line drawings will not import as renderable objects in 3D Studio, and that a 3D Face drawing will have to be created. This can be created in AutoCAD by overlaying the line drawing with 3D Faces with the Object Snap set to END. As with the radiation patterns, vertex creation order should be consistent with outwards-pointing normals. Showing the antenna in the same image as its radiation pattern is probably best avoided as it occasionally invokes the question ' Is that as far as the signal goes?'.

Lights must be created in the scene to properly illuminate the radiation pattern object. Spotlights have been found to be of most use, and up to three have been used at different angles to properly illuminate the object. Ambient lighting and omnidirectional lights may also be needed to give proper illumination to the ground surface object. Care should be taken in positioning the lights so that they are sufficiently far away from the largest of the radiation pattern objects as lights unexpected buried within an object can cause some puzzling effects.

The next entity to create is a camera. Like the lights, this must be positioned sufficiently far away from any objects. The camera has two parameters under the heading of RANGES. These control the distance/strength relationship of certain atmospheric effects such as fog. The NEAR distance should be set approximately four times the distance from the furthermost point of any radiation pattern object. The FAR setting should be set about twice that distance.

To provide a suitable background to the scene an image such as 3D Studio's SKY.JPG is used. To enhance the impression of distance, a fog atmospher is also applied. The fog colour should be approximately the same colour as the proposed background, with NEAR and FAR settings of 0 and 40% respectively. With the previously set camera ranges, this should add a suitable haze to distant parts of the scene.

Text can be created using the 2D Editor, and imported into the scene either directly or via the Lofter if some character depth is desired. Alternatively it can be created in an image format in 3D Studio or elsewhere, and an appropriate material created. This is then attached to an appropriate object in the scene. This method saves the repeated processing of the large number of text vertices for every image frame and rendering is significantly faster. Animated text can be added in a similar way using multiple objects. This has been used successfully in other visualisation work, but was not used in the training aid images as other windows outside the antenna pattern image area provide textual information.

Both the camera and lights need to move to set up the various viewpoints and maintain proper lighting. This is a rotary motion and is determined by specifying angles with respect to object pivot points. As neither cameras nor lights can be assigned object pivot points directly, two dummy objects (POINTER01 and POINTER02) are created, the lights and camera deriving their rotational motion by linkage to these objects. As the dummy objects will eventually be hidden, their shape is unimportant except as a visual guide to verifying their correct movement. Long cylinders or cones have been found to be useful shapes. If they are centered at (0,0,0), this will be their default object pivot point.

The next step is to enter the Keyframer to create an animation. This editor allows the hierarchy of objects to be specified, as well as the setting of the various 'keys' which control the object position, rotation, scale, and morphing, lighting and cameras at the appropriate frames of the animation. At this point the scene contains some 32 objects, all but four of which are hidden. Those still visible are the first radiation pattern RP02, the ground and the two pointers. Apart from the ground, animation keys must be assigned to all of these. For the training aid, a frequency step of 1/4 MHz was used to give a smooth image transition with frequency. As the patterns objects are created at 1 MHz increments, intermediate pattern shapes need to be created. This is done by morphing RP02 to a successive patterns (RP03 to RP30) every four frames, 3D Studio creating the intermediate geometries by interpolation. This gives 114 frames per frequency sweep.

Morphing is performed with reference to a fixed reference point for each shape. This will normally be the centroid, although with a some effort it can be manually forced to other locations. However, without specifically setting the reference point for every radiation pattern object, morphing will generally cause the pattern origin (0,0,0) to move, the pattern centroid remaining fixed. This problem was originally corrected manually at each morph key, by making a position adjustment (usually in each of the three dimensions) to maintain the origin of the morphed pattern at (0,0,0). This required a significant effort to achieve a satisfactory result. Another method was to generate a path of position keys calculated from the image shapes within AutoCAD. The current method makes use of Keyscript, a language embedded in 3D Studio and will be mentioned later. The 114 frame key sequence is repeated once for each viewing angle, thus repeating the morphing of RP02 through the patterns from 2 to 30 MHz.

Control of the camera is the next concern. This should be initially set in the 3D Editor to view the pattern from 0 degrees in both azimuth and elevation. Both the camera and its target location and field of view need to be set to accommodate the largest radiation pattern from all the proposed viewing angles.

As POINTER01 and POINTER02 have been created centered on (0,0,0), they can readily be rotated about this point in each axis. At the end of every 114 frames, POINTER01 is stepped 22.5 degrees around a vertical axis. Each step requires 2 keys, the first a step of 0 degrees at the end of the sequence (113th frame) to hold its position, and the second at the next frame of 22.5 degrees to cause an immediate step. POINTER02 is linked to POINTER01 so that the two then move together. Any spotlights lighting the radiation pattern should also have their targets and sources linked to POINTER01 so that they move with it, thus maintaining proper lighting on the radiation pattern.

POINTER02 is stepped by 30 degrees about a horizontal axis at the end of every sequence of POINTER01 (1824 frames), again requiring 2 keys to generate an immediate step. POINTER02 thus steps in azimuth by virtue of its linkage to POINTER01, and in elevation in response to its own rotation keys.

The preceeding key sequences have created three nested loops. The inner loop controlling the morphing of the radiation pattern object RP02 from 2 to 30 MHz, the next stepping POINTER01 in azimuth in 22.5 degrees increments, and the outer loop stepping POINTER02 in elevation in 30 degree increments.

The camera target and its body are then linked to POINTER02, thus following its motion and allowing the radiation pattern frequency sequence to be viewed with 22.5 degree steps in azimuth and 30 degree steps in elevation. The complete sequence spans 5537 frames. It requires the creation of over 11000 keys and presents a formidable task if done manually. Fortunately 3D Studio now has an embedded language called Keyscript - a BASIC-like language with Pascal record constructs. It has the ability to extract and manipulate the parameters of 3D Studio objects. The extents of the morph objects can be read and used to adjust the position of RP02 to maintain its origin at (0,0,0) during morphing. Only 70 lines of code is needed to generate the required keys, reducing the time needed to set up keys from over a week to less than a minute. The code can be reused providing the structure of object names, locations, hierarchies and linkages is maintained.
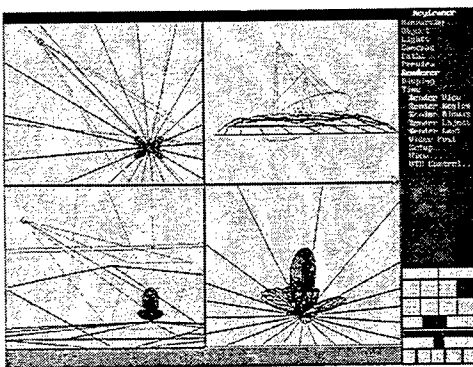
Fig 1: 3D Studio keyframer screen showing lights, camera, the radiation pattern and the ground objects.
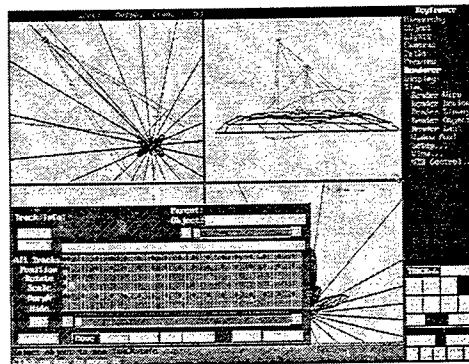
Fig 2: showing some of the 11000 keys set up in the keyframer.

The images are created by invoking the Renderer. The Renderer will produce images in a number of different screen resolutions. A resolution of 640 X 480 pixels is used in the training aids as it gives the best compromise between image quality and viewing speed. Images can also be created in a number of formats including a number of the standard single-image formats such as .GIF, .TGA, .TIF, .JPG and .BMP as well as the animation format (.FLC). The Joint Photographic Experts Group (JPEG) .JPG format, provides excellent image quality for non-textual images, and with proper choice of compression, generates a small file without materially degrading image quality. File sizes of 10 to 30 kbyte are typical, compared with 100 to 300 kbyte for other common formats. For these reasons .JPG was chosen for use in the training aid. When producing single images, the Renderer generates a file name consisting of the first four characters supplied by the user, the remaining four being the frame number.

Rendering time is a function of the complexity of the scene geometry, lighting, and materials. For the images created for the training aid typical times were between 20 and 50 seconds per frame with a 150 MHz Pentium processor. Each sequence of 5537 frames takes just on three days to complete. Images for one antenna, over three grounds and at three different heights takes about 1 month of CPU time.

Viewer
A special purpose viewer is being developed for this application. In addition to displaying the radiation pattern images themselves, auxiliary textual parameters associated with the antenna pattern are displayed in a small window. These include the antenna name and description, together with details of its current configuration, frequency, height above ground, ground type, and the viewpoint azimuth and elevation. Because of the amount

of information, this is split into three scrollable pages. To provide correct perception of the antenna orientation, a second window displays a line drawing of the antenna viewed from the same viewpoint as the antenna pattern. In addition a linear display indicates frequency, and other windows show viewpoint elevation and azimuth scales. A further window displays current program status and other parameters associated with debugging. It is planned to add a conventional plot of a horizontal cut of the radiation pattern at a nominated takeoff angle. This would be overlaid on the azimuth scale.
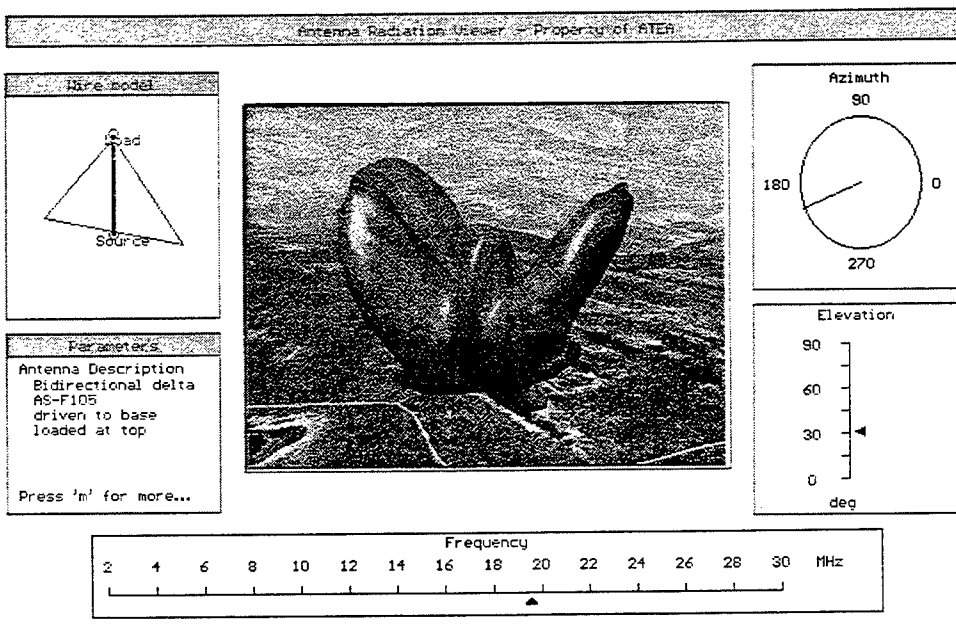
The frequency, viewpoint elevation and azimuth can be changed by the user under keyboard control. These functions will eventually be transferred to mouse control. Selection of antenna type, ground type and height above ground can also be user selected. These parameters are processed by the program to uniquely define a directory and file name, the file then being displayed in the radiation pattern image window and the other displays updated.

Radiation pattern display.
The radiation pattern images are created in 640 X 480 pixel format, with 256 colours, requiring a SVGA display. This mode was chosen as it provides a suitable large display space with an adequate palette range. Its wide support across the diverse range of personal computer platforms also made it a practical choice with regard to the issues of hardware and software support.

As previously noted, the file format is .JPG. Since .JPG is a compressed image format, a decompression procedure had to be written. A number of the decompression parameters are not fixed and require a careful

choice for optimum performance, particularly where the parameters interact. The choices include the final image dimensions, single or double pass quantisation, a range of discrete inverse cosine transforms, the method or absence of image dithering, and the number of colours used in the final image. For this application, single pass quantisation is used for its timely processing of reasonable quality images. The standard (type 3) transform is fast and provides adequate images. Floyd-Steinberg dithering was found to provide the most realistic image quality with minimal overheads. As the generation of a new screen image takes about 0.5 second with a 150 MHz Pentium, the operation appears relatively interactive.

Implementation issues.
Because of the target computing environment, the training aid had to be capable of operating with a Microsoft DOS 6.2 operating system. This presented some interesting problems as there is little support for the required screen resolution. Code had to be developed in full, rather than relying on such luxuries as dynamically linked libraries to supply many of the functions. The image processing routines were adapted from those of the Independant JPEG Group (IJG). While these routines were largely successful and reliable and are easily incorporated into the mainline program, over-reliance on these codes may have resulted in palette control problems.

Palette aspects.
In order to achieve the greatest flexibility, the number of colours available for image display should be as high as possible. For SVGA, the colours available for display are stored in a palette of 256 24 bit locations. During loading of the .JPG image, its palette information is transferred to the display palette. This was done by code supplied by the IJG. Depending on the number of colours used in the image, this code may not always load the full 256 colours. However, if 256 colours are loaded, those palette locations already designated for display of the auxiliary data will be overwritten. The radiation pattern image will display correctly but other sections of the display will appear in unpredictable colours. To overcome this a technique had to be devised to force those colours required for the auxiliary display to be present in all the .JPG images, and to have the same palette location. This involves the capture of palette data from a sufficient number of the images of each series, and the creation of a new palette which includes these colours and the colours required for the auxiliary display. The colour order is then adjusted to force the colours for the auxiliary display into the required locations. This palette is then used in 3D Studio to generate the complete suite of .JPG images.

Mouse problems.
Considerable difficulty has been experienced in achieving the desired program control from the mouse. Mouse implementations which work well with a 320 X 200 screen resolution had to be rewritten to accommodate the 640 X 480 resolution. Although mouse movement can be sensed and position information extracted, the cursor is not visible in the 640 X 480 mode. In addition the range of vertical cursor movement available is limited to the top half of the screen. Coding at a low level will no doubt be needed and other priorities have prevented fully addressing this problem at this time.

Memory issues.
Due to the limitations of the DOS environment, memory usage is a sensitive issue. Problems often do not become evident immediately but occur when other unrelated programs are run, indicating over-writing of areas of the operating system. Careful construction and checking of the code is required to prevent sporadic corruption of critical memory areas.

Conclusions.
The training aid being developed has shown considerable potential in the conveying of the complexities of antenna radiation patterns. Reusable procedures have been devised that greatly simplify the process of image creation. Although skill in both antenna modelling and the use of 3D Studio are re-requisites, the process itself is largely routine providing that the established procedures, structures and hierarchies are observed. Some work is still to be done in developing a reliable and intuitive viewer for the images.

References
[1]   A. Nott "AutoNEC - A Marriage of Convenience" published in the Proceedings of ACES 10th Annual Review of Progress in Applied Computational Electromagnetics, Monterey, CA, March 21-26, 1994, Volume 2, pp 380 - 387.

[2]   H.A. Nott "Electromagnetic Visualisation Using Commercial Software" published in the Proceedings of ACES 12th Annual Review of Progress in Applied Computational Electromagnetics, Monterey, CA, March 18-22, 1996, Volume 1, pp 326 - 333.

The Fieldinspector: A Graphic Field Representation System

P. Leuchtmann and A. Witzig

Lab. of El.-mag. fields and Microwave Electronics, ETH Zurich
CH-8092 Zurich, Switzerland
e-mail: `leuchtmann@ifh.ee.ethz.ch`

Abstract: *The paper describes the* `fieldinspec-`
`tor`*, a 3D system for graphical EM-field represen-*
tations including animations. Conceptually the user
may interactively construct both flat and curved sur-
faces in 3D. Then, the EM-field is drawn on these al-
most arbitrarily located surfaces, using arrows, shad-
ing, contour lines, field lines etc.

The `fieldinspector` *needs any calculation pro-*
gram being able to give the $\vec{E}$*- and* $\vec{H}$*-vectors in any*
particular point. The interface to this external pro-
gram is described in this paper. The `fieldinspec-`
`tor` *calculates all other vectors and scalar quantities*
and 'draws' them into an arbitrary number of viewers
to show the same field from different view points and
in different magnifications. In each viewer a sep-
arate animated representation may be created. For
teaching purposes the `fieldinspector` *is currently*
installed in the students computer network at the
Swiss Federal Institute of Technology.

1. Introduction

The graphic representation of EM fields is very useful
for getting a deep understanding of the field behav-
ior. In this paper we describe the `fieldinspector`,
a 3D system for graphical field representations in-
cluding animations. Note that the `fieldinspector`
is not a field calculation program but only a tool to
draw nice pictures of electromagnetic fields which are
calculated by a second program called `fieldcalcu-`
`lator`. For the examples in this paper the MMP-
package [1] was the `fieldcalculator`.

Figure 1 gives the principle interaction scheme
between the `fieldinspector` and the `fieldcalcu-`
`lator`.

In the first (and main) part of this paper we de-
scribe the `fieldinspector` from the users point of
view. Section 2 treats the principles of construct-
ing geometrical objects such as lines and surfaces on
which the fields are to be represented. In section
3 we discuss all the possibilities for 'drawing' fields,
while section 4 deals with animations. The features
for numerical field output as well as the integration
of specific field quantities is treated in section 5. Fi-
nally, in section 6 we discribe the `fieldinspector`
form the 's point of view and discuss the interface

between the two programs.

2. The Construction of Geometrical Objects

The fields to be drawn are real 3D vector fields. Since
it is usually too complicated to look at real 3D fields
at one time the `fieldinspector` shows fields only on
surfaces being constructed by the user. For this pur-
pose the `fieldinspector` includes a 3D construction
tool which we briefly describe in this section.

The `fieldinspector` allows you to look at all
constructed object by *viewers* (i.e., a window on the
screen). Each viewer gives a picture of the same
situation but from a different point of view. The
mouse cursor may be used in any viewer to set *points*.
In the second construction step several points define
lines. Both straight lines and circular arcs are pos-
sible. The third construction step produces *surfaces*
from lines and/or points. E.g., three points define a
parallelogramm or, as a second example, a line to-
gether with a revolution axis and a revolution angle
define a surface of revolution.

Any point, line or surface may be both moved
along an arbitrary vector at any time and/or ro-
tated around an arbitrary axis and/or stretched or
shrinked with different factors in different directions.
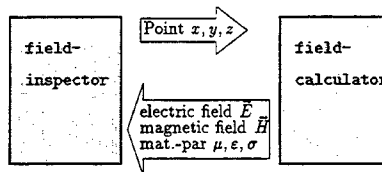
Figure 1: Two programs are working together. The
`fieldinspector` asks for the field values — electric
field $\vec{E}$ and magnetic field $\vec{H}$ — and the material
properties (permittivity ϵ, permeability μ and con-
ductivity σ) at a given location x, y, z. The field-
calculator delivers these values and then the field-
inspector draws nice pictures.

Since we want to draw fields on these geometrical objects, there is a grid on the surfaces which may be adjusted at any time in order to draw, e.g., more arrows on the same surface.

Note that the (fixed) geometry of the situation is constructed and then drawn in the same way as the surfaces for field representations. However, for a typical fieldinspector-session the fixed model of the particular problem is usually preloaded and drawn in a non transparent way while the surfaces for field representations are drawn as wire grids in order to look through them.

3. The Representation of Fields

Points, lines or surfaces (being constructed interactively as described in the previous section) may be selected by simple mouse click. A further click on "Compute field" makes the fieldinspector asking the fieldcalculator for the field values on the selected locations. Let us use the generic term *field surface* for the geometrical object including the calculated field values, even when the field is calculated only on a line. Thus, each click on "Compute field" creates a field surface.

Since the fieldinspector is basically written for the representation of time harmonic fields (with angular frequency ω and $e^{-i\omega t}$ time dependency) the knowledge of the complex values of both the electric field $\vec{E}$, the magnetic field $\vec{H}$ and the possibly complex material parameters ε (permittivity), μ (permeability) and σ (conductivity) are sufficient for calculating the still complex fields

$$\vec{D} = \varepsilon\vec{E} \quad \text{displacement current density}$$
$$\vec{B} = \mu\vec{H} \quad \text{magnetic induction} \tag{1}$$
$$\vec{j} = \sigma\vec{E} \quad \text{conduction current density}$$

and the complex Poynting vectors

$$\vec{S}^{\sim} = \vec{E} \times \vec{H},$$
$$\vec{S} = \vec{E} \times \vec{H}^{*}. \tag{2}$$

Instantaneous values at the time t for these field quantities are easily obtained by multiplying the complex vectors by $e^{-i\omega t}$ and then taking the real part[1]. The fieldinspector always draws instantaneous values of (in general) time dependent values[2].

For each field surface the fieldinspector may execute one or more *plot jobs*. A plot job is specified by

- the field to be drawn ($\vec{E}$, $\vec{H}$, $\vec{D}$, $\vec{B}$, $\vec{j}$, $\vec{S}$ or $\langle\vec{S}\rangle$)

---

[1] The Poynting vector is $\vec{S}(t) = \frac{1}{2}\Re\left(\vec{S} + \vec{S}^{\sim}\cdot e^{-2i\omega t}\right)$.

[2] The time mean value of the Poynting vector, $\langle\vec{S}\rangle := \frac{1}{2}\Re\vec{S}$ is also possible.
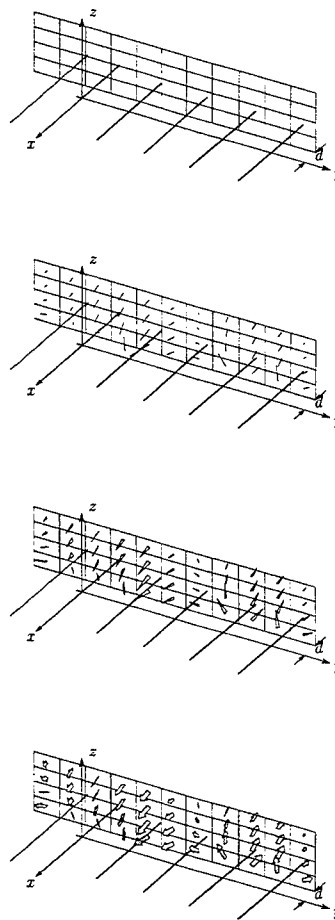
Figure 2: All pictures show the instantaneous value of the electric field. The field is evaluated on the 4×11 rectangle (44 field points) which is at a distance d parallel to the y-z-plane. The underlying problem is a sending yagi antenna with the active element on the x-axis, four directors along $y > 0$ and the reflector at $y < 0$. The picture at the top gives the geometry of the situation only, the second pictures draws simple needles while the two pictures at the bottom give two differently shaped arrows. Note the grid lines which are partly in front, partly behind the arrows/triangles. This is done for giving a more spacial impression of the field.

Figure 3 on the next page gives more drawings of the same field.

- the time phase angle (obsolete for $\langle \tilde{S} \rangle$ and for animated representations [see below!])
- a scaling factor (depends on the field to be drawn)
- the kind of field representation (vectorial: needles, triangles, thick arrows, octagons; scalar: shading, contour lines [flat or lifted with optional logarithmic scaling]). See figs 2 and 3.
- Grid option: Turns the drawing of the geometrical object on/off.

Note that the combination of different plot jobs for the same field surface opens a wide variety of more sophisticated representations. One can draw both $\bar{E}$- and $\bar{H}$-fields at the same time, or the combination of triangles and octagons for the same field leads to the "thumb nail arrows" (middle of fig. 3) giving an improved impression of the fields spatial direction.
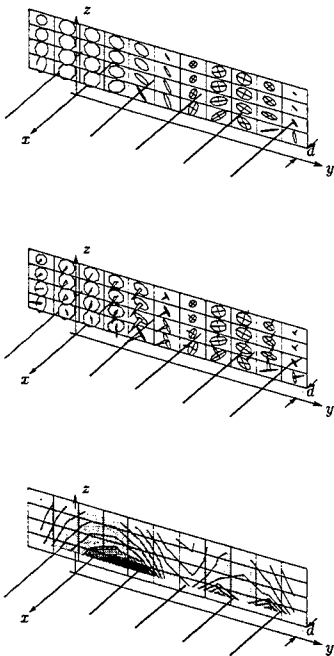
Figure 3: The field of the yagi antenna shown in fig. 2 may be drawn in different ways. While the octagons on top are less impressive the "thumb nail arrows" — obtained as a simple 'superposition' of the triangles in fig. 2 and the octagons at the top of this figure — in the middle are much more instructive. At the bottom contour lines of the field are shown.

More sophisticated representations as well as radiation patterns are given in figs 4–6.
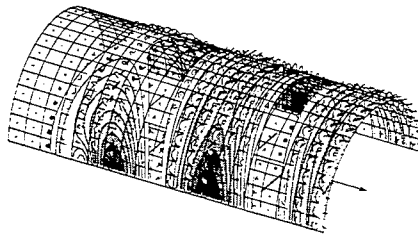
Figure 4: The field around the yagi antenna shown in figs 2 and 3 may also be shown on curved surfaces. The picture shows the instantaneous value of the Poynting vector using both contour lines and "thumb nails" which makes a total of three plot jobs for the same field (two for the thumb nails, one for the contour lines).
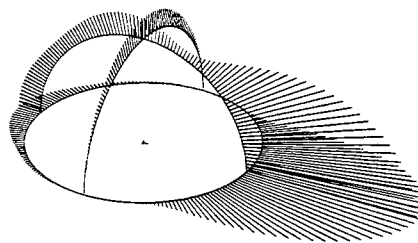
Figure 5: This figure shows the radiation pattern of the yagi antenna shown in previous figures. The antenna is located in the center of the circles. The needles on the circles represent the time mean value of the Poynting vector.

The **fieldinspector** offers also *field lines* to show the spacial behavior of the Poynting vectors time mean value. (Time dependent field lines are hardly ever useful nor are they supported by the **fieldinspector**.) Starting on the $n \times m$ points of a surface, field lines of $\langle \bar{S} \rangle$ may be drawn. In many cases true 3D field lines are more disturbing than clearing your mind. The **fieldinspector** partly overcomes this problem by drawing a grid which may be moved along the field lines, i.e., each grid points is shifted along its field line. The result is a moving grid regularly starting on the field surface and later being distorted in space. See figs 7 and 8 for an example.
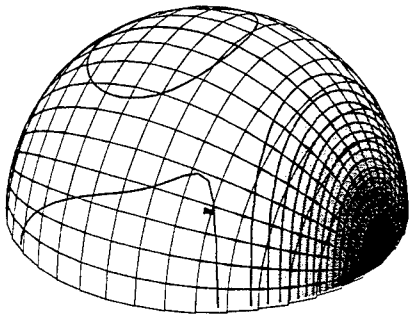
Figure 6: The radiation pattern of the yagi antenna (located in the center of the sphere) is shown using a contour plot of the Poynting vector's time mean value on a half sphere with a radius of 15 wavelengths.

4. Animations

Picture field plots are nice to look at but it is even nicer to see movies. First of all, time dependencies are quite naturally shown in turn, one situation after the other. In such a way the time behavior of fields is easily understood. However, a second aspect of animated representation is evenly important: Since the true 3D-fields must be mapped onto a two dimensional screen, some information is lost in any case. By moving (most preferable: rotating) a 3D static object the human observer becomes a much better idea of the spaciousness.

The **fieldinspector** offers both options: the time film and the rotation film. A click to "Create Film" builds up a normal time film which automatically advances the time phase of all field plots by 20° resulting in 18 pictures per full cicle. A second "Create Film" option only rotates the viewer around an axis by a certain angle. Both the axis and the angle may be specified by the user. Finally the moving field line grid mentioned at the end of section 3 and shown in figs 7 and 8 may also be shown in an animated way.

Creating a film actually produces a series of bitmaps which may be run later on, either by stepping forward or backward one picture a click or by running it at a rate of about 10 pictures per second. For time harmonic fields the film is repeated always starting from the first picture while for rotation films (with total rotation angle less than 360°) and for moving field line grids the film may be repeatedly run forward and backward.
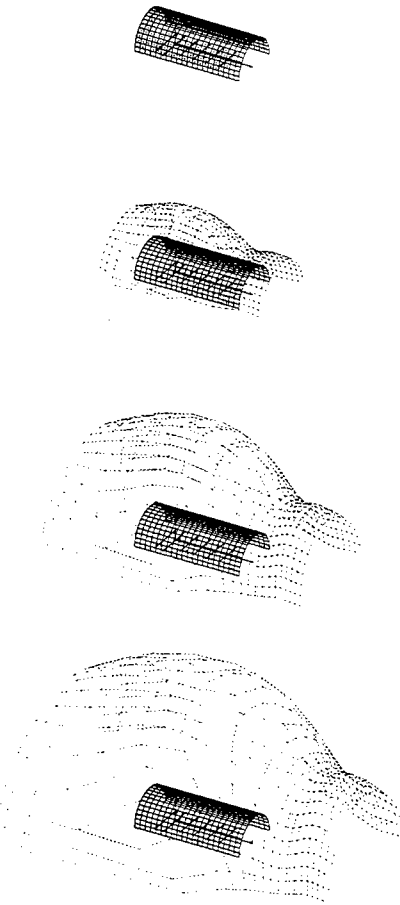
Figure 7: The picture shows a series of dotted grids which follow the field lines of the Poynting vectors time mean value. See fig. 8 on the next page for the field lines itself.
Note that the field lines start on the curved surface which was already used in fig. 4. The distortion of the grid towards the right hand side indicates a stronger radiation in that direction: The finer the distorted grid the stronger is the radiation.
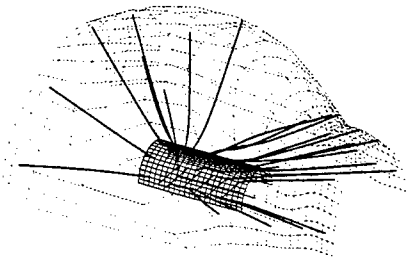
Figure 8: The same as the bottom picture of fig. 7 but with added field lines of the Poynting vectors time mean value. Most field lines are pointing to the right which is the direction of main ration.

5. Integrals and Numerical Output

Though graphic field representations are very useful to obtain a qualitative impression of the EM-field behavior one may be interested in numerical values as well. The **fieldinspector** offers two features for this purpose:

- numerical field values at any location, both complex amplitudes or instantaneous values of

$$\vec{E}, \ \vec{H}, \ \vec{D}, \ \vec{B}, \ \vec{j}, \ \vec{S} \text{ or } \langle \vec{S} \rangle$$

- integrals of fields along user definable lines or surfaces:
    - $\int \vec{E} \cdot \vec{dl}$ (voltage)
    - $\int \vec{H} \cdot \vec{dl}$ (current, if closed line)
    - $\int \vec{D} \cdot \vec{dA}$ (charge)
    - $\int \vec{B} \cdot \vec{dA}$ (magnetic flux)
    - $\int \vec{j} \cdot \vec{dA}$ (conduction current)
    - $-i\omega \int \vec{D} \cdot \vec{dA}$ (displacement current)
    - $\int (\vec{j} - i\omega \vec{D}) \cdot \vec{dA}$ (total current)
    - $\int \vec{S} \cdot \vec{dA}, \int \vec{S}^{\sim} \cdot \vec{dA}$ (complex powers)

Thereby, $\vec{dl}$ is the vectorial line element and $\vec{dA}$ is the vectorial surface element pointing normal to the surface.

6. The Interface

fieldinspector — fieldcalculator

As already mentioned in the introduction the **field-inspector** works together with the **fieldcalculator**. The latter is a second program performing the evaluation of the EM field. The name of the **field-calculator** program may be specified in a command line option of the **fieldinspector**. Note that the **fieldcalculator** is only started on request.

It is supposed that all the information needed for one particular problem is stored in files located in the same directory. This information is split into two groups: the file for the **fieldinspector** (with default name MODEL) and the file(s) for the **fieldcalculator**. To make things more clear we describe the actual procedure to be performed for calculating the field in a single point of a particular problem. After having started the **fieldinspector**, you have to

① find the working directory in the **fieldinspector**'s filer and double click MODEL. This file contains the geometry of the problem in **fieldinspector** format. If MODEL is empty the following procedure still works but you see at the beginning only free space (i.e., nothing than the coordinate axes) in the **fieldinspector**'s viewers. The **fieldinspector** automatically opens unix-pipes and starts the **fieldcalculator** as a child process using the command which has been specified in the respective command line option of the **fieldinspector**. The **fieldcalculator** usually assumes the presence of some input files containing the full information of the problem in its own format.

② Now the **fieldcalculator** is in a "waiting for input" status. As soon as the **fieldinspector** needs a field value the following two line string is sent to the **fieldcalculator**:

<div align="center">

102 0

1 x y z

</div>

The first line contains the key sequence for single points and the second line contains an integer key[3] plus the coordinates of the field point. The **fieldcalculator**'s answer on this request are the six lines

<div align="center">

202 0

domain number

E_{xr} E_{xi} E_{yr} E_{yi} E_{zr} E_{zi}

H_{xr} H_{xi} H_{yr} H_{yi} H_{zr} H_{zi}

waiting for input

waiting for input

</div>

The first line is the answer key sequence for single points, the second line contains the integer number of the domain[4], the third line is for $\vec{E}$ (cartesian components, real and imaginary parts) and the forth line is for $\vec{H}$.

For a full regular $m \times n$-array of field points, the

---

[3] 1 stands for total field. −1 for the scattered field only.

[4] A list of domains and their material parameters is stored in MODEL. If MODEL is empty, the **fieldinspector** uses vacuum parameters.

53

`fieldinspector` sends only five lines:

$$104\ 0$$
$$x_c\ y_c\ z_c$$
$$x_1\ y_1\ z_1$$
$$x_2\ y_2\ z_2$$
$$m\ n\ 0\ 1$$

where the vectors $\vec{r}_c = (x_c, y_c, z_c)$, $\vec{v}_1 = (x_1, y_1, z_1)$ and $\vec{v}_2 = (x_2, y_2, z_2)$ specify a parallelogram (center $\vec{r}_c$ and sides $\vec{v}_1$ and $\vec{v}_2$). m and n are the number of points along $\vec{v}_1$ and $\vec{v}_2$ respectively. The `fieldcalculator`'s answer for this request is

$$204\ 0$$
domain number
$$E_{xr}\ E_{xi}\ E_{yr}\ E_{yi}\ E_{zr}\ E_{zi}$$
$$H_{xr}\ H_{xi}\ H_{yr}\ H_{yi}\ H_{zr}\ H_{zi}$$
$$\vdots$$
`waiting for input`
`waiting for input`

with lines 2–4 repeated $m{\cdot}n$ times. The order of the points is 'row by row' where one row contains m fieldpoints on a line parallel to $\vec{v}_1$.

7. Closing Remarks

The `fieldinspector` is essentially the graphic part of Peter Regli's mmptool [2]. Several features have been removed, others are new. The goal was to create a tool being independent from a particular field calculation program. The `fieldinspector` is currently installed in the students computer network at the Swiss federal institute of technology to give students the opportunity to look at the fields in their way rather than in the teachers way.

The program runs on sun workstations (Solaris 2.5). It is available from the author.

8. References

[1] Ch. Hafner and Lars H. Bomholt. *The 3D Electrodynamic Wave Simulator*. John Wiley & Sons, 1993.

[2] Peter Regli. mmptool 2.4, program running on sun workstations, available from Peter Regli, email: regli@iis.ee.ethz.ch, 1995. ETH Zurich.

A Data Compression Technique for Antenna Pattern Storage and Retrieval.

Alan Nott, BEE, CEng, MIEE
Senior Electromagnetics and Software Engineer
Army Technology and Engineering Agency (ATEA)
Department of Defence, Australia.
email:nott@atea.mat.army.defence.gov.au

Abstract.
Antenna radiation patterns can be represented as three-dimensional surfaces in space, with gain being specified with respect to azimuth and elevation. The data required to specify a wide band antenna pattern over its upper hemisphere, at angular and frequency resolutions, sufficiently fine to capture its salient features and for its complete frequency range, is not insignificant. Timely access to this amount of data in a limited computing environment can present difficulties. This paper describes some of the work being done at ATEA using data compression techniques to reduce this problem.

Background.
The Australian Defence Force, particularly the Army and Navy make significant use of High Frequency (HF) communications for a variety of scenarios. The effectiveness or otherwise of HF communications depends considerably on the proper choice and use of the antennas at both ends of the communications path. Reliable over-the-horizon (OTH) HF communications continue to present an interesting and complex challenge.

One part of the OTH communications equation is the temporal and spatial characteristics of the ionosphere. Computer packages provide a systematic approach to working with the vagaries of the ionosphere. They exploit the daily, yearly and 11-yearly cyclic nature of the ionosphere, refined with current measurements of ionospheric parameters. They have met with varying degrees of success in predicting path loss, critical frequencies, propagation mode and many other HF communications parameters.

Another vital part of the equation is the proper application of antennas. This involves a knowledge of the radiation characteristics of antennas at both ends of the communications path. Most predictors contain some representation of antenna patterns for a range of different antennas. This embedded data, possibly because of data-storage limitations, generally represents either a single elevation cut of the pattern along the major electromagnetic axis of the antenna, or at worst an omnidirectional radiator. The latter represents a trivial solution. The former assumes that the antenna is always pointed directly towards the distant station - not always the case, particularly when communicating with multiple locations. A further complication arises because the radiation pattern not only changes shape with frequency, but the major axis may not necessarily remain aligned relative to the antenna. If the predictor has access to antenna gain data across the frequency band then these problems can be accommodated. For this reason Australia's ATEA is developing software which incorporates an ionospheric predictor and full circle antenna pattern data. This capability is being developed to optimise the choice of antenna types, locations and orientations, frequencies and transmission times over wide areas and with a variety of geographic and communications scenarios. The package has been called HAGGAI and its 'MAP' screen is shown in Figure 1.
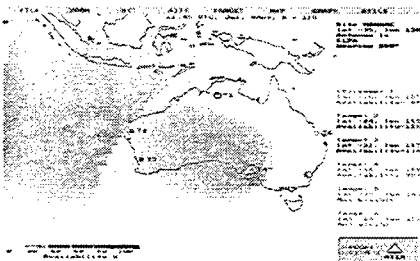
Fig 1: HAGGAI in its 'map' mode (geographic display of data) showing a prediction of percentage availability using a steerable log periodic antenna. This mode is the most computationally intensive, each screen image requiring some 5000 calls to the antenna gain data for each transmission mode under consideration. This is further increased for each alternate antenna which may be considered in an optimising strategy. It is a two pass operation, initially creating large 'pixels' of data with coarse steps of latitude and longitude, followed by one tenth this resolution in user-designated target areas. This considerably reduces processing time, quickly displaying the overall perspective, while still providing fine resolution where needed.

Compression of the antenna data in a way which will also provide fast retrieval as well as interpolation between the original data points, is clearly desirable and is the subject of work at ATEA.

Antenna pattern datasets.
The antenna data is generated using ATEA's AutoNEC capability. This uses a customised version of AutoCAD® as a pre- and post- processor for the Lawrence Livermore Laboratory's Numeric Electromagnetics Code (NEC), to create antenna model geometry. ATEA is currently running NEC-2. The outputs of multiple NEC runs over the frequency range of interest are collated into single files of antenna gain data. If needed, these can be read by AutoCAD to generate three dimensional surfaces of antenna gain for visualisation purposes.

When the work was commenced, a range of antenna pattern datasets was already available from other activities. Antenna types ranged from simple dipoles in free space, or above real grounds, through vehicle and aircraft mounted antennas, to large antennas such as log periodic arrays and rhombics. Five antennas were selected for this investigation to provide a diverse range of pattern types. These were the vertical whip, horizontal dipole, steerable log periodic, vertical delta, and a helicopter wire antenna. Some work was also done with a rhombic antenna. As the antennas were essentially ground-based, the datasets only contained data on the upper hemisphere. Polarisation effects were also ignored at this stage, although they could be processed by the same techniques.
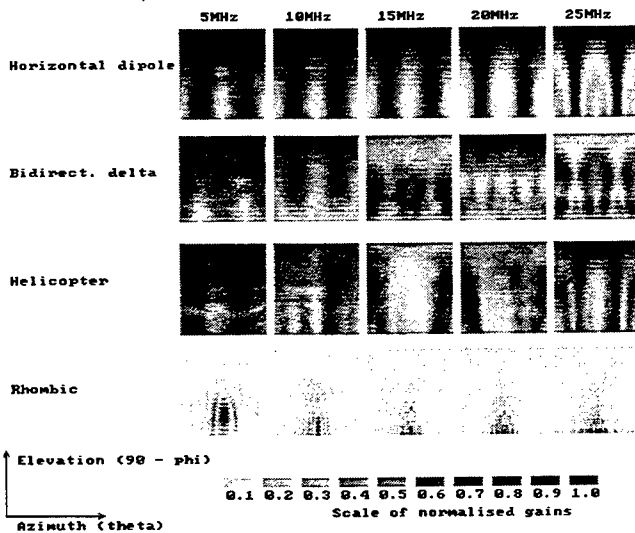
Fig 2: Normalised gain plots for the horizontal dipole, bidirectional delta, helicopter and rhombic antennas.

These images represent antenna gain patterns, sampled at 5 degrees in azimuth and elevation, and at five frequencies across the band.

Antenna pattern statistics.
Examination of many antenna pattern datasets indicates that for most 'well behaved' antennas (those that are not physically large or at a significant distance above the earth) antenna gain data sampled at 5 degree increments in azimuth and elevation provides sufficient resolution. This gives 1368 points per frequency for the upper hemisphere. To store this data as real numbers at 1 MHz steps across the HF band (perhaps an overkill), 169 kbytes is required. Larger antennas such as rhombics, or antennas significantly above the ground can have quite complex patterns and require finer angular resolution to specify the detailed structure. Thus, the rhombic antenna, some 600 feet in length, is undersampled at 5 degree increments. In addition, this antenna was modelled up to 30 MHz, well above the operating frequency range. This greatly contributes to sidelobe

---

®,AutoCAD is a registered trademark of Autodesk Inc.

development, particularly at higher frequencies. It was included in this work to investigate the limitations of the compression techniques and was to prove difficult to compress successfully across the whole band.

Compression techniques.
The compression of any dataset is a process which extracts the essence of the data. This is generally performed by means of transformations based on sets of orthonormal functions. The compressed data only contains those coefficients considered 'significant', the discarded terms resulting in at least part of the compression. A number of transforms could be candidates for this application. They include the Discrete Fourier Transform (DFT), the Discrete Cosine Transform (DCT), and the Discrete Walsh (or Hadamard) Transform (DWT). Literature abounds with references to the use of these transforms, often in relation to image compression or enhancement. Fractal compression is another possible technique, but it was considered too esoteric at this stage to yield a solution in the time required. In this investigation, the Fourier, Cosine and Walsh Transforms were considered. Early work with the DWT showed some initial promise and it is well suited to fast computer coding. However it introduced discontinuities in the recovered data which could only be reduced by increasing the number of significant terms at the expense of compression ratio. The end application also required interpolation of data between the original data points, and the DWT does not readily support this. Both the DFT and DCT performed well, with the DCT providing marginally better compression in most cases. Thus the development has concentrated on the DCT.

The Discrete Cosine Transform is given by

$$F(u,v) = \frac{2}{\sqrt{N_1 N_2}} C(u)\, C(v) \left[\sum_{x=0}^{N_1-1} \sum_{y=0}^{N_2-1} f(x,y) \cos\frac{(2x+1)u\pi}{2N_1} \cos\frac{(2y+1)v\pi}{2N_2} \right]$$

where:

$f(x,y)$ is the input data, in this case an antenna radiation pattern dataset having N_1 points in azimuth and N_2 points in elevation,

$F(u,v)$ is a N_1 by N_2 set of DCT coefficients,

$C(z)=1 / \sqrt{2}$ if $z = 0$ otherwise $C(z)=0$, and

N_1 = the number of azimuth data points is 72, and N_2 = the number of elevation points is 19 (for the upper hemisphere of 5 degree resolution antenna patterns).

As HAGGAI uses frequencies which are integer MegaHertz, it was not considered necessary at this point to address compression in the frequency domain. Further work may show that this is also feasible resulting in a further reduction of the total dataset size for any particular antenna. This will inevitably increase the decompression time, and is not warranted in an application which does not require frequency interpolation.

The DCT is not a component by component transformation as all the output values, $F(u,v)$, depend on all the input values, $f(x,y)$. The transformation is also lossless (within the limits of computer rounding) and the original values can be recovered from the full set of coefficients by applying the inverse transform:

$$f(x,y) = \frac{2}{\sqrt{N_1 N_2}} \left[\sum_{u=0}^{N_1-1} \sum_{v=0}^{N_2-1} C(u)\, C(v)\, F(u,v) \cos\frac{(2x+1)u\pi}{2N_1} \cos\frac{(2y+1)v\pi}{2N_2} \right]$$

Allowing x and y to assume non-integer values in the inverse transform permits interpolation in azimuth and elevation between the points of the original dataset.

Many of the DCT coefficients are at or near to zero. If those terms below a given threshold are neglected, a compression results. A higher threshold will result in greater compression. However, if the threshold is set too high then the decompression will become lossy and tracking between the input and output datasets will be degraded. The choice of this threshold will depend on the nature of the input dataset, and on the required tracking accuracy.

Compression criteria.
In order to compare different compression techniques and parameters, a set of test criteria needed to be developed. The choice will vary depending on the nature of the end. The maximum tracking error between input data and the decompressed data should be appropriate in the context of input data uncertainty. This in turn will depend not only on the accuracy of the antenna pattern data computed by NEC, but also on the degree to which the NEC model represents the actual antenna, and the antenna's day-to-day variability. If the compressed model is to be embedded in an ionospheric predictor then predictor uncertainties should also be considered. For incorporation in the ionospheric prediction software described above, the following were considered appropriate:

- The dynamic range of the decompressed antenna pattern should not be less than 20 db.
- Accuracy of the maximum antenna gain is of prime significance
- Accuracy of the minimum antenna gain is of the next significance
- Accuracies of antenna gains between maximum and minimum are of less significance.
- Tracking of antenna gains should be better than 0.5 db at the maximum gain, increasing linearly to 3 db at -20 db below maximum gain.

Methodology.
The antenna pattern data generated by NEC was first converted from db to numeric gain in preparation for compression. Numeric gain is required by HAGGAI and will be recovered by decompression without additional conversion. For each frequency, the maximum gain Gn was extracted and the gains normalised to 1.0. It was envisaged that the compressed data will be stored as this gain factor plus a series of coefficients, thus retaining the same dynamic range for low and high gain antennas. This method also allows a simple comparison of the process against both low and high gain antennas data.

The 72 X 19 array of (normalised) antenna data was then passed through a two dimensional DCT, yielding a 72 X 19 array of coefficients. In image compression, the picture space is typically subdivided, usually into groups of 8 X 8 pixels, and compression applied to these. Ideally the array size is a sub-multiple of the data space size. A 19 X 18 subdivision was considered in this application and although processing was marginally faster, the total number of coefficients was invariable greater for the same tracking error because of the number of groups of coefficients generated. This technique may have advantages for 'busy' antenna patterns such as that of the rhombic.

In order to monitor the quality of the processing, the inverse transform was applied and the original and decompressed datasets compared. For this purpose a special display was devised. This consisted of a 256 colour display of the original data as square blocks, colour corresponding to antenna gain. This was overlaid with a similar display of the decompressed data using smaller circular patches centred on the original squares. The differences in colour not only provide a very sensitive indicator of the tracking between the two datasets, but also show where errors occur. Other sections of the display showed a plot of the 'significant' coefficients, a scatter plot of input/output tracking and various other parameters associated with the processing.

At this point it became apparent that the tracking limits applied at gains less than -20 db should not simply be linearly varying db limits as first envisaged. For this application an antenna gain of -30 db below the maximum could be equally well represented by a gain anywhere between -20 and -1000 db. A revised set of limits were chosen with a constant offset from the input numeric gain rather than an increasing offset from the gain in db, _viz_ if Gi is the normalised input numeric gain, then the upper limit is $Gi+k$, and the lower limit is $Gi-k$. By setting k $=0.1*(\sqrt{2}-1)$, the upper and lower limits at maximum gain ($Gi=1$) are just under 0.5 db, while for 20 db below maximum gain ($Gi=0.1$), the upper limit is -17.9 db, thus approximating the limits originally envisaged for 0 and -

20 db. The corresponding lower limit is -24.6db. At even lower antenna gains, the upper limit asymptotes to -27.6 db, while the lower limit falls to large negative values. This 'exponential' variation of tracking limits provide a more realistic metric for comparison of compression strategies over a wide dynamic range as shown in Figure 3.
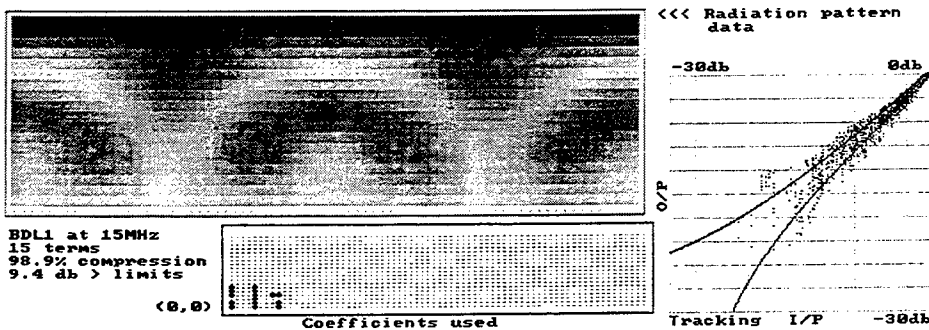
Fig 3: Display for bidirectional delta antenna, showing tracking with 15 coefficients. The tracking error limits are shown as the solid lines on the scatter plot. The grid lines represent 3 db steps from 0 to -30 db. I/P = original data and O/P = data after compression and decompression.

As the array pointers of each DCT term are required during decompression as the variables u and v, each DCT coefficient was tagged with its pointers and sorted in descending order of absolute magnitude.

Tracking error variation with number of terms used in the decompression.

To determine its effect on the tracking error of the decompressed data decompression was applied to the range of antennas and frequencies, using different numbers of terms in the expansion. The following series of plots show the variation of worst case tracking error with the number of terms used in the decompression The results indicate that, with the exception of the rhombic antenna, 100 terms is adequate to recover the original antenna pattern within the proposed tracking error limits. A rough extrapolation suggests that 200 terms might be sufficient for the rhombic. However, if the rhombic antenna pattern were sampled at a resolution finer than 5 degrees, the number could be different.
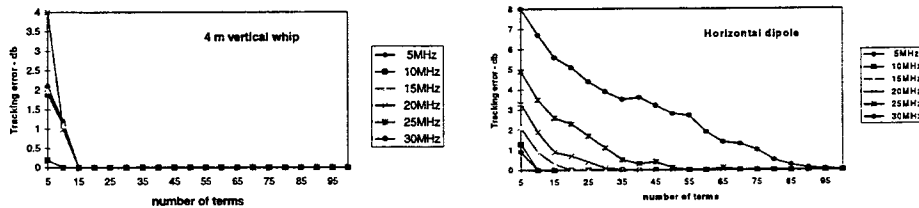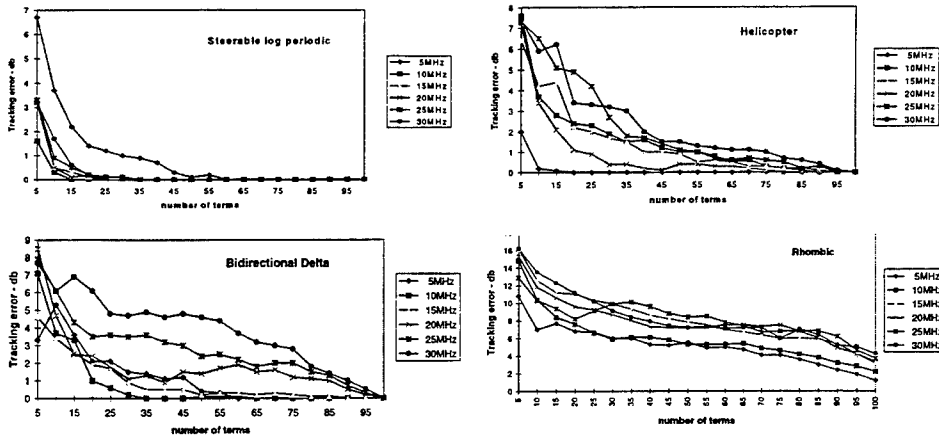
Fig 4: Worst case tracking errors outside proposed limits plotted against number of terms for vertical whip, horizontal dipole, steerable log periodic, helicopter, bidirectional delta, and rhombic antennas.

Figures 5 to 9 are scatter plots showing data recovered by decompression against the original data. These are termed 'output - db' and 'input - db' respectively. If the process is lossless - *i.e.* no tracking error exists, all points will lie on a straight line with a slope of +1 and passing through (0,0). Each plot contains 1368 data points, many of which are co-incident. With the exception of the rhombic, the plots cover a 30 db dynamic range.
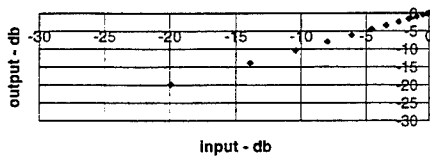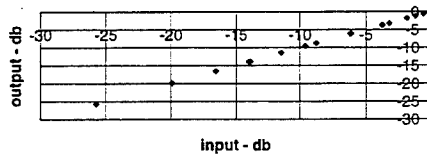
Fig 5: The vertical whip was modelled in isolation above a real ground. It has no azimuthal changes in gain, the variations in elevation being well behaved. Tracking error data is for 35 terms at 5 and 30 MHz. The whip pattern can be recovered adequately from as low as 10 terms per frequency over much of the frequency band.
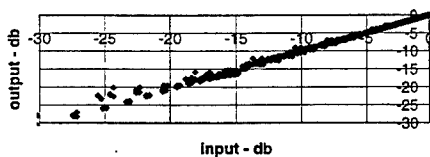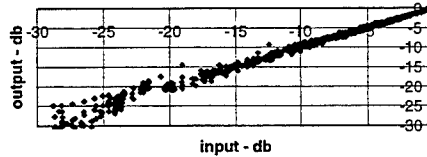
Fig 6: The horizontal dipole is modelled above a real ground. Its gain varies considerably with both azimuth and elevation. Significant changes in the character of its radiation pattern also occur with frequency and height above ground. Although the tracking error is not as low as that of the vertical whip, 35 terms is adequate at 10 MHz, and 100 terms at 30 MHz.

Bidirectional delta @ 30 MHz, 65 terms

Bidirectional delta @ 30 MHz, 100 terms
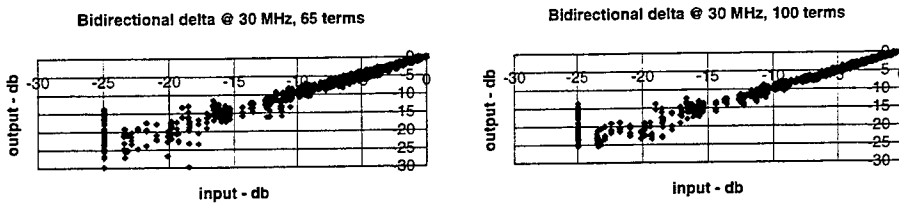
Fig 7: The bidirectional delta is a larger antenna and thus produces a more complex pattern. Although 65 terms are sufficient at 10 MHz, 100 terms must be used at 30 MHz. These patterns show an unexplained 'singularity' type behaviour at an input of -25 db. A single input data value is recovered as a range of output values, depending on its values of azimuth and elevation on the radiation pattern hemisphere. There is also evidence of this at other input values, although the magnitude reduces with the number of terms in the expansion. This behaviour has also been observed on other antennas, but fortunately it seems to be restricted to normalised gains below -20 db, and generally lies within the proposed error limits.

Rhombic @ 10 MHz, 35 terms

Rhombic @ 10 MHz, 100 terms
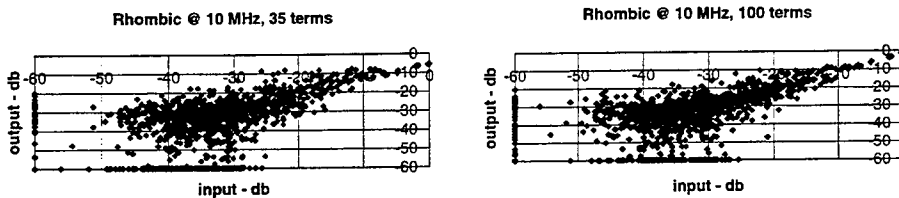
Fig 8: The rhombic data, as previously noted, has very complex patterns. This may be aggravated by undersampling in azimuth and elevation. Plots have been extended down to -60 db as a considerable number of the data points occur below -20 db. At 10 MHz, near the upper frequency limit of the rhombic, the pattern cannot be recovered with the required tracking error with 100 terms. However because the major tracking errors occur at low gains, 100 terms does provide a first approximation which could be used in the coarse resolution mode for HAGGAI. One solution for such 'difficult' antennas would be to save 200 coefficients as two records, with appropriate changes to the decompression code to handle the extra data. Although this will approximately double processing time, it will still yield a useful result with only minor code changes. This proposal will have to be re-examined when finer resolution rhombic data is available.

Horizontal dipole @ 5 MHz, 5 terms

Horizontal dipole @ 5 MHz, 5 terms - adjusted
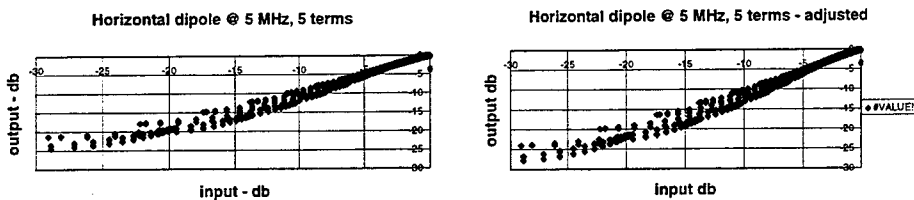
Fig 9: A number of the antennas showed an upwards trend in the scatter plots below -20 db, particularly when low numbers of terms are used in the decompression. Increasing the number of terms reduces this. However a fixed offset applied to the numeric gain, together with an adjustment to the overall gain to maintain the data passing through (0,0), the performance with only five terms can approach that with 35 or more terms. Although not needed in HAGGAI, the addition of the single offset term could provide a dramatic reduction in the data storage requirements in other applications.

File structure.
The work has shown that 100 terms is adequate for all the evaluation antennas except the rhombic. Based on this assumption a record structure for the compressed antenna data was adopted. This consisted of a single record containing the normalising gain factor Gn, the frequency Fq, plus an array of 100 coefficient terms, with their attached pointers. The file contains one record per frequency. Although the fixed record size of 100 coefficients will provide more terms than necessary for antennas such as the vertical whip and the steerable log periodic, the record structure is small enough to be readily handled within the proposed computing environment, and the complication of processing variable size records is avoided.

Performance parameters.
Both Gn and Fq are stored as single precision real numbers, each occupying 4 bytes. The dynamic range of the DCT coefficients is too great for single byte representation, thus integer format is used. Together with their byte array pointers each coefficient occupies 4 bytes. Thus each frequency occupies 408 bytes, compared with the original data size of 5472 bytes (1368 real numbers). Specifying an antenna across the HF band takes 12240 bytes compared with 154 kbytes, a compression of 92%.

The 5000 antenna gain points needed to refresh the HAGGAI map screen are computed in just under six seconds using a 150 MHz Pentium processor. Although this is slightly longer that the processing time of the ionospheric predictor currently employed to cover the same area, it does not greatly increase the overall display refresh time.

Further development.
As the coefficients are stored in descending order of magnitude, an opportunity exists to use a subset of the DCT terms to generate an initial estimate of the antenna gain, thus reducing processing time at the expense of accuracy. This has application to quickly determine whether a particular location is outside the footprint of the selected antenna, so that processing is not wasted on locations that are not visible. Some work has commenced on developing a convergence test to determine where to truncate the number of terms to achieve a given accuracy. This will be a function of the entropy of the antenna pattern and may require an additional control parameter to be stored for each frequency.

Another opportunity for faster decompression arises because the variation in antenna gain with azimuth at high elevations will be less than that at low elevations, degenerating to a single gain figure at 90 degrees (vertical). It would be reasonable to expect that the number of DCT terms required for a specific tracking error would be considerably less for near vertical radiation and this has been demonstrated in a number of cases.

The opportunity also exists to exploit the symmetrical nature of patterns from antennas in isolation and with one or more axes of symmetry, to achieve a corresponding increase in the number of effective terms in the decompression. This will reduce the tracking error without materially increasing data storage requirements.

Conclusions.
The compression techniques developed around the Discrete Cosine Transform have shown significant potential in the reduction of storage requirements for antenna gain data. The technique is simply implemented and yields good results in reasonable processing times from minimal data. It has a built in interpolation capability for generation of data not in the original dataset. It has been shown to be applicable to a wide range of different antenna types, and although not demonstrated to satisfactorily handle the rhombic antenna data as presently available, improvements to the data and extensions to the process should overcome these difficulties. Opportunities exist to refine the techniques to achieve better speed and tracking performance and will be the subject of ongoing work.

SESSION 2:

ADVANCED TIME-DOMAIN METHODS

Chair: S. Gedney

Solution of Boundary Value Problems in Time Domain Using Multiresolution Analysis

Linda P.B. Katehi, The University of Michigan

James Harvey, Army Research Office

1.0 Abstract

The application of multiresolution analysis directly to Maxwell's equations results in new time domain schemes with unparalleled properties. This time domain approach, MRTD (Multiresolution Time Domain Method), allows for the development of schemes which are based on scaling functions only or on a combination of scaling functions and wavelets for the development of a variable griding. The dispersion of the MRTD schemes compared to the conventional FDTD Yee's scheme shows an excellent capability to approach the exact solution with negligible error for sampling rates which approach the Nyquist limit. Furthermore, due to the weak-interaction properties of the wavelets, MRTD schemes allow for time/space-adaptive grids. These recent developments in time domain techniques at the University of Michigan have strongly indicated the potential of MRTDs in creating a major impact to the area of computational electromagnetics [10,11]. MRTD is not a new methodology. It is a correct and accurate generalization of the conventional discretization approaches. It provides the correct mathematical frame for solving problems in time domain and allows for the understanding of important issues in time-domain computational electromagnetics.

2.0 Introduction to MRTD

The finite-difference time-domain method (FDTD) has proven to be a powerful numerical technique in electromagnetic field computations [1,2]. However, despite its simplicity and modeling versatility, the technique suffers from serious limitations due to the substantial computer resources required to

model electromagnetic problems with medium or large computational volumes. In addition, the FDTD method cannot provide the accuracy required for computer simulations of time-dependent electromagnetic interactions in electrically long regions or in regions which contain non-linear materials. Such simulations are very important for integrated device modeling, especially in relation to the design of non-linear photonic devices. The above limitations have always made it a matter of great interest to improve the efficiency of Yee's FDTD scheme and have led researchers to the development of hybrid combinations of FDTD with other propagation methods [3,4] and higher order FDTD schemes based on Yee's grid [5]. The method of moments provides a mathematically correct approach for the discretization of integral and partial differential equations. [6]. Its application to the discretization of Maxwell's partial differential equations has provided the field theoretical foundation for TLM [7,8]. In addition, it has been shown recently [9] that Yee's FDTD scheme can be derived from the same approach when using pulse functions for the expansion of the unknown fields. Since the method of moments allows for the use of any complete and orthonormal set, the choice of an appropriate expansion set may lead to new powerful time domain schemes. The application of the method of moments using scaling and wavelet functions, known as multiresolution analysis (MRA), has been applied to Maxwell's partial differential equations and has lead to novel and powerful time domain schemes [10] and [11].

In a MRTD scheme the electromagnetic fields are represented by a two-fold expansion in scaling and wavelet functions with respect to space. The expansion in terms of scaling functions allows for a correct modeling of smoothly-varying electromagnetic fields. In regions characterized by strong field variations or field singularities, additional field sampling points are introduced by incorporating wavelets in the field expansions. These additional points are introduced only at specific locations, thus, allowing for a variable grid capability. The use of different families of functions leads to various time domain schemes. The exclusive use of scaling functions provides a variety of conventional schemes including FDTD and TLM. The MRTDs which have been recently developed at Michigan have used pulse functions as expansion and testing functions in the time domain in order to obtain a two-step finite difference scheme with respect to time.

MRTD schemes based on cubic spline Battle-Lemarie scaling and wavelet functions have been developed and applied to a variety of problems. An extensive presentation of these derivations is presented in [10]. This orthonormal wavelet expansion has already been applied successfully to the computation of electromagnetic-field problems in the frequency domain and results have been presented for both 2-D and 3-D problems [17,18]. The Battle-Lemarie scaling and wavelet functions do not have compact support, thus the MRTD schemes have to be truncated with respect to space (see Figure 1). However, this disadvantage is offset by the low-pass and band-pass characteristics in spectral domain, allowing for an a priori estimate of the number of resolution levels necessary for a correct field mod-

eling. Furthermore, for this type of scaling and wavelet functions, the evaluation of the moment method integrals during the discretization of Maxwell's PDEs is simplified due to the existence of closed form expressions in spectral domain and simple representations in terms of cubic spline functions in space domain. The use of non-localized basis functions cannot accommodate localized boundary conditions and cannot allow for a localized modeling of material properties. To overcome this difficulty, the image principle is used to model perfect electric and magnetic boundary conditions. As for the description of material parameters, the constitutive relations are discretized accordingly and the relationships between the electric/magnetic flux and the electric/magnetic field are given by two matrix equations.

FIGURE 1.   **Battle-Lemarie Scaling and Mother Wavelet Functions and their Fourier Transforms.**
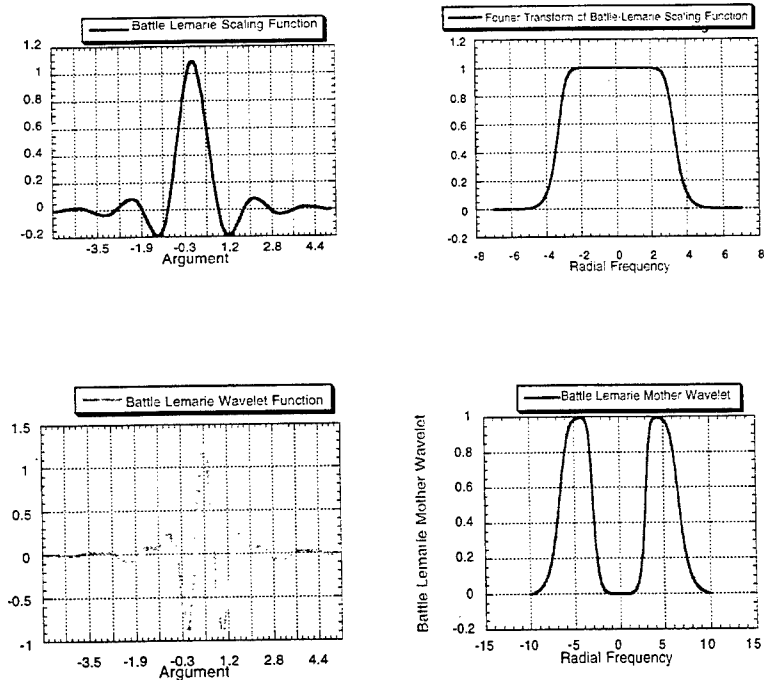
Complete dispersion analyses of the MRTD schemes including applications to 3-D problems and comparisons to Yee's FDTD scheme are given in [10] and show the superiority of MRTDs to all other existing discretization techniques. Specifically, the results show the capability of the MRTD method to provide excellent accuracy with up two points per wavelength which is the Nyquist sampling limit.

The use of Battle Lemarie scaling and wavelet functions has provided very efficient solutions to open and shielded circuit problems. Figure 2 shows field calculations for the even mode excited in coupled strips operating in an open environment. The open boundaries have been accounted for by incorporating PML regions within the MRTD technique. The use of MRTD allowed for the placement of the matching layer right at the planar lines while it provided very high accuracy and high computational efficiency. Figure 3 shows the even-mode electric field distributions for a similar coupled strip geometry operating in a shielded environment [22].

FIGURE 2. **Even-Mode Electric Field Distribution in an Open Coupled Strip Line**
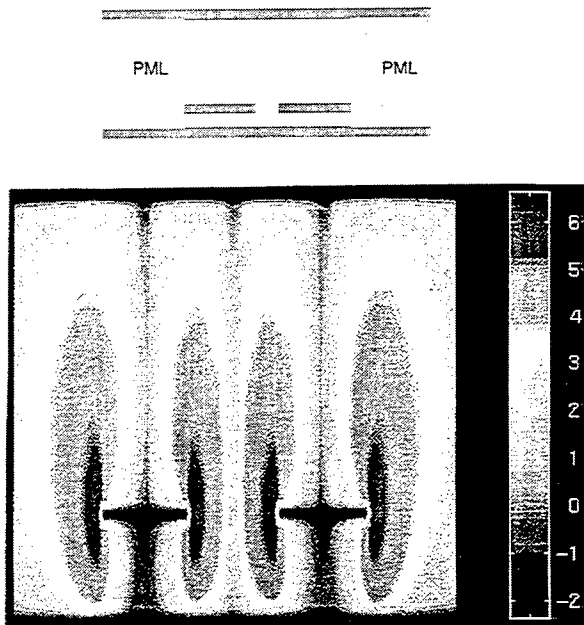
FIGURE 3.   **Even-Mode Electric Field Distribution in a Shielded Coupled Strip Line**
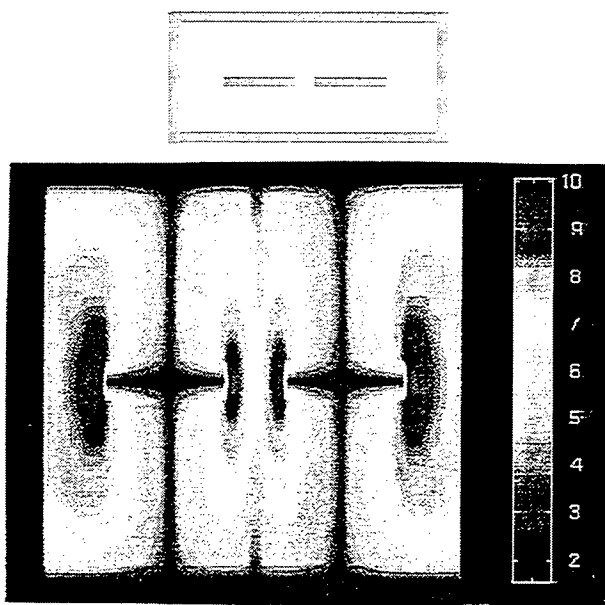
As with Battle-Lemarie functions, the application of the Haar basis functions (see Figure 4) has led into the development of a multigrid FDTD technique [23, 24] and has demonstrated the capability for a spatially adaptive grid in 2-dimensional waveguide and transmission line problems. Figure 5 shows the field distribution in a two-dimensional shielded stripline. On the same figure the spatially adaptive grid utilized in this problem is shown.

3.0 Spatially Adaptive MRTD Schemes

The major advantage of the use of Multiresolution analysis to time domain is the capability to develop time and space adaptive schemes for an open as well as shielded space, and its application to linear and non-linear problems. The effectiveness of the technique will be measured in terms of its accuracy and computational efficiency in comparison to conventional time domain techniques (FDTD, TLM). The development of a spatially and temporally adaptive MRTD method is based on the property of

wavelet expansion functions to interact weakly and allow for a spatial sparsity that may vary with time as needed through a thresholding process [12-19]. The availability of such an adaptive method is extremely important for the accurate modeling of sharp field variations of the type encountered in beam focusing in nonlinear optics, wave propagation through narrow slits and apertures etc. A brief presentation of the fundamental steps required for such a adaptive grid is given in the following section.

FIGURE 4.   Haar Scaling Functions and Wavelets
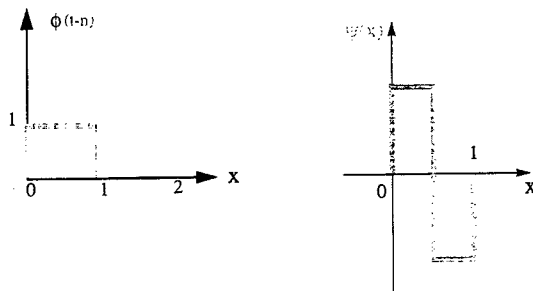
The use of multiresolution analysis for adaptive grid computations for PDEs has been suggested by Perrier and Basdevant [20] and Liantdrat and Tchamitchian [21]. To describe the basic ideas of such an adaptive scheme for Maxwell's hyperbolic system, let us cast Maxwell's equations in one spatial dimension in the form:

$$\frac{\partial}{\partial t}\hat{u} = A\hat{u} \tag{1}$$

where $\hat{u} = (E(z,t), H(z,t))^T$, and A is the operator:

$$A = \begin{bmatrix} 0 & -\varepsilon(z)^{-1}\frac{\partial}{\partial z} \\ -\mu(z)^{-1}\frac{\partial}{\partial z} & 0 \end{bmatrix}. \tag{2}$$

FIGURE 5. Field Distribution in a Printed Stripline Using MRTD Based on Haar Functions
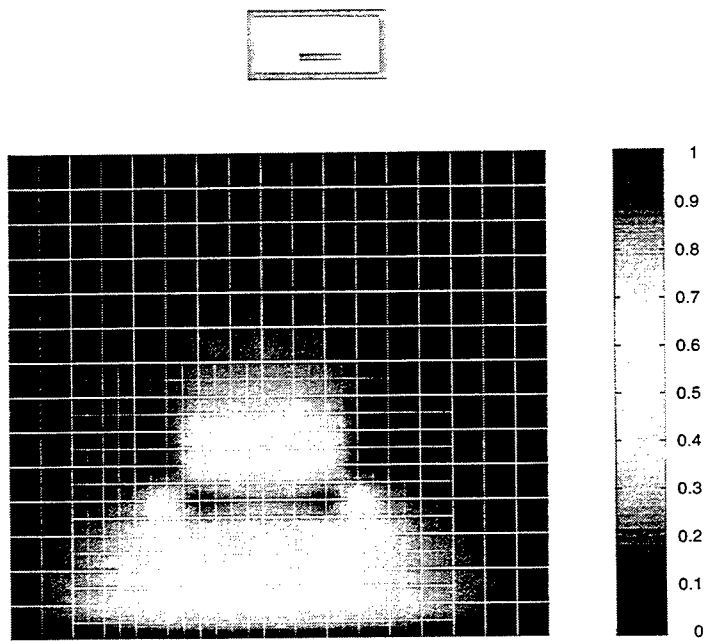
The numerical solution of (1) subject to initial conditions and appropriate boundary conditions at the two boundary points is sought. Following appropriate derivations, the above equation can be written in the following form:

$$M \ |U\rangle = 0 \tag{3}$$

where

$$M = \begin{bmatrix} \varepsilon T^\dagger{}_h d_t & T^\dagger{}_h D_z \\ Z^\dagger{}_h D_z & \mu Z^\dagger{}_h d_t \end{bmatrix} \tag{4}$$

70

In equation 4, Z_h, T_h are half shift operators for the spatial and temporal coordinates z, t respectively and $Z^\dagger_h, T^\dagger_h$ are their Hermitian conjugates. Furthermore, d_t, D_z are difference operators given by the following equations:

$$d_t = \frac{1}{\Delta t}(T^\dagger_h - T_h) \tag{5}$$

and

$$D_z = \frac{1}{\Delta z}\left(Z^\dagger_h \sum_{i=-9}^{8} \alpha_\varphi(i)Z^{-i} + \sum_{i=-9}^{8} \alpha_\psi(i)Z^{-i}\right) \tag{6}$$

where

$$Z^\dagger = Z^{-1}. \tag{7}$$

In equation 6, $\alpha_\varphi(i), \alpha_\psi(i)$ are the coefficients associated with the scalar functions or wavelet expansion functions respectively. Since M is represented by block of band matrices, it can be shown that the domain where the field coefficients of $u^{(n+1)}$ are non-negligible is at most equal to the corresponding domain of $u^{(n)}$ plus the width of the bands in matrix M that represent the operator A in the wavelet basis. If N_φ, N_ψ are the total number of nonzero scaling and wavelet field coefficients (grid points), the number of operations required to compute M is of the order of $O(N_\varphi + N_\psi)$. As it has been shown in [10,11], the total number of scaling grid points can be as low as two per wavelength. However, the resolution required in the wavelet grid points is determined by the nature of the boundaries in the problem of interest.

We are now ready to describe the method suggested in [20,21] to adapt in space and time the wavelet grid and thus follow the sharp features of the waves as they develop and/or move on the grid. At each time step we keep both the wavelet field values that are larger than a given threshold as well as the adjacent values. An adjacent wavelet field value is defined on the basis of the wavelet resolution level(s) incorporated in the solution. The development of an appropriate definition can be considered. Let $G_{(n)}$ be the wavelet field values (grid points) which are kept and represent the approximate solution at the nth time step. From these let us call fundamental the wavelet coefficients that are greater than the threshold and adjacent the ones as defined above. From equation 3 we compute the wavelet field coefficients of $u^{(n+1)}$ corresponding to the fundamental and adjacent coefficients that constitute

grid $G_{(n)}$. We then adjust $G_{(n)}$ by changing into "fundamental" those field coefficients that are greater than the threshold and changing into adjacent their adjacent ones. This process creates the new grid $G_{(n+1)}$. We project u onto the space corresponding to $G_{(n+1)}$ and we are ready for the next step update

Clearly the basic assumption behind this algorithm is that during a time Δt, the domain of the fundamental field coefficients does no spread beyond its border of adjacent coefficients. This method has already been applied to a variety of circuit problems and results will be discussed during the presentation [25].

4.0 References

1. K.S. Yee, "Numerical Solution of Initial Boundary Value Problems Involving Maxwell's Equations in Isotropic Media", IEEE Trans. on Antennas and Propagation, vol. 14, no. 3, pp. 302-307, May 1966.

2. J.C.Strikwerda, "Finite Difference Schemes and Partial Differential Equations", Wadsworth & Brooks, Pacific Grove, 1989.

3. P.H. Aoyagi, J.F. Lee, R. Mittra, "A Hybrid Yee Algorithm/Scalar--Wave Equation Approach", IEEE Trans. Microwave Theory Tech., vol. 41, no. 9, pp. 1593-1600, September 1993.

4. M. Mrozowski, "A Hybrid PEE--FDTD Algorithm for Accelerated Time Domain Analysis of Electromagnetic Waves in Shielded Structures", IEEE Microwave Guided Wave Letters, vol. 4, no. 10, pp. 323-325, October 1994.

5. L. Lapidus, G.F. Pinder, "Numerical Solution of Partial Differential Equations in Science and Engineering", J. Wiley, New York 1982, pp. 171-179.

6. R.F. Harrington, "Field Computation by Moment Methods", Krieger Publishing Company, Inc., Malabar, Florida, 1982.

7. M. Krumpholz, P. Russer, "Two--Dimensional FDTD and TLM", Int. Journal of Num. Modelling, vol. 7, no. 2, pp. 141-153, February 1993.

8. M. Krumpholz, P. Russer,"A Field Theoretical Derivation of TLM", IEEE Trans. on Microwave Theory and Tech., vol. 42, no. 9, pp. 1660-1668, September 1994.

9. M. Krumpholz, C. Huber, P. Russer, "A Field Theoretical Comparison of FDTD and TLM", to be published in the IEEE Transactions on Microwave Theory and Techniques.

10. M. Krumpholz and Linda P.B. Katehi, "MRTD: New Time Domain Schemes Based on Multiresolution Analysis," submitted to IEEE Transactions on Microwave Theory and Techniques, May 1995.

11. M. Krumpholz and Linda P.B. Katehi, New Prospectives for FDTD," submitted to Microwave and Guided Wave Letters, April 1995.

12. S.G. Mallat, "A Theory for Multiresolution Signal Decomposition: The Wavelet Representation", IEEE Trans. Pattern Anal. Machine Intell., vol. 11, pp. 674-693, July 1989.

13. B. Jawerth, W. Sweldens, "An Overview of Wavelet Based Multiresolution Analyses", SIAM Review, vol. 36, no. 3, pp. 377-412, September 1994.

14. G. Battle, "A block spin construction of ondelettes", Comm. Math. Phys., vol. 110, pp. 601-615, 1987.

15. P.G. Lemarie, "Ondelettes a localization exponentielle", J. Math. Pures Appl., vol. 67, pp. 227-236, 1988.

16. B.Z. Steinberg, Y. Leviatan, "On the Use of Wavelet Expansions in the Method of Moments", IEEE Trans. Antennas Propagation, vol. 41, no. 5, pp. 610-619, May 1993.

17. K. Sabetfakhri, L.P.B. Katehi, "Analysis of Integrated Millimeter--Wave and Submillimeter--Wave Waveguides Using Orthonormal Wavelet Expansions", IEEE Trans. on Microwave Theory and Tech., vol. 42, no. 12, pp. 2412-2422, December 1994.

18. K. Sabetfakhri and L.P.B. Katehi, "Fast Wavelet Algorithm (FWA) for Moment Method Analysis of Electromagnetic Problems," 1995 ACES Proceedings, vol. I, pp. 568-575, March 1995.

19. I. Daubechies, "Ten Lectures on Wavelets", Philadelphia, PA: Society for Industrial and Applied Mathematics, 1992.

20. V. Perrier and C. Basdevant, "La decompositionen ondelettes periodiques un outil pour l'analyse des champs inhomogenes. Theorie et algorithmes," La Recherche Aerospatiales, no. 3, pp. 53-67, 1989.

21. J. Liandrat and P. Tchamitchian, "Resolution of the 1D regularized Burgers equation using a spatial wavelet approximation, NASA Report, ICASE Report no. 90-83, Dec. 1990.

22. E.Tentzeris, M.Krumpholz and L.P.B.Katehi, "Characterization of Microwave Circuit Components Using teh MRTD Technique,", submitted to the IEEE MTT Transactions.

23. K.Goverdhanam, E.Tentzeris, M.Krumpholz and L.P.B. Katehi, "An FDTD Multigrid based on Multiresolution Analysis", Proc. AP-S 1996, pp. 352-355. MTT paper:

24. K.Goverdhanam, L. P.B. Katehi, A. Cangellaris, "Applications Of Multiresolution Based FDTD Multigrid", Accepted for publication in the 1997 IEEE MTT-S Microwave Conference Digest.

25. E.Tentzeris, Robert Robertson, L.P.B.Katehi and Andreas Cangellaris, "Space- and Time- Adaptive Gridding Using MRTD Technique," Accepted for publication in the 1997 IEEE MTT-S Microwave Conference Digest.

High Resolution Schemes for Maxwell Equations in the Time Domain

J.S. Shang*
Flight Dynamics Directorate
Wright Laboratory
Wright-Patterson AFB, OH 45433-7913

Abstract

A bidiagonal compact-difference and a finite-volume procedure of fourth-order temporal and third-order spatial accuracy have been developed for solving three-dimensional, time-dependent Maxwell equations. Solutions of a three-dimensional waveguide and the scattering by a perfectly electrical conducting sphere and an ogive cylinder are validated. The bidiagonal compact difference scheme applied to the waveguide shows exceptional resolution characteristics over a wide range of wavenumber. The high resolution finite-volume scheme demonstrates improved numerical efficiency over previous efforts in RCS calculations.

Introduction

For simulating wave diffraction and refraction phenomena, numerical resolution for high frequency spectrum is clearly needed [1-4]. The accuracy requirement in computational electromagnetics (CEM) is so demanding that it has become a pacing item for this technology development. In time-dependent calculations, the truncation error of a numerical result is manifested as dissipation and dispersion. The numerical error accumulation during a sustained period of calculations or in an extensive computational domain may lead to a situation where the wave modulation and phase errors become unacceptable. In principle, the numerical accuracy can be improved either by refining the mesh point density or by adopting a high resolution numerical procedure. The more fundamental approach of devising high resolution numerical procedures has the potential to expand the application range of CEM, thus is much more appealing.

Using exclusively the formal order of accuracy of temporal and spatial truncation errors to select an algorithm for time dependent simulation is an over simplification [5-7]. Although the dispersive error is dominated by the spatial discretization [5], this error can still be alleviated by more accurate time integration options. No dissipation is also achievable by some schemes by a stencil construction that provides symmetry with respect to time [8]. Even the perfect shift condition can be achieved under certain restrictions through temporal and spatial truncation error cancellation [9]. An algorithm that meets the perfect shift condition at specific Courant-Friedrichs-Lewy (CFL) numbers, can generate an exact one dimensional solution. The perfect shift property, however, is not preserved for multi-dimensional problems. In fact, an additional error in terms of the numerical anisotropy will be present.

The numerical resolution can be quantified by the Fourier analysis in terms of normalized wavenumber. In applications the quantification is measured by the grid-point density per wavelength. However, this simple grid density criterion is insufficient when the computational domain contains multiple media with a wide range of characteristic impedances, because all numerical schemes have a limited wavenumber range for accurate computations. At the present, for a high frequency CEM simulation associated with a large-scale configuration, the required number of mesh points to meet an accuracy specification is often beyond the reach of conventional computing systems. In order to extend the present simulation capability to higher frequency spectra, the need to develop high resolution schemes for CEM is urgent.

Compact differencing [5,6], optimized difference [7], and spectral methods [10] are viable options to achieve high resolution. The idea of the compact and optimized methods is closely linked. Both approaches seek algorithms that have a small stencil dimension and yet maintain a lower level of dispersive and dissipative error than conventional numerical schemes. Collatz [11] has pointed out that the compact difference scheme is based on the Hermite's

generalization of the Taylor series. The accuracy gain is acquired through additional derivative data to be specified at the boundary [5-7]. Although the stencil structure for most popular compact differencing formulas is tridiagonal, they still requires a transitional scheme from the boundary to the interior domain. The numerical boundary scheme must transmit data from the boundary and also preserves the stability and accuracy of the interior calculations for the global resolution. For this reason, the development of a numerical boundary scheme is emerging as a major challenge for high resolution methods.

The need for higher order resolution is equally applicable to both temporal and spatial variables. In the present analysis, a Runge-Kutta method [12] up to fourth order accuracy is used for the integration with respect to time. This high temporal resolution procedure is implemented to a finite-volume MUSCL procedure in a general curvilinear frame of reference [13] and several flux vector splitting finite-difference methods [14,15] including a bidiagonal compact difference scheme. Only the bidiagonal compact difference scheme will be described in detail. All validating efforts are concentrated on three-dimensional simulations to emphasizes the focus on practical application and on understanding multi-dimensional numerical procedure development. All numerical schemes are first evaluated by simulating transverse electrical wave propagation in a three-dimensional rectangular guide. Then some selected procedures are used to simulate the scattering phenomenon around a perfectly electrical conducting (PEC) scatterer.

Governing Equations

The time-dependent Maxwell equations for an electromagnetic field are [16,17]:

$$\frac{\partial B}{\partial t} + \nabla \times E = 0 \tag{1}$$

$$\frac{\partial D}{\partial t} - \nabla \times H = -J \tag{2}$$

$$\nabla \cdot B = 0, \quad B = \mu H \tag{3}$$

$$\nabla \cdot D = 0, \quad D = \epsilon E \tag{4}$$

where ϵ and μ are the electric permittivity and the magnetic permeability which relate the electric displacement,D, to the electric field intensity, E, and magnetic flux density, B to the magnetic field intensity,H, respectively.

The time-dependent Maxwell equations can be cast in flux-vector form on a curvilinear frame of reference by a coordinate transformation from the Cartesian system. The governing equations become [13-15]:

$$\frac{\partial U}{\partial t} + \frac{\partial F_\xi}{\partial \xi} + \frac{\partial F_\eta}{\partial \eta} + \frac{\partial F_\zeta}{\partial \zeta} = -J \tag{5}$$

where the dependent variable U in the present formulation is now scaled by the local cell volume, V, or the reciprocal of the Jacobian of the coordinate transformation.

$$U = \{B_x V, B_y V, B_z V, D_x V, D_y V, D_z V\}^T \tag{6}$$

F_ξ, F_η, and F_ζ are the contravariant components of the flux vectors of the Cartesian coordinates which is the basic frame of reference of the present analysis [13,15].

$$\begin{aligned} F_\xi &= \xi_x F_x + \xi_y F_y + \xi_z F_z \\ F_\eta &= \eta_x F_x + \eta_y F_y + \eta_z F_z \\ F_\zeta &= \zeta_x F_x + \zeta_y F_y + \zeta_z F_z \end{aligned} \tag{7}$$

and ξ_x, η_x, ζ_x, ξ_y, η_y, ζ_y, ξ_z, η_z, and ζ_z are the nine metrics of the coordinate transformation.

The characteristic-based finite-volume and finite-difference approximations are achieved by splitting the flux vector according to the signs of eigenvalues of the coefficient matrix in each spatial direction [13-15]. The flux vector in the discretized space is represented by a superposition of two components; F_ξ^+, F_ξ^-, F_η^+, F_η^-, F_ζ^+, and F_ζ^- according to eigenvalue structure [15]. The formal order of accuracy for these schemes is exclusively dependent on how either the subsequent difference quotients or the flux vectors are reconstructed. For the finite-volume scheme at

the cell surfaces the split flux vectors are calculated by the reconstructed dependent variables on either side of the interface according to the MUSCL scheme [18]:

$$F_{\xi,i+\frac{1}{2}} = F_\xi^+(U_{i+\frac{1}{2}}^L) + F_\xi^-(U_{i+\frac{1}{2}}^R)$$
$$F_{\eta,j+\frac{1}{2}} = F_\eta^+(U_{j+\frac{1}{2}}^L) + F_\eta^-(U_{j+\frac{1}{2}}^R) \tag{8}$$
$$F_{\zeta,k+\frac{1}{2}} = F_\zeta^+(U_{k+\frac{1}{2}}^L) + F_\zeta^-(U_{k+\frac{1}{2}}^R)$$

where U^L and U^R denote the reconstructed dependent variables at the left and right side of the cell interface. The split flux vectors in respective ξ-t, η-t, and ζ-t planes are obtained by straightforward matrix multiplications and are given in reference 15.

Initial Conditions and Boundary Values

For the present analysis, the incident wave of the waveguide and the scattering simulations consist of a linearly polarized harmonic field propagating in the negative z-axis direction. On the media interface the transverse electrical wave, TE(1,1), within a rectangular waveguide and the scattering simulations must satisfy the identical bounadry conditions, therefore the boundary condition implementation can also be shared. Since the surface of the scatterer and the waveguide are assumed to have perfect electrical conductivity, the appropriate boundary conditions at the surfaces are [16,17];

$$\begin{aligned}
\vec{n} \times (E_1 - E_2) &= 0 \\
\vec{n} \times (H_1 - H_2) &= J_s \\
\vec{n} \cdot (B_1 - B_2) &= 0 \\
\vec{n} \cdot (D_1 - D_2) &= \rho_s
\end{aligned} \tag{9}$$

Following previous efforts [3,4], the unknown surface current and charge densities, J_s and ρ_s are treated as finite jumps of constant value. Extrapolated numerical boundary conditions for the finite jump of properties at the surface are introduced to replace the equations that contain unknowns. This formulation is compatible with the basic attribute of the hyperbolic partial differential system which allows piecewise continuous data to propagate unaltered along a characteristic.

The advantage of the characteristic-based formulation is also revealed in the implementation of the far field boundary condition. In principle, if one of the coordinates is aligned with the direction of wave motion, the split flux of the characteristic-based scheme is identical to the compatibility condition at the truncated far field boundary [13-15]. An effective approximation is easily implemented by setting the incoming flux component to the null value at the truncated far field boundary.

For the rectangular waveguide

$$F_\zeta^-(\xi, \eta, \zeta_{exit}) = 0 \tag{10}$$

For the PEC Scatterer

$$F_\xi^+(\xi_\infty, \eta, \zeta) = 0 \tag{11}$$

Temporal and Spatial Discretization

The present approach uses Runge-Kutta schemes for time integration. This first-order derivative evaluation procedure can be fitted into a Taylor's series by the constraint of weighting coefficients to retain a prescribed order of accuracy [12]. Only the four-stage or the fourth-order accurate Kutta method is presented here.

$$\begin{aligned}
U^{n+1} &= U^n + (\Delta t/6) \cdot (U_{t,1} + 2U_{t,2} + 2U_{t,3} + U_{t,4}) \\
U_{t,1} &= U_t(t, U^n) \\
U_{t,2} &= U_t(t + \Delta t/2, U^n + \Delta t/2 \cdot U_{t,1}) \\
U_{t,3} &= U_t(t + \Delta t/2, U^n + \Delta t/2 \cdot U_{t,2}) \\
U_{t,4} &= U_t(t + \Delta t, U^n + \Delta t \cdot U_{t,3})
\end{aligned} \tag{12}$$

The four-stage procedure needs twice as many arithmetic operations to advance the solution one time step as the two-stage scheme. An additional array of dynamic memory for the derivatives, U_t is also needed for completing a time sweep. However, the allowable CFL number nearly doubles from the two-stage to the four-stage procedure. The CFL number increases from 0.876 for the two-stage to 1.740 for the four-stage procedure.

The accuracy gain by compact differencing methods over conventional methods is obtained not by increasing mesh point stencil, but rather by incorporating adjacent derivatives of the function [11]. Since the formulation is based on the Taylor series expansion, the compact differencing formulation is valid only in the domain where the dependent variables are continuous and differentiable. The most general compact difference or the Hermitian formula can be written to include first- and second-order derivatives [14]. For CEM in the time domain, the formula containing only the first derivatives is sufficient. The general spatial formula can be written as:

$$\alpha U'_{i-1} + \beta U'_i + \gamma U'_{i+1} = C_1 U_{i-3} + C_2 U_{i-2} + C_3 U_{i-1} + C_4 U_i + C_5 U_{i+1} + C_6 U_{i+2} + C_7 U_{i+3} \tag{13}$$

The present scheme incorpoates a third-order accurate compact formula which was developed by Adam [19]. This formula has a bidiagonal structure for the first-order derivatives.

For the forward biased differencing

$\alpha = 4$, $\beta = 2$, $\gamma = 0$, $C_1 = 0$, $C_2 = $ -1, $C_3 = $ -4, $C_4 = 5$, $C_5 = 0$, $C_6 = 0$, $C_7 = 0$.

For the backward difference

$\alpha = 0$, $\beta = 2$, $\gamma = 4$, $C_1 = 0$, $C_2 = 0$, $C_3 = 0$, $C_4 = $ -5, $C_5 = 4$, $C_6 = 1$, $C_7 = 0$.

It is immediately recognizable that the third-order compact difference has a smaller stencil dimension than its explicit counterpart [6,9]. The compact stencil consists of three points, and the associated first derivatives have a bidiagonal-diagonal structure. From the Fourier analysis of this algorithm when applied to the one-dimensional model wave equation, the maximum allowable CFL number has a value of 0.696 and exhibits a characteristic of lower dispersive error. The bidiagonal compact difference procedure even outperforms fourth-order compact difference schemes of the same family [5].

For numerical solutions of initial-value problem, the issues of consistency, well-posedness, and stability are paramount. Unfortunately, most known numerical stability analyses lack the ability to take the boundary condition into consideration. For high-order methods, the effects of boundary formulations are also no longer masked by the built-in dissipation of the lower-order schemes. Numerical stability is a critical concern for high-order compact difference method, which must include a stable transitional boundary scheme to preserve the formal accuracy [20,21]. The Adam's bidiagonal compact difference algorithm has been demonstrated to be a stable and compatible transition boundary scheme to a fourth-order accurate method [4].

Numerical Results

All results are processed on the Cray C916/16256 computing system. The presentation of numerical results is separated into three groups. The first group addresses the dispersion and dissipation of the adopted finite-difference numerical algorithms when applied to the one-dimensional model wave equation. The second group summarizes the performance of the present characteristic-based codes [13-15] applied to a three-dimensional transverse electric wave in a rectangular waveguide. The wave speed and the time elapsed during the computation are fixed for all simulations to permit the wave to transverse the entire length of the waveguide twice. At the highest frequency, the transmitted wave travels a total distance of 36.6 wavelengths. The last group details computations of a PEC sphere and an ogive cylinder over a wavenumber range from 1.06 to 20.0 by the finite-volume procedure using the two-stage and the four-stage Runga-Kutta temporal integration.

The dissipative error of the mid-point leapfrog, the upwind, and the bidiagonal compact-difference algorithm are presented in Figure 1. The mid-point leapfrog scheme is included as a reference point for comparison [1]. All numerical results are obtained by solving the one-dimensional model wave equation. In spite of the fact that, the mid-point leapfrog is a second-order scheme, the one-dimensional solution does not contain any dissipative error. The upwind scheme of Warming and Beam [8] possesses the same feature at the CFL value of 1 and 2 but exhibits error when CFL differs from the aforementioned values. The bidiagonal compact-differencing and the windward scheme reveals numerical diffusion.

Figure 2 depicts the corresponding dispersive error of all schemes examined. The bidiagonal compact-difference scheme shows the least dispersion. This compact difference scheme even outperforms a fourth-order compact scheme of the same family [5,7]. The dispersive error expressed in terms of the normalized wave number, spans a usable range from 0.0 to 2.4. However the one-dimensional result should be used only as a general guide for numerical procedure development, because the additional numerical error such as anisotropy will be present in multi-dimensional problems.

77

In Figure 3, the y-component of electric displacements in the waveguide are depicted at three different frequencies. All numerical solutions are generated by the second-order accurate upwind scheme of Warming and Beam [8] on a uniformly spaced grid (25 × 24 × 96). The instantaneous D_y distributions along the entire length of the waveguide are accompanied by the theoretical values for validation [16,17]. The comparison with the theory for frequency spectra from 3π to 5π corresponds to a grid-point density of 18.3 to 9.15 per wavelength. For the lowest frequency simulation, the dissipation error is confined to less than one percent. As the wavenumber increases and the grid-point density decreases accordingly, the numerical error becomes unacceptable.

Figure 4 displays the resolution characteristics for the four-stage Runge-Kutta and spatially third-order compact difference method, RK4S3CD in the waveguide simulation. These results of the RK4S3CD method are far superior in the higher frequency range than the upwind method given in Figure 3. The numerical results obtained on mesh systems with the grid-point density of 18.3 and 13.7 per wavelength are accurate. As the grid-point density is further decreased to the value of 9.15 ($\omega = 5\pi$), the numerical resolution starts to degrade and yields a maximum error of 0.331 percent near the middle point of the waveguide. The third-order accurate compact differencing method has also been use to generate waveguide solutions for the angular frequencies of 6π and 7π, which correspond to the grid-point densities of 8.34 and 7.25 points per wavelength. Under these circumstances, the maximum dissipative errors have values of 1.60 and 9.72 percent respectively.

The horizontal polarized bi-static RCS distributions of the PEC sphere, $\sigma(\theta,0.0)$ at a wavenumber of 20 by the third-order finite-volume, two-stage (RK2S3) and four-stage Runge-Kutta (RK4S3) methods are given in Figure 5. Although these solutions are obtained by different time steps for data sampling, the maximum difference between the two numerical results is negligible. The maximum discrepancy of numerical results from the theoretical value occurs at the viewing angle of 114.5 degree with an absolute value of 0.1308. For these simulations, the far-field boundary is placed at 2.86 wavelengths away from the sphere. On the (73 × 60 × 96) grid system, the grid-point density along the circumferential coordinate is now reduced to a value of 9.6. In comparing with an earlier calculation at the same wavenumber [3], the present calculations require fewer number of grid points by a factor of 4.25.

The finite-volume result (RK4S3) for bi-static RCS of the ogive cylinder in horizontal polarization is presented in Figure 6. The calculations simulate the scattering phenomena when the ogive cylinder is illuminated by a head-on incident wave at 2 Giga hertz. The wavenumber at this frequency is scaled by the scatterer length of 54.6 cm to yield a value of 1.065. The numerical simulation is performed using a two-block grid system with the respective dimensions of (143 × 109 × 43) and (53 × 109 × 75). The agreement with the calculation of a method of moment [23] is excellent. A nearly identical result was also produced by the two-stage Runge-Kutta time integration scheme, (RK2S3) but at a cost of 11.2 % more CPU seconds.

Concluding Remarks

The bidiagonal, compact-difference scheme when applied to the simple wave model exhibits the lowest dispersive error among all the algorithms considered. The compact-difference approximations shows promising potential for extending the frequency spectra simulations by solving the three-dimensional, time-dependent Maxwell equations.

The temporally fourth-order and spatially third-order windward biased finite-volume method exhibits a numerical efficiency gain over the lower order temporal accuracy method. The improved accuracy in time enhances the stability of this method permitting a doubling of the CFL number from 0.876 to 1.740.

Acknowledgments

References

1. Taflove, A., Reinventing Electromagnetics: Super Computing Solution of Maxwell's Equations Via Direct Time Integration on Space Grids, Computing Sys in Engineering Vol 3, Nos 1-4, 1992, pp.153-168.

2. Shankar, V., Research to Application - Supercomputing Trends for the 90's and Opportunities for Interdisciplinary Computations, AIAA 91-0002, Jan. 1991.

3. Shang, J.S., Time-Domain Electromagnetic Scattering Simulations on Multicomputers, J. Computational Physics, Vol 128, 1996, pp.381-390.

4. Shang, J.S. and Gaitonde, D., Scattered Electromagnetic Field of a Reentry Vehicle, AIAA 94-0231, Reno, NV Jan. 1994, also AIAA J Spacecraft and Rockets, Vol 32, No 2, March-April 1995, pp.294-301.

5. Lele, S.K., Compact Finite Difference Schemes with Spectral-Like Resolution, J. Comp Physics, Vol 103, 1992, pp.16-42.

6. Shang, J.S. and Gaitonde, D. On High Resolution Schemes for Time-dependent Maxwell Equations, AIAA 96-0832, 34th Aerospace Science Meeting, January 15-18, Reno NV, 1996.

7. Gaitonde, D. and Shang, J.S., High-Order Accurate Schemes in Wave Propagation Phenomena, AIAA 96-2335, 27th Plasmadynamics and Laser Conferences, New Orleans LA, 17-20 June,1996

8. Thomas, J.P., Kim, C., and Roe, P.L., Progress Toward a New Computational Scheme for Aeroacoustics, AIAA 95-1758-CP, San Diego, CA, June 1965, pp.1325-1336.

9. Anderson, D.A, Tannehill, J.C., and Fletcher, R.H., Computational Fluid Dynamics and Heat Transfer, McGraw Hill Book Co., New York, 1984, pp.87-169.

10. Gottlieb, D. and Orszag, Numerical Analysis of Spectral Methods, SIAM, Philadelphia PA, 1977.

11. Colatz, L., The Numerical Treatment of Differential Equations, Springer-Verlag, New York, 1966, p.538.

12. Carnahan, B., Luther, H.A., and Wilkes, J.O., Applied Numerical Methods, John Wiley & Sons Inc, New York, 1969, pp.361-366.

13. Shang, J.S. and Gaitonde, D., Characteristic-Based, Time-Dependent Maxwell Equations Solvers on a General Curvilinear Frame, AIAA 93-3178, also AIAA J. Vol 33 No 3, March 1995, pp.491-498.

14. Shang, J.S., A Fractional-Step Method for the Time Domain Maxwell Equations, AIAA 93-0461, Jan. 1993, also J Comp Physics, Vol 118 No 1, April 1995, pp.109-119.

15. Shang, J.S. and Fithen, R.M., A Comparative Study of Characteristic- based Algorithms for the Maxwell Equations, J. Computational Phys., Vol 125, 1996, pp.378-394.

16. Harrington, R.F., Time-Harmonic Electromagnetic Field, McGraw Hill Co., New York. 1961.

17. Stratton, J.A., Electromagnetic Theory, McGraw Hill Co., New York, 1941.

18. Anderson, W.K., Thomas, J.L., and Van Leer, B., A Comparison of Finite Volume Flux Splittings for the Euler Equations, AIAA 85- 0122, also AIAA J., Vol 24, No. 9, Sept 1986, pp.1453-1460.

19. Adam, Y., Highly Accurate Compact Implicit Methods and Boundary Conditions, J. Comp. Physics, Vol 24, 1977, pp 10-22.

20. Gustafsson, B., Kreiss, H.-O., and Sundstrom, A., Stability Theory of Difference Approximations for Mixed Initial Boundary Value Problems. II, Math. Comp. Vol 26, 1972, pp 649-686.

21. Carpenter, M.K., Gottlieb, D., and Abarbanel, S., Time-Stable boundary Conditions for Finite-Difference Schemes Solving Hyperbolic Systems: Methodology and Application to High-Order Compact Schemes, J. Comp. Physics, Vol. 111, No 2, April 1994, pp 220-236.

22. Bowman, J.J., Senior, T.B.A., and Uslenghi, P.L.E., Editors, Electromagnetic and Acoustic Scattering by Simple Shapes, Hemisphere Pub. Corp., New York, 1987 pp. 353-415.

23. Putnam, J.N. and Gedera, M.B., CARLOS-3D (TM):, A General-Purpose Three-Dimensional Method of Moment Scattering Code, IEEE Antennas & Propagation Magazine, Vol 35, No 2, April 1933 pp.69-71.
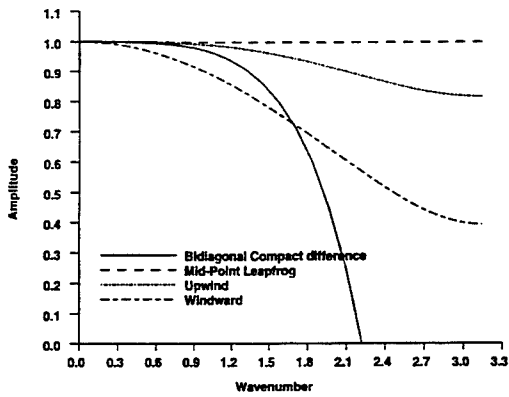
Figure 1: Dissipative Error of selected Finite-Difference Algorithms, CFL=0.7
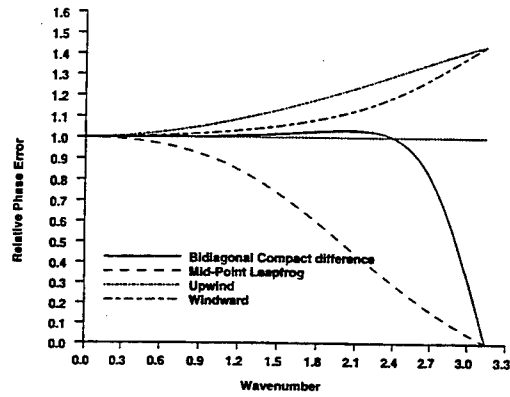
Figure 2: Dispersive Error of selected Finite-Differencing Algorithm, CFL=0.7
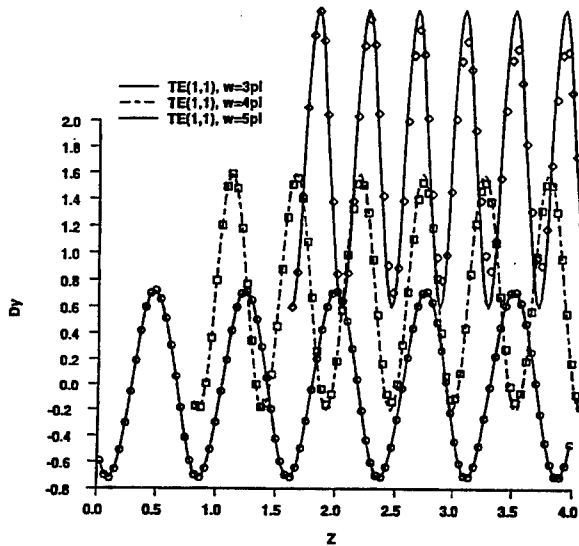
Figure 3: Resolution Characteristics of the Upwind Method Over a Wavenumber Range
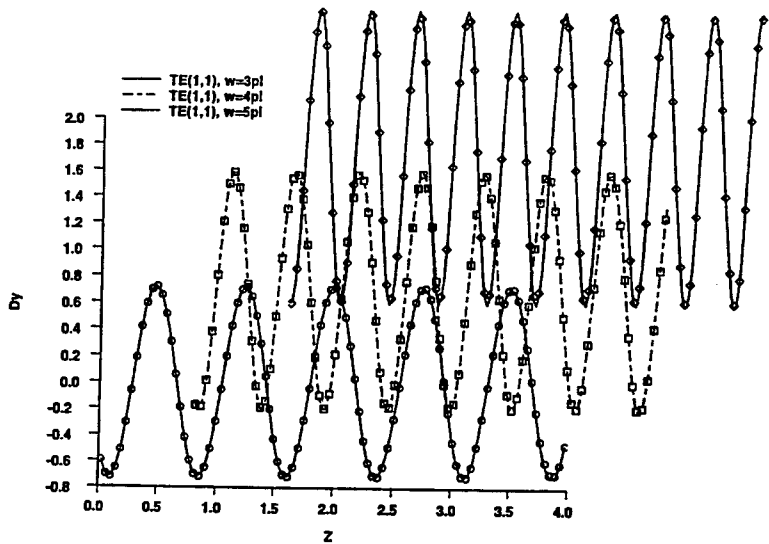
Figure 4: Resolution Characteristics of a Compact Difference Method Over a Wavenumber Range
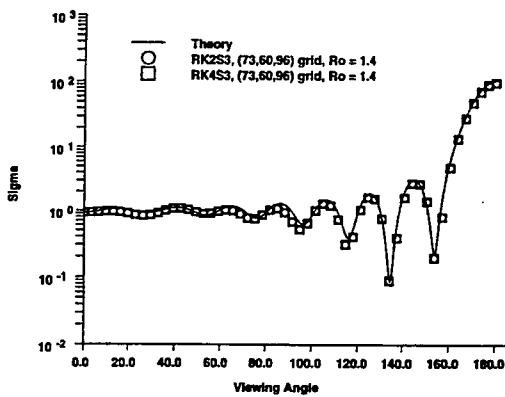
Figure 5: RCS of a PEC Sphere, $\sigma(\theta, 0.0)$, ka=10.0
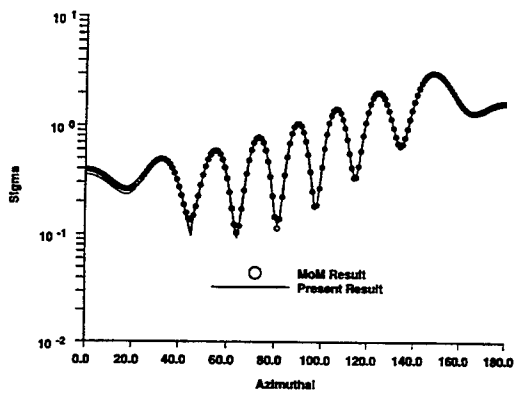
Figure 6: RCS of a ogive Cylinder, Head-On illumination, 2 Giga Hertz

FD-TD M24 Dispersion and Stability in Three Dimensions

G. Haussmann and M. Piket-May
Department of Electrical and Computing Engineering
University of Colorado at Boulder
Boulder CO 80309-0425

1 Introduction

The original Finite-Difference Time-Domain electromagnetic simulation method, first proposed by Yee [1] in 1966, has spawned numerous variants in an attempt to emphasize desirable characteristics, such as simplicity and stability. This paper examines the dispersion and stability properties of some of these variants.

The dispersion relation for a given method or variant expresses the error in propagation speed. This error, a phenomenon resulting from grid discretization, varies with propagation angle and grid resolution. Switching to different FD-TD variants can reduce or aggravate the overall dispersion error.

Stability must also be examined since the explicit nature of the FD-TD method exerts a stability condition [2]. The stability requirements restrict the possible time and space resolution used in FD-TD simulations.

2 General Forms of Dispersion and Stability Equations

In this section the dispersion relation and stability requirements are examined using a general difference operator D. After these general equations are derived, they later can be used to examine FD-TD methods by substituting in specific difference operators.

2.1 Dispersion

The dispersion relation is derived via the wave equation

$$\nabla^2 \vec{V} - \left(\frac{\partial}{\partial t}\right)^2 \vec{V} = 0 \tag{1}$$

which is expressed using difference operators as

$$D_t^2 - D_x^2 - D_y^2 - D_z^2 = 0 \tag{2}$$

A special requirement, which only shows up in a more detailed derivation, is that the difference operators must be linear. Certain methods satisfy this requirement for two dimensional simulations only, and must be modified for use in three dimensions.

2.2 Stability

The stability analysis of an FD-TD simulation is traditionally performed in two stages. The simulation is examined as a large discrete linear system, and restrictions are placed on this system's eigenvalues to provide stability. First, the temporal eigenvalues are examined to find the allowed range of stable eigenvalues. Then the spatial operators are used to produce a criteria which only allows propagation of the stable eigenvalues found in the first step.

While this process is normally done with a specific FD-TD method, (second or fourth order) it is possible to derive a stability criteria up to a certain point using only generic difference operators, as was done with the dispersion relation.

2.2.1 Temporal Eigenvalues

The temporal eigenvalues are found by analyzing the difference equation

$$\vec{V}|_{i,j,k}^n = \vec{V}|_{i,j,k}^n + \triangle t D_t \vec{V}|_{i,j,k}^n \tag{3}$$

and defining a time shift operator Q such that $Q^2 \vec{V}|_{i,j,k}^n = \vec{V}|_{i,j,k}^{n+1}$. This leads to

$$
\begin{aligned}
Q^2 \vec{V}|_{i,j,k}^n &= \vec{V}|_{i,j,k}^n + \triangle t Q D_t \vec{V}|_{i,j,k}^n \\
Q^2 \vec{V}|_{i,j,k}^n &= \left(1 + \triangle t\, Q\, D_t\right) \vec{V}|_{i,j,k}^n \\
Q^2 &= 1 + \triangle t\, Q\, D_t \\
0 &= Q^2 - \triangle t\, Q\, D_t - 1 \\
Q &= \frac{D_t \triangle t}{2}\left(1 \pm \sqrt{1 + \left(\frac{2}{D_t \triangle t}\right)^2}\right)
\end{aligned}
\tag{4}
$$

To enforce stability we must limit the growth factor of $\vec{V}|_{i,j,k}^n$ over time, meaning that

$$\left|\frac{\vec{V}|_{i,j,k}^{n+1}}{\vec{V}|_{i,j,k}^n}\right| = \left|\frac{Q^2}{1}\frac{\vec{V}|_{i,j,k}^n}{\vec{V}|_{i,j,k}^n}\right| = \left|Q^2\right| \le 1 \tag{5}$$

Substituting (4) into (5) produces a limit on the temporal operator D, such that

$$\frac{D_t \triangle t}{2}\left(1 \pm \sqrt{1 + \left(\frac{2}{D_t \triangle t}\right)^2}\right) \le 1 \tag{6}$$

which requires that D_t be imaginary and bounded by

$$|D_t| = \frac{2}{\triangle t} \tag{7}$$

The corresponding eigenvalue equation

$$D_t \vec{V}|_{i,j,k}^n = \Lambda \vec{V}|_{i,j,k}^n \tag{8}$$

tells us that $D_t = \Lambda$, and so Λ is restricted in the same manner as D_t.

2.2.2 Spatial Eigenvalues

Derivation of the possible spatial eigenvalues starts with

$$\nabla^2 \vec{V}|_{i,j,k}^n = \Lambda \vec{V}|_{i,j,k}^n \tag{9}$$

which, in difference form, becomes

$$(D_x^2 + D_y^2 + D_z^2)\vec{V}|_{i,j,k}^n = \Lambda \vec{V}|_{i,j,k}^n \tag{10}$$

Solving for Λ produces the eigenvalues

$$\Lambda = \pm\sqrt{D_x^2 + D_y^2 + D_z^2} \tag{11}$$

which, when combined with the restriction found for the temporal equations, gives the stability restriction

$$\sqrt{D_x^2 + D_y^2 + D_z^2} \le \frac{2}{\triangle t} \tag{12}$$

2.3 Difference Operators for Specific FD-TD methods

In this section the difference operators used for various FD-TD methods are defined. After these operators are defined, they are then applied to the general dispersion equations to find the dispersion relation and stability criterion for each method.

2.3.1 The Second Order Difference

The difference operator D most commonly used is the second order difference, defined in FD-TD as

$$D_x\vec{V}|_{i,j,k}^n = \frac{\vec{V}|_{i+1/2,j,k}^n - \vec{V}|_{i-1/2,j,k}^n}{\triangle} \tag{13}$$

where $\vec{V}|_{i,j,k}^n$ represents an Electric or Magnetic vector field. When $\vec{V}|_{i,j,k}^n$ is in the plane wave form

$$\vec{V}|_{i,j,k}^n = \vec{V}_0\, e^{j(k_x(i)\triangle x + k_y(j)\triangle y + k_z(k)\triangle z - \omega(n)\triangle t)} \tag{14}$$

we can rewrite the difference as a constant term, independent of the field it operates on:

$$D_x = \frac{2j}{\triangle x}\sin\left(\frac{k_x\triangle x}{2}\right) \tag{15}$$

The second order difference is then extended to the other spatial axes (y and z) and the time axis t. The complete array of second order difference equations is given by

$$D_x = \frac{2j}{\triangle x}\sin\left(\frac{k_x\triangle x}{2}\right) \tag{16}$$

$$D_y = \frac{2j}{\triangle y}\sin\left(\frac{k_y\triangle y}{2}\right) \tag{17}$$

$$D_z = \frac{2j}{\triangle z}\sin\left(\frac{k_z\triangle z}{2}\right) \tag{18}$$

$$D_t = \frac{2j}{\triangle t}\sin\left(\frac{\omega\triangle t}{2}\right) \tag{19}$$

2.3.2 The Basic Fourth Order Difference

There are many types of fourth order difference operators. The simplest fourth order operator is a simple extension of the second order operator, given by

$$D_x = -\frac{1}{24\triangle}\left[\vec{V}|_{i+3/2,j,k}^n - \vec{V}|_{i-3/2,j,k}^n\right] + \frac{9}{8\triangle}\left[\vec{V}|_{i+1/2,j,k}^n - \vec{V}|_{i-1/2,j,k}^n\right] \tag{20}$$

With a plane wave excitation this operator, like the second order difference, becomes a linear term

$$D_x = -\frac{1}{24}\frac{2j}{\triangle x}\sin\left(\frac{3k_x\triangle x}{2}\right) + \frac{9}{8}\frac{2j}{\triangle x}\sin\left(\frac{k_x\triangle x}{2}\right) \tag{21}$$

2.3.3 The Modified Fourth Order operator

One fourth order method (herein referred to as 'M24') [3] augments the basic fourth order difference operator with additional terms, and allows for some varying of coefficients in the operator. By varying the coefficient values, one can produce operators which have a very low dispersion error. The full equation is of the form

$$D_x V_y|_{i,j,k}^n = k_1 D_1 V_y|_{i,j,k}^n + k_2 D_2 V_y|_{i,j,k}^n + k_3 D_3 V_y|_{i,j,k}^n \tag{22}$$

which combines both second and fourth order differences. The three parts of the difference are defined to be

$$D_1\vec{V}|_{i,j,k}^n = \frac{V_y|_{i+1/2,j,k}^n - V_y|_{i-1/2,j,k}^n}{\triangle} \tag{23}$$

$$D_2\vec{V}|_{i,j,k}^n = \frac{1}{3\triangle}\left(\vec{V}|_{i+3/2,j,k}^n - \vec{V}|_{i-3/2,j,k}^n\right)$$

$$D_3\vec{V}|_{i,j,k}^n = \frac{1}{2}\left[\frac{1}{3\triangle}\left(\vec{V}|_{i+3/2,j+1,k}^n - \vec{V}|_{i-3/2,j+1,k}^n\right) + \frac{1}{3\triangle}\left(\vec{V}|_{i+3/2,j-1,k}^n - \vec{V}|_{i-3/2,j-1,k}^n\right)\right]$$

For a plane wave excitation the difference operator becomes a simple coefficient, just as the second and basic fourth order operators did.

$$D_x V_y|_{i,j,k}^n = \left[k_1\frac{2j}{\triangle x}\sin\left(\frac{k_x\triangle x}{2}\right) + k_2\frac{2j}{\triangle x}\sin\left(\frac{3k_x\triangle x}{2}\right) + \right. \tag{24}$$

$$\left. k_3\frac{2j}{\triangle x}\sin\left(\frac{3k_x\triangle x}{2}\right)\cos\left(k_y\triangle y\right)\right]V_y|_{i,j,k}^n \tag{25}$$

At this point the operators cannot be substituted into the general dispersion and stability equations, due to the fact that the operators change depending on what field component they are applied to. As an example, consider applying the same D_x operator to $V_z|_{i,j,k}^n$. This produces

$$D_x V_z|_{i,j,k}^n = \left[k_1\frac{2j}{\triangle x}\sin\left(\frac{k_x\triangle x}{2}\right) + k_2\frac{2j}{\triangle x}\sin\left(\frac{3k_x\triangle x}{2}\right) + \right. \tag{26}$$

$$\left. k_3\frac{2j}{\triangle x}\sin\left(\frac{3k_x\triangle x}{2}\right)\cos\left(k_z\triangle z\right)\right]V_z|_{i,j,k}^n \tag{27}$$

85

which differs from the original D_x operator (applied to $V_y|_{i,j,k}^n$) by a single cosine term.

The difference operators for M24 are not linear operators; the operators change form when applied to different components. Identities such as $D_x V_y|_{i,j,k}^n + D_x V_z|_{i,j,k}^n = D_x(V_y|_{i,j,k}^n + V_z|_{i,j,k}^n)$ are not true, and one cannot use the dispersion and stability equations derived using generalized difference operators. Instead separate operators for different fields must be defined, for example $D_x^y V_y|_{i,j,k}^n$ and $D_x^z V_z|_{i,j,k}^n$.

The M24 method was originally proposed and examined in two dimensions, which in some part explains the problems encountered when applying it to three dimensional problems. This method can be slightly modified to produce linear operators in three dimensions. Define the difference components as

$$D_1 V_y|_{i,j,k}^n = \frac{V_y|_{i+1/2,j,k}^n - V_y|_{i-1/2,j,k}^n}{\triangle} \tag{28}$$

$$D_2 V_y|_{i,j,k}^n = \frac{1}{3\triangle}\left(\vec{V}|_{i+3/2,j,k}^n - \vec{V}|_{i-3/2,j,k}^n\right)$$

$$D_3 V_y|_{i,j,k}^n = \frac{1}{4}\left[\frac{1}{3\triangle}\left(\vec{V}|_{i+3/2,j+1,k}^n - \vec{V}|_{i-3/2,j-1,k}^n\right) + \right.$$
$$\frac{1}{3\triangle}\left(\vec{V}|_{i+3/2,j-1,k}^n - \vec{V}|_{i-3/2,j-1,k}^n\right) +$$
$$\frac{1}{3\triangle}\left(\vec{V}|_{i+3/2,j,k+1}^n - \vec{V}|_{i-3/2,j,k+1}^n\right) +$$
$$\left.\frac{1}{3\triangle}\left(\vec{V}|_{i-3/2,j,k-1}^n - \vec{V}|_{i-3/2,j,k-1}^n\right)\right]$$

When $\vec{V}|_{i,j,k}^n$ is expressed as a plane wave, the difference operator becomes

$$D_x = \left[k_1\frac{2j}{\triangle x}\sin\left(\frac{k_x\triangle x}{2}\right) + k_2\frac{2j}{3\triangle x}\sin\left(\frac{3k_x\triangle x}{2}\right) + \right. \tag{29}$$
$$\left. k_3\frac{2j}{12\triangle x}\sin\left(\frac{3k_x\triangle x}{2}\right)\left(\cos\left(k_y\triangle y\right) + \cos\left(k_z\triangle z\right)\right)\right]$$

for both the $V_y|_{i,j,k}^n$ and $V_z|_{i,j,k}^n$ components, making D_x a linear operator.

3 Specific Dispersion and Stability Equations

3.1 Dispersion for Various Methods

The difference operators for specific update methods can be substituted into the general dispersion equation (2) to produce a dispersion relation for that specific scheme. The relations produced here are normalized, with $c = 1$.

3.1.1 Dispersion Relation For The Second Order Difference

$$\left[\frac{1}{\triangle t}\sin\left(\frac{\omega\triangle t}{2}\right)\right]^2 = \left[\frac{1}{\triangle x}\sin\left(\frac{k_x\triangle x}{2}\right)\right]^2 + \left[\frac{1}{\triangle y}\sin\left(\frac{k_y\triangle y}{2}\right)\right]^2 + \tag{30}$$

$$\left[\frac{1}{\triangle z}\sin\left(\frac{k_z\triangle z}{2}\right)\right]^2$$

3.1.2 Dispersion Relation For The Fourth Order Difference

$$\left[\frac{1}{\triangle t}\sin\left(\frac{\omega\triangle t}{2}\right)\right]^2 = \left(\frac{1}{\triangle x}\right)^2\left[\frac{9}{8}\sin\left(\frac{k_x\triangle x}{2}\right) - \frac{1}{24}\sin\left(\frac{3k_x\triangle x}{2}\right)\right]^2 + \tag{31}$$

$$\left(\frac{1}{\triangle y}\right)^2\left[\frac{9}{8}\sin\left(\frac{k_y\triangle y}{2}\right) - \frac{1}{24}\sin\left(\frac{3k_y\triangle y}{2}\right)\right]^2 +$$

$$\left(\frac{1}{\triangle z}\right)^2\left[\frac{9}{8}\sin\left(\frac{k_z\triangle z}{2}\right) - \frac{1}{24}\sin\left(\frac{3k_z\triangle z}{2}\right)\right]^2$$

3.1.3 Dispersion Relation For The Three Dimensional Modified (2,4) Scheme

To preserve space, only a third of the equation is displayed, with the understanding that this equation holds to the same form as the second order and fourth order dispersion equations.

$$\frac{1}{\triangle t^2}\sin^2\left(\frac{\omega\triangle t}{2}\right) = \frac{1}{144(\triangle x)^2}\left[144k_1^2\sin^2\left(\frac{k_x\triangle x}{2}\right) + 16k_2^2\sin^2\left(\frac{3k_x\triangle x}{2}\right) + \tag{32}\right.$$

$$96k_1k_2\sin\left(\frac{k_x\triangle x}{2}\right)\sin\left(\frac{3k_x\triangle x}{2}\right) +$$

$$k_3^2\sin^2\left(\frac{3k_x\triangle x}{2}\right)\Big(\cos\left(k_y\triangle y\right) + \cos\left(k_z\triangle z\right)\Big) +$$

$$2\Big(12k_1\sin\left(\frac{k_x\triangle x}{2}\right) + 4k_2\sin\left(\frac{3k_x\triangle x}{2}\right)\Big)k_3\sin\left(\frac{k_x\triangle x}{2}\right)\cdot$$

$$\left.\sin\left(\frac{3k_x\triangle x}{2}\right)\Big(\cos\left(k_y\triangle y\right) + \cos\left(k_z\triangle z\right)\Big)\right] +$$

$$\ldots\ldots$$

3.2 Stability for Various Schemes

3.2.1 Stability for the Second Order Difference

Substituting the second order operators into the stability requirement (12) produces

$$\left(\frac{2}{\triangle x}\sin\left(\frac{k_x\triangle x}{2}\right)\right)^2 + \left(\frac{2}{\triangle y}\sin\left(\frac{k_y\triangle y}{2}\right)\right)^2 + \tag{33}$$

$$\left(\frac{2}{\triangle z}\sin\left(\frac{k_z\triangle z}{2}\right)\right)^2 \leq \left(\frac{2}{\triangle t}\right)^2$$

This equation can be simplified by assuming equal grid spacing in all three dimensions, and also renormalizing the equations to include the propagation speed (c). This is expressed more

87

succinctly by $\triangle x = \triangle y = \triangle z = \frac{\triangle}{c}$. With the knowledge that $|\sin(x)| \leq 1$, these simplifications give

$$\frac{2\sqrt{3}}{\triangle} \leq \frac{2}{\triangle t} \tag{34}$$

$$\triangle t \leq \frac{\triangle}{c\sqrt{3}} \tag{35}$$

3.2.2 Stability for the Fourth Order Difference

Substituting the fourth order operators into the stability requirement (12), in the same way we looked at the second order stability equation, produces

$$\left(\frac{2}{\triangle}\right)^2 \left[\frac{9}{8}\sin\left(\frac{k_x\triangle x}{2}\right) - \frac{1}{24}\sin\left(\frac{3k_x\triangle x}{2}\right)\right]^2 + \tag{36}$$

$$\left(\frac{2}{\triangle}\right)^2 \left[\frac{9}{8}\sin\left(\frac{k_y\triangle y}{2}\right) - \frac{1}{24}\sin\left(\frac{3k_y\triangle y}{2}\right)\right]^2 +$$

$$\left(\frac{2}{\triangle}\right)^2 \left[\frac{9}{8}\sin\left(\frac{k_z\triangle z}{2}\right) - \frac{1}{24}\sin\left(\frac{3k_z\triangle z}{2}\right)\right]^2 \leq \frac{2}{\triangle t}$$

Making the same assumptions that we made for the second order operator, we can simplify this equation into

$$\frac{2c^2}{\triangle}\frac{28^2}{24} + \frac{2c^2}{\triangle}\frac{28^2}{24} + \frac{2c^2}{\triangle}\frac{28^2}{24} \leq \left(\frac{2}{\triangle t}\right)^2 \tag{37}$$

$$\sqrt{3}\frac{28c}{12\triangle} \leq \frac{2}{\triangle t}$$

$$\triangle t \leq \frac{24\triangle}{28c\sqrt{3}} = \frac{6\triangle}{7c\sqrt{3}}$$

3.2.3 Stability for the Three Dimensional Modified (2,4) Scheme

The spatial eigenvalues are of the form

$$\Lambda^2 = \frac{1}{144(\triangle x)^2}\left[144k_1^2\sin^2\left(\frac{k_x\triangle x}{2}\right) + 16k_2^2\sin^2\left(\frac{3k_x\triangle x}{2}\right) + \tag{38}\right.$$

$$96k_1k_2\sin\left(\frac{k_x\triangle x}{2}\right)\sin\left(\frac{3k_x\triangle x}{2}\right) +$$

$$k_3^2\sin^2\left(\frac{3k_x\triangle x}{2}\right)\left(\cos\left(k_y\triangle y\right) + \cos\left(k_z\triangle z\right)\right) +$$

$$2\left(12k_1\sin\left(\frac{k_x\triangle x}{2}\right) + 4k_2\sin\left(\frac{3k_x\triangle x}{2}\right)\right)k_3\sin\left(\frac{k_x\triangle x}{2}\right) \cdot$$

$$\left. \sin\left(\frac{3k_x\triangle x}{2}\right)\left(\cos\left(k_y\triangle y\right) + \cos\left(k_z\triangle z\right)\right)\right] +$$

$$\ldots$$

which, using the same assumptions as for the second order difference, produces

$$3 \cdot \left(\frac{2}{144\triangle}\right)^2 \left[144k_1^2 + 16k_2^2 + 96k_1k_2 + \sqrt{2}k_3\left(k3 + 2(12k_1 + 4k_2)\right)\right] \le \left(\frac{2}{\triangle t}\right)^2 \tag{39}$$

and, solving for the same stability form as the other difference methods, produces

$$\triangle t \le \frac{\triangle}{c\sqrt{3\left[144k_1^2 + 16k_2^2 + 96k_1k_2 + \sqrt{2}k_3\left(k3 + 2(12k_1 + 4k_2)\right)\right]}} \tag{40}$$

where is it also assumed that the largest value for $\left(\cos(k_y\triangle y) + \cos(k_z\triangle z)\right)$ is $\sqrt{2}$.

For the case where $k_1 = 1$, $k_2 = k_3 = 0$, the difference operators collapse to second order and the stability requirement reduces to the second order stability equation

$$\triangle t \le \frac{\triangle}{c\sqrt{3}} \tag{41}$$

and in the case where $k_1 = 9/8$, $k_2 = -1/9$, $k_3 = 0$, the difference operators reduce to the standard fourth order case producing

$$\triangle t \le \frac{\triangle}{c\sqrt{3 \cdot \frac{12544}{9216}}} = \frac{6\triangle}{7c\sqrt{3}} \tag{42}$$

4   Conclusions and Future Work

The dispersion and stability relations become more complex as one progresses from the original second-order method to the three dimensional M24 method. However, since the relations for dispersion and stability can be expressed in terms of general difference operators, analysis of any specific difference method consists of straightforward substitution into the general equations. Care must taken to avoid occurrences such as the non-linear difference operators that appear in the modified (2,4) method (section 2.3.3).

We are currently constructing a three dimensional electromagnetic simulator using the M24 method, with the global dispersion error minimized using the dispersion equations derived in this paper. Using the generalized equations, the M24 method and other variations - such as a proposed "compact" M24 version - can be easily analyzed for dispersion and stability characteristics.

References

[1] K. Yee, "Numerical solution of initial boundary value problems involving maxwell's equations in isotropic media," *IEEE Trans. on Antennas and Propagat.*, vol. 14, pp. 302–307, 1966.

[2] W. F. Ames, *Numerical Methods for Partial Differential Equations.* New York: Barnes and Noble, Inc., 1969.

[3] M. Hadi, *A Modified (2,4) Scheme For Modeling Electrically Large Structures With High Phase Accuracy.* PhD thesis, University of Colorado at Boulder, January 1996.

Transparent Absorbing Boundary (TAB): Truncation of Computational Domain without Reflections [1]

Jian Peng and Constantine A. Balanis
Department of Electrical Engineering
Telecommunications Research Center
Arizona State University
Tempe, AZ 85287-7206

Abstract

A new approach to truncate computational domains without reflection is proposed for finite methods, such as finite difference and finite element. By a *transparent* amplitude modulation, the open-space Maxwell equations, along with boundary conditions, are transformed to an equivalent hyperbolic system with a homogeneous closed boundary. Like the popular Perfectly Matched Layer (PML), the TAB is independent of frequency and incident angle. The unique feature of this method is that it does not need the absorption region of the PML, and the physical fields can be found from the attenuated ones through an inverse transformation.

1 Introduction

An important issue in computational electromagnetics is to simulate an unbounded space in a finite domain with a minimal computational space. Figure 1 shows a diagram of a traditional finite computational domain. The subject domain contains the system under investigation within which field components are of interest. Surrounding it is a transition domain which is used to truncate the unbounded space. A variety of techniques have been proposed [1]-[6] to represent the fields with some prescribed conditions either at the exterior boundary of the computational domain or at the interfaces between the subject domain and the transition domain. The Perfectly Matched Layer (PML), proposed by Berenger [6], is presently the state-of-art of truncation techniques. It is independent of frequency and incident angle, and is virtually reflection free. Its shortcoming is the storage-intensiveness because of the split formulation. A variety of alternative approaches have since been proposed to avoid splitting fields [7, 8]. However, the transition region is still used to absorb the outgoing waves in these techniques. Besides, the Berenger's approach is easy to implement in time domain, while the others are suitable in frequency domain.

The truncation technique we propose here is an analytical approach that can be directly applied to various finite methods, such as finite difference and finite element, in either time or frequency domain. Without introducing reflections, the *transparent absorbing boundary* (TAB) forces the magnitudes of the field components to decay inside the subject domain and to become exactly zero at the domain's boundary. Thus, the transition domain used in most of the existing truncation methods is no longer needed. In this paper, we will present the idea of the technique, along with some examples to demonstrate its characteristics.
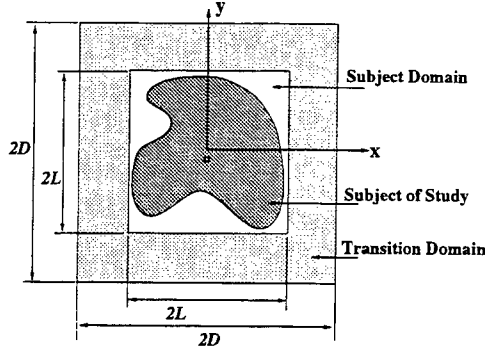
Figure 1: Configuration of a traditional computational domain.

2 Transparent Absorbing Boundary

The proposed *transparent absorbing boundary* (TAB) method begins with the introduction of auxiliary fields. Governing equations for the auxiliary system are then derived from Maxwell's equations. Let $\mathbf{E}_o(t,r)$ and $\mathbf{H}_o(t,r)$ be the electric and magnetic fields of a physical problem in an unbounded space, satisfying Maxwell's equations and the boundary conditions of the problem. Assume that $F(r)$ is a scalar amplitude modulation function, defined in the subject domain whose boundary is indicated by r_o. Then, the auxiliary fields $\mathbf{E}(t,r)$ and $\mathbf{H}(t,r)$ are defined as:

$$\mathbf{E}(t,r) = F(r)\mathbf{E}_o(t,r) \tag{1a}$$

$$\mathbf{H}(t,r) = F(r)\mathbf{H}_o(t,r) \tag{1b}$$

If $F(r) \neq 0$ for $r < r_o$, one can express $(\mathbf{E}_o, \mathbf{H}_o)$ in terms of $(\mathbf{E}, \mathbf{H})$ and substitute them into Maxwell's equations. Then, the governing equations that the auxiliary fields must satisfy are, for interior points $r < r_o$,

$$\frac{\partial \mathbf{E}}{\partial t} = \frac{1}{\epsilon}\left(\nabla \times \mathbf{H} - \frac{1}{F}\nabla F \times \mathbf{H}\right) - \frac{\sigma}{\epsilon}\mathbf{E} - \frac{F}{\epsilon}j_i \tag{2a}$$

$$\frac{\partial \mathbf{H}}{\partial t} = -\frac{1}{\mu}\left(\nabla \times \mathbf{E} - \frac{1}{F}\nabla F \times \mathbf{E}\right) - \frac{\sigma^*}{\mu}\mathbf{H} - \frac{F}{\mu}m_i \tag{2b}$$

$$\nabla \cdot \mathbf{E} = F\rho + \frac{1}{F}\nabla F \cdot \mathbf{E} \tag{2c}$$

$$\nabla \cdot \mathbf{H} = F\rho^* + \frac{1}{F}\nabla F \cdot \mathbf{H} \tag{2d}$$

where σ, σ^*, j_i, m_i, ρ and ρ^* retain their meanings of the physical problem [9]; and for boundary points $r = r_o$,

$$\mathbf{E} = F(r_o)\mathbf{E}_o \tag{3a}$$

$$\mathbf{H} = F(r_o)\mathbf{H}_o \tag{3b}$$

Apparently, homogeneous boundary conditions can be obtained for the auxiliary system if F is chosen to decay outwardly and to become zero at the boundary r_o. The most important feature of (2a) and (2b) is the introduction of $\frac{1}{F}\nabla F \times \mathbf{E}$ and $\frac{1}{F}\nabla F \times \mathbf{H}$. According to the theory of hyperbolic partial differential equations [10, 11], it is these terms that make the field attenuate and result in the homogeneous boundary conditions, regardless of the physical interpretations of the loss mechanism. Therefore, the effect of the outwardly-decaying F on the auxiliary system is equivalent to the absorption of the fields by these lossy terms.

In addition to the governing equations, all the boundary conditions of the physical problem are also transformed properly to establish an equivalence between the physical and auxiliary systems. Hence, instead of solving Maxwell's equations in the unbounded space, one can first solve the auxiliary system (2) with homogeneous boundary conditions. The physical fields interior to boundary r_o are then found using (1a) and (1b). It is important to ensure that no additional reflection is created during the transformation of boundary conditions.

Thus, the critical part of the *transparent absorbing boundary* is to impose constraints upon the amplitude modulation function $F(r)$ so that the artificial loss mechanism creates no reflections. It is well-known that there will be no reflection from a medium discontinuity if both the phase velocities and wave impedances are identical across it. Furthermore, the physical reflection at the medium discontinuity will not be affected by an artificial loss mechanism if the boundary conditions $[BC]$, the phase velocities v, and the wave impedances η are unchanged across the interface by the loss mechanism; i.e.,

$$[BC]_a = [BC]_o, \qquad v_a = v_o, \qquad \text{and} \qquad \eta_a = \eta_o \tag{4}$$

where subscript a indicates the auxiliary system while o stands for the original one. Such a characteristics of zero reflection is independent of frequency, incident angle, and material properties. Note that, in [6], it is indicated that the PML satisfies these conditions, which explains mathematically why the PML is a reflection-free loss mechanism.

Since $F(r) \neq 0$ in the interior domain $r < r_o$, the auxiliary system has the same wave impedance as that of the physical system, i.e., $\eta_a(r) = \frac{|\mathbf{E}(t,r)|}{|\mathbf{H}(t,r)|} = \frac{|\mathbf{E}_o(t,r)|}{|\mathbf{H}_o(t,r)|} = \eta_o(r)$. Meanwhile, a real and continuous F makes the boundary conditions and phase terms identical in the two systems. Thus, no additional reflection is created at the discontinuities. In other words, the artificial loss seems *transparent*. Consequently, the proposed method is referred to as the *Transparent Absorbing Boundary* (TAB). In addition to being non-zero, real, continuous, and outwardly-decaying, F should have at least first-order differentiability so that it does not introduce discontinuity to cause reflection. For simplicity, it is also preferred that the function is single-valued and independent of field information. These conditions are quite easy to satisfy; and the following

$$F(x,y,z) = \left[1 - \left(\frac{|x|}{L_x}\right)^m\right]^n \left[1 - \left(\frac{|y|}{L_y}\right)^p\right]^q \left[1 - \left(\frac{|z|}{L_z}\right)^u\right]^v \tag{5a}$$

and

$$F(x,y,z) = \cos^m\left[\frac{\pi}{2}\left(\frac{|x|}{L_x}\right)^n\right] \cos^p\left[\frac{\pi}{2}\left(\frac{|y|}{L_y}\right)^q\right] \cos^u\left[\frac{\pi}{2}\left(\frac{|z|}{L_z}\right)^v\right] \tag{5b}$$

are two examples of F in Cartesian coordinates, if m, n, p, q, u and v are greater than zero. L_x, L_y and L_z are the lengths of attenuation paths in the x, y and z directions, respectively.
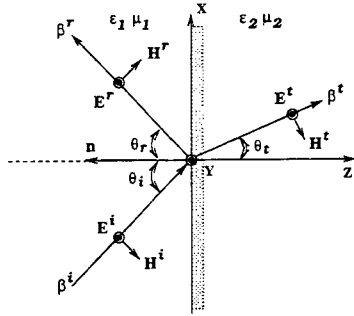
Figure 2: TE (horizontal) polarized plane wave incident at an oblique angle on an interface.

3   Reflection Coefficient

The following analytical example is intended to demonstrate that the physical reflection at a medium discontinuity will not be affected if (4) is satisfied. The derivation is similar to the plane wave case in [9]. Assume that a TE (perpendicular) polarized plane wave is incident obliquely on the interface of medium 1 and medium 2, as shown in Figure 2. The auxiliary incident fields can be expressed as:

$$\mathbf{E}^i = \hat{a}_y |E^i(x,z)| e^{-j\frac{\omega}{v_1}(x\sin\theta_i + z\cos\theta_i)} \tag{6a}$$

$$\mathbf{H}^i = (-\hat{a}_x \cos\theta_i + \hat{a}_z \sin\theta_i)|H^i(x,z)| e^{-j\frac{\omega}{v_1}(x\sin\theta_i + z\cos\theta_i)} \tag{6b}$$

where v_1 is the phase velocity of the auxiliary fields in region 1, and i indicates the incident fields. The reflected and transmitted fields of the auxiliary system can be expressed accordingly.

Under (4), the tangential components of the auxiliary fields are continuous, like the physical fields. Substituting the incident, reflected and transmitted field expressions into the continuity equations leads to Snell's laws of reflection and transmission:

$$\theta_i = \theta_r \tag{7a}$$

$$\frac{1}{v_1}\sin\theta_i = \frac{1}{v_2}\sin\theta_t \tag{7b}$$

as well as the reflection and transmission coefficients Γ and T:

$$\Gamma = \frac{|E^r(x,z=0)|}{|E^i(x,z=0)|} = \frac{\eta_2 \cos\theta_i - \eta_1 cos\theta_t}{\eta_2 \cos\theta_i + \eta_1 cos\theta_t} \tag{8}$$

$$T = \frac{|E^t(x,z=0)|}{|E^i(x,z=0)|} = \frac{2\eta_2 \cos\theta_i}{\eta_2 \cos\theta_i + \eta_1 cos\theta_t} \tag{9}$$

where $\eta_1 = \frac{|E^i|}{|H^i|} = \frac{|E^r|}{|H^r|}$ is the wave impedance of the auxiliary waves in medium 1, and $\eta_2 = \frac{|E^t|}{|H^t|}$ represents that in medium 2. Since the phase velocities and wave impedances are identical in the physical and auxiliary systems, the propagation directions, dictated by Snell's laws, are maintained and the coefficients given in (8) and (9) are equal to those of the physical case given in [9]. Therefore, the *transparent absorbing boundary* does not introduce additional reflections, regardless of the frequency and incident angle of the waves.
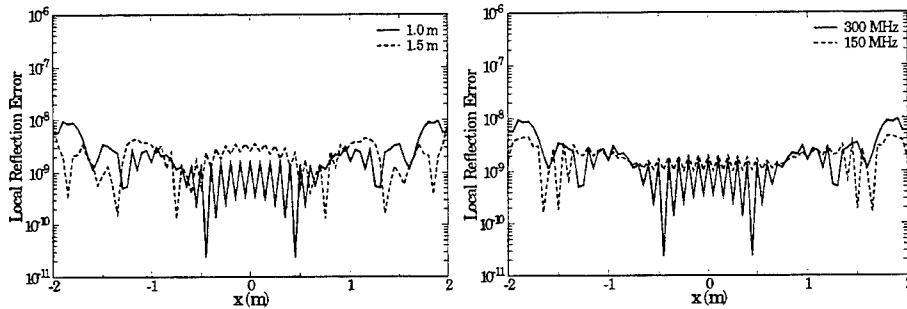
Figure 3: Local reflection errors that are due to the TAB absorption.

4 Numerical Reflections

To show the TAB's characteristics numerically, the reflection errors of a two-dimensional TM polarized cylindrical wave are computed, using the methodology suggested by Moore [12]. The computational domain is shown in Figure 1, with the source in the center of the subject domain that is free space now. The dimensions of the domains are $2L = 4\ m$ and $2D = 8\ m$. The amplitude modulation function is given as below:

$$F(x,y) = \begin{cases} \left[1 - \left(\frac{|x|-L}{D-L}\right)^4\right]\left[1 - \left(\frac{|y|-L}{D-L}\right)^4\right] & \text{if } (x,y) \text{ in the transition domain} \\ 1 & \text{otherwise} \end{cases} \qquad (10)$$

The transition region is still used to measure the reflections caused by the TAB's loss mechanism. Yee's algorithm [13, 14] is used to approximate (2a) and (2b). The cells are 0.05 m × 0.05 m in dimension, which makes the transition domain 40 cells thick. The Courant number $\gamma = \frac{c\delta t}{\Delta}$ is taken to be 0.7, and the time duration is 100 steps. The computations were made with double precision.

Figure 3 shows the distributions of local reflection errors. They are lower than 10^{-8} (i.e., -160 dB); in other words, the TAB is *reflection-free*, as expected. The data shown on the left are the errors at 300 MHz, collected along two horizontal lines off the symmetry line by some distances. Since the distributions are along the different observation lines, the low reflections in the two cases indicates that the TAB is independent of the incident angles of the source. The data shown on the right were computed at 150 MHz and 300 MHz, and collected along the horizontal line that is 1 m off the symmetry line. It is clear that the operating frequency has little effects on the low reflection of the TAB; i.e., the loss mechanism is independent of frequency.

It should be pointed out that the reflection errors shown in Figure 3 are solely due to the artificial loss mechanism. It is this kind of reflection that limits the applications of most absorption-based truncation methods. Like the PML, the TAB is virtually reflection-free and independent of frequency and incident angle at the interface between the free space and the artificial lossy media. The other type of reflection into the free space region is caused by the numerical implementation at the exterior boundary, such as the perfect electric conducing (PEC) termination used in the PML. Such a reflection is not intrinsic to the analytical absorbing mechanism and may vary with different numerical implementations. Therefore, it is eliminated during the computations by stopping the computation before such a reflected wave reaches the subject domain.
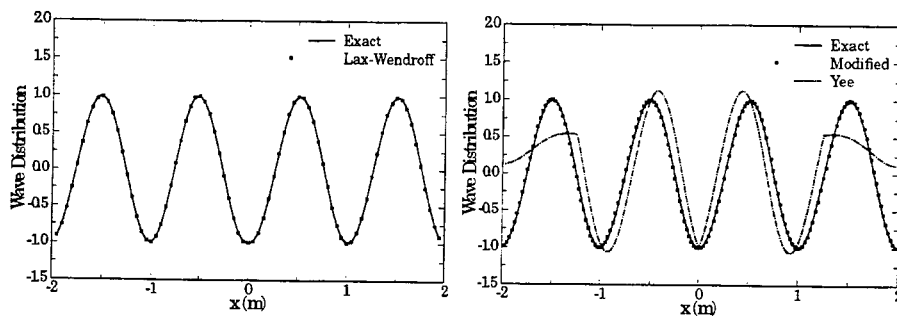
Figure 4: The numerical solutions of the E_o of a plane wave traveling outwardly in both directions.

5 Domain Truncation for Finite Difference Methods

It is mentioned in the previous section that the imperfection due to the numerical implementation near the exterior boundary may cause some reflections. They are not intrinsic to the analytical reflection-free loss mechanism. In this section, we use two one-dimensional examples to show that that kind of reflections are indeed caused by the finite difference schemes, instead of the analytical absorbing method.

Assume that a plane wave source is located in the middle of an one-dimensional free-space domain, and the wave propagates in both directions. The entire domain amplitude modulation function

$$f(x) = 1 - \left(\frac{|x|}{L}\right)^4, \qquad \qquad \text{if } |x| \leq L \qquad (11)$$

is used to truncate the computational domain of $2L = 4\ m$. Both Yee's algorithm and the Lax-Wendroff scheme [15] are applied to find the auxiliary E field. The results are then converted back to E_o, and compared with the exact solution. In the computations, the Courant number is equal to 1, the cell size is 0.025λ, and the time duration is 400 steps which is sufficiently long for the reflected waves to bounce back and forth a few times in the domain. The numerical results are shown in Figure 4, along with the exact solution of the problem.

The computed results on the left-hand side were obtained using the Lax-Wendroff scheme in which the E and H fields are collocated. The numerical solution agrees excellently with the exact solution. Those on the right-hand side were computed with Yee's algorithm where the E and H grids are staggered. Without modifications, the result is contaminated by the reflections generated near the two boundary ends, as shown by the dashed line. The reflections are caused by the staggered finite difference approximation, which can be illustrated with the help of Figure 5. At the last H grid (a half cell away from the boundary), the Yee equation for the magnetic field is

$$H|_{N-0.5}^{n+\frac{1}{2}} = H|_{N-0.5}^{n-\frac{1}{2}} + \frac{\gamma}{\eta_o}\left(1 + \frac{\Delta f'_{N-0.5}}{2f_{N-0.5}}\right) E|_{N-1}^{n} \approx H|_{N-0.5}^{n-\frac{1}{2}} + \frac{\gamma}{\eta_o}\frac{f_N}{f_{N-0.5}} E|_{N-1}^{n} = H|_{N-0.5}^{n-\frac{1}{2}} \quad (12)$$

because of $f_N = 0$. If the initial value is zero, $H|_{N-\frac{1}{2}}$ will be always close to zero, which is equivalent to a magnetic conducting wall at the grid point. An identical wall occurs at the other end of the
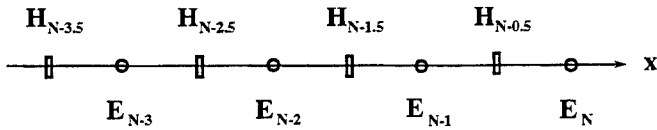
Figure 5: The one-dimensional illustration of a staggered grid, such as the Yee's.

domain. Modifications, such as the following,

$$H|_{N-0.5}^{n+\frac{1}{2}} = \frac{1}{2}\left(H|_{N-0.5}^{n-\frac{1}{2}} + H|_{N-1.5}^{n-\frac{1}{2}}\right) + \frac{\gamma}{\eta_o}\left(1 + \frac{\Delta f'_{N-0.5}}{2f_{N-0.5}}\right)E|_{N-1}^n \qquad (13)$$

are needed to avoid the problem. With (13), the formation of the magnetic walls are prevented; and the computed result, shown as the dot, agrees well with the exact solution. Thus, such reflections are associated with the particular numerical scheme, instead of the artificial loss mechanism. It is noticed that the effectiveness of (13) depends upon the values of the Courant number γ, and varies with the dimensions of the problems. Further research is necessary in order to prevent the numerical reflection walls associated with the staggered scheme.

6 Conclusion

A new analytical approach, the *Transparent Absorbing Boundary* (TAB), has been proposed. The TAB introduces an artificial loss mechanism that can be mathematically identified. With the TAB method, a physical problem in an unbounded space can be solved in a closed domain, with the aid of the auxiliary fields.

Like the popular PML method, the TAB is reflection-free, independent of frequency, and unconstrained by the incident angle. The uniqueness of the TAB is that it does not need the additional transitional domain. Besides, it can be directly applied to time- and frequency-domain finite methods, such as the Finite Difference Time Domain (FDTD) and the Finite Element Method (FEM). Potentially, it is suitable to truncate an arbitrary convex domain by defining the amplitude modulation function F according to the shape of the domain.

Analytical and numerical examples showed that the TAB itself does not create reflections. The method has been successfully implemented to truncate the collocated Lax-Wendroff scheme. However, when used along with the popular Yee staggered algorithm, an artificial magnetic conducting wall is formed near the exterior boundary. It should be noted that this is associated only with staggered schemes and is presented as a future challenge. Hopefully, the strengths and challenging issues of the TAB will stimulate new ideas and further research to improve the computational efficiency and accuracy of finite methods.

References

[1] B. Engquist, and A. Majda, "Absorbing boundary conditions for the numerical simulation of waves," *Mathematics of Computation*, vol. 31, 1977, pp. 629-651.

[2] G. Mur, "Absorbing boundary conditions for the finite-difference approximation of the time-domain electromagnetic field equations," *IEEE Trans. Electromagnetic Compatibility*, vol. 23, 1981, pp. 377-382.

[3] Z. P. Liao, H. L. Wong, B. P. Yang, and Y. F. Yuan, "A transmitting boundary for transient wave analyses," *Scientia Sinica* (series A), vol. XXVII, 1984, pp. 1063-1076.

[4] R. L. Higdon, "Numerical absorbing boundary conditions for the wave equation," *Mathematics of Computation*, vol. 49, 1987, pp. 65-90.

[5] K. K. Mei and J. Fang, "Superabsorption - a method to improve absorbing boundary conditions," *IEEE Trans. Antennas and Propagation*, vol. 40, 1992, pp. 1001-1010.

[6] J. P. Berenger, "A perfectly matched layer for the absorption of electromagnetic waves," *J. Computational Phys.*, vol. 114, no. 2, Oct. 1994, pp. 185-200.

[7] Z. S. Sacks, D. M. Kingsland, R. Lee and J. Lee, "A perfectly matched anisotropic absorber for use as an absorbing boundary condition," *IEEE Trans. Antennas Propagat.*, vol. 43, no. 12, Dec. 1995, pp. 1460-1463.

[8] W. C. Cho and W. H. Weedon, "3D perfectly matched medium from modified Maxwell's equations with stretched coordinates," *Microwave and Optical Technology Letters*, vol 7, no. 13, Sept. 1994.

[9] C. A. Balanis, *Advanced Engineering Electromagnetics*, New York: John Wiley & Sons, 1989.

[10] P. R. Garabedian, *Partial Differential Equations*, New York: John Wiley, 1964.

[11] F. Mainardi and D. Cocci, "Energy propagation in linear hyperbolic systems in the presence of dissipation," *Nonlinear Hyperbolic Problems: Theoretical, Applied, and Computational Aspects*, Procceedings of the fourth international conference on hyperbolic problems, Taormina, Italy, April 1992, pp. 409-415.

[12] T. G. Moore *et al.*, "Theory and application of radiation boundary operators," *IEEE Antenn. Propagat.*, vol. 36, Dec. 1988, pp. 1797-1812.

[13] K. S. Yee, "Numerical solution of initial boundary value problems involving Maxwell's equations in isotropic media," *IEEE Trans. Antennas and Propagation*, vol. 14, 1966, pp. 302-307.

[14] A. Taflove, *Computational Electromagnetics*, Boston: Artech House, 1995.

[15] P. D. Lax and B. Wendroff, "Systems of conservation laws," *Comm. Pure and Appl. Math.*, vol. 13, 1960, pp. 217-237.

THE DESIGN OF MAXWELLIAN SMART SKINS

Richard W. ZIOLKOWSKI, *Electromagnetics Laboratory,*
Dept. of Electrical and Computer Engineering, Univ. of Arizona
Fabrice AUZANNEAU, *CEA CESTA, BP 2, 33114 Le Barp, FRANCE*

1 - INTRODUCTION

Electromagnetic absorbers have many practical usages and demand for them is increasing. These include the now famous stealth technologies and practical EMI/EMC countermeasures for personnel communications and computers, as well as the more traditional cone absorbing materials for anechoic chambers. The immense interest in complex media such as artificial chiral materials [1-4] has arisen from such needs. The artificial chiral materials such as the helix-loaded substrates [3] are worthy of particular note since they represent a very nice example of our current ability to engineer absorbers which have strong magnetic, as well as electric, properties designed into them. In contrast, artificial dielectrics have been known for many years [5-7] and have found uses, for example, as light-weight lenses and currently as photonic band-gaps [8].

Absorbers have also attracted much attention recently in the computational electromagnetics community. The need to truncate the simulation domain in any finite difference or finite element approach is well-known. Many approaches have been developed to achieve this truncation; they are generally classified now simply as absorbing boundary conditions (ABCs). Like with any real-life absorber, the perfect ABC would absorb perfectly any frequency of electromagnetic radiation incident upon it from any angle of incidence. The Berenger perfectly matched layer (PML) ABC [9] comes quite close to this goal. However, the PML ABC is implemented in a non-Maxwellian fashion through the field equation splitting introduced by Berenger [9]. This is not a serious drawback numerically, but it does mean that a PML region can not be realized physically.

A broad bandwidth absorbing material that is Maxwellian has been introduced in [10]. It is based upon a generalization of the Lorentz model for the polarization and magnetization fields that includes the time derivative of the driving fields as a source term. The physical basis for this time-derivative Lorentz material (TD-LM) model has been discussed [11]. Suggestions have been made [10] for potential realizations of this TD-LM material with a proper engineering of artificial materials. This paper represents a more detailed look at the use of electrically small radiating elements combined with a proper selection of circuits to achieve a perfect absorber. Because they are small, these artificial molecules can be integrated into the surfaces of an object and can be designed to cause active or passive variations in the responses (active or passive components in the circuits) from the electromagnetic field interactions with these structures. Potential applications include novel sensors and detectors as well as smart RCS surfaces and absorbers.

The electrically small antennas we have considered to date are discussed in Sections 2 and 3. The corresponding artificial electric and magnetic molecules are detailed in Sections 4 and 5. The results from modeling these smart structures with the finite difference time domain approach are discussed in Section 6. Conclusions are drawn in Section 7.

2 - DIPOLE ANTENNA

We consider an electrically small dipole antenna (i.e. $kl_0 \ll 1$, where $2l_0$ is the physical length of the antenna and k is the free space wavenumber) as shown in figure 1-a.

(a) dipole   (b) loop
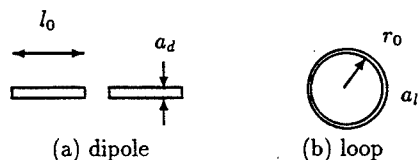
figure 1

For an induced current law on the dipole of the triangular form

$$I(z) = I_0(1 - \frac{|z|}{l_0})$$

the effective length h of the antenna is $\vec{h} = -l_0 \sin\theta\, \hat{a}_\theta$ and the induced open circuit voltage at the dipole terminals is

$$V_{OC} = \vec{E} \cdot \vec{h}$$

Using Thévenin's equivalent circuit for the dipole and its load, we find the current at the terminals to be

$$I_{in} = I(z = 0) = \frac{V_{OC}}{Z_{in} + Z_L}$$

where Z_{in} is the input impedance of the antenna and Z_L is the impedance of the load.

The equivalent polarization of the resulting 'electric molecule', i.e., the small dipole antenna coupled to the load, is thus given by

$$P = \frac{I_{in} l_0}{j\omega V} = \epsilon_0 \chi_e E$$

where

$$\chi_e = \frac{K_e}{-j\omega Z_d(\omega)} \qquad (1)$$

is the equivalent electric susceptibility of the composite material,

$$K_e = \frac{l_0^2}{\epsilon_0 V} \cos\psi_e \sin\theta$$

is a positive constant, ψ_e is the polarization angle between the dipole and the incident electric field, V is the effective volume in which the composite permittivity is constant, $Z_d(\omega) = Z_{in} + Z_L$ is the total impedance, and ϵ_0 is the permittivity of vacuum.

The input impedance of an electrically short dipole antenna is approximately

$$Z_{in}(\omega) = \frac{1}{-j\omega C_d}$$

where $C_d = \pi\epsilon_0 l_0/\Omega$ is the equivalent capacitance of the dipole, and $\Omega = \ln(2l_0/a_d)$ is the antenna thickness factor. The load is defined by passive elements. Various combinations are considered in Section 4.

3 - LOOP ANTENNA

For an electrically small loop antenna (i.e. $kr_0 \ll 1$, where r_0 is the loop's radius) as shown in figure 1-b, the induced current is a constant I_0. Using Norton's equivalent circuit for the loop and its load, we find the current at the terminals to be

$$I_0 = 2r_0 H = I_a + I_L$$

where I_a is the current flowing through the antenna impedance and I_L is the current through the load. The voltage at the load is

$$V_L = I_L Z_L = I_a Z_{in}$$

so we derive the expression for the current I_a

$$I_a = I_0/(1 + \frac{Z_{in}}{Z_L})$$

The input impedance of an electrically small loop antenna is approximately

$$Z_{in}(\omega) = -j\omega L_l$$

where $L_l = \mu_0 r_0 (\ln\frac{8r_0}{a_l} - 2)$ is the equivalent inductance of the loop.

The equivalent magnetization of the resulting "magnetic molecule", i.e., the small loop antenna coupled to the load, is thus given by

$$M = \frac{\pi r_0^2}{V} I_a = \chi_m H$$

where

$$\chi_m = \frac{K_h}{1 + Z_{in}/Z_L} \qquad (2)$$

is the equivalent magnetic susceptibility of the composite material,

$$K_h = \frac{2\pi r_0^3}{V} \cos \psi_h \sin \theta$$

with similar notations as before.

4 - EXAMPLES OF LOADS
4.1 - Global EM properties of the composite material
Due to the fact that the electric molecule produces only dielectric properties, and the magnetic molecule only magnetic properties, we can have different and unrelated behaviors on the 'dielectric side' and on the 'magnetic side'. Furthermore, if every dipole (or loop) is oriented in the same direction (under the action of an electric field for example) we obtain a dielectrically (or magnetically) anisotropic material.

Also, it appears possible to design a matched material based upon the dipole and the loop, i.e. a material with $\epsilon_r = \mu_r$ on a large frequency band, because of the apparent duality between the dielectric molecule and the magnetic molecule.

Assuming that the load has only passive components, the impedance Z_L can be written as the fraction of two polynomials of $-j\omega$

$$Z_L(\omega) = \frac{P_n(-j\omega)}{Q_m(-j\omega)} = \frac{\sum\limits_{i=0}^{n} p_i(-j\omega)^i}{\sum\limits_{i=0}^{m} q_i(-j\omega)^i} \qquad (3)$$

where the p_i and q_i are positive real numbers.

4.2 - Resistor load
The simplest load is a single resistor R. When connected to the dipole, the total impedance is $Z_d = R - 1/(jC_d\omega)$ and the electric susceptibility is given by

$$\chi_e = \frac{K_e C_d}{1 - j\omega R C_d}$$

which is similar to the Debye model.

When connected to the loop, the load impedance is $Z_L = R$ and the magnetic susceptibility is given by

$$\chi_m = \frac{K_h}{1 - j\omega L_l/R}$$

which is a *magnetic* Debye model.

In each case, the material has positive losses, since the components are passive.

4.3 - LRC loads
When connected to the dipole, an LRC *series* load gives the following electric susceptibility

$$\chi_e = \frac{K_e C_{tot} \omega_0^2}{\omega_0^2 - \omega^2 - j\omega R/L}$$

where $C_{tot} = C_d C/(C_d + C)$ is the resultant capacitance and $\omega_0 = 1/\sqrt{LC_{tot}}$ is the resonant frequency of the total circuit. This results in the well known Lorentz dispersion model. Note that $\omega_0^2 = 1/LC_{tot}$ is the resonant frequency of the total circuit, including the antenna.

When connected to the loop, the LRC *parallel* load gives the following magnetic susceptibility

$$\chi_m = \frac{\omega_0^2 K_h}{\omega_0^2 - \omega^2 - j\omega/RC}$$

where $L_{tot} = L_l L / (L_l + L)$ is the resultant inductance and $\omega_0 = 1/\sqrt{L_{tot}C}$ is the resonant frequency of the total circuit. This results in the *magnetic* Lorentz dispersion model.

4.4 - Other loads

When a parallel RC circuit is connected to the dipole, or by duality a series LR is connected to the loop, we obtain a *time derivative* Debye dielectric or magnetic model, caracterized by

$$\chi_e = C_d K_e \frac{1 - jRC\omega}{1 - jR(C + C_d)\omega} \qquad \chi_m = K_h \frac{R - jL\omega}{R - j(L + L_l)\omega}$$

When a parallel LR circuit is connected to the dipole, or by duality a series RC is connected to the loop, we obtain a *time derivative* Lorentz dielectric (presented in [10] and [11]) or magnetic model (TD-LM), characterized by

$$\chi_e = K_e C_d \frac{\omega_0^2 - j\omega/RC_d}{\omega_0^2 - \omega^2 - j\omega/RC_d} \qquad \chi_m = K_h \frac{\omega_0^2 - j\omega R/L_l}{\omega_0^2 - \omega^2 - j\omega R/L_l}$$

It is also possible to derive a double time derivative Debye or Lorentz Material by changing the loads. For example, the 2TD-LM dielectric material is obtained for a parallel LRC load, while the 2TD-LM magnetic material is for the series LRC load.

In each of the cases described above, the possibility of having a matched material (i.e. $\epsilon_r = \mu_r$) is subject to the condition

$$1 - \frac{jL_l\omega}{Z_L^{loop}} = -j\omega \frac{K_h}{K_e} \left(-\frac{1}{jC_d\omega} + Z_L^{dipole} \right) \tag{4}$$

5 - FDTD IMPLEMENTATION

The FDTD implementation is made by using an algorithm analogous to the Auxiliary Differential Equation Method. The electric (resp. magnetic) susceptibility is explicitly written employing equation 1 (resp. 2), where the load impedance Z_L is written as a fraction, employing relation 3. Then, after reduction of the denominators, the equation obtained is transformed into a partial differential equation, assuming a time derivative $\partial^n/\partial t^n$ for each term $(-j\omega)^n$. We show hereafter some examples of these partial differential equations.

5.1 - Resistor load : Debye models

Thus the simple resistor load leads to the following equations, relating P and E, M and H

$$\frac{\partial P}{\partial t} + \frac{1}{RC_d}P = \frac{\epsilon_0 K_e}{R}E$$

$$\frac{\partial M}{\partial t} + \frac{R}{L_l}M = \frac{K_h R}{L_l}H$$

5.2 - LRC loads : Lorentz models

A series LRC load, connected to the dipole and a parallel LRC to the loop lead to the following equations

$$\frac{\partial^2 P}{\partial t^2} + \frac{R}{L}\frac{\partial P}{\partial t} + \frac{1}{LC_{tot}}P = \frac{\epsilon_0 K_e}{L}E$$

$$\frac{\partial^2 M}{\partial t^2} + \frac{1}{RC}\frac{\partial M}{\partial t} + \frac{1}{L_{tot}C}M = \frac{K_h}{L_{tot}C}H$$

5.3 - Time Derivative Lorentz Materials

The parallel LR load connected to the dipole and the series RC connected to the loop lead to the following differential equations

$$\frac{\partial^2 P}{\partial t^2} + \frac{1}{RC_d}\frac{\partial P}{\partial t} + \frac{1}{LC_d}P = \frac{\epsilon_0 K_e}{R}\frac{\partial E}{\partial t} + \frac{\epsilon_0 K_e}{L}E$$

$$\frac{\partial^2 M}{\partial t^2} + \frac{R}{L_l}\frac{\partial M}{\partial t} + \frac{1}{L_l C}M = \frac{K_h R}{L_l}\frac{\partial H}{\partial t} + \frac{K_h}{L_l C}H$$

6 - NUMERICAL RESULTS
6.1 - Matched Debye material

In order to have a reflectionless material, equation 4 leads to

$$K_e C_d = K_h \qquad R_l R_d C_d = L_l$$

The first equation enables us to choose the dimensions of the antennas, while the second provides their respective loads. We designed a matched absorbing multilayer material, with a taper on the loads. The following picture shows that, for an incident wave of unit amplitude, the reflected wave is less than 2.10^{-4}V/m, and the transmitted wave is attenuated in its propagation through the material.

E-field at t=18ns vs. distance (m)
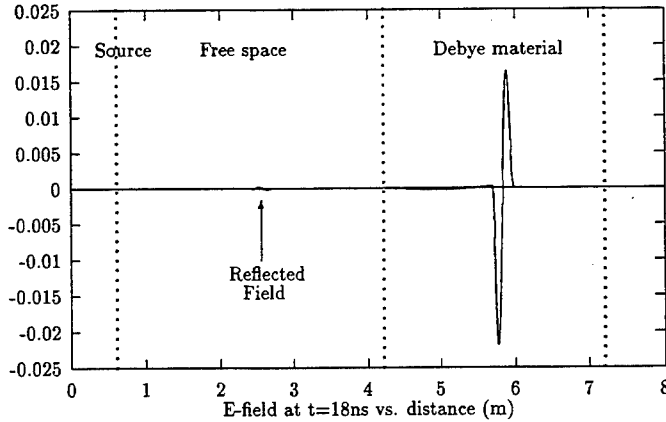
6.2 - Matched Lorentz and TD-LM materials

In order to have a reflectionless material, equation 4 leads to the two previous equations plus

$$L_d C_d = L_l C_l$$

This leads essentially to the same analytical and numerical results as was obtained with the matched Debye material for normally incident electromagnetic (i.e., 1D plane) waves.

7 - CONCLUSIONS

The possibility of constructing artificial molecules from loaded elementary electric and magnetic dipole antennas has been examined. The design of the loads of these molecules allows one to achieve particular polarization and magnetization properties. The resultant characteristics of these artificial molecules lead to lossy electric and magnetic material designs. For instance, since the polarization and magnetization properties can be properly proportioned, one can realize extremely interesting reflectionless electromagnetic absorbers. These "smart skins" have many potential uses.

102

Several basic cases were discussed. They have been tested numerically with FDTD implementations in 1D. Many more parameter studies must be made and are currently under investigation. The response of the matched materials to various incident pulse shapes are being considered as well as their behavior when their thickness and loss parameters are varied significantly. Obliquely incident plane waves cases are also being considered. Future studies will include the use of active molecules achieved with nonlinear loads and their reponse to broad bandwidth incident pulses.

References

[1] I. V. Lindell, A. H. Sihvola, S. A. Tretyakov, and A. J. Vitanen *Electromagnetic Waves in Chiral and Bi-isotropic Media*, Artech House, Boston, 1994, pp. 8-14.

[2] F. Mariotte, S. A. Tretyakov, and B. Sauviac "Isotropic chiral composite modeling: comparison between analytical, numerical, and experimental results," *Microwave and Optical Technology Letters*, vol 7(18), pp. 861-864, December 1994.

[3] *Proceedings Chiral'94 Workshop*, 3rd International Workshop on Chiral, Bi-isotropic and Bi-anisotropic Media Eds. F. Mariotte and J.-P. Parneix, Perigueux France, May 18-20, 1994 (C.E.A. / C.E.S.T.A., Le Barp France, 1994).

[4] R. E. Raab and J. H. Cloete "An eigenvalue theory of circular birefringence and dichroism in a non-magnetic chiral media," *J. Electromagnetic Waves and Applications*, vol. 8(8), pp. 1073-1089, 1994.

[5] J. Brown, "Artificial dielectrics," in *Progress in Dielectrics*, vol. 2, Heywood, London, 1960, pp. 194-225.

[6] M. M. Z. Kharadly, W. Jackson "The properties of artificial dielectrics comprising arrays of conducting elements," *Proc. IEE (London)*, vol. 100, pp. 199-212, July 1953.

[7] Z. A. Kaprielian "Dielectric properties of a lattice of anisotropic particles,", *J. Appl. Phys.*, vol. 27(1), pp. 24-32, January 1956.

[8] J. D. Joannopoulos, R. D. Meade, and J. N. Winn, *Photonic Crystals* (Princeton University Press, Princeton, New Jersey, 1995).

[9] J.-P. Berenger "A perfectly matched layer for the absorption of electromagnetic waves," *J. Comp. Phys.*, vol. 114, pp. 185-200, October 1994.

[10] R. W. Ziolkowski, "The design of Maxwellian absorbers for numerical boundary conditions and for practical applications using engineered artificial materials," to appear in *IEEE Trans. Antennas and Propagation*, 1997.

[11] R. W. Ziolkowski, "Time-derivative Lorentz-materials and their utilization as electromagnetic absorbers," submitted to *Phys. Rev. E*, November 1996.

Numerical Analysis of Periodic Structures Using the Split Field Update Algorithm

Paul H. Harms, J. Alan Roden, James G. Maloney, Morris P. Kesler, Eric J. Kuster
Signature Technology Lab
Georgia Tech Research Institute
Atlanta, GA 30332

Stephen D. Gedney
Department of Electrical Engineering
University of Kentucky

1. Introduction

The numerical modeling of periodic structures, such as photonic band gap (PBG) structures and frequency selective surfaces (FSS), is important in the design of antennas and other devices [1]. Currently, most available techniques are based in the frequency domain and thus can analyze periodic structures for only one frequency at a time. This can be a severe limitation for analyzing periodic structures which operate over a broad frequency band. An alternative approach is to employ time-domain techniques such as the finite-difference time-domain algorithm. A primary consideration with using a time-domain approach for a periodic structure, however, has been the implementation of an efficient technique for modeling the periodic boundary condition for plane waves at arbitrary angles of incidence. Recently, progress has been made in this area with the development of a simple two-dimensional technique called the split-field update (SFU) method that incorporates a periodic boundary condition in the time-domain and maintains the capacity to compute wide bandwidth responses [2]. In this work, this methodology is extended to three dimensions, and the resultant algorithm is employed to analyze a PBG structure and a thick FSS. Comparisons of the results of the method are made with data from measurements and other numerical methods.

2. Formulation

The periodic boundary condition is taken into consideration through a Floquet related transformation of Maxwell's equations which is presented in [3] and [4] and briefly described below. Since these equations are unstable when the traditional leap-frog approach of the finite-difference time-domain algorithm is employed, and the approach given in [4] is complex to implement, a split-field update (SFU) technique was developed [2]. The SFU technique uses field splitting in discretizing the transformed field equations. The fields are staggered in space, but for stability some of the split electric and magnetic fields are updated with the leap frog method at each half time step, and the rest of the split fields are computed with additional equations. For the problems under consideration, the propagation direction of the incident wave is in the x-z plane only, but the structure is periodic in both $\hat{x}$ and $\hat{y}$. The three dimensional formulation for an incident plane wave approaching the origin as shown in Fig. 1 is given by the equation

$$E^{inc}(x,y,z,t) = E_o^{inc} f\left(\frac{x\sin\theta}{c} + \frac{y}{c} + \frac{z\cos\theta}{c} + t\right) \tag{1}$$

where c is the velocity of light in free space, and θ is the angle of incidence. Using the frequency domain transform given by

$$\begin{Bmatrix} P \\ Q \end{Bmatrix} = \begin{Bmatrix} E \\ H \end{Bmatrix} e^{-jk_x x} \tag{2}$$

where $k_x = k_o \sin\theta$ the Floquet condition in the time domain simplifies to

$$P(x+T_x, y+T_y) = P(x,y) \tag{3}$$

for P and similarly for Q [3, 4]. After transforming Maxwell's equations in the frequency domain with (2), they are converted back to the time domain, and the field splitting approach is employed to discretize them. For example, P_y is given by

$$\frac{\partial P_y}{\partial t} = \frac{c\eta_o}{\varepsilon_r}\left(\frac{\partial Q_x}{\partial z} - \frac{\partial Q_z}{\partial x} + \frac{\sin(\theta)}{c}\frac{\partial Q_z}{\partial t}\right) \tag{4}$$

which is expressed in the split field form as

$$\frac{\partial P_{ya}}{\partial t} = \frac{c\eta_o}{\varepsilon_r}\left(\frac{\partial Q_x}{\partial z} - \frac{\partial Q_z}{\partial x}\right) \tag{5}$$

and

$$P_y = P_{ya} + \frac{\eta_o \sin(\theta)}{\varepsilon_r} Q_z \tag{6}$$

where η_o is the free space wave impedance, and c is the velocity of light in free space. Following the procedure given in [2], the SFU equations for the three dimensional case can be expressed as

$$Q_x^{n+1/2} = Q_x^{n-1/2} + \frac{c\Delta t}{\mu_r \eta_o}\left(\partial_z P_y^n - \partial_y P_z^n\right) \tag{7}$$

$$P_x^{n+1/2} = P_x^{n-1/2} - \frac{c\Delta t \eta_o}{\varepsilon_r}\left(\partial_z Q_y^n - \partial_y Q_z^n\right) \tag{8}$$

$$Q_{ya}^{n+1/2} = Q_{ya}^{n-1/2} + \frac{c\Delta t}{\mu_r \eta_o}\left(\partial_x P_z^n - \partial_z P_x^n\right) \tag{9}$$

$$P_{ya}^{n+1/2} = P_{ya}^{n-1/2} - \frac{c\Delta t \eta_o}{\varepsilon_r}\left(\partial_x Q_z^n - \partial_z Q_x^n\right) \tag{10}$$

$$Q_{za}^{n+1/2} = Q_{za}^{n-1/2} - \frac{c\Delta t}{\mu_r \eta_o}\left(\partial_x P_y^n - \partial_y P_x^n\right) \tag{11}$$

$$P_{za}^{n+1/2} = P_{za}^{n-1/2} + \frac{c\Delta t \eta_o}{\varepsilon_r}\left(\partial_x Q_y^n - \partial_y Q_x^n\right) \tag{12}$$

$$Q_z^{n+1/2} = \frac{Q_{za}^{n+1/2} + \dfrac{\sin\theta}{\mu_r \eta_o} P_{ya}^{n+1/2}}{1 - \dfrac{\sin^2\theta}{\mu_r \varepsilon_r}} \tag{13}$$

$$P_z^{n+1/2} = \frac{P_{za}^{n+1/2} - \sin(\theta)\dfrac{\eta_o}{\varepsilon_r} Q_{ya}^{n+1/2}}{1 - \dfrac{\sin^2\theta}{\mu_r \varepsilon_r}} \tag{14}$$

$$Q_y^{n+1/2} = Q_{ya}^{n+1/2} - \frac{\sin\theta}{\mu_r \eta_o} P_z^{n+1/2} \tag{15}$$

$$P_y^{n+1/2} = P_{ya}^{n+1/2} + \sin(\theta)\frac{\eta_o}{\varepsilon_r} Q_z^{n+1/2}. \tag{16}$$

Equations (7) - (12) are the finite difference updates, and (13) - (16) account for the periodicity. In (13) - (16) the fields are averaged in space where appropriate to maintain second-order accuracy.

The stability condition was derived for this formulation using a Von Neuman eigenvalue analysis [2] (including the spatial averaging) and is given by

$$\Delta t = \frac{\cos^2\theta}{c\dfrac{|\sin\theta|\sin\xi\cos\xi}{\Delta x} + c\sqrt{D}} \tag{17}$$

where

$$D = \frac{\sin^2\xi\cos^2\xi\sin^2\theta}{\Delta x^2} + \frac{\sin^2\xi\cos^2\theta}{\Delta x^2} + \frac{\cos^4\theta}{\Delta z^2} + \frac{\cos^2\xi\cos^2\theta\sin^2\theta}{\Delta z^2} + \frac{\cos^2\theta}{\Delta y^2} \tag{18}$$

$$\xi = \cos^{-1}\left(\frac{1}{2}\sqrt{2R}\right) \tag{19}$$

$$R = \frac{\Delta y^2 \Delta x^4 c_\theta^2 s_\theta^4 + \Delta y^2 \Delta z^4\left(2s_\theta^2 + 1\right) + 4\Delta x^2 \Delta z^4 s_\theta^2 + \Delta x^2 \Delta y^2 \Delta z^2 s_\theta^2\left(1 + c_\theta^2\right)}{\Delta y^2 \Delta x^4 c_\theta^2 s_\theta^4 + \Delta y^2 \Delta z^4\left(1 + s_\theta^2\right) + 4\Delta x^2 \Delta z^4 s_\theta^2 + 2\Delta x^2 \Delta y^2 \Delta z^2 s_\theta^2} +$$

$$\frac{\left(\Delta y \Delta x^2 s_\theta^2 - \Delta y \Delta z^2\right)\sqrt{\Delta y^2 \Delta x^4 s_\theta^4 c_\theta^4 + 2\Delta x^2 \Delta y^2 \Delta z^2 s_\theta^2 c_\theta^2 + 4\Delta x^2 \Delta z^4 s_\theta^2 c_\theta^2 + \Delta y^2 \Delta z^4}}{\Delta y^2 \Delta x^4 c_\theta^2 s_\theta^4 + \Delta y^2 \Delta z^4 \left(1 + s_\theta^2\right) + 4\Delta x^2 \Delta z^4 s_\theta^2 + 2\Delta x^2 \Delta y^2 \Delta z^2 s_\theta^2} \quad (20)$$

$s_\theta = \sin\theta$, and $c_\theta = \cos\theta$.

At normal incidence ($\theta = 0$), the stability criterion given by (17) - (20) reduces to the standard FDTD stability relation. As the angle of incidence increases, the required time step decreases, and as θ approaches grazing incidence (90°), the time step becomes very small which results in an impractical number of iterations. Due to this limitation, the SFU approach becomes computationally intensive for incident angles above approximately 80° degrees (at which point the time-step has been reduced by approximately a factor of 20). For the larger angles, other methods can be used, see for example [5, 6, 7, 10].

3. Boundary Conditions

The mesh is truncated with periodic boundary conditions (PBCs) at the surfaces normal to the $\hat{x}$ and $\hat{y}$ directions and a radiation or absorbing boundary condition in the $\pm\hat{z}$ coordinate directions. The PBC is implemented by setting the transformed magnetic fields one-half cell outside of the periodic cell boundaries to those fields one periodic cell away but within the periodic boundaries using (3).

The anisotropic perfectly matched layer (PML) boundary condition is employed to absorb radiation from the periodic structure that impinges upon the mesh truncation boundaries in $\pm\hat{z}$ [9]. Note that the conductivity in the PML needs to be increased for larger angles of incidence to provide better absorption.

4. Analysis of a Woodpile Photonic Band Gap Geometry and a Thick, Double, Concentric Square Loop

The SFU method is used to analyze a wood pile PBG structure and a thick, double, concentric square loop FSS. The SFU results for the PBG are compared with results from a frequency domain multi-mode matching (MMM) method and measurements [7]. The woodpile and its dimensions are shown in Figure 1. Each stick forming the woodpile is the same size and has the same permittivity. The structure is doubly periodic in $\hat{x}$ and $\hat{y}$. The results are given for normal incidence in Figure 2 and for an incident angle of 30 degrees in Figure 3. The numerical results from the SFU agree well with the data from the MMM technique, and the results are similar to the measured data. Note that the measurements at the high frequencies are more inaccurate.

A top view of one cell of the doubly-periodic, thick FSS is shown in Figure 4 [6, 8]. Thick conductors with square cross sections form the loops. The percentage of power reflected is computed for this case, and the results of the SFU calculations are compared with method of moments (MM) and the single-frequency finite difference time domain (SF-FDTD) results given in [6, 8]. Figure 5 shows the analysis for a plane wave at an incident angle of 0 degrees, and Figure 6 shows the results for a TM plane wave (H_y) at an incident angle of 60 degrees. For the 0 degrees incident angle, the SFU results agree best with the SF-FDTD results. For the 60 degrees case shown in Figure 6, the SFU results are slightly shifted from the other results, but good general agreement is observed.

5. Conclusions

The two-dimensional SFU method was extended to three dimensions where the propagation direction of the incident plane wave was limited to the x-z plane, but the periodic structures were doubly periodic in $\hat{x}$ and $\hat{y}$. Comparison of the numerical results with those from measurements and other methods showed the technique modeled both geometries well over a band of frequencies. This approach is being extended to the general three dimensional case for a plane wave at an arbitrary angle of incidence.
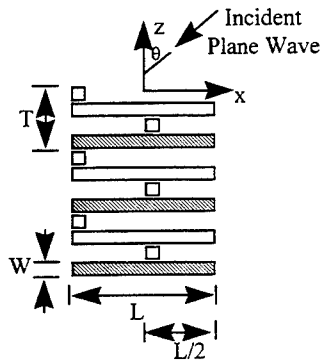
Figure 1. Side view of wood pile doubly-periodic in x and y. (Each stick has dimensions of W = 1/8 in, L = 0.4375 in and dielectric constant of $\varepsilon_r = 8.0$. The periodic cell is LxL. The diagonally shaded sticks along $\hat{x}$ are offset from each other in the same fashion as the sticks along $\hat{y}$.)
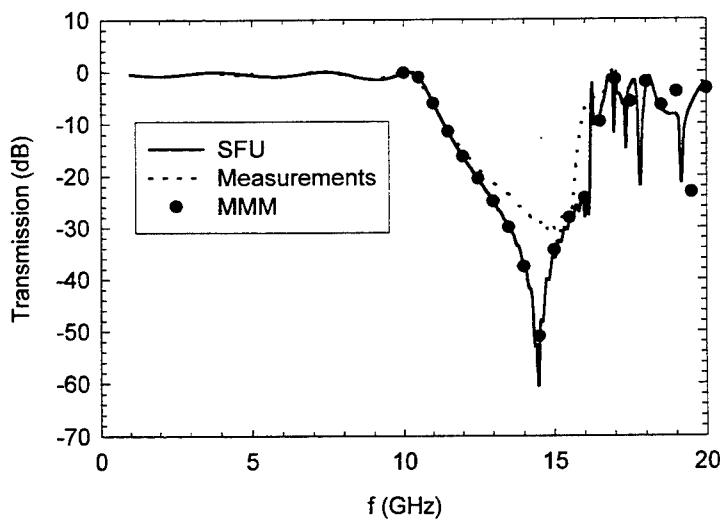
Figure 2. Comparison of results for the transmission through a woodpile PBG with normal incidence.
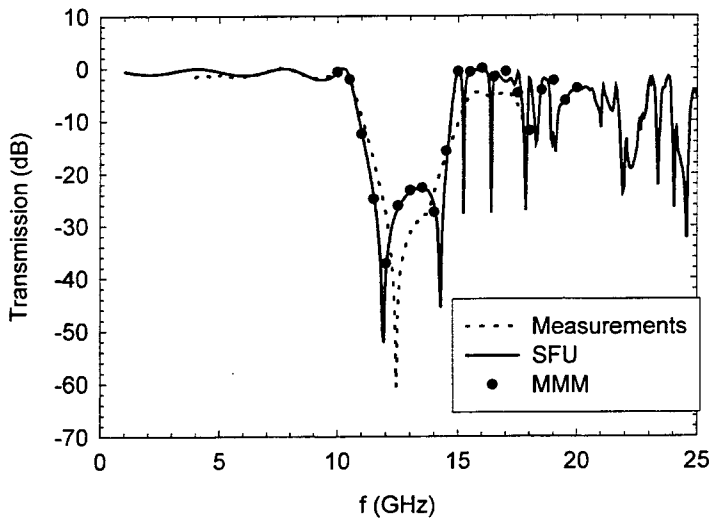
Figure 3. Comparison of results for the transmission through the woodpile PBG for an incident angle of 30 degrees.
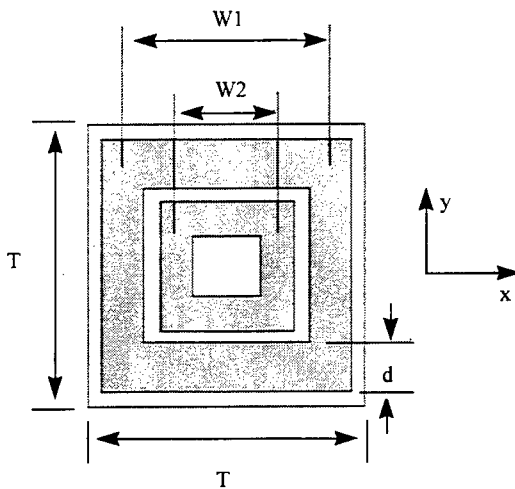
Figure 4. Top view of thick, double, concentric square loop doubly periodic in $\hat{x}$ and $\hat{y}$. The conductors forming the loops have a square cross section of T/16 x T/16 where T is the periodic cell dimension, d = T/16. W1/T = 0.875 and W2/T = 0.6875 where W1 and W2 are measured from the centers of the conductor widths.
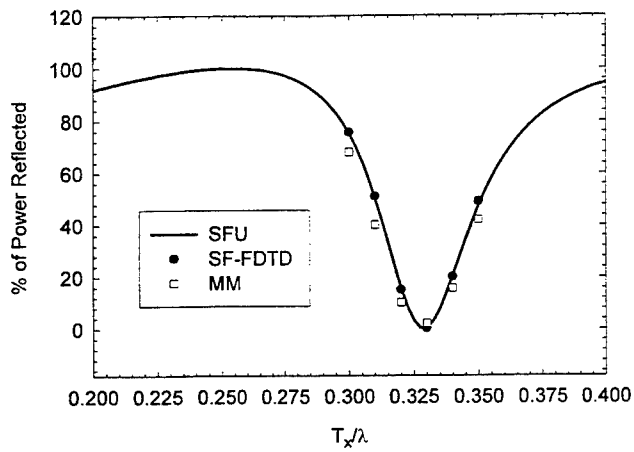
Figure 5. Percentage of power reflected for the thick, double, concentric square loop for a plane wave at an incident angle of 0 Degrees.
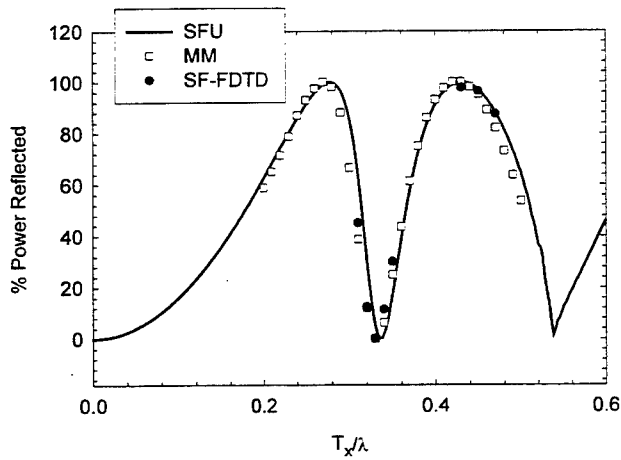
Figure 6. Percentage of power reflected for the thick, double, concentric square loop for a plane wave at an incident angle of 60 Degrees.

References

[1]   J. D. Joannopoulos, R. D. Meade and J. N. Winn, *Photonic Crystals*. Princeton, NJ: Princeton University Press, 1995.

[2]   J. A. Roden, M. P. Kesler, J. G. Maloney, P. H. Harms and S. D. Gedney, "Time domain analysis of periodic structures at oblique incidence: orthogonal and non-orthogonal FDTD implementations," submitted to *IEEE Trans. Microwave Theory Tech.*

[3]   M. E. Veysoglu, R. T. Shin and J. A. Kong, "A finite-difference time-domain analysis of wave scattering from periodic surface: oblique incidence case," *Journal of Electromagnetic Waves and Applications*, vol. 7, no. 12, pp. 1432-1435.

[4]   Y. Chun, A. Kao and R. G. Atkins, "A finite difference-time domain approach for frequency selective surfaces at oblique incidence," in *1996 IEEE APS Int. Symp. Dig.*, July 21 - 26, vol. 2, pp. 1432-1435.

[5]   W. L. Ko and R. Mittra, "Implementation of Floquet boundary condition in FDTD for FSS analysis," in *1993 IEEE APS Int. Symp. Dig.*, June 28-July 2, vol. 1, pp. 14-17.

[6]   P. Harms, R. Mittra and W. Ko, "Implementation of the periodic boundary condition in the finite-difference time-domain algorithm for FSS structures," IEEE Trans. Antennas Propagat., vol. 42, pp. 1317-1324, September 1994.

[7]   R. Moore, E. Kuster, P. Friederich, P. Kemper and J. Meadors, "Percolationg systems-Phase II," Final Report, Contract No. 94-C-0021, Georgia Tech Research Institute, December 1995.

[8]   D. B. Webb and R. Mittra, "Design techniques for bandpass frequency selective surfaces," M.S. thesis, Univ. of Illinois, Urbana-Champaign, 1992.

[9]   Stephen D. Gedney, "An anisotropic perfectly matched layer-absorbing medium for the truncation of FDTD lattices," IEEE Trans. Antennas Propagat., vol 44, pp. 1630 - 1639, December 1996.

[10]   T. K. Wu, Ed., *Frequency selective Surface and Grid Array*. New York, NY. John Wiley and Sons, Inc., 1995.

Modeling Dispersive Soil for FDTD Computation By Fitting Conductivity Parameters

Carey M. Rappaport and Scott C. Winton
Center for Electromagnetics Research
Northeastern University
Boston. MA 02115

Abstract The electrical parameters of soils are strongly dependent on their type, physical characteristics, and electromagnetic excitation frequency. When numerically modeling soil for subsurface sensing simulation, it is particularly important to account for this dispersion. When computations are done in the time domain, this dispersion becomes problematic. Using a difference equation relation—and its corresponding Z-transform—to model dispersion between electric field and current leads to an approximation of complex conductivity in the form of a ratio of polynomials in Z^{-1} (where $Z = e^{j\omega t}$).

It is shown that if the real dielectric constant is held constant at an average value and conductivity only is matched with a single (2,2) Padé approximant $\sigma(f) = (b_0 + b_1 Z^{-1} + b_2 Z^{-2})/(1 + a_1 Z^{-1} + a_2 Z^{-2})$. then the resulting propagation number $\beta(f)$ and decay rate $\alpha(f)$ will both closely match those corresponding to real soil measurements. In particular, a simple relation governing the frequency behavior of conductivity as a function of soil moisture and density is presented, allowing for the efficient numerical prediction of wave propagation in soils of varying environmental characteristics. Computed FDTD results for scattering in soil—with the computational lattice terminated with a "soil-tuned" PML absorbing boundary condition—clearly show the significance of media dispersion

I. INTRODUCTION

Recent interest in ground penetrating radar for locating and identifying buried waste. land mines, and excavation obstacles has motivated the development of advanced computational tools to simulate wave propagation in soil. In particular, the need exists to analyze ultra-wideband signals which might balance the trade-off between penetration depth and target resolution. Soil is a difficult medium to model since it is inhomogeneous, lossy, dispersive, and has an irregular surface boundary. For flexibility in predicting radar scattering from both metal and plastic targets buried in soil with rock inclusions and topped with vegetation, the Finite Difference Time Domain offers significant advantages over other standard computational techniques.

To include the effects of frequency-dependent conductivity and dielectric constant. a dispersive variant of the FDTD algorithm must be employed.

This variant is nontrivial, since unlike with the frequency domain constituitive relation, electric flux and field are related by convolution in the time domain: $\mathbf{D} = \epsilon * \mathbf{E}$. The electric current is also a more complicated function of electric field in the time domain, since conductivity cannot merely be included as part of a complex permittivity.

The standard approaches to modeling dispersion in the FDTD method involve either recursively computing the convolution (as cleverly developed by Luebbers, *et. al.* [1]); or by approximating the frequency domain dispersive complex dielectric constant with a series of simple rational functions (Debye or Lorentz models) of $j\omega$ [2,3], and then by multiplying the constituitive relation by the denominator and inverse Fourier transforming the result into the time domain. While these methods are effective, they are suffer from the limitations of numerical computation. Namely, that for good dispersive media modeling, higher-order, multiple-pole dielectric constant functions are necessary; but as the order of the function increases, so does the required storage of previous time field values for the entire grid, along with the sensitivity and numerical instability of the algorithm. In particular, to suit the conceptual elegance and simplicity of the FDTD method, it is important to keep the media model to at worst second-order. This presents a problem for the conventional complex dielectric constant models, which must accurately approximate both real and imaginary frequency dependencies simultaneously, using at most two poles.

For certain types of media, however, it is possible to separate the modeling of real dielectric constant and conductivity. In both biological tissue and soil, for instance, the lossy dispersive wave propagation is governed almost entirely by the frequency-dependent conductivity. For these media, the real dielectric constant, though frequency-dependent, does not significantly affect either the real propagation constant β, nor the decay rate α [4]. As such. their electrical characteristics can be well-modeled with a constant relative permittivity ϵ', and a second-order-in-frequency conductivity σ. Further, by modeling σ in terms of powers of the Z-transform variable Z^{-1} (which readily transform to time delays), the conversion of the generalized dispersive Ohm's Law $\mathbf{J}(Z) = \sigma(Z)\mathbf{E}(Z)$ to the time domain is particularly straightforward [5]. The problem addressed with this report is the specific selection of modeling parameters for a typical, well-studied soil, that simply and efficiently accounts for variations in density and moisture content.

112

Modeling Puerto Rican Clay Loam Using Second-Order Conductivity

Arguably the most widely-cited soil measurement study is that of Hipp [6], which provides conductivity and real permittivity of San Antonio and Puerto Rican clay loam as a function of moisture (as a percent of dry weight) m, and density (g/cc) d, for the frequency range 30 to 3840 MHz. The method for developing the general second-order conductivity soil model is based on this experimental data set. While other soils will have different electrical characteristics, it is expected that general trends will be similar to that of Puerto Rican clay loam. Also, because of the wide variety of soils, and the difficulty in obtaining carefully generated soil measurements. every attempt was made to keep the model parameters as simple as possible, with mostly linear dependence on their physical characteristics.

First, to maintain easy conversion to time domain it is essential that the conductivity for all moisture and density cases have the form:

$$\sigma(Z) = \frac{J(Z)}{E(Z)} = \frac{b_0 + b_1 Z^{-1} + b_2 Z^{-2}}{1 + a_1 Z^{-1} + a_2 Z^{-2}} \qquad (1)$$

The b_i and a_i coefficients will each be independent functions of m and d. The actual measured values of conductivity correspond to the real part of $\sigma(Z)$, with $Z = e^{j2\pi f \Delta t}$, for FDTD time step Δt. The imaginary part, divided by $j2\pi f \epsilon_0$ adds to the frequency-independent dielectric constant ϵ'. In the time domain, Eqn. (1) becomes:

$$J^n + a_1 J^{n-1} + a_2 J^{n-2} = b_0 E^n + b_1 E^{n-1} + b_2 E^{n-2} \qquad (2)$$

and Ampere's Law, as usual, is given by:

$$\nabla \times H^{n+1/2} = \epsilon_0 \epsilon' \frac{E^{n+1} - E^n}{\Delta t} + \frac{J^{n+1} + J^n}{2} \qquad (3)$$

In a previous publication [7], the best coefficients for Puerto Rican clay loam were determined for each separate sample of moisture and density. Although useful from a numerical view, these coefficients are not very helpful for the practical problem of determining wave propagation for an intermediate soil condition. To address this difficulty, a more unified approach is developed.

For the various moisture and density cases measured in [6], the best modeling coefficient values of Eqn. (1) vary considerably. However, the denominator coefficients: a_1 and a_2, only differ at most by about 15%. Choosing fixed values $a_1 = -1.6$ and $a_2 = .64$ and allowing variation of the b_i coefficients gives up a little accuracy but provides a more simple model. Instead of finding the values of b_i which minimize a non-linear cost function for each moisture/density case, the current modeling

method simply solves for b_1, b_2, and b_3 by setting the real parts of $\sigma(Z)$ in Eqn. (1) to the measured values, at three particular frequencies: 120, 960, and 3840 MHz. While this method arbitrarily emphasizes the fit at these frequencies, it avoids justifying what type of cost function to use. A least-squares cost function for normalized error in σ and ϵ', for example, is not as precise as for normalized error in the real and imaginary parts of the wave number $k = \beta - j\alpha$; and neither appropriately weighs the error on decaying wave amplitude across the frequency range.

The b_i coefficients for constant density and moisture levels $m = 2.5$, 5, 10, and 20 are first determined, and then fit to simple functions of m: $b_i \approx b_{i0} + b_{i1} \log m$. It was found that while a very good fit is possible for each b_i, the numerator of Eqn. (1) is small for low frequencies (where $Z \approx 1$), so that small errors in the b_i approximations lead to large errors in $\sigma(f)$. To avoid this cancellation problem, approximations are determined for b_1, b_2, and the sum $bs = b_0 + b_1 + b_2$, with the sum having the form $bs \approx bs_0 + bs_1 m + bs_2 m^2$. The resulting coefficients for $d = 1.2$, 1.4, and 1.6 are given in Table 1. The average dielectric constant chosen for these models is simply the measured value at 960 MHz. A quadratic least-squares fit to these data for each density, $\epsilon(m) = \epsilon_0 + \epsilon_1 m + \epsilon_2 m^2$ is given in Table 2.

Table 1: Conductivity Numerator Coefficients

Coeff.	Density (g/cc)		
	1.2	1.4	1.6
b_{10}	0.0484917	0.0540739	0.0160977
b_{11}	−0.136191	−0.162553	−0.188476
b_{20}	−0.0125623	−0.220495	−0.0004839
b_{21}	0.0574154	0.0722359	0.0808164
bs_0	1.14562E−4	7.06024E−5	1.1323E−3
bs_1	−3.9964E−6	−4.218E−6	−1.2685E−5
bs_2	1.01241E−6	1.92513E−6	3.54086E−6

Table 2: Dielectric Constant Coefficients

Coeff.	Density (g/cc)		
	1.2	1.4	1.6
ϵ_0	2.8	2.817	3.95
ϵ_1	0.14	0.171	0.0632
ϵ_2	0.012	0.181	0.0318

Figure 1 shows the accuracy of the approximation for $d = 1.4$, and the extreme moisture cases, $m = 2.5$ and 20%. Plotted in this figure are the magnitude of the propagation constant β and decay rate
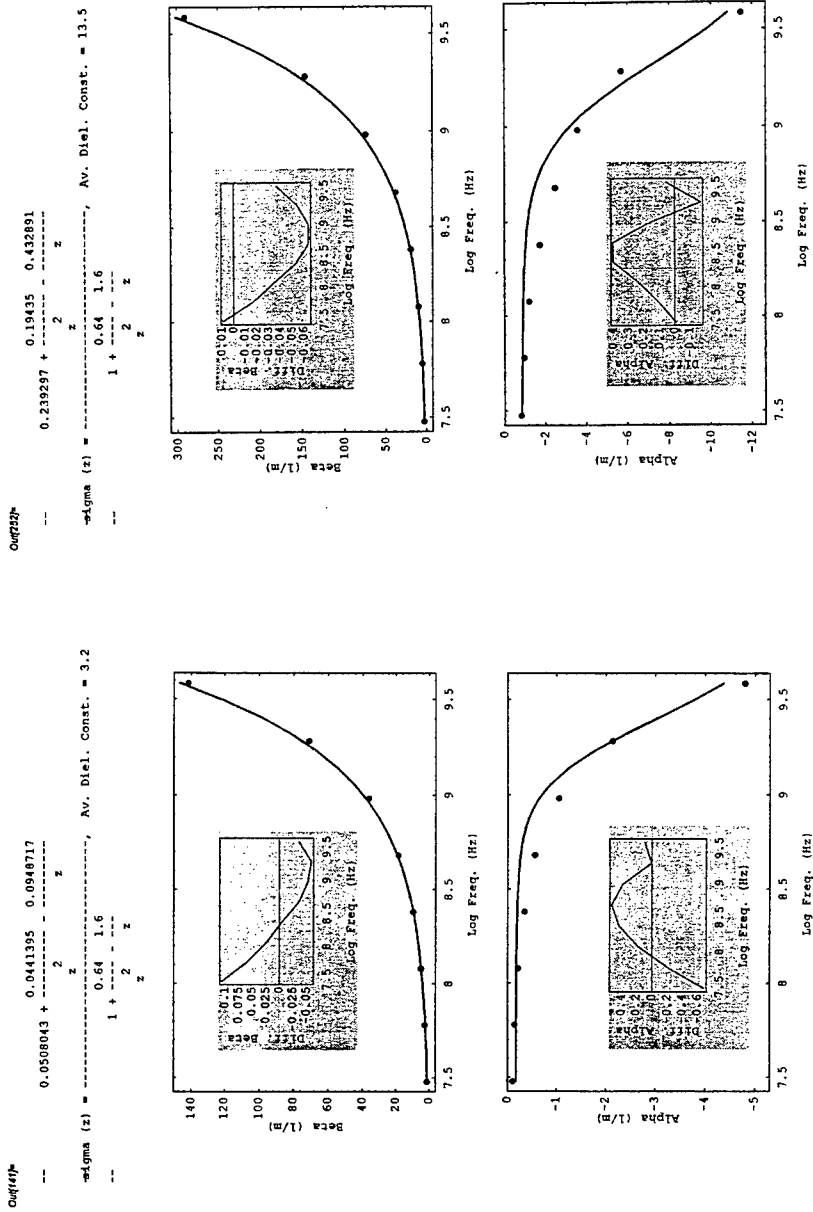
Figure 1 Complex conductivity, frequency-independent dielectric constant, wave propagation number, decay rate, and normalized error, as a function of log frequency, for conductivity model (———), and measured (· · ·) data for a) $m = 2.5\%$, and b) $m = 20\%$.

α of the model and the measured values of Puerto Rican clay loam as a function of frequency for the entire measured frequency range 30 to 3840 MHz. Also shown in the inserts are the fractional errors $\Delta\beta/\beta$ and $\Delta\alpha/\alpha$. The agreement is surprisingly good for such a simple model across two decades of frequency. It should be noted that the fit is even better for the intermediate moisture values 5 and 10%, and similar for the other density cases.

Soil-Tuned PML ABC

With all FDTD scattering problems, it is necessary to minimize reflections from the lattice boundaries with absorbing boundary conditions (ABC). A novel ABC, the "soil-tuned" Perfectly Matched Layer (PML), has been developed. The soil-tuned PML is a modified version of the Berenger ABC [8,9] which specifically absorbs waves incident from dispersive media. Since the efficiency of transmission of waves into the PML is dependent on the closeness of match of the transverse wave impedance on both sides of the layer, it is essential to select the electrical parameters of the PML appropriately. For soil parameters ϵ'_{soil}, σ_{soil}, μ'_{soil}, the desired impedance match condition is:

$$
\begin{aligned}
\eta_{soil} &= \sqrt{\frac{\mu'_{soil}\mu_0}{(\epsilon'_{soil} - j\sigma_{soil}/\omega\epsilon_0)\epsilon_0}} \\
&= \sqrt{\frac{\mu'_{soil}\mu_0(1 - j\sigma_P/\omega\epsilon_0)}{(\epsilon'_{soil} - j\sigma_{soil}/\omega\epsilon_0)\epsilon_0(1 - j\sigma_P/\omega\epsilon_0)}} \quad (4) \\
&= \eta_{PML}
\end{aligned}
$$

where σ_P is the usual increasing conductivity profile of the PML layer. While the relations of Eqn. (4) correspond to the transverse impedance only for normal incidence on the PML layer, the split-field or auxiliary equation PML formulation ensure impedance match for all incidence angles, provided a match occurs for normal incidence.

Eqn. (4) therefore specifies the effective dielectric constant and conductivity in the PML layer,

$$
\begin{aligned}
\epsilon'_{PML} &= \epsilon'_{soil} \\
\mu'_{PML} &= \mu'_{soil} \\
\sigma_{PML} &= \sigma_{soil} + \epsilon'_{soil}\sigma_P \\
\sigma^m_{PML} &= \sigma_P\mu_0/\epsilon_0
\end{aligned} \quad (5)
$$

where the double conductivity term $-\sigma_{soil}\sigma_P/(\omega\epsilon_0)^2$ is neglected as negligible compared to ϵ'_{soil} for all but the largest PML conductivity layers. If σ_{soil} were frequency independent, Eqn. (5) would provide constant constituitive parameters for the PML equations which could be used directly in the time domain. Since σ_{soil} is dispersive, however, the PML equations must make use of the auxiliary difference

Eqn. (2), with b_i coefficients in Eqn. (1) adjusted to account for the new conductivity values of Eqn. (5c). The soil-tuned PML can be thought of a modification of the dispersive media calculation with split fields and magnetic loss.

Numerical Test Case

Using the formula derived in the above section to specify the electrical characteristics of Puerto Rican clay loam with density 1. g/cc, and 10% moisture, a 2-dimensional FDTD calculation simulating plane wave scattering from a buried one wavelength diameter circular metal cylinder was performed. The geometry of the scattering lattice is shown in Figure 2. The lattice is oversized in width, 500 grid points, to prevent reflections from the sides, and is terminated with an 8-cell soil-tuned PML, to prevent reflections from the back lattice boundary. A 0.96 GHz modulated, gaussian envelope plane wave is initiated along the front grid boundary. One-dimensional FDTD calculations on the left and right edges ensure that the plane wave propagates from front to back without distortion. The time and space steps used are $\Delta t = 20$ ps and $\Delta x = 4.6$ mm, the nominal phase velocity is $v = c/\sqrt{\epsilon'} = .383c$, and the Courant number is held at 0.5.
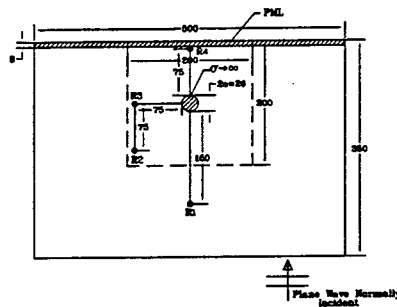
Figure 2 Geometry of the scattering problem

The four surface plots of Figure 3 show the electric field distribution across the central 200 by 200 grid point section of the computational grid (indicated in Figure 2) at various times. The upper left and right plots show the total and scattered field as the incident wave begins scattering from the circular cylinder. The lower two plots show scattered field 100 and 300 time steps later. The scattering is symmetric, as expected. For the $1100\Delta t$ plot, the residual reflections from the PML ABC, at $x = 100$, are visible. The amplitude of these reflections are of the order of 10^{-3}, which is about 3% of the field amplitude incident on the back boundary. Although

Total Field, 800 dt
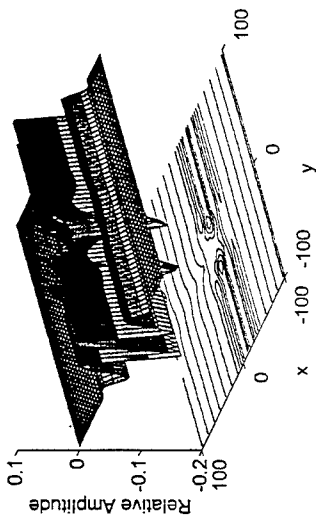
Scattered Field, 800 dt
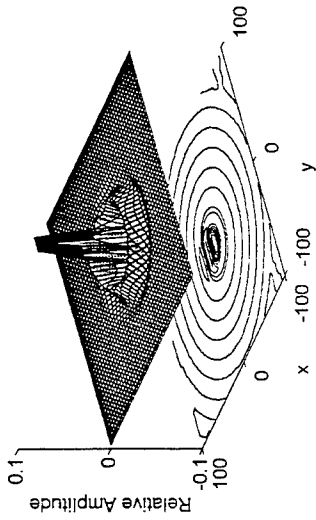
Scattered Field, 900 dt
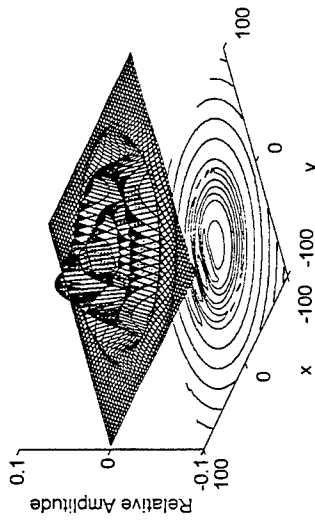
Scattered Field, 1100 dt
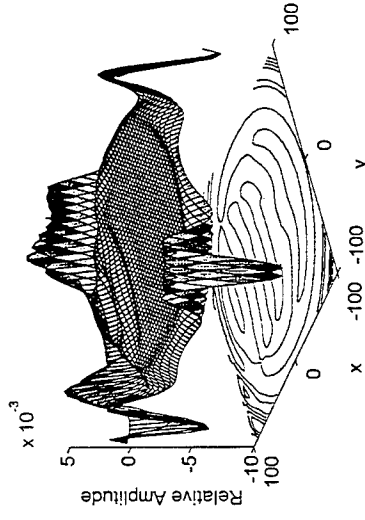
Figure 3 FDTD field plots simulating scattering by a perfectly conducting circular cylinder, surrounded by dispersive clay loam, $d = 1.4$, $m = 10\%$, with plane wave incidence.

still rather significant, the soil-tuned PML generates about one-half the reflections of generated by a conventional PML used to terminate this dispersive medium.

Figure 4 compares frequency independent and dispersive propagation, by showing the received signals at a single point ($R1$ in Figure 2) 150 grid points, directly in front of the circular scatterer. For the frequency independent case (left plots), the conductivity is kept constant at the measured value at 960 MHz, 0.032 S/m. The upper plots give the total field for the two cases, indicating only minor differences in the modulated plane wave propagation. It is interesting to note the much more significant differences in the lower, scattered field plots. In particular, the wave amplitude of the dispersive medium is twice that of the uniform conductivity case, the propagation speed is slightly different, and the higher frequencies have been attenuated—with only nine discernible maxima compared to ten in the uniform case.

CONCLUSIONS

A model of dispersive soil—with simple functional dependence on moisture and density—that can easily be adapted into the FDTD method has been developed. Based on a (2,2) Padé approximant in transform variable Z^{-1}, the model requires storing at most four additional arrays per time calculation. For simplicity, the model maintains constant denominator coefficients, with numerator coefficients being limited to a worst second order in moisture.

Also presented is a soil-tuned PML absorbing boundary condition, which is a modified variant of the PML used to terminate dispersive media lattices. In this new formulation, the PML constitutive parameters are adjusted to ensure transverse impedance matching with the dispersive medium. Its performance for soil is twice as good as the conventional PML.

Clearly, dispersion is important, and may have a greater effect in two or three dimensional scattering applications. Neglecting to model the frequency dependence of soil in wave propagation simulation can lead to significant errors. The current model simply and effectively approximates the dispersion for Puerto Rican clay loam through the entire 30 to 3840 MHz band.

ACKNOWLEDGEMENTS

REFERENCES

[1] Luebbers, R., Hunsberger, F., Kunz, K., Standler, R., and Schneider, M., "A Frequency-Dependent Finite Difference Time Domain Formulation for Dispersive Materials", *IEEE Transactions on Electromagnetic Compatibility*, pp. 222-227, Vol. 32, No. 3, March 1990.

[2] Kashiwa, T. and Fukai, I., "A Treatment by the FD-TD Method for the Dispersive Characteristics Associated with Electronic Polarization", *Microwave and Guided Wave Letters*, Vol. 16, No. 6, pp. 203-205, June 1990.

[3] Gandhi, O., "A Frequency-Dependent Finite Difference Time Domain Formulation for General Dispersive Media", *IEEE Transactions on Microwave Theory and Techniques*, Vol. 41, No. 4, pp. 658-665, April 1993.

[4] Rappaport, C., and Weedon, W., "Efficient Modeling of Electromagnetic Characteristics of Soil for FDTD Ground Penetrating Radar Simulation", *1996 IEEE Antenna and Propagation Society/URSI Symposium Digest*, pp. 620-623, June 1996.

[5] Weedon, W., and Rappaport, C., "A General Method for FDTD Modeling of Wave Propagation in Arbitrary Frequency-Dispersive Media", *IEEE Transactions on Antennas and Propagation*, accepted for publication March 1997.

[6] Hipp, J., "Soil Electromagnetic Parameters as Functions of Frequency, Soil Density, and Soil Moisture", *Proceedings of the IEEE*, Vol. 62, No. 1, pp. 98-103, January 1974.

[7] Weedon W., Rappaport, C., and Silevitch, D., "Modeling and Stability Considerations for FDTD Analysis of Wave Propagation in Soils", *1996 SPIE Aerosense Symposium*, pp. 245-252, April 1996.

[8] Berenger, J., "A Perfectly Matched Layer for the Absorption of Electromagnetic Waves", *Journal of Computational Physics*, Vol. 114, No. 1, pp. 185-200, October 1994.

[9] Rappaport, C., "Interpreting and Improving the PML Absorbing Boundary Condition Using Anisotropic Lossy Mapping of Space", *IEEE Transactions on Magnetics*, Vol. 32, No. 3, May 1996. pp. 968-974,
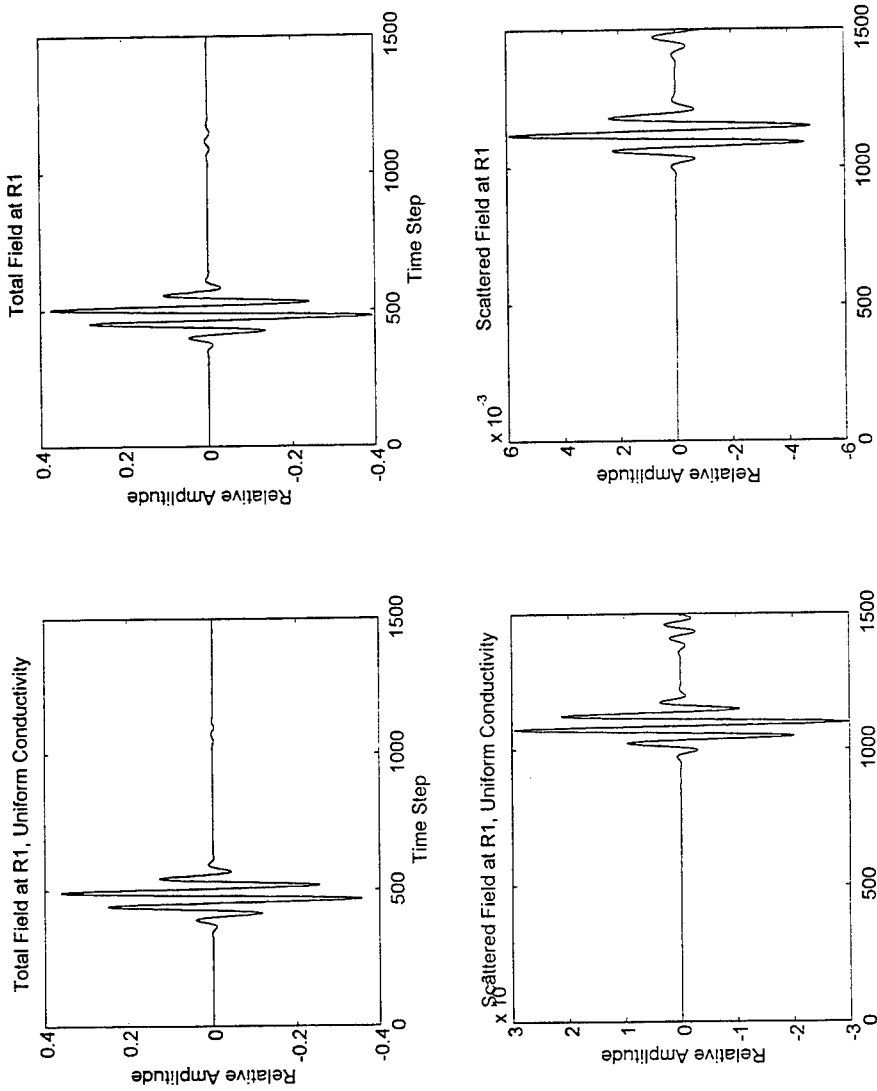
Figure 4 Received signals at point $R1$ for soil $d = 1.4$, $m = 10\%$, with frequency independent $\sigma_c = 0.032$ S/m, $\epsilon' = 6.8$; and for conductivity model.

A Hybrid Analysis Using FDTD and FETD
for Locally Arbitrarily Shaped Structures

Dongsoo Koh, Hong-bae Lee, Bijan Houshmand*, and Tatsuo Itoh

Electrical Engineering Department
University of California, Los Angeles
Los Angeles, CA90095

*Jet Propulsion Laboratory
Oak Grove Drive
Pasadena, CA91109

ABSTRACT

A hybrid analysis incorporating the FETD(Finite Element Time Domain) method into the FDTD(Finite Difference Time Domain) method has been developed to analyze locally detailed and arbitrary structures. This method has been applied to rectangular waveguides with an iris of finite thickness. The comparison of calculated results and the method of moments solutions verifies this analysis.

I. Introduction

The FDTD method has been extensively used for the full-wave analyses of three-dimensional microwave structures due to its simplicity and numerical efficiency. However, modeling structures using box-shaped uniform meshes in the conventional FDTD algorithm gives difficulty in dealing with locally detailed and curved structures. Typically, curved structures are modeled using stair-casing, which requires finer meshes and dramatic increase in memory size. The locally detailed structures demand globally fine meshes as well.

The FETD algorithm is suitable for analyzing arbitrarily shaped structures because of its flexibility. However, the FETD method is not so efficient as the FDTD method because it requires solving a system of simultaneous equations in each time step. When the arbitrarily shaped parts are located locally in the analyzed structure, combining the FDTD algorithm and the FETD algorithm can give salient features which have both the efficiency and the flexibility [1].

The hybrid method applies the standard FDTD algorithm and the edge-based

FETD algorithm. The rectangular waveguide with an iris of finite thickness has been characterized using this hybrid method by applying the FETD to the iris region and the FDTD elsewhere. When the iris thickness is zero, the calculated results are compared with the published method of moments solutions.

II. Hybrid method

This method hybridizes the FDTD method with Super absorbing Mur's 1st order ABC(absorbing boundary condition) and the FETD method with the regular brick element.

The FETD method formulation starts from the vector wave equation in a linear isotropic region,

$$\nabla \times \nabla \times \vec{E} + \mu\epsilon\frac{\partial^2 \vec{E}}{\partial t^2} = 0. \tag{1}$$

The weak form formulation of (1) gives

$$\int (\nabla \times \vec{E}) \cdot (\nabla \times \vec{N})dv + \int \mu\epsilon\vec{N} \cdot \frac{\partial^2 \vec{E}}{\partial t^2}dv = \int \vec{N} \cdot (\nabla \times \vec{E} \times \hat{n})ds, \tag{2}$$

where $\vec{N}$ is the testing function based on the regular brick element. The electric field can be interpolated using the same regular brick element as

$$\vec{E}(r,t) = \hat{x}\sum_{i=1}^{4} N_{xi}\mathcal{E}_{xi}(t) + \hat{y}\sum_{i=1}^{4} N_{yi}\mathcal{E}_{yi}(t) + \hat{z}\sum_{i=1}^{4} N_{zi}\mathcal{E}_{zi}(t), \tag{3}$$

where N_{xi}, N_{yi}, and N_{zi} are defined in Fig. 1 [2].

The unconditionally stable backward difference has been used for the finite differencing of (2) in time [3], which gives:

$$\left[\int (\nabla \times \vec{N}) \cdot (\nabla \times \vec{N})dv + \frac{\mu\epsilon}{\delta t^2}\int \vec{N} \cdot \vec{N}dv\right]\mathcal{E}^n$$

$$= \mathcal{E}^n \int \vec{N} \cdot (\nabla \times \vec{N} \times \hat{n})ds$$

$$+ \frac{\mu\epsilon}{\delta t^2}\left[2\mathcal{E}^{n-1}\int \vec{N} \cdot \vec{N}dv - \mathcal{E}^{n-2}\int \vec{N} \cdot \vec{N}dv\right], \tag{4}$$

where $\mathcal{E}^n$ represents the electric field at the time step n.

In order to calculate $\mathcal{E}^n$, the electric field values for one and two time steps ahead are required. In addition, the boundary values at the present time step which are obtained from the the FDTD computation will play a vital role to communicate the FDTD field and the FETD field.

At the interface, the FDTD region and the FETD region share one layer. When calculating the FETD electric field, the FETD boundary electric field updated by FDTD will make the Dirichlet boundary condition for the FETD electric field calculation. The FDTD boundary electric field will be interpolated from the calculated FETD electric field.

Since the electric field inside the regular brick element can be interpolated from the edge elements through (3), the FDTD cells and the FETD meshes do not have to be matched at the interface. However, this work makes use of the matched FDTD cells and FETD meshes at the interface.

III. Numerical results

The Hybrid method has been applied to the waveguide with an iris as shown in Fig. 2. The iris region is analyzed by FETD so that the iris thickness can be considered regardless of the FDTD Δz size, while both outsides of the iris region are characterized by FDTD. For simulation, the standard WR90 waveguide (0.9 inches $\times$ 0.4 inches) was chosen. The FETD volume corresponds to $14 \times 32 \times 4$ computational domain of FDTD.

Fig. 3 depicts the normalized inductive iris susceptance versus the iris width when the iris thickness is zero. The normalized iris susceptance can be calculated from S_{11} using

$$\frac{Y}{G_0} = -\frac{2S_{11}e^{j2\beta L}}{1 + S_{11}e^{j2\beta L}}, \tag{5}$$

where L is the distance from the iris to the reference plane for S_{11} [4]. The calculated results by the hybrid method show very good agreement with the Marcuvitz's curve [5], the method of moments solutions [5], and the FDTD data.

When the iris has a finite thickness, the flexible FETD method can be effectively employed, while the FDTD Δz size is not affected. Fig. 4 shows the $|S_{11}|$ of the waveguide with an iris of different thickness. The waveguide of an iris of 20 mil thickness has been analyzed while the Δz size of the FDTD domains is 28 mil.

IV. Conclusion

A hybrid analysis using the FDTD method and the FETD method has been developed to analyze microwave structures of locally arbitrary shape. This method has been successfully applied to analyze the waveguide with an iris of a finite thickness. This study shows that this hybrid method can be effectively employed to analyze the three dimensional locally arbitrary or detailed structures.

References

[1] R.-B. Wu and T. Itoh, "Hybridizing FD-TD analysis with unconditionally stable FEM for objects of curved boundary," *IEEE MTT-S Digest*, pp. 833-836, May 1995.

[2] J. Jin, *The Finite Element Method in Electromagnetics*. New York: Wiley, 1993.

[3] J.-F. Lee, "WETD - A finite element time-domain approach for solving Maxwell's equations," *IEEE Microwave and Guided Wave Lett.*, vol. 4, pp. 11-13, Jan. 1994.

[4] R. S. Elliott, *An Introduction to Guided Waves and Microwave Circuits*. Englewood Cliffs, NJ: Prentice-Hall, 1993.

[5] W. E. Kummer, *Iris-Excited Shunt Slots in Rectangular Waveguide, Theory and Experiment*, Ph. D. Dissertation, Electrical Engineering Dept., University of California, Los Angeles, 1989.
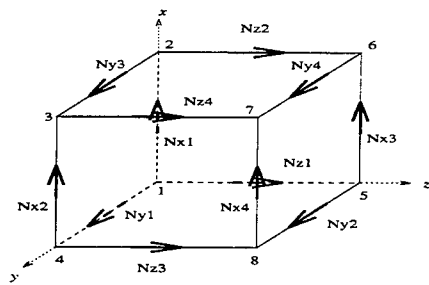
Figure 1: The regular brick element.
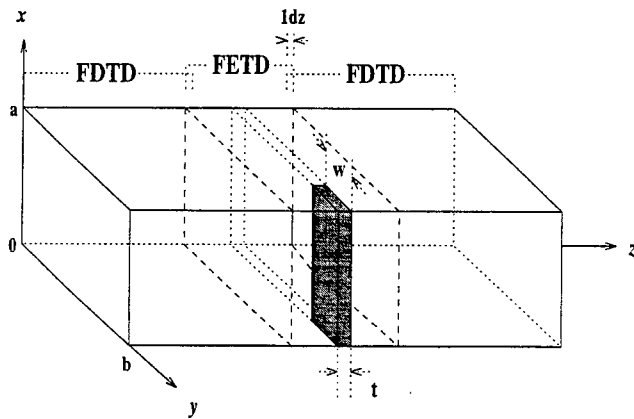
Figure 2: The waveguide with an iris of finite thickness.

123
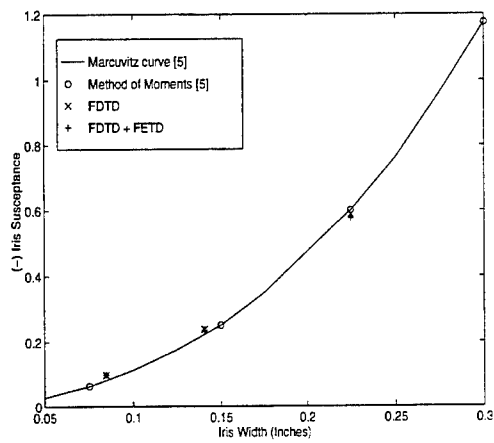
Figure 3: Normalized inductive iris susceptance vs. iris width.
(Waveguide dimensions : a = 0.9", b = 0.4", Freq. = 9.375 GHz)
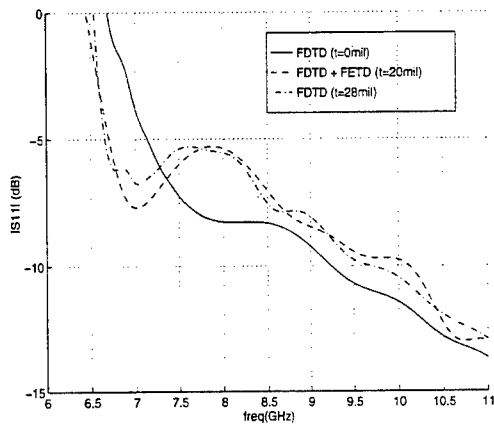
Figure 4: $|S_{11}|$ of the waveguide with an inductive iris.
(Waveguide dimensions : a = 0.9", b = 0.4", w/a = 0.25)

A Simple Method for Distributed Parallel Processing with a Cartesian Coordinate System Based Finite-Difference Time-Domain Code

E. A. Baca, J. T. MacGillivray, D. Dietz, S. A. Blocher, C. E. Davis
Phillips Laboratory Electromagnetic Effects Division
Kirtland AFB, NM 87117-5776

Abstract

A simple and very easily implemented method for parallel processing with a Cartesian coordinate system based Finite-Difference Time-Domain (FDTD) algorithm using two or more networked computers is discussed. The algorithm consists of less than 30 lines of standard FORTRAN code which is easily inserted into an existing serial FDTD code used on computers having an operating system which allows the computers to access a common file. The method is useful when sophisticated distributed parallelization software is either unavailable or when the time and cost of obtaining and using such software is undesirable.

1. Overview

The computational problem space is subdivided into roughly equal-sized subdomains with each allocated to a separate computer memory. The serial FDTD software is modified to allow for the proper calculation of the individual subdomains and a simple algorithm which allows communication between the computers is installed into the software located on each machine. The communication algorithm provides for the controlled exchange of the necessary E and/or H field values at the boundary of adjacent subdomains via hard disk data files, whose access is controlled by flag files. The resulting run time is reduced due to the multiple processors and is equal to the run time of the slowest computer. The run time includes overhead incurred by the exchange of boundary data. For certain volumes of several million cells, the efficiency of the method is greater than 91% when used on computers of similar speed and with subdomains appropriately sized to balance the load. (The efficiency referred to here is the ratio of the run time using a single computer with the run time of the slowest computer using multiple computers.) In addition to reduced run times, the total memory space available to store a problem volume is increased to the sum of the core memory of the computers, thus allowing computation of very large problems. For instance, calculations requiring up to about 2 GBytes of memory can be easily performed using four fully loaded SUN SPARC workstations.

2. Algorithm Implementation

The following explicit update equation for E_y,

$$E_y\big|_{x,y,z}^{t+\Delta t} = AE_y\big|_{x,y,z}^{t} + B\left[\frac{H_x\big|_{x,y,z+\Delta z/2}^{t+\Delta t/2} - H_x\big|_{x,y,z-\Delta z/2}^{t+\Delta t/2}}{\Delta z} - \frac{H_z\big|_{x+\Delta x/2,y,z}^{t+\Delta t/2} - H_z\big|_{x-\Delta x/2,y,z}^{t+\Delta t/2}}{\Delta x}\right],$$

derived from Maxwell's curl equation for the total E field, shows that only the previous time E_y value and the nearest neighbor H_x and H_z values are needed in the calculation. Furthermore, the needed H components specified by the curl equation are perpendicular to the E component. The same is true for all other field components. This property allows a volume to be easily divided into several subvolumes for calculation purposes.

Two methods for dividing the volume are depicted in Figs. 1 and 2 where it is seen that the basic computational volume is easily divided along cell boundaries. For these methods, calculation of transverse field components on the boundary in each subvolume requires transverse field components from both subvolumes while the field components normal to the boundary are calculated with component information present within their respective subvolumes. For the first approach, depicted in Fig. 1, it is seen that the first subvolume needs transverse E field components on the boundary of the second subvolume for calculation of its boundary transverse H field components while the second subvolume needs transverse H fields for its E fields. The second method involves a 1/2 cell overlap of the two subvolumes. As seen in Fig. 2, the transverse E data at the boundary is exchanged to calculate the boundary transverse H fields in each subvolume. This approach involves a redundant calculation of the H fields on the boundary but allows for fewer modifications to the serial FDTD code resulting in a faster implementation as well as some speed advantages for a two subvolume problem. The action of the two methods with respect to the field update algorithms in the software is illustrated in Figure 3. With the first method, transfer of field data takes place after both E and H field updates. This requires transfer of data at four separate intervals. However, in the second method, data transfer happens only after the E field updates. This allows for the possibility of some data transfer in parallel if transferred data is written to the local hard disk and read across the network.

Modifications to the serial FDTD code for use on multiple machines depends on the type of absorbing boundary condition (ABC) utilized and choice of the volume subdividing method. A boundary condition algorithm such as the Liao ABC uses E field information interior to the face for transverse E field components on the boundary. Thus, in order to apply the first method discussed above, adjustment of the Liao ABC loop parameters and nullification of the BCs on adjacent faces is necessary. In addition, adjustment of field, material ID, and Liao ABC array dimensions is required for storage of transferred boundary data. If the second method is used with the Liao ABC, no modification of the boundary condition is needed since adjacent face E field data is overwritten if the data exchange is performed after the boundary values are calculated. However, for increased efficiency, nullification of the BCs on adjacent faces and adjustment of the Liao loop parameters is easily accomplished. In addition, no adjustment of the field and material ID array dimensions is required since storage is already present due to the cell overlap.

The data exchange between subvolumes is performed via data files with access controlled by flag files to insure that information is sent or received only when necessary. Data and flag files reside on the hard disk of each computer. It was discovered that the i/o time is substantially reduced if each computer writes field data needed by the other computers to its own hard disk and reads needed data across the network from the other computers hard disks. Fig. 4 has a general logic flow chart for both received and transmitted data illustrating

126

the simplicity of the data exchange algorithm. A self-adapting delay is used to reduce network traffic and improve computational efficiency.

3. Numerical Results

Code runs for several differing volumes were performed to check the utility and efficiency of the technique. The computations were done utilizing four networked SUN workstations on volumes ranging from 140,000 cells to 12,635,000 cells. Each volume was computed on a single workstation and then sub-divided along its length and computed on all four workstation for comparison. Minor variations in computational speed between the computers exist due to differences in the respective hardware configurations. Also, the two outer subvolumes have more boundary value calculations than the inner subvolumes. Therefore, minor adjustments were made to the relative size of each volume in order to balance the load across the computers. Since dynamic load balancing was not incorporated, small variations in individual machine run times occurred and a small computational overhead resulted due to the slightly unbalanced volume distribution. It is important to note that static load balancing is not time consuming unless one is determined to obtain the last few percent of efficiency. The efficiency of the process was calculated as 1/4 the run time on the single machine divided by the run time of the slowest of the four machines. The problem specification, computation time, and efficiency of four different sized volumes are listed in Table 1. The efficiency for the small 140,000 cell problem is only 38%. However, the efficiency quickly grows for volume sizes more representative of practical problems and is better than 91% for the 12,636,000 cell calculation. The favorable trend is due in part to the fact that the hard disk access and write times are not significant compared to volume computation for large volumes.

4. Conclusion

The utility of this distributed parallelization approach rests in its simplicity, high efficiency, and ease of implementation. Data transfer across the network between computer main memories rather than through the hard disks requires much less time and is done with a variety of sophisticated software. But costs and time associated with obtaining, installing, integrating, and debugging such software are often considerable. The algorithm presented above, together with the second method of dividing into subvolumes was installed into an existing serial FDTD code and validated in one day. Since this hard disk method is better than 91% efficient for large problems and is easily installed and used, it may be more desirable (at least initially) than other more sophisticated parallelization software for the scientist or engineer with limited time and resources. It turned out to be a great benefit to our group.

127
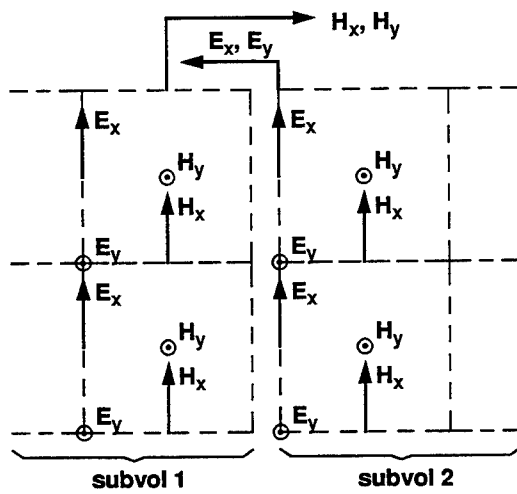
Figure 1. A computational volume is divided along a cell boundary. H_x and H_y on the boundary of subvolume 1 are used for calculation of E_x and E_y on the boundary of subvolume 2 while E_x and E_y in subvolume 2 are used for calculation of H_x and H_y in subvolume 1.
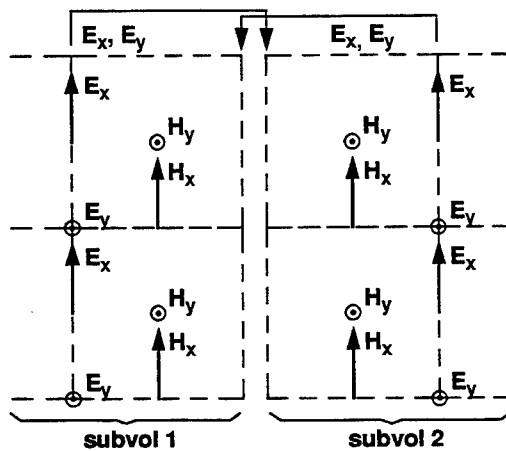
Figure 2. A computational volume is divided in a manner that allows a 1/2 cell overlap. Nearest transverse E_x and E_y components are used in adjacent subvolumes for calculation of boundary H_x and H_y components. The H_x and H_y fields on the boundary are therefore common to both subvolumes.
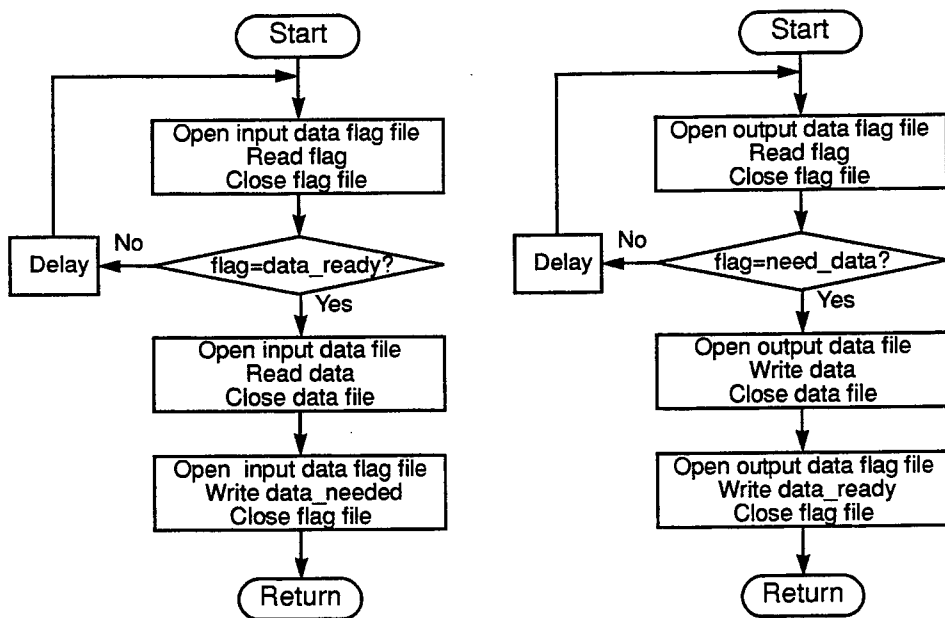
Figure 4. Logic flow charts for the data exchange algorithm at one interface. The flag files allow controlled access to the data files. An adaptable delay minimizes bus activity in between data transfer and increases overall efficiency.
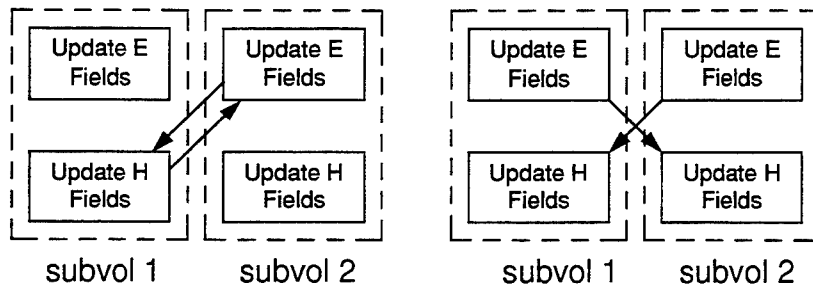
Figure 3. Illustration of the each method for a two subvolume computation. The first method involves transfer of boundary data at the end of E field updates in volume 1 and at the end of H updates in volume 2. The second method involves transfer of boundary data at the end of E field updates in both subvolumes.

Problem	Computational time (sec)					Eff(%)
Size (cells)	#1 only	#1	#2	#3	#4	
20x20x350 140,000	95	63	63	63	63	38
40x40x350 560,000	391	124	124	123	123	79
110x110x350 4,235,000	2997	839	840	840	840	89
190x190x350 12,635,000	8945	2443	2445	2447	2447	91

Table 1. Results from several problem sizes run on four computers. The efficiency is determined as 1 /4 the time of the single machine run divided by the time of the slowest of the four computers.

MODEL REDUCTION METHODS FOR COMPUTATIONAL ELECTROMAGNETICS

Chairs:J.-F. Lee and K.-K. Sun

Computation of Transient Electromagnetic Wavefields in Inhomogeneous Media Using a Modified Lanczos Algorithm

R.F. Remis and **P.M. van den Berg**

Laboratory of Electromagnetic Research, Faculty of Electrical Engineering,
Centre for Technical Geoscience, Delft University of Technology,
P.O. Box 5031, 2600 GA Delft, The Netherlands

1. Introduction

The Finite-Difference Time-Domain method (FDTD method) is one of the methods commonly used to compute transient electromagnetic wavefields in inhomogeneous media. The method employs finite-differences for the derivatives with respect to the space and time variables that occur in Maxwell's equations. It is well known that, in order to get a stable result, the time-step in this method is limited by the Courant-Friedrichs-Lewy stability condition. In case one is dealing with diffusive electromagnetic fields (neglecting the displacement currents) the stability condition in explicit time-stepping methods puts an even stricter limitation on the time-step compared to the wavefield case.

Recently, Druskin and Knizhnerman [1] have proposed a much more efficient approach to solving Maxwell's equations in the diffusive regime. Their method, called the Spectral Lanczos Decomposition Method (SLDM), is based on a second-order differential equation for either the electric field strength or the magnetic field strength and utilizes a Lanczos algorithm via which one can compute the transient diffusive field without having to discretize the time variable, i.e. their method is not an explicit time-stepping method.

We present a non-explicit time-stepping method for computing transient electromagnetic wavefields in inhomogeneous media based on Maxwell's equations as a system of first-order differential equations. Our method utilizes a modified Lanczos algorithm and via this algorithm a so-called reduced model can be constructed that gives an accurate representation of the electromagnetic wavefield on a certain bounded interval in time. Constructing a reduced model via the modified Lanczos algorithm makes the discretization of the time-variable superfluous.

2. Basic Equations

Maxwell's equations governing the electromagnetic field in a domain in which an inhomogeneous, anisotropic and lossy medium is present are written in the form

$$(\mathcal{D} + \mathcal{M}_1 + \mathcal{M}_2\partial_t)\mathcal{F} = \mathcal{Q}', \tag{1}$$

where $\mathcal{D}$ is a symmetric spatial differential operator matrix given by

$$\mathcal{D} = \begin{pmatrix} 0 & 0 & 0 & 0 & \partial_3 & -\partial_2 \\ 0 & 0 & 0 & -\partial_3 & 0 & \partial_1 \\ 0 & 0 & 0 & \partial_2 & -\partial_1 & 0 \\ 0 & -\partial_3 & \partial_2 & 0 & 0 & 0 \\ \partial_3 & 0 & -\partial_1 & 0 & 0 & 0 \\ -\partial_2 & \partial_1 & 0 & 0 & 0 & 0 \end{pmatrix} \tag{2}$$

and the time-independent matrices $\mathcal{M}_1$ and $\mathcal{M}_2$ are medium matrices given by

$$
\mathcal{M}_1 = \begin{pmatrix}
\sigma_{1,1} & \sigma_{1,2} & \sigma_{1,3} & 0 & 0 & 0 \\
\sigma_{2,1} & \sigma_{2,2} & \sigma_{2,3} & 0 & 0 & 0 \\
\sigma_{3,1} & \sigma_{3,2} & \sigma_{3,3} & 0 & 0 & 0 \\
0 & 0 & 0 & 0 & 0 & 0 \\
0 & 0 & 0 & 0 & 0 & 0 \\
0 & 0 & 0 & 0 & 0 & 0
\end{pmatrix}
\tag{3}
$$

and

$$
\mathcal{M}_2 = \begin{pmatrix}
\varepsilon_{1,1} & \varepsilon_{1,2} & \varepsilon_{1,3} & 0 & 0 & 0 \\
\varepsilon_{2,1} & \varepsilon_{2,2} & \varepsilon_{2,3} & 0 & 0 & 0 \\
\varepsilon_{3,1} & \varepsilon_{3,2} & \varepsilon_{3,3} & 0 & 0 & 0 \\
0 & 0 & 0 & \mu_{1,1} & \mu_{1,2} & \mu_{1,3} \\
0 & 0 & 0 & \mu_{2,1} & \mu_{2,2} & \mu_{2,3} \\
0 & 0 & 0 & \mu_{3,1} & \mu_{3,2} & \mu_{3,3}
\end{pmatrix}.
\tag{4}
$$

Using energy considerations it can be shown that both medium matrices are symmetric and that matrix $\mathcal{M}_1$ is positive semidefinite, while matrix $\mathcal{M}_2$ is positive definite. The field vector $\mathcal{F} = \mathcal{F}(\boldsymbol{x}, t)$ consists of the components of the electric field strength $\boldsymbol{E}$ and the magnetic field strength $\boldsymbol{H}$ and is given by

$$
\mathcal{F} = [E_1, E_2, E_3, H_1, H_2, H_3]^T,
\tag{5}
$$

while the source vector $\mathcal{Q}' = \mathcal{Q}'(\boldsymbol{x}, t)$ is composed of the components of the external electric-current source $\boldsymbol{J}^{\mathrm{e}}$ and the external magnetic-current source $\boldsymbol{K}^{\mathrm{e}}$ as

$$
\mathcal{Q}' = -[J_1^{\mathrm{e}}, J_2^{\mathrm{e}}, J_3^{\mathrm{e}}, K_1^{\mathrm{e}}, K_2^{\mathrm{e}}, K_3^{\mathrm{e}}]^T.
\tag{6}
$$

Further, the signature matrix δ^- is introduced as

$$
\delta^- = \operatorname{diag}(1, 1, 1, -1, -1, -1)
\tag{7}
$$

and we observe that this signature matrix anti-commutes with matrix $\mathcal{D}$, i.e.

$$
\mathcal{D}\delta^- = -\delta^-\mathcal{D}
\tag{8}
$$

and that it commutes with the medium matrices $\mathcal{M}_1$ and $\mathcal{M}_2$, i.e.

$$
\mathcal{M}_1\delta^- = \delta^-\mathcal{M}_1
\tag{9}
$$

and

$$
\mathcal{M}_2\delta^- = \delta^-\mathcal{M}_2.
\tag{10}
$$

Now, consider source vectors of the form $\mathcal{Q}'(\boldsymbol{x}, t) = w(t)\mathcal{Q}(\boldsymbol{x})$, where $w(t)$ is the source wavelet that vanishes for $t < 0$ and $\mathcal{Q}$ is a time-independent vector. Then, because of causality, the field vector $\mathcal{F}$ must vanish everywhere for $t < 0$. Applying a one-sided Laplace tranformation to Eq. (1) with respect to time results in the equation

$$
(\mathcal{D} + \mathcal{M}_1 + s\mathcal{M}_2)\hat{\mathcal{F}}(\boldsymbol{x}, s) = \hat{w}(s)\mathcal{Q}(\boldsymbol{x}),
\tag{11}
$$

with $\operatorname{Re}(s) > 0$. In our further analysis we take s real and positive. Then, Lerch's theorem (see Widder [2]) ensures that there is a one-to-one correspondence between a causal time function

and its Laplace-transform-domain counterpart, provided that the time function is continuous and is, at most, of exponential growth as $t \to \infty$ and that equality in the definition of the Laplace transform is invoked at the real set of points $\{s_n = s_0 + nh; n = 0, 1, 2, \cdots\}$, where s_0 is sufficiently large and positive and h is positive.

As a next step, we discretize in space using standard spatial finite-differences (cf. Yee [3]) with a Dirichlet boundary condition. The use of more sophisticated boundary conditions is not studied in this paper. In practice, the boundary of the computational domain is taken such that reflections that occur due to the Dirichlet boundary condition, are not observed in the observation points on the time-interval of interest. The discrete counterparts of $\mathcal{D}$, $\mathcal{M}_1$, $\mathcal{M}_2$, $\mathcal{F}$ and $\mathcal{Q}$ are denoted by D, M_1, M_2, F and Q, respectively, while the discrete counterpart of matrix δ^- is denoted by the same symbol. The matrices obtained after discretization satisfy the following equations

$$D\delta^- = -\delta^- D, \tag{12}$$

$$M_1\delta^- = \delta^- M_1, \tag{13}$$

$$M_2\delta^- = \delta^- M_2, \tag{14}$$

and

$$(D + M_1 + sM_2)\hat{F}(s) = \hat{w}(s)Q, \tag{15}$$

with $s \in \mathbb{R}^+$. All the matrices occuring in Eq. (15) are square $N \times N$ matrices. Matrix D is real and anti-symmetric, matrix M_1 is real, symmetric and positive semidefinite and matrix M_2 is real, symmetric and positive definite.

Solving $\hat{F}(s)$ from Eq. (15), we end up with

$$\hat{F}(s) = \hat{w}(s)M_2^{-1}(A + sE)^{-1}Q, \tag{16}$$

with $s \in \mathbb{R}^+$. In this equation, E is the identity matrix and matrix A is defined as

$$A = (D + M_1)M_2^{-1}. \tag{17}$$

Via inspection and by Lerch's theorem the unique and causal time-domain counterpart of $\hat{F}(s)$ is obtained as

$$F(t) = w(t) * \chi(t)M_2^{-1}\exp(-At)Q, \tag{18}$$

where $\chi(t)$ denotes the Heaviside unit step function and $*$ denotes convolution in time.

3. A Modified Lanczos Algorithm

First of all, let us define the bilinear form

$$\langle \cdot, \cdot \rangle_b = \langle M_2^{-1}\delta^- \cdot, \cdot \rangle, \tag{19}$$

where $\langle \cdot, \cdot \rangle$ denotes the standard inner product of two real vectors of the appropriate size. It is easily seen that matrix A is symmetric with respect to this bilinear form. This enables us to carry out the following Lanczos algorithm

$$\left.\begin{array}{rcl} \beta_1 v_1 = Q & & \\ w_i & = & Av_i - \beta_i v_{i-1} \\ \alpha_i & = & \langle v_i, w_i \rangle_b \\ \beta_{i+1}v_{i+1} & = & w_i - \alpha_i v_i \end{array}\right\} \quad i = 1, 2, \cdots, \tag{20}$$
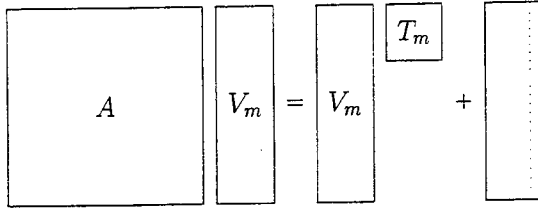
Figure 1. A picture of Eq. (21) for $m \ll N$.

with $v_0 = 0$. In each step, β_i is determined from the condition that $\langle v_i, v_i \rangle_b = 1$ for $i \geq 1$. After m steps of this algorithm we have the summarizing equation

$$AV_m = V_m T_m + \beta_{m+1} v_{m+1} e_m^T, \tag{21}$$

where the $N \times m$ matrix V_m has the column partitioning $V_m = (v_1, v_2, \cdots, v_m)$, T_m is a complex symmetric tridiagonal $m \times m$ matrix given by $T_m = \mathrm{tridiag}(\beta_i, \alpha_i, \beta_{i+1})$ and e_m is the m-th column of the $m \times m$ identity matrix E_m. We are interested in situations where m is much smaller than N, the order of matrix A (see Figure 1).

4. The Reduced-model Approximation

After carrying out m steps of the modified Lanczos algorithm, one can prove the following result

$$A^j Q = \beta_1 V_m T_m^j e_1, \qquad j = 0, 1, 2, \cdots, m - 1. \tag{22}$$

The proof is by induction over j and uses Eq. (21). Now, consider the vector $(A + sE)^{-1}Q$ with $s > s_0$ and s_0 defined by

$$s_0 = \max\{\|A\|, \|T_m\|\}, \tag{23}$$

where $\| \cdot \|$ denotes the matrix 2-norm. Using the result of Eq. (22) we can write this vector as

$$(A + sE)^{-1}Q = \beta_1 V_m \frac{1}{s} \sum_{k=0}^{m-1} (-\frac{1}{s} T_m)^k e_1 + \frac{1}{s} \sum_{k=m}^{\infty} (-\frac{1}{s} A)^k Q, \tag{24}$$

with $s > s_0$. Equation (24) is rewritten as

$$(A + sE)^{-1}Q = \beta_1 V_m (T_m + sE_m)^{-1} e_1 + \hat{R}_m(s), \tag{25}$$

with $s > s_0$ and where $\hat{R}_m(s)$ is given by

$$\hat{R}(s) = (-A)^m \frac{1}{s^m} (A + sE)^{-1} Q - \beta_1 V_m (-T_m)^m \frac{1}{s^m} (T_m + sE_m)^{-1} e_1. \tag{26}$$

Again, via inspection and relying on Lerch's theorem, the time-domain counterpart of Eq. (25) is obtained as

$$\chi(t) \exp(-At)Q = \chi(t)\beta_1 V_m \exp(-T_m t)e_1 + R_m(t), \tag{27}$$

where the vector $R_m(t)$ is given by

$$\begin{aligned}
R_m(t) &= \chi(t)\left\{ \frac{(-A)^m}{(m-1)!} \int_{\tau=0}^{t} \exp[-A(t - \tau)]\tau^{m-1} \mathrm{d}\tau \, Q \right. \\
&\quad - \left. \beta_1 V_m \frac{(-T_m)^m}{(m-1)!} \int_{\tau=0}^{t} \exp[-T_m(t - \tau)]\tau^{m-1} \mathrm{d}\tau \, e_1 \right\}.
\end{aligned} \tag{28}$$

135

Substitution of Eq. (27) into Eq. (18) gives

$$F(t) = F_m(t) + w(t) * M_2^{-1} R_m(t), \tag{29}$$

where we have defined the reduced model as

$$F_m(t) = w(t) * \chi(t)\beta_1 M_2^{-1} V_m \exp(-T_m t)e_1. \tag{30}$$

time [ns] →
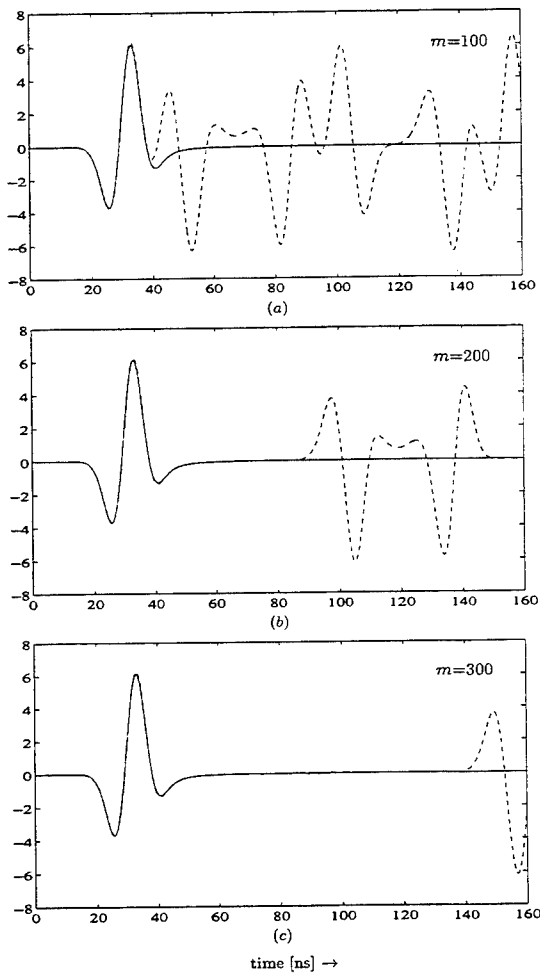
Figure 2. Electric field strength as measured by the receiver. Solid line is the exact result. Dashed line is the reduced-model approximation after 100 Lanczos steps (a), after 200 Lanczos steps (b) and after 300 Lanczos steps (c).

This reduced model is now taken as an approximation to the vector $F(t)$ on a certain bounded interval $(0, t_{max}]$. It can be shown that $\|\hat{R}_m(t)\|$ becomes negligible for all $t \in (0, t_{max}]$ as soon as $m > t_{max}\, e\, s_0$, where s_0 is defined in Eq. (23).

5. Numerical Examples

The reduced-model technique has been implemented for two-dimensional E- or H-polarized waves in inhomogeneous, isotropic and lossy media. The configuration is invariant in the x_2-direction and the x_3-direction is chosen downwardly. The source wavelet is taken to be a Ricker wavelet and is given by

$$w(t) = \chi(t) C \sqrt{\frac{e}{2\theta}} \frac{d}{dt} \exp[-\theta(t-t_0)^2], \qquad (31)$$

where C is a normalization constant. The parameter t_0 allows us to shift the non-zero part of the wavelet and by varying the parameter θ we can vary the peak frequency of this wavelet. The parameter θ is chosen such that this peak frequency is 40 MHz. The spatial discretization is such that we have about 34 points$/\lambda$, where λ is the free-space wavelength corresponding to the peak frequency of 40 MHz.

As a first example, we consider E-polarized waves (electric field strength parallel to the invariance direction) generated by the external electric-current source $J_2^e(x_1, x_3, t) = w(t)\delta(x_1, x_3)$. For this particular example, the electric field strength E_2 is known in closed form as

$$E_2(x_1, x_3, t) = \begin{cases} 0, & t < T, \\ -\dfrac{\mu_0}{2\pi} \displaystyle\int_{\tau=T}^{t} \dfrac{\partial_t w(t-\tau)}{\sqrt{\tau^2 - T^2}} d\tau, & t > T, \end{cases} \qquad (32)$$

where $T = (x_1^2 + x_3^2)^{1/2}/c_0$ is the arrival time for the wave to travel from the source location to the observation point, c_0 is the electromagnetic wave speed in vacuum and μ_0 is the permeability of vacuum. In our finite-difference approximation, the delta function is approximated by a two-dimensional triangular distribution and the expression for the electric field strength as given by Eq. (32) is therefore weighted over this distribution.

For an observation point located 4.84 m from the source, we then obtain the result as given by the solid line in Figure 2. The dashed line is the reduced-model approximation after 100 Lanczos steps (Figure 2a), after 200 Lanczos steps (Figure 2b) and after 300 Lanczos steps (Figure 2c). We observe that increasing the number of Lanczos steps extends the interval in which the solution is correct.

As a second example, we consider the two-dimensional configuration of Figure 3 in which E-polarized waves are excited by the same source as in the previous example.
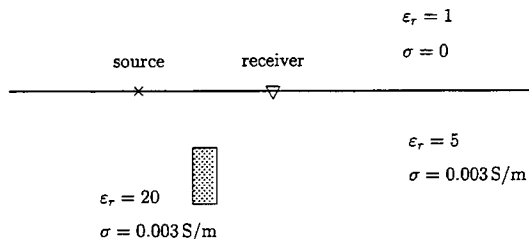
Figure 3. Source and receiver located 4.84 m apart at the interface of a lossy halfspace. The buried object of 0.88 m × 1.98 m is located 1.98 m below the interface.
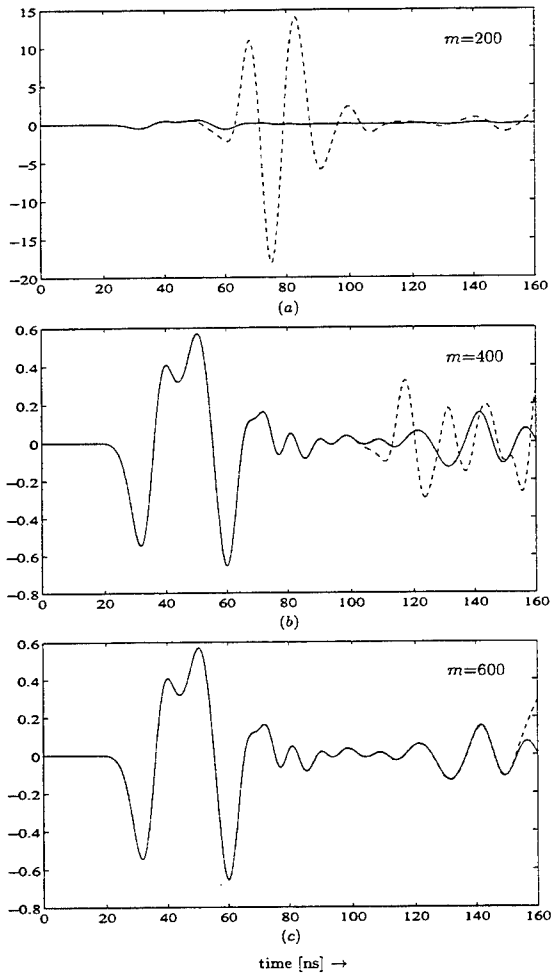
Figure 4. Electric field strength as measured by the receiver. Solid line is the reduced-model approximation after 650 Lanczos steps. Dashed line is the reduced-model approximation after 200 Lanczos steps (a), after 400 Lanczos step (b) and after 600 Lanczos steps (c).

Figure 4 shows the electric field strength as measured by the receiver. The solid line in Figure 4 is the reduced-model approximation after 650 Lanczos steps. The dashed line in Figure 4a is the reduced-model approximation after 200 Lanczos steps (note the scale), in Figure 4b after 400 Lanczos steps and in Figure 4c after 600 Lanczos steps. Again, we observe that increasing the number of Lanczos steps, extends the length of the interval in which the solution is correct.

138

We have also compared the reduced-model approximation after 650 Lanczos steps with the result obtained via the FDTD method using the same spatial discretization as in the reduced-model technique on the time interval of Figure 4. The results show a good overall agreement if the time-step in the FDTD method is chosen sufficiently small. In fact, our numerical experiments show that by decreasing the time-step in the FDTD method, the FDTD result converges to the reduced-model approximation.

6. Conclusions

A new method for computing transient electromagnetic wavefields in inhomogeneous media is presented. The method is based on a modified Lanczos algorithm and via this algorithm so-called reduced models can be constructed. A reduced model gives an accurate representation of the electromagnetic wavefield on a certain bounded interval in time. The length of this interval can be extended by performing more steps of the Lanczos algorithm. The numerical results indicate that the present method leads to a powerful technique for the computation of time-domain electromagnetic wavefields without discretization of the time variable.

The method can also be applied to the case of diffusive electromagnetic fields (neglecting the displacement currents). The stability condition in an explicit time-stepping method puts an even sticter limitation on the time-step than the one for wave propagation problems. As far as computation time is concerned, our present approach will lead to a superior technique for the computation of diffusive fields.

The Lanczos algorithm is a Krylov subspace iterative method. The convergence of such subspace methods can be accelerated by using suitable preconditioning techniques. For our type of problem, we can use techniques similar to the ones presented by Druskin and Knizhnerman [4]. These techniques are based on Padé approximations to the matrix exponential. Although the reduced-model technique is a reasonable efficient method in itself, it is to be expected that these preconditioning techniques will considerably speed up the convergence of the method.

References

[1] V.L. DRUSKIN AND L.A. KNIZHNERMAN, "Spectral approach to solving three-dimensional Maxwell's equations in the time and frequency domains," *Radio Science*, vol. 29, no.4, pp. 937-953, 1994.

[2] D.V. WIDDER, *The Laplace Transform*, Princeton Unviversity Press, 1946.

[3] K.S. YEE, "Numerical solution of initial boundary value problems involving Maxwell's equations in isotropic media," *IEEE Transactions on Antennas and Propagation*, vol. 14, no.3, pp. 302-307, 1966.

[4] V.L. DRUSKIN AND L.A. KNIZHNERMAN, "Krylov subspace approximation of eigenpairs and matrix functions in exact and computer arithmetic," *Numerical Linear Algebra with Applications*, vol. 2(3), pp. 205-217, 1995.

S–Parameters of Microwave Resonators Computed by Direct Frequency and Modal Frequency Finite Element Analysis

John Brauer
Ansoft Corporation
4300 West Brown Deer Road
Milwaukee, WI 53223 USA
brauer@ansoft.com, 414/357–0333

Avraham Frenkel
Ansoft Corporation
1 Haganim St., P.O.Box 5301
Kiryat Bialik, ISRAEL
msinord@mail.netvision.net.il

Abstract— S–parameters of microwave resonator filters are computed using two types of finite element analysis. The first method is the conventional direct frequency method, in which the number of unknowns is equal to the number of edge degrees of freedom. The second method is the new modal frequency method, which first computes the 3D modes and then uses them as basis functions, thereby greatly reducing the number of degrees of freedom. The two methods are applied to the ACES/TEAM19 filter and a variation of the Microwave Engineering Europe benchmark filter. For a large number of analyzed frequencies, the modal method is shown to obtain good results with speedup factors ranging up to 23.

INTRODUCTION

Microwave resonators often are used to make filters. If the coupling coefficients are small and the Q is high, then narrow passbands or stopbands may require analysis at a large number of frequencies. In conventional direct frequency finite element analysis (FEA) [1], total solution time is directly proportional to the number of frequencies analyzed. To reduce computer time, asymptotic waveform analysis (AWE) has recently been successfully combined with FEA [2], but AWE may have limitations when there are many resonances.

In a new technique called modal frequency FEA [3], a 3D eigenvalue analysis is first performed to reliably find all resonances of low loss devices. The resulting eigenvectors are used as basis functions for solutions over a range of frequencies, thereby possibly saving computer time if S–parameters are needed for a large number of frequencies.

A 1997 paper [3] describes the theory of modal frequency FEA and applies it to computing S–parameters of two filters. One filter is a cutoff–coupled rectangular dielectric resonator filter, and the other is a coax–fed rectangular box containing cylindrical dielectric resonators. Modal frequency results obtained are similar to those of direct frequency, and speedup factors obtained range from 1.4 to 4.

After a brief review of theory, this paper compares modal frequency FEA with direct frequency FEA for analyzing two new resonator filters. The first new example is the one–port ACES/TEAM Workshop problem 19 [4]. The next example is a variation of a benchmark problem from the magazine *Microwave Engineering Europe* and is a two–port cylindrical six–cavity filter with iris coupling to rectangular waveguides.

BRIEF THEORY OF MODAL FREQUENCY FEA

Direct frequency FEA consists of solving the matrix equation [1], [5] with angular frequency ω:

$$[-\omega^2[M] + j\omega[C] + [K]]\{u\} = \{P\} \tag{1}$$

where [M] is the permittance matrix (proportional to permittivity), [C] is the conductance matrix (proportional to conductivity), and [K] is the reluctance matrix (inversely proportional to permeability). For the edge finite elements used here, the unknown vector $\{u\}$ consists of edge magnetic vector potentials $\overline{A}$. Electric field is then $-j\omega\overline{A}$. $\{P\}$ is the excitation vector, which for S–parameter computations is located at the ports. The $\{u\}$ vector has as many degrees of freedom as there are finite element edge unknowns, which usually number in the tens of thousands. Note that the left hand matrix changes with frequency and thus solution time is proportional to the number of frequencies analyzed.

Instead of solving (1) directly, we can first solve for the 3D eigenvalues and eigenvectors, denoted by $\{\phi_i\}$. Then a *modal frequency* solution is assumed to be a linear combination of the eigenvectors, expressed as [3]:

$$\{u\} = [\phi]\{q\} \tag{2}$$

where the matrix $[\phi]$ is made up of m columns of individual orthogonal eigenvectors $\{\phi_i\}$, and the vector $\{q\}$ contains all of the coefficients. If there are n direct degrees of freedom in a problem (the length of the column vector $\{u\}$), then $[\phi]$ is an (n x m) matrix. This transformation can be highly accurate when all n eigenvectors of the system are used. In many cases only a small approximation is introduced if a limited number of eigenvectors in a specified frequency range is used.

The frequency range of the eigensolution should include all modes that are expected to be excited. All of the real modes over any finite frequency range are rigorously computed in Ansoft's MicroWaveLab[TM] [3] using a Sturm sequenced Lanczos algorithm. Then the final solution is obtained by substituting (2) into (1):

$$- \omega^2[M][\phi]\{q\} + j\omega[C][\phi]\{q\} + [K][\phi]\{q\} = \{P\} \tag{3}$$

Premultiplying both sides by $[\phi]^T$ results in:

$$- \omega^2[\phi]^T[M][\phi]\{q\} + j\omega[\phi]^T[C][\phi]\{q\} + [\phi]^T[K][\phi]\{q\} = [\phi]^T\{P\} \tag{4}$$

which can be rewritten as the *modal frequency equation* [3]:

$$(- \omega^2[m] + j\omega[c] + [k])\{q\} = \{p\} \tag{5}$$

where the three new *modal* matrices are:

$$[m] = [\phi]^T[M][\phi] \quad , \qquad [c] = [\phi]^T[C][\phi] \, , \qquad [k] = [\phi]^T[K][\phi] \tag{6}$$

Note that the modal frequency equation (5) has only as many unknowns as the selected number of modes. This reduction in the number of unknowns can often lead to a substantial computational speedup compared with direct frequency FEA.

Because real modes are assumed in MicroWaveLab, the modal frequency method is applicable only to low loss problems. While material losses can be analyzed, wall losses can only be analyzed indirectly using equivalent lossy air or other filler material. Other important limitations and assumptions are detailed in [3]. Recently, Professor Jin—Fa Lee has formulated a rigorous method that avoids the approximate port boundary conditions assumed by us.

ACES/TEAM PROBLEM 19

The first example analyzed here is the ACES/TEAM Workshop problem 19 [4]. Fig. 1 shows the geometry and finite element mesh developed for one—quarter of the problem, which is a cylindrical cavity coupled through an iris to a feed waveguide. Measurements are available [4] for $|S_{11}|$ versus frequency. Here $|S_{11}|$ is computed both by direct frequency FEA and modal frequency FEA using the software MicroWaveLab from Ansoft.

The cases analyzed here are for a 15 mm iris width with or without a concentric 9 mm diameter dielectric rod in the cavity. MicroWaveLab direct frequency results from 2.4 to 2.6 GHz have been presented elsewhere [6], using lossy 3D air finite elements instead of lossy 2D wall finite elements. There are 680 hexahedral and pentahedral H1—curl edge elements in the model of Fig. 1.

The modal frequency method applied to the empty cavity computed four modes up to the selected top frequency of 4 GHz. One of the modes, at 2.5315 GHz, is the cavity mode. The other three computed modes, at 1.9158, 2.3696, and 2.9846 GHz, are standing modes in the waveguide feed. These frequencies depend on the length of the waveguide section.
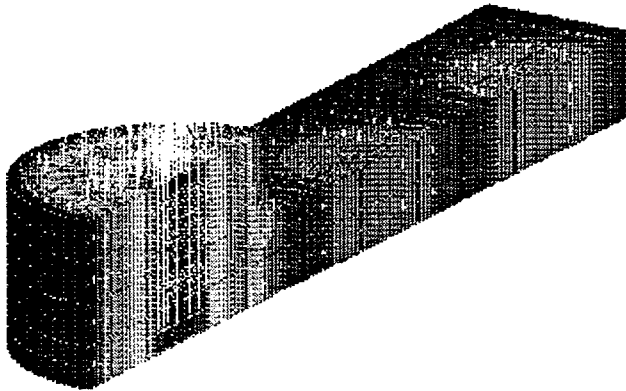
Fig 1. Geometry, finite element model, and electric field computed at 2.5315 GHz for the empty cavity case of ACES/TEAM19.

Fig. 2 compares the $|S_{11}|$ for the empty cavity case over the frequency range of interest (2.5 to 2.6 GHz) computed by MicroWaveLab's direct frequency and modal frequency techniques. Note that the two results are very similar. However, modal frequency FEA for 41 frequencies takes only 0.25 minutes per frequency, compared with 5 minutes per frequency for the standard direct frequency FEA. This speedup factor of 20 is further increased if more frequencies are analyzed.
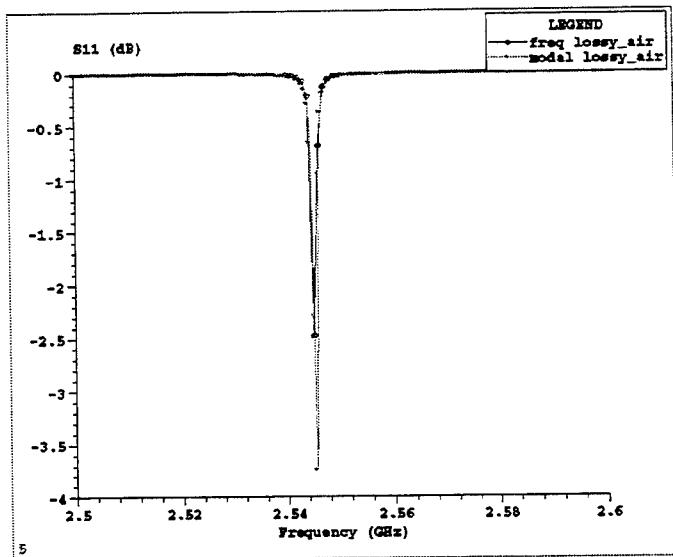
Fig. 2. Comparison of direct frequency and modal frequency reflection coefficients for the empty ACES/TEAM19 filter with lossy air.

Fig. 3 compares the results of the two methods when the cavity contains a dielectric rod made of plexiglass. The assumed plexiglass relative permittivity is $2.7 - j0.01$. Note again that the modal frequency $|S_{11}|$ plot agrees well with that computed by the standard direct frequency method.
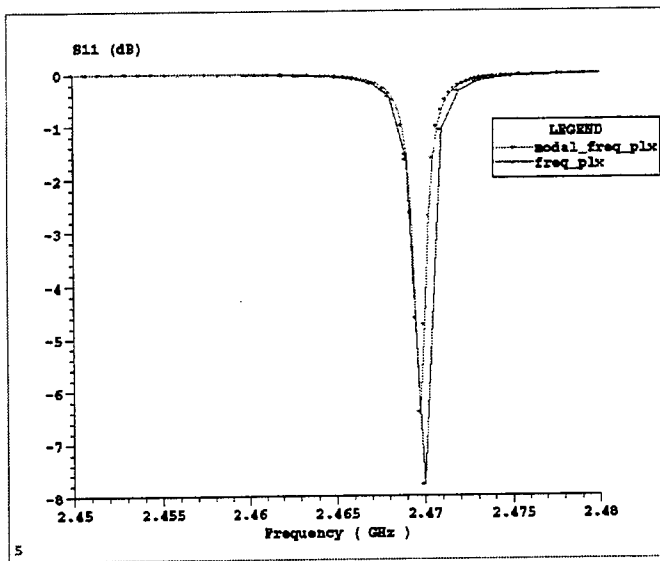
Fig. 3. Comparison of direct frequency and modal frequency reflection coefficients for the ACES/TEAM19 filter with a lossy plexiglass rod.

The final case analyzed was for the dielectric rod made of PVC, which has an assumed relative permittivity of 4.0 $-j0.05$. Table 1 lists its resonant frequency along with those of the other cases. The table shows that while the other two cases agree well with measurements, the PVC case does not. Computations by others [7], [8] agree closely with ours. Thus the assumed PVC material properties evidently are incorrect. The overall conclusion from Table 1 is that the modal frequency method of MicroWaveLab gives good results for the ACES/TEAM19 problem.

Table 1.

Resonant frequency (GHz) of ACES/TEAM19 cavity for an iris width of 15mm and rod diameter of 9 mm.

METHOD	Empty cavity	Plexiglass rod	PVC rod
Experiment	2.5446	2.4645	2.4494
Real modes FEA	2.5315	2.4621	2.4146
Direct frequency FEA	2.545	2.470	-
Modal frequency FEA	2.545	2.469	2.411
Computed by others [7]	2.5448	2.4650	2.4003
Computed by others [8]	2.545	2.4647	2.4020

VARIANT OF MICROWAVE ENGINEERING EUROPE FILTER

The final example analyzed in this paper is a variation of the dual mode 10–12 GHz filter benchmark problem from the magazine *Microwave Engineering Europe* [9]. Fig. 4 shows the geometry of its six cylindrical cavities fed by two rectangular waveguide ports. The filter is assumed lossless.
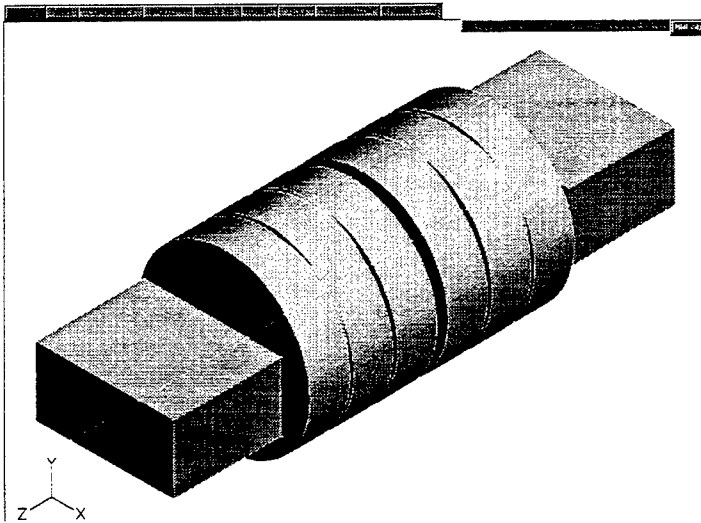
Fig. 4. Exterior geometry of two–port six–cavity filter from Microwave Engineering Europe magazine.

The interior of the filter of Fig. 4 is assumed here to be as shown in Fig. 5. Note that the cavity apertures are large and small ellipses. Fig. 6 shows that the assumed major axes of the ellipses are at 0, 45, and 90 degrees.
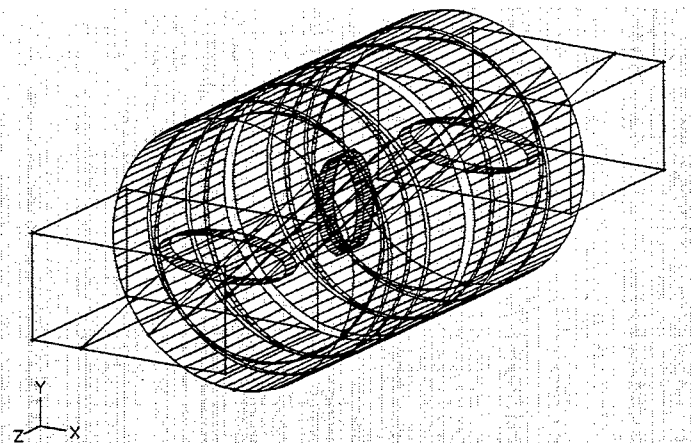
Fig. 5. Assumed interior geometry of two–port six–cavity filter of Fig. 4.
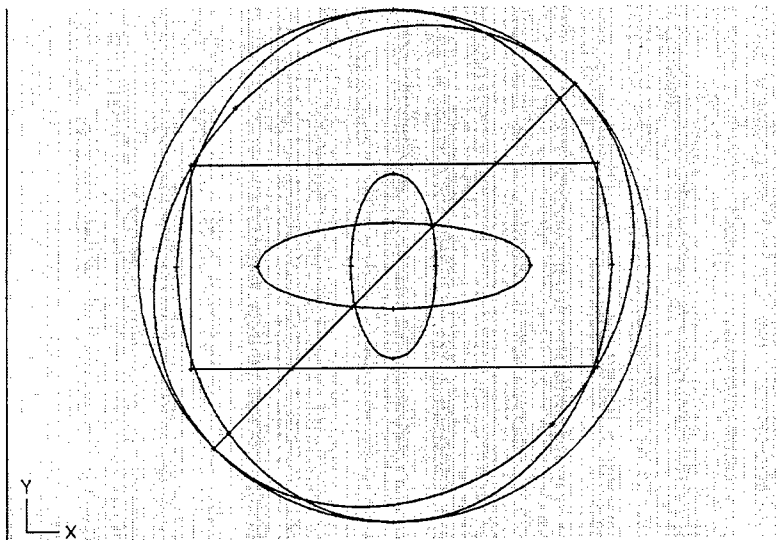
Fig. 6. Cross section of Fig. 5, showing elliptical cavity apertures.

The apertures assumed in Figs. 5 and 6 are not those of the measured filter [9] because they do not progress as needed for an ideal dual—mode filter [10]. One of the two large elliptical major axes at +45 degrees should have been rotated to −45 degrees. With both major axes at +45 degrees, the assumed filter of Fig. 5 possesses mirror symmetry about a plane midway between its 3rd and 4th cavities, which may not be true in practice.

Due to the assumed symmetry in Fig. 5, only a one—half model containing three cavities is required. The half model must, however, be analyzed twice. One analysis has an electric wall (PEC) boundary condition at the symmetry plane, which obtains the odd solution. The second analysis has a magnetic wall (PMC) boundary condition at the symmetry plane and obtains the even solution. These one—port lossless models both obtain reflection coefficients of magnitude equal to 1. The phase of these two reflection coefficients determines the overall S—parameters of the two—port filter. Denoting the phase of the even solution by ψ_{even} and the phase of the odd solution by ψ_{odd}, the overall two—port S—parameters are computed by:

$$|S_{11}| = \cos[0.5(\psi_{even} - \psi_{odd})] \ , \qquad |S_{21}| = \sin[0.5(\psi_{even} - \psi_{odd})] \qquad (7)$$

Fig. 7 shows the finite element model developed for the MicroWaveLab direct frequency and modal frequency computations of the S—parameters of (7). The two different boundary conditions are applied to the right—hand boundary plane. The model contains 5,772 tetrahedral H1—curl finite elements with 33,626 degrees of freedom. Note that because of the finite thickness irises, the elements shown in Fig. 7 need not match up from waveguide to adjacent cavity and between adjacent cavities.

The modal frequency analysis used all modes between 0.1 and 14.9 GHz. Fig. 8 compares direct frequency and modal frequency results for $|S_{11}|$; they agree well except near 11.24 GHz where the dips differ in magnitude by about 6 dB. Fig. 9 compares direct frequency and modal frequency computations for $|S_{21}|$. In general, the modal frequency S—parameters agree well with those computed by the standard direct frequency FEA.

On an HP 735/125 computer, time for each run (even or odd) at 201 frequencies is reduced from 41,535 seconds for direct frequency FEA to 1,775 seconds for modal frequency FEA. Thus the speedup factor is greater than 23.

145
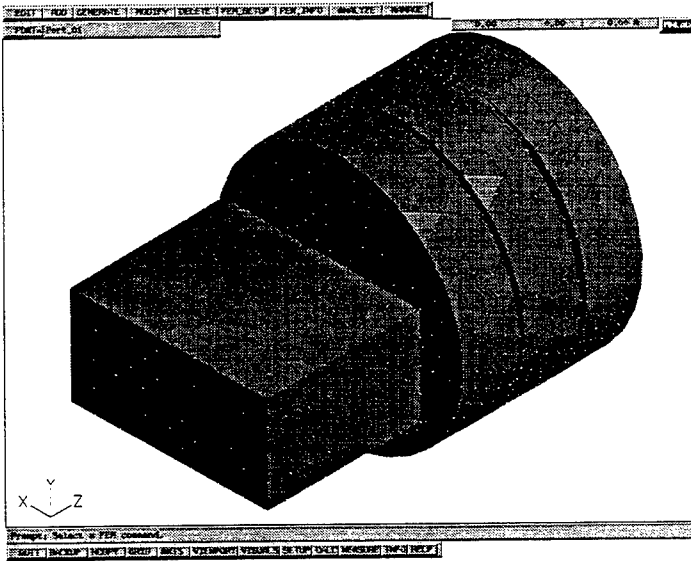
Fig. 7. Finite element model of one–half of two–port six–cavity filter of Fig. 5.
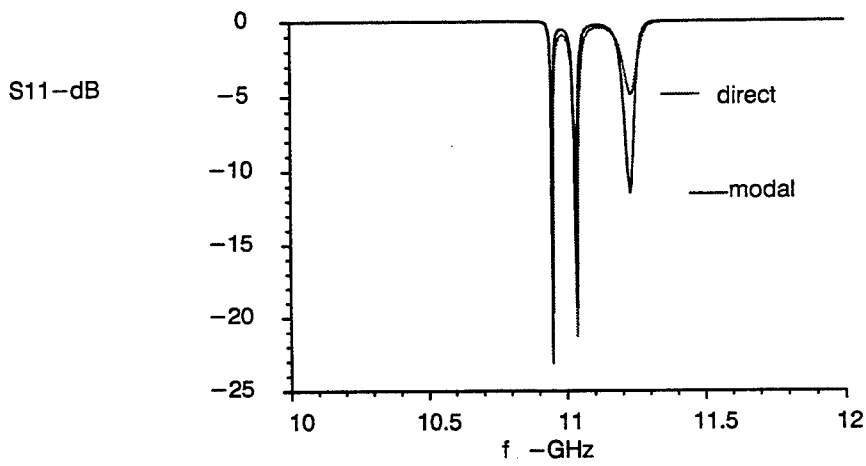
Fig. 8. Comparison of direct frequency and modal frequency reflection coefficients computed for the six–cavity filter of Fig. 5.
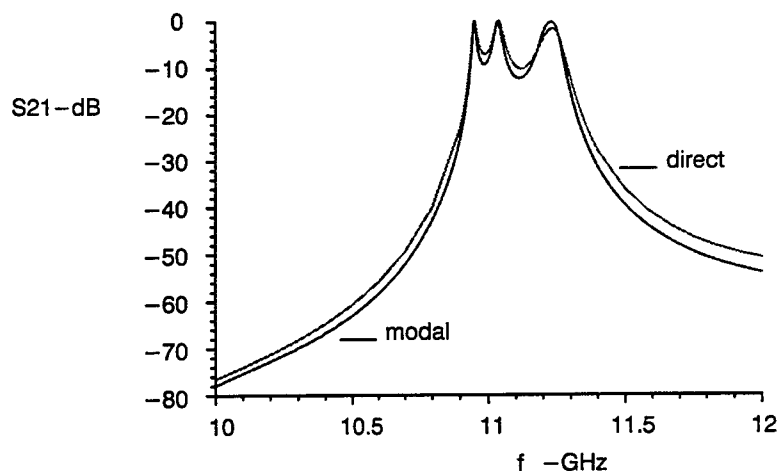
Fig. 9. Comparison of direct frequency and modal frequency transmission coefficients computed for the six-cavity filter of Fig. 5.

CONCLUSION

The new modal frequency method of FEA has been compared with conventional direct frequency FEA. Modal FEA S—parameters for the ACES/TEAM 19 single—cavity filter compare well with those of direct FEA and with measurements. Modal and direct S—parameters also compare well for a variation of a six—cavity dual—mode filter. The modal frequency method yields computer time speedups of 20 and 23, respectively, for the two filters.

REFERENCES

[1] Gary C. Lizalek, Jeffrey J. Ruehl, and John R. Brauer, "Multi—mode S—parameter computation using finite elements and perfectly matched absorbers," *Proc. ACES Symposium*, Monterey, CA, March 1996, pp. 946—953.

[2] Din Sun, John Manges, Xingchao Yuan, and Zoltan Cendes, "Spurious modes in finite—element methods," *IEEE Antennas & Propagation Magazine*, v. 37, October 1995, pp. 12—24.

[3] John R. Brauer and Gary C. Lizalek, "Microwave filter analysis using a new 3D finite element modal frequency method," *IEEE Trans. Microwave Theory & Techniques*, v. 45, May 1997, in press.

[4] A. Bossavit, J. F. Lamaudier, and B. Maestrali, "ACES/Team Workshop Problem 19," *Proceedings of TEAM Workshop*, Sapporo, Japan, Jan. 30, 1993, pp. 68-72.

[5] John R. Brauer (ed.), *What Every Engineer Should Know About Finite Element Analysis*, 2nd edition, Marcel Dekker, Inc., New York, 1993.

[6] A. Frenkel, "Simulation of an aperture coupled loaded cavity TEAM problem 19," presented at TEAM Workshop, Graz, Austria, Sep. 26, 1996.

[7] R. Dyczij—Edlinger, "Solution of TEAM benchmark problem 19", *Proceedings of TEAM Workshop*, Aix—le—Bains, France, July 1994, pp. 7—9.

[8] R. Ehmann, M. Burkhardt, H. Wolter, and T. Weiland, "Electromagnetic simulation of a loaded cavity," *IEEE Trans. Magnetics*, v. 32, May 1996, pp. 922—925.

[9] "CAD benchmark takes on filter design," *Microwave Engineering Europe*, Dec./Jan. 1997, pp. 7—12.

[10] Luciano Accatino, Giorgio Bertin, and Mauro Mongiardo, "A four—pole dual mode elliptic filter realized in circular cavity without screws," *IEEE Trans. Microwave Theory & Techniques*, v. 44, Dec. 1996, pp. 2680—2687.

REDUCED-ORDER MODELING OF ELECTROMAGNETIC SYSTEMS WITH PADÉ VIA LANCZOS APPROXIMATIONS

Andreas C. Cangellaris and Li Zhao
Center for Electronic Packaging Research
and the Electromagnetics Laboratory
Department of Electrical and Computer Engineering
University of Arizona, Tucson, AZ 85721

Abstract. This paper discusses the extension of a class of model order reduction techniques based on the Lanczos algorithm to distributed, vectorial electromagnetic systems. The reduced-order model generated by this approach can be used for the efficient broadband response calculation of the system. The proposed technique is more robust than the asymptotic waveform evaluation-based methodology used recently in conjunction with finite element electromagnetic modeling in the frequency domain. Numerical examples from wave propagation in waveguides are used to validate the proposed methodology and demonstrate its capabilities.

1. Introduction

Except for very simple systems, distributed electromagnetic analysis is hindered by the large number of degrees of freedom involved in the mathematical model. This suggests that in addition to the development of more efficient techniques for the solution of the large matrices resulting from the numerical approximation, the development of reduced-order modeling techniques, which allow the replacement of most of the mathematical model of the electromagnetic system with a substantially smaller model that approximates sufficiently its behavior, is of equal importance to advances in efficiency and modeling capability of electromagnetic simulators.

Reduced-order modeling of physical systems is a common practice in engineering. In particular, in the discipline of electrical engineering several examples of *physical* model order reduction come to mind. Perhaps the most important is the reduction of Maxwell's equations to Kirchhoff's laws for the mathematical description of the electrical behavior of circuits for frequencies such that the physical dimensions of the circuits are only a fraction of the wavelength. The impact that Kirchhoff's laws have had on the advancement of electronic technology is indeed profound. Other applications of physical model order reduction that have contributed significantly to the analysis of electromagnetic wave interactions in complex environments include: a) the development of telegrapher's equations for the description of one-dimensional wave propagation in two- and multi-conductor transmission lines; b) the concept of impedance boundary condition; c) the geometric theory of diffraction.

In parallel to the aforementioned physical model order reduction procedures, model order reduction can be effected in a purely mathematical way. The objective of the mathematical approach to reduced-order modeling of a linear electromagnetic system may be stated in a generic form as follows. Given a linear system, construct a sufficiently accurate approximation of its transfer function $H(s)$ using only a relatively small number of dominant poles and zeros. This approximation is capable of capturing with satisfactory accuracy the behavior of the system on some desirable temporal (and/or spatial) scale.

This *mathematical* model order reduction has been explored and used significantly over the years for efficient modeling of large-scale dynamical systems in a variety of engineering disciplines. In the area of elctromagnetic modeling, some of the earlier efforts include the application of model-based parameter estimation for the rapid generation of broadband electromagnetic responses using integral equation techniques [1]. More recently, the asymptotic waveform evaluation

(AWE) method, which has been used with great success in the efficient simulation of large circuits including both lumped elements and transmission lines [2]-[6], was used in conjunction with the finite element method for the broadband characterization of waveguide and planar microwave passive components. Several examples of such applications can be found in these proceedings.

Despite its success, the AWE algorithm has inherent numerical limitations which restrict its applicability to systems that can be modeled accurately using only a relatively small number of poles. Clearly, this is an issue of concern when the approximation of distributed electromagnetic systems is of interest. Earlier efforts in conjunction with modeling of wave propagation in transmission lines have led to enhancements which, however, come at the cost of increased computational complexity. The most successful of these is the so-called complex frequency hopping (CFH) [6], and is the one used currently in conjunction with the aforementioned finite element modeling of electromagnetic systems.

Recently, a robust alternative to the AWE algorithm was proposed by Feldmann and Freund [7]. The algorithm they proposed was called Padé approximation via Lanczos (PVL). PVL uses a numerically robust Lanczos-type process to compute Padé approximations of linear network transfer functions, up to any order, as required by the desired level of accuracy. The successful extension of this algorithm to the modeling of circuits with transmission line systems was presented in [8].

In this paper, the PVL algorithm is used for the efficient broadband simulation of three-dimensional electromagnetic systems. The presentation includes the underlying mathematical framework used in conjunction with model order reduction. Examples from the application of this methodology to the simulation of wave propagation in metallic waveguides with discontinuities are presented in order to ellaborate on its numerical implementation and demonstrate its numerical efficiency.

2. The Mathematical Framework for PVL

The mathematical framework for the development of Padé approximations using Lanczos and Arnoldi-type algorithms is discussed next in a general fashion considering a linear time-invariant system. For distributed electromagnetic problems, such a system results from the numerical approximation of spatial derivatives in Maxwell's time-dependent equations. A development of such an approximation using the Yee's lattice will be discussed in Section 3. Let M be the total number of state variables in the system, and let m be the number of outputs of interest. The state-space representation of the system may be cast in the form

$$\mathbf{C}\frac{d}{dt}\mathbf{x}(t) = -\mathbf{G}\mathbf{x}(t) + \mathbf{u}(t) \tag{1}$$

$$\mathbf{y}(t) = \mathbf{Z}^T\mathbf{x}(t) \tag{2}$$

where $\mathbf{x} = [\mathbf{y}, \mathbf{x}_{in}]^T$ is the vector of the state variables of the system with $\mathbf{x}_{in}$ the vector of internal variables and $\mathbf{y}$ the vector of the m state variables that constitute the outputs of interest. $\mathbf{u}$ is a vector associated with the forcing function, while $\mathbf{Z} = [\mathbf{I}_m, \mathbf{0}]^T$ is the matrix that selects $\mathbf{y}$ from $\mathbf{x}$. $\mathbf{I}_m$ denotes the identity matrix of dimension m and the superscript T denotes matrix transposition. $\mathbf{C}$ and $\mathbf{G}$ are constant matrices.

In Laplace domain (1),(2) become

$$s\mathbf{C}\mathbf{x}(s) = -\mathbf{G}\mathbf{x}(s) + \mathbf{u}(s) \tag{3}$$

$$\mathbf{y}(s) = \mathbf{Z}^T\mathbf{x}(s) \tag{4}$$

149

from which, the transfer-function matrix for the circuit is easily obtained as

$$H(s) = Z^T (G + sC)^{-1} \tag{5}$$

With the change of variables $s = s_0 + \sigma$ (5) may be cast in the form

$$H(s_0 + \sigma) = Z^T (I - \sigma A)^{-1} R \tag{6}$$

where $A = -(G + s_0 C)^{-1}C$ and $R = (G + s_0 C)^{-1}$.

Without loss of generality let us consider the simple case of a system with one output ($m = 1$). Then H is a scalar function. With the assumption that A is diagonalizable, we have

$$A = Q \Lambda Q^{-1}$$
$$\Lambda = diag\{\lambda_1, \lambda_2, \ldots, \lambda_M\}$$

With the definitions $f^T = z^T Q$, $g = Q^{-1}r$, and after some matrix manipulations, the transfer function of the single-output system may be cast in the form

$$H(s_0 + \sigma) = z^T Q (I - \sigma \Lambda)^{-1} Q^{-1} r \tag{7}$$

or

$$H(s_0 + \sigma) = \sum_{j=1}^{M} \frac{f_j g_j}{1 - \sigma \lambda_j} \tag{8}$$

The difficulty with this pole-residue representation of the system response is that the calculation of all the poles becomes prohibitively expensive as M becomes large. It is the goal of reduced-order modeling to approximate (8) with a pole-residue representation that includes only the poles needed for sufficient accuracy in the temporal scale of interest.

More specifically, the fundamental idea behind reduced-order modeling is the following. Instead of calculating exactly the transfer function, $H(s)$, of the linear system, seek an approximation of it that describes adequately its properties. One of the possible approaches is Padé approximation. The qth Padé approximation to $H(s_0 + \sigma)$ is the rational function

$$H_q(s_0 + \sigma) = \frac{b_0 + b_1 \sigma + \cdots + b_{q-1} \sigma^{q-1}}{1 + a_1 \sigma + \cdots + a_q \sigma^q} \tag{9}$$

the Taylor series of which about s_0 agrees with the Taylor series of $H(s_0 + \sigma)$ in at least the first $2q$ terms:

$$H_q(s_0 + \sigma) = H(s_0 + \sigma) + \mathcal{O}\left(\sigma^{2q}\right)$$

The coefficients $a_1, a_2, \ldots, a_q$, $b_0, b_1, \ldots, b_{q-1}$, are uniquely determined by matching the first $2q$ Taylor coefficients (moments), m_n, of the exact transfer function with those of the approximate transfer function,

$$\frac{1}{n!} \frac{d^n H_q}{ds^n} = \frac{1}{n!} \frac{d^n H}{ds^n} = m_n, \quad n = 0, 1, \cdots, 2q - 1 \tag{10}$$

Considering the general case of a system with m outputs, the specific form of (6) leads to the following Taylor series for the transfer-function matrix $H(s_0 + \sigma)$,

$$H(s_0 + \sigma) = Z^T \left(I + \sigma A + \sigma^2 A^2 + \ldots\right) R = \sum_{n=0}^{\infty} M_n \sigma^n \tag{11}$$

150

where the matrices, M_n, $M_n = Z^T A^n R$, $n = 0, 1, 2, \ldots$, are the moments of the system response.

It is clear from this last expression that the moments can be generated in a computationally efficient, recursive manner once the matrix A has been computed. This moment generation phase is then followed by the moment matching process described by (10), which eventually leads to a pole-residue representation of the elements of the transfer function matrix H. What is achieved by the AWE algorithm is the solution of the approximated problem over a range of frequencies at the cost of a single matrix inversion at a properly selected frequency (s_0). However, as already mentioned earlier, the moment-matching phase of the AWE algorithm has inherent limitations which limit its applicability to systems with small number of poles only. As an alternative Padé approximations for systems with large numbers of significant poles can be generated up to any order, as required by the desired level of accuracy, in a more robust way using Krylov subspace iteration techniques.

For the purposes of this paper we concentrate on the use of the Lanczos algorithm for the development of Padé approximations, as proposed by Feldmann and Freund [7] and Gallivan, Grimme and Doren [9]. At this point it is appropriate to recall that, given an $N \times N$ matrix A which, in general, is non-Hermitian, the Lanczos algorithm generates a sequence of $n \times n$ tridiagonal matrices, T_n, $n = 1, 2, \ldots$, which, in a certain sense, approximate A [10]. More specifically, under the assumption of exact arithmetic and no breakdowns, the Lanczos algorithm terminates after at most Q steps, where $Q \leq N$, and the tridiagonal matrix T_Q represents the restriction of A or A^T to an A-invariant or A^T-invariant subspace of $\mathcal{C}^N$, respectively. All eigenvalues of T_Q are also eigenvalues of A and the algorithm generates basis vectors for the resulting A-invariant or A^T-invariant subspaces. Clearly, it is the spectrum of the tridiagonal matrices T_n that is of immediate relevance to reduced-order modeling. Typically, the spectrum of T_n offers good approximations to some of the eigenvalues of A even for $n \ll N$. To summarize, the tridiagonal matrix T_q, resulting from the qth iteration ($q \ll N$), is a good approximation to the matrix A. Furthermore, Feldmann and Freund demonstrated that

$$H_q(s) = \left(z^T r\right) \cdot e_1{}^T (I - \sigma T_q)^{-1} e_1 \tag{12}$$

where $e_1 = [1, 0, \ldots, 0]^T$. Hence, the tridiagonal matrix T_q leads directly to the qth order Padé approximation of $H(s)$. A pole-residue representation is obtained from (12) in a straightforward fashion as follows. Rewriting (12) in terms of the eigendecomposition of the matrix T_q,

$$T_q = S_q \Lambda_q S_q^{-1} \tag{13}$$

where $\Lambda_q = \text{diag}(\lambda_1, \lambda_2, \cdots, \lambda_q)$, and defining the vectors $\mu = S_q^T e_1$ and $v = S_q^{-1} e_1$ one obtains

$$H_q(s) = \left(z^T r\right) \cdot \mu^T (I - \sigma \Lambda_q)^{-1} v = \sum_{i=1}^{q} \frac{z^T r \cdot \mu_i v_i}{1 - \sigma \lambda_i} \tag{14}$$

Clearly, PVL generates the Padé approximation of A directly; thus the ill-conditioned moment matching phase of AWE is avoided. The computational procedure of the PVL algorithm can be found in [7]. We only comment here on the selection of the expansion point s_0. If the frequency range of interest is $f_{\min} \leq f \leq f_{\max}$, where $f_{\min} < f_{\max}$ and $f_{\max} > 0$, s_0 is selected to be

$$s_0 = (f_{\max} - f_{\min})\pi + j(f_{\max} + f_{\min})\pi \tag{15}$$

For the special case where the frequency range of interest is $0 \leq f \leq f_{\max}$, the property that the impulse responses of the systems of interest are real, i.e. $H^*(j2\pi f) = H(-j2\pi f)$, is used to define

the equivalent frequency range $-f_{max} \leq f \leq f_{max}$. Thus, from (15), the expansion point is found to be $s_0 = 2\pi f_{max}$.

In general, the matrix $\mathbf{A} = -(\mathbf{G}+s_0\mathbf{C})^{-1}\mathbf{C}$ is nonsymmetric. It is well known that the Lanczos algorithm may break down for nonsymmetric matrices. This breakdown is well understood and several look-ahead implementations have been proposed to overcome it (when possible) [11]. It is pointed out that the dominating cost of the algorithm is the computation of the LU factorization of the matrix $\mathbf{G} + s_0\mathbf{C}$, which is done only once.

3. State-Space Representation of the Discrete Electromagnetic System

Before we proceed with the development of the state-space representation of the Maxwell's time-dependent curl equations, it is important to recall that numerical approximations of electromagnetic boundary value problems using finite methods result in discrete models of finite order. Thus, the approximate response of the system is bandlimited, with cutoff frequency dependent on the grid size and the order of the approximation. Consequently, the pole-residue representation of the transfer function of the approximated electromagnetic system will be of finite order.

For the purposes of this paper, the spatial approximation of the curl terms in Maxwell's time-dependent equations is effected using the Yee's lattice. The two curl equations can be written in a compact form as follows

$$-\mathbf{P}\frac{\partial}{\partial t}\mathbf{x}(\vec{r},t) = \mathbf{L}\mathbf{x} + \mathbf{D}\mathbf{x} + \mathbf{f}(\vec{r},t) \tag{16}$$

where $\mathbf{x} = [E_x, E_y, E_z, H_x, H_y, H_z]^T$; $\mathbf{D}$ is the spatial differential operator matrix representation of the curl operators; $\mathbf{P}$ and $\mathbf{L}$ are time-independent matrices that include the permittivities/permeabilities and conductivities, respectively, at the specific point in space; $\mathbf{f}$ is the vector of source current densities. Assuming a causal system with sources that turn on at $t = 0$ and zero initial conditions, the results in [12] are used to develop the Laplace-domain form of the discrete approximation of (16) on a Yee's lattice over the volume of interest

$$-[s\hat{\mathbf{P}} + (\hat{\mathbf{L}} + \hat{\mathbf{D}})]\hat{\mathbf{x}}(s) = \hat{\mathbf{b}}u(s) \tag{17}$$

where the symbol $\hat{\mathbf{P}}$ is used to denote the discrete form of the matrix operator $\mathbf{P}$ with similar notation for the other matrices and vectors. The source currents are assumed to be of the form $\mathbf{f}(\vec{r},t) = u(t)\mathbf{b}(\vec{r})$. Clearly, the discrete model is of the form in (3), with $\mathbf{C} = \hat{\mathbf{P}}$ and $\mathbf{G} = \hat{\mathbf{L}} + \hat{\mathbf{D}}$.

For radiation and scattering problems, absorbing boundary conditions need to be used for reflectionless grid truncation. The grid truncation scheme based on Berenger's perfectly matched layer (PML) [13] appears to be most suitable for our purposes since the splitting of the fields preserves the linearity in s of the discrete problem. The performance of Berenger's PML in conjunction with the development of Padé approximations for unbounded problems using the Lanczos algorithm is currently under investigation. An alternative implementation of PMLs using the generalized theory for PML (GT-PML) [14] is possible also, and its performance in conjunction with the PVL model order reduction process is also under investigation. The results from these studies will be published in a future paper.

4. Numerical Experiments

The first example deals with the simple problem of wave propagation inside an air-filled rectangular waveguide. The cross section of the guide is on the $x - y$ plane; its width along x is 7.62 cm and its height along y is 3.81 cm. An electric current sheet source placed at the center of a finite segment of the guide is used to excite the TE_{10} mode. The guide is terminated at both ends using four-cell thick PMLs designed for a 10^{-5} reflection coefficient at normal incidence.

The desired output is the amplitude of the y component of the electric field along the axis of the waveguide. The expansion point for the PVL approximation is taken to be $s_0 = 2\pi f_0$, where $f_0 = 6$ GHz. In Fig. 1 the magnitude of the field calculated from a PVL approximation of order 40 is compared with the analytic result over the frequency range from cutoff to 5 GHz. Excellent agreement is observed. Fig. 2 depicts the comparison of the analytic result with that obtained from the PVL for the real part of E_y for the TE_{10} mode along the axis of the guide at $f = 3$ GHz. The agreement is very good for both approximations of orders 20 and 40, generated using the expansion point $f_0 = 6$ GHz.

The second example deals with the calculation of the return loss for a dielectric post inside a WR90 waveguide. The post is placed at the center of the guide as shown in Fig. 3. Its width, c, is 12 mm, its length, d, is 6 mm, and its its dielectric constant is 8.2. Measured results for the return loss for this structure are available in [15]. Figure 4 depicts the comparison of the measured data with those generated using PVL approximations of order 40 and 60 and expansion point $s_0 = 2\pi f_0$ with $f_0 = 13$ GHz. Very good agreement is observed.

5. Concluding Remarks

As electromagnetic CAD technology continues to mature, a new computer modeling and simulation environment is expected to emerge, capable of supporting design iteration and prototyping of high-speed, high-frequency electronic components and systems. Since the accurate resolution of the electromagnetic interactions in such components and systems result in numerical approximations with a very large number of degrees of freedom, model order reduction is anticipated to play an important role in the development of efficient electromagnetic CAD tools.

The process of model order reduction was discussed in this paper from both a physical and a mathematical point of view. It was shown that robust model order reduction techniques, used currently for simulation of very large lumped circuits, can be extended to handle distributed electromagnetic systems. In particular, it was demonstrated how the Padé via Lanczos (PVL) algorithm can be used effectively for the generation of very accurate single-point Padé approximations for the broadband electromagnetic response of waveguiding structures.

In addition to facilitating the broadband response calculation from, essentially, a single frequency solution of the the boundary value problem, the pole-residue form of the Padé approximation of the transfer function can be used to generate in a very efficient and accurate fashion the transient response of the system for a given excitation. Indeed, even for those cases that the inverse Laplace tranform cannot be carried out analytically, the exponential character of the time-domain form of the PVL approximation of the transfer function permits the use of efficient, recursive time-domain convolutions of $\mathcal{O}(N)$ complexity (where N is the number of steps in the time integration). Finally, the generated reduced-order models for the port responses of a "multiport" linear electromagnetic system result in the development of broadband *macromodels* of the multiport, which can be used subsequently for the rapid simulation of more complicated linear/nonlinear systems that contain the specific multiport as a subsystem.

References

[1] G.J. Burke, E.K. Miller, S. Chakrabarti and K. Demarest, "Using model-based parameter estimation to increase the efficiency of computing electromagnetic transfer functions," *IEEE Trans. Magnetics*, Vol. 25, pp. 2807–2809, 1989.

[2] L.T. Pillage and R.A. Rohrer, "Asymptotic waveform evaluation for timing analysis," *IEEE Trans. on Computer-Aided Design*, Vol. CAD-9, pp. 352–366, 1990.

[3] T.K. Tang and M.S. Nakhla, "Analysis of high-speed VLSI interconnects using the asymprotic waveform evaluation technique," *IEEE Trans. on Computer-Aided Design*, Vol. CAD-11,

pp. 341–352, 1992.

[4] S.-Y. Kim, N. Gopal, and L.T. Pillage, "Time-domain macromodels for VLSI interconnect analysis," *IEEE Trans. on Computer-Aided Design*, Vol. CAD-13, pp. 1257–1270, 1994.

[5] E. Chiprout and M.S. Nakhla, *Asymptotic Waveform Evaluation And Moment Matching for Interconnect Analysis*. Kluwer Academic Publishers, Dordrecht, 1994.

[6] E. Chiprout and M.S. Nakhla, "Analysis of interconnect networks using complex frequency hopping (CFH)," *IEEE Trans. on Computer-Aided Design*, Vol. CAD-14, pp. 186–200, 1995.

[7] P. Feldmann and R.W. Freund, "Efficient linear circuit analysis by Padé approximation via the Lanczos process," *IEEE Trans. on Computer-Aided Design*, Vol. CAD-14, pp. 639–649, 1995.

[8] M. Celik and A.C. Cangellaris "Simulation of dispersive multiconductor transmission lines by Padé approximation via the Lanczos process," *IEEE Trans. Microwave Theory Tech.*, pp. 2525–2535, 1996.

[9] K. Gallivan, E. Grimme and P. Van Dooren, "Asymptotic waveform evaluation via a Lanczos method," *Appl. Math. Lett.*, Vol. 7, pp. 75–80, 1994.

[10] C. Lanczos, "An iteration method for the solution of the eigenvalue problem of linear differential and integral operators," *J. Res. Nat. Bur. Standards*, Vol. 45, pp. 255–282, 1950.

[11] R.W. Freund, M.H. Gutknecht, and N.M. Nachtigal, "An implementation of the look-ahead Lanczos algorithm for non-Hermitian matrices," *SIAM J. Sci. Comput.*, Vol. 14, pp. 137–158, 1993.

[12] T. Weiland, "On the unique numerical solution of Maxwellian eigenvalue problems in three dimensions," *Particle Accelerators*, Vol. 17, pp. 227–242, 1985.

[13] J.P. Berenger, "A perfectly matched layer for the absorption of electromagnetic waves," *J. Computational Physics*, Vol. 114, pp. 185–200, 1994.

[14] L. Zhao and A.C. Cangellaris, "GT-PML: Generalized theory of perfectly matched layers and its application to the reflectionless truncation of finite-difference time-domain grids," *IEEE Trans. Microwave Theory Tech.*, pp. 2555–2563, 1996.

[15] J. Ritter, V.J. Brankovic, D.V. Krupezevic and F. Arndt, "A wide-band s-parameter extraction procedure for arbitrarily shaped, inhomogeneous structures using time domain numerical techniques," *1995 IEEE International Microwave Theory Symposium Digest*, pp. 273–276, Orlando, Florida, 1995.
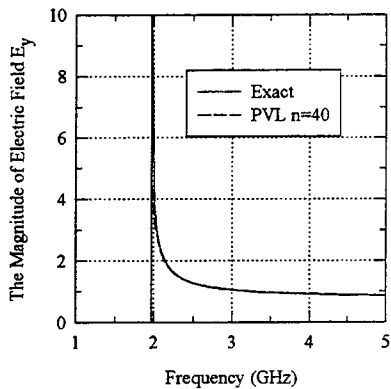
Fig.1 Magnitude of the electric field of the TE_{10} mode in a uniform rectangular waveguide versus frequency. The expansion point is $f_0 = 6\ GHz$.
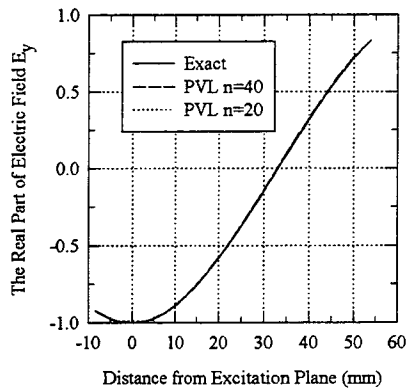
Fig.2 Real part of the electric field of the TE_{10} mode at $f = 3\ GHz$ along the axis of the waveguide. Excitation plane is at $z = 0$. Expansion point is $f_0 = 6\ GHz$.
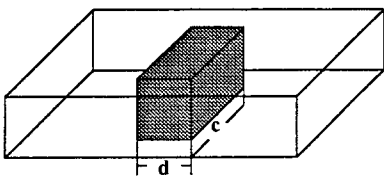
Fig. 3 Dielectric post inside WR90 waveguide (ε_r=8.2). $d = 6\ mm$, $c = 12\ mm$.
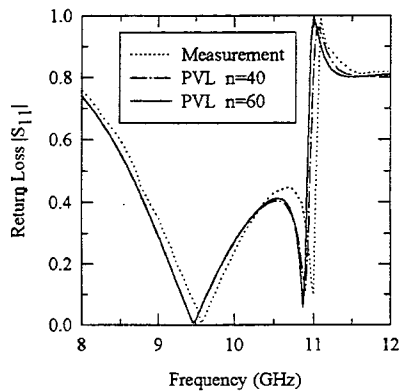
Fig. 4 Return loss simulated and measured in [15] for the geometry of Fig. 3. Expansion point is $f_0 = 13\ GHz$ for all cases.

Integrating Data Obtained From Electromagnetic Field Analysis into Circuit Simulations

Wendemagegnehu T. Beyene and José E. Schutt-Ainé

Department of Electrical and Computer Engineering
University of Illinois at Urbana-Champaign
1406 W. Green St., Urbana, IL 61801

A b s t r a c t - In this paper, a new approach to integrate data obtained from electromagnetic field analysis into circuit simulations is presented. The method is based on a robust rational approximation of the multiport scattering parameters that characterize the electromagnetic system and a recursive convolution to convert the rational functions into macromodels of multiterminal networks. The multiport representations of the scattering parameters (measured or simulated) are incorporated into traditional circuit simulation as Norton equivalent circuits with conductances and dependent current sources. This allows the accurate simulations of electromagnetic systems with nonlinear terminal networks. The method avoids numerical transforms, band-limiting windowing, and explicit convolution of a large number of points that are required in conventional methods. Examples of transient simulations of linear and nonlinear networks are given to illustrate the method.

I. INTRODUCTION

THE transient simulation of microwave devices, and high-speed analog and digital integrated circuits requires electromagnetic analysis of the distributed systems. The microstrip structures such as filters, couplers, and impedance transformers have to be represented in detail to determine the performance of the systems. The microstrip discontinuities, dispersions and dielectric losses can be accurately represented by data from field solutions than by equivalent circuits. In order to provide a means of rigorous simulation of such distributed components, an efficient method of integrating data obtained from electromagnetic field analysis into circuit simulations is indispensable.

Recently, research has been directed to combine the electromagnetic and circuit simulations into one platform. The approaches can be categorized in two groups. The first approach is to extend the existing electromagnetic techniques by introducing the concept of a lumped device model to handle circuit components that represent passive and active devices [1]-[4]. Resistors and capacitors are implemented as three-dimensional block resistors and parallel-plate capacitors selecting the conductance and the permittivity of the regions. The semiconductor devices are implemented either as analytical grid models or using the concepts of voltage-variable resistors and capacitors. The second approach concentrates on integrating the fundamental parameters of the electromagnetic systems into a circuit simulation environment. The fundamental parameters, such as impedance, admittance or scattering parameters, are directly used in circuit simulation to solve the terminal voltages and currents of an arbitrary network using convolution [5], [6]. An alternative approach is to extract equivalent circuit representations directly from simulated or measured time- or frequency-domain data [7]. The time-domain approximation of impulse response involves costly optimization and the method does not guarantee physically meaningful (positive) values for the circuit elements. Often the automatic extraction fails to give useful information for complex problems [8].

In this paper, a new approach is presented to integrate data obtained from electromagnetic field analysis into circuit simulations. The scattering parameters of a multiport network are extracted from electromag-

netic simulations, and measurements. The equation describing the electromagnetic (EM) system is formulated using the scattering matrix, terminal voltages and currents, reference impedances and virtual dependent sources. The scattering matrix is approximated using a rational function and recursive convolution is applied to convert the rational functions into macromodels of multiterminal networks that can be used as system matrix stamps. The approach bypasses explicit convolution, inverse Fourier transforms, and low-pass filtering of a large number of points in order to avoid aliasing and time-domain ripples associated with the transformation of data between the frequency and time domains. The circuit representations of an EM system using Norton equivalent circuits with a conductance and a time-dependent current source is compatible with those of conventional time-domain simulators such as SPICE [9] and ASTAP [10] or with methods based on reduced-order techniques such as asymptotic waveform evaluation (AWE) [11], complex frequency hopping (CFH) [12], and Padé via Lanczos (PVL) [13].

In Section II, the method of implementing the scattering parameter formulation of a multiport network in conventional circuit simulators is described. Then, the rational approximation technique of a network function is presented in Section III. The use of recursive convolution for efficient calculation of the system response of an arbitrary input is described in Section IV. Examples of linear and nonlinear networks are given in Section V. The conclusion is given in Section VI.

II. SCATTERING PARAMETER

A general network can be partitioned into a number of subnetworks. The EM subsystems, such as microstrip structures and interconnect geometries, can be represented as a multiport subnetwork that can be characterized by scattering parameters. The N-port scattering parameters of complex structures can be calculated using full-wave analysis techniques. For example, one FDTD simulation can generate the time-domain scattering matrix and eliminate the adverse effects from the imperfect boundary conditions. The corresponding frequency-domain scattering parameters are defined in terms of the Fourier transforms of the time signatures of the incident, reflected and transmitted voltages.

It is possible to obtain scattering parameters of an EM system from frequency-domain measurements with high accuracy using one of the commercially available network analyzers. They are easier to measure over a wider frequency range using careful calibration techniques. The N-port time-domain impulse response can also be obtained from reflection and transmission measurements using a high-speed oscilloscope with TDR and TDT options.

The analysis of the EM system characterized by scattering parameters is done using the following incident and reflected voltage wave definitions:

$$A(j\omega) = \frac{1}{2}\left(V(j\omega) + Z_{ref}I(j\omega)\right)$$

$$B(j\omega) = \frac{1}{2}\left(V(j\omega) - Z_{ref}I(j\omega)\right)$$

(1)

The impedance matrix Z_{ref} describes the reference impedance of an N-port network and is used to describe the scattering parameters in the calculation or measurement of the scattering parameters. The scattering matrix $S(j\omega)$ relates the incident wave $A(j\omega)$ to the reflected wave $B(j\omega)$ as

$$B(j\omega) = S(j\omega) A(j\omega)$$

(2)

In order to express the terminal voltages and currents at each port, instead of dealing with voltage waves, we terminate the system by the reference impedance, Z_{ref}. Then the terminal relation can be represented by the equation

$$[S(j\omega)-1]V(j\omega) + Z_{ref}[S(j\omega)+1] I(j\omega) = 0$$

(3)

157

where $V(j\omega)$ and $I(j\omega)$ are the terminal voltages and the currents flowing into the electromagnetic system, and I is the identity matrix. To obtain the response of the EM system connected to an arbitrary network, the system is separated into an EM system and arbitrary networks as shown in Figure 1. The ports of the EM system are terminated by a reference system, Z_{ref}, and virtual source, $e(t)$, determined from the nonlinear terminal networks.
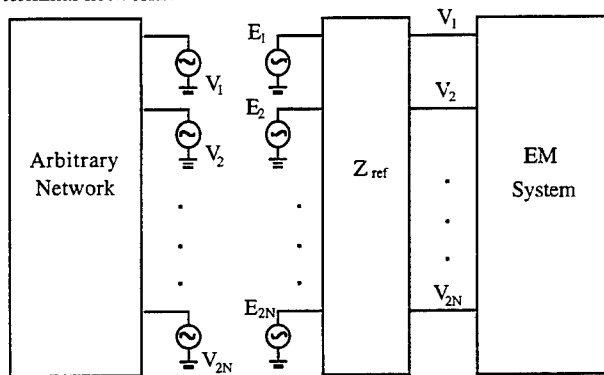
Figure 1. EM system and arbitrary network partitions with overlapping reference systems.

The voltage at the ports of the EM system and the virtual voltage, $e(t)$, are related by

$$e(t) = v(t) + Z_{ref}\, i(t) \tag{4}$$

where $i(t)$ is the current flowing out of the arbitrary network. By overlapping the EM system and the arbitrary network partitions, the currents flowing out of the arbitrary networks are equated with the current flowing into the EM system. In [6], a negative impedance system, $-Z_{ref}$, is inserted in order to remove the effect of the reference impedance. Thus, the stamp of the MNA, a matrix formulation used by circuit simulation [14], corresponding to the EM system is given by

$$\begin{pmatrix} -\mathbf{Z}_{ref}^{-1} & \mathbf{Z}_{ref}^{-1} & 1 \\ 0 & (S-1) & \mathbf{Z}_{ref}\,(S+1) \end{pmatrix} \begin{pmatrix} E \\ V \\ I \end{pmatrix} \tag{5}$$

where S, Z_{ref} and I are the scattering, the reference impedance, and the identity matrices, respectively. This scattering matrix formulation uses terminal voltages and currents and can directly be implemented in conventional simulators. In [15], the convolution relation in (2) is used to derive the time-dependent relationships between the terminal voltages and currents. Although this approach does not introduce additional variables to the MNA matrix, the method requires special subroutines to generate the wave vectors and matrix inversions to calculate the time-dependent conductances.

III. Rational Approximation

Although the time-domain impulse response of an EM system can be approximated by a polynomial of exponential functions using such methods as Prony's or Pencil-of-function, the approximation procedures involve costly nonlinear optimization. Since linear electromagnetic systems are well characterized

in the frequency-domain, a frequency-domain approximation is more efficient and can give better results.

The transfer functions of EM systems can be approximated by the least maximum error by rational functions rather than that by polynomial functions of comparable order. The computational procedures of rational approximations are numerically sensitive and limited by the precision of the computer. The approximation matrices are ill-conditioned. In [16], optimal conditioning and Householder orthogonal triangularization are used to guarantee the existence of a stable rational approximation of a complex system over a wide approximation domain.

The scattering parameters, $S_{i,j}(j\omega)$, of a linear system can be approximated by a rational function of degree (ξ, ϑ) as

$$H_{\xi,\vartheta}(s) = \frac{Q_\xi(s_i)}{P_\vartheta(s_i)} = \frac{q_0 + q_1 s + q_2 s^2 + \ldots + q_\xi s^\xi}{1 + p_1 s + p_2 s^2 + \ldots + p_\vartheta s^\vartheta} \tag{6}$$

with p_0 normalized to unity. Equation (6) contains $n = \xi + \vartheta + 1$ free coefficients, hence, at most n independent parameters. The coefficients are determined so that the approximating function evaluated at the same frequency points gives close approximations to the function $S(s)$. For specified finite functional values $y_i = S(s_i)$, $(i = 0, \ldots k-1)$ and k specified distinct points, s_i, the resulting equations give

$$\frac{Q_\xi(s_i)}{P_\vartheta(s_i)} - y_i = 0 \tag{7}$$

By canceling the denominators in (7), one obtains the linear homogenous system of k equations in n unknowns:

$$\underbrace{\begin{bmatrix} 1 & s_0 & s_0^2 & \cdots & s_0^\xi & -s_0 y_0 & -s_0^2 y_0 & \cdots & -s_0^\vartheta y_0 \\ 1 & s_1 & s_1^2 & \cdots & s_1^\xi & -s_1 y_1 & -s_1^2 y_1 & \cdots & -s_1^\vartheta y_1 \\ & \vdots & & & & & & & \\ 1 & s_{k-1} & s_{k-1}^2 & \cdots & s_{k-1}^\xi & -s_{k-1} y_{k-1} & -s_{k-1}^2 y_{k-1} & \cdots & -s_{k-1}^\vartheta y_{k-1} \end{bmatrix}}_{V} \underbrace{\begin{bmatrix} q_0 \\ q_1 \\ q_2 \\ \vdots \\ q_\xi \\ p_1 \\ p_2 \\ \vdots \\ p_\vartheta \end{bmatrix}}_{X} = \underbrace{\begin{bmatrix} y_0 \\ y_1 \\ \vdots \\ y_{k-1} \end{bmatrix}}_{Y} \tag{8}$$

The columns of $V \in R^{k \times n}$ form independent vectors and often $k \geq n$, and (8) is a full-rank overdetermined system. When $k > n$ Equation (8) can be reformulated as a square consistent system that has a unique solution $X = \hat{V}^{-1} Y$ for any $Y \in R^n$, where $\hat{V} \in R^{n \times n}$ is the reformulated V.

For higher-order approximations over a wider approximation range, the system in (8) is highly ill-conditioned and nearly singular because of the large difference between the maximum and minimum frequencies raised to the order of approximation. The condition number can be improved by normalizing the maximum frequency to unity and shifting the domain variable.

Due to numerical difficulties, solving the consistent equation obtained from (8) using the direct method may give inaccurate results. The problem can be transformed into a more numerically robust equivalent one, yet still produce the solution. The Householder QR orthogonalization can be used to solve Equation (8). The total computational complexity of the approximation method is one polynomial factorization, two Householder QR transformations, and two backsubstitutions.

The approximation algorithm can be made more efficient and accurate by utilizing the special properties of the EM system fundamental parameters. The functions are analytic functions of a complex variable; hence, their real and imaginary parts are related by Cauchy-Riemann equations. The consequence of this property is that only the real part, imaginary part, angle, or magnitude of the network function have to be approximated and the network function itself can be found from the resulting approximation. Details of the approximation can be found in [16]. The scattering parameters are approximated by stable partial fraction expansion given as

$$H(s) = k_\infty + \sum_{i=1}^{\vartheta'} \frac{k_i}{s + p_i} \tag{9}$$

This partial fraction expansion is used to characterize the EM system. In the next section, the partial fraction expansion is used to perform convolution efficiently to obtain system response for an arbitrary input.

IV. RECURSIVE CONVOLUTION

We established the fact that the transient response of an electromagnetic system can be approximated by the exponential functions in the time domain or rational function in the frequency domain. In the preceding sections, we have successively derived a robust frequency-domain rational approximation method for the transfer functions of electromagnetic systems. The response of the system for an arbitrary input is obtained in the form

$$Y(s) = \underbrace{\left(k_\infty + \sum_{i=1}^{\vartheta} \frac{k_i}{s + p_i} \right)}_{H(s)} X(s) \tag{10}$$

where $X(s)$, $Y(s)$ and $H(s)$ are the Laplace domain input, output and transfer function of the system, respectively. The time-domain response is obtained by calculating the convolution integral given as

$$y(t) = \int_0^t x(\tau) h(t - \tau) \, d\tau \tag{11}$$

where $x(\tau)$ and $y(\tau)$ are the input and output to the linear system, respectively, $h(\tau)$ is the impulse-response or the kernel function of the system. The convolution integral in (11) becomes progressively more expensive as the simulation time increases. Since the transfer function of the electromagnetic system is expressed as a sum of partial fraction expansions (9), the time for the numerical convolution in (11) can greatly be reduced by taking advantage of the recursive convolution.

The advantage of a recursive convolution for calculating the switching response of frequency-dependent transmission lines was first recognized in the early 70's by power and systems experts. In 1975, Semlyen and Dabuleanu developed the recursive convolution and showed its computational efficiency and usefulness [17]. The time-domain response can be written in terms of the last response and a single time-step convolution as

$$y(t) = k_\infty x(t) + \sum_{i=1}^{\vartheta} \left(e^{p_i \delta t} y(t - \delta t) + \int_0^{\delta t} k_i e^{p_i t} x(t - \tau) \, d\tau \right) \tag{12}$$

Knowledge of the values of $x(t)$ at a discrete number of points is not sufficient to specify $y(t)$ uniquely by the above equation. It is necessary to make assumptions about the nature of $x(t)$ such that its values at a discrete set of the points suffice to specify $y(t)$ uniquely. If the excitation is assumed to be piecewise constant, $x(t)=c$, where $t_{n-1} \le t \le t_n$, Equation in (12) reduces to

$$y(t_n) = k_\infty x(t_n) + \sum_{i=1}^{q} \tilde{y}_i(t_n) \tag{13}$$

where $\tilde{y}_i(t_n) = k_i(1 - e^{-p_i \delta t_n}) x(t_n - \delta t_n) + e^{-p_i \delta t_n} \tilde{y}_i(t_n - \delta t_n))$

and $\delta t_n = t_n - t_{n-1}$.

160

The recursive convolution gives exact results if the assumption made about $x(t)$ is valid. The stability of the convolution method depends on the nature of the system impulse response function, $h(t)$.

Each entry in the submatrix of the scattering parameters of the electromagnetic system is approximated by a rational function, and the inverse Laplace transform of the pole-residue model, is found symbolically. This corresponds to the macromodel stencils of the MNA matrix. Equation (13) is implemented as a Norton equivalent circuit consisting of a conductance of constant value, k_∞, and a current source, $-\sum_{i=1}^{q} \tilde{y}_i(t_n)$, which is updated at each time iteration based on the pole-residue pairs and the voltage at a previous time point. Since the number of pole-residue pairs is much smaller than the number of time points in the total simulation time, the integration routine is linear in time.

V. NUMERICAL RESULTS

An interconnect with a V-shaped cross-section is characterized using a scattering matrix. The scattering parameters are measured in the frequency range *45 MHz-10 GHz* with a *HP8510B* vector network analyzer. The measured scattering parameters of the interconnect are approximated over a frequency range using a rational function. Although the method is able to generate a stable, very high-order rational approximation, a *24th-* and a *27th-* order rational function is used to approximate S_{12} and S_{11}, respectively. The measured and approximated scattering parameters are shown in Figures 2 to 5. The magnitude and phase plots of S_{12} and S_{11} are almost indistinguishable.
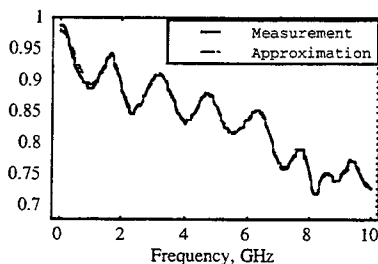
Figure 2. Magnitude plots of S_{12}, the measured data and the *24th*-order rational approximation.
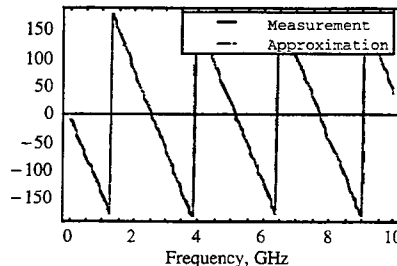
Figure 3. Phase plots of S_{12}, the measured data and the *24th*-order rational approximation.
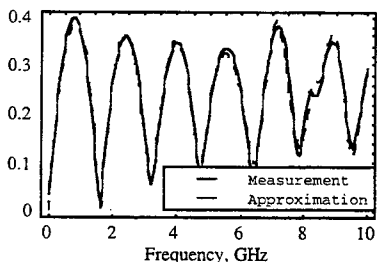
Figure 4. Magnitude plots of S_{11}, the measured data and the *27th*-order rational approximation.
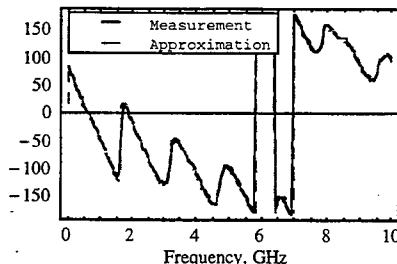
Figure 5. Phase plots of S_{11}, the measured data and the *27th*-order rational approximation.

161

The proposed method is used to study resistive and diode terminations. The network in Figure 6 consists of a measured subnetwork, a diode-pair termination and a resistive termination. For the measured sub-network, the rational function approximations of the scattering parameters of the V-shaped interconnect are used. First, the measured S-parameters are extrapolated to low frequencies for the dc solution. Then, the scattering parameters are incorporated into the MNA matrix using Equation (5). The network is exited by a pulse with rise and fall times of *0.3 ns* and pulse magnitude and width of *5 V* and *7 ns*, respectively. The network is simulated with the diode-pair termination and with the *5 kΩ* resistor replacing the diodes shown in Figure 6.
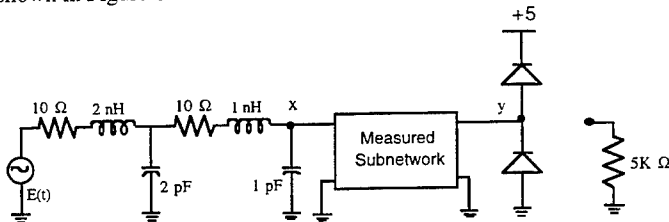
Figure 6. The diode-pair terminated network. (The *5 kΩ* resistor replaces the diode-pair.)

The transient responses of the diode-pair termination at nodes *x* and *y* are compared to those of a *5 kΩ* resistor termination. At the far end, node *y*, the voltage response of the *5 kΩ* resistor, shows voltage overshoots and undershoots while the diode-pair termination squelch the voltage overshoots as shown in Figure 7. The voltage waveforms at the near-end, node *x*, for the two cases are almost identical as shown in Figure 8. Thus, the time-domain analysis of a nonlinear network can be performed efficiently using the proposed method.
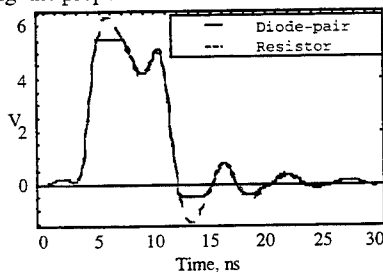
Figure 9. The transient response at node *y*.
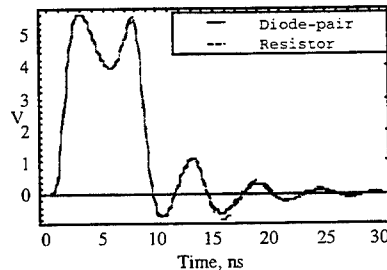
Figure 8. The transient response at node *x*.

VI. CONCLUSIONS

An efficient method of integrating data obtained from electromagnetic analysis into circuit simulations is presented. The frequency-dependent scattering matrix characterizing the EM system is approximated by rational function, and recursive convolution is used to construct the macromodels and to incorporate them into time-domain nonlinear solvers. The MNA stamps corresponding to the EM systems are constructed as Norton equivalent circuits with conductances of constant values and time-dependent current sources that are compatible with the formulations of conventional circuit simulators. The method s efficiency over traditional methods is obtained by avoiding the use of time-consuming IFFT, low-pass filtering and convolution that are required in traditional methods.

REFERENCES

[1] P. B. Johns and M. O'Brien, "Use of the transmission line modelling (T.L.M.) method to solve nonlinear lumped networks," Radio Electronic Engineering, vol. 50, nos. 1-2, pp. 59-70, January-February 1980.

[2] R. Voelker and R. Lomax, "A finite-difference transmission matrix method incorporating a nonlinear device," IEEE Transactions on Microwave Theory and Techniques, vol. 38, no. 3, pp. 302-312, March 1990.

[3] T. Shibata, "Circuit simulations combined with electromagnetic field analysis," IEEE Transactions on Microwave Theory and Techniques, vol. 39, no. 11, pp. 1862-1868, November 1991.

[4] W. Sui, D. A. Christensen, and C. H. Durney, "Extending the two-dimensional FDTD method to hybrid electromagnetic systems with active and passive lumped elements," IEEE Transactions on Microwave Theory and Techniques, vol. 40, no. 4, pp. 724-730, April 1992.

[5] T. K. Liu and F. M. Tesche, "Analysis of antennas and scattering with nonlinear loads," IEEE Transactions on Antennas and Propagation, vol. AP-24, pp. 131-139, March 1976.

[6] D. Winklestein, M. B. Steer, and R. Pomerleau, " Simulation of arbitrary transmission line networks with nonlinear terminations," IEEE Transactions on Circuits and Systems, vol. 38, no. 4, pp. 418-422, April 1991.

[7] Y. Chen, P. Harms, R. Mittra, and W. Beyene, "Analysis of complex electronic packages using FDTD / TOUCHSTONE hybrid technique," Microwave and Optical Technology Letters, vol. 12, no. 6, pp. 313-315, August 1996.

[8] S. D. Corey, K. J. Kerns and A. T. Yang, "Automatic measurement-based characterization of lossy MCM line using lumped elements," IEEE 5th Topical Meeting on Electrical Performance of Electric Packaging, Napa, CA, October 28-30, 1996.

[9] L. W. Nagel, "SPICE2: A computer program to simulate semiconductor circuits," Technical Report ERL-M520, University of California, Berkeley, May 1975.

[10] W. T. Weeks, A. J. Jininez, G. W. Mahoney, D. Mehta, H. Qassemzadeh, and T. R. Scott, "Algorithms for ASTAP-A network analysis program," IEEE Transactions on Circuit Theory, vol. CT-20, pp. 628-634, November 1973.

[11] J. Bracken, V. Raghavan and R. Rohrer, "Interconnect simulation with asymptotic waveform evaluation (AWE)," IEEE Transactions on Circuits and Systems, vol. CAS-39, no. 11, pp. 869-878, November 1992.

[12] E. Chiprout and M. S. Nakhla, "Transient waveform estimation of high-speed MCM networks using complex frequency hopping," Proceedings of Multi-Chip Module Conference (MCMC), pp. 134-139, March 1993.

[13] K. Gallivan, E. Grimme and P. Van Dooren, "Asymptotic waveform evaluation via Lanczos methods," Applied Mathematics Letters, vol. 7, pp. 75-80, 1994.

[14] C. Ho, A. Ruehli, and P. Brennan, "The modified nodal approach to network analysis," IEEE Transactions on Circuits and Systems, vol. CAS-22, pp. 504-509, June 1975.

[15] S. D. Corey and A. T. Yang, "Interconnect characterization using time-domain reflectometry," IEEE Transactions on Microwave Theory and Techniques, vol. 43, no. 9, pp. 2151-2156, September 1995.

[16] W. T. Beyene and J. E. Schutt-Ainé, "Efficient transient simulation of high-speed interconnects characterized by sampled data," submitted to IEEE Transactions on Components, Packaging, and Manufacturing Technology-Part B: Advanced Packaging.

[17] A. Semlyen and A. Dabuleanu, "Fast and accurate switching transient calculations on transmission lines with ground return using recursive convolutions," IEEE Transactions on Power Apparatus and Systems, vol. PAS-94, no. 2, March/April 1975.

Application of AWE Method to the Spectral Responses of 3D TVFEM Modeling of Passive Microwave Devices

Xiaoming Zhang and Jin-Fa Lee
ECE Dept., WPI
100 Institute Road
Worcester, MA 01609
jinlee@ece.wpi.edu
(508)831-5778

Romanus Dyczij-Edlinger
Motorola Corp., System Technologies
Motorola CCRL, IL02-EA901
1301 East Algonquin Road
Schaumburg, IL 60796

Spectral responses of electromagnetic devices in a range of frequency are often of great value for analysis and design purpose. Among various approaches for solid modeling of microwave devices, finite element methods (FEM), especially tangential vector finite element method (TVFEM), has been demonstrated to be very successful. The TVFEM formulation of EM problems usually leads to a matrix equation of high dimension. And in order to obtain the system responses within a certain frequency band, this equation used to be solved directly at a set of discrete frequency points and the results are interpolated to form a continuous curve. However with the increasing size of the system, solving this system equation at many discrete frequency points can be very time consuming. Especially when the system posses a complex spectral behavior, the points that this approach needs can be 50 or even more.

This paper describes an efficient approach for evaluating the spectral responses of the passive microwave devices. This method is based on the TVFEM formulation of the EM problems and the AWE technique. Through choosing the expansion point from the entire frequency plane as well as with selective orthogonalization in the Lanczos process, the spectral responses of the system can always be obtained by the expansion at a single frequency point. An adaptive algorithm based on this approach is developed and applied to several practical problems.

Solution of EM Problems Using Reduced-order models by Complex Frequency Hopping

M. A. Kolbedhari, M. Nakhla, R. Achar and M. Srinivasan

Department of Electronics Engineering,
Carleton University, Ottawa, Ont., Canada, K1S 5B6
Ph: 613-520-5780   Fax: 613-520-5708   e-mail: msn@doe.carleton.ca

Abstract

This paper describes an efficient method for both spectral- and time-domain solution of general EM problems using reduced-order models. In this technique, EM problems described by generalized FEM formulation (both homogeneous and inhomogeneous cases) which usually result in large sets of algebraic equations are reduced to lower-order models using complex frequency hopping. Proposed technique can also handle formulations consisting of hybrid finite element - boundary integral systems. Several electromagnetic problems have been studied using the proposed technique and a speed up of one to three orders of magnitude is achieved for a comparable accuracy with conventional techniques.

I. INTRODUCTION

Efficient solution of electromagnetic field formulations are important for accurate and quick analysis/design of high-speed circuits and systems. Most common approach used for the solution of EM problems is the finite element method (FEM) [1] - [3] and the formulation can be in space/frequency or space/time domain. The formulations in the spectral-domain lead to a set of algebraic equations which have to be solved repeatedly at many frequency points, while the one in the latter domain leads to a set of ordinary differential equations which have to be solved in time-domain. Generally, the size of the resulting equations is large and the conventional solution algorithms are restricted by computing time and stability conditions [4]. Also in most applications both frequency- and time-domain results are required to be computed. In order to address the above issues efficiently, a new solution method based on reduced-order models using CFH [5] - [7] has been developed.

Complex Frequency Hopping (CFH) is a moment-matching technique that has been recently developed in the circuit simulation area which yields a speed-up factor of 10-1000 over conventional circuit simulators. It has been extended to solution of static fields in VLSI interconnects, in ground/power planes and thermal equations [5] - [9]. CFH uses the concept of moment-matching [6], [10] to obtain both frequency- and time-domain responses of large linear networks through a lower-order multipoint Padé approximation. It extracts a relatively small set of dominant poles to represent a large network that may contain hundreds to thousands of actual poles. CFH is particularly suitable for solving large set of ordinary differential equations which makes it a logical candidate for solving general class of EM equations. The main advantages of the proposed model-reduction technique can be summarized as follows:

- 10-1000 times faster than the conventional FEM solution techniques
- Produces simultaneously both the frequency- and time-domain results.
- Can handle general case of EM problems: both homogeneous and inhomogeneous formulations.
- Solution algorithm does not suffer from instability problems associated with the conventional methods.
- Problems consisting of Dirichlet, Neumann and combined boundary conditions can be solved and the proposed model-reduction technique can be easily integrated with conventional EM simulators.

Integration of CFH with nodal-based FEM for solution of homogeneous EM problems is described in [11]. This paper presents formulation/solution of general case of EM problems (both homogeneous and inhomogeneous) based on the proposed model-reduction algorithm. Also, presented is the extension of the proposed model-reduction technique for the more involved case of hybrid finite element - boundary integral systems.

Rest of the paper is organized as follows: A brief discussion of general EM formulations is given in section II. Section III gives a brief outline of the CFH algorithm. Section IV presents the proposed model-reduction algorithm. Numerical examples and conclusions are presented in section V and VI, respectively.

II. FORMULATION

For general time-harmonic case, starting from Maxwell's equations an expression in terms of electric field E can be derived as [2]

$$\nabla \times \left(\frac{1}{\mu_r} \nabla \times E \right) - k_o^2 \varepsilon_r E = -j k_o Z_0 J \tag{1}$$

The boundary conditions often encountered are those to be applied at the electrically and magnetically conducting surfaces and are given by,

$$\hat{n} \times E = 0; \qquad \hat{n} \times \nabla \times E = 0; \qquad \frac{1}{\mu_r}(\hat{n} \times \nabla \times E) + \gamma_e \times \hat{n} \times \hat{n} \times E = 0 \tag{2}$$

respectively. The continuity conditions at the interfaces separating two different media are

$$\hat{n} \times E^+ = \hat{n} \times E^- \tag{3}$$

where $\hat{n}$ is the unit vector normal to the interface. J represents the excitation source current. $\varepsilon_r = \varepsilon/\varepsilon_0$ and $\mu_r = \mu/\mu_0$ denote the relative permittivity and permeability, respectively. $k_0 = \sqrt{\mu_0 \varepsilon_0}$ and $Z_0 = \mu_0/\varepsilon_0$ are the wave number and intrinsic impedance of the free space, respectively.

In accordance to the variational principle, the solution to the electric field governed by (1) - (3) can be obtained by seeking the stationary point of the functional

$$F(E) = \frac{1}{2} \iiint_\Omega \left[\left(\frac{1}{\mu_r} \nabla \times E \right) \cdot \nabla \times E - k_o^2 \varepsilon_r E \cdot E \right] d\Omega \; + \iint_s \left[\frac{\gamma_e}{2} \hat{n} \times E \cdot \hat{n} \times E \right] dS \; + j k_0 Z_0 \iiint_\Omega E \cdot J d\Omega \tag{4}$$

where Ω represents the finite element domain. A similar functional can also be derived in terms of magnetic field. Alternatively, above kind of functional can also be obtained in terms of magnetic vector potential [2]. By minimizing the functional of the problem and applying associated Dirichlet and Neumann boundary conditions, a system of ordinary differential equations in Laplace-domain can be obtained as

$$(Cs^2 + Bs + A)X(s) = R(s) \tag{5}$$

or

$$Y(s)X(s) = R(s) \tag{6}$$

where A, B, C are $N \times N$ symmetric, positive definite matrices assembled from $[S]_{e_p}$ and $[T]_{e_p}$ and N is the total number of nodes. $R(s)$ is a vector of dimension N, assembled from $[G]_{ep}$ which contains the forced terms attributed to space or time excitation. $X(s)$ is a vector containing discretized unknown field components. $[S]_{e_p}$, $[T]_{e_p}$ are real square elemental matrices and $[G]_{e_p}$ is a column vector, defined as

$$[S_{ij}]_{e_p} = \int_{\Omega_{e_p}} \nabla \alpha_i^p \cdot \nabla \alpha_j^p \, d\Omega_{e_p}; \qquad [T_{ij}]_{e_p} = \int_{\Omega_{e_p}} \alpha_i^p \alpha_j^p d\Omega_{e_p}; \qquad [G_i]_{ep} = \int_{\Omega_{e_p}} \alpha_i^p f(t) d\Omega_{e_p} \tag{7}$$

where Ω_{e_p} represents the domain of finite elements. Here p refers to either 1, 2 or 3 corresponding to one-, two- or three-dimensional FEM formulation with finite elements e_p and shape functions α^p.

III. COMPLEX FREQUENCY HOPPING

Complex frequency hopping(CFH) [5] - [7] is a recently developed model-reduction algorithm in the circuit simulation area. It has been successfully and efficiently applied for obtaining the solution of large set of ordinary differential equations and it uses the moment-matching for obtaining reduced-order description of a linear system. In general, moment matching technique approximates the frequency response of a Taylor series expansion in the complex s plane. The cost of an expansion is approximately one frequency point analysis. The moments (coefficients of the expansion) are matched to a lower-order transfer function using a rational Padé approximation. This transfer function can be used to obtain the output response. Single Padé approximations are accurate near the point of expansion in the complex s plane and decrease in accuracy with increased distance from the point of expansion. CFH overcomes this problem by performing multiple Taylor expansions in the complex plane using a binary search algorithm. With a minimized number of frequency point expansions, enough information is obtained to enable the generation of an approximate transfer function that matches the original function up to a pre-defined highest frequency. The transfer function or set of transfer functions then acts much as the entire network up to that frequency, both in time and frequency-domains.

Expanding $X(s)$ in (5) about the complex frequency point $s = \alpha$ yields,

$$X(s) = \sum_i M_n (s - \alpha)^n \tag{8}$$

where M_n is the nth vector of coefficients (moments) of the Taylor expansion. A recursive relation for

the evaluation of moments can be obtained in the form

$$[Y(\alpha)]M_n = -\sum_{r=1}^{n} \frac{Y(s)^{(r)}\big|_{s=\alpha} M_{n-r}}{r!} \tag{9}$$

The transfer function of the system is then found by matching a Padé approximation to the moments of the system in (8). The reduced-order model which is obtained in terms of approximate dominant poles $\hat{p}_i$ and residues $\hat{k}_i$ of the system can be represented as

$$H(s) \approx \hat{H}(s) = \hat{c} + \sum_{i=0}^{L} \frac{\hat{k}_i}{s - \hat{p}_i} \tag{10}$$

where $\hat{c}$ is the direct coupling constant between the input and the output and L is the total number of dominant poles extracted. Corresponding approximate time-domain impulse response is given by

$$h(t) \approx \hat{h}(t) = \hat{c}\delta t + \sum_{i=0}^{L} \hat{k}_i e^{\hat{p}_i t} \tag{11}$$

In order to compute moments in (9), we need the derivatives $Y^{(r)}(s)$. Computation of $Y^{(r)}(s)$ has been discussed extensively in circuit simulation area where in the Y matrix comprises of circuit elements such as inductors/capacitors and quasi-TEM interconnect models. However, computation of these moments in case of EM formulations has not been addressed previously in the literature. In the following section we propose an efficient method to compute these derivatives for EM formulations.

IV. MOMENTS-GENERATION.

To obtain the derivatives of $Y(s)$ in (9), a recursive relationship has been developed and is summarized below:

$$[C\alpha^2 + B\alpha + A]M_0 = R(\alpha) \tag{12}$$

$$[C\alpha^2 + B\alpha + A]M_1 = -[B + 2\alpha C]M_0 + R'(\alpha) \tag{13}$$

$$[C\alpha^2 + B\alpha + A]M_n = -BM_{n-1} - C[2\alpha M_{n-1} + M_{n-2}] + \frac{R''(\alpha)}{n!} \tag{14}$$

for $n \geq 2$. Here (12), (13) and (14) give the system moments recursively at a given expansion point $s = \alpha$. In case of hybrid finite element boundary systems, moments-generation gets little complicated as the matrices involved here, A, B and C are frequency dependent [2]. In this case also the moments can be recursively computed as

$$[\Gamma(\alpha)]M_n = \sum_{r=1}^{n} \varphi^{(r)}(s)\big|_{s=\alpha} M_{n-r} \tag{15}$$

where $\Gamma(\alpha)$ and $\varphi^{(r)}(\alpha)$ are functions of the derivatives of $A(\alpha)$, $B(\alpha)$ and $C(\alpha)$.

V. COMPUTATIONAL RESULTS

Numerical examples involving formulations for the case of homogeneous EM problems are presented in [11]. In this paper two numerical examples are given to demonstrate the applicability and the speed-up achieved in case of inhomogeneous EM problems. Problems chosen here are the extraction of resonance frequencies of inhomogeneous dielectric resonators. For these examples, formulations indicated in section II were carried out in cylindrical co-ordinates and the resulting $Y(s)$ represented by (6) has the form $Y(s) = Cs^2 + A$.

Example 1:

In this example resonant frequencies of an inhomogeneous dielectric resonator shown in Fig. 1 are evaluated using the proposed model-reduction technique. This example is reported in [12] with FEM formulation containing 325 nodes. Using a similar kind of discretization and equations (12) - (14), required moments are generated and the resonant frequencies are extracted using the CFH algorithm. In Table 1, accuracy comparison of resonant frequencies obtained using the proposed model-reduction technique and the conventional FEM frequency-domain (FEMFD) approaches are given and as seen they match accurately. Also, the accuracy of resonant frequencies obtained using the proposed technique are compared with one reported in [12] and they agree reasonably. Speed-up achieved using the proposed technique compared to FEMFD is given in Table 2.

$L = 5mm \quad R_1 = 15mm$
$R = 5mm \quad R = 0.635mm$
$\varepsilon_R = 100 \quad \varepsilon_s = 9.6$

Normalized parameters:

$\varepsilon_n = \varepsilon_s / \varepsilon_R = 0.096$
$t_n = t/R = 0.127$
$R_n = R_1/R = 1.5$
$L_n = L/R = 1.5$
$H_n = H/R$
$f_n = 2Rf_0 \sqrt{\mu_0 \varepsilon_0 \varepsilon_R}$

Fig. 1. Cross-section of an inhomogeneous dielectric resonator
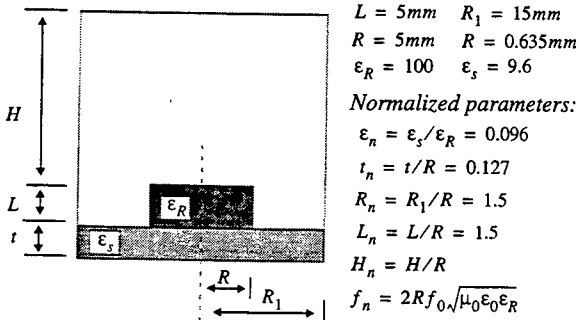
Table 1. Accuracy comparison of resonant frequencies (325 nodes)

H_n	Proposed method-f_n(Ghz)	FEMFD f_n (GHz)
0.20	1.2427	1.2427
0.30	1.2199	1.2199
0.40	1.2069	1.2069
0.50	1.1988	1.1988
0.60	1.1939	1.1939
0.75	1.1890	1.1890
1.00	1.1874	1.1874
1.50	1.1857	1.1857
2.00	1.1857	1.1857
2.50	1.1857	1.1857

Table 2. CPU comparison (SUN Sparc 10)

Matrix Size	H_n	Proposed method (secs)	FEMFD (secs)	Speed-up Ratio	No. of hops
293 x 293	0.20	2.35	423.8	180	2
292 x 292	0.30	2.61	426.7	163	2
304 x 304	0.40	2.73	564.3	206	2
301 x 301	0.50	2.65	597.3	225	2
304 x 304	0.60	2.37	498.4	210	2
313 x 313	0.75	2.58	454.0	176	2
313 x 313	1.00	3.28	578.9	176	2
326 x 326	1.50	3.35	706.7	211	2

Example 2:

This example consisting of an inhomogeneous dielectric resonator (Fig. 2) [13] is chosen for the purpose of demonstrating the accuracy and CPU speed-up of the proposed model-reduction technique. The configuration consists of a cylindrical high-dielectric constant material (region 3) positioned between three layers of different dielectrics. The structure is analyzed using the proposed technique and the resonant frequencies are evaluated. Table 3 and Fig. 3 give the CPU/accuracy comparison of the proposed technique with the conventional FEMFD approach. As seen the results match accurately while the proposed technique yields a very high-speed up (approximately 200). Also accuracy of the results from the proposed technique are compared with the results reported in [13] and they agree reasonably.

$h_1 = 0.0635 cm$

$h_3 = 0.48 cm$

$R_1 = 0.635 cm$

$R_2 = 1.4R_1$

$\varepsilon_1 = 10\varepsilon_0$

$\varepsilon_3 = 37\varepsilon_0$

$\varepsilon_5 = 1.4\varepsilon_0$
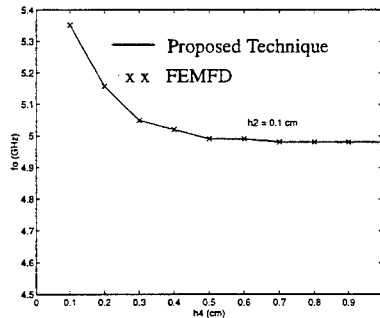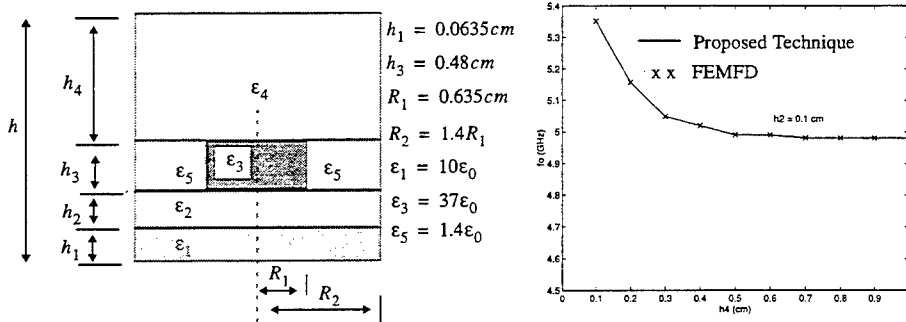
Fig. 2. Cross-section of the resonator for example 2   Fig. 3. Resonant frequencies for various h_4

Table 3. CPU comparison (SUN Sparc 10)

Matrix Size	h_4	Proposed method (secs)	FEMFD (secs)	Speed-up Ratio	No. of hops
367 x 367	0.1	5.01	943.1	188	3
385 x 385	0.2	5.25	1075.2	204	3
405 x 405	0.3	5.07	1284.6	253	3
398 x 398	0.4	5.38	1099.0	204	3
397 x 397	0.5	5.05	1171.3	231	3
386 x 386	0.6	5.95	1216.0	204	3
398 x 398	0.7	5.70	1436.5	252	3
383 x 383	0.8	5.10	1220.5	239	3
404 x 404	0.9	5.70	1106.6	194	3
402 x 402	1.0	5.45	1314.2	241	3

VI. CONCLUSIONS

An efficient model-reduction technique based on CFH and FEM for solution of both homogeneous and inhomogeneous EM problems is presented in this paper. Several electromagnetic problems including inhomogeneous dielectric resonators were analyzed using the proposed technique and a speed-up of two orders of magnitude is achieved compared to conventional techniques. Proposed model-reduction technique yields both frequency- and time-responses and can be easily integrated with conventional EM simulators.

References

[1] P. P. Silvester and R. L. Ferrari, *Finite Elements for Electrical Engineer*, Cambridge University Press: NY, 1990.

[2] J. Jin, *The Finite Element Method in Electromagnetics*, John Wiley and Sons Inc: NY, 1993.

[3] X. D. Cai and G. I. Costache, "A Laplace-domain finite element method (LDFEM) applied to diffusion and propagation problems in electrical engineering", *Intl. J. of NMENDF, vol 7*, pp. 419-432, 1994.

[4] R. Harrington, *Time-Harmonic Electromagnetic Fields,* McGraw-Hill Book Co. Inc: NY 1961.

[5] E. Chiprout and M. S. Nakhla, "Analysis of interconnect networks using complex frequency hopping," *IEEE Trans. CAD*, vol. 14, No. 2, pp. 186-199, Feb. 95.

[6] E. Chiprout and M. S. Nakhla, *Asymptotic Waveform Evaluation and Moment Matching for Interconnect Analysis*, Boston: Kluwer Academic Publishers, 1993.

[7] R. Sanaie, E. Chiprout, M. S. Nakhla, and Q. J. Zhang, "A fast method for frequency and time domain simulation of high-speed VLSI interconnects," *IEEE Trans. Microwave Theory Tech.*, vol. 42, No. 12, pp. 2562-2571, Dec. 1994.

[8] T. Tang and M. S. Nakhla, "Analysis of high-speed VLSI interconnect using the asymptotic waveform evaluation technique," *IEEE Trans. CAD*, vol 11, pp. 2107-2116, Mar. 1992.

[9] D. G. Liu, V. Phanilatha, Q. J. Zhang and M. S. Nakhla, "Asymptotic thermal analysis of electronic packages and printed circuit boards", *IEEE Trans.CPMT*, Part A, vol 18, pp. 781-787. 1995.

[10] L. T. Pillage and R. A. Rohrer, "Asymptotic waveform evaluation for timing analysis," *IEEE Trans. CAD*, vol. 9, PP. 352-366, Apr. 1990.

[11] M. A. Kolbedhari, M. Srinivasan, M. Nakhla, Q. J. Zhang and R. Achar, "Simultaneous time and frequency domain solutions of EM problems using finite element and CFH techniques.", *IEEE Trans. MTT*, vol. 44, pp. 1526-1534, Sept. 1996.

[12] P. S. Kooi, M. S. Leong, and A. L. Satyaprakash, "Finite-element analysis of the shielded cylindrical dielectric resonator", IEE Proceedings, Vol 132, No H-1, pp. 7-16, Feb. 1985

[13] R. R. Bonetti and A. E. Atia, "Design of cylindrical dielectrical resonators in inhomogeneous media", *IEEE Trans. Microwave Theory Tech.*, vol. 29, No. 4, pp. 2562-2571, Apr. 1981.

Transient Analysis via Electromagnetic Fast-Sweep Methods and Circuit Models

J. Eric Bracken and Zoltan J. Cendes
Ansoft Corporation
Four Station Square, Suite 660
Pittsburgh, PA 15219-1119

Abstract—This paper presents an efficient method for the computation of electromagnetic transients. We employ fast frequency-sweep methods, such as Asymptotic Waveform Evaluation (AWE) or the Lanczos-based ALPS procedure, to determine the frequency response of an electromagnetic system over a broad frequency band. Using a rational function fitting procedure, we compute a reduced-order model of the system's port parameters. Next, an equivalent circuit model is formed. A circuit simulator such as SPICE or SPECTRE can then be used to compute the transient response of the system in conjunction with nonlinear driver and load devices. We provide examples to demonstrate the accuracy and efficiency of this technique.

1 Introduction

Electromagnetic transients are often computed by using time-stepping methods in the space domain using the FDTD or similar algorithms[1]. In this approach, the geometry of the structure is represented by thousands of grid points and the electromagnetic field at each point is computed at thousands of tiny (e.g. picoseconds) time steps directly from Maxwell's equations.

This paper presents a efficient alternative to this computation-intensive approach. We use fast-sweep methods such as AWE[2][3] or ALPS[4] to determine the frequency response of an electromagnetic system over a broad bandwidth. This information is used to compute a reduced-order model of the transfer function of the system; then an equivalent circuit is derived from this reduced-order model. This equivalent circuit is subsequently used in circuit analysis to determine the transient response of the system using circuit simulators such as SPICE[5][6] or SPECTRE [7].

There are several advantages to the new approach. First, the electromagnetic field is computed only once. Electromagnetic fields in many systems are linear and are completely characterized by a few dozen parameters derived by using linear analysis. Second, the electromagnetic analysis may be performed by using either differential or integral equation methods. In this paper, we employ both finite element analysis and boundary element analysis to perform the frequency domain electromagnetic field computation. Third, the time-domain solution is computed in the circuit domain. This means that the transient simulation is very fast and memory efficient since it is based on reduced-order models involving only a few dozen parameters. Fourth, the resulting electromagnetic model is readily combined with external sources and loads. Since both the electromagnetic fields and the external sources and loads are represented by circuit elements, they are analyzed simultaneously in the circuit simulator. And fifth, it is very easy to use these reduced-order models in what-if design variations. Since the electromagnetics

is done once and for all, it is possible to pass these detailed models on to design groups working at the system level. The new transient/fast sweep procedure has been implemented in Ansoft's High-Frequency Structure Simulator (HFSS). This paper will illustrate the theory with solutions from microwave circuit design obtained by using this technique.

2 Fast Frequency Sweep Techniques for Electromagnetics

Numerical solutions of Maxwell's equations typically involve a discretization process which reduces the field problem to a matrix equation of the form

$$A(s)x(s) = b(s). \tag{1}$$

Here, $x(s)$ is a vector consisting of the desired solution quantities (for example, electric fields or current densities), $b(s)$ is a vector containing the contributions of applied sources, and $A(s)$ is a square matrix formed by stamping in the various finite element or integral equation contributions. Since A and b are frequency-dependent quantities, it is necessary to repeat the solution of (1) for every frequency point desired. This process is obviously expensive if a large number of frequency points is required.

Fast frequency sweep methods attempt to accelerate the procedure by breaking apart the operator $A(s)$ into more manageable pieces. In the simplest lossless cases, it is possible to rewrite $A(s)$ as

$$A(s) = A_0 + s^2 A_2 \tag{2}$$

where A_0 and A_2 are frequency-independent matrices. In this case, it is possible to solve (1) using a series expansion technique; we represent $x(s)$ and $b(s)$ by their Taylor series, and then use (2) to determine the coefficients of the series for $x(s)$. For a direct-method equation solver, it is possible to show that only a *single* computation-intensive *LU* factorization is required to determine all of the series coefficients, as opposed to one per frequency point in the conventional approach. This is the core idea behind the asymptotic waveform evaluation (AWE) technique[3].

Once the Taylor series' coefficients have been found, it is possible to derive a low-order model for the response using Padé approximation techniques[8]. A Padé approximation represents the desired response $f(s)$ as a rational function:

$$f(s) \cong \frac{\beta_0 + \beta_1 s + \beta_2 s^2 + \ldots + \beta_q s^q}{\alpha_0 + \alpha_1 s + \alpha_2 s^2 + \ldots + \alpha_q s^q} \tag{3}$$

An approximation accurate over a broad frequency band can often be determined with just 10-20 terms of the Taylor series expansion. Once we have a formula such as (3), characterized in terms of just a few parameters α and β, it is a simple matter to evaluate the frequency response by substituting a particular value of s.

A more numerically stable procedure than AWE is the Padé-via-Lanczos, or PVL procedure[9]. With either AWE or PVL, the fast sweep procedure may easily be 10-1000 times faster than the conventional "discrete" frequency sweep technique. The amount of speed-up depends upon the desired number of frequency points.

In the more general case of lossy problems, a splitting such as (2) is still possible, but unfortunately the matrices A_0 and A_2 depend upon frequency. The Padé approximation can still be computed in the vicinity of a particular frequency point, but the band of validity is more limited. In this case, it is necessary to use a few (perhaps 5) frequency expansion points and to merge the results using an adaptive procedure such as the ALPS algorithm[4].

To summarize, various computationally efficient procedures exist to compute rational function models such as (3) which are valid in a piece-wise fashion over different sections of the frequency band of interest. When taken together, these models will cover the entire band and permit the rapid evaluation of the frequency response at any point within the band.

3   Reduced Order Modeling

Given a frequency response $f(s)$, it is desirable to create a single rational function model valid over the *entire* frequency band of interest. If this can be achieved, then it is a simple matter to determine the time domain response of the system. The first step is to determine the q poles of the rational function, and then represent the frequency response in pole-residue form as

$$k_\infty + \frac{k_1}{s - p_1} + \frac{k_2}{s - p_2} + \ldots + \frac{k_q}{s - p_q}. \tag{4}$$

It is then trivial to carry out the inverse Laplace transform of the function to find the time response. In order to compute a model such as (4), we use a procedure based upon rational function interpolation, pole pruning and least squares fitting. The initial "unconstrained" rational function interpolation procedure[10] is carried out in order to find a model that passes through the computed data at a set of equally spaced points along the line $s = j\omega$. To choose the interpolant's order, we start with a small number of interpolation points and then increase the number of points until an acceptably accurate fit is achieved between the interpolation points.

The unconstrained interpolation procedure may produce nonphysical, unstable right half-plane poles. In the pole pruning stage, these poles are eliminated from the model. This makes the model stable, but introduces additional approximation errors. To minimize these errors, a final least squares fitting procedure is used to adjust the residues $\{k_i\}$ of the remaining poles. Typically, we find that a maximum error of about 1% is achievable with 5-30 poles.

4   Modeling Electromagnetic Structures in a Circuit Simulator

In order to carry out simulation of complete digital or microwave circuits, it is desirable to include both

the electromagnetic effects of interconnects as well as the nonlinear effects of transistors and diodes. Thus, we wish to incorporate the reduced-order models we derive within circuit simulation packages such as SPICE and Spectre. The main challenge in doing this is translating between the scattering parameter models of high-frequency electromagnetics and the circuit models of SPICE. The problem is illustrated in Figure 1.
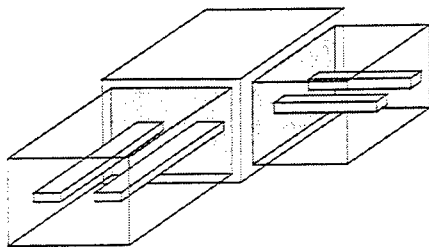
Figure 1.   Three-dimensional "black box" fed by two triaxial cables.
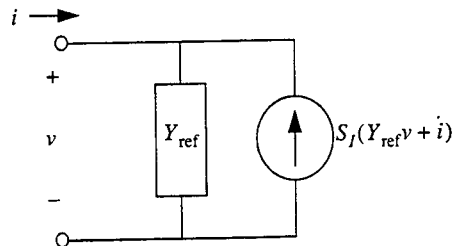
Figure 2.   A circuit interpretation of the current scattering relationship in (8).

This figure depicts a three-dimensional structure (contained inside a "black box") which we wish to characterize via electromagnetic analysis. The structure has two "feeds," each consisting of a pair of wires within a shield. Each feed will support two quasi-TEM modes of propagation, as well as higher-order modes. Microwave circuit theory conventionally defines each mode as a "port" into the structure; scattering parameter matrices represent the relationship between the incident and reflected powers of these modes. In order to communicate with a circuit simulator, we must develop a relationship between the modal fields and certain "voltage" and "current" signals. In circuit theory, the voltages are typically defined as potential differences between each signal conductor and a "ground" conductor.

Formally, a voltage v_m is the integral of the transverse electric field $\vec{E}_t$ over an open path C_m.

$$v_m = -\int_{C_m} \vec{E}_t(x, y) \cdot \vec{dl}. \tag{5}$$

If the transverse electric field can be represented in terms of incident and reflected modes, with intensities a_n and b_n, respectively, then we have

$$\vec{E}_t = \sum_n a_n \vec{e}_n(x, y) + \sum_n b_n \vec{e}_n(x, y)$$

Therefore, in terms of modal intensities, the voltage v_m becomes

$$v_m = \sum_n a_n t_{mn} + \sum_n b_n t_{mn}$$

where $t_{mn} = -\int_{C_m} \vec{e}_n(x, y) \cdot \vec{dl}$ is an integral of the modal electric field.

Collecting all of the voltages and wave intensities together as vectors, the relationship becomes

$$v = T(a + b) \tag{6}$$

where $T = [t_{mn}]$ is a square matrix (4x4 for Figure 1) defining the transformation from mode intensities to port voltages. We need another such transformation to compute the port currents; this can be derived from (6) by enforcing energy conservation between the circuit and electromagnetic models. Then it is possible to derive a "pseudo-scattering" matrix S_p relating incident and reflected pseudo-waves. We define the pseudo-wave intensities in terms of circuit quantities:

$$a_p = \frac{1}{2}(Z_{\text{ref}}^{-1/2}v + Z_{\text{ref}}^{1/2}i)$$
$$b_p = \frac{1}{2}(Z_{\text{ref}}^{-1/2}v - Z_{\text{ref}}^{1/2}i) \tag{7}$$

Then we have a simple relationship: $b_p = S_p a_p$.

5   Implementation of Reduced Order Models in a Circuit Simulator

Using (7), we can rewrite the relationship $b_p = S_p a_p$ in terms of voltages and currents:

$$Y_{\text{ref}}v - i = S_I(Y_{\text{ref}}v + i) \text{ where } S_I = Z_{\text{ref}}^{-1/2}S_p Z_{\text{ref}}^{1/2}. \tag{8}$$

We introduce $Y_{\text{ref}} = Z_{\text{ref}}^{-1}$ as well as the *current-scattering matrix* S_I. The advantage of (8) is that it lends itself to direct implementation in a circuit simulator. An equivalent circuit model for this relationship is shown in Figure 2. The overall procedure for producing the equivalent circuit is now summarized:

1. Run an electromagnetic analysis on the structure of interest, using fast-sweep methods to find the modal scattering parameter matrix S over a broad frequency band.

2. Determine the transformation matrix T from the modal field patterns at the ports.

3. Compute the pseudo-scattering matrix S_p and then convert it into a current-scattering matrix S_I.

4. Perform reduced-order modeling on the entries of the current-scattering matrix.

5. Write out the reduced-order models as frequency-dependent controlled sources in the form of a circuit deck for SPICE or Spectre.

6 Examples

The first example is a low-pass filter (Figure 3a). This was analyzed using Strata™, a full-wave boundary element code with ALPS-based fast frequency sweep. The computed scattering parameters were modeled with rational functions of 16-18 poles. A comparison of the sweep results with the reduced-
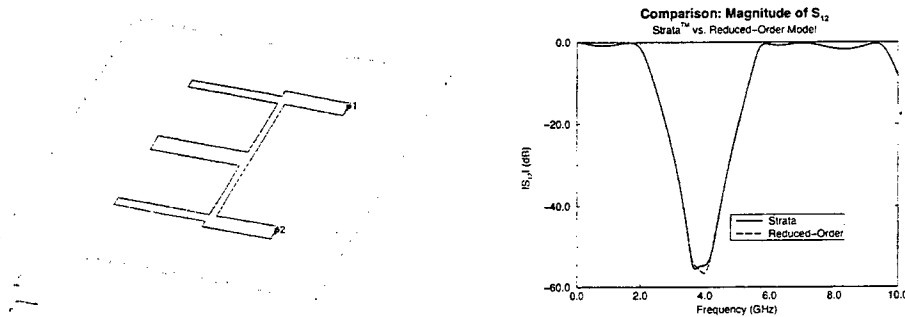
Figure 3. (a) Chebyshev 3rd-order low-pass filter structure; and (b) comparison of Strata's frequency response (computed by fast sweep) and the reduced-order model.

order model is shown in Figure 3(b).

A 2-port equivalent circuit model for the structure was then generated; this was connected to a nonlinear MOS inverter driver. The transmitted and reflected pulses from a transient simulation are shown below in Figure 4.
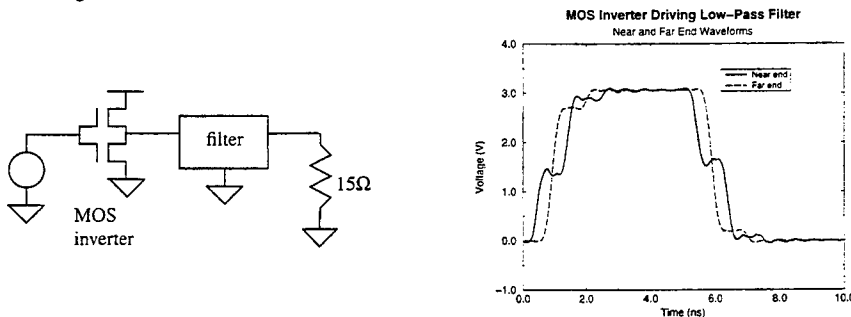
Figure 4. Transient simulation results from HSPICE analysis of the combined MOS driver and reduced order model.

The second example (Figure 5a) is taken from printed circuit board design. It consists of two symmetrical wires used in a differential signalling scheme; the wires make a 90° bend, which includes a transition from an x-routing layer to a y-layer through a pair of vias. There are ground planes above and below the structure. We wish to investigate the crosstalk between the undesired common mode (even mode) of propagation and the signal-carrying differential mode (odd mode). The structure was analyzed

in Ansoft HFSS using both a standard discrete frequency sweep and fast frequency sweep techniques; the modal S-parameters were converted into circuit-based parameters for even and odd modes and then
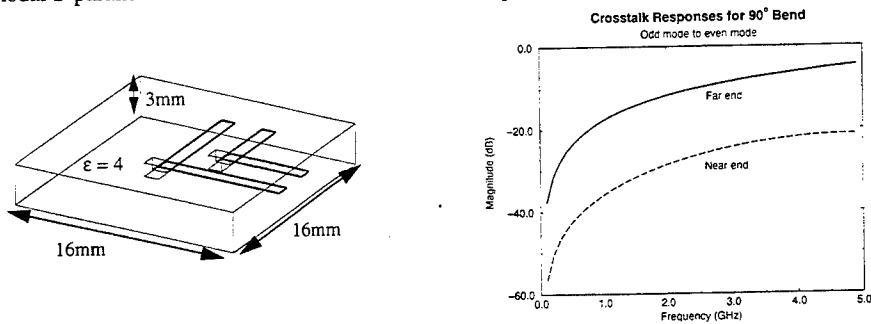
Figure 5.   (a) 3-d printed circuit board structure including vias and 90-degree bend; and (b) the simulated far-end crosstalk response between odd and even modes.

fitted by reduced order models. The point-by-point frequency sweep (100 points) took 2.5 hours of CPU time on a DEC Alpha 3000/800 workstation, while the fast frequency sweep took less than 0.2 CPU-hours. Plots of the near and far end crosstalk magnitudes are shown as a function of frequency in Figure 5b. In addition, we have computed the time-domain crosstalk waveforms for the structure, assuming that input pulses with 0.1ns rise times drive the even and odd modes. Plots of these waveforms are given in Figure 6a. This information could be used to create "design rules" for the maximum number of right-angle bends allowed for a certain maximum crosstalk.
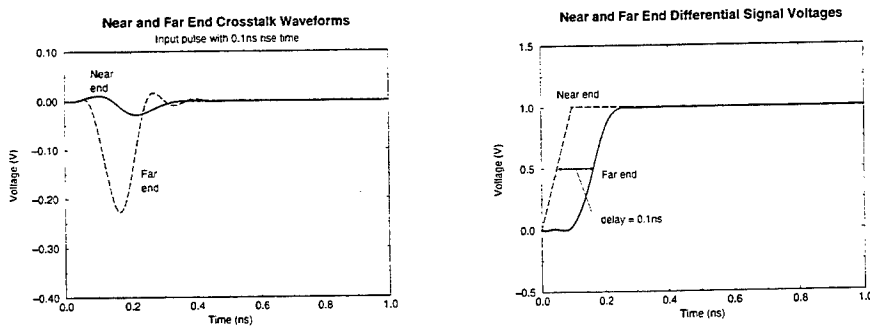
Figure 6.   (a) Time-domain crosstalk waveforms at the input (near) and output (far) ports; and (b) time-domain differential signal waveforms at the near and far ends.

Also shown (Figure 6b) are the signal waveforms at the near and far ends. Notice that the waveforms predict a delay of approximately 0.1ns from input to output. This is consistent with the relative dielectric constant ($\varepsilon = 4$, leading to a velocity of 1.5×10^8 m/s) and the total distance travelled (about 16mm.)

178

7 Conclusions

Fast frequency sweep methods provide a powerful tool for characterizing the electromagnetic behavior of structures that are intended to operate over a broad frequency band, or whose time-domain characteristics are important. Reduced-order models can be generated with a low additional cost. These models are very useful for circuit simulation, which can be used to explore the time-domain behavior of a system that includes both electromagnetic structures and nonlinear device models. We have presented several examples to demonstrate the usefulness of this technique.

8 Bibliography

[1]   A. Taflove, *Computational Electrodynamics: The Finite-Difference Time-Domain Method*. Boston: Artech House, 1995.

[2]   L. T. Pillage and R. A. Rohrer, "Asymptotic waveform evaluation for timing analysis," *IEEE Trans. on CAD*, vol. 9, no. 4, pp. 352-366, April 1990.

[3]   V. Raghavan, R. A. Rohrer, L. T. Pillage, J. Y. Lee, J. E. Bracken and M. M. Alaybeyi, "AWE-Inspired," *Proc. IEEE Custom IC Conf.*, pp. 18.1.1-18.1.8, May 1993.

[4]   D.-K. Sun, "ALPS—an adaptive Lanczos-Padé approximation for the spectral solution of mixed-potential integral equations," *USNC/URSI Radio Sci. Mtg. Digest*, p. 30, July 1996.

[5]   L. W. Nagel, "SPICE2: A computer program to simulate semiconductor circuits," UC Berkeley Electronics Research Labs memo. no. UCB/ERL M520, May 1975.

[6]   T. L. Quarles, "Analysis of performance and convergence issues for circuit simulation," UC Berkeley Electronics Research Labs memo. no. UCB/ERL M89/42, April 1989.

[7]   Cadence Design Systems, Inc. *Spectre Reference Manual*, March 1994.

[8]   G. A. Baker, Jr. *Essentials of Padé Approximants*, Academic Press, 1975.

[9]   P. Feldmann and R. W. Freund, "Efficient linear circuit analysis by Padé approximation via the Lanczos process," *IEEE Trans. on CAD*, vol. 14, no. 5, pp. 639-649, May 1995.

[10]   C. Hwang and Y.-C. Lee, "Multifrequency Padé approximation via Jordan continued-fraction expansion," *IEEE Trans. Automatic Control*, vol. 34, no. 4, pp. 444-446, April 1989.

COMPUTER
SIMULATION
OF ANTENNAS

Chairs:B. Tomasic and R. Haupt

APPLICATION OF COMPUTATIONAL ELECTROMAGNETICS TO SHIPBOARD HFDF SYSTEM SIMULATION

Jeffrey B. Knorr
Department of Electrical and Computer Engineering
Naval Postgraduate School
Monterey, California 93943-5121

Abstract

This paper describes a computer simulation of a shipboard high frequency direction finding system which was developed to study the effect of ship topside reconfiguration on DF system accuracy. Numerical models of DD963 Spruance Class destroyers in two different configurations were developed. The numerical models were then calibrated by computing the responses of the DF antennas as a function of azimuth. The numerical calibration data were used to study the effect of topside changes on the performance of the direction finding system. Numerical results were validated using experimental calibration data. The overall objective of the investigation was to determine the feasibility of using a computer simulation as a ship recalibration decision support system.

I. Introduction

A computer simulation of a shipboard correlation interferometry direction finding (CIDF) system for the high frequency (HF) band has been developed as shown in Figure 1. The simulation utilizes a module which implements the CIDF algorithm [1] and will correlate DF antenna responses for a signal of interest (SOI) with calibration data to derive an estimate of the angle of arrival of the SOI. As illustrated in Figure 1, this can be accomplished using data obtained from numerical ship models, scale ship models, or real ships. The use of numerical models to compute DF antenna responses as well as the comparison of numerical data with data from measurements on scale models was presented previously [2], [3]. It was shown that numerical and experimental DF antenna responses were in good agreement at 1.85, 6.34, and 9.25 MHz.

Two configurations of the DD963 were investigated; one in which the ship was configured with an anti-submarine rocket (ASROC) launcher as shown in Figure 2a, and one in which the ASROC launcher was removed and replaced with a vertical launch system (VLS) as shown in Figure 2b. The VLS has a much lower profile than the ASROC launcher and it can be anticipated that the difference in coupling to the DF antennas will affect their responses, and therefore the performance of the DF system. Experimental data for validation of numerical results was obtained

using the 1/48th scale brass model ship shown in Figure 3.

Recently, DF antenna responses were computed at a fourth frequency, 20.075 MHz. Also, both numerical and experimental data for the VLS configuration of the DD963 were cross-correlated with data for the ASROC configuration and bearing error was computed at all four frequencies. This cross-correlation simulated the effect of calibrating the ship in the ASROC configuration, and then using the calibration data to estimate arrival angles for signals received in the VLS configuration. The primary purpose of this paper is to present these correlation and bearing error results.

II. DF Antenna Responses

DF antenna responses for 1.85, 6.34, and 9.25 MHz were previously reported [2]. Numerical and experimental data for these frequencies were in good agreement, although results for 9.25 MHz were not as satisfying as those at 1.85 and 6.34 MHz. Figure 4a shows the numerical patterns for DF antennas P-3 and S-3 at 20.075 MHz. These antennas are mounted on the deckhouse and angled about 20 degrees to port and starboard, respectively. Figure 4b shows the experimental patterns for these same antennas. The experimental patterns were obtained using the 1/48th scale brass model of the ship which is shown in Figure 3. Both the numerical and experimental patterns show these antennas have maximum response about 40 degrees off the bow (bow is 0 degrees). The experimental results, however, show a much lower response in the opposite direction than predicted numerically. It should be noted that experimentally, azimuth is plotted clockwise from the bow according to nautical convention (Figure 4b) while numerically, azimuth is plotted counter-clockwise from the bow according to mathematical convention (Figure 4a).

Numerical and experimental results for antennas P-12 and S-12 are shown in Figures 5a and 5b, respectively. These antennas are mounted on the stern of the ship, looking aft. Figure 5b shows that experimentally, the maximum response is aft, as would be expected at 20.075 MHz. Response in the bow sector is down 10-30 dB. Figure 5a shows the numerical patterns are in poor agreement.

Computations of DF antenna response at 20.075 MHz using the existing numerical models have not yielded satisfactory results. The existing models have several openings in the side of the hull, between the deck and the waterline, which are on the order of 1 wavelength in width and 1/2 wavelength in height at 20 MHz. Also, the space inside the hull (excluding bow) is about 1/2 x 1 wavelength at 20 MHz and is therefore capable of supporting waveguide modes. It appears that the openings in the hull permit incident plane waves to excite fields inside the hull, and that these fields corrupt the DF antenna responses at the higher frequencies. Current plans are to upgrade the numerical models.

III. Correlation and Bearing Error

DF antenna responses for the VLS configuration were cross-correlated with the DF antenna responses for the ASROC configuration to determine the error in bearing estimate caused by the change in configuration. Figures 6a and 6b show the cross-correlation surfaces obtained using 1.85 MHz numerical and experimental data, respectively. In these figures, the vertical axis gives the magnitude of the complex correlation coefficient (0-1). The axis receeding into the figure gives the angle of arrival (0-360, or bow-stern-bow) for the signal of interest received in the VLS configuration. The remaining axis gives the difference (-180 - +180) between the angle of arrival of the SOI and the arrival angle of the signal from the database for the ASROC configuration. It can be seen that the numerical and experimental surfaces are very nearly the same. Both show a well defined central ridge and low sidelobes, indicating that bearing estimates should be reasonably accurate.

A cut through the cross correlation surface gives the cross-correlation curve for a specific angle of arrival. This curve gives the response of the DF array, and when plotted in a polar format, looks much like an antenna pattern. Figures 7a and 7b show such a plot for 1.85 MHz signal with an arrival angle of 232 degrees, as indicated by the cursor. The numerical and experimental results are in good agreement.

Lastly, Figures 8a and 8b show the bearing error (bearing estimate - actual bearing) as a function of azimuth at 1.85 MHz. Again, numerical and experimental results are in reasonable agreement.

Another measure of DF system performance is RMS bearing error (root mean squared bearing error averaged over all azimuths) at a given frequency. Table 1 shows the numerical and experimental RMS bearing error predicted by the simulation at all four frequencies investigated. It is interesting that this integrated performance measure show good agreement between numerical and experimental data even though the agreement between the numerical and experimental DF antenna responses deteriorates with increasing frequency.

Table 1. RMS Bearing Error
Predicted by Simulation

Frequency (MHz)	1.85	6.34	9.25	20.075
Numerical Bearing Error in Degrees	1.11	0.86	2.80	7.38
Exp'tal Bearing Error in Degrees	1.20	0.39	1.51	6.20

IV. Conclusions

Comparison of results predicted by this simulation using numerical and experimental data show that DF antenna responses (amplitude and phase) are in good agreement at the low end of the HF band but do not agree well at the high end of the band. The same statement is true for cross-correlation and bearing error curves. Numerical and experimental values of RMS bearing error agree quite well at all four frequencies investigated, however. It is believed that the degradataion of numerical results, particularly above 10 MHz, is due to the fact that the numerical models do not meet modeling guidelines at the higher frequencies. It is anticipated that additional work on the numerical models would correct this problem.

This simulation, in which computational electromagnetics plays a key role, has yielded results which show that such an approach could eventually be used to construct a ship recalibration decision support system. It has also highlighted areas which require additional work if such a simulation were to be cost effective and used routinely. These include (1) generation of numerical models from ship CAD files, (2) parallelization of CEM codes to decrease computation time, (3) comparison of the performance of CEM codes (NEC and PATCH, for example), (4) development of CEM code pre/post processors with capabilities which simplify editing, visualization and display of results for large files.

Acknowledgements

References

[1] N. Saucier and K. Struckman, "Direction finding using correlation techniques", *Proc. IEEE International Symposium on Antennas and Propagation*, pp. 260-263, June 1975.

[2] J. B. Knorr, "A numerical and experimental investigation of a shipboard DF antenna array", *12th Annual Review of Progress in Applied Compuataional Electromagnetics*, pp. 792-801, Monterey, CA, March 18-22, 1996.

[3] J. B. Knorr and D. C. Jenn, "A numerical and experimental investigation of a semi-loop antenna on a metal box", *12th Annual Review of Progress in Applied Computational Electromagnetics*, pp. 832-841, Monterey, CA, March 18-22, 1996.
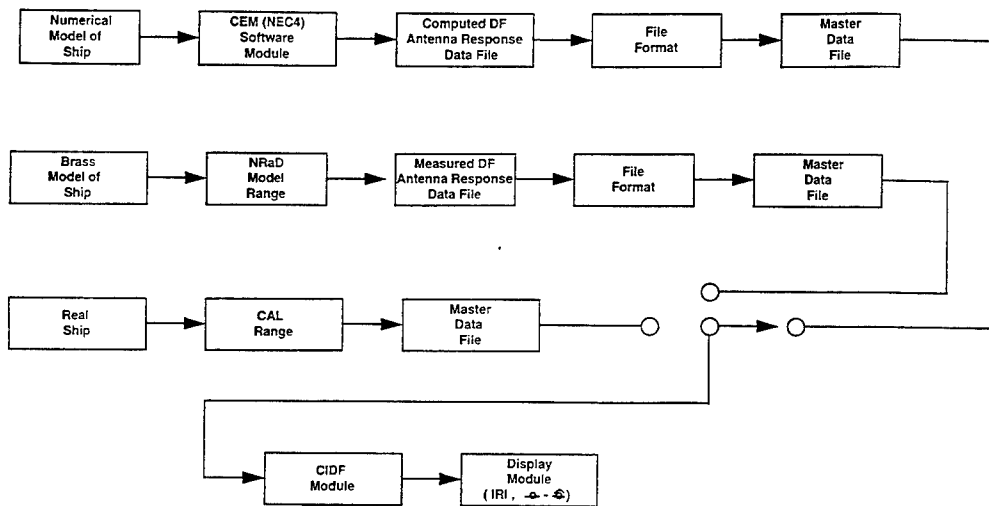
Figure 1. Block diagram for computer simulation of shipboard correlation interferometery direction finding (CIDF) system.
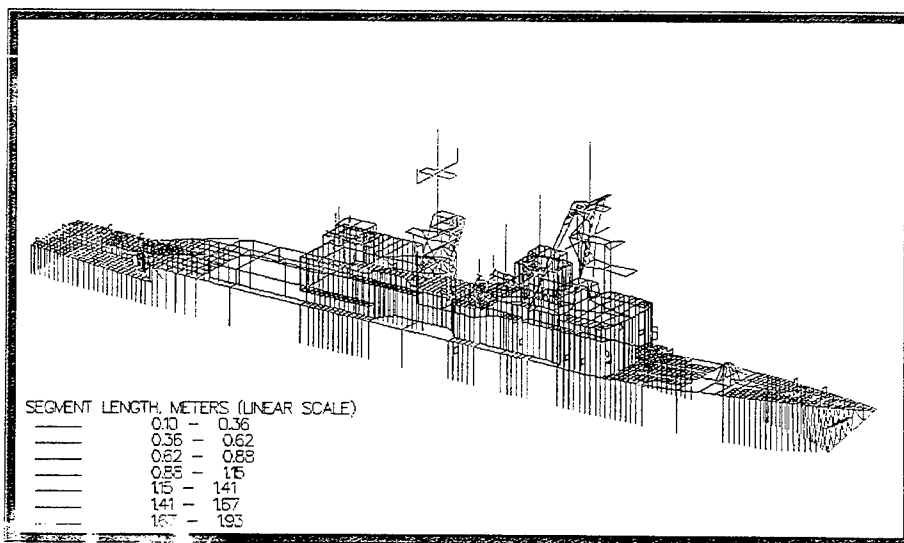
Figure 2a. Visualization of numerical model of DD963 Spruance Class destroyer with ASROC launcher located forward from the deckhouse.
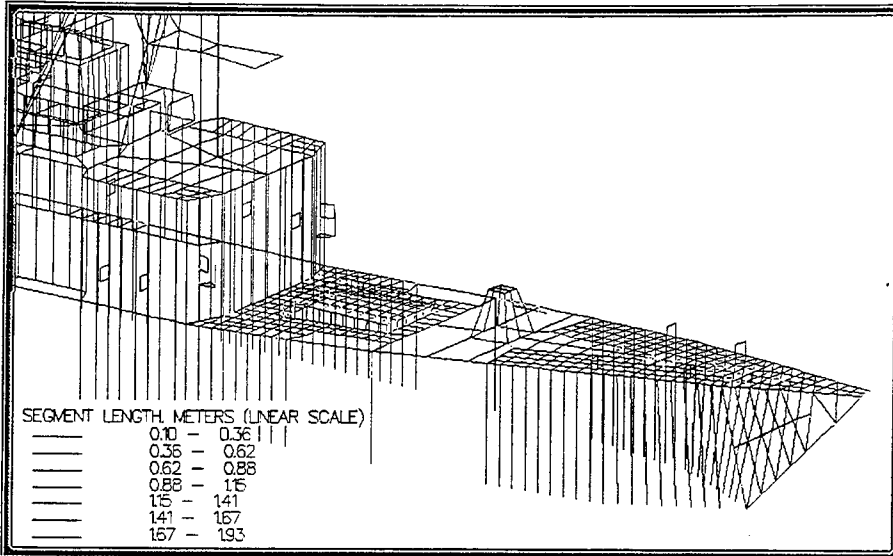
Figure 2b. Visualization of bow area of DD963 Spruance Class destroyer configured with vertical launch system (VLS). DF loop antenna pairs P-1, S-1, through P-5, S-5 (fore-aft) can be seen.
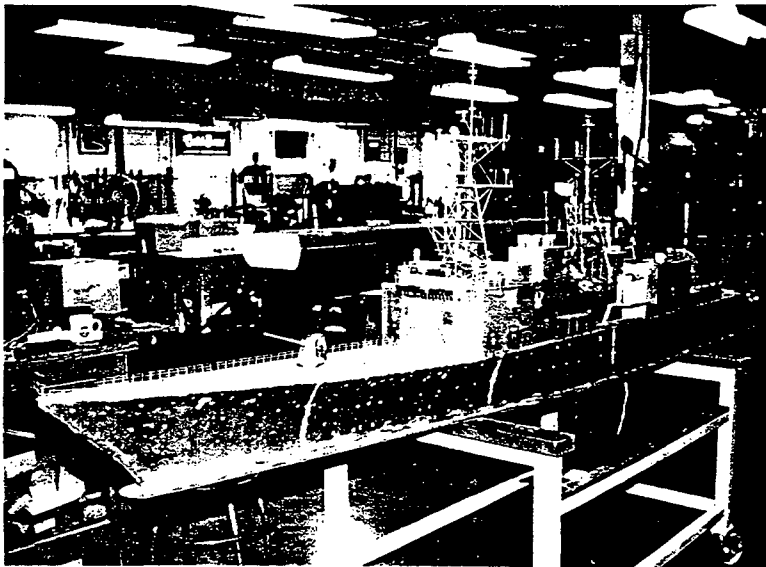
Figure 3. Photograph of brass model of DD963 Spruance Class destroyer, VLS configuration. Scale is 1/48th.
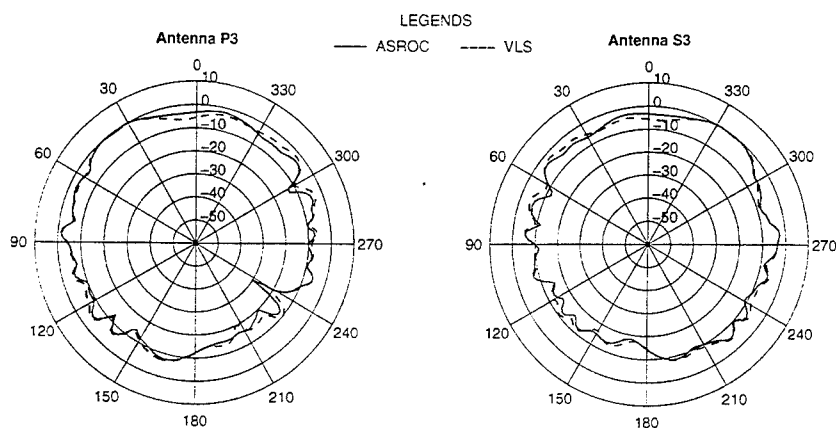
Antenna P3   —— ASROC   ---- VLS   **Antenna S3**

Figure 4a.   Numerical patterns for antennas P-3 and S-3 for ASROC and
VLS configurations of DD963.   Elevation angle is 5 degrees, frequency
is 20.075 MHz.

LEGENDS

Antenna P3   —— ASROC   ---- VLS   **Antenna S3**
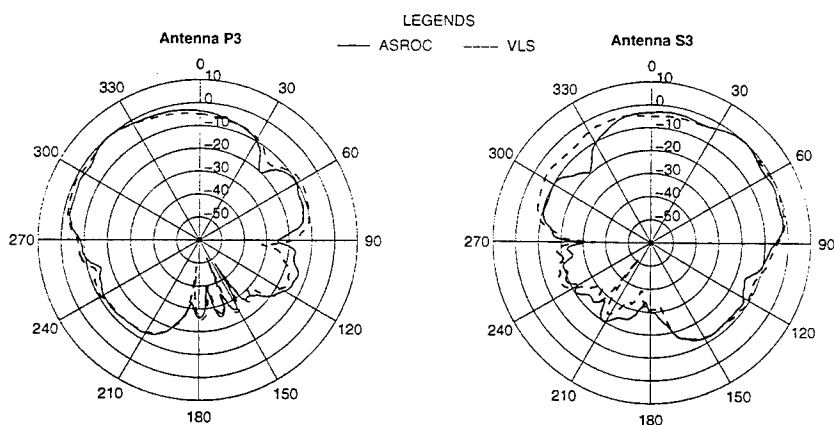
Figure 4b.   Experimental patterns for antennas P-3 and S-3 for ASROC
and VLS configurations of DD963.   Elevation angle is 5 degrees, scaled
frequency is 20.075 MHz.
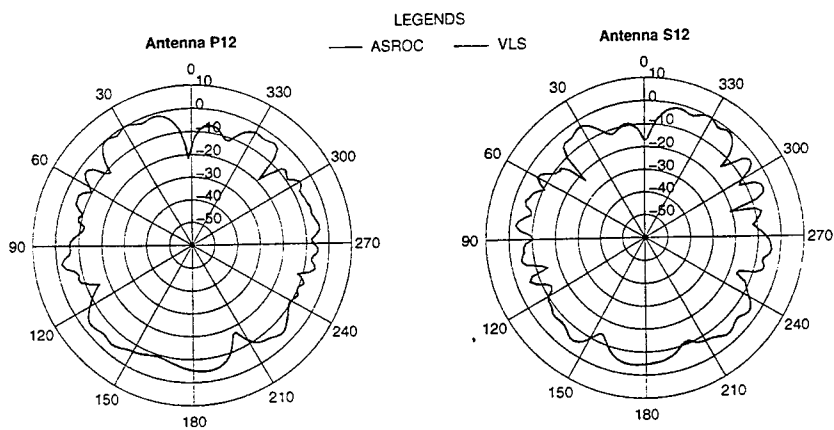
Figure 5a. Numerical patterns for antennas P-12 and S-12 for ASROC and VLS configurations of DD963. Elevation angle is 5 degrees, frequency is 20.075 MHz.
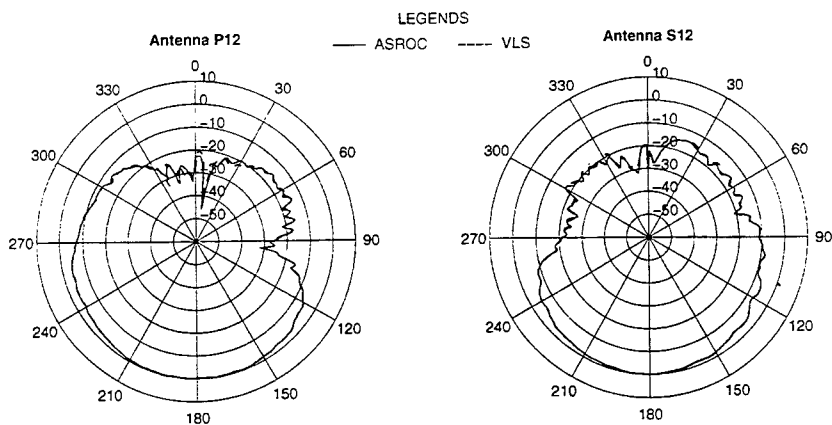
Figure 5b. Experimental patterns for antennas P-12 and S-12 for ASROC and VLS configurations of DD963. Elevation angle is 5 degrees, scaled frequency is 20.075 MHz.
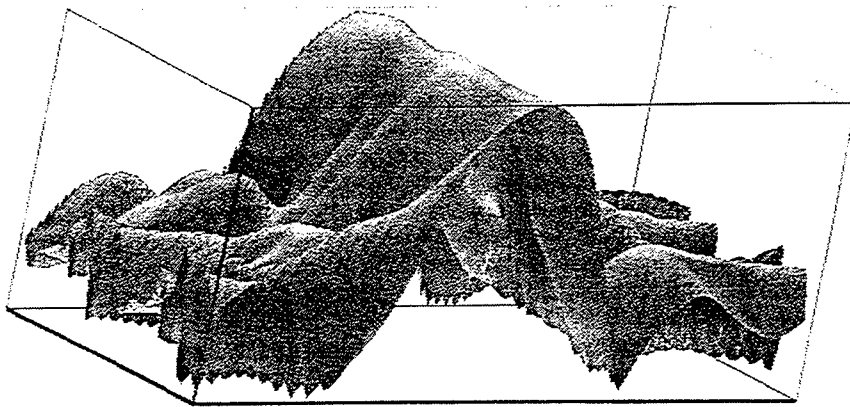
Figure 6a.   Numerical   cross-correlation   surface,   VLS   vs.   ASROC
configuration of DD963.   Frequency is 1.85 MHz.
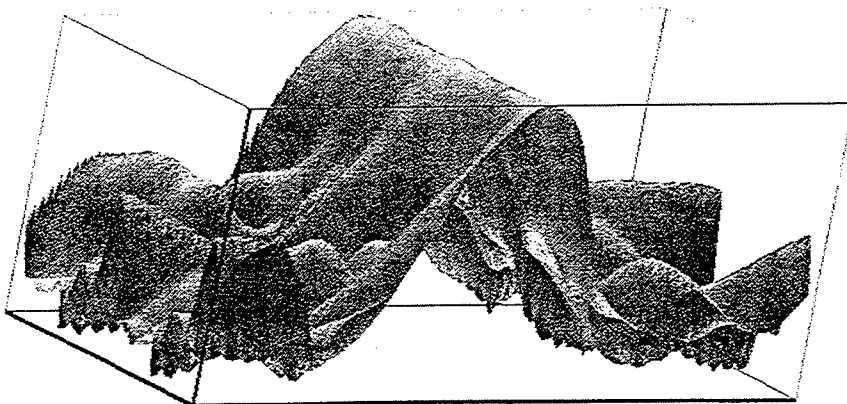
Figure 6b.   Experimental cross-correlation surface, VLS vs. ASROC
configuration of DD963.   Frequency is 1.85 MHz.
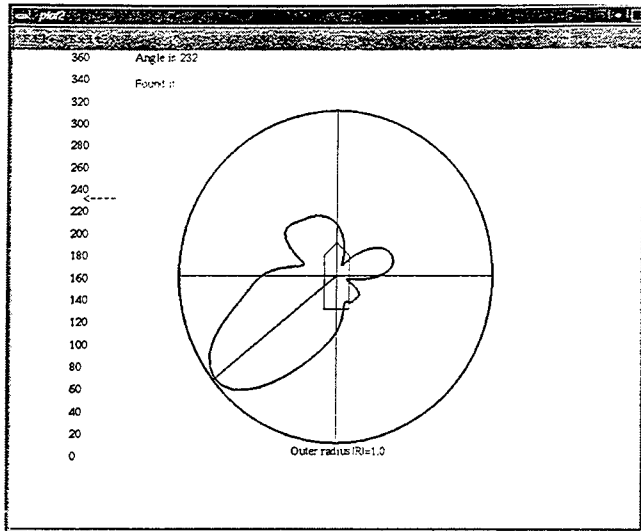
Figure 7a. Numerical curve of correlation vs. azimuth, VLS vs. ASROC configuration of DD963. Signal arrival angle is 232 degrees, signal frequency is 1.85 MHz.
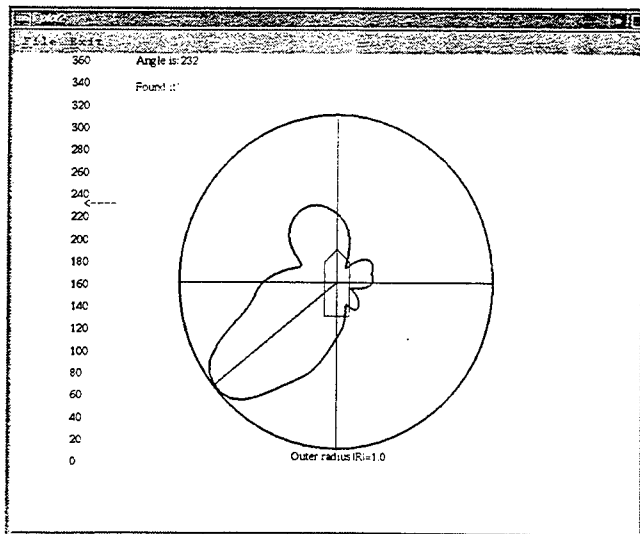
Figure 7b. Experimental curve of correlation vs. azimuth, VLS vs. ASROC configuration of DD963. Signal arrival angle is 232 degrees, signal frequency is 1.85 MHz.
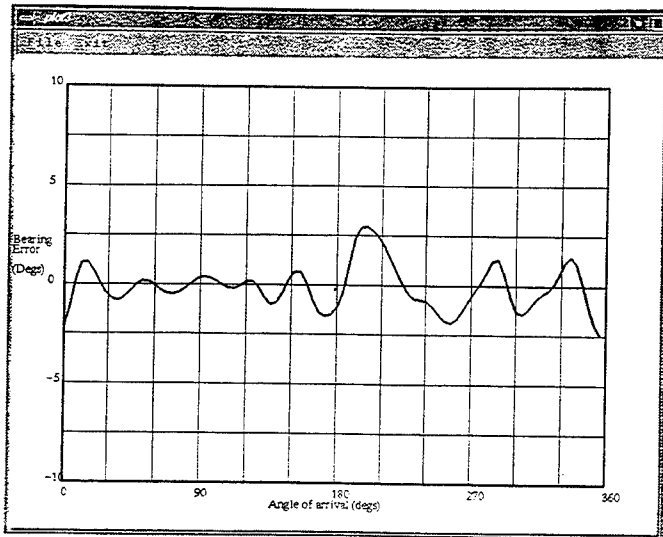
Figure 8a. Numerical curve of bearing error vs. azimuth, VLS vs. ASROC configuration of DD963. Frequency is 1.85 MHz.
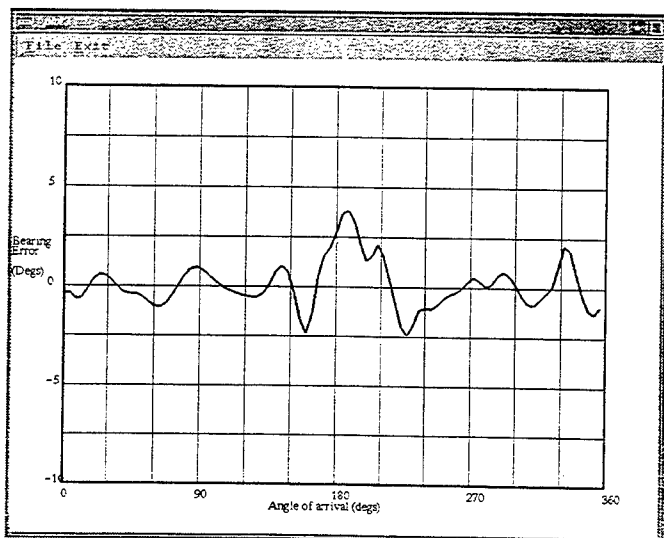
Figure 8b. Experimental curve of bearing error vs. azimuth, VLS vs. ASROC configuration of DD963. Frequency is 1.85 MHz.

Calculation of the near fields of a large complex antenna structure and comparison with *in situ*
measurements.*

C. Selcher[1], E. Kennedy[1], and P. Elliot[2]

[1] Code 5550
Naval Research Laboratory
Washington, D. C., 20375

[2] Raytheon, Inc.
M/S T1SS13
P.O. Box 1201
Tewkesbury, MA 01876

Abstract

*The near electric and magnetic fields of the High Frequency Active Auroral Research Program
(HAARP) Developmental Prototype (DP) were calculated using the Numerical Electromagnetics Code
(NEC4). The DP, at its present stage of development, consists of 18 active antenna elements arranged
into a three by six array. Each element is composed of both a high band and a low band crossed
dipole. The entire currently active array was modeled, including both the high and low band dipoles, the
towers used to support the antenna structure, a gridded aluminum ground screen located below the
dipoles and raised fifteen feet above the earth, as well as the effects of an imperfectly conducting earth.
Segmentation model analysis on the ground screen component will be described, the results of which
indicated that the use of a ground screen consisting of a larger cell size than the actual screen
introduced only small errors into the calculation and led to a significant reduction in the number of
segments included in the model. This permitted the modeling of this large complex structure using
fewer than 7000 segments. Features of the calculated near fields, including those introduced by
modeling the full three by six array in place of a previous model which consisted of a two by two array,
will be reviewed and will be compared to electric field values measured at several locations at the
HAARP site. Preliminary measurements at the site have indicated good agreement with NEC4
computations. The calculated and measured RMS near fields, scaled to the maximum transmitter
power, are shown to satisfy the IEEE safety standards for maximum permissible exposure to RF
electromagnetic fields as specified in IEEE C 95.1-1991*

Introduction

A high performance scientific observatory is being constructed in Alaska under the High
Frequency Active Auroral Research Program (HAARP). The primary purpose of this facility is to study
and investigate the fundamental physical processes occurring within the earth's ionosphere. The HAARP
facility will consist of a high power radio frequency transmitter and antenna array, operating in the High
Frequency (HF) band, which will be used to perturb or heat a small, localized region of the ionosphere
above the HAARP facility. A diverse suite of sensitive monitoring instruments located at or near the site
will be used to observe ionospheric processes occurring either both natural conditions and when
influenced by the HAARP HF transmitter.

Based of research experience at other ionospheric research facilities, the HAARP HF transmitter
and antenna array has been designed to be capable of generating a power density of approximately 1 - 3
microwatts per square centimeter ($\mu W/cm^2$) in the ionospheric layers above the site. This power density
will be obtained through a combination of transmitter power and antenna gain producing an effective
radiated power (ERP) ranging from about 86 dBW at 2.8 MHz to 95 dBW at 10 MHz. Rather than use
very high power sources and a small number of antennas, the adopted design approach distributes
transmitter power among 180 antennas constructed as a planar, phased array. This approach has several
advantages including (1) the ability to form a narrow beam that can be tailored in shape and steered in
azimuth and elevation angle, (2) the ability to divide the array to produce independent beams, and (3)
reduced cost associated with using lower power radio frequency (RF) power components.

One of the major concerns for any high power transmitting facility is the generation of high electromagnetic (EM) field strengths in the vicinity of the antenna array. The HAARP antenna system architecture minimizes electromagnetic fields on the ground while achieving the scientific goals for ERP, through the use of a large array of relatively low power transmitters. Even though the aggregate power produced by the HAARP array is large, at any given point on the ground near the antenna array, the net electric (or magnetic) field is dominated only by the closest antenna elements.

At its current phase of completion, the Developmental Prototype (DP) HAARP antenna array consists of 48 antenna elements arranged as eight rows by six columns. Transmitters are connected to a smaller portion of this array consisting of six rows by three columns for a total of 18 active elements. The purpose of the DP is to validate the engineering design of the array at a scale that is both realistic from a performance perspective while small enough that changes can be made to the design at relatively low cost.

This report describes studies that have been completed using the Numerical Electromagnetic Code (NEC) [LLNL, 1992] to predict the electromagnetic fields around and under the HAARP DP antenna array. The crossed dipole antenna elements employed in the HAARP array achieve a broad frequency response through a wire frame, polyhedral shape. Additional metallic elements in the array including supporting towers, a segmented ground screen and supporting piles has led to the development of a sophisticated numerical model.

The DP array represents the first opportunity to compare predicted array performance with measurements. The NEC predictions have been verified during recent testing periods at the site of the HAARP observatory in Alaska and results have not only confirmed the accuracy of the antenna model but have also shown that the array will be capable of meeting scientific research requirements while maintaining a safe level of field in the areas around the site.

NEC Modeling

Model Description

The NEC model used in most of the calculations described here consisted of eighteen crossed dipole elements radiating 10 kW each suspended thirty feet above a ground screen which was in turn located fifteen feet above an imperfect earth. The earth was modeled as a infinite half-space through the use of the Sommerfeld ground option included in NEC, using values of conductivity and permitivity measured in the Gulkana and Tok region. Since the interest in this study is in terms of worst-case conditions, wet earth values were used. The ground screen consisted of an interlocking series of horizontal wires, with an inter-wire spacing of 120 inches. Two sets of towers were also included in the model. The full height towers were centered on each dipole, with electrically shorted gaps to accommodate the sources, while stub towers were used on the perimeter of the ground screen. All towers were wired into the ground screen, and extend twenty feet below the surface of the earth. This model was excited by driving balanced currents on source segments for each element which were connected through a manifold to each dipole structure. This precluded any even mode currents on the full height towers. For this reason, and to conserve computer memory, the full height towers were not electrically connected to the dipoles. Any deviation from this baseline DP model will be noted. All calculations were performed on a Hughes Data Systems TAC-3 model 755 99 MHz computer capable of 40 MFLOPS with 448 Megabytes of RAM.

Segmentation Analysis

The DP model described above requires between 6400 and 6800 wire segments, depending on the frequency of interest. Well over one half of these segments are part of the ground screen and tower structure rather than the elements themselves. Previous models exhibited an even greater disparity between segments (and therefore computer memory and execution time) consumed in modeling the ground screen and those used to model the antenna structure. Because of this, it had previously only been possible to model a two-by-two version of the DP.

The two-by-two HAARP models used a spacing of forty inches between the ground screen wires. However, it was found that the field strengths under the screen were not very sensitive to variations of the ground screen spacing. The table below shows a comparison of the maximum and mean electric fields under the screen using four-element models with spacings of 40 and 120 inches, for cases of broadside excitation and 30 degree pointing angle.

Table 1

Case	40" Spacing		120" Spacing	
	Max	Mean	Max	Mean
Broadside	167.5	68.5	139.5	71.5
Scanned	227.3	60	220.2	62.6

It was determined that the small errors introduced by the increased screen spacing were acceptable, since enough segments were now free to allow the modeling of the entire DP at its current stage of development. This allowed for the study of array effects on the near field, such as the location and structure of field nulls.

Calculated Near Field Features

Using the baseline model, electric fields strengths were calculated in the near field region of the array, at frequencies spanning the HAARP transmission band. In all cases, the vertical electric field is the predominate field component that exists underneath the ground screen. This is due in part to the reduction of the horizontal field components by the ground screen and the earth. The vertical field is not reduced as strongly in this manner, and so dominates the total electric field.

Figures 1 and 2 are raster plots of the calculated total electric field strength in the region beneath the ground screen and surrounding the HAARP site. Two of the salient features which can be observed in the plot are the variation in the azimuthal gain due to array effects, and the fact that at no point does the field exceed the Maximum Permissible Exposures (MPE) levels discussed in the next section, and is in fact several orders of magnitude less than the MPE throughout the vast majority of the region.

Figures 3 and 4 are line plots of the calculated total electric field along a Bureau of Land Management (BLM) trail and the Tok cut-off highway which runs past the HAARP site. As expected, all electric field values are well below the MPE. The Tok cut-off highway plot is interesting in that it clearly demonstrates the transition from the near-field to the far-field.

Electromagnetic Safety Standards

One of the primary purposes of the modeling analysis is to be able to predict the electromagnetic fields not only in the main beam of the antenna pattern but also at points on the ground near the array to ensure that the HAARP facility can be operated in a safe manner. Two organizations have developed standards for safe levels of electromagnetic field and power density, C 95.1 -1991 [IEEE, 1992-1] developed by the Institute of Electrical and Electronic Engineers (IEEE) and the American National Standards Institute (ANSI) and Report No. 86 [NCRP, 1995], developed by the National Council on Radiation Protection and Measurements. In the frequency range where the HAARP array operates, both of these standards define the safe level of power density for public environments (where there is no attempt made to restrict access) as $P_d = 180/F^2$, where P_d is the power density in milliwatts per square centimeter (mw/cm^2) and F is the frequency in MHz.

The maximum safe level of P_d for the frequency range 2.8 - 10 MHz ranges from 22.9 mw/cm^2 to 1.8 mw/cm^2 respectively. Safe levels of electric and magnetic field are also defined in both standards and are derived from the level of power density under the assumption that the field can be described as a plane wave and that the electric and magnetic fields are related by the intrinsic impedance of free space.

Measurements Conducted on the HAARP antenna array

Beginning in December 1994, measurements have been made of fields around the HAARP array whenever transmitting tests were conducted. Early measurements identified the need for improvements to the antenna feed network (primarily the balun) and served as motivation for developing the current, comprehensive NEC model. Field strength levels observed during those measurements are no longer descriptive of the current array. Early predictions based on a simple model including only the antenna elements did not accurately describe the electromagnetic field strength that was observed. The predominate vertical electric field at all points away from the array indicates the existence of vertical currents within the antenna structure, and independent measurements have shown the existence of antenna currents on the supporting towers.

During November 1996, following completion of antenna modification work, measurements were again conducted of field strength at several points around the DP array. At each geographic point, measurements were conducted at three frequencies, 3.155 MHz, 5.95 MHz and 9.1 MHz. At each frequency, measurements were obtained for three beam pointing angles: $0°$ (straight up), $30°$ North and $30°$ South (along the major axis of the DP array).

For each of the frequency-pointing angle conditions, measurements were made using calibrated electric and magnetic field probes. The field strength receiver was calibrated prior to each measurement and the calibration source was checked at the end of the test against a standard signal generator. Electric field strengths were then calculated for each of the probes using calibration charts supplied with the instrument. The measured field strengths were then converted to *equivalent plane wave power density*, P_d [IEEE, 1992-2], using the relation $P_d = E_e \cdot E_m / 377$, where E_e and E_m are the electric field strengths measured using the electric and magnetic probes respectively.

Measurement results for each of the frequencies are shown in Table 2 for the case of antenna main beam pointed vertically. The table also shows predicted NEC field strengths for each of the geographic points and the ratio between the measured field strength and the NEC prediction. In addition, Table 2 shows the predicted power density at each of the geographic points and the ratio of the measured power density, P_d (as calculated above) and the NEC prediction.

With the a few exceptions, the agreement between measured and predicted field strengths is good. Measured power density is always well below the MPE at all geographic points studied. At geographic point 4, located at a distance of 16.8 km from the HAARP site, the field strength measured using the magnetic probe exhibited deep fading at both 3.155 MHz and 5.95 MHz, indicating either contamination of the measurement by a skywave component of nearly equal magnitude to the weak ground wave component, or multimode skywave fading without a ground wave. At this geographic point, the electric field probe exhibited no fading but was much weaker than the field measured with the magnetic field probe (this probe would have no response to a downward propagating skywave component).

Figure 4 is a plot of the field variation expected along the closest public access road to the HAARP site. The variation of field exhibits a minimum associated with the pattern null off the southeast corner of the array as shown in Figure 2. This pattern null, labeled point 1 in Table 2, was obtained experimentally by driving along the Tok highway to find a local minimum. Its position coincides geographically with the NEC prediction.

Measurements made at the Tok road entrance to the facility are much lower than predicted using NEC. We believe the inaccuracy at this point only, is due to the proximity of a large metallic building lying between the measurement position and the antenna array leading to either shadowing or destructive interference from scattered energy. Further numeric investigation is planned to evaluate this case.

Conclusions

The work described in this paper was motivated by the need to develop an accurate model of the HAARP antenna array that could be used to confirm that desired scientific performance would be obtained simultaneously with safe levels of electromagnetic field at all points along the ground in the vicinity of the facility. To realize a reasonably accurate model, it was found necessary to model all

metallic structures in the vicinity of the antenna. A tractable numerical model was achieved through a careful study of ground screen grid spacing and by using symmetry procedures in the NEC specification statements describing the complete structure.

Calculations of the field strength under the antenna (in the area described by Figure 1) indicate the power density will be close to but below the MPE for all operating frequencies. Spot measurements that have been made of field strengths under the array have confirmed this. The field strength measured at points near the array and in the near field are highly variable within a short distance but are in general agreement with NEC predictions and remain below the MPE for all points measured.

Measurements at considerable distance from the array along the Tok highway, taking into account possible skywave contamination or scattering components, are in good agreement with NEC predictions and show a field strength many orders of magnitude below the safe level of electromagnetic field as established by IEEE/ANSI C 95.1-1991.

References

LLNL (1992) Numerical Electromagnetics Code - NEC-4 Method of Moments, Gerald Burke, Lawrence Livermore National Laboratory Report #UCRL-MA-109338. Refer requests to Commander, US Army Information Systems Engineering Command, Attn: ASQB-OSE-TP, Fort Huachuca, AZ 85613-5300

IEEE (1992-1) IEEE Standard for Safety Levels with Respect to Human Exposure to Radio Frequency Electromagnetic Fields, 3 kHz to 300 GHz., Report No. C95.1-1991 (The Institute of Electrical and Electronic Engineers, Inc., New York).

IEEE (1992-2) IEEE Recommended Practice for the Measurement of Potentially Hazardous Electromagnetic Fields - RF and Microwave., Report No. C95.3-1991 (The Institute of Electrical and Electronic Engineers, Inc., New York).

NCRP (1995) Biological Effects and Exposure Criteria for Radiofrequency Electromagnetic Fields, Report No. 86. (National Council on Radiation Protection and Measurements. Bethesda, MD).

Figure 1: Near electric fields underneath ground screen at a height of 1.5 meters
Broadside o-mode excitation at 3.155 MHz with 360 kW radiated power

Diamonds indicate approximate source locations

Magnitude of Total Electric Field (V/m)
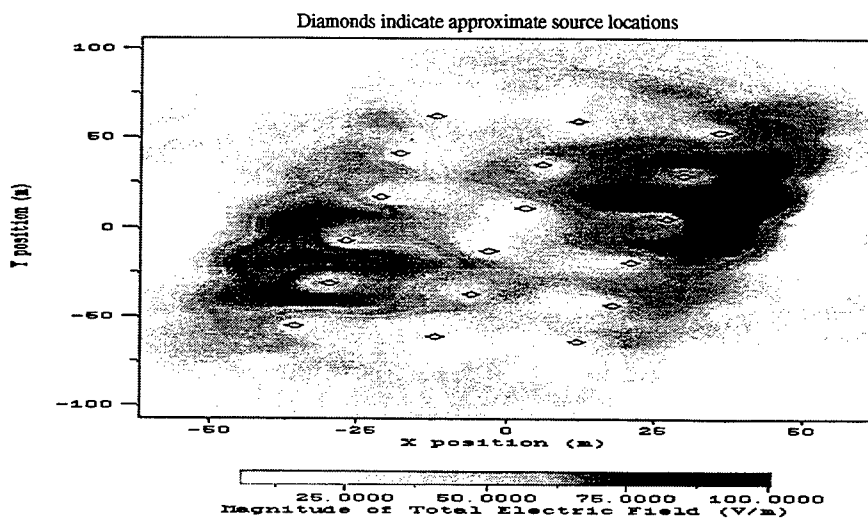
Figure 2: Near electric fields in vicinity of HAARP site at a height of 1.5 meters
Broadside o-mode excitation at 3.155 MHz with 360 kW radiated power

Magnitude of Total Electric Field (V/m)
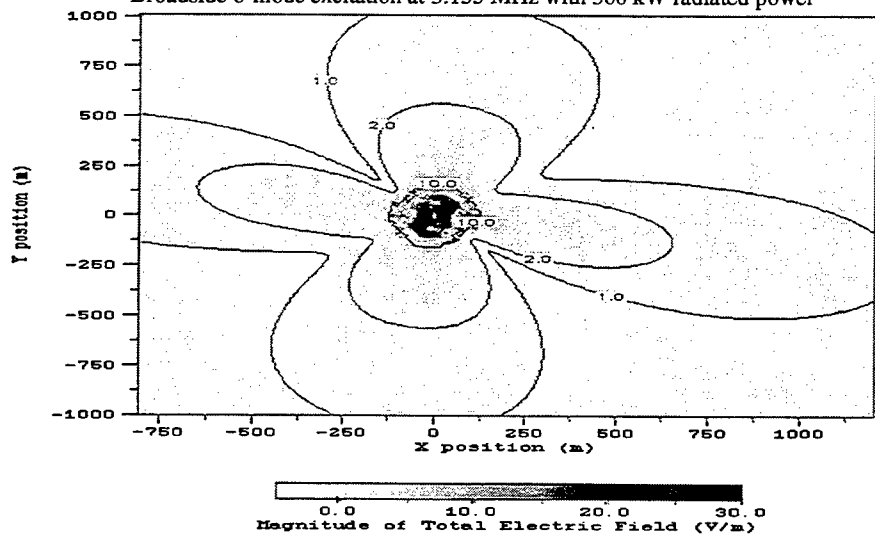
Figure 3: Near electric fields along BLM trail at a height of 1.5 meters
Broadside o-mode excitation at 3.155 MHz with 360 kW radiated power
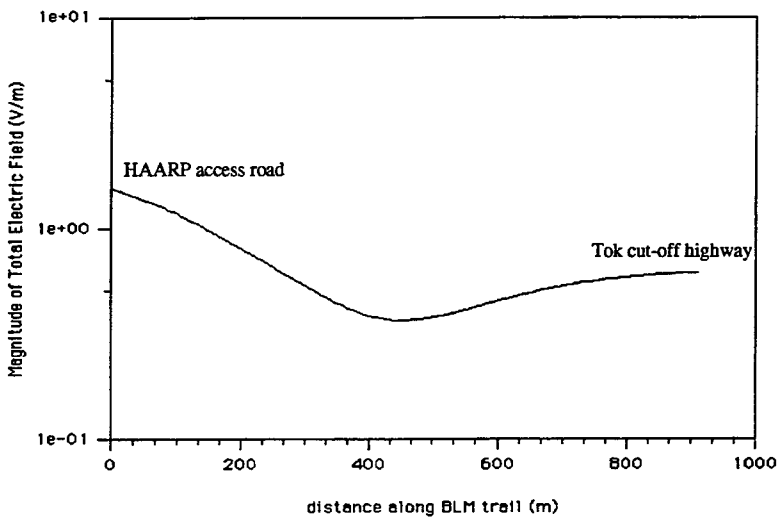
Figure 4: Near electric fields along Tok Cutoff Highway at a height of 1.5 meters
Broadside o-mode excitation at 3.155 MHz with 360 kW radiated power
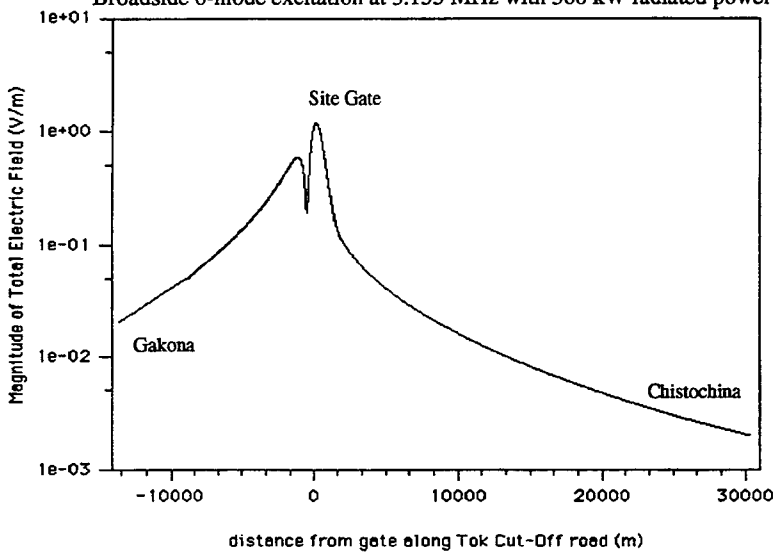
Table 2: Results of Field Measurements and Comparison to NEC Calculations
Broadside o-mode excitation with 360 kW radiated power

Site #	Frequency (MHz)	NEC E-field (V/m)	E Field Probe (V/m)	E Probe/NEC	H Field Probe (V/m)	H Probe/NEC	Calculated Power Density	Pd/MPE
1	3.155	0.362	1.540	4.25	0.776	2.14	3.17E-04	1.75E-05
2	3.155	0.113	0.389	3.45	0.245	2.18	2.53E-05	1.40E-06
3	3.155	0.024	0.031	1.27	0.025	1.01	2.01E-07	1.11E-08
4	3.155	0.001	0.001	0.77	0.011	8.46	2.92E-09	1.61E-10
5	3.155	0.027	0.976	35.63	0.616	22.48	1.60E-04	8.81E-06
6	3.155	0.035	0.069	1.99	0.044	1.26	7.99E-07	4.42E-08
7	3.155	0.698	0.062	0.09	0.035	0.05	5.65E-07	3.12E-08
1	5.95	0.362	0.489	1.35	0.245	0.68	3.18E-05	1.76E-06
2	5.95	0.113	0.017	0.15	0.069	0.61	3.19E-07	1.76E-08
3	5.95	0.024	0.022	0.90	0.016	0.64	9.00E-08	4.97E-09
4	5.95	0.001	0.001	0.62	0.001	0.54	1.49E-10	8.21E-12
5	5.95	0.027	0.976	35.63	0.616	22.48	1.60E-04	8.81E-06
6	5.95	0.035	0.006	0.18	0.004	0.11	6.41E-09	3.54E-10
7	5.95	0.698	0.005	0.01	0.003	0.00	3.64E-09	2.01E-10
1	9.1	0.134	0.174	1.29	0.069	0.51	3.18E-06	1.76E-07
2	9.1	0.029	0.020	0.66	0.025	0.83	1.27E-07	7.00E-09
3	9.1	0.007	0.014	1.94	0.008	1.10	2.86E-08	1.58E-09
4	9.1	0.000	0.000	0.33	0.000	0.33	2.65E-12	1.47E-13
5	9.1	0.004	0.549	144.47	0.346	91.16	5.04E-05	2.79E-06
6	9.1	0.016	0.007	0.44	0.007	0.44	1.26E-08	6.98E-10
7	9.1	0.153	0.001	0.00	0.000	0.00	5.31E-11	2.93E-12

Site Locations Relative to Center of Array

Site #	Bearing (degrees)	Range (meters)
1	141	1,086
2	181	2,389
3	199	5,042
4	222	17,217
5	71	4,767
6	55	2,324
7	125	949

THEORETICAL STUDIES ON THE EFFECT OF WAVEGUIDE GEOMETRY ON THE RADIATING SLOT

PRAKASH VVS, BALAKRISHNAN N* and CHRISTOPHER S

ELECTRONICS AND RADAR DEVELOPMENT ESTABLISHMENT
* INDIAN INSTITUTE OF SCIENCE
BANGALORE, INDIA

ABSTRACT :- The longitudinal offset radiating slot in the broadwall of rectangular waveguide has been analyzed using a spectrum of 2-dimensional solutions. All the fields and the sources are Fourier transformed with respect to the longitudinal axis of the waveguide and the resulting 2D problem has been solved using two different approaches namely, Finite difference method (FDM) wherein the grid truncation is with Measured Equation of Invariance (MEI) and the Moment method(MoM). This analysis accurately models the effect of finite waveguide outer geometry on the radiating slot. Comparative studies have been made on the spectral solutions of the MEI and the MoM. Effect of the waveguide geometry on the slot characteristics has been presented.

1. INTRODUCTION

Longitudinal offset slots cut on the broadwall of rectangular waveguide are widely used as radiating elements in high performance slotted array applications. One of its advantages is the control over the radiated power by means of changing the offset of the slot from the center line of the waveguide. To achieve the required aperture distribution precisely, it is essential that the behavior of the slot, as a function of length, offset, width, etc., be analyzed as accurately as possible. One of the assumptions made in the slot characterization is that the slots are radiating into an infinite ground plane for computing the external radiated fields[1-3]. Since the waveguide outer cross-section is rectangular in shape, this assumption is not valid for large offsets.

This paper attempts to solve the problem of a longitudinal offset slot radiating into a rectangular outer geometry. Using equivalence principle, the slot is covered by a perfect electric conductor and a magnetic current of $+M_z$ on the exterior side and a $-M_z$ on the interior side of the slot to ensure the continuity of tangential electric fields. The continuity of the tangential magnetic fields on either side of the slot is enforced at the slot aperture. The unknown magnetic current is obtained by the solving the resulting integral equation using Galerkin method. The finite wall thickness of the

waveguide also can be considered in the same way. The internal scattered fields are computed using Stevenson's Greens functions[1]. To find the external radiated fields, all the fields and the sources are Fourier transformed along the waveguide axis, thereby converting the original 3D problem into a 2D problem[4]. Two approaches have been used to solve the resulting 2D problem in spectral domain, namely the Finite difference method coupled with Measured Equation of Invariance(MEI) and the other is Moment method coupled with electric field integral equation (EFIE). The solutions of these two methods have been compared in terms of accuracy and convergence behavior.

The dominant element of external admittance matrix has been computed using the above mentioned two methods and is compared with that of the Half space Green's function approach. The admittance properties of the radiating slot have been computed using these two methods and are compared with that available in the literature[2].

2. THEORY

The geometry of broadwall longitudinal offset radiating slot is shown in Fig.1a. The slot is assumed to be narrow so that the only significant component of the slot aperture electric field is in the x-direction. Using the Schelkunoff's equivalence principle, the domain of the radiating slot is divided in to two regions; the waveguide interior and exterior regions. The continuity of tangential electric fields is ensured by placing suitable magnetic current sheet at the location of slot. A coupled integral equation is obtained by enforcing the continuity of tangential magnetic fields at the slot location as

$$\overline{H}^{ext}(\overline{M}) \quad + \quad \overline{H}^{int}(\overline{M}) \quad = \quad \overline{H}_{10}^{inc} \qquad \qquad ...(1)$$

The unknown slot magnetic current is expanded in to a set of N basis functions as

$$M_z \quad = \quad \sum_{n=1}^{N} \alpha_p \; \sin\frac{p\pi}{2L}(z+L) \quad = \quad \sum_{p=1}^{N} \alpha_p \; M_p \qquad \qquad ...(2)$$

and following the Galerkin's method, the coupled integral Eq.1 is converted in to a set of linear algebraic equations as

$$[Y^{ext} \quad + \quad Y^{int}] \; [V] \quad = \quad [h^{inc}] \qquad \qquad ...(3)$$

where Y^{ext} and Y^{int} are the external and internal admittance matrices respectively and V is the matrix composed of the expansion coefficients of the magnetic current. Computation of Y^{int} is straight forward and is done using Stevenson's internal waveguide Green's function[1].

For computing the Y^{ext}, the method of 2D spectral solutions is used. Here all the sources and the fields are Fourier transformed with respect to the longitudinal axis of the waveguide i.e. z-axis, thereby reducing a 3D problem to a 2D one. The 2D problem is solved using two different approaches as follows.

(1) <u>Computation of exterior magnetic field by MEI</u> :

The wave equation for the magnetic vector potential, F_z is solved using MEI and the external tangential magnetic field is obtained from it. The magnetic vector potential which is due to p[th] basis function excitation at the slot aperture is obtained by solving

$$\nabla_t^2 \, \tilde{F}_z^p \;+\; (k_o^2 - k_z^2) \, \tilde{F}_z^p \;=\; 0 \qquad\qquad \ldots(4)$$

under the boundary condition that the electric field tangential to the waveguide surface is zero except at the slot region where it is equal to the slot aperture electric field, i.e.

$$\frac{\partial \tilde{F}_z^p}{\partial n} \;=\; - \,\varepsilon_o \, \tilde{E}_x^p \quad \text{at the position of slot.}$$

$$\frac{\partial \tilde{F}_z^p}{\partial n} \;=\; 0 \quad \text{on the rest of the waveguide surface.} \qquad \ldots(5)$$

where 'n' is the normal direction away from the waveguide surface in to the exterior region and $\tilde{E}_x$ is the Fourier transformed slot aperture electric field corresponding to p[th] expansion function. Finite difference method is used to solve Eq.4 in the exterior region of the 2D problem(Fig.1b). The finite difference grid is truncated using MEI, after a few buffer layers from the waveguide surface[4]. A 5-point MEI is employed and the coefficients of MEI are extracted using

(a) linearly independent set of metrons on the surface of the waveguide as

$$\begin{aligned} \psi_n \;&=\; \cos\frac{n\pi l}{T} \quad \text{for n even or n = 0} \\[1mm] &=\; \sin\frac{n\pi l}{T} \quad \text{for n odd} \end{aligned} \qquad \ldots(6)$$

where n = 0,1,...,4, T = total circumference of waveguide = 2 a + 2 b and l is a parameter along the cross-section of the waveguide.

(b) plane waves at the point of application of MEI as

$$\psi \;=\; e^{-j\,k\rho\,(\cos\phi_i \; x \; + \; \sin\phi_i \; y)} \qquad\qquad \ldots(7)$$

where ϕ_i is the angle of incidence of plane wave and (x,y) are the coordinates of the point under consideration. For each of the expansion coefficients $\tilde{M}_p$, Eq.4 is solved subjected to the boundary conditions of Eq.5. The tangential magnetic field at the slot aperture is given in terms of $\tilde{F}_z^p$ as

$$H_{z,p}^{ext} = \frac{1}{j\omega\,\mu_0\,\varepsilon_0\,2\pi} \int_{K_z=-\infty}^{\infty} \widetilde{F}_z^p(k_z)\,k_\rho^2\,e^{-j\,k_z\,z}\,dk_z \qquad ...(8)$$

(2) Computation of exterior magnetic field by Moment method:

Using physical equivalence, the waveguide surface is replaced by unknown surface electric currents. The surface electric currents are computed for each spectral wavenumber by solving the electric field integral equation given by

$$\widetilde{\widetilde{E}}_t^{inc}(\overline{\rho}) \cdot \hat{s}(\overline{\rho}) = jk_o\eta_o \int_s \hat{s}(\overline{\rho}) \cdot \hat{s}(\overline{\rho}')\,\widetilde{J}_s(\overline{\rho}')\,G(\overline{\rho},\overline{\rho}')\,ds'$$

$$+ \frac{jk_o\eta_o}{k_\rho^2}\,\frac{\partial}{\partial s}\int_s \frac{\partial\,\widetilde{J}_s(\overline{\rho}')}{\partial s'}\,G(\overline{\rho},\overline{\rho}')\,ds' \quad ...(9)$$

where $\widetilde{\widetilde{E}}_t^{inc}$ is the transverse incident electric field due to the magnetic current $\widetilde{M}_z(k_z)$, $k_\rho^2 = k_o^2 - k_z^2$ and $G(\overline{\rho},\overline{\rho}')$ is the 2D free space Green's function[5]. The unknown surface electric currents are expanded in to piecewise constant pulses and using collocation method, the Eq.9 is solved for each spectral wavenumber k_z.

The tangential magnetic field at the slot aperture is then calculated as

$$\hat{n} \times \overline{H}^{ext} = \overline{J} = \overline{J}_s\,\hat{s} + J_z\,\hat{z} \qquad\qquad ...(10)$$

Once the exterior magnetic field is computed by one of the methods described above, the elements of exterior admittance matrix Y^{ext} are given by,

$$Y_{mn}^{ext} = \iint_s \overline{H}_m^{ext}(\overline{\rho},z) \cdot \overline{M}_n(\overline{\rho},z)\,ds = \frac{1}{2\pi}\int_{k_z} R_{mn}(k_z)\,dk_z \quad ...(11)$$

where $R_{mn}(k_z) = \int_s \widetilde{\widetilde{H}}_m^{ext}(\overline{\rho},k_z) \cdot \widetilde{M}_n(\overline{\rho},-k_z)\,ds$ and $m,n = 1,2,....,N.$

3. RESULTS

The proposed method has been applied to a longitudinal offset radiating slot on the broadwall of a standard S-band rectangular waveguide of a = 7.214cm and b = 3.404cm. For simplicity, the wall thickness is taken to be zero and the slot width is 0.3cm. For a slot offset of 0.75cm and a length of 4.6cm, the dominant element of the external admittance matrix (Y_{11}^{ext}) has been computed as a function of spectral wave number and is plotted in Fig.2. As can be seen, the solution obtained using MEI is found to be exhibiting irregular behavior with k_z where as the MoM solution is smooth. It is found that the using surface currents as metrons does not give any marked advantage over the use of

planewave functions, as far as accuracy is concerned in this case. The use of plane wave functions for extracting the MEI coefficients leads to unacceptable errors in the spectral solution. For large K_z all the solutions approach that of the infinite half space method.

The reflection coefficient of the radiating slot is computed as a function of slot length and is presented in Fig.3. The phase of the reflection coefficient is shifted by 180^0 and is plotted in Fig.3. For the FDM+MEI approach, five buffer layers are used between the MEI boundary and the waveguide surface. The grid spacing is taken to be $\lambda/50$ leading to a large system of linear equations to be solved for each spectral wavenumber. Moreover, the convergence of the spectral solution of FDM is found to be poor over the range of practicable grid spacings. Even though pulse expansion and point matching is used with MoM, good convergence is obtained with 118 unknowns.

For a typical slot length of 4.25cm, the slot reflection coefficient has been computed as a function of slot offset using Moment method and is presented in Fig.4. Also presented are the results of Half space Green's function approach. It is found that the effect of waveguide outer geometry is negligible for small offsets. As the offset of the slot increases, it comes close to the waveguide corner which effects the reflection coefficient and the present method has to be used for an accurate computation of slot reflection coefficient.

CONCLUSION:- The admittance properties of longitudinal offset radiating slot on the broadwall of rectangular waveguide have been studied using a method of spectrum of 2D solutions. Both the Finite difference + MEI and the MoM approaches have been studied. It has been shown that the use of FDM leads to unacceptable errors in the admittance computations with normally used set of metrons. It might be possible to find an optimum set of metrons which will reduce the error in MEI boundary truncation. It should be noted that the excitation is not a plane wave but a sheet of magnetic current on the waveguide surface. The moment method is relatively free of oscillations leading to an accurate solution. The half space Green's function approach has been found to be applicable for small slot offsets. For a more accurate solution, the finite outer cross-section of the waveguide has to be considered.

References:-

[1] Stevenson,"Theory of slots in rectangular waveguides," J.Appl. phys., vol.19,pp.24-38, Jan. 1948.
[2] Stern,G.J. and Elliot,R.S.,"Resonant length of longitudinal slots and validity of circuit representation: theory and experiment",IEEE Trans.,AP-33,pp.1264-1271, 1985.
[3] Lyon,R.W. and Sangster,A.J.,"Efficient moment method analysis of radiating slots in a thick walled rectangular waveguide", IEEE Trans.,1981,128H,pp.197-205.
[4] Mei,K.K., Pous,R., Chen,Z., Liu,Y.W., and Prouty,M.D.,"Measured equation of invariance: a new concept in field computations", IEEE Trans. Antennas Propagat., vol.42, pp.320-328, 1994.
[5] J.Wettergren and P.Slattman,"Electric field integral equation for cylindrical structures," IEE Proc. Microw. Antennas Propagat., Part.H, vol.143, pp.147-151, April 1996.
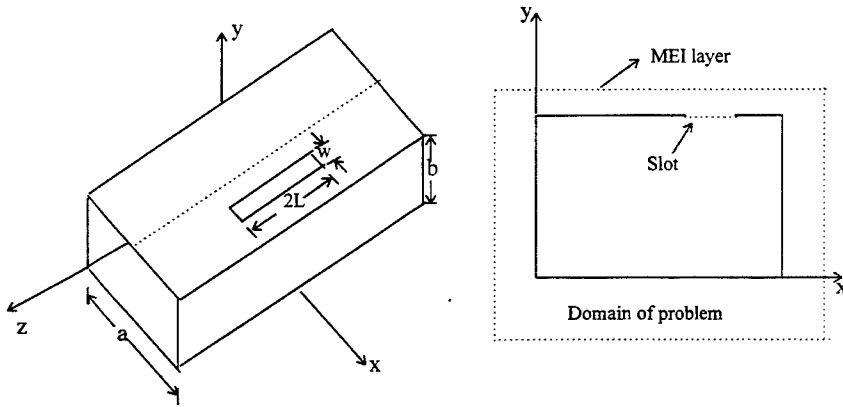
(a) Broadwall longitudinal offset slot   (b) 2D problem in Fourier domain

Fig.1 Geometry of radiating slot cut on a rectangular waveguide
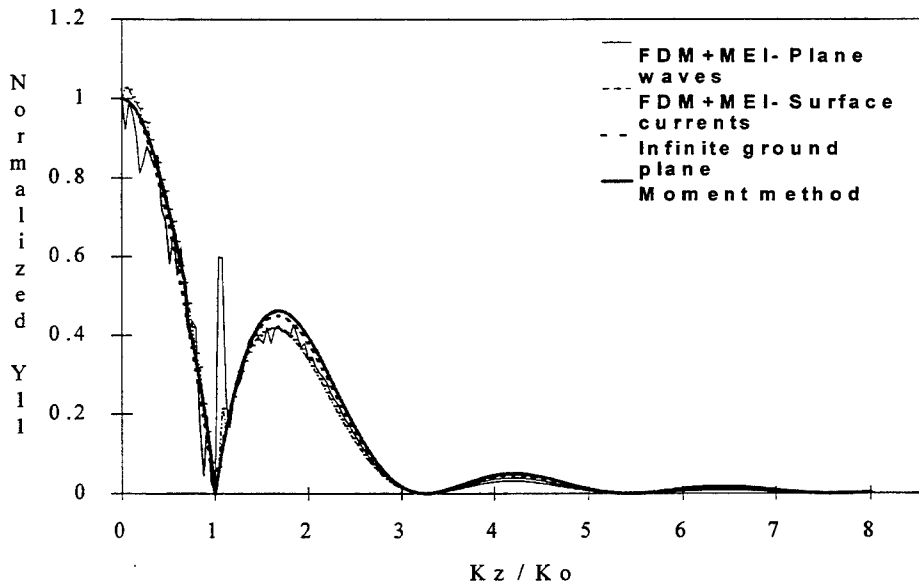
Fig.2 Normalized magnitude of Y_{11} -vs- K_z / K_o
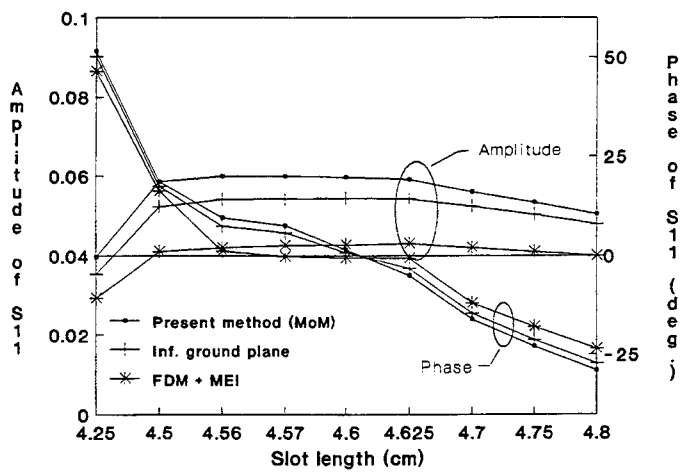
Fig.3 S11 of longitudinal slot -vs- slot length at 3GHz.
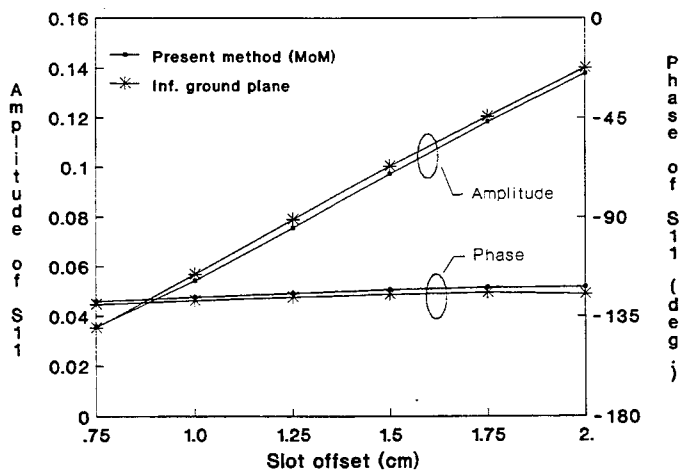
Fig.4 S11 of longitudinal slot -vs- slot offset at 3GHz.

COMPUTED AND MEASURED RADIATION PATTERNS OF ANTENNAS WITH AERODYNAMIC RADOMES

David Jenn and Scott Herzog
Naval Postgraduate School
Monterey, CA 93943

I. INTRODUCTION

Radomes are a crucial component of communications and radar systems deployed on aircraft. The electrical characteristics of the radome must not significantly degrade the antenna performance, yet aerodynamic, structural, and thermal requirements must also be satisfied. Tradeoffs in the design process are facilitated by an accurate analytical model of the antenna and radome. A rigorous model that includes the effects of multiple reflections, attenuation by the radome walls, and surface waves favors the method of moments over ray tracing techniques.

A previous solution [1] used the method of moments with basis functions limited to bodies of revolution. The antenna is modeled as an aperture with a specified field distribution. The method of moments excitation vector is computed using the complete expressions for the radiated field from the aperture. All powers of $1/R$ (R being the distance from an aperture point to an observation point on the radome) and all vector components are included in the calculation. Therefore, the model can accommodate geometries where the radome is in the near-field of the antenna.

A shortcoming of the model in [1] is that no antenna surfaces are included in the antenna representation; it is simply an equivalent current distribution suspended in free space. Thus the antenna aperture is transparent to reflections from the radome that would either return to the antenna port and affect its VSWR or be scattered a second time around. Consequently there is a limit to the accuracy of the model's data because the interactions between the radome and antenna are neglected.

The model presented here and described in detail in [2] utilizes a voltage source representation available in the computer code PATCH [3]. The antenna aperture is represented by an array of thin short slots that are weighted in amplitude and phase to reproduce the radiation pattern of the actual antenna. The plate resistivity can be specified so that any desired aperture transparency, and hence reflection coefficient, can be achieved. Computed and measured data are presented for HARM and AIM-9 radomes.

II. COMPUTER MODEL

PATCH is a FORTRAN code that computes electromagnetic scattering and radiation based on a method of moments (MM) solution of the E-field integral equation (EFIE). Triangular facets (subdomains) and overlapping basis functions of the type developed by Wilton and Rao [4] are used in PATCH. The method of moments reduces the EFIE to a set of linear equations that can be solved using standard matrix methods. The number of unknowns, and hence the size of the matrix equation that must be solved, depends on the number of triangular patches are used to represent the antenna and radome. Therefore the application of MM is usually limited by the size of the computer available.

Faceted models of the HARM and AIM-9 radomes along with the antenna apertures are shown in Figure 1. Both radomes are axially symmetric. The HARM is ogive-shaped in the forward section with the straight line segments near the back, while the AIM-9 radome is hemispherical. A general rule of thumb for convergence of the far-field radiation pattern is that triangle edge lengths should not exceed 0.1λ, where λ is the wavelength. The models in Figure 1 are accurate up to about 12 GHz.

PATCH allows the user to define impressed voltage sources at an edge. An approximate aperture model for a Microline 56X1 horn is shown in Figure 2. The dots denote edges that are excited simul-
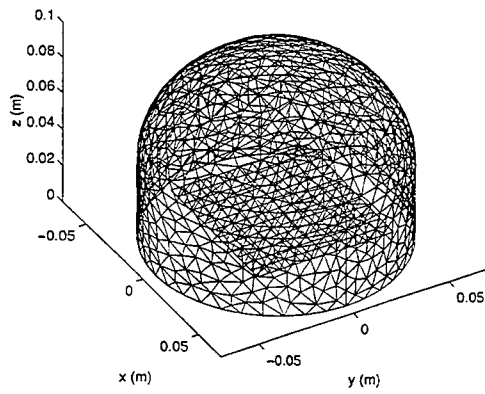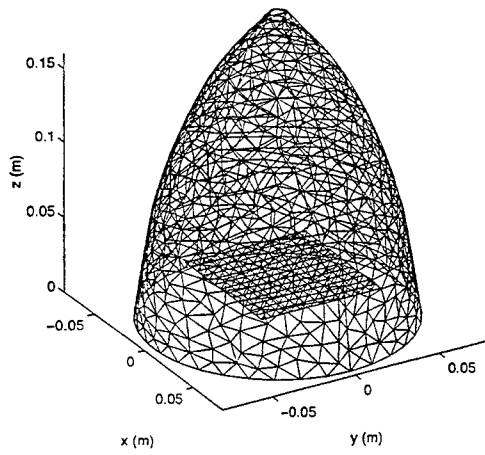
Figure 1: Facet models for the HARM and AIM-9 radomes with antenna apertures.
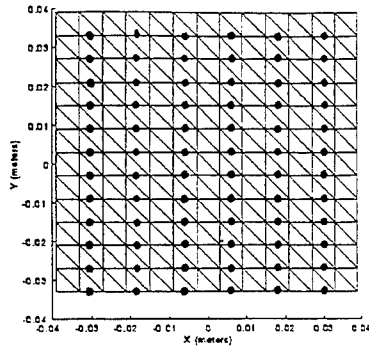
Figure 2: Horn aperture approximation by a plate with excited slots.

taneously using voltage sources. The amplitude and phase of each source is chosen so that the far-field pattern of the aperture approximates the measured far-field pattern of the horn. The required distribution is close to that of the TE_{10} mode with a quadratic phase error in both principal planes. Typical antenna patterns in the absence of a radome are shown in Figure 3 for PATCH, RADOME (the code described in [1]), and measured data. All data presented is for a frequency of 10 GHz.

III. RADOME WALL MODEL

The radome walls are represented by thin dielectric shells [5]. The equivalent surface impedance is determined using a transmission line representation. Two radome walls were modeled: (1) HARM three-layer sandwich and, (2) AIM-9 single-layer wall. The surface impedance of an infinite flat panel of the HARM radome is shown in Figure 4. The surface impedance used by PATCH must be independent of angle; the value for normal incidence ($Z_s = 234 - j166$ Ω) is a good approximation up to about 60°.

IV. COMPARISON OF COMPUTED AND MEASURED DATA

The radome and antenna configuration is depicted in Figure 5. In the calculation the antenna aperture was placed so that it was coincident with the phase center of the measurement horn. The resistivity of the aperture plate was adjusted by trial and error to obtain the best agreement with measured data.

Comparisons of the E- and H-plane patterns for the two radomes are given in Figures 6 and 7. The measured patterns contain some error due to an asymmetrical chamber configuration (as evidenced by the asymmetrical patterns). On the measured HARM radome there is a hard plastic rim with mounting holes and a metal tip that are not included in the facet model. The AIM-9 radome has a 3 inch metal base that is not modeled in PATCH. In spite of these differences the measured and computed patterns have the same essential features.

V. ACKNOWLEDGEMENTS
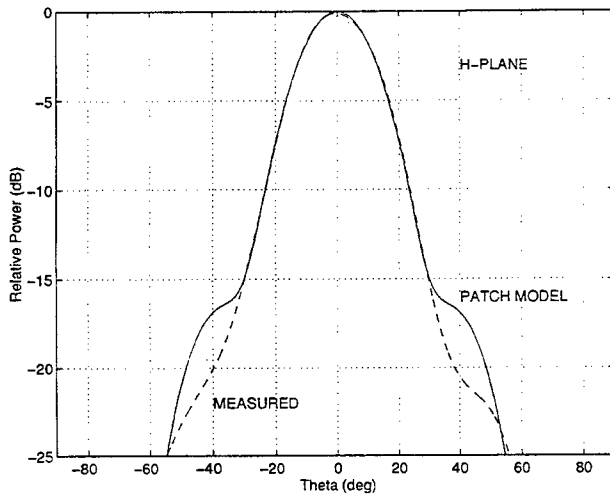
Figure 3: Sample comparison of approximate antenna model and measured data (H-plane).
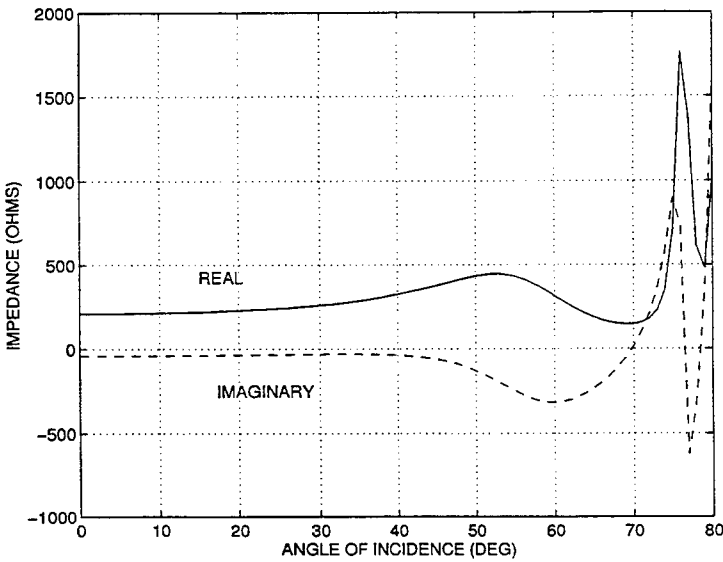
Figure 4: HARM radome surface impedance.
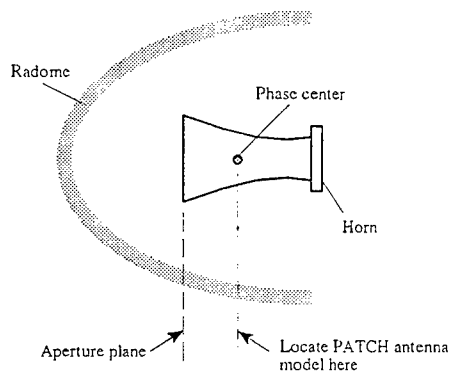
Figure 5: Antenna and radome configuration.
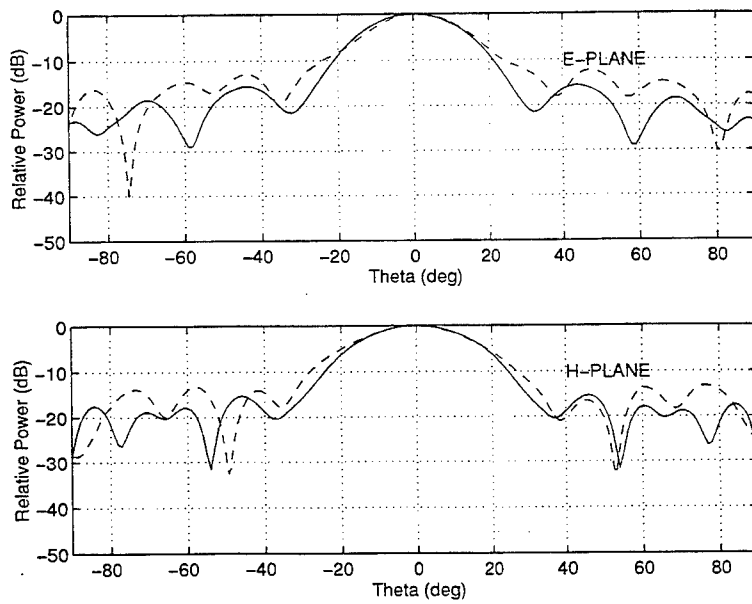
Figure 6: Comparison of calculated and measured data for the HARM radome.
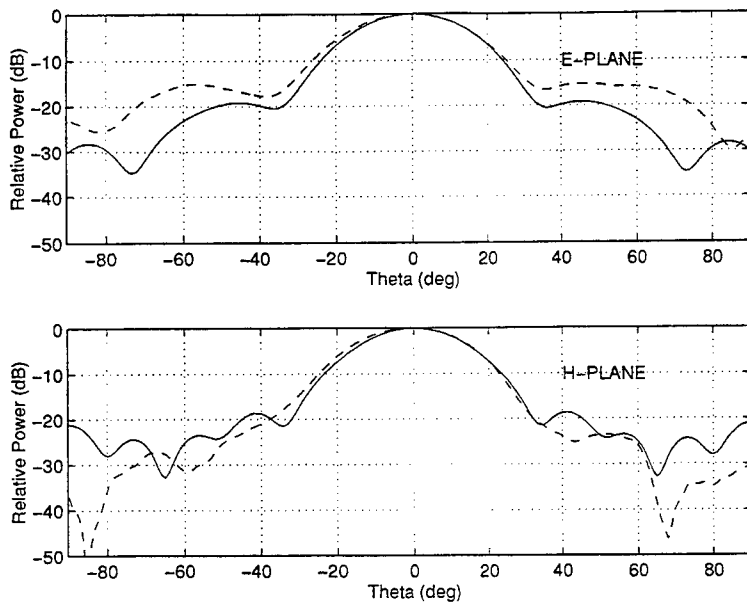
Figure 7: Comparison of calculated and measured data for the AIM-9 radome.

VI. REFERENCES

[1] D. C. Jenn, R. M. Francis and K. A. Klopp, "Computer Model for Axially Symmetric Dielectric Radomes in the Near Field of a Circular Aperture," *Applied Computational Electromagnetics Symposium*, March 1993, p. 785.

[2] S. M. Herzog, "Radiation Pattern Calculation for Missile Radomes in the Near Field of an Antenna," Naval Postgraduate School Masters Thesis, September 1995.

[3] W. Johnson, et al,"PATCH Code Users Manual," Sandia Laboratory Report SAND87-2991, May 1988.

[4] S. M. Rao, D. R. Wilton and A. W. Glisson, "Electromagnetic Scattering by Surfaces of Arbitrary Shape," *IEEE Trans. on Ant. and Prop.*, vol. AP-30, no. 3, May 1982, p. 409.

[5] R. F. Harrington and J. R. Mautz, "An Impedance Sheet Approximation for Thin Dielectric Shells," *IEEE Trans. on Ant. and Prop.*, vol. AP-29, no. 4, May 1975, p. 531.

SAF Analysis Codes for Computing Shipboard Antenna Pattern Performance, Antenna Coupling, and RADHAZ*

Barry J. Cown[1] and John P. Estrada[2]

(1) GEMTECH Microwaves, Inc. 1318 Chandler Court, Acworth, GA 30102
(2) Georgia Tech Research Institute, ATDD/SEAL, Atlanta, GA 30332

A. INTRODUCTION

This paper describes computer codes based on the near-field (NF) spectral analysis method known as the Spherical Angular Function (SAF) technique for predicting antenna pattern performance, antenna coupling, and RADHAZ for shipboard antennas operating in the presence of nearby scattering obstacles and other antennas [1-11]. Emphasis is given to the application of the SAF codes to the mostly-metallic topsides of present surface vessels. However, the progression to composite topsides is also indicated herein.

The complexity of the scattering environments encountered by topside antennas can be appreciated by considering, for example, the topside of the DDG shown in Figure 1. The shipboard directive antennas must operate in close proximity to other antennas and various topside structures including round masts, open masts, platforms, yardarms, equipment, stacks, decks, and deckhouses. Frequently, the entire ship topside is well within the radiating near-field region of a directive transmitting antenna at microwave/millimeter wave frequencies. In addition, two or more ship structures may be simultaneously illuminated by the transmitting antenna. The fields scattered from these multiple obstacles can combine with the directly-transmitted antenna fields to produce far-field pattern distortions and to produce local "hot-spots" and relative nulls that can significantly impact both RADHAZ near-field power density profiles and equipment interference levels.

Computer codes based on the Spherical Angular Function (SAF) near-field analysis technique has been developed to expedite the analysis and design of shipboard antenna arrangements to achieve maximum electromagnetic effectiveness for current topsides [1-11]. The FORTRAN 77-compliant SAF codes have proven to be accurate engineering tools for predicting pattern performance, coupling, and RADHAZ levels for antennas operating in the presence of metallic structures, and they are readily extended to handle integrated antenna/composite mast topsides. The SAF analysis technique and validation results are succinctly described in the following paragraphs. More detailed expositions of the SAF analysis can be found in References 1, 3, 4, and 11. Extensive applications of the SAF codes to modern ship topside antennas are contained in References 4 through 7.

The progression toward antennas that are increasingly integrated with composite structures to both increase antenna performance and control topside RCS is illustrated by Figures 2 through 5. Figure 2 shows the concept for the ATD (Advanced Technology Development) hexagonal composite mast that encloses two existing widely-used topside microwave antennas, namely the TAS antenna and the SPS-40 antenna. Figure 3 illustrates the MERS (Multifunction Electromagnetic Radiating System) concept where UHF communication antennas, JTIDS, combat DF, and IFF antennas are embedded in a single composite structure. Figure 4 also illustrates the embedded sensor concept. Figures 2, 3, and 4 illustrate mixed topsides involving both composite structures and traditional topside structures. In the longer term, it is envisioned that the unified composite superstructure concept shown in Figure 5 will be realized.

B. SAF MATHEMATICAL MODELS

The radiating near-field of an antenna or scattering obstacle may be represented as a vectorial angular spectrum of outwardly propagating plane waves. This vectorial angular spectrum of plane waves is completely described by the Spherical Angular Function (SAF) for the antenna, and it is denoted as $\bar{F}(\theta,\phi)$, where (θ,ϕ) are the elevation and azimuth angles, respectively, in a standard vertically-oriented system of spherical coordinates. $\bar{F}(\theta,\phi)$ may be expressed directly in terms of the vectorial complex far-field electric field $\bar{E}_{ff}(\theta,\phi)$ as $\bar{F}(\theta,\phi) = r \{\exp[jkr]\}\bar{E}_{ff}(\theta,\phi)$, where $k = \frac{2\pi}{\lambda}$, λ is the free-space wavelength, and r is the distance to the far-field pattern point.

Consider the case depicted in Figure 2 involving 3 scattering obstacles. The resultant total SAF for the antenna operating in the presence of the multiple obstacles is computed via the "Marching In Range Method", or MIRM for short. In the MIRM, the antenna SAF is propagated to the first obstacle, the scattered SAF is computed and added to the incident antenna SAF to obtain the total SAF. This total SAF is just the distorted SAF for the antenna operating in the presence of the first obstacle. This total SAF after this first step is then allowed to be incident on the second obstacle, the scattered SAF from the second obstacle is computed and added to the total SAF for the first obstacle to obtain the distorted total SAF for the antenna operating in the presence of the two obstacles. Obviously, this process is repeated N times if there are N obstacles blocking the antenna. This process can be expressed mathematically as

$$\bar{F}_N^{tot}(\theta,\phi) = \prod_{n=0}^{N} \bar{\bar{\Gamma}}_n\left(\theta,\phi|\theta',\phi'|\bar{R}_n\right) \bullet \bar{F}^a\left(\theta',\phi'\right), \tag{1}$$

where the SAF integral operator $\bar{\bar{\Gamma}}_n\left(\theta,\phi|\theta',\phi'|\bar{R}_n\right)$ is defined as

$$\overline{\overline{\Gamma}}_n\left(\theta,\phi|\theta',\phi'|\overline{R}_n\right) =$$
$$\iint_\Omega d\Omega' \exp\left\{j\left[\overline{k}(\theta,\phi) - \overline{k}(\theta',\phi')\right] \bullet \overline{R}_n\right\}\left\{\overline{\overline{I}} + \overline{\overline{S}}_n\left(\theta,\phi|\theta',\phi'\right)\right\}, \tag{2}$$

where $\overline{\overline{S}}_n\left(\theta,\phi|\theta',\phi'\right)$ is the plane-wave (PW) scattering dyad for the $n^{\underline{th}}$ obstacle, $\overline{R}_n$ is the vector distance from the antenna to the $n^{\underline{th}}$ obstacle, as indicated in Figure 6, and where $\overline{k}(\theta,\phi)$ and $\overline{k}(\theta',\phi')$ are the wave vectors for the scattered and incident fields, respectively. $\overline{\overline{I}}$ is the identity dyad. The SAF antenna pattern performance code GMULT and the antenna gain loss code GLOSS utilize finite circular and elliptical cylinders, circular cone frusta, flat rectangular plates, and flat triangular plates to model the ship topside structural elements.

The voltage induced at the terminals of a nearby receiving antenna, as per Figure 7, is expressed in terms of the resultant SAF, $\overline{F}_N^{tot}$, for the transmitting antenna operating in the presence of the N multiple obstacles and the clear-site SAF $\overline{F}_{rec.}^b$ for the receiving antenna:

$$v(\overline{R}^{ab}|\beta,\alpha|\xi,\eta) =$$
$$\iint_\Omega\left\{\overline{F}_{rec.}^b(\theta-\beta,\phi-\alpha) \bullet \overline{F}_N^{tot}(\theta-\xi,\phi-\eta)\exp\left[-j\overline{k}(\theta,\phi) \bullet \overline{R}^{ab}\left(\theta_o,\phi_o\right)\right]\right\}\sin(\theta)d\theta d\phi, \tag{3}$$

where (β,α) are the elevation and azimuth pointing angles of the receiving antenna, and (ξ,η) are the elevation and azimuth pointing angles of the transmitting antenna referenced to the $\left(\theta_o,\phi_o\right)$ angular coordinates of the receiving antenna rotation center, and $\overline{R}^{ab}$ is the vector from the transmitting antenna to the receiving antenna. This near-field coupling analysis is implemented in the antenna coupling code GCUPL.

C. VALIDATIONS WITH MEASURED DATA

Figure 8 shows measured and computed antenna patterns for a 4-foot diameter parabolic antenna blocked by a quadrapod open-mast obstacle for the operating frequency of 5.5 GHz for horizontal polarization [6,8]. Only the 14 cylindrical elements shown in the inset of Figure 4 were used to obtain the computed curve; additional elements cause only small changes in the sidelobe details. Figure 10 shows measured and computed azimuth antenna patterns for the TAS antenna installed aboard the U. S. S. Kennedy, as depicted in Figure 9, for a case involving severe blockage by the ship topside structures [6,8]. The TAS antenna is operating vertically-polarized at an L-band frequency.

Figure 11 shows the measured and GCUPL-computed coupling curves for two 4-foot diameter C-band antennas blocked by an intervening round mast. Figure 12 compares RADHAZ power density curves computed via GCUPL from the measured blocked SAF and from the GMULT-computed blocked SAF, for the 4-foot diameter C-band antenna operating in the presence of the quadrapod open-mast obstacle for the blockage geometry shown in Figure 13.

D. APPLICATION TO INTEGRATED ANTENNA/COMPOSITE TOPSIDES

The pattern performance, coupling, and RADHAZ of antennas located either in the interior or the exterior regions of composite structures may be computed via Equations (1), (2) and (3), as appropriate, once the PW scattering dyad is specified. PW scattering dyads for basic canonical shapes such as flat polygonal panels composed of multilayer dielectric and/or frequency selective surfaces (FSS) are readily derived by combining a) Physical Optics (PO) formulas for opaque polygonal plates and b) the Periodic Moment Method (PMM) code [12,13]. The PO formulas account for the shape of the panels and the PMM code is used to compute the PW transmission and reflection coefficients for the panels as a function of the PW incidence angles. Exact PW scattering dyads are, of course, known for transversely-infinite multilayer dielectric panels and for multilayer dielectric circular cylinders and spheres [13,14]. The PW scattering dyad for general curved multilayer composite structures that have electrically-large radii of curvature can be modeled as the superposition of an ensemble of polygonal facets that are chosen to closely approximate the shape of the actual structure; this first-order approximation can be improved by accounting for the propagation of circumferential modes in the multilayer structure. The resultant RCS for the enclosed antenna and the enclosing composite structure may be computed via Equations 1 and 2 by straightforward adaptation of the MIRM method for the externally-incident PW. The SAFs and RCS for antennas embedded in flat multilayer dielectric and/or FSS panels can be computed with the aid of moment method codes adapted for these purposes [15].

E. CONCLUDING REMARKS

Good agreement between computed and measured results is achieved for the near-field scenarios presented in Part C and for other validation scenarios [4-7]. It is concluded that the SAF technique is well-suited for analysis of directive antenna far-field and near-field radiation characteristics and near-field antenna coupling in complex near-field scattering environments such as ship topsides, space stations, and congested terrestrial antenna sites. The SAF analysis technique combined with the Marching In Range Method (MIRM) is applicable to micro/millimeter wave antennas operating in close proximity to arbitrary metallic and/or composite structures for which the individual SAFs of the constituent scattering structures are known or can be derived.

217

Present Ship Topside

TAS antenna
at 90 feet ABL

Figure 1. Topside of DDG.

LIGHTNING ROD
TACAN ANTENNA
INTEGRATED
COMMUNICATIONS
ANTENNA
MMBA (RESERVE)
ROS
TAS ANTENNA
SPS40 ANTENNA
IFF ANTENNA
BALLISTIC
TRUNK
SHIELDED
SPACE
HVAC

ATD P/C BASELINE
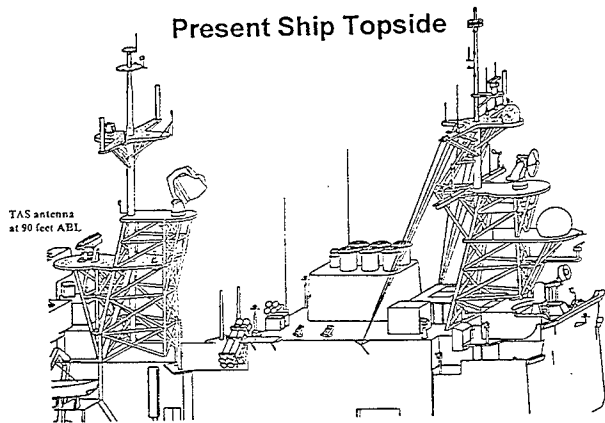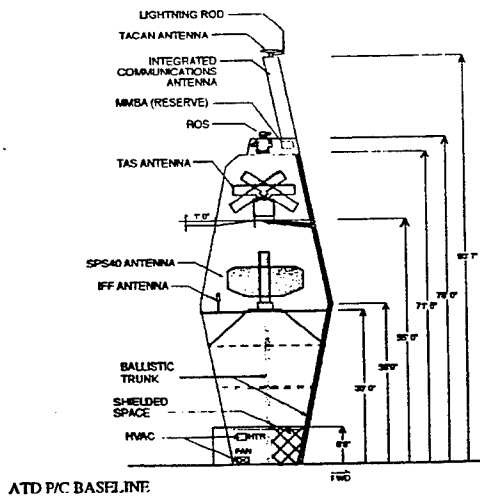
Figure 2. ATD hexagonal mast concept.

MAST

Demonstrate operational
system at sea

6 feet vs. 30 feet
(Frees up 80% of
the mast design
volume)

Weight: 450 lbs
vs. 1.5 tons/hull

5 feet
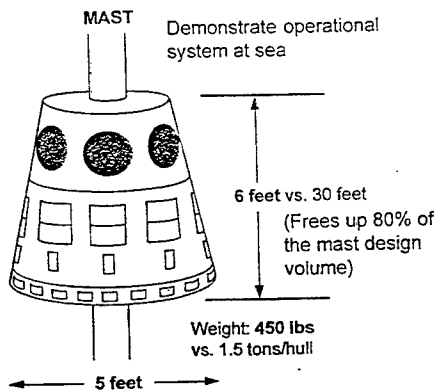
**Figure 3. MERS ATD concept for UHF comm.,
JTIDS, Combat DF, and IFF antennas.**
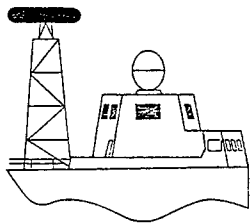
Figure 4. Embedded sensor concept for FFG-7.
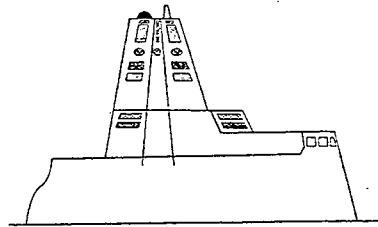
Figure 5. Unified composite superstrucure concept.
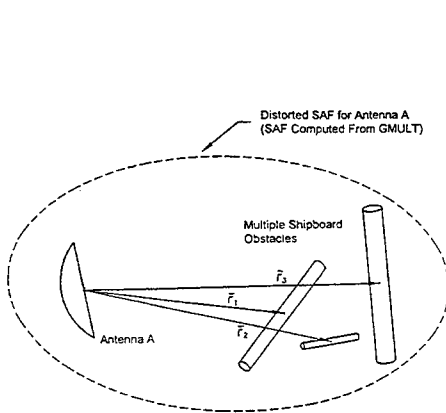
Figure 6. SAF MIRM concept for multiple obstacles.
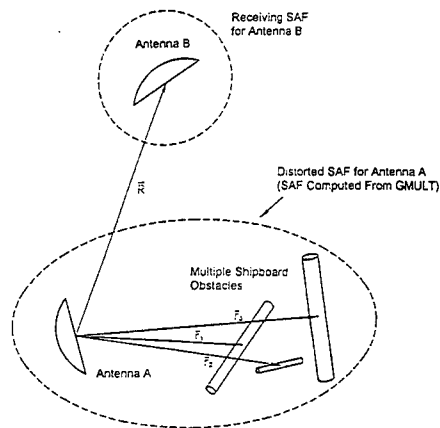
Figure 7. SAF antenna coupling concept.
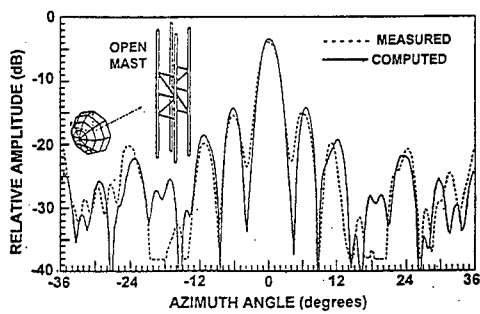
Figure 8. Azimuth patterns for the 4.0-foot diameter antenna blocked by the quadrapod open-mast obstacle.

219
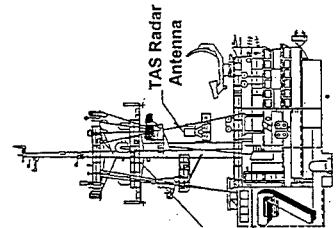
Figure 9. Topside of U. S. S. Kennedy.
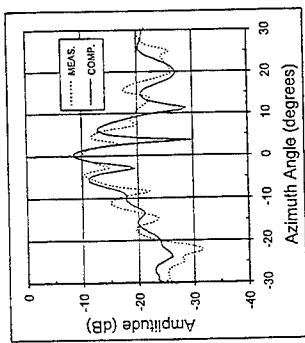
Figure 10. Azimuth patterns for the TAS radar antenna.

Figure 11. Antenna coupling for two 4.0-foot diameter antennas blocked by intervening 2.0 foot diameter mast.

Figure 12. Near-field power density versus azimuth angle for the 4.0-foot diameter antenna blocked by the quadrapod mast.
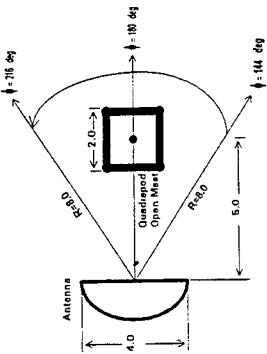
Figure 13. Plan view of the blockage geometry for Figure 12.

F. REFERENCES

1. Barry J. Cown, "Antenna Pattern Performance and Coupling in the Presence of Near-Field Shipboard Obstacles", Final Technical Report, GTRI, Prime Contract No. N00024-82-K-5329, July 1984.

2. Barry J. Cown, R. W. Cravey, and C. D. Papanicolopoulos, "Analysis of Antenna Coupling and Scattering Via Spherical Angular Functions", 1986 IEEE International Antenna and Propagation Symposium Proceedings. Philadelphia, PA, June 13-18, 1986.

3. B. J. Cown and C. E. Ryan, Jr., "Near-Field Scattering Measurements for Determining Complex Target RCS", *IEEE Trans. Ant. and Prop.*, Vol 37, No. 5, May 1989, pp. 576-585.

4. B. J. Cown, J. P. Estrada, Brian L Shirley, and C. E. Ryan, Jr., "Shipboard Near-Field Energy Determination", Final Technical Report, GMT-9101 and GTRI A-9275, Task SCEEE-NSWC/ 9C-0123 (Navy Prime Contract N6092C-87-D-A315-0123), September, 1992.

5. B. J. Cown, John P. Estrada, C. E. Ryan, Jr., and C. D. Papanicolopoulos, "Shipboard Antenna Analysis Using SAF Computer Codes GMULT11 and GCUPL7B", Final Technical Report, GMT-9201 and GTRI A-9184, Task NCEE/A303/C-92 & /1A-92 (Navy Prime Contract No. N6092-92-D-A303), March, 1993.

6. B. J. Cown and J. P. Estrada, "Shipboard Directive Antenna Modeling Via the GMULT/GCUPL Computer Codes", Final Technical Report, GMT-9301 and GTRI A-9275, P. O. #'s NCEE/A303/10-92 and 10A-92, (Navy Prime Contract N-6092C-92-D-A303, March 1994.

7. Barry J. Cown and John P. Estrada, "SAF Analysis of Shipboard Directive Antenna Performance and Coupling", Final Technical Report, GMT-9401 and GTRI A-9462, Task NCEE/A303/24-93 &24A-93 (Navy Prime Contract No. N6092C-92-D-A303), January 1995.

8. B. J. Cown and John P. Estrada, "SAF Analysis of Shipboard Antenna Performance, Coupling, and RADHAZ in Complex Near-Field Scattering Environments", IEEE Antennas and Propagation Symposium Proceedings, Newport Beach, CA, June 18-23, 1995, pp. 6-9.

9. B. J. Cown, J. Ch. Bolomey, D. Picard, and J. P. Estrada, "Hybrid Near-Field Measurement/Analysis Technique for Predicting Installed Antenna Performance and Coupling", 1995 URSI Meeting Digest. Newport Beach, CA, June 18-23, 1995, pp. 57

10. Ph. Garreau, B. J. Cown, F. Gallet, *et. al*, "Applicability of Rapid NF Techniques and SAF Numerical Approach to Bistatic RCS", 1995 AMTA Proceedings. Williamsburg, VA, Nov 13-17, 1995, pp 375-380.

11. B. J. Cown, C. D. Papincolopoulos, and R. W. Cravey, "In-Band Antenna Coupling Research", Final Technical Report, Contract CECOM-TR-82-J069-F, June 1986.

12. William B. Gordon, "Far-Field Approximations to the Kirchoff-Helmholtz Representations of Scattered Fields", IEEE Trans. on Antennas and Propagation, July 1975, pp 590-592.

13. L. W. Henderson, "Introduction to PMM, Version 4.0", Technical Report 725347-1, Contract No. SC-SP18-91-0001, July 1993.

14. M. Kerker, The Scattering of Light and Other Electromagnetic Radiation, Academic Press, NY, 1966.

15. B. J. Cown, "SAF Analysis Techniques for Hybrid Composite/Metallic Topsides", GEMTECH IRAD Report No. GMT-9602, June, 1996.

221

FAR FIELD PATTERNS OF COMBINED TE/TM APERTURE DISTRIBUTIONS

Ross A. Speciale

Redondo Beach, California

polytope@msn.com

A recent paper [1] has shown the quite unique properties of a very specific planar aperture distribution, obtained by linearly combining a TE , and a TM cylindrical mode, both having the same amplitude, the same phase, and the same $m = 1$ cylindrical symmetry index.

The two modes are defined in Reference [1] in closed form, on both the $z = 0$ aperture plane, and on the whole $z > 0$ half-space above the aperture, using only Bessel functions J_v of the first kind for the radial dependence.

For a unitary value $m = 1$ of the cylindrical symmetry index, a rigorous expression of the complex Poynting vector shows a) a high concentration of axially radiated power density in an electrically small region of the circular aperture, close to its center, b) a relatively small power density in alternate azimuth directions, around the z-axis, and c) an *identically-zero radial power-flow density*, everywhere in the $z > 0$ half-space.

This quite unique aperture distribution has now been combined with the well-known Hansen's One Parameter Aperture Distribution for Circular Apertures [2], in order to introduce a controlled amount of radial amplitude decay, and a controlled amount of edge-taper, thus obtaining a smooth aperture truncation.

The particular choice of the Hansen's One Parameter Aperture Distribution for Circular Apertures appears most appropriate, as it uses the Bessel function I_0 of the second kind, a circumstance that is expected to lead to the existence of a closed-form expression for the far-field pattern.

The closed-form integration of the resulting, truncated aperture distribution is being performed, by using the very enhanced formal-integration capabilities of Mathematica 3.0 .

The paper presented in session will report both the formal, as well as the quantitative results of this investigation.

REFERENCES.

[1] Speciale R. A. ,"New Results in the Synthesis of Aperture-Field Distributions for Ultra-High Gain Pased Arrays," Proceedings of the 12th Review of Progress in Applied Computational Electromagnetics, Monterey, California, March 18-22, 1996, pages 914-917.

[2] Hansen R. C. ,"A One-Parameter Circular Aperture Distribution with Narrow Beamwidth and Low Sidelobes," IEEE Trans. AP-24, 1976, pp. 477-480 (See also the Handbook of Antenna Design, A. W. Rudge et al. Editors, Chapter 10, pp. 159-161).

Calculation of Equivalent Generator Voltage and Generator Internal Impedance for Cylindrical Antennas in the Receiving Mode

Ching-Chuan Su
Department of Electrical Engineering
National Tsinghua University
Hsinchu, TAIWAN

Abstract— The power absorbed at the load connected to a receiving antenna can be modeled by an equivalent circuit composed of an equivalent generator voltage and an generator internal impedance. In many of the literature the equivalent generator voltage is taken to be the open-circuit voltage and the generator internal impedance is taken to be the input impedance in the transmitting mode. If these are correct, the generator voltage will be uncoupled from the load impedance and the internal impedance uncoupled from both the load impedance and the angle of incidence. In this investigation, these voltages and impedances are computed numerically for cylindrical antennas. From the numerical results, it is found that the aforementioned uncoupling is not correct. While, it is found that the uncoupled-circuit model, where the open-circuit voltage and the input impedance are taken as the generator voltage and the internal impedance, can yield valid results of the load current. The validness of the uncoupled-circuit formula of the load current can be proved by using the reciprocity theorem. Thereby, it is concluded that the uncoupled-circuit model can yield the exactly correct result of the load current, but the open-circuit voltage and the input impedance are not at all identical to the equivalent generator voltage and the generator internal impedance, respectively.

I. Introduction

The complex power P_L absorbed at a load connected to the terminals of a receiving antenna can be modeled by constructing an equivalent circuit, which consists of an equivalent generator with output voltage V_g, an internal impedance Z_g of the equivalent generator, and the load of impedance Z_L. In many of popular antenna books [1]-[4] the Thevenin theorem is used to derive the equivalent generator voltage V_g. Thereby, the equivalent generator voltage V_g is taken to be the open-circuit voltage V_{oc}, the voltage induced between the two terminals of the receiving antenna when the load is removed. Further, the generator internal impedance Z_g is taken to be the input impedance Z_{in} of the same antenna in the transmitting mode. If these two replacements are correct, the equivalent generator voltage will be independent of the load impedance and the generator internal impedance independent of both the load impedance and the angle of incidence.

In this investigation we compute the equivalent generator voltage V_g and the generator internal voltage Z_g numerically for cylindrical antennas in the receiving mode. Then, the dependences of V_g and Z_g on the load impedance and the angle of incidence are examined. From the results, the open-circuit voltage V_{oc} can be determined immediately, since it corresponds to the voltage across the load as the load impedance Z_L approaches infinity. The input impedance Z_{in} of the same antenna in the transmitting mode will also be computed. Then, a direct comparison between V_g and V_{oc} and that between Z_g and Z_{in} can be made. Thereafter, the load current determined in terms of V_g and Z_g is compared with that of V_{oc} and Z_{in}.

II. Equivalent Generator Voltage and Generator Internal Impedance

Under the illumination of an incident electric field $\mathbf{E}^i$, an electric current will be induced over the surface of a receiving antenna and in the load connected to the terminals of the antenna. The induced current will re-radiate a scattered electric field $\mathbf{E}^s$ into the space. It is well-known that the total field $\mathbf{E}$ is equal to the sum of the incident field $\mathbf{E}^i$ and the scattered field $\mathbf{E}^s$. For a lossless antenna the magnitude of the tangential component of the total field is given as

$$E_{\parallel} = \begin{cases} 0 & \text{on } S_{ant} \\ \dfrac{Z_L I_L}{g}, & \text{on } S_{gap} \end{cases} \tag{1}$$

where the subscript $\parallel$ denotes the field component tangential to the surfaces S_{ant} and S_{gap}, S_{ant} is the surface of the antenna. S_{gap} is the surface of the load, I_L is the current induced at the load, and g is the terminal separation. Thus, the complex power P_L absorbed at the load is given as

$$P_L = \frac{1}{2} |I_L|^2 Z_L = \frac{1}{2} \iint_S \mathbf{E}(\mathbf{r}') \cdot \mathbf{J}_s^*(\mathbf{r}') ds', \tag{2}$$

where surface $S = S_{ant} + S_{gap}$ and $\mathbf{J}_s$ is the surface current density induced on the surface S of the receiving antenna and the load.

Since, for an arbitrary but lossless antenna the power delivered to the antenna is equal to the sum of the power absorbed at the load and the re-radiated power. Thus, the complex power P_a delivered from an incident electric field $\mathbf{E}^i$ to the antenna in the receiving mode should be given as

$$P_a = \frac{1}{2} \iint_S \mathbf{E}^i(\mathbf{r}') \cdot \mathbf{J}_s^*(\mathbf{r}') ds'. \tag{3}$$

And, the complex re-radiated power P_s should be given as

$$P_s = -\frac{1}{2} \iint_S \mathbf{E}^s(\mathbf{r}') \cdot \mathbf{J}_s^*(\mathbf{r}') ds', \tag{4}$$

where the scattered electric field $\mathbf{E}^s$ is originated from $\mathbf{J}_s$. Note that the powers P_a, P_s, and P_L are associated with the surface integrals of the inner products of the induced surface current density $\mathbf{J}_s^*$ with the incident field $\mathbf{E}^i$, the scattered field $\mathbf{E}^s$, and the total

field $\mathbf{E}$, respectively. And the power conservation $P_a = P_L + P_s$ is a direct consequence of the relation $\mathbf{E}^i = \mathbf{E} - \mathbf{E}^s$.

In terms of the power P_a delivered to the antenna and the re-radiated power P_s, the equivalent generator voltage V_g and the internal impedance Z_g of the equivalent generator can be defined as

$$V_g = \frac{1}{I_L^*} \iint_S \mathbf{E}^i(\mathbf{r}') \cdot \mathbf{J}_s^*(\mathbf{r}') ds' \tag{5}$$

$$Z_g = -\frac{1}{|I_L|^2} \iint_S \mathbf{E}^s(\mathbf{r}') \cdot \mathbf{J}_s^*(\mathbf{r}') ds'. \tag{6}$$

Then, according to the equivalent circuit or the power conservation relation, the load current I_L is given as

$$I_L = \frac{V_g}{Z_g + Z_L}. \tag{7}$$

III. Formulations and Numerical Procedure

For a z-directed cylindrical antenna of circular shape with radius a and of length ℓ, the z-directed surface current density J_s induced on the receiving antenna under the illumination of an incident electric field $\mathbf{E}^i$ is governed by the integral equation:

$$-jk_0\eta_0 a \int_{-\ell/2}^{\ell/2} \int_0^{2\pi} \left[G(R) + \frac{\partial^2}{k_0^2 \partial z^2} G(R) \right] J_s(\phi', z') d\phi' dz' - 2\pi a J_s(\phi, z) \Re_0(z) = -E_z^i(\phi, z), \tag{8}$$

where Green's function

$$G(R) = \frac{e^{-jk_0 R}}{4\pi R}, \tag{9}$$

distance $R = \sqrt{[2a\sin\frac{1}{2}(\phi - \phi')]^2 + (z - z')^2}$, field $E_z^i = \hat{z} \cdot \mathbf{E}^i$, and $\Re_0(z)$, associated with the load impedance per unit length, is given as

$$\Re_0(z) = \begin{cases} 0 & \text{on } S_{ant} \\ \dfrac{Z_L}{g} & \text{on } S_{gap} \end{cases} \tag{10}$$

If the antenna is thin enough, such that the incident field and the induced current can be deemed as circumferentially uniform, that is, their variations over the azimuthal angle ϕ can be ignored, one has

$$jk_0\eta_0 \frac{1}{2\pi} \int_{-\ell/2}^{\ell/2} \int_0^{2\pi} \left[G(R) + \frac{\partial^2}{k_0^2 \partial z^2} G(R) \right] d\phi' I(z') dz' + \Re_0(z) I(z) = E_z^i(z). \tag{11}$$

Here $R = \sqrt{(2a\sin\frac{1}{2}\phi')^2 + (z - z')^2}$ and $I(z) = 2\pi a J_s(z)$. In the transmitting mode, the governing equation becomes

$$jk_0\eta_0\frac{1}{2\pi}\int_{-\ell/2}^{\ell/2}\int_0^{2\pi}\left[G(R)+\frac{\partial^2}{k_0^2\partial z^2}G(R)\right]d\phi' I(z')dz' = s(z), \qquad (12)$$

where

$$s(z) = \begin{cases} 0 & \text{on } S_{ant} \\ -\dfrac{V_i}{g}. & \text{on } S_{gap} \end{cases} \qquad (13)$$

If the distance R in (12) is approximated as $R = \sqrt{a^2+(z-z')^2}$, the integration over ϕ' just contributes to a factor of 2π. Then, (12) reduces to the well-known Pocklington equation.

To solve the above two integral equations, the antenna cylinder (including the gap) is divided equally into N segments. Then, N pulse functions are used to expand the unknown current distribution $I(z)$ and the point-matching technique is used to render the integral equation into the $N \times N$ matrix equation:

$$\mathbf{Ax = b}, \qquad (14)$$

where $\mathbf{A}$ is a matrix, $\mathbf{x}$ is a vector whose elements are the induced current to be solved, and $\mathbf{b}$ is also a vector corresponding to the incident field or the impressed voltage. In the transmitting mode, the elements b_m of vector $\mathbf{b}$ are given as

$$b_m = \begin{cases} 0 & \text{on } S_{ant} \\ -\dfrac{V_i}{g}; & \text{on } S_{gap} \end{cases} \qquad (15a)$$

and in the receiving mode the elements are given as

$$b_m = E_z^i(z_m), \qquad m = 1, 2, \cdots, N \qquad (15b)$$

where $z_m = (m-\frac{1}{2})\triangle z - \frac{1}{2}\ell$, and $\triangle z = \ell/N$. In (14) the matrix elements $[\mathbf{A}]_{mn}$ are given as

$$[\mathbf{A}]_{mn} = jk_0\eta_0\left[P(|m-n|) + \frac{1}{k_0^2}P_{zz}(|m-n|)\right] + \Re_0(z_m)\delta_{mn}, \qquad (16)$$

where

$$\delta_{mn} = \begin{cases} 1 & m=n \\ 0. & m \neq n \end{cases} \qquad (17)$$

and in the transmitting mode $\Re_0(z_m) = 0$ for all z_m. In (16), P and P_{zz} are given as

$$P(i) = \frac{1}{2\pi}\int_0^{2\pi}\int_{i\triangle z-\triangle z/2}^{i\triangle z+\triangle z/2} G[R(\phi',z')]dz'd\phi' \qquad (18)$$

$$P_{zz}(i) = \frac{1}{2\pi}\int_0^{2\pi}\left\{G_z[R(\phi',i\triangle z+\frac{1}{2}\triangle z)] - G_z[R(\phi',i\triangle z-\frac{1}{2}\triangle z)]\right\}d\phi'. \qquad (19)$$

where

$$G_z[R(\phi',z')] = \frac{\partial G[R(\phi',z')]}{\partial z'} = G(R)\left(-jk_0 - \frac{1}{R}\right)\frac{z'}{R}, \qquad (20)$$

and $R(\phi',z') = \sqrt{(2a\sin\frac{1}{2}\phi')^2 + z'^2}$. Numerical integration was used to evaluate the $P(i)$ and $P_{zz}(i)$ by dividing each cylinder segment into even smaller subdivisions in both ϕ and z directions. For the self-term $P(0)$, singularity was encountered. However, this singularity is integrable. In the numerical integration of the self-term $P(0)$ over the subdivisions in ϕ and z, the subdivision containing the singular term is removed. Accordingly, its contribution κ to the integral is evaluated analytically by approximating the subdivision by a planar circular disk of radius ξ, where $\pi\xi^2$ is equal to the area of the subdivision. Thereby, it can be shown that

$$\kappa = \frac{1}{2\pi a}\frac{1 - e^{-jk_0\xi}}{j2k_0}. \qquad (21)$$

Numerical results indicate that subdivision of an elongated shape may lead to poorer accuracy. Thus, the subdivision is chosen to be close to a square. The proposed numerical procedure can be generalized to a lossy cylindrical antenna in both the transmitting and the receiving modes. For this the values of $\Re_0(z_m)$ on S_{ant} in (16) are replaced with the resistance per unit length along the antenna.

IV. Numerical Demonstration
The component of incident electric field tangential to the antenna is given as

$$E_z^i(z_m) = \sin\theta_i e^{jk_0\cos\theta_i z_m}, \qquad (22)$$

where θ_i denotes the angle of incidence as measured from the z axis. Based on the computed distributions of current induced on the receiving antenna, the equivalent generator voltage V_g is calculated according to (5) by numerical integration. And the generator internal impedance Z_g defined by (6) is calculated simply by $Z_g = V_g/I_L - Z_L$.

A. Generator Voltage and Internal Impedance
The dependences of V_g (amplitude and phase angle) and Z_g (real and imaginary parts) on the incident angle θ_i and the load impedance Z_L are shown on Tables I and II, respectively. It is seen definitely that V_g and Z_g do depend on θ_i and Z_L. When the load impedance is high enough, V_g and Z_g grow linearly and quadratically with Z_L, respectively. This is due to that the load current decreases inversely with a high load impedance.

To compare the internal impedance with the input impedance, the Z_{in} of the same antenna in the transmitting mode was also computed. The result of input impedance is $Z_{in} = (104.3 + j42.90)\ \Omega$. It is seen that the result of Z_{in} disagrees with all the results of the generator internal impedance Z_g listed on Tables I and II.

The open-circuit voltage V_{oc} can be replaced by the voltage V_L $(= Z_L I_L)$ across the load when the load impedance is high enough. In this investigation, the impedance is chosen to

227

be as high as $10^6\ \Omega$. For higher load resistances, no substantial variation in the calculated value of V_L was observed. The calculated results of V_{oc} for various incident angle θ_i are listed in Table III. Again, all the calculated results of the open-circuit voltage V_{oc} disagree with those of the corresponding equivalent generator voltage V_g listed on Table I.

B. Load Current

The results of the load current I_L for various loading conditions are listed on Table IV. These results of I_L are just picked up from the solutions of induced current at the loading point. While, the current I'_L determined by the uncoupled-circuit model, where the generator voltage V_g in (7) is taken to be the open-circuit voltage V_{oc} and the internal impedance Z_g to be the input impedance Z_{in} in the transmitting mode, is calculated according to

$$I'_L = \frac{V_{oc}}{Z_{in} + Z_L}. \tag{23}$$

The results of this current are listed on the last column in Table IV. By comparing the results of current I'_L with those of the load current I_L, it is seen that, except for some small discrepancies,

$$I'_L = I_L \tag{24}$$

over various loading conditions. The above equality can be shown to be true [5] and hence the small discrepancies are just numerical errors. Thus, the current determined by using the uncoupled-circuit model is actually identical to the load current, although V_g and Z_g are not identical to V_{oc} and Z_{in}, respectively.

V. Conclusion

From the numerical results, it is apparently seen that the equivalent generator voltage V_g and the generator internal impedance Z_g do depend on the incident angle θ_i and the load impedance Z_L. Qualitatively speaking, V_g and Z_g suffer a loading effect, that is, their values depend on the load impedance. Whereas, V_{oc} corresponds to an infinite load impedance and Z_{in} has nothing to do with the load impedance. Further, Z_{in} has nothing to do with the incident angle. Thus, V_g and Z_g can not be V_{oc} and Z_{in}, respectively. In other words, the open-circuit voltage V_{oc} does not correspond to the power delivered to a receiving antenna and the input impedance Z_{in} does not correspond to the re-radiated power from that receiving antenna.

However, the numerical results indicate that the uncoupled-circuit model, where V_g is replaced with V_{oc} and Z_g with Z_{in}, can yield correct result of load current. The validiness of the uncoupled-circuit formula of load current cab be proved rigorously by using the reciprocity theorem. Based on these, we can state that the two replacements in the uncoupled-circuit model together can yield the exactly correct result of the load current, but each individual replacement itself is not correct, physically or quantitatively.

References

[1] S. Silver, "Circuit relations, reciprocity theorems." in *Microwave Antenna Theory and Design*, S. Silver, Ed. New York: McGraw-Hill, 1949, ch. 2.

[2] R.E. Collin, *Antennas and Radiowave Propagation*. New York: McGraw-Hill, 1985, ch. 5.

[3] D.H. Staelin, A.W. Morgenthaler, and J.A. Kong, *Electromagnetic Waves*. Englewood Cliffs: Prentice-Hall, 1994, ch. 9.

[4] S. Ramo, J.R. Whinnery, and T. Van Duzer, *Fields and Waves in Communication Electronics*, 3rd ed. New York: Wiley, 1994, ch. 12.

[5] C.C. Su, "On the Equivalent Generator Voltage and Generator Internal Impedance for Antennas in the Receiving Mode," submitted for publication.

Table I The Equivalent Generator Voltage V_g and the Generator Internal Impedance Z_g as Functions of the Incident Angle θ_i in Degree for a Center-Loaded Cylindrical Antenna of Length $\ell = 0.5\lambda$ and Radius $a = 0.005\lambda$. The Load Impedance $Z_L = 100\ \Omega$.

θ_i	V_g (in V)	Z_g (in Ω)
10	$0.0456\ \angle -22.02°$	$88.03 + j\ 5.34$
20	$0.0921\ \angle -21.08°$	$87.84 + j\ 8.74$
30	$0.1399\ \angle -19.75°$	$87.56 + j13.63$
40	$0.1886\ \angle -18.24°$	$87.24 + j19.14$
50	$0.2364\ \angle -16.79°$	$86.91 + j24.49$
60	$0.2802\ \angle -15.56°$	$86.62 + j29.08$
70	$0.3158\ \angle -14.64°$	$86.39 + j32.54$
80	$0.3393\ \angle -14.08°$	$86.25 + j34.67$
90	$0.3475\ \angle -13.89°$	$86.20 + j35.39$

Table II The Equivalent Generator Voltage V_g and the Generator Internal Impedance Z_g as Functions of the Load Impedance Z_L for the Cylindrical Antenna in Table I. The Incident Angle $\theta_i = 90°$.

Z_L (in Ω)	V_g	Z_g
1	$0.3376 \angle - 0.32°$	$81.50 + j57.01$
10	$0.3377 \angle - 1.58°$	$81.55 + j56.75$
100	$0.3475 \angle - 13.89°$	$86.20 + j35.39$
1 000	$0.8903 \angle - 67.89°$	$0.5519 \times 10^3 - j0.2050 \times 10^4$
10 000	$8.245 \angle - 87.83°$	$0.4712 \times 10^5 - j0.2101 \times 10^6$
100 000	$82.38 \angle - 89.94°$	$0.4703 \times 10^7 - j0.2101 \times 10^8$

Table III The Open-Circuit Voltage V_{oc} as a Function of the Incident Angle θ_i for the Cylindrical Antenna in Table I.

θ_i	V_{oc} (in V)
10	$0.0506 \angle - 11.79°$
20	$0.1022 \angle - 11.89°$
30	$0.1553 \angle - 12.04°$
40	$0.2092 \angle - 12.22°$
50	$0.2618 \angle - 12.40°$
60	$0.3096 \angle - 12.56°$
70	$0.3484 \angle - 12.69°$
80	$0.3738 \angle - 12.77°$
90	$0.3826 \angle - 12.80°$

Table IV The Load Currents I_L and I'_L as Functions of the Load Impedance Z_L for the Cylindrical Antenna in Table I. The Incident Angle $\theta_i = 90°$.

Z_L (in Ω)	I_L (in A)	I'_L
1	$0.3366 \times 10^{-2} \angle - 34.96°$	$0.3367 \times 10^{-2} \angle - 34.96°$
10	$0.3135 \times 10^{-2} \angle - 33.37°$	$0.3135 \times 10^{-2} \angle - 33.37°$
100	$0.1833 \times 10^{-2} \angle - 24.65°$	$0.1833 \times 10^{-2} \angle - 24.65°$
1 000	$0.3463 \times 10^{-3} \angle - 15.02°$	$0.3463 \times 10^{-3} \angle - 15.01°$
10 000	$0.3787 \times 10^{-4} \angle - 13.04°$	$0.3787 \times 10^{-4} \angle - 13.03°$
100 000	$0.3823 \times 10^{-5} \angle - 12.82°$	$0.3823 \times 10^{-5} \angle - 12.81°$

ARRAYS OF SLEEVED MONOPOLES - COMPUTER CODE

Boris Tomasic*
Rome Laboratory/ERA
31 Grenier st., Hanscom AFB, MA 01731

Edward Cohen
ARCON Corporation
260 Bear Hill Rd., Waltham, MA 02154

Kondagunta Sivaprasad
University of New Hampshire
Dept. of El. Eng. and Comp. Eng., Durham, NH 03824

ABSTRACT

Arrays of sleeved monopoles have very good off-broadside characteristics and so they can be used for such applications as the Over-The-Horizon (OTH) Radar. We developed an accurate analysis and computer codes for arrays of arbitrarily spaced sleeved monopole elements. The analysis treats the sleeved monopoles in an array environment and takes into account the actual feed configuration. With such codes, a high performance array can be designed by simulation, thereby avoiding a costly iterative experimental procedure.

INTRODUCTION

The analysis of the array of sleeved monopoles and the array design tradeoffs were discussed and reported in [1]. In this paper, after a brief overview of the analysis, emphasis will be placed on computational techniques used, along with a description of the user-friendly computer codes.

Three versions of code were developed from a Galerkin solution procedure for monopole currents: 1) a dense matrix code based on cosine expansion and test functions; 2) a dense matrix code based on roof-top basis and test functions; and 3) a sparse matrix code specifically tailored to very large arrays. Both 1) and 2) are for small and medium size arrays. Version 3) employs a sparse matrix approximation that yields results which are virtually indistinguishable from the full matrix codes, but requires sugnificantly less matrix fill and solve times. The computer code architectures and block diagrams are also presented.

The theory and codes were validated against a simple experiment consisting of a 3-element array. Typical simulated results for active admittance, element patterns and scattering (coupling) coefficients are compared with measured data and given in [2]. In this paper we present some typical results for 31-element and 101-element linear arrays.

ANALYSIS - AN OVERVIEW

Fig. 1 shows the array element under consideration. It consists of a vertically extended inner conductor (probe) of height L and radius a, and an outer conductor (sleeve) of height ℓ with inner and outer radii b and c, respectively. The identical feed lines have the characteristic admittance Y_c and are filled with a dielectric material of relative permittivity ϵ_r. The top view of the array is shown in Fig. 2. The total number of array elements is N, with m denoting the reference element.

Since $a \ll \lambda$ and $c \ll \lambda$, it is assumed that the probe and sleeve currents have only an axial component and no angular variation. Furthermore, it is assumed that the field distribution in each coaxial aperture is that of the coaxial feed-line TEM mode. An integral equation is formulated for the unknown probe and sleeve current distributions by requiring that the total tangential electric field vanishes on the reference monopole surface. The tangential field is produced by currents on the m-th reference element (self term) and currents on the rest of the array elements (coupling terms). The procedure is carried out in the following steps:

1. All elements are excited with aperture voltages $V_n = |V_n| \exp(j\phi_n)$. $n = 1, 2, \ldots, m, \ldots, N$.

2. In view of the equivalence principle, we close the coaxial aperture with a perfect conductor. The problem is now divided into two parts, one for the internal and the other for the external region. In the external region, at $z = \ell$, the coaxial TEM aperture electric fields are replaced by magnetic current frills $M_{\phi m}$.

3. Expressions are obtained for $E_z^0(\rho, z)$, $E_\rho^0(\rho, z)$ and $H_\phi^0(\rho, z)$ due to a probe current $J_z^p(a, z)$, sleeve current $J_z^s(c, z)$, annulus current $J_\rho^a(\rho, z = \ell)$ and magnetic frill $M_\phi(\rho, z = \ell)$ of a single (isolated) monopole.

4. The total E_{zm}^p on the probe of the reference element is then obtained by summing the contributions from the element itself and the rest of the array elements, and can be written as

$$E_{zm}(a, z) = E_{zm}^0(a, z)) + \sum_{\substack{n = 1 \\ n \neq m}}^{N} E_{zn}^0(|\,\boldsymbol{\rho}_m - \boldsymbol{\rho}_n + \mathbf{a}\,|, z). \tag{1}$$

5. In order to apply the boundary conditions on the reference probe, the Addition Theorem for Hankel functions is used,

$$H_0^{(2)}(\kappa\,|\,\boldsymbol{\rho}_m - \boldsymbol{\rho}_n + \mathbf{a}\,|) \simeq J_0(\kappa a) H_0^{(2)}(\kappa R_{mn}), \tag{2a}$$

$$R_{mn} = |\,\boldsymbol{\rho}_m - \boldsymbol{\rho}_n\,|, \tag{2b}$$

the field E_{zn}^0 is expanded about a cylindrical axis at the reference element. Following the procedure indicated in steps 3 and 4, total fields $E_{zm}(c, z)$ on the sleeve and $E_{\rho m}(\rho, z = \ell)$ in the annulus are obtained.

6. To determine the external currents **J**, we impose the boundary conditions that the total tangential electric field vanishes on the surface of the reference monopole, i.e.,

$$E_t(\mathbf{J}, \mathbf{M}) = 0, \quad \text{on} \quad S \tag{3}$$

where $m = 1, 2, \ldots, N$ and **M** are the known magnetic frill currents. This can be written as:

$$\mathbf{E}_{tm}^0(\mathbf{J}_m) + \sum_{\substack{n=1 \\ n \neq m}}^{N} \mathbf{E}_{tn}^0(\mathbf{J}_n) = -\mathbf{E}_{tm}^0(M_{\phi m}) - \sum_{\substack{n=1 \\ n \neq m}}^{N} \mathbf{E}_{tn}^0(M_{\phi n}) \tag{4}$$

which is an integral equation for the determination of the electric currents $\mathbf{J}_m$ and $\mathbf{J}_n$.

7. Eq. (4) is now solved by the method of moments (MoM). To that end, the monopole electric current on the n-th element is expanded in the following series:

$$\mathbf{J}_n = \sum_{j=1}^{I} c_n^j \psi_j \quad n = 1, 2, \ldots, m, \ldots, N. \tag{5}$$

Two different expansion functions, (ψ_j), for the unknown currents are used: the entire domain cosine functions and the roof top functions.

8. Substituting (5) into (4), and using the Galerkin procedure yields a set of linear inhomogeneous equations for the determination of the expansion coefficients, c_n^j, of the unknown probe and sleeve currents. The system of equations can be conveniently written in a block matrix form as follows:

$$[\underline{\mathbf{A}}_{mn}] \, [\mathbf{C_n}] = [\mathbf{B_m}]\mathbf{V} \tag{8a}$$

where

$$\underline{\mathbf{A}}_{mn} = [a_{mn}^{ij}] \tag{8b}$$

$$\mathbf{C_n} = [c_n^j] \tag{8c}$$

$$\mathbf{B_m} = [b_{mn}^i] \tag{8d}$$

$$\mathbf{V} = [V_n]. \tag{8e}$$

where $[\underline{\mathbf{A}}_{mn}]$ is an $N \times N$ block matrix (each block or submatrix contains $I \times I$ elements) representing the interaction between elements m and n, $[\mathbf{C_n}]$ is block column vector (each block of size I) representing the unknown expansion coefficients, $\mathbf{B_m}$ is also a block column matrix whose elements (blocks) are the $I \times N$ submatrices, and $\mathbf{V}$ is the excitation vector.

9. Once the probe and sleeve currents have been found, the total magnetic field $H_\phi(\rho, z = 0^+)$ in the aperture of the reference element is determined following the procedure indicated in steps 3 and 4.

10. Imposing continuity of $H_\phi(\rho, z = 0)$ across the coaxial aperture of the reference element, we obtained expressions for active admittance, active reflection coefficient, array scattering

parameters (coupling coefficients), element gain, radiation pattern, and other array characteristics. The details of the derivation are given in [2].

NUMERICAL ANALYSIS

The core of the numerical analysis work involved the evaluation of matrix element integrals in (8a). As already mentioned, two types of basis and test functions were (separately) used, cosine (entire domain) functions and roof-top functions. In both cases, the k_z-integrals defining the matrix elements were evaluated along the same path in the complex plane, and in the same manner using both real-axis and arc integrations around the same singularities. By having programs based on two different solution methods, one could also expect to discern any glaring discrepancy between their calculated final results and also point the way for correction of any analysis or programming errors. Both programs produced practically identical results. We noticed that the 30 term roof function program calculated the current at the feed point ($z = \ell$) slightly more accurately than the equivalent cosine expansion. Although both codes produced very accurate results, the computational time, for large arrays, was very high. For example for a 30-element array, using 10 current terms, the computational time on Sun SPARC station 10 was obout one day. Because of that, for the study of large arrays, we developed a more efficient method for creating the left- and right-hand side Galerkin matrices, $\underline{\mathbf{A}}$, and $\underline{\mathbf{B}}$, respectively. Only cosine basis and test functions were used in this code development. The method is based on matrix sparsification procedure, and is described below.

To that end, it is important to note that the coupling between the two elements spaced farthest apart, say element m and n in a large array, is relatively small (-50 dB for example). Because of that, interaction between current modes on element m and current modes on element n can be approximated by the interaction between their dominant modes only. In other words, all elements in submatrix $\underline{\mathbf{A}}_{\mathrm{mn}}$ are set to zero except the first one, a_{mn}^{11}. The magnitude of this element is used as a threshold. All elements in other submatrices with smaller magnitudes were then also set to zero. This simple procedure generates sparse, off-diagonal submatrices that require considerably less fill-time than for the full, dense matrix situation. In this fashion, the direct interaction of each monopole on every other is optimally taken into consideration to some extent. Fig. 3 depicts a sparse matrix structure resulting from this procedure. The resulting sparse matrix system was then solved using an IMSL sparse solver. The sparse matrix filled only about 5 % of the total matix elements. In addition, the sparse matrix solver was much faster than dense matrix solver. The results from the sparse matrix codes and full-dense matrix codes were compared on a 31-element linear array case. Practically identical results were obtained from both codes.

COMPUTER CODE

A FORTRAN computer code was generated for evaluation of active admittance, scattering (coupling) coefficients and the far-field patterns. Three versions of the code were developed: 1) a dense matrix code based on cosine expansion and test functions; 2) a dense matrix code based on roof-top basis and test functions; and 3) a sparse matrix code specifically tailored to very large arrays. In addition, each of these codes comes with graphics (IMSL) and without a graphics package. For convenience these code versions are schematically shown in Fig. 4.

234

The program flow chart is given in Fig. 5. In NAMELIST we input element geometry and options. In file xyvv.f we define array geometry and excitation. Program xx.f computes $\underline{\mathbf{A}}$ and $\underline{\mathbf{B}}$ matrices. The results are dumped into xx.res ABDATA files. The program yy.f inverts the matrix $\underline{\mathbf{A}}$, and computes scattering matrix and other array parameters. The file yy.res stores numerical results. The results can be also presented graphically and interactively on the screen. Input and output program capabilities and corresponding flow charts will be described at the presentation.

NUMERICAL RESULTS FOR A LARGE ARRAY

Fig. 6 shows the end element gain pattern - $G_1(\theta, \phi = 0^0)$ of a 31-element linear array. The element dimensions are: $L = 0.750$", $\ell = 0.250$", $a = 0.025$", $b = 0.081$", $c = 0.090$", and $\epsilon_r = 2.0$. The array element spacing is $d/\lambda = 0.5$ at $f = 3.7GHz$. In MoM we used a 15 term cosine expansion. Computations were performed with sparse matrix code. The sparse matrix filled about 5.3 % of the total matrix elements. Identical results were obtained with the dense matrix code which was roughly 10 times slower. For the same array, Fig. 7 shows the magnitude of the coupling coefficients $\mid S_{1n} \mid$ vs. element serial number. Notice that the coupling between two end elements is approximately -40 dB. More results on this array and the larger, 101-element array, will be given at the presentation.

REFERENCES

[1] B. Tomasic, E. Cohen, and K. Sivaprasad, "Large Array of Sleeved Monopoles," IEEE AP-S Int. Symposium, Seattle, Washington, June 1994, pp. 502-505.

[2] B. Tomasic, E. Cohen, and K. Sivaprasad, "Large Array of Sleeved Monopoles," RL Technical Report, in publication.
For info. Tel.: (617) 377-2055, e-mail:tomasic@bessel.rl.plh.af.mil .
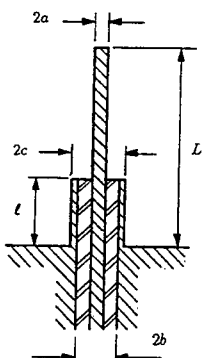
Fig. 1 Monopole array element
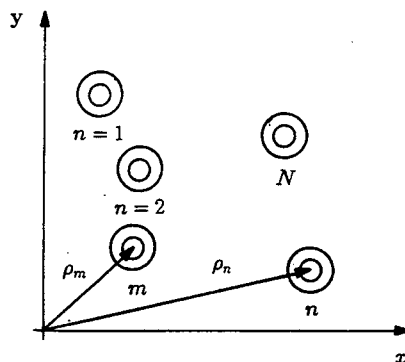
Fig. 2 Top view of the array
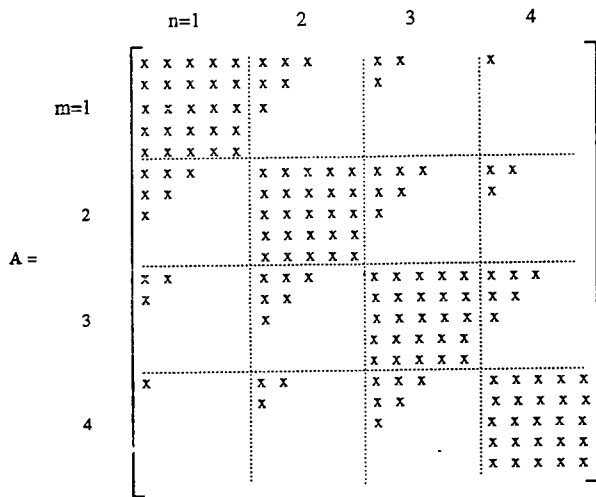
Fig. 3 Sparse matrix structure, N=4, I=5
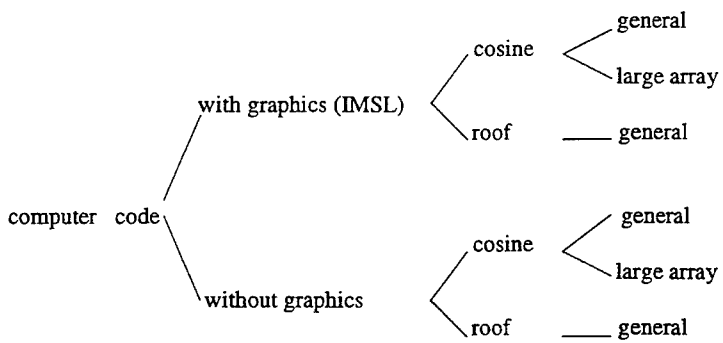
Fig. 4 Computer code versions
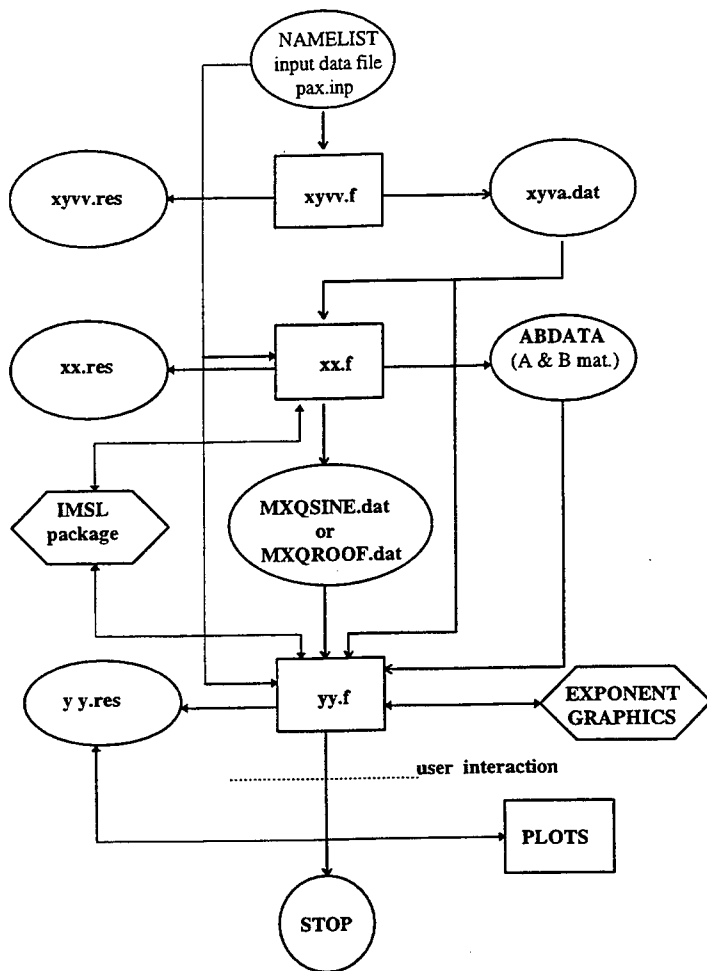
Fig. 5 Program flow chart
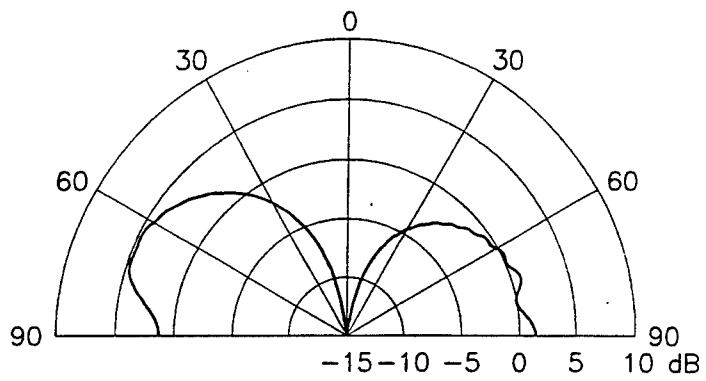
Fig. 6 Element gain pattern $G_1(\theta, \phi = 0^0)$, $N = 31$
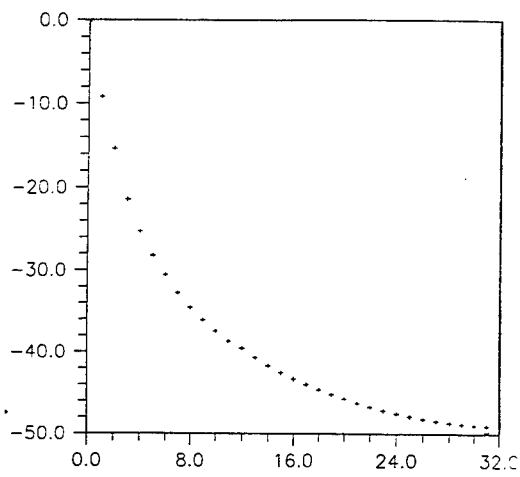
Fig. 7 Coupling coefficients $| S_{1n} |$ vs. n

SESSION 5:

RADIATION PHYSICS

Chairs: E.K. Miller and R. Bevensee

AN EXPLORATION OF RADIATION PHYSICS IN ELECTROMAGNETICS

E. K. Miller

3225 Calle Celestial, Santa Fe, NM 87501-9613

505-820-7371, emiller@esa.lanl.gov

0.0 ABSTRACT

All external electromagnetics (EM) originate from the process of radiation. There would be no radiated, propagated or scattered fields were it not for this phenomenon. In spite of this self-evident truth, our understanding of how and why radiation occurs is relatively superficial at both a fundamental and practical level. It's true that mathematical analysis shows radiation occurs due to charge acceleration. It's also true that the we are able to solve for the near and far fields of rather complex objects subject to arbitrary excitation and can thus analyze and design EM systems. However, for example, if the problem is to determine the spatial distribution of radiation over the surface of a conducting body, a solution becomes less obvious. Either this particular problem has no answer, or it has eluded us, possibly because it hasn't been found necessary for most applications. Whatever the reason for this situation, it seems undeniable that knowing where radiation originates is worth knowing, if for no other reason than acquiring a better understanding of EM physics.

A conceptual way to think about this problem could be to ask, were our eyes sensitive to X-band frequencies and capable of resolving source distributions a few wavelengths in extent, what kind of image would such simple objects as dipoles, circular loops, conical spirals, log-periodic structures, continuous conducting surfaces, etc. present when excited as antennas or scatterers? Various kinds of measurements, analyses and computations have been made over the years that bear on this question. This presentation will summarize some relevant observations concerning radiation physics in both the time and frequency domains for a variety of observables. While it may not be possible to provide a quantitative recipe that permits direction computation of a radiation image from a source distribution obtained from a numerical model, a variety of qualitative statements can be made that bear on this question. Note that not all of the observations made here are necessarily rigorously provable, representing the author's belief about possibly debatable points.

2.0 BACKGROUND

It is a physical fact that the $1/r$ components of the electric and magnetic fields produced by a source distribution, i.e., the so-called far or radiation fields because their Poynting's vector falls as $1/r^2$ to maintain a constant total power flow over a sphere of radius R, are due solely to accelerated charge. The Lienard-Wiechert potentials show explicitly that accelerated charge alone produces a $1/r$ field [Panofsky and Phillips (1956)]. Thus, with the charge velocity given by $\mathbf{u}$ and $\mathbf{r}$ the observation vector to its retarded position, the electric field of a point charge e can be written as

$$\mathbf{E} = \frac{e}{4\pi\varepsilon_0}\left[\frac{1}{s^3}\left(\mathbf{r} - \frac{r\mathbf{u}}{c}\right)\left(1 - \frac{u^2}{c^2}\right) + \frac{1}{c^2 s^3}\left\{\mathbf{r}\times\left[\left(\mathbf{r} - \frac{r\mathbf{u}}{c}\right)\times\frac{d\mathbf{u}}{dt'}\right]\right\}\right],$$

where

$$s = r - (\mathbf{u}\cdot\mathbf{r})/c, \tag{1}$$

where the differentiation is with respect to retarded time t' and c is the speed of light. The magnetic field is obtained as

240

$$\mathbf{B} = \mathbf{r} \mathbf{x} \mathbf{E}/rc. \tag{2}$$

It can be seen in (1) that taking the limit $r \text{---} > \infty$ of r|E|, only the charge-acceleration term, du/dt', remains, which means acceleration alone contributes to the radiation field.

However, charge acceleration need never be dealt with in the majority of EM analysis, unless one seeks specifically to account for radiation in more physical terms. Indeed, if the question "What causes radiation?" is put to a typical EM student, the typical answer tends to focus on current, being something like "Current causes radiation." While this answer can be accepted as not being incorrect, at least superficially, it doesn't really get to the fundamental cause of radiation. Without moving charge, there is no conduction current, and without charge motion or the onset of motion, there can be no acceleration (the term 'acceleration' is used here whatever the sign of the velocity change). Current inextricably involves charge motion, but the presence or not of accelerated charge associated with that current may be less obvious.

In any case, it seems that we should look for accelerated charge in our solutions as providing the radiation component. This may also not be as easy as it first appears to be. Places where charge acceleration occurs on a simple dipole antenna may be fairly obvious after a little thought; at the ends where the current goes to zero because of charge reflection and at the feedpoint where the excitation sets the charge into motion. It may also appear that charge is accelerated along the entire length of the antenna since the current varies periodically both in time and direction all along its length. But if the charge is accelerated everywhere, why then doesn't the total power radiated from a time-harmonic, spatially sinusoidal current filament (SCF) increase linearly with length rather than about a mean value that grows as the log of the length (shown below)? This seems to imply that not all parts of that sinusoid are radiating equally. On the other hand, if all of the current isn't radiating, is it then necessary to integrate over all of it to obtain the radiated power? A more careful examination of radiation from the SCF is considered next.

2.0 RADIATION FROM A SINUSOIDAL CURRENT FILAMENT
Because its far field and radiated power are analytically available, and it well-approximates the actual current on a thin-wire antenna, it's instructive to examine the far field radiated by the SCF of length L

$$I(z) = I_0 \sin(\omega t)\sin[k(L/2 - |z|)], \quad -L/2 \le z \le L/2 \tag{3}$$

for which the far field is given by

$$E_\theta \approx K_1 I_0 [\exp(ikL\cos(\theta)/2 + \exp(-ikL\cos(\theta)/2 - 2\cos(kL/2)]\exp(-ikr_0)/[r_0\sin(\theta)]$$
$$= K_1 I_0 \{\cos[kL\cos(\theta)/2] - \cos(kL/2)\}\exp(-ikr_0)/[r_0\sin(\theta)]. \tag{4}$$

where $K_1 = j\eta/(2\pi)$, with η the medium wave impedance, and an $\exp(j\omega t)$ time dependence is assumed. Note that (4) consists of three point sources radiating spherical waves, located at $z = \pm L/2$ and $z = 0$, respectively, except for the $\sin(\theta)$ term in the denominator. The presence of this latter term, however, significantly alters the situation, as can be seen in the expression for the total radiated power

$$P_{rad} = (\eta/4\pi)|I_0|^2\{C + \ln(kL) - C_i(kL) + 0.5\sin(kL)[S_i(2kL) - 2S_i(kL)] \tag{5}$$
$$+ 0.5\cos(kL)[C + \ln(kL/2) + C_i(2kL) - 2C_i(kL)]\}$$

where C is Euler's constant, C_i and S_i are the cosine and sine integrals and η is the medium impedance [Balanis (1982)]. The various non oscillatory contributions in Eq. (5), including terms containing $\ln(kL)$, indicate that there must be some radiation mechanism besides a simple three-point-source model also at work. This is discussed further below.

2.1 Radiation from a Sinusoid and Constant Current Compared

If radiation were correctly to be simply attributable to current, then it seems reasonable to expect that as the amount of current increases, e.g., as a filament gets longer, the radiated power would increase proportionally. This is not evident in Eq. (5) nor from numerical evaluation of P_{rad} which produces the results plotted in Fig. 1 for a filament 0 to 2 and 49 to 51 wavelengths long. The mean of the radiated power is seen to increase only very slowly at large values of L, while its L-dependence is more pronounced for the smaller-L range. Clearly, however, the radiated power is not linearly dependent on L over the entire length-range shown, but does, it turns out, exhibit an average trend proportional to log(kL).

It's interesting to compare the radiated power produced by a SCF with that from a spatially uniform or constant current, also plotted in Fig. 1 [Miller (1996a)]. In contrast to the sinusoid, the power radiated by the constant current increases linearly with length. It seems, perhaps not surprising given their different spatial characteristics, that the constant current must embody different charge-acceleration properties from that of the sinusoid, one explanation being that to produce a constant current requires a spatially distributed exciting field as further discussed by Miller (1996b).
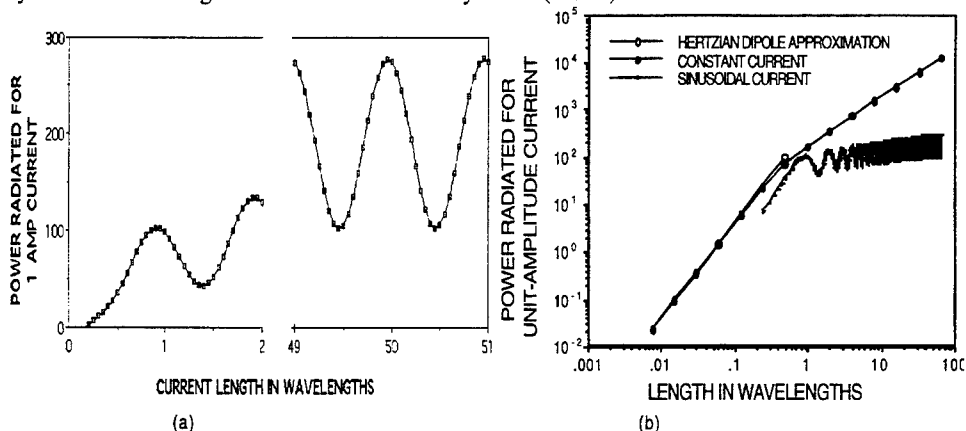
Figure 1. Power radiated by a unit-amplitude sinusoidal current filament of length L in wavelengths for the range L = 0 to 2 and 49 to 51 (a) and power radiated by a unit-amplitude constant current compared with that of a sinusoid as a function of current length (b). The constant current at first exhibits the well-known dependence on length squared up to about 0.5 wavelengths where it changes to a linear dependence. The sinusoid radiated power exhibits an oscillatory behavior with a logarithmic trend.

2.2 Oscillating Current and Accelerated Charge

Returning to the fundamental observation that accelerated charge causes radiation, it would seem to follow that the average total amount of accelerated charge associated with the SCF somehow grows only as log(kL) rather than as L. If this is true, then it must also follow that the oscillating charge which superficially seems to accompany an oscillating current is not necessarily itself accelerating, since otherwise a different L-dependence of radiated power would result with increasing length of the SCF. But how can a charge oscillate and not be accelerated?

The answer seems to be that the standing current wave of which the SCF is comprised, can also be written as the sum of two oppositely propagating traveling waves initiated at the driving point or source, here taken to be z = 0. In Eq. (1), these current/charge waves are implicitly assumed to be propagating at a constant value c, the speed of light, so that the wavelength = c/frequency. From this viewpoint, there is no charge acceleration along the filament, but only at its ends where reflected waves are produced. These in turn propagate towards the opposite ends of the filament, where they reflect again. A length-dependent reflection can also occur at the source, as determined by the degree of current-slope discontinuity that exists there due to a localized excitation. This latter effect evidently accounts for the

oscillation of the radiated power as a function of length [Miller (1996b)].

The reason for the radiated power depending also on log(kL) is less obvious, but may be explained as follows. First, let's examine the in-phase electric field parallel to the current filament (the quadrature field is reasonably similar to this). This field is plotted in Fig. 2a at a distance of 10^{-6} wavelengths (an arbitrary distance, but chosen as representative of a thin wire) from the axis of a filament 20 wavelengths long. Although a purely SCF is known to provide a reasonably good approximation for computing the far field of a wire antenna, it's clear from this plot that its near-field does not yield a good result for the $E_{tan} = 0$ boundary condition required on the surface of a perfect conductor.

(a) In-phase tangential electric field   (b) Differential power for filament
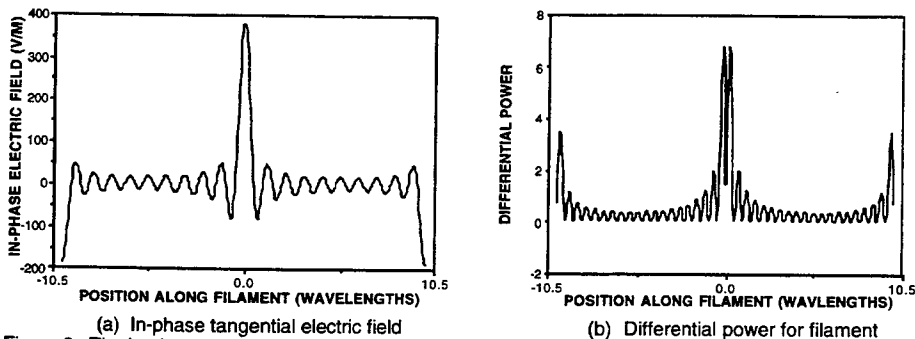
Figure 2. The in-phase, parallel electric field produced by a 20-wavelength, sinusoidal current filament at a distance of 10^{-6} wavelengths from its axis (a). As is expected, the field is largest at the ends of the filament, and also at the midpoint of a magnitude dependent on the degree of current-slope discontinuity that exists there. Whether the midpoint field is positive or negative (or zero) depends on whether the filament is an even or odd (or half-integer) number of wavelengths long. The differential power for a 20-wavelength, sinusoidal current filament (b), is obtained from $0.5Re[E_{tan}(z)I^*(z)]$. By examining other lengths [Miller (1996b)], it's found that the end contribution is basically independent of filament length whereas that from the center changes systematically with length and is responsible for the oscillation seen in the total radiated power. The differential power away from these two regions is inversely proportional to distance from the end and/or center, accounting for the log(kL) dependence of the mean power.

What this [and similar field plots in Miller (1996b)] demonstrates is that for a purely sinusoidal current to be excited on a perfectly conducting, thin wire, solved as a boundary-value problem, single-point excitation would not suffice. Rather, the excitation would have to be distributed along the entire length of the wire so as to cancel the complex tangential electric (scattered) field produced by the sinusoidal current. Thus, power would be provided to the antenna all along its length as well, with the ends and center "feedpoint" apparently the regions where most of the source power would be delivered. Since an applied field causes charge acceleration we might expect that the sinusoidal current would radiate along its length in an analogous fashion.

It's possible to evaluate the input power needed to produce a sinusoidal current on an actual wire having a radius equal to the field offset from the filament axis by computing the integral of the differential power along the filament, a computation that also yields the radiated power. This is the induced EMF method that was widely used before computer models for such problems were available. It required a "reasonable" approximation for the current from which $E_{tan}(z)$ could be obtained and the integral thus performed. This can be regarded as a generalization of the special case where the tangential electric field due to the induced current is zero everywhere along a wire except in the feed region where the wire is excited and where the input power can be obtained from $0.5Re[V_{ex}I^*]$.

In order to illustrate the spatial characteristics of the power flow associated with the SCF, a plot of

$0.5\text{Re}[E_{tan}(z)I*(z)]dz$, the differential, or per-unit-length power, is included in Fig. 2, for the same 20-wavelength filament. The end contributions for this case is within 1% or so of those obtained for filaments varying between 20 and 21 wavelengths, about 3.4 watts/wavelength. The constancy of the end contribution seems reasonable, in that an end-reflected unit-amplitude wave can be expected to generate a fixed amount of power regardless of the filament length. The primary length dependence is due to the degree to which power is provided at the midpoint region, and to a lesser extent in the region between the midpoint and the ends.

The origin for the log(kL) dependence of the mean power in Eq. (5) is apparent from Fig. 2. It can be observed there (and confirmed from the numerical data and the analytical field expressions) that the differential power decreases inversely proportional to distance from the ends and center of the filament. Since integrating dx/x produces log(x), the log(kL) terms in the radiated-power expression seem to come from this contribution. Thus, a simple sinusoid must radiate appreciably along its entire length. Note that the integral of $0.5\text{Re}[E_{tan}(z)I*(z)]$ along the filament agrees to within 5% or so with (5), confirming the applicability of the EMF method for the radiated-power computation for even a "simulated" wire consisting of only a current filament. The log(kL) trend apparently must be due to the sin(θ) in the denominator, as otherwise the radiation field is the sum of three spherical waves whose total power would only be oscillatory with L. In effect, the sin(θ) term causes the point sources to have angle-dependent amplitudes, resulting in the log(kL) dependence.

Additional calculations were done for a center-fed dipole using NEC to determine if the log(kL) radiated-power trend is a property shared by a real antenna. The radius was maintained at a constant value of 0.001 λ while the dipole length and number of segments were systematically increased over an L/λ range of 1.0 to 10. The input (and radiated) power needed to produce a current of unit amplitude at the first maximum away from the source was then determined, for comparison with the SCF result, and is plotted in Fig. 3, where SCF results are included for comparison. It's interesting to see that the NEC solution also exhibits a log(kL) trend, and overlays the SCF result over most of the power range except at the higher values where it becomes systematically less than the SCF result with increasing L. Since the power maxima occur where source-region radiation is a maximum, this difference suggests that it may be due to a difference in how the source is treated. Apparently, the SCF and NEC currents are very similar with respect to how their total radiated powers depend on length, a somewhat unexpected result. For comparison, a line is also included on Fig. 3 that shows the power radiated by an infinite, circular antenna having a 1-amp maximum current.

Figure 3. Radiated power from a sinusoidal current filament and NEC model of a dipole, as a function of length. The NEC results agree within a few per cent of the SCF over most of the curve, but depart systematically towards the higher values of radiated power. The NEC minimum power values lie on a curve modeled by A + Blog(kL).

3.0 OTHER MANIFESTATIONS OF RADIATION
A wide variety of phenomena can offer insight concerning EM radiation. A few of the examples accumulated by the author follow below.

3.1 The "Kink" Model of Radiation Fields
The finite propagation speed of EM waves makes possible a graphical presentation for depicting the electric fields of accelerating charges, thus providing a visual illustration of their radiative behavior. The basis for the field-kink model is illustrated in Fig. 4, where a point charge, originally at rest at position 1, is abruptly
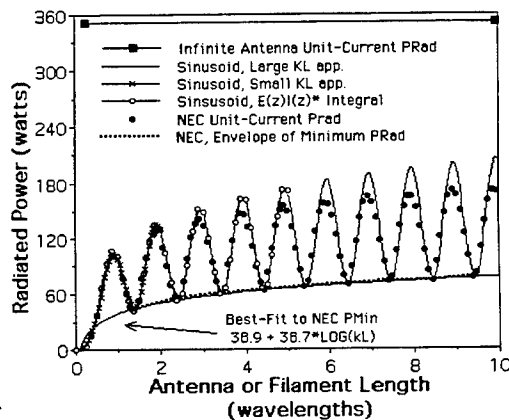
moved a short distance to new position, 2. The electric-field lines that terminated on the charge at its initial position require a finite time to adjust to the new location. This time "retardation" means that information about the charge's move reaches an observation point, r, centered on the charge's original position, after a propagation time t =R/c where R is the distance from r to 2. Because the new E-field lines point to position 2 while the original ones point to position one, an non-radial, or transverse, component is needed to make them continuous, forming a wave-propagation front, as shown in the figure. This is the radiation component produced by the charge's acceleration.
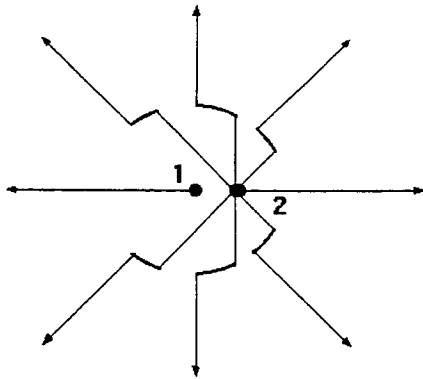
Figure 4. Field-kink model for depicting radiation. Using the propagation speed of EM waves and the continuity of E-field lines in a charge-free region, a simple model can be developed that illustrates how a non-radial, or transverse field is caused by charge acceleration. The kinked lines only occur when charges are accelerated; charges in uniform motion have a radially directed field accompanying them whose density per unit solid angle becomes non-uniform when the speed approaches c [Jackson (1975)].

3.2 Imaging Current Distributions

One of the earliest examples of microwave holography is due to Izuka and Gregoris (1970) who measured the near field of a 10-wavelength monopole and generated an optical image of the result in various planes relative to the monopole's location. Some results from this experiment are shown in Fig. 5, where the image in the plane of the monopole is seen to consist of two bright spots, at the end and feedpoint, showing where the predominant sources of radiation appear to be located.

Figure 5. Results from microwave-holography experiment of Izuka and Gregoris (1970). Part (a) is a photograph of the monopole, while optically reconstructed field distributions are shown (b) at the antenna plane, (c) at a plane in the Fresnel region, and (d) at the Fraunhofer region.

(a)   (b)

(c)   (d)

It's also possible to develop images from far-field data. One way to do this is to process the data using Prony's Method [Miller and Lager (1983)], an example of which is shown in Fig. 6. Because the most straightforward application of Prony's Method requires that the amplitudes of the exponential series be independent of the observation variable, the field values were first multiplied by $\sin(\theta)$ to remove the effect discussed in connection with Eq. (4). A number of computer experiments using this imaging technique consistently found discrete sources to be located at points where charge acceleration is expected and which are thus expected to be sources of radiation.

3.3 Body Resonances

Another kind of pole, those due to object resonances, can also be insightful concerning radiation, although in a less direct way than the space poles just discussed. Some results for body-resonance, or SEM (singularity-expansion method), poles are shown in Fig. 7. The imaginary, or os-

cillatory, axis is vertical with the loss axis being horizontal on these plots. Results for a nearly straight wire (there are 15 deg bends one quarter of the way from each end) are compared with those for a circular loop and a wire having a right-angle bend at its center, with all wires being of the same length. The increased loss component of the loop is due to its continuous curvature, which results in a directional charge acceleration along it. Also, it has half as many resonances per unit frequency change as the straight wire because it can support only even current modes. The bent wire, by comparison, has two layers of poles, with the less lossy layer being similar to those for the straight wire. The alternate ones, however, associated with the odd modes having a current zero in the center, are substantially more lossy, due to the associated charge maximum there and the consequent directional acceleration as the charge moves around the bend.
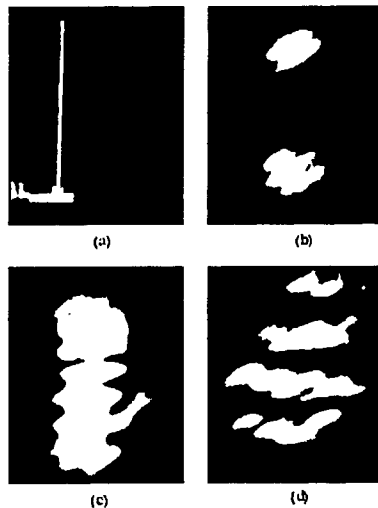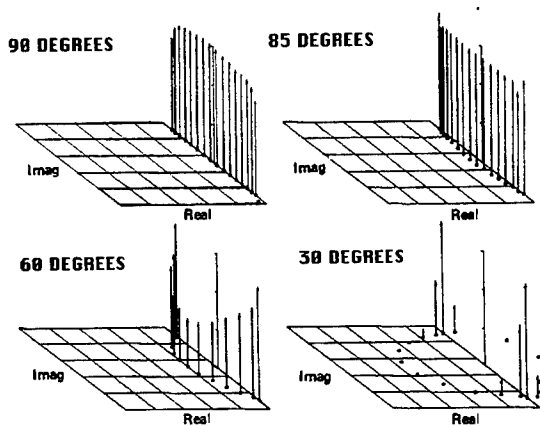
Figure 6. Space poles determined from applying Prony's Method to the far field scattered by a plane wave from a nine-wavelength-long wire for: (a) broadside incidence, (b) 5 deg from broadside, (c) 30 deg from broadside, and (d) 60 deg from broadside [Miller and Lager (1983)]. Poles are shown in a complex space plane where the pole position corresponds to $\exp[k\cos\theta(d_{re} - id_{im})]$, so that a purely imaginary pole is located in real space, and an imaginary component implies angular directivity. The amplitude of each source is indicated by the vertical lines on a three-decade log scale. At broadside incidence, the source poles are about one-half wavelength apart, evidently due to the uniform excitation along the wire's length, with a transition to GTD-like behavior of near-axial incidence.
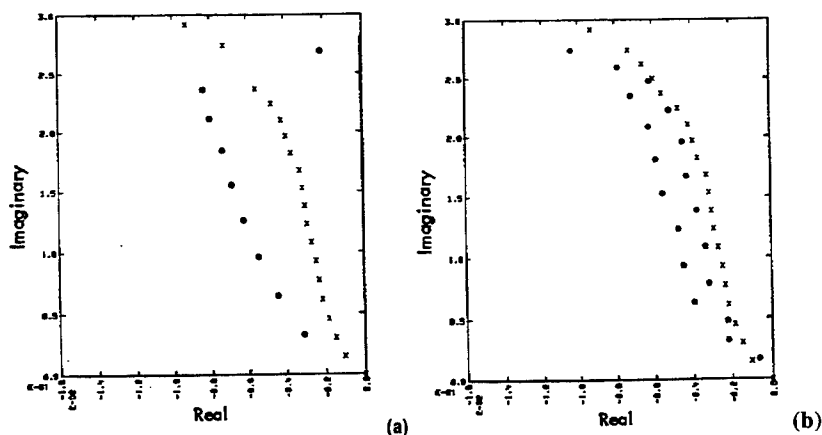
Figure 7. Pole results for a (a) a circular loop and (b) a bent wire, both shown by •, compared with a straight wire of the same length shown by x. The real part of a pole is the loss component and the imaginary part is the oscillatory component. The systematic difference between these pole plots for wires of the same length is due to their different geometries and the consequent effect on how the object radiates. Increased pole loss (the negative real axis) signifies a corresponding increase in radiative loss, due to the added charge acceleration that the circular loop and bent wire cause relative to a straight wire.

246

3.4 Space-Time Contour Plots of Time-Domain Fields

Time-domain solutions offer an opportunity to identify localized radiation sources because of the time resolution short-pulse excitation makes possible. Examples of this possibility are shown in Fig. 8, where a space-time contour format is used to plot the electric field near a center-excited, straight wire and its corresponding far field [Miller and Landt (1980)], obtained using the Thin-Wire Time-Domain model. For the near-field plot, the field values are multiplied by radial distance to compensate for the geometrical fall off, while the propagation time-delay is removed in the far-field plot.
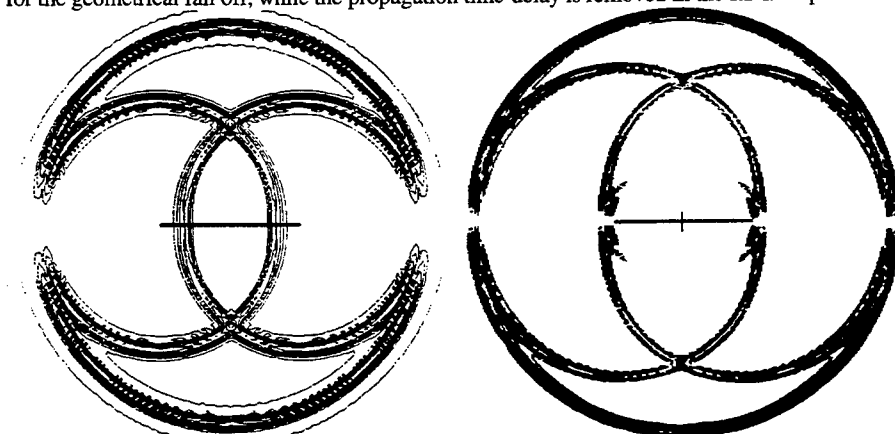
Figure 8. Early-time, space-time contour plots of the electric field produced by an impulsively excited, center-fed straight wire on approximately the same scale [Miller and Landt (1980)]. The near field shown in the left-hand plot and the far field in the right identify the sources of radiation as the wire center and the two ends, places where maximum charge acceleration occurs.

4.0 CONCLUDING COMMENTS

Were it not for the process of radiation, electromagnetics would be a much different subject. Yet, the physical basis for radiation does not seem to be well-understood, at least in terms of unambiguously and quantitatively determining the incremental contribution that each part of a source distribution makes to the total power it radiates, even though Maxwell's equations show that charge acceleration is the only way to produce a radiation field. It's undeniable that the mathematical and computational tools that are available provide correct solutions to a wide variety of problems, so perhaps attempting to develop a charge-acceleration-based perspective of EM is not necessary. On the other hand, if a clear, quantitative answer to the question "Why and from where does an object radiate?" can not be given, can we claim to have an adequate comprehension of electromagnetic physics?

5.0 REFERENCES

Balanis, C. A. (1982), *"Antenna Theory, Analysis and Design,"* Harper & Row, Publishers, New, York, NY.

Izuka, K. and L. G. Gregoris (1970), "Application of Microwave Holography in the Study of the Field from a Radiating Source," *Applied Physics Letters*, V17, N12, pp. 509-512.

Jackson, J. D. (1975), *"Classical Electrodynamics,"* John Wiley & Sons, New York, NY.

Miller, E. K. (1996a), "PCs for AP and Other EM Reflections," *IEEE AP-S Magazine*, June.

Miller, E. K. (1996b), "PCs for AP and Other EM Reflections," *IEEE AP-S Magazine*, Oct.

Miller, E. K. and J. A. Landt (1980), "Direct Time-Domain Techniques for Transient Radiation and Scattering from Wires", Invited Paper in *Proceedings of the IEEE*, **68**, pp. 1396-1423.

Miller, E. K. and D. L. Lager (1983), "Imaging of Linear Source Distributions," *Electromagnetics*, **3**, pp. 21-40.

Panofsky, W. K. H. and M. Phillips (1956), *"Classical Electricity and Magnetism,"* Addison-Wesley Publishing Company, Inc., Reading, MA.

Formulae for Total Energy and Time-average Power Radiated from Charge-Current Distributions

by

R. M. Bevensee

BOMA ENTERPRISES

P.O. Box 812   Alamo, CA, 94507-0812 USA

1. Summary

This paper will validate, by specific examples, general expressions for the total energy radiated during a time interval T by a space-time charge current distribution on an antenna surface or in free space. The examples include an accelerating "electron", a triangular distribution of sinusoidal current on a straight dipole, and a uniform sinusoidal current on a circular loop. The general expression is W_{rad} of Eq. (2). derived from the Panofsky-Phillips' expressions for the fields $\overline{E}(\overline{r}, t)$ and $\overline{H}(\overline{r}, t)$. The integrand of Eq. (2) contains a $\overline{J} \bullet \partial \overline{J}/\partial t$-component which, when applied to the spherical electron of uniform charge density, yields the power to accelerate the electron, $\frac{\partial}{\partial t}(\frac{1}{2} m_{ke} v^2)$. The "kinetic energy" mass, m_{ke} is *twice* the classical mass evaluated from the electrostatic energy required to construct the electron. m_{ke} represents this electrostatic energy *plus* the electric field energy stored inside and outside (to ∞) the electron.

This component of $\overline{J} \bullet \partial \overline{J}/\partial t$ is the power required to accelerate the electron mass consisting of *initial field energy*, distinct from the power radiated to the radiation sphere!

By expanding $\overline{J}(\overline{r}', t' = t - R/c)$ and similarly $q(\overline{r}', t')$, with $R = |\overline{r} - \overline{r}'|$ in Eq. (2) in a Taylor series in powers of R/c about t we find the two predominant non-kinetic energy terms yield the power radiated by an accelerating electron, as evaluated from the Poynting vector on the radiation sphere.

For sinusoidal steady state, $T = 2\pi/\omega$. and we obtain the time-average radiated power of Eq. (31). This contains no kinetic-power component. It yields the correct power radiated by the straight dipole and loop described above.

Eqs. (2) and (31) assume that the excitation to support a given charge-current distribution is provided, and that any boundary conditions, which might be imposed on antenna surfaces, are satisfied. This implies generator support of tangential E-field which might otherwise fall on perfectly conducting surfaces.

Eqs. (2) and (31) are convenient *mathematical* statements of energy radiated (including the flow into kinetic energy) due to charge-current interactions but do not explain fully the radiation *physics*.

2. Derivation of Eq. (2) for W_{rad}.

This derivation from Eq. (1),

$$W_{rad}(T) = - \int_T dt \oint_{S_a} dS \, \overline{E}(\overline{r}, t) \bullet \overline{J}(\overline{r}, t) , \tag{1}$$

is carried out in the Appendix from the Panofsky-Phillips' expressions [1] for $\overline{E}(\overline{r}, t)$ and $\overline{H}(\overline{r}, t)$. The integrand of Eq. (1) is evaluated from the near- and far-field components of these fields and their vector and scalar potentials. The power flowing into spatial stored energy (distinct from the "mass" field energy) is evident and is separated out. Upon integrating some of the terms in the final expression, Eq. (A18). by parts over time we obtain Eq. (2):

$$W_{rad}(T) = \frac{\mu_0}{4\pi} \int_T dt \oint_{S_a} dS \oint_{S_a} dS' \frac{1}{R} \left[\overline{J}(\overline{r}, t) - \frac{\overline{R}}{R} cq(\overline{r}, t) \right] \bullet \left[\frac{\partial}{\partial t} \overline{J}(\overline{r}', t' = t - \frac{R}{c}) + \frac{\overline{R}}{R} \frac{\partial}{\partial t} cq(\overline{r}', t') \right] \tag{2}$$

where $\overline{R} = \overline{r} - \overline{r}'$, $R = |\overline{R}|$, and c is light velocity.

Notice the integrand of Eq. (2) does *not* represent instantaneous power $P_{rad}(t)$ radiated at time t because of the time-integration by parts in its derivation. The rule for obtaining instantaneous power terms

in Eq. (2) which we employ below is this: *any term in the integrand which can be rearranged (by time-integration by parts, addition of itself to the time-integration-by-parts term and division by 2), so as to yield a non-zero power term when the double spatial integration is carried out is a physically meaningful power flow.*

3. Evaluation of $P_{rad}(t)$ from the integrand of Eq. (2) for a spherical "electron" of uniform charge distribution within radius r_o.

For the electron moving in the z-direction, $\bar{p}$ designating a transverse position, we can write very generally

$$q(\bar{r},t) = g(\bar{p},z,t) = g\left(\bar{p}, z - \int^t v(\tau)d\tau\right), \qquad \int_{V} g\,dV = -e , \tag{3}$$

$$\bar{J}(\bar{r},t) = \bar{J}(\bar{p},z,t) = \bar{a}_z g v(t) \tag{4}$$

Note

$$\nabla \bullet \bar{J} = \frac{\partial J}{\partial z} = g' v(t) = -\dot{q}, \qquad ' = \frac{\partial}{\partial(arg)} \tag{5}$$

Now expand $g(\bar{r}', t' = t - R/c)$ about t:

$$g(\bar{r}',t' = t - R/c) = g(\bar{r}',t) - \frac{R}{c}\dot{g}(\bar{r}',t' = t) + \frac{1}{2}\left(\frac{R}{c}\right)^2 \ddot{g}(\bar{r}',t) - \frac{1}{6}\left(\frac{R}{c}\right)^3 \dddot{g}(\bar{r}',t) + ... \tag{6}$$

and similarly $\bar{J}(\bar{r}',t')$. Then P_{rad} reads

$$P_{rad}(t) = \frac{\mu_0}{4\pi} \int dV \int dV' \frac{1}{R}\left\{\bar{a}_z J(\bar{r},t) - \frac{\bar{R}}{R}cq(\bar{r},t)\right\} \bullet \left\{\bar{a}_z\left[J(\bar{r}',t) - \frac{R}{c}\dot{J}(\bar{r}',t) + \frac{1}{2}\left(\frac{R}{c}\right)^2 \ddot{J}(\bar{r}',t) - ...\right]\right.$$

$$\left. + \left(\frac{\bar{R}}{R}\right)c\left[\dot{q}(\bar{r}',t) - \frac{R}{c}\ddot{q} + \frac{1}{2}\left(\frac{R}{c}\right)^2 \dddot{q} - \frac{1}{6}\left(\frac{R}{c}\right)^3 \ddddot{q} + ...\right]\right\} \tag{7}$$

3.1 the $J(\bar{r},t)\dot{J}(\bar{r}',t) - term.$

If we take half of the $J\dot{J}$-term in Eq. (7) added to the term with $\bar{r}$ and $\bar{r}'$ interchanged we obtain

$$P_1 = \frac{\mu_0}{4\pi} \int dV \int dV' \frac{1}{R}\frac{\partial}{\partial t}\frac{1}{2}\left[J(\bar{r},t)J(\bar{r}',t)\right] \tag{8}$$

and can be interpreted as an instantaneous power component. Since $J = qv$ and $q = -e/(4\pi r_o^3/3)$, this is clearly the rate of change of kinetic energy, $\partial(\frac{1}{2}m_{ke}v^2)/\partial t$. When we evaluate the kinetic mass, m_{ke}, we find

$$m_{ke} = \frac{\mu_0}{4\pi}\left(\frac{3e}{4\pi r_o^3}\right)^2 \int dV \int dV' \frac{1}{R} \tag{9}$$

The double integrals evaluates in spherical coordinates to $(32/15)r_o^5\pi^2$, and we obtain

$$m_{ke} = \frac{3}{10\pi}\frac{\mu_0 e^2}{r_0}, \tag{10}$$

which is *double* the classical mass, m_{cl}, obtained by integrating the electrostatic energy required to build the electron and equating it to $m_{cl}c^2$ [2].

However, this calculation of classical mass ignores stored electric field energy. When we add the field energy stored inside and outside the electron (to ∞) to the electrostatic energy required to build the electron and equate all these to mc^2 we find this mass is equal to m_{ke}.

We conclude P_1 is consistent with our non-quantum description of the electron.

3.2 The $J(\overline{r},t)\ddot{J}(\overline{r}',t)$ – term in Eq. (7)

The R-factors cancel, and when we integrate by parts over time, from the beginning to the end of the response, we obtain

$$P_2 = \frac{\mu_0}{4\pi c} \int dV \int dV'' \dot{J}(\overline{r},t)\dot{J}(\overline{r}',t) \tag{11}$$

$J = qv(t)$ and $\dot{J} = \dot{q}v + q\dot{v}$, with $\dot{q} = -\partial J/\partial z$; the only term which survives the z-integration is the $q(\overline{r},t)\dot{v}q(\overline{r}',t)\dot{v}$- portion. Since $\int q \, dV = -e$ we obtain

$$P_2 = \frac{\mu_0 e^2}{4\pi c}(\dot{v})^2 \tag{12}$$

This is larger than the power obtained by integrating the Poynting vector over the radiation sphere.

3.3 The $J(\overline{r},t)\dddot{J}\overline{r}',t)$ – term in Eq. (7)

Here we evaluate

$$T_3 = \int dV \int dV'' \frac{R}{c} J(\overline{r},t)\dddot{J}(\overline{r}',t) \tag{13}$$

We can integrate by parts over time twice and obtain

$$T_3 = \int dV \int dV'' \frac{R}{c} \ddot{J}(\overline{r},t)\dot{J}(\overline{r}';,t) \tag{14}$$

We can interchange $\overline{r}$ and $\overline{r}'$ in Eq. (13) without changing R, again integrate by parts, and obtain the *negative* of Eq. (14). Hence Eqs. (13) and (14) add to *zero!*

4. The $[\overline{J}(\overline{r},t)\dot{q}(\overline{r}',t') - q(\overline{r},t)\dot{\overline{J}}(\overline{r}',t')]$ cross terms

The cross-term integrand in Eq. (2) is, with $\overline{J} = \overline{a}_z J$,

$$\frac{c}{R}\left[J(\overline{r},t)\frac{z-z'}{R}\dot{q}(\overline{r}',t') - \frac{z-z'}{R}q(\overline{r},t)\dot{J}(\overline{r}',t')\right] \tag{15}$$

Integration over time by parts of the second term yields, for $\dot{q} = -\partial J/\partial z$ and fixed $\overline{R} = \overline{p} - \overline{p}' + \overline{a}_z(z - z')$,

$$-\frac{c}{R^2}\left[J(\overline{r},t)(z-z')\frac{\partial J}{\partial z'}(\overline{r}',t') + \frac{\partial J(\overline{r},t)}{\partial z}(z-z')J(\overline{r}',t')\right] \tag{16}$$

The easiest way to see that this integrates to zero over z and z' for fixed $\overline{p}$ and $\overline{p}'$ is to index the z and z' coordinates by n and n', such that $z_n = z_0 + n\delta z$, etc. Then we evaluate $\int dz \int dz'$ as

$$\sum_n \sum_{n'} J_n(\overline{p},t)(z_n - z_{n'})[J_{n'+1}(\overline{p}',t') - J_{n'-1}(\overline{p}',t')] + \sum_n \sum_{n'} [J_{n+1}(\overline{p},t) - J_{n-1}(\overline{p},t)](z_n - z_{n'})[J_{n'}(\overline{p}',t')] \tag{17}$$

In the second sum change $n+1$ and n' to n and $n'-1$ for the J_{n+1}- portion and $n-1, n'$ to $n, n'+1$ for the J_{n-1}-portion. This doesn't change R. Than that sum reads

$$\sum_n \sum_{n'} J_n(\overline{p},t)(z_{n-1} - z_{n'-1})[J_{n'-1}(\overline{p}',t') - \sum_n \sum_{n'} J_n(\overline{p},t)(z_{n+1} - z_{n'+1})J_{n'+1}(\overline{p}',t'). \tag{18}$$

This exactly cancels the first sum in Eq. (17).

This cancellation occurs for all combinations of $\overline{p}$ and $\overline{p'}$ So the cross-term integrand of Eq. (15) integrates to *zero*.

5. The $q(\overline{r},t)\dot{q}(\overline{r'},t')$-terms in Eq. (2)

We now examine these terms with $\dot{q}$ expanded as in the last [ ] of Eq. (7). The $q(\overline{r},t)\dot{q}(\overline{r'},t)$-term obviously integrates to zero, for if we add it to the term with $\overline{r},\overline{r'}$ interchanged and take one-half we get

$$-\frac{1}{2}\int dV \int dV'' \frac{c^2}{R}\frac{\partial}{\partial t}[q(\overline{r},t)q(\overline{r'},t)] \sim \frac{\partial}{\partial t}\int dV \int dV'' \frac{1}{R}q(\overline{r},t)q(\overline{r'},t) = 0, \tag{19}$$

because the double integral is independent of t.

5.1 The $q(\overline{r},t)\ddot{q}(\overline{r'},t)$ − term in Eq. (7)

This simplifies after time-integration by parts to

$$-c\int dV \int dV' \dot{q}(\overline{r},t)\dot{q}(\overline{r'},t) \tag{20}$$

Since $\dot{q}(\overline{r},t) = -\frac{\partial}{\partial z}J(\overline{r},t)$ and similarly for $\dot{q}(\overline{r'},t)$. we can integrate these J-derivatives through the entire electron sphere and obtain *zero* for this term.

5.2 The $q\ddot{q}$ − term in Eq. (7)

Integration by parts over time yields $\dot{q}(\overline{r},t)\ddot{q}(\overline{r'},t)$ in the integrand. Interchange of $\overline{r}$ and $\overline{r'}$, addition to the first integrand and division by 2. yields a spatial integral of the form

$$\frac{1}{4}\frac{\partial}{\partial t}\int dV \int dV'' R \frac{\partial J(\overline{r},t)}{\partial z}\frac{\partial J(\overline{r'},t)}{\partial z'} \tag{21}$$

This is zero: for fixed $\overline{p}$ and $\overline{p'}$ the double integral may be integrated over z as

$$\int dz \frac{\partial J(\overline{p},z,t)}{\partial z}\left[\int_{-\infty}^{z}(z-z')\frac{\partial J(\overline{p'},z',t)}{\partial z'}dz' + \int_{z}^{\infty}(z'-z)\frac{\partial J(\overline{p'},z',t)}{\partial z'}dz'\right] \tag{22}$$

Evaluation of the [ ]-term and integration by parts over z yields

$$-2\int dz J(\overline{p},z,t)J(\overline{p'},z',t), \qquad independent\ of\ time \tag{23}$$

Therefore Eq. (21) is *zero*.

5.3 The $q\dddot{q}$ − term in Eq. (7)

This term is

$$P_3 = \frac{1}{6}\frac{\mu_0}{4\pi c}\int dV \int dV' q(\overline{r},t)R^2\dddot{q}(\overline{r'},t), \qquad R^2 = |\overline{p}-\overline{p'}|^2 + (z-z')^2 \tag{24}$$

Integration by parts over time twice and substitution of $\ddot{q}(\overline{r},t) = -\partial\dot{J}(\overline{r},t)/\partial z$. etc., yields

$$P_3 = \frac{1}{6}\frac{\mu_0}{4\pi c}\int d\overline{p} \int d\overline{p'} \int dz \int dz' \frac{\partial \dot{J}(\overline{r},t)}{\partial z}\left[|\overline{p}-\overline{p'}|^2 + (z-z')^2\right]\frac{\partial \dot{J}(\overline{r'},t)}{\partial z'} \tag{25}$$

The $|\overline{p}-\overline{p'}|^2$-term yields zero; only the $-2zz'$ within the brackets yields a finite answer. Integrating by parts over z,z', we obtain

$$P_3 = -\frac{1}{3}\frac{\mu_0}{4\pi c} \int d\bar{p} \int d\bar{p}' \int dz \int dz'\, \dot{J}(\bar{p},z,t)\dot{J}(\bar{p}',z',t) \tag{26}$$

With

$$\dot{J}(\bar{r},t) = \dot{g}v + g\dot{v} = -\frac{\partial J}{\partial z}v(t) + q(\bar{r},t)\dot{v} \tag{27}$$

and similarly for $\dot{J}(\bar{r}',t)$, we see the $\frac{\partial J}{\partial z}v$-term integrates over z to zero. The final result is

$$P_3 = -\frac{1}{3}\frac{\mu_0}{4\pi c}(\dot{v})^2 \left(\int dV q(\bar{r},t) \right)^2 = -\frac{1}{3}\frac{\mu_0 e^2}{4\pi c}\dot{v}^2 \tag{28}$$

When this is added to Eq. (12) for the $J\ddot{J}$-contribution to the radiated power we obtain the correct instantaneous power radiated by an accelerating electron,

$$P_{rad} = \frac{2}{3}\frac{\mu_0 e^2}{4\pi c}(\dot{v})^2 \tag{29}$$

6. The sinusoidal steady state, time-average power radiated.

For sinusoidal steady state, $T = 2\pi/\omega$, and we substitute

$$\bar{J}(\bar{r},t) = \frac{1}{2}[\hat{J}(\bar{r})e^{j\omega t} + complex\ conjugate] = Real\,[\hat{J}(\bar{r})e^{j\omega t}] \qquad etc. \tag{30}$$

and obtain for the time-average radiated power, P_{rad}:

$$P_{rad}(\omega) = -\frac{1}{2}Real \oint_{S_a} \hat{\mathcal{E}}^*(\bar{r})\bullet\hat{J}(\bar{r})\,dS = \frac{\mu_0}{8\pi}Real\left\{ j\omega \oint_{S_a}\oint_{S_a} dSdS'\left[\hat{J}^*(\bar{r})\bullet\hat{J}(\bar{r}') - c^2\hat{q}^*(\bar{r})\hat{q}(\bar{r}')\right]\frac{e^{-jkR}}{R}\right\} \tag{31}$$

The two Jq cross terms have cancelled.

6.1 A straight dipole of length $2\ell_0$ along the $z-axis$, with a triangular distribution of sinlusoidal current of amplitude 1 at low frequency.

Eqw. (31) can be evaluated independent of the dipole radius. Approximating $exp(-jkR)$ as $1 - jkR + \frac{1}{2}(-jkR)^2 + \frac{1}{6}(-jkR)^3$, with $R = |z - z'|$, we find the $J^*(z)\bullet\dot{J}(z')$-contribution–via the $-jkR$ term in this expansion is [3]

$$P_4 = \frac{(\omega\ell_0)^2}{8\pi\epsilon_0 c^3} = \frac{(\omega\ell_0)^2\mu_0}{8\pi c} \tag{32}$$

The first term to contribute in the $\hat{q}^*(z)\hat{q}(z')$-product comes from the $(-jkR)^3$-term in the above expansion (!), and yields $-\frac{1}{3}P_4$. So the total time-average radiated power, $\frac{2}{3}P_4$, equated to $\frac{1}{2}J(0)^2 R_{rad}$ yields the correct radiation resistance:

$$R_{rad} = 20(k\ell_0)^2, \qquad k = \omega/c \tag{33}$$

6.2 A small circular loop of radius a_0 and spatially uniform sinusoidal current of amplitude 1. $q = 0$.

Now the first term to contribute is the $(-jkR)^3$-term in the preceding expansion for $J^*(\bar{r})\bullet\dot{J}(\bar{r}')$. The result of the double integration around the circle of radius a_0 in Eq. (31) is:

$$P_5 = \frac{\mu_0 c\pi}{12}\left(\frac{\omega a_0}{c}\right)^4 = \frac{1}{2}R_r, \tag{34}$$

and this yields the correct low-frequency radiation resistance, R_r:

$$R_r = 20\pi^2(ka_0)^4. \tag{35}$$

7. Interpretation of these results

Eqs. (2) and (31) are the result of radiation *mathematics* but do not explain fully the radiation *physics*. Radiation is ordinarily ascribed to charge *acceleration*, but the only acceleration term in Eq. (2) is the $q(\bar{r}',t')\partial\bar{v}(\bar{r}',t')/\partial t$-term from $\partial\bar{J}/\partial t$, and this may not dominate the remaining $\partial q/\partial t\bar{v})$- and $\overline{R}/R\partial cq/\partial t$-terms. The equation only says that we can evaluate the radiated energy by integrating over space-time the "coupling" between one charge-current pair and the time derivative of another charge-current pair.

The physics of radiation are even more obscure in Eq. (31), where there is no obvious acceleration term. It merely says that we can evaluate the time-average power by integrating over current density pairs and charge density pairs, each pair multiplied by the Green function.

References

[1] W.K.H. Panofsky and M. Phillips, *Classical Electricity and Magnetism*, Addison- Wesley, 1962. pp. 246 et. seq.
[2] Alonso-Finn, *Fundamental University Physics*, Addison-Wesley, 1967, p. 584.
[3] R. M. Bevensee, *Foundations for Power Flow* notes, 1976.

Appendix. Outline of one derivation of Eq. (2)

This derivation could be carried out directly from Eq. (1) and Eqs. (A1)-(A3) below, but instead is based on near- and far-field expressions and their potentials.

The Panofsky-Phillips' expressions for the space-time electric and magnetic fields due to surface charge $q(\bar{r},t)$ and surface current $\overline{J}(\bar{r},t)$ are

$$\overline{E}(\bar{r},t) = \overline{E}_{ne} + \overline{E}_{ra}, \tag{A1}$$

where the near (ne) and radiation (ra) components are

$$\overline{E}_{ne} = \frac{1}{4\pi\epsilon_0}\oint_{S_a}\frac{[q]\overline{R}}{R^3}dS', + \frac{1}{c}\oint_{S_a}\frac{[\overline{J}]\bullet\overline{RR} - \overline{R}\times([\overline{J}]\times\overline{R})}{R^4}dS' \tag{A2}$$

$$\overline{E}_{ra} = \frac{1}{4\pi\epsilon_0 c^2}\oint_{S_a}\frac{([\dot{\overline{J}}]\times\overline{R})\times\overline{R}}{R^3}dS', \tag{A3}$$

with the definitions

$$[\overline{J}] = \overline{J}(\bar{r}',t'=t-R/c), \quad [q] = q(\bar{r}',t'), \quad \dot{X} = \frac{\partial X}{\partial t} \quad \overline{R} = (\bar{r}-\bar{r}'), \quad R = |\overline{R}| \quad.$$

The associated magnetic field is

$$\overline{H}(\bar{r},t) = \overline{H}_{ne} + \overline{H}_{ra}, \tag{A4}$$

where

$$\overline{H}_{ne} = \frac{1}{4\pi} \oint_{S_a} \frac{[\overline{J}] \times \overline{R}}{R^3} dS', \quad \overline{H}_{ra} = \frac{1}{4\pi c} \oint_{S_a} \frac{[\dot{\overline{J}}] \times \overline{R}}{R^2} dS' \qquad (A5)$$

Defining the scalar and vector potentials ϕ and $\overline{A}$,

$$4\pi\epsilon_0 \phi_{ne}(\overline{r}, t) = \oint_{S_a} \left(\frac{[q]}{R} + \frac{1}{c}\frac{[\overline{J}] \bullet \overline{R}}{R^2} \right) dS', \quad 4\pi\epsilon_0 \phi_{ra}(\overline{r}, t) = \frac{1}{c^2} \oint_{S_a} \frac{[\dot{\overline{J}}] \bullet \overline{R}}{R} dS' \qquad (A6)$$

$$4\pi\epsilon_0 \overline{A}_{ne}(\overline{r}, t) = \frac{1}{c} \oint_{S_a} \left(\frac{[q]\overline{R}}{R^2} + \frac{1}{c}\frac{[\overline{J}] \bullet \overline{R}}{R^3} \right) dS', \quad 4\pi\epsilon_0 \overline{A}_{ra}(\overline{r}, t) = \frac{1}{c^3} \oint_{S_a} \frac{[\dot{\overline{J}}] \bullet \overline{R}\overline{R}}{R^2} dS', \qquad (A7)$$

we have

$$\overline{E}_{ne} = -\nabla \phi_{ne} - \dot{\overline{A}}_{ne}, \qquad \overline{E}_{ra} = -\nabla \phi_{ra} - \dot{\overline{A}}_{ra} \qquad (A8)$$

$$\overline{H}_{ne} = \nabla \times \overline{A}_{ne}, \qquad \overline{H}_{ra} = \nabla \times \overline{A}_{ra} \qquad (A9)$$

By dot-multiplying $\nabla \times \overline{H} = \epsilon_0 \dot{\overline{E}}$ with $\overline{E}_{ne}$ and $\nabla \times \overline{E}_{ne} = -\mu_0 \dot{\overline{H}}_{ne}$ with $\overline{H}$, and integrating over the volume outside the antenna surfaces we obtain

$$-\oint_{S_a} \overline{E}_{ne} \times \overline{H} \bullet \overline{dS} = -\oint_{S_a} \overline{E}_{ne} \bullet \overline{J} dS = \dot{W}_{ne} + \epsilon_0 \int_V \dot{\overline{E}}_{ra} \bullet \overline{E}_{ne} dV + \mu_0 \int_V \overline{H}_{ra} \bullet \dot{\overline{H}}_{ne} dV \qquad (A10)$$

with

$$W_{ne} = \frac{1}{2} \left(\epsilon_0 \int_V |\overline{E}_{ne}|^2 dV + \mu_0 \int_V |\overline{H}_{ne}|^2 dV \right) \qquad (A11)$$

We also have

$$-\oint_{S_a} \overline{E}_{ne} \bullet \overline{J} dS = \oint_{S_a} \left(\phi_{ne}\dot{q} + \overline{J} \bullet \dot{\overline{A}}_{ne} \right) dS \qquad (A12)$$

Analogous to Eq. (A10) we obtain

$$-\oint_{S_a} \overline{E}_{ra} \bullet \overline{J} dS = P_{rad} + \dot{W}_{ra} + \epsilon_0 \int_V \overline{E}_{ra} \bullet \dot{\overline{E}}_{ne} dV + \mu_0 \int_V \dot{\overline{H}}_{ra} \bullet \overline{H}_{ne} dV \qquad (A13)$$

with

$$W_{ra} = \frac{1}{2} \left(\epsilon_0 \int_V |\overline{E}_{ra}|^2 dV + \mu_0 \int_V |\overline{H}_{ra}|^2 dV \right) \qquad (A14)$$

and

$$P_{rad} = power\ radiated\ at\ time\ t\ on\ the\ radiation\ sphere.$$

We also have

$$-\oint_{S_a} \overline{E}_{ra} \bullet \overline{J} dS = \oint_{S_a} \left(\phi_{ra}\dot{q} + \overline{J} \bullet \dot{\overline{A}}_{ra} \right) dS \qquad (A15)$$

Adding Eqs. (A10) and (A13) we obtain

$$-\oint_{S_a} \overline{E} \bullet \overline{J} dS = P_{rad} + \dot{W}_{ne} + \dot{W}_{ra} + \frac{\partial}{\partial t} \left(\epsilon_0 \int_V \overline{E}_{ra} \bullet \overline{E}_{ne} dV + \mu_0 \int_V \overline{H}_{ne} \bullet \overline{H}_{ra} dV \right). \qquad (A16)$$

Equivalently. adding Eqs. (A12) and (A15) we obtain

$$-\oint_{S_a} \overline{E} \bullet \overline{J} dS = \oint_{S_a} \left(\phi_{ne}\dot{q} + \overline{J} \bullet \dot{\overline{A}}_{ne} + \phi_{ra}\dot{q} + \overline{J} \bullet \dot{\overline{A}}_{ra} \right) dS \qquad (A17)$$

Taking $\int_{-\infty}^{+\infty} dt$ of Eqs.(A16) and (A17) we find

$$-\int dt \oint_{s_a} \overline{E} \bullet \overline{J} dS = W_{rad} = \int dt \oint_{S_a} \left(\phi_{ne}\dot{q} + \overline{J} \bullet \dot{\overline{A}}_{ne} + \phi_{ra}\dot{q} + \overline{J} \bullet \dot{\overline{A}}_{ra} \right) dS \qquad (A18)$$

Substituting Eqs. (A6) and (A7) and $\nabla \bullet \overline{J} = -\dot{q}$ and integrating the first. third, and fourth terms by parts over time we obtain an expression in which one more term must be integrated over time by parts to obtain the final Eq. (2).

An Overview of Antenna Radiation Basic Principles

W.P. Wheless, Jr. and L.T. Wurtz
Department of Electrical Engineering
University of Alabama
Tuscaloosa, Alabama 35487

Abstract - **This paper is to provide an intuitive introduction to the fundamental phenomena which result in antenna radiation. It is tutorial in nature, and written such that practical antenna experimenters, as well as CEM practitioners, may acquire a useful appreciation of what contributes to antenna operation at the most basic level. The concepts discussed here are refined and extended, analytically and computationally, by other authors in separate papers.**

I. I. INTRODUCTION

To facilitate discussion, the specific context of wire antennas (the $\lambda/2$ dipole, in particular), operated at frequencies in the 3-30 MHz HF range, has been chosen. The discussion begins with some background information which contributes to subsequent examination of basic operational mechanisms.

First, consider causing a radiated field by the periodic oscillation of a single electron about an equilibrium point. If one could grasp an electron with a tiny pair of non-conducting tongs and wave it back and forth over, say, a 10 cm displacement at a rate of 5 oscillations per second, a nearby sufficiently sensitive receiver tuned to a wavelength of 60 Mm would detect the resultant electromagnetic signal.

The free electrons in an electric conductor (copper, for example) are able to travel freely in the interatomic space under the influence of any electric fields that are present. Alternating current in an antenna wire is simply the net effect of a massive electron migration: individual electrons still oscillate about their respective average positions and emulate the single electron in the rudimentary experiment above.

It is relevant and informative to calculate some typical displacements and speeds for free electrons in an electric conductor. Consider a wire antenna of #10 gauge copper wire, and subjected to an electric field excitation at 20 MHz so that the rms antenna current at the plane of interest is 1.0 Ampere. The diameter of #10 AWG wire is 101.9 mils, there are $n = 8.4 \times 10^{28}$ free electrons/m^3 [1], and each electron represents $e = 1.602 \times 10^{-19}$ Coulombs. The skin depth

$$\delta = \frac{1}{\sqrt{\pi f \mu \sigma}} \tag{1}$$

at 20 MHz is 1.48×10^{-5} m. For an approximate calculation, a simplifying assumption that the current is accounted for in a thickness of two skin depths is taken, so the area associated with the current flow is approximately 2.41×10^{-7} m^2. For sinusoidal oscillations, the average free electron drift velocity in the wire is then

$$v = \frac{1}{Ane} \approx 3.1 \times 10^{-4} \text{ m/s} \tag{2}$$

and the peak speed is about 4.8×10^{-4} m/s. Since at 20 MHz, the oscillations are repetitive with period $T = 50$ nanoseconds, a free electron can only travel on the order of 8×10^{-12} m during a half cycle. A surprising number of graduate electrical engineers believe that electrons flow back and forth from one side of a center-fed $\lambda/2$ dipole to the other, but the reality is that their motion is quite localized! These displacements

are nonetheless quite significant relative to the size of an electron, however, as the classical radius for an electron is a minuscule 1.41 fm [2].

More impressive than the electron displacements is the associated accelerations. At 20 MHz, electrons are accelerated from zero to peak speed in 1.25×10^{-8} second or, conversely, decelerated from peak speed to zero in the same amount of time. Therefore, the average acceleration over a quarter cycle is approximately 38,640 m/s^2, equivalent to 3,943 g's (where acceleration unit $g = 9.8$ m/s^2).

In general, fields divide into *velocity fields*, which are independent of acceleration, and *acceleration fields* [3]. The velocity fields are essentially static fields and decay with the inverse of distance squared (i.e., as r^{-2}); on the other hand, acceleration fields are typical radiation fields and fall off as r^{-1}. An accelerating or decelerating electron, therefore, is a source of electromagnetic radiation.

II. Fields of an Oscillating Single Electron

The coulomb field of a stationary electron is illustrated by the common depiction of Figure 1. The coulomb field is always present, whether the electron is in motion or not, but is electrostatic in nature. This most elementary field, it turns out, is critical to the successful operation of antennas.

Assume now that we mechanically oscillate the electron at a radio frequency rate. The oscillatory motion gives rise to two new fields which are qualitatively discussed in this section, namely, the magnetic field and the dynamic electric field.

By moving the electron, a small current is created, and that current is accompanied by a magnetic field (with field orientation in accord with the right-hand rule). The oscillating current associated with the electron may be analyzed as a short electric dipole [4], which provides the conclusion that the phase of the magnetic field at the electron's "surface" has negligible lag, experiences a small lag out to a radius of $\frac{\lambda}{2\pi}$ and then, for larger radial distances r, settles at a constant rate of 360° per wavelength. Numerous textbook

analyses show that the field energy at distances up to $\frac{\lambda}{2\pi}$ is mostly stored, and becomes mostly radiated at larger distances from the current source.
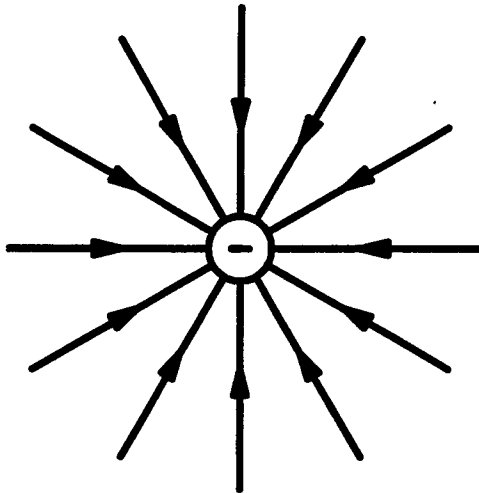
Figure 1. The coulomb field associated with an electron.

The other new field resulting from the electron's acceleration/deceleration is also an electric field, referred to as the dynamic electric field because of its dynamic origin. It is useful to view the dynamic electric field as two components, one of which is referred to as the radiation field and the other as the induction field. The distinction between the two is that one is in-phase with the magnetic field and the other is 90° out of phase with the magnetic field. The excitation current has been taken to be sinusoidally oscillating along a line in space and, since the system is linear, the response induction and radiation fields also vary sinusoidally at the same frequency. It can be shown [4] that the induction and radiation fields become equal in magnitude at the distance $\frac{\lambda}{2\pi}$ broadside to the small length of current formed by the oscillating electron. The radiation field decays much less rapidly than the induction

field, however, and thus quickly becomes dominant with increasing distance from the source. In most practical applications, engineer are concerned with the transmission of energy by the radiation field produced by masses of oscillating electrons, at relatively large distances.

III. KINK CONCEPT OF ACCELERATING ELECTRON RADIATION

Consider the event illustrated in Figure 2, where an electron initially at rest at point A is accelerated very briefly toward point B. Assume that the electron continues at constant speed toward the right after the brief acceleration period ends. Take reference time $t = 0$ to be the time when acceleration of the electron (at point A) begins, let $t = t_e$ be the time at which acceleration ends and, finally, let the time of passage through point B be $t = t_0$. Hence, $0 < t_e < t_0$.

Note that the larger dotted circle in Figure 2 is centered at point A. Its radius is equal to the distance an electromagnetic wave in free space travels in time t_0. The field outside this circle at time t_0 is the coulomb field for the electron at rest at point A up to time $t = 0$.

The smaller dotted circle is centered on the point where the acceleration ends (just slightly to the right of point A), and its radius is the distance an electromagnetic wave travels in time $t_0 - t_e$. The distance between points A and B is quite small, in accord with the earlier displacement calculations, and has been exaggerated in the figure for clarity. The field inside the smaller circle at time t_0 is a moving coulomb field centered on the electron's present position at point B.

The gap between circles represents the distance of propagation in time $t_e - 0 = t_e$, while the electron is being accelerated. The field lines in the gap region must be intermediate to the values on the circles, and connecting the field lines across the gap results in a "kink" in each field line across this gap region. These kinks are an electromagnetic disturbance which propagates outward with advancing time. The superimposed vectors in the insert of Figure 2 show the resultant field at a point in the gap resolved into radial and transverse components. The transverse component is the radiation field, which has originated from the (radial) coulomb field by virtue of acceleration of the electron. The radiation field from an oscillating electron, then, is comprised of a series of such disturbances, caused by the periodic electron acceleration and deceleration.

IV. RADIATION RESISTANCE AND INDUCTANCE

Among others, Feynman [5] has contemplated the origins of radiation resistance. His brief description of a model concluded:

> "This model of the origin of the resistance to acceleration, the radiation resistance of a moving charge, has run into many difficulties, because our present view of the electron is that it is not a 'little ball'; this problem has never been solved. Nonetheless we can calculate exactly, of course, what the net radiation resistance force must be, i.e., how much loss there must be when we accelerate a charge, in spite of not knowing directly the mechanism of how that force works."

Efforts continue to fully understand and describe the mechanism. Toward that end, consider that the vibrating charged electron experiences forces from the induction and radiation fields it has produced. The source of energy, which causes the electron to oscillate, must therefore overcome these self, or "bootstrap," forces. It is widely accepted that radiation resistance and inductance are manifestations of the bootstrap forces, but modeling of all the details remains incomplete. The following discussion, although lacking the intimate details, offers a basis for appreciation of what is involved in the radiation resistance and inductance phenomena.

At the surface of an oscillating electron, the magnetic field is essentially in phase with the current (i.e., the electron's speed). The electric radiation field is in phase with the magnetic field,

258
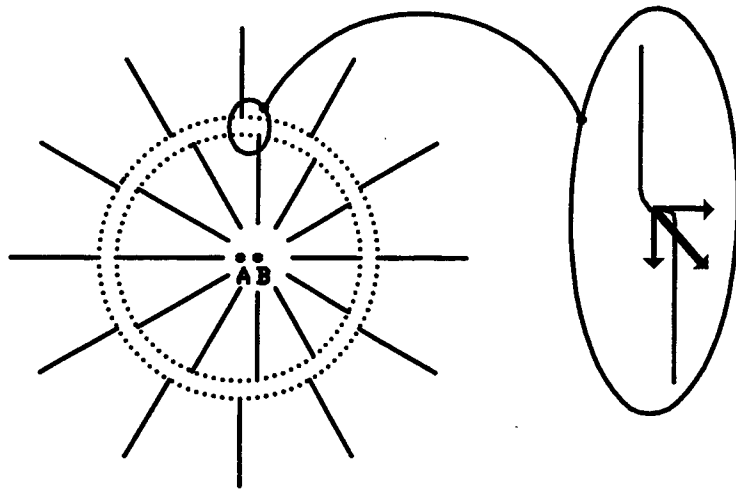
Figure 2. Kink concept of radiation field production by an accelerated charge.
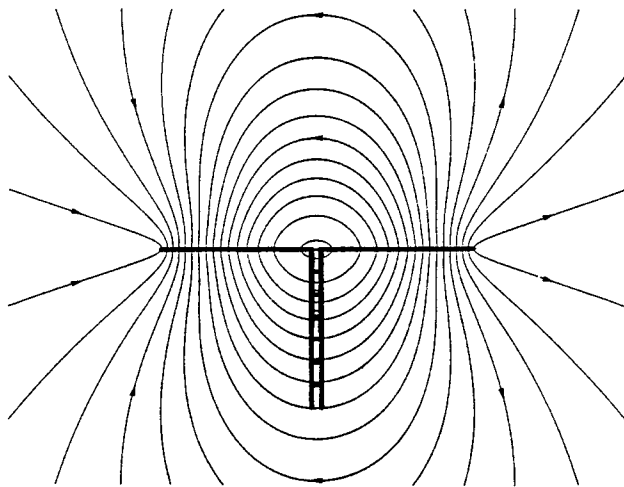
Figure 3. Qualitative illustration of coulomb field associated with a $\lambda/2$ dipole antenna.

and so an "in-phase bootstrap force" which opposes the electron's motion results. This drag force is the essential cause of radiation resistance, and is distinct from the other drag force known as ohmic resistance, which results from collisions of a moving electron with atomic obstacles in its path. Both resistances dissipate energy according to the familiar I^2R relationship, but ohmic loss results in heat (because of its mechanical collision nature) while radiation resistance serves to transform electrical source energy into an electric radiation field.

For efficient antenna operation, the radiation resistance (Ω/cm) must be much greater than the ohmic resistance. Because the radiation field from a $\lambda/2$ dipole is well emulated by a "three-point" model that emphasizes the center and end points, it is reasonable to expect that radiation resistance must rise substantially in value toward the dipole ends.

On the other hand, the induction field at the electron's surface is 90° out of phase with the current/magnetic field, and thus produces a force that opposes the time rate of change of current rather than the current itself. That is, the bootstrap force associated with the induction field is proportional to acceleration. In this case, the energy source driving the electron oscillation therefore expends work on the electron, which is stored in its magnetic field, during periods of acceleration. The magnetic field then collapses and returns energy to the source during periods of deceleration. Because the induction field bootstrap force acts to oppose acceleration, the net effect is analogous to inertia in mechanical systems and the gravitational mass of the electron is effectively increased.

V. Extension to Antennas

In this section, a straight copper wire $\frac{\lambda}{2}$ dipole antenna, isolated in free space, is considered as an representative case and reference is made to Figure 3. Prior discussion dealt with the coulomb field of a single electron, but now we will consider the antenna's coulomb field, combined from all the charged particles (both positive and neg-

ative) in the antenna wire. The antenna, as a whole, also has a magnetic field with is the vector sum of the magnetic fields of all its moving free electrons. Similarly, there is a dynamic electric field for the antenna which is the resultant of all the free electron dynamic fields. We can once more resolve the dynamic field at any point in space into the radiation field (in phase with the total magnetic field) and the induction field (90° out of phase), and note that, at the antenna wire, these fields contribute forces which are parallel to the wire axis. Again, the radiation field decays more slowly with distance than the other components, and the term *far field* is applied to that region of space where the radiation field has become dominant.

Figure 3 is a qualitative view of the coulomb field in space, near a $\lambda/2$ dipole, at a selected fixed point in time. The field line density in Figure 3 depicts field strength. The figure indicates that the field lines are nearly, but not exactly, perpendicular to the wire surface, so there are both perpendicular and parallel field components present there. The perpendicular component exerts a force attempting to pull electrons from the surface, which is possible but uncommon, and the parallel component exerts a force which pushes or pulls free electrons parallel to the wire axis.

Even though the travel of any individual electron is restricted to a fraction of a centimeter, one half of the dipole will accumulate a net excess of electrons during one half-cycle of the feed-point rf excitation and a net deficiency of electrons (that is, positively charged metal ions) will accumulate on the other half of the dipole. The net charge condition reverses during the subsequent rf half-cycle. The force of the coulomb field associated with the charge imbalance between dipole halves opposes the charge motion, and the increasing coulomb field force (as charge accumulates) will eventually become sufficient first to stop the flow, and then reverse it. The reversal process continues periodically, driven at the frequency of the feed-point source, resulting in the oscillating wire currents that produce heat from ohmic resistance and electromagnetic radiation from radiation re-

sistance.

Newton's $F = ma$ law allows a useful approximation, where the three forces involved are the coulomb field component parallel to the wire axis, the dynamic electric field bootstrap force, and the drag force from ohmic resistance. If the ma product is taken to be negligibly small due to the tiny electron gravitational mass, then we conclude the dynamic electric field and antenna coulomb field partially cancel, and the difference field is just sufficient to overcome the ohmic resistance drag force. If the material is idealized to a perfect electric conductor, the coulomb field at a point on the wire surface is the vector opposite of the dynamic electric field.

VI. The Dipole as a Resonant Circuit

Real power is associated with the antenna's radiation field and reactive power is associated with the induction field, but the coulomb field carries both real and reactive power.

As with transmission lines, rf energy is transported from the feed-point to other antenna points by the field in space surrounding the dipole. The real power transported to free electrons along the dipole wire via the coulomb field replinishes the energy lost to ohmic and radiation losses.

Current and charge at a given location along the antenna are 90° out of phase, so that one is zero when the other is maximized. Where the zero current condition occurs, the magnetic field vanishes and energy stored in the coulomb field is maximized; this can be viewed as capacitive (reactive) energy associated with the antenna's distributed capacitance. Conversely, for the zero charge condition, the coulomb field vanishes and the same energy level is now stored in the current's magnetic field; this can be regarded as inductive energy associated with the antenna's distributed inductance. Thus, a meaningful equivalent-circuit model of the resonant $\lambda/2$ dipole is a series resonant RLC circuit where both kinds of distributed resistance (ohmic and radiation) contribute to the value of R.

VII. Topics for Future Research

Reliable calculations of radiation resistance values at points along the length of a dipole antenna wire are feasible, but have not been achieved by the authors to date. CEM techniques, such as the method of moments, may be applied to compute the current and charge distributions on a dipole wire antenna, followed by application of the principles presented in this paper in order to quantitatively characterize the operational details of the antenna as a system.

An accurate simulation and graphical depiction of the power flow associated with a $\lambda/2$ resonant dipole antenna would substantially enhance the visualization and understanding of energy transport from the feed-point to other parts of the antenna. This also remains a project for additional future work.

VIII. Acknowledgment

The authors gratefully acknowledge the earlier work on this subject and contributions to the content of this paper by Ken Macleish.

References

[1] M.A. Plonus, *Applied Electromagnetics*, New York: McGraw-Hill Book Company, p. 58.

[2] D. Halliday and R. Resnick, *Fundamentals of Physics, Third Edition*, New York: John Wiley & Sons, p. 638.

[3] J.D. Jackson, *Classical Electrodynamics, Second Edition*, New York: John Wiley & Sons, Ch. 14.

[4] J.D. Kraus, *Antennas, Second Edition*, New York: McGraw-Hill, Ch. 5.

[5] R.P. Feynman, R.B. Leighton, and M. Sands, *The Feynman Lectures on Physics, Volume I*, Reading, MA: Addison-Wesley Publishing Company, Ch. 32.

[6] K. Macleish, "Why an antenna radiates," QST, November 1992, p. 59-63.

COMPUTATIONAL METHODS FOR INVERSE SCATTERING

Chairs: B. Weedon and G. Newman

Application of Kaczmarz's Method
to Nonlinear Inverse Scattering

WILLIAM H. WEEDON
APPLIED RADAR ANALYSIS
14 UNION STREET. SUITE 2
WATERTOWN, MA 02172
(whw@world.std.com)

ABSTRACT

The use of Kaczmarz's method is investigated as an iterative solver for nonlinear inverse scattering. The distorted-Born approximation is used to linearize the inverse problem at each stage of the outer loop in Kaczmarz's method. resulting in a nonlinear inversion algorithm. Typically, the conjugate gradient (CG) method is used as the iterative solver of choice for nonlinear inverse scattering. The CG method is known to converge quickly when the actual scattering object differs greatly from the initial value used in the inversion. but converges slowly in the final steps of the inversion when the computer model for the scatterer is close to the actual object. A combined Kaczmarz's/CG solution method is suggested where CG is used in the initial steps of the inversion, but Kaczmarz's method is used in the later steps.

1. Introduction

The inverse problems in acoustics and electromagnetics are well known to be non-linear and non-unique. In acoustics. the inverse problem is to reconstruct a quantitative profile of wave velocity and/or attenuation. The problem in electromagnetics is to reconstruct permittivity and/or conductivity distributions of a scatterer. Nonlinear inverse scattering algorithms solve the nonlinear inverse problem directly by employing a computational forward solver. and successively linearizing the inverse problem at each stage in an iterative procedure [1-5].

The conjugate gradient (CG) method is often used as the iterative solver in a nonlinear inversion due to the robustness of the solution. even when the initial scattering object profile differs greatly from the actual object. Experience has shown, however. that while the initial convergence with CG is quite fast. the convergence rate is reduced greatly after approximately 20-30 iterations [4]. Hence. the CG method works well for the initial iterations. but poorly for the final iterations where the reconstruction is close to the true profile.

Kaczmarz's method has been used previously in the contest of computed tomography for X-ray imaging [6] and diffraction tomography [7-8]. to solve linear inverse problems. We investigate the use of Kaczmarz's method in a distorted-Born iterative method algorithm [1-5] to solve the nonlinear inverse problem. That is. we replace the usual CG iterative solver with a Kaczmarz's method solver. We compare the convergence using the Kaczmarz solver with the CG results.

2. Kaczmarz's Method

Kaczmarz's method is used to solve a set of coupled linear equations

$$b_k = \overline{A}_k \cdot x, \qquad k = 1, \ldots, K. \tag{1}$$

In inverse scattering problems, the problem may be subdivided so that k represents a measurement, such as a particular view angle or frequency of illumination.

We summarize Kaczmarz's method solution below:

$$
\begin{aligned}
& x^{(0)} = \text{initial value assigned} \\
& For\ j = 1\ to\ J \\
& \quad x_0 = x^{(j-1)} \\
& \quad x_k = x_{k-1} + \overline{A}_k^\dagger (\overline{A}_k \overline{A}_k^\dagger)^{-1} (b_k - \overline{A}_k x_{k-1}), \quad k = 1, \ldots, K \\
& end\ for\ j \\
& x^{(j)} = x_k.
\end{aligned}
\tag{2}
$$

A pseudoinverse is used in the inner iteration loop of the above procedure. Also, it can be shown that $x^{(J)}$ converges monotonically to a solution to Eqs. (1), if a solution exists. Otherwise, the solution converges to the minimum $\mathcal{L}^2$ norm to Eqs. (1). A more complete discussion of the convergence properties to Kaczmarz's method may be found in [6-8].

3. Linearization using the Distorted Born Approximation

As we mentioned previously, the inverse scattering problem is inherently nonlinear due to multiple scattering. The Kaczmarz method solution applies to linear equations. Hence, we linearize the inverse problem using the distorted Born approximation [9]. In the discussion below, we restrict our attention to electromagnetic scattering in a lossless medium.

We assume an inhomogeneous background medium with permittivity $\epsilon_b(r)$. The actual permittivity is represented as $\epsilon(r)$, and we let $\delta\epsilon(r) = \epsilon(r) - \epsilon_b(r)$. Assuming a two-dimensional TM geometry, the field inside the scatterer and at the receivers in the presence of the background permittivity $\epsilon_b(r)$ is $E_{z0}(r)$. The actual field in the presence of scatterer $\epsilon(r)$ is $E_z(r)$, and the difference is $\delta E_z(r) = E_z(r) - E_{z0}(r)$.

The field perturbation $\delta E_z(r)$ may be thought of as the field perturbation due to the object perturbation $\delta\epsilon(r)$. Using the distorted-Born approximation, the field and object perturbation are related as

$$
\begin{aligned}
\delta E_z(r) &= \mathcal{F}\{\delta\epsilon(r)\} \\
&= k_0^2 \int dr'\, g(r, r')\, E_{z0}(r')\epsilon(r')
\end{aligned}
\tag{3}
$$

The operator $\mathcal{F}$ is known as the Freche't derivative operator, and it is an integral equation relating the object perturbation $\delta\epsilon(r)$ to the field perturbation $\delta E_z(r)$. Hence, the Freche't operator is analogous to the matrix $\overline{A}$ in Kaczmarz's method above. Kaczmarz's method may then be used to solve for $\delta\epsilon(r)$ at a particular iteration of the nonlinear inversion if Equation (3) above is discretized and solved numerically.

4. Kaczmarz-DBIM algorithm

The various steps of our Kaczmarz-DBIM algorithm are summarized below.

1. Choose initial background permittivity ϵ^0

2. for $j = 1$ to J

3. Linearize problem using distorted-Born approximation

4. Compute field inside object $E_{z0}(r)$ and Green's function $g(r, r')$ using current background profile ϵ^{j-1}.

5. Set $\delta\epsilon_0 = 0$

6. Inner loop on experiment k, varying transmitter and frequency

7. Compute $\delta\epsilon_k = \delta\epsilon_{k-1} + \overline{F}_k^\dagger \cdot (\overline{F}_k \cdot \overline{F}_k^\dagger)^{-1} \cdot (\delta E_z^{\text{meas}} - \overline{F}_k \cdot \delta\epsilon_{k-1})$

8. end loop on k

9. $\epsilon^j = \epsilon^{j-1} + \delta\epsilon_K$

10. end loop on j

References

[1] W. C. Chew and Y. M. Wang, "Reconstruction of two-dimensional permittivity using the distorted Born iterative method. *IEEE Trans. Medical Imaging*. Vol. 9, pp. 218-225, 1990.

[2] M. Moghaddam and W. C. Chew, "Study of some practical issues in inversion with the Born iterative method using time-domain data," *IEEE Trans. Antennas Propagat.* Vol 41, pp. 177-184, 1993.

[3] M. Moghaddam, W. C. Chew and M. Oristaglio, "Comparison of the Born Iterative Method and Tarantola's Method for an Electromagnetic Time-domain Inverse Problem", *Internat. J. Imaging Sys. Technol.* Vol. 3, pp. 318-333, 1991.

[4] W. H. Weedon and W. C. Chew, "Time-domain inverse scattering using the local shape function (LSF) method," *Inverse Probl.* Vol. 9, pp. 551-564, 1993.

[5] W. C. Chew, G. P. Otto, W. H. Weedon, J. H. Lin, C. C. Lu, Y. Wang and M. Moghaddam, "Nonlinear diffraction tomography—the use of inverse scattering for imaging," *Int. J. Imaging Sys. Technol.*, Vol. 7, pp. 16-24, 1996.

[6] F. Natterer, *The Mathematics of Computerized Tomography*, Wiley, New York, 1986.

[7] K. T. Ladas and A. J. Devaney, "Generalized ART algorithm for diffraction tomography," *Inverse Problems*, Vol. 7, pp. 109-128, 1991.

[8] R. W. Deming, *New Tomographic Imaging Methods for Geophysical and Medical Ap-*

plications, Ph.D. Dissertation, Northeastern University, Boston, MA, 1996.

[9] M. Born and E. Wolf, *Principles of Optics, Sixth Ed.*, Pergamon, New York, 1980.

STATISTICAL CHARACTERISTICS OF REFLECTION AND SCATTERING OF ELECTROMAGNETIC RADAR PULSES BY ROUGH SURFACE AND BURIED OBJECTS

Yasumitsu MIYAZAKI, Koichi TAKAHASHI and Stefan KNEDLIK*

Department of Information and Computer Sciences

Toyohashi University of Technology

Tempaku-cho, Hibarigaoka, Toyohashi, 441, Japan

miyazaki@emlab.tutics.tut.ac.jp, FAX 0532-48-3422

*Universität GH-Siegen, Hölderlinstrasse, 57068 Siegen, Germany.

1 Introduction

In this paper, electromagnetic wave reflection and scattering of mono-pulses generated by SA radar and GP radar are statistically studied for target objects, buried under the random ground surface and built on rough surface, using FD-TD method. Statistical analysis of electromagnetic wave reflection and scattering from complicated media condition is important for improving of resoluton of imaging radar, and actualize more safety radio commucation. So, many theoretical and experimental papers are reported. Rapid progress of computers in recent years made possible the numerical analysis of electromagnetic wave scattering using FD-TD (Finite-Difference Time-Domain) method. By using FD-TD method, numerical simulations are accomplished for main reflection and multiple scattering.

2 Analysis model

2.1 GP Radar case

The detection of underground objects with GP radars is difficult for effects of unwanted underground scatterer, such as stone, air gaps, etc. So, we analyzed the relationship between the complication of underground and the randomness of received signal with GP radar, using statistical functions, such as deviation and correlation function. Analysis model of GP radar case is shown in Fig. 1. Analysis region is made up of two parts, 0.5 m above the ground and 2.5 m below the ground. The target is a rectanglar air gap which is placed at 1.0 m depth and is 0.5 m by 0.3 m in size. For the soil, the relative permittivity is defined as 4.0, relative permeability as 1.0 conductivity is 10^{-7}. And around an air gap are the many obstacles with random permittivity. Source antenna is a plane antenna of width is 0.3 m and placed 0.1 m above the ground. Incident wave is Gaussian as shown in Fig. 2 and current distribution of plane antenna is defined as in Fig. 3.

2.2 SA radar case

In the case of remote sensing of the building on the surface of the earth, using SA radar with radar platform as aircraft or satellite, the rough surface consist of moutains, trees, and any other buildings which often produce serious effect on the radar signal. So we considered one building on the rough surface as a target of remote sensing. After the FDTD analysis, statistical analysis similar to the GP radar case is acheived. Analysis model of SA radar case is shown in Fig. 4. Analysis region is made up from 280 m above the ground and 20 m under the ground and the target is a building of height 20 m and width 20 m. Actually, radar for remote

sensing uses microwave frequency (wavelength of the order cm) because microwave radar can image the surface of the earth independent of atmosphere or clouds. But due to computer memory limitations, we used the pulse wave 20 m in wavelength and analyzed the relationship between the wavelength and roughness of the surface of the earth, using statistical function described in the previous section. As a source of radar, we used plane antenna which width is 80 m. In this case, the antenna is almost non-directional, so we used weighted function shown in Fig. 5 and generate the directive pulse.
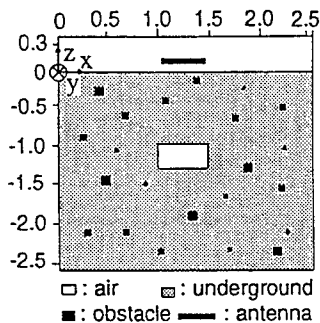
Fig. 1 Analysis model of GP radar case
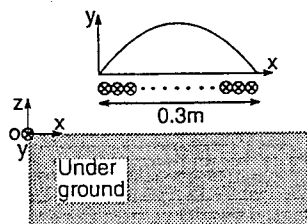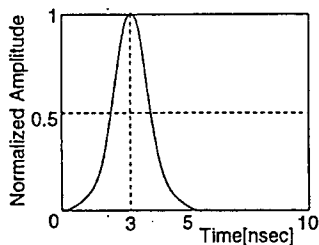
Fig. 2 Incident wave of GP radar

Fig. 3 Current disribution of plane antenna
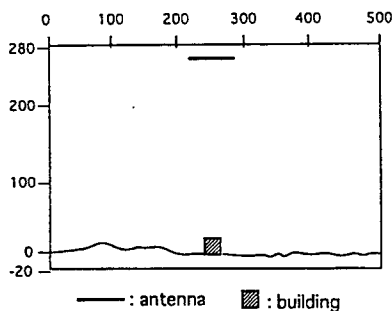
Fig. 4 Analysis model of SA radar

3 FD-TD formulation

When the two dimensional analysis region are given as shown in Fig. 1 or Fig. 2, the region is divided into small cells as shown in Fig. 6 and components of electromagnetic fields are displaced in individual cells as shown in Fig. 7. There is cells shown as Yee's cells. The FD-TD method is formulated by discretization of Maxwell equation as follows: i,j indicate the position in x-z plane, and n is the number of time step,

Fig. 5 Weighted function of SA radar pulse

$$H_x^{n+\frac{1}{2}}\left(i, j+\frac{1}{2}\right) = H_x^{n-\frac{1}{2}}\left(i, j+\frac{1}{2}\right) + C_1\{E_y^n(i, j+1) - E_y^n(i, j)\} \tag{1}$$

$$H_z^{n+\frac{1}{2}}\left(i+\frac{1}{2}, j\right) = H_z^{n-\frac{1}{2}}\left(i+\frac{1}{2}, j\right) + C_1\{E_y^n(i+1, j) - E_y^n(i, j)\} \tag{2}$$

$$\begin{aligned} E_y^n(i, j) = & \ C_2 E_y^{n-1}(i, j) - C_3 J^{n-\frac{1}{2}}(i, j) + C_4 \left\{ H_x^{n-\frac{1}{2}}\left(i, j+\frac{1}{2}\right) \right. \\ & \left. - H_x^{n-\frac{1}{2}}\left(i, j-\frac{1}{2}\right) - H_z^{n-\frac{1}{2}}\left(i+\frac{1}{2}, j\right) + H_z^{n-\frac{1}{2}}\left(i-\frac{1}{2}, j\right) \right\} \end{aligned} \tag{3}$$

where $C_1 \sim C_4$ are constants,

$$C_1 = \frac{\Delta t}{\Delta s\, \mu(i,j)} \tag{4}$$

$$C_2 = \frac{1 - \Delta t\, \sigma(i,j)/2\,\varepsilon(i,j)}{1 + \Delta t \sigma(i,j)/2\,\varepsilon(i,j)} \tag{5}$$

$$C_3 = \frac{\Delta t/\varepsilon(i,j)}{1 + \Delta t \sigma(i,j)/2\,\varepsilon(i,j)} \tag{6}$$

$$C_4 = \frac{\Delta t/\Delta s\, \mu(i,j)}{1 + \Delta t \sigma(i,j)/2\,\varepsilon(i,j)} \tag{7}$$

$\Delta s = \Delta x = \Delta z$ is space increment, and Δt is time increment. For stability of the FD-TD solution, Δs and Δt should satisfy the condition,

$$\Delta t \le \frac{\Delta s}{2c} \tag{8}$$

By using these equations, propagation of electromagnetic wave in an infinite analysis region is modeled, but since infinite computer memory is not possible, an appropriate boundary conditions must be applied. The absorbing boundary condition, proposed by G. Mur, to solve this is

$$\left(\frac{\partial}{\partial n} + \frac{1}{v}\frac{\partial}{\partial t} \right) E = 0 \tag{9}$$

where n is the symbol for the component normal to the boundary, and v is the velocity of electromagnetic wave.
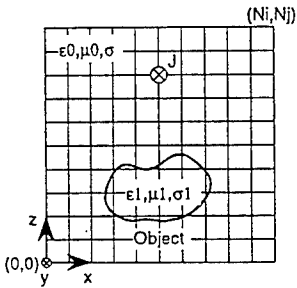
Fig. 6 Division of analysis region
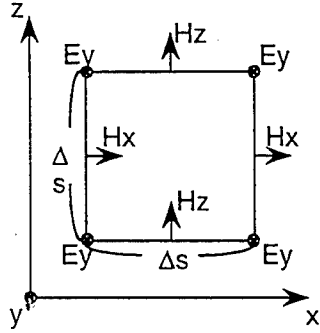
Fig. 7 Displacement of electromagnetic components

4   Statistical analysis of electromagnetic wave scattering

4.1   random surface analysis

To study the roughness of random surface, we used standard deviation of surface height(σ_z) and correlation length(l). When the height of surface at distance $i = (i-1)\Delta x$ is given by $z(i)$, standard deviation σ_z is given by

$$\sigma_z = \left[\frac{1}{N-1} \left(\sum_{i=1}^{N} z(i)^2 - N(\bar{z}^2) \right) \right]^{1/2} \tag{10}$$

where

$$\bar{z} = \frac{1}{N} \sum_{i=1}^{N} z(i), \tag{11}$$

and N is the number of samples.

270

Next, autoautocorrelation function of surface is given by

$$R(x') = \frac{\sum_{i=1}^{N+1-j} z(i)z(j+1-1)}{\sum_{i=1}^{N} z(i)^2} \tag{12}$$

where x' is distance $(j-1)\Delta x$. The distance l for which $R(l)$ is equal to $1/e$, is defined as correlation length.

4.2 Random wave analysis

To analyze effect of roughness of the surface or complication of media on scattered wave from radar, the following statistical functions are used.

The received signal on plane surface model is defined as E_h, and the one on random surface is defined as E_r. The relationship between E_r and E_h is studied statistically. The second order averaged error is given by

$$\sigma_{Ey}^2 = \sum_{i=1}^{N} \frac{(E_r(t_i) - E_h(t_i))^2}{T} \tag{13}$$

$$T = t_N - t1 + \Delta t \tag{14}$$

where t_1 is the time taken by radar pulse to reach the ground in both cases of GP and SA radar. But if only the phase of reflected wave is shifted, forward error grows so large, therefore correlative analysis is nessesary. The corresponding correlation coefficient, R_{E_r,E_h} is given by

$$R_{E_r,E_h} = \frac{C(E_r, E_h)}{\sigma_{E_r} \cdot \sigma_{E_h}} \tag{15}$$

$$\sigma_{E_r}^2 = \frac{1}{T} \sum_{i=1}^{N} \{E_r(t_i) - \mu_{E_r}\}^2 \tag{16}$$

$$\sigma_{E_h}^2 = \frac{1}{T} \sum_{i=1}^{N} \{E_r(t_i) - \mu_{E_r}\}^2 \tag{17}$$

$$C(E_r, E_h) = \frac{1}{T} \sum_{i=1}^{N} \{E_r(t_i) - \mu_{E_h}\}\{E_h(t_i) - \mu_{E_h}\} \tag{18}$$

5 Results

We analyzed at six models for which randomness or complication of media is various. Model Case $1 \sim 3$ are GP radar case and model Case $4 \sim 6$ are SA radar case. And received signal given by FD-TD analysis are also shown.
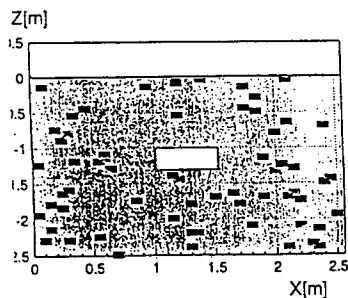
Fig. 8 Model of case 1
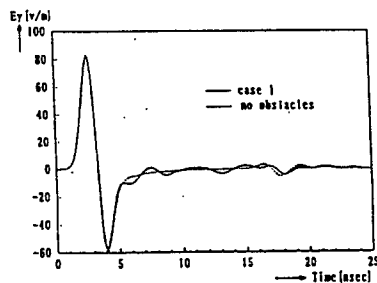
Fig. 9 Received signal by FD-TD analysis
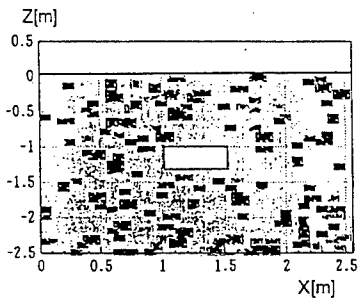
Fig. 10 Model of case 2
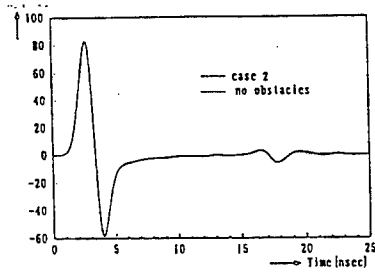
Fig. 11 Received signal by FD-TD analysis
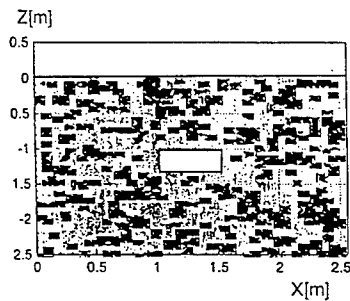
Fig. 12 Model of case 3
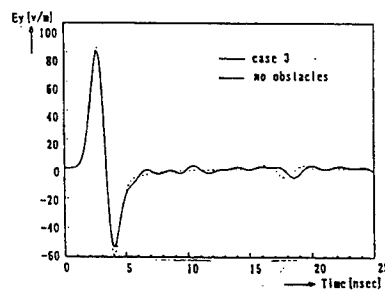
Fig. 13 Received signal by FD-TD analysis
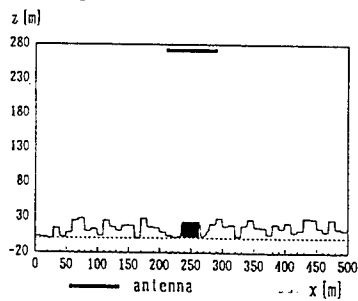
Fig. 14 Model of case 4
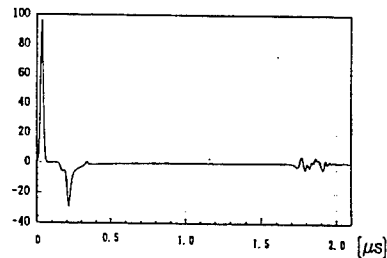
Fig. 15 Received signal by FD-TD analysis
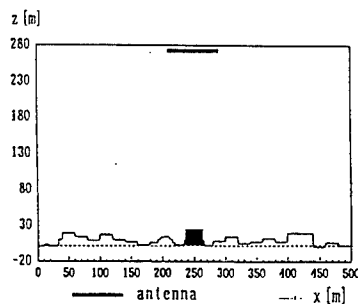
Fig. 16 Model of case 5
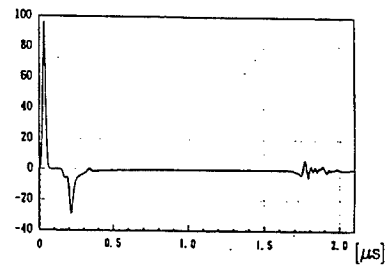
Fig. 17 Received signal by FD-TD analysis
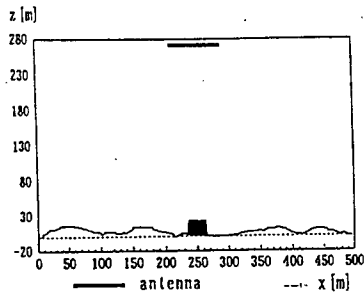
Fig. 18 Model of case 6
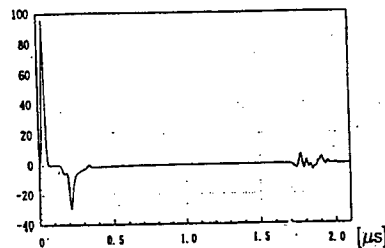
Fig. 19 Received signal by FD-TD analysis

6 conclusion

The result of statistical analysis is shown in Table 1, with roughness of surface indicated by the standard deviation and correlation length, and complication of media is described as correlation length of media constant at height $z = 0$. The table shows that when the roughness or complication of media increases, the randomness of received signal increases. In this paper, statistical analysis of wave scattering is validated. As future work, effective signal processing of random scattered wave to improve radar imaging will be considered.

Table 1 Result of statistical analysis

Model	Complication of media		Effect of random scatterer	
	σ_f	$\mathcal{L}$	σ_{ε_r}	$R_{\varepsilon_r, \varepsilon_h}$
case 1	0.0395	14.5 cm	0.2376	0.9833
case 2	0.0291	10.0 cm	3.446	0.7908
case 3	0.0227	6.0 cm	3.713	0.7727
case 4	6.2189	12.0 m	9.4529	0.2493
case 5	8.4094	7.0 m	7.1579	0.5549
case 6	5.2600	15.0 m	7.5270	0.7795

References

(1) J. Sonoda and Y. Miyazaki, "Dynamic Characteristics of Electromagnetic Scattering of Pulse Wave by Buried Object Using FD-TD Method", Proc. of Int. Symp. on EMC'94, Sendai, Japan, 18P407, pp.382-385,1994

(2) K. Taketomi and Y. Miyazaki, "Analysis of Scattering by Buried Objects using FD-TD Method and Spectrum Separate Calculation Method", Proc. of ISAP'92, Sapporo, Japan, 4E3-1, pp.433-438,1992

(3) Y.Miyazaki and Y.Jyonori, "Statistical Reflection Properties of Electromagnetic Monopulse by Buried Objects in Subsurface Random Ground Using FD-TD", Proc. of 12th Annual Review of Program in Applied Computational Electromagnetics, Monterey CA USA, pp.492–499, 1996

(4) Adrian K. Fung, Milind R. Shah, and Saibun Tjuatja, "Numerical Simulation of Scattering from Three-Dimensional Randomly Rough Surfaces", IEEE Trans. GRS, Vol. 32, No. 5, 1994

(5) Fawwatz T. Ulaby, Richard K. Moore, and Adrian K. Fung, "Microwave Remote Sensing", Vol. II, Addison-Wesley Publishing Company, Inc., 1982

(6) John C. Curlander and Robert N. McDonough, "SYNTHETIC APERTURE RADAR Systems and Signal Processing", A Wiley-Interscience publication, 1991

(7) K.S.Yee: "Numerical Solution of Initial Boundary Value Problems Involving Maxwell's Equations in Isotropic Media", IEEE Trans.AP, Vol.14-3, pp.302–307, 1966.

(8) G.Mur: "Absorbing Boundary Conditions for the Finite-Difference Approximation of the Time Domain Electromagnetic-Field Equations", IEEE Trans.EMC, Vol.23-4, pp.377–382, 1981.

Nondestructive Materials Measurement of Electrical

Parameters with Readily Made Coaxial Probes

Timothy R. Holzheimer* and Dr. Charles V. Smith, Jr. **

*Raytheon E-Systems/UT Arlington, P. O. Box 75403,
Greenville, Texas 75403
**UT Arlington, Department of Electrical Engineering, P. O.
Box 19167, Arlington, Texas 76019

The electrical parameters of materials is required in the design and construction of loaded antennas and all devices using dielectric substrates. Methods of nondestructive measurement are desired due to cost and availability of limited materials and for simplicity in making the electrical parameter measurements. The approach described makes use of coaxial probes, made of readily available components, as compared to techniques implementing cavity resonators, coaxial lines, various waveguide types and free space measurements. These probes do require minor machining of their plates.

The material parameters to be measured include complex permittivity (i.e. dielectric constant and loss tangent) and complex permeability. This investigation required measured material electrical parameters for inclusion in the analysis and design of cavity backed antennas. Full two-port measurements were made using a network analyzer. The measured data was

then input to an analytical program in order to reduce the S-parameter data to the electrical parameters of the materials investigated. The analytical program includes airgaps between both upper and lower surfaces of the material to be measured. This analysis builds upon previously reported results of Baker-Jarvis, Janezic, Stafford and Ching-Lieh. [1,2,3]

Several materials were measured with these practically built coaxial probes. . In particular, a YBCO high temperature superconducting thin film was measured and is reported here. A technique is also described whereby T-parameters are used in order to back out the electrical parameters of the thin film by itself, that is not including the lanthanum aluminate substrate.

Potential measurement problems are addressed in using these coaxial probes for performing nondestructive measurements of the material electrical parameters. An assessment is made in the accuracy of the measurement and what is required for a loaded antenna. Measured data, for one case, of a loaded cavity backed antenna is compared using the measured electrical parameters in a hybrid finite element/boundary element/method of moments analytical prediction code.

References:

1. Baker-Jarvis, J., Janezic, M.D. and Stafford, R. B., "Shielded Open-Circuited Sample Holders For Dielectric and Magnetic Measurement of Liquids and Powers," NIST, Tech Report NISTIR 5001, March, 1993.

2. Baker-Jarvis, J. and Janezic, M.D., "Analysis of a Two-Port Flanged Coaxial Holder for Shielding Effectiveness and Dielectric Measurements of Thin Films and Thin Materials," IEEE Transactions EMC, Vol. 38, No. 1, February, 1996, pp. 67-70.

3. Ching-Lieh, Li, "Measurement of Electromagnetic Properties of Materials Via Coaxial Probe Systems," PhD Dissertation, Michigan State University, 1993.

A VOLUME-INTEGRAL CODE FOR ELECTROMAGNETIC NONDESTRUCTIVE EVALUATION

R. Kim Murphy, Harold A. Sabbagh, Anthony Chan, and Elias H. Sabbagh
Sabbagh Associates, Inc., 4635 Morningside Drive, Bloomington, IN 47408, USA

Introduction. In [1] we developed a volume-integral eddy-current model that is designed to solve problems in nondestructive evaluation. The integral equations are discretized on a regular grid, which means that the resulting matrices are either Toeplitz, which implies a convolutional structure, or Hankel, which implies a correlational structure. In either case, large problems can be solved using conjugate-gradients, with the matrix-vector multiplies computed using the three-dimensional fast Fourier transform. The default scheme for solving the equations is the LU-decomposition.

The model is now implemented in the computer code VIC-3D[1], and in this paper we present some results computed with it. Our first results are aimed at validating the model and code by comparing data from two benchmark experiments, and in the second part of the paper we give model calculations that are typical of the nuclear power industry.

Two Validation Problems. The first problem, which is illustrated in Figure 1, consists of a coil that is scanned over a flaw in a conducting workpiece [3]. The flaw is a long, thin, empty slot, and

Host: $\sigma = 3.06 \times 10^7$ S/m
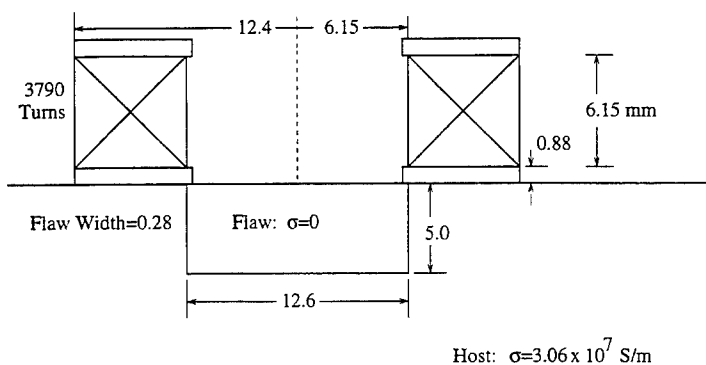
Figure 1: Validation Problem No. 1, consisting of a coil being scanned over a long, narrow, empty slot in a half-space of aluminum. All dimensions are in millimeters.

the workpiece is a half-space of aluminum. The excitation frequency is 900 Hz, and the objective is to compute the change in impedance seen by the probe coil, as the coil is scanned over the flaw, and compare with the measured values listed in [3]. The results for the real and imaginary parts of the impedance-change are shown in Figure 2.
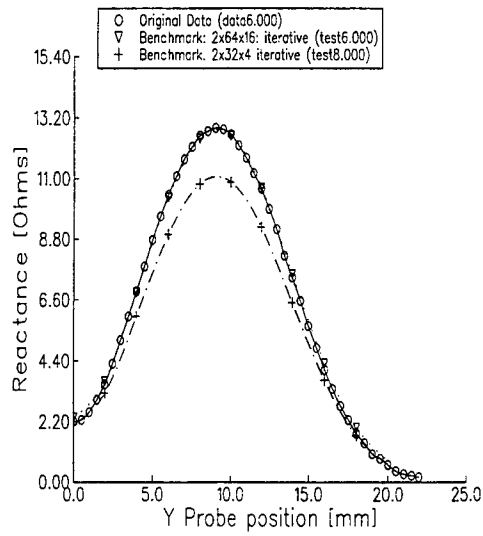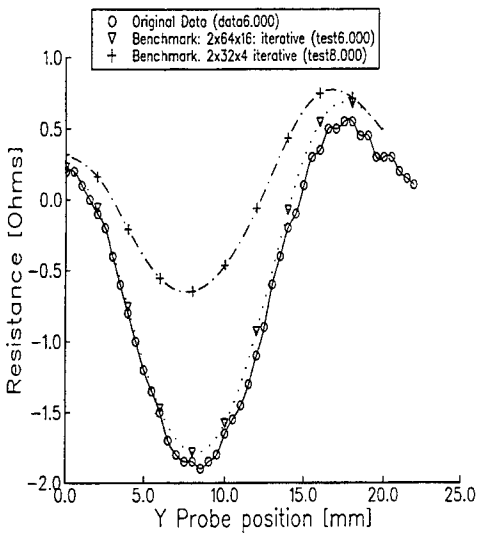
Figure 2: Comparison of measured and computed changes-of-impedances for Validation Problem No.1. The ∇'s label results for a mesh of $2 \times 64 \times 16$ (width $\times$ length $\times$ depth) cells, and the $+$'s label results for a mesh of $2 \times 32 \times 4$ cells. The original data, which are the experimental benchmark results, are labeled with the 0's.

The conjugate gradient iterative method was used to compute the results shown in Figure 2; in the following figure we show the reduction of the normalized residual as the algorithm converges.

```
                PERCENT ERROR in RESIDUAL
            0      25     50     75    100
            |       |      |      |      |
Iteration   ----------------------------------    dR [Ohm]    dX [Ohm]
    0       |******************************  100.00    .0000E+00   .0000E+00
    5       |****************************    91.28   -.2454E+00   .4074E+00
   10       |*************************       82.58   -.7444E+00   .1189E+01
   15       |************************        76.78   -.1048E+01   .1950E+01
   20       |**********************          72.85   -.1192E+01   .2689E+01
   25       |*********************           64.93   -.1341E+01   .4485E+01
   30       |*****************       52.23           -.1469E+01   .7168E+01
   35       |***********     35.40                   -.1541E+01   .9996E+01
   40       |*******      22.34                      -.1563E+01   .1149E+02
   45       |******      17.31                       -.1567E+01   .1190E+02
   50       |*****      14.82                        -.1569E+01   .1208E+02
   55       |****      11.77                         -.1573E+01   .1225E+02
   60       |***      9.76                           -.1578E+01   .1235E+02
   65       |**      7.56                            -.1586E+01   .1244E+02
   70       |**      5.09                            -.1594E+01   .1251E+02
   75       |*      3.72                             -.1597E+01   .1253E+02
   80       |*      2.81                             -.1597E+01   .1254E+02
   85       |*      2.20                             -.1593E+01   .1255E+02
   90       |       1.43                             -.1585E+01   .1256E+02
   95       |        .86                             -.1580E+01   .1256E+02
  100       |        .49                             -.1578E+01   .1256E+02
  105       |        .30                             -.1577E+01   .1256E+02
  110       |        .19                             -.1577E+01   .1256E+02
  115       |        .11                             -.1577E+01   .1256E+02
  120       |        .05                             -.1577E+01   .1256E+02
|Z| converged
```

The result is for the fine mesh ($2 \times 64 \times 16$ cells), with the probe located at 10 mm. There are 4960 unknowns in this problem.

In the second validation test, we compare model predictions with measurements performed at the Oak Ridge National Laboratory and communicated to us by Dr. C. V. Dodd. The test that we have modeled is shown in Figure 3. It consists of a bobbin coil within an aluminum tube ($\sigma = 2.58 \times 10^7$ S/m), which has four through-wall holes symmetrically placed around the circumference of the tube. The coil is excited at 500 Hz. In modeling this test, we compute the change in impedance due to one hole, and divide the measured impedance-changes by four.

The magnitude and phase of the impedance-change due to the holes is shown in Figure 4. The differences between measurement and model calculation may be due to the fact that in computing the matrix elements for the scattering from the flaw, we treat the tube as being a flat workpiece. This allows us to use a Green's function for a layered, plane-parallel host, of the type that was used in the first test problem. Another possibility for the discrepancy is that the signal from four holes is not simply four times the signal from a single hole.
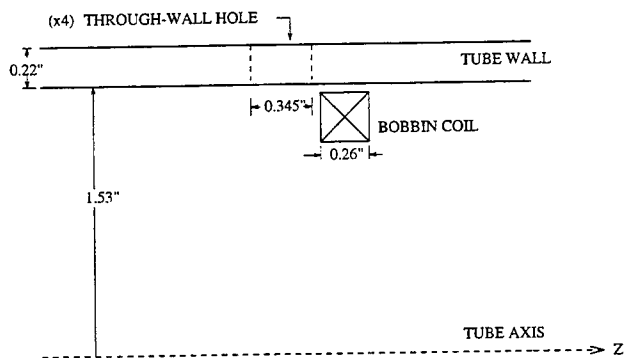
Figure 3: Validation Problem No. 2, consisting of a bobbin coil within an aluminum tube with a circular hole.
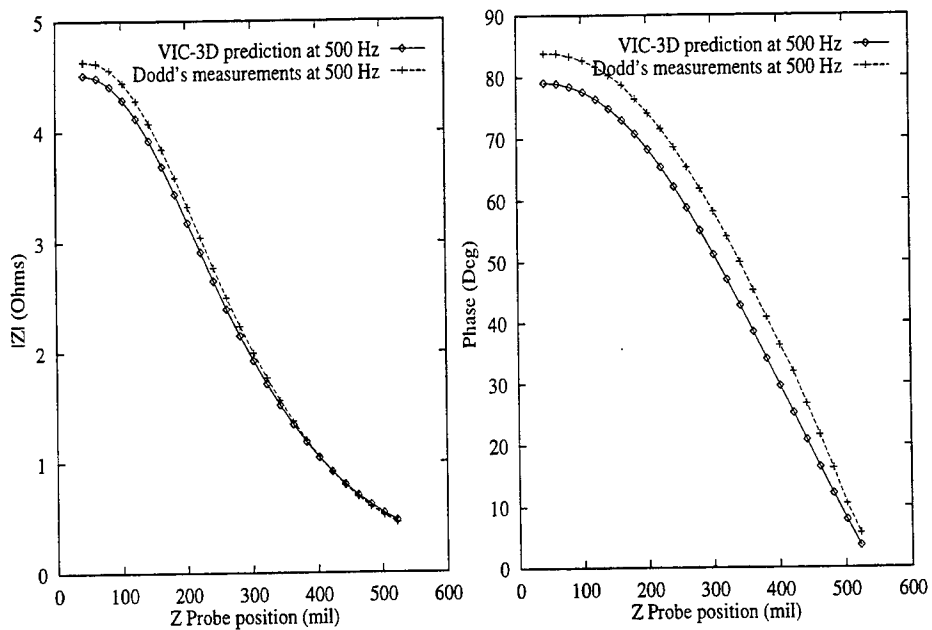
Figure 4: Comparison of measured and computed changes-of-impedances for Validation Problem No.2.

Axisymmetric Problems in Nuclear Power. In [2] we specialized the general three-dimensional formulation of [1] to axisymmetric problems, such as those typically found in steam generator tubing for the nuclear power industry. These problems, which are defined by means of a few parameters, are solved in a module called Tube Support Plate. Figure 5 illustrates the manner in which the parameters may vary in order to define problems ranging in complexity from a simple tube support plate with a magnetite gap to a tube with a non-uniform radius, support plate, magnetite gap, and sludge region. All axisymmetric problems are solved using the LU-decomposition. because the resulting equations lack the Toeplitz or Hankel structure in the radial direction, which negates the advantage of using the conjugate-gradient/FFT algorithm.

A Model Calculation. Figure 6 illustrates a common situation in the nuclear power industry, in which an axial flaw exists on the outer surface of a tube, and is centered under a ferromagnetic tube support that may even contain a layer of magnetite. The detector is a standard differential bobbin probe. The challenge is to detect and classify flaws, which produce a relatively small signal, in the presence of the large signal presented by the tube support or the magnetite layer. The results shown in Figure 6 are for a model calculation, only. We do not have experimental data to support this calculation.

References

[1] R. Kim Murphy, Harold A. Sabbagh, Jeff C. Treece, and Lai Wan Woo, "A Volume-Integral Code for Electromagnetic Nondestructive Evaluation," Conference Proceedings, 11th Annual Review of Progress in Applied Computational Electromagnetics, March 1995, pp. 109-116.

[2] H. A. Sabbagh, R. K. Murphy, J. C. Treece, and L. W. Woo, "Application of Volume-Integral Models to Steam Generator Tubing," in *Review of Progress in Quantitative Nondestructive Evaluation*, Vol. 14, D. O. Thompson and D. E. Chimenti, eds., Plenum Press, New York, 1995, pp. 283-289.

[3] S. Burke, "A Benchmark Problem for Computation of ΔZ in Eddy-Current NDE," Journal of Nondestructive Evaluation, Vol. 7, Nos. 1/2, 1988, pp. 35-41.
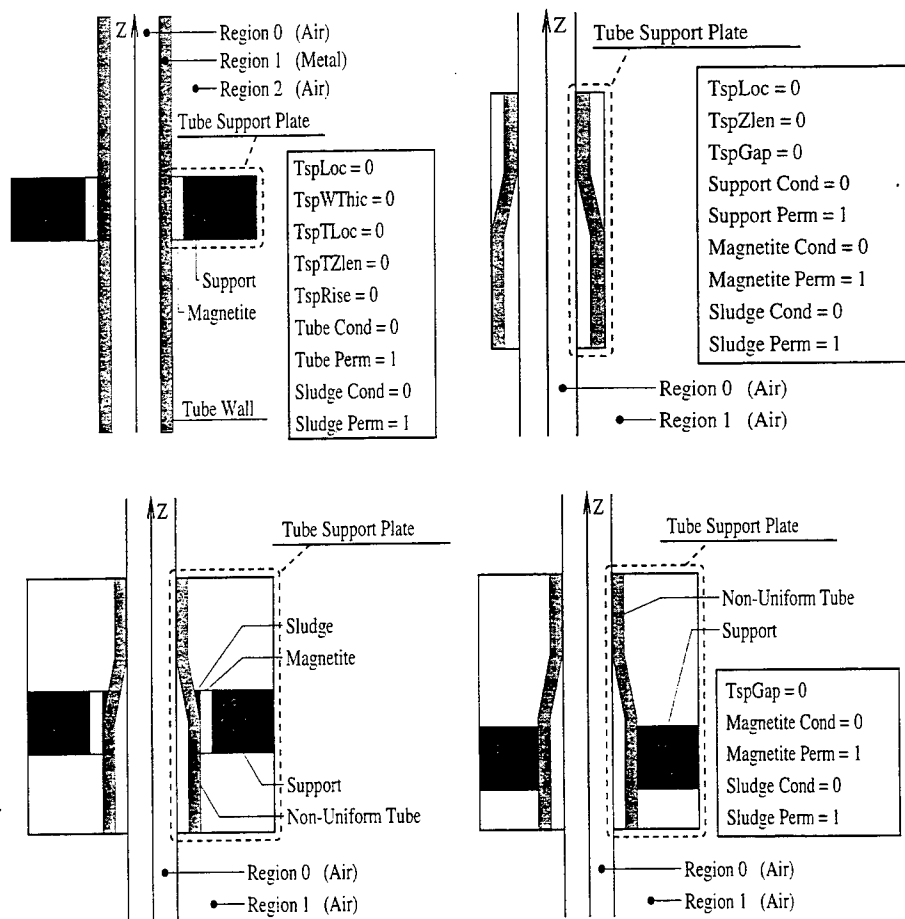
Figure 5: Examples of axi-symmetric regions modeled with the Tube Support Plate. Clockwise from upper left: 1. Tube support plate with magnetite gap; 2. Tube with non-uniform radius; 3. Tube with non-uniform radius and support plate; 4. Tube with non-uniform radius, support plate, magnetite gap, and sludge region.
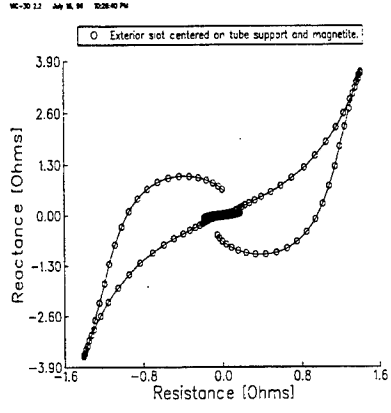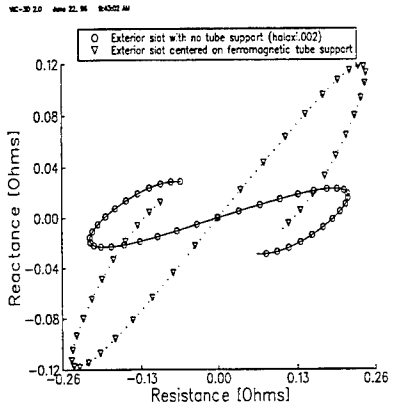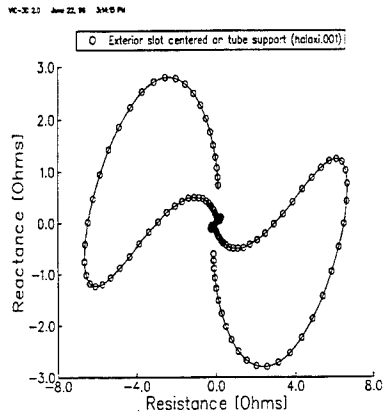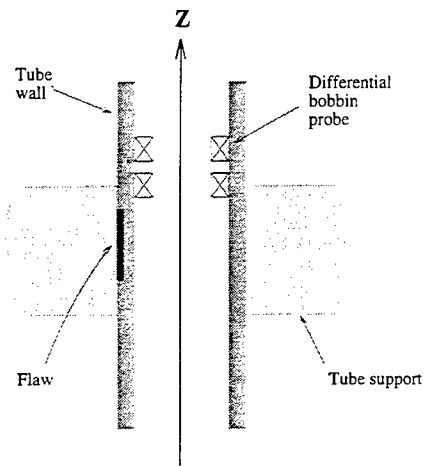
Figure 6: 1) An external axial flaw, centered under a ferromagnetic tube support is shown in the upper left. 2) The response of the differential bobbin probe to the flaw and tube support is shown in the upper right. The signal from the edges of the tube support dwarf the flaw signal, which is buried in the middle of the curve. 3) The flaw signal alone is shown in the lower left; the tube support signal has been subtracted ('balanced out'). Also shown is the flaw signal from a tube with no support. 4) The effect of a large magnetite layer on the curve in the upper right is shown in the lower right.

SESSION 7:

WAVELETS
AND
FRACTALS

Chairs: R. Haupt and D. Werner

Application of Coifman Wavelets to the Solution of Integral Equations

Mikhail Toupikov and Guangwen Pan

Department of Electrical Engineering
Arizona State University

Abstract

A topic of considerable current interest in engineering and applied mathematics is wavelets. In electromagnetics, wavelets have been used in conjunction with the method of moments (MoM) and the finite difference time domain (FDTD). It has been demonstrated that very sparse impedance matrices can be obtained when wavelets basis and testing functions are employed in the MoM. However, there are concerns against the use of the wavelets in the MoM. It seems that the advantage of having sparse matrices is outweighted by the complexity and time consuming evaluations of the numerical integration, due to the poor regularity and lack of closed forms of the wavelets.

In this presentation, we propose the use of the Coifman wavelets, where the majority of the matrix entries can be carried out without performing the time consuming Gausian quadrature. For electrically large problems, the new algorithm will be more efficient than the Collocation method (pulse expansion and point matching approach). A numerical example of 3D Mie scattering showed good agreement with analytic solution. The relative error of this method is rigorously studied by means of analytic expressions.

1 INTRODUCTION

Wavelet functions have been employed recently as basis functions in the method of moments (MoM) solution of integral equations [1],[2],[3]. In conventional MoM, the integration domain is discretized into several subdomains. Then, the unknown function (usually the current density on the scatterer) is expanded in terms of the basis functions with unknown coefficients. Basis functions may be defined on the whole integration domain or be defined on one or several subdomains. Finally, the resultant equations are tested with the weighting functions resulting in a set of linear algebraic equations whose solution gives the unknown coefficients. The resulting matrix is dense and solution of such a system of linear equation is very time consuming, especially for electrically large objects.

Using wavelets as basis functions in a Galerkin method leads to highly localized system matrices. Due to local supports and vanishing moment properties of wavelets, many of the matrix elements are very small compared to the largest element and

can be dropped without significantly degrading the solution. The big disadvantage of such approach is that before applying a threshold procedure one must calculate all matrix elements.

Fast Wavelet Transforms (FWT) have been used to produce matrix representation of integral operators [4], but only Calderon-Zigmund type kernels on real line have been considered. Nonetheless, most integral equations in Electromagnetics do not satisfy the Caldoren-Zigmund conditions.

In this paper we propose the use of a special class of wavelets, Coifman wavelets, which allow us to apriory identify all small elements of the system matrix and to perform threshold procedure without having these elements calculated. In this article, the new approach is applied to real world problems, and error estimate is presented.

2 BASIC FORMULATIONS OF WAVELET THEORY

2.1 Scaling Function

A multiresolution analysis of $L^2(\mathcal{R})$ is defined as a nested sequence of closed subspaces $\{V_j\}_{j \in \mathcal{Z}}$ of $L^2(\mathcal{R})$, such that

$$\cdots \subset V_j \subset V_{j+1} \subset \cdots \subset L^2(\mathcal{R})$$

$$v(x) \in V_j \Leftrightarrow v(2x) \in V_{j+1}$$

$$v(x) \in V_0 \Rightarrow v(x+n) \in V_0, \text{ for all } n \in \mathcal{Z} \tag{1}$$

$$\bigcap_{j \in \mathcal{Z}} V_j = \{0\}, \quad \overline{\bigcup_{j \in \mathcal{Z}} V_j} = L^2(\mathcal{R})$$

A scaling function $\varphi(x) \in V_0$, with a non-vanishing integral, exists such that the set $\{\varphi(t-l) \mid l \in \mathcal{Z}\}$ forms an orthogonal basis of V_0. Since $\varphi \in V_0 \subset V_1$, a sequence $\{h_k\} \in l^2(\mathcal{R})$ exists such that the scaling function satisfies

$$\varphi(x) = \sqrt{2} \sum_k h_k \varphi(2x - k) \tag{2}$$

This functional equation is referred to as the dilation equation, where $\{h_k\}$ satisfies

$$\sum_k h_k = 1 \tag{3}$$

The set of functions $\{\varphi_{j,l} \mid j, l \in \mathcal{Z}\}$, with

$$\varphi_{j,l}(x) = 2^{j/2} \varphi(2^j x - l) \ . \tag{4}$$

forms an orthonormal basis of V_j.

2.2 Wavelets

Let us use W_j to denote a space complementing V_j in V_{j+1}, that is, a space that satisfies

$$V_{j+1} = V_j \oplus W_j \tag{5}$$

A function ψ is called a wavelet if the set of functions $\{\psi(x-m) \mid m \in \mathcal{Z}\}$ forms an orthonormal basis of W_0. If such a function can be found, then the set of wavelet functions $\{\psi_{j,m} \mid m, j \in \mathcal{Z}\}$ forms an orthonormal basis of W_m, with

$$\psi_{j,m}(x) = 2^{j/2}\psi(2^j x - m)$$

From the definition of multiresolution analysis (1), it follows that

$$\bigoplus_{j \in \mathcal{Z}} W_j = L^2(\mathcal{R}) \tag{6}$$

and hence $\{\psi_{j,m}\}_{j,m \in \mathcal{Z}}$ is an orthonormal basis of $L^2(\mathcal{R})$.

Since the wavelet ψ is an element of V_1, a sequence $\{g_k\} \in l^2$ exists such that

$$\psi(x) = \sqrt{2}\sum_k g_k \varphi(2x - k) \tag{7}$$

It then suffices to take

$$g_k = (-1)^k h_{1-k} \tag{8}$$

An orthonormal wavelet system with compact support is called an orthogonal Coifman wavelet system of order N (N must be even) or Coiflets [5] if the scaling functions $\varphi(x)$ and wavelets $\psi(x)$ both have N vanishing moments, i.e.

$$\int_S x^p \varphi(x)dx = 0, \quad \text{for } p = 1, ..., N-1 \tag{9}$$

$$\int_S x^p \psi(x)dx = 0, \quad \text{for } p = 0, ..., N-1 \tag{10}$$

The support widths of $\varphi(x)$ and $\psi(x)$ are both equal to $3N - 1$.

3 SOLVING THE INTEGRAL EQUATIONS

In this section, we apply the Coifman wavelets to solve the integral equation

$$\int f(x')K(x, x')dx' + c(x)f(x) = g(x) \tag{11}$$

where $c(x)$ is a known function.

3.1 Expansion in Terms of Coifman Wavelets

For a bounded interval or closed contour, the unknown function $f(x)$ in the integral equation can be approximated by its projection to space V_J of the highest level J

$$V_J = V_{J-J_0} \bigoplus_{j=1}^{J_0} W_{J-j}$$

yielding

$$f(x) = \sum_{k=1}^{2^{J-J_0}} f_{J-J_0,k}^{\varphi} \varphi_{J-J_0,k}(x) + \sum_{j=J_0}^{1} \sum_{k=1}^{2^{J-j}} f_{J-j,k}^{\psi} \psi_{J-j,k}(x) \qquad (12)$$

Define

$$
\begin{aligned}
\{B_i(x)\} &= \{\varphi_{J-J_0,i}(x), ..., \psi_{J-J_0,i}(x), ..., \psi_{J-1,i}(x)\} \\
\{a_i\} &= \{f_{J-J_0,k}^{\varphi}, ..., f_{J-J_0,k}^{\psi}, ..., f_{J-1,k}^{\psi}\}
\end{aligned}
$$

The expansion of $f(x)$ is substituted into the integral equation (11), and the resultant equation is tested with the same set of the expansion functions.

Substituting the expansion of (12) into (11), and applying the Galerkin's procedure, we obtain

$$\sum_n a_n \{ \int c(x) B_m(x) B_n(x) dx + \int \int K(x,x') B_n(x') B_m(x) dx' dx \}$$
$$= \int g(x) B_m(x) dx \qquad (13)$$

As a result, a set of linear equations is formed

$$\mathbf{Ax} = \mathbf{g}$$

where

$$a_{m,n} = \int c(x) B_m(x) B_n(x) dx + \int \int K(x,x') B_n(x') B_m(x) dx' dx \qquad (14)$$

$$g_m = \int g(x) B_m(x) dx \qquad (15)$$

When $c(x)$ is constant, the first term of (14) is equal to

$$\int c B_m(x) B_n(x) dx = c\delta_{m,n}$$

4 NUMERICAL INTEGRATION

The evaluation of the coefficient matrix entries usually involves time consuming numerical integrations. However, by taking advantage of the vanishing moments and compact support of the wavelets, many entries can be directly identified or calculated without performing the quadrature procedures. Away from the singular points the

kernel is a smooth function and it behaves as a polynomial locally. Consequently, the integral that contains at least one wavelet function $\psi(x)$, as the basis or the testing function, will result in a very small value and can be set to zero. For example, if matrix elements contain only Coifman wavelet functions on levels J_1 and J_2, then they can be written as

$$c_{n,m} = \int_{S_n} \int_{S_m} K(x;y)\psi_{J_1,n}(x)\psi_{J_2,m}(y)dxdy \qquad (16)$$

It follows that the error between the exact value of (16) and the Coiflet approximation for a zero entry is

$$|c_{n,m}| \leq 2^{-(J_1+J_2)/2}\{ \sum_{l,p\geq N} 2^{-(J_1p+J_2l)}|\frac{K_{x,y}^{(l)(p)}(2^{-J_2}n, 2^{-J_1}m)}{l!p!}||$$
$$\int_S y^l\psi(y)dy|| \int_S y^p\psi(y)dy|\} \qquad (17)$$

where S_m in (16) is a support of the m-th scaling function, S is the same support after a coordinate transform. We need just a few items of the summation in (17) to estimate the order of this error. The moment integrals

$$\int_S y^n\varphi(y)dy, \quad \int_S y^n\psi(y)dy, \quad n \geq N \qquad (18)$$

can be calculated directly, using the wavelet theory. These errors depend on the values of n and m, on levels J_1 and J_2, and on the shape of the integration contour.

On the other hand, the integral that only contains scaling functions as basis and testing functions, will take the zero order moment of the kernel. Such one point quadrature formulas for smooth functions which include scaling functions have been considered in [4], [6].

For those integrals in which the basis and testing functions overlap, causing the kernel singular point to lie within the integration interval, numerical integration has to be conducted. Even though if supports of the basis and testing functions overlap but not coincide we can partially incorporate the above technique to the numeric integration formulas.

5 Example

In our example we use the Coifman wavelets and scaling functions of order $N = 4$ as basis functions to expand the unknown function in the integral equation. Althow higher order Coifman wavelets give us more vanishing moments and produce better approximation, the supports of these wavelets are wider and it would take a longer time to calculate the singular integrals. Choice of $N = 4$ is a good trade off between accuracy and calculation time. We used two different classes of the Coifman wavelets which are defined on the segment (intervallic) and on the closed contour.

As an example of application of the Coifman wavelets to 3D geometries we consider a perfectly conducting sphere excited by a uniform plane wave which is incident on the sphere along the direction of the positive z-axis. The total electric current
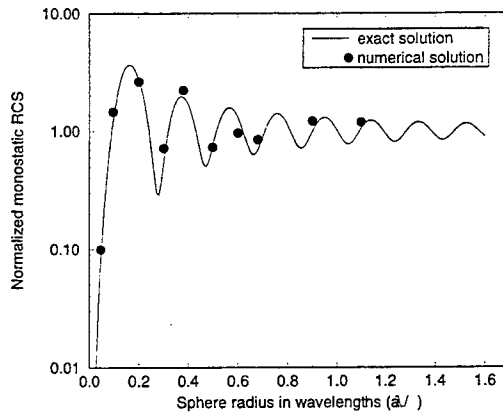
Figure 1: Normalized monostatic radar cross section (RCS) $(\sigma/\pi a^2)$ for a conducting sphere.

density $\mathbf{J}_s(\mathbf{r})$ induced at any point $\mathbf{r}$ on the surface of the sphere can be found from the Magnetic Field Integral Equation

$$\mathbf{J} = 2\hat{\mathbf{n}} \times \mathbf{H}^i + \frac{1}{2\pi}\hat{\mathbf{n}} \times \int_S \mathbf{J}(\mathbf{r}') \times \nabla' G(\mathbf{r},\mathbf{r}')dS'$$

where ∇' is the surface gradient defined on the primed coordinates; $\hat{\mathbf{n}}$ is the unit surface normal. The integral is interpreted in the Cauchy principal value sense.

In a spherical coordinate system $\{r, \theta, \varphi\}$ tangential electric current density on a surface of the sphere can be described by its two components $\{J_\theta, J_\varphi\}$.

For a surface of the sphere, coordinates θ and φ vary in the range of $0 \leq \theta \leq \pi$ and $0 \leq \varphi \leq 2\pi$. Formally, we can consider that coordinate θ is defined on a bounded interval and coordinate φ is defined on a closed contour.

Following the wavelet approach in Section 3, the unknown components of the surface current are expanded in finite series of basis functions

$$J_\theta(\theta, \varphi) = \sum_i a_i^\theta B_i(\theta, \varphi)$$

$$J_\varphi(\theta, \varphi) = \sum_i a_i^\varphi B_i(\theta, \varphi)$$

where

$$B_i(\theta, \varphi) = B_m(\theta)B_n(\varphi)$$

Functions $B_m(\theta)$ are the intervallic Coifman scaling functions of level J_1; functions $B_n(\varphi)$ are ordinary Coifman scaling function of level J_2 which are defined on a closed

contour; $i = \{m, n\}$ is a double index. To demonstrate the effectiveness of the 2D wavelet expansion, we did not utilize the rotational symmetry.

For an incident plane wave

$$\mathbf{E}^i = \hat{x}e^{-jkz}, \quad \mathbf{H}^i = \hat{y}e^{-jkz}$$

the normalized monostatic radar cross section $\sigma/\pi a^2$ are evaluated. The normalized monostatic radar cross section (Figure 1) are calculated for a sphere at frequencies which do not coincide with the eigen frequencies of the spherical resonator. These results are in a good agreement with the exact solution.

References

[1] B. Z. Steinberg and Y. Leviatan, "Om the Use of Wavelet Expansions in the Method of Moments," *IEEE Trans. Antennas and Propagation*, vol. 41, pp. 610-619, May 1993.

[2] G. Wang and G. W. Pan, "Full Wave Analysis of Microstrip Floating Line Structures by Wavelet Expansion Method," *IEEE Trans. Microwave Theory Thch.*, vol. 43, pp. 131-142, Jan. 1995.

[3] G. Wang, G. Pan, and B. K. Gilbert, "A Hybrid Wavelet Expansion and Boundary Element Analysis for Multiconductor Transmission Line in Multilayered Dielectric Media," *IEEE Trans. Microwave Theory Tech.*, vol. 43, pp. 664-675, March 1995.

[4] G. Beylkin, R. Coifman, and V. Roklin, Fast Wavelet Transforms and Numerical Algorithm I, *Commun. pure Appl. Math.*, vol. 44, pp. 141-183, 1991

[5] I. Daubechies, *Ten Lectures on Wavelets*, SIAM, Philadelphia, 1992.

[6] Wim Sweldens, R. Piessens, "Quadrature Formulae and Asymptotic Error Expansions for Wavelet Approximations of Smooth Functions," *SIAM journal on numerical analysis* , vol. 31, pp. 1240-1237, Aug. 1994.

Fast Array Factor Calculations for Fractal Arrays

Randy L. Haupt
HQ USAFA/DFEE
2354 Fairchild Dr, Suite 2F6
USAF Academy, CO 80840-6236
and
Douglas H. Werner
Applied Research Laboratory
Pennsylvania State University
PO Box 30
State College, PA 16804-0030

Abstract: Arrays are thinned to reduce sidelobe levels in the far field pattern. In this paper, we approach thinning with the sole purpose of arranging the elements in a fractal pattern to investigate the usefulness of fractal array designs. In particular, the multiscaling of the fractal makes them attractive for wideband applications. In the course of our investigations, we discovered that the array factor for fractal arrays can be very quickly calculated using a product rule compared to the normal discrete Fourier transform approach. Results for both the Cantor linear array and the Sierpinski carpet array are presented.

I. Introduction

The term fractal, which means broken or irregular fragments, was originally coined by Mandelbrot [1] to describe complex shapes that can't be defined by classical Euclidean geometry. Since the pioneering work of Mandelbrot and others, fractal applications have appeared in many branches of engineering and science. One such area is fractal electrodynamics in which fractal geometry is combined with electro-magnetics. An introduction to the subject of fractal electrodynamics is found in the excellent review by Jaggard [2] . More recent developments in the field are summarized by Jaggard [3] and Werner [4] . This paper focuses on the application of fractal geometric concepts to the analysis and design of thinned fractal linear as well as planar arrays.

There are many applications where it is advantageous to apply thinning techniques to the design of antenna arrays [5] . In this paper, we approach thinning with the sole purpose of arranging the elements in a fractal pattern to investigate the usefulness of fractal array designs. In particular, the multiscaling of the fractal makes them attractive for wideband applications. Another advantage of these fractal arrays is that the self-similarity in their geometrical structure may be exploited in order to develop algorithms for rapid computation of radiation patterns. These algorithms are based on convenient product representations for

the array factors and are much quicker to calculate than the discrete Fourier transform approach. Results for both the Cantor linear array and the Sierpinski carpet planar array are presented.

II. Fractal Linear Arrays

The array factors for an arbitrary row of symmetric elements along the z-axis are given by

$$AF(u) = \begin{cases} a_0 + 2 \sum_{m=1}^{M} a_m \cos{[m\Psi]} & \text{odd number of elements } (2M+1) \\ 2 \sum_{m=1}^{M} a_m \cos{[(m-.5)\dot{\Psi}]} & \text{even number of elements } (2M) \end{cases} \tag{1}$$

where

N = number of elements

$a_m = \begin{cases} 1 = \text{element turned on or connected to feed network} \\ 0 = \text{element turned off or connected to matched load} \end{cases}$

$\Psi = kdu_s$

$k = \frac{2\pi}{\lambda}$

λ = wavelength

d = constant spacing between elements

$u_s = \cos\theta - \cos\theta_s$

θ = angle of incidence of electromagnetic plane wave

θ_s = direction of mainbeam

Element weights are either 1 or 0 and indicate whether or not the individual elements contribute to the total radiation pattern of the array.

It is easier to generate the Cantor array by starting with a three element generating array, then applying the generator to P scales. The generating array for the Cantor array has three elements with the center element turned off. An expression for this generating subarray may be easily obtained from (1) using the fact that $m = 2$, $a_1 = 0$, and $a_2 = 1$ in order to arrive at

$$GA(\Psi) = 2\cos{[\Psi]} \tag{2}$$

Applying this rule a total of P times results in the following array factor for the Cantor array:

$$AF_P(\Psi) = \left(\frac{2}{3}\right)^P \prod_{p=1}^{P} \cos\left(3^{p-1}\Psi\right) \tag{3}$$

Table 1 shows the array factor expression and plot for scales 1, 2, and 4.

One of the interesting properties of this Cantor array is the ability to quickly calculate the array factor. If (1) is used to calculate the array factor for an odd number of elements, then M cosine functions must be evaluated and M additions performed for each angle. Using (3), only P cosine function evaluations and $P-1$ multiplications are required. For the case of the 81 element array, the fractal array factor is at least $\frac{M}{P} = \frac{40}{4} = 10$ times faster to calculate than the conventional discrete Fourier transform approach.

The procedure outlined above for constructing the Cantor array from a three-element subarray can be generalized by expressing the array factor in the following way:

$$AF_P(\Psi) = \left(\frac{1}{s}\right)^P \prod_{p=1}^{P} GA\left(s^{p-1}\Psi\right) \tag{4}$$

where
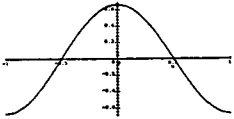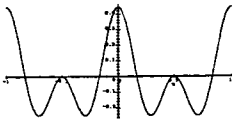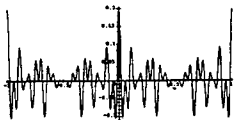
Scale	Array Factor	Array Factor Plot
1	$\left(\frac{2}{3}\right)\cos\left(\Psi\right)$	
2	$\left(\frac{4}{9}\right)\cos\left(\Psi\right)\cos\left(3\Psi\right)$	
4	$\left(\frac{16}{81}\right)\cos\left(\Psi\right)\cos\left(3\Psi\right)\cos\left(9\Psi\right)\cos(27\Psi)$	

Table 1: Column 1 is the scale at which the array factor is calculated. Scale 1 is the generator array. Column 2 is the array factor and Column 3 is a plot of the Cantor linear array.

s = total number of elements in the generating array (turned on and turned off)
GA = radiation pattern of the generating subarray
P = number of fractal levels

Note that s also acts like a scale factor in (4). Consequently, a fractal dimension may be calculated from

$$D = \frac{log\left(\sum_{n=1}^{s} a_n\right)}{log\left(s\right)} \qquad (5)$$

There are many different ways to calculate a fractal dimension. This approach is called the scale dimension and seems best suited for the array. As a check for reasonableness, a uniform subarray of five

elements has $D = log(5)/log(5) = 1$ which is the dimension of a uniform linear array. On the other hand, a three element subarray with weights given by $a = [0, 1, 0]$ has $D = log(1)/log(3) = 0$ which is the dimension of a single point source. Thus, the bounds of D appear to check with Euclidean geometry. Finally, (5) may be used to show that the fractal dimension of the infinite Cantor array ($P \rightarrow \infty$) with subarray element weights $a = [1, 0, 1]$ is $D = log(2)/log(3) = 0.6309$.

III. Fractal Planar Arrays

A symmetric planar array with an odd number of elements in the x and y directions has an array factor given by

$$ff = A_{11} + 2\sum_{m=2}^{M} A_{m1} \cos\left[(m-1)\Psi_x\right] + 2\sum_{n=2}^{N} A_{1n} \cos\left[(n-1)\Psi_y\right] + \qquad (6)$$

$$4\sum_{n=2}^{N}\sum_{m=2}^{M} A_{mn} \cos\left[(m-1)\Psi_x\right] \cos\left[(n-1)\Psi_y\right]$$

where
M = number of elements in the x-direction
N = number of elements in the y-direction
$A_{mn} = A_{mn}e^{j\Omega_{mn}}$ = complex weight at element (m, n)
d_x and d_y are the element spacings in the x and y directions
$u_{sx} = \sin\theta\cos\phi - \sin\theta_s\cos\phi_s$
$u_{sy} = \sin\theta\sin\phi - \sin\theta_s\sin\phi_s$
(θ_s, ϕ_s) = steering angles
$\Psi_x = kd_x u_{sx}$
$\Psi_y = kd_y u_{sy}$

A Sierpinski carpet is a two-dimensional version of the Cantor set and applies to thinning planar arrays. Consider the simple generator array

$$\begin{matrix} 1 & 1 & 1 \\ 1 & 0 & 1 \\ 1 & 1 & 1 \end{matrix}$$

This array is generated by the rule of turning off the center element of a nine element square. as a pattern. The array factor for $d_0 = .5\lambda$ simplifies to

$$GA(u_{sx}, u_{sy}) = 2\cos\left(\pi u_{sx}\right) + 2\cos\left(\pi u_{sy}\right) + 4\cos\left(\pi u_{sx}\right)\cos\left(\pi u_{sy}\right) \qquad (7)$$

The array factor at scale P is

$$AF_P = \prod_{p=1}^{P} \left[2\cos\left(3^{p-1}\pi u_{sx}\right) + 2\cos\left(3^{p-1}\pi u_{sy}\right) + 4\cos\left(3^{p-1}\pi u_{sx}\right)\cos\left(3^{p-1}\pi u_{sy}\right) \right] \qquad (8)$$

Table 2 shows a view of the fractal array at scales 1,2, and 4.

IV. Conclusions

A fractal antenna array factor is very fast to calculate, because it may be formulated as a product of generating array factors. This paper derived these formulations for linear and planar arrays and showed some of the interesting fractal antenna patterns resulting from their application.

References

[1] B. B. Mandelbrot, *The Fractal Geometry of Nature*, New York: W. H. Freeman and Company, 1977.
[2] D. L. Jaggard, "On fractal electrodynamics," in Recent Advances in Electromagnetic Theory, D. L. Jaggard and H. N. Kritikos, Eds., New York: Springer-Verlag, 1990, pp. 183-224.
[3] D. L. Jaggard, "Fractal electrodynamics: Wave interactions with discretely self-similar structures," in Electromagnetic Symmetry, C. E. Baum and H. N. Kritikos, Eds., Bristol, PA: Taylor
[4] D. H. Werner, "An overview of fractal electrodynamics research," Proceedings of the 11th Annual Review of Progress in Applied Computational Electromagnetics, Naval Postgraduate School, Monterey, CA, Mar 20-25, 1995, pp. 964-969.
[5] Y. T. Lo, "Aperiodic arrays," in *Antenna Handbook: Theory, Applications, and Design*, Y. T. Lo and S. W. Lee, Eds., New York: Van Nostrand Reinhold, 1988, pp. 14.1-14.37.
[6] C.Puente-Baliarda and R. Pous, "Fractal design of multiband and low sidelobe arrays," IEEE AP-S Trans., Vol. 44, No. 5, pp. 730-739, May 96.
[7] D. H. Werner and P. L. Werner, "Frequency-independent features of self-similar fractal antennas," Radio Science, Vol. 31, No. 6, pp. 1331-1343, Nov-Dec 96.
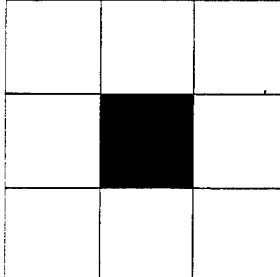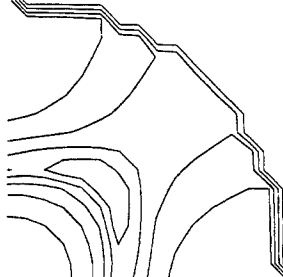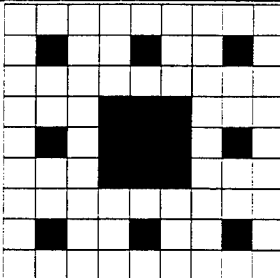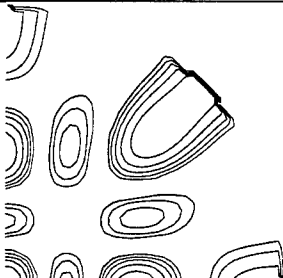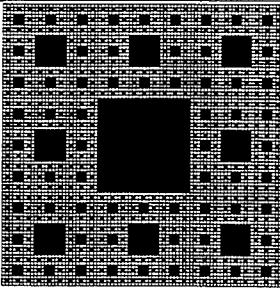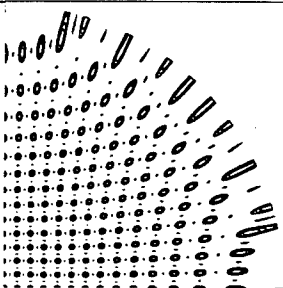
Scale	Fractal Array	Array Factor Plot
1		
2		
4		

Table 2: Column 1 is the scale at which the array factor is calculated. Scale 1 is the generator array. Column 2 is a view of the thinned array: white blocks are elements turned on and black blocks are elements turned off. Column 3 is the array factor. The angle phi is measured around the circumference of the plot, while theta is radially measured from the lower left.

NEC2 MODELING OF FRACTAL-ELEMENT ANTENNAS (FEA's)

Nathan Cohen, Fractal Antenna Systems, Inc.
2 Ledgewood Place
Belmont MA 02178

ABSTRACT

Since antennas comprised of generalized fractal elements were reported growing interest has concentrated on the ability to model then with NEC and other engines. Here we report NEC2 results of three FEA and compare their model observables with experimental results. The results appear compatible. This promises hope for modeling a variety of FEA and FEA arrays. Broad bandwidths; reduced resonant frequencies; field strengths; power patterns; and others may be studied successfully with NEC2 for simple to somewhat complex FEA's. Extremely complex FEA will require other modeling approaches as the modeling engine limitations are reached.

INTRODUCTION

In recent years, antenna design has entertained the peculiar twist of antennas built upon geometric patterns which are fractal (Cohen, 1995; Puente-Baliarda et.al,1996). Such antennas incorporate some degree of self-similarity in their structure, whether it is 'deterministic' or 'random/chaotic' in its nature. Fractal antennas also extend to array distributions (see, for example, Werner and Werner, 1996), where they appear to be an extension of log-periodic/self complementary antennae. In general however, fractal antennae remain an inchoate aspect of applied electromagnetics and are not well known. Here, I will concentrate on some characteristics of 3 simple antennas comprised of fractal elements from a modeling standpoint and compare, when possible, to experimental results. This is provided as confirming information between model and data, and also as an incentive for others to pursue these exotic antennae as viable candidates for future modeling and testing.

CHARACTERISTICS AND EARLIER WORK

Much of the principle of a fractal-element antenna may be extrapolated from the fractal 'coastline' problem (Mandlebrot,1983). In this, it is noted that a fractal can manifest a very large perimeter while maintaining a very small area. In three dimensions this becomes a large surface area over a small volume. For an antenna a fractal is a compact way of 'accordioning' a perimeter into a small two dimensional region.

There is no *a priori* reason to assume that any perimeter distribution which is closely packed would radiate well, nor that the impedance would be purely real at some frequencies However, fractal structure appears to produce self-reactance which yields resonances (Cohen 1996a). Furthermore, a perimeter in excess of a wavelength also produces more than one current

maximum. Analogous to a multiturn (three dimensional) helix, this perimeter length yields a higher radiation resistance than intuition may suggest.

Early studies of fractal-element antennae did not reach conclusions which were entirely correct. For example, Robin and Soulliard (1993), based on a simple theoretical analysis predicted that diffusion limited aggregates (DLA's) would produce antennae with harmonic resonances, while actual DLA's produce broad band/multiband resonances only vaguely harmonically related. Cohen's(1995) conjecture of diffraction as an important process in fractal wire antennas, following the approach of Berry (1979) was later corrected (Cohen and Hohlfeld, 1996).

Most importantly, a study of fractal loops (Cohen and Hohlfeld,1996) drew an incorrect interpretation that electrically small fractal loops would make superior antennae based upon higher radiation resistance. Indeed, save for the very small electrical sizes, fractal loops do have higher radiation resistances than a Euclidean loop. However, the point is spurious, as the fractal loop perimeter is substantially longer than a Euclidean one and hence its ohmic losses are, in turn, higher. With electrically small fractal loops, the radiation resistance is quite small and hence any ohmic loss dramatically reduces field strength. As a result an (electrically small) fractal loop has lower field strength than a Euclidean one and hence a fractal loop is an *inferior antenna in the electrically small case*. Electrically 'medium' cases (say, 1/12-1/4 wave maximum dimension) are different stories and here fractal loops are multiband/broadband affairs where some resonances have substantial gain (Cohen and Hohlfeld,1996).

Despite these wrong turns, previous efforts were not without some valuable findings. First, fractal element antennae were found to be multiband with non-harmonically defined resonances(Cohen,1995; Puente-Baliarda et al., 1996). When extended to sufficient numbers of iterations, the structure produces fractal loading and causes these antennae to have merged resonance clusters and become the general case of frequency-independent antennae (Cohen,1996b). The fractal loading tends to lower the resonant frequencies (Cohen, 1995). A practical aspect of fractal antennae is that the fractal loading yields resonant antenna from the structure itself, so no additional components are needed to obtain a resonant antenna. This makes fractal antennae viable miniature antenna (as long as they are not electrically small).

The electrical behavior of the fractal structure not only produced a fractal loading effect, but, not surprisingly, yields phasing lines within the element. This allows some fractal element antennae to contained phased elements with gain properties (see, for example, Landstorfer and Sacher, 1985; Cohen, 1996a). The gain can be substantial and, at least, pose alternatives to discretely phased arrays and parasitics (see, for example, Kraus, 1988).

MODELLING AND TESTING

Fractals have been around for over two centuries (some called 'pathological curves') so it comes as some surprise that they have not been explored electromagnetically until recently. In fact, the self-similarity argues for simplicity, but their overall complex structure makes them almost impossible to explore for wave properties analytically. Yet fractal-element antennae would not exist if they couldn't be computationally produced and computationally modelled, in numerical

fashion. That they CAN be modelled with extant tools--at least for simple fractals--is demonstrated here where I demonstrate some simple fractal element-antenna properties through simulation using the EZNEC-M (Lewallen, 1996) version of NEC2.

First, some caveats. In modeling complex wire antennae such as FEA's, the limitations are all too easily probed. Line segments can easily become very close to imposed length limits and any structure may begin to take on small looped-shapes, which are known not to be modelled well (Burke,1987) The objective is thus to see what general characteristics are discernable from modeling.

To check the modeling, testing was done using 900 MHz versions of the antennae built upon thin, FR4 substrates. An HP 8754a with S parameter test set (HP 8748a) were used to obtain S11 and S12. From these, various parameters were inferred. A modest range measurement was used to infer pattern and maximum gain by a comparison of S12 to a test dipole or 1/4 wave monopole.

For the sake of an introductory illustration I will describe a fractal monopole, dipole, and loop. Each is comprised of a Minkowski fractal for the sake of this introduction. Here I present these results and compare with data.

A: Fractal Monopole

This monopole is one of a family of optimized top-loaded fractal antennae meant to be structurally compact and resonant, without additional discrete component loading. End-loading is believed to be the most efficient means of shortening the length of the antenna and a variety of schemes abound, especially in the amateur radio literature (see, for example, Moxon,1983).

The fractal monopole is shown in Figure 1 A) and incorporates a first iteration Minkowski generator (Lauwerier,1991) upon an open square. Table 1 lists its observables as simulated by EZNEC-M. It should be noted that this is a form factor that is smaller than other two-dimensional end-loaded resonant antenna.
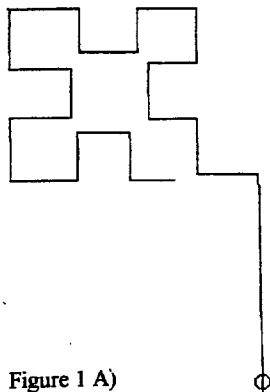
Figure 1 A)
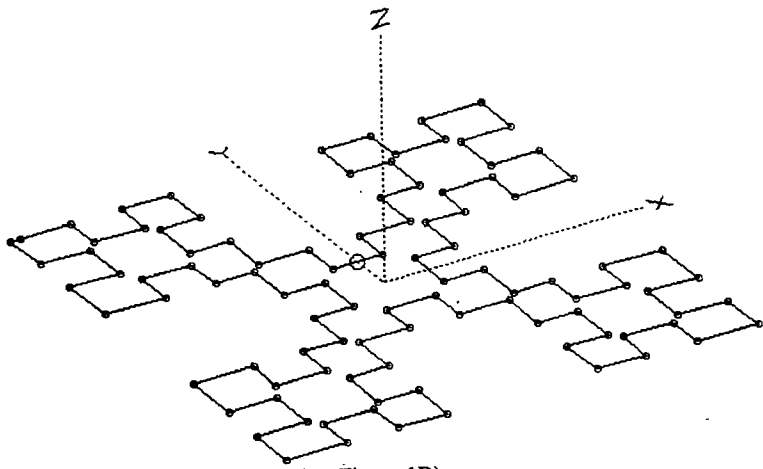
Figure 1B)
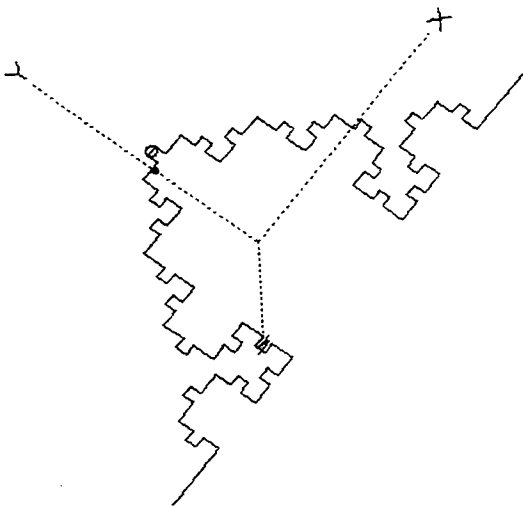
Figure 1 C)

The antenna was mounted above a circular ground plane (an approximation to an infinite plane) for the measurements. The data compare favorably with the model: gain 2dBi; BW 5 % (2:1 VSWR); omni pattern in azimuth. Return loss was 12 dB . Hence this small fractal structure imposed few inaccuracies to this NEC2 model.

TABLE 1
EZNECM Modeling Results

Antenna	Wire Width (waves)	Max. Dimension(λ)	Impedance (ohms)	FS Gain (dBi)	Bandwidth(%)	Comments
1A)	0.001	0.28	23-j0.5	1.7	6	omni
1B)	0.0002	0.14	27+j3.0	1.8	3	narrow '8'
1C)	0.001	0.53	15+j1.2	5.8	1.6	bidirectional

b: Fractal Loop

Using the same motif, only in second iteration and applying it to an entire square, the loop of Figure 1B) is shown. At its lowest resonance, the loop had characteristics modeled by EZNECM as shown in Table 1.

The actual loop is a balanced antenna, with very close values to the model. The BW was 4.5 %; best return loss was 14 dB;field strength was 2 dBi. It is also multiband, as discussed in Cohen (1996b).

c. Fractal Dipole

The fractal dipole of Figure 1 C) is effectively a section of the fractal loop, only shown here in a third iteration. It's lowest resonance gives a largest dimension of 0.17 waves (14 ohms drive) and is a modest loaded dipole at that frequency. However, the next resonance, listed in Table 1, employs the fractal structure to acheive gain. This antenna appears to be akin to shaped dipoles, described by Landstorfer and Sacher (1985) and Cohen (1996a).

The gain was confirmed through measurement as being 3.5 dBλ. Return loss was 8dB and BW was 2 %. The gain seems to occur because the iterations produce collinear and echelon structures which phase to produce it. The current distribution and power pattern are shown in Figure 2.
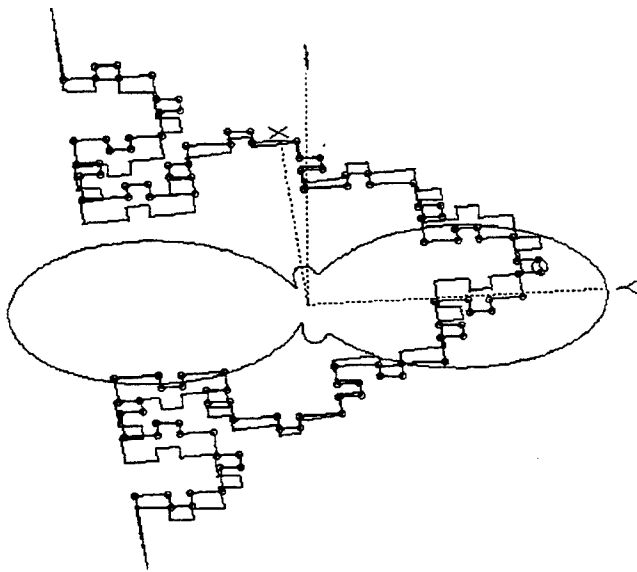
Figure 2

DISCUSSION

These simple fractal-element antennae simulations compare well with modest measurements. This implies that more complex fractal antennae such as those encountered by Linden and Altschuler,(1996) will be modeled successfully. But where does the limit begin?

Most fractals are far more complex affairs. Modeling these structures as antennas (whether in patch, monopole, or other configurations) will take considerable effort. In fact, it is improper to extend the capabilities of NEC2 to model very complex antenna, such as 'filled' fractals of many iterations. Wire gridding, for example, is bound to fail on iterative details because the detail will ultimately be undersampled--or the grid spacing will be too close by for NEC2 to model. Fractal element antennae thus take antenna modeling into a complex regime.

As an incentive I pose the following fractal element antenna shown, in part, in Figure 3. It is a 'fractal ribbon' an unusual meander-like structure defined by a Sierpinski motif (Lauwerier,1991)

to a fourth iteration. With dimensions of 13 cm long and 1.62 cm across, the fractal ribbon resembles a 1/7 wave,albeit resonant, with a return loss of 10 dB and a 100 MHz bandwidth at 400 MHz resonance. Mounted upon the circular ground plane, the antenna was indistinguishable in gain from a 1/4 wave vertical on the same ground plane (RMS 0.7 db). Obviously the meander aspect is providing some inductive loading, but a pure meander alone (that is, without the fractal holes) failed to produce a resonance below 500 MHz and with far less (about 15%) bandwidth.

Figure 3

A wire grid version on NEC2 was not possible due to segment limitations. Other modeling schemes should be able to pose some insight.

SUMMARY

NEC2 modeling is a valuable tool for simple fractal antenna modeling and provides a useful introduction to fractal electromagnetics. Accuracy to actual data appears acceptable and thus modeling presents a good opportunity to explore these complex structures. However, for the truly complex--and interesting fractals-- modeling limitations are all too easily met. Thus fractal electromagnetics poses interesting challenges to more sophisticated modeling schemes in the future.

Acknowledgements

Aspects of this work are patent pending.

REFERENCES

Berry,M.,1979,"Diffractals", Journal of Physics, A12,781.
Burke, G.,1987,"Enhancements and Limitations of the Code NEC for Modeling Electrically Small Antennas",UCID-20970 Report.
Cohen,N.,1995,"Fractal Antennas Part 1",Communications Quarterly,Summer,7.
Cohen,N.,1996a,"Fractal and Shaped Dipoles",Communicatiosn Quarterly,Spring,25.

Cohen,N.,1996b,"Fractal Antennas Part 2", <u>Communications Quarterly,Summer,</u>53.

Cohen,N., and Hohlfeld,R.,1996,"Fractal Loops and the Small Loop Approximation",
 <u>Communications Quarterly,Winter,</u>77.

Landstorfer,F., and Sacher,R.,1985,**Optimization of Wire Antennas**,Wiley,New York.

Lauwerier,H.,1991,**Fractals**,Princeton University Press,Princeton.

Lewallen,R.,1996, **EZNECM** software.

Linden,D., and Alstschuler,E.,1996,"Automatic Wire Antenna Design Using Genetic
 Algorithms",<u>Microwave Journal,March,</u>74.

Kraus,J.,1988,**Antennas**, McGraw Hill, New York.

Mandlebrot,B.,1983,**Fractal Geometry of Nature**,Freeman,San Fracisco.

Moxon,L.,1982,**HF Antennas for All Locations**,RSGB,Herts.

Puente-Baliarda,C.,Romeau,J.,Pous,R.,Garcia,X., and Benitez,F.,1996,"New Fractal Multiband
 Antenna Based on the Sierpinski Gasket", <u>IEE Electronics Letters,January,</u> 28.

Robin,T., and Souilliard,B.,1993,"Electromagnetic Properties of Fractal Aggregates",<u>Europhysics
 Letters,21,</u>273.

Werner,D., and Werner,P.,1996,"Frequency-Independent Features of Self-Similar Fractal
 Antennas", <u>Radio Science,31,</u>6,1331.

GENETIC ANTENNA OPTIMIZATION WITH FRACTAL CHROMOSOMES

Nathan Cohen, Fractal Antenna Systems, Inc., and GenSonics, Inc.
2 Ledgewood Place Belmont MA 02178

ABSTRACT

We describe a method of multiparameter optimization of antennas through a hybrid optimization engine. The engine incorporates a genetic algorithm. However, it's parametrization is fractal. The self-similarity of the fractal assures even a complex structure can be described with very few independent parameters. The size of the gene is reduced, allowing for more simplified crossover and mutation.

INTRODUCTION

Optimization in electromagnetics is a daunting task. The problem lies with the abilities of the optimization engines (OE's) to arrive at optimized solutions accurately, and with a minimum of computational cycles. Genetic algorithms (GA's) are the latest method of optimization to be applied to electromagnetics with success. Although this invites investigation of optimized antennae which could not be simulated before, it also invites the simulation of extremely complex antenna geometries. The number of independent parameters in complex structures can be enormous and thus provide a practical limitation to approaching optimized solutions. In this paper, I discuss a variation of the genetic algorithm approach, whereby the number of independent parameters is reduced through a fractal coding of the antenna's geometry. This reduction in gene size may prove practical in obtaining convergence in fewer iterations, or reducing the optimization stagnation sometimes encountered over several generations. As a caveat, there are situations in which divergence is likely.

GENETIC ALGORITHMS

GA's are a class of optimization method which emulate the survival of the fittest imperative of biological Darwinian evolution. At their heart is the notion of the generational selection--through die off--of individuals whose genetic makeup does not allow then the opportunity to escape the environmental filters . These would otherwise lead to survival and a new generation which incorporates their specific genes. The culling is a 'dumb' algorithmic approach in the sense that there is no memory of previous generations or other individuals being assessed. 'Pass or chop' is an expression often used to describe the heart of the GA approach. The GA approach may be seen in a variety of references, including Davis (1996), and Michalewicz(1994).

Parameters are treated in GA's through their coding as chromosomes which themselves comprise a gene. Each parameter is made part of a string which sequentially is made of all the paremeter/string segments. The string segment is usually written as a binary number for ease of manipulation. Hence all the parameters are represented as a string of 1's and 0's. Different model parameters produce a different

string and hence a different gene. Replacing/changing string segments, or the numbers within a segment, relates to crossover and mutation.

GA's have three distinct features which are common to all variations. First, breeding of new generations from parents occurs. Here the parameter chromosomes from two parents are chopped up and parts from one are merged with parts of the other to make up a child with a slightly different gene from the parents. This is crossover. Next, mutation is incorporated through an occasional wildcard change of a chromosome value. Finally, there is an 'objective' function--actually a figure of merit--which assesses the vitality of a given gene. The best genes from each generation are kept and allowed to produce another generation. This continues until some best family of genes with the highest objective function values are obtained.

It is important to keep in mind that the OE is a separate engine from the simulator engine; it produces model parameter values and assesses them, but does not itself simulate the observables, such as gain, pattern, impedance, and so on.

FRACTALS AND FRACTAL CODING

To date, the limited but emerging interest of GA's in electromagnetics has concentrated on fairly simple structures. This has been dictated, in part, by the fact that each part of the antenna model--a line segment on a wire antenna for example-- must be specified by several parameters. The gene thus becomes extremely large very quickly. To wit: a 10 wire model may have 3 or more degrees of freedom with 30 plus parameters to be coded into the gene. Clearly a large gene will invite a huge possibility for genetic variation and the situation becomes potentially intractable.

Of course, one can use a 'compressed' coding whereby the the model is represented by a user-defined short hand. Fractal and related compression codings has already demonstrated considerable robustness and accuracy in data and images (see, for example,Barnsley and Hurd,1993). Thus they invite an extension to other types of problems, such as encountered in GA genes. No claim is made to anything 'magical' to a fractal approach, but it has proven of some utility and is adopted here as a working compression model in GA .

One of the advantages of fractals is that their complex structure can be represented by a handful of variables, even though the overall structure can be very complex. This arises because of the self-similarity nature of fractals; the few parameters define the structure of many size scales. Further versatility is evinced through a 'randomizing' parameter and employing random fractals rather than categorically self-similar ones. Fractal compression of data and images exploits this aspect, hence the seemingly huge compression ratios (some in the 1000's) often touted for this scheme.

A variety of fractal codes may be utilized. They usually specify a coding for the 'generator function' (the pattern applied in self similarity); a parameter for iteration, and one or more randomization parameter. So-called iterative function system (IFS)(Barnsley,1988; Barnsely and Hurd; 1993) codings are popular because they have very few parameters, which seek to specify the affine transformations which comprise the iterative process. Since fractal coding is treated in depth in the aformentioned references, the details will not be repeated here.

SIMPLE EXAMPLE

As a simple example, I show an optimization of a two dimensional monopole defined around a small family of fractal tree shapes. This antenna is not being presented as THE optimized monopole any more than a structure of 7 or 10 line segments can make that claim. However it does illustrate the merging of GA with a simple fractal coding, and the reduction of free parameters.

Since trees and related structures such as diffusion limited aggregates are not well known antenna · shapes, it helps to pose this example as an 'optimized' antenna which just happens to be a fractal.

The objective function chosen seeks to optimize the gain for a vertical-ground plane antenna with a narrow (1%) bandwidth. It was restricted to about 1/3 wave maximum height and 1/3 wave sideways; it must be a 2 dimensional antenna, with a single feedpoint and no parasitic elements. It's impedance must be real. The motivation was to find a wire antenna whose attributes were not defined by additional LC components, such as the approach described for optimization of wire antennae by Landstorfer and Sacher (1985).

Explicitly the objective function chosen was:

$$O = (5G + 3B - 2X)/10 \quad [1]$$

where G is field strength (incorporating ohmic losses to gain) in dbi; B is percent bandwidth; X is absolute value of reactance in ohms.

EZNECM (Lewallen,1996), a version of NEC2, was used as the modeling engine.

The antenna at its simplest is a simple vertical monopole with elaboration through iteration to form branches of various lengths, with length decreasing with height from the ground. The chromosome had the following parameters: iteration number n (0 to 3); ratio of branch length to trunk length (0 to 1 in 15 increments); angle from trunk to branch (40 to 90 in 10 degree increments); randomization offset for opposing branches (0 to 0.1 branch length in 7 increments); randomization offset of affine translation for iteration m of n (used in mutation otherwise set to zero). Note all binary values were normalized to meet the above. The gene looked like (with some typical values):

$$01 \quad 01001 \quad 011 \; 101 \; 01 \qquad [2]$$

Spacing indicates the next parameter, starting with iteration number from left to right.

In comparison, a standard parametrization would have, say, up to eight branches. Each branch would have a length, and angle, and a placement parameter and might look like

111110111 101000001 101010011 1111111100 010101101 101110011 001110101 001111010 [3]

This is much longer and the possible variations and length of the computational task is obvious.

Convergence was started with a gene pool of 5 examples. Culling was obtained for the best 4 of each generation. Convergence was obtained in 10 generations. The survivor is an odd looking antenna shown in Figure 1. This 'urban christmas tree' is shown with its current distribution superposed and its power pattern offset above a perfect ground plane. It has a bandwidth of 0.8% ; a feedpoint impedance of 4.5-j0.8 ohms. Maximum height was 0.34 waves and wire width was 0.001 waves. Field strength was 9.0 dBi; gain was 10.3dBi.
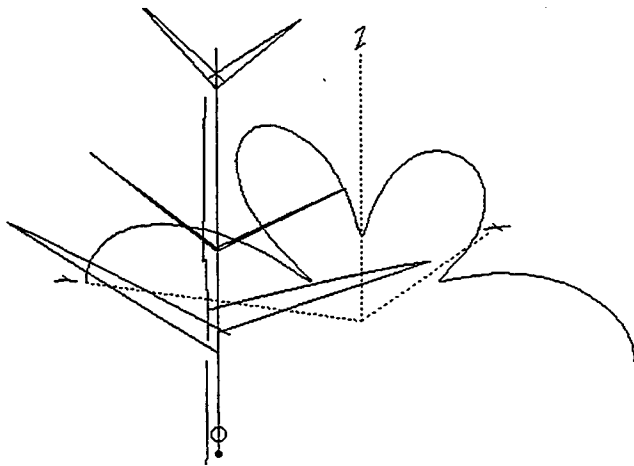
Figure 1

DISCUSSION

In any scheme of optimization, there is some a priori qualification that the scheme will converge within certain boundaries of execution. In GA's this qualification is less than intuitive and invited a criticism that GA's are not well understood. In fact, Davis's description (1996) emphasizes almost a strict, cookbook approach, lest the user deviate into the many cold abysses of divergence. Fractal coding seems to invite further criticism of GA's in general--how do they work? That they work is clear; WHY they work is still somewhat ill-posed (Coveney and Highfield,1995). In addition there are two obvious criticisms of fractal coding: 1) in very simple cases they provide less parameter freedom than a regular approach; 2) crossover can produce bizarre hybrids which could be very far from convergence.

Point 1 is merely an example of a sophisticated technique applied to a simple program. As in all such cases, the advantage is moot or dubious. The fact that some form of coding compression is not commonly used in GA electromagnetic problems (see, for example, Altschuler and Linden, 1997) indicates the fact that they weren't needed.

However, it is very easy to envision problems where the fractal coding IS needed in optimization. One obvious one is in fractal arrays (Werner and Werner, 1996). Here the distribution of elements is fractally related so using a non-fractal parametrization to describe the positions and lengths of the elements is a sheer waste of computational cycles. A similar situation may be attributed to fractal-element antennas (Cohen,1995,1996) where the elements are sought to be optimized.And since any complex structure can be *approximated* by a fractal or 'fractal collage' (Barnsley and Hurd,1993) the technique promises advantages to any complex structure modeling in electromagnetics.

A great deal of experimentation will be necessary to see if convergence will always emerge with a fractal coding. One obvious benefit is that the crossover hybrids can remove the parameters from a 'convergence rut' sometimes encountered over several generations. These ruts relate to Darwinian evolution's punctuated equilibrium and represent local maxima in the objective function (see Hillis, in Coveny and Highfield,1995). On the flip side, the radical changes in actual structure caused by fractal coding and crossover may yield the opposite situation and produce a convergence rut. There is the temptation to stop after x generations if no obvious improvement are evident. This is a clear bias based upon Newton-Raphson approaches to incremental improvements in optimization. A fair warning: improvements in the objective function with fractal coding will NOT necessarily be incremental as a function of generation, any more than they are in actual Darwinian evolution.

SUMMARY

Fractal coding of the model parameters offers a possible means of simplifying the optimization process in GA's in electromagnetics. Reduction in the number of iterations and crossovers is clear--within certain 'cookbook' limits, yet to be fully explored.

Acknowledgements

REFERENCES

Altschuler,E., and Linden,D.,1997, "Design of a Loaded Monopole Having Hemispherical Coverage Using a Genetic Algorithm", IEEE Transactions on Antennas and Propagation,45,1,1.

Barnsley,M.,1988,**Fractals Everywhere**,Academic Press,Boston.

Barnsley,M., and Hurd,L.,1993,**Fractal Image Compression**,AK Peters,Ltd.,Wellesley MA.

Cohen,N.,1995,"Fractal Antennas Part 1",Communications Quarterly,Summer,7.

Cohen,N.,1996,"Fractal and Shaped Dipoles",Communications Quarterly,Spring,25.

Coveney,P., and Highfield,R.,1995,**Frontiers of Complexity**,Random House,New York.

Davis,L.,1996, **Handbook of Genetic Algorithms**,ITP,Boston.

Landstorfer,F., and Sacher,R.,1985,**Optimization of Wire Antennas**,Wiley,New York.

Lewallen,R.,1996, **EZNECM** software.

Michalewicz,Z.,1994,**Genetic Algorithms and Data Structures**,Springer-Verlag,New York.

Werner, D., and Werner, P.,1996,"Frequency-Independent Features of Self-Similar Fractal Antennas",Radio Science,31,6,1331.

SESSION 8:

FDTD AND FVTD I

Chair: M. Picket-May

An FDTD/FVTD 2D-algorithm to solve Maxwell's equations for a thinly coated cylinder

Jei S. Chen and Kane S. Yee
Lockheed Palo Alto Research Laboratories
Palo Alto, California, August 1995

Abstract

A recently devised finite difference and finite volume time domain hybrid scheme [1] has simplified the process for calculating the electromagnetic scattering for a large class of 2-D scattering problems [2]. The computational grid is conformal to the object. This paper expands further the capability of the FDTD/FVTD hybrid to 2-D objects coated with a physically thin and optically thick layer of dielectric. The formulation is general but the computations were carried out for a circular cylinder. The results compare quite good with infinite series solution.

1. Introduction

This paper is a further extension of the previous publications [1, 2]. We refer interested readers to the following references for a historical account of the work various researchers have contributed to the conformal time domain techniques [1, 2, 3]. The modeling of an object coated with a physically thin but optically thick layer of dielectric has been a challenging problem for the numerical electromagnetists. It is now quite simple to model conformally PEC object coated with a thin layer of dielectric. Modeling thin layer structure with the FDTD has been considered by Tikras and Demarest [4]. In this paper we specialize our 3-D FDTD/FVTD technique for 2-D calculations. The calculation is further simplified with the substitution of the traditional radiation boundary condition (RBC) by a newly discovered tapered damping technique near the outer computational boundary [5].

The general relations on which the FDTD and FVTD algorithms are based as well as PEC boundary conditionare are given in the above references. Here we shall only give enough details to make this paper comprehensive. We start from the Maxwell's equations in integral forms.

$$-\int_A \dot{\vec{B}} \bullet d\bar{a} = \int_{\partial A} \vec{E} \bullet d\bar{l} \qquad \text{Faraday's Law (line-surface)} \qquad (1a)$$

$$\int_A \dot{\vec{D}} \bullet \hat{n} ds = \int_{\partial A} \vec{H} \bullet d\bar{l} \qquad \text{Ampere's Law (line-surface)} \qquad (1b)$$

$$\int_V \dot{\vec{D}} dv = \int_{\partial V} \hat{n} \times \vec{H} da \qquad \text{Faraday's Law (surface-volume)} \qquad (2a)$$

$$\int_V \dot{\vec{D}} dv = \int_{\partial V} \hat{n} \times \vec{H} da \qquad \text{Ampere's Law (surface-volume)} \qquad (2b)$$

We refer to the line integral in equation (1a) as the electric circulation; the line integral in equation (1b) as the magnetic circulation; the surface integral in equation (2a) as the electric vorticity; and the surface integral in equation (2b) as the magnetic vorticity. The (generalized) FDTD algorithm is developed from the discretization of Equations 1, while the FVTD algorithm is based on the discretization of Equations 2. In specializing to 2-D, we take the volume, in Eqs. 2, to be prisms with height equal to one unit length, and the trace of a prism in the x-y plane to be a curve. For numerical calculations the volumes and areas should be taken to be small compared to the wavelength of interest for accuracy and the volumes and areas can not be too irregular. The sampling point for the integrands should be at the centroid of the volume or the centroid of the area whenever it is possible.

3. Grid and variable location for FDTD and FVTD

Given a computational grid we call it an FDTD grid if an electric field component is associated with each edge at the "edge center" and a magnetic field component is associated with a face at the "face center". The grid will be an FVTD grid if the electric vector **E** is associated with each vertex and the magnetic vector **H** is associated with the "center" of each "element". These terminologies are illustrated in rectangular grids in 2-D in Figures 1a-1c.

3.1 Grids for PEC object coated with a thin layer of dielectric

The spatially staggered and time leap frogging FDTD/FVTD give us the flexibility to have arbitrary grids. Our PEC object is coated with a physically thin but optically thick layer of dielectric. It is common knowledge that the variation of the total field in the direction normal to the surface is more drastic than in the tangential direction. Therefore, we use a finer spatial discretization in the normal direction and a coarser discretization in the tangential direction. We show such a grid for a circular cylinder coated in Figure 2. The FDTD algorithm is very simple in an orthogonal grid and it is very convenient for the simulation of the boundary condition; it is , however, quite clumsy in an unstructured non-orthogonal grid. Our FVTD is convenient in unstructured grids and not as convenient as the FDTD to simulate boundary condition. We therefore propose to use the FDTD in the region near the body (region 1, Figure 2) and use the FVTD in the outer region (region 2, Figure 2).

4. Boundary Conditions

The FDTD alogrithm is natural for PEC boundary condition since the component of the electric field along a boundary edge is known. It is also quite natural across an interface of two media since only tangential components of the electric field are located there. The PEC boundary condition simulation for FVTD is given in [2]. Here we shall give more details on the boundary condition simulation between two media for FDTD.

4.1. Boundary Condition Between Two Media

The 2-D boundary condition between two different media is a specialization of that for 3-D. The magnetic contour needed to update the electric field component at point **p** (Fig. 3) is shown. Let **t** be the direction for this component. The normal component of the magnetic field at the boundary points are not continuous. Therefore in the evaluation of the line integral one must take into account of this discontinuities. The equation for the updating of this electric field component is (based on (1b) with loss)

$$\int_{\partial A} \vec{H} \bullet d\vec{s} = \int_A \hat{\imath} \bullet (\dot{\vec{D}} + \sigma\vec{E}) da \approx A_1 \hat{\imath} \bullet (\dot{\vec{D}}_1 + \sigma_1 \vec{E}_1) + A_2 \hat{\imath} \bullet (\dot{\vec{D}}_2 + \sigma_2 \vec{E}_2)$$

$$= \varepsilon_a A \hat{\imath} \bullet \dot{\vec{E}}_1 + \sigma_a A \hat{\imath} \bullet \vec{E}_1 = \varepsilon_a A \hat{\imath} \bullet \dot{\vec{E}}_2 + \sigma_a A \hat{\imath} \bullet \vec{E}_2 \qquad (3)$$

where A_1 and A_2 are the fractional areas enclosed by the contour in the medium 1 and the medium 2 respectively and where

$$\varepsilon_a = (A_1 \varepsilon_1 + A_2 \varepsilon_2)/A; \quad \sigma_a = (A_1 \sigma_1 + A_2 \sigma_2)/A; \quad A = A_1 + A_2$$

4.2 A more accurate FDTD boundary condition simulation across a dielectric boundary (roof top approximation)

The FDTD boundary condition approximation in section **4.1** assumes that the electric field in each area A_1 and A_2 are constant (in this case they are the same constant). In the evaluation of the magnetic line integral, the magnetic field components are also assumed to be piece wise constant. This assumption may introduce intolerable error if the dielectric constants in the two medium differ greatly. We make the following observation:

If we approximate an area integral by multiplying the area by the value of the integrand at the center of the area, we introduces an error of $0(\Delta x)^2$. This accuracy can only be attained if the variable has a continuous second derivatives. Across an interface the electric field components and/or the magnetic field components may or may not be continuous. Definitively, they are not continuously differentiable twice. Therefore the approximation used in the ordinary FDTD will be of lower accuracy. We can improve the accuracy by noticing that the variable are continuously differentiable twice in the tangential directions and in the interior of each region; but the first derivative along the normal may not be the same. Therefore, we assume that the variables are piece wise linear in the normal direction. For clarity of discussion we refer to Fig. 3 with the following notations

$\quad$ **T** is the unit normal to the area enclosed by the contour 2-4-8-10-2.

$\quad$ t_3 is the unit tangent along the side 2-4.

$\quad$ t_7 is the unit tangent along the side 4-8.

$\quad$ t_9 is the unit tangent along the side 8-10.

t_{11} is the unit tangent along the side 10-2.

$T*E = E_T$ is the component of the electric field in the T direction.

$t_3*H = H3$ is the magnetic field component along the side 2-4.

$t_7*H = H7$ is the magnetic field component along the side 4-8.

$t_9*H = H9$ is the magnetic field component along the side 8-10.

$t_{11}*H = H11$ is the magnetic field component along the side 10-2.

Note that H3 may not be continuous across the point 3. But H7 has continuous second derivative in the direction of 4-8. In the evaluation of the area integral we assume that E_T is linear from the point p to the point q; and E_T is also linear from the point r to the point p. These two linear functions do not have to be the same. Also in the evaluation of the magnetic circulation from the point 3 to point 4 we assume that H3 is linear from the points 3 to the point 5. The approximation made here is intuitively more accurate than that in the previous section and we shall show this with computations in a later section. Let S_{ij} denote the arc length from points i to point j we refer to Fig. 3 to get the following approximations:

$$\int_2^3 \vec{H} \cdot d\vec{l} = \frac{1}{4}[3H_3(3^-)+H_3(1)]S_{23} \qquad \int_3^4 \vec{H} \cdot d\vec{l} = \frac{1}{4}[3H_3(3^+)+H_3(5)]S_{34} \, .$$

$$\int_4^8 \vec{H} \cdot d\vec{l} = H_7(7)S_{48} \qquad \int_8^9 \vec{H} \cdot d\vec{l} = \frac{1}{4}[3H_9(9^+)+H_9(6)]S_{89}$$

$$\int_9^{10} \vec{H} \cdot d\vec{l} = \frac{1}{4}[3H_9(9^-)+H_9(12)]S_{9\,10} \qquad \int_{10}^2 \vec{H} \cdot d\vec{l} = H_{11}(11)S_{10\,2}$$

$$\int_A \dot{\vec{D}} \cdot d\vec{a} = \frac{A_2\varepsilon_2}{4}[3\dot{E}_T(p)+\dot{E}_T(q)]+\frac{A_1\varepsilon_1}{4}[3\dot{E}_T(p)+\dot{E}_T(r)]$$

4.3 FDTD Boundary Condition Simulation Across a Dielectric Boundary (flat top approximation, explicit expressions from section 4.1)

The flat top approximation, which is more crude than the approximation given in section 4.2 would have the following approximations:

$$\int_2^3 \bar{H} \cdot d\bar{l} = H_3(3^-)S_{23} \qquad \int_3^4 \bar{H} \cdot d\bar{l} = H_3(3^+)S_{34} .$$

$$\int_4^8 \bar{H} \cdot d\bar{l} = H_7(7)S_{48} \qquad \int_8^9 \bar{H} \cdot d\bar{l} = H_9(9^+)S_{89} \qquad \int_9^{10} \bar{H} \cdot d\bar{l} = H_9(9^-)S_{9\,10}$$

$$\int_{10}^2 \bar{H} \cdot d\bar{l} = H_{11}(11)S_{10\,2} \qquad \int_A \dot{\bar{D}} \cdot d\bar{a} = (A_1\varepsilon_1 + A_2\varepsilon_2)\dot{E}_T(p)$$

4.4a Roof top approximation across a cylindrical dielectric boundary for TM wave.

The free space zone thickness is Δ and the dielectric zone thickens is δ . (Figure 4) The index i corresponds to the radial (r or n) direction and the index j corresponds to the angular (theta or s) direction. The boundary corresponds to i = I. For convenience we introduce the following notations:

$$S_{I,j} = |\bar{r}(I, j+1/2) - \bar{r}(I, j-1/2)|$$

$$S'_{I,j} = |\bar{r}(I-1/2, j+1/2) - \bar{r}(I-1/2, j-1/2)|$$

$$S''_{I,j} = |\bar{r}(I+1/2, j+1/2) - \bar{r}(I+1/2, j-1/2)|$$

The resulting equation are (based on the discussion of **4.2**):

$$E_z^{n+1}(I,j) = E_z^n(I,j) - \frac{\varepsilon\delta}{3\varepsilon\delta + 3\varepsilon_o\Delta}[E_z^{n+1}(I-1,j) - E_z^n(I,j)]$$

$$-\frac{\varepsilon_o\Delta}{3\varepsilon\delta + 3\varepsilon_o\Delta}[E_z^{n+1}(I+1,j) - E_z^n(I+1,j)]$$

$$+\frac{8\Delta t}{S_{I,j}(3\varepsilon\delta + 3\varepsilon_o\Delta)}\{S'_{I,j}H_\theta^{n+1/2}(I-1/2, j+1/2) - S''_{I,j}H_\theta^{n+1/2}(I+1/2, j+1/2)$$

$$+(\frac{3\Delta}{8}\frac{\mu}{\mu_o} + \frac{3\delta}{8})[H_r^{n+1/2}(I, j+1/2) - H_r^{n+1/2}(I, j-1/2)]$$

$$+\frac{\delta}{8}[H_r^{n+1/2}(I-1, j+1/2) - H_r^{n+1/2}(I-1, j-1/2)]$$

$$+\frac{\Delta}{8}[H_r^{n+1/2}(I+1, j+1/2) - H_r^{n+1/2}(I+1, j-1/2)]\} \tag{4a}$$

$$H_\theta^{n+1/2}(I+1/2, j) = H_\theta^{n-1/2}(I+1/2, j) - \frac{\Delta t}{\mu_o\Delta}[E_z^n(I+1, j) - E_z^n(I, j)] \tag{4b}$$

$$H_\theta^{n+1/2}(I-1/2, j) = H_\theta^{n-1/2}(I-1/2, j) - \frac{\Delta t}{\mu\delta}[E_z^n(I, j) - E_z^n(I-1, j)] \tag{4c}$$

$$H_r^{n+1/2}(I, j+1/2) = H_r^{n-1/2}(I, j+1/2) - \frac{\Delta t}{\mu r_{Ij}}[E_z^n(I, j) - E_z^n(I, j+1)] \tag{4d}$$

4.4b Roof top approximation across a cylindrical dielectric boundary for TE wave.

Following the notations of the last section, we can derive the equation to update the z-component of the electric vector.

$$E_\theta^{n+1}(I, j+1/2) = E_\theta^n(I, j+1/2) - \frac{\varepsilon\delta}{3\varepsilon\delta + 3\varepsilon_o\Delta}[E_\theta^{n+1}(I-1, j+1/2) - E_\theta^n(I-1, j+1/2)]$$

$$- \frac{\varepsilon_o\Delta}{3\varepsilon\delta + 3\varepsilon_o\Delta}[E_\theta^{n+1}(I+1, j+1/2) - E_\theta^n(I+1, j+1/2)]$$

$$+ \frac{8\Delta t}{(3\varepsilon\delta + 3\varepsilon_o\Delta)}[H_z^{n+1/2}(I+1/2, j+1/2) - H_z^{n+1/2}(I-1/2, j+1/2)]$$

(5)

5. Computational results

We present calculations in this section of both TM and TE waves scattering from circular cylinders coated with a thin layer of dielectric. The radius of the circular cylinder is 1 meter, the thickness of the dielectric medium is 0.025m, the grid size is delx=0.05m. For all the calculations, the thin layer material is divided into 5 zones in the radial direction. We use the FDTD algorithm in the orthogonal cylindrical grid (region 1, Figure 2) in the neighborhood of the body and use FVTD in the irregular grid (region 2, Figure 2). The distance from the outer boundary of FVTD computational grid to the surface is 30 zones which includes 10 zones of tapered damping. The input signal is a Gaussian shape pulse with the half width of the pulse equal to $20\Delta t$. The bistatic RCS calculation at f=300 MHz are presented along with the theoretical value based on the series solution [6]. The wavelength in the medium is 0.1m for a medium with the index of refraction equal to 10 at 300MHz; and the thickness of the thin layer is equal to a quarter of wavelength in the medium at this frequency. Figures 5a and Figure 5b are the Bistatic TM RCS for two different sets of eps and mu. Figure 6a and Figure 6b are the Bistatic TE RCS for two different sets of eps and mu. The difference in RCS using flat-top and roof-top approximation for the TE wave is small, but the difference in RCS for TM is pronounced.

318

6. Conclusion

We have presented some calculation of the RCS by a circular cylinder coated with a thin layer of dielectric. In this paper we make use of the flexibility of the FVTD in an unstructured grid away from the scatterer and the FDTD in an orthogonal grid next to the scatterer. We also employed the easy to implement outer boundary condition simulation [5] to allow us to . truncate the computational region not with a rectangular outer boundary but with an irregular boundary. The realization and the implementation of the piece wise linear approximation of the variables across he interface of two media further improve the accuracy of our algorithm.

7. References

1. Kane S. Yee and J. S. Chen, "Conformal Hybrid Finite Difference Time Domain and Finite Volume Time Domain ", *IEEE. Trans. Antennas Propag.* vol. 42. No. 10, Oct. 1994.

2. Jei S. Chen, John Prodan, and Kane. S. Yee, " An FDTD/FVTD 2D-Algorithm to Solve Maxwell's Equations, " *Proceeding of the 1995 ACES conference.*

3. K. S. Yee, "Ten years of evolution of the FDTD-like conformal techniques," *Proceeding of the 1995 ACES conference.*

4. P.A. Tikras and K. R. Demarest, "Modeling of thin dielectric structures using the finite difference time domain technique", *IEEE trans. Antenna and Propagation,* Vol. 39, pp 1338-1345, Sept. 1991.

5. Jei S. Chen, and Kane S. Yee, " Artificial tapered damping near the outer computational boundary," submitted to IEEE for publication. Also *1995 IEEE APS Conference Digest* pp. 620-23

6. G. T. Ruck, editor, <u>Radar Cross Section Handbook</u>, Vol. 1, Ch. 4, New York, Plenum Press, 1970.
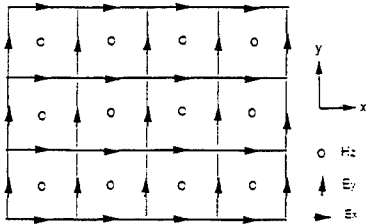
Fig. 1a FDTD Grid for 2-D TE Waves

○ Hz
▲ Ey
▶ Ex

Fig. 2 The FDTD grid (1) and the FVTD (2) grid for a circular cylinder coated with a dielectric layer

Dielectric boundary

Boundary of the FDTD and FVTD grids

Outer computation boundary

Fig. 1b FDTD Grid for 2-D TM Waves

● Ez
▲ Hy
▶ Hx
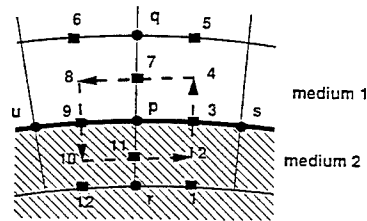
Fig. 3 The magnetic contour to update the electric field at the point p (illustrating the use of the roof top function variation

medium 1

medium 2

Fig. 1c FVTD Rectangular Grids

● E
○ H
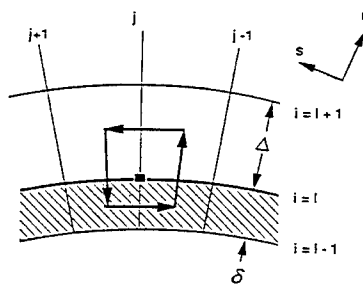
Fig. 4 The contour used to update Ez at the interface

320
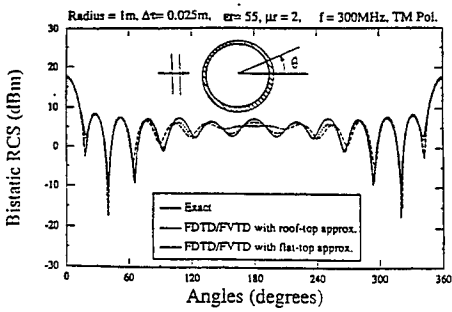
Figure 5a   TM Bistatic RCS for a circular cylinder coated with a thin layer
of dielectric (eps = 55; mu=2)
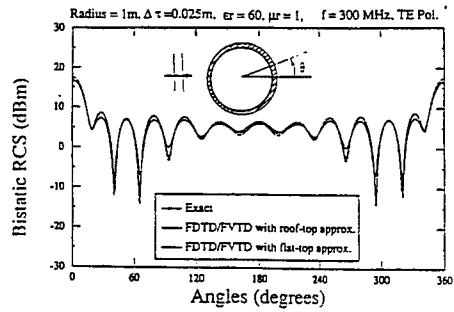
Figure 6a   TE Bistatic RCS for a circular cylinder coated with a thin layer
of dielectric (eps = 60; mu=1)
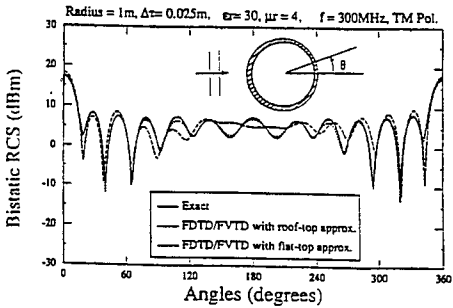
Figure 5b   TM Bistatic RCS for a circular cylinder coated with a thin layer
of dielectric (eps = 30; mu=4)
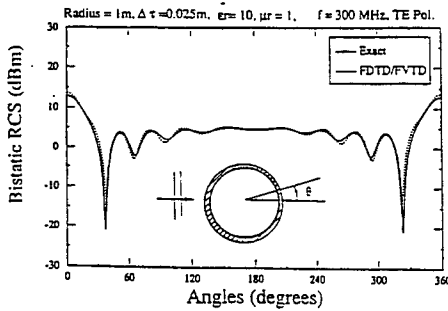
Figure 6b   TE Bistatic RCS for a circular cylinder coated with a thin layer
of dielectric (eps = 10; mu=1)

Improved computational efficiency by using sub-regions in FDTD simulations

Eric A. Jones and William T. Joines [*]

Abstract

This paper presents a method of dividing a Finite Difference Time Domain Method (FDTD) problem space into multiple sub-regions. Each sub-region has its own set of field arrays and uses update equations customized to the properties of the sub-region. After each half-time step, neighboring sub-regions communicate the field values shared at their common boundary so that waves travel uncorrupted from one sub-region to another. This regional FDTD method produces the same results as the standard FDTD method, but it is both computationally more efficient and less memory intensive. It is particulary well-suited for rectangular waveguide simulations where it provides a speed up of as much as 3.83 and a memory savings of up to 94%, as shown by an example.

1 . Introduction

The versatility of the Finite Difference Time Domain Method (FDTD) makes it suitable for solving a variety of problems in electromagnetics. The standard approach of implementing the FDTD algorithm treats the problem space of a simulation as one computational region. The entire problem space is represented with a single set of field arrays, and these arrays are updated using a single set of update equations. Here we present a method of dividing the problem space into multiple sub-regions. Each sub-region has its own set of field arrays and uses update equations customized to the properties of the sub-region. After each half-time step, neighboring sub-regions communicate the field values shared at their common boundary so that waves travel uncorrupted from one sub-region to another. This regional FDTD method produces the same results as the standard FDTD method, but it is both more computationally efficient and less memory intensive.

Dividing the problem space into multiple sub-regions has the following five advantages over treating it as a single large region. First, since the update equations only have to be valid over a small sub-region, they are often more efficient than using a single set of general purpose update equations for the entire region. For example, the update equations for a homogeneous-lossless medium are less complex than the update equations necessary to simulate an inhomogeneous-lossy region. Second, by separating out homogenous regions, memory is saved because there is no need to store a material array to identify the type of material at each grid point inside the sub-region. The entire sub-region can use the same material constants and the efficient homogeneous update equations. Third, the shape of the problem space is no longer restricted to a single rectangular region. The problem space can consist of several connected cubical sub-regions. This is particularly useful for waveguide problems that do not fit efficiently into a single rectangular region. Fourth, it should be possible to use sub-regions with

different grid-densities within the same problem space. This would allow the intricate features in one sub-region to be resolved without increasing the grid density of the entire problem space. It should also be possible to use sub-regions with unstructured grids to model parts of a problem that do not fit on a rectangular grid while the rest of the problem is modeled with sub-regions that use more efficient rectangular grids. Fifth, while all of the suggested advantages are realizable on single processor machines, the sub-region approach is also well-suited for parallel processing.

This paper is organized in the following manner. Section 2 looks at the difference in computational complexity of several different FDTD update equations as a motivation for developing the regional FDTD method. Section 3 then discusses the implementation issues of the method. Section 4 applies the method to two different types of problems: 1) scattering from a lossy, dielectric object, and 2) simulation of a magic-tee waveguide structure.

2. FDTD Update Equations

The computational complexity of the update equations for FDTD is dependent on the type of region under simulation. Equations (1) and (2) show two of the six general FDTD update equations necessary to update the electric and magnetic field components of an inhomogeneous medium of lossy materials where $\Delta x \neq \Delta y \neq \Delta z$. The other four equations are very similar to these.[1, ch. 3]

$$
\begin{aligned}
E_{x\,[i+1/2,j,k]}^{n+1/2} &= C_{a[i+1/2,j,k]}\, E_{x\,[i+1/2,j,k]}^{n-1/2} \\
&\quad + C_{b[i+1/2,j,k]}\Big[H_{z\,[i+1/2,j+1/2,k]}^{n} - H_{z\,[i+1/2,j-1/2,k]}^{n}\Big] \\
&\quad - C_{c[i+1/2,j,k]}\Big[H_{y\,[i+1/2,j,k+1/2]}^{n} - H_{y\,[i+1/2,j,k-1/2]}^{n}\Big]
\end{aligned}
\tag{1}
$$

$$
\begin{aligned}
H_{y\,[i+1/2,j,k+1/2]}^{n+1} &= C_{d[i+1/2,j,k+1/2]}\, H_{y\,[i+1/2,j,k+1/2]}^{n} \\
&\quad + C_{e[i+1/2,j,k+1/2]}\Big[E_{z\,[i+1,j,k+1/2]}^{n+1/2} - E_{z\,[i,j,k+1/2]}^{n+1/2}\Big] \\
&\quad - C_{f\,[i+1/2,j,k+1/2]}\Big[E_{x\,[i+1/2,j,k+1]}^{n+1/2} - E_{x\,[i+1/2,j,k]}^{n+1/2}\Big]
\end{aligned}
\tag{2}
$$

where C_a through C_f are determined by the material constants present at a specific grid point. The set of six update equations requires a total of 18 multiplications to calculate the field values at a point for a single time step. It is also necessary to access an array to determine what material exists at each field point. A method outlined in [2] uses an integer(or byte) value to indicate the type of material present at each grid point. Because all of the E-field and H-field values are staggered in space, six different material arrays, one for each field component, are needed to store the material types. This uses less memory than creating an array for each of the material constants.

Of course, equations (1) and (2) are also valid for a homogeneous region of lossless material where $\Delta x \neq \Delta y \neq \Delta z$, but they are not the most efficient equations for this simplified situation. For homogeneous-lossless regions, equations (1) and (2) simplify to the following equations:

$$E_x^{n+1/2}{}_{[i+1/2,j,k]} = E_x^{n-1/2}{}_{[i+1/2,j,k]}$$

$$+ C_b \left[H_z^n{}_{[i+1/2,j+1/2,k]} - H_z^n{}_{[i+1/2,j-1/2,k]} \right] \tag{3}$$

$$- C_c \left[H_y^n{}_{[i+1/2,j,k+1/2]} - H_y^n{}_{[i+1/2,j,k-1/2]} \right]$$

$$H_y^{n+1}{}_{[i+1/2,j,k+1/2]} = H_y^n{}_{[i+1/2,j,k+1/2]}$$

$$+ C_e \left[E_z^{n+1/2}{}_{[i+1,j,k+1/2]} - E_z^{n+1/2}{}_{[i,j,k+1/2]} \right] \tag{4}$$

$$- C_f \left[E_x^{n+1/2}{}_{[i+1/2,j,k+1]} - E_x^{n+1/2}{}_{[i+1/2,j,k]} \right]$$

There are two major differences between equations (3) and (4) and their slower cousins. First, because the region is lossless, $C_a = C_d = 1$, and therefore they can be left out of the equation. This reduces the required number of multiplications for the set of six update equations from 18 down to 12 and results in equations that are more computationally efficient. Second, because the region is homogeneous, C_b, C_c, C_e, and C_f do not vary from grid point to grid point. This saves memory because the arrays that track which material is present at each grid point are no longer necessary. Also, now C_b, C_c, C_e, and C_f can be stored in registers. This is also more computationally efficient because it reduces the amount of data that is retrieved from memory and leaves more space in the memory cache for the field arrays.

There are many different special case update equations. Table 1 compares the memory and computational requirements for several different update equations used on a 50x50x50 region where $\Delta x \neq \Delta y \neq \Delta z$. The run time is the amount of time required to execute 100 time steps on a Dell XPS Pentium-120. Floating point numbers (4 bytes) were used to store field values and short integers (2 bytes) were used to store material types.

Type of Medium	Run Time (seconds)	Total Memory (MB)	Speed Up	Memory Savings
Perfectly Matched Boundary Layer (PML)	63.4	7.50	0.63	-67 %
Lossy Inhomogeneous	40.2	4.50	1.00	0%
Electrically Lossy and Inhomogeneous Magnetically Lossless and Homogeneous	31.1	3.75	1.29	17%
Lossless Homogeneous	22.6	3.00	1.78	33 %
Perfect Electric Conductor (PEC)	00.0	0.00	-	100 %

Table 1: This table compares the run time and memory requirements for several different FDTD update equations used to update a 50x50x50 grid for 100 time steps on a Dell XPS Pentium 120 with 40 MB of RAM. Field values were 4-byte floating point numbers and material types were 2-byte integer values. Speed up and memory savings are calculated using the lossy-inhomogeneous case as a reference.

The table shows that the homogeneous-lossless case provides a speed up of 1.78 over the inhomogeneous-lossy case. The homogeneous-lossless case also provides a 33% memory savings over the inhomogeneous-lossy case. Here the following definitions have been used:

$$SpeedUp = \frac{RunTime_{old}}{RunTime_{improved}} \qquad MemorySavings = \frac{Memory_{old} - Memory_{improved}}{Memory_{old}} * 100\%$$

The perfectly matched boundary layer condition (PML) update equations are also included in this table. The split-field formulation originally developed by Berenger is used to implement these update equations [3]. They are much more computationally intensive than any of the other cases. This implies that when the split-field PML layer is used to truncate a problem space, most of the computation time is spent updating the boundary region. Recently a more efficient form of the PML has been developed by Gedney which should ameliorate this situation [4].

3 . Dividing a Problem Space into Regions

Standard FDTD simulations represent the problem space using a single large grid. If there is a single inhomogeneous-lossy region in an otherwise homogeneous-lossless problem space, the whole problem space is updated using the inhomogeneous-lossy equations. It is obvious from Table 1 that a price is paid for using these equations. If instead the problem is split up into sub-regions so that each sub-region uses the most efficient update equations that are valid in the region, both time and memory are saved.
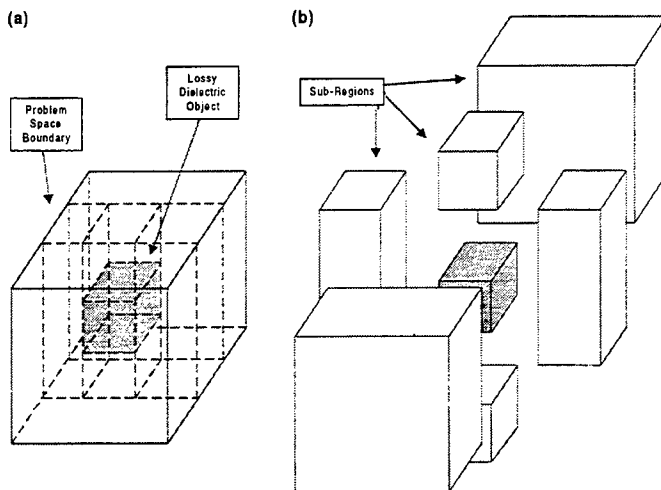
Figure 1: a) Shows an FDTD problem space containing a single lossy dielectric object. b) The problem space divided into sub-regions of homogeneous materials.

Figure 1 illustrates how the regional method is applied to a problem with a block of lossy material suspended in air. In the regional FDTD method, the simulation region is divided into seven blocks as shown in Figure 1b. Now the lossy material is in its own sub-region isolated from the air surroundings, and it can use the homogeneous-lossy update equations. The other six regions of air will use the homogeneous-lossless update equations.

While dividing the problem space into smaller sub-regions improves the efficiency of the update equations, it also adds some complexity to the problem. After each field update, the sub-regions must communicate the field values along their borders with their neighboring sub-regions. In this way, fields that propagate out of one sub-region seamlessly propagate into a neighboring sub-region. For this to work, neighboring grids must overlap slightly so that they share the border grid points between them. Only one of the grids is responsible for updating the border grid points. It then sends the calculated values to its neighboring grid. It is easier to illustrate how this is done on a two-dimensional grid rather than on a three-dimensional grid. Three two-dimensional sub-grids are shown in Figure 2a.
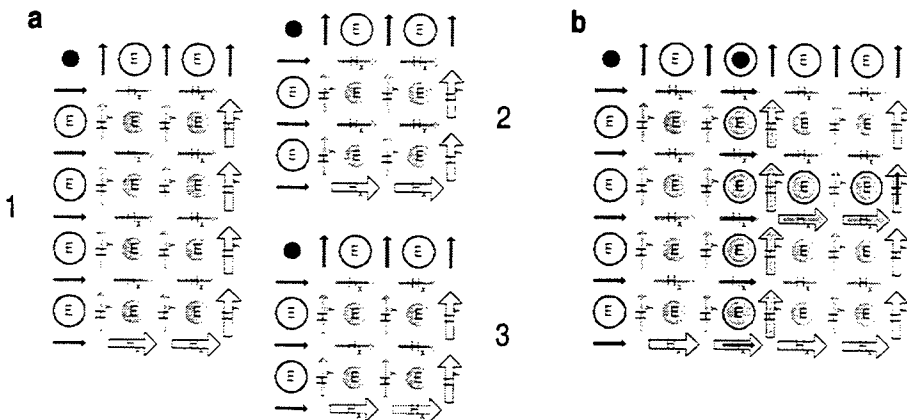
Figure 2: a) This figure shows the computational grids for three neighboring sub-regions of a two-dimensional FDTD problem. Solid gray circles indicate E_z field points that the sub-grids are responsible for computing. Solid gray arrows indicate H_x and H_y fields that the sub-grids are responsible for computing. Empty circles and arrows indicate field values that the sub-grid expects to receive from a neighbor. Black circles and arrows indicate field values that are never used in any computations by the sub-grids. b) The three sub-grids from (a) are assembled to form the entire rectangular problem space. All of the hollow circles and arrows in the middle of the problem are now filled in by a neighboring sub-grid. The hollow circles and arrows along the boundary of the problem are determined from boundary conditions.

These three grids fit together to form a square as shown in Figure 2b. The solid gray circles in each sub-grid represent the E_z field values that the grid is responsible for updating. The empty circles are the E_z field values that the sub-grid expects to receive from a neighbor. After each n+½th time step, grid 1 has calculated E-field values that are needed by grids 2 and 3, so it sends them the appropriate E-field values. In a similar fashion, the solid gray arrows in each sub-grid represent the H_x and H_y field values

that the grid is responsible for updating, and the empty gray arrows are the H_x and H_y field values that the grid expects to receive from a neighbor. After each nth time step, grids 2 and 3 have calculated H-field values that are needed by grid 1, so they send it the appropriate field values. Black circles and arrows on a sub-grid represent field values that are never used in any calculations made in that particular sub-grid. Therefore, it is not necessary to exchange or operate on the field at black grid locations.

As an inhomogenoues region is divided into multiple homogeneous sub-regions, the communications overhead becomes greater and greater. Also, as the size of sub-regions becomes smaller, the size of the field arrays also becomes smaller. This reduces the efficiency of the update equation loops. Test runs on a 60x60x60 inhomogenoues cube indicate that the region can be divided into about 35 homogeneous sub-regions before these costs outway the computational benefits of using more efficient homogeneous equations.

Dividing the problem space into sub-regions is not the only way to take advantage of more efficient update equations at individual grid points in a problem space. It also possible to use "if-then" statements inside the field update loops to determine which update equation is valid for a particular grid point. The regional FDTD method has several advantages over this approach. First, the regional FDTD method offers a memory savings while the "if-then" method does not. Second, "if-then" statements inside inner loops are usually handled well by standard processors, but they are extremely expensive on vector processors [1, ch.16]. And finally, there are situations where the "if-then" approach would not work, and the regional FDTD method may work. These include using sub-regions with different grid densities or even unstructured grids in the same problem space with normal cartesian sub-regions. These topics are subjects of current research. In the next section, the regional FDTD method developed in this section is applied to two example problems.

4. Two Examples
In the first problem, a 80x80x10 lossy, dielectric block is suspended in a 100x100x30 free-space region. This problem is similar to the simulation of a planar antenna on a dielectric substrate. Table 2 compares the run time and memory usage for both the standard FDTD method and the regional FDTD method. For the standard FDTD method, the problem space was treated as an inhomogeneous-lossy region. For the regional FDTD method, the problem space was divided into homogeneous sub-regions as discussed in the previous section. The first part of Table 2 shows that the regional FDTD method provides a computational speed-up of 1.12 and a 14.4% memory savings over the standard FDTD method.

Most practical problems must be truncated by an absorbing boundary condition. The second part of Table 2 adds a five layer PML region around the problem space. This PML region is composed of six adjoining sub-regions that form a cubical shell around the problem space for both the standard and regional FDTD methods. As evidenced by the increased run time, the computational and memory burden of the PML region are much larger than that of the problem space. This reduces the benefits of the regional FDTD method considerably because it does not optimize performance in the boundary region. Now the regional FDTD method provides a computational speed-up of only 1.023 and a 6.4% memory savings over the standard FDTD method. Again it is noted that the split-field implementation

of the PML method which was used in these simulations is not as efficient as recently developed implementations of the PML [4].

No PML				
Algorithm	**Run Time (sec)**	**Memory Used (MB)**	**Speed Up**	**Memory Savings**
Standard FDTD	65.8	9.0	1.00	0.0 %
Regional FDTD	58.8	7.7	1.12	14.4 %
With 5 Layer PML				
Algorithm	**Run Time (sec)**	**Memory Used (MB)**	**Speed Up**	**Memory Savings**
Standard FDTD	172.4	20.0	1.00	0.0 %
Regional FDTD	168.8	18.8	1.02	6.4 %

Table 2: Compares the standard FDTD method and the regional FDTD method for an FDTD simulation of a 80x80x20 lossy dielectric block imbedded in a 100x100x30 free-space region. Results are shown for simulation with and without a PML boundary region. The standard FDTD method is used as the reference for speed up and memory savings calculations.

The second example concerns the simulation of a waveguide component. If a magic-tee is simulated using the standard FDTD method, the cubical region outlined in Figure 3a must be simulated. Much of this space lies outside of the waveguide and is therefore irrelevant to the problem. Figure 3b shows how the irrelevant regions can be trimmed away using the regional FDTD method so that only regions inside the waveguide are left in the problem. This results in a substantial savings in memory. It is also more computationally efficient. Even if the standard FDTD method only calculates field values that are inside the problem space, it must still take the time to look at every grid point to determine if it is within the waveguide. The regional FDTD method avoids this unecessary overhead.
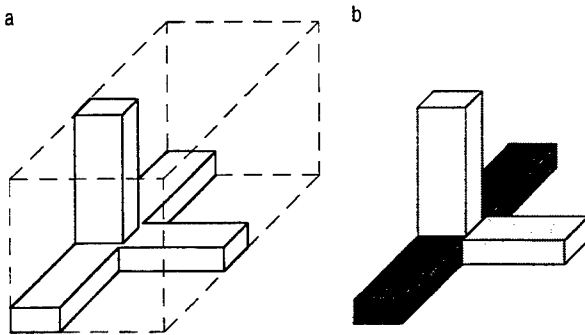
Figure 3: FDTD simulation of a magic-tee. The outline in (a) defines the region that is simulated using the standard FDTD method. In the regional FDTD method, the problem is divided into 3 sub-regions as shown in (b).

Consider the case where each arm of the magic-tee has the dimensions of 10x20x50 cells. The problem space for a standard FDTD implementation would have to be 60x70x120 cells. This requires 15.12 MB of memory. Calculating field values inside the wave guide for 100 time steps requires 38.12 seconds on a Dell XPS Pentium-120. In contrast, the problem can be separated into three separate sub-regions which measure 10x20x50, 10x20x50, and 10x20x120. Using this regional approach, the problem only requires 1.03 MB of memory and only requires 9.94 seconds to execute 100 time steps resulting in a speed up of 3.83 and a memory savings of 93% over the standard FDTD method. This is a very substantial improvement. These results are shown in Table 3.

Magic-Tee Waveguide Comparison				
Algorithm	Run Time (sec)	Memory Used (MB)	Speed Up	Memory Savings
Standard FDTD	38.12	15.12	1.00	0.0 %
Regional FDTD	9.94	1.03	3.83	93.2 %

Table 3: Compares the standard FDTD method and the regional FDTD method for an FDTD simulation of magic-tee waveguide component. The standard FDTD method is used as the reference for speed up and memory savings calculations.

5 . Conclusion

A regional FDTD method has been presented which connects multiple sub-regions to form a single problem space. Each sub-region updates its field values with the most efficient, valid update equations. This results in a method that is more efficient, both computationally and in memory requirements, than the standard FDTD method. Two examples using the method were presented. The first example applies the regional FDTD method to a typical inhomogenous FDTD problem with modest computational and memory savings. The second example shows that the method is particularly well-suited for waveguide simulations and provides a substantial computational speed up and memory savings for such problems. There is still quite a lot to be done that will extend and improve the regional FDTD method. It is hoped that further research will develop methods for combining unstructured grids and rectangular grids within the same problem space. Also, the inherently parallel structure of the regional FDTD method makes it a great candidate for distributed processing.

[1] A. Taflove, Computational ElectroDynamics The Finite-Difference Time-Domain Method," Boston: Artech House, 1995.

[2] A. Taflove and M. E. Brodwin, "Computation of the electromagnetic fields and induced temperature within a model of the microwave-irradiated human eye," IEEE Transaction on Microwave Theory and Techniques, vol. 23, no. 11, Nov 1975, pp. 888-896.

[3] J. P. Berenger, "A Perfectly Matched Layer for the Absorption of Electromagnetic Waves," Journal of Computational Physics, vol. 114, pp. 185-200, Oct. 1994.

[4] S. D. Gedney, "An Anisotropic Perfectly Matched Layer-Absorbing Medium for the Truncation of FDTD Lattices," IEEE Transactions on Antenna and Propagation, vol. 44, no. 12, Dec 1996, pp. 1630-1639.

FINITE DIFFERENCE TIME DOMAIN ELECTROMAGNETIC CODE VALIDATION USING AN INFRARED MEASUREMENT TECHNIQUE

Christopher Reuter, Mike Seifert, Tom Karle
Rome Laboratory
525 Brooks Road
Rome, NY 13441-4505
reuterc@rl.af.mil, seifertm@rl.af.mil, karlet@rl.af.mil

ABSTRACT

This paper describes the on-going Rome Laboratory computational electromagnetics effort associated with the Air Force's Command, Control, Communication, Computers, and Intelligence (C4I) mission. This effort is based on the need to predict how electromagnetic energy from an external environment is coupled into the interior of cavities in aircraft in which electronic circuits and modules are housed. The paper addresses the capability of using finite difference time domain to predict the energy that is coupled into a cavity. The validation of this technique is obtained through comparisons with experimental data from infrared images of the coupled energy.

INTRODUCTION

Miniaturization of electronic circuitry presents a major challenge in both the commercial and military world. The design of aircraft circuitry for the Air Force has additional challenges, one being the need for circuitry to operate under hostile electromagnetic environments such as electromagnetic radiation from both friendly and hostile sources including lightning, electrostatic discharge, and electronic warfare jammers. The success of the circuitry design rests on the ability to simulate and predict the performance of the circuitry in adverse electromagnetic environments prior to the prototype being built. Since aircraft circuitry is housed within some type of cavity, the first step in determining the circuit performance is to identify effective methodologies to predict how the external electromagnetic energy is coupled within the cavities.

Numerous methods, including Finite Difference Time Domain (FD-TD) and Method of Moments, are used in analyzing the problem of coupled energy into cavities. Advancements of FD-TD modeling [1] in the area of subcell models of fine geometrical features has resulted in greater applicability and has been viewed with great interest. This paper addresses the coupling problem from the aspect of FD-TD.

The validation of the FD-TD simulations is conducted through direct comparisons of Infrared (IR) images of the energy within the cavity. The IR imaging technique is a minimally perturbing approach that provides a fast, accurate two or three dimensional visual representation of the electromagnetic field distribution. The IR technique uses a planar detection screen to absorb a portion of the coupled microwave energy. The temperature at each location on the detection screen is proportional to the electromagnetic field intensity at that location [2]. This technique

has many advantages over conventional field probing techniques in that the latter technique tends to interact with and distort the fields being measured. Furthermore, the conventional probing technique collects data at single point in space and requires repositioning of the probes to obtain additional data. this process is not only time consuming but is error prone due to the repositioning of the probes. The IR technique has been successfully used in measuring the modal distributions of excited electromagnetic fields inside metal cavities [3].

This paper addresses the FD-TD methodology of predicting the coupled energy and microwave field distribution in a cylindrical waveguide with a thin axial slot. Comparisons are made between the field strengths predicted by the FD-TD simulations and the IR measured field strengths at various locations along the cylindrical axis.

FDTD MODELING AND SIMULATION

The chosen FD-TD implementation consists of the standard Yee grid using second order accurate central difference expressions to approximate the spatial and temporal derivatives in Maxwell's two curl equations. The computational space is characterized by a total-field/scattered-field formulation [4] of the FD-TD algorithm to provide a compact wave source realization. Also, a perfectly matched layer is introduced to minimize the reflected electromagnetic waves which reach the boundary of the computational space.

The problem of interest consists of a cylindrical waveguide with a thin axial slot as shown in Figure 1. The 13.25 inch cylinder with a 3 inch inside diameter contains a 2 inch by .03125 inch slot located 8.8 inches from one end. The brass cylinder has a thickness of .25 inches and is modeled with σ = 32.7 Msiemens/meter. To generate a more accurate model the characteristics of IR detector disk with styrofoam backing that is placed inside the cylinder during the IR measurements is also incorporated. The IR detector is modeled as an infinitely thin layer having σ = 94.3 siemens/meter; and the 0.2 inch styrofoam backing is modeled with a relative permittivity of 1.03. In addition, to ensure that steady state is achieved within a reasonable number of time steps (roughly 4000), the remaining material within the cavity is assigned the characteristics of a small loss medium (σ = .05 siemens/meter).

The simulations are based on a time and spatial discretization of .13 nanoseconds and .08 inches, respectively. The computational space encompasses a volume of 66 x 66 x186 cells. A plane wave source of frequency 3.5 GHz is introduced at the total field/scattered field boundary.

INFRARED EXPERIMENTAL SETUP

The experimental setup is shown in Figure 2. The IR measurements were performed in the large anechoic chamber in the Electromagnetic Environmental Effects Research Facility (E3RF) at Rome Laboratory. This facility provides control of interference to minimize unintentional EM field reflections and interactions from distorting the measurement results and for temperature stability.

A brass cylinder with dimensions as shown in Figure 1 is placed on a styrofoam block aligned parallel to the aperture of a 2-4 GHz standard gain horn antenna. One end of the cylinder is
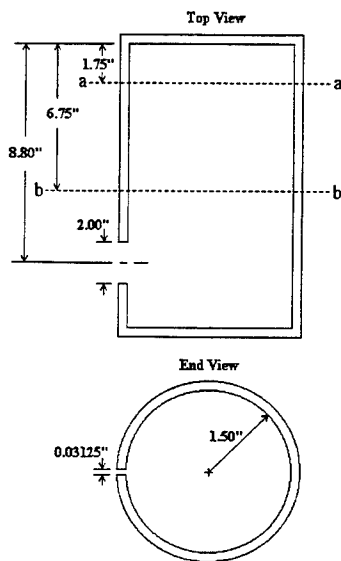
Figure 1. Geometry of Slotted Cylinder
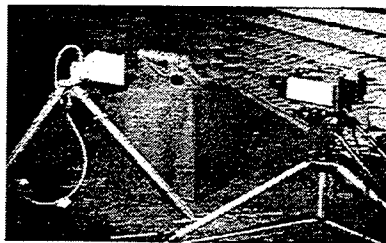
Figure 2. Experimental setup.

completely closed while the other end is covered with a fine wire mesh which allows the IR camera to view the internal fields and modal distributions while representing a somewhat solid end at the frequencies used in this experiment. The horn is located 20 inches from the cylinder directly in front of the slot aperture. The cylinder is illuminated with an incident electric field polarized perpendicular to the cylinder axis

The IR detector and styrofoam fit tightly inside the cylinder and are moved to various points of interest. The IR detector used in this experiment is a carbon loaded Kapton material mounted on a styrofoam poster board having a surface resistance of 100 ohms/square at 4 GHz and $\sigma = 94.3$ siemens/meter with d = 100µm. The conductivity and the imaginary components of the permittivity and permeability cause the temperature of the detector to rise above the ambient temperature. The increase in temperature is proportional to the local electric intensity at every location on the detector, producing a two-dimensional map of the field intensity. An Agema Thermovision 900 Infrared measurement system records, digitizes and stores the absolute temperature of the IR detector.

The IR measurement system records the thermal pattern at various planes along the axis of the cylinder. The carbon paper heats for several minutes to obtain a steady state condition. A long wave IR scanner having a spectral response of 8-12 microns detects temperature changes as small as 0.08C. The IR scanner samples data at 136 lines per frame and 272 samples per line and the data is recorded, digitized and stored. A synthesized sweep generator produces the transmit signal. The signal is pre-amplified and then amplified by a 200 Watt TWT Amplifier. The IR measurements begin by recording the thermal distribution of the IR detector without any applied

microwave field. The ambient temperatures are subtracted from the RF induced temperatures. This step insures that only the contribution from the coupled microwave signal is used to determine the internal field intensities.

SIMULATION VALIDATION

FD-TD simulations and IR measurements were conducted for various positions of the IR detector material within the cylindrical cavity. Figure 1 identifies two of these positions (denoted by the aa and bb planes) in reference to the location of the aperture of the cylinder. The simulation and measurement results are presented in Figures 3 and 4. The steady state simulation data (shown in Figures 3a and 4a) represent the sum of the squared electric field components; whereas, the measured data (shown in Figures 3b and 4b) represent the power absorbed by the heating of the IR detector material. The results are individually normalized and plotted with the shown gray scale.

Figures 3 and 4 represent two distinctive electromagnetic modes within the cylinder. For each mode there is good correlation between the simulated and measured data. Improvement in the correlation would result from a finer gridding of the aperture region and a more realistic energy source implementation within the simulation.

a   b
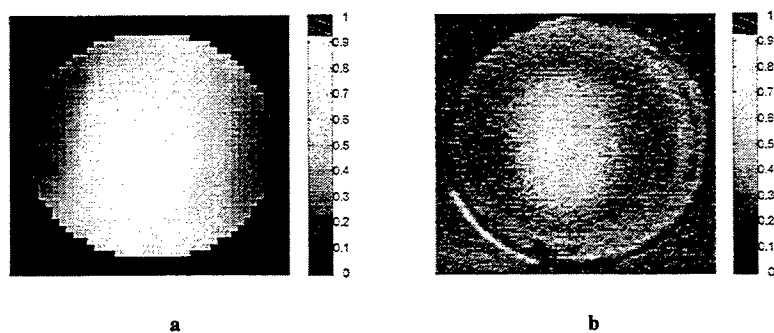
Figure 3. Simulated (a) and measured (b) modes in cylinder: 1.75 inches from the back

(at the aa-plane)

CONCLUSIONS

This paper has described an IR validation methodology for computational electromagnetic analysis tools and models. The validation process was conducted on a cylindrical waveguide with a narrow slot aperture. The results indicate that this validation technique can provide insight in the area of model development, model enhancement, and simulation techniques.
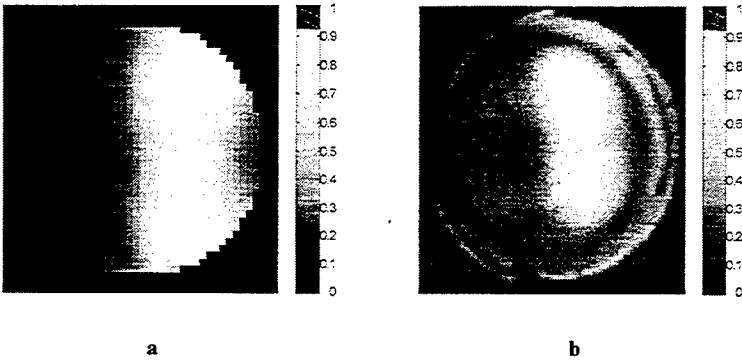
Figure 4. Simulated (a) and measured (b) modes in cylinder: 6.75 inches from the back

(at the bb-plane)

REFERENCES

[1] Taflove, A., K. R. Umashankar, B. Beker, F. Harfoush, and K. S., "Detailed FD-TD Analysis of Electromagnetic Fields Penetrating Narrow Slots and Lapped Joints in Thick Conducting Screens," IEEE Trans. Antennas and Propagation, vol. 36, 1988, pp.247-257.

[2] Pesta, A. J., M. F. Seifert, "Infrared Measurements of Electromagnetic Field", Dual-Use Technologies and Application Conference, SUNY Institute of Technology, Marcy NY, May 1993.

[3] Norgard, J. D., R. M. Sega, " Resonant Coupling Through a Slot to a Loaded Cylindrical Cavity - Experimental Results", Final Technical Report: RADC-TR-89-382, Rome Air Defense Center, March 1990.

[4] Taflove, A., Computational Electrodynamics: The Finite-Difference Time-Domain Method, Artech House, Boston, MA.

PML-FDTD Simulation for
Dispersive, Inhomogeneous, and Conductive Earth

W.C. Chew[1], M. Oristaglio[2], and T. Wang[3]

[1]Center for Computational Electromagnetics
University of Illinois, Urbana, IL 61801
[2]Schlumberger-Doll Research
Old Quarry Road, Ridefield, CT 06877
[3]Western Atlas Wireline Services
10201 Westheimer, Houston, TX 77042

1. Introduction

Dispersive media are often encountered in rocks, earth and biological media [1-7]. The dispersive phenomenon can result from dielectric relaxation in the media. This could be a consequence of geometrical effect of insulating rock platelets immersed in a conductive host [6]. It could also be the result of the interaction of electromagnetic fields with the double layer around colloidal suspensions in a saline solution [7]. When the permittivity varies as a function of frequencies, the conductivity also varies as a function of frequencies as dictated by the causality requirement of the Kramers-Kronig relations [8].

Therefore, to have a realistic model of the lossy earth, it is prudent that we include the effect of dispersion in the media. For the model, we will assume either a Debye relaxation model or the Lorentzian relaxation model [9-11]. The Debye relaxation model is a special case of the Lorentzian model. Therefore, we need only to address the Lorentzian model, albeit developing a code tailored especially for the Debye model will be more efficient than a general purpose code for a general relaxation model. The model is causal so that the Kramers-Krong relationship is automatically satisfied. Because of this, the permittivity value will be complex having both a frequency dependent real and imaginary parts. The imaginary part can be thought of as frequency-dependent loss or conductivity.

We will use the recursive convolution approach [9-11] for modeling a dispersive medium and using the split Maxwell's equations with PML as the absorbing boundary condition [12-14] to simulate an infinite conductive region.

As will be noted, the modeling of the dispersive, conductive media comes not without a cost. More storage and computation is needed in order to model the conductive dispersive media appropriately.

2. PML-FDTD Formulation

The PML can be related to a complex coordinates stretching in the frequency domain [14]. This is necessitated by a splitting of Maxwell's equations in the time domain. This splitting generally doubles the memory requirements of an FDTD simulation. When conductive loss is added, this further increases the memory requirements because of an added conductivity term in the PML equation. We will see that the inclusion of dispersion further increases the memory requirement.

The stretched coordinates Maxwell's equations are

$$\nabla_s \times \mathbf{E} = i\omega\mathbf{B}, \tag{1}$$

$$\nabla_s \times \mathbf{H} = -i\omega\mathbf{D} + \sigma\mathbf{E}, \tag{2}$$

for a conductive medium in the frequency domain with $e^{-i\omega t}$ dependent. In the above

$$\nabla_s = \hat{x}\frac{1}{s_x}\partial_x + \hat{y}\frac{1}{s_y}\partial_y + \hat{z}\frac{1}{s_z}\partial_z, \tag{3}$$

335

where s_x, s_y, and s_z are frequency dependent complex stretching variables. To facilitate the solution in the time domain, (1) and (2) are usually split as follows:

$$i\omega \mathbf{B}_{sx} = \frac{1}{s_x} \partial_x \hat{x} \times \mathbf{E}, \tag{4}$$

$$-i\omega \mathbf{D}_{sx} + \sigma \mathbf{E}_{sx} = \frac{1}{s_x} \partial_x \hat{x} \times \mathbf{H}, \tag{5}$$

where the same is repeated for y and z replacing x.

By letting $s_x = a_x + i\frac{\Omega_x}{\omega}$, where a_x and Ω_x are frequency independent, the above becomes

$$i\omega a_x \mathbf{B}_{sx} - \Omega_x \mathbf{B}_{sx} = \partial_x \hat{x} \times \mathbf{E}, \tag{6}$$

$$-i\omega a_x \mathbf{D}_{sx} + \Omega_x \mathbf{D}_{sx} + a_x \sigma \mathbf{E}_{sx} + i\frac{\Omega_x}{\omega} \sigma \mathbf{E}_{sx} = \partial_x \hat{x} \times \mathbf{H}_{sx}. \tag{7}$$

Transforming the above back into the time domain, one obtains

$$-a_x \partial_t \mathbf{B}_{sx} - \Omega_x \mathbf{B}_{sx} = \partial_x \hat{x} \times \mathbf{E}, \tag{8}$$

$$a_x \partial_t \mathbf{D}_{sx} + \Omega_x \mathbf{D}_{sx} + a_x \sigma \mathbf{E}_{sx} + \Omega_x \sigma \int_0^t \mathbf{E}_{sx}(\tau) \, d\tau = \partial_x \hat{x} \times \mathbf{H}. \tag{9}$$

In the above, for a dispersive medium, we let $\mathbf{B}_{sx} = \mu \mathbf{H}_{sx}$ while

$$\mathbf{D}_{sx}(t) = \epsilon(t) * \mathbf{E}_{sx}(t). \tag{10}$$

3. Recursive Convolution

A Lorentzian dispersive medium is characterized by [11]

$$\chi(t) = \sum_{p=1}^{P} \gamma_p e^{-\alpha_p t} \sin(\beta_p t) u(t), \tag{11}$$

where

$$\beta_p = \sqrt{\omega_p^2 - \alpha_p^2}, \tag{12}$$

$$\gamma_p = \frac{\omega_p^2 G_p (\epsilon_s - \epsilon_\infty)}{\sqrt{\omega_p^2 - \alpha_p^2}}, \tag{13}$$

and

$$\sum_{p=1}^{P} G_p = 1,$$

$$\epsilon(t) = \epsilon_0 \left[\epsilon_\infty + \chi(t) \right]. \tag{14}$$

We can define a complex susceptibility

$$\hat{\chi}(t) = \sum_{p=1}^{P} i\gamma_p e^{(-\alpha_p - i\beta_p)t} u(t), \tag{15}$$

336

so that $\chi(t) = \Re e[\hat{\chi}(t)]$. Note that Debye relaxation is the special case where $\beta_p = 0$, and $i\gamma_p$ is real or when $\gamma_p > \omega_p$. The electric flux is related to the electric field via

$$\mathbf{D}(t) = \epsilon_0 \epsilon_\infty \mathbf{E}(t) + \epsilon_0 \chi(t) * \mathbf{E}(t). \tag{16}$$

Using (15) in (16), we have

$$\mathbf{D}(t) = \epsilon_0 \epsilon_\infty \mathbf{E}(t) + \epsilon_0 \sum_{p=1}^{P} \Re e \left[\hat{\chi}(t) * \mathbf{E}(t) \right]. \tag{17}$$

When $t = l\Delta_t$, the above becomes

$$\mathbf{D}^l = \epsilon_0 \epsilon_\infty \mathbf{E}^l + \epsilon_0 \sum_{p=1}^{P} \Re e \left[\hat{\chi}_p^0 \mathbf{Q}_p^l \right], \tag{18}$$

where

$$\mathbf{Q}_p^l = \sum_{m=0}^{l-1} \mathbf{E}^{l-m} e^{(-\alpha_p - i\beta_p) m \Delta_t}, \tag{19}$$

$$\mathbf{Q}_p^l = \begin{cases} 0, & l = 0 \\ \mathbf{E}^l + \mathbf{Q}_p^{l-1} e^{-i\bar{\omega}_p \Delta_t}, & l > 0 \end{cases}, \tag{20}$$

and $\bar{\omega}_p = \beta_p - i\alpha_p$.

The above equations allow the computation of $\mathbf{D}^l$ given $\mathbf{E}^l$ as the input. However, one would like to compute $\mathbf{E}^l$ given $\mathbf{D}^l$ as the input in an FDTD scheme as we shall see later. To this end, we substitute (20) into (18) to obtain

$$\mathbf{D}^l = \epsilon_0 \left(\epsilon_\infty + \sum_{p=1}^{P} \Re e \left[\hat{\chi}_p^0 \right] \right) \mathbf{E}^l + \epsilon_0 \sum_{p=1}^{P} \Re e \left[\hat{\chi}_p^0 \mathbf{Q}_p^{l-1} e^{-i\bar{\omega}_p \Delta_t} \right], \tag{21}$$

or that

$$\mathbf{D}^l = \epsilon_0 \left(\alpha \mathbf{E}^l + \mathbf{P}^{l-1} \right), \tag{22a}$$

where

$$\alpha = \epsilon_\infty + \sum_{p=1}^{P} \Re e [\hat{\chi}_p^0], \tag{22b}$$

$$\mathbf{P}^{l-1} = \sum_{p=1}^{P} \Re e \left(\hat{\chi}_p^0 \mathbf{Q}_p^{l-1} e^{-i\bar{\omega}_p \Delta_t} \right), \tag{22c}$$

depends only on $\mathbf{Q}_p^{l-1}$.

4. The Time-Stepping Scheme

We need to devise a time-stepping scheme for Equations (8) and (9). The space discretization is done according to the Yee scheme [15] so that we will not discuss it here. The time discretization for them are as follows:

$$\frac{-a_x \left(\mathbf{B}_{sx}^{l+\frac{1}{2}} - \mathbf{B}_{sx}^{l-\frac{1}{2}} \right)}{\Delta_t} - \Omega_x \mathbf{B}_{sx}^{l+\frac{1}{2}} = \partial_x \hat{x} \times \mathbf{E}^l, \tag{23}$$

337

$$\frac{a_x\left(\mathbf{D}_{sx}^{l+1} - \mathbf{D}_{sx}^l\right)}{\Delta_t} + \Omega_x\mathbf{D}_{sx}^{l+1} + a_x\sigma\mathbf{E}_{sx}^{l+1} + \sigma\Omega_x\mathbf{F}_{sx}^l = \partial_x\hat{x} \times \mathbf{H}^{l+\frac{1}{2}}, \tag{24}$$

where $\mathbf{F}(t) = \int_0^t \mathbf{E}(\tau)\,d\tau$. Equation (23) can be easily rearranged for time stepping

$$\mathbf{B}_{sx}^{l+\frac{1}{2}} = -(a_x + \Omega_x\Delta_t)^{-1}\left[\Delta_t\left(\partial_x\hat{x} \times \mathbf{E}^l\right) - a_x\mathbf{B}_{sx}^{l-\frac{1}{2}}\right], \tag{25}$$

$$(a_x + \Omega_x\Delta_t)\mathbf{D}_{sx}^{l+1} + a_x\sigma\Delta_t\mathbf{E}_{sx}^{l+1} = \Delta_t\left(\partial_x\hat{x} \times \mathbf{H}^{l-\frac{1}{2}}\right) + a_x\mathbf{D}_{sx}^l - \sigma\Omega_x\Delta_t\mathbf{F}_{sx}^l. \tag{26}$$

However, the left-hand side of (26) depends on both $\mathbf{D}_{sx}^{l+1}$ and $\mathbf{E}_{sx}^{l+1}$ making it unsuitable for time stepping. To remove this problem, we substitute (22a) into the left-hand side of (26) so that we have

$$\begin{aligned}[(a_x + \Omega_x\Delta_t)\,\alpha\epsilon_0 + a_x\sigma\Delta_t]\,\mathbf{E}_{sx}^{l+1} =&\, \Delta_t\left(\partial_x\hat{x} \times \mathbf{H}^{l+\frac{1}{2}}\right) + a_x\mathbf{D}_{sx}^l \\ &- \sigma\Omega_x\Delta_t\mathbf{F}_{sx}^l - (a_x + \Omega_x\Delta_t)\epsilon_0 P_{sx}^l.\end{aligned} \tag{27}$$

The above equation is now suitable for time stepping and updating $\mathbf{E}_{sx}^{l+1}$. After $\mathbf{E}_{sx}^{l+1}$ is updated, it is used in the right-hand side of (26) to update $\mathbf{B}_{sx}^{l+\frac{1}{2}}$ and hence $\mathbf{H}_{sx}^{l+\frac{1}{2}}$. On the right-hand side of (27), the pertinent quantities are updated as follows:

$$\mathbf{D}_{sx}^l = \epsilon_0\left(\alpha\mathbf{E}_{sx}^l + \mathbf{P}_{sx}^{l-1}\right), \tag{28a}$$

$$\mathbf{F}_{sx}^l = \mathbf{F}_{sx}^{l-1} + \mathbf{E}_{sx}^l\Delta_t, \tag{28b}$$

$$\mathbf{P}_{sx}^l = \sum_{p=1}^P \Re e\left[\hat{\chi}_p^0\mathbf{Q}_{p,sx}^{l-1}e^{-i\tilde{\omega}_p\Delta_t}\right], \tag{28c}$$

$$\mathbf{Q}_{p,sx}^l = \mathbf{E}_{sx}^l + \mathbf{Q}_{p,sx}^{l-1}e^{-i\tilde{\omega}_p\Delta t}. \tag{28d}$$

The above schemes are repeated for x replaced with y and z. Hence, (25) and (27) constitute the updating schemes for the electromagnetic fields. Storage are required for $\mathbf{H}_{s\xi}$, $\mathbf{E}_{s\xi}$, $\mathbf{F}_{s\xi}$. $\mathbf{Q}_{p,s\xi}$, $p = 1, \cdots, P$, $\xi = x, y, z$ and since each $\mathbf{A}_{s\xi}$ has two vector components, we need to store $(18 + 6P)N$ values where N is the number of simulation nodes, and P is the number of species in the relation model. The added storage cost of simulating a PML dispersive medium is $6PN$ while the added cost of a PML conductive medium is to store $\mathbf{F}_{s\xi}$ which is $6N$. A non-dispersive, non-conductive PML medium will require $12N$ storage as opposed to the $6N$ needed in the plain Yee scheme.

5. Numerical Results

An FDTD code has been written using the above formulation. A PML medium is assumed everywhere so that the code can be easily parallelized allowing the parallel computer to work in a SIMD (single instruction multiple data) mode. The code is used to simulate the response of a vertical electric dipole on top of a half space that is dispersive and conductive.

The half space is assumed to have $\epsilon_s = 50.$, $\epsilon_\infty = 5.$, and a $\sigma = 0.3\,\mathrm{mho/m}$. A two species Lorentz medium is assumed where $G_1 = 0.4$ and $G_2 = 1 - G_1$, $f_1 = 2. \times 10^8$, $f_2 = 5. \times 10^8$ from which we obtain $\omega_1 = 2\pi f_1$ $\omega_2 = 2\pi f_2$. We let $\alpha_1 = a_1\omega_1$ $\alpha_2 = a_2\omega_2$, where $a_i < 1$ for Lorentz media and $a_i > 1$ for Debye media. The PML is set up with 7 parabolic-profile layers. The center frequency of the Blackman-Harris pulse is 0.5 GHz. The Courant factor is 0.8. The half space occupies 60 % of the vertical height of the cubic simulation region. The simulation is done with $50 \times 50 \times 50$ grid with a space discretization size $\Delta_s = 8.47\,\mathrm{mm}$ and a time step $\Delta_t = 13\,\mathrm{ps}$. Assuming that the origin is at a corner of the cube, then the source

is located at $\mathbf{r}_s = (0.5, 0.7, 0.5)L$, while the receive is located at $\mathbf{r}_r = (0.3, 0.5, 0.5)L$ where L is the length of the cube, which in this case is $50\Delta_s$. The receiver is deliberately buried in the half-space so that it is more sensitive to the wave propagating through the half-space.

Figure 1a and Figure 1b show the dispersive behavior of the permittivity for two Lorentz media. In Figure 1a, the $a_1 = a_2 = 0.8$ so that the Lorentz poles are quite far from the real ω axis. In this case, the two-species dispersion is not distinct. In Figure 1b, $a_1 = a_2 = 0.5$ so that the Lorentz poles are nearer to the real ω axis. One can discern distinctly two resonance peaks for this Lorentz medium. For soil, the dispersive behaviour resembles more like that of the Figure 1a.

Figure 2a shows the time response of the E_y component of the field at the receiver for the conductive medium without dispersion (solid line), with dispersion of Figure 1a (dash-dot line), and with dispersion of Figure 1b (dotted line). It is seen that the pulse is distorted to different extent by the dispersive media. The dispersive media also seems to slow down the pulse.

Figure 2b simulates the case of the dispersive media of Figure 1b for a larger number of time steps (1000) with no visible instability.

Figure 3 shows cases where the locations of the Lorentz poles are being moved by changing the Lorentz frequencies f_1 and f_2. The center frequency of the exciting pulse in this case is 1 GHz. The Lorentz frequencies are respectively, (i) 100× (dashed line), (ii) 10× (dotted line), (iii) the same (dash-dot line), and (iv) 0.1× (heavy solid line) those shown at the begining of this section. In this case, $a_1 = a_2 = 0.5$. It is seen that different Lorentz frequencies affect the pulse propagation differently. When the exciting pulse has a center frequency close to that of the poles (case ii), the pulse is severely distorted. When the Lorentz frequencies are too high, the pulse is little affected while lower Lorentz frequencies will still distort the pulse. However, this kind of dispersive media is hardly encountered in rocks or soil.

Figure 4 shows a snap shot of the profile of the field at 1,000 time steps. It is shown that the field is well absorbed by the PML at the edge of the simulation region with no noticeable reflection or instability.

The code has been parallelized to run on a SGI Power Challenge Array. The Array has six R8000 processors running at 90 MHz. Altogether, the Array has a total of 2 GB RAM. The machine has been rated at 126 Mf/s by the Netlib Performance database. Figure 5 shows the speed of the code versus the number of processors for 100 time steps. It takes about 85 seconds to calculate 100 time steps for the aforementioned grid size with dispersion and conductive loss. The vertical axis here is the number of processors divided by the total CPU times of all the processors involved. It is noted that for a small number of processors, an almost linear speed-up is observed. When the number of processors is larger than four, the speed-up deteriorates because of contention with other ongoing codes running on the same machine.

6. Conclusions

The PML-FDTD formulation has been developed for a dispersive Lorentz medium with conductive loss. By a proper choice of the parameters, a Lorentz medium exhibits dispersions observed in some soil and rocks. It is shown that such dispersion can distort pulse shape as the pulse propagates through such a medium. It may have ramification on the design of ground penetrating radar and impulse radar for probing soil and rock formation [16].

Also, the use of the PML absorbing boundary condition allows the easy parallelization of the code compared to the use of the Liao absorbing boundary condition [17]. The stabilized Liao absorbing boundary condition generally requires double precision computation, while single precision computation suffices for PML computation. However, the use of PML in a dispersive medium comes with the added cost of more memory requirements and computational time. It is observed to take about twice as long in terms of CPU time compared to a

nondispersive conductive medium calculation. A PML-conductive media modeling requires about 1.5 times the PML media modeling, while a PML-conductive-dispersive media modeling with two Lorentz species may take about 3 times the ordinary PML media modeling.

ACKNOWLEDGEMENTS

REFERENCES

1. J. E. Hipp, 1974, Soil electromagnetic parameters as functions of frequency, soil density, and soil moisture:*Proc. IEEE*, **62**, 98-103.
2. W. D. Hurt, 1985, Multiterm Debye dispersion relations for permittivity of muscle: *IEEE Trans. Biomed. Eng.*, **BME-32**, 60-64.
3. D. Sullivan, 1992a, A frequency-dependent FDTD method for biological applications: IEEE Trans. Microwave Theory Tech., **40**, 532-539.
4. D. Sullivan, 1992b, Frequency-dependent FDTD methods using z transforms: IEEE Trans. Ant. Propagat., **40**, 1223-1230.
5. O. P. Gandhi, B. Q. Gao, and J. Y. Chen, 1993, A frequency-dependent finite-difference time-domain formulation for general dispersive media: *IEEE Trans. Microwave Theory Tech.*,**41**, 658-664.
6. P. N. Sen and W. C. Chew, 1983, The frequency dependent dielectric and conductivity response of sedimentary rocks, *J. Microwave Power*, **18**, no. 1, p. 95.
7. W. C. Chew and P. N. Sen, 1982, Dielectric enhancement due to electrochemical double layer: thin double layer approximation, *J. Chem. Phys.*, **77**, no. 9, p. 4683.
8. W. C. Chew, 1990, *Waves and Fields in Inhomogeneous Media*, Van Nostrand Reinhold: New York. Reprinted by IEEE Press, 1995.
9. R. Luebbers, F. P. Hunsberger, 1992, FDTD for N-th order dispersive media: *IEEE Trans. Ant. Propagat.*, **40**, 1297-1301.
10. R. Luebbers, F. P. Hunsgerger, K. S. Katz, R. B. Standler, and M. Schneider, 1990, A frequency-dependent finite-difference time-domain formulation for dispersive materials:*IEEE Trans. Electromag. Compat.*, **32**, 222-227.
11. C. M. Rappaport and W. H. Weedon, 1994, Computational issues in ground penetrating radar, unpublished report.
12. J. P. Berenger, 1994, A perfectly matched layer for the absorption of electromagnetic waves: *J. Comp. Phys.*, **114**, 185-200.
13. D. S. Katz, E. T. Thiele, and A. Taflove, 1994, Validation and extension to three dimensions of the Berenger PML absorbing boundary condition for FD-TD meshes: *IEEE Microwave and Guided Wave Lett.*, **4**, 268-270.
14. W. C. Chew and W. H. Weedon, 1994, A 3D perfectly matched medium from modified Maxwell's equations with stretched coordinates:*Micro. Opt. Tech. Lett.*,**7**, 599-604.
15. K. S. Yee, 1966, Numerical solution of initial boundary value problems involving Maxwell's equation in isotropic media: *IEEE Trans. Antennas Propagat.*, **AP-14**, 302-307.
16. M. Moghaddam, E. J. Yannakakis, W. C. Chew, and C. Randall, C., 1991, Modeling of the subserface interface radar: J. Electromag. Waves App., **5**, 17-39.
17. Z. P. Liao, H. L. Wong, B. P. Yang, and Y. F. Yuan, 1984, A transmitting boundary for transient wave analysis:*Scientia Sinca*, **27A**, 1063-1076

(a)   **(b)**
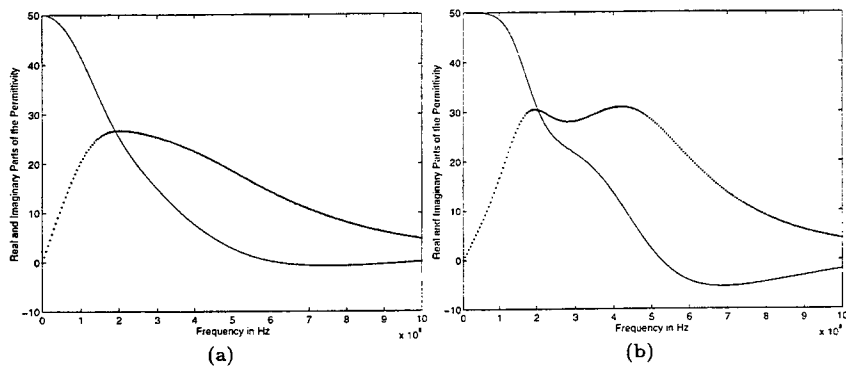
Figure 1. Permittivity dispersion for a two species Lorentz medium with (a) $a_1 = a_2 = 0.8$. See text for more details, (b) $a_1 = a_2 = 0.5$. In this case, the poles are closer to the real ω axis, and two distinct resonances are observable.

(a)   **(b)**
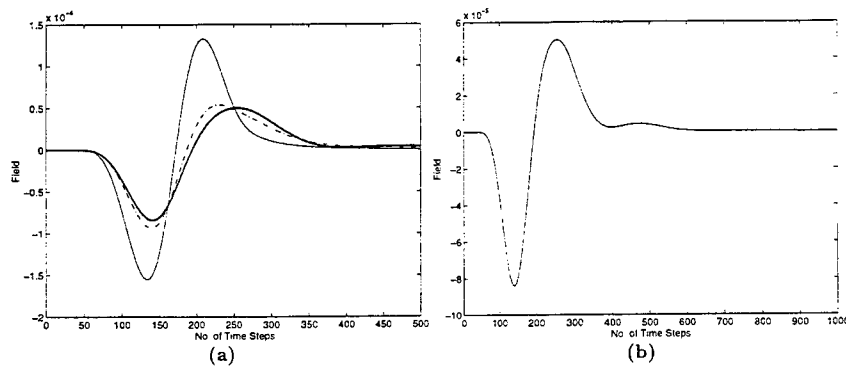
Figure 2. (a) Pulse distortion for different Lorentz medium with conductivity loss. (i) No dispersion (solid line), (ii) dispersion with the case of Figure 1a (dash-dot line), and (iii) dispersion with the case of Figure 1b (heavy dotted line). See text for more details. (b) Same as case (iii) of (a), but run for 1000 time steps. No reflection and instability are visible.

341
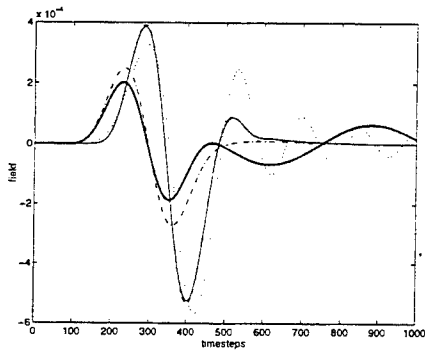
Figure 3. Different pulse distortion for different frequencies of the Lorentz poles. The center frequency of the exciting pulse is 1 GHz. The Lorentz media have the Lorentz frequencies (ω_1 and ω_2) (i) 100 times (dashed line), (ii) 10 times (dotted line), (iii) same (dashed-dot line), and (iii) 0.1 time (heavy solid line) those of Figure 1.
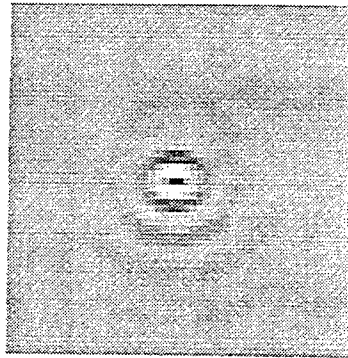
Figure 4. A snapshot of the field profile at 1,000 time steps. No reflection and instability are visible from the edge of the simulation region.
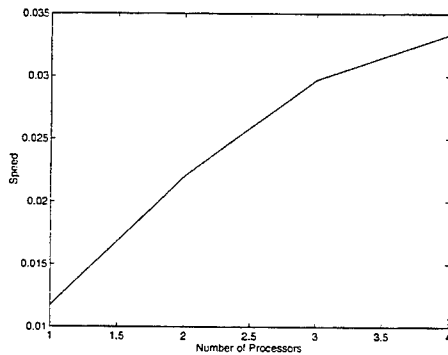
Figure 5. Speedup of the code for 100 time steps for different number of processors on a SGI Power Challenge Array. Linear speedup is observed for a small number of processors, but performance deteriotes as the number of processors increases.

Study of Absorbing Boundary Conditions in the Context of the Hybrid Ray-FDTD Moving Window Solution

Y. Pemper[†], B. Fidel[†], E. Heyman[†], R. Kastner[†], and R.W. Ziolkowski[‡]

[†]Tel-Aviv University,
Department of Electrical Engineering
- Physical Electronics
Tel-Aviv 69978, Israel

[‡]University of Arizona,
Department of Electrical and Computer Engineering
Tucson, AZ 85721

I Introduction

The hybrid ray-FDTD moving window scheme has been presented recently for the propagation of electromagnetic pulses in homogeneous and inhomogeneous media [1]. This method has been cast in the Lagrange formulation, where the continuous field equations have been transformed into the moving frame and then discretized. The moving frame equations exhibit different characteristics in terms of both numerical dispersion and absorbing boundary conditions (ABC's), compared with the stationary equations.

Theoretically, if no numerical dispersion is present, the sampling rate in the FDTD algorithm will be reduced by about five to ten times for a comparable error level, thereby relaxing the demands on computational resources by a similar factor. It has been shown that the Lagrangian formulation reduces the effects of numerical dispersion compared with the stationary frame, as long as the pulse is propagating in a direction that coincides with the moving frame.

We show a unified derivation of numerical dispersion and stability conditions. The stability condition is extracted from the numerical dispersion relations in a method less cumbersome than the transition matrix eigenvalue formalism.

Boundary conditions for the moving frame scheme are derived by diagonalizing the field equations and identifying the backward propagating and stationary eigenfunctions as the basic two independent unknowns. For a given boundary, the outgoing eigenvectors are treated with a first order Mur boundary condition, the incoming eigenvectors are specified, and the stationary eigenvectors are calculated either according to the original field equation (if the eigenvector is an original unknown of the problem), or through a stationary specification. The method is demonstrated for the moving frame in inhomogeneous media. Another possible application is the treatment of two dimensional waveguides with obstacles.

II Basic Equations

We consider the acoustic wave equations

$$\partial_t \vec{V} = -\frac{1}{\rho}\nabla P, \qquad \partial_t P = -c^2 \rho \nabla \cdot \vec{V} , \tag{1}$$

where P is the pressure, $\vec{V}$ is the velocity vector, ρ and c are density and sound velocity of the medium, respectively.

We shall consider a plane stratified medium with $c = c(z)$, $\rho = 1$ and normally propagating cylindrically symmetric solutions. Denoting $V = V_z$ and $U = V_r$, the cylindrical representation of (1) is

$$\partial_t V = -\partial_z P, \qquad \partial_t U = -\partial_r P, \qquad \partial_t P = -c^2(z)\partial_z V - c^2(z)\frac{1}{r}\partial_r(rU) \tag{2}$$

with the conditions $U = 0$, $\partial_r P = 0$, $\partial_r V = 0$ at $r = 0$.

The Lagrangian formulation involves a moving coordinate frame ζ, defined by

$$\zeta = \int_0^z \frac{c_0}{c(z')}dz' - c_0 t , \tag{3}$$

343

where c_0 is an arbitrary constant reference velocity. We choose a uniform sampling of the time steps and the optical length coordinate ζ. This renders the spatial grid z non-uniform, with Δz now proportional to $1/c(z)$, while the propagation times between any two adjacent grid points along z remain the same.

With this transformation equations (2) become:

$$\partial_t V = c_0 \partial_\zeta V - \frac{c_0}{\tilde{c}} \partial_\zeta P, \qquad \partial_t U = c_0 \partial_\zeta U - \partial_r P, \qquad \partial_t P = c_0 \frac{\partial P}{\partial \zeta} - c_0 c \partial_\zeta V - \tilde{c}^2 \frac{1}{r} \partial_r (rU), \qquad (4)$$

where $\tilde{c}(\zeta) = c[z(\zeta)]$. The central-difference discretized form of (7), organized in a "marching in time" form is thus:

$$V_{i,j}^{n+1} = V_{i,j}^{n-1} + \gamma_\zeta (V_{i+1,j}^n - V_{i-1,j}^n) - (\gamma_\zeta/\tilde{c}_i)(P_{i+1,j}^n - P_{i-1,j}^n) \qquad (5a)$$

$$U_{i,j}^{n+1} = U_{i,j}^{n-1} + \gamma_\zeta (U_{i+1,j}^n - U_{i-1,j}^n) - \gamma_r c_0^{-1}(P_{i,j+1}^n - P_{i,j-1}^n) \qquad (5b)$$

$$P_{i,j}^{n+1} = P_{i,j}^{n-1} + \gamma_\zeta (P_{i+1,j}^n - P_{i-1,j}^n) - \tilde{c}_i \gamma_\zeta (V_{i+1,j}^n - V_{i-1,j}^n) - \tilde{c}_i^2 c_0^{-1} \gamma_r \frac{1}{r_j}(r_{j+1} U_{i,j+1}^n - r_{j-1} U_{i,j-1}^n) \qquad (5c)$$

Here, the grid is defined as described above, i.e., it is uniform in t, ζ and r and sampled at the points $t_n = n\Delta t$, $\zeta_i' = i\Delta\zeta$, $r_j = j\Delta r$. We denote $\gamma_\zeta = \frac{c_0\Delta t}{\Delta\zeta}$ and $\gamma_r = \frac{c_0\Delta t}{\Delta r}$ and also $\tilde{c}_i = \tilde{c}(i\Delta\zeta)$.

Eq. (5a) applies for $j \geq 0$, while (5b) and (5c) apply for $j \geq 1$. In (5b) we have $U = 0$ for $j = 0$. The singularity of (5c) at $r = 0$ is addressed by integrating the corresponding continuous equation in (4) within the elementary volume $dv = 2\pi r\, dr\, d\zeta$ around the $r = 0$ axis and using the divergence theorem, yielding

$$\int_0^{\Delta r} r\, dr\, \partial_t P = c_0 \int_0^{\Delta r} r\, dr\, [\partial_\zeta P - c_0 \tilde{c}(\zeta) \partial_\zeta V] - \int_0^{\Delta r} \tilde{c}^2(\zeta) \frac{1}{r} \partial_r(rU) r\, dr \qquad (6)$$

and thus

$$\partial_t P|_{r=0} = c_o\, \partial_\zeta P|_{r=0} - c_0 \tilde{c}\, \partial_\zeta V|_{r=0} - \frac{2}{\Delta r} \tilde{c}^2 U \Big|_{r=\Delta r} \qquad (7)$$

or, in discretized form

$$P_{i,0}^{n+1} = P_{i,0}^{n-1} + \gamma_\zeta (P_{i+1,0}^n - P_{i-1,0}^n) - \tilde{c}_i \gamma_\zeta (V_{i+1,0}^n - V_{i-1,0}^n) - 2\tilde{c}_i^2 c_0^{-1} \gamma_r U_{i,1}^n \qquad (8)$$

This equation replaces (5c) for $j = 0$.

III Numerical Dispersion

In the analysis we may assume that the medium is locally uniform and make the following ansatz for a space-time harmonic solution of the form

$$\begin{pmatrix} V_{i,j}^n \\ U_{i,j}^n \\ P_{i,j}^n \end{pmatrix} = \begin{pmatrix} V_0 J_0(k_r r_j) \\ U_0 J_1(k_r r_j) \\ P_0 J_0(k_r r_j) \end{pmatrix} e^{-i[\omega t_n - k_\zeta \zeta_i']} \qquad (9)$$

where k_r and k_ζ are wave numbers; J_0 and J_1 are Bessel functions of the zero and first order, respectively. Substituting into (5), we obtain the matrix equation

$$\begin{pmatrix} \sin\Omega + \gamma_\zeta \sin K_\zeta & 0 & -\gamma_\zeta c_0^{-1} \sin K_\zeta \\ 0 & \sin\Omega + \gamma_\zeta \sin K_\zeta & -i\gamma_r c_0^{-1} K_r \\ -\gamma_\zeta c_0 \sin K_\zeta & i\gamma_r c_0 K_r & \sin\Omega + \gamma_\zeta \sin K_\zeta \end{pmatrix} \begin{pmatrix} V_0 \\ U_0 \\ P_0 \end{pmatrix} = 0 \qquad (10)$$

where $K_\zeta = k_\zeta \Delta\zeta$, $K_r = k_r \Delta r$, and $\Omega = \omega \Delta t$. In this derivation we have used $J_n(k_r r_{j+1}) \approx J_n(k_r r_j) + J_n'(k_r r_j) k_r \Delta r$ and also $J_0'(z) = -J_1(z)$, $J_1'(z) = J_0(z) - z^{-1} J_1(z)$. The local numerical dispersion relation is described by the zeros of the determinant

$$\sin\Omega + \gamma_\zeta \sin K_\zeta = 0, \qquad (\sin\Omega + \gamma_\zeta \sin K_\zeta)^2 - \gamma_\zeta^2 \sin^2 K_\zeta - \gamma_r^2 K_r^2 = 0 \qquad (11)$$

The first equation in (11) describes backward propagation dispersion. In particular for small Ω and K_ζ it reads $\frac{\omega}{k_\zeta} = -c_0$. This velocity in the moving frame corresponds to the radial propagation of U in the stationary frame. The second equation in (11) is rewritten as

$$\sin \Omega + \gamma_\zeta \sin K_\zeta = \pm \gamma_\zeta \sin K_\zeta \sqrt{1 + \frac{\gamma_r^2}{\gamma_\zeta^2} \frac{K_r^2}{\sin^2 K_\zeta}} \approx \pm \gamma_\zeta \sin K_\zeta \sqrt{1 + \frac{k_r}{k_\zeta}^2} , \tag{12}$$

where in the approximation we used $\sin K_\zeta \approx K_\zeta$.

We shall estimate the resulting numerical dispersion assuming an excitation by a collimated pulsed-beam with $(k_r/k_\zeta)^2 \equiv \epsilon \ll 1$. For example, a collimated pulsed-beam (see section VI below) satisfies the spectral estimates $k_r \sim \mathcal{O}((c_0 b T)^{-1/2})$, $k_\zeta \sim \mathcal{O}((c_0 T)^{-1})$, where T is the pulse length and b is the collimation distance and typically $c_0 T/b \ll 1$. Thus we have $(k_r/k_\zeta)^2 \sim \mathcal{O}(c_0 T/b) \ll 1$. Eq. (12) reduces to

$$\sin \Omega + \gamma_\zeta \sin K_\zeta \approx \pm \gamma_\zeta \sin K_\zeta (1 + \epsilon/2) . \tag{13}$$

Thus, for the forward propagating spectrum $\sin \Omega = \frac{\epsilon}{2}\gamma_\zeta \sin K_\zeta$, which for small Ω yields $\frac{\omega}{k_\zeta} \approx \frac{\epsilon}{2} c_0 \ll c_0$. For the backward propagating wave $\sin \Omega = -\gamma_\zeta (2 + \epsilon/2) \sin K_\zeta \approx -2\gamma_\zeta \sin K_\zeta$, giving, for small Ω $\frac{\omega}{k_\zeta} \approx -2c_0$.

IV   Stability Analysis

In general, the stability condition is implicitly contained in the numerical dispersion equations. This follows by substituting $g = e^{-i\Omega}$ into (11), arriving at:

$$g^{-1} - g + i2\gamma_\zeta \sin K_\zeta = 0 , \qquad (g^{-1} - g + i2\gamma_\zeta \sin K_\zeta)^2 + 4\gamma_r^2 K_r^2 + 4\gamma_\zeta^2 \sin^2 K_\zeta = 0 . \tag{14}$$

The first equation in (14) yields

$$g = i\gamma_\zeta \sin K_\zeta \pm \sqrt{1 - \gamma_\zeta^2 \sin^2 K_\zeta} \tag{15}$$

The stability condition $gg^* \leq 1$ is satisfied only if $\gamma_\zeta^2 \sin^2 K_\zeta \leq \gamma_\zeta^2 \leq 1$ (in which case $|g| = 1$). This yields the following CFL criterion: $c_0 \Delta t \leq \Delta \zeta$. The second equation in (14) gives

$$g^{-1} - g + i2\gamma_\zeta \sin K_\zeta = \pm i2\gamma_\zeta \sin K_\zeta \sqrt{1 + \frac{\gamma_r^2}{\gamma_\zeta^2} \frac{K_r^2}{\sin^2 K_\zeta}} \approx \pm i2\gamma_\zeta \sin K_\zeta \sqrt{1 + \epsilon^2} \tag{16}$$

where we used the same approximation as in (12). For collimated pulses, the correction term inside the square root is small and may be neglected. For small ϵ we obtain the following two equations:

$$g^2 - i4g\gamma_\zeta \sin K_\zeta (1 + \epsilon/4) - 1 = 0 , \qquad g^2 + ig\epsilon\gamma_\zeta \sin K_\zeta - 1 = 0 . \tag{17}$$

The solution of the first equation in (17) gives $g = i2\gamma_\zeta(1 + \epsilon/4)\sin K_\zeta \pm \sqrt{1 - 4\gamma_\zeta^2(1 + \epsilon/4)^2 \sin^2 K_\zeta}$. The stability condition $gg^* \leq 1$ yields $4\gamma_\zeta^2(1 + \epsilon/4)^2 \sin^2 K_\zeta \leq 4\gamma_\zeta^2(1 + \epsilon/4)^2 \leq 1$, and finally

$$c_0 \Delta t \leq \frac{1}{2}\Delta \zeta(1 - \epsilon/4) \approx \frac{1}{2}\Delta \zeta . \tag{18}$$

Since $\epsilon \ll 1$ for well collimated pulsed beams, the small correction term may be neglected. The stability condition above is stronger than the previous one and therefore will be used throughout. It is the analog of the CFL condition in the stationary coordinate frame, recalling that in the moving coordinate frame the greatest wave speed is $2c_0$ (for the backward propagating wave).

The second equation in (17) gives the solution $g = i(\epsilon/2)\gamma_\zeta \sin K_\zeta \pm \sqrt{1 - (\epsilon/2)^2 \gamma_\zeta^2 \sin^2 K_\zeta}$, with the stability condition $(\epsilon/2)^2 \gamma_\zeta^2 \sin^2 K_\zeta \leq (\epsilon/2)^2 \gamma_\zeta^2 \leq 1$, and thus $c_0 \Delta t \leq \frac{1}{2}\Delta \zeta \epsilon^{-1}$. Since $\epsilon \ll 1$ this condition is much weaker than the CFL condition.

V Boundary Conditions

We assume, without loss of generality, that our grid is located in the region $0 \leq \zeta \leq \zeta_{max}$, $0 \leq r \leq r_{max}$. In general, when considering first order boundary condition schemes, it is necessary to analyze the field components moving in the direction normal to the boundary at hand. Consequently, when considering the boundaries $\zeta = 0$ and $\zeta = \zeta_{max}$, we assume $\partial_r \approx 0$ in (4), obtaining:

$$\partial_t V = c_0 \partial_\zeta V - \frac{c_0}{\tilde{c}} \partial_\zeta P \tag{19a}$$

$$\partial_t U = c_0 \partial_\zeta U \tag{19b}$$

$$\partial_t P = c_0 \partial_\zeta P - c_0 \tilde{c} \partial_\zeta V. \tag{19c}$$

This system can be rewritten in matrix form as

$$\partial_t \mathbf{q} + \mathbf{A} \partial_\zeta \mathbf{q} = 0, \qquad \mathbf{A} = \begin{pmatrix} -c_0 & 0 & c_0 \tilde{c} \\ 0 & -c_0 & 0 \\ c_0/\tilde{c} & 0 & -c_0 \end{pmatrix}, \tag{20}$$

where $\mathbf{q}$ is the vector of the unknown field variables $\begin{pmatrix} P & U & V \end{pmatrix}^T$. $\mathbf{A}$ has eigenvalues $\lambda_1 = 0$, $\lambda_2 = -2c_0$, $\lambda_3 = -c_0$ and eigenvectors $\begin{pmatrix} \tilde{c} & 0 & 1 \end{pmatrix}^T$, $\begin{pmatrix} \tilde{c} & 0 & -1 \end{pmatrix}^T$, $\begin{pmatrix} 0 & 1 & 0 \end{pmatrix}^T$ respectively. Assuming $\tilde{c}(\zeta)$ changes slowly in the vicinity of the boundaries, transformation of (20) to the eigenbase yields:

$$\partial_t \mathbf{w} + \mathbf{\Lambda} \partial_\zeta \mathbf{w} = 0, \tag{21}$$

where $\mathbf{w} = \mathbf{T}^{-1} \mathbf{q} = \frac{1}{2\tilde{c}} \begin{pmatrix} P + \tilde{c}V & P - \tilde{c}V & 2\tilde{c}U \end{pmatrix}^T$, $\mathbf{\Lambda} = \mathbf{T}^{-1} \mathbf{A} \mathbf{T} = \lambda_i \delta_{ij}$ and $\mathbf{T}$ is the base transformation matrix whose columns are the eigenvectors. This gives rise to new variables

$$\overset{+}{W} = P + \tilde{c}V, \qquad \overset{-}{W} = P - \tilde{c}V \tag{22}$$

and a diagonalized system

$$\partial_t \overset{+}{W} = 0 \tag{23a}$$

$$\partial_t \overset{-}{W} = 2c_0 \partial_\zeta \overset{-}{W} \tag{23b}$$

$$\partial_t U = c_0 \partial_\zeta U. \tag{23c}$$

From (23) we readily recognize that $\overset{+}{W}$, $\overset{-}{W}$, U propagate at velocities 0, $-2c_0$, $-c_0$, respectively, in the ζ direction.

At the boundary $\zeta = 0$, $\overset{-}{W}$ and U exit the computational grid and have to be computationally absorbed. $\overset{-}{W}$ and U are absorbed using (23b) and (23c), respectively, which are the standard Engquist-Majda one-way wave equations [2]. For $\overset{+}{W}$ we use (23a). We end up with the following discretized boundary conditions:

$$\overset{+}{W}_{0,j}^{n+1} = \overset{+}{W}_{0,j}^{n-1} \tag{24a}$$

$$\overset{-}{W}_{0,j}^{n+1} = \overset{-}{W}_{0,j}^{n} + 2\gamma_\zeta (\overset{-}{W}_{1,j}^{n} - \overset{-}{W}_{0,j}^{n}) \tag{24b}$$

$$U_{0,j}^{n+1} = U_{0,j}^{n} + \gamma_\zeta (U_{1,j}^{n} - U_{0,j}^{n}). \tag{24c}$$

Eq. (24b) and (24c) were derived from (23b) and (23c), respectively, using forward differencing in ζ (since we are on the back boundary) and also forward differencing in time (because of stability considerations — see discussion below).

To test stability, we note that (24) does not involve r dependence and thus we may substitute a space time harmonic ansatz:

$$\psi = \psi_0 e^{-i(\Omega n - K_\zeta i)}. \tag{25}$$

346

Substituting ψ into (24) at $\zeta = 0$, for example, we get an expression of the form:

$$B(\Omega, K_\zeta; \gamma_\zeta) = 0. \tag{26}$$

Stability exists if'f $\forall K_\zeta \in \mathcal{R}$, $\left| e^{-i\Omega} \right| \leq 1$. We shall demonstrate the stability analysis by using temporal central differencing instead of forward differencing in (23b), yielding:

$$\bar{W}_{0,j}^{n+1} = \bar{W}_{0,j}^{n-1} + 4\gamma_\zeta(\bar{W}_{1,j}^n - \bar{W}_{0,j}^n). \tag{27}$$

Substituting $\bar{W}_{i,j}^n = \psi$ as in (25), Eq. (27) transforms to $e^{-i\Omega} = e^{i\Omega} + 4\gamma_\zeta(e^{iK_\zeta} - 1)$ or $g^2 - 4\gamma_\zeta(e^{iK_\zeta} - 1)g - 1 = 0$, where $g = e^{-i\Omega}$. Choosing $K_\zeta = \pi$ we obtain $g^2 - 8\gamma_\zeta g - 1 = 0$, which is a quadratic equation with real roots $g_1 \neq g_2$. Furthermore, $|g_1||g_2| = 1$, meaning one of the roots must satisfy $|g| > 1$. Thus, (27) is unstable.

Via a similar procedure it can be shown that (24b) and (24c), which utilize forward differencing in time, are stable.

Finally, rewriting (24) explicitly in terms of the field constituents we have:

$$P_{0,j}^{n+1} = \frac{1}{2}(\overset{+}{W}_{0,j}^{n+1} + \bar{W}_{0,j}^{n+1}) \tag{28a}$$
$$= \frac{1}{2}[P_{0,j}^{n-1} + \tilde{c}_0 V_{0,j}^{n-1} + P_{0,j}^n - \tilde{c}_0 V_{0,j}^n + 2\gamma_\zeta(P_{1,j}^n - \tilde{c}_1 V_{1,j}^n - P_{0,j}^n + \tilde{c}_0 V_{0,j}^n)]$$

$$V_{0,j}^{n+1} = \frac{1}{2\tilde{c}_0}(\overset{+}{W}_{0,j}^{n+1} - \bar{W}_{0,j}^{n+1}) \tag{28b}$$
$$= \frac{1}{2\tilde{c}_0}[P_{0,j}^{n-1} + \tilde{c}_0 V_{0,j}^{n-1} - P_{0,j}^n + \tilde{c}_0 V_{0,j}^n - 2\gamma_\zeta(P_{1,j}^n - \tilde{c}_1 V_{1,j}^n - P_{0,j}^n + \tilde{c}_0 V_{0,j}^n)].$$

At the boundary $\zeta = \zeta_{\max}$, $\bar{W}$ and U enter the grid from the outside and should be specified according to the external excitation. Here we set $\bar{W}|_{\zeta=\zeta_{\max}} = U|_{\zeta=\zeta_{\max}} = 0$. For $\overset{+}{W}$ we use (23a), as before. Thus we have

$$\overset{+}{W}_{I,j}^{n+1} = \overset{+}{W}_{I,j}^{n-1} \tag{29a}$$

$$\bar{W}_{I,j}^{n+1} = 0 \tag{29b}$$

$$U_{I,j}^{n+1} = 0, \tag{29c}$$

where $I\Delta\zeta = \zeta_{\max}$ and finally, in the field constituents

$$P_{I,j}^{n+1} = \frac{1}{2}\overset{+}{W}_{I,j}^{n+1} = \frac{1}{2}(P_{I,j}^{n-1} + \tilde{c}_I V_{I,j}^{n-1}) \tag{30a}$$

$$V_{I,j}^{n+1} = \frac{1}{2\tilde{c}_I}\overset{+}{W}_{I,j}^{n+1} = \frac{1}{2\tilde{c}_I}(P_{I,j}^{n-1} + \tilde{c}_I V_{I,j}^{n-1}). \tag{30b}$$

At the boundary $r = r_{\max}$ we assume $\partial_\zeta \approx 0$, yielding:

$$\partial_t V = 0 \tag{31a}$$
$$\partial_t U = -\partial_r P \tag{31b}$$

$$\partial_t P = -\tilde{c}^2 \frac{1}{r}\partial_r(rU) \tag{31c}$$

For high frequency signals with $kr_{\max} \gg 1$, we may replace $\frac{1}{r}\partial_r(rU) \approx \partial_r U$. Following the procedure described above we get:

$$\partial_t \overset{+}{F} = -\tilde{c}\partial_r \overset{+}{F} \tag{32a}$$

$$\partial_t \bar{F} = \tilde{c}\partial_r \bar{F} \tag{32b}$$
$$\partial_t V = 0, \tag{32c}$$

where $\overset{+}{F} = P + \tilde{c}U$, $\bar{F} = P - \tilde{c}U$. Using similar arguments as above we obtain:

$$\overset{+}{F}{}_{i,J}^{n+1} = \overset{+}{F}{}_{i,J}^{n} - \tilde{c}_i c_0^{-1} \gamma_r(\overset{+}{F}{}_{i,J}^{n} - \overset{+}{F}{}_{i,J-1}^{n}) \tag{33a}$$

$$\bar{F}_{i,J}^{n+1} = 0 \tag{33b}$$

$$V_{i,J}^{n+1} = V_{i,J}^{n-1} + \gamma_\zeta(V_{i+1,J}^{n} - V_{i-1,J}^{n}) - (\gamma_\zeta/\tilde{c}_i)(P_{i+1,J}^{n} - P_{i-1,J}^{n}), \tag{33c}$$

where $J\Delta r = r_{\max}$, and finally, the physical field constituents are

$$P_{i,J}^{n+1} = \frac{1}{2}\overset{+}{F}{}_{i,J}^{n+1}$$
$$= \frac{1}{2}[P_{i,J}^{n} + \tilde{c}_i U_{i,J}^{n} - \tilde{c}_i c_0^{-1}\gamma_r(P_{i,J}^{n} + \tilde{c}_i U_{i,J}^{n} - P_{i,J-1}^{n} + \tilde{c}_i U_{i,J-1}^{n})] \tag{34a}$$

$$U_{i,J}^{n+1} = \frac{1}{2\tilde{c}_i}\overset{+}{F}{}_{i,J}^{n+1}$$
$$= \frac{1}{2\tilde{c}_i}[P_{i,J}^{n} + \tilde{c}_i U_{i,J}^{n} - \tilde{c}_i c_0^{-1}\gamma_r(P_{i,J}^{n} + \tilde{c}_i U_{i,J}^{n} - P_{i,J-1}^{n} + \tilde{c}_i U_{i,J-1}^{n})]. \tag{34b}$$

Eq. (33a) is derived using forward differencing in time and backward differencing in the r direction, and is stable provided $\frac{\Delta r}{\Delta t} \leq \frac{1}{c(z)}$. Since typically Δr is kept constant as the frame moves along the z axis, we must choose $\frac{\Delta r}{\Delta t} \leq \frac{1}{\max[c(z)]}$. Eq. (33c) is the regular field equation (5a) for V applied at (i, J).

VI Example

We used the moving window FDTD scheme on the "complex source pulsed beam" (PB) [3], that has the exact expression

$$P = 1/4\pi s \overset{+}{f}(t - iT/2 - s/ - ib/), \text{ where } \sqrt{r^2 + (z - ib)^2}, \text{ with } \operatorname{Re} s \geq 0. \tag{35}$$

The parameter $b > 0$ is recognized as the collimation (or Fresnel) distance. We chose $\overset{+}{f}(t) = \overset{+}{\delta}(t) = 1/\pi it$, $\operatorname{Im} t \leq 0$. A more localized wavepacket can be obtained with $\overset{+}{f}(t) = \overset{+}{\delta}{}^{(2)}(t) = 2/\pi it^3$, but to demonstrate the interaction with the boundaries we chose $\overset{+}{f} = \overset{+}{\delta}$, which is a PB with slower axial decay. With this choice we identify T as the 3dB pulse width, and $W = W_0\sqrt{1 + (z/b)^2}$, $W_0 = 2\sqrt{cTb}$, as the half-amplitude beamwidth, with W_0 being the beamwidth at the waist $z = 0$. In the numerical examples we use $c = 1$, $b = 1$, without loss of generality. Figures 1–3 depict results of numerical runs with $T = 2 \times 10^{-3}$, $\Delta\zeta = 2 \times 10^{-4}$, $\Delta r = 8 \times 10^{-3}$ and $\gamma_\zeta = 0.495$ at normalized times $t = 0.1, 1, 2$, i.e., when the PB is in the near Fresnel zone, at the Fresnel distance and at twice the Fresnel distance (far zone). A comparison of the axial distributions at $r = 0$ for the numerical solution versus the exact solution is shown in Figure 4. Because of (24a), there is a static error at the $\zeta = \zeta_{\min}$ boundary. This error exists only on the boundary, and has no effect on the numerical solution within the computational grid, since it cannot forward propagate into the moving frame. In figures 1–3 we showed the numerical solution without the boundary $\zeta = \zeta_{\min}$. To demonstrate this phenomenon, we show the numerical solution of the PB at $t = 2$ with the boundary $\zeta = \zeta_{\min}$ in figure 5.

References

1. B. Fidel, E. Heyman, R. Kastner and R. W. Ziolkowski, "Hybrid ray-FDTD moving frame approach to pulse propagation," *Proc. of the 1994 International IEEE/AP-S Symposium*, Seattle, WA, pp. 1414–1417.

2. B. Engquist and A. Majda, "Absorbing boundary conditions for the numerical simulation of waves," *Mathematics of Computation*, vol. 31, pp. 629–651, 1977.

3. E. Heyman, "Pulsed beam propagation in inhomogeneous medium," *IEEE Trans. Antennas Propagat.*, vol. 42, pp. 311–319, 1994.

Figure 1: P field distribution of the PB at $t = 0.1$.
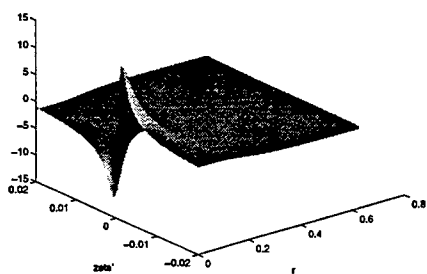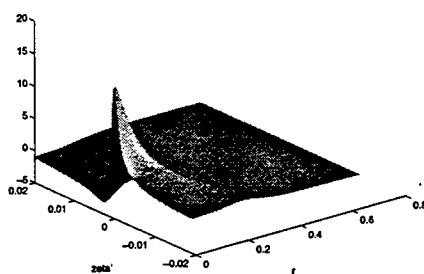

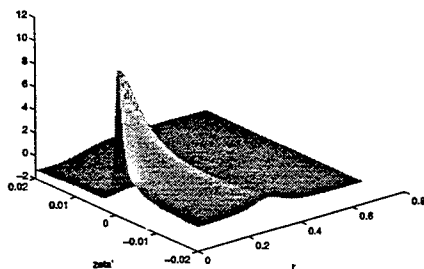Figure 2: P field distribution of the PB at $t = 1$.

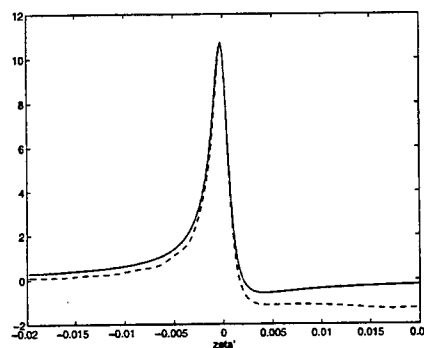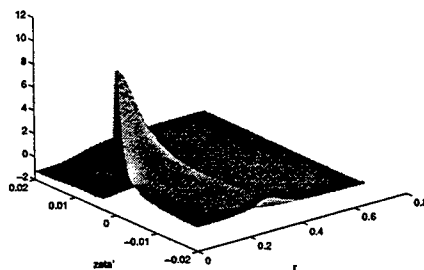

Figure 3: P field distribution of the PB at $t = 2$.

Figure 4: Numerical solution (dashed) versus exact solution (solid) of the P field distribution of the PB at $t = 2$, $r = 0$.

Figure 5: Same as figure 3 with the boundary $\zeta = \zeta_{\min}$ included.

INTERACTIVE TECHNICAL SESSION

9A THROUGH 9G

A Generalized Finite-Volume Time-Domain Algorithm for Microwave Heating Problems on Arbitrary Irregular Grids

H. Zhao, I. Turner
School of Mathematics, Queensland University of Technology,
Brisbane, Qld 4001, Australia
Tel : +61 7 3864 4309   Fax : +61 7 3864 5252   Email : h.zhao@fsc.qut.edu.au

Abstract

A finite-volume time-domain (FVTD) formulation to solve microwave heating problems on general two- and three-dimensional arbitrarily shaped irregular grids is developed. The method is directly applied to the integral form of the Faraday and Ampere laws in the time-domain and allows coupling with a heat transfer equation. The new scheme uses discrete unknown variables based on the cell edge and remains consistent with the staggered-grid methodology of the FDTD method. It is shown that the FVTD method is equivalent with the FDTD technique for regular meshes, however, a significant advantage of the new method is that it is suitable for arbitrarily shaped geometries. Furthermore, the FVTD and FDTD methods can be combined within a single strategy to provide an efficient numerical solution. The method is tested and verified on a simple waveguide example for which an analytic solution is available. The technique is applied subsequently to a horn applicator device and to a more complicated cavity problem where the solutions for the power density distribution are compared directly with experimental results previously reported in the literature.

1. Introduction

In the mid-1960s, Yee [1] introduced a computationally efficient means of solving directly Maxwell's time-dependent curl equations using finite difference techniques. Nowadays, the Finite-Difference Time-Domain method (FDTD) has become one of the most popular and widely used computational methods in electromagnetics. In recent years, there has been an increasing interest in the numerical simulation of microwave heating problems via a direct solution of Maxwell's equations using the FDTD method [2] [4] [5] [6] [8]. The finer details of the FDTD method, together with an investigation of it's performance for solving microwave heating problems has been given in a previous paper by the authors [11]. For problems involving general non-rectangular domains, 'staircased' orthogonal approximations have been used. Unfortunately, although relatively simple to implement, this approach often gives rather poor approximations to the boundary shape unless a very fine mesh is used. However, a substantial refinement of the mesh can lead to increases in both memory and computation time. Another technique that has been used in the past to treat irregularly shaped conducting boundaries is the contour path method [9]. This scheme is implemented in essentially the same manner as the FDTD method except at the boundaries, where the Faraday and Ampere laws are integrated over the surfaces of the boundary elements.

The solution of Maxwell's equations on irregularly shaped computation domains generally is carried out using the Finite-Element or Finite-Volume numerical techniques. However, Finite-Element methods can be rather expensive when solving Maxwell's equations in the Time-Domain, since the method has to solve a large sparse matrix system at every iteration [10]. On the other hand, the Finite-Volume technique can be implemented explicitly using an appropriately chosen time marching strategy to advance the solution in time. In this case, matrix inversion is avoided, however, more stringent time step restrictions must be imposed before stability can be achieved.

Recently, the finite volume method has been used to solve Maxwell's equations in the time domain [3] [7]. In [3], the concept of a dual and a primary cells was introduced. The dual cell is constructed from the primary cell by joining its barycentres which is located at the average of the coordinates of the nodes of the primary cell. The electric field is computed by using a volume integration around the dual cell which contains the primary cell edges where the electric field components are located. The magnetic field was computed in a similar manner using the primary cell. The scheme is marched in time by the explicit leap-frog algorithm.

In [7], volume integration of the time-domain Maxwell equations was used. Discrete unknowns are thus volume integrals or cell averages of electric and magnetic field variables. Arbitrary sets of basis functions are introduced in constructing local representations of the fields and evaluating the volume and surface integrals. Electric and magnetic fields are approximated by linear combinations of these basis functions. The staggered leap-frog scheme and the Runge-Kutta methods are utilized for the time integration.

In this paper, a new Finite-Volume Time-Domain (FVTD) technique for solving microwave heating problems has been developed. Both the cavity and the load can be of arbitrary shape. The mesh can consist of structured and unstructured primary cells that can be of any shape and form. A dual cell is constructed around the primary cell by connecting the centres of the primary cells in a similar fashion to that described in [3]. The FVTD method is applied directly to the integral form of the Faraday and Ampere Laws in the Time-Domain. One of the benefits of this scheme is that FDTD and FVTD can be combined within the one code to produce optimal processing times. Although not discussed in great detail within this article, the new FVTD technique has been combined with a complete heat and mass transfer code so that drying and heating operations can be analysed.

The method is tested and verified on a simple waveguide problem for which an analytic solution is available. The technique is applied subsequently to a horn applicator device and to a more complicated cavity problem where the solution for the power density distribution is compared directly with experimental results previously reported in the literature.

2. Formulation of the Microwave Heating Mathematical Model

In a simple microwave heating system, such as that exhibited in Figure 1, an input microwave power signal is
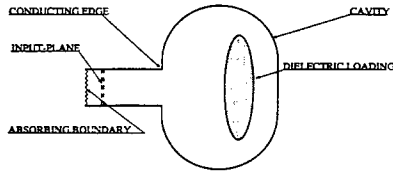
Figure 1: *Schematic of the Microwave Heating System*

propagated along a waveguide into a cavity and used subsequently to irradiate and heat a lossy material that is loaded at some specified position within the cavity. Typically, this simple system can not be resolved using classical analytic techniques and numerical methods often become the best means for analysing the field interaction within such a configuration. However, even the numerical treatment of this problem can be quite difficult.

The fundamental laws of electromagnetism are referred to as Maxwell's equations and can be cast in terms of a compact integral representation. In general, the time-dependent electric and magnetic fields that exist in any given region of space should satisfy the classical Maxwell's equations in order to be unique. The Faraday and Ampere Laws provide a system of equations that form an independent set of coupled relationships between the time-varying electric field and magnetic field quantities. These equations allow the determination of the volumetric power density distribution within the load. This microwave power source can then be coupled further with the heat transfer equation in order to determine the thermal distribution of the load. These equations are summarised as follows:

$$\int_A \frac{\partial \mathbf{B}}{\partial t} \cdot ds = -\oint_{\partial A} \mathbf{E} \cdot dl \tag{1}$$

$$\int_A \left(\frac{\partial \mathbf{D}}{\partial t} + \mathbf{J} \right) \cdot ds = \oint_{\partial A} \mathbf{H} \cdot dl \tag{2}$$

$$\int_V \rho C_p \frac{\partial T}{\partial t} dv = \oint_{\partial V} \kappa \nabla T \cdot ds + \int_V Q dv \tag{3}$$

where: $\mathbf{E}$ and $\mathbf{H}$ are the electromagnetic fields intensity, $\mathbf{D}$ and $\mathbf{B}$ are the electromagnetic flux density. T, ρ, C_p, κ and Q are the temperature, density, heat capacity, heat conductivity and power density. V, A, s and l are the volume, surface area, surface area vector and surface boundary edge length vector. The constitutive relations are:

$$\mathbf{D} = \epsilon \mathbf{E} \tag{4}$$

$$\mathbf{B} = \mu \mathbf{E} \tag{5}$$

$$\mathbf{J} = \sigma \mathbf{E} \tag{6}$$

$$Q = \frac{1}{\tau} \int_{n\tau}^{(n+1)\tau} \sigma \mathbf{E}^2 dt \tag{7}$$

where ε is the permittivity, μ is the permeability and σ is the electric conductivity of the medium. τ is microwave time of the period.

3. Finite-Volume Time-Domain Formulation

The basic philosophy of the new FVTD method remains consistent with the Leap-Frog Two-Step Methods in time, and solves the integral form of the system equations (1)-(3) on the discretized space. The scheme seeks to achieve second order accuracy in both space and time. Assuming that equations (1)-(3) have to be solved on an irregular three-dimensional domain R having an outer boundary ∂R, the domain R is first discretized into a network of tetrahedral cells which will be called primary cells. Next, dual tetradecahedron cells are created around the primary cells by simply connecting the primary cell centers. The $\mathbf{E}$ field is located on the primary cell edges at the points where the edge intersects with the dual cell face. The $\mathbf{H}$ field is located on the dual cell edge at the point of intersection with the primary cell face, see Figure 2. The system equations (1) and (2) can be written in
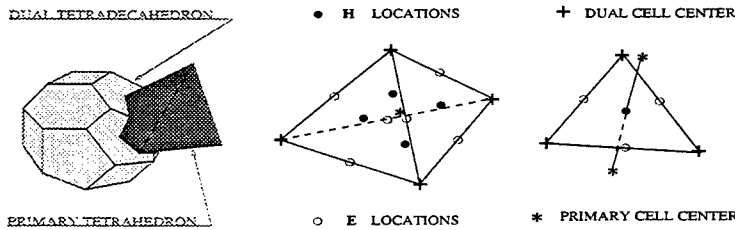
Figure 2: *Discrete electric and magnetic field components locations relative to the primary and dual cells.*

discretized form as follows:

$$\mathbf{H}_i^{t+1/2} \cdot \hat{d}_{ni} = \mathbf{H}_i^{t-1/2} \cdot \hat{d}_{ni} - C_{hi}\frac{1}{A_i}\sum_{k=1}^{n}(\mathbf{E}_k^t \cdot \hat{d}_{ek})l_k \tag{8}$$

$$\mathbf{E}_j^{t+1} \cdot \tilde{d}_{ni} = C_{e1j}\mathbf{E}_j^{t-1} \cdot \tilde{d}_{ni} - C_{e2j}\frac{1}{A_j'}\sum_{k=1}^{m}(\mathbf{H}_k^{t+1/2} \cdot \tilde{d}_{ek})l_k' \tag{9}$$

where, A_i, $\hat{d}_{ni}$, $\hat{d}_{ek}$ and l_k are the face area, unit normal direction vector of the face, unit direction vector of the edge and edge length of the primary cell respectively; A_j', $\tilde{d}_{nj}$, $\tilde{d}_{ek}$, l_k' are the face area, unit normal vector of the face, unit vector direction of the edge and edge length of the dual cell respectively; $C_{hi} = \delta t/\mu_i$, $C_{e1j} = (2\varepsilon_j - \sigma_j\delta t)/(2\varepsilon_j + \sigma_j\delta t)$ and $C_{e2j} = (2\delta t)/(2\varepsilon_j + \sigma_j\delta t)$; and n and m are the number of the edges for the primary face and the dual face respectively.

Equations (8) and (9) are used to determine the components of the magnetic ($\mathbf{H} \cdot \hat{d}_n$) and electric ($\mathbf{E} \cdot \tilde{d}_n$) fields in the direction of the normal to the primary and dual cell faces respectively. In order to resolve these vectors in the directions of the edge face vectors, a 3×3 system of equations is generated, solved and subsequently projected along the edge direction. If more than three edges connect to either a dual or primary cell center, then a least-squares algorithm can be used to obtain the best approximation for $\mathbf{E}$ and $\mathbf{H}$ (refer figure 2).

The data structure used to store the information necessary for the computations is edge based. It is considered more efficient to store all of the information following the order of the primary cell edge and dual cell edge separately. The unknown normal components of the electric and magnetic fields are stored following the order of their primary cell edges and dual cell edges respectively. Therefore, all the information will follow the indices of the edge, and is stored in the following ways:

$$\begin{array}{cccccc} \{ & H_{ni} & A_i & \hat{d}_{ni} & \tilde{d}_{ei} & l_i' \cdot & \} \\ \{ & E_{nj} & A_j' & \tilde{d}_{nj} & \tilde{d}_{ej} & l_j & \} \end{array}$$

354

In addition, the primary cell volume V_i has to stored only in the dielectric material domain for computing the temperature distribution. According to the above data structure, the grid can be structured or unstructured and ordered by the edges.

Electromagnetic waves carry with them electromagnetic power. When an external electric field is applied to a dielectric material, an isolated motion of the conduction electrons and dipolar reorientation will result, dissipating part of the electrons kinetic energy as heat. In the FVTD scheme, after the steady state solutions for $\mathbf{E}$ are determined, linear interpolation is used to obtain the power at the center of the primary cell. Then, the power density distribution can be calculated by equation (7), and the temperature distribution can be calculated by equation (3). When the temperature distribution changes the dielectric properties of the material significantly, it is necessary to re-solve equations (8) and (9) so that the power density distribution can be updated. This procedure is repeated until the microwave heating is finished.

It is easy to see that this new FVTD method is unlike other unstructured formulations used in computational fluid dynamics which usually compute the field quantities by volume integration, together with some form of interpolation scheme. In particular, the new FVTD method uses surface integration to compute the field quantities in a very efficient manner. Moreover, the FVTD method reduces to the FDTD method when it is applied to an orthogonal regular grid. A significant advantage of the method proposed here is that the FVTD and FDTD methods can be combined within a single strategy to provide a computationally effective numerical solution strategy. The details of the dielectric interface boundary condition and field singularity behaviour are presented in [11]. The stability and error analysis of the new scheme will be reported in a future paper.

4 Comparison of the Numerical Simulation Results

Based on the above formulation, three different case studies using three different applicator configurations are used to investigate the accuracy of the proposed numerical model. The FVTD method has been implemented in Fortran-77 and all the computations were performed on a SGI Power Challenge L R10000. In all cases a standard TE_{10} mode input waveguide operating at the microwave frequency 2.45 GHz is used.

Case Study 1

In this case study, a two-dimensional code that combines the FDTD and the FVTD methodologies together is tested by using a combination of orthogonal and triangular cells within a closed waveguide system, refer to Figure 3(b). The system was discretised using a mesh of dimension 20×100, with 40 mesh points along the waveguide being used for the orthogonal mesh component and 60 mesh points along the waveguide being used for the triangular component. The triangular mesh was constructed by subdividing each rectangular cell into two triangles. The electric field distributions in the TE_{10} mode waveguide has been compared with the analytical solution in Figure 3. The numerical results indicate that the new FVTD scheme matches the analytical solution almost exactly and shows that the FDTD and FVTD methods work well together.

Case Study 2

In this case study, a three-dimensional version of the FVTD model is used to compute the electromagnetic field density distribution inside a waveguide that is connected with a horn region. Such devices are quite often used in microwave heating systems. The details of the configuration are given in Figure 4 (a), and the system was discretised using a body fitted hexahedral mesh of dimensions $80 \times 40 \times 323$. The numerical solutions of the electromagnetic field density distribution are presented in Figure 4 (b)-(e). These numerical results show that the FVTD method produces a realistic field behaviour that conforms with the shape of the horn device. In particular, Figure 4(b) exhibits a perfectly symmetrical field pattern and the existence of a double mode close to the short circuit. Furthermore, at the junction between the TE10 waveguide and the horn, it is possible to observe a distinct change in the TE10 mode field pattern.

Case Study 3

In this case study, an experimentally determined thermal image for a arbitrarily shaped high lossy food material (batter) is used to validate the simulation results obtained by the FVTD method. The reader is referred to [10] for obtaining all of the finer details concerning the experiments. The cavity had the dimensions of $0.391 \times 0.292 \times 0.300$ (m) with respect to the X, Y and Z directions, see Figure 5 (a), and was fed by a TE_{10} mode waveguide, operating with frequence 2.45 GHz, and located at the center of the top of the cavity. The dimensions of the batter were given as $Diameter = 0.135$ (m) and $Depth = 0.030$ (m). The disk shape material of batter was placed on the long centerline of the cavity, 0.020 (m) from the side and 0.050(m) from the bottom. The relative permittivity of the

(a. TE_{10} waveguide $0.086 \times 0.043 \times 0.43$ (m^3))

(b. 2D mixed orthogonal and triangular mesh)

(c. numerical solution of electric
field density distribution)

(d. (O O O) analytical solution,
and ($\triangle$ $\triangle$ $\triangle$) numerical solution)
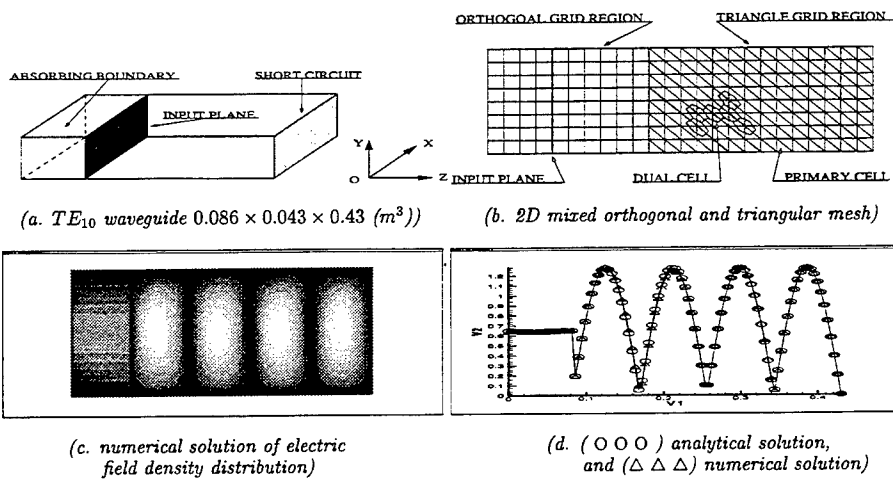
Figure 3: *Two-Dimensional Model*

(a. configuration of the system)

(b. electric field in X-Z plane)

(c. electric field in Y-Z plane)   (d. magnetic field in X-Z plane)   (e. magnetic field in Y-Z plane)
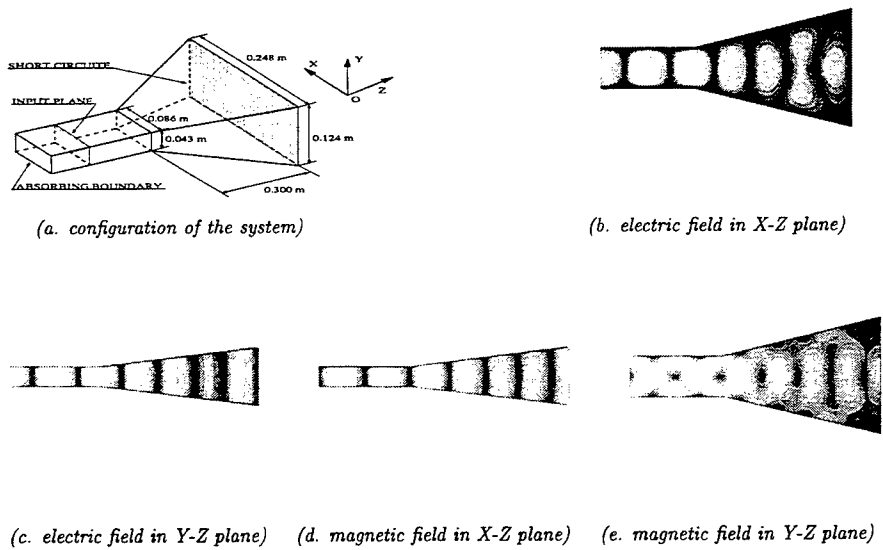
Figure 4: *Electromagnetic field density distribution.*

356
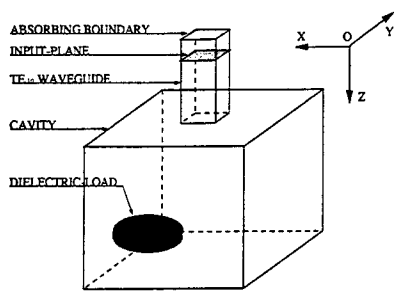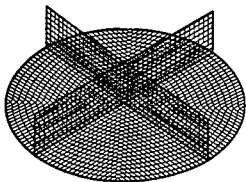
Figure 1: *Power density distributions. (a) configuration of the system, (b) thermal image on the top surface of the material, (c) mesh inside the material, (d) the contour plot of power at top surface of the material in X-Y plane, (e) the contour plot of power at middle of the material in X-Y plane, (f) the contour plot of power at bottom surface of the material in X-Y plane.*

batter was given as $38.3 - 9.2j$. Unfortunately, the heating parameters of the batter were unable to obtained, so that the temperature distribution was not computed in this case. Consequently, the power density distribution, rather than a thermal distribution, is displayed here.

Since a commercial mesh generator was unavailable, a hexahedral mesh was generated to match the inner interface boundary of the load. The entire mesh dimensions were $117 \times 88 \times 90$. The computational time of the FVTD scheme for this case required 4.5 hours to run for 40 microwave periods for a total of 5320 iterations. In Figure 5 (d)-(f), it can be seen that the power density distribution matches the thermal image more than adequately.

Note that the power profiles exhibited in Figure 5 (d)-(f) provide a suitably accurate map of where distinct heating patterns should arise within the materials throughout microwave irradiation. In this sense, a comparison of the results shown here and the thermal images shown in [10] highlights that the solutions obtained using the FVTD method are representative of reality. In particular, the higher temperature locations evident within the material in the thermal images coincide precisely with the power density maxima established by the FVTD model.

5 Conclusions

This paper provides a detailed formulation of a new FVTD method, and presents three case studies which test the performance and validity of the proposed algorithm. In conclusion, the new FVTD code was used successfully to model microwave heating in multimode cavities and was able to predict accurately the microwave heating phenomena that arise during experiments. The next stage in this research concerns the further analyses of the stability of the FVTD scheme and how different mesh structures influence the numerical errors.

References

[1] Yee,K.S. 1966. Numerical solution of initial boundary value problem involving Maxwell's equations in isotropic media. IEEE Trans. on Antennas and Propagation VOL. 14, 302-307.

[2] M.de Pourcq 1985. Field and power-density calculations in closed microwave systems by three-dimensional finite differences, IEE PROCEEDINGS, Vol.132, Pt.H,No.6, 360-368

[3] Niel K. Madsen and Richard W. Ziolkowski, 1990. A THREE-DIMENSIONAL MODIFIED FINITE VOLUME TECHNIQUE FOR MAXWELL'S EQUATIONS, Electromagnetics 10: 147-161.

[4] F. Liu, I. Turner and M.E. Bialkowski, 1994. A Finite-difference time-domain simulation of power density distribution in a dielectric loaded microwave cavity, J. Microwave Power and Electromagnetic Energy, Vol.29, No 3, 138-148.

[5] Magdy F. Iskander, Ray L. Smith, A. Octavio M. Andrade, Hal Kimrey, Jr., and Lee M. Walsh. 1994. FDTD Simulation of Microwave Sintering of Ceramics in Multinode Cavities, IEEE TRANSACTIONS ON MICROWAVE THEORY AND TECHNIQUES, VOL. 42, NO. 5, 793-800.

[6] Pierre-Yves,C., Christophe,M., Luc,D., Maurice,C., and Joseph,P. 1994. Complete Three-Dimensional Modeling of New Microstrip-Microslot Applicators for Microwave Hyperthermia Using the FDTD Method, IEEE TRANSACTIONS ON MICROWAVE THEORY AND TECHNIQUES, VOL. 42, NO. 12, 2657-2666.

[7] Yen Liu, 1994. A Generalized Finite-Volume Algorithm for Solving the Maxwell Equations on Arbitrary Grids, 10th Annual Review of Progress in Applied Computational Electromagnetics, the Applied Computational Electromagnetics Society, 487-494.

[8] Lin-Kun,W. and William,K.N. 1995. FDTD Analysis of the Radiometric Temperature Measurement of a Bilayered Biological Tissue Using a Body-Contacting Waveguide Probe, IEEE TRANSACTIONS ON MICROWAVE THEORY AND TECHNIQUES, VOL. 43, NO. 7, 1576-1582.
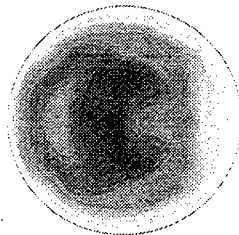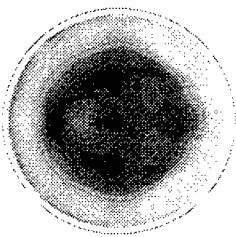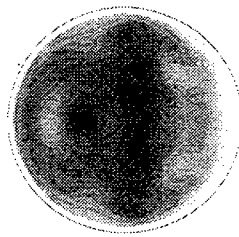
[9] F. Liu and I. Turner, 1996. Numerical Modelling Techniques for Simulating the Microwave Heating of Polymer Materials Inside a Ridge Waveguide, Computational Techniques and Applications: CTAC95. World Scientific Publishing Co.

[10] D.H. Malan, Dibben, D.C. and Metaxas, A.C. 1996. Analyzing loaded multimode cavities using the FETD method, Proc, INTERNATIONAL SCIENTIFIC AND INDUSTRIAL RF & MICROWAVE APPLICATIONS. A2.1-4.

[11] Zhao, H. and Turner, I.W. 1996. An Analysis of the Finite-Difference Time-Domain Method for Modelling the Microwave Heating of Dielectric Materials Within a Three-Dimensional Cavity System, submitted for publication in the Journal of Microwave Power and Electromagnetic Energy.

A PARALLEL FVTD MAXWELL SOLVER USING 3D UNSTRUCTURED MESHES

Jean-Pierre CIONI†‡, Loula FEZOUI†, Laurent ANNE‡, Frédéric POUPAUD*

†INRIA Sophia-Antipolis, BP 93, route des Lucioles, 06 902 Sophia-Antipolis Cedex (France)
‡SIMULOG SA, les Taissounières HB2, route des dolines, 06 560 Valbonne (France).
*Université de Nice Sophia-Antipolis, CNRS URA 168, BP 71, 06 108 Nice Cedex 02 (France).

1 Introduction

The method being presented in this paper is devoted to the simulation of the three dimensional electromagnetic devices using the time domain Maxwell equations and a parallel finite volume solver with unstructured meshes (tetrahedral elements). Such methods have been initially developed with element centered finite volumes [3] and usually with second order Lax-Wendroff schemes on regular grids [6]. We will present here a node centered finite volume method together with the scheme we have written to treat multi layer materials and heterogeneities. In particular, this Godunov scheme is able to deal with large variations of material indices and surface currents. Furthermore, the resulting scheme is third order accurate both in time and space and completely explicit in time. From this method, the software named MAXWELL/VF has been developed jointly by the INRIA Sophia-Antipolis institute and the SIMULOG SA society. Concerning the parallelisation, the reader may find some further information in [5, 7] and particularly about high performance computing with FDTD methods on massively parallel computers. The aim remains different in this paper since some numerical results (with unstructured meshes) as well as performance results obtained with MAXWELL/VF on sets of clusters of workstations or personal computers will be presented.

2 The finite volume Maxwell solver

2.1 Description of the numerical method

The time domain Maxwell equations are among the most general governing equations in electromagnetism which involve the electromagnetic field $^t(\mathbf{E}, \mathbf{H}) \in I\!\!R^6$ and the inductions $\mathbf{Q} = {}^t(\mathbf{B}, \mathbf{D}) \in I\!\!R^6$. In order to complete the model, we have joined the classical linear constitutive equations which involve the electric permittivity $\varepsilon(\mathbf{x})$ and the magnetic permeability $\mu(\mathbf{x})$. Here, we only consider isotropic materials with ε and μ as piecewise constant functions. Maxwell system may be finally written in terms of the inductions as the following condensed conservative form :

$$\mathbf{Q}_t + \vec{\nabla}.\mathbf{F}(\mathbf{x}, \mathbf{Q}) = -\mathbf{J} \tag{1}$$

where $\mathbf{F}(\mathbf{x}, \mathbf{Q}) = {}^t(\mathbf{F}_1(\mathbf{x}, \mathbf{Q}); \mathbf{F}_2(\mathbf{x}, \mathbf{Q}); \mathbf{F}_3(\mathbf{x}, \mathbf{Q}))$ with $\mathbf{F}_l(\mathbf{x}, .) \in \mathcal{L}(I\!\!R^6)$, $l = 1, 2, 3$. The right-hand-side is some eventual volumic source terms. System (1) is hyperbolic and one may refer to [1] for further details about this point.

As the Maxwell system in transient state is hyperbolic and may be rewritten in conservative form, it is natural to use a numerical approximation based on conservative upwind schemes, developed for solving such systems. Let us recall now briefly the main characteristics of the used approximation. Consider a discretisation of the computational domain Ω by nt finite elements (triangles or tetrahedra). Another partition of Ω is then constructed as $\Omega = \bigcup_{i=1}^{ns} C_i$ where ns is the number of nodes and C_i is a cell [1]. Contrary to most finite volume type methods used in electromagnetism, the degrees of freedom here are located in the mesh nodes. A weak formulation is obtained by integrating system (1) on each cell C_i taking the characteristics functions of the cell as test functions. Assuming partial derivative $\mathbf{Q}_t$ to be constant in space on C_i yields the equation for each mesh node using a Green formula :

$$Vol(C_i) (\mathbf{Q}_t)_i + \int_{\partial C_i} \mathbf{F}(\mathbf{x}, \mathbf{Q}).\nu \, d\sigma = - \int_{C_i} \mathbf{J} \, d\sigma \tag{2}$$

where ν is the unit normal exterior to ∂C_i.

Eq. (2) is then broken down into a sum of internal fluxes, boundary terms and sources :

$$Vol(C_i)\,(\mathbf{Q}_t)_i + \sum_{j=1}^{N_i} \Phi_{ij} + \text{boundary terms} + \text{sources} = 0 \qquad (3)$$

where N_i is the number of neighbors of the central node of C_i and Φ_{ij} is an approximation of the internal flux $\int_{\partial C_i \cap \partial C_j} \mathbf{F}(\mathbf{x}, \mathbf{Q}).\nu\, d\sigma$. Since the Maxwell system is hyperbolic, we choose an upwind approximation for the numerical fluxes Φ_{ij} depending on states $\mathbf{Q}_i$ and $\mathbf{Q}_j$ that are constant per cell. To evaluate these internal fluxes, we introduce the notation $\eta = \int_{\partial C_i \cap \partial C_j} \nu\, d\sigma$ and the numerical flux function Φ to express the fluxes as $\Phi_{ij} = \Phi(\mathbf{x}_i, \mathbf{x}_j, \mathbf{Q}_i, \mathbf{Q}_j, \eta)$. We assum here that $\mathbf{F}(\mathbf{x}, \mathbf{Q})$ does not depend on variable $\mathbf{x}$ in each cell and is noted $\mathbf{F}(\mathbf{x}_i, \mathbf{Q})$ in C_i.

2.2 The Godunov scheme

Unlike the homogeneous case, the first order upwind schemes are not all identical when dealing with heterogeneous or multi-layer materials. We have first extended a flux decomposition according to the sign of the eigenvalues of Maxwell system [1] : $\Phi_{ij} = \mathcal{A}^+(\mathbf{x}_i, \eta)\mathbf{Q}_i + \mathcal{A}^-(\mathbf{x}_j, \eta)\mathbf{Q}_j$ where $\mathcal{A}(\mathbf{x}) = \sum_{l=1,3} \frac{\partial \mathbf{F}_l(\mathbf{x}, \mathbf{Q})}{\partial \mathbf{Q}}.\eta_l$. As it is shown in fig. 4.A, this scheme does not satisfy numerically the continuity of the EM field tangential components and produces oscillations. We have used so a Godunov scheme for Maxwell equations which satisfies by construction the jump conditions. The fluxes associated to the Godunov scheme in cell C_i lead to $\Phi_{ij} = \mathcal{A}(\mathbf{x}_i, \eta)\mathbf{Q}_{II}$ where $\mathbf{Q}_{II}(\mathbf{Q}_i, \mathbf{Q}_j)$ is solution of a Riemann problem which is solved exactly.

After a change of variable, $\Phi_{ij} \in I\!R^6$ is completely defined by solving the two 1D-subsystems (4) locally at the interface $S = \partial C_i \cap \partial C_j$ (placed at $y = y_{\frac{i+j}{2}}$) and between the time steps τ_n and τ_{n+1}. The Riemann problem is the following Cauchy problem which corresponds to the Maxwell system written in the η-direction :

$$\frac{\partial \mathbf{w}}{\partial \tau} \pm \frac{\partial}{\partial y}(A(y)\mathbf{w}) = 0, \; A = \begin{bmatrix} 0 & \frac{1}{\varepsilon} \\ \frac{1}{\mu} & 0 \end{bmatrix}, \; \mathbf{w}(y, \tau = \tau_n) = \begin{cases} \mathbf{W}_i^n & if \quad y < y_{\frac{i+j}{2}} \\ \mathbf{W}_j^n & if \quad y > y_{\frac{i+j}{2}} \end{cases} \qquad (4)$$

where the components of $\mathbf{w} \in I\!R^2$ stands for two sets of linear combinations of the EM field components. A source of currents may be present at the interface and is noted $\mathcal{J}_s(\tau) = {}^t(-M_s, J_s)$. The boundary conditions (or jump conditions) at the interface write $\left[\; Aw \;\right]_s = \mathcal{J}_s(\tau)$. This system may be solved entirely and analytically (see [4]) and a representation of the solution is shown on fig. 1. It consists in four constant states in the (y, τ) plane : the initial states $\mathbf{W}_{I,i} = \mathbf{W}_i^n$, $\mathbf{W}_{IV,j} = \mathbf{W}_j^n$ and the ones at the interface which has to be defined ($\mathbf{W}_{II,i}$ and $\mathbf{W}_{III,j}$).
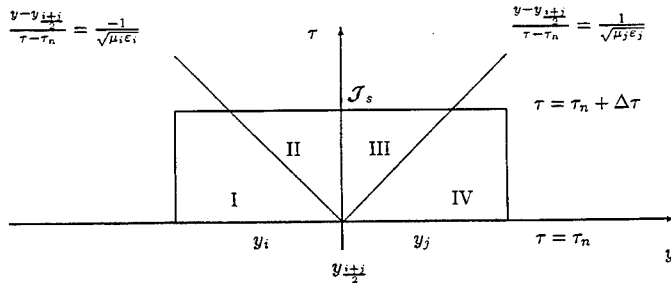

Figure 1: Local Riemann problem.

Finally, the solution (associated to the positive sign in subsystem (4) and cell C_i) writes :

$$
\begin{cases}
W_{1,II} &= \dfrac{\delta}{2}\dfrac{\mu_i}{\mu_j}(W_{1,j}^n - Z_j W_{2,j}^n) + \dfrac{\beta}{2}(W_{1,i}^n + Z_i W_{2,i}^n) - \dfrac{\delta}{2}\mu_i(J_s + \dfrac{1}{Z_j}M_s) \\[2mm]
W_{2,II} &= \dfrac{\delta}{2}(W_{2,i}^n + Y_i W_{1,i}^n) + \dfrac{\beta}{2}\dfrac{\varepsilon_i}{\varepsilon_j}(W_{2,j}^n - Y_j W_{1,j}^n) + \dfrac{\delta}{2Z_i}\mu_i(J_s + \dfrac{1}{Z_j}M_s)
\end{cases}
\tag{5}
$$

with $\delta = \frac{2Z_j}{Z_i + Z_j}$, $\beta = \frac{2Z_i}{Z_i + Z_j}$ where $Z_i = \frac{1}{Y_i} = \sqrt{\dfrac{\mu_i}{\varepsilon_i}}$ is the impedance of the material associated to cell C_i.
The jump conditions give :

$$
W_{1,III} = \frac{\mu_j}{\mu_i}W_{1,II} + \mu_j J_s \quad \text{and} \quad W_{2,III} = \frac{\varepsilon_j}{\varepsilon_i}W_{2,II} - \varepsilon_j M_s .
$$

and the Godunov scheme is now completely defined. In presence of currents, $\Phi_{ij} \neq -\Phi_{ji}$ and $\Phi_{ji} = -\mathcal{A}(x_j, \eta)\mathbf{Q}_{III}$. Let us note that $\mathbf{Q}$ is not constant across the interface but the fluxes are if no current is present at the interface.

The linear flux function leads to a first order scheme no matter if we use a flux decomposition (Steger-Warming) type scheme [2] or a Godunov scheme [4]. The MUSCL method increases the accuracy by raising the degree of interpolation of unknown $\mathbf{Q}$ on the cell. We have to define some new values on the cell interfaces which requires defining gradients of the approximated solution in the mesh nodes. We extended here the numerical flux to the second and the third order in space using a β-scheme. The higher order flux is written as follows on the cell interfaces using the interpolated fields $\mathbf{Q}_{ij}$ and $\mathbf{Q}_{ji}$:

$$
\Phi_{ij} = \Phi(\mathbf{Q}_{ij}, \mathbf{Q}_{ji}, \eta) \quad , \quad \mathbf{Q}_{ij} = \mathbf{Q}_i + \tfrac{1}{2}\{(1 - 2\beta)(\mathbf{Q}_j - \mathbf{Q}_i) + 2\beta\overrightarrow{\nabla}\mathbf{Q}_i.\overrightarrow{ij}\} .
$$

The gradients at node i are evaluated by means of the Galerkin gradients [1] and the value of the parameter β is chosen here to be 1/3. Concerning the time integration, we use the explicit Runge-Kutta scheme with three steps and low storage. The resulting scheme is third-order accurate both in time and space and conditionally stable.

3 Parallelisation

The Maxwell solver previously presented is included in a whole software chain starting from the mesh generator and going to the graphic visualisation. Particularly this chain allows to perform calculations with one processor (or with a workstation) as well as with several ones. The parallelisation of MAXWELL/VF has been performed using the PVM[1] library of communications. So, we have chosen to use a SPMD approach based on the splitting of data and message passing. This approach is adapted to a large variety of computers and some modifications of the initial sequential source code have to be done. However, these modifications are very few as they consist essentially in adding communication routines.

First of all, we have to make a pre-processing step in order to split the initial global mesh into several subdomains. Each subdomain is then associated to a node of calculation (a processor or a workstation). This splitting includes the generation of information used for communications (PVM) and this phase is realised by means of the MS3D[2] tool. A decomposition with subdomain overlapping has been chosen : the interface layer is one element width for the first order scheme and also for the third order accurate one. An update of the boundary points is so required and is made by the means of communications between the subdomains (for the solutions and the gradients). The parallel program is made of a *HOST* program which initialises the parallel processes and leads several *NODE* programs executed by the nodes of calculation. Finally, the local solutions are merged by a post-processing procedure which uses information issued from MS3D to recompose the global solution. The merged solution may then be viewed through a visualisation tool as ENSIGHT[3] in our case.

---

[1] Parallel Virtual Machine, version 3.2
[2] SIMULOG software
[3] CEI software
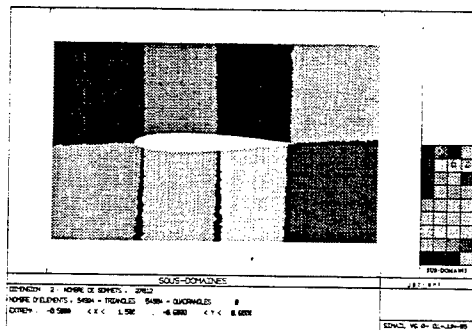
Figure 2: Decomposition of a 2D triangular mesh in 8 subdomains.

4 Numerical results

4.1 Exemples of mesh decomposition

The MS3D tool is a necessary step before a parallel execution of MAXWELL/VF. A first example of decomposition is presented in fig. 2 for a two dimensional airfoil mesh splitted in 8 subdomains. The global triangular mesh is made of approximately 28 000 nodes.

The mesh generator SIMAIL[2] has been used to build the volumic mesh around a sphere. The global mesh is made of 35 686 nodes and 191 312 elements. On fig. 3.A, one part of a two subdomain decomposition is shown whereas a four subdomain decomposition is presented on fig. 3.B.
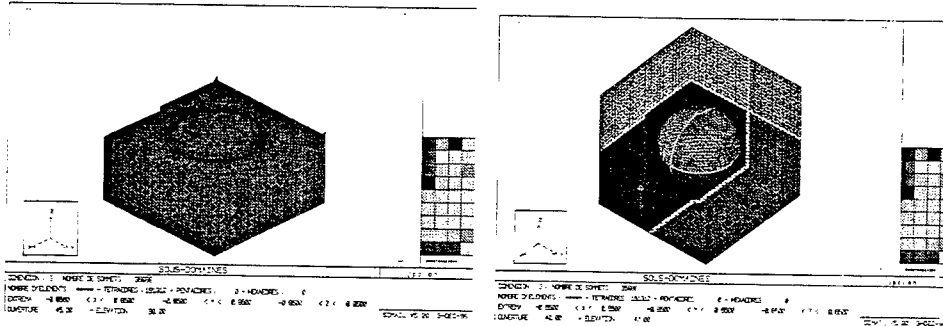
Figure 3:

3.A : Volumic view of one subdomain out of two.

3.B : View of the mesh skin with a four subdomains decomposition.

4.2 Numerical experiments

4.2.1 A 2D coated airfoil

Let us consider now a 2D perfectly conducting NACA0012 airfoil coated by a thin layer of lossless dielectric. The airfoil is illuminated by a TM impulse at zero incidence and the value of the permittivity in the layer is 4. We compare in fig. 4 the decomposition of fluxes (Steger-Warming) and the Godunov scheme (exact Riemann solver) by means of H_z isovalues. One can notice that only the Godunov scheme satisfies the H_z field continuity in this case.
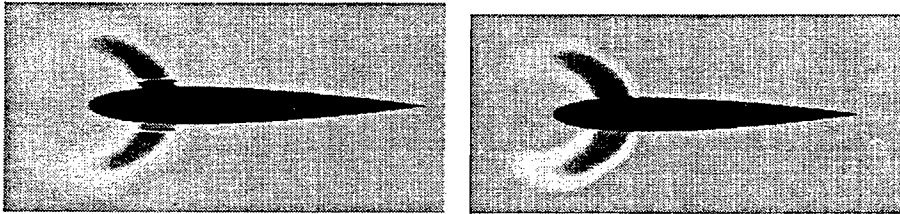
Figure 4:

4.A : Flux decomposition scheme.   4.B : Godunov scheme.

4.2.2 The sphere

We present now a three dimensional simulation which consists in computing the radar cross section (RCS) of a perfectly conducting sphere. The artificial boundary which limits the computational domain is placed at a distance of one wavelength (λ) from the body. The radius r and the frequence f of the incoming wave satisfy the relation $k * r = 4.78$. In order to compute the RCS, the sphere is illuminated by a plane wave and the time evolution of the electromagnetic field is computed until a periodic state is reached. A Fourier transformation is then applied to get the solution in the frequency domain. Finally, we use a near field to far field transformation to get the RCS. One can observe a good agreement between the exact and numerical solutions on fig. 6.A. This result has been obtained with a boundary surface set only at a distance of one wavelength from the sphere and a first order absorbing condition. Besides, the number of points per wavelength varies from 6 to 15 in the whole mesh.

4.2.3 The cylindrical cavity

This test case involves a perfectly conducting cavity having a closed side and vacuum inside. More precisely, the cavity consists of a right hollow cylinder and we look for unsteady solutions relative to the initial incident wave front given by an impulse. This test case has been realised for the workshop [8] and further details may be found in the proceedings. The evolution of the total electric field at point O (shown in fig. 5) is reported in fig. 6.B during 12 periods.
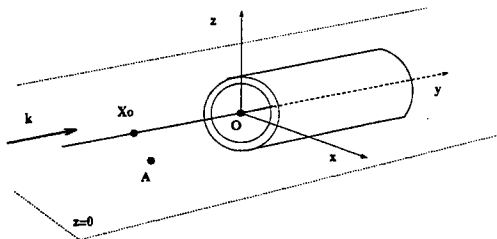
Figure 5: Geometry and observation point O.

4.3 Performance results

We have reported in this section the CPU times and the performance results in terms of Mflop/s concerning two test cases. The results reported in this section concern single precision (32 bit). One can add an amount of 30% to the following results in order to have an evaluation for double precision. In the following tables, the times TCPU and TCOM concern only the Maxwell solver and refer to the CPU time and the communication time. Unless specified, the reported times always refer to the duration of the numerical simulation for one time step.
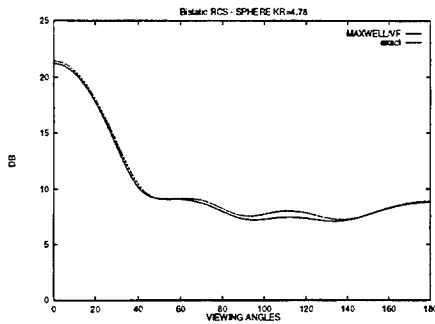
Figure 6:

6.A : Radar Cross Section of the sphere.   6.B : Time evolution at point 0 (cylindrical cavity).
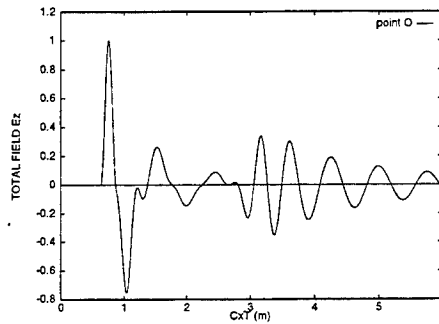
Let us note that the performance calculations are based on the maximum of the measured times over the NMAX different nodes of calculation. The percentage of communication time over the CPU time is noted PERCOM and MF represents the performance results in terms of Mflop/s.

We present now some performance results obtained with clusters of workstations. A set of four DEC-ALPHA 500 (333 MHz) has been used but measurements with Pentium Pro PC's (200 MHz) are also presented. Let us note that the network links of these two sets have both a rate of 10 Mbytes/s. We recall that the mesh of the sphere is composed of 35 686 nodes and 191 312 tetrahedras. The test case related here is the calculation of the RCS after the convergence of the solution towards a periodic state (see fig. 6.A). The third order scheme both in time and space has been used. The performance results versus the number of workstations are shown in tab. 1 for the DEC ALPHA's set. Both CPU and communication times have been also reported in tab. 1. The field TOTCPU refers to the total CPU time needed to obtain the final result of this test case, that is to say the RCS diagram. These measurements reveal a good speed-up of MAXWELL/VF whose value is 3.7 with four nodes of calculation. In particular, MAXWELL/VF reaches 469 Mflop/s with four nodes.

N	TCPU (s/iter.)	TCOMM (s/iter.)	PERCOMM (%)	TOTCPU (min)	MF (Mflop/s)	SPEED-UP
1	3.21	0	0	24	128	1
2	1.71	0.08	4.8	13	241	1.9
4	0.87	0.08	9.8	7	469	3.7

Table 1: CPU and communication times with DEC-ALPHA's.

The same experience has been made with the set of PC's and results are shown on tab. 2. Performances are less benefit that the ones obtained with DEC-ALPHA's but very encouraging for such new installations (speed-up of 3.5 and 122 Mflop/s with four nodes). One can observe that the performance obtained with one DEC-ALPHA is reached equivalently with four PC's (see tabs. 1 and 2). However, these results show that scientific computing may be envisaged with such PC's.

N	TCPU (s/iter.)	TCOMM (s/iter.)	PERCOMM (%)	TOTCPU (min)	MF (Mflop/s)	SPEED-UP
1	12.6	0	0	92	35	1
2	6.6	0.11	1.6	48	67	1.9
4	3.57	0.12	2.2	26	122	3.5

Table 2: CPU and communication times with Pentium PC's.

5 Conclusion

We have developed a finite volume method of a high order accuracy for solving the 3D time domain Maxwell equations where the use of unstructured meshes is adapted to any geometry. Furthermore, the MAXWELL/VF software has been parallelised by using a message passing technic. The parallel version is of a confortable use since it is included in a whole chain of softwares. As for the performance results, they show the ability of this software to run on workstations such as personal computers. We have also proposed a Godunov scheme which satisfies the jump conditions at a surface discontinuity in a discrete way. The continuity of the tangential components of the EM field is insured and currents may be introduced. At the moment, this software is still being developed to increase its modelling capabilities and all its characteristics allow to consider the simulation of complex devices and large scale applications.

References

[1] CIONI J.P. - FEZOUI L. - ISSAUTIER D., *High-order upwind schemes for solving time-domain Maxwell equations*, La Recherche Aérospatiale, Vol 5, pp. 319-328, (1994).

[2] CIONI J.P. - FEZOUI L. - STEVE H., *A parallel time-domain Maxwell solver using upwind schemes and triangular meshes*, IMPACT in computing in science and engeenering, Vol 5, pp. 215-247, (1993).

[3] PETITJEAN B. - LÖHNER R., *Finite element solvers for Radar Cross-Section (RCS) calculations*, AIAA paper 92-0455, (1992).

[4] GIMONET G. - CIONI J.P. - FEZOUI L. - POUPAUD F., *Approximation numérique des équations de Maxwell en milieu hétérogène monodimensionnel par un solveur de Riemann exact*, CERMICS report N° 95-37, (April 1995).

[5] ROWELL C. - SHANKAR V. - HALL W.F. - MOHAMMADIAN A., *Advances in time-domain CEM using massively parallel architectures*, 11th annual review of progress in applied computational electromagnetics, Vol 1, pp. 839-846, Monteray (US), (March 1995).

[6] SHANKAR V. - HALL W.F. - MOHAMMADIAN A.H., *A time-domain differential solver for electromagnetic scattering problems*, Proceedings on the IEEE, Vol 77, pp. 709-721, No 5, (1989).

[7] TAFLOVE A., *Re-inventing electromagnetics: supercomputing solution of Maxwell's equations via direct time integration on space grids*, AIAA paper 92-0333, (1992).

[8] WORKSHOP and 3rd international conference on *Approximations and numerical methods for the solution of the Maxwell equations*, Oxford, (1995).

ADAPTING AN ALGORITHM OF COMPUTATIONAL FLUID DYNAMICS FOR COMPUTATIONAL ELECTROMAGNETICS

T.E. Hodgetts and C.C. Lytton
Defence Research Agency
St. Andrew's Road, Malvern, Worcs., WR14 3PS, United Kingdom

INTRODUCTION

Computational electromagnetics and computational fluid dynamics have evolved as independent areas of numerical analysis, but the equations which are solved in these two areas are fundamentally similar. It therefore seems plausible that methods developed in one area should also be applicable to the other, with possible savings of time and computer resources. This paper describes a test of this idea: a general method originally developed for aerodynamic calculations by specialists at the Farnborough site of the Defence Research Agency (DRA) is now being adapted for electromagnetic calculations, with the collaboration of specialists at the DRA's Malvern site.

Apart from quasi-optical techniques at high frequencies, the usual methods of computational electromagnetics (CEM) for scattering bodies are all variations of the so-called "method of moments". This method has a long and successful history — some thirty years in its modern form (e.g. Harrington [1]), with ideas traceable back to the last century — but its computational demands grow very rapidly with increasing frequency, typically according to the well-known sixth-power law. Our wish to improve on this growth rate provided the motive for investigating the methods of computational fluid dynamics (CFD). We have focused our attention on one of these methods, the finite-difference flux-balance method described by Hall [2], which is being progressively modified and re-programmed by one of us (C.C.L.). Before describing the Hall-Lytton method in detail, we give an overview of it in relation to the method of moments.

OVERVIEW

The method of moments, as applied to general scattering problems, is a finite-element method. It essentially consists of formulating a set of simultaneous linear equations, which express the field scattered by a body in terms of currents induced on (or in) small elements of the body by the incident field. These equations are then solved for the currents, from which the scattered field may be calculated. However, no finite element may be larger in any dimension than some modest fraction of the wavelength (typically 1/8), so the number of elements required to cover a body's surface is proportional to the square of the frequency; and so is the number of simultaneous equations. The work of solving them is then proportional to the cube of their number, and so to the sixth power of the frequency (if every current significantly affects every equation, which is the usual case). If the scattering body is penetrated by the incident field, the finite elements may have to fill its volume as well as covering its surface, and their number is even greater. Another problem is that the method of moments is essentially applied to one frequency at a time, so a body's response to a broad-band radar (for example) can only be determined by repeating the entire calculation for many closely-spaced single frequencies.

The Hall-Lytton method, in contrast to the finite elements of the method of moments, uses finite differences, operating directly with Maxwell's partial differential equations for the components of the electromagnetic field; these are calculated

on a grid (sometimes called a mesh or an array) of points in space with stepping in time. Since the method uses time-stepping rather than working with a specified frequency, it is directly suited to calculating a scattering body's response to broad-band or pulsed transmissions; and since finite-difference methods work by propagating changes from each grid point to and from its neighbours at each step, we do not have to manipulate a dense matrix of coefficients representing the interaction of every point with every other point. The total amount of computation still depends strongly on the highest significant frequency of excitation through its effect on the spacing and step size required for stability, but the growth rate is proportional to the fourth or fifth power of the frequency instead of the sixth.

The use of finite differences directly in Maxwell's equations is not an original idea in itself; simple algorithms on Cartesian grids have been studied at least since the work by Yee [3] in 1966. However, to make the idea competitive with the method of moments, three things are necessary: (i) a good finite-difference algorithm (accurate, self-consistent and stable); (ii) a good grid (well-conformed to the scattering body's irregularities, and spaced more finely where the field components are changing rapidly); and (iii) a good outer boundary condition (to prevent spurious reflections from the outside edges or surfaces of the grid, so that a pure outgoing field is obtained). Each of these requirements (and particularly the third) has attracted much attention, and the literature is now vast, with new papers almost every month in such journals as *IEEE Transactions MTT* and *Microwave Letters;* but most publications describe their authors' *ad hoc* inventions for particular problems. In contrast, we present a universal algorithm, applicable to a whole family of partial differential equations, and already extensively tested in aerodynamic applications; our methods of generating conforming grids have been tested in the same way (although we do not discuss them in detail here). Designing finite-difference algorithms and grid generators is a branch of numerical analysis, which is a complex and specialised mathematical art; the well-known book *Numerical Recipes* [4] has done much to popularise its techniques, but also gives many illustrations of its hidden dangers. We think, therefore, that by adapting well-tested general methods rather than inventing new special ones, we have chosen the better way.

We now begin to describe what the Hall-Lytton method is.

THE HALL-LYTTON METHOD: OUTLINE

The heart of Hall's method for CFD is an algorithm for treating an equation of the general form

$$\frac{\partial U}{\partial t} = -\left(\frac{\partial F}{\partial x} + \frac{\partial G}{\partial y} + S\right) \tag{1}$$

where U, F and G are column vectors of dependent variables, which may have functional equations (but not other differential equations) relating them, and S is a column vector of source terms (which may vanish). (The equation is written in its original two-dimensional form from [2]; a term $(\partial H/\partial z)$ may be added in three dimensions.) The space derivatives in this equation can be used to express a vector curl or divergence; so, since Maxwell's equations all take the form of a curl or a divergence equated to a first-order time derivative (sometimes added to a source term), they can all be put in the form (1).

This method, as remarked earlier, works directly with the fundamental first-order differential equations of electromagnetics or fluid dynamics. That is to say, we do not need to use any of the conventional transformations into higher-order equations satisfied by potential functions (in CEM) or stream functions (in CFD), nor does it matter whether such transformations would give a scalar problem (depending on only one potential or stream function) or a vector problem (depending on two or more such functions). The use of first-order equations is generally agreed to give better stability, and greater freedom from spurious solutions which finite-differencing may create. It also allows greater flexibility; separating the two principal electromagnetic polarisations is not necessary in principle, although doing so may still be convenient in practice. (In fact, we have done so for our two-dimensional tests, to reduce the number of independent variables.) Moreover, it is much more convenient to apply the interface boundary conditions directly in terms of field components rather than in terms of potential functions; and this is also true of the constitutive relations which define the permeability, permittivity and conductivity of material media (which require special treatment in time-domain

analysis, unless the properties of all the media are independent of the frequency). These points will be considered below in more detail.

THE HALL-LYTTON METHOD: DETAILS OF THE ALGORITHM

We solve eqn.(1) numerically in the following way (Hall [2]); this description is given for one component in the column vectors U, F, G and S, but the extension to several components is immediate (likewise the extension if the additional term $(\partial H / \partial z)$ is present).

Suppose we have calculated the values after n time steps, and we now wish to proceed to the $(n+1)$-th step; then, by Taylor's theorem

$$
\delta U = \left(\frac{\partial U}{\partial t} \right)^{(n)} \delta t + \frac{1}{2} \left(\frac{\partial}{\partial t} \left(\frac{\partial U}{\partial t} \right) \right)^{(n)} (\delta t)^2
\tag{2a}
$$

to the second order, where $\delta U = U^{(n+1)} - U^{(n)}$ and $\delta t = t^{(n+1)} - t^{(n)}$. On substituting into eqn.(2a) from eqn.(1) and interchanging orders of differentiation, we get

$$
\delta U = -\left[\frac{\partial F}{\partial x} + \frac{\partial G}{\partial y} + S \right]^{(n)} \delta t - \frac{1}{2} \left[\frac{\partial}{\partial x} \left\{ \frac{\partial F}{\partial U} \cdot \frac{\partial U}{\partial t} \right\} + \frac{\partial}{\partial y} \left\{ \frac{\partial G}{\partial U} \cdot \frac{\partial U}{\partial t} \right\} + \left\{ \frac{\partial S}{\partial U} \cdot \frac{\partial U}{\partial t} \right\} \right]^{(n)} (\delta t)^2
\tag{2b}
$$

where the terms like $(\partial F / \partial U)$ and $(\partial U / \partial t)$ are in general square matrices and column vectors, respectively. Now, U is defined at the nodes of a grid, and the grid may also be considered to be made up of cells, each cell being defined by four nodes like A, B, C, D (see the Figure page). We may calculate the functions F and G at the node corners of a cell, and then apply Gauss' theorem to the cell, giving

$$
\iint \left\{ \frac{\partial F}{\partial x} + \frac{\partial G}{\partial y} \right\}^{(n)} ds = \oint \left(F \, \underline{\hat{n}}_x + G \, \underline{\hat{n}}_y \right)^{(n)} \cdot \underline{dl}
\tag{3}
$$

where $\underline{n}_x$ and $\underline{n}_y$ are unit normal vectors, and their dot product is taken with the differential vector $\underline{dl}$. The right-hand side of eqn.(3) may be evaluated using the trapezium rule; this has second-order relative error, but we are using it to calculate a first-order correction in eqn.(2b), so the absolute error is third-order. On dividing this right-hand side by the negative of the cell's area (defined by integrating (ds), for which also we use the trapezium rule), we have the value of

$$
-\left\{ \frac{\partial F}{\partial x} + \frac{\partial G}{\partial y} \right\}^{(n)}
\tag{4}
$$

at the centroid of the cell ABCD (the point 1 in the Figure); and the first-order change in U, ΔU, is obtained by subtracting S from this and then multiplying the result by (δt), as is obvious from eqn.(2b). However, this first-order change is referred to the wrong place — a cell's centroid, instead of a node (cell's vertex). We remove this difficulty by noting that each node is itself the centroid of four cells' centroids (thus, C is the centroid of 1, 2, 3, 4 in the Figure); so we take ΔU at C to be the weighted mean of ΔU at 1, 2, 3, 4, with the weightings being the areas of the cells containing each of the four points 1, 2, 3, 4. This weighting was shown by Hall [2] to give better stability when the cells vary markedly in size, which is likely to happen in our electromagnetic problems; we remarked in the "Overview" on the importance of a well-conformed and well-spaced grid when attempting to follow accurately the surface of an irregular scattering body.

To complete the calculation of δU in eqn.(2b), we need to determine the factor multiplying $(\delta t)^2$. We note first that in this factor we may replace $(\partial U/\partial t)$ by $(\Delta U/\delta t)$, since we require only first-order relative accuracy. It is then trivial to evaluate the second-order contributions due to S (involving $(\partial S/\partial U)$). To treat the other two terms in the square brackets multiplying $(\delta t)^2$, we write them as

$$\left[\frac{\partial}{\partial x} \left\{ \frac{\partial F}{\partial U} \cdot \Delta U \right\} + \frac{\partial}{\partial y} \left\{ \frac{\partial G}{\partial U} \cdot \Delta U \right\} \right]^{(n)} (\delta t)^{-1} \tag{5}$$

and we calculate the expressions in brackets at the centroids of the cells to first-order relative accuracy, which is done by taking the mean of the values at each centroid's four neighbouring nodes; then we again apply Gauss' theorem (in the form of eqn.(3)) to a dual cell like the one shown in dotted lines in the Figure — defined by four centroids instead of four nodes — to obtain the second-order part of δU at the node enclosed by the dual cell. When the first-order and second-order changes have thus been calculated for every node, the values of U at the nodes are updated; and the $(n+1)$-th time step is complete. (The size of the time step is governed by the conventional Courant-Friedrichs-Levy criterion.)

A summary of the process is included in the Figure. Methods of this kind, which make direct use of Gauss' theorem, are often called "flux-balance" methods; the name "cell-vertex" is also used (e.g. [2]) to summarise the movement back-and-forth between the cells' centroids and their vertices.

APPLICATION TO MAXWELL'S EQUATIONS

In the description just given, the components of the vectors U, F, G and S can be taken as the conventional components of the three-dimensional field vectors $\underline{E}$, $\underline{H}$, $\underline{B}$ and $\underline{D}$. In the most general case there are eight scalar partial differential equations relating these (three from each Maxwellian curl equation and one from each divergence equation); but whenever a simplification is supplied by theoretical considerations it can be incorporated into the computer programming, because of the generality of eqn.(1). Such simplifications naturally include the standard linear relations between $\underline{B}$ and $\underline{H}$ and between $\underline{D}$ and $\underline{E}$ (with the current density $\underline{J}$ included, if a conducting medium is present). These relations require special attention if the excitation covers a broad frequency band, because the parameters of a medium with conductivity or hysteresis depend on the frequency. However, this problem has been treated by Luebbers *et al.* [5] in a form which is applicable to any finite-difference method which works directly with field components, and we are implementing a version of their treatment. As remarked earlier, we have also used in our numerical experiments the convenient fact that in two dimensions the eight scalar Maxwellian equations separate into two independent sets of four, one for each polarisation (at least when all media are isotropic; e.g. Jones [6]); again, there is nothing about this separation which is special to our method. There are special features of the grid and its boundaries, however, and we outline these next.

GRIDS AND BOUNDARY CONDITIONS

Nothing in the mathematics which has been presented so far requires the edges of any cell (or its walls, in three dimensions) to be aligned with any particular direction; on the Figure page, we can take the x-variable in eqn.(1) as horizontally-directed and the y-variable as vertically-directed, while the grid is represented as not even straight-edged, much less perpendicular. Our algorithm can therefore be used with a separate conforming grid generator, since there are no built-in assumptions about the grid except the obvious implication that it is sufficiently fine to follow all necessary detail; it need not be everywhere orthogonal, for instance. The separate generator can be one proven in aerodynamic applications using the original form of our program, since there are no requirements fundamentally different from the electromagnetic case; in both cases we wish to cover a surface or surfaces and to divide up the volume around and between the surfaces (although a sophisticated generator is not needed to do this for the simple bodies we have studied so far). In both cases also, the surface-specific boundary conditions take the form of tangential and normal conditions at the surfaces, and again there is no fundamental difference; although when an element of U is to be continuous across a surface, it is convenient if the cells which actually touch the surface are orthogonal to it. Even singular points or lines do not create any fundamental distinctions, since both in aerodynamics and electromagnetics the possible singularities must

satisfy requirements of finite energy. In fact, the only important difference between the two cases is the treatment of the outer boundary of the grid, which is our next topic.

TREATMENT OF THE OUTER BOUNDARY

The computational treatment of the outer boundary of a finite-difference grid has become a very fashionable subject since Berenger [7] described his "Perfectly-Matched Layer" in 1994, and we intend to contribute to the literature in due course. We are implementing the variant of Berenger's hypothetical material which was described by Sacks *et al.* [8], because the "splitting" of Maxwell's equations introduced by Berenger is an inconvenience in applying our general algorithm (eqn.(1)), and it also complicates the separation of the polarisations for testing purposes (which is already complicated because these materials are anisotropic). Sacks' type of material is also more convenient for constructing an outer boundary without corners, which is more natural for use with an algorithm based on the flow patterns around aerofoils. We are studying the theoretical extension of the Perfectly-Matched Layer from plane layers to cylindrical and spherical ones, which are the simplest forms without corners as well as being the logical choices when far-field radiation is considered.

There has been some recent controversy about the numerical stability of finite-difference methods in the presence of these hypothetical materials (Nehrbass *et al.* [9], Gedney [10]). We are still considering this problem; but our tests so far indicate that, if our algorithm is unstable when Sacks' material is used, the instability is so weak that it can be suppressed by numerical "smoothing". This technique is commonplace in algorithms for CFD, and it was already incorporated in Hall's original work [2] before we began our adaptation to CEM; so again we have been able to carry over a trusted numerical procedure.

PROGRESS AND PRELIMINARY RESULTS

The work described above is still in progress, so we report here only on our early results. We did not implement a Perfectly-Matched boundary material at the beginning; so our first numerical experiments were tests of the propagation of a sinusoidal pulse from the front to the back of simple scattering objects, since these tests could be truncated in time so that reflections from the outer boundary would not seriously affect the results. Comparisons with theoretical predictions of the response to an infinite sinusoid gave very encouraging agreement, particularly since our numerical sinusoid was necessarily "switched on" at time zero and therefore had an associated initial transient. Since this early work, we have been experimenting with the boundary materials, and some interesting results using these will be reported at the conference. Our plans for the future include going beyond simple objects to ones with edges; we believe that our algorithm should be well-suited to studying these, because in CFD it has already demonstrated the ability to predict behaviour near the trailing edge of an aerofoil.

As this paper is already approaching the recommended maximum length, we present only a sample of our algorithm's behaviour. Our graph shows a comparison between results from two sizes of two-dimensional grid, one with half the spacing of the other, and theoretical predictions. These data exhibit the response of an infinite circular lossless dielectric cylinder, with relative permittivity 2.56 and relative permeability 1, to a transverse electric (TE) sinusoid whose frequency is such that the circumference of the cylinder is 5 free-space wavelengths (chosen as a resonance condition). The horizontal co-ordinate of the graph is angle in degrees, measured around the cylinder from the line of normal incidence (0°); the vertical co-ordinate is amplitude relative to unit excitation. The two sets of grid results are plotted continuously, while the predictions are plotted as individual points at intervals of 6° around the cylinder.

ACKNOWLEDGEMENTS

REFERENCES

1.   Harrington, R.F., "Field Computation by Moment Methods", Macmillan, New York and London, 1968.

2.   Hall, M.G., "Cell-Vertex Multigrid Schemes for Solution of the Euler Equations", Royal Aircraft Establishment Technical Memorandum AERO 2029, 1985.

3.   Yee, K.S., "Numerical Solution of Initial Boundary Value Problems Involving Maxwell's Equations in Isotropic Media", IEEE Trans. Antennas and Propagation, vol. AP-14, 1966, pp. 302-306.

4.   Press, W.H., Flannery, B.P., Teukolsky, S.A. and Vetterling, W.T., "Numerical Recipes: The Art of Scientific Computing", Cambridge University Press, Cambridge and New York, 1986 (and later editions).

5.   Luebbers, R., Steich, D. and Kunz, K., "FDTD Calculation of Scattering from Frequency-Dependent Materials", IEEE Trans. Antennas and Propagation, vol. AP-41, 1993, pp. 1249-1257.

6.   Jones, D.S., "The Theory of Electromagnetism" (International Series of Monographs on Pure and Applied Mathematics, vol. 47), Pergamon Press, Oxford and New York, 1964.

7.   Berenger, J.-P., "A Perfectly Matched Layer for the Absorption of Electromagnetic Waves", J. Comp. Physics, vol. 114, 1994, pp. 185-200.

8.   Sacks, Z.S., Kingsland, D.M., Lee, R. and Lee, J.-F., "A Perfectly Matched Anisotropic Absorber for Use as an Absorbing Boundary Condition", IEEE Trans. Antennas and Propagation, vol. AP-43, 1995, pp. 1460-1463.

9.   Nehrbass, J.W., Lee, J.-F. and Lee, R., "Stability Analysis for Perfectly Matched Layered Absorbers", Electromagnetics, vol. 16, 1996, pp. 385-397.

10.   Gedney, S.D., "An Anisotropic PML Absorbing Media for the FDTD Simulation of Fields in Lossy and Dispersive Media", Electromagnetics, vol. 16, 1996, pp. 399-415.

11.   Brewitt-Taylor, C.R., "Program MIESCAT: Scattering from Cylinders and Spheres", Defence Research Agency (Malvern) Radar Sensors and Techniques Divisional Memorandum AD2-43/91, 1991.

12.   Stratton, J.A., "Electromagnetic Theory" (International Series in Physics), McGraw-Hill, New York and London, 1941.

MECHANICS OF CELL-VERTEX METHOD

Figure
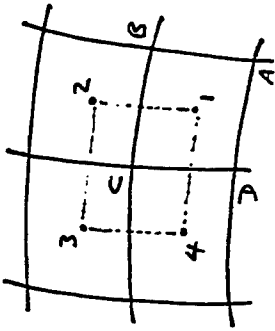
- U defined at grid nodes like A,B,C,D

- Compute F, G at nodes, then apply Gauss' Theorem over cell ABCD:

$$\int\int_s \left(\frac{\partial F}{\partial x} + \frac{\partial G}{\partial y}\right) ds = \oint \left(F\hat{n}_x + G\hat{n}_y\right) \cdot dl$$

- Right side can be evaluated approximately by trapezium rule

- Left side yields approximation for first-order term $\left(\frac{\partial F}{\partial x} + \frac{\partial G}{\partial y}\right)$ at centroid 1

- The second-order divergence term can be written in terms of first-order flux increments known at cell centroids like 1,2,3,4. Apply Gauss' Theorem again over the dual cell 1234, of which node C is regarded as being the centroid, to get approximation for second-order term at node C
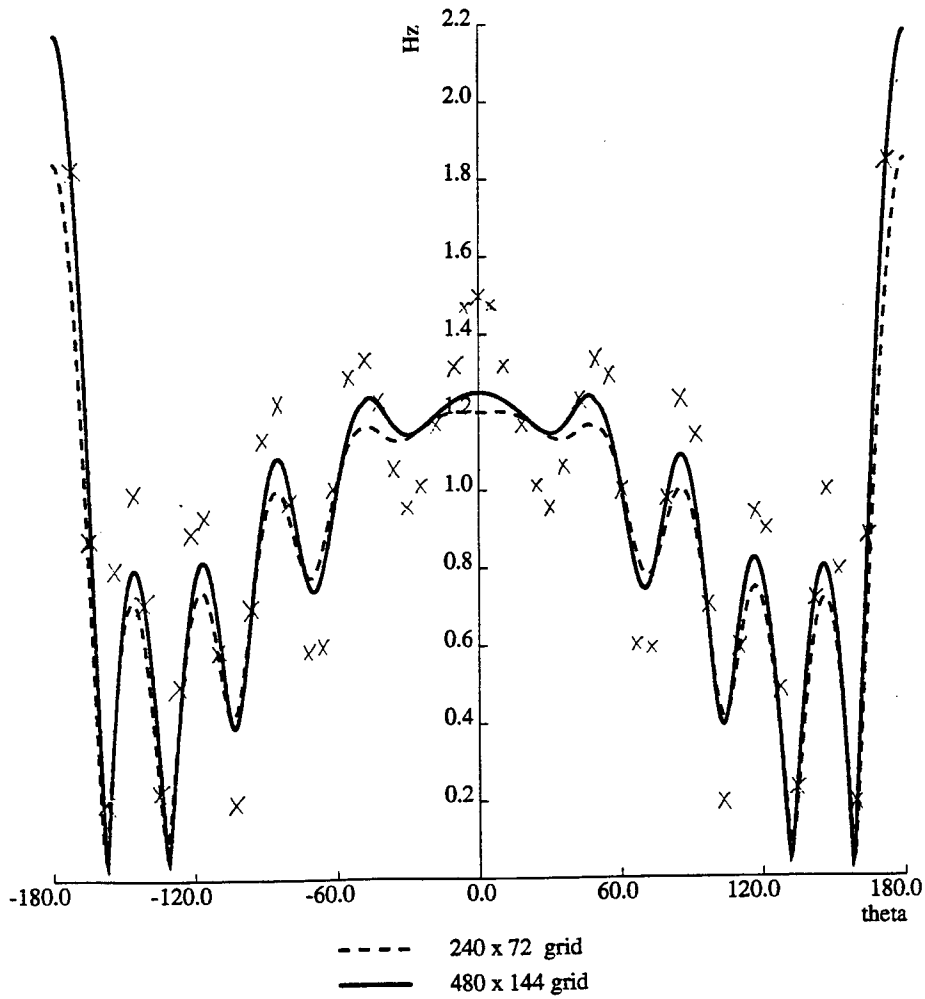
Amplitude, total Hz field along cylinder surface

Circular Cylinder; TE mode; mu = 1.0, eps = 2.56; beta = 0.0, ka = 5

Grid Refinement Comparison

- - - - 240 x 72 grid
——— 480 x 144 grid

APPLICATION OF A FINITE-VOLUME TIME-DOMAIN
TECHNIQUE TO THREE-DIMENSIONAL OBJECTS

Frederick G. Harmon, Andrew J. Terzuoli, Jr.
Air Force Institute of Technology

Abstract-Concurrent engineering approaches for the disciplines of computational fluid dynamics (CFD) and electromagnetics (CEM) are necessary for designing future high-performance aircraft. A characteristic-based finite-volume time-domain (FVTD) computational algorithm used by CFD and herein applied to CEM is implemented to analyze the radar cross section (RCS) of two three-dimensional objects, the ogive and cone-sphere, by utilizing a scattered-field formulation of the time-dependent Maxwell equations. The FVTD formulation uses a monotone upstream-centered scheme for conservation laws (MUSCL) for the flux evaluation and a Runge-Kutta multi-stage scheme for the time integration. The RCS results are obtained from the electromagnetic fields via a Fourier transform and a near-to-far field transformation.

The FVTD code and algorithm are evaluated for electromagnetic scattering problems by comparing FVTD code RCS results to data obtained from a Moment Method (MoM) code (CICERO) and empirical RCS data published by the Electromagnetic Code Consortium (EMCC). The FVTD RCS results for the ogive and cone-sphere are within 3.0 dB of the bistatic MoM results and 3.1 dB of the monostatic empirical RCS data. Accurate FVTD computations of diffraction, traveling waves, and creeping waves require a surface grid point density of 15-30 cells/λ, dependent on frequency.

I. FVTD Formulation of Maxwell Equations

The FVTD computational technique is capable of concurrently solving the Euler equations of fluid dynamics and the Maxwell equations of electromagnetics. CFD has used the FVTD technique since the early 1980's [21] to analyze the airflow about an aircraft or airfoil and the technique has recently been applied to CEM. Several engineers, Blake, Shang, Shankar [2-3, 7-20] and others are exploring and advancing the application of the FVTD technique to the Maxwell equations of electromagnetics. The FVTD formulation and numerical procedure implemented in Shang's FVTD code is discussed and used to obtain the RCS results for the ogive and cone-sphere.

A. Grid Generation of Finite-Volume Cells

To use FVTD, the physical space surrounding an object of interest must be discretized into volumetric cells. The space containing the finite-volume cells is referred to as the space grid [22]. The frequency of interest and the electrical length of the object determines the number of cells in the grid.

For the characteristic-based FVTD formulation, a structured grid using curvilinear coordinates is used so the wave propagation is aligned closely with one of the coordinate axes [10]. The compatibility condition used for the radiation boundary condition is exact if the wave propagation parallels a coordinate axis. In addition, the curvilinear coordinates permit higher accuracy in the computation of the electric and magnetic scattered fields.

B. Maxwell's Equations in Conservation Form

The two time-domain Maxwell curl equations, in differential form, are shown below and will be used in the development of the electromagnetic FVTD equations:

Faraday's Law: $\nabla \times E = -\dfrac{\partial B}{\partial t}$ (1)   Ampere's Law: $\nabla \times H = \dfrac{\partial D}{\partial t} + J$ (2)

where E: Electric field strength vector (V/m) B: Magnetic flux density vector (Wb/m^2 or T)
D: Electric flux density vector (C/m^2) J: Electric current density vector (A/m^2)
H: Magnetic field strength vector (A/m)

Using the constitutive parameters to relate the field strength vectors and the flux density vectors, when the material is linear and isotropic, the constitutive relations are $D = \varepsilon E$ and $B = \mu H$ where ε is the electric permittivity (F/m) and μ is the magnetic permeability (H/m).

For use in FVTD, the two Maxwell equations are cast in conservation form [12]. The solution of Maxwell's equations do not require the conservation form; however, the form is required by the Euler equations to conserve physical properties such as energy, mass, and momentum. The Maxwell equations are cast in conservation form solely to take advantage of the

same computational technique used to solve the Euler equations. To this end, the curl operations are carried out and the constitutive parameters are implemented. The result is given by

$$\frac{\partial U}{\partial t} + \frac{\partial F}{\partial x} + \frac{\partial G}{\partial y} + \frac{\partial H}{\partial z} = -J \qquad (3)$$

where

$$U = \begin{bmatrix} B_x \\ B_y \\ B_z \\ D_x \\ D_y \\ D_z \end{bmatrix} \quad F = \begin{bmatrix} 0 \\ -D_z/\varepsilon \\ D_y/\varepsilon \\ 0 \\ B_z/\mu \\ -B_y/\mu \end{bmatrix} \quad G = \begin{bmatrix} D_z/\varepsilon \\ 0 \\ -D_x/\varepsilon \\ -B_z/\mu \\ 0 \\ B_x/\mu \end{bmatrix} \quad H = \begin{bmatrix} -D_y/\varepsilon \\ D_x/\varepsilon \\ 0 \\ B_y/\mu \\ -B_x/\mu \\ 0 \end{bmatrix} \quad J = \begin{bmatrix} 0 \\ 0 \\ 0 \\ J_x \\ J_y \\ J_z \end{bmatrix}$$

Equation (3) is a system of six linear equations. U is the independent variable and the F, G, and H flux vectors are the dependent variables. The equations are not linearly independent; therefore, a characteristic-based technique is used to uncouple the six equations.

C. Coordinate Transformation

To analyze the scattering of various objects, such as the ogive and cone-sphere, a curvilinear coordinate transformation is required. A curvilinear structured grid minimizes the errors introduced in the cell metrics and the flux calculations. The variables ξ, η, and ζ are used to convert the Cartesian coordinates to curvilinear coordinates. After a coordinate transformation, Equation (3) becomes [12, 13]

$$\frac{\partial \hat{U}}{\partial t} + \frac{\partial \hat{F}}{\partial \xi} + \frac{\partial \hat{G}}{\partial \eta} + \frac{\partial \hat{H}}{\partial \zeta} = -\hat{J} \qquad (4)$$

where $\quad \hat{U} = \dfrac{U}{V} \qquad \hat{J} = \dfrac{J}{V}$

$$\hat{F} = \left(\frac{\partial \xi}{\partial x} F + \frac{\partial \xi}{\partial y} G + \frac{\partial \xi}{\partial z} H \right) \frac{1}{V} \qquad \hat{G} = \left(\frac{\partial \eta}{\partial x} F + \frac{\partial \eta}{\partial y} G + \frac{\partial \eta}{\partial z} H \right) \frac{1}{V} \qquad \hat{H} = \left(\frac{\partial \zeta}{\partial x} F + \frac{\partial \zeta}{\partial y} G + \frac{\partial \zeta}{\partial z} H \right) \frac{1}{V}$$

and V is the Jacobian of the coordinate transformation.

D. Finite-Volume Formulation

Equation (4) is applied to every finite-volume cell in the grid. An integration is performed over each finite-volume cell:

$$\iiint_V \frac{\partial \hat{U}}{\partial t} dV + \iiint_V \left(\frac{\partial \hat{F}}{\partial \xi} + \frac{\partial \hat{G}}{\partial \eta} + \frac{\partial \hat{H}}{\partial \zeta} \right) dV = - \iiint_V \hat{J} \, dV \qquad (5)$$

The divergence theorem is then applied to the second integral:

$$\iiint_V \frac{\partial \hat{U}}{\partial t} dV + \oiint_S \left(\hat{F} + \hat{G} + \hat{H} \right) \cdot \mathbf{n} \, dS = - \iiint_V \hat{J} \, dV \qquad (6)$$

where $\mathbf{n}$: Unit vector normal to the surface (ξ, η, and ζ for $\hat{F}$, $\hat{G}$, and $\hat{H}$, respectively)

S: Closed surface bounding the finite volume (m^2)

Equation (6) is the expression for a generic FVTD formulation. The unknown components of the $\hat{U}$ vector are the magnetic and electric flux densities. The vectors $\hat{F}$, $\hat{G}$, and $\hat{H}$ are the flux vectors and can be expressed in terms of the magnetic and flux densities. A multitude of techniques are used to solve Equation (6) giving rise to the myriad of FVTD numerical algorithms.

E. Flux Evaluation and Time Integration

The flux vectors in Equation (6) can be evaluated numerically using one of several techniques. The technique implemented by Shang is an explicit characteristic-based scheme that produces third-order accuracy. The van Leer's kappa

scheme calculates the flux on a surface of a cell by extrapolating data from adjacent cell centers [10]. The scheme is referred to as a Monotone Upstream-Centered Scheme for Conservation Laws (MUSCL) and is a windward approach that considers the direction of wave propagation. A flux-vector splitting algorithm developed by Steger and Warming [21] is used to calculate the fluxes from the independent variable $\hat{U}$ calculated at the cell faces. The incoming and outgoing electromagnetic waves are split based on the positive and negative sign of the eigenvalue, hence, the name split-flux vectors.

Equation (6), in the temporal or time-stepping domain, can be solved using several techniques, just as in the spatial domain. Shang uses a Runge-Kutta family of single-step multi-stage procedures [13] which gives varying degrees of accuracy. For example, with van Leer's kappa scheme for the flux evaluation, Shang uses a four-stage Runge-Kutta method that produces fourth-order accuracy [10].

F. Boundary Conditions

Shang uses a first-order accurate radiation boundary condition [7-16] in which the incoming flux component is set to zero at the boundary. For the compatibility condition, the fields traveling perpendicular to the boundary are not reflected. For example, in the case of the propagation of a wave from a dipole, the BC is exact since the wave travels along the radial coordinate direction. However, numerical errors can result if the wave is not traveling perpendicular to th : boundary. The coordinate transformation discussed previously increases the component of the wave traveling perpendicular to the outer boundary [12].

A surface boundary condition is implemented on the surface of PEC scatterers. The boundary condition sets the tangential electric field equal to zero and the normal component of the magnetic flux density equal to zero [2-3,8].

G. Green's-Function-Based Near-to-Far Field Transformation

The spatial and time integration of Equation (6) gives time-domain results in the near-field whereas the RCS is a far-field calculation. Green's-function-based transformations allow the scattered fields in the far-field to be easily calculated from the near-field results subsequent to a Fourier transform [22].

The far-field results are obtained by creating a virtual surface around the object. An imaginary surface in the FVTD grid space can serve as a virtual surface. The surface equivalence theorem is applied to the surface to obtain the equivalent time-harmonic electric and magnetic currents and charges. The currents and charges on the virtual surface are then weighted by a free-space Green's function to obtain the far-field E and H fields [22]. The far-field is easily calculated from the far-field scattered E and H fields.

II. Electromagnetic Scattering Results

The RCS using the fourth-order accurate characteristic-based FVTD algorithm, implemented by Shang [7-16], for the ogive and cone-sphere test bodies are discussed [24]. Bistatic and monostatic RCS are presented for each perfect electric conducting (PEC) test body and compared to MoM and empirical data to evaluate the FVTD algorithm and code for CEM.

To analyze the scattering from the ogive, a grid convergent study was performed to obtain the optimum grid point density (GPD) for each coordinate direction (r,θ,φ). The radial direction is approximately orthogonal to the surface and the theta and phi directions correspond to the surface of the object. The grid for the cone-sphere was generated using the optimal GPDs. The RCS results for the cone-sphere confirm the grid requirements obtained for the ogive and validate the FVTD algorithm for another PEC test body.

A. Ogive Electromagnetic Scattering Results

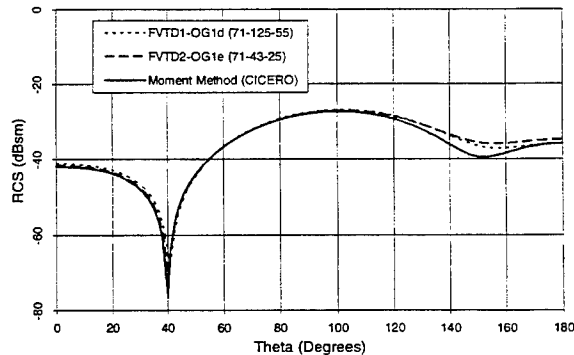Three ogive tests, including several subtests, are labeled with a character

Figure 1: Ogive Bistatic RCS, 1.18 GHz, HH, Fine (71-125-55) vs. Coarse (71-43-25) Grid
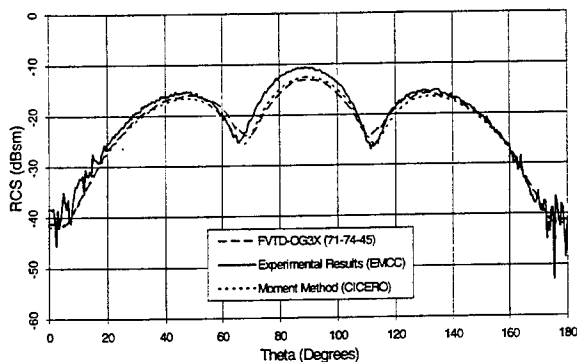
376

Figure 2: Ogive Monostatic RCS, 1.18 GHz, HH

designator. "OG" in the test designator refers to a test for the ogive, and the number in the test designator refers to the test number. The last letter in each test designator refers to the subtest. The subtests are groups of tests that use a specific frequency or grid size. A designator such as OG3X refers to the entire group of subtests.

The RCS for the ogive for each test are compared to MoM RCS results and experimental data for either VV (transmit vertical, receive vertical) or HH (transmit horizontal, receive horizontal) polarization. The first ogive tests, OG1X, use a sinusoid incident wave at 1.18 GHz. Tests OG3X are monostatic calculations at 1.18 GHz. The bistatic RCS for the ogive at 9.0 GHz is test OG4a. For all of the bistatic tests, the angle of incidence is tip-on at 0°.

The bistatic RCS is calculated for the ogive at 1.18 GHz using a sinusoid incident wave. The ogive is one wavelength long at this frequency. The HH polarization RCS is shown in Figure 1 and compares the RCS for the coarse grid (OG1e) to the fine grid (OG1d). The fine grid has a surface grid point density of 80-116 cells/λ and the coarse grid has a grid point density of 22-32 cells/λ. The FVTD results are within 3.0 dB of the MoM data for the coarse grid and for the fine grid are within 2.0 dB of the MoM.

The frequency data for tests OG1d and OG1e were taken from the fourth to the fifth periods. These tests reveal that for 1.18 GHz the transients introduced with the sinusoid incident wave require at least four periods to diminish before frequency data can be taken for the RCS calculations. Taflove [22] recommends that at least four times the electrical length (in periods) is required. The ogive results show that this approximation is appropriate for this frequency; however, fewer periods are used for higher frequencies to obtain accurate data.

In addition to bistatic RCS, the FVTD code can also obtain monostatic data. Multiple simulations must be completed to obtain monostatic data for one frequency as compared to one test for bistatic data. One simulation produces a bistatic plot for 0° to 180°. The simulation produces a monostatic result for only the angle of incidence. To obtain a full monostatic sweep, a bistatic-to-monostatic approximation is used. The approximation requires tests to be completed every 10° and bistatic data completes the monostatic approximation [6]. Tests OG3X are monostatic calculations for the ogive at 1.18 GHz. A test was completed for an angle of incidence every 10° from 0° to 90°. The ogive is symmetric about the xy plane resulting in a symmetric monostatic plot about θ=90°.

The monostatic approximation for HH polarization is plotted in Figure 2. The HH monostatic test used a moderate grid size of (71-74-45) and frequency data was taken from the fifth to the seventh period. The FVTD RCS is plotted against MoM results and empirical data. As can be seen in the plot, the MoM and FVTD results are almost identical and differ from the empirical data by nearly the same value. FVTD results differ from the MoM by no more than 2.5 dB. If the large fluctuations are ignored in the empirical data, the FVTD results are within 3.1 dB of the empirical data.

Further analysis is completed for the ogive using FVTD by running a test, OG4a, for the ogive at 9.0 GHz. The ogive is approximately 7.6 wavelengths long at this frequency. The grid size
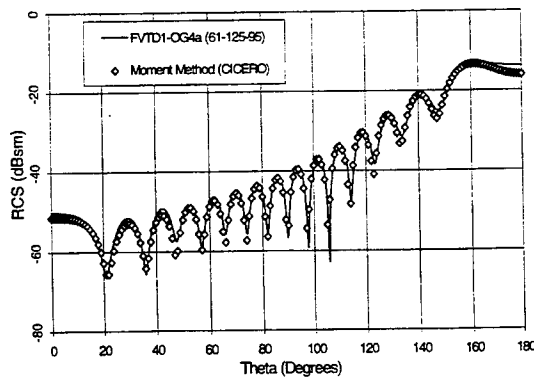

Figure 3: Ogive Bistatic RCS, 9.0 GHz, VV

required for this frequency is much larger (61-125-95). The FVTD results for 9.0 GHz, VV, are shown in Figure 3. The FVTD results are plotted against MoM RCS data. The results are excellent except there are small discrepancies in the backscatter and forward scattering regions. The surface grid point densities (GPD) for these tests are smaller than for 1.18 GHz. The grid point densities in the theta and phi directions are 15.2 cells/λ and 18.8 cells/λ, respectively. The results for the ogive at 1.18 GHz showed that a GPD of at least 22-32 cells/λ gives the best data. These results depict the dependence of the required GPD on the electrical size of the object. The GPD can be 15-20 cells/λ if the electrical length of the object increases.

The 9.0 GHz results for the ogive illustrate the dependence of the length of simulation time (in periods) to the length of the object. At 1.18 GHz, the test had to be at least four times (in periods) the length of the object. The same factor would require

Figure 4: Cone-Sphere Bistatic RCS, 0.869 GHz, VV, Tip-On Incidence

a simulation time of 30 periods for 9.0 GHz. This is not required because, at 9.0 GHz, the ogive is in the optical region. At 9.0 GHz, the diffraction and the traveling waves can be considered to be more of a local phenomena than for 1.18 GHz. This reduces the simulation time for the test to approximately three times the length of the object (in periods) instead of four.

B. Cone-Sphere Electromagnetic Scattering Results

The RCS calculations for the cone-sphere provide further validation of the FVTD code and algorithm. The cone-sphere is a common RCS test body but the narrow cone portion and the sphere cap provide a unique body for analysis. At lower frequencies, the scattering from the cone-sphere can be modeled as traveling waves along the narrow cone, creeping waves around the sphere cap, and diffraction from the tip. Three tests were completed which include several subtests with designators "CS" instead of "OG" to refer to the cone-sphere.

The electromagnetic scattering via FVTD are compared to MoM RCS results and experimental data for VV and HH polarization. The cone-sphere is two wavelengths long at 0.869 GHz. An incident angle of 0° corresponds to incidence on the cone-sphere along the axis of symmetry directly onto the sphere-cap. Tests CS2X are bistatic tests at 0.869 GHz with a sinusoid incident wave at 180° (tip-on incidence). Tests CS3X are tests for the monostatic calculations at 0.869 GHz. The monostatic RCS is computed every 10° from 0° to 180°, and bistatic data completes the monostatic plot. CS5a is a bistatic simulation for the cone-sphere at 3.0 GHz using a sinusoid incident wave at tip-on incidence (θ=180).

FVTD RCS data for tip-on incidence were obtained in test OG2X. The incident wave propagates toward the cone-sphere from 180°. The accuracy of the bistatic RCS depends on the correct calculation of creeping waves, traveling waves, and tip diffraction. The VV polarization case is shown in Figure 4. The finer grid, CS2b,
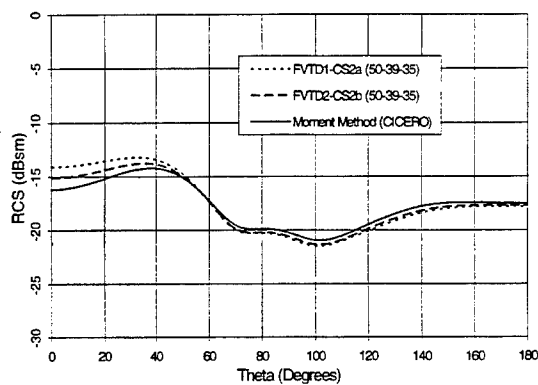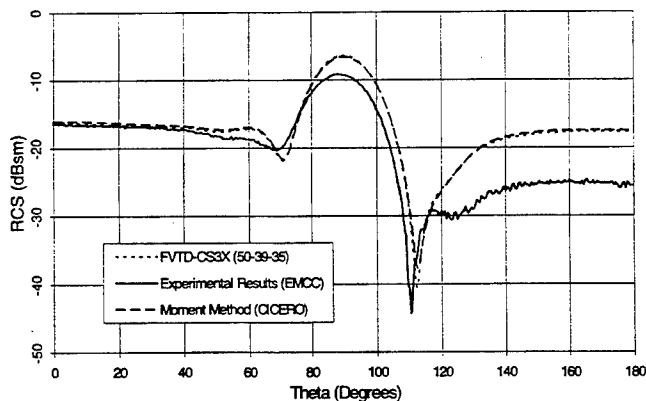

Figure 5: Cone-Sphere Monostatic RCS, 0.869 GHz, HH

produces much better results than the grid with the coarser spacing (CS2a) in the radial direction. The forward scatter results ($\theta=0°$) are only accurate if the fine grid is used (CS2b).

The monostatic RCS data for the cone-sphere, HH polarization, is plotted in Figure 5. The FVTD and MoM RCS match each other much closer than they match the empirical data. Volakis [24] states that errors exist in the experimental data, especially in the forward sector (120°-180°). The MoM and FVTD results are almost identical for every location except for several of the bistatic-to-monostatic approximation junctions. The agreement between the techniques suggest that the empirical data is not correct from 120°-180°.

Figure 6: Cone-Sphere Bistatic RCS, 3.0 GHz, VV, Tip-On Incidence

The bistatic RCS for the cone-sphere at 3.0 GHz is presented. Test CS5a is the tip-on incidence test. The length of the cone-sphere is 6.9 wavelengths at this specific frequency. The cone-sphere at this frequency is in the optical region, just as the ogive was for 9.0 GHz. The electromagnetic phenomena, such as diffraction, creeping waves, and traveling waves, are local and the test time (in periods) is not as long as for lower frequencies.

Figure 6 is the VV polarization RCS for tip-on incidence (CS5a). The FVTD results are almost identical to the MoM RCS results. The FVTD RCS data for the forward scatter region, from the sphere-cap ($\theta=0°$), differs by 1.0 dB from the MoM data. The FVTD data for the backscatter region ($\theta=180°$) from the tip differs by 1.2 dB from the MoM RCS results. As seen with the ogive, errors in the FVTD RCS calculations first occur at the tips.
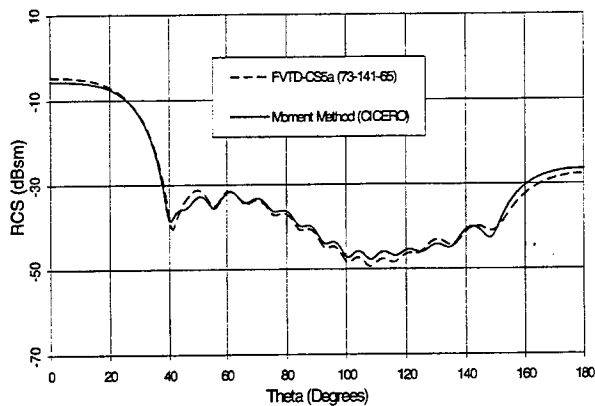
III. Conclusions

The electromagnetic scattering and RCS results for the ogive and cone-sphere test bodies were presented. Bistatic and monostatic RCS results were compared to MoM and empirical RCS results.

The FVTD RCS for the ogive is excellent compared to MoM and empirical data. Several bistatic and monostatic tests at various frequencies showed that a grid point density (GPD) on the surface of approximately 22-32 cells/λ produced the best results for lower frequencies (1.18 GHz) and could be reduced to 15.2-18.8 cells/λ for larger frequencies (9.0 GHz). Shankar [17] reports a GPD requirement of 30-50 cells/λ for objects with edges or tips, like the ogive, for his second-order accurate algorithm. The lower GPD requirement for Shang's fourth-order accurate FVTD code is consistent with the order of accuracy of the algorithms. As the GPD decreases, the errors in the RCS occur first in the backscatter and forward scatter direction as would be expected because of the diffraction at the tips of the ogive. As the electrical size of the object increases, traveling waves and diffraction contribute less to the RCS. These phenomena become local and the grid point density does not have to be as large to accurately compute the propagation of the wave. The bistatic tests for 1.18 GHz differed from the MoM results by no more than 3.0 dB. The FVTD calculations for the monostatic tests were compared to empirical results in addition to MoM results. The FVTD results are within 2.5 dB of the MoM monostatic values and within 3.1 dB of the empirical results.

The bistatic and monostatic cone-sphere results confirm the accuracy and grid requirements for the ogive. For 0.869 GHz, the surface grid spacing required is 22-26 cells/λ. The results differed by no more than 1.6 dB from the MoM results and 0.5 dB from the empirical results. The bistatic RCS for 3.0 GHz differed by no more than 2.1 dB from the MoM results. Accurate results required a surface grid spacing of 14-26 cells/λ to accurately consider diffraction and traveling waves. These grid point density requirements confirm the ogive conclusion that a lower grid point density is needed for electrically larger objects since diffraction and traveling waves contribute less to the RCS.

The electromagnetic phenomena which occurs from the surfaces of an ogive and cone-sphere are challenging for many computational codes. The smooth curved surfaces, tips, and diffraction points are surface characteristics which can pose difficulties for accurately computing scattering results. Based on the FVTD results for the ogive and cone-sphere, the

electrical size of the object is critical when determining grid size and spacing. For a small object, 1-2λ, the grid spacing must be 22-25 cells/λ on the surface. For an object which is electrically larger (7λ-8λ), the surface grid spacing may be reduced to 15-19 cells. These findings are critical for the expansion of the code to studying electrically larger objects such as airfoils and aircraft shaped bodies. A grid must be generated which will incorporate these features for a particular frequency.

Acknowledgments

Bibliography

1. Constantine A. Balanis, *Advanced Engineering Electromagnetics*. New York: John Wiley & Sons, 1989.

2. D.C. Blake and T.A. Buter, "Domain Decomposition Strategies for Solving Hyperbolic Systems on Distributed Parallel Architectures," *AIAA Paper 96-0834*. 34th Aerospace Sciences Meeting and Exhibit, Reno NV, Jan. 1996.

3. D.C. Blake and T.A. Buter, "Overset Grid Methods Applied to a Finite-Volume Time-Domain Maxwell Equation Solver," *AIAA Paper 96-0834*. 27th Fluid Dynamics, Plasmadynamics and Lasers Conference, New Orleans LA, June 1996.

4. J.W. Crispin, Jr. and K.M. Siegel, *Methods of Radar Cross Section Analysis*. New York: Academic Press, 1968.

5. Karl S. Kunz and Raymond J. Luebbers, *The Finite Difference Time Domain Method for Electromagnetics*. Boca Raton: CRC Press, 1993.

6. Michael J. Schuh, Alex C. Woo, and Michael P. Simon, "The Monostatic/Bistatic Approximation," *IEEE Antennas and Propagation Magazine*, vol. 36, no. 4, pp. 76-78, Aug. 1994.

7. J.S. Shang, "A Characteristic-Based Algorithm for Solving 3-D, Time-Domain Maxwell Equations," *AIAA Paper 92-0452*. 30th Aerospace Sciences Meeting and Exhibit, Reno NV, Jan. 1992.

8. J.S. Shang, "Characteristic-Based Algorithms for Solving Maxwell's Equations in the Time-Domain," *IEEE Antennas and Propagation Magazine*, vol. 37, no. 3, pp. 15-25, June 1995.

9. J.S. Shang, "A Fractional-Step Method for Solving 3-D Time-Domain Maxwell Equations," *Journal of Computational Physics*, vol. 118, pp. 109-119, 1995.

10. J.S. Shang and Robert M. Fithen, "A Comparative Study of Numerical Algorithms for Computational Electromagnetics," *AIAA Paper 94-2410*. 25th AIAA Plasmadynamics and Lasers Conference, Colorado Springs CO, June 1994.

11. J.S. Shang, D.A. Calahan, and B. Vikstrom, "Performance of a Finite Volume CEM Code on Multicomputers," *AIAA Paper 94-0236*. 32nd Aerospace Sciences Meeting and Exhibit, Reno NV, Jan. 1994.

12. J.S. Shang and D. Gaitonde, "Characteristic-Based Time-Dependent Maxwell Equations Solvers on a General Curvilinear Frame," *AIAA Paper 93-3178*. 24th AIAA Plasmadynamics and Laser Conference, Orlando FL, July 1993.

13. J.S. Shang and D. Gaitonde, "On High Resolution Schemes for Time-Dependent Maxwell Equations," *AIAA Paper 96-0832*. 34th Aerospace Sciences Meeting and Exhibit, Reno NV, Jan. 1996.

14. J.S. Shang and D. Gaitonde, "Scattered Electromagnetic Field of a Reentry Vehicle," *AIAA Paper 94-0231*. 32nd Aerospace Sciences Meeting and Exhibit, Reno NV, Jan. 1996.

15. J.S. Shang and S.J. Scherr, "Time-Domain Electromagnetic Scattering Simulations on Multicomputers," *AIAA Paper 95-1966*. 26th AIAA Plasmadynamics and Lasers Conference, San Diego CA, June 1995.

16. J.S. Shang and C.C. Shang, "Concurrent Computation of Electromagnetic Phenomena on the Paragon," *AIAA Paper 95-0592*. 33rd Aerospace Sciences Meeting and Exhibit, Reno NV, Jan. 1995.

17. Vijaya Shankar, "Computational Electromagnetics (CEM) - Development of a Finite-Volume, Time-Domain Solver for Maxwell's Equations," Report NAWCADWAR-93052-60, Contract N62269-90-C-0257, Thousand Oaks, CA: Rockwell International Science Center, 1993.

18. Vijaya Shankar, "Research to Application - Supercomputing Trends for the 90's, Opportunities for Interdisciplinary Computations," *AIAA Paper 91-0002*. 29th Aerospace Sciences Meeting, Reno NV, Jan. 1991.

19. Vijaya Shankar, W.F. Hall, and A.H. Mohammadian, "A CFD-based Finite-Volume Procedure for Computational Electromagnetics - Interdisciplinary Applications of CFD Methods," *AIAA Paper 89-1987*. 9th AIAA Computational Fluid Dynamics Conference, Buffalo NY, June 1989.

20. Vijaya Shankar, W.F. Hall, and A.H. Mohammadian, "A Time-Domain, Finite-Volume Treatment for the Maxwell Equations," *Electromagnetics*, vol. 10, pp. 127-145, 1990.

21. Joseph L. Steger and R.F. Warming, "Flux Vector Splitting of the Inviscid Gasdynamic Equations with Application to Finite-Difference Methods," *Journal of Computational Physics*, vol. 40, pp. 263-293, 1981.

22. Allen Taflove, *Computational Electrodynamics: The Finite-Difference Time-Domain Method*. Boston: Artech House, 1995.

23. Bram van Leer, "Flux-Vector Splitting For the Euler Equations," Eighth International Conference on Numerical Methods in Fluid Dynamics, Berlin: Springer-Verlag, pp. 507-512, 1982.

24. John L. Volakis, Alex C. Woo, Helen T.G. Wang, Michael J. Schuh, and Michael L. Sanders, "Benchmark Radar Targets for the Validation of Computational Electromagnetics Programs," *IEEE Antennas and Propagation Magazine*, vol. 35, no. 1, pp. 84-89, Feb. 1993.

COMPARISON OF EQUATIONS FOR THE FDTD SOLUTION
IN ANISOTROPIC AND DISPERSIVE MEDIA *

G. J. Burke and D. J. Steich
Lawrence Livermore National Laboratory
P.O. Box 5504, L-156, Livermore, CA 94550

I. Introduction

The finite-difference time-domain (FDTD) solution procedure developed by Yee [1], has in recent years been extended to dispersive and anisotropic media to handle materials such as magnetized ferrites and plasmas. The solution for dispersive media has been accomplished through a recursive update of a convolution integral in the constitutive relations for the fields [2], [3], [4], [5], by numerical solution of the differential equation form of the constitutive relations [6], [7] and using Z transforms [8]. The extension of the recursive convolution (RC) method to gyrotropic materials, which are both dispersive and anisotropic, was developed in [9] and [10] where it was applied to 1D problems. The anisotropic media results in coupling of field components and the need for averaging to obtain field components at locations where they are not directly available in the Yee formulation. The RC solution for gyrotropic media is reviewed in [4], and results validating the method are also given. The solution was developed for 3D Gyrotropic materials in [11] for a ferrite with biasing field in an arbitrary direction, and the issue of minimizing the storage added by the recursive convolution evaluation was also considered there. A piecewise linear RC method has also been developed that is more accurate than the pulse approximation considered here [12].

In published work on dispersive material there are some differences in the equations resulting from application of the RC method. The time derivative of the convolution integral can involve the derivative of the field, or integrating by parts can put the derivative on the susceptibility function. Reduction of these two results to discrete form leads to slightly different update equations. Also, the choice of the evaluation time and integration limit of the convolution integral can lead to differences in the discrete update equation. These different forms of the solution are compared here for accuracy and stability for time increments approaching the Courant limit. It is found that slightly greater accuracy and greater stability are obtained with the convolution evaluated at the time of the equation, a half step before the field being evaluated, using a pulse approximation of the integral ending in a half pulse. Modifications of this result lead to somewhat simpler but less stable equations. In the case that the susceptibility function starts at zero for time equal to zero the equations for anisotropic and dispersive material simplify greatly, requiring only the addition of the RC term to the normal FDTD equations, without further coupling of the field components. While 3D solutions are considered here, the accuracy and stability are demonstrated for the 1D problem of normal incidence on a slab of ferrite or plasma with biasing field in the direction of propagation, since simple analytic solutions are available for this problem.

II. Equations for Gyrotropic Media

The solution for anisotropic and dispersive magnetic material will be considered here. The magnetic field update equation for such material is obtained by combining the Maxwell's equation

$$\frac{\partial \mathbf{B}}{\partial t} = -\nabla \times \mathbf{E} \tag{1}$$

and the equation relating $\mathbf{B}$ and $\mathbf{H}$ in convolution form

$$\mathbf{B}(t) = \mu_0 \left[\mathbf{H}(t) + \int_0^t \bar{\bar{\chi}}_m(t-\tau) \cdot \mathbf{H}(\tau)\, d\tau \right] \tag{2}$$

where $\bar{\bar{\chi}}_m(t)$ is the susceptibility tensor representing the impulse response of the material. In the usual convention, equation (1) is solved together with the equation $\epsilon \partial \mathbf{E}/\partial t = \nabla \times \mathbf{H}$ with $\mathbf{E}$ evaluated at integral time steps $n\Delta t$, and $\mathbf{H}$ and $\mathbf{B}$ evaluated at half time steps $(n+1/2)\Delta t$. The time derivatives in Maxwell's equations are approximated with central differences so that $\mathbf{E}$ and $\mathbf{H}$ can be computed in a leap-frog scheme in time.

Equation (2) can be reduced to discrete form by assuming that $\mathbf{H}(t)$ is constant with value $\mathbf{H}^{n+1/2}$ for $n\Delta t < t < (n+1)\Delta t$ with the result

$$
\begin{aligned}
\mathbf{B}^{n+1/2} =\mu_0 &\left[\mathbf{H}^{n+1/2} + \sum_{i=0}^{n-1} \int_{i\Delta t}^{(i+1)\Delta t} \bar{\bar{\chi}}_m \left[(n+\tfrac{1}{2})\Delta t - \tau \right] d\tau \cdot \mathbf{H}^{i+1/2} \right.\\
&\left. + \int_{n\Delta t}^{(n+1/2)\Delta t} \bar{\bar{\chi}}_m \left[(n+\tfrac{1}{2})\Delta t - \tau \right] d\tau \cdot \mathbf{H}^{n+1/2} \right]\\
=\mu_0 &\left[\mathbf{H}^{n+1/2} + \sum_{i=0}^{n-1} \int_{(n-i-1/2)\Delta t}^{(n-i+1/2)\Delta t} \bar{\bar{\chi}}_m(\tau')\, d\tau' \cdot \mathbf{H}^{i+1/2} + \int_0^{\frac{1}{2}\Delta t} \bar{\bar{\chi}}_m(\tau')\, d\tau' \cdot \mathbf{H}^{n+1/2} \right].
\end{aligned}
$$

If the integrals over $\bar{\bar{\chi}}_m(\tau')$ are also approximated by sums of pulses the result for $\mathbf{B}^{n+1/2}$ is

$$\mathbf{B}^{n+1/2} = \mu_0 \left[\left(\bar{\bar{\mathbf{I}}} + \tfrac{1}{2}\Delta t\, \bar{\bar{\chi}}_m(0) \right) \cdot \mathbf{H}^{n+1/2} + \Delta t \sum_{i=0}^{n-1} \bar{\bar{\chi}}_m\left[(n-i)\Delta t \right] \cdot \mathbf{H}^{i+1/2} \right].$$

With a similar representation for $\mathbf{B}^{n-1/2}$ the central difference approximation of $\partial \mathbf{B}(t)/\partial t$ in equation (1) leads to the update equation

$$\mathbf{H}^{n+1/2} = \left[\bar{\bar{\mathbf{I}}} + \frac{\Delta t}{2} \bar{\bar{\chi}}_m(0) \right]^{-1} \cdot \left\{ \left[\bar{\bar{\mathbf{I}}} - \frac{\Delta t}{2} \bar{\bar{\chi}}_m(0) \right] \cdot \mathbf{H}^{n-1/2} - \Delta t\, \boldsymbol{\Psi}^n - \frac{\Delta t}{\mu_0} \nabla \times \mathbf{E}^n \right\} \tag{3}$$

where

$$\boldsymbol{\Psi}^n = \sum_{i=0}^{n-1} \left[\bar{\bar{\chi}}_m[(n-i)\Delta t] - \bar{\bar{\chi}}_m[(n-i-1)\Delta t] \right] \cdot \mathbf{H}^{i+1/2}. \tag{4}$$

In the recursive convolution solution the elements of the susceptibility tensor are sums of exponentials, $\chi_{ij} = \sum_\ell a_{ij\ell} e^{b_\ell t}$, in which case $\boldsymbol{\Psi}^n$ in (4) can be updated by a simple recursion relation

$$\boldsymbol{\Psi}_\ell^{n+1} = e^{b_\ell \Delta t} \boldsymbol{\Psi}_\ell^n + (e^{b_\ell \Delta t} - 1) \bar{\bar{a}}_\ell \cdot \mathbf{H}^{n+1/2}, \qquad \boldsymbol{\Psi}_\ell^0 = 0 \tag{5}$$

383

and $\Psi^{n+1} = \sum_\ell \Psi_\ell^{n+1}$.

A result differing somewhat from equation (3) can be obtained by evaluating the derivative of equation (2) as

$$\frac{\partial}{\partial t}\mathbf{B}(t) = \mu_0 \left[\frac{\partial}{\partial t}\mathbf{H}(t) + \bar{\bar{\chi}}(t) \cdot \mathbf{H}(0) + \int_0^t \bar{\bar{\chi}}(\tau) \cdot \frac{\partial}{\partial t}\mathbf{H}(t-\tau)\, d\tau \right] \tag{6}$$

or, integrating by parts, as

$$\frac{\partial}{\partial t}\mathbf{B}(t) = \mu_0 \left[\frac{\partial}{\partial t}\mathbf{H}(t) + \bar{\bar{\chi}}(0) \cdot \dot{\mathbf{H}}(t) + \int_0^t \frac{d}{dt}\bar{\bar{\chi}}(t-\tau) \cdot \mathbf{H}(\tau)\, d\tau \right]. \tag{7}$$

Converting equation (6) to discrete form with a pulse approximation of the integral leads to a result close to that of equation (3). Starting with equation (7) and representing $\partial \mathbf{H}(t)/\partial t$ with a central difference and $\bar{\bar{\chi}}(0) \cdot \mathbf{H}(n\Delta t)$ with an average of $\mathbf{H}$ from times $(n-1/2)\Delta t$ and $(n+1/2)\Delta t$ leads to an equation similar to (3), but with Ψ^n replaced by $\Delta t\, \Psi'^n$ where the prime indicates a derivative and

$$\Psi'^n = \sum_{i=0}^{n-1} \bar{\bar{\chi}}'_m[(n - i - \tfrac{1}{2})\Delta t] \cdot \mathbf{H}^{i+1/2}.$$

Somewhat different results can also be obtained for equation (3) from different interpretations of the pulse approximation of the integral, or in the equation derived from equation (7) by using the value at the forward or back time step rather than the average for $\mathbf{H}(n\Delta t)$. In fact, adding the same small quantity to both square-bracketed terms in (3) results in a second-order change in the product multiplying $\mathbf{H}^{n-1/2}$ and relatively small changes in the solution. Hence equation (3) can be reduced to

$$\mathbf{H}^{n+1/2} = \left[\bar{\bar{\mathbf{I}}} + \Delta t \bar{\bar{\chi}}_m(0) \right]^{-1} \cdot \left(\mathbf{H}^{n-1/2} - \Delta t \Psi^n - \frac{\Delta t}{\mu_0} \nabla \times \mathbf{E}^n \right) \tag{8}$$

by adding $(\Delta t/2)\bar{\bar{\chi}}(0)$ to both coefficients, or by subtracting the same quantity

$$\mathbf{H}^{n+1/2} = \left[\bar{\bar{\mathbf{I}}} - \Delta t \bar{\bar{\chi}}_m(0) \right] \cdot \mathbf{H}^{n-1/2} - \Delta t \Psi^n - \frac{\Delta t}{\mu_0} \nabla \times \mathbf{E}^n. \tag{9}$$

These modifications of equation (3) result in small errors when the elements of $\Delta t\bar{\bar{\chi}}(0)$ have magnitudes much less than one, as demonstrated in the next section, but the solutions show increased late-time instability when Δt is near the Courant limit. Equation (9) seems to be a nicer form for solving, but it still mixes values of $\mathbf{H}^{n-1/2}$ in averaging for field components in the product with the tensor. The evaluation of a single vector component of the product of a tensor and $\nabla \times \mathbf{E}$ involves 36 field components in the Yee cell, but this can be reduced to 20 components by combining and canceling terms.

When $\bar{\bar{\chi}}(0) = 0$, which occurs in materials such as Lorentz dielectrics, equations (3), (8) and (9) all reduce to the simpler and easier to use form

$$\mathbf{H}^{n+1/2} = \mathbf{H}^{n-1/2} - \Delta t \Psi^n - \frac{\Delta t}{\mu_0} \nabla \times \mathbf{E}^n. \tag{10}$$

The above discussion has assumed total fields. The generalization of equation (3) for separate incident and scattered fields is

$$\mathbf{H}_s^{n+1/2} = \left[\bar{\bar{\mathbf{I}}} + \frac{\Delta t}{2}\bar{\bar{\chi}}_m(0)\right]^{-1} \cdot \left\{\left[\bar{\bar{\mathbf{I}}} - \frac{\Delta t}{2}\bar{\bar{\chi}}_m(0)\right] \cdot \mathbf{H}_s^{n-1/2} - \Delta t \Psi_s^n\right.$$
$$\left. - \Delta t \frac{d}{dt}\int_0^t \bar{\bar{\chi}}_m(\tau)\cdot\mathbf{H}_i(t-\tau)\,d\tau\bigg|_{t=n\Delta t} - \frac{\Delta t}{\mu_0}\nabla\times\mathbf{E}_s^n\right\}$$

where $\mathbf{H}_i$ is the incident field, which satisfies Maxwell's equations for free space everywhere in the problem space, and

$$\Psi_s^n = \sum_{i=0}^{n-1}\left[\bar{\bar{\chi}}_m[(n-i)\Delta t] - \bar{\bar{\chi}}_m[(n-i-1)\Delta t]\right]\cdot\mathbf{H}_s^{i+1/2}.$$

The convolution integral with $\mathbf{H}_i$ can be evaluated analytically for some special incident field functions [5], or otherwise is evaluated numerically along with the scattered field.

III. Results

The FDTD solution for gyrotropic media was validated for a plane wave normally incident on a ferrite slab with the biasing magnetic field in the direction of propagation, along the z axis. This problem was also solved in [4] and [9], and is chosen because the reflection and transmission coefficients for the slab are available in simple analytic form. In this case a 3D code was written, using the equations from the preceding section. Codes solving equations (3), (8) and (9) were compared for accuracy and stability with time increments approaching the Courant limit. Since a plane wave propagating through the ferrite in the direction of the biasing field splits into right-hand and left-hand circularly polarized waves with different propagation constants, the problem space was terminated in even-symmetry boundary conditions in both x and y boundary planes. In the direction of propagation z the problem space was made large enough to gate out reflections, thus eliminating the boundary conditions as a source of error.

The components of the susceptibility tensor $\bar{\bar{\chi}}(t)$ for the ferrite are

$$\chi_{11}(t) = \chi_{22}(t) = \text{Re}\left\{\frac{\omega_m}{\alpha+j}\exp\left[\frac{-\omega_0 t}{\alpha+j}\right]\right\}U(t)$$

$$\chi_{12}(t) = -\chi_{21}(t) = \text{Re}\left\{\frac{j\omega_m}{\alpha+j}\exp\left[\frac{-\omega_0 t}{\alpha+j}\right]\right\}U(t).$$

where $U(t)$ is the unit step function. The parameters of the ferrite modeled here were

$$\omega_0 = (2\pi)\cdot 20\times 10^9 \text{ rad/s}$$
$$\omega_m = (2\pi)\cdot 10\times 10^9 \text{ rad/s}$$
$$\alpha = 0.1$$

Results from solving equation (3) for this ferrite with $\Delta x = 75(10^{-6})$ m and $\Delta t = \Delta x/(2c\sqrt{3})$ with 6000 time steps are shown in Figure 1. The source was a Gaussian-pulse plane wave with

full-width-half-max equal to 0.001 m. Since the solution is uniform in the x and y directions the problem was solved with 3 cells in x and y and 4000 cells in z to eliminate the radiating boundaries, and the ferrite filled 50 cells ($k = 2000$ through 2049) for a thickness of 0.00375 m. The reflection and transmission coefficients were obtained by numerical deconvolution of the reflected fields, with right and left-hand circular polarizations obtained as

$$R_{\mathrm{rcp}}(\omega) = R_x(\omega) + jR_y(\omega)$$

and

$$R_{\mathrm{lcp}}(\omega) = R_x(\omega) - jR_y(\omega).$$

In Figure 1 the magnitudes of the numerically determined reflection and transmission coefficients for left-hand polarization are compared with the exact results, and the relative errors in the complex quantities are also shown. The error increases with frequency due mainly to dispersion in the FDTD mesh. Although these results were obtained with a 3D code for which the Courant limit is $\Delta t \leq \Delta x/c\sqrt{3}$ the problem is actually 1D. As a result Δt can be extended to the 1D Courant limit of $\Delta x/c$, and the resulting dispersion errors in solving equation (3) are reduced by one to two orders of magnitude above about 200 GHz.

The errors from solving the simpler equations (8) and (9) are compared with the errors from equation (3) in Figure 2 for $\Delta t = \Delta x/2c\sqrt{3}$. Below about 100 GHz equations (8) and (9) yield slightly higher error than (3). Above 100 GHz the results of equation (8) have slightly lower error than (3) for reflected field while all errors become the same for transmitted field. Solving equations (8) or (9) at the Courant limit of $\Delta t = \Delta x/c$ resulted in a rapid blowup in the ferrite, as shown in Figure 3. Equation (3) also became unstable at late time with $\Delta t = \Delta x/c$, but the instability did not become significant until after about 4000 time steps, which was late enough to get useful results. The fields plotted in Figure 3 were at 60 cells in front of the ferrite slab. When the solution of equation (8) was stopped at $t = 0.15$ ns the field in the ferrite was over 10^{13}. With $\Delta t = \Delta x/c\sqrt{3}$ equation (8) still showed an instability at a reduced rate, as shown in Figure 4. No significant instability was seen in equation (3) at this Δt. Equation (9) showed a stability close to that of equation (8). The equation derived with using equation (7), which was used in [13], yielded about a factor of two lower error than equation (3) below 50 GHz and the errors were identical at higher frequencies. Stability of this equation was also similar to (3).

IV. Conclusion

The recursive-convolution solution for anisotropic and dispersive media was seen to yield accurate results for reflection from ferrite slabs up to a frequency limit set by the sampling interval. Depending on the application, the results shown might be considered usable up to about 300 GHz, which corresponds to about 13 cells per wavelength. Results at still higher frequencies might be usable when a time delay or frequency shift due to dispersion can be tolerated.

Several different forms of the update equations were considered which can result from different approximations in reducing the continuous equations to discrete form. Equation (3) and the alternate form derived with equation (7), and used in [13], result from direct application of the pulse approximations of the fields and susceptibilities, and differ only in the way that the time derivative of the convolution integral is approximated. Equations (8) and (9) are similar to equation (3) with the limit of the convolution interval shifted by a half time step. These

equations correspond to the different forms for a conductive medium when the field multiplying the conductivity is taken as the forward or back value in time or the average. Equation (3) was found to be more stable than (8) or (9), and slightly more accurate at low frequencies. Since equation (9) does not involve a tensor multiplying the curl operation it could be considerably faster to evaluate.

References

[1] K. S. Yee, "Numerical solution of initial boundary value problems involving Maxwell's equations in isotropic media," *IEEE Trans. Antennas Propagat.*, Vol. AP-14, pp. 302-307, May 1966.

[2] R. J. Luebbers, F. P. Hunsberger, K. S. Kunz, R. B. Standler and M. Schneider, "A frequency-dependent finite-difference time-domain formulation for dispersive materials," *IEEE Trans. Electromagn. Compat.*, Vol. EMC-32, pp. 222-227, August 1990.

[3] R. J. Luebbers and F. P. Hunsberger, "FDTD for Nth-Order Dispersive Media," *IEEE Trans. Antennas Propagat.*, Vol. AP-40, pp. 1297-1301, November 1992.

[4] K. S. Kunz and R. J. Luebbers, *The Finite Difference Time Domain Method for Electromagnetics.*, CRC Press, Boca Raton, 1993.

[5] R. Luebbers, D. Steich and K. Kunz, "FDTD calculation of scattering from frequency-dependent materials," *IEEE Trans. Antennas Propagat.*, Vol. AP-41, pp. 1249-1257, September 1993.

[6] T. Kashiwa and I. Fukai, "A treatment of the dispersive characteristics associated with electronic polarization," *Microwave Opt. Technol. Lett.*, Vol. 3, No. 6, p. 203, 1990.

[7] R. Joseph, S. Hagness and A. Taflove, "Direct time integration of Maxwell's equations in linear dispersive media with absorption for scattering and propagation of femtosecond electromagnetic pulses," *Opt. Lett.*, Vol. 16, no. 18, p. 1412, 1991.

[8] D. M. Sullivan, "A Frequency-Dependent FDTD Method for Biological Applications," *IEEE Trans. Microwave Theory Tech.*, Vol. 40, pp. 532-539, 1992.

[9] F. P. Hunsberger, "Extension of the finite-difference time-domain method to gyrotropic media," Ph. D. Thesis, Pennsylvania State University, 1991.

[10] F. Hunsberger, R. Luebbers and K. Kunz, "Finite-Difference Time-Domain Analysis of Gyrotropic Media — I: Magnetized Plasma," *IEEE Trans. Antennas Propagat.*, Vol. AP-40, pp. 1489-1495, December 1992.

[11] J. Schuster and R. Luebbers, " Application of the FDTD method to three-dimensional propagation in a magnetized ferrite," *Proceedings of the 12th Annual Review of Progress in Applied Computational Electromagnetics*, Monterey, CA, March 1996.

[12] D. F. Kelley and R. J. Luebbers, " The Piecewise Linear Recursive Convolution Method for Incorporating Dispersive Media into FDTD," *Proceedings of the 11th Annual Review of Progress in Applied Computational Electromagnetics*, Monterey, CA, March 1995.

[13] J. F. DeFord, G. Kamin, G. D. Craig and L. Walling, "Dispersive soft ferrite models for time domain simulation and their application to accelerator component modeling," Lawrence Livermore National Laboratory, UCRL-JC-109495-Rev 1, 1993.
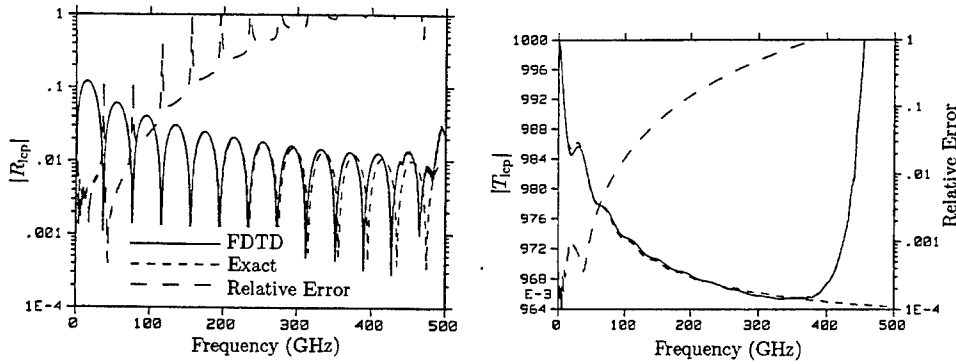
Fig. 1. Magnitudes of the left-hand polarized reflection and transmission coefficients for normal incidence of a plane wave on a ferrite slab from the FDTD solution are compared with the exact solutions. The relative errors in the complex quantities are also shown.
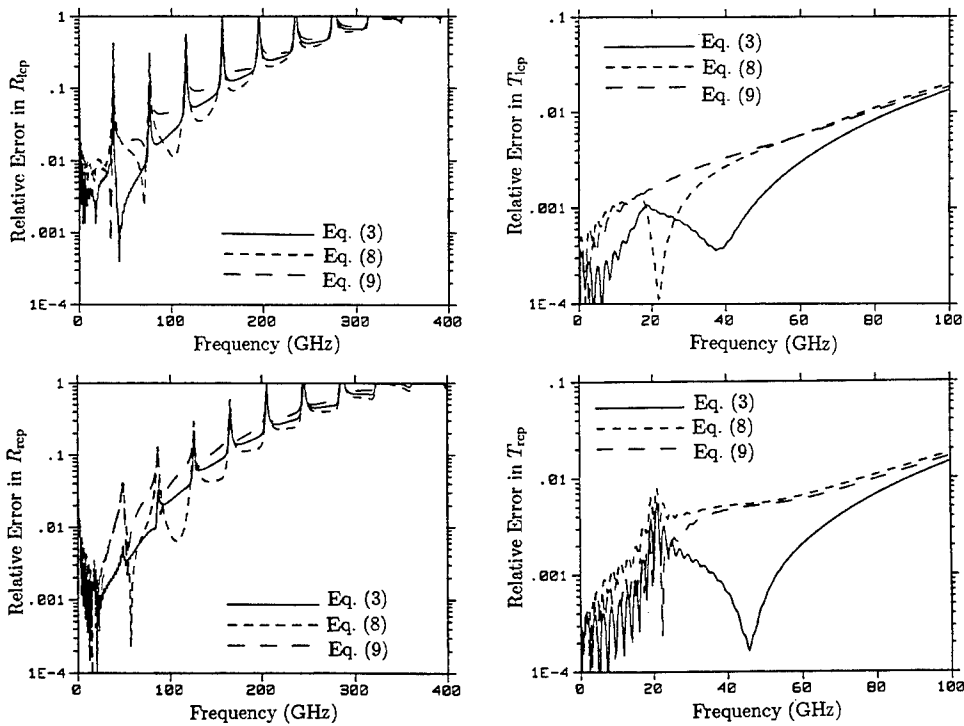

Fig. 2. Relative errors in the complex reflection and transmission coefficients from solving equations (3), (8) and (8) for normal incidence on a ferrite slab with $\Delta t = \Delta x / 2c\sqrt{3}$.
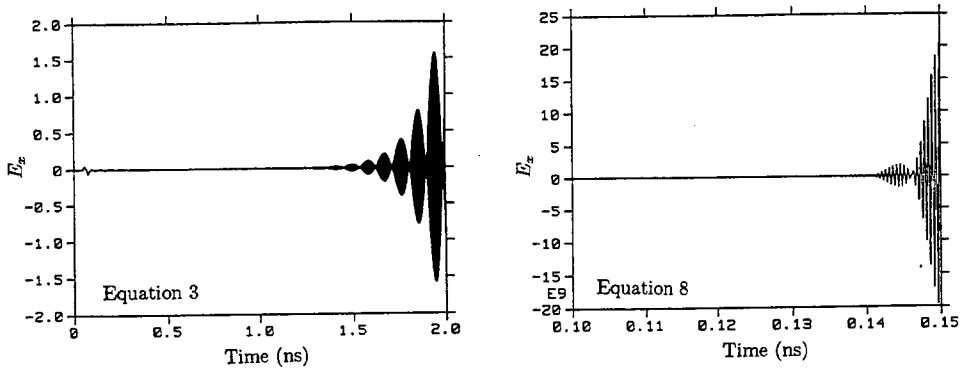
Fig. 3. Electric field in front of the ferrite slab showing the difference in stability of equations (3) and (8) solved at the 1D Courant limit of $\Delta t = \Delta x/c$.
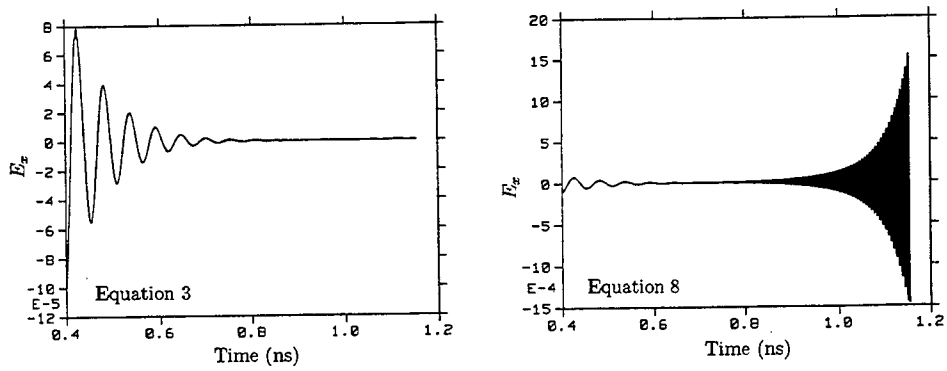

Fig. 4. Electric field in front of the ferrite slab showing the difference in stability of equations (3) and (8) solved at a time step of $\Delta t = \Delta x/c\sqrt{3}$.

A NEAR-FIELD TO NEAR-FIELD TRANSFORMATION FOR STEADY-STATE FDTD

K. A. Lysiak[1] and D. H. Werner[2]

[1]Southwest Research Institute, P.O. Drawer 28510, San Antonio, TX 78228-0510
[2]The Pennsylvania State University, Applied Research Laboratory
P.O. Box 30, State College, PA 16804

Abstract - A two-dimensional steady-state near-field transformation is presented which may be used to calculate scattered fields over a large area, thus reducing memory requirements and dispersion errors associated with a direct application of FDTD. The derivation is based on the surface equivalence principle applied in two dimensions. This method is developed to work in conjunction with a scattered-field FDTD formulation and requires the transformed fields to radiate from within the closed FDTD space. For a scattered-field FDTD calculation, the scattered tangential components on the surface are known and the transform application is shown to be straight forward. The FDTD code calculates the scattered near-fields close to the scattering object. These fields are then transformed to the area of interest.

I. INTRODUCTION

A number of applications requiring near-zone scattered fields are of interest. The desired field may be a considerable distance away from the scattering object yet still require a full near field solution. In cases like this, the solution would necessitate extensive computer resources using a standard Finite Difference Time Domain (FDTD) method. An alternative approach to solving such problems is to use a Near Field Transformation (NFT) technique in conjunction with FDTD. This allows the required FDTD space to be considerably smaller, thereby decreasing memory requirements as well as minimizing dispersion errors.

The purpose of the NFT is to provide a method to predict scattered fields outside an FDTD region. There are four combinations of transforms possible; time-domain near-field to far-field, time-domain near-field to near-field, frequency-domain near-field to far-field and frequency-domain near-field to near-field. Many of these techniques have been developed for FDTD [1,2]. For instance, Barth et al. [3] presented both time-domain and frequency-domain far-field techniques. Shlager and Smith [4] more recently presented a time-domain near-field to near-field approach. Luebbers et al. [5] developed a three-dimensional technique for the time-domain near-field to far-field transformation and later published a two-dimensional version of this technique [6]. The transformation introduced in this paper is a two-dimensional frequency-domain near-field to near-field transform similar to the two-dimensional formulation mentioned in [6]. The major difference here is the calculation of frequency-domain near-fields rather than time-domain far-fields.

The FDTD technique is used to calculate the electric and magnetic fields along a closed rectangular path of integration around the aperture boundary surrounding the object. This allows scattered near fields outside the FDTD region to be predicted based on the surface equivalence

principle. The NFT implementation is used to calculate scattered fields outside the FDTD region due to objects contained within the FDTD region. The advantage of the NFT is that it only requires a small FDTD calculation space.

This method enables large area calculations using a desk-top PC rather than a supercomputer. Its original application calculated propagation path loss for a 167 by 667 wavelength area requiring only 100 MBytes of memory [7]. Without this method 40 GBytes of memory would have been required to perform this calculation with acceptable dispersion errors. The method is particularly appealing when evaluation of only a few field points is required.

II. THEORETICAL DEVELOPMENT

This section discusses the derivation based on an application of the surface equivalence theorem (Huygen's principle) to two-dimensional frequency-domain scattering problems. The surface equivalence theorem states that the fields outside an imaginary closed surface may be obtained by determining the appropriate set of electric and magnetic current densities which, when placed over the closed surface, satisfy the boundary conditions [8]. This is accomplished by selecting the current densities in such a way that fields inside the closed surface are zero, whereas outside the surface the fields are equal to the radiation produced by the actual sources. These radiated or scattered fields are determined through integration over the closed surface which requires a knowledge of the tangential components of the fields at the surface. For this reason, the surface equivalence theorem is well suited for application to the FDTD algorithm since the electric and magnetic fields are known at all locations and times throughout the FDTD region.

The derivation begins by considering the full three-dimensional form of the magnetic vector potential $\vec{A}$ due to an electric current density $\vec{J}$. The expression for $\vec{A}$ is given by [8]

$$\vec{A}(x,y,z) = \frac{\mu}{4\pi} \int_V \vec{J}(x',y',z') \frac{e^{-j\beta R'}}{R'} dv' \tag{1}$$

where $R' = \sqrt{(x-x')^2 + (y-y')^2 + (z-z')^2}$ represents the distance between the source point (x',y',z') and the observation point (x,y,z). The propagation constant is $\beta = 2\pi/\lambda$ where λ is the wavelength. Suppose it is assumed that the scattering object extends infinitely along the z-axis and that the current density $\vec{J}$ is independent of z'. Then the following identity

$$\int_{-\infty}^{\infty} \frac{e^{-j\beta R'}}{R'} dz' = -j\pi H_0^{(2)}(\beta R) \tag{2}$$

can be used in order to show that Equation 1 may be written as the surface integral

$$\vec{A}(x,y) = -j \frac{\mu}{4} \int_S \vec{J}(x',y') H_0^{(2)}(\beta R) ds' \tag{3}$$

where $H_0^{(2)}$ is the zero-order Hankel function of the second kind and $R = \sqrt{(x-x')^2 + (y-y')^2}$. Application of the surface equivalence principle requires that the current should be confined to lie on the outer edge of the two-dimensional surface. In this case, Equation 3 can be reduced to a line integral of the form

$$\vec{A}(x,y) = -j \frac{\mu}{4} \oint_C \vec{J}(x',y') \, H_0^{(2)}(\beta R) \, d\ell' \tag{4}$$

An expression for the magnetic field $\vec{H}_e$ may now be obtained from Equation 4 according to

$$\vec{H}_e(x,y) = \frac{1}{\mu} (\vec{\nabla} \times \vec{A}) = -\frac{j}{4} \oint_C \vec{\nabla} \times [\vec{J}(x',y') \, H_0^{(2)}(\beta R)] \, d\ell' \tag{5}$$

where the subscript e denotes the contribution attributed to the electric current density $\vec{J}$. By making use of well-known vector identities, equation 5 can be simplified to an expression for $\vec{H}_e$ given by

$$\vec{H}_e = \frac{j\beta}{4} \oint_C [\hat{R} \times \vec{J}(x',y')] \, H_1^{(2)}(\beta R) \, d\ell' \tag{6}$$

Performing the indicated cross product, yields $\vec{H}_e(x,y) = H_{ez}(x,y) \, \hat{z}$ where

$$H_{ez}(x,y) = \frac{j\beta}{4} \oint_C [(x-x') J_y(x',y') - (y-y') J_x(x',y')] \, \frac{H_1^{(2)}(\beta R)}{R} \, d\ell' \tag{7}$$

The electric field $\vec{E}_e$ is related to the corresponding magnetic field $\vec{H}_e$ through the expression

$$\vec{E}_e(x,y) = \frac{1}{j\omega\varepsilon} (\vec{\nabla} \times \vec{H}_e) \tag{8}$$

Combining Equations 7 and 8 suggests that $\vec{E}_e(x,y) = E_{ex}(x,y) \hat{x} + E_{ey}(x,y) \hat{y}$ where

$$E_{ey}(x,y) = -\frac{1}{j\omega\varepsilon} \frac{\partial H_{ez}}{\partial x} \tag{9}$$

Substituting Equation 7 into 9 and carrying out the required differentiations leads to the following integral representations of the electric field components

$$E_{ey}(x,y) = \frac{\eta}{4} \oint_C \left\{ \beta(x-x') [(x-x') J_y(x',y') - (y-y') J_x(x',y')] \frac{H_2^{(2)}(\beta R)}{R^2} - J_y(x',y') \frac{H_1^{(2)}(\beta R)}{R} \right\} d\ell' \quad (10)$$

where

$$\eta = \sqrt{\frac{\mu}{\epsilon}} \quad (11)$$

and $H_2^{(2)}$ is the second-order Hankel functions of the second kind.

Similar expressions can be derived for the electric field components due to a magnetic current density $\vec{M}$ by starting with the three-dimensional form of the electric vector potential $\vec{F}$ given by

$$\vec{F}(x,y,z) = \frac{\epsilon}{4\pi} \int_V \vec{M}(x',y',z') \frac{e^{-j\beta R'}}{R'} dv' \quad (12)$$

It can easily be shown that Equation 12 may be reduced to the form

$$\vec{F}(x,y) = -j \frac{\epsilon}{4} \oint_C \vec{M}(x',y') H_0^{(2)}(\beta R) d\ell' \quad (13)$$

by following an analogous procedure to that used to derive Equation 4 from 1. An expression for the electric field $\vec{E}_m$ may now be found from $\vec{F}$ by using

$$\vec{E}_m(x,y) = -\frac{1}{\epsilon}(\vec{\nabla} \times \vec{F}) = \frac{j}{4} \oint_C \vec{\nabla} \times [\vec{M}(x',y') H_0^{(2)}(\beta R)] d\ell' \quad (14)$$

where the subscript m denotes the contribution attributed to the magnetic current density $\vec{M}$. If $\vec{J}$ is replaced by $\vec{M}$ in Equation 5, then it follows that Equation 14 may be written as

$$\vec{E}_m(x,y) = -\frac{j\beta}{4} \oint_C [\hat{R} \times \vec{M}(x',y')] H_1^{(2)}(\beta R) d\ell' \quad (15)$$

Performing the indicated cross product yields $\vec{E}_m(x,y) = E_{mx}(x,y) \hat{x} + E_{my}(x,y) \hat{y}$ where

$$E_{my}(x,y) = \frac{j\beta}{4} \oint_C (x-x') \, M_z(x',y') \, \frac{H_1^{(2)}(\beta R)}{R} \, d\ell' \tag{16}$$

The NFT scheme requires that the aperture (or surface) fields be calculated by FDTD. Once the aperture fields have been determined, then Equations 10 and 16 can be used to derive scattered fields outside the FDTD region. The accuracy of this technique depends on the knowledge of the aperture fields. The surface currents $\vec{J}_s$ and $\vec{M}_s$ are related to the aperture fields by $\vec{J}_s = \hat{n} \times \vec{H}_a$ and $\vec{M}_s = -\hat{n} \times \vec{E}_a$ where $\hat{n}$ is the unit normal vector pointing out of the surface. In this paper, the aperture fields are sampled along a rectangular surface positioned 10 cells inside the FDTD region with a sampling resolution of at least 10 cells per wavelength. The choice of a rectangular aperture makes it possible to conveniently discretize Equations 10 and 16 in the following way for the x-faces where $J_{sy}=0$ and:

$$\Delta E_{ey} = -\frac{\eta}{4} \left[\beta(x-x')(y-y') \, \frac{H_2^{(2)}(\beta R)}{R^2} \, J_{sx} \right] \Delta x \tag{17}$$

$$\Delta E_{my} = \frac{j\beta}{4} \left[(x-x') \, \frac{H_1^{(2)}(\beta R)}{R} \, M_{sz} \right] \Delta x \tag{18}$$

and for the y-faces where $J_{sx}=0$

$$\Delta E_{ey} = \frac{\eta}{4} \left[\left\{ \beta(x-x')^2 \, \frac{H_2^{(2)}(\beta R)}{R^2} - \frac{H_1^{(2)}(\beta R)}{R} \right\} J_{sy} \right] \Delta y \tag{19}$$

$$\Delta E_{my} = \frac{j\beta}{4} \left[(x-x') \, \frac{H_1^{(2)}(\beta R)}{R} \, M_{sz} \right] \Delta y \tag{20}$$

Initially, the values of the E_{ax}, E_{ay} and H_{az} field components over the surface of the rectangular aperture are calculated by FDTD and stored in a file. The NFT makes use of these aperture fields to compute the associated electric and magnetic surface current densities (J_{sx}, J_{sy} and M_{sz}). The desired near field location for the scattered field calculation is then specified and Equations 17 through 20 are used to compute the field contribution due to each aperture boundary segment of length Δx or Δy. The total near

zone scattered field component E_y may then be determined by summing the fields produced by each individual segment of the rectangular boundary.

III. APPLICATIONS AND RESULTS

A simple application of the FDTD/NFT algorithm will be presented and compared to an available exact solution. The problem consists of a two-dimensional PEC cylinder excited by an ideal TE plane wave with a magnitude of 1 V/m. Vertical near fields are calculated over a 10 by 10 wavelength area surrounding the cylinder. The geometry is shown in Figure 1 where a denotes the radius of the cylinder and is equal to 2.5 wavelengths. FDTD is used to calculate the scattered fields around the cylinder in an 8 by 10 wavelength area shown in Figure 2. The FDTD calculations use 50 cells per wavelength. The NFT is then used to calculate the scattered field in a 2 by 10 wavelength area to the right of the cylinder. The NFT calculations are performed with 25 samples per wavelength. This demonstrates the fact that the NFT calculations can be run on a sparse grid. The incident portion of the field is derived analytically and added to the scattered portion to provide the total field results. It should be noted that, in this case, the entire problem can be easily solved on a desktop PC using only FDTD, but is evaluated instead using the FDTD/NFT method for demonstration purposes. The exact solution is compared to results obtained using the FDTD/NFT approach. Portions of the shadow region are greater than 40 dB below the incident field magnitude and there is no noticeable difference between this solution and the exact solution, even along the FDTD/NFT boundary.

The second application consists of a two-dimensional diamond shaped PEC cylinder. The cylinder height is 6.5 wavelengths and its width is three wavelengths. The excitation is the same as in the case of the circular cylinder considered previously. Near fields are calculated over a 10 by 20 wavelength area surrounding the cylinder using the FDTD\NFT method. The scattered fields in a 10 by 10 wavelength area around the cylinder are calculated using FDTD. The NFT is then applied to calculate the fields in the remaining 10 by 10 wavelength area. A smooth transition between the FDTD and NFT regions is observed in both cases. It was found that these results compare well with the GTD solution for this problem.

The NFT algorithm applied here was derived to efficiently increase the area over which FDTD calculations could be performed, especially for electrically large objects. The algorithm works in conjunction with a two-dimensional scattered-field steady-state FDTD code. The algorithm can be applied in two-dimensions or could be modified to work in three dimensions with any steady-state radiating field. The only requirement is that the fields must be known over the entire closed surface. The accuracy of the NFT will depend on the spacial sampling interval. An interval of 10 or more samples per wavelength are recommended although as few as four may provide reasonably accurate results.

IV. CONCLUSION

A near-field steady-state transformation was developed to calculate near-fields outside an FDTD space during post-processing. This method can be applied to accurately and efficiently calculate radiated fields over a large area. It is also extremely efficient if the fields at only a few points outside the FDTD space are of interest. Dispersion errors inherent in FDTD are compounded by the number of cells. Therefore, the use of the NFT will reduce these errors by reducing the number of cells required for the FDTD calculation. Another advantage of the NFT is that it can be used in conjunction with FDTD to significantly reduce the memory requirements associated with large problem spaces. Results of the

FDTD/NFT technique were found to be in excellent agreement when compared to the well-known exact solution for scattering from a circular cylinder and compared well to GTD results.

ACKNOWLEDGMENTS

REFERENCES

[1]   A. Taflove, *Computational Electrodynamics, The Finite-Difference Time-Domain Method*, Artech House, Boston, 1995.

[2]   K. S. Kunz and R. J. Luebbers, *The Finite Difference Time Domain Method for Electromagnetics*, CRC Press, Boca Raton, Florida, 1993.

[3]   M. Barth, R. McLeod and R. Ziolkowshi, "A Near and Far-Field Projection Algorithm for Finite-Difference Time-Domain Codes," *Journal of Electromagnetic Waves and Applications*, Vol. 6, No. 1, 6, 1992.

[4]   K. Shlager and G. Smith, "Near-field to near-field transformation for use with FDTD method and its application to pulsed antenna problems," *Electronic Letters*, Vol. 30, No. 16, 1262, August 1994.

[5]   R. Luebbers, K. Kunz, M. Schnieder, and F. Hunsburger, "A Finite-Difference Time-Domain Near Zone to Far Zone Transformation," *IEEE Trans. Ant. Prop.*, 39(4), 429, 1991.

[6]   R. Luebbers, D. Ryan, J. Beggs, "A Two-Dimensional Time-Domain Near-Zone to Far-Zone Transformation," *IEEE Trans. Ant. Prop.*, 40(7), 848, 1992.

[7]   K. A. Lysiak, J. K. Breakall and J. S. Zmyslo, "UHF/VHF Propagation Model Characterization of Irregular Terrain using MoM/FDTD," *Proceedings of the 12th Annual Review of Progress in Applied Computational Electromagnetics*, Vol. I, pp. 502-507, March 18-22, 1996.

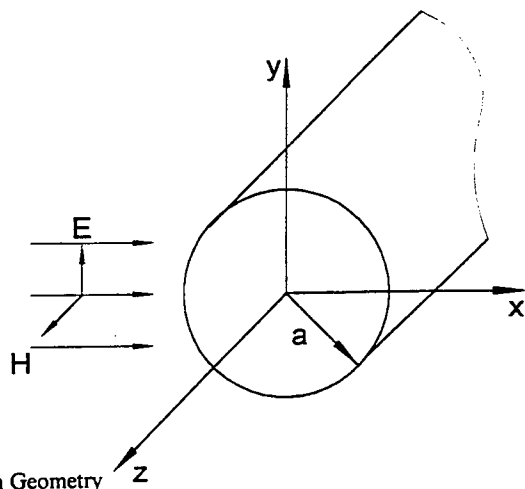[8]   C. A. Balanis, *Advanced Engineering Electromagnetics*, Wiley, New York, 1989.
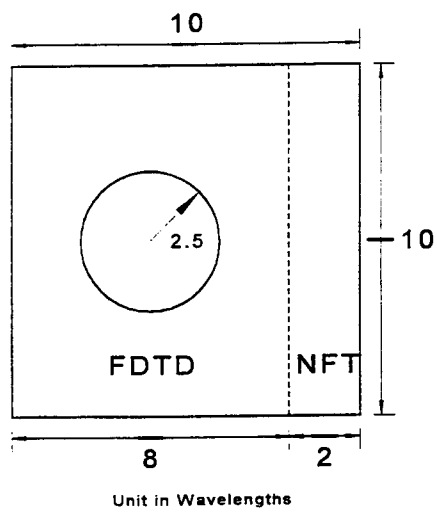
Figure 1. Transform Geometry

Unit in Wavelengths

Figure 2. FDTD/NFT Space Geometry

Transient Simulation of Breakdown Characteristics of a Miniaturized MOSFET based on a Non-Isothermal Non-Equilibrium Transport Model

W.-C. Choi, H. Kawashima and R. Dang

Hosei university, Tokyo, Japan

Abstract

The conventional semiconductor device simulation technique, based on the Drift-Diffusion Model (DDM), neglects the thermal and other energy-related properties of a miniaturized device. We, therefore, developed a simulator based on the Thermally Coupled Energy Transport Model (TCETM) which treats not only steady-state but also transient phenomena of such a small-size MOSFET. In particular, the present paper investigates the breakdown characteristics in transient conditions. As a result, we found that the breakdown voltage has been largely underestimated by the DDM in transient conditions.

Introduction

As a consequence of the present trend in microminiaturization, with the MOSFET being shrinked to smaller and smaller size, it was well conceivable that the current density increase at the Si/SiO$_2$ channel interface and the electric field concentration in the drain vicinity, should be conspicuous. In such situation, the non-equilibrium of localized carrier energy and the increase of device temperature due to heat generation, must be duly taken into account.

However, simulation techniques have not been able to cope with the situation. So far either the DDM [1] plus the heat flow equation, or the non-isothermal non-equilibrium model [2]-[4], have been solved in the steady-state. The loss of information due to the neglect of the transient state should be considerable. We, therefore, adopt both non-isothermal and non-equilibrium models in our study of the transient characteristics and in the following, report the newly obtained result for breakdown characteristics in transient conditions.

Basic Equations

Basic equations for two-dimensional transient simulation, consisting of Poisson equation (1), current continuity equations for electrons (2) and holes (3), energy transport equation for electrons (4) and heat flow equation (5), are given as follow.

$$\text{div}(\varepsilon \text{ grad } \psi) = -q(N_D - N_A + p - n) \tag{1}$$

$$\frac{\partial n}{\partial t} = \text{div}(\frac{J_n}{q}) + U \tag{2}$$

$$\frac{\partial p}{\partial t} = -\operatorname{div}\left(\frac{J_p}{q}\right) + U \tag{3}$$

$$\frac{\partial(n\xi_n)}{\partial t} + \operatorname{div} S_n = J_n \cdot E - nC_n + \xi_n U \tag{4}$$

$$\rho C \frac{\partial T_L}{\partial t} - \operatorname{div}(k_L \operatorname{grad} T_L) = Q_L \tag{5}$$

where ε, ψ, n, p, N_A, N_D and U represent permittivity, electric potential, electron density, hole density, acceptor doping concentration, donor doping concentration, and generation-recombination of carriers, respectively. J_n and J_p are electron and hole current densities. E is electric field . S_n and C_n are energy flux and mean energy loss rate for electron. ξ_n is electron mean energy. ρ, C, k_L, Q_L and T_L stand for density, specific heat capacity, thermal conductivity, lattice heat generation rate and lattice temperature, respectively. Note that equations (1)-(3) form what is conventionally called the drift-diffusion model, equation (4) is the energy balance equation for electrons and equation (5) is the heat flow equation which have been added here to account for the non-isothermal and non-equilibrium conditions. As for the energy balance equation, we consider electrons only, and assume that the hole and lattice temperatures are equal.

The electron mean energy ξ_n is assumed to be totally thermal, since thermal energy is much larger than the average kinetic energy in most cases. Here, the mean energy loss rate C_n is given as follows.

$$C_n = \frac{\xi_n - \xi_L}{\tau_{wn}} = \frac{3}{2} k_B \frac{T_n - T_L}{\tau_{wn}} \tag{6}$$

where τ_{wn} is energy relaxation time for electrons, T_n is electron temperature and ξ_L is lattice energy. Variables n, p, J_n, J_p are interrelated with each others by following auxiliary equations.

$$n = n_i \exp \frac{q(\psi - \phi_n)}{k_B T_n} \tag{7}$$

$$p = n_i \exp \frac{q(\phi_p - \psi)}{k_B T_p} \tag{8}$$

$$J_n = q D_n \operatorname{grad} n - q\mu_n n E + k_B n \alpha_n \mu_n \operatorname{grad} T_n \tag{9}$$

$$J_p = -q D_p \operatorname{grad} p - q\mu_p p E - k_B p \alpha_p \mu_p \operatorname{grad} T_p \tag{10}$$

$$S_n = -k_n \operatorname{grad} T_n - (\xi_n + k_B T_n) \tag{11}$$

Furthermore, the thermal energy is related to the total current as follows.

$$J = J_n + J_p + J_{disp} \tag{12}$$

$$Q_L = E \cdot J - E_g U \tag{13}$$

with

$$J_{disp} = -\varepsilon \frac{\partial}{\partial t} \operatorname{grad} \psi \tag{14}$$

where T_p, n_i, k_n and k_B are hole temperature, intrinsic carrier density, thermal conductivity for electron and Boltzmann constant. ϕ_n, ϕ_p, μ_n, μ_p, D_n and D_p represent quasi-Fermi potentials, mobilities and

diffusion constants for electrons and holes, respectively. a_n and a_n are transport coefficients for electrons and holes. J is total current and J_{disp} is displacement current.

Generation due to impact ionization (G_{IMP}) of carriers and recombination based on Shockley-Read-Hall model (R_{SHR}) and Auger model (R_{AUG}) are calculated using the following formulae [5].

$$G_{IMP} = \frac{J_n}{q} A_n \exp(-a_n \Delta n^2 + b_n \Delta n + c_n) + \frac{J_p}{q} A_p \exp(-a_p \Delta p^2 + b_p \Delta p + c_p) \qquad (15)$$

where

$$\Delta n = \frac{|J_n|}{|E \cdot J_n|} , \qquad \Delta p = \frac{|J_p|}{|E \cdot J_p|} \qquad (16)$$

$$R_{SHR} = \frac{n_i^2 - n p}{\tau_n(p + n_i) + \tau_p(n + n_i)} \qquad (17)$$

$$R_{AUG} = (n_i^2 + n p)(C_n n + C_p p) \qquad (18)$$

$$\tau_n = \frac{\tau_{n0}}{1 + \frac{|N|}{\tau_{ne}}} , \qquad \tau_p = \frac{\tau_{p0}}{1 + \frac{|N|}{\tau_{pe}}}$$

with

$A_n = 7.35 \times 10^5 [\text{cm}^{-1}], A_p = 7.83 \times 10^5 [\text{cm}^{-1}],$

$a_n = 4.1777 \times 10^{11} [\text{Vcm}^{-1}], a_p = 5.732 \times 10^{11} [\text{Vcm}^{-1}],$

$b_n = -1.787 \times 10^5 [\text{Vcm}^{-1}], b_p = -1.261 \times 10^6 [\text{Vcm}^{-1}],$

$c_n = 42.137, c_p = 43.32,$

$C_n = 2.7 \times 10^{-31} [\text{cm}^{-6} \text{sec}^{-1}], C_p = 9.9 \times 10^{-31} [\text{cm}^{-6} \text{sec}^{-1}],$

$\tau_{n0} = 3.95 \times 10^{-5} [\text{sec}], \tau_{p0} = 3.52 \times 10^{-5} [\text{sec}],$

$\tau_{ne} = \tau_{np} = 7.1 \times 10^{15} [\text{cm}^{-3}].$

Other physical parameters not enumerated above are identical with those in Ref. [6].

NUMERICAL METHOD

Equations (1)-(14) are now numerically solved self-consistently. We used a modified Scharfetter-Gummel formula by Tang [7], and the backward time differencing by Mock [8].

A simplified algorithm of the simulation is shown in Fig.1. This algorithm is composed of four computing loops, namely drift diffusion loop, energy transport loop, heat flow loop for solving the governing equations and the last transient loop for controlling the time flow.

First of all, structure parameters of the MOSFET are calculated as initial settings. Then the gate voltage is increased until a given bias, e.g. 3.0 [V]. After setting time t, equations (1)-(3), (7)-(10) are solved first by means of a coupled method for ψ, n, p. Equations (4), (5) and (11), (13) are solved next using the just-obtained ψ, n, p. This process is reiterated until convergence is achieved for each time step. The time is now renewed to $t + \Delta t$ and the whole thing is repeated until the prescribed simulation time is exhausted.

SIMULATION RESULT

A gate transient simulation is performed on a MOSFET structure shown in Fig. 2, with channel length L_{eff} =0.2 [μ m], oxide thickness t_{ox} = 8 [nm], junction depth x_j = 0.08 [μ m], substrate doping density N_{sub} = 3.9 × 10^{17} [atoms/cm^{-3}], respectively. Gate bias is initially fixed at 3.0 [V], bulk and source biases at 0 [V]. Then the drain potential is raised from 0 [V] to 10 [V] with various rising time lengths (e.g. 50, 100, 1000 [ps]). Terminal currents are taken positive in their outward direction.
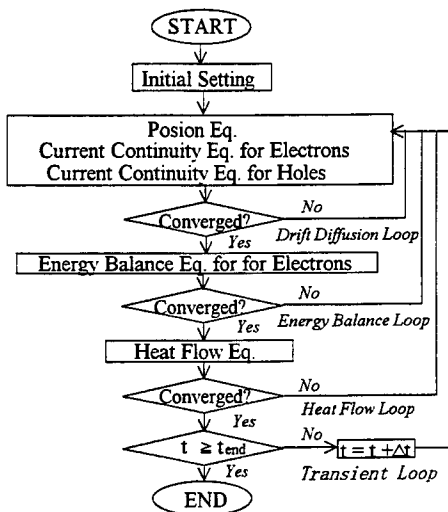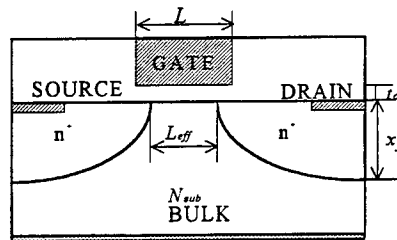

Fig.1. The algorithm of the simulation


Fig. 2. Geometry of a n-channel MOSFET

Fig. 3 shows the characteristics of the drain current on drain voltage based on (a) DDM and (b) TCETM with three different rising times. We found that the breakdown voltage based on the TCETM is higher than that of the DDM. This is due to the lower electric field strength dependent of carrier energy of the TCETM [9]. Furthermore, the breakdown voltage is lower with shorter rising time due to the delay of carrier transport for variable drain voltage. And the drain currents are higher with shorter rising time for increasing of gate current and bulk current at pre-breakdown.

Fig.4 shows the gate displacement current in TCETM. The corresponding transverse electric field within the gate oxid at the middle of the channel is shown in Fig. 6. It is found that the slope is steeper when the rising time is shorter.

The bulk current in Fig. 5 also increases with shorter rising time due to increasing of carrier generation by the impact ionization near the drain.
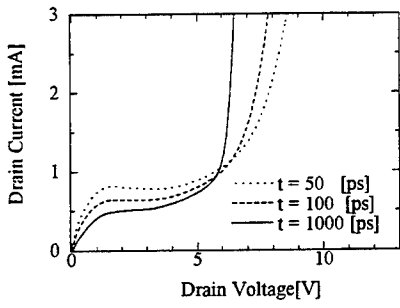
(a) DDM
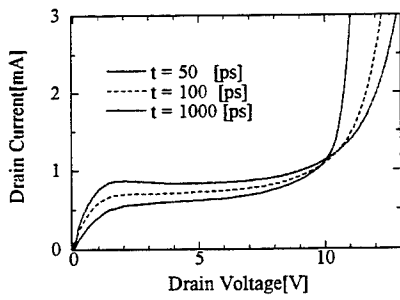
(b) TCETM

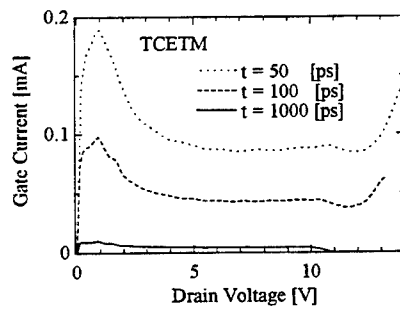Fig. 3. The characteristics of the drain current

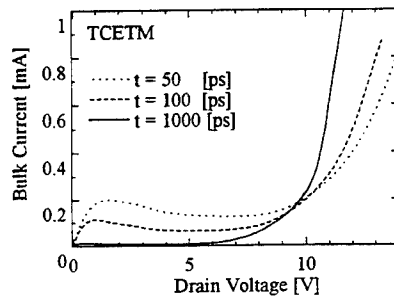Fig.4. The characteristics of gate current
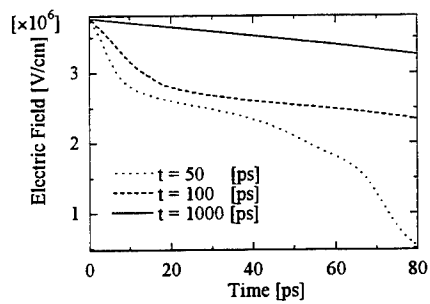

Fig. 5. The characteristics of bulk current

Fig. 6. Electric field at transient conditions

Conclusion

We have reported transient simulation of breakdown characteristics of a miniaturized MOSFET based on a non-isothermal non-equilibrium transport model. We found again that breakdown voltage is under estimated by the DDM. Furthermore, we also observed an increase of drain current and breakdown voltage with short rising time. Therefore, it is necessary to adopt TCETM and transient conditions when investigating breakdown characteristics of a deep submicron MOSFET.

References

[1] For example, D. L. Scharfetter and H. K. Gummel, "Large-Signal Analysis of a Silicon Read Diode Oscillator," *IEEE Trans. Electron Devices*, Vol. ED-16, No.1, pp. 64-77, 1969.

[2] D. Chen, Z. Yu,K.-C. Wu, R. Goossens and R. W. Dutton, "Dual Energy Transport Model with Couple Lattice and Carrier Temperatures," *SIMULATION OF SEMICONDUCTOR DEVICE AND PROCESSES*, Vol. 5, pp. 157-160, 1993.

[3] M. Liang and M. E. Law, "Influence of Lattice Self-Heating and Hot-Carrier Transport on Device Performance," *IEEE Trans. Electron Devices*, Vol. 41, No. 12, pp. 2391-2398, 1994.

[4] Y. Apanovich, P. Blacky, R. Cottle, E. Lyumkis, B. Polsky, A. Shur and A. Tcherniaev, "Numerical Simulation of Submicrometer Devices Including Coupled Nonlocal Transport and Nonisothermal Effects," *IEEE Trans. Electron Devices*, Vol. 42, No. 5, pp. 890-898, 1995.

[5] R. Dang, K. Matsushita and H. Hayashi, "A highly Efficient Adaptive Mesh Approach to Semiconductor Devices Simulation, " *IEEE Trans. Magnetics*, Vol. MAG-27, No. 5, pp. 4162-4165, 1991.

[6] H. Hayashi, H. Kawashima and R. Dang, "Non-Isothermal Device Simulation Taking Account of Both Carrier and Lattice Heating, " *ICVC '93*, pp. 147-150, 1993.

[7] T. W. Tang "Extention of the Scharfetter-Gummel Algorithm to the Energy Balance Equation," *IEEE Trans. Electron Devices*, Vol. ED-31, No. 12, pp. 1912-1914, 1984.

[8] M. S. Mock, "A Time-dependent Numerical Model of the Insulated-Gate Field-Effect Transistor," *Solid-State Electronics*, Vol. 24, No. 10, pp. 959-966, 1981.

[9] H. Hayashi, H. kawashima and R. Dang,"Semiconductor Device Simulation Taking Account of energy Transport under Non-isothermal Conditions," *Journal of the Japan Society for Simulation Technology*, Vol. 14, No. 4, pp. 61-70, 1994.

Numerical Simulation of Electro-thermal Characteristics of Semiconductor Devices Taking Account of Chip Self-heating and In-chip Thermal Interdependence

H. Kawashima [1], C. Moglestue [2], M. Schlechtweg [2], and R. Dang [1]

1) College of Engineering, Hosei University, Tokyo, Japan
2) Fraunhofer Institute of Applied Solid State Physics, Freiburg, Germany

ABSTRACT

In this paper, we report electro-thermal characteristics of a transistor mounted on a chip in various arrangements by solving heat flow equation together with other basic semiconductor equations. To calculate accurately the temperature distribution inside a single transistor taking account of in-chip thermal interdependence, we combine a three-dimensional thermal simulator with a two-dimensional electrical simulator. As a result, we found that influences on electrical characteristics of the transistor caused by the self-heating effect and the in-chip thermal interdependence, can not be neglected.

I. INTRODUCTION

As the sizes of a transistor and a circuit are decreasing, the temperature inside a chip becomes very high at the same bias. Transistors designed without considering thermal effects, may give rise to hot spots on the chip. To cope with this situation, it is necessary to consider not only electrical but also thermal characteristics.

The temperature distribution in both two and three dimensions has been widely reported [1-9]. In general, there are two viewpoints on the temperature analysis inside a semiconductor device. One, the macroscopic one [1-4], solves heat flow equation analytically or numerically in the entire chip by considering a transistor to be a lumped heat source. The other, the microscopic one [5-9], couples the solution of the heat flow equation with electrical semiconductor equations, namely, Poisson equation, current continuity equations, and so on, within the area surrounding a single transistor. It is difficult for the former approach to calculate the detailed temperature distribution inside each transistor and electro-thermal characteristics of the transistor caused by the self-heating effect. On the other hand, as heat flow spreads widely and deeply into the substrate, it is difficult for the latter approach to set up an appropriate simulation area and efficient boundary conditions that accurately reflect physical models. Combining both approaches with a view of profiting their respective merits enables us to calculate temperature distribution in the transistor taking account of the global structure of the entire circuit. This combination is realized in the present paper by a two-step calculation, first by considering the transistor as a lumped heat source; then restricting the simulation area to the nearest surroundings of the

transistor with the detailed heat generation provided by the electrical simulator. Using these simulators, electro-thermal characteristics of a transistor taking account of chip self-heating and in-chip thermal interdependence are investigated.

II. BASIC EQUATIONS

A. Thermal Model

The heat flow equation for steady state reads

$$\text{div } (k \text{ grad } T) = -Q \tag{1}$$

where k, T, and Q represent thermal conductivity of material at stake, temperature, and heat generation rate, respectively.

The temperature dependence of the thermal conductivity of each material to be considered is given as follows [1-5].

Si	: $3122.86\ T^{-4/3}$	(1.55 at 300 K)
SiO$_2$	: $1.43 \times 10^{-2} + 3.84 \times 10^{-6}\ (T - 273) + 2 \times 10^{-8}\ (T - 273)^2$	(0.0144 at 300 K)
GaAs	: $550\ T^{-1.25}$	(0.44 at 300 K)
Al	: 2.3	
Au	: 3.12	

Unit : [W cm^{-1} K^{-1}]

B. Electrical Model

Electrical basic equations for steady state, consisting of Poisson equation (2) and current continuity equations for electrons (3) and holes (4), are given as follows.

$$\text{div} \left(\varepsilon \text{ grad } \psi \right) = -q \left(N_D - N_A + p - n \right) \tag{2}$$

$$\text{div} \left(\frac{-J_n}{q} \right) = U \tag{3}$$

$$\text{div} \left(\frac{J_p}{q} \right) = U \tag{4}$$

where ε, ψ, q, N_D, N_A, and U represent permittivity, electric potential, electronic charge, donor doping concentration, acceptor doping concentration, and generation-recombination rate of carriers, respectively. n and p are electron density and hole density, as follows.

$$n = n_i \exp \frac{q(\psi - \phi_n)}{k_B T} \tag{5}$$

$$p = n_i \exp \frac{q(\phi_p - \psi)}{k_B T} \tag{6}$$

where n_i and k_B stand for intrinsic carrier density and Boltzmann constant. ϕ_n and ϕ_p are quasi-Fermi potentials for electrons and holes, respectively.

J_n and J_p represent electron and hole current densities, including the effect of temperature gradient, and are given as follows.

$$J_n = -q\mu_n n \operatorname{grad}\psi + qD_n \operatorname{grad}n + k_B n\, a_n \mu_n \operatorname{grad}T \tag{7}$$

$$J_p = -q\mu_p p \operatorname{grad}\psi - qD_p \operatorname{grad}p - k_B p\, a_p \mu_p \operatorname{grad}T \tag{8}$$

where $\mu_n, \mu_p, D_n, D_p, a_n$, and a_p are mobilities, diffusion constants, and transport coefficients for electrons and holes, respectively.

C. Physical Model

In order to consider effects of the self-heating and the thermal interdependence in electrical characteristics, we use carrier mobility models [10-12] as a function of temperature, concentration, and electric field for Si MOSFET, as follows.

$$\mu_{n,p}(N,T,E_G,E_D) = \frac{\mu_{n,p}(N,T,E_G)}{\sqrt{1 + \dfrac{(\mu_{n,p}(N,T,E_G)\,E_D/v_c)^2}{\mu_{n,p}(N,T,E_G)\,E_D/v_c + G} + (\mu_{n,p}(N,T,E_G)\,E_D/v_s(T))^2}} \tag{9}$$

$$\mu_{n,p}(N,T,E_G) = \mu_{n,p}(N,T)\,(1 + aE_G)^{-0.5} \tag{10}$$

$$\mu_n(N,T) = 88\,T_0^{-0.57} + \frac{7.4\times10^8\,T^{-2.33}}{1 + 0.88\,T_0^{-0.146}\,N/(1.26\times10^{17}\,T_0^{2.4})} \tag{11}$$

$$\mu_p(N,T) = 54.3\,T_0^{-0.57} + \frac{1.36\times10^8\,T^{-2.33}}{1 + 0.88\,T_0^{-0.146}\,N/(2.35\times10^{17}\,T_0^{2.4})} \quad,\quad T_0 = T/300 \tag{12}$$

$$v_s(T) = \frac{2.4\times10^{17}}{1 + 0.8\exp(T/600)} \tag{13}$$

where E_D and E_G represent electric fields defined by components perpendicular and parallel to the current density vector. N is concentration and other parameters are identical with those in Ref. [12].

Temperature dependent intrinsic carrier density for silicon is given as follows [9].

$$n_i(T) = 3.88\times10^{16}\,T^{1.5}\exp\left(\frac{-7000}{T}\right) \tag{14}$$

D. Numerical Implementation

We solve these equations by finite difference method on an orthogonal mesh using Newton's method in three (thermal simulator) or two (electrical simulator) dimensions.

To ensure the flexibility of coupling the thermal simulator to the electrical simulator, the calculation is carried out in two stages. First, by replacing each transistor as a lumped heat source, the calculation of temperature distribution taking account of design parameters of a circuit, such as the number of transistors, the distance between each transistor, the number of transistors, the layout of the circuit, and so on, is carried out using the thermal simulator. Then, the simulation area is reduced to the surrounding of the single transistor, and both electrical and thermal simulators are carried out by means of

setting boundary conditions of heat flow equation from temperature distribution obtained from the first stage in order to consider effects of design parameters.

III. SIMULATION RESULTS

A. Thermal Simulation of Si MOSFET

The simulated structure, a Si MOSFET of 12 equidistant parallel channels, is shown in Fig. 1. Each channel (heat source) is 1 micron long, 50 micron wide with a heat dissipating rate of 0.1 W. The spacing between them is 8 microns, the chip thickness 100 microns. The top surface is covered with a 0.02 micron thick layer of SiO_2 as gate oxide, and a 1 micron thick layer of Aluminum as gate electrode. The bottom face is connected to a heat sink at room temperature (300 K). This structure is separated from other devices by 150 microns to ensure thermal isolation.

Fig. 2 shows temperature distributions in the first quadrant of the structure. Distributions in other quadrants can be obtained easily by virtue of symmetry. Under these conditions, the peak temperature rises to about 355 K. The temperature variation along the width of the transistors clearly indicate that a three-dimensional analysis is necessary in order to get a realistic temperature distribution.
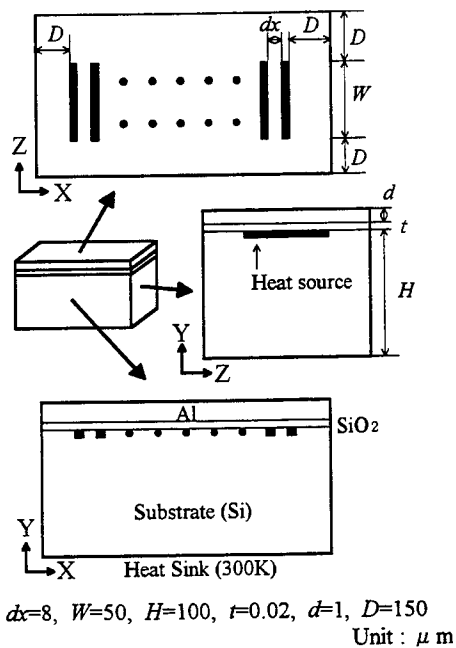

dx=8, W=50, H=100, t=0.02, d=1, D=150

Unit : μ m

Fig. 1 Simulated structure with Si MOSFETs

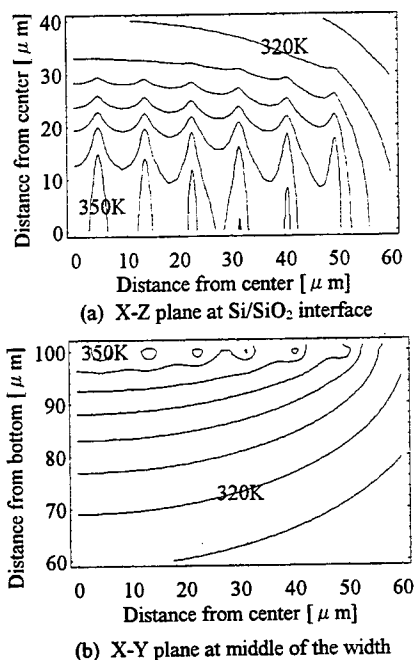(a) X-Z plane at Si/SiO$_2$ interface

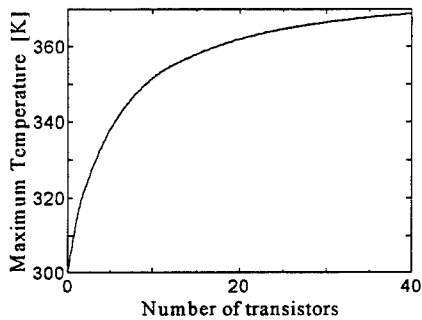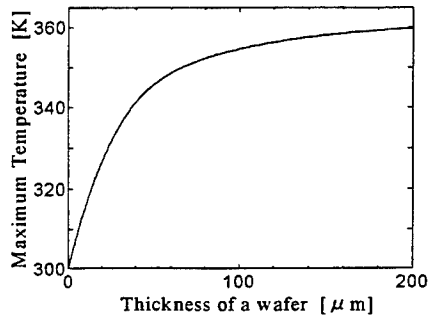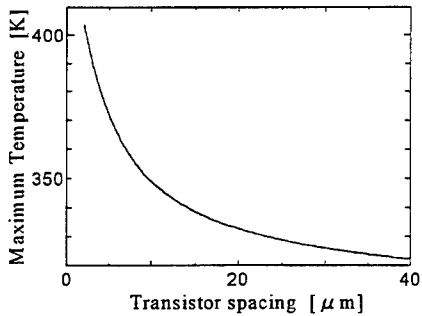(b) X-Y plane at middle of the width

Fig. 2 Temperature distribution

(a) Dependence on the number of transistors

(c) Dependence on the thickness of a wafer

(b) Dependence on the transistor spacing

Fig. 3 Dependence of maximum temperature on design parameters of a circuit

Fig. 3 shows the dependence of maximum temperature on (a) the number of transistors while keeping the transistor spacing constant, (b) the varying transistor spacing, and (c) the wafer thickness. As seen, with the variation of the number of transistors, the maximum temperature rises steeply, but levels off at about 40 and the maximum temperature converges to about 371 K. The temperature also depends largely on the transistor spacing of under 20 microns. In other words, it is difficult to separate each transistor in an integrated circuit in terms of thermal characteristics. Furthermore, if the spacing becomes smaller than 5 microns, the peak temperature rises sharply and the circuit may eventually cause functioning stop. On the other hand, by thinning the wafer to less than 100 microns (on this condition), it is possible to hold down the rise of maximum temperature. As a result, we can see that the interaction between each transistor and the effect of design parameters can not be neglected on a thermal analysis.

B. Thermal Simulation of GaAs MESFET

Fig. 4 shows the simulated structure, a GaAs MESFET of 12 gates. This structure has same geometry of Si MOSFET in Fig. 1, except of materials of the substrate and the electrode.

Fig. 5 shows the temperature distribution at GaAs/Au interface. Under these conditions, the peak temperature rises to about 488 K. The temperature in this structure is very high as compared with one of a Si substrate under same conditions, because of low thermal conductivity of GaAs.
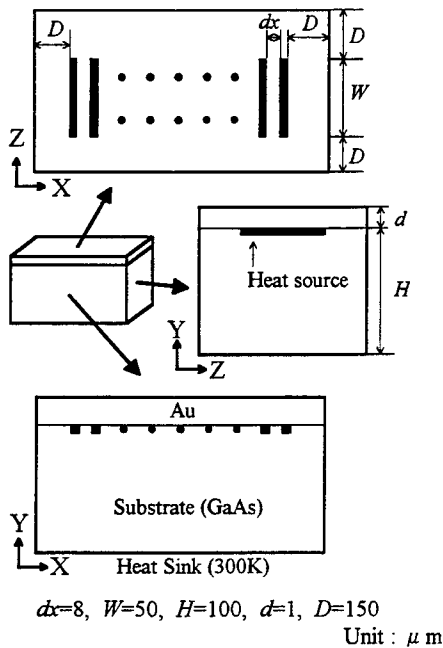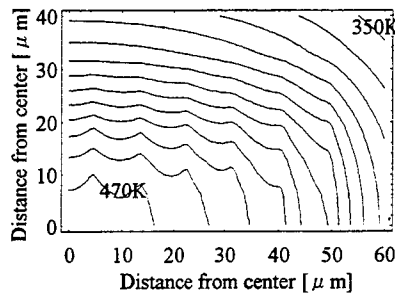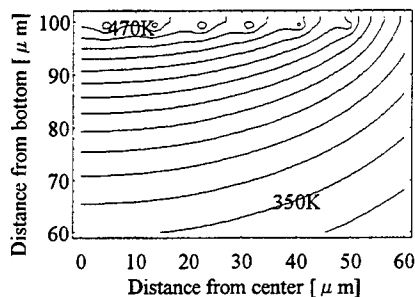
dx=8, W=50, H=100, d=1, D=150

Unit : μ m

Fig. 4 Simulated structure with GaAs MESFETs

(a) X-Z plane at GaAs/Au interface

(b) X-Y plane at middle of the width

Fig. 5 Temperature distribution

C. Electro-thermal Simulation of Si MOSFET

Fig. 6 shows the detailed geometry of a single n-channel Si MOSFET for the two-dimensional electrical device simulator which is shown as a black stripe in Fig. 1. The gate length is 1.0 micron, the gate oxide thickness 0.02 microns, the depth of the diffusion layer 0.2 microns and the bulk doping concentration 10^{17} cm^{-3}.
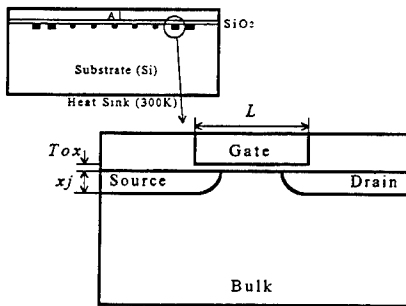
Fig. 7 shows the dependence of drain current and total heat generation rate in the MOSFET on drain voltage by the electrical device simulator under isothermal condition, when gate voltage is fixed at 5 V.

After this simulation, by replacing total heat generation rate of the single MOSFET as heat generation rate of each lumped heat source on each voltage condition, the thermal simulation taking account of effects of a global structure as shown Fig. 1, is carried out. Then the simulation region is reduced to a small area around the single transistor and electrical characteristics are calculated again using the electrical device simulator including the solution of heat flow equation just obtained the temperature resulted from the thermal simulation as new boundary conditions.

Fig. 8 shows drain current versus drain voltage under non-isothermal or isothermal condition. We can see that the drain current based on the isothermal model, is overestimated due to the neglect of

temperature rise. Furthermore, the drain current based on the non-isothermal model with 12 MOSFETs is very different from the one with 1 MOSFET due to the thermal interdependence.

Fig. 9 shows the temperature distribution inside the MOSFET resulted from the non-isothermal model with 12 MOSFETs, when both gate and drain voltages are 5 V. Under these conditions, the temperature shows a localized increase of about 353 K, and heat flow spreads through whole MOSFET device.

L=1, T_{ox}=0.02, x_j=0.2   Unit : μ m

Fig. 6 n-channel Si MOSFET
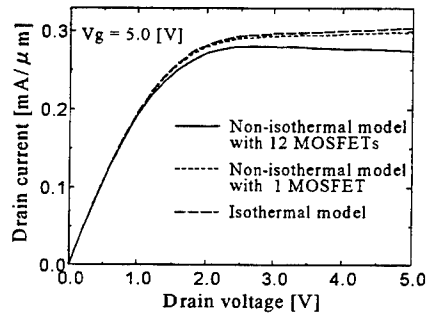
Fig. 8 Drain current versus drain voltage
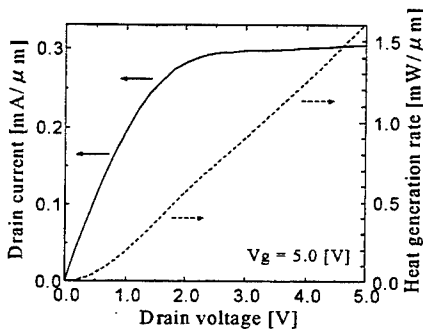
Fig. 7 Dependence of drain current and heat generation rate on drain voltage
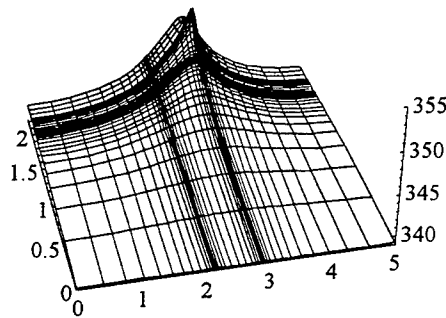
Fig. 9 Temperature distribution in Si MOSFET

IV. CONCLUSION

We calculated the temperature distribution either in a global structure embedded with a pluralty of transistors or a single transistor using a thermal simulator and an electrical simulator. As a result, we found that the temperature inside the chip largely depends on design parameters of the circuit, such as the number of transistors, the distance between them, and the thickness of the wafer. Therefore, we can

see that it is necessary to simulate a global structure taking account of the thermal interdependence from other devices.

Furthermore, by combining the thermal simulator treating the entire chip globally, with the electrical simulator dealing with a single transistor locally, electro-thermal characteristics of Si MOSFET are compared with those by electrical simulator under isothermal condition. As a result, we found that influences on electrical characteristics of the transistor caused by the chip self-heating and the in-chip thermal interdependence, can not be neglected.

REFERENCES

[1] C. G. Shirley, "Steady-state temperature profiles in narrow thin-film conductors," *J. Appl. Phys.*, Vol. 57, No. 3, pp. 777-784, 1985.

[2] W. Nakwaski, "Thermal model of the catastrophic degradation of high-power stripe-geometry GaAs/(AlGa)As double-heterostructure diode lasers," *J. Appl. Phys.*, Vol. 67, No. 4, pp. 1659-1668, 1990.

[3] M. Berger and Z. Chai, "Estimation of heat transfer in SOI-MOSFET's," *IEEE Trans. Electron Devices*, Vol. 38, No. 4, pp.871-875, 1991.

[4] X. Gui, P. W. Webb, and G.-b. Gao, "Use of the three-dimensional TLM method in the thermal simulation and design of semiconductor devices," *IEEE Trans. Electron Devices*, Vol. 39, No. 6, pp. 1295-1302, 1992.

[5] S. Szeto and R. Reif, "A unified electrothermal hot-carrier transport model for silicon bipolar transistor simulations," *Solid-State Electronics*, Vol. 32, No. 4, pp. 307-315, 1989.

[6] M. Liang and M. E. Law, "Influence of lattice self-heating and hot-carrier transport on device performance," *IEEE Trans. Electron Devices*, Vol. 41, No. 12, pp. 2391-2398, 1994.

[7] Y. Apanovich, P. Blakey, R. Cottle, E. Lyumkis, B. Polsky, A. Shur, and A. Tcherniaev, "Numerical simulation of submicrometer devices including coupled nonlocal transport and nonisothermal effects," *IEEE Trans. Electron Devices*, Vol. 42, No. 5, pp. 890-898, 1995.

[8] H. Kawashima, H. Hayashi, and R. Dang, "MOSFET's lattice temperature effect in non-isothermal and non-equilibrium transport," *The Fourth International Seminar on Simulation of Devices and Technologies (ISSDT'95)*, South Africa, pp.188-191, 1995.

[9] S. P. Gaur and D. H. Navon, "Two-dimensional carrier flow in a transistor structure under nonisothermal conditions," *IEEE Trans. Electron Devices*, Vol. 23, No. 1, pp. 50-57, 1976.

[10] C. Jacoboni, C. Canali, G. Ottaviani, and A. Quaranta, "A review of some charge transport properties of silicon," *Solid-State Electronics*, Vol. 20, pp. 77-89, 1977.

[11] N. D. Arora, J. R. Hauser, and D. J. Roulston, "Electron and hole mobilities in silicon as a function of concentration and temperature," *IEEE Trans. Electron Devices*, Vol. 29, No. 2, pp. 292-295, 1982.

[12] K. Yamaguchi, "A mobility model for carriers in the MOS inversion layer," *IEEE Trans. Electron Devices*, Vol. 30, No. 6, pp. 658-663, 1983.

APPLICATIONS OF PHOTONIC BAND GAP MATERIALS

M. M. Sigalas[1], R. Biswas[1], K. M. Ho[1], W. Leung[2], G. Tuttle[2], and D. Crouch[3]

[1]Ames Laboratory and Department of Physics and Astronomy, Iowa State University, Ames IA 50011

[2]Microelectronics Research Center and Department of Electrical Engineering and Computer Engineering, Iowa State University, Ames IA 50011

[3]Advanced Electromagnetic Technologies Center, Hughes Electronics Corporation, Rancho Cucamonga, CA 91729

1. INTRODUCTION

A novel class of periodic dielectric structures has been developed where propagation of electromagnetic (EM) waves is forbidden for all frequencies in the stop band or photonic band gap (PBG).[1-2] These PBG structures have been fabricated at a variety of microwave and millimeter-wave length scales with three-dimensional PBG frequencies ranging between 10 and 500 GHz. [2-5] An extremely attractive application of these PBG crystals is as reflecting substrates for integrated circuit antennas.

A serious disadvantage of conventional antennas on a semi-infinite semiconductor substrate (with dielectric constant ϵ) is that the power radiated into the substrate is a factor $\epsilon^{3/2}$ larger than the power into the free space.[6] Hence, antennas on GaAs or Si, radiate only 2-3% of their power into free space. A large fraction of the power radiated into the substrate is in the form of trapped waves propagating at angles larger than the critical angle.[6] By fabricating the antenna on a PBG material with a driving frequency in the stop band, no power should be transmitted into the PBG material and all power should be radiated in the free space, provided there are no surface modes.

Brown et al.[7] demonstrated this concept by fabricating a bow-tie antenna on their 3-cylinder PBG crystal and found a complex radiation pattern in air. They improved the directionality by placing the antenna on different high and low-dielectric surfaces.[8,9] Cheng et al .[11] measured the dipole radiation pattern on the layer-by-layer PBG crystal and found the pattern to be strongly dependent on the position of the dipole in the unit cell. Kesler et al.[11] measured the radiation of antennas placed on top of two-dimensional (2D) and three-dimensional (3D) PBG materials and found insensitivity of the antenna patterns when the dipole was raised sufficiently high above the surface.

In this paper we measure and calculate the radiation pattern of a dipole antenna on our layer-by-layer PBG crystal.[5] The layer-by-layer PBG crystal was fabricated by stacking alumina rods, and has a 3-dimensional stop band gap between 12 and 14 GHz with an attenuation of more than 40 db within the stop band.[5] The 4 variables controlling the antenna radiation pattern are 1) the

412

position of the antenna in the surface unit cell, 2) the height of the antenna above the surface, 3) the orientation of the antenna, and 4) the driving frequency.

There are two high symmetry positions in the unit cell corresponding to the antenna either in a 'solid' position on top of the rod i.e. intersection of the 1st and 2nd layer rods, or ii) in the 'void' position with no dielectric rod directly beneath it, but above the third and fourth layer rods. At each of these two surface positions there are two orientations, corresponding to the dipole parallel or perpendicular to the first layer rods. The height z is expressed as a ratio of the rod diameter d (d=0.318 cm). Other lower symmetry positions in the unit cell were not found to have any particular advantage. Experimentally, the minimum height of the dipole above the top of the first layer rods is the coaxial feed cable radius, corresponding to a minimum height of $z/d \approx 0.53$.

Experimentally a Ku-band synthesizer generated an input signal that was divided by a 3 db hybrid coupler into two components that were $180°$ out of phase. Each component signal was routed through adjustable phase shifters and 50 ohm coaxial cables. [11] The dipole was fabricated by bending the center conductors of the two coaxial cables and minimizing the feed gap. Measurements were performed in an anechoic chamber with an HP8510B network analyzer, with the dipole as a rotating source and the pyramidal feedhorn as the receiving antenna. Feedwires rotated with the dipole, to minimize electromagnetic interference. Exceptional care in fabrication was used so that the radiation of the free dipole was found to be very close to the expected result.

The FDTD calculations [12] were performed for a finite length dipole (1.6 cm) and utilized the symmetry of the crystal to reduce the computational space to one-fourth of the actual PBG crystal cell.

2. RESULTS

For the dipole above the first layer rod with its center at the intersection of the rods of the first and second layers, at its minimum height ($z/d = 0.53$), both experiment and FDTD calculations predict a central lobe in the E-plane and a broader but still centrally peaked pattern in the H-plane (Fig. 2). As the dipole is raised ($z/d = 1.3 - 1.5$) the E-plane intensity weakens with two side-lobes developing at about $40°$ to the normal. The H-plane pattern weakens but remains broad. As the dipole is lifted higher ($z/d = 2.5$), both the E-plane and H-plane intensities decrease further, with a central lobe and 2 side-lobes. at about $40°$ to the normal. The weakening radiation arises from a phase cancellation between the direct wave and the wave reflected from the photonic crystal. There is very good agreement between experiment and FDTD calculation. It is desirable to place the dipole close to the surface to achieve strong central peak patterns.

In Fig. 2, we compare the intensity patterns for three different frequencies inside the PBG. The dipole is above the first layer rod with its center at the intersection of the first and second layers and z/d=0. For the dipole perpendicular to the first layer of rods, we get the maximum intensities for frequencies close to the upper edge of the PBG. For the parallel dipole case, however, we get the maximum intensities for frequencies close to the lower edge of the gap.

We find that that antenna patterns become insensitive to position when the antenna is raised high enough above the substrate (e.g. $z/d > 3$), where the E-fields are uniform, and results for void and solid positions are similar. This is in agreement with previous theoretical studies.[10,13]

In all positions there is virtually no power propagating through the PBG crystal with all radiation emerging from the front side, illustrating the PBG crystal behaving as a perfect dissipationless

Perpendicular-void
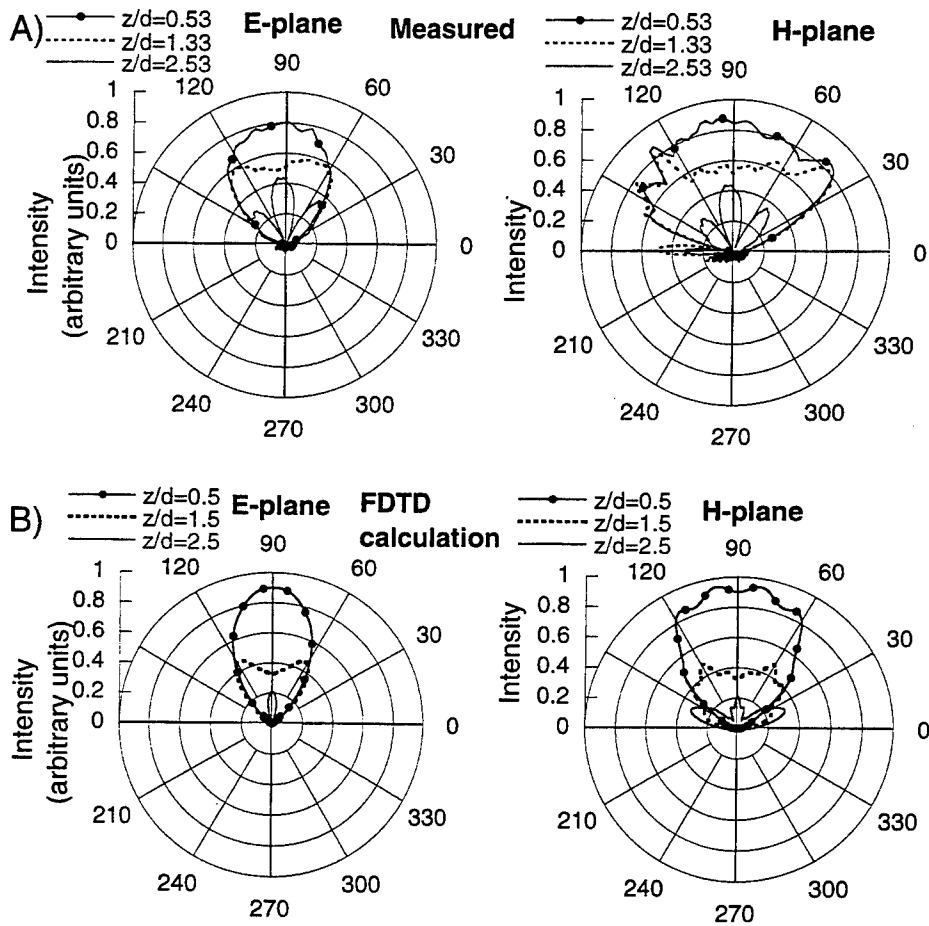
Figure 1: Measured (A) and FDTD calcuations (B) of the antenna radiation in the E- and H-planes when the antenna is in the Perpendicular solid position. The three sets of curves correspond to different heights z of the antenna above the top of the first layer rod. Heights z are expressed as a ratio z/d where d is the diameter of the dielectric rod (0.318 cm). Experimental uncertainty in z/d is approximately 0.1.
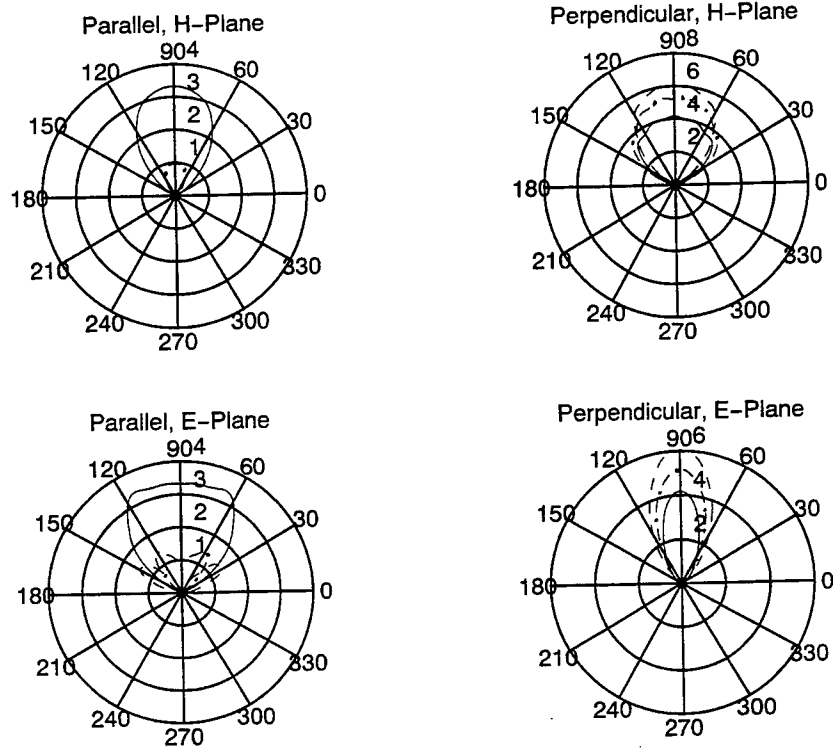
Figure ¯.2: FDTD calcuations of the antenna radiation in the E- and H-planes when the antenna is in the solid position (either parallel or perpendicular) with z/d=0. Results for three different frequencies 11.5, 12.5, and 13.5 GHz (solid, dotted dashed, and dashed lines, respectively) lying inside the PBG are shown.

415

reflector.

3. CONCLUSIONS

The antenna pattern for a dipole antenna on the surface of a PBG crystal has been measured and calculated with the FDTD method for different surface positions, heights, and orientations of the dipole. Within the stop band the PBG crystal behaves as a dissipiationless reflector and all the antenna power is reflected into the air side.

The antenna radiation strongly depends on the position of the dipole antenna, since the dipole radiation depends on the rapidly varying local E-field at the surface of the photonic crystal. When the dipole is raised high enough above the surface the patterns become insensitive to dipole position, since the E-field is uniform. For our layer-by-layer PBG crystal we find the two dipole orientations directly on top of the dielectric rod to be the most suitable for central lobe type of patterns. It is advantageous to have the dipole placed directly above a dielectric. At several geometries when the dipole is raised above the surface we find strong lobes in the H-plane that may be useful for directional antennas.

There is good agreement between the measurements and the FDTD calculations especially in the angular dependence of the patterns. FDTD simulations can be used as a powerful design tool to optimize antenna patterns on any photonic crystal surface. Antennas in cavity geometries may be designed on PBG crystal surfaces, to optimize the antenna radiation. PBG crystals have immense potential for novel microwave and miilimeter wave applications.

REFERENCES
1. See the proceedings of the NATO ASI, *Photonic Band Gap Materials* ed. C. M. Soukoulis, (Plenum, New York, 1996).
2. E. Yablonovitch, T. J. Gmitter, and K. M. Leung, Phys. Rev. Lett. **67**, 2295 (1991).
3. E. Ozbay, A. Abeyta, G. Tuttle, M. Tringides, R. Biswas, C. T. Chan, C. M. Soukoulis, and K. M. Ho, "Measurements of a Three Dimensional Photonic Band Gap in a Crystal structure Made of Dielectric Rods," Phys. Rev. B, Vol. 50, July 1994, pp. 1945-1948.
4. E. Ozbay, E. Michel, G. Tuttle, M. Sigalas, R. Biswas, and K. M. Ho, "Micromachined Millimeter Wave Photonic Band Gap Crystals," Appl. Phys. Lett., Vol. 64, April 1994, pp. 2059-2061.
5. E. Ozbay, E. Michel, G. Tuttle, R. Biswas, K. M. Ho, J. Bostak, and D. M. Bloom, Opt. Lett. **19**, 1155 (1994).
6. D. B. Rutledge, D. P. Neikirk, and D. P. Kasilingam, in *Infrared and Millimeter Waves* (Academic, Orlando, 1983), Vol. 10, p. 1.
7. E. R. Brown, C. D. Parker, and E. J. Yablonovitch, "Radiation Properties of a Planar Antenna on a Photonic Crystal Substrate," J. Opt. Soc. Am. B, Vol. 10, Feb. 1993, pp. 404-407.

8. E. R. Brown, C. D. Parker, and O. B. McMahon, "Effect of Surface Composition on the Radiation Pattern from a Photonic Planar Dipole Antenna," Appl. Phys. Lett., Vol. 64, June 1994, pp. 3345-3347.

9. E. R. Brown and O. B. McMahon, "High zenithal directivity from a dipole antenna on a photonic crystal," Appl. Phys. Lett., Vol. 68, June 1994, pp. 1300-1302.

10. M. P. Kesler, J. G. Maloney, B. L. Shirley, and G. S. Smith, "Antenna Design with the Use of Photonic Band Gap Materials as All Dielectric Planar Reflectors," Microwave Opt. Tech. Lett., Vol. 11, March 1996, pp. 169-174.

11. S. D. Cheng, R. Biswas, E. Ozbay, S. McCalmont, G. Tuttle, and K.-M. Ho, "Optimized Dipole Antennas on Photonic Band Gap Crystals," Appl. Phys. Lett., Vol. 67, December 1995, pp. 3399-3401.

12. K. Umashankar and A. Taflove, "Computational Electromagnetics," (Artech House, Boston, 1993).

13. M. M. Sigalas, R. Biswas, and K. M. Ho, "Theoretical Study of Dipole Antennas on Photonic Band Gap Materials," Microwave Opt. Tech. Lett., Vol. 13, November 1996, pp. 205-209.

INVESTIGATING THE USE OF MODEL-BASED PARAMETER ESTIMATION FOR ELECTROMAGNETIC-DATA PHASE RECOVERY

E. K. Miller
3225 Calle Celestial, Santa Fe, NM 87501-9613
505-820-7371, e-mail: emiller@esa.lanl.gov

INTRODUCTION
When conducting electromagnetic (EM) experiments, it is sometimes the case that only the magnitude of the desired observable is easily accessible, e.g., when the power balance in a system is being measured. Having access to the phase in such cases would be an added benefit, however, since knowledge of the complex reflected, absorbed, and transmitted power in a component is useful for tuning and other purposes.

Model-based parameter estimation (MBPE) using rational functions has been demonstrated to be applicable in developing a simple, analytic representation of pole-like transfer functions, such as EM frequency responses [Miller (1996)]. Until now, this MBPE application has employed complex data for the parameter-estimation process. In this presentation, we explore the application of MBPE to frequency transfer functions where only the data magnitude is available and the goal is to estimate the complex response, a problem that is known as "phase recovery" in optics. The approach will be summarized and some initial results will be presented for MBPE phase recovery.

BRIEF REVIEW OF MBPE
MBPE can be simply described as "smart" curve fitting, where the fitting model (FM) that is used to smooth or fit the data of interest is based on the physics of the problem which generated that data, the "model-based" part of MBPE. The parameters of MBPE are the coefficients of the FM whose numerical values are found by matching the FM to the data, the "parameter-estimation" part of MBPE.

Two complementary FMs that have widespread utility for MBPE applications in electromagnetics (EM) are series of exponentials or poles, which are related by a Laplace transform. These particular FMs can be used to represent the generic EM responses

$$f(x) = f_p(x) + f_{np}(x) = \Sigma R_\alpha \exp(s_\alpha x) + f_{np}(x) = m(x) + f_{np}(x), \qquad (1)$$

and

$$F(X) = F_p(X) + F_{np}(X) = \Sigma R_\alpha/(X - s_\alpha) + F_{np}(X) = M(X) + F_{np}(X), \ \alpha = 1, \ldots, P \qquad (2)$$

where "x" and "X" are the independent variables in the exponential- and pole-series FMs, respectively, and the R_α and s_α are the FM residues and poles, which are complex in general. The exponential-series FM, $m(x)$, can be regraded as representing a general waveform of which a specific example is a transient response. The pole-series FM, $M(X)$, can represent a general spectral response of which a specific example is a frequency spectrum. Thus, Eqs. (1) an (2) can be conveniently described as waveform-domain (WD) and spectral-domain (SD) responses with corresponding FMs $m(x)$ and $M(X)$, respectively. Since the WD or SD response of interest may not be fully described by an exponential or pole series, the additional terms in (1) and (2), $f_{np}(x)$ and $F_{np}(X)$, are included to allow for this fact where the subscript "np" denotes a "non-pole" contribution.

Given data samples from either $f(x)$ or $F(X)$, it is straightforward, at least conceptually, to develop a way of obtaining the coefficients for either kind of data and FM [Miller (1995)]. Because of difficulties caused by noise, limited data-sample dynamic range, and similar issues, actually computing the FM

parameters can encounter various kinds of problems that enter the realm of signal processing. These will not be discussed further here, as we instead focus instead on outlining use the SD FM for modeling magnitude-only data.

USING MBPE FOR PHASE RECOVERY

First, observe that there are several variants of SD parameter estimation, depending on the specific problem circumstances [Brittingham et al. (1980)].

1) If the poles comprising $F_p(X)$ are unconstrained, then a P-pole spectrum would require 2P complex samples of $F(X)$, at a minimum, for the 2P complex parameters represented by P complex residues and P complex poles, to be obtained.

2) When the residues and poles occur in conjugate pairs, as is the case for EM responses, then the number of required data samples can be halved, if knowledge that the parameters are complex conjugates can be exploited. It turns out for this particular situation, that the coefficients of the numerator and denominator polynomials obtained by expanding the pole series in (2) in common-denominator form become pure real, thus halving the number of real unknowns and requiring P complex samples of $F(X)$.

3) A further variation arises when using magnitude-only samples of $F(X)$ are used in the parameter-estimation step. We then obtain

$$|F_p(X)|^2 = \sum_{\alpha=1}^{P} \frac{R_\alpha}{X - s_\alpha} \sum_{\alpha=1}^{P} \frac{R_\alpha^*}{(X - s_\alpha)^*} = a_{P-1}^2 \frac{\prod_{\alpha=1}^{P-1}(X - z_\alpha)(X - z_\alpha)^*}{\prod_{\alpha=1}^{P}(X - s_\alpha)(X - s_\alpha)^*} = \frac{N_{2P-2}(X)}{D_{2P}(X)} \quad (3)$$

where the z_α are zeros of the numerator polynomial, which depend on the poles and residues together, and a_{P-1} is a normalizing parameter. The number of unknowns is doubled when squaring the FM, with the poles and zeros reflecting about the jω axis. Valid poles and zeros are those having negative real parts, however, so that upon factoring the numerator and denominator polynomials, only those roots having negative real parts are retained. Thus, the real and imaginary parts, or the magnitude and phase, of $F_p(X)$, can be estimated from ~ 4P real samples of $|F_p(X)|^2$.

As also can happen in implementing approaches (1) and (2), a potential difficulty arises here in that it's only feasible to use a relatively small number of poles and zeros in the FM since the matrix being solved to obtain its parameters becomes increasingly ill-conditioned with increasing P. This means that it's necessary to window the data being modeled which results in some ambiguity in the FM-parameter values. This is because the data in a given frequency window is affected by poles and zeros lying outside it and the data rank (i.e., P) is itself ambiguous [Miller (1995)]. Finally, modeling in the SD has its primary goal that of providing an acceptable match to a transfer function between its data samples, which doesn't require that the poles and residues (or zeros) even be computed, nor imply how accurate they should be if they were computed. For the phase-recovery application, however, the poles and zeros are needed, since otherwise those arising from squaring the complex transfer function can not be identified and removed. These issues will be discussed in the presentation.

REFERENCES

Brittingham, J. N., E. K. Miller and J. L. Willows (1980), "Pole Extraction from Real-Frequency Information", *Proceedings of the IEEE*, **68**, pp. 263-273.

Miller, E. K. (1995), "Model-Based Parameter Estimation in Electromagnetics: I--Background and Theoretical Development," *Applied Computational Electromagnetics Society Newsletter*, 10 (3), November.

Miller, E. K. (1996), "Model-Based Parameter Estimation in Electromagnetics: II--Applications to EM Observables," *Applied Computational Electromagnetics Society Newsletter*, 11 (1), pp. 35-56, March.

Real Time Adaptive Forward Error Correction Scheme

S. VELUSWAMY.
Electronics and Radar Development Establishment,
Bangalore - 560 093, INDIA.

Abstract

A new Real Time Adaptive Error Correction Scheme for use in Packet Radio network over noisy time varying channels has been investigated. Different rate codes are suggested on an adaptive manner for an efficient transmission, based on the link quality in the network. The proposed scheme is shown to provide better throughput performance than the fixed rate error correction schemes, and the conventional diversity systems.

Introduction :

Highly reliable and efficient data transmission over land mobile channels is complicated and problematic due to its time varying nature. The time varying characteristics results in variable rate Rayleigh fading due to multipath reflections and time dispersions. These in turn causes multiple random and burst errors resulting in unreliable communication. The aim of a Packet Radio Network is to achieve a high throughput at desirable levels of bit error performance, using available bandwidth and at acceptable complexity.

Several systems are available to protect the data over the time varying channels. These utilize the facilities like channel quality estimates, feedback links, and the availability of independent multi channels (diversity systems). When these facilities are not available as in a typical packet radio network, the protection of the data in the time varying channels becomes very difficult. The possible solution is to go for Forward Error Correction (FEC) schemes. In order to substantially improve the end-to-end bit error rate of the transferred message one must carefully consider the noise and fading process in question. The land mobile radio channel used for packet radio network is characterised by fadings of Rayleigh type. The fading process causes bursts of errors to appear with varying frequency and duration, in the received data stream. For a typical time dispersion of the order of 10 milliseconds encountered and for a transmission rate of 16 Kbps a burst error of 160 bits length are common.

To maximize the throughput of the system, the code rate has to be maximized (i.e redundancy has to be minimized). For this one may have to select a code that performs an averaging function, spreading out the effects of the deep fades over the rest of the signal. [1, 2]. The objective is the minimization of the variance of the number of errors occuring in a code word for redundancy is wasted if some code words encounter a large number of errors while others encounter none. The averaging function can be achieved through the selection of codes with very long code words. Considering a 16 Kbps channel, a typical vehicle speed of say 40 Km/hr and a carrier frequency of 60 MHz the fade rate is calculated to be of the order of 4 Hz . Then a code length of 4000 bits or more must be selected to average out the effects of fading process. Given an average BER of 1×10^{-2} or more the code has to correct a large amount of bit errors also. As the hardware complexity is a direct function of code length and the number of errors to be corrected the system to meet the above requirements will be complex. Therefore the scheme designed to cater for the worst case error conditions of the channel will be complex and in addition results in a poor average throughput efficiency of the systems in normal conditions [3]. Therefore it is a must to

420

have an adaptive forward error correction scheme to provide as high a throughput as possible with available bandwidth and allowed complexity.

Real Time Adaptive Forward Error Correction Scheme :

By monitoring the channel in some way it is possible to adjust different transmission parameters , such as the power , and / or the transmission rate , so as to match the transmission to the prevailing channel conditions [4-8]. In this paper a Real Time Adaptive Forward Error Correction Scheme is proposed for an efficient and reliable data transmission using Packet Radio Network in which most of the nodes may be mobile nodes which are affected by the time-varying fading channels. The scheme makes use of the availability the Radio channel link quality information between each node in the network. The information regarding the link quality is used at the transmitting node to adaptively encode the data portion of the packet, for transmission from that node. So different rate FEC codes are used at different instant of time depending upon the link quality at the time of transmission. It is assumed that the channels are of equal transmission rate (BW) between each node and the total transmitted power are the same for different transmissions. Unlike conventional scheme which uses a fixed (low) rate error correction system the proposed scheme uses fixed length codes and variable length information in each code word. The number of information bits in each code word is based on the link quality estimation and it is this that gives the adaptive nature of the scheme.

It will be appreciated that the link quality estimation is an essential part of the system. Such units are employed in a number of existing practical communication systems operating over fading time varying channels. This may involve complex hardware for link quality estimation. However in the case of a packet radio network the link quality between each node are estimated already for the purpose of selecting the best link for a destination node which may have many neighbours of the same tier from a transmitting node. This available information itself can be used for the real time adaptive FEC scheme and no extra link quality estimation is required . The error control encoding for the data portion of the packet can be done using a suitable code based on the link quality. The link quality information can be included as one of the field in the header of the packet. This information can be used at the receiver to select the correct code for decoding. It is assumed that the header of the packet is protected from error by a separate powerful fixed (low) rate FEC code.

System Analysis :

Let it be assumed that the estimates of the channel qualities are updated periodically. The estimates will be based on the received energy per bit to noise ratio measurement . Let β_1, β_2 , β_3 ...... β_m be the estimates during " m" time periods (i.e during m packet transmission periods). Let this be denoted as

$$\beta_i = \alpha_i^2 \frac{E_b}{N_0} \tag{1}$$

where α_i is the attenuation factor during i [th] packet transmission period, E_b is the transmitted energy per bit and N_0 is the power spectral density of the noise which is assumed to be AWGN. It is assumed that the estimates , β_i , remains constant during one adaptation period i.e during the transmission of one packet period . That is

$$\beta_i = \text{constant} \qquad \text{for } m\tau \leq t \leq (m+1)\tau \qquad (2)$$

where τ is the time for one packet transmission. Based on β_i, let r_i redundant bits be added as check bits to k_i information bits during the ith packet transmission .The set of information bits k_i and check bits r_i constitute an (n, k_i) error correcting code, where $n = (k_i + r_i)$ for $i = 1, 2, \ldots\ldots m$, capable of correcting all error patterns of weight t_i. The overall purpose is to minimize the system residual bit error rate and improve the overall system throughput rate R. The throughput is defined as the ratio of the number of information bits to the total number of bits, transmitted per unit time. In this case the system throughput, R, (for the data portion of the packet is concerned) during transmission of "m" packets is given by

$$R = \left(\sum_{i=1}^{m} k_i \right) / n \cdot m \qquad (3)$$

If p_i is the residual decoding bit error probability during the ith packet transmission the average residual bit error probability at the system output for the transmission of m packets is given by

$$P_{e,m} = \left(\sum_{i=1}^{m} k_i \right) / K \qquad (4)$$

$$\text{where} \quad K = \sum_{i=1}^{m} k_i$$

The main objective of the Real time adaptive FEC scheme will be to select the set $\{ k_i \}$ which minimizes the residual error probability $P_{e,m}$. In other words the goal is to determine the optimum set $\{ k_i \}$ as a function of the set $\{ \beta_i \}$ to maximize the system average throughput R.

To evaluate the average residual bit error probability the values of p_i's should be known. For a "t" error correcting code of block length "n", operating over a random error channel the probability of correct decoding of a code word is given by

$$P_c = \sum_{i=0}^{t} {}^n c_i \; q^i (1-q)^{n-i} \qquad (5)$$

where q is the channel transition probability . This channel transition probability, q can be calculated from the knowledge of the signals and modulation technique used, the probability distribution of the noise and the output quantization threshold of the demodulator. The probability that a decoded codeword will be in error is given by

$$P_E = 1 - P_c \qquad (6)$$

In general the relationship between P_E and p_i depends on the structure of the code word used. There are many approximation for the residual bit error probability in terms of the codeword

error probability , [10, 11]. If the number of information bits is reasonably large then $p_i \cong (1/2) P_E$ as a worst case. This approximation $p_i = (1/2) P_E$ is used in this paper.

For given type of error correction codes the set $\{ k_i \}$ determines the set $\{ t_i \}$ and for a given $\{ \beta_i \}$ the corresponding set of channel transition probabilities, $\{ q_i \}$, are determined by the modulation technique used. The set $\{ t_i \}$ and the set $\{ q_i \}$ determine the residual bit error probability $\{ p_i \}$ of the system during a given packet transmission .

Using U, T and Q to denote the vectors whose elements are k_i, t_i and q_i respectively, then the expression for the system residual bit error probability $P_{e,m}$ given in equation (4) can be modified as

$$P_{e,m} [U,T,Q] = \frac{1}{K} \sum_{i=1}^{m} \frac{k_i}{2} \left\{ 1 - \sum_{j=0}^{t_i} {}^n c_i \ q_i^j \ (1-q_i)^{n-j} \right\} \tag{7}$$

Since for a given code length the vector T is related to and fully determined by the vector U, one of them can be expressed in terms of the other in the argument of $P_{e,m}$ in equation (7) . Also since Q is mathematically related to the vector V of β_i's the analysis of the bit error probability in equation (7) can be carried out in terms of " U " and " V " which is more convenient. The aim then will be to find out the information vector , U, as a function of the Bit Error Rate (BER) vector , Q. So that the average residual bit error probability is minimized subject to the limitation that throughput R is maximized.

The channel over which the packets are transmitted can be considered to be slowly - varying Rayleigh fading channel that is subjected to AWGN. Here slowly varying means the signal fade level, and hence the received signal energy, remains constant over the period of one packet duration which can be the duration of a code word and this level may vary during the next packet transmission following Rayleigh distribution. Then the β_i 's will have the probability density function given by

$$p_\beta (\beta) = (1 / \beta') \ exp (- \beta / \beta') \quad for \ \beta \geq 0 \tag{8}$$

where β' is the average per bit signal to noise ratio. Then the probability density function associated with the vector constituted by the β_i's over m number of packet transmission is given by

$$p_v (V) = \prod_{i=1}^{m} \frac{1}{\beta'} \ exp\left(-\frac{\beta}{\beta'}\right) \quad for \ \beta \geq 0 \tag{9}$$

Therefore the overall average bit error probability of the system is given by

$$\overline{P_e} = \int_0^\infty \int_0^\infty .... \int_0^\infty P_{e,m}[U,V] \ p_v \ (V) \ dv \tag{10}$$

and the aim is to minimize the equation (10) subject to the constraint that

$$R = \left(\sum_{i=1}^{m} k_i \right) / n . m$$

For a given estimate of V obtained from the channel quality monitor a set of say N codes are selected which will minimize the $P_{e,m} [U , V]$ and hence the equation (9). Depending on the estimate of V one of the code belonging to the set of N codes is selected during a particular packet transmission .

In order to properly decode a received code vector the decoder , in this case , should know which code is used during that particular transmission. The information regarding the code used for data portion of the packet is passed on to the receiver in the header portion of the packet. The header being comparatively very small than the data portion, the header can be protected from errors by using an appropriate (separate) code and hence the reliability of the system can be made as high as needed.

In this paper a class of Linear block codes is used. But the application of the idea of Real time adaptive FEC is not restricted to this class. This class is selected here because of their simplicity and availability of large range of information bits for a given code word length n . The process of error minimization referred to earlier involves first selecting the appropriate codes for a given range of channel signal-to-noise ratio (in terms of E_b / N_o) and channel BER . Next allocation of appropriate code during different packet transmission depending on the channel quality information (β_i). This involves allotting a high-rate code during best channel condition and lowest-rate code during worst case channel condition. A set of four codes are chosen and the codes in the form (n,k,t) are (24,00,00) , (24,08,05) , (24,12,03) and (25,15,02). For E_b / N_o values of 0 to 2 dB the code (24,00,00); for values 2 to 6 dB the code (24,08,05); for values of 6 to 10 dB the code (24,12,03) and for E_b / N_o values of 10 dB and above (24,15,02) code are used during the packet transmission.

Results :

The performance of the Real Time Adaptive FEC scheme has been analysed numerically for different values of E_b / N_o . It is assumed that the transmission power during each transmission is the same. The performance has been compared with a system using fixed rate code for all transmission irrespective of the channel quality i.e. designed for worst case condition. The system performance is shown in figure . It can be seen that the system throughput is high in the case of the Real Time Adaptive FEC scheme for the same value of E_b / N_o and for a required value of error rate. The improvement can be even hundred percent. The system has also been compared with a multi channel (L) maximal-ratio combining (MRC) diversity system. The advantage of Real Time Adaptive FEC scheme is that it is better able to take account of those periods when the channels are good than is a diversity system, whose rate is fixed at 1 / L where L is the number of channels used [9]. This advantage is important in practical systems. For example in the case of speech communication system where a BER of 10^{-4} is acceptable, the multichannel diversity system requires atleast 4 dB more E_b / N_o than the proposed system for that BER.

Conclusion :

A new Real Time Adaptive Forward Error Correction has been proposed for use in Packet Radio network. The advantage over the fixed code rate system arises mainly due to the fact that when the channel is highly noisy, low rate code is used than when the channel is less noisy. It has been shown that for a given E_b / N_o range and required residual BER the throughput is higher than in the case of a fixed code rate system and conventional diversity systems.
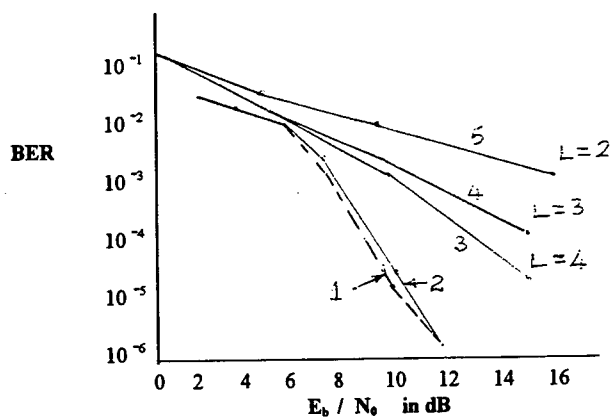

FIG : Performance of Real Time Adaptive FEC Scheme

1 Fixed Rate Code System (24, 08, 05)
2 Real Time Adaptive FEC Scheme
3,4,5 MRC Diversity System.

References :

1. SIEW, C.K., and GOODMAN, D.J., : ' Packet - Data Transmission over Mobile Radio Channels' , IEE Trans. Veh., Tech., Vol 38, No : 2, May 1989.
2. STEPHEN, B.,WICKER, : ' Highly Reliability Data transfer over the Land Mobile Radio Channel' , IEEE Trans. Veh., Tech., Vol 39, No :1, Feb 1990.
3. VUCETIC, B., DRAJIC, D., and PERISIC, D. : ' Algorithm for adaptive error control system synthesis', Proc. IEE F, Feb. 1988, pp. 85-94.
4. HAYES, J.F. : ' Adaptive feedback communication'. IEEE Trans. Commun. Technol., Feb. 1968, COM-16, (1), pp. 29-34.
5. CAVERS, J.K. : ' Variable-rate transmission for Rayleigh fading channel', IEEE Trans. Commun. Technol., Feb.1972, COM-20, (1), pp. 15-22.
6. HENTINEN, V. : 'Error performance for adaptive transmission on fading channels', IEEE Trans. Commun., Sept. 1974, COM-22, (9), pp. 1331 - 1337.
7. CHANG, S., : ' A feedback adaptive variable rate meteor burst communication system'. Proc.IEEE International Conference on Communication, July 1988, pp. 14.2.1 - 14.2.7.

8. SKINNER, T., and CAVERS, J. : ' Selective diversity for Rayleigh fading channels with feedback link', IEEE Trans. Commun., Feb 1973, **COM-21**, (2), pp. 117 - 126.

9. KOUSA, M.A., and TURNER, L.F., : ' Multichannel adaptive forward error-correction system', IEE Proceedings-I, Vol. 140, No.5, Oct. 1993.

10. PROAKIS J.G. : ' Digital communiocations' (McGraw - Hill, New York, 1983.)

11. MICHELSON, A.M., and LEVESQUE, A.H. : ' Error - control techniques for digital communication' (John Wiley & Sons, New York, 1985)

A NOVEL SPATIAL MODULATION SPREAD-SPECTRUM TECHNIQUE

S.A. Pradels, N. Marshall, N. Aery and O.R. Baiocchi
Center for Telecommunications
College of Engineering, Computer Science, and Technology
California State University, Chico

ABSTRACT:

Spread Spectrum technology, originally developed for covert and interference resistant communications, has now become one of the significant enabling technologies for high density cellular telephone communications and for wireless computer local area networks. One spreading modulation technique, known as direct sequence spread spectrum, involves convolving the digital data stream with a much higher rate pseudo-random sequence as a phase modulation. This combined waveform, spread over a wide spectrum but with a correspondingly lower spectral density, is transmitted to a receiver that carries out a matched de-convolution to extract the original data stream. The focus of this study is to replace the convolution process with a switching process between multiple antennas.

This technique will generate receivable spread spectrum signals at very geographically specific points, but will present a reduced coherence at other points. The implication of the approach, beyond the obvious use for secure communications, is that the potential exists to reduce the mutual interference between fixed geographical locations, and to operate general communication systems at a lower spectral density than would otherwise be practical. Initial investigation of this technique has been done through computer simulation using the HP-EEsof Series IV software package running on UNIX workstations. The simulation consists of a single array of two transmitting antennas separated by a quarter wave distance and in line with a single receiver which are switched by a data sequence. It is demonstrated that the coherence of the signal peaks at the receiver and decays rapidly with the distance from the receiver. Applications and variations of this technique to practical wireless systems are also discussed.

INTRODUCTION:

Similar to the Direct Sequence Spread Spectrum (DSSS) systems, the spatial modulation technique relies on the phase angle of a carrier waveform to relay data across the wireless link. Unlike DSSS where the modulating sequence is directly mixed with a carrier signal to generate the phase modulation, Spatial Modulation relies on an array of transmitting antennas to produce the desired effect. The antennas are placed in such a way as to produce a carrier signal with a different phase for each antenna. The modulation is implemented by using the modulo-2 (exclusive OR) sum of the data sequence and the pseudonoise (PN) to control which antenna transmits at a time. Although the

427

antennas all transmit at the same carrier frequency, the switching of the antennas produces a resultant signal that appears to have a wideband spectrum.

For the purposes of our initial investigation, an array of two antennas placed λ/2 apart were used to represent the transmitters and a single receiver antenna was placed in the far-field on axis with the transmitting array (see Figure 1). At the receiver location a matched deconvolution is performed and the original data sequence is recovered. As the location deviates from the axis the coherence of the signal is expected to decay due to improper phase modulation.

```
           λ/2                        Far Field
     X <-------> X                        O
       \      /                           |
       Transmitters                    Receiver
```

FIGURE 1

The situation becomes more complicated with the introduction of a large antenna array. After the location of the receiver antenna has been determined, each antenna would be driven with a controllable phase angle an a PN sequence used to select which of the several antennas is transmitting at any given point in time. There are of course several different radio architectures which could be implemented using this technique.

SIMULATION:

The HP-EEsof series IV software was used to simulate the previously described situation where two transmitting antennas are placed 180 degrees (λ/2) out of phase with respect to each other and the receiver antenna is in the far-field. The OMNISYS system simulator was used to layout the schematic of the desired system as well as to run the discrete time test bench simulation.

The schematic layout in Figure 2 shows the internals of the simulated system. It consists of a linear feedback shift register with maximal taps of {20, 3} used to produce a 20 bit PN sequence of length $2^{20} - 1$.[Dixon, 1994] An exclusive-OR gate was used to modulo-2 add the data and the PN sequence resulting in the switch controlling sequence. A single pole double throw switch is used to select which of the two transmitting antennas will emit the carrier signal. The transmitter antennas are "linkt" elements with gains specified to be 0 dB. The phase shifts of 0 and 180 degrees expected as resultant of transmitter locations were used to specify the phase shifts caused by the "linkt" elements. The receiver antenna was also specified to have a 0 dB gain and a phase shift of 0 degrees. The received signal is mixed with a local carrier to downconvert the incoming signal to basedband frequencies. For simplicity, the PN sequence used for the transmitter was directly used to despread the received signal by the use an exclusive-OR resulting in the desired data sequence. Of course in a practical system, the PN sequence would have to be locally generated and synchronized with the transmitted sequence. Several ports were used to inject various signals such as the RF carrier tone, data sequence, and the PN clock as well as for the purpose of making measurements.
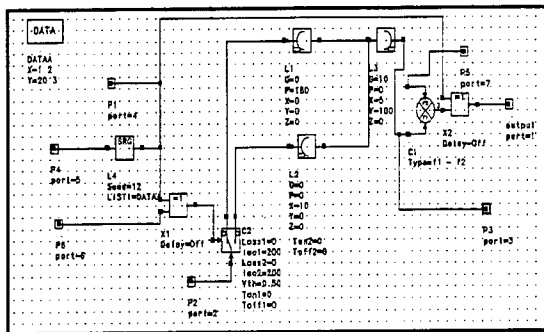
428

Figure 2

This schematic was imported into the test bench and the ports of the element were connected as shown in Figure 3. Port 4 was used to inject the clock for the PN generator which was set to have a period of .01ns. A data source provided by the program was configured to have a 1ns period and was differentially encoded before being applied to port 6 of the schematic. Differential encoding and decoding was used to provide coherent detection of the transmitted signal. This eliminates the phase ambiguity of the received signal. In order to interface with the encoder and decoder elements some signal level shifts were performed through Logic_to_NRZ and NRZ_to_Logic elements. RF_1 tone elements were used to provide the transmitter and receiver carrier waves through ports 2 and 5 respectively. Port 1 was the output of the schematic and all other ports were made available for system analysis.
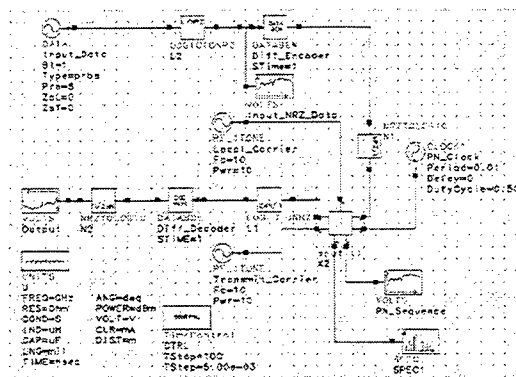
Figure 3

The simulation was initiated and the resulting waveforms were captured. Figure 4 shows the input NRZ (polar) data stream that was fed into the system and Figure 5 was the data waveform captured at the output of the system. As can be seen the output waveform at the desired location follows the input data stream, and the PN sequence has been removed.
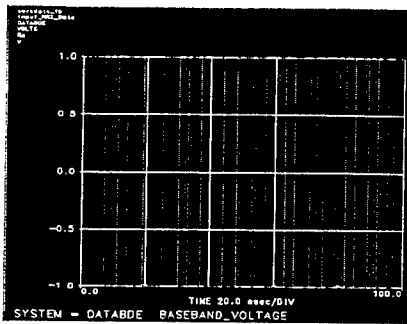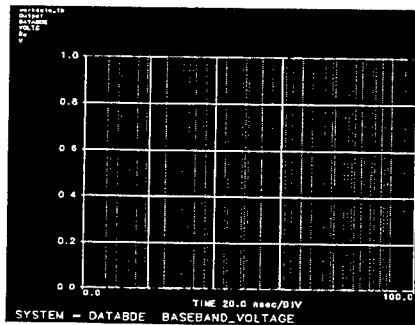
Figure 4 (Input)

Figure 5 (Output)

EXTENSIONS:

This paper has illustrated the principle of spatial modulation to achieve geographically focused spread spectrum modulation. In order to set the foundations for future investigation, a canonical model was analyzed. However, the greatest potential for the technique lies in the extension to multiple radiator scenarios.

There are two obvious extensions, each involving numerous radiators randomly placed within a cluster. Each case benefits from the focusing of decodable communication to within a defined area.

Cluster / cluster communications

In this situation, transmission modulation occurs by phase and amplitude modulation of a number of radiators that are randomly placed, but grouped together in a cluster. The reception is performed by a second cluster of antennas, that may be contiguous with the transmitting cluster, or may be far removed.

In either case, the transmission modulation pattern is optimized to minimize the intelligibility of the radiation beyond the boundaries of the target reception area. The reception array is designed to sum the incident signals during the demodulation and correlation processes.

The most obvious applications of this technique are for jam-resistant communications, and for minimum intercept communications.

Cluster / point communications

Transmission modulation is carried out as in the previous case, but with the additional criterion that the intelligibility of the transmitted information is highly focused at a single point, at the same time as minimizing the intelligibility in all other regions. Of the two discussed extensions, this is the simpler to implement.

430

There are two sub-classes of this technique:

a) Communication to a single point within the geographical boundary of the cluster. Far field radiation beyond the cluster falls off rapidly, allowing frequency re-use to be deployed on a denser basis than would otherwise be possible. Applications lie in increasing the overall spectral efficiency of urban communication systems, such as CDMA/PCS.

b) Communication to a single point far removed from the cluster. Again, far field radiation falls off rapidly, but the intelligible signal is focused at a single distant point. This characteristic can be beneficially used in rural wireless telephone communications, where frequency allocations are scarce, but the "spill over" from one distant zone to another distant zone frequently reduces the benefits obtainable from the frequency re-use. In this application, the spatial modulation technique combines the benefits of CDMA modulation with the advantages of aperture synthesis, again, to increase the ultimate data carrying capacity of the available spectrum.

The two cases illustrate some of the potential to be derived from further analysis and extension of the concept of combining spatial modulation with spread spectrum technology. As the demand for spectrum becomes more pressing, a natural migration of this technology to the commercial arena can be expected.

REFERENCES:

1. Dixon, Robert C. *Spread Spectrum Systems with Commercial Applications*, J Wiley & Sons, New York, 1994.
2. Series IV, Release 6.0 - *System Network Items*, HP EEsof , July 1995.
3. Series IV, Release 6.0 - *Simulating and Testing*, HP EEsof , July 1995.

Time-Frequency and Time-Scale Analysis
for Electromagnetics — Spectrograms, Wavelets and More

Christopher J. McCormack

Rome Laboratory / ERCS

Hanscom AFB, MA 01731

c.mccormack@ieee.org

Abstract

This paper presents a brief introduction to using time-frequency and time-scale methods for signal analysis. The basic characteristics of the spectrogram, Wigner-Ville distribution, reduced interference distribution, and wavelet representations are presented. These techniques offer additional insight compared with traditional Fourier analysis when working with non-stationary signals.

1 Introduction

Electromagnetic scattering signals have been analyzied using time-frequency transformations [11] and time-scale transformations [9] to obtain insights into signal characteristics that are not obvious using traditional Fourier-based frequency domain analysis. These newer techniques are particularly useful when dealing with non-stationary signals or when considering dispersive materials or structures.

The shortcomings of regular Fourier analysis can be illustrated by considering two signals taken from the WaveLab toolbox [1]. The first signal is a linear chirp with a frequency increasing linearly with time. Figure 1 shows a portion of this waveform. This can be generated in Matlab using

```
t = ( 1 :  512 ) / 512 ;
x = sin ( pi * ( 512 * t / 2 ) .* t ) ;
```

The second test signal consists of three components: a high frequency sinusoid, a linear chirp, and a quadratic chirp. This waveform is show in Figure 2. The Matlab definition for this signal is

```
t = ( 1 :  512 ) / 512 ;
x = sin ( pi * ( 512 * .6902 ) * t ) ...
+ sin ( pi * ( 512 * t / 8 ) .* t ) ...
+ sin ( pi * ( 512 * ( t .* t ) / 2 ) .* t );
```
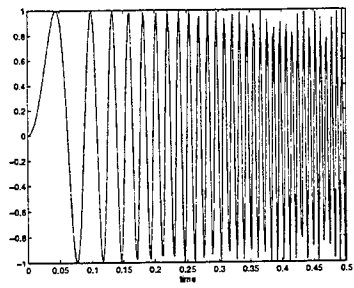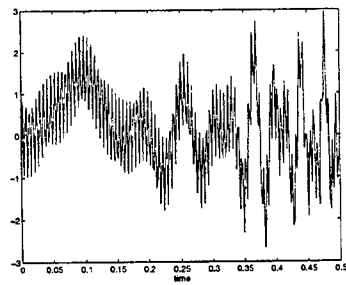
Figure 1: Linear Chirp Waveform

Figure 2: Three Component Waveform

The major difficulty with these signals is the spectra changes as time advances. Figure 3 shows the magnitude of the Fourier transform for these two signals, using the relationship

$$X(f) = \mathcal{F}\{x\} = \int_{\infty}^{-\infty} x(\tau)e^{-j2\pi f\tau}d\tau$$

or the discrete equivalent

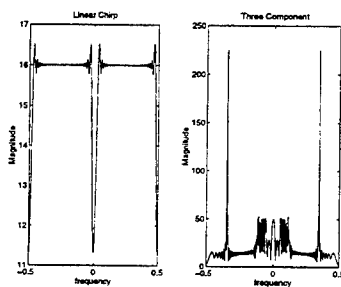$$X(k) = \sum_{m=1}^{N} x(m)e^{-j2\pi mk/N}$$

Figure 3: Magnitude of Fourier Transforms

It is important to remember the Fourier transform is a complete representation of the signal, and the inverse transform will exactly reproduce the original waveform. The problem is a magnitude plot only provides part of the story — the transform's phase contains significant information which may be difficult to decipher.

2   Spectrogram

The simplest way to characterize a time-varying signal is to take multiple Fourier transforms, each giving a snapshot of the signal. The spectrogram, or short-time Fourier transform (STFT), is generated by centering a window at the time of interest then taking the squared magnitude of the Fourier transform. This can be expressed as

$$S_x(t,f) = \left| \int_{-\infty}^{\infty} h(t,\tau)x(\tau)e^{-j2\pi f\tau}d\tau \right|^2$$

The choice of a proper window function, $h(t,\tau)$, is essential for obtaining a clear spectrogram. A narrow window allows the spectrogram to react quickly to changes in the signal, but the short observation time gives poor frequency resolution. On the other hand, a long window will yield high frequency resolution, but will react slowly to signal changes, smearing the result along the time axis. Figure 4 shows the difference between a 16 point and a 128 point window function when applied to the three-component signal.
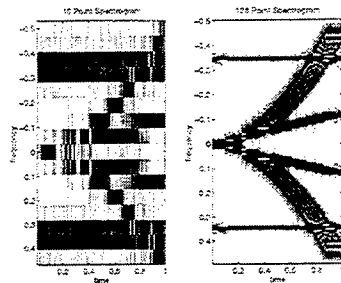
434

Figure 4: Short and Long Window Spectrograms

The tradeoff between time and frequency resolution is the fundamental characteristic of the spectrogram. While this does not cause much difficulty for slowly changing signals, it does present problems for complex, rapidly changing signals.

3 Wigner-Ville

The Wigner-Ville distribution avoids the time and frequency resolution tradeoff found in the spectrogram and gives high resolution along both the time and frequency axes. The drawback of this method is the existence of large cross terms which arise between legitimate signal components and interfere with the desired result. The distribution is calculated using the expression

$$W(t,f) = \int_{-\infty}^{\infty} x(t+\tau/2)x^*(t-\tau/2)e^{-j2\pi f\tau}d\tau$$

The Wigner-Ville distribution gives a two-dimensional energy distribution, analogous to a two-dimensional probability density function. Like the probability distribution, integrating or summing along one axis will provide the marginal distribution. The marginals of the Wigner-Ville are equivalent to the signal power, $|x(t)|^2$, and the power spectral density, $|X(f)|^2$. To satisfy these marginals, some portions of the distribution take on negative values. Figure 5 shows the Wigner-Ville distribution for the two example signals.

4 Reduced Interference Distributions

The reduced interference distribution, or RID, was developed as an improvement to the Wigner-Ville distribution. The goal was to maintain the high resolution and marginal properties of the Wigner-Ville while reducing the cross terms [7]. RIDs, as well as the Wigner-Ville and spectrogram, can be considered members of Cohen's class with the general form [3]

$$C_x(t,f;\phi) = \int\int\int x(t+u/2)x^*(t-u/2)e^{-j2\pi\nu u}\phi(\nu,\tau)e^{j2\pi f\tau}e^{-j2\pi\nu t}du\ d\tau\ d\nu$$
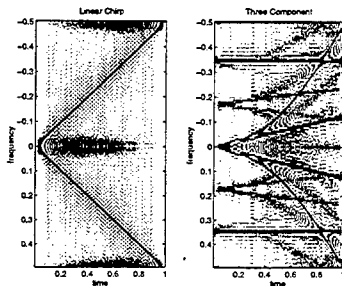
Figure 5: Wigner-Ville Distributions

The difference between all these distributions is the selection of the kernel function, $\phi(\nu, \tau)$. Design rules have been developed for selecting ϕ, and it can be selected using adaptive techniques [8].

A discrete version of the RID known as the binomial distribution provides a kernel that performs reasonably well in most situations. Figure 6 shows the binomial distributions for the test signals.
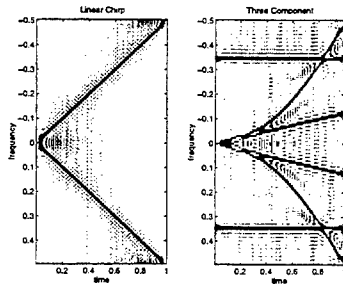

Figure 6: Binomial Distributions

The reduced interference displayed in the binomial distribution does not come without a disadvantage. The Wigner-Ville distribution exhibits the highest possible resolution along each axis. The binomial distribution sacrifices some of that resolution to reduce the interference. This is analogous to allowing a wider main beam pattern in an antenna to obtain low sidelobes.

5   Wavelets

The three techniques presented above all are closely related to the Fourier transform and have resolution cells that are uniform throughout the time-frequency plane. An alternative to generating a time-frequency distribution is to apply the wavelet transformation and create a time-scale

distribution. Instead of using complex sinusoids as basis functions, the wavelet transform uses scaled and shifted versions of a mother wavelet. Compressing the time scale of a signal corresponds to increasing its frequency, allowing a time-scale distribution to be treated as a time-frequency distribution also.

For a given mother wavelet, $h(t)$, the wavelet transform is defined as [12]

$$\text{WT}_x(\tau, a) = \int_{-\infty}^{\infty} x(t) h_{a,\tau}^*(t) dt$$

where the basis functions

$$h_{a,\tau}(t) = \frac{1}{\sqrt{a}} h\left(\frac{t-\tau}{a}\right)$$

are called wavelets.

The representation of the signal using a wavelet transform has some major differences from the preceeding distributions. The time-scale distribution changes drastically with the use of different mother wavelets. In general, the distribution follows the concepts of multi-resolution analysis (MRA) or constant Q analysis [2]. As the scale compresses, the shifts tracked become finer. That means time and frequency resolution are inversely related — low frequencies have good frequency resolution and poor time resolution, while high frequencies have poor frequency resolution and good time resolution.

Figure 7 shows the wavelet representation for the two example signals based on a Morlet mother wavelet [13]. Some differences stand out from the proceeding time-frequency plots. The time-scale plot gives a one-sided spectra with logarithmic spacing along the scale (frequency) axis. The time-frequency distributions appear clearer for these signals since they consist of sinusoidal functions, exactly matching the basis functions used.
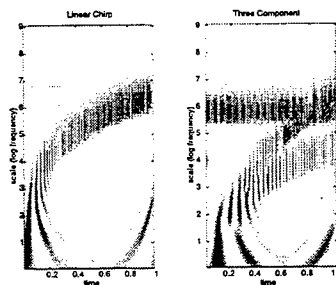

Figure 7: Wavelet Distributions

6   Conclusions

This paper provides an introduction to time-frequency and time-scale analysis. The references included provide the path to further investigating this field, both with understandable introductions to time-frequency techniques [11], wavelets [14], and samples of how to implement these techniques on a computer [11, 1].

References

[1] Jonathan Buckheit, et. al. "WaveLab." *MATLAB* Library available on the World Wide Web from `http://playfair.stanford.edu/ wavelab`.

[2] Y. T. Chan. *Wavelet Basics*. Kluwer Academic Publishers, 1995.

[3] Leon Cohen, "Time-Frequency Distributions — A Review." *Proceedings of the IEEE*, Volume 77, Number 7, 1989.

[4] Nikola Hess-Nielsen and Mladen Victor Wickerhauser, "Wavelets and Time-Frequency Analysis." *Proceedings of the IEEE*, Volume 84, Number 4, April 1996.

[5] Guillermo C. Gaunaurd and Hans C. Stifors. "Signal Analysis by Means of Time-Frequency (Wigner-Type) Distributions — Applications to Sonar and Radar Echoes.

[6] Amara Graps, "An Introduction to Wavelets." *IEEE Computational Science and Engineering*, Volume 2, Number 2, Summer 1996.

[7] Jechang Jeong and William J. Williams. "Kernel Design for Reduced Interference Distributions." *IEEE Transactions on Signal Processing*, Volume 40, Number 2, February 1992.

[8] Jechang Jeong and William J. Williams. "Alias-Free Generalized Discrete-Time Time-Frequency Distributions." *IEEE Transactions on Signal Processing*, Volume 40, Number 7, November 1992.

[9] Hyeongdong Kim and Hao Ling. "Wavelet Analysis of Radar Echo from Finite-Size Targets". *IEEE Transactions on Antennas and Propagation*, Volume 41, Number 2, February 1993.

[10] Stephane G. Mallat, "A Theory for Multiresolution Signal Decomposition: The Wavelet Representation." *IEEE Transactions on Pattern Analysis and Machine Intelligence*, Volume 11, Number 7, July 1989.

[11] Christopher J. McCormack. "Time-Frequency Analysis in Radar Backscatter Problems". Ph.D. Thesis, The University of Michigan, 1996.

[12] Olivier Rioul and Martin Vetterli, "Wavelets and Signal Processing." *IEEE Signal Processing Magazine*, October 1991.

[13] John Sadowsky, "Investigation of Signal Characteristics Using the Continuous Wavelet Transform." *Johns Hopkins APL Technical Digest*, Volume 17, Number 3, 1996.

[14] Brani Vidatović and Peter Müller, "Wavelets for Kids: A Tutorial Introduction." 1994. Unpublished. Available by FTP from `ftp.isds.duke.edu` in the directory `/pub/Users/brini/papers/wav4kids[A-B].ps.Z`

Antenna Array Factors for Dipole Antennas Above an Imperfectly Conducting Half- Space

John W. Williams
Science Applications International Corporation
20201 Century Boulevard, Germantown, Maryland 20874
(301) 353-8227 / (301) 428-3482 (FAX)
John.W.Williams@cpmx.saic.com

Abstract

This paper presents a formalism for calculating antenna array factors for arrays of vertical dipoles positioned above an imperfectly conducting half-space. Using expressions for incident, reflected, and surface-wave contributions to the total field, antenna array factors are derived for a linear arrays with array axis parallel and perpendicular to the ground plane. The approach introduces the concept of surface-wave coefficients which are treated in a manner similar to that for plane wave reflection coefficients in the development of expressions for the antenna array factors. Reflected and surface-wave contributions to the array factors are calculated as the product of the free space field radiated by a reference element, a geometrical factor, and the plane wave reflection and surface-wave coefficients, respectively. It is shown that for a linear array of vertical dipoles with array axis parallel to the ground plane, the geometrical factor is identical in magnitude to that for the same array radiating in free space. However, if the array axis is normal to the ground plane, the geometrical factor required for calculation of the reflected and surface-wave contributions to the far fields differs in magnitude and phase from the free space geometrical factor. Applications and limitations of the formalism are illustrated for arrays of vertical dipoles positioned above soil and water media.

1. Introduction

Few problems in electromagnetic theory have a longer history of investigation than that of radiating dipoles above an imperfectly conducting ground. This is because the electromagnetic fields cannot be treated as the sum of incident and reflected plane waves alone. Solutions near the boundary of the half-space must include an inhomogeneous lateral wave which includes a surface-wave term in addition to the plane wave components [1-3]. In this paper, total far fields radiated from linear arrays of vertical dipoles are calculated as the sum of incident, reflected, and surface-wave components. The objective is to quantify the effects of an imperfectly conducting half-space on antenna array factors. Antenna array factors for arrays in free space are well known for a variety of configurations [4-6]. Because reflected and surface-wave components can add either constructively or destructively with the incident component, the free space antenna array factors can be noticeably altered in the presence of an imperfectly conducting ground.

Basic expressions for far fields radiated by a single dipole positioned above a ground plane are discussed in Section 2. These expressions are then used in Section 3 to calculate antenna array factors for linear arrays of vertical dipoles spaced uniformly along the y- or z-axes. Section 4 presents comparisons of free antenna array factors and electric fields with those obtained in presence of a ground plane. Conclusions are given in Section 5.

2. Expressions for the Dipole Fields

Far fields from a single radiating dipole positioned above an imperfectly conducting ground plane can be written as the sum of incident, reflected and surface-wave contributions to the total fields [1].

$$E^{(total)} = E^{(inc)} + E^{(ref)} + E^{(sur)} \tag{1}$$

Figure 1 illustrates the geometry for a single dipole and its image. Expressions used in this paper for the dipole far fields were developed by Norton [1]. For a vertical dipole, radiated electric field have two components, E_p and E_z. The ϕ-component of the electric field vanishes. Non-vanishing components are given by:
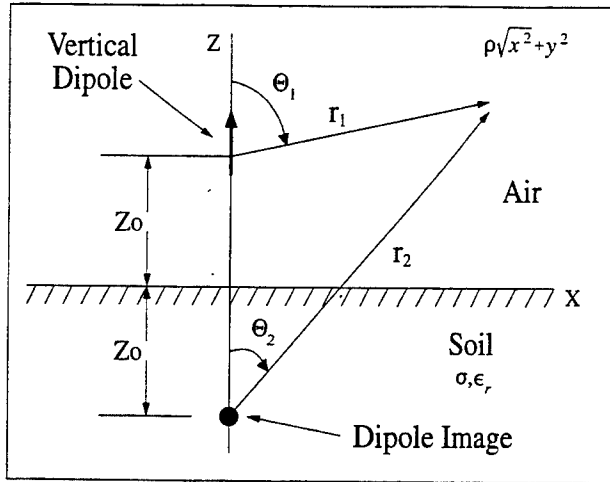
Figure 1 Geometry for the calculations

$$E_z = V[\sin^2\theta_1 \frac{e^{ikr_1}}{r_1} + R_v(\theta_2)\sin^2\theta_2\frac{e^{ikr_2}}{r_2} + (1-R_v)(1-u^2+u^4\sin^2\theta_2)F(w)\frac{e^{ikr_2}}{r_2}$$ (2)

and

$$E_\rho = -V[\sin\theta_1\cos\theta_1\frac{e^{ikr_1}}{r_1} + \sin\theta_2\cos\theta_2 R_v(\theta_2)\frac{e^{ikr_2}}{r_2}$$

$$-(1-R_v)\sin\theta_2 u\sqrt{1-u^2\sin^2\theta_2}\left[1 - \frac{u^2(1-u^2\sin^2\theta_2)}{2} + \frac{\cos^2\theta_2}{2}\right]F(w)\frac{e^{ikr_2}}{r_2}$$ (3)

where V represents the dipole source strength, $V = ik\eta_0 Idl/4\pi$, and R_v denotes the reflection coefficient for a plane wave with its electric vector in the plane of incidence,

$$R_v = \frac{\cos\theta_2 - u\sqrt{1-u^2\sin^2\theta_2}}{\cos\theta_2 + u\sqrt{1-u^2\sin^2\theta_2}}$$ (4)

Factor "u" is defined as the ratio of the propagation constant for air, $k^2 = \omega^2\epsilon_0\mu_0$, and the propagation constant for the half-plane, $k_g = \omega^2\epsilon_0\epsilon_r\mu_0 + i\omega\sigma\mu_0$, i.e. $u = k/k_g$. The Norton surface wave attenuation function, $F(w)$, is defined in terms of the complex error function as [7,8]:

$$F = 1 + i\sqrt{\pi w}e^{-w}efrc(-i\sqrt{w})$$ (5)

where

$$w = ikr_2u^2\left(\frac{1-u^2\sin^2\theta_2}{2}\right)\left(1 + \frac{\cos\theta_2}{u\sqrt{1-u^2\sin^2\theta_2}}\right)^2$$ (6)

In developing the formalism for evaluation of antenna array factors, it will prove convenient to recast equations for the components of the electric field in the following form:

$$E_\xi = V\left\{ g_\xi(\theta_1)\frac{e^{ikf_1}}{r_1} + g_\xi(\theta_2)\left[R_\nu(\theta_2) + \Psi_\xi(r_2,\theta_2)\right]\frac{e^{ikr_2}}{r_2} \right\} \tag{7}$$

where $g_z(\theta) = \sin^2\theta$ and $g_\rho(\theta) = \sin(\theta)\cos(\theta)$. We will refer to functions Ψ_ξ as surface-wave coefficients. These are given by:

$$\Psi_z(\theta) = (1 - R_\nu)csc^2\theta(1 - u^2 + u^4\sin^2\theta)F(w) \tag{8}$$

and

$$\Psi_\rho(\theta) = (1 - R_\nu)\tan\theta\, u\sqrt{1 - u^2\sin^2\theta}\left[1 - \frac{u^2(1 - u^2\sin^2\theta)}{2} + \frac{\cos^2\theta}{2}\right]F(w) \tag{9}$$

Although the products $g_\xi\Psi_\xi$ ($\xi = z,\rho$) which define the ξ-components of the electric field are non-singular for all values of the polar angle θ, Ψ_z is singular where θ equals an integer multiple of π radians and Ψ_ρ is singular when the polar angle equals an integer multiple of $\pi/2$ radians.

3. Antenna Array Factors

The concept of an antenna array factor has long been used for the analysis of antenna arrays ([4]-[6]). This concept is computationally efficient tool for the design of antenna arrays. If E_ξ represents the ξ-component of the radiated far field from an antenna array and $E_{\xi,0}$ denotes the ξ-component of the far field radiated by a reference element, then E_ξ can be expressed as the product of the radiated field from the reference element and the antenna array factor $f(\theta,\phi)$:

$$E_\xi = E_{\xi,0}\, f(\theta,\phi) \tag{10}$$

This paper examines an analogous formalism for antenna arrays above an imperfectly conducting half-space. For an array in free space, the antenna array factor depends on the array geometry alone and is independent of distance between the source and observation point. However, as shown below, for an antenna array positioned over an imperfectly conducting half-space, the array factor is dependent upon both the array geometry and the distance between the observation point and the array.

In order to examine the effects of an imperfectly conducting ground on antenna array performance, it is assumed that the antenna array is composed of radiating dipoles positioned above an imperfectly conducting half-space. Expressions for the far fields radiated by individual elements of the array are those discussed in Section 2.1 above. Throughout this paper, it is assumed that the reference element for the array is located at the centroid of the array. If an element of the array is located at the centroid, then it is selected as the reference element. If no element of the array is positioned at the centroid, then a reference element is assumed to exist at the centroid.

First consider an array of N_y vertical or horizontal dipoles spaced uniformly along the y-axis a distance Z_0 above the half-space. Using equation 7 above, far fields radiated by the array of either horizontal or vertical dipoles can be written as:

$$E_\xi = E_{\xi,0}\left\{ \sum_{n=1}^{N_y} \frac{|V_n|}{|V_0|}\left[\frac{g_\xi(\theta_{1,n},\phi_{1,n})}{g_\xi(\theta_0,\phi_0)}\frac{r_0}{r_{1,n}}e^{ik(r_{1,n} - r_0 + \beta_n)} \right. \right.$$

$$\left. \left. + (R_\nu + \psi_\xi)\frac{g_\xi(\theta_{2,n},\phi_{2,n})}{g_\xi(\theta_0,\phi_0)}\frac{r_0}{r_{2,n}}e^{ik(r_{2,n} - r_0 + \beta_n)} \right] \right\} \tag{11}$$

441

where β_n denotes the phase of the nth source, γ , relative to the reference source, $_0V$, $_{1,n}r$ represents the radial distance from the nth element of the array to the observation point, and $r_{2,n}$ represents the radial distance from the image of the nth element of the array to the observation point. Here, $E_{\xi,0}$ denotes the incident field radiated by the reference element located at the centroid of the array.

$$E_\xi = E_{\xi,0}\left[\sum_{n=1}^{N_y} e^{ik(r_{1,n}-r_0-\beta_n)} + (R_v+\psi_\xi)e^{ik(r_{2,n}-r_0-\beta_n)}\right] \tag{12}$$

For the far fields, it is reasonable to assume that $r_0/r_{1,n} \approx r_0/r_{2,n} \approx 1$, $\theta_{1,n} \approx \theta_{2,n} \approx \theta_0$, and $\phi_{1,n} \approx \phi_{2,n} \approx \phi_0$ for all values of n. In order to obtain analytical expressions for array factors, we shall also assume that $|V_n| = |V_0|$ for all values of n. With these simplifications, equation 11 becomes:

Since specific forms for the antenna array factors depend on whether the array contains an even or odd number of elements, it is convenient to define $M_{0y} = (N_y-1)/2$ and $M_{ey} = N_y/2$. The nth element of the array is positioned at $(x_{1,n}, y_{1,n}, z_{1,n}) = (0, y_{1,n}, Z_0)$, while the image of the nth element is located at $(x_{2,n}, y_{2,n}, z_{2,n}) = (0, y_{2,n}, -Z_0)$. If N_y is an odd integer and "a" denotes the distance between adjacent elements of the array, it will prove convenient to number the elements so that elements assigned an odd (even) number are aligned along the negative (positive) y-axis as follows: $y_{1,2m+1} = y_{2,2m+1} = -yma$ for m = 0,1, ..., M_{0y} and $y_{1,2m} = y_{2,2m} = yma$ for m = 1,2, ..., M_{0y}, where y denotes unit vector in the y-direction. We also assume that phases of the elements are selected as: $\beta_{2m+1}=-m\Delta$ for m = 0,1, ..., M_{0y}, and $\beta_{2m} = m\Delta$ for m = 1,2, ..., M_{0y}. Under these assumptions:

$$\begin{aligned}r_{1,2m+1}-r_0 &= ma\sin\theta_0\sin\phi_0 \quad m = 0,1,....,M_{oy} \ , \\ r_{1,2m}-r_0 &= -ma\sin\theta_0\sin\phi_0 \quad m = 1,2,...,M_{oy}\end{aligned} \tag{13}$$

and

$$\begin{aligned}r_{2,2m+1}-r_0 &= 2Z_0\cos\theta_0+ma\sin\theta_0\sin\phi_0 \quad m = 0,1,....,M_{oy} \ , \\ r_{2,2m}-r_0 &= 2Z_0\cos\theta_0-ma\sin\theta_0\sin\phi_0 \quad m = 1,2,...,M_{oy}\end{aligned} \tag{14}$$

If we then define argument γ_y as:

$$\gamma_y = (\Delta-ka\sin\theta_0\sin\phi_0)/2 \tag{15}$$

then equation 11 reduces to:

$$E_\xi = E_{\xi,0}\left[1+\sum_{m=1}^{M_{oy}}(e^{-2im\gamma_y}+e^{2im\gamma_y})\right]\left[1+(R_v+\Psi_\xi)e^{2ikZ_0\cos\theta_0}\right] \tag{16}$$

Using the relation

$$\sum_{m=1}^{M_{oy}} x^m = \frac{x(1-x^{M_{oy}})}{1-x} \ , \tag{17}$$

equation 16 can be recast:

$$E_\xi = E_{\xi,0}\left\{\frac{1+\cos[(N_y+1)\gamma_y/2]\sin[(N_y-1)\gamma_y/2]}{\sin\gamma_y}\right\}\left[1+(R_v+\Psi_\xi)e^{2ikZ_0\cos\theta_0}\right] \tag{18}$$

where N_y is an odd integer. The first term in brackets on the right side of equation 16 is the free space antenna factor which depends on the array geometry and is independent of the distance between the source and observation point. Terms in the second bracket show the incident, reflected, and surface wave contributions to the antenna array factor and the resulting ξ-component of the radiated field.

Equation 18 holds if N_y is an odd integer. If the array of dipoles contains an even number of elements, then it will prove convenient to adopt the following scheme: $y_{1,2m-1} = (\frac{1}{2} - m)$ and $y_{1,2m} = (m - \frac{1}{2})$ for $m = 1, 2, ..., M_{ey}$. Selecting phases β_n so that $\beta_{2m-1} = (\frac{1}{2} - m)\Delta$ and $\beta_{2m} = (m - \frac{1}{2})\Delta$ for $m = 1, 2, ..., M_{ey}$ and using the relation:

$$\sum_{m=1}^{M_{ey}} x^{m-1/2} = \frac{x^{1/2}(1 - x^{M_{ey}})}{1 - x} \quad , \tag{19}$$

the ξ-component of the radiated field can be written:

$$E_\xi = E_{\xi,0} \left[\frac{\sin(N_y \gamma_y)}{\sin \gamma_y} \right] \left[1 + (R_v + \Psi_\xi) e^{2ikZ_0 \cos\theta_0} \right] \tag{20}$$

where N_y is an even integer.

Similar reasoning can be used to calculate the antenna array factors for a uniform linear array of N_z dipoles aligned parallel to the z-axis. Let $M_{oz} = (N_z - 1)/2$ and $M_{ez} = N_z/2$. First consider the case in which N_z is an odd integer and let "b" denote the distance between adjacent elements. Elements of the array are numbered so that $z_{1,2m+1} = -mb$ for $m = 0, 1, ..., M_{oz}$ and $z_{1,2m} = mb$ for $m = 1, 2, ..., M_{oz}$. Without loss of generality we select $x_{1,n} = x_{2,n} = y_{1,n} = y_{2,n} = 0$. Equations for the phase factors appearing in equation 12 (with N_z replacing N_y) become:

$$\begin{aligned}
r_{1,2m+1} - r_0 &= mb\cos\theta_0 \quad & m &= 0,1,....,M_{oz} \quad , \\
r_{1,2m} - r_0 &= -mb\cos\theta_0 \quad & m &= 1,2,...,M_{oz}
\end{aligned} \tag{21}$$

and

$$\begin{aligned}
r_{2,2m+1} - r_0 &= 2Z_0\cos\theta_0 - mb\cos\theta_0 \quad & m &= 0,1,....,M_{oz} \quad , \\
r_{2,2m} - r_0 &= 2Z_0\cos\theta_0 + mb\cos\theta_0 \quad & m &= 1,2,...,M_{oz}
\end{aligned} \tag{22}$$

Phases β_n are selected as follows: $\beta_{2m+1} = -m\Delta$ for $m = 0, 1, ..., M_{oz}$ and $\beta_{2m} = m\Delta$ for $m = 1, 2, ..., M_{oz}$. Arguments γ_z and γ'_z are defined:

$$\gamma_z = (\Delta - kb\cos\theta_0)/2 \quad \wedge \quad \gamma'_z = (\Delta + kb\cos\theta_0)/2 \tag{23}$$

Substitution in equation 12 yields:

$$\begin{aligned}
E_\xi = E_{\xi,0} & \left\{ \frac{1 + \cos[(N_z + 1)\gamma_z/2]\sin[(N_z - 1)\gamma_z/2]}{\sin\gamma_z} \right\} \\
&+ E_{\xi,0} \left\{ \frac{1 + \cos[(N_z + 1)\gamma'_z/2]\sin[(N_z - 1)\gamma'_z/2]}{\sin\gamma'_z} \right\} \left[(R_v + \Psi_\xi) e^{2ikZ_0\cos\theta_0} \right]
\end{aligned} \tag{24}$$

where N_z is an odd integer. The first term on the right side of equation 24 arises from the summation of incident fields and is identical to the free space antenna array factor for a uniform linear array of antenna elements parallel

to the z-axis. In contrast to the antenna array factor for a uniform linear array parallel to the y-axis given in equation 18, array factors for the reflected and surface wave contributions are functions of γ'_z, while the free space array factor depends on γ_z.

If N_z is an even integer, elements of the array can be numbered as follows: $z_{2m-1} = (\frac{1}{2} - m)b$ and $z_{2m} = (m - \frac{1}{2})b$ for m = 1, 2, ..., M_{ez}. Phases β_n are given by: $\beta_{2m-1} = (\frac{1}{2} - m)\Delta$ and $\beta_{2m} = (m - \frac{1}{2})\Delta$ for m = 1, 2, ..., M_{ez}. Factors in the phase become:

$$
\begin{aligned}
r_{1,2m-1} - r_0 &= (m-1/2)b\cos\theta_0 \quad m = 1,2,....,M_{ez} \quad , \\
r_{1,2m} - r_0 &= (1/2-m)b\cos\theta_0 \quad m = 1,2,...,M_{ez}
\end{aligned}
\tag{25}
$$

and

$$
\begin{aligned}
r_{2,2m-1} - r_0 &= [2Z_0 - (m-1/2)b]\cos\theta_0 \quad m = 1,2,...,M_{ez} \quad , \\
r_{2,2m} - r_0 &= [2Z_0 + (m-1/2)b]\cos\theta_0 \quad m = 1,2,...,M_{ez}
\end{aligned}
\tag{26}
$$

Substitution into equation 12 then yields:

$$
E_\xi = E_{\xi,0}\left[\frac{\sin(N_z\gamma_z)}{\sin\gamma_z} + \frac{\sin(N_z\gamma_z')}{\sin\gamma_z'}(R_v + \Psi_\xi e^{2ikZ_0\cos\theta_0})\right]
\tag{27}
$$

4.   Calculations

This section presents examples of antenna array factors calculated from equations 18, 20, 24 and 27 for dipole arrays positioned above various ground planes. Table 1 shows the values of ϵ_r and σ used in the calculations [3]].

Table 1 Soil Conductivity, σ, and Relative Dielectric Constant, ϵ_r, for Various Media
(Extracted from Reference 3)

Description	σ (S/m)	ϵ_r
Sea Water	4.000	80
Wet Earth	0.400	12
Dry Earth	0.040	8
Lake Water	0.004	80
Dry Sand	0.000	2

We begin with the simpler case of an array of dipoles with elements positioned at intervals "a" along the y-axis. Figure 2 shows antenna array factors for the ρ-component of the electric field obtained by using equation 18 for a fifty-element array of dipoles driven at a frequency of 100 MHZ. Elements of the array are separated by 0.2 λ_0 with centroid 1 λ_0 above the ground plane. The radial distance from the centroid to the observation points was 100 λ_0. Phase differences among the dipoles were obtained by choosing angle θ and ϕ appearing in equation 15 to yield a main lobe in the radiation pattern at $\phi = 50°$ and $\theta = $ arc $\cos[\pi/(kZ_0)] = 60$. This choice for θ reduces the exponential factor appearing in equation 18 to unity. Therefore, alterations to the free space antenna array factor arise from the sum of the plane wave reflection coefficient and the surface wave coefficient. Results shown in Figure 2 are obtained from equation 18 when normalized to the number of elements in the array. For an antenna

array in free space, the normalized antenna array factor is less than or equal to one. However, due to constructive interference between the incident and reflected fields, antenna array factors for arrays above a partially conducting ground plane can exceed unity. For the dry earth medium, the angle of reflection exceeds the quasi-Brewster angle for the medium, and the reflected wave is out of phase with the incident component. As a result the peak value of the array factor is reduced to value less than one. For this array configuration and the media described in Table 1, the surface wave contributions were unimportant.
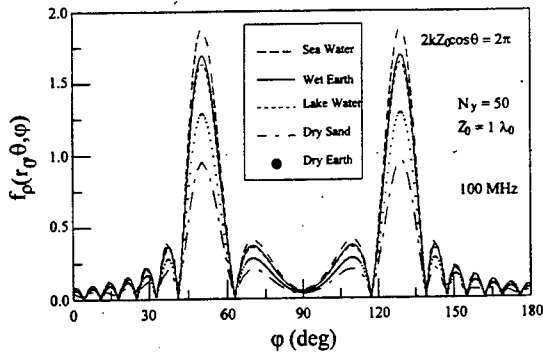
Figure 2 Antenna Array Factor for $N_y = 50$ and $2kZ_0 \cos\theta = 2\pi$

Figure 3 shows the results obtained for the same configuration of dipoles except that the dipoles phases were chosen to yield a main lobe at $\phi = 50°$ and $\theta = \text{arc } \cos[\pi/(2kZ_0)] \approx 75.5°$. In this example the difference in geometrical path length for rays drawn from the reference element and its image result in a value of π radians for the phase of the exponential factor in equation 18. For the water and wet earth media, the angle of reflection is less than the quasi-Brewster angle, and the phase resulting from the product of the plane wave reflection coefficient and exponential factor results in a significant reduction in the main lobe of the radiation pattern. For the dry earth and sand media, the angle of incidence exceeds the quasi-Brewster angle and the result is an enhancement of the main lobe relative to the free space value.
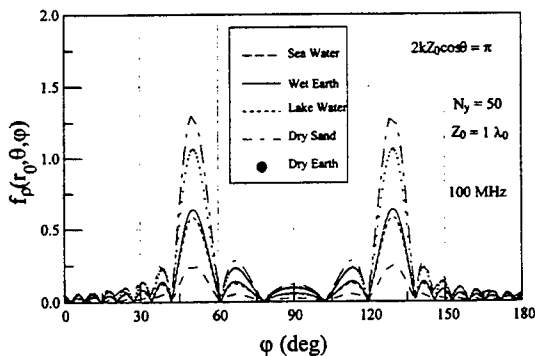

Figure 3 Antenna Array Factor for $N_y = 50$ and $2kZ_0 \cos\theta = \pi$

Figure 4 shows the antenna array factor for the z-component of electric fields radiated from a configuration in which the surface wave contributions are dominant contributors. The calculation applies to a 20 element, linear array of vertical dipoles parallel to the y-axis. Dipoles in the array are driven at a frequency of 1 GHz and are separated by a distance of $0.25 \lambda_0$. The centroid of the array is $0.1 \lambda_0$ above the ground plane. Phase differences between adjacent elements were selected from the condition $\gamma_y = 0$ (equation 15) so that the main lobe of the radiation pattern occurs in the direction defined by $\theta = 90°$ and $\phi = 30°$. Observation points are a distance of $10 \lambda_0$ from the centroid of the array. For this configuration, the angle of reflection is approximately $89°$. The angle of reflection exceeds the quasi-Brewster angle for all of the media, and the plane wave reflection coefficient approaches a value of -1. The path difference between rays originating at the reference dipole and its image is small in terms of wavelength. As a result, the incident and reflected fields nearly cancel one another due to destructive interference. Figure 4 shows the total antenna array factor and the surface-wave portion the array factor for the z-component of the radiated fields. The main lobe of the array factor exceeds unity only for the sea water medium which is characterized by the largest quasi-Brewster angle among the five media.
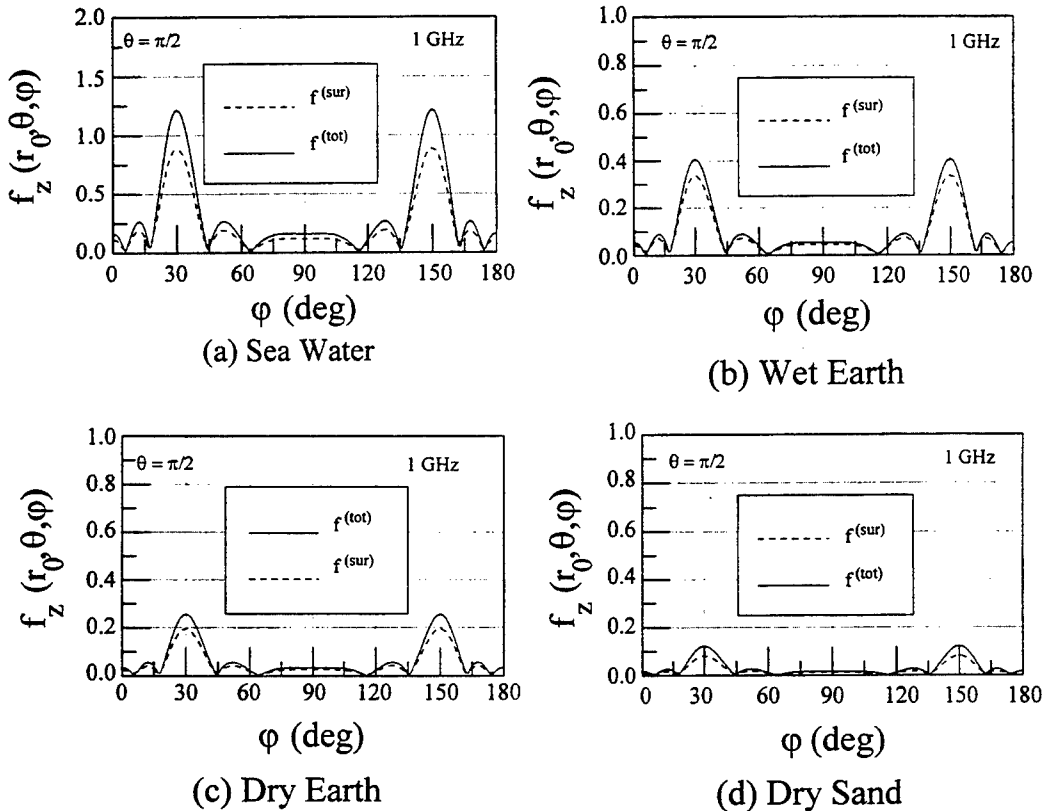

(a) Sea Water

(b) Wet Earth

(c) Dry Earth

(d) Dry Sand

Figure 4 Antenna Array Factors for Near-Grazing Incidence

As a final example, Figure 5 shows the calculated values of E z for a uniform linear array of 10 vertical, radiating dipoles with elements equally spaced $0.1\ \lambda_0$ along the z-axis. The elements are driven at a frequency of 10 GHz. The centroid of the array is $2\lambda_0$ above the ground plane. Phases differences between adjacent elements were selected (using $\gamma_z = 0$ in equation 23) to yield a maximum in the free field radiation pattern at $\theta = 50°$. Angle θ in Figure 5 is the polar angle measured by an observer at the centroid. As the angle of incidence approaches grazing incidence, $\theta \approx 90°$, the incident and reflected fields interefere destructively. Surface wave terms near grazing incidence are relatively small in comparison to values of the total field observed at smaller angles of incidence where the incident and reflected terms add constructively or where the destructive interference is less severe. Maxima and minima seen in Figure 5 for $30° \leq \theta \leq 60°$ occur where values of the plane wave reflection coefficient are relatively constant, and the extremes are due largely to the exponential factor in equation 24. As indicated in equation 2, the surface wave component of E_z does not vanish as θ approaches zero. The surface wave coefficient defined in equation 8 is singular along the z-axis. While the product $g_z \Psi_z$ remains finite everywhere, it is clear that the results become non-physical near $\theta = 0°$. This is a fundamental limitation·in this particular approach and can be resolved only if the theory is reformulated in terms of expressions for the surface-waves that vanish at least as rapidly as $\sin^2\theta$ as θ approaches zero.
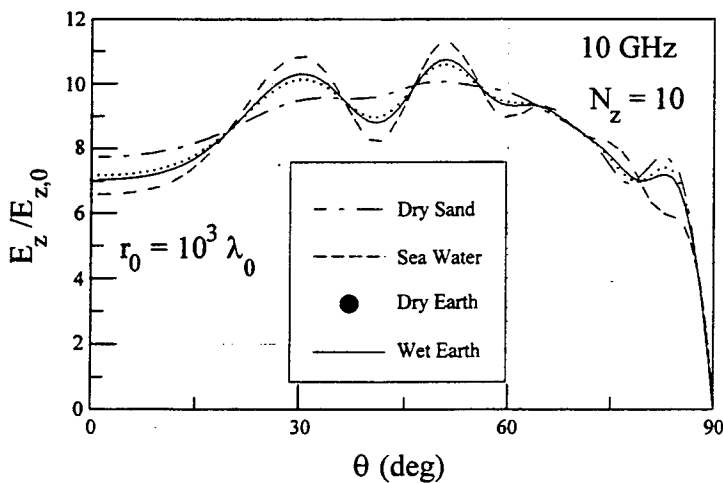

Figure 5 Calculated Far Fields Calculated for a 10 Element Array with Elements Positioned Along the Z-Axis

5. Conclusion

This paper has presented a formalism for calculating antenna array factors for linear arrays of vertical dipoles positioned above an imperfectly conducting ground plane. Surface-wave coefficients introduced in Section 3 are a theoretical convenience that allow a straightforward calculation of antenna array factors in a manner analogous to that for free space antenna arrays. The resulting expressions are useful for many cases of practical interest. However, the surface-wave coefficients are singular at the zeros of the incident field because expressions for the surface-wave components do not vanish with the incident field. This is a fundamental limitation in the approach.

References

[1]   K.A. Norton, "The Propogation of Radio Waves over the Surface of the Earth and in the Upper Atmosphere, Part II," *Proc. IRE*, Vol. 24, pp.1203-1236, September 1937.

[2]   Alfred Banos, Jr., *Dipole Radiation in the Presence of a Conducting Half-Space*, Pergamon Press, New York, NY., 1966.

[3]   Ronold W.P. King and Sheldon S. Sandler, "The Electromagnetic Field of a Vertical Electric Dipole over the Earth or Sea," *IEEE Trans. Antennas Propagat.*, Vol. 42, pp. 382-389, March 1994.

[4]   Robert E. Collin and Francis J. Zucker, *Antenna Theory, Part 1*, McGraw-Hill, Inc., New York, NY, pp. 138-206, 1969.

[5]   M.T. Ma, *Theory and Applications of Antenna Arrays*, John Wiley & Sons, New York, NY, pp. 4-19, 1974.

[6]   Julius Adams Stratton, *Electromagnetic Theory*, McGraw-Hill, Inc., New York, NY, pp. 505-511, 1941

[7]   Milton Abramowitz and Irene A. Stegun, Editors, *Handbook of Mathematical Functions*, Dover Publications, Inc., New York, NY, Chapter 7, 1972.

[8]   Ira Kohlberg, "Electromagnetic Fields of a Vertical Electromagnetic Pulse Simulator Including Surface Wave Contribution," HDL-CR-89-052-2, U.S. Army Harry Diamond Laboratory (now the U.S. Army Reseach Laboratory), Adelpi Maryland, August 1989.

Energy Transfer from Free Space Transient Waveforms Through HF Antennas to Arbitrary Loads

Malcolm J. Packer

Harris Corporation, RF Communications Division
1680 University Avenue, Rochester, NY 14610

ABSTRACT

A single electromagnetic pulse created by a high-altitude detonation of a nuclear weapon creates an intense electromagnetic transient that can cover an immense geographical area. The energy contained within the transient waveform is capable of disabling communications by destroying susceptible semiconductors within radio equipment. In particular, HF equipment is susceptible due to the receive aperture size presented by large transmit antennas. This paper summarizes an effort to understand the effects of a pulse on certain HF antennas and the subsequent voltages and currents seen by radio equipment attached to them.

First we discuss the free space transient electromagnetic waveform created and its spectral content. Next, the calculated short-circuit current and open-circuit voltage induced on a dipole as a function of height above ground. This is followed by calculations of currents in different resistive loads connected to this dipole. Then, five antennas are analyzed to observe how they coupled transient energy into complex loads required to match the antenna impedance at 4, 8, and 20 MHz. These antennas are: a 46 m dipole, 9.7 m and 14.4 m monopoles, a crossed dipole, and a fan dipole.

To date, a 46 m dipole, a 14.4 meter monopole, and a fan dipole have been tested. Direct validation of calculated responses of the different antennas are not practical. However, a comparison of calculated and empirical results provides useful insight, and is provided for the following parameters: rise-time, peak short-circuit current, peak open-circuit voltage, load current, and load voltage. There is good correlation between numerical and empirical results, providing validation of the numerical method. Therefore, the empirical results provides evidence that the other antenna's numerical results are accurate.

INCIDENT TRANSIENT WAVEFORM

The electromagnetic transient peak magnitude, as well as rise- and fall-times of the EMP, are functions of the detonation altitude and distance of the detonation to susceptible equipment. If detonation is directly overhead (vertical distance equals distance to antenna), the rise-time (0.1 to 0.9 E_{peak}) is 5 nanoseconds and the half-value width (0.5 to 0.5 E_{peak}) is 20 nanoseconds, but the electric field only reaches about 0.1 of E_{max}. The E_{max} value of 50 kvolts/meter is reached when the distance from the detonation point to the point-of-contact with the earth's surface is approximately twice the vertical height. In this case, the rise-time is just under 10 nanoseconds and the half-value width is 50 nanoseconds. At the point of farthest distance from the detonation, i.e., tangential to the earth surface ($\approx$5 x vertical height), the rise-time is just longer than 10 nanoseconds with a half-value width of 200 nanoseconds, and the peak value reached is approximately 0.5 E_{max}. The incident wave-shapes vary greatly due to uncertainty of the antenna location relative to the point-of-detonation. To overcome this variable, a general waveform has been adopted. It contains the worst case attributes of all three waveforms: 5 nanosecond rise-time, 200 nanosecond half-value and 50 kilovolt peak. The double exponential equation for the generalized High-altitude EMP Electric Field Waveform[1] is displayed in equation (1) and the Fourier Transform in (2).

$e(t) = Eo\left[e^{-\alpha t} - e^{-\beta t}\right]$ volts/meter   (1)   where, Eo = 52.5 kvolts

$\qquad\qquad\qquad\qquad\qquad\qquad\qquad\qquad\qquad\qquad\qquad\quad \alpha = 4.0 \times 10^{6}$

$E(\omega) = Eo\dfrac{\beta - \alpha}{\beta\alpha - \omega^2 + j(\alpha + \beta)}$ volt/meter/Hz   (2) $\beta = 4.76 \times 10^{8}$

This quick rise-time yields strong spectral components in the HF band. Therefore, HF radio systems are extremely vulnerable because their antennas are tuned to receive these spectral components. The generalized Electric Field threat waveform is shown in Fig. 1. The magnetic field waveform is equivalent in transient shape with H_{max} obtaining 130 amps/meter.

To determine the frequency response, equation 1 can be Fourier Transformed symbolically, or the waveform can be inverted with a Discrete Fourier Transformation[2] (DFT).

Choosing the best sampling rate is not trivial. The sampling rate of e(t) requires rapid sampling

Fig. 1 Generalized High Altitude EMP Electric Field Waveform

during the quick rise-time, then a slower sampling rate throughout the fall-time[3]. This is ideal for sampling, but adds difficulty when performing the DFT; therefore uniform sampling is preferred. Since we know that the transient waveform contains 99% of its energy below 100 MHz, the minimum sampling frequency, ω_s, is 100 MHz, or a time domain sampling rate of $1/\omega_s$, 10 nsec. This is not quick enough to retain the 10 nsec rise-time shape. Therefore we sample every 2 nsec, which results in a band limited spectrum of ω_s equaling 500 MHz, and a folding frequency of 250 MHz. This creates 2000 samples across the spectrum; in the time domain it results in 4 μseconds, where the electric field is negligible.

Using MATHCAD[4] to perform the DFT insures retention of the phase information, equation (3). This converts e(t) into $E(\omega)$, the spectral domain, which is shown on a Bode plot in Fig. 2. As noted earlier, the quick rise-time in the time domain yields frequency components in the High Frequency band. This Bode plot has two breakpoints; at 630 kHz it declines at 20 dB per decade and at 76 MHz it declines at 40 dB per decade. The solid line is the DFT and the dashed line is the symbolic Fourier Transform, equation 2. The two curves are very similar in the frequency band of interest. The DFT has a folding frequency at 250 MHz, generating a mirror image. This does not affect our calculations, but must be retained for the correct inverse DFT.

$E(k) = \sum_{n=0}^{N-1} e(n) e^{-j(2\pi/N)kn}$

$e(n) = \dfrac{1}{N}\sum_{n=0}^{N-1} E(k) e^{j(2\pi/N)kn}$ (3)

Any antenna that is resonant
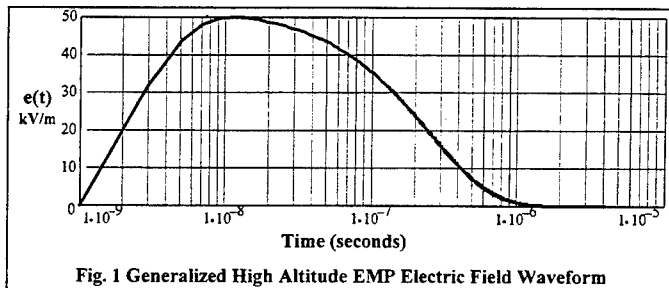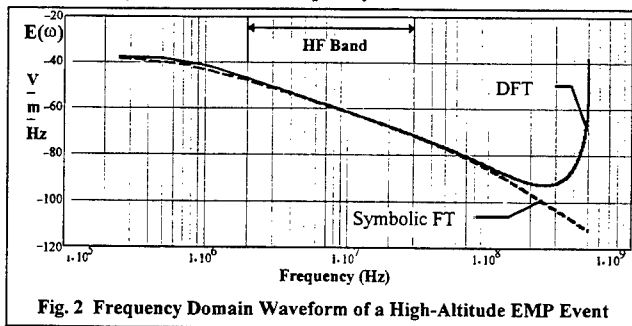

Fig. 2 Frequency Domain Waveform of a High-Altitude EMP Event

at a frequency within the transient waveform's spectrum will have voltages and current induced upon it via this incident waveform. The amount of energy induced depends on the incident angle, antenna size and orientation of antenna elements. For the five antennas analyzed, the worst case incident angle and wave polarization for each antenna type was chosen. The dipoles had the incident angle from zenith; the monopoles had an incident angle at the horizon.

ANTENNA VOLTAGES AND CURRENTS

For a simple cylindrical antenna structure in free space, it is possible to derive the plane wave impulse response, then convolve that response with the transient waveform to determine the resultant transient impulse responses. Unfortunately, complex antenna geometries combined with finite grounds make classic analytical treatment impractical. A numerical technique was needed to analyze different antenna structures.

This was accomplished with the use of the Numerical Electromagnetic Code[5] (NEC). The linear relationship between excitation and response allows the transient response to be developed in a two step procedure. With the Numerical Electromagnetic Code (NEC), a 1 volt/meter plane wave excites the wire-grid antenna model every 250 kHz across the frequency band from 250 kHz to 100 MHz. The result of this simulation represents a highly accurate calculation of the antenna's short-circuit current impulse response in the frequency domain. The magnitude of the 400 discrete short circuit currents is shown in Fig. 3 for a 46 m dipole in free space and situated at 2 m and 9 m above a finite earth. When an earth model is included, a finite ground relative permitivity, ε_r, of 10 and a conductivity, σ, of 0.01 Si/m, which represents average soil, is used.

The 46 m dipole receives maximum energy at its resonant frequencies, i.e., 3.25 MHz, 9.75 MHz, etc. At anti-resonance frequencies, i.e., 6.5 MHz, 13 MHz, etc, the antenna receives minimum energy.

This calculated plane wave impulse response contains 400 complex values from 0.25 MHz to 100 MHz while the incident waveform
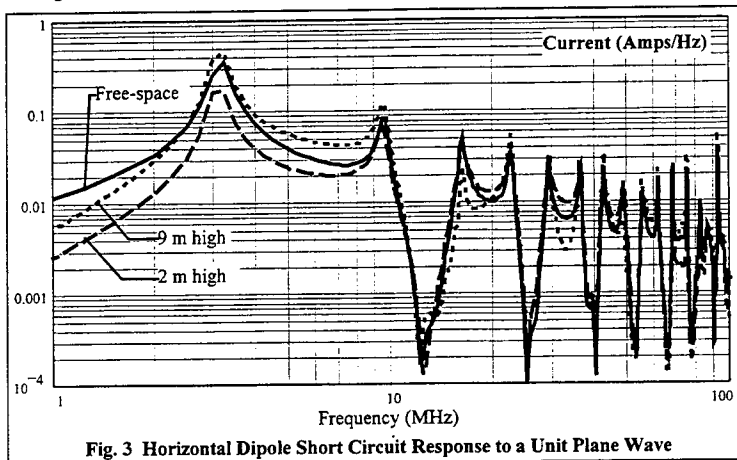

Fig. 3 Horizontal Dipole Short Circuit Response to a Unit Plane Wave

contains 2000 complex values from 0.25 MHz to 500 MHz. The real part of the impulse response was padded with 600 zeros, then the remaining 1000 values were an even function of the first thousand. The imaginary part of the impulse response was padded with zeros, then the next 1000 values were replicated as an odd function. This complete impulse response can be multiplied with the spectral waveform of the generalized high-altitude double exponential electric field waveform using MATHCAD. The results very closely approximate the actual measured short-circuit current impulse response of an antenna when it is subjected to an incident electromagnetic transient. Fig. 4 shows the

resulting short circuit current (A/Hz) from the transient waveform. The resonant and anti-resonant features can clearly still be seen in the spectral response.

The short-circuit current transient response, Fig 5, is obtained by performing an Inverse DFT (IDFT) on the spectral response. The current response is the expected damped exponential sinusoid. Sinusoidal oscillations occur every 310 nsec for a resonant frequency of 3.25 MHz. The rise-time has significantly slowed to 80 nsec, due to the bandpass nature of the dipole, which attenuates spectral components that are not natural resonant frequencies.
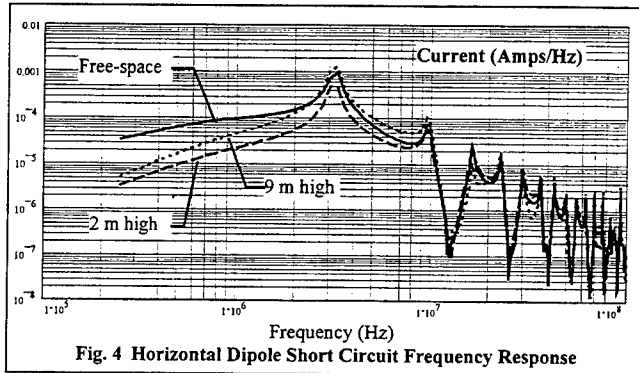
Fig. 4 Horizontal Dipole Short Circuit Frequency Response

Of the three curves displayed, the free space case has the highest current of 1800 amps. For both 2 m and 9 m heights, the direct and indirect waves add destructively. If the dipole was $\lambda/4$ high at 3.25 MHz ($\approx$23m) then the direct and indirect waves will add constructively.

RESISTIVE LOAD RESPONSE

An antenna, analyzed as a short-circuit current with the antenna impedance in shunt,
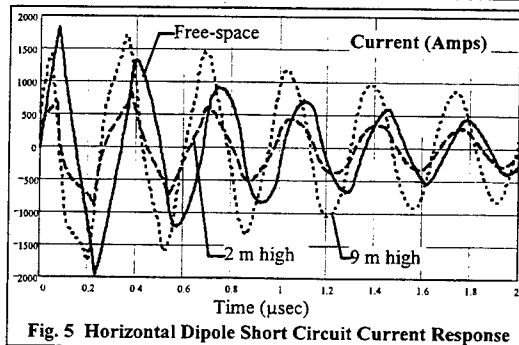
Fig. 5 Horizontal Dipole Short Circuit Current Response

provides the driving source for an arbitrary load impedance, such as a 50 Ω transmission line. The Norton current driving source can be converted into a Thevenin open-circuit voltage with the antenna impedance in series. With either source, the energy transfer to any arbitrary load can be calculated in the frequency domain.

Antenna impedance varies as a function of frequency. The NEC was used to calculate the complex antenna input impedance versus frequency. For the 46 m free-space dipole, the complex antenna impedance is shown in Fig. 6. The resistance starts at a small resistance and rises to the highest peak of 5000 Ω at the first anti-resonance, then repeats the cycle throughout the
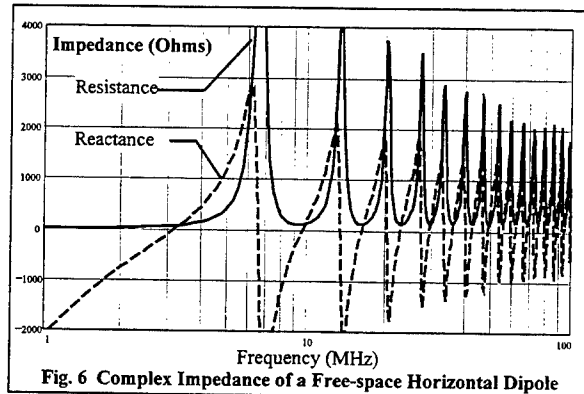

Fig. 6 Complex Impedance of a Free-space Horizontal Dipole

452

frequency band with decreasing peaks. The reactance starts at 9000 Ω capacitive and passes zero at resonance (3.25 MHz) and goes inductive (positive reactance). This cycle also repeats itself with decreasing peaks through the band. Although each antenna has a different input impedance, this cyclical nature is typical of any open-ended antenna structure.

With the driving source and source impedance defined in the spectral domain, any arbitrary load can be attached to the source's terminals. Under matched conditions, the maximum

$$I_L(\omega) = \frac{I_{SC}(\omega)Z_{ant}(\omega)}{Z_{ant}(\omega) + Z_L(\omega)} \quad (4)$$

load transient stress is $I_{sc}(\omega)/2$. The load current is calculated by current division between the antenna impedance and the load impedance, equation (4). Fig. 7 displays the current through three resistive loads and the source current in the frequency and time domains. In the frequency domain, the decreased current flow in the load is seen at the antenna resonance as the load impedance increases. At anti-resonance, when the antenna resistance is high, almost all the current flows through the load resistor. In the time domain, the increased resistive load tends to attenuate the ringing. The current in the load reaches a peak current of 1800 amps in 80 nsec, which agrees with early theoretical work[6].
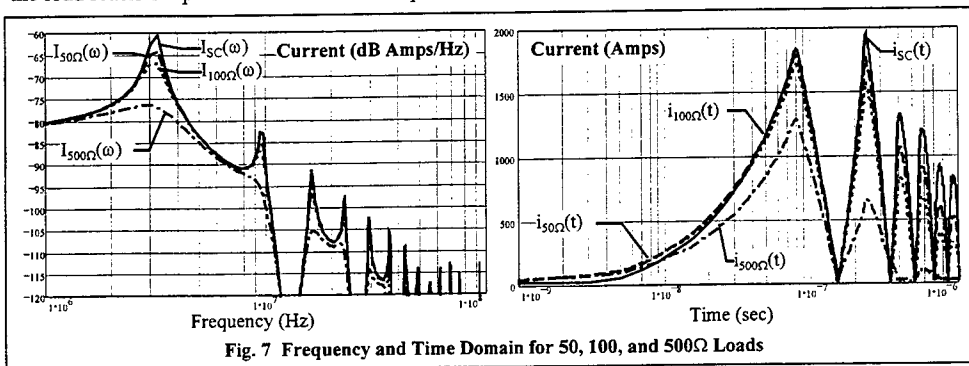

Fig. 7 Frequency and Time Domain for 50, 100, and 500Ω Loads

ARBITRARY COMPLEX LOAD RESPONSE

In reality, an antenna matches a 50 Ω transmission line when frequencies are selected such that the antenna input impedance is near 50+j0 Ω. Antenna couplers are available that provide near instantaneous matching to a 50 Ω transmission line at any frequency within the HF band. To meet fast Automatic Link Establishment timing requirements, these antenna couplers switch combinations of series inductors and shunt capacitors to form a low-pass network within several milli-seconds. To meet this rapid matching requirement, the coupler is under microprocessor control. Semiconductors employed within the coupler are susceptible to damage from transient energy.

Connecting the open-circuited antenna voltage to the arbitrary load impedance of the coupler causes a load impedance as a function of tune frequency. As shown in Fig. 8, the coupler is modeled as a simple shunt capacitor and a series inductor. The shunt 200 Ω resistor represents the transmission line impedance as seen through an auto-transformer. Different capacitors and inductors are connected as a function of desired frequency. Once tuned to a specific frequency, the capacitors and inductors remain constant until a retune command is issued. As the incident energy's frequency is varied, the coupler remains tuned to a singular frequency. The impedance seen by the incident energy varies as a function of specific $j\omega L + R_L$ and $1/j\omega C$. Therefore, each of the spectral components of the source

spectral waveform will see a different load impedance as opposed to the constant resistive loads discussed in the previous section.

The value of capacitors and inductors to tune the 46 m dipole at frequencies of 4, 8, and 20 MHz are 900pF and 28μH, 100pF and 5μH, and 63pF and 2.6μH, respectively. Fig. 9 displays the results for load voltage and current in the time domain. The open circuit antenna voltage reaches 2 MV in 80 nsec. An approximate method to bound the voltage is to multiply the free-field electric field peak, 50 kV, by the length, 46 m.

Fig. 8 Simple Model of Coupler and Open-circuit Driving Source

Therefore, maximum open-circuit voltage equals $E_0h = 2.3$ MV. The worst case load voltage is 0.5 MV at 80 nsec. The load current is close to the same current received by the antenna from the transient waveform. These voltages and currents contain significant energy and will damage internal components of the coupler. In general, couplers are equipped with gas-filled spark-gap protection devices that trigger at approximately 10 KV. Proper gap sparking limits the transferred energy from antenna to load from 10 to 30 Joules to under 10 mJ.

Several more antennas were analyzed, a 9.7 m and 14.4 m monopole, crossed dipole at 4.6 m above a finite ground, and a fan dipole at 9.2 m above a finite ground plane. The resultant voltages and currents are shown in Figs. 10, 11, 12, and 13 for load voltages and currents in the time domain.
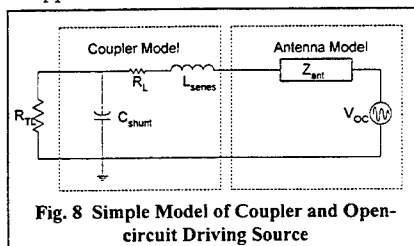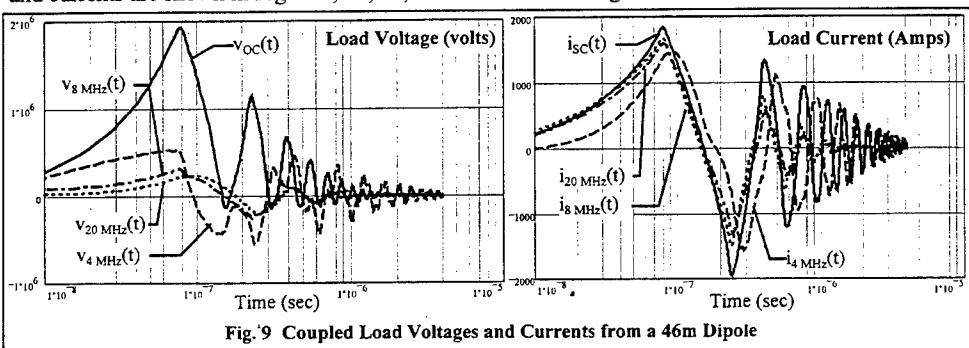

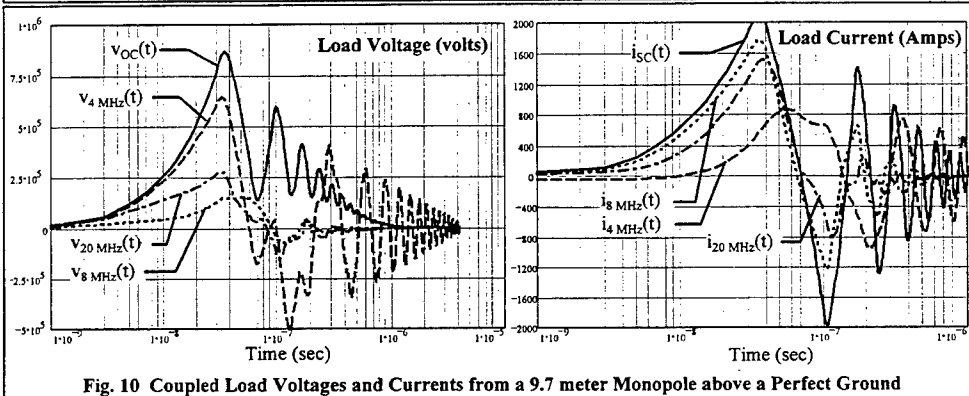**Fig. 9 Coupled Load Voltages and Currents from a 46m Dipole**

Fig. 10 Coupled Load Voltages and Currents from a 9.7 meter Monopole above a Perfect Ground

Fig. 11 Coupled Load Voltages and Currents from a 14 meter Monopole above a Perfect Ground

Fig. 12 Coupled Load Voltages and Currents from a Crossed Dipole 4.6m above an Average Ground
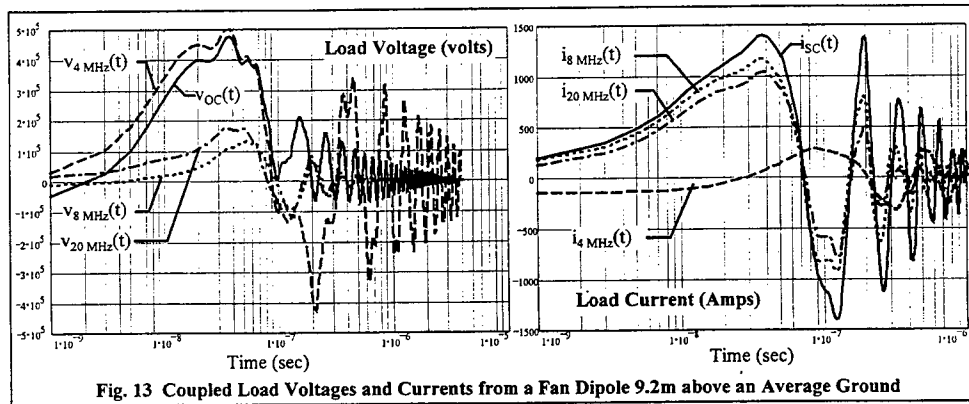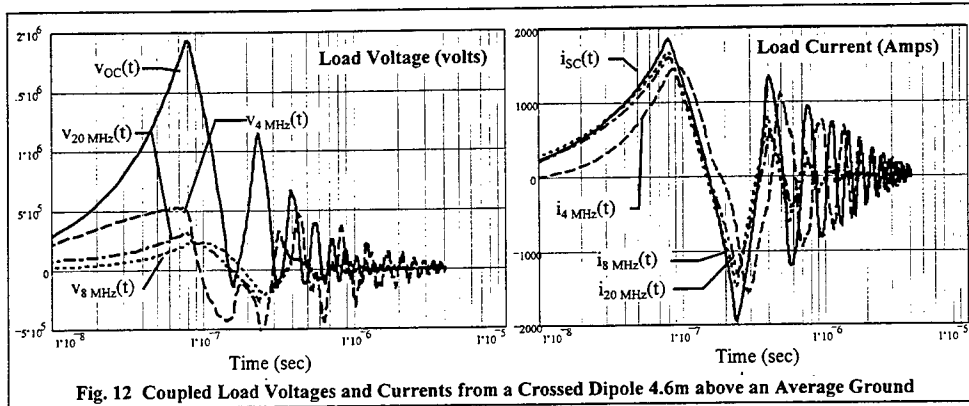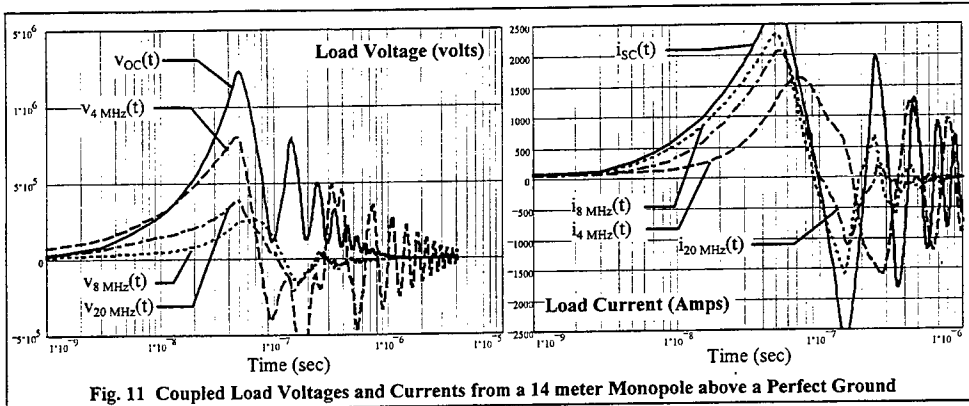

Fig. 13 Coupled Load Voltages and Currents from a Fan Dipole 9.2m above an Average Ground

455

Three antennas also have been tested to date, a 46 m dipole, a 14.4 m monopole, and a fan dipole. Direct comparisons of their test results to their calculated responses are not practical due to the difficulty in generating the transient waveform shown in Fig. 1. However, when we compare calculated and empirical results for each antenna, Table 1, we see good correlation in: rise-time, peak short-circuit current, peak open-circuit voltage, load current, and load voltage. Table 1 also shows numerically calculated energy quantities: charge, action integral, and Joules. The good correlation between numerical and empirical results validates the numerical technique. This indicated that the other antenna's numerical results are correct.

	46 m Dipole	46 m[7] Dipole	14.4 m Monopole	14.4 m[7] Monopole	Fan Dipole	Fan[7] Dipole
	Numerical	Empirical	Numerical	Empirical	Numerical	Empirical
Peak Eo (kV/m)	16	16	50	50	16	16
t_r (nanoseconds)	80		50	70	38	
I_{SC} (amps)	360		2700	1900	400	140
V_{OC} (volts)	150K		1200 K	400 K	150K	
I_{LOAD} (amps)	400	160	2000	1600	130	140
V_{LOAD} (volts)	150K		75 K	60 K	150K	
Charge (Coulombs)	$3.0(10^{-4})$		$1.0(10^{-3})$		$9.2(10^{-5})$	
Action Integral (amps^{2}sec)	.072		1.0		0.005	
Energy (Joules)	3.6		16.4		0.14	

Table 1 Comparison of Numerical and Empirical Results for Several Antennas

CONCLUSIONS

The numerical method using NEC and MATHCAD provides a method to analyze current and voltages induced on any antenna structure and arbitrary load. There was very good agreement with resonant length and sinusoidal oscillations in the time domain. The five antennas analyzed were: a 46 m dipole, 9.7 m monopole, 14.4 m monopole, a crossed dipole and a fan dipole. The longer the element, the worse the induced currents and voltages for a collinear antenna. The 46 m dipole had peak current of 1800 amps and a voltage of 2 MV. A 500 ft sloping-V antenna was analyzed in both polarizations. When polarization was aligned with the 500 ft V's length profile, the transient energy canceled at the feed point. In the other polarization, induced energy was still far below all the other antennas.

The analytical and empirical data for the 14.4 m monopole agrees. However, the analyzed values are greater than the empirical values because the analysis used a perfect ground plane. The short circuit currents are close, but the open-circuit voltages have a greater discrepancy. This infers that the numerical antenna impedance is different. The relationship between antenna parameters to load values correlate. These results provide high confidence in the remaining numerical results.

[1] *EMP Engineering and Design Principles*, Bell Laboratories, Technical Publications Department, Whippany, NJ, 1975.

[2] A.V. Oppenheim, R.W. Schafer, *Digital Signal Processing, Prentice-Hall, Inc.*, Englewood Cliffs, New Jersey, 1975.

[3] M. Dion, S. Kashyap, "Some Considerations on the use of NEC for Computing EMP Response", Applied Computational Electromagnetic Society Journal, Vol. 4, No. 2, 1989.

[4] MATHCAD, MathSoft Inc., 101 Main St. Cambridge, Massachusetts, 1995.

[5] G. J. Burke, "Numerical Electromagnetics Code - NEC-4, Method of Moments," Part I: User's Manual, Lawrence Livermore National Laboratory, Jan. 1992.

[6] W.O. Coburn, E. Nguyen, R.J. Reyzer, M.H. Mar, "High-Altitude Electromagnetic Pulse Survivability Assessment of the Harris RF-3200 Transceiver," US Army Laboratory Command, Harry Diamond Laboratories, Adelphi, MD.

[7] Personal Communications, Excerpts from NRAD Test Report on a 14.4 m monopole, Communications Systems Engineering and Integration Division.

A 12 Beam Cylindrical Array Antenna for AMPS and PCS Applications

G.A. Martek, J. Todd Elson
Metawave Communications Corporation, Redmond, WA
January 15, 1997

1 Abstract

The use of sector antennas or multiple narrow-beam antennas rather than omni-directional antennas has become a trend in cellular technology. Because property is becoming increasingly difficult to acquire for cellular communication base stations, wireless service providers are looking at enhancement of antennas as a way to increase system capacity, improve call quality, and extend portable range. Enhancement comes in the form of an increase in gain and a decrease of side and back lobes. Panel antennas, which are planar arrays of dipoles backed by a conductor, have recently been implemented for such a purpose.

This paper discusses the design and test of a cylindrical array of vertical dipoles for use in advanced mobile phone system (AMPS) applications. The cylindrical array provides 12 beams, equally spaced in the azimuth plane. One of the advantages of a 12-beam array compared to a series of panel antennas is the elimination of scan loss. Of equal importance, the size of the cylindrical array is considerably less than the farm of panel antennas that is required to achieve the same beam function. The aesthetics of the cylindrical array make it much less objectionable to local communities, which often obstruct or delay the construction of conventional base station antenna towers because of their clutter of antennas.

The design of the antenna was assisted by two numerical methods, the method of moments (MoM) and the finite difference time domain (FDTD) method. The popular numerical electromagnetics code (NEC) was the interface to MoM, and is well suited to the cylindrical antenna. The FDTD method provides a second opinion to the problem. Two models were put into NEC, one simply with a cylindrical-shaped conductor and array of dipoles, and another with the same conductor and array, plus the feed system.

A prototype was constructed and tested in an urban environment. The gain and front-to-back ratio of the antenna are estimated from the field data by comparison with a monopole antenna located near the cylindrical array. Results indicate that all three models give reasonable predictions of the performance of the antenna. Future efforts will be directed toward providing different polarizations and implementing electrical downtilt.

2 Introduction

A new class of aesthetic communications antennas for use with cellular radio base stations is discussed. Cellular radio [1] in North America is also referred to as Advanced Mobile Phone

System(AMPS). This popular communications service, begun in 1978, enjoys a rather substantial market penetration of about 12 percent. Continual increase in demand for this service has generated increasing need for more capacity, lower interference, better call quality, and longer portable range. This in turn has spurred the construction of a substantial number of base stations, which connect the user to the public telephone network. See Figure 1.

Construction of a base station is a substantial capital investment, in radio and switching equipment, in hard-to-acquire property, and in antenna tower and base station. See Figure 2.

Wireless service providers typically divide coverage around a cell site into three 120-degree sectors. Each has at least one transmitting antenna and two receive antennas. Spatial diversity schemes are often implemented, in which two antennas are used to receive the same signal with different fading envelopes. When two fading envelopes are combined, fading is reduced, providing an improvement to system performance [2]. The antennas that cover a sector are usually mounted on a facet of a triangular platform structure on top of the tower, as seen in Figure 3. At the ends of such a facet two or more antennas are mounted and usually separated by at least ten wavelengths.

A large number of these base stations and towers are deployed and many more are needed. However, community resistance to tower construction has grown dramatically in recent years. Many communities have stopped or seriously delayed the construction of antenna towers. The most aesthetically objectionable element of antenna towers are the triangular antenna mounting platforms with their clutter of antennas. The cylindrical antenna system presented in this paper relies on angular and later, polarization diversity to eliminate the need for an antenna mounting platform, and its cylindrical shape is more pleasing to the eye (Figure 4). Figure 5 shows a standard antenna tower with antenna mounting platform. Figure 6 shows the same tower, with the cylindrical antenna superimposed.

3 Cylindrical Array Design

Cellular towers are often populated with many monopole antennas, to boost gain and provide spatial diversity. Sector antennas, which typically have 60°, 90°, or 120° beam widths, are also widely used for spatial diversity because directional antennas have a higher gain than the monopoles; thus, fewer can be used. The drawback to using sectored antennas is that mobiles must be tracked as they move out of the coverage area of one beam and into another.

The sectored concept can be extended to several beams covering the entire 360° azimuth. The drawback to this antenna configuration is the vastly more complicated task of tracking mobiles into and out of the multiple beam patterns. For example, consider three panel-antennas, each covering 120° in the azimuth plane, with each panel providing four 30° beams. This configuration covers the entire azimuth. While that 12-beam configuration has distinct benefits, it also has a serious scan-loss problem, which is inherent in planar arrays. It was this important problem with multiple beam planar antenna arrays that led to the development of the cylindrical array, which provides the same beam coverage without scan loss.

The cylindrical array is composed of 12 cylindrically symmetric columns of half-wave dipoles placed a quarter of a wavelength above a cylindrical shaped conductor. Figure 7 is a schematic representation of the cylindrical antenna array. The array possesses four horizontal rows of dipole elements, with a spacing of one λ, while the columns are circumferentially spaced $\lambda/2$ apart. Each beam is generated by four adjacent columns of elements (12 columns total), with the inner two columns delayed by 90° relative to the outer two columns. This yields a beam with its axis centered relative to the

columns. The numerical electromagnetics code (NEC) and finite difference time domain (FDTD) were used to fine tune this concept. More details about the prototype are provided in the next section.

NEC [3] is a widely used tool for numerical analysis of wire antennas. It is well-suited to an antenna composed of conductors and ground with no dielectrics because it utilizes the method of moments, and the necessary Green's function is known exactly. A straightforward model of the cylindrical antenna is shown in Figure 7. The dipoles are oriented vertically, so the ground reflector is represented by cylindrically arranged vertical wires. The wires are spaced approximately $\lambda/10$ apart and have segmentation equal to $\lambda/5$. This segmentation gave nearly identical results to cases with such segmentation equal to $\lambda/10$ or $\lambda/20$. The remaining eight dipoles, not excited as sources, are represented as 50-ohm loads.

Figure 10 displays far-field plots of one beam of the antenna generated by this model. The beam width is near 30°and the side lobes are about 12 dB down from maximum gain. The front-to-back ratio is about 27 dB.

The FDTD method [4] is not as well-suited to the current problem, but because to its ease of use it was chosen for a second analysis of the antenna, to verify beam width and side and back lobe levels. A two dimensional slice of the antenna appears in Figure 9, showing the region as seen by the FDTD code. A rectangular mesh with segmentation of $\lambda/40$ is laid over the domain of interest. This dense segmentation renders a fairly accurate staircase approximation of the cylinder and allows the placement of sources very close to their desired positions. Figure 11 displays a far-field plot of the azimuth pattern generated by this model. The beam width is near 36 degrees and the side lobes are about 15 dB down. The front-to-back ratio is about 25 dB.

Finally, a more detailed model of the antenna was fed into NEC. The result is shown in Figure 8. This model includes the airline feed system existing just above the surface of the cylinder. Such an addition requires a large increase in memory, which is required for analysis, as horizontal segments of the feed system are connected to the cylinder. This adds several wires to the mesh. Figure 12 displays far-field plots generated by this model. The beam width is again near 30 degrees and the side lobes are about 8 dB down. The front-to-back ratio is about 15 dB. There appears to be significant radiation in undesired directions.

The simpler NEC model and the FDTD model give very good indications of the beam width, peak gain, side lobe level, and front-to-back ratio of the current antenna. The more detailed model predicts similar results, with some degradation in gain due to the feed system and modeling errors. The side and back lobes are a bit higher as well.

4 Prototype Constructed

A prototype was built, composed of a cylindrical conductor and 12 "columns". Each column consists of four dipoles fed through an airline and baluns. Internal to the antenna array, each column feed is connected by an N connector. The internal beam-forming network consists of discrete hybrid couplers and Wilkinson splitters with phase-matched cables. At the bottom of the antenna assembly are 12 input connectors. The topology of the beam-forming network is such that at any one input the excitation is split in four with the phase relationship of 0°,-90°,-90°,0°. Thus, the appropriate four columns are excited with the central two columns being delayed electrically by 90° in the azimuth plane. This allows the wave fronts of the outer two columns to catch up with the two central columns. The beam-forming

topology compensates for the curvature of the cylinder by phase advancing the outer columns, bringing the beam's wave in-phase. Due to mutual coupling of the dipoles, a series of tuning iterations were required to bring the driving point impedance of each column close to 50 ohms. The antenna was tuned from 820 to 895 MHz with a return loss of 10 dB at the band edges and 25 to 40 dB at the center of this range. Stagger tuning could improve the width of this input response, but was not pursued.

A far-field antenna range was not used in the testing of the antenna system. A mobile equipped with a source was driven around the antenna site. A data acquisition system at the antenna site collected signal in a realistic scattering environment. A total of 12 signals were recorded over time, one for each beam of the antenna. From these data, gain and front-to-back ratio could be estimated. A commercial brand monopole antenna with known gain was used to measure gain of the antenna under test. Figure 13 plots instantaneous maximum signal among the 12 beams versus time. The signal recorded 6 beams away from the maximum (180° around in azimuth) is also shown as a means of estimating the front-to-back ratio. Both traces are normalized with respect to the trace generated by the monopole antenna, which has a gain of 11.1 dBi. On average, the gain of the antenna is about 3 dB higher than the monopole, putting it at about 14 dBi. As there is a 3 dB loss associated with the feed system, this value is fairly close to the theoretical predictions. The front-to-back ratio appears to be about 20 dB, which is also reasonably close to theory.

5 Future Work

An antenna of this type should have elevation beam-adjustment for users that require that groups of beams or individual beams be adjusted routinely. The issue of an economical phase shifter becomes important as well as its range in phase shift. The underlying concept is to subdivide the array into sub-arrays with their own relative phase relationship to the adjacent sub-array. Control of the amount of this relative phase yields the required amount of elevation plane beam-steering. The concept of polarization diversity can be employed by using orthogonal array elements such as crossed dipoles fed with baluns. The advantage here is that the phase centers for the elements are collocated, producing a high degree of cross polarization purity. This should translate into a good non-correlation of any collocated beam formation; that is, slant-left and slant-right linear polarization covering the same beam direction.

Preliminary investigation indicates that this antenna can be scaled down for use in personal communication system (PCS) applications.

Bibliography
William C.Y.Lee, *Mobile Cellular Telecommunications 2nd Ed*. McGraw-Hill, New York, 1995
William C.Y.Lee *Mobile Communications Design Fundamentals* John Wiley and Sons, Inc. 1993
NEC-2, The Numerical Electromagnetics Code-Method of Moments, Lawrence Livermore National Laboratory, Livermore, CA, 1981
K. S. Yee, "Numerical Solution of Initial Boundary Value Problems Involving Maxwell's Equations in Isotropic Media," *IEEE Trans. On Ant. Prop.*, Vol. 14, 1966, pp. 302-7.
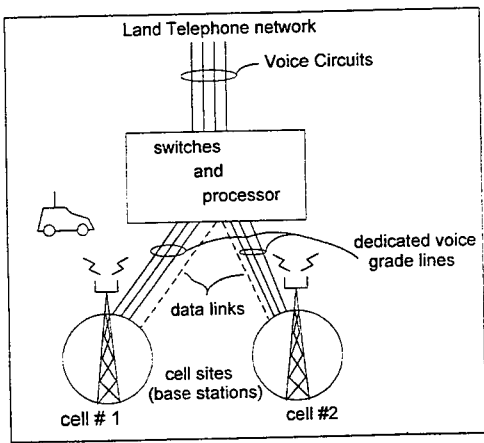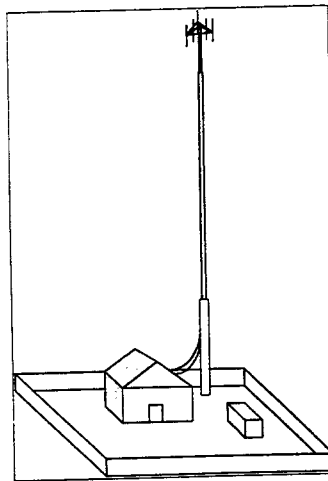
Figure 1 Typical Cellular Topology

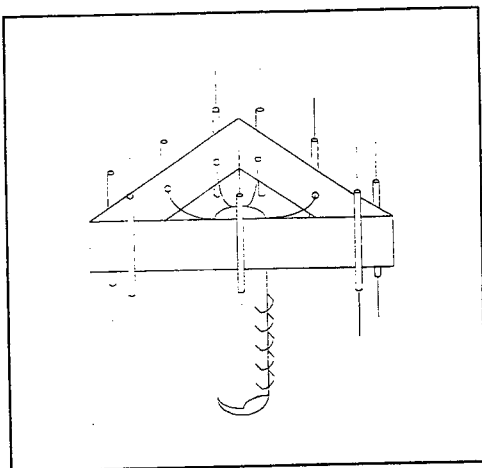Figure 2 A Cellular Base Station

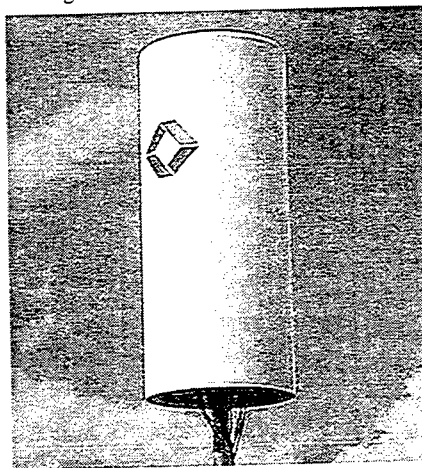Figure 3 Cellular Antenna Platform on Tower
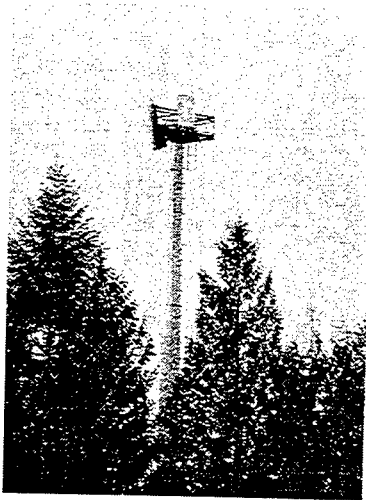

Figure 4 Conical Multibeam Antenna

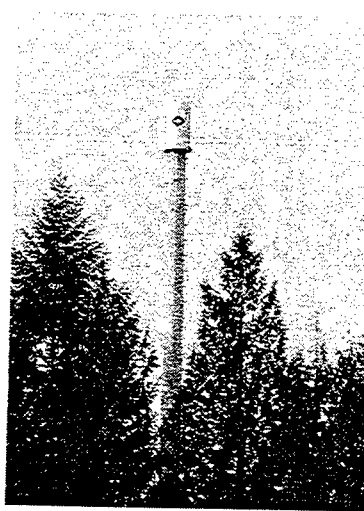Figure 5 Typical Cell Platform Antennas

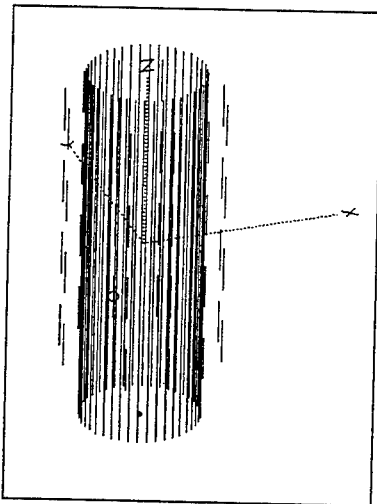

Figure 6 Conidal Antenna on Same Tower

Figure 7 Wire Grid Model for NEC

Figure 8 Wire Grid Model with Feed System
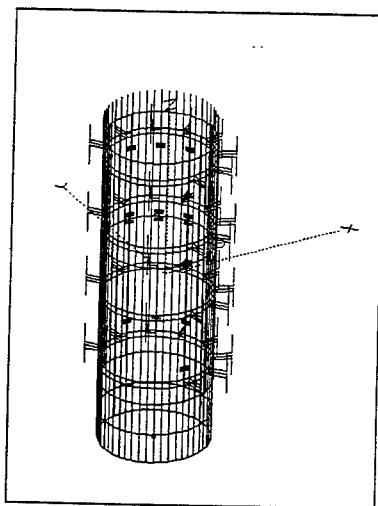
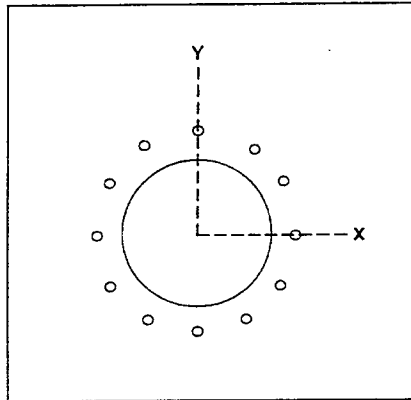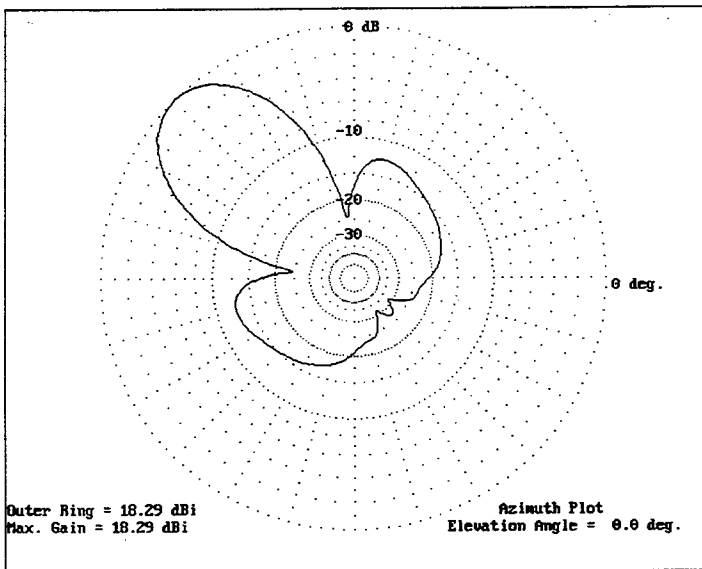Figure 9 Cross Section of Cylindrical Array (FDTD Model)

Outer Ring = 18.29 dBi
Max. Gain = 18.29 dBi

Azimuth Plot
Elevation Angle = 0.0 deg.

Figure 10 Azimuth Plot of Far Field for Model of Figure 7
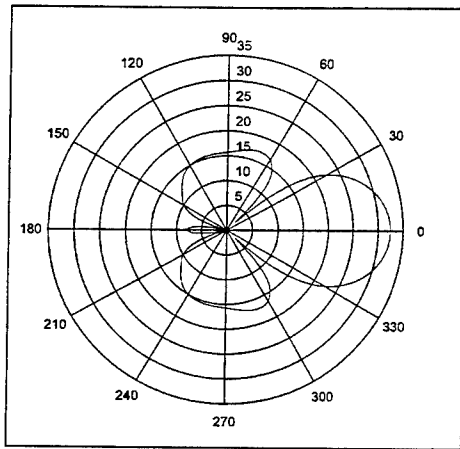
Figure 11 Far Field Plot for FDTD Model

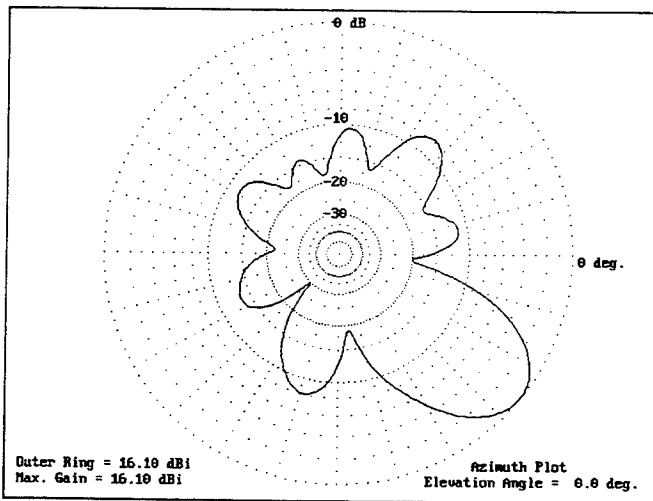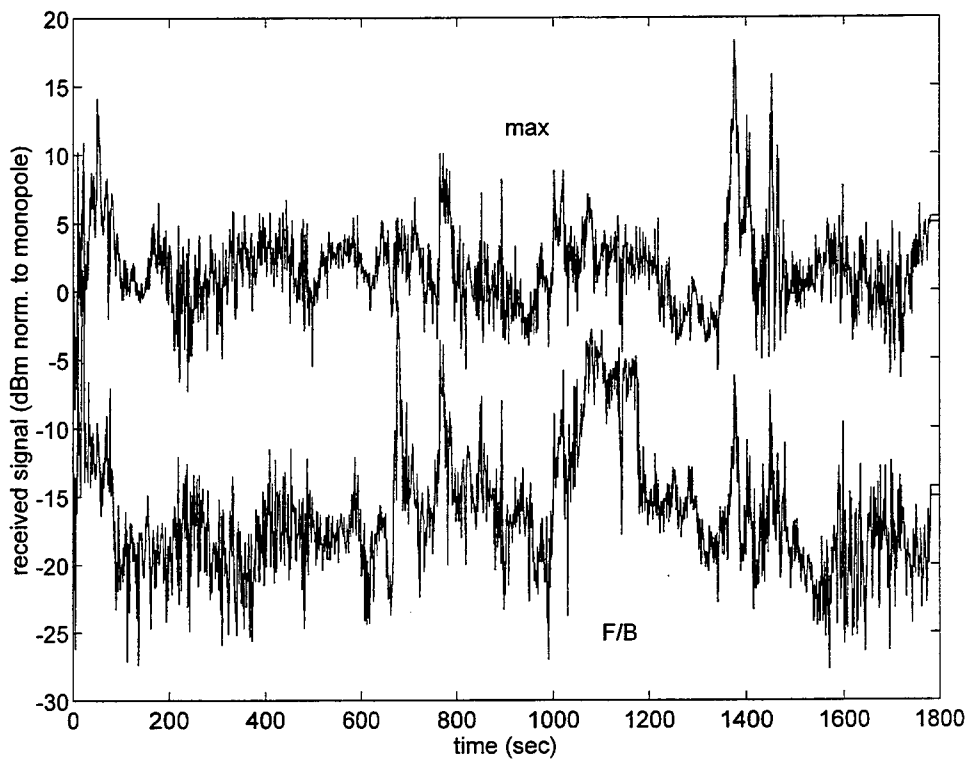

Figure 12 Azimuth Plot of Far Field of Figure 8

Figure 13 Maximum signal and F/B ratio for drive test

A HYBRID -METHOD SYNTHESIS OF
A RADIOMETRIC ANTENNA FOR NEAR-FIELD SENSING

E. Di Giampaolo° and F. Bardati#
° Dipartimento di Ingegneria Elettrica, Università dell'Aquila, L'Aquila, Italy
DISP, Università di Roma "Tor Vergata", Roma, Italy

ABSTRACT

Feasibility of non-contacting radiometry for temperature retrieval has been considered. A two-dimensional problem has been investigated, both the body and the antenna exhibiting cylindrical symmetry. The antenna is composed by two reflectors and a horn. The reflector shaping has been performed by geometrical optics, and one-to-one mapping of points of two wavefronts, on the horn aperture and on a surface close to the body, respectively. A local technique for the analysis of the field radiated in the close vicinity of the objects can be used to single out the wavefronts needed by the synthesis.

INTRODUCTION

Multi-frequency radiometry is the spectral measurement of the electromagnetic field spontaneously irradiated by a lossy body in the microwave frequency range. The spectrum of the radiation detected by a radiometer is dependent on the local temperature distribution inside the body. It is this dependency that allows multi-frequency radiometry to be used for near-field sensing of body temperature. In fact, information about interior temperature is contained in radiometric data measured externally to the body and can be extracted through a temperature retrieval. A major source of system errors or even impracticability of microwave radiometry for body temperature measurement is the antenna.

In a previous paper [1] we have proposed a cylindrical dual-reflector antenna as a possible non-contacting device to collect thermal radiation. Preliminary 2-D design and analysis have been performed on a cross-section of the antenna system including a TEM horn, two reflectors and a layered lossy cylinder simulating a human body. The synthesis has been performed by extension of a method developped by Kildal [2] for the Arecibo radio telescope.

Due to reciprocity in antenna theory, the problem of collecting thermal radiation emitted by (a portion of) a body is that of focusing antenna radiation to (that portion of) the body. Since body permittivity and electrical conductivity attain high values at radiometric frequencies, a plane wave impinging the body from a free-space is reflected at the skin-air boundary. Moreover, radiation transmitted to the body undergoes strong damping when it propagates through tissues. Therefore, our synthesis has been oriented to match the electromagnetic field radiated by the antenna to the field that is generated, in a region close to the body, by a deep-seated source within the body.

In the method, ray optics is used to map the wavefront, Γ_H, on the horn aperture into a corresponding wavefront, Γ_B, on a surface enclosing the body and close to it. To deal with problems on a plane, body, horn, reflectors and sources are assumed as cylinders, the z-axis being normal to the plane. Due to the simple geometry of the horn (two metal strips from two planes at angle β) and the body (a dielectric circular cylinder), the computation of Γ_H and Γ_B has been performed analytically. In more general instances, it would be performed numerically. So our method is hybrid because a local numerical technique (e.g., FDTD) can be used together with geometrical optics. Since diffraction effects are neglected in the reflector shaping, we finally used FDTD to analyse the electromagnetic field radiated by the system.

A FOUNDATION FOR NEAR-FIELD NON-CONTACTING RADIOMETRY

Microwave radiometry is based on the measurement of spontaneous temperature-dependent electromagnetic emission from lossy bodies. Maps of sub superficial temperatures can be obtained by inversion of data measured by a radiometer operating at various microwave frequencies. The mathematical problem can be formulated as the solution of the following Fredholm integral equation of first kind in the temperature T with discrete data g

$$g(f_n) = \int_{\Omega_B} W(\underline{r}, f_n) T(\underline{r}) d\underline{r} \qquad (1)$$

where Ω_B is the emitting body and W is a weighting function depending on the antenna in use. Because reciprocity in antenna theory, W can be obtained by the power loss term at points $\underline{r}$ of Ω_B when the antenna radiates onto the body at frequency f_n [3]. Note that a particular antenna affects radiometric resolution and accuracy through the weighting function. Spurious effects, which are due to antenna sidelobes and thermal noise, must be kept low.

In most radiometric systems the antenna is a dielectrically-filled truncated waveguide which contacts the surface, $\partial\Omega_B$, of the body. Since a contacting antenna has some disadvantages, we are considering the feasibility of a non-contacting device. As a first non-contacting device let us consider plane-wave observation, i.e., far-field radiation to an antenna focused to infinity. We assume a layered cylindrical model for Ω_B, the physical parameters being those of skin, fat, muscle and bone in this order, and a TE_z x-propagating plane-wave. $\omega_{h.s.} \subset \Omega_B$ is a hot-spot to be retrieved radiometrically (Fig. 1). For this geometry closed form computations can be performed. The weighting function is reported in Fig. 2 for some frequencies in a band commonly used for medical applications of microwave radiometry. The hot spot has been retrieved by means of a singular-function expansion detailed, e.g., in [4]. Results are shown in Fig. 3 in the absence of noise and system errors. Poor resolution can be appreciated.
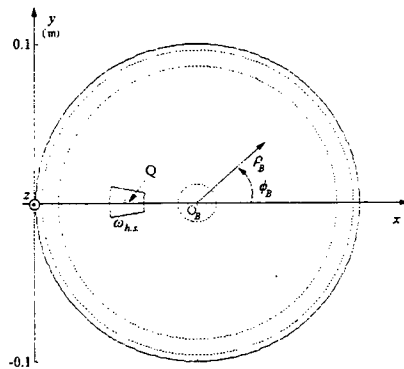

Fig. 1- Cross-section of a layered skin-fat-muscle-bone cylinder. Hot spot $\omega_{h.s.}$ to be retrieved radiometrically, $Q \in \omega_{h.s.}$. Cartesian (x,y,z), and cylindrical (ρ_B, φ_B, z) co-ordinate systems also shown.

We expect improved resolution from a finite-extent plane-wave. Therefore the impinging H_z-field has been assumed to be a gaussian pulse on α, where α is the plane $x = 0$, tangent to the cylinder:

$$H_z^{(\alpha)}(y) = H_0 \, e^{-\frac{y^2}{w^2}} \qquad\qquad\qquad (2)$$

w is the gaussian-pulse waist and $H_0 = 1$ A/m. The field computation was performed analytically by expansion of the gaussian pulse into a finite sum of uniform plane waves, for proper values of the amplitudes and phases. Once the gaussian-pulse response has been calculated and the weighting function has been obtained as the power loss inside Ω_B, the retrieval of $\omega_{h.s.}$ is performed as before. The diagrams of Fig. 4 show that better resolution is achieved with respect to single plane-wave observation. We conclude that improved retrievals are expected by a non-contacting antenna radiating a beam the cross-section of which is a finite-extent (like a gaussian) pulse on α.
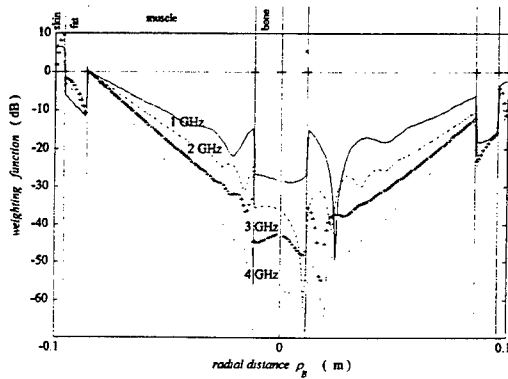

Fig. 2 - Weighting function $W(\rho_B, \varphi_B; f)$ vs. ρ_B for $\varphi_B = 0, \pi$. 0 dB level at fat-muscle interface.
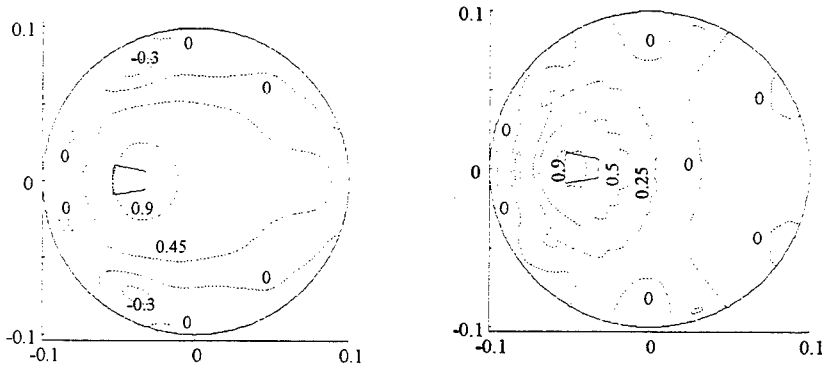

Fig. 3 - Hot-spot temperature retrieval by data at 8 equi-spaced frequencies in the band 1-4.5 GHz and (a) plane-wave observation from direction $\varphi_B = \pi$, (b) finite-extent beam, Gaussian pulse waist about $\lambda/2$ at each frequency. Contour levels are fractions of the maximum.

REFLECTOR SHAPING

In this paper the synthesis of the radiometric antenna is concentrated on reflector shaping by geometrical optics. A wavefront, Γ_H, is assumed on the horn aperture. For the sake of simplicity, Γ_H is a cylinder, whose cross-section on is a circle, centre O_H and radius R_H. If ρ_H, φ_H are polar co-ordinates, the field radiated by the horn is assumed as

$$H_z(\rho_H, \varphi_H) = A \frac{\Phi(\varphi_H)}{\sqrt{\rho_H}} e^{-jk_0 \rho_H} \tag{3}$$

where A is a constant, k_0 is free-space wavenumber, and $\Phi = 1$ for $0 \leq \varphi_H \leq \beta$, vanishing elsewhere.

A ray-optics model for body radiation deserves more consideration. Thermal emission from an elemental volume can be modelled as radiation from currents densities within the element. In cylindrical structures z-directed magnetic currents radiate TE_z polarized fields. Therefore the following magnetic source is considered on the $z = 0$ plane:

$$J_m(x,y) = I_m \delta(x - x_Q, y - y_Q) \tag{4}$$

where $Q \equiv (x_Q, y_Q)$ is a point of $\omega_{h.s.}$ and δ is Dirac delta function. The Green function, $G(P/Q)$, for a homogeneous dielectric cylinder is well known [5]. To compute the field at points outside the body we use the Green function for a homogeneous muscle cylinder instead of the Green function of the multilayer cylinder, because it is faster. In fact, ϵ and σ of skin and muscle coincide, moreover the narrow fat layer and the bone core lightly affect radiation from the body. Due to the cylindrical symmetry, the field radiated by the magnetic source of equation (4) is computed at points $P \equiv (\rho_B, \varphi_B)$ of a polar frame centred in O_B (Fig. 1).

A wavefront of the field radiated by the magnetic source of equation (4) is obtained by solving the following non -linear equation in ρ_B

$$Arg[G(\rho_B, \varphi_B / x_Q, y_Q)] - \eta = 0 \tag{5}$$

for $\pi/2 \leq \varphi_B \leq 3\pi/2$, where η is a real number. This procedure identifies an equiphase surface, Γ , for radiated H_z field (Fig. 4). To verify that Γ is also a wavefront at some distance from the body, the normal $\hat{n}$ is computed at points belonging to Γ, then the dot product of $\hat{n}$ with the unit vector directed as the real part of the Poynting vector is verified to be 1. Moreover, if Γ' is a different wavefront corresponding to η', the straight line through corresponding points of Γ and Γ' is verified to be at right angles with the two surfaces. This proves the line to be a ray. Γ_B, which is the second wavefront for the synthesis, is a surface Γ very close to $\partial \Omega_B$.

The synthesis is performed on the plane $z = 0$ and is aimed at determining N points for each S_1 and S_2 together with curvature parameters: normal and curvature radius (the second curvature radius being ∞). The synthesis is based on one-to-one mapping of points $P_H^{(n)}$ of Γ_H to corresponding points $P_B^{(n)}$ of Γ_B, by enforcing power conservation inside ray-tubes and ray reflection at points of S_1 and S_2 (Fig. 5). Let the n-th ray path, $L^{(n)}$, be known. Therefore $P_1^{(n)}$ and $P_2^{(n)}$ as well as the normals, $\hat{n}_1^{(n)}$ and $\hat{n}_2^{(n)}$, are also known. The curvature radii, $\rho_1^{(n)}$ and $\rho_2^{(n)}$, can be obtained by enforcing ray tube matching after reflection by reflectors (to perform this calculation, backward ray

propagation is assumed from Γ_B to S_2). Once $\hat{n}_1^{(n)}$ and $\rho_1^{(n)}$ have been determined, a parabola $\gamma_1^{(n)}$ can be found through $P_1^{(n)}$ as a local approximation of S_1. The intersection of $\gamma_1^{(n)}$ and the $n+1$–th ray gives $P_1^{(n+1)}$ and $\hat{n}_1^{(n+1)}$. Analogous computation can be made for the second reflector, then a new iteration can start. The initial ray path $L^{(0)}$ is passing through an edge of each surface involved in the synthesis. Since the overall size of the antenna depends on $L^{(0)}$ also, it must be selected carefully. To be useful in a clinical environment, the radiometer system should be relatively small and allow simultaneous different operations on the patient. This observation adds further requirements to the antenna design. A result is shown in Fig. 6.
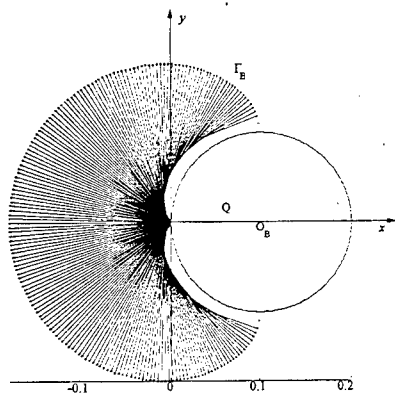

Fig. 4 - Wavefront Γ_B for the electromagnetic field radiated by a magnetic-current Dirac source at Q. Ray congruence also shown.
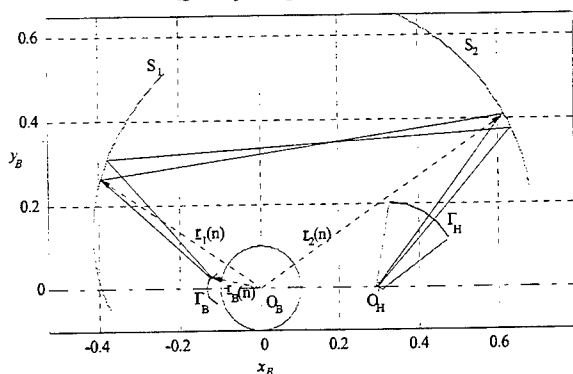

Fig. 5 - Scheme for reflector shaping. A ray path from Γ_H (horn) to Γ_B (body) is reflected by S_1 (main reflector) and S_2 (sub-reflector). Vectors $\underline{r}_B, \underline{r}_1, \underline{r}_2$ from O_B to Γ_B, S_1, S_2 also shown.

Some approximations have been made in the above procedure, especially where the wavefronts on the horn and the body are determined. Moreover, diffraction effects are not negligible due to small

size of the various objects and relative distances in terms of wavelength. So an analysis of the electromagnetic field inside a 2D domain, including the antenna and the body, has been performed by FDTD, 400x400 cells and Mur first-order ABC (Fig. 7). Diagrams of $|H_z|$ on the α plane are shown in Fig. 8 for various frequencies. Each diagram has a central part in front of Ω_B, where the curve is a good approximation of a gaussian pulse, and sidelobes.
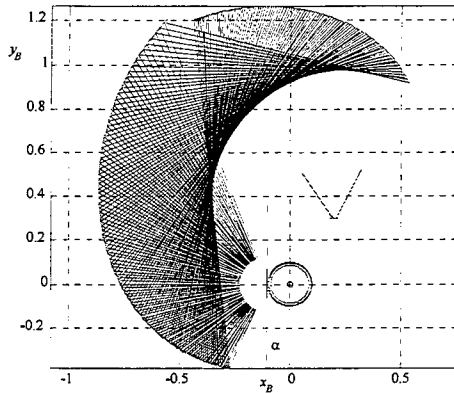

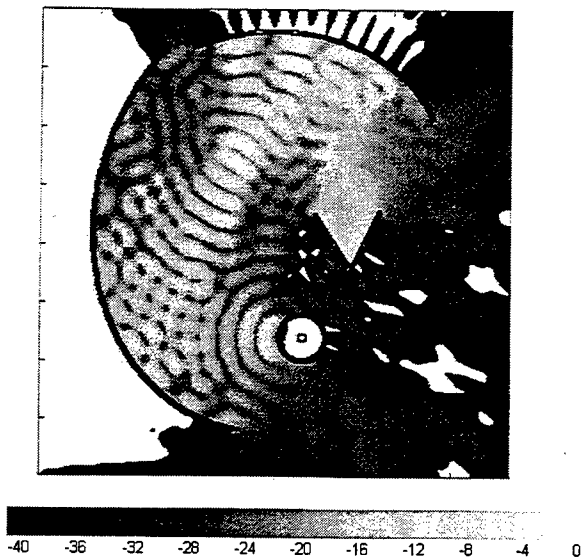Fig. 6 - Result of the synthesis. Ray congruence also shown

Fig. 7 - 2D FDTD analysis. Field radiated by a magnetic source at the horn vertex.

CONCLUSION

The problem of the synthesis of a dual-reflector antenna for non-contacting microwave radiometry has been considered. A finite-extent antenna beam on a plane tangent to the body has been shown to allow improved thermal resolution with respect to plane-wave observation. The reflector shaping has been performed by geometrical optics, provided the wavefronts close to the receiving horn and the body are determined. The wavefronts have been approximated by means of analytical models, while they could be obtained numerically in a more realistic case. FDTD analysis of the electromagnetic field for the synthesised antenna provides results in agreement with the requirements.

REFERENCES

[1] E. Di Giampaolo, G. Marrocco, F. Bardati, "A shaped dual-reflector antenna for non-contacting radiometry of human body", USNC/URSI Radio Science Meeting, Baltimore, MD, July 21-26, 1996, p. 131

[2] P.-S. Kildal "Synthesis of multireflector antennas by kinematic and dynamic ray tracing", IEEE Trans. Antenna Propagat. Vol. AP-38, pp. 1587-1599, 1990

[3] F. Bardati, V. J. Brown, P. Tognolatti (1995) "Spectral microwave radiometry for subcutaneous temperature imaging" in *Non-Invasive Thermometry of the Human Body*, M. Miyakawa and C. Bolomey Eds., CRC Press, Boca Raton, FL, 1995, pp. 225-253.

[4] F. Bardati, V. J. Brown, and P. Tognolatti (1993) "Temperature reconstructions in a dielectric cylinder by multifrequency microwave radiometry", J. Electromagnetic Waves Applications, vol. 7, n. 11, pp. 1549-1571

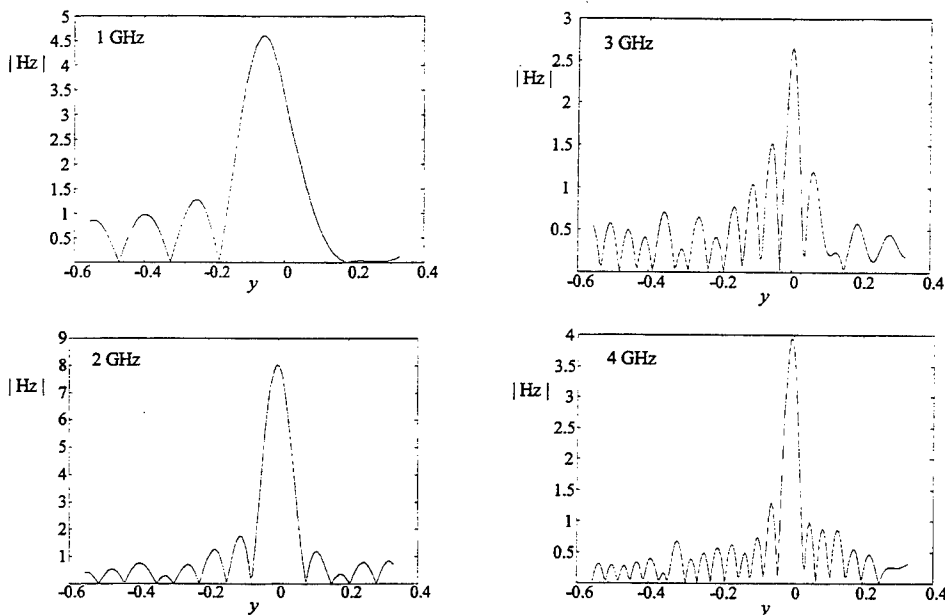[5] J. R. Wait, *Introduction to Antennas and Propagation*, Peregrinus, London, 1986, p. 193.

Fig. 8 - $|H_z|$ vs. y on the $x = 0$ plane (α plane)

An Evaluation of Software Packages Based on Moment Methods for TV Antenna Design

By Ignacio F. Anitzine, Cristina Jaureguibeitia and J. A. Romo

Abstract: **The fact of having to design a new real antenna has let us make an evaluation of different programs for antenna design, which is here presented. The programs involved are Antenna Optimizer AO 6.5, Mininec Professional 1.5 and NecWin Professional 1.0. All of them are based on the method of moments. The analysis is as well about the friendliness for work as about the way of working. Concretely, we deal about the way of approximating current distribution, the proper number of segments and execution rate.**

1. Introduction

Last year we developed a new antenna design for TDTV (Terrestrial Digital Television) in the bands IV and V (450-900 MHz). In order to arrive at good results without a great cost of time, we began looking for the best antenna design software tools. At last we decided to use three different software packages to be sure of our design results before constructing prototypes: Antenna Optimizer (AO 6.5), Mininec Professional 1.5 and NecWin Professional 1.0.

We have had to use them for a long time. The aim of this article is to present our experience with these three programs and to present an evaluation of these tools which all based in method of moments. We give our own opinions about the visualising tools included in the packages and about other aspects as the kindness for introducing geometries.

After this subjective analysis, we began with an evaluation of the programs in purely teorethical terms. In regard to this point we analysed if they used point matching or a certain approximation for the current along each wire segment, and in this latest case which one.

On another hand we studied about how to determine the number of segments which drives to better results. At first we describe the ways of introducing this number, if it is an automatic or a handily one. Later we put our attention on the criteria of the software packages to decide if the geometry is well defined in regard to the number of segments, that is, if the segment length is not too large compared to the wave length but if it is large enough to the wire radius and others. Finally we made programs run with a same geometry but different number of elements, comparing the obtained results in terms of gain, radiation patterns and impedance for each number of segments to the corresponding values with experimental measurements.

Besides we probed the programs about execution rate, determining which hardware characteristic if more important for each program to operate at the highest rate.

2. About visualising tools, way of introducing geometries and other topics

We are going to present our particular point of view about some characteristics of the three programs evaluated: Antenna Optimizer Professional 6.5, NecWin Professional 1.0 and Mininec Profesional 1.5. AO works at a higher computational rate than the other programs. NecWin is the slowest whilst Mininec is fast but, for a complex geometry as ours, it is necessary to calculate the radiation patterns frequency by frequency. A useful characteristic offered by AO and Mininec is the indication about the evolution of the execution, so you can guess how much time is necessary to finish.

These two latest programs run on Windows and have a presentation interface kinder than AO, which must be run on MS-DOS. The way of introducing the geometry under study is simple in the three programs. In NecWin and AO you define each wire indicating the coordinates of the start and end points and the radius, whilst in Mininec, first you define each node and later the start and end nodes of each wire. In this latest program you can not use edit tools as "copy" and "paste" ones, that simplify the geometry introducing task. AO allows you to define some variables so in this way, changes of dimensions are faster. For example you can define all the antenna as a function of a dimension, typically the wavelength at the design frequency, and then modify this variable. This is one of the greatest characteristics of AO. Nevertheless, NecWin and Mininec have another tools as "scale", "translate" and "rotate". On another hand, Mininec gives an evaluation of the geometry according to the criteria we will explain later.

In regard to the visualising tools, AO presents less possibilities of presentation. For example, it is not possible to obtain plots in colour or scale them. Moreover, in the other two programs, currents can be analysed in a graphical quantitative way. NecWin can be used to obtain comparative plots in a very easy way. All of the programs allow to display in 3D as well the model geometry as the radiation patterns, but only NecWin and Mininec give printed copies of the model geometry.

But the main and differential characteristic of AO is its capacity of optimization, despite of the great time required in this mode to reach at good results. With our experience in TV antenna design we developed the first approximation of our geometry. Later this AO capability was fundamental to arrive at more exact dimensions.

3. Approximating the current distribution

There are several moment methods depending on the way to approximate the current distribution.

AO uses the wire segmentation to model conductor current in sections called pulses. Within each pulse the current is considered as uniform. These pulses are centred at segment junctions and have the same length as segments. No pulse overlaps the last half segment of an unconnected wire end. A pulse is placed at each wire junction and overlaps onto two wires, so in a junction of n wires there are only n-1 pulses.

On the other side, in Mininec the wire is subdivided into segments and the current is expanded in triangles centred in the adjacent segment junctions as it is illustrated in Figure 3.1 (a) extracted from the Mininec reference manual. The end points have no triangles. If a second wire is attached to one end of the first, the triangles in the second wire are located as in the first case. However a full triangle is located at the attachment end as it is illustrated in Figure 3.1 (b). Each half of the triangle assumes the dimensions appropriate to the segment of each wire. So, as in the case of AO, in a junction of n wires there are only n-1 overlapping triangle pulses.

(a)   (b)
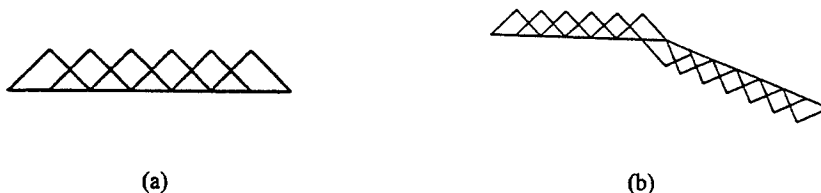
□ Figure 3.1

Finally, we are sorry to inform you that we have no information about how NecWin Pro approaches the current because this information is not provided in its reference manual and manuals have been our sources for this point.

4. How to decide about the proper number of segments

There are four key factors that determine how close a computer analysis is to the "real world" performance of an antenna. These factors are:

1.- The numerical methods employed and how well these methods are implemented in a computer code.
2.- The inherent accuracy of the computer.
3.- How well the numerical model corresponds to the physical model.
4.- The user's experience in recognising problem areas.

In the previous chapter we have seen how the method of moments approaches to the current distribution. Now we can discuss about the best way to determine the number of segments, directly regarded to the accuracy of the results. The moment methods makes some suppositions whose validity depends on the dimensions of the segments considered. It assumes that all the current is in the axial direction on the segment and there is no allowance for variation of the current around the wire, so the relation between radius, length, and wavelengths should accomplish some rules.

In AO you can let it segment wires automatically or you can specify the number of segment for one or more wires. Increasing the number of segments generally improves accuracy but analysis takes more time and there is always a limit. Generally between 4 and 40 segments per halfwave of wire provides useful results. Besides the segments should not be too short. The length of each segment must be greater than 0.0001λ and greater than the wire diameter. A warning message is displayed when either of these limits is exceeded.

The maximum number of pulses (and consequently the number of segments) you can define in AO is only determined by the available memory. For our case, in which we have 32 MB of memory and our design is a free-space symmetric model, there are 4026 pulses available.

In regard to wire junctions, the segment lengths in the wires involved should not be too disimilar. When automatic segment-length tapering is enabled, AO analyses the junctions and correct them. By default, a ratio of 2 is set and it is the highest value which leads to valid results but it can be modified.

Mininec allows to establish your own criteria used for the Definition evaluation but it gives a set of default values. Each wire should be subdivided into segments comparable to less than 0.1λ. The accuracy is seriously reduced if segments are greater than 0.2λ. At the same time, the shortest permissible segment is determined by the wire radius. The ratio of segment length to wire radius should be maintained greater than 8. Some reasonable results can be obtained down to 2. Besides the wire radius should satisfy that it is thinner than 0.01λ. If wires are fatter than 0.03λ the results may be in error. In this program the maximum number of wire segments is

At wire junctions there must not be great differences between the wires involved. For good results. the length ratio should be less than 2 and values greater than 5 should always be avoided. the ratio of the radii of wires at a junction should be minor than 10 but ratios of 100 have also shown reasonable results.

When the definition evaluation criteria are not accomplished the violations are indicated in the Evaluation summary.

Finally, in NecWin Pro the length of a segment should be, at least, less than 0.1λ and $2\Pi a/\lambda$, where "a" is the radius of the wire, has to be much less than 1 for valid results. In wire junctions a large radius change between connected segments may decrease accuracy but there are no numerical rules in this program. We can follow the criteria of the other software packages. We can define until 2000 segments in a model.

In all the programs crossed wires are not modelled and close wires should also be avoided. There should be several radii apart.

All of these are rules indicated in the corresponding manuals of each program. In the following graphics and tables there is a comparison of the results obtained when you consider a different number of segments for a given geometry within a frequency band. We introduced the geometry of our antenna design (Figure 4.1) with 330, 661 and 1321 segments.
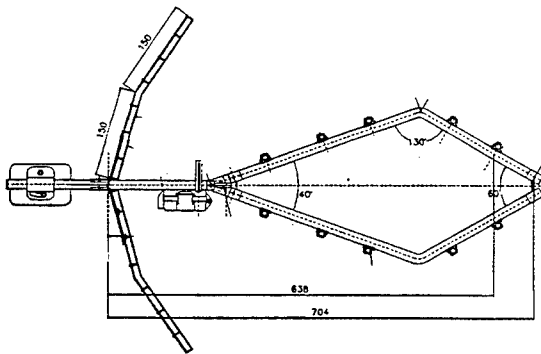
□ Figure 4.1

We can say that the values of gain and the radiation patterns are maintained more or less unaffected with the number of segments. The values of gain obtained with the three programs are similar, a bit more optimistic in NecWin Basic and Mininec than in AO. But if we compare them with experimental measurements, we will find out that the nearest ones are the values from Mininec. In any way, experimental results are better than simulations, so we can trust in the designs. There is also accordance between simulated radiation patterns and measured ones.

Frequency	AO Prof. 6.5	NecWin Prof.1.0.	Mininec Prof. 1.5	Measurements
450 MHz	9.25 dB	9.87 dB	9.69 dB	9.80 dB
500 MHz	9.69 dB	10.39 dB	10.19 dB	10.20 dB
550 MHz	10.20 dB	11.01 dB	10.77 dB	11.10 dB
600 MHz	10.83 dB	11.78 dB	11.48 dB	12.03 dB
650 MHz	11.61 dB	12.63 dB	12.29 dB	12.48 dB
700 MHz	12.37 dB	13.23 dB	12.93 dB	12.11 dB
750 MHz	12.68 dB	13.32 dB	13.20 dB	13.10 dB
800 MHz	13.13 dB	13.98 dB	13.74 dB	14.68 dB
850 MHz	14.53 dB	14.83 dB	15.04 dB	15.30 dB
900 MHz	14.91 dB	13.75 dB	15.25 dB	14.92 dB

□ Table 4.1

For the measurements, we used a network analyser (HP 8753C) controlled by a PC through our own HPVEE programs to measure S parameters, gain, F/B and radiation patterns. The measurements took place in the "L" outdoors measurement field.

Bigger differences are found in the impedance values and, consequently, in the VSWR, due to the selected number of segments. We have made three graphics (Figure 4.2)in which it can be observed the differences between the results of each program in case of using a certain number of segments and the real values obtained by experimental measurements.

476

□ Figure 4.2

477
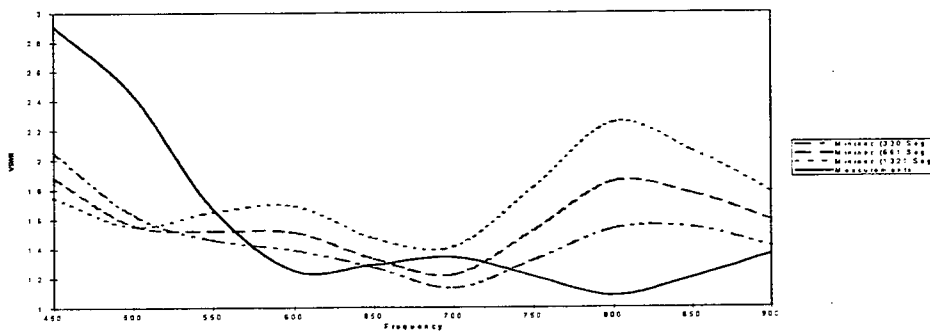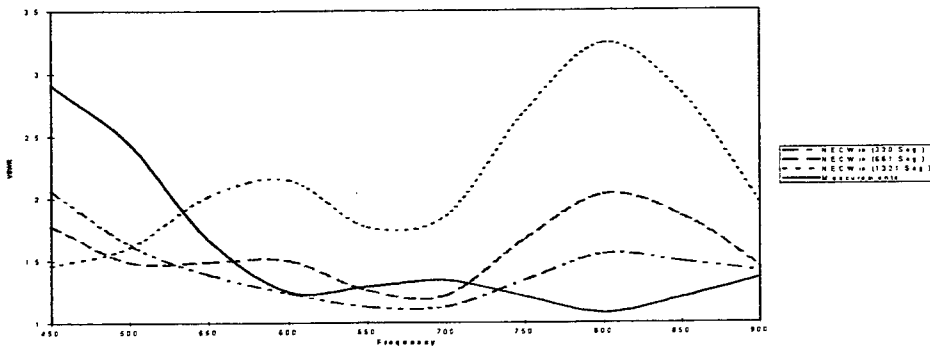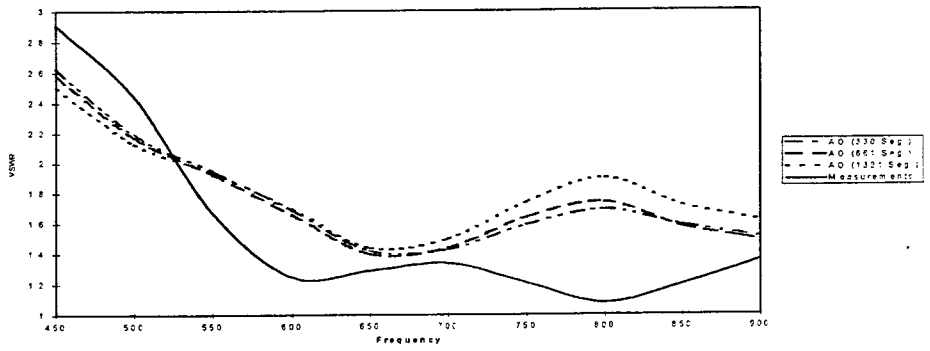
In regard to VSWR, only given by AO and NecWin (Mininec presents impedance values, with which one must calculate VSWR if you want to know), AO's ones appear to be more reliable.

5. About execution time

One of the most important point of evaluation of the software packages is the execution time. When the process requires a considerable time to give good results the simulation task becomes in a boring one. We have analysed the operation time of each program.

We have found that the time required by each program to give results is more or less proportional to the number of frequencies. However, the execution time increases rapidly, more than proportionally, as the number of specified segments grows up. The software package which appears to be faster is Antenna Optimizer (AO 6.5), in which there are no time differences in using automatic or not-automatic segmentation. In the second place it could be Mininec Professional but, as we said before, it has the drawback that radiation patterns at every frequency must be calculated separately, so it is needed a person to be in front of the computer to obtain the results that, in the two other programs, are obtained without human interaction. The measured times required by each program to calculate currents and radiation patterns at 10 frequencies are presented in the following table (Table 5.1). Tests have been made with a PC Pentium at 120 MHz and with 32 MB RAM.

	AO Prof.6.5	NecWin Prof.1.0	Mininec Prof. 1.5
330 Segments	1 min 10 s.	10 min. 20 s.	1 min. 49 s.*
661 Segments	4 min 25 s.	1h. 14 min. 10 s.	12 min. 4 s.**
1321 Segments	21 min. 56 s.	9h. 54 min. 20s.	1h. 20 min. 55 s.***

❑ Table 5.1

This is the time required for current calculation at 10 frequencies. To calculate currents and radiation patterns at each frequency they are necessary 1 min 4 s.** In this case they are necessary 2 min. 39 s.*** They are necessary 11 min. 25 s. for currents and radiation patterns at each frequency.

On another hand we have made a more exhaustive analysis of Mininec and NECWin programs using one of the utilities provided by Windows NT, the Monitoring Performance. In this way, we have been able to discover the bottlenecks of the process, that is, which hardware characteristic is determining in a greater way the execution time. We have centred our attention in three main points: the processor time, which includes as well the processor as the RAM memory, the disk access time and finally, the virtual memory pages per second. The last item gives us an idea of the lack of RAM memory: as higher as its number is, more RAM memory would be necessary. In Figure 5.1 it could be seen a comparison of the obtained diagrams for NecWin and Mininec in the case of 661 segments.

We have repeated the same tests with a computer 486 DX4 at 100 MHz with 16 MB RAM. As it would be expected, execution takes more time. There is no a great increasing of virtual memory pages per second in Mininec so it can be said that it is limited by the micro used. As it can be seen in the figure, in certain moments, NecWin Professional requires a great number of virtual memory pages per second, which shows us that this program is mainly limited by the RAM memory.

478
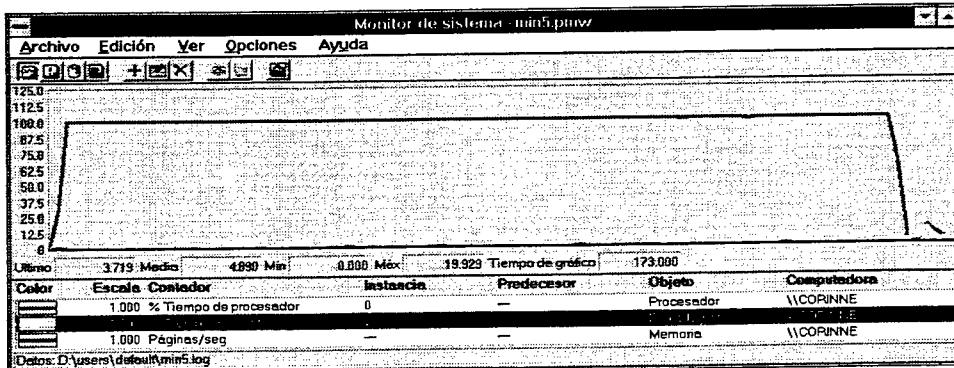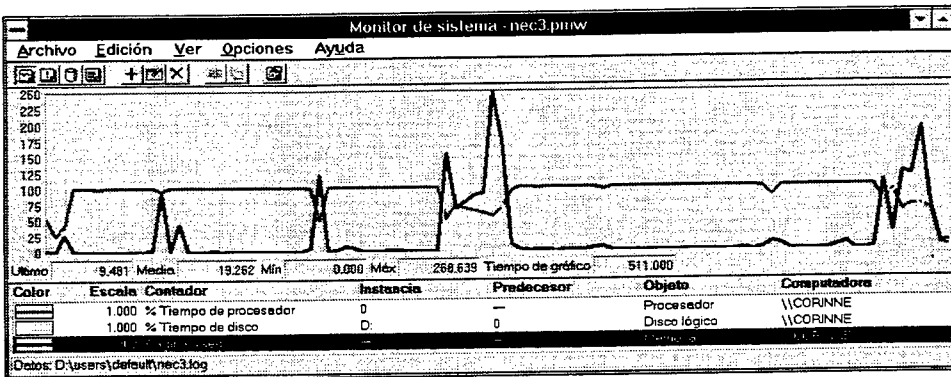
Figure 5.1

6. Conclusions

We can say that the selected number of segments is the most important point in simulation task. For the study of our geometry we have decided to use 661 segments, so we can obtain good results in a reasonable period of time. Besides, a greater number does not always drive to better results because some of the assumptions of the method of moments begin not to be true. This is the case of NecWin in VSWR calculation. The influence of the number of segments is variable depending on the software, being AO 6.5 the most unaffected.

Nevertheless, we can not forget that simulations are simulations, and it is always necessary to make experimental measurements which gives us the real behaviour of the involved antenna. The results about gain and radiation patterns are more or less reliable but VSWR values from the three programs differ from the real world. Despite these differences, software packages are a decisive tool in antenna design because, through their capabilities as optimization, they allow to reduce the task of constructing prototypes.

References

[1]   John Rockway, James Logan. "Advances in Mininec" IEEE Antennas & Propagation Vol. 37, N°4, August 1995, pp 7-12

[2]   Brian Beezley. "The Antenna Optimizer AO Manual". Brian Beezley. Linda Vista 1994

[3]   J.W. Rockway, J.C. Logan. "The Mininec Professional for Windows Manual". EM Scientific, Inc. Carson City, Nevada 1995

[4]   J. Shapiro, J. Finnerty, M. Nye. "The Nec-Win Professional User's Manual". Paragon Technology, Inc. 1996

[5]   R.F. Harrington. "Field Computation By Moment Methods" The Macmillan Company, New York, 1968

ALGORITHM FOR PREDICTION OF SCATTERING FROM THIN CYLINDRICAL CONDUCTORS USING FIELD DECOMPOSTITION

P K Bishop[1], J R James[1], R T Biggs[2]

[1]Royal Military College of Science, Cranfield University, UK
[2]DERA, UK

INTRODUCTION

The scattering of radio waves from cylindrical structures, Felsen and Marcuvitz (1), such as underground pipes etc. continues to be of interest in radar, communications and navigation. Numerical methods can of course model such situations using techniques such as the method of moments or finite elements but the computational resources demanded are often excessive for many practical applications and a simpler, yet reliable method of estimating the scattering behaviour would be useful. As far as we are aware no simple closed form solution exists that will accommodate a variety of application needs. In evolving a simpler solution we have been influenced by the present trend of supplementing computational procedures with analytical expressions to reduce the volume of processing and hence the computational resources demanded. Such hybrid analytical / computational methods will of course only be applicable over the narrower range of physical conditions delineated by the analytical content but over that range, the simplified hybrid method will out-perform a large scale numerical computational programme provided the analytical content skilfully embodies the physical action taking place. We will demonstrate that this is so for the simpler methods presented here and we use NEC, Burke (2), as a comparative of a large versatile computational routine.

In this paper we demonstrate adaptable algorithms for the near, intermediate and far scattered fields of a thin conducting cylinder which is generally one quarter of the free space wavelength or longer in electrical length. The technique described arises from the approximate decomposition of the scattered fields into the well known modal solution of an infinite length cylinder together with an amplitude scaling function which comprises of the current and charge distribution on a finite length cylinder derived in a novel manner. The sequence of the present paper commences with the formulation of the Field Decomposition (FD) technique leading to the scattering algorithms. In its simplest form the algorithm is applicable to configurations of connected thin conducting cylinders immersed in a lossy medium and subject to oblique multiple frequency illumination. Extension of the algorithm to other cylindrical scatterers with dielectric boundary conditions is possible and the subject of ongoing research.

FIELD DECOMPOSITION

The basis of the FD technique arises from analysis of the resonator action taking place in the fields around a conducting cylinder generally having a very large length to diameter ratio. Physically we can identify travelling wave fields characteristic of an infinite length cylinder and these fields will be used as analytical content in our algorithms. Dielectric waveguide and opto-electronic guides exhibit similar mechanisms whereby an incident wave excites a travelling wave which is reflected from the terminations depending on the terminal impedances, and this leads to simplifying hybrid computational methods, Chiang (3).

Transverse Fields

The travelling wave on a finite length conducting circular cylinder, Balanis (4), of radius $a \ll \lambda_o$, where λ_o = free space wavelength, will have, except in the region of the terminations, the near field structure of the fields of a cylinder of the same radius but of infinite length. When $ka \ll 1$, where k is the propagation constant, the Transverse Magnetic (TM) fields are dominated by the first term of the modal expansion and the solution to the transverse wave equation is axially symmetric, leading to the isotropic scattered fields in equation (1).

$$E_x = E_o R(\rho,\alpha)\cos\alpha\cos\phi \qquad E_y = E_o R(\rho,\alpha)\cos\alpha\sin\phi \qquad E_z = -E_o\sin\alpha\frac{\ln(k\rho\sin\alpha)}{\ln(ka\sin\alpha)} \qquad H_x = H_o R(\rho,\alpha)\sin\phi$$

$$\hspace{6cm} (1)$$

$$H_y = H_o R(\rho,\alpha)\cos\phi \qquad R(\rho,\alpha) = \frac{1}{k\rho\sin\alpha(\ln(ka\sin\alpha))} \qquad H_o = E_o\sqrt{\frac{\varepsilon}{\mu}}$$

Where E_{xyz} and H_{xy} are the Cartesian field components. H_z is zero for the TM case. ρ and ϕ are cylindrical coordinates of the scattered field and the plane wave of amplitude E_o is incident at an angle α to the cylinder axis as shown in Fig. 1. The permittivity ε and permeability μ are of the surrounding medium and $k^2=\omega^2\mu\varepsilon-j\omega\mu\sigma$.

Curents

We assume open circuit terminations and present methods of obtaining the travelling wave current based on physical action. The fields in equation (1) are normalised and scaled along the cylinder axis in proportion to the travelling wave current and charge which for electrically long cylinders have many minima created by the terminal reflections. The incident field excitation is applied at N=s+1 equispaced points along the cylinder axis, where s is the number of segments between the excitation points, Fig. 2, to produce N asymmetrical dipole current distributions. The currents generated by the N dipoles are then summed to produce the required current distribution for a finite length cylinder. We now describe two algorithms for scattering behaviour that can be derived from this field decomposition. A very simple yet surprisingly effective method. algorithm I. is based on heuristic reasoning while algorithm II is a precise method based on established antenna theory.

Algorithm I. A simple graphical process can be employed to describe the steps involved in the mathematical implementation of this method as follows:
- Draw a cylinder scaled in wavelengths.
- Discretise the cylinder into a small number of segments. Fig. 2.
- Each segment end will be used as a source location. providing approximate representation of the current on the individual. unbalanced. dipoles. To construct these individual dipole currents draw sine waves. with period λ. starting from the source location and travelling outward in both directions to the cylinder ends. Repeat this procedure for each of the individual sources.
- Add the resulting waveforms and take the absolute value of the result to provide an approximate graphical representation of the current density distribution on the cylinder due to a plane wave source.
- Normalisation is carried out by subtracting the amplitude of the first point from the entire result and dividing the new curve by its new maximum. Graphically this is interpreted as shifting the curve (ends) down to the x axis (y=0) and making the peak y value equal to 1.

Fig. 3 shows the graphical implementation of algorithm I for a cylinder which is $5\lambda/4$ in length and discretised into 8 segments.

Algorithm II. The mathematical derivation of the travelling wave current I(z) is again based upon the summation of dipole current distributions. now taking into account dissipative losses and radiation. The current on an infinitely-long dipole driven at z=0 is simply $I_{inf}(z)=(E_o/2Z_{inf})e^{jkz}$. King and Smith (5). which can be expressed as the integral equation (2).

$$I_{inf}(z) = \frac{2jk}{\eta_o}\int_{C_o}\frac{e^{i\zeta z}}{(k^2-\zeta^2)\overline{K}(\zeta)}d\zeta \hspace{4cm} (2)$$

where $\overline{K}(\zeta) = \pi j J_o H_o^{(1)}$ and J_o and $H_o^{(1)}$ are Bessel functions with arguments $\{a(k^2-\zeta^2)^{1/2}\}$. C_o is the contour of integration and η_o is the intrinsic impedance of free space. A good approximation of the current. except quite close to the generator where the imaginary part is somewhat in error. is given in equation (3).

$$I_{\inf}(z) = \frac{je^{jkz}}{\eta_0} \ln\left[1 - \frac{2\pi j}{2C_w + \ln\left(kz + \sqrt{(kz)^2 + e^{-2\gamma}}\right) + \gamma + j\frac{3}{2}\pi}\right]$$ (3)

The current on a finite antenna may be expressed as the superposition of the current $I_{\inf}(z)$ and currents reflected from the cylinder ends which are proportional to $I_{\inf}(h_1+z)$ and $I_{\inf}(h_2-z)$, respectively, where the ends of the antenna are at $z=-h_1$ and $z=h_2$. The current on a symmetrical dipole antenna with its driving point at $z=0$ is given by King and Smith (5) and modified for the asymmetrical dipole with its driving point still at $z=0$, by Shen and King (6) resulting in equation (4) below.

$$I(z) = I_{\inf}(z) + C_d I_{\inf}(h_1 + z) + C_u I_{\inf}(h_2 - z)$$ (4)

Where the amplitude coefficients C_d and C_u satisfying the boundary condition of zero current at the cylinder ends, are shown to be:

$$C_d = -R\left[\frac{I_{\inf}(h_1) - RI_{\inf}(h_2)I_{\inf}(h_1 + h_2)}{1 - R^2[I_{\inf}(h_1 + h_2)]^2}\right] \qquad C_u = -R\left[\frac{I_{\inf}(h_2) - RI_{\inf}(h_1)I_{\inf}(h_1 + h_2)}{1 - R^2[I_{\inf}(h_1 + h_2)]^2}\right]$$ (5)

Where $R = \frac{\eta_0}{2\pi}[2C_w + j\pi]$, $C_w = \ln(1/ka) - \gamma$, and $\gamma = 0.577$.

In our solution we show that the current on a parasitic element, or finite length cylinder, consists of a summation of elementary asymmetrical dipole current distributions of the form of equation (4) but with shifted driving points. The cylinder is discretised into segments as shown in Fig. 2 and a 'source' placed at the end of each segment. Each individual source represents the voltage induced at that point by the illuminating wave and produces a single dipole current distribution. These voltage sources could be, for example, 1V at 1m intervals for a normally incident plane wave of 1V/m amplitude, however, allowance must be made for the varying amplitude and phase relationship between these sources for a plane wave that has oblique incidence. These individual distributions are summed to represent the total current distribution on the finite length cylinder due to the incident illumination. Although the solution is not limited to plane wave illumination, as discussed later, it is the given scenario in equation (6) with appropriate phase and amplitude variation included within the summation for oblique plane wave incidence.

$$I(z) = \left[\sum_{n=1}^{n=N}\left\{I_{\inf}(|z|) + C_d I_{\inf}\left(\left|h - (n-1)\frac{h}{s} + z\right|\right) + C_u I_{\inf}\left(\left|(n-1)\frac{h}{s} - z\right|\right)\right\}e^{-jk\left(\frac{h}{2} - (n-1)\frac{h}{s}\right)\cos\alpha}\right]\sin\alpha$$ (6)

where h is the total cylinder length and the coefficients become:

$$C_d = -R\left[\frac{I_{\inf}\left(h - (n-1)\frac{h}{s}\right) - RI_{\inf}\left((n-1)\frac{h}{s}\right)I_{\inf}(h)}{1 - R^2[I_{\inf}(h)]^2}\right] \qquad C_u = -R\left[\frac{I_{\inf}\left((n-1)\frac{h}{s}\right) - RI_{\inf}\left(h - (n-1)\frac{h}{s}\right)I_{\inf}(h)}{1 - R^2[I_{\inf}(h)]^2}\right]$$ (7)

When the cylinder is surrounded by a lossy medium η_0 is replaced by $\sqrt{\dfrac{\mu}{\varepsilon + \dfrac{j\sigma}{\omega}}}$. The travelling wave charge is related to the current through the continuity equation.

The algorithm consists of a few modular steps:

- The current on an infinite cylinder with one source located at z=0, equation (3), is computed, providing the current emanating from the three sources associated with each individual dipole in the summation, the source itself and the points of reflection at either end of the cylinder.
- The dipole current is then calculated for each source location individually, equation (6).
- The resultant current distributions are then summed to provide the total current distribution on the finite length cylinder.
- The charge distribution is then computed by application of the continuity equation to the current distribution.

Scattered Field Components

The field decomposition method provides the scattered field components around the finite cylinder, within its axial bounds, using a combination of the transverse fields of equation (1) scaled by axial fields given by algorithm I or algorithm II, equation (6). For the precise solution required of algorithm II the current and charge must be respectively scaled using equation (8) to provide the scattered E_x, E_y, E_z, and H_x, H_y fields.

$$\frac{\rho(z)}{2\pi\varepsilon r} \qquad\qquad \frac{I(z)}{2\pi r} \qquad\qquad (8)$$

Where ρ is the charge density and r the distance of the measurement plane from the cylinder axis. It is seen from equation (1) that if the incident wave is normal to the cylinder axis, $\alpha=\pi/2$, the transverse electric field components E_x and E_y are zero for an infinite cylinder. These components are non zero for a finite length cylinder. A simple solution of the electric fields that exist for axial distances off of the cylinder ends, due to a finite value of charge at the cylinder ends, is possible. These additional fields are defined in equation (9). It is seen that the x and y components of the electric field decay with increasing distance from the cylinder ends and the z component rises to a peak some distance from the cylinder end before decaying with further distance.

$$Eoe_x = \frac{E_x \rho_{end}\cos\gamma}{2\pi\varepsilon\delta} \qquad Eoe_y = \frac{E_y \rho_{end}\cos\gamma}{2\pi\varepsilon\delta} \qquad Eoe_z = \frac{(E_x + E_y)\rho_{end}\sin\rho}{2\pi\varepsilon\delta} \qquad (9)$$

Eoe is the scattered field from the cylinder ends, γ and δ are the angle and distance from the cylinder end as defined in Fig. 1.
The sequence of steps to obtain the scattered fields is as followed:
- The transverse scattered field components for an infinite length cylinder, equation (1), are computed and normalised.
- These transverse fields are then made to follow the scaled current and charge distributions, equation (8), along the cylinder axis, resulting in the three dimensional scattered fields of the finite length cylinder within the axial bounds of the cylinder length.
- The electric fields off of the cylinder ends, equation (9), are then added based upon the normalised transverse fields components and the terminal values of charge.

Multiple connected cylinders, used to represent bends along the cylinder length, are analysed by varying the source amplitude and phase appropriately for each connected element. Multiple frequency illumination is analysed by superposition of currents, either several discrete frequencies can be modelled or a broadband pulse. Illumination other than plane wave can be modelled simply by substitution of the sources, at each segment end, with those due to a radiation lobe or other illumination at the same points. Far field radiation is obtained by integration of the cylinder current along its length.

APPLICATION AND RESULTS

Algorithm I

This algorithm can be employed to provide a very simple approximation to the current distribution which can then either be used to provide physical interpretation or as part of the decomposition process in place of algorithm II when high accuracy is of less importance than computational resources. Although it can be implemented simply with pen and paper,

a simple mathematical interpretation executed on Matlab is used here. Fig. 4 shows results obtained using algorithm I to obtain the current distribution for a finite length cylinder employing 8 segments, compared to those produced by the NEC program employing 30 segments for cylinder lengths from $\lambda/4$ to 2λ in steps of $\lambda/4$. This simple implementation of algorithm I for so few segments is seen to agree surprisingly well with the NEC solution. Note that this technique is only effective for wire lengths $\lambda/2$ or greater and hence no comparison with NEC is present in the first view.

Algorithm II

For ease of implementation, modification and graphical output, Matlab has so far been used to implement the algorithm. Figs. 5 and 6 show the E_x component of scattered field on a plane 0.1m above the cylinder axis using algorithm II and NEC respectively, for a cylinder of radius 0.002m and $5\lambda_0/4$ in length, where λ_0 is 300m. The surrounding medium is free space and the cylinder is subjected to oblique plane wave illumination where $\alpha=30^0$ and amplitude 1V/m. Figs. 7 and 8 show the E_x component of scattered field for the same scenario as Figs. 5 and 6 but with the surrounded medium now having the properties $\mu=\mu_0$, $\epsilon_r=3$ and $\sigma=0.0001$S/m. Figs. 9 and 10 show the scattered H_x component of scattered field on a plane 10m above the cylinder axis produced by algorithm II and NEC respectively for a cylinder bent at a right angle in its middle, where the middle is located at the origin and each of the two arms make an angle of 45^0 with the z axis; the surrounding medium is free space and the plane wave is normally incident to the z axis. Figs. 11 and 12 show the same cylinder as the last pair of figures but for a lossy surrounding medium as in Figs. 7 and 8. In Figs 5-12 the distances from the cylinder axis and centre are scaled in wavelengths. In all cases the comparison between the scattered fields produced by algorithm II and NEC is extremely good.

CONCLUSIONS

Adaptable algorithms have been demonstrated that accurately predict the scattering from thin connected conducting cylinders in a lossy medium with the advantage that they employ excitation at the cylinder ends compared to NEC's centre segment excitation resulting in a more accurate boundary value solution of zero current at the cylinder ends. These algorithms are suitable for use as either stand alone tools or hybrid components that will enhance the efficiency of existing numerical methods. The current distribution can be found in one of two ways, depending on the accuracy required, with algorithm I producing an excellent insight into the physical properties of the scattering mechanisms associated with a finite length cylinder and algorithm II producing an exact formulation of the scattered fields.

REFERENCES

1. Felsen L B and Marcuvitz N, 1973. "Radiation and scattering of waves", Prentice-Hall.

2. Burke G J, 1981. "Numerical Electromagnetics Code", Lawrence Livermore Laboratory.

3. Chiang K S. 1994. "Review of numerical and approximate methods for the modal analysis of general optical dielectric waveguides", Optical and Quantum Electronics, 26, (3), 113-134.

4. Balanis C A. 1989. "Advanced engineering electromagnetics", John Wiley & Sons.

5. King R W P and Smith G S. 1981, "Antennas in matter", MIT Press.

6. Shen L and King R W P. 1968. "A simple formula of current in dipole antennas", IEEE Trans. Antennas and Propagation, AP-16, (5), 542-547.
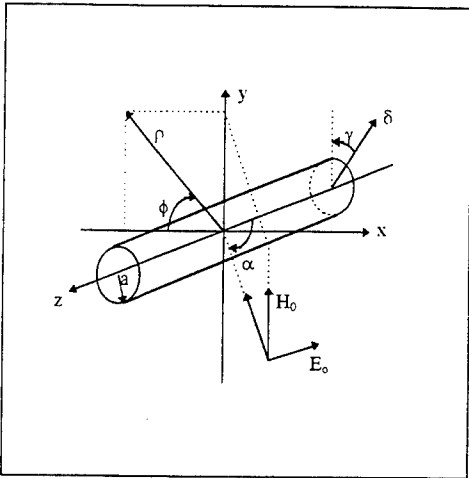
Figure 1: Coordinate system for cylinder scattering into media with electrical properties μ, ε and σ.

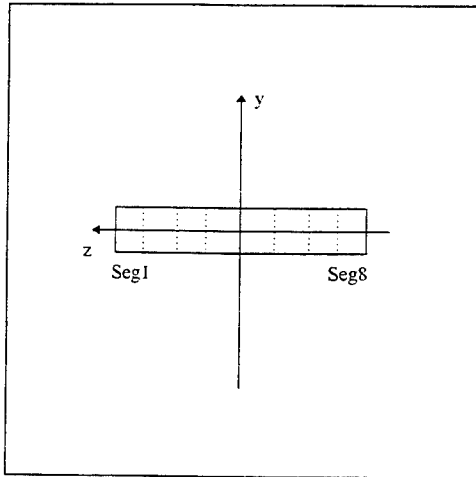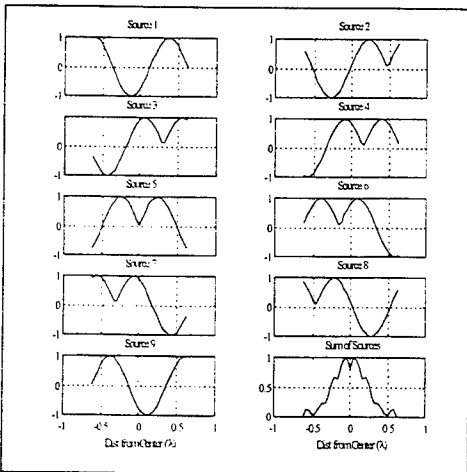Figure 2: Cylinder segmentation.

Figure 3: Graphical implementation of the normalised current distributions of algorithm I, for 8 segment cylinder $5\lambda/4$ in length.
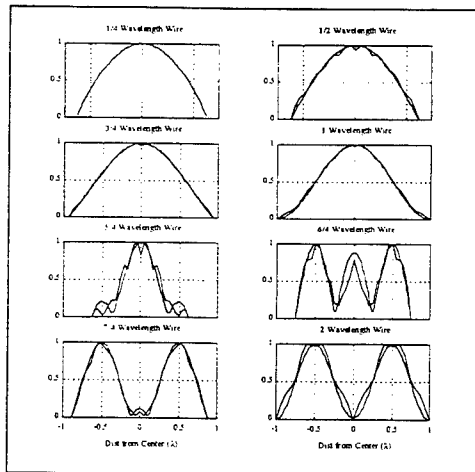

Figure 4: Normalised Current distributions using 8 segment implementation of algorithm I compared to 30 segment implementation using NEC (smooth curves).
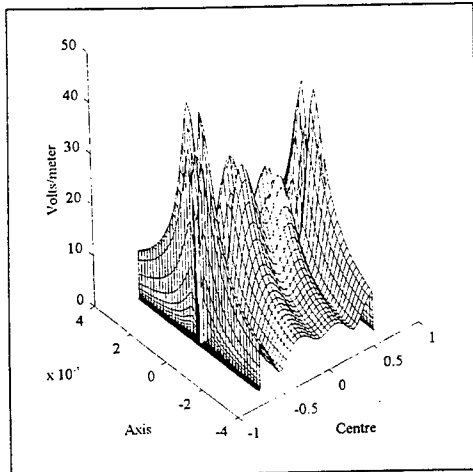
Figure 5: E_x, algorithm II. Cylinder radius=0.002m, $5\lambda_0/4$ in length. λ_0=300m. free space. oblique plane wave illumination of 1V/m amplitude. α=30^0. 5m off of either end shown. Measurement plane 0.1m above cylinder axis.
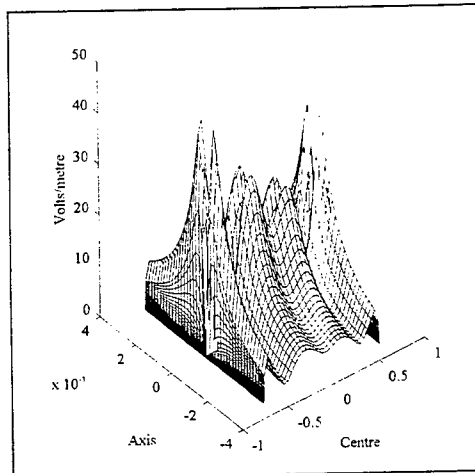

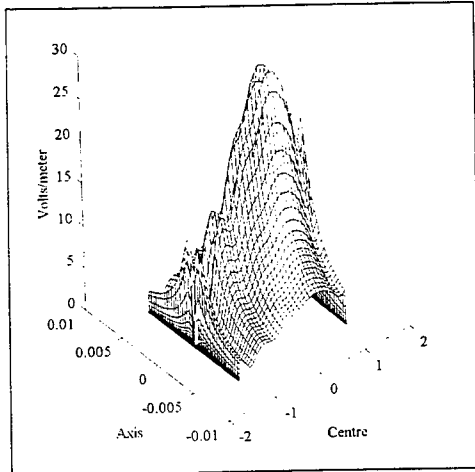Figure 6: E_x component of scattered field as Fig. 5 but using NEC.

Figure 7: E_x component of scattered field using algorithm II, as Fig. 5 but with surrounding medium properties $\mu=\mu_0$, ε_r=3 and σ=0.0001S/m.
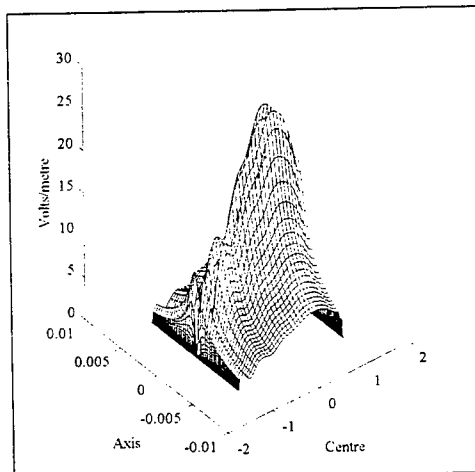

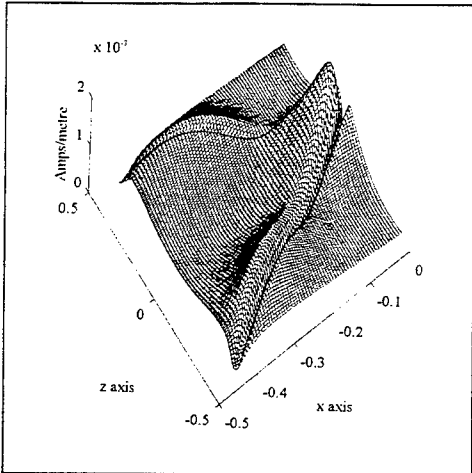Figure 8: E_x component of scattered field as Fig. 7 but using NEC.

487

Figure 9: H_y. algorithm II. Cylinder is as Fig. 5 but bent at a right angle in its middle at the origin. each arm 45^0 to the z axis. Normal plane wave illumination of 1V/m amplitude. Measurement plane 10m above cylinder axis.
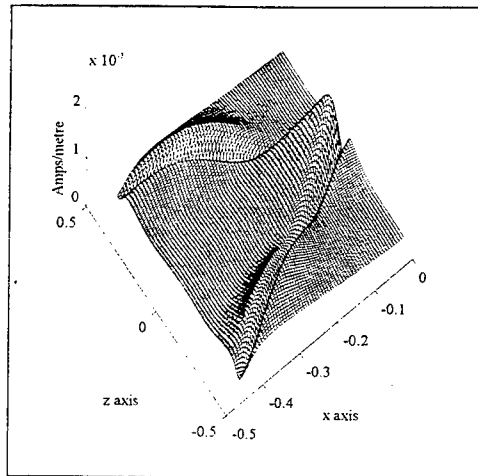

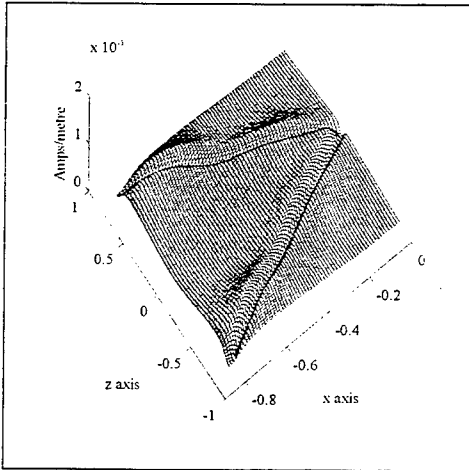Figure 10: H_y component of scattered field as Fig. 9 but using NEC.

Figure 11: H_y component of scattered field using algorithm II. as Fig. 9 but in a surrounding medium with properties $\mu=\mu_0$. $\varepsilon_r=3$ and $\sigma=0.0001$S/m.
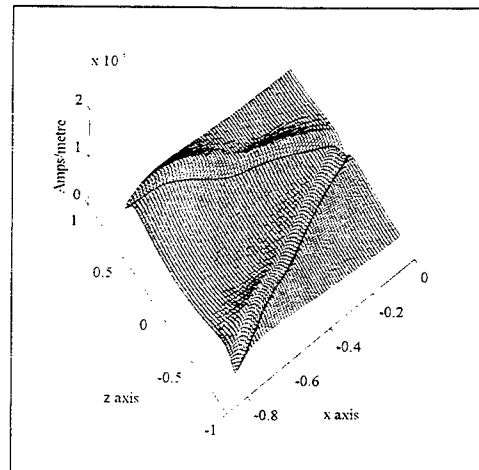

Figure 12: H_y component of scattered field as Fig. 12 but using NEC.

488

NUMERICALLY EXACT ALGORITHM
FOR THE H AND E-WAVE SCATTERING FROM
A RESISTIVE FLAT-STRIP PERIODIC GRATING

T. L. Zinenko, A. I. Nosich*, Y. Okuno, A. Matsushima

Kumamoto University, Kumamoto 860, Japan
*Institute of Radiophysics and Electronics,
National Academy of Sciences, Kharkov 310085, Ukraine

1. Introduction

A flat-strip zero-thickness periodic grating is one of the canonical scattering geometries. In a great number of papers such a scatterer has been analyzed under the assumption of the perfect electric conductivity (PEC) [1-4]. The most accurate results are obtained by methods based on the analytical inversion (i.e., regularization) of the static part of the full-wave equations. Among important applications of this analysis is a modeling of printed-circuit structures. A solution to a flat-strip grating may also be considered as a reference for validating more general-purpose numerical codes. However, assuming a perfect conductivity prevents studying lossy or absorbing materials. The scattering of waves from imperfect scatterers is of considerable interest for many practical applications of microwaves. One of the important cases is the thin partially transparent dielectric or metal strip grating. It is known that the latter can be simulated by *resistive* boundary conditions [5-7]. Thus the scattering of E and H-polarized plane wave from a resistive-strip grating is the key problem in this area, addressed by several papers published recently [8-10]. However, a closer view reveals that in the case of H-polarization, results are obtained by computing a matrix which is not convergent to the exact solution when increasing the number of equations. In the E-polarization case, they deal with algorithms that lose accuracy for narrow strips and slots. Thus, our goal is to develop an algorithm based on reducing the problem to a Fredholm 2-nd kind (regularized) matrix, solvable equally efficiently for arbitrary strip widths.

2. Formulation

We consider the scattering of a normally incident H- or E-polarized plane wave $U^{in}(y,z) = e^{-ikz}$, where U stands for the H_x or E_x component depending on the polarization, from a grating made of resistive strips, of the width w each. The period of the grating is l (see Fig. 1), hence the slot width is $d = l - w$.

The total field $U = U^{in} + U^{sc}$ has to solve the 2-D Helmholtz equation

$$(\nabla^2 + k^2)U(\vec{r}) = 0, \qquad k = \omega(\epsilon_0\mu_0)^{1/2}, \tag{1}$$

with a number of conditions known to guarantee uniqueness of the solution.

Resistive-type boundary conditions [6] couple the tangential field components

$$1/2[\vec{E}_T^+(\vec{r}) + \vec{E}_T^-(\vec{r})] = R\vec{n} \times [\vec{H}_T^+(\vec{r}) - \vec{H}_T^-(\vec{r})], \qquad \vec{E}_T^+(\vec{r}) = \vec{E}_T^-(\vec{r}) \tag{2}$$
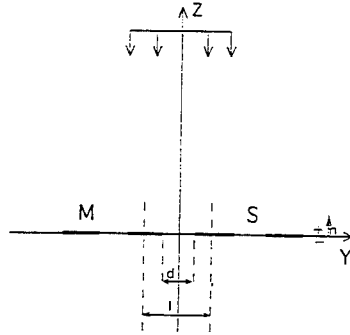
Figure 1: Geometry of the problem.

for all $(y, z) \in M$: $\{z = 0, |y - l/2 - ml| < w/2, m = 0, \pm 1, ...\}$. Here, $\vec{n} = \vec{z}_0$, R is the resistivity simulating a thin dielectric layer of high permittivity, or a thinner-than-skin-depth layer of imperfect metal. The respective formulas are $R_{diel} = iZ_0[kh(\epsilon/\epsilon_0 - 1)]^{-1}$ and $R_{metal} = (h\sigma)^{-1}$, where h is the layer thickness, Z_0 is the free-space impedance, and σ is the conductivity. Strictly speaking, (2) does not hold near the sharp edges, where a special condition is to be held locally: the limited energy contained in any finite domain D enclosing the edge:

$$\int_D (\epsilon_0 |\vec{E}|^2 + \mu_0 |\vec{H}|^2) dy dz < \infty, \qquad D \subset (y, z) \tag{3}$$

The radiation condition specifies the field behavior at infinity, and thus is closely tied to the arrangement of the host medium at infinity. In our case of a periodic grating placed in a lossless free space, it can be shown that, when the incident field U^{in} is a normally coming plane wave, the adequate radiation condition is given by

$$U^{sc\pm}(y, z) = \sum_{n=-\infty}^{\infty} \{a_n, b_n\} e^{\pm i g_n z} e^{i \frac{2\pi n}{l} y}, \qquad z \to \pm \infty \tag{4}$$

k is the wavenumber, a_n and b_n are the numbers depending on the frequency and other parameters of the grating, and $g_n = [k^2 - (2\pi n/l)^2]^{1/2}$, with the sign of the square root chosen such as either $\mathrm{Re}\, g_n > 0$, or $\mathrm{Im}\, g_n > 0$.

3. H-polarization

In the case of H-polarization $\vec{E}_T = E_y \vec{y}_0$, with $E_y = -(Z_0/ik)\partial H_x/\partial z$, because the totality of M is a periodic set of the infinite number of strips along the y-axis, and the incident field $H^{in}(y, z)$ does not depend on y, the scattered field $H^{sc}(y, z)$ is also a periodic function of y with the same period l. Hence, it can be expanded in terms of the Fourier-Floquet-Rayleigh series like (4). The numbers a_n and b_n are coupled by the equation $E_y^+ = E_y^-$, which is valid at $z = 0$ and all y. This enables one to find that all $b_n = -a_n$, and later eliminate one set, say of b_n, from further consideration.

490

To determine the coefficients a_n, let us use the dual set of the boundary conditions which hold on the complementary sub-intervals of the y-axis, namely

$$1/2(E_y^+ + E_y^-) = R(H_x^+ - H_x^-), \qquad (y,z) \in M \tag{5}$$

$$H_x^+(y,z) = H_x^-(y,z), \qquad (y,z) \in S \tag{6}$$

By introducing the notations $\phi = 2\pi y/l$, $\theta = \pi d/l$, and $\kappa = kl/2\pi$, $r_n = |n| + i(\kappa^2 - n^2)^{1/2}$ and substituting the series expansions (4), we arrive at the dual series equations (DSE)

$$\begin{cases} \sum_{n=-\infty}^{\infty} a_n |n| e^{in\phi} = -i\kappa + \sum_{n=-\infty}^{\infty} a_n(r_n + 2ikR/Z_0)e^{in\phi}, & \theta < |\phi| \le \pi \\ \sum_{n=-\infty}^{\infty} a_n e^{in\phi} = 0, & |\phi| < \theta \end{cases} \tag{7}$$

The latter equations are of canonical form, the left hand side of which forms the Riemann-Hilbert Problem (RHP) [11,12,2]. An exact analytical solution to RHP, as it is given in [12], yields an infinite-matrix equation eqivalent to the DSE (7):

$$a_m = \sum_{n=-\infty}^{\infty} A_{mn} a_n + B_m, \qquad m = 0, \pm 1, \pm 2, \ldots \tag{8}$$

where

$$A_{mn} = (r_n + 2ikR/Z_0)T_{mn}(\theta), \qquad B_m = -i\kappa T_{m0}(\theta) \tag{9}$$

where the functions $T_{mn}(\theta)$ are given in [12]. Based on the large-index asymptotics of the Legendre polynomials, it can be shown that $T_{mn} = O([|mn|^{1/2}|m - n + 1|]^{-1})$ uniformly for all θ. This is enough to prove that the operator norm $||A|| = \sum_{n,m=-\infty}^{\infty} |A_{mn}|^2 < \infty$, and, hence, the matrix equation (8) is a *regularized* equation, i.e., of the Fredholm 2-nd kind. It can be shown also (see [12]) that the solution of (8) satisfies the condition (3), because the edge behavior is explicitly taken into account when inverting the RHP [11,12,2].

The obtained equation set can be solved numerically to find the coefficients a_n whatever are the parameters κ and d/l. The number of equations (i.e., the truncation number), needed for arbitrary d/l and a 3-digit accuracy, is found from numerical experiments such as $N_{tr} = \kappa(1 + |R/Z_0|^{1/2}) + 5$. However, the potential accuracy is limited only by the digital precision of the computer used. Comparing this matrix with those from [8,9,10], one may see that the latter have elements which do not decay with larger m, n, and hence cannot result in a convergent solution. In Fig. 2, we present the dependence of the solution relative error versus N_{tr}. The plots in Fig. 3 demonstrate the behavior of the transmitted, reflected and absorbed power fractions as a function of the normalized period of grating.

The coefficients a_n and b_n are coupled by the energy conservation law

$$1 - k^{-1} \sum_{|n|<\kappa} g_n(|a_n|^2 + |b_n + \delta_{0n}|^2) = P_{abs} \tag{10}$$

where δ_{mn} is the Kronecker symbol, P_{abs} is the power absorbed by the grating (zero in the lossless case of $ReR = 0$). This relation served as a partial validation test and always displayed the digital

precision level.

4. E-polarization

Considering the case of E-polarized plane wave scattering, we obtain DSE as follows

$$\sum_{n=-\infty}^{\infty} a_n g_n e^{in\phi} = \begin{cases} -\frac{k}{2(R/Z_0)}\left(1 + \sum_{n=-\infty}^{\infty} a_n e^{in\phi}\right), & \theta < |\phi| \le \pi \\ 0, & |\phi| < \theta \end{cases} \tag{11}$$

This equation can be patially inverted analytically by using the inverse Fourier transform and the orthogonality of the exponents. The result is an infinite-matrix equation

$$a_m = -\frac{k}{2(R/Z_0)g_m} \sum_{n=-\infty}^{\infty} a_n S_{mn}(\theta) - \frac{k}{2(R/Z_0)g_m} S_{0m}(\theta), \quad m = 0, \pm 1, \dots \tag{12}$$

where

$$S_{mn}(\theta) = -\frac{\sin[(n-m)\theta]}{\pi(n-m)}, \quad m \ne n; \quad S_{nn}(\theta) = 1 - \frac{\theta}{\pi} \tag{13}$$

This matrix again is a regularized one and is somewhat similar to those in [8,9]. However, as we have used a set of entire-period exponents as expansion functions, the efficiency does not depend on d/l value. The number of equations needed for a 3-digit accuracy is estimated similarly to the H-case, with R/Z_0 replaced by its inverse value. Fig. 4 shows the dependence of the solution error on the matrix order N_{tr}. Fig. 5 demonstrates the values of the transmitted, reflected and absorbed power fractions as a function of the normalized period of the grating.
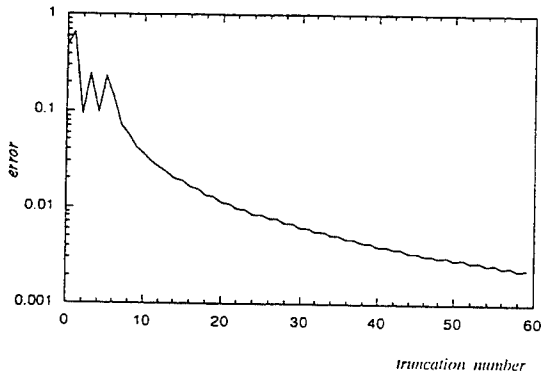

Fig.2. $l/\lambda = 5.5$. $R/Z_0 = 0.1i$. $d/l = 0.5$. $H - pol$.
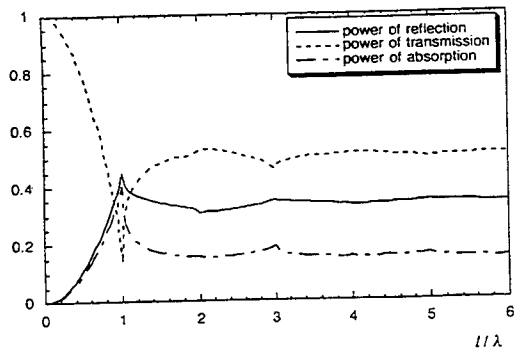
492

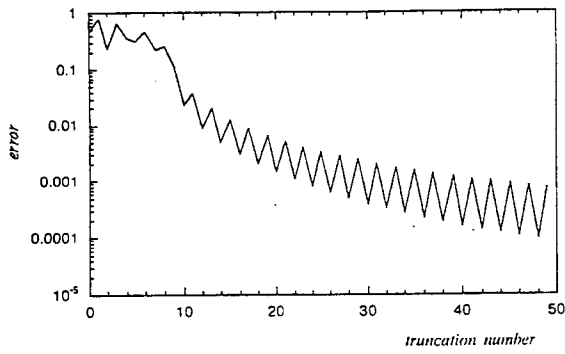Fig.3. *Power versus l / λ plotted for $R / Z_n = 0.1$, $d / l = 0.5$. $H - pol$.*

Fig.4. $l / \lambda = 1.5$, $R / Z_n = 0.1i$, $d / l = 0.5$. $E - pol$.
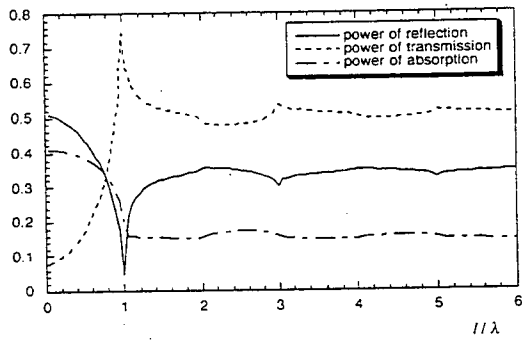

Fig.5. *Power versus l / λ plotted for $R / Z_n = 0.1$, $d / l = 0.5$. $E - pol$.*

References

1. H. Lamb, On the reflection and transmission of electric waves by metallic grating, *Proc. London Math. Society (1)*, v. 29, no 1, pp. 523-545, 1898.

2. Z. S. Agranovich, V. A. Marchenko, V. P. Shestopalov, Diffraction of a plane electromagnetic wave from plane metalic lattices, *Soviet Physics - Technical Physics, Engl. Transl.*, v. 7, pp. 277-286, 1962.

3. T. Uchida, T. Noda, T. Matsunaga, Spectral domain analysis of electromagnetic wave scattering by an infinite plane metallic grating, *IEEE Trans. Antennas and Propagation*, v. AP-35, no 1, pp. 46-52, 1987.

4. A. Matsushima, T. Itakura, Singular inttegral equation approach to plane wave diffrraction by an infinite strip grating at oblique incidence, *J. Electromagnetic Waves and Applications*, v. 4, no 6, pp. 505-5519, 1990

5. G. Bouchittè, R. Petit, On the concept of a perfectly conducting material and a perfectly conducting and infinitely thin screen, *Radio Science*, v. 24, no 1, pp. 13-26, 1989.

6. E. Bleszynski, M. Bleszynski, T. Jaroszewicz, Surface-integral equations for electromagnetic scattering from impenetrable and penetrable sheets, *IEEE Antennas and Propagation Magazine*, v. 36, no 6, pp. 14-25, 1993.

7. T. B. A. Senior, J. Volakis, *Approximate Boundary Conditions in Electromagnetics*, London: IEEE Press, 1995.

8. R. C. Hall, R. Mittra, Analysis of multilayered periodic structures using generalized scattering matrix theory, *IEEE Trans. Antennas and Propagation*, v. AP-36, no 4, pp. 511-517, 1988.

9. R. Petit, G. Tayeb, Theoretical and numerical study of gratings consisting of periodic arrays of thin and lossy strips, *J. Optical Society America (A)*, v. 7, no 9, pp. 1686-1692, 1990.

10. J. L. Volakis, Y. C. Lin, H. Anastassiu, TE characterization of resistive strip gratings on a dielectric slab using a single edge-mode expansion, *IEEE Trans. antennas and Propagation*, v. AP-42, no 2, pp. 205-213, 1994.

11 R. W. Ziolkowski, n-series problems and the coupling of the electromagnetic waves to apertures: Riemann-Hilbert approach, *SIAM J. Applied Math.*, v. 16, pp. 358-378, 1985.

12. A. I. Nosich, Green's function – dual series approach in wave scattering from combined resonant scatterers, in M. Hashimoto, M. Idemen, and O. A. Tretyakov (Eds.), *Analytical and Numerical Methods in Electromagnetic Wave Theory*, Tokyo: Science House, pp. 419-469, 1993.

494

NUMERICAL CONVERGENCE AND RICHARDSON EXTRAPOLATION

Richard C. Booton, Jr.
2983 Foothills Ranch Rd.
Boulder, CO 80302

INTRODUCTION

This paper addresses two principal questions:
1. How can be the accuracy of a numerical computation be determined?
2. How can extrapolation be used to speed the computation?

CONVERGENCE AND ACCURACY

Many, if not all, numerical methods for electromagnetics contain a parameter that governs the fineness of the mathematical model. For example, with finite-difference and finite-element methods, some measure of cell size serves as this parameter. For moment-method solutions, model fineness is determined by the number of basis functions. If the problem is well-posed, improving model fineness improves the accuracy of the solution. A sensible approach to examining accuracy is to form a sequence of solutions, improving fineness by a factor of two for each solution and observing the improving accuracy.

A sequence of such calculations is being performed with results C_1, C_2, C_3,···, C_N. After N steps, has the sequence converged "enough" or should the calculations continue? Such sequences never converge exactly but approach a limit to some degree of accuracy! Two approaches can be followed:
1. Round the C_n to some desired accuracy and continue until two successive results agree:
   rounded (C_N) = *rounded* (C_{N-1}).
2. Calculate the changes $\Delta_N = C_N - C_{N-1}$ and continue until $|\Delta_N| \leq$ *tolerance*, where, as will be seen, the tolerance is approximately equal to the desired accuracy. For example, a tolerance of 0.05 usually corresponds to an accuracy of 0.05, which in term means that the first digit after the decimal point is correct.

These topics are illustrated first by consideration of a simple problem for which an analytical solution is available, namely the computation of the capacitance per unit length of a coaxial-type cable with square inner and outer conductors, with sides of A and 2 A, respectively, as shown in Fig.1. For comparison with numerical results, the capacitance per unit length is 90.61455 pF/m, to five digits after the decimal point..The finite-element method is used with isosceles right triangular elements, which corresponds roughly to the finite-difference method. The largest value of h is $h_1 = A/2$ and successive values of h are taken as h_1/N where $N = 1,2,4,··· = 2^{k-1}$. Thus far we have concentrated on the convergence with respect to decrease of h (or equivalently with respect to increase of N). Two convergence problems are involved here. Not only are we concerned with convergence as h is decreased, but also the capacitance for each h is the result of a sequence of iterations. For each value of cell size h_n, the potential values must be iterated until desired accuracy for that value of h_n is
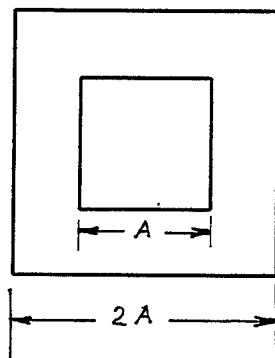
Figure 1. Square coaxial cable

achieved.. Then the cell size must be decreased until desired accuracy is achieved. The tolerance for the iteration process (the inner process) should be smaller than the limit for the h convergence (the outer process) in order that the iterations have adequately converged for each value of h. Experience shows that a tolerance for the iterations of two-fifths the tolerance for the convergence with respect to h gives satisfactory results. For an outer tolerance of 0.05 and an inner tolerance of 0.02, Table 1 shows as a function of N the sequence of resulting values of capacitance (where these and other values of capacitance are in the units of pF/m), together with the error which makes use of use of the result 90.6146 derived from an analytical solution. A fourth column shows the difference Δ of successive values. Comparison of the third and fourth columns shows that the error and Δ are approximately equal and the error is less than Δ. Note that at N=128 Δ is 0.0284, which satisfies the tolerance inequality. Greater accuracy can be achieved, but because the convergence with respect to decreasing h is very slow, achieving a tolerance of 0.005, which for this example means an accuracy of less than 0.005) requires a run time of approximately 1.35 days.

The relation between error and change Δ depends upon the manner in which the error varies with h. If the error is proportional to h, then the error is easily shown to be equal to Δ. If the error variation is stronger, then the error is less than Δ. Experience suggests that the latter is usually the case. Examination of the results in Table 1 show that the magnitude of error is approximately proportional to $h^{1.3}$, which is consistent with the numerical relation between the error and Δ, namely that the error is less than the change Δ.

Table 1. Values of capacitance for triangular elements with tolerances of 0.05

N=A/2h	cap	error	Δ_N	run time/s
1	106.2503	-15.6357	N/A	0
2	96.0188	-5.4042	-10.2315	0
4	92.6346	-2.0201	-3.3841	0
8	91.3924	-0.7779	-1.2422	0
16	90.9181	-0.3035	-0.4743	0
32	90.7339	-0.1193	-0.1842	1
64	90.6617	-0.0471	-0.0722	13
128	90.6332	-0.0186	-0.0284	210

Total run time = 224 sec = 3.73 min

RICHARDSON EXTRAPOLATION

Although satisfactory results can be obtained from such sequences of calculations, the computational time required for such a simple problem is excessive. Such considerations led Lewis Richardson to introduce the concept of extrapolation in papers published in 1910 and 1927.This concept is very broad and as used here the basic approach of Richardson extrapolation is to pass a polynomial through the calculated values and take as the extrapolated value the value of the polynomial for h equal to zero. The concept first is illustrated graphically as an extension of a plot of the first few values. An algebraic way of implementing this process is to pass a polynomial in powers of h through the points and use the constant term (the polynomial value when h is zero) as the extrapolated value. An efficient method that can be employed with a larger number of computed values is presented in such a way that it can be easily incorporated in a computer program. The numerical results of computations using the extrapolation yield the results obtained without the extrapolation much more quickly and also can give more accurate results. The analytical solution verifies the results obtained for this problem. Additional examples will be presented to demonstrate this approach for finite-element and moment-methods solutions of a microstrip problem, moment-method solutions for antenna input impedance and finite-difference-time-domain method to determine a cavity resonant frequency.

For example, with two values of h, namely, h_1 and $h_2 = h_1/2$ the coefficient a_0 of the polynomial $C(h) = a_0 + a_1 h$ is determined by solution of the equations

$$a_0 + a_1(2\ h_2) = C(2h_2)$$
$$a_0 + a_2\ h_2 = C(h_2)$$

Elimination of the first-degree term yields

$$a_0 = 2\ C(h_2) - C(2h_2)$$

,With three values of h, the polynomial

$$C(h) = a_0 + a_1 h + a_2 h^2$$

can be used to derive

$$a_0 = \frac{8}{3}\ C(h_3) - \frac{6}{3}\ C(2h_3) + \frac{1}{3}C(4h_3)$$

The coefficients in these and similar expressions multiply any errors in the calculated values, which may cause an error in the result. The calculated values in the inner process should be determined to a slightly higher accuracy to avoid this problem. For example, when the tolerance in the convergence with respect to h is set at 0.05, a reasonable tolerance for determination of each value of capacitance is 0.01.

If N values of h have been used, a polynomial of degree $N - 1$ can be determined to agree with the values of $C(h_k)$ for k=1, 2, 3,$\cdots$ N. In terms of the N calculated values, the appropriate polynomial satisfies the N equations

$$C(h_k) = \sum_{n=0}^{N-1} a_n h_k^n$$

and an efficient way to solve for a_0 is to successively eliminate the terms $a_k h^k$ for $k>0$. To eliminate the first degree term, form the N-1 first-order extrapolations

$$E_1(h_k) = 2\ C(h_k) - C(h_{k-1})$$

Then the N-2 second order extrapolations can be formed as

$$E_2(h_k) = \frac{4\,E_1(h_k) - E_1(h_{k-1})}{3}$$

Continuing in this way, the general expression is

$$E_n(h_k) = \frac{2^n\,E_{n-1}(h_k) - E_{n-1}(h_{k-1})}{2^n - 1}$$

After N such steps, we reach the extrapolation

$$E_{N-1}(h_N) = a_0$$

because all the higher-degree terms have been eliminated and the multiplier of a_0 remains as unity after each step. These equations easily can be inserted into a computer program.

Table 2 illustrates the results obtained with the use of Richardson extrapolation for a tolerance of 0.005 and Table 3 compares the total run times with and without extrapolation for tolerances of 0.05 and 0.005. The improvements given by extrapolation are clear.

Table 2. Extrapolated values of capacitance for triangular elements with tolerances of 0.005.

N=A/2h	capacity	extrapolation	run time/s
1	106.2503	106.2503	0
2	96.0188	85.7872	0
4	92.6346	90.4049	0
8	91.3924	90.4566	0
16	90.9181	90.5612	0
32	90.7338	90.5945	2
64	90.6616	90.6068	27
128	90.6332	90.6115	420

total run time = 448 sec = 7.47 min

Table 3. Summary of finite-element results for triangular elements

Tolerance	Rounded result	Run time without extrapolation	Run time with extrapolation
0.05	90.6	3.73 min	1 sec
0.005	90.61	1.35 days	7.47 min

Consider now the quasi-TEM solution for the shielded microstrip shown in Fig. 1. If the moment method is used, calculated values of capacitance should converge as the number of basis functions N is increased. To used the extrapolation process derived earlier, the polynomials are written in terms of the variable 1/N. This variable goes to zero as the number N becomes infinite. As in the finite-element case, there is a second convergence process, which in this case is the convergence of the Fourier series which defines the Green's function:

$$G(x,x') = \sum_{n=1}^{\infty} g_{2n-1} \cos\left(\frac{(2n-1)\pi x}{a}\right) \cos\left(\frac{(2n-1)\pi x'}{a}\right)$$

Numerical results are shown in Table 4. The shielded microstrip can also be analyzed with the finite-element method, and results from the two methods are compared in Table 5.
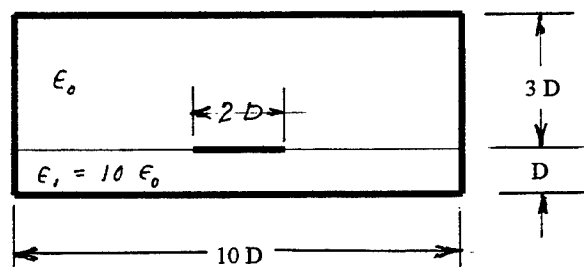

Figure 2. Shielded microstrip example.

Table 4. Moment-method solution of shielded microstrip
with pulse functions and point matching (tolerance = 0.005)

N	capacity	extrapolation	run time/s
1	255.84	255.84	0
2	262.84	269.85	1
4	266.59	270.51	7
8	268.54	270.52	27
16	269.52	270.52	218

total run time = 253 s

Table 5. Summary of results for microstrip

Tolerance	Rounded result	Run time for triangular elements	Run time for moment method
0.05	270.5	11 sec	16 sec
0.005	270.52	11 sec	4.22 min
0.0005	270.521	1.52 hr	9.37 min
0.00005	270.5212	1.02 day	34.52 min

CONCLUSIONS

We have demonstrated two principal points: (1) Accuracy can best be determined by performing not one solution but rather a sequence of computations with increasing fineness of the mathematical model, and (2) Richardson extrapolation greatly decreases the time required to achieve a fixed level of accuracy.

POWERFUL RECURSIVE ALGORITHM FOR THE EXHAUSTIVE RESOLUTION OF A NONLINEAR EIGENVALUE PROBLEM

Ph.Riondet*, D.Bajon*, H.Baudrand**

*SUPAERO, Laboratoire Electronique, 10 avenue Ed.Belin, 31055 Toulouse Cedex, France
**ENSEEIHT, Groupe de Modelisation Microonde, 2 rue Ch.Camichel, 31071 Toulouse Cedex, France

Abstract - **This work deals with the introduction of a monotonous function allowing the resolution of a nonlinear eigenvalue problem with a great saving of computation time and with an improved reliability. Thanks to the intrinsic properties of this function, it is possible to automatize the computation of the solutions using a general recursive algorithm. This technique has been successfully implemented to determine the resonance frequencies of a large number of microwave and millimeter-wave structures.**

I. INTRODUCTION

In the case of a source-free problem, the application of many existing techniques leads to a homogeneous system of linear equations depending on a parameter ω (the resonance frequency) whose nonzero solution can be obtained thanks to the resolution of a nonlinear eigenvalue problem, i.e. for certain particular values of ω enforcing the determinant of the matrix system to vanish.

It is common practice to detect the zeros of the determinant function [1],[2]. Unfortunately, the determinant is a nonlinear function of the frequency containing many extrema that can not be analytically explicited. Therefore, due to the lack of suitable zero searching procedure, any search algorithm, to our knowledge, is not automatized and hence, has to operate at small step widths, which considerably slows down the resolution of the matrix system. Few years ago, an alternative approach had been reported in [3] to eliminate numerical problems related to poles. This technique consists in computing a singular value decomposition (SVD) of the matrix and to detect the minima of its lowest singular value σ_m. Accordingly, the presence of poles can be eliminated, providing this method with a good reliability and numerical stability. Nevertheless, computing a singular value decomposition is not economical in computation time.

In this work, a particular combination of the matrix entries is used rather than the determinant to solve the problem. This built function has the intrinsic properties to be monotonous with ω and to have the same zeros as the determinant function. The monotonicity ensures that poles and zeros must alternate in position along the ω axis so that once calculated the poles, zeros are easily computable, providing this technique with a good reliability. In addition, it is possible to automatize the pre-location of the searching intervals using a recursive procedure so that the resolution can be totally automatized without any consideration about the initial location of the solutions. Since one single evaluation of the function needs $2(n-1)^3/3$ flops, which is less than for the determinant, computation time can be then highly speeded up. This technique makes the characterization of any resonance problems numerically systematic and automatic.

502

II. FORMULATION

The analysis of a planar circuit in inhomogeneous medium reduces to the writing on the printed plane S (Fig.1) of the continuity conditions of the tangential components of the electric and magnetic fields

$$\begin{cases} \mathbf{E}_{1T} = \mathbf{E}_{2T} = \mathbf{E} \\ \mathbf{H}_{1T} - \mathbf{H}_{2T} = \mathbf{J} \wedge \mathbf{n} \end{cases} \tag{1}$$
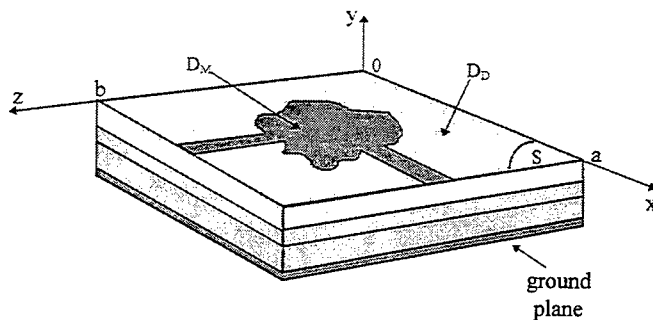

Fig.1: Planar circuit

For commodity reasons, we introduce $\mathbf{J} = \mathbf{H} \wedge \mathbf{n}$ so that $\mathbf{J} = \hat{\mathbf{Y}}\mathbf{E}$ where $\hat{\mathbf{Y}}$ represents the admittance operator of a finite or infinite half-space C as illustrated on Fig.2. Owing to that, the tangential components of the fields are such that on each side of the S-plane

$$\begin{cases} \mathbf{J}_1 = \hat{\mathbf{Y}}_1 \mathbf{E}_1 \\ \mathbf{J}_2 = \hat{\mathbf{Y}}_2 \mathbf{E}_2 \end{cases} \tag{2}$$

Therefore, replacing (2) in (1) yields

$$\begin{cases} \mathbf{E}_1 = \mathbf{E}_2 = \mathbf{E} \\ \mathbf{J}_1 + \mathbf{J}_2 = \mathbf{J} \end{cases} \tag{3}$$

The resolution of the problem is obtained thanks to the writing of the boundary conditions on S :

$$\begin{cases} \mathbf{E} = \mathbf{0} & \text{on } D_M \\ \mathbf{J} = \mathbf{0} & \text{on } D_D \end{cases} \tag{4}$$

where D_M and D_D correspond respectively to the metallic and dielectric subdomains of S.
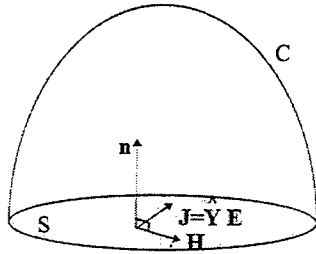
Fig. 2 : admittance operator of a finite or infinite half-space C

Equating the problem leads to the resolution on D_M of the following equation :

$$\left(\hat{Y}_1 + \hat{Y}_2\right)^{-1} J = \hat{Z}J = 0 \qquad (5)$$

On the S-plane, the unknown current J is expanded in terms of piecewise or extended testing functions $\left|g_k\right\rangle$, independent of the frequency anyhow, which must be chosen to approximate the true but unknown distribution of the current on D_M and to vanish on the dual domain D_D :

$$J = \sum_{k=1}^{p} x_k \left|g_k\right\rangle \qquad (6)$$

so that (5) can be written as an homogeneous linear equation with p unknowns coefficients $\left(x_1 \cdots x_p\right)$

$$\sum_{k=1}^{p} \hat{Z} \left|g_k\right\rangle x_k = 0 \qquad (7)$$

The application of Galerkin's method leads to the numerical resolution of (7) as a homogeneous system of p linear equations with p unknowns x_k. The matrix representation of (7) is given by

$$\left[\hat{Z}\right][X] = 0 \qquad (8)$$

where $[X]$ is a vector containing the p coefficients $\left(x_1 \cdots x_p\right)$ and $\left[\hat{Z}\right]$ is a p-by-p matrix, depending on a parameter ω (the resonance frequency), the ij entry of which is given by

$$\left[\hat{Z}(\omega)\right]_{i,j} = \left\langle g_i \hat{Z}(\omega) g_j \right\rangle \qquad (9)$$

504

The condition of existence of a nonzero vector $[\mathbf{X}]$ in (8) is obtained by computing the values of ω making the $[\hat{\mathbf{Z}}]$ matrix singular, i.e. enforcing its determinant to vanish

$$det\left[\hat{\mathbf{Z}}(\omega)\right] = 0 \tag{10}$$

Equation (10) is known as the *generalized resonance condition* [5] and constitutes in fact a nonlinear eigenvalue problem.

It is then common practise to look for the zeros of the determinant function. However, the lack of property of the determinant versus ω makes this task tedious. On one hand, the determinant contains poles and zeros in close neighborhood [3], and on the other hand, more than one zero can be found between any two consecutive poles, making any standard zero searching procedure inefficient. Owing to that, it would be more convenient to find a monotonous equivalent of (10).

III. RESOLUTION OF THE NONLINEAR EIGENVALUE PROBLEM

Firstly, it will be assumed that any quadratic form constructed with $\hat{\mathbf{Z}}(\omega)$ is a monotonous function of ω. Accordingly, it can be readily proved that any quadratic form constructed with $\hat{\mathbf{Z}}^{-1}(\omega)$ is also a monotonous function of ω. This property applies itself to the diagonal terms of $\left[\hat{\mathbf{Z}}^{-1}(\omega)\right]$ and in particular to the first, so that

$$\left[\hat{Z}^{-1}(\omega)\right]_{1,1} = \frac{det\left[\hat{Z}_{2,2}(\omega)\right]}{det\left[\hat{Z}(\omega)\right]} = \frac{1}{z_{1,1}(\omega) - \left[\hat{Z}_{1,2}(\omega)\right]\left[\hat{Z}_{2,2}(\omega)\right]^{-1}\left[\hat{Z}_{2,1}(\omega)\right]} \tag{11}$$

is a monotonous function of ω. The denominator of (11) is the result of the following partition of $\left[\hat{Z}\right]$

$$\left[\hat{Z}\right] = \begin{bmatrix} z_{1,1} & \vdots & \hat{Z}_{1,2} \\ \cdots & \cdots & \cdots & \cdots & \cdots \\ & \vdots & \\ \hat{Z}_{2,1} & \vdots & \hat{Z}_{2,2} \\ & \vdots & \end{bmatrix} \tag{12}$$

According to the assumption, it is clear that the denominator of (11)

$$f_p(\omega) = z_{1,1}(\omega) - \left[\hat{Z}_{1,2}(\omega)\right]\left[\hat{Z}_{2,2}(\omega)\right]^{-1}\left[\hat{Z}_{2,1}(\omega)\right] \tag{13}$$

is also a monotonous function of ω. Moreover $f_p(\omega) = \dfrac{det\left[\hat{Z}(\omega)\right]}{det\left[\hat{Z}_{2,2}(\omega)\right]} = 0$ (14)

is equivalent to (10). Once the monotonicity of $f_p(\omega)$ established, it follows that poles and zeros must alternate in position along the ω axis. The zeros location being ensured by the poles location, it is necessary to look for the poles of (13).

We can see in (13) that the poles contained in the $\left[\hat{Z}\right]$ entries vanish by construction in $f_p(\omega)$. Thus, according to (14), the poles of $f_p(\omega)$ are obtained by computing the values of ω such that

$$det\left[\hat{Z}_{2,2}(\omega)\right] = 0 \tag{15}$$

This is in fact a nonlinear eigenvalue problem of order (p-1) which can be solved equivalently, i.e. introducing a function $f_{p-1}(\omega)$ which is the result of the partition of $\left[\hat{Z}_{2,2}\right]$ as in (12). This process iterates until the last diagonal term of the initial matrix $z_{p,p}(\omega)$ that has also the property to be monotonous and whose poles are easily computable. It is then possible to automatize the resolution of (10) using a recursive procedure based on the calculation of the zeros of the determinants of principal submatrix of $\left[\hat{Z}\right]$ as illustrated in Fig.3.

Poles of $z_{p,p}(\omega)$

iteration 1

zeros of $z_{p,p}(\omega)$ = poles of $f_2(\omega)$

iteration 2

zeros of $f_2(\omega)$= poles of $f_3(\omega)$

zeros of $f_{p-1}(\omega)$= poles of $f_p(\omega)$
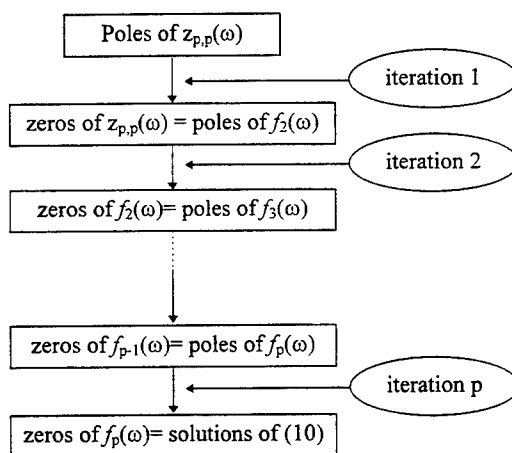
iteration p

zeros of $f_p(\omega)$= solutions of (10)

Fig. 3 : Recursive algorithm for the resolution of the nonlinear eigenvalue problem

IV. APPLICATION AND RESULTS

The spectral representation of the $\hat{Z}$ operator is given by

$$\hat{Z}(\omega) = \sum_{n}^{TE,TM} |\mathbf{f_n}\rangle\left(Y_{1n}(\omega) + Y_{2n}(\omega)\right)^{-1}\langle\mathbf{f_n}| \qquad (16)$$

The $|\mathbf{f_n}\rangle$ functions are the eigenfunctions of the Helmholtz operator for the two-dimensional boundary-value problem on S (x=0,x=a,z=0,z=b in Fig.1). These functions constitute the complete set of *transverse* $TE^{(y)}$ *and* $TM^{(y)}$ *mode functions* [1] and the modal components E_n and J_n of electric and magnetic fields are such that for the ith region $J_{in} = Y_{in}E_{in}$. Since functions $|\mathbf{f_n}\rangle$ and $|\mathbf{g_k}\rangle$ are independent of ω, the ω-dependence of the matrix entries (9) is carried out by $Y_{1n}(\omega)$ and $Y_{2n}(\omega)$. It can be readily proved that $Y_{1n}(\omega)$ and $Y_{2n}(\omega)$ have the property to be monotonous versus ω, which ensures the initial assumption about the quadratic form of $\hat{Z}$. Briefly established in the spectral domain, this property is maintained in the spatial domain.

The technique developped in section III had been successfully implemented to determine the resonance frequencies of a patch antenna (Fig. 4).
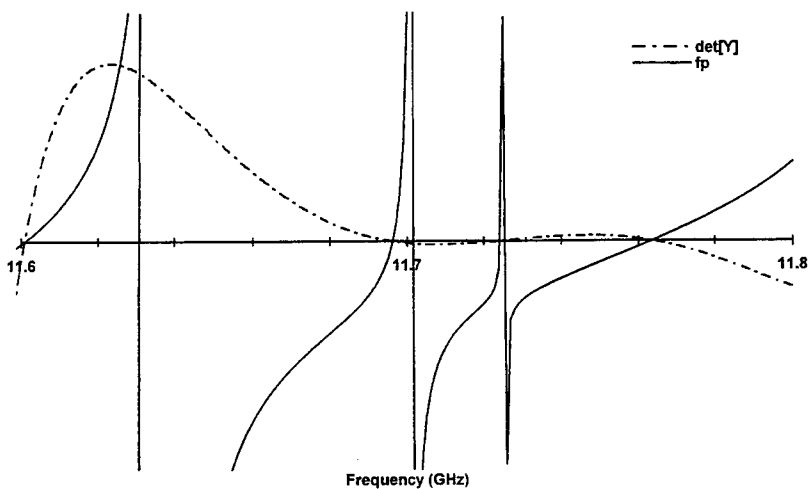

Fig. 4 : Resonance frequencies of a patch antenna as example of application.

507

In Fig. 4 are plotted both the determinant function and the $f_p(\omega)$ defined in (13). The scale of the frequency axis had been intentionally zoomed in order to see how difficult it would have been to look for the zeros of the determinant. It is clear that since poles and zeros alternate, and once calculated poles, missing solutions is avoided with this function.

The algorithm consist in fact in an automatic pre-location of the poles of $f_p(\omega)$. Since one single evaluation of $f_p(\omega)$ needs only $2(p-1)^3/3$ flops (compared to $2p^3/3$ for a determinant [6]), computation time can be highly speeded up.

V. CONCLUSION

A general recursive algorithm has been presented to solve a nonlinear eigenvalue problem. This technique is general and takes full advantage of what an operator may have properties versus a parameter. It allows the automatic resolution of a nonlinear eigenvalue problem with an extremely reduced CPU time and an improved reliability. With this method, the features of a large number of microwave and millimeter-wave structures can be systematically and automatically studied.

REFERENCES

[1]   T.Itoh, Ed., *Numerical Techniques for Microwave and Millimeter-Wave Passive Structures*. New York: John Wiley, 1989

[2]   R. Sorrentino, Ed., *Numerical Methods for Passive Microwave and Millimeter-Wave Structures*. New York: IEEE Press, 1989

[3]   V.A.Labay and J.Bornemann, *"Matrix Singular Value Decomposition for Pole-Free Solutions of Homogeneous Matrix Equation as Applied to Numerical Modeling Methods"*, IEEE Microwave and Guided Wave Lett., vol. 2, pp. 49-51, Feb 1992

[4]   C.J.Railton and T.Rozzi, *"Complex Modes in Boxed Microstrip"*, IEEE Trans. Microwave Theory Tech., vol. MTT-36, pp. 865-874, May 1988

[5]   S.T.Peng, A.A.Oliner, *"Guidance and Leakage Properties of a Class of Open Dielectric Waveguides : Part I - Mathematical Formulations"*, IEEE Trans. Microwave Theory Tech., vol. MTT-29, pp. 843-854, Sept 1981

[6]   G.H.Golub, C.F.Van loan, *Matrix computations*. John Hopkins University Press, 1989

A Dense Out-of-Core Solver for Workstation Environments

Dr. Cullen E. Lee
Sandia National Laboratories

Dr. Raymond M. Zazworsky
Sandia National Laboratories

<u>ABSTRACT</u>

In general, the application of solvers to systems of linear equations are limited by the available random access memory (RAM) on the host computer. For typical workstations, this may limit the size of the problem to a few thousand unknowns (complex, double precision). This paper discusses a dense out-of-core (DOC) solver which operates on a partitioned system matrix where the submatrices can be sized in a way consistent with available RAM. The application of this DOC solver, given a moderate amount of RAM, is limited only by the amount of available disk space and the desired solution time. Results from a series of run-time trials are given, comparing the run time of the DOC solver to that of a standard in-core solver. Finally, both sequential and parallel components within the DOC solver have been identified; providing a clear path to a distributed implementation of the algorithm.

<u>1. INTRODUCTION</u>

The purpose of this paper is to present a dense out-of-core (DOC) solver for large complex linear systems of equations that would normally exceed the in-core capacity of the host computer. Since the amount of available RAM on a workstation can be quite limited and disk space is considerably less expensive than RAM, out-of-core solvers are a cost effective means for extending the solution capability of the machine as long as the solution time can be maintained at a reasonable level. Of course, the capabilities of computing platforms vary dramatically for different installations and a "reasonable" time will depend on, among other things, the number of users and availability of the machine. As a result, this paper does not attempt to provide an "optimum" solver for our host computer, but examines the requirements (RAM and disk space) and performance (problem size and computation time) of an algorithm that represents a compromise between RAM usage and solution time. In addition, this compromise allowed for the examination of a rather wide range of requirement and performance parameters. The host computer used to generate these results is a Silicon Graphics workstation (64-bit, R8000 processor) with 384 MB of RAM, a 2GB system disk drive, and four 9 GB external data disk drives.

The following discussion presents the general problem and assumptions, describes the solution approach with a more detailed definition of the out-of-core algorithm, provides a discussion of the run-time performance results, and examines the relationship of RAM and data transfer requirements with problem size and partitioning. This is followed by a brief discussion of the potential run-time improvement realized through a distributed implementation of the DOC solver.

2. PROBLEM DESCRIPTION

The DOC solver determines the unknown matrix **X** in the equation

$$AX = \begin{bmatrix} A_{11} & \cdots & A_{1m} \\ \vdots & \ddots & \vdots \\ A_{m1} & \cdots & A_{mm} \end{bmatrix} \begin{bmatrix} X_1 \\ \vdots \\ X_m \end{bmatrix} = \begin{bmatrix} B_1 \\ \vdots \\ B_m \end{bmatrix} = B \tag{1}$$

where A is the nxn system matrix (impedence matrix), B is the nxk matrix of right-hand-sides (RHSs or excitation vectors), and m is the number of partitions. For electromagnetics problems, all of the matrices are, in general, complex and the system matrix is typically dense. Before the algorithm is applied, all of the matrices are partitioned into submatrices that are read from disk as needed and overwritten with intermediate results as they are calculated. The size of the partitions is chosen to be consistent with the available RAM and acceptable run times. Furthermore, this DOC solver can be used on less-than-dense system matrices. It is, however, advisable to use a pre-conditioner on such system matrices before applying this solver to ensure the diagonal submatrices are nonsingular. For problems considered in this paper, pre-conditioning was not required.

3. APPROACH

The approach is similar to the standard solution that uses LU decomposition except that it is divided into a collection of sequential steps to obtain

$$LUX = \begin{bmatrix} L_{11} & 0 & 0 \\ \vdots & \ddots & 0 \\ L_{m1} & \cdots & L_{mm} \end{bmatrix} \begin{bmatrix} U_{11} & \cdots & U_{1m} \\ 0 & \ddots & \vdots \\ 0 & 0 & U_{mm} \end{bmatrix} \begin{bmatrix} X_1 \\ \vdots \\ X_m \end{bmatrix} = \begin{bmatrix} B_1 \\ \vdots \\ B_m \end{bmatrix} = B \tag{2}$$

where L and U are partitioned in a manner consistent with the original system matrix. First, the system matrix is partitioned into submatrix blocks that are consistent with the available RAM. Although it is not quite the most efficient partition, the first (m-1) by (m-1) submatrices in the system matrix are assigned the same dimension, s, such that the dimension, q (q<=s), of A_{mm} is as close to s as possible while maintaining (m-1)s+q=n. After partitioning, the sequential steps begin with A_{11} and each step in the sequence factors the block diagonal submatrix, A_{ii}, into its L_{ii} and U_{ii} factors, solves for the submatrices below (L_{ji}, i<j<=m) and to the right (U_{ij}, i<j<=m) of the diagonal submatrix, calculates the intermediate solution of $L_{ii}Y_i = B_i$ for the corresponding block, updates the unused blocks in the RHS and system matrix before proceeding to the next submatrix on the diagonal. When this sequence of steps is complete, the matrices U and Y are stored on the disk, and all that remains is to backsolve $UX = Y$ for the unknown matrix, X. This sequential procedure is less complicated but involves a solve and update repetition similar to the above sequence. Beginning with U_{mm}, each block diagonal matrix, U_{ii}, and its corresponding RHS, Y_i, are used to solve for X_i which is then used to update the RHS (Y_j, 1<=j<i) above the current block row.

It is clear that this implementation reduces RAM usage at the expense of data transfer time and will increase the overall run time of the application. The following section defines the algorithm that was used in the run-time trials discussed in Sec. 5. It is also the basis for the RAM and data transfer requirements that are discussed in Sec. 6.

4. ALGORITHM DEFINITION

A. First m-1 LU Decomposition Steps.

For i=1 to m-1:

1. Perform a standard LU decomposition [1] on A_{ii} and calculate the ith intermediate solution.
   a. Retrieve A_{ii} and B_i from the disk.
   b. Obtain $L_{ii}U_{ii} = A_{ii}$ and p_i from the LU decomposition where p_i is the row permutation vector.
   c. Permute B_i using p_i, and solve $L_{ii}Y_i = B_i$ for Y_i.
   d. Replace B_i and A_{ii} on the disk with Y_i and $L_{ii}U_{ii}$, respectively.

2. Forward solve $L_{ii}U_{ij} = A_{ij}$ for U_{ij}. (j = i+1,...,m).
   For j = i+1 to m
       a. Retrieve A_{ij} from the disk and permute using p_i.
       b. Solve $L_{ii}U_{ij} = A_{ij}$ for U_{ij}.
       c. Replace A_{ij} on the disk with U_{ij}.
   End of j Loop

3. Solve $L_{ji}U_{ii} = A_{ji}$ for L_{ji} (j = i+1,...,m) and update the RHS and the system matrix.
   For j = i+1 to m
       a. Retrieve A_{ji} from the disk.
       b. Solve $L_{ji}U_{ii} = A_{ji}$ for L_{ji}.
       c. Retrieve B_j from the disk and subtract $L_{ji}Y_i$.
       d. Replace B_j on the disk with the difference.
       e. Update remainder of system matrix with outer product.
           For r = i+1 to m
               1. Retrieve U_{ir} and A_{jr} from disk.
               2. Subtract $L_{ji}U_{ir}$ from A_{jr}.
               3. Replace A_{jr} on disk with the difference.
           End of r Loop
   End of j Loop

End of i Loop

B. Last LU decomposition and completion of the intermediate solution.
       1. Retrieve A_{mm} from disk.
       2. Obtain $L_{mm}U_{mm} = A_{mm}$ and p_m from the LU decomposition.
       3. Permute B_m using p_m, and solve $L_{mm}Y_m = B_m$ for Y_m.
       4. Backsolve $U_{mm}X_m = Y_m$ to obtain X_m.
       5. Replace Y_m on disk with X_m.

6. Update Y.
    For i=m-1 to 1
       a. Retrieve Y_i and U_{im} then subtract $U_{im}X_m$ from Y_i.
       b. Replace Y_i on disk with difference.
       End of i Loop
C. Backsolve for solution matrix.
    For $i = m-1$ to 1
       1. Retrieve U_{ii} and Y_i from disk.
       2. Solve $U_{ii}X_i = Y_i$ for X_i .
       3. Replace Y_i on disk with X_i .
       4. If i is greater than 1, update Y.
         For $j = m-1$ to 1
           a. Retrieve Y_j and U_{ji} then subtract $U_{ji}X_i$ from Y_j.
           b. Replace Y_j on disk with difference.
         End of j Loop
    End of i Loop

5. RUN-TIME PERFORMANCE VIA PATCH

The PATCH code is an EFIE based MoM code that can be used to predict the RCS of faceted bodies, see, e.g., [2-3]. In this regard, PATCH is an ideal tool for generating dense complex linear systems. Over the past four years PATCH has been extensively modified (by CEL) to provide a more efficient environment in which electromagnetic predictions can be done. In particular, PATCH has been divided into functionally dissimilar routines. These routines are (1) geometry manipulation, (2) impedance matrix fill, (3) excitation matrix fill, (3) linear system solve, and (4) RCS computation. Each of these routines are now executed independently of one another, although output from one routine may be required as input to another.

Most recently, PATCH was modified to provide partitioned linear systems in a format compatible with the DOC solver and in its current form, PATCH computes both the impedance and the excitation matrix elements to double precision. However, to minimize disk storage, all matrices written to the external disk drives are stored as single precision. So the DOC solve portion of this RCS prediction process is done as single precision.

When PATCH is used in combination with the DOC solver, the impedance matrix fill routine can distribute the partitions of an impedance matrix onto at most four user specified external disk drives as does the excitation matrix fill routine. The excitation matrix fill routine stacks dual polarization excitation (column) vectors per incident direction into a matrix that forms the RHS of the linear system. The DOC solver reads the partitioned data from the external disk drives as needed and writes out the partitioned solution matrix. Finally, the RCS computation routine reads the partitioned solution matrix along with geometry data and computes the RCS data corresponding to the faceted body and given excitation matrix. Timing results for the DOC solver portion of this process are provided in Fig. 1 for the m=4 and m=20 DOC solvers, see Sec. 3. These results are compared with those of an in-core solver, based on the LU decomposition technique described in [1], and are also shown in Fig. 1.
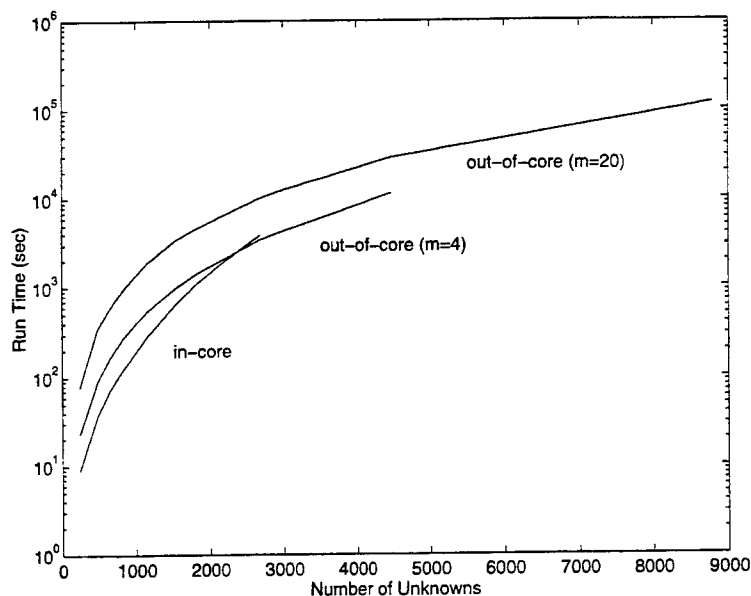
512

Figure 1. Run-Time Comparisons

The run-time comparison given in Fig. 1 clearly illustrates the trade-off between in-core and out-of-core solvers, i.e., between RAM usage and solution time. The m=20 DOC solver, where the system matrix is partitioned into 400 submatrices requires a great deal more disk I/O than does the m=4 DOC solver with its 16 submatrices; accounting for the longer run times shown in Fig. 1.

The in-core solver requires no disk I/O and as a result one would expect it to require even less run time than the m=4 DOC solver. This is true until one approaches the RAM limit of the host computer, in which case there is apparently some memory management overhead that begins to influence the run time. For near RAM limit applications, this causes the in-core solver to run slower than the m=4 DOC solver.

6. MEMORY AND DATA TRANSFER REQUIREMENTS

Assuming that the number of RHSs, k, is less than or equal to the dimension, s, of a system submatrix, the algorithm defined in Sec. 4 requires three complex $s \times s$ matrices and one integer permutation vector ($s \times 1$) in RAM. Assuming a single precision calculation (4 byte real), the amount of memory (RAM) required to execute the algorithm is illustrated in Fig. 2 for various values of system dimension and

513

partition. The memory requirement for the partitioned systems is capable of handling problems with as many as s RHSs. The memory requirement for the in-core solver was calculated using only one RHS.
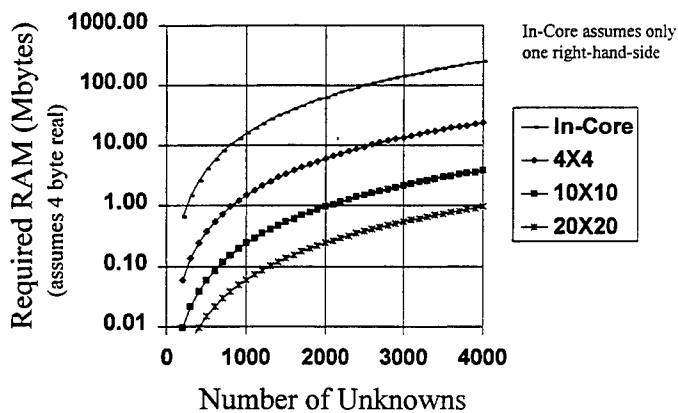
Figure 2. RAM Requirements

Besides RAM, another significant factor influencing the problem run time is the amount of data that must be transferred to and from the disk (or disks) during the solution process. Fig. 3 illustrates that there is about twice as much data read as written. This ratio between reads and writes will be the same for all problems where the number of RHSs is small relative to the submatrix dimension. Another variable that might be considered here is the number of times that an external disk drive is accessed. However, this number is dependent only on the number of partitions, m, and not the size of the problem, and compared to the data transfer times, it will typically be small.
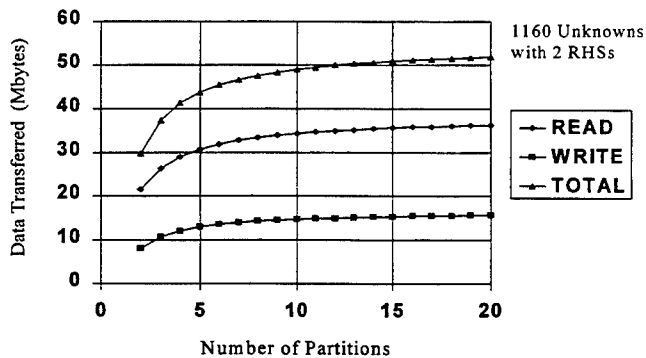
Figure 3. Amount of Data Transferred

7. ALGORITHM IMPLEMENTATION FOR NETWORK ENVIRONMENTS

The choice of a linear system solver depends greatly on the computing environment in which it will be used. The attributes of a networked (distributed) computing environment differs significantly from those of a machine designed specifically for parallel computations. A networked computing environment is characterized by processors which have different speeds, local memory, and local disk storage. In addition, the communication times within the network are considerably longer so that data transfer among network nodes is less than optimum. This problem is countered by the fact that a networked computing environment can provide a significant reduction in application run time if there is an appreciable amount of mutually independent [4] calculations in the solution algorithm such as those described in Sec. 4. In particular, steps A2, A3, B6, and C4 of the algorithm make up a large portion of the total run time, are clearly independent, and do not share the same data. These steps include the mutually independent calculations of the U_{ij}, L_{ji}, and Y_i; the outer product obtained from these matrices; the update of the system and excitation matrices; and updates to the RHS which are part of the backsolve steps. Exploitation of these mutually independent operations will depend on the unique properties of a given network and will require an approach which accommodates these properties when attempting to maintain proper load balancing while limiting interprocessor communications.

8. SUMMARY

The dense out-of-core solver described here was written with workstation users specifically in mind although it is not restricted to such computing environments. This implementation trades RAM usage for solution time and external disk space, and is well suited for solving large linear systems of equations. This particular implementation of the DOC solver has been used in combination with the PATCH code for computing the RCS of various test-bed objects at frequencies up to 10 GHz.

9. ACKNOWLEDGEMENT

10. REFERENCES

[1] W. H. Press, S. A. Teukolsky, W. T. Vetterling, and B. P. Flannery, 1992, *Numerical Recipes in Fortran*, 2nd ed., (New York: Cambridge UP).

[2] W. A. Johnson, D. R. Wilton, and R. M. Sharpe, "Patch Code Users' Manual", Sandia National Laboratories SAND87-2991, May, 1988.

[3] S. Rao, D. R. Wilton, and A. W. Glisson, "Electromagnetic Scattering by Surfaces of Arbitrary Shape", IEEE Trans., AP-30(3), May, 1982, pp. 409-418.

[4] A. Jennings, J. J. McKeown, 1992, *Matrix Computation*, 2nd ed., (New York: John Wiley & Sons).

MATHEMATICAL REPRESENTATION OF MULTIPORT RESONATOR TEST DATA

Ross A. Speciale

Redondo Beach, California

polytope@msn.com

1 - MODELING OF RESONATOR TEST DATA.

Closed-form mathematical expressions have been developed, that accurately characterize a large class of multiport cavity resonators, in terms of scattering, impedance, and image parameters.

Surprisingly simple closed-form expressions, developed by fitting the impedance-matrix eigenvalues with rational functions, have been extracted from calibrated scattering parameter data.

Calibrated scattering parameter measurements were performed on representative physical models of a large class of multiport resonators, machined with high precision in the form of straight cylinders with either circular, square, or hexagonal cross-sections.

2 - MULTIPLE RESONANT-IRIS COUPLINGS.

The multiport resonators tested and analyzed in this study have either six, four, three or two direct-coupling ports, in the form of mutually-identical coupling irises cut out of either the resonator cylindrical wall (Fig. 1), or cut out of the resonator top and bottom shorting planes.

The cross-sections of the iris apertures are carefully designed to make all the irises resonant at the same frequency as either the TE or the TM fundamental resonator modes. The coupling irises are always cut at equally-spaced azimuth locations around the resonator axis, with iris-to-iris azimuth spacing of either $60°$, $90°$, $120°$, or $180°$, depending on the total number of ports.

The coupling irises that are cut out of the resonator cylindrical wall are either centered around the median plane between the top and bottom shorting planes (Fig.1), or symmetrically *offset* above and below it in alternating pairs.

All the multiport resonators tested and analyzed in this study exhibit very specific rotation, and reflection symmetries, identified by the symbols C_{6V}, C_{4V}, C_{3V}, and C_{2V}.

In the case of the six-port, or four-port resonators with *offset* cylindrical-wall irises, however, the symmetry classifications are given by either $S_6 = C_6\,\sigma_2$, for the six-port case, or $S_4 = C_4\,\sigma_2$, for the four-port case, (drehspiegelung [1]).

3 - PRACTICAL APPLICATIONS.

The six-port, and four-port resonators with coupling irises cut out of the cylindrical wall at equidistant azimuth angles around the cylinder axes, have a quite remarkable practical applications as the *"unit cells"* of two rather unique, two-dimensional wave-guiding structures, with either an *hexagonal* or a *square lattice*. These two types of structure resemble thus a *"honeycomb"* and respectively an *"egg-crate"*.

Indeed, such slow-wave structures have already been theoretically analyzed in substantial depth [2-6], and experimentally evaluated as low-loss, wide-band signal-distribution networks for electronically-steered phased arrays [7-8].

In this specific application, each of the mutually-coupled resonators in the structure feeds one of the array elements with the resultant vector-sum of signals generated by a comparatively small number of mutually-coherent sources. This system configuration leads to large reductions in the required number of electronic beam-steering control-devices, as compared to the notoriously expensive active-aperture arrays (Fig. 2 & 3).

4 - TWIN STACKED HONEYCOMB STRUCTURES.

Similarly, the three-port resonators with coupling irises cut out of either shorting-plane at 120° azimuth angles around the cylinder axis, can be used as the *"unit cells"* of a two level, *"twin-stacked-honeycomb"* slow-wave structure, where each top-level resonator only has three bottom-shorting-plane irises, and *symmetrically overlaps* three bottom-level resonators, that only have three top-shorting-plane irises (Fig. 6).

The twin-honeycomb structure exhibits a geometrical *"relative shift"* of its top-level honeycomb relative to the bottom-level honeycomb. The shift is equal to the uniform spacing between resonator axes of both honeycombs divided by $\sqrt{3}$, and oriented in one of the six azimuth directions that bisect the 60° angles between the reflection-symmetry planes of the structure.

The wave-propagation properties of the two-level twin-honeycomb structure are intrinsically different, because of the guided waves only coupling and propagating *down*, from the top level to the bottom level, and *back up* to the top level, while there are no coupling irises between adjacent resonators of each single level. The twin-honeycomb structure exhibits, besides the rotation and reflection symmetries, also *"glide"* symmetry.

5 - SYMMETRIES OF THE PARAMETER MATRICES.

The rotation, and reflection symmetries of the described resonators, and the implied *reciprocity*, are strongly correlated to the very specific mathematical structure of all the representative parameter matrices.

Indeed, save for unavoidable machining imperfections of the models, the multidimensional scattering, impedance, and admittance matrices of the described resonators are all nominally *"symmetric"* (around the main diagonal) and *"circulant"* [9].

The unique structure of these matrices leads to very substantial reductions of the dimensionality of the mathematical representations of resonator performance, and to quite

remarkable simplifications of the ensuing analysis of the wave-propagation properties of the described slow-wave structures.

6 - CALIBRATED SCATTERING PARAMETER MEASUREMENTS.

Physical models of four-port cavity resonators were precision-machined out of solid copper blocks, in three pieces : the cylindrical outer wall with the four resonant irises, and the top and bottom shorting planes. The spacing between any two external, parallel mating surfaces are equal to the uniform spacing between resonator axes in the full *"egg-crate"* structure, so that each resonator model strictly resembles a single unit cell (Fig. 1 & 2).

Six calibrated, two-port scattering parameter measurements were performed on each resonator model, in all the six possible combinations of input and output ports(Fig. 4 & 5).

These redundant measurement had a three-fold purpose :

a) confirming the expected symmetries of the scattering matrix.

b) evaluating the precision of the machining operations.

c) use the redundant data to extract strictly *symmetric* and *circulant* matrices.

A single, strictly symmetric and *circulant* scattering matrix was obtained by performing a simple, constrained least-squares fitting operation on the acquired six sets of calibrated scattering-parameter data.

The least-squares fitting operation further enhances the accuracy of the extracted data, by using *"a priory"* knowledge of the symmetry structure of the nominal scattering matrix of the device under test.

7 - FITTING THE IMPEDANCE MATRIX EIGENVALUES.

The elements and the eigenvalues of the corresponding *symmetric* and *circulant* impedance matrix were computed from the extracted scattering matrix, by means of simple scalar transformations. Indeed, the necessary mathematical operations are greatly simplified by the unique *symmetric* and *circulant* structure of all the parameter matrices, that reduce the number of different matrix elements, and the number of different eigenvalues to at most *three*, and in the most relevant case to *only two*.

Surprisingly accurate, closed-form mathematical representations of all the resonator parameters were obtained by heuristically fitting the eigenvalues of the impedance-matrix, with simple rational functions. The functions were designed to match the frequency-axis locations of the poles and zeros of the impedance matrix eigenvalues.

The accuracy of the fitting was even further improved by adding small polynomial correction terms.

8 - THE PARAMETERS OF 6-PORT, 3-PORT, AND 2-PORT RESONATORS.

Rigorous closed-form expressions have also been derived for the few different elements of the impedance and scattering matrices of *six-port*, *three-port*, and *two-port* resonators, having the same internal cross-section, axial depth, and iris-aperture size and shape as the tested four-port resonator models.

The derivations of these expressions are based on the *functional equivalence* between a *four-port* resonator, and a *six-port* resonator both having *all but two* diametrically opposite coupling irises *shorted* (Fig. 7).

This functional equivalence is mathematically expressed by equating the 2×2 *admittance* matrices of a *four-port*, and of a *six-port* resonator with *all but two* diametrically-opposite ports shorted.

Obviously, the admittance matrices to be equated are simply 2×2 sub-matrices of the full 6 $\times$ 6 and 4×4 admittance matrices of the *six-port*, and respectively of the *four-port* resonator.

The full admittance matrices are very easily computed, as the inverses of the corresponding *symmetric* and *circulant* impedance matrices, by means of peculiarly simple linear transformations, performed on the reciprocals of the impedance-matrix eigenvalues.

Similarly, closed-form expressions of the two different elements of the 3×3 impedance matrix of a *three-port* resonator, with coupling irises at 120° azimuth angles, have been obtained by equating its 3×3 admittance matrix to that of a *six-port* resonator with *three* out of the six coupling irises *shorted* (Fig. 8).

9 - RESULTS.

The Figures 9-12 show comparisons between the scattering parameters of two-port, three-port, four-port, and six-port resonators with equal internal geometry and coupling irises of equal size and shape. The data displayed in the figures were all obtained from the described calibrated scattering parameter measurements, performed *only* on physical models of *four-port* resonators.

10 - REFERENCES.

[1] Hamermesh M. ,"Group Theory and its Application to Physical Problems," Addison-Wesley Publishing Company Inc. , Reading, Massachusetts, USA , 1962, Chapter 2, page 36.

[2] Speciale R. A. ,"Sectored Cylindrical Cavity Resonators," Proceedings of the 8th Review of Progress in Applied Computational Electromagnetics, Monterey, California, March 16-20, 1992, pages 274-281.

[3] Speciale R. A. ,"Symmetry Analysis of Large Two Dimensional Clusters of Coupled Cavity Resonators," Proceedings of the 9th Review of Progress in Applied Computational Electromagnetics, Monterey, California, March 22-26, 1993, pages 281-288.

[4] Speciale R. A. ,"Wave-Field Patterns on Electrically Large Networks," Proceedings of the 11th Review of Progress in Applied Computational Electromagnetics, Monterey, California, March 20-25, 1995, pages 656-663.

[5] Speciale R. A. ,"Advanced Design of Phased Array Beam-Forming Networks," Proceedings of the 12th Review of Progress in Applied Computational Electromagnetics, Monterey, California, March 18-22, 1996, pages 918-930.

[6] Speciale R. A. ,"Synthesis of Phased ArrayAperture Distributions," Proceedings of the 12th Review of Progress in Applied Computational Electromagnetics, Monterey, California, March 18-22, 1996, pages 898-913.

[7] Speciale R. A. , US Patent No. 5,347,287 Awarded September 13, 1994.

[8] Speciale R. A. , US Patent No. 5,512,906 Awarded April 30, 1996.

[9] Davis J. P. ,"Circulant Matrices," John Wiley & Sons, New York, 1979, Pure and Applied Mathematics Series, Chapter 3, pages 66-107, and Chapter 5, pages 155-191.
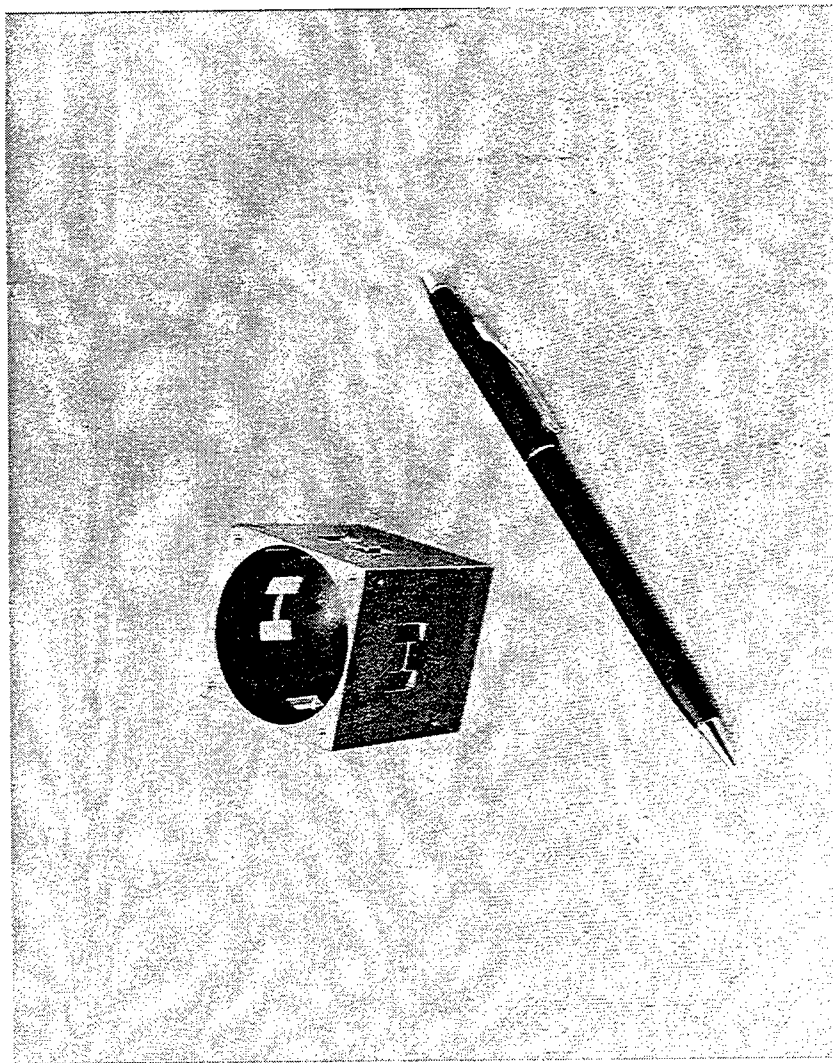
Figure 1 - Physical Test-Model of a Four-Port Cylindrical, Cavity Resonator. The Resonant Dumbbell-Shaped Irises, Oriented Orthogonal to the Axis, Couple to the Fundamental TM_{010} Mode.
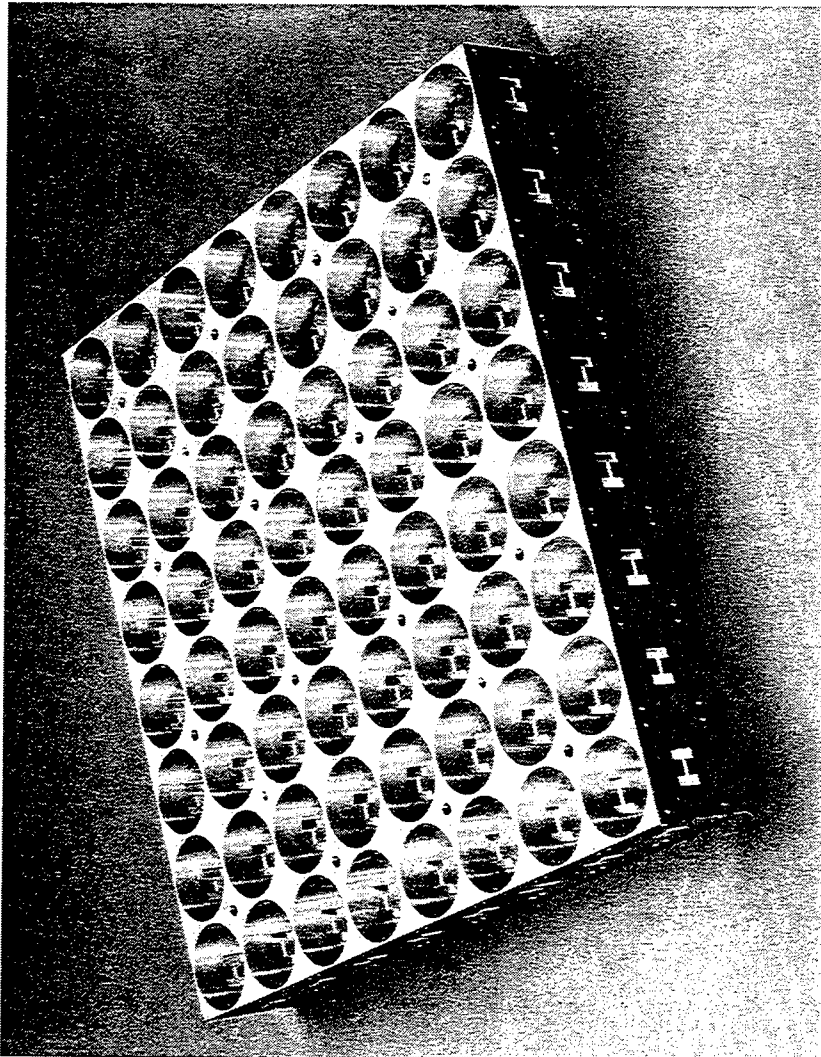
Figure 2 - Typical Slow-Wave Structure Composed of Directly-Coupled Cylindrical Resonators, All Tightly Clustered in a Two Dimensional, Square Lattice (Resembling an *"Egg-Crate"*).
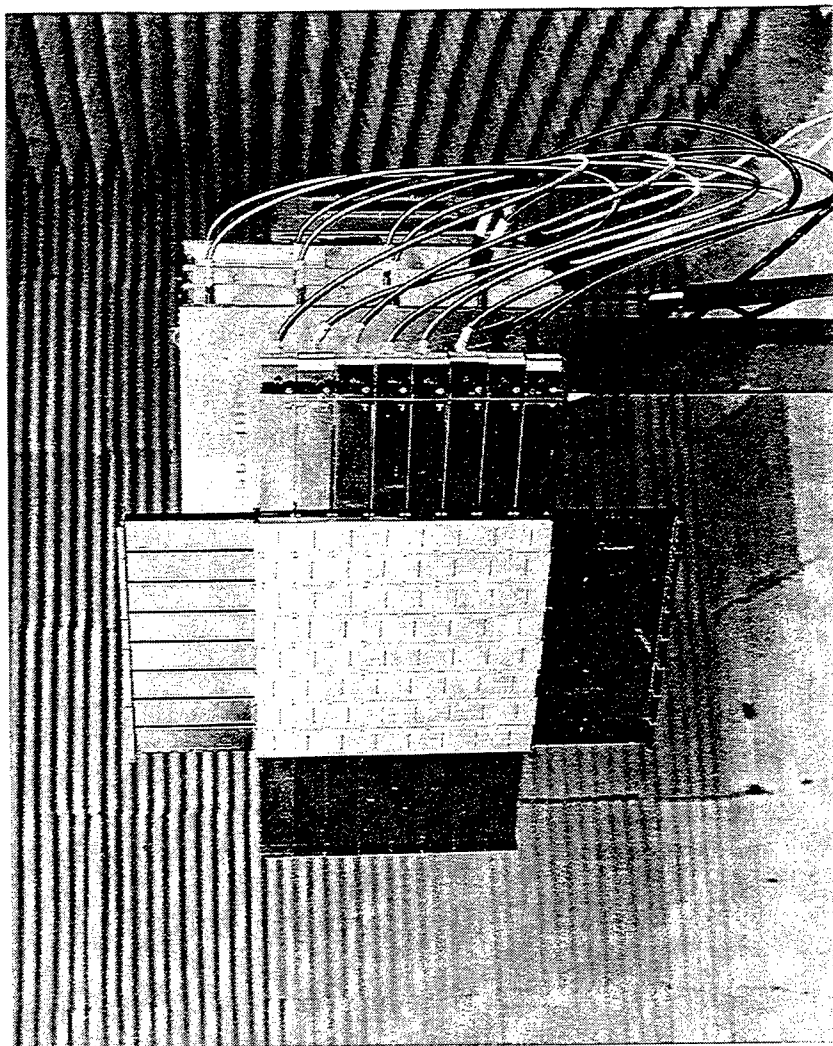
Figure 3 - Physical Test-Model of an 8 × 8 Cavity-Backed-Slot Phased Array, Synergistically Excited by 32 External, Mutually-Coherent Controlled Sources (The 32 Input Waveguides are WR-137).
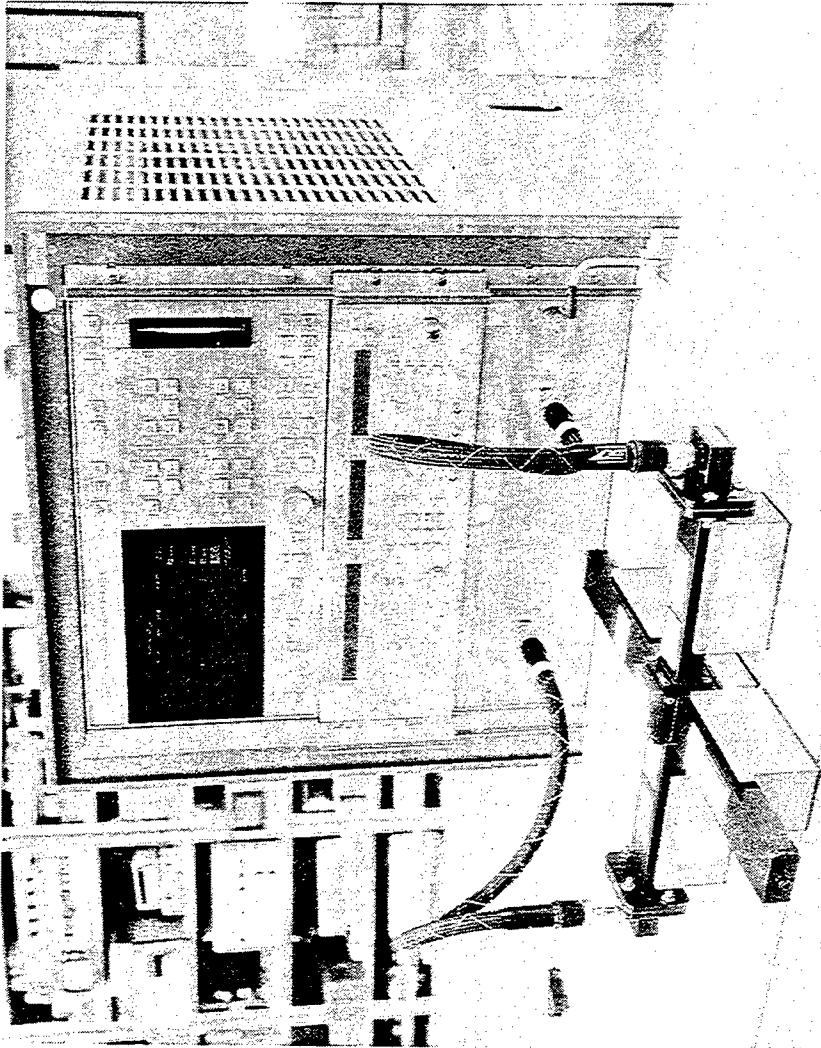
Figure 4 - The Calibrated Scattering Parameter Measurement Set Up. An Automated Vector Network Analyzer is Shown Connected to a Physical Model of Four-Port Cylindrical Cavity Resonator.
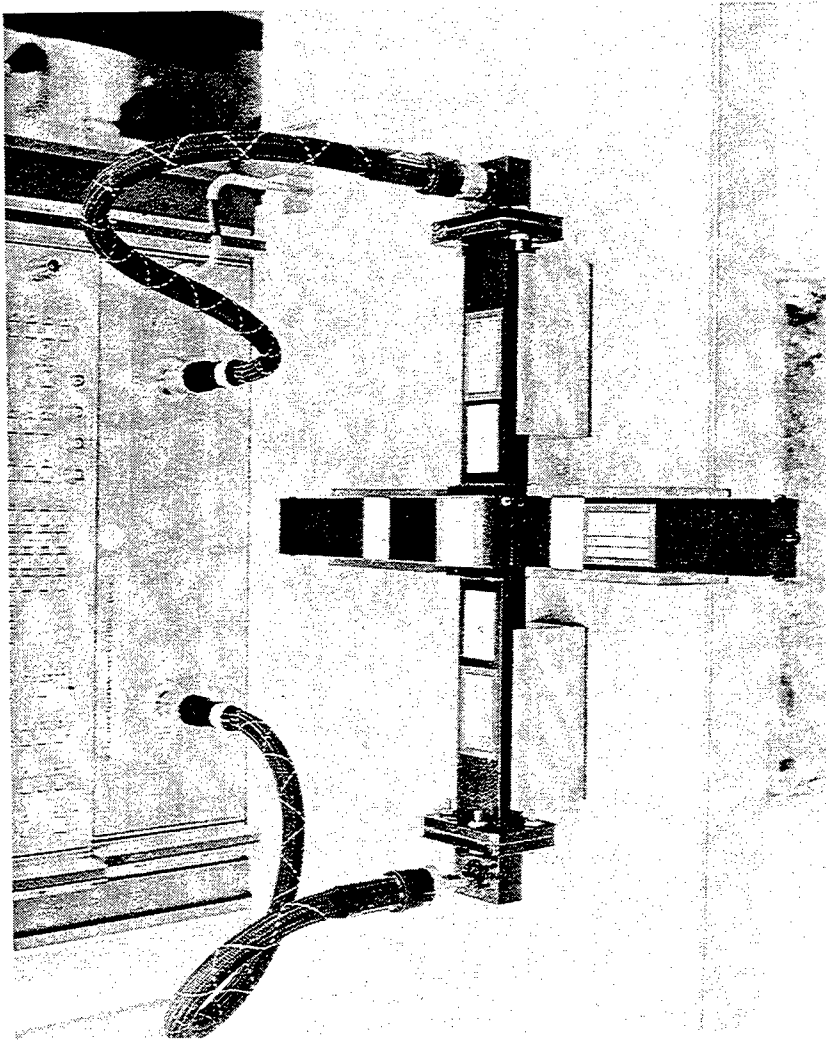
Figure 5 - The Calibrated Scattering Parameter Measurement Set Up. Detail of the Waveguide Fixture Connecting the Network Analyzer to a Physical Model of Four-Port Cavity Resonator.
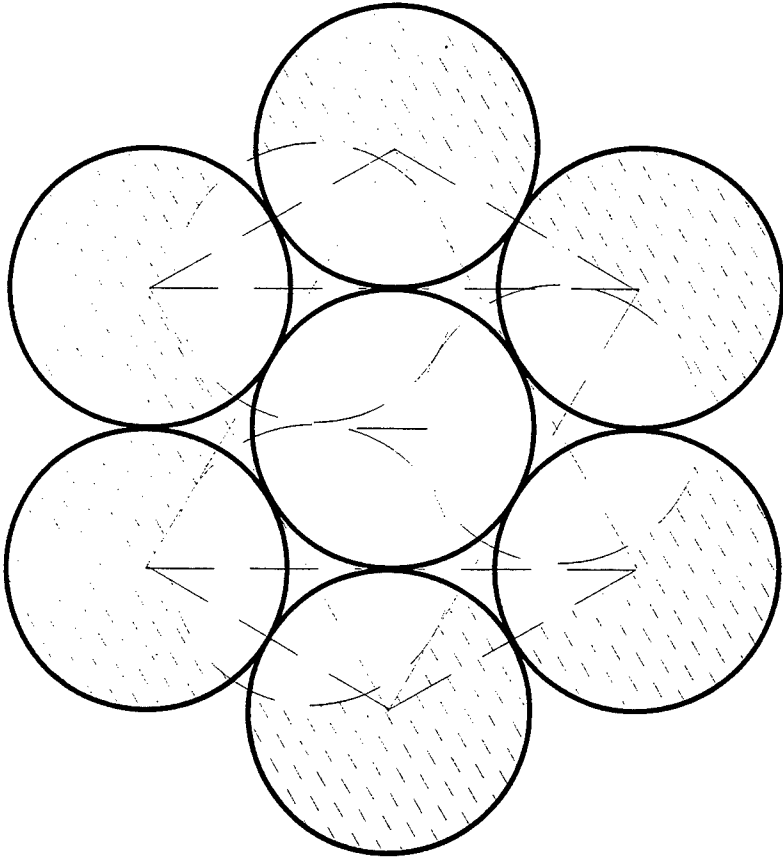
Figure 6 - Representative Geometry of a "Twin Stacked Honeycomb" Slow-Wave Structure. The Dashed Circles Represent here the Upper-Level Cylindrical Three-Port Resonators.
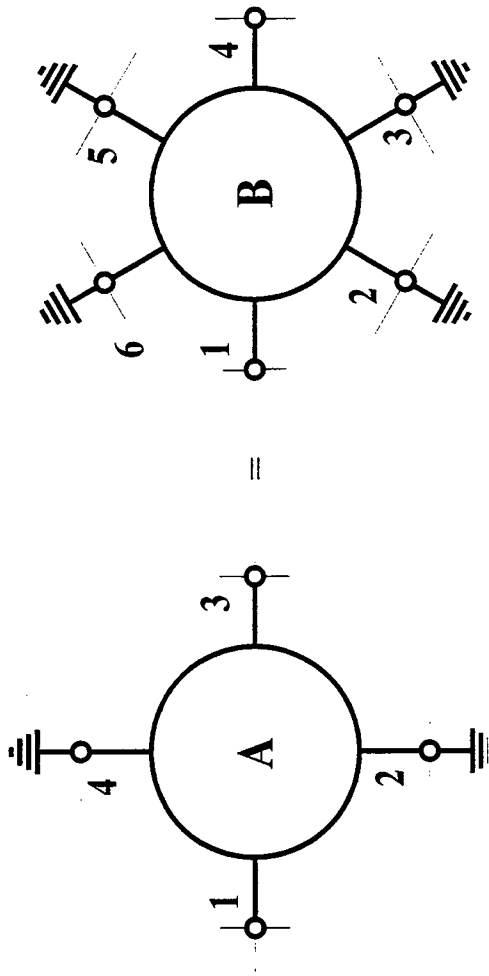
Figure 7 - Equivalence between Four-Port, and Six-Port Resonators with All But Two Diametrically Opposite Ports Shorted.
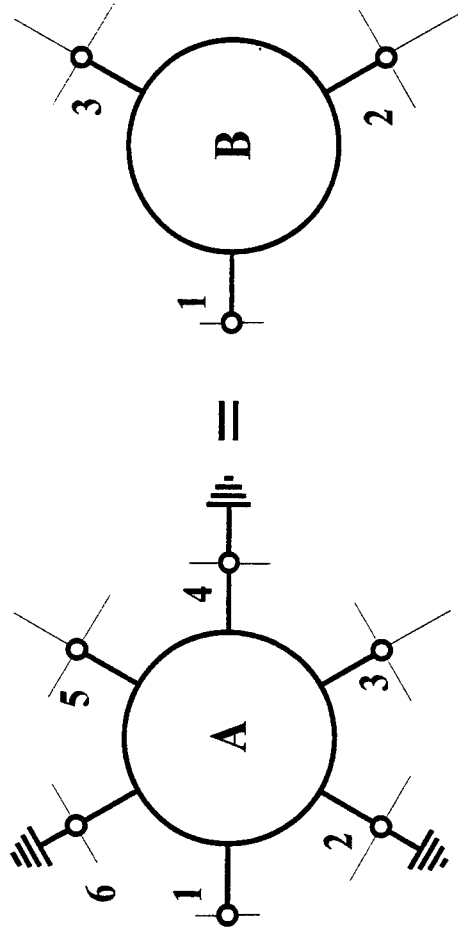
Figure 8 - Equivalence Between a Six-Port Resonator with Every Second Port Shorted and a C-3V Symmetric Three-Port Cylindrical Resonator.

S12—MAG dB : 6-PORT (SOLID), 4-PORT (DASHED), 3-PORT (DASH/DOT), AND 2-PORT (DOTTED) RESONATORS
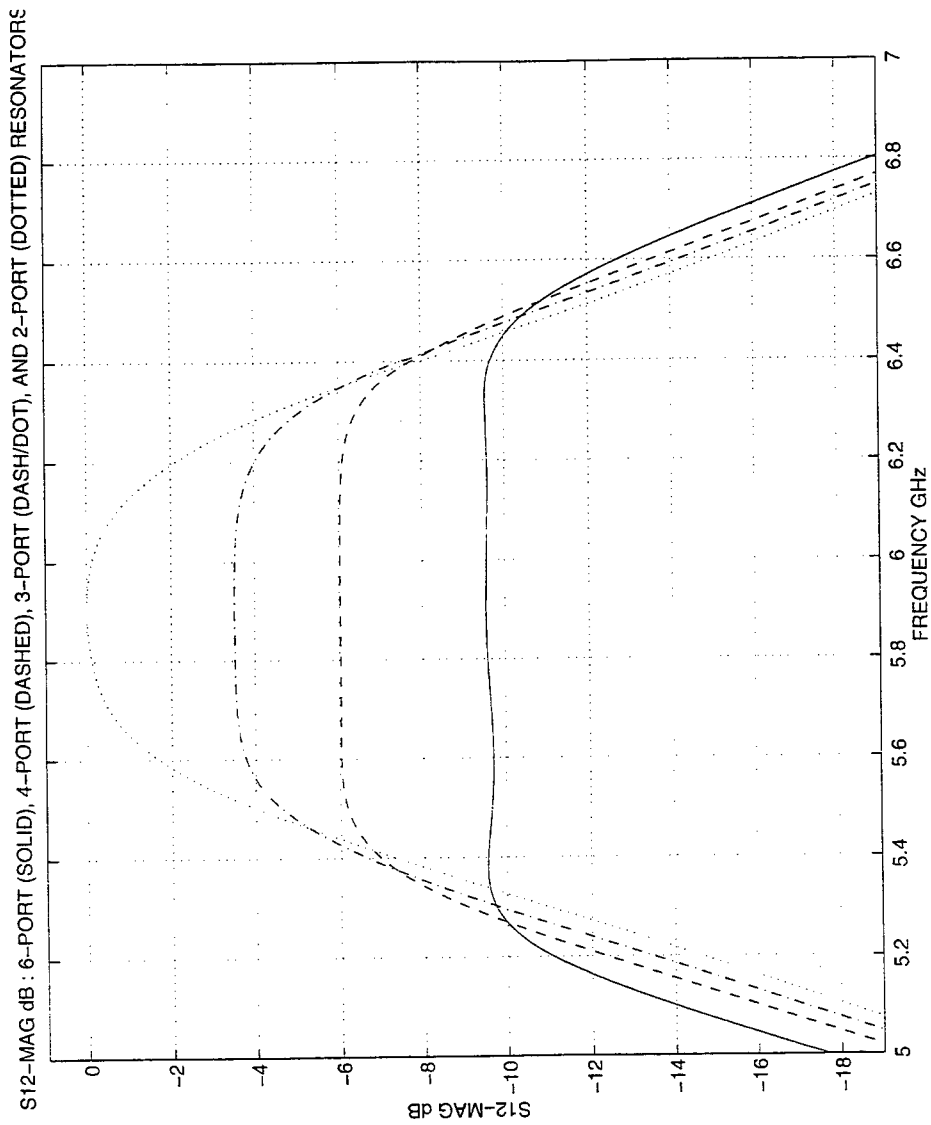
Figure 9 - Magnitude of the Transmission Parameter S_{12} for a 6-Port (Solid Line), a 4-Port (Dashed Line), a 3-Port (Dash/Dot Line), and a 2-Port (Dotted Line) Circular-Cylindrical Resonator, all having 1.505" Diameter, 1.527" Axial Depth, and Equal-Size Coupling Irises.

S12-PHA deg : 6-PORT (SOLID),, 4-PORT (DASHED), 3-PORT (DASH/DOT), AND 2-PORT (DOTTED) RESONATORS
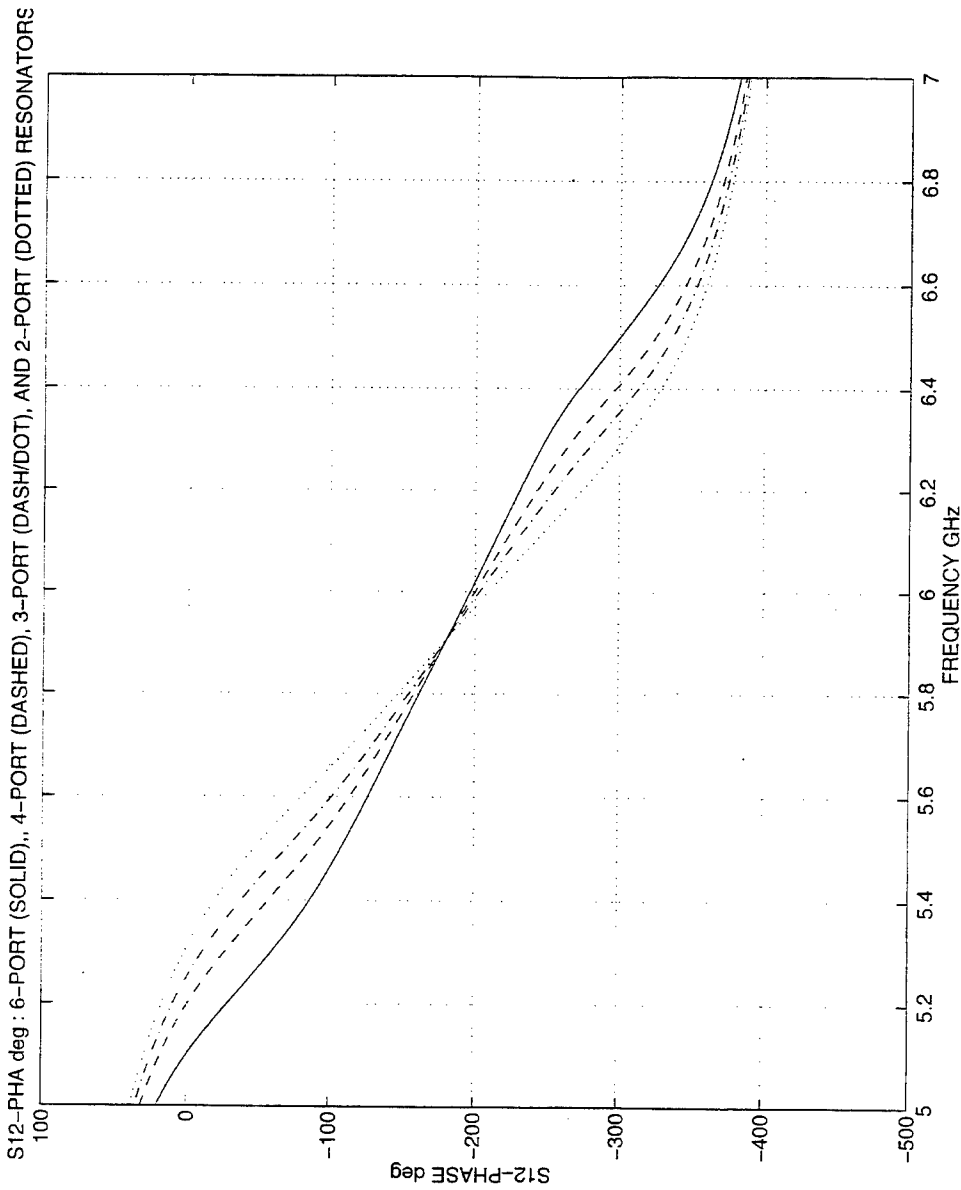
Figure 10 - Phase of the Transmission Parameter S_{12} for a 6-Port (Solid Line), a 4-Port (Dashed Line), a 3-Port (Dash/Dot Line), and a 2-Port (Dotted Line) Circular-Cylindrical Resonator, all having 1.505" Diameter, 1.527" Axial Depth, and Equal-Size Coupling Irises.

POLAR PLOT OF THE S12 ELEMENTS OF THE S2, S3, S4, AND S6 MATRICES
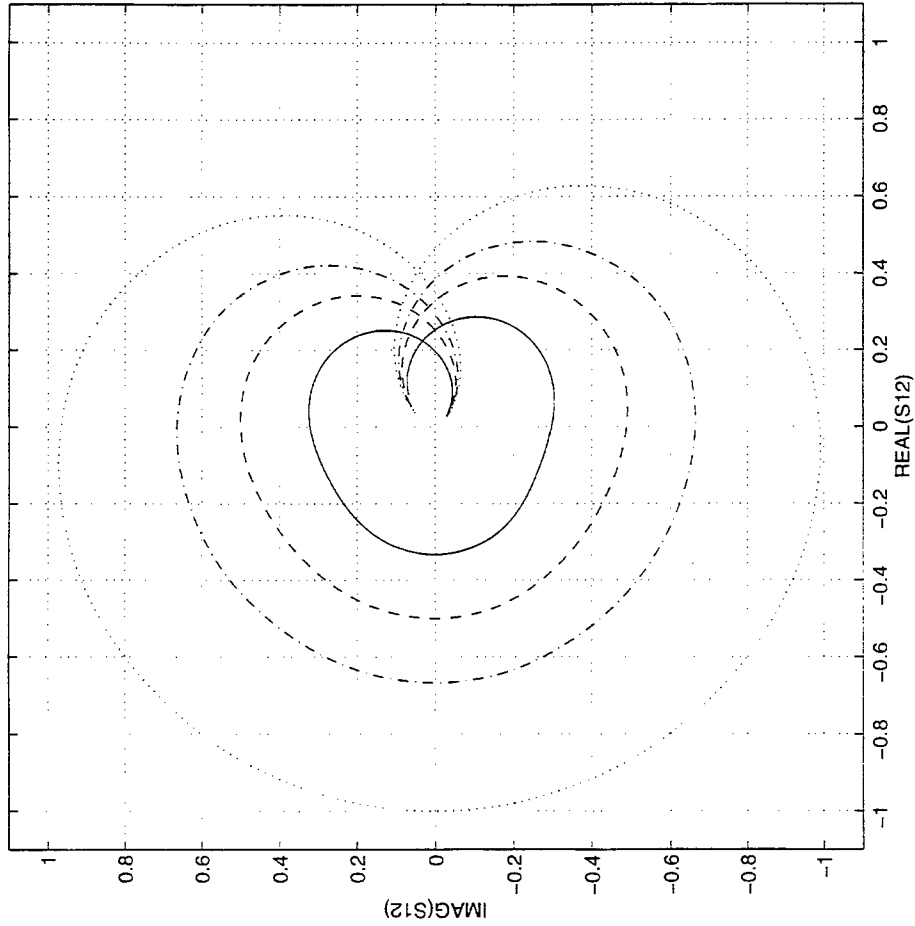
Figure 11 - Polar Plot of the Transmission Parameter S_{12} for a 6-Port (Solid Line), a 4-Port (Dashed Line), a 3-Port (Dash/Dot Line), and a 2-Port (Dotted Line) Circular-Cylindrical Resonator, all having 1.505" Diameter, 1.527" Axial Depth, and Equal-Size Coupling Irises.

POLAR PLOT OF THE S11 ELEMENTS OF THE S2, S3, S4 AND S6 MATRICES
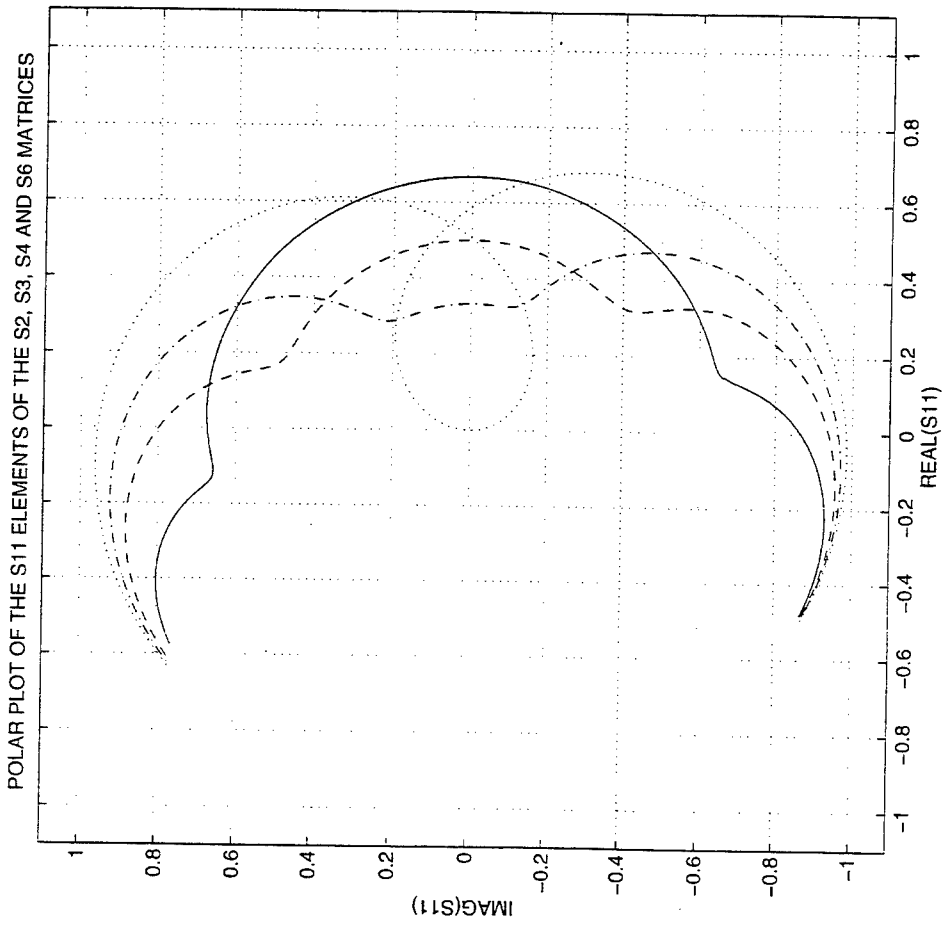
Figure 12 - Polar Plot of the Reflection Parameter S_{11} for a 6-Port (Solid Line), a 4-Port (Dashed Line), a 3-Port (Dash/Dot Line), and a 2-Port (Dotted Line) Circular-Cylindrical Resonator, all having 1.505" Diameter, 1.527" Axial Depth, and Equal-Size Coupling Irises.

A Comparison of Analytical and Numerical Solutions for Induction in a Sphere with Equatorially Varying Conductivity by Low-Frequency Uniform Magnetic Fields of Arbitrary Orientation

Trevor W. Dawson   and   Maria A. Stuchly
Department of Electrical and Computer Engineering
University of Victoria, P.O. Box 3055
Victoria, British Columbia, Canada V8W 3P6

Abstract

This paper considers analytical and numerical solutions to the problem of induction, by horizontal uniform low-frequency time-harmonic magnetic fields, in an equatorially stratified sphere having the conductivity distribution $\sigma(\varphi) = \sigma_0 e^{-\lambda \cos(p\varphi)}$, with $p \in \{1, 2\}$ and $\lambda > 0$. The resulting induced electric and current density fields are fully three-dimensional and exhibit interesting yet physically reasonable behaviour. While of interest in its own right, the analytical solution is particularly useful for the validation of low-frequency electromagnetic computer modelling codes. Fields computed by a numerical implementation of a scalar potential finite different method are found to compare favorably with the analytic ones, except for surface errors due to staircasing, and differences along the vertical axis where the numerical implementation poorly approximates the rapid conductivity variation.

1   Introduction

The problem of low-frequency electromagnetic induction in isolated non-magnetic compact conducting bodies is amenable to solution using Stevenson's method [1]. This approach is valid near the conductor, provided that the conductor is much smaller than the wavelength of the incident field, and that the conducting body is small with respect to all of its internal skin depths, so that the phase of the fields is known. Each of the incident, reflected and interior fields is expanded formally in a power series in wavenumber. The coefficients of like powers of wavenumber are related through Maxwell's equations. The result is a sequence of differential equations for the various coefficients. The lowest-order problem has (i) a magnetic field unperturbed by the conductor, and so is equal to the source field everywhere, and (ii) an electric field which is zero inside the conductor, and satisfies Laplace's equation outside the conductor, with the body replaced by a perfect conductor bearing a surface charge density $\rho_{s0}(\boldsymbol{u})$.

The quantity of interest in the present work is the lowest-order internal electric field, which is in quadrature with the external field. With an $e^{j\omega t}$ factor dropped, this can be represented as

$$\boldsymbol{E}_1^i(\boldsymbol{u}) = -i\omega \left\{ \boldsymbol{\nabla}\psi(\boldsymbol{u}) + \boldsymbol{A}_0(\boldsymbol{u}) \right\}. \tag{1.1}$$

Here $\boldsymbol{A}_0(\boldsymbol{u})$ is a vector potential for the static limit of the incident magnetic field, and $\psi(\boldsymbol{u})$ is a scalar conduction potential. A differential equation for the scalar potential is obtained upon requiring that the conduction current be conserved inside the conductor, $\boldsymbol{\nabla} \cdot \left[\sigma(\boldsymbol{u}) \boldsymbol{E}_1^i(\boldsymbol{u})\right] = 0$, so that

$$\boldsymbol{\nabla} \cdot \left[\sigma(\boldsymbol{u}) \, \boldsymbol{\nabla}\psi(\boldsymbol{u})\right] = -\boldsymbol{\nabla} \cdot \left[\sigma(\boldsymbol{u}) \, \boldsymbol{A}_0(\boldsymbol{u})\right]. \tag{1.2}$$

Specification of the problem is completed by imposition of the boundary condition

$$\sigma(\boldsymbol{u}) \, \hat{n}(\boldsymbol{u}) \cdot \boldsymbol{E}_1^i(\boldsymbol{u}) = i\omega \rho_{s0}(\boldsymbol{u}). \tag{1.3}$$

In low-frequency induction, the electric and magnetic fields can be considered decoupled, and attention can be focussed on electric or magnetic forcing in isolation by alternatively setting $A_0(u)$ or $\rho_{s_0}(u)$ to zero. The remainder of this paper is concerned with magnetic excitation, and so it will be assumed from here on that $\rho_{s_0}(u) = 0$. The excitation is therefore solely due to the magnetic scalar potential, distributed throughout the conductor volume.

The authors have developed an efficient computer code implementing the Scalar Potential Finite Difference (SPFD) Method based on equations (1.1), (1.2) and (1.3), and are using this code for the modelling of magnetically-induced power line frequency fields in realistic human full-body models. As with any numerical method, it is desirable to validate the results, minimally by comparison with an independent numerical technique, and preferably by comparison with an analytical solution. However, suitable analytic solutions are relatively rare, particularly for fully three-dimensional problems. A recent paper [2] described one test of the code, in which the results for whole-body SPFD computations in a human model composed of 7.2-mm voxels were compared voxel-by-voxel with fields computed in the same model using a quasistatic finite-difference time-domain (FDTD) code [3]. Excellent agreement was obtained, with typical voxel fields agreeing to three significant figures.

As a second test of the code, the authors recently developed [4] an analytic solution to the problem of induction in an equatorially-stratified conducting sphere by an applied uniform axial harmonic magnetic field. When $\lambda > 0$, the induced current is forced though a conductivity gradient, and a fully three-dimensional current flow results. A recent paper [5] is concerned with a comparison of the numerical SPFD results with the analytic ones. There, it was shown that the two sets of calculations agree quite well, except at the surface (where staircasing errors were apparent) and near the central axis, where the discrete conductivity inherent in the numerical approximation poorly approximates the rapid true conductivity variation.

The analytic solution [4] was formulated in terms of a general Green's function, involving expansions in terms of eigenfunctions of azimuthal and equatorial ordinary differential equations. Solutions of the latter are similar to Mathieu functions and are obtained as Fourier series. The Green's function also involves radial functions that have zero slope at the surface to ensure that the surface electric field is tangential to the sphere. The Green's function formulation led to an exact solution, for the case of axial magnetic excitation, also in the form of an eigenfunction expansion. However, as the authors noted [4], the Green's function formulation is quite general, and so can serve as the basis for analytic solutions for other source fields.

In the present work, the original analytic solution is extended to encompass excitation by horizontal magnetic fields, thereby completing the problem of low-frequency induction in the equatorially-stratified sphere by uniform quasi-static magnetic fields. The solution is outlined in Section 2. The Green's function formulation [4] is described briefly, and the eigenfunction expansion coefficients for the new solutions are developed. Once the scalar potential is available, its gradients can be combined with a knowledge of the applied magnetic vector potential to compute the induced electric field. Illustrations of typical solutions are presented in Section 4, along with a comparison of analytic results with fields computed using the SPFD numerical code.

2   Model and Analytic Solution

Coordinates and vectors will be be interchangeably defined in terms of a Cartesian coordinate system (x, y, z) with associated unit vectors $\{\hat{x}, \hat{y}, \hat{z}\}$, and a spherical polar coordinate system (r, θ, φ) with corresponding unit vectors $\left\{\hat{r}, \hat{\theta}, \hat{\varphi}\right\}$. The two systems are related by

$$x = r \sin\theta \cos\varphi, \quad y = r \sin\theta \sin\varphi \quad \text{and} \quad z = r\cos\theta. \tag{2.1}$$

A typical position vector is $u = x\,\hat{x} + y\,\hat{y} + z\,\hat{z}$. The conducting body is a sphere of radius a, centred at the origin, and having the particular positive, periodic, and equatorially stratified conductivity distribution

$$\sigma(\varphi) = \sigma_0 e^{-\lambda \cos(p\varphi)}, \tag{2.2}$$

with $p \in \{1, 2\}$ and $\lambda > 0$. This model has p conductivity maxima and minima for $-\pi < \varphi \leq \pi$, and a maximum conductivity contrast of $e^{2\lambda}$. The logarithmic derivative of the conductivity is

$$s'(\varphi) \equiv \sigma'(\varphi) / \sigma(\varphi) = \lambda p \sin(p\varphi). \tag{2.3}$$

The excitation field under consideration has the form $\boldsymbol{B}^e = B_x^e \hat{\boldsymbol{x}} + B_y^e \hat{\boldsymbol{y}}$, so that a suitable divergence-free vector potential is then

$$\boldsymbol{A}_0 = B_x^e \left(y\hat{\boldsymbol{z}} - z\hat{\boldsymbol{y}} \right)/2 + B_y^e \left(z\hat{\boldsymbol{x}} - x\hat{\boldsymbol{z}} \right)/2. \tag{2.4}$$

For the conductivity distribution (2.2), the differential equation (1.2) attains the form

$$\boldsymbol{\nabla}\cdot\left[\sigma(\boldsymbol{u})\,\boldsymbol{\nabla}\psi(\boldsymbol{u})\right] = -S(\boldsymbol{u}) \equiv \tfrac{1}{2}\cot\theta \left\{ B_x^e\cos\varphi + B_y^e\sin\varphi \right\} \sigma'(\varphi). \tag{2.5}$$

Since the external electric field is being ignored, and the magnetic vector potential (2.4) is tangential to the sphere surface, the requisite boundary condition reduces to

$$\partial\psi(\boldsymbol{u})\,/\partial r = 0 \qquad (r = a). \tag{2.6}$$

As in the case of axial forcing [4], a solution to the above boundary-value problem can be expressed in terms of a modified Green's function as

$$\psi(\boldsymbol{u}') = \iiint_V S(\boldsymbol{u}) G_e\left(\boldsymbol{u}'|\boldsymbol{u}\right) dv(\boldsymbol{u}). \tag{2.7}$$

This Green's function has the form of the expansion

$$G_e\left(\boldsymbol{u}'|\boldsymbol{u}\right) = \sum_{\varpi\in\{e,o\}} \sum_{m,n=0}^{\infty}{}' \left\{ \hat{F}_m^{\varpi}(\varphi')\,\hat{F}_m^{\varpi}(\varphi)\,\hat{Q}_{mn}^{\varpi}(\theta')\,\hat{Q}_{mn}^{\varpi}(\theta)\,R_{\nu_{mn}^{\varpi}}(r'|r) \right\} \tag{2.8}$$

in eigenfunctions of the two angular coordinates, the prime indicating that the $m = n = 0$ term is to be omitted. A principal point to note here is that the functions $R_{\nu_{mn}^{\varpi}}(r'|r)$ in the expansion all satisfy the outer boundary condition (2.6), and hence so does $G_e\left(\boldsymbol{u}'|\boldsymbol{u}\right)$. The terms $\hat{F}_m^{\varpi}(\varphi')$ are the even and odd normalized eigenfunctions of the differential equation

$$F''(\varphi) + s'(\varphi)\,F'(\varphi) + \mu^2 F(\varphi) = 0, \tag{2.9}$$

subject to a boundary condition of periodicity and regularity. This additionally defines the equatorial eigenvalues μ_m^{ϖ}, $m = 0, 1, \ldots$. In the case $p = 2$, the eigenfunctions additionally fall into π- and 2π-periodic classes. All are defined in terms of Fourier series. Eigenfunctions corresponding to different eigenvalues are orthogonal under the inner product

$$\langle f\,|\,g \rangle_{\varphi} \equiv \int_{-\pi}^{+\pi} \sigma(\varphi)\,f(\varphi)\,g(\varphi)\,d\varphi, \tag{2.10}$$

Similarly, the terms $\hat{Q}_{mn}^{\varpi}(\theta)$ denote the normalized eigenfunctions of the associated Legendre equation

$$[\sin\theta\,Q'(\theta)]' + \left[\nu\left(1+\nu\right)\sin\theta - \mu^2/\sin\theta\right]Q(\theta) = 0. \tag{2.11}$$

Boundary conditions of regularity at the sphere poles lead to the eigenvalues

$$\nu \in \left\{ \nu_{mn}^{\varpi} \equiv \mu_m^{\varpi} + n\,|\,n = 0, 1, \ldots \right\}. \tag{2.12}$$

The functions

$$Q_{mn}^{\varpi}(\theta) = \sin^{\mu}\theta\,C_n^{(\mu+1/2)}(\cos\theta), \qquad (n = 0, 1, \ldots) \tag{2.13}$$

form a suitable set of unnormalized azimuthal eigenfunctions, in terms of the Gegenbauer [6] (ultraspherical) orthogonal polynomials. Pairs of eigenfunctions (2.13) of different azimuthal orders are orthogonal under the inner product

$$\langle f\,|\,g \rangle_{\theta} \equiv \int_0^{\pi} f(\theta)\,g(\theta)\,\sin\theta\,d\theta. \tag{2.14}$$

The volume integration in eq.(2.7) can be carried out, using the expansion for the modified Green's function. This leads to the solution

$$\psi(\boldsymbol{u}') = -\tfrac{1}{2}C \sum_{\varpi\in\{e,o\}} \sum_{m,n=0}^{\infty}{}' V_{m.n}^{\varpi} \left(B_x^e U_{m\,x}^{\varpi} + B_y^e U_{m\,y}^{\varpi} \right) \hat{F}_m^{\varpi}(\varphi')\,\hat{Q}_{mn}^{\varpi}(\theta')\,\bar{R}_{\nu_{mn}^{\varpi}}(r') \tag{2.15}$$

for the potential, where

$$U_{m\,x}^{\varpi} \equiv \left\langle s' \cos\varphi \,\middle|\, \hat{F}_m^{\varpi} \right\rangle_{\varphi}, \quad U_{m\,y}^{\varpi} \equiv \left\langle s' \sin\varphi \,\middle|\, \hat{F}_m^{\varpi} \right\rangle_{\varphi} \quad \text{and} \quad V_{m.n}^{\varpi} \equiv \left\langle \cot\theta \,\middle|\, \hat{Q}_{mn}^{\varpi} \right\rangle_{\theta}. \tag{2.16}$$

The integrals (2.16a) and (2.16b) can be integrated either numerically, or analytically in terms of the Fourier coefficients. The non-zero excitation pattern for the two horizontal excitations is indicated in Table 1, along with that for the previously-published axial excitation case. The integrals (2.16c) can similarly be evaluated analytically.

	$p=1$		$p=2$			
	F_m^e	F_m^o	F_{2m}^e	F_{2m-1}^e	F_{2m}^o	F_{2m-1}^o
B_x	0	•	0	0	0	•
B_y	•	0	0	•	0	0
B_z	0	•	0	0	•	0

Table 1: Equatorial eigenfunction excitation pattern for the three canonical source fields.

3 The SPFD Method

In the numerical implementation of the SPFD to solve equations (1.2) and (1.3), the three-dimensional computational domain is discretized into a uniform set of elementary parallelepipeds or voxels. Within each voxel the electrical properties are assumed constant. The potential method is naturally confined only to the conductor, with potentials defined at the vertices of the voxels. The electric fields are defined as a set of discrete vectors on the staggered array defined by the voxel edges, with field values defined at the edge centers. These are computed *a posteriori*, using finite differences of the potential field. To allow for physical interpretation of the results, electric field vectors are defined at the voxel centers by averaging the three sets of four parallel edge components. The magnetic vector potential contribution indicated in eq.(1.1) must also be included. The current density is then computed by multiplication by the voxel conductivity.

A finite-difference approximation of equation (1.2) at a given node can be constructed by an application of the divergence theorem to an imaginary shifted voxel with that node at its centroid. It is convenient to adopt a local indexing scheme, where the target node is labeled 0 and both the nodes and edges connected to it on the $+x$, $-x$, $+y$, $-y$, $+z$ and $-z$ sides are indexed from 1 to 6 respectively. Quantities associated with nodes or edges are then labeled with the local index of the associated object. With this shorthand, a simple finite difference equation results :

$$\left(\sum_{r=1}^{6} s_r \right) \psi_0 - \sum_{r=1}^{6} s_r \psi_r = i\omega \sum_{r=1}^{6} (-1)^{r+1} s_r \ell_r A_{0r} \tag{3.17}$$

In this equation, ℓ_r denotes the various edge lengths in the local indexing scheme, and A_{0r} denotes the component of the external magnetic vector potential tangent to the rth edge, evaluated at the edge centre. The coefficients are the edge conductances $s_r \equiv \bar{\sigma}_r a_r / \ell_r$, where $\bar{\sigma}_r$ denotes the average conductivity of the four voxels contacting edge r and a_r is the area of the voxel face normal to edge r. The above equations need to be modified in an obvious manner if the central point is connected to less than 6 neighbouring nodes in the conductor. It may be noted here that the above equations can be viewed as modelling a Cartesian lattice of resistors associated with the voxel edges, and in this sense, the induced currents may be considered to be confined to these edges. This interpretation has consequences for the surface discrepancies. observed in Section 4, between numerical and analytic calculations.

When equations of the above form are written for each vertex of every conducting voxel in the distribution, the result is a heptadiagonal system of equations which may be written as $(N - E)\,y = f$. This set of equations is diagonally dominant, symmetric, positive semi-definite. It is also singular, since the potential is indeterminate

to within an additive constant. This system may be left-preconditioned to the form $\left(I - N^{-1}E\right)y = N^{-1}f$, or symmetrically preconditioned to the form $(I - A)x = b$, where $A = N^{-1/2}EN^{-1/2}$, $y = N^{-1/2}x$ and $b = N^{-1/2}f$. The singularity can be removed by augmenting the system with an equation requiring that the potential have zero mean. Either form is well-suited for solution on a computer, particularly using an iterative solvers [7]. The restarted Generalized Minimum Residual method converges well for the augmented and left-preconditioned system. However, the Conjugate Gradient Method applied to the symmetrically-preconditioned and augmented system proved to be the most efficient.

4 Results

To illustrate the nature of the resulting field behavior, Figure 1 depicts in a pseudo-Cartesian format, the surface
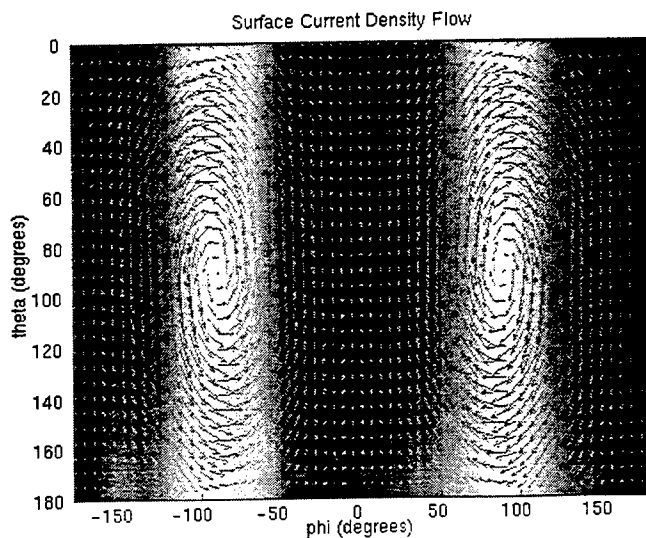
Figure 1: Surface current density pattern for excitation by a uniform 1-T, 60-Hz magnetic field directed along the y-axis.

current density induced by a source oriented along the y-axis. All of the results in this section pertain to a 1-m diameter sphere with a periodicity factor of $p = 2$, a contrast factor $\lambda = \ln\sqrt{50}$ and a scale factor $\sigma_0 = e^{-\lambda}$. The conductivity distribution is therefore $\sigma(\varphi) = 50^{-(1-\cos 2\varphi)/2}$ S m^{-1}, with a maximum contrast of 50-to-1 and a maximum value of 1 S m^{-1}. The conductivity maxima both lie along the y-axis, while the minima lie along the x-axis. All magnetic source fields have a frequency of 60 Hz, with a strength of 1 T. The relative arrow lengths are proportional to the local current density magnitude. They are superimposed on a greyscale representation of the conductivity, white being associated with the highest values. As might be expected, the current flow is dominantly associated with the higher conductivity and shows the anticipated circulation around the source vector in accordance with Faraday's law.

To further illustrate the nature of the analytic solution, Figure 2 depicts the current flow, induced by a magnetic field directed along the x-axis, in the plane $x = 5$ mm. The most notable feature is again the presence of a current

vortex associated with each conductivity maximum. There is also a net flow around the perimeter of the sphere. These features are further illustrated in the lower left panel of Figure 3, which depicts the modulus of the induced current density in the plane $z = 5$ mm. The associated electric field intensity is depicted on the top left panel of this same Figure. The two current vortices are clearly visible, more so in the electric field.
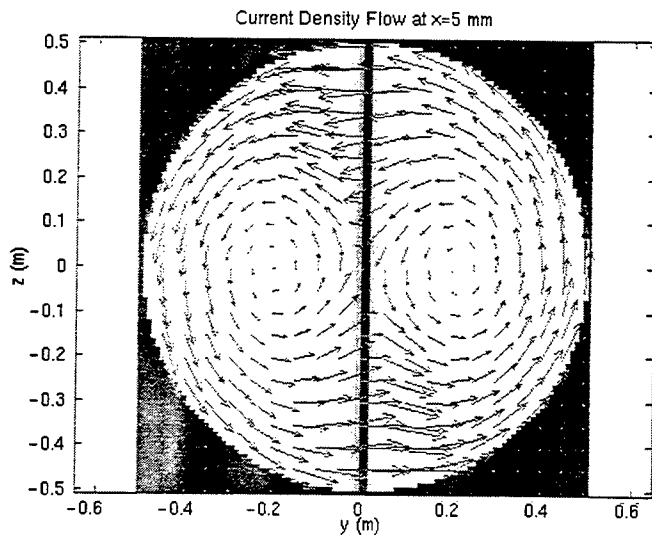
Figure 2: Current density pattern in the plane $x = 5$ mm induced by a uniform 1-T, 60-Hz magnetic field directed along the x-axis.

Figure 3 also depicts results typical of comparisons between data computed from the SPFD numerical code and the analytical model. The right-hand panels show the voxel-wise difference between the modulus of the electric field (top) and current density (bottom) computed by the two methods. Significant discrepancies are confined to the vicinity of the surface of the sphere and of the z-axis. The former are largely associated with the staircasing errors, where the voxel-edge-based numerical representation of the electric field poorly represents the true spherical surface current pathways. The latter are associated with the inability of the discrete voxels to capture the rue rapid variation of the conductivity with angle.

Table 2 presents a numerical comparison between the field moduli computed by the analytical and numerical methods, for both source orientations. The upper section of the table is concerned with the maximum values. These are in good agreement, for both the electric field and current density, for the source along the x-axis. Furthermore, the maximum value of the electric difference field is only 5% of the corresponding field maximum. The maximum current density discrepancy is about 17% of the maximum. The agreement is worse for the y-directed source. Here the numerical electric field and current density maxima are much smaller than those generated by the x-directed source, and differ from each other by 26% and 12% respectively. Similarly the corresponding maximum differences are 26% and 18% of the associated global maximum. The table also presents two global comparison measures, namely the average and variance of each field. These are in much better agreement. The averages all agree to better than 0.4% relative error, and the variances are in only slightly worse agreement. Finally, the table indicates in the last row, the three-dimensional correlation coefficient between the analytic and numerical computations. These exceed 99.3% for the x-directed source and 99.9% for the y-directed source. The better agreement for the
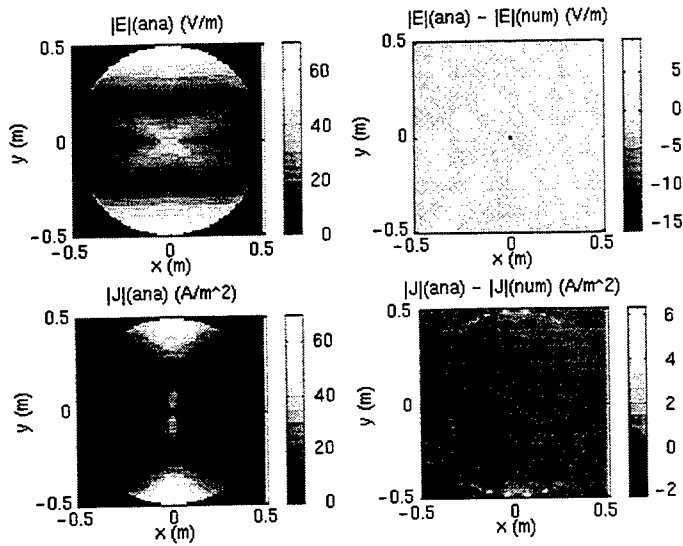
Figure 3: Modulus of the analytically-computed electric field and current density (left column), and of the associated differences between the analytic and numerical solutions, in the plane $z = 5$ mm. Excitation is by a uniform 1-T, 60-Hz magnetic field directed along the x-axis.

		B_x		B_y	
		$|E|$	$|J|$	$|E|$	$|J|$
Max	Ana	+1.22, +3	+1.77, +2	+1.11, +2	+3.58, +1
	Num	+1.22, +3	+1.77, +2	+1.40, +2	+4.01, +1
	Δ	+6.61, +1	+2.92, +1	+2.91, +1	+6.27, +0
Avg	Ana	+3.11, +1	+7.06, +0	+2.84, +1	+5.06, +0
	Num	+3.12, +1	+7.07, +0	+2.84, +1	+5.05, +0
	Δ	−7.15, −2	−1.07, −2	+5.31, −2	+7.26, −3
Var	Ana	+5.87, +1	+1.44, +1	+3.54, +1	+7.86, +0
	Num	+6.00, +1	+1.44, +1	+3.53, +1	+7.85, +0
	Δ	+8.02, +0	+1.27, +0	+1.17, +0	+2.09, −1
Cor		+0.99300	+0.99688	+0.99967	+0.99975

Table 2: Comparisons between the modulus of the electric field (in volts per meter) and current density (in amperes per square meter) computed by the numerical (labeled "Num") and analytical ("Ana") solutions, for excitation by 60-Hz, 1-T uniform magnetic fields directed along the x- and y- axes. The tabulated data are the maximum ("Max"), average ("Avg") and the variation ("Var") for each field. The quantities are also tabulated for the voxel-wise difference between the analytic and numerical solutions. In the bottom row are the full three- dimensional correlation coefficient between the two solutions. The numerical values are in an abbreviated scientific notation, with the exponent of 10 following the comma.

539

latter source orientation is corroborated by the average and variance data, despite the worse agreement between the global maxima.

5 Conclusions

The overall agreement between the results obtained from the analytical solution and the numerical SPFD code is good. The differences can be explained in terms of the straightforward implementation of the SPFD code. The agreement provides a degree of confidence in the correctness of the coding of the numerical model. An improved version of the code, based on conformal voxels for example, might be expected to provide an even better agreement. The analytic model, extended to general source orientations, clearly provides a useful addition to the limited set of three-dimensional analytic solutions that can be used in the verification of numerical electromagnetic modelling codes.

Acknowledgment

References

[1] J. Van Bladel. *Electromagnetic Fields*. Hemisphere Publishing Corporation, Washington D.C., revised printing edition, 1985.

[2] Trevor W. Dawson, Jan De Moerloose, and Maria A. Stuchly. Comparison of magnetically induced ELF fields in humans computed by FDTD and scalar potential FD codes. *Applied Computational Electromagnetics Society Journal*, 11(3):63–71, November 1996.

[3] Jan De Moerloose, Trevor W. Dawson, and Maria A. Stuchly. Application of FDTD to quasi-static field analysis. *Radio Science*, 1997. manuscript accepted for publication.

[4] Trevor W. Dawson and Maria A. Stuchly. An analytic solution for verification of computer models for low-frequency magnetic induction. *Radio Science*, 1997. manuscript accepted for publication.

[5] Trevor W. Dawson and Maria A. Stuchly. Analytic validation of a three-dimensional scalar-potential finite-difference code for low-frequency magnetic induction. *Applied Computational Electromagnetics Society Journal*, 11(3):72–81, November 1996.

[6] Philip M. Morse and Herman Feshbach. *Methods of Theoretical Physics*. McGraw-Hill Book Company, New York, 1953.

[7] R.D. da Cunha and T.R. Hopkins. PIM 2.0 : Parallel Iterative Methods package for systems of linear equations; (FORTRAN 77 version), 1993. ©1993 R.D. da Cunha, T.R. Hopkins and Computing Laboratory, University of Kent at Canterbury, Canterbury, U.K. and Centro de Processamento de Dados, Universidade Federal do Rio Grande do Sul, Porto Alegre, Brasil.

Modeling of Laminated Cores by Homogeneous Anisotropic Cores for Magnetics Simulation

J. E. Kiwitt, A. Dietermann, K. Reiß

Universität Karlsruhe, Inst. f. Theoretische Elektrotechnik
D-76128 Karlsruhe, Germany
kiwitt@tem.etec.uni-karlsruhe.de

Abstract: In this paper a new model of laminated iron cores for numerical field computations considering eddy currents is presented. An equivalent core with homogeneous, but anisotropic constitutive parameters is derived analytically and verified numerically. The choice of parameters is valid for all frequencies, as long as wave propagation can be neglected. It is independent of core width and frequency, which allows easy time–domain simulation.

1   Introduction

Realistic magnetic devices, like transformers or sensors often have laminated cores to reduce eddy current losses. Nevertheless, in many cases eddy currents have an influence on the behavior of the devices which cannot be neglected. The 3D numerical simulation of laminated cores, taking into account eddy currents, requires so many mesh points that it is still far too time-costly.

As shown in [1], a laminated core can be modeled by a homogeneous core with anisotropic constitutive parameters, which needs much less mesh points. An approach was presented how to determine the equivalent constitutive parameters.

In the next sections, a different approach with several advantages is presented, which remarkably improve practical applicability.

2   Analytical solution with idealized geometry

Since the laminated core and its equivalent homogeneous core cannot be equivalent in every aspect, the most relevant one for the design of magnetic devices has to be taken. This is usually the V-I characteristic, measured at a coil around the core. The geometries of the laminated core and the equivalent core are shown in Fig. 1. For both geometries, the V-I characteristic is calculated and compared.

2.1   Simplifications

To make an analytical solution possible, some simplifications have to be assumed. First, only a 2D–geometry is calculated analytically which means, that the whole geometry extends from $-\infty$ up to ∞ in z-direction. A real 3D–geometry in simulations has to be built by straight parts.

The coil around the core is modeled by a sheet current. Because of this ideal modeling, we can assume that all flux remains within the coil. The eddy current approximation of Maxwell's equations ($\dot{\mathbf{D}} \ll \mathbf{J}$) is used and the material is linear.
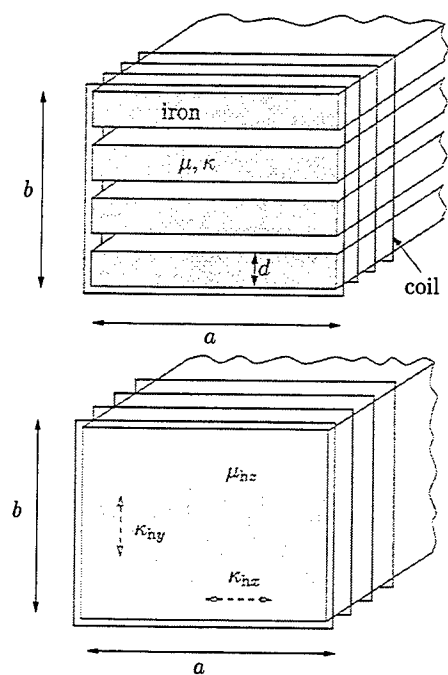
Figure 1: Laminated core with p sheets, and equivalent homogeneous core

2.2 Calculation of homogeneous core

The geometry for the calculation is shown in Fig. 2. This geometry can be considered as a linear system with an impressed sheet current as input quantity and the induced voltage in a loop around the core as output quantity. For both cores the response to a unit step function is calculated and compared. This was done because two linear systems with the same unit step response respond equally to arbitrary time functions as input signal. For easier calculation, not an ordinary unit step function was used, but the function depicted in Fig. 3.

The constitutive equations are:
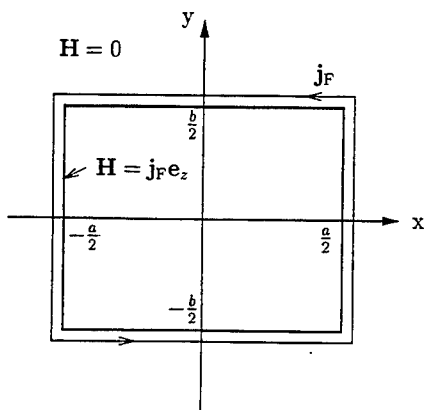
Figure 2: Geometry for the analytical solution

$$\mathbf{J} = \begin{pmatrix} \kappa_{\mathrm{h}x} & 0 & 0 \\ 0 & \kappa_{\mathrm{h}y} & 0 \\ 0 & 0 & \kappa \end{pmatrix} \mathbf{E} \tag{1}$$

$$\mathbf{B} = \begin{pmatrix} \mu & 0 & 0 \\ 0 & \mu & 0 \\ 0 & 0 & \mu_{\mathrm{h}z} \end{pmatrix} \mathbf{H} \tag{2}$$

The fields have the following components and dependencies:

$$\mathbf{H} = \begin{pmatrix} 0 \\ 0 \\ H(x,y,t) \end{pmatrix} \tag{3}$$

$$\mathbf{J} = \begin{pmatrix} J_x(x,y,t) \\ J_y(x,y,t) \\ 0 \end{pmatrix} \tag{4}$$

$$\mathbf{E} = \begin{pmatrix} E_x(x,y,t) \\ E_y(x,y,t) \\ 0 \end{pmatrix} \tag{5}$$

542

With this ansatz, the eddy current approximation of Maxwell's equations leads to the following parabolic differential equation:

$$\kappa_{\mathrm{h}x}\frac{\partial^2 H}{\partial x^2} + \kappa_{\mathrm{h}y}\frac{\partial^2 H}{\partial y^2} = \mu_{\mathrm{h}z}\kappa_{\mathrm{h}x}\kappa_{\mathrm{h}y}\dot{H}. \quad (6)$$
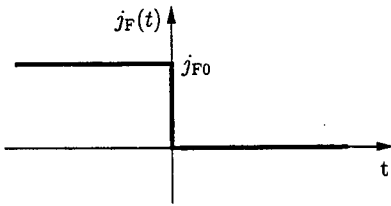
Figure 3: Time dependence of impressed sheet current used as excitation

This type of differential equation can be solved with given boundary values for all times and starting values given in the whole area where it shall be solved.

The sheet current represents an ideal coil. Therefore we can assume that there is no magnetic field outside. The impressed sheet current, together with $\mathrm{Curl}\,\mathbf{H} = j_{\mathrm{F}}(t)$, leads to appropriate boundary conditions.

A look at Fig. 3 shows that $H|_{\mathrm{border}} = 0$ for $t \geq 0$ is valid at the border of the core. For $t < 0$, we have a stationary problem which leads to following initial condition:

$$H(|x| \leq \frac{a}{2}, |y| \leq \frac{b}{2}, t = 0) = H_0 = j_{\mathrm{F}0} \quad (7)$$

Now eq. (6) can be solved with separation of variables:

$$H(x,y,t) = \sum_{i=0}^{\infty}\sum_{k=0}^{\infty} D_{ik}\cos\left(\frac{\pi}{a}(1+2i)x\right)$$

$$\cos\left(\frac{\pi}{b}(1+2k)y\right)e^{-\alpha_{ik}t} \quad (8)$$

with

$$D_{ik} = \frac{16H_0(-1)^{i+k}}{\pi^2(1+2i)(1+2k)} \quad (9)$$

$$\alpha_{ik} = \frac{(1+2i)^2\left(\frac{\pi}{a}\right)^2\kappa_{\mathrm{h}x} + (1+2k)^2\left(\frac{\pi}{b}\right)^2\kappa_{\mathrm{h}y}}{\mu_{\mathrm{h}z}\kappa_{\mathrm{h}x}\kappa_{\mathrm{h}y}} \quad (10)$$

The magnetomotive force can be calculated by:

$$V_{\mathrm{hom}} = \int_{y=-\frac{b}{2}}^{\frac{b}{2}}\int_{x=-\frac{a}{2}}^{\frac{a}{2}} \dot{\mathbf{B}}dxdy \quad (11)$$

$$V_{\mathrm{hom}} = \frac{64}{\pi^4}\mu_{\mathrm{h}z}H_0ab\sum_{i=0}^{\infty}\sum_{k=0}^{\infty} C_{ik}\frac{\mathrm{d}}{\mathrm{d}t}e^{-\alpha_{ik}t}, \quad (12)$$

$$C_{ik} = \frac{(-1)^{i+k}}{(1+2i)^2(1+2k)^2}. \quad (13)$$

2.3 Calculation of laminated core

The laminated core is put together by single plates. For each single plate we know the solution already. We can take equations (8), (9), (10) and set $\mu_{\mathrm{h}z} = \mu$, $b = d$ and $\kappa_{\mathrm{h}x} = \kappa_{\mathrm{h}y} = \kappa$. The sheet current does not need to be located directly on the surface. We assume it has a distance of half the spacing between two plates. This does not change the boundary conditions. The solution in one plate is given by:

$$H(x,y,t) = \sum_{i=0}^{\infty}\sum_{k=0}^{\infty} D_{ik}\cos\left(\frac{\pi}{a}(1+2i)x\right)$$

$$\cos\left(\frac{\pi}{d}(1+2k)y\right)e^{-\alpha_{ik}t} \quad (14)$$

with

$$D_{ik} = \frac{16H_0(-1)^{i+k}}{\pi^2(1+2i)(1+2k)} \quad (15)$$

$$\alpha_{ik} = \frac{(1+2i)^2\left(\frac{\pi}{a}\right)^2 + (1+2k)^2\left(\frac{\pi}{b}\right)^2}{\mu\kappa} \qquad (16)$$

Each plate has a magnetic field of zero outside the sheet current. To get the solution of the laminated core we superpose the solutions of the single layers. Two plates are brought together in a way that the sheet currents of the single plates just touch each other and compensate themselves between the layers. Thus, a sheet current around the whole core accrues. Such a proceeding means a not quite justified superposition of boundary conditions, since the electric field is not zero outside the sheet currents although the magnetic field is. Therefore, a numerical verification of the result will be necessary.

The gaps between the layers are quite small and the relative permeability of iron is much greater than one. Therefore, the flux through the gaps between the plates can be neglected.

$$V_{\text{hom}} = p \int\limits_{y=-\frac{d}{2}}^{\frac{d}{2}} \int\limits_{x=-\frac{a}{2}}^{\frac{a}{2}} \dot{B} \, dx \, dy \qquad (17)$$

$$V_{\text{lam}} = p\frac{64}{\pi^4}\mu H_0 ab \sum_{i=0}^{\infty}\sum_{k=0}^{\infty} C_{ik}\frac{\mathrm{d}}{\mathrm{d}t}e^{-\alpha_{ik}t} \qquad (18)$$

2.4 Determination of equivalent parameters

Now V_{hom} (eq. 12) and V_{lam} (eq. 18) can be set equal to determine $\mu_{\text{h}z}$, $\kappa_{\text{h}x}$, $\kappa_{\text{h}y}$. The two voltages are equal if

$$\mu_{hz} = \mu p\frac{d}{b}. \qquad (19)$$

There are two possibilities for the choice of $\kappa_{\text{h}x}$ and $\kappa_{\text{h}y}$. First,

$$\kappa_{\text{h}x} = \kappa\frac{d}{pb}, \qquad \kappa_{\text{h}y} = \kappa\frac{b}{pd}, \qquad (20)$$

and second,

$$\kappa_{\text{h}x} = \kappa\frac{a^2}{pbd}, \qquad \kappa_{\text{h}y} = \kappa\frac{bd}{pa^2}, \qquad (21)$$

The second choice of parameters (21) has the disadvantage that it depends on the width a. This means that a geometry with various widths of the iron core has to be split up in various parts with different constitutive parameters. So parameter setting (20) should be preferred. Beyond, it can be interpreted physically.

3 Interpretation

For very small air gaps, parameter setting (20) means that $\kappa_{\text{h}y} \approx \kappa$, whereas $\kappa_{\text{h}x} \approx \kappa/p^2$. (For parameter setting (21) the ratio of magnitudes is converse.) Fig.'s 4 and 5 insinuate that in y-direction in both cores the same cross-section is available for the current. Therefore the same conductivity can be used to achieve the same voltage.

In x-direction, the whole current is restricted to a cross-section of half the thickness of one layer, due to the lamination. In the equivalent homogeneous core a cross-section of $b/2$ is available. To compensate this, the conductivity has to be reduced to one p-th. Additionally, the current flows $2p$ times through this small cross-section, whereas it flows only twice through the bigger cross-section available in the homogeneous core. Thus the conductivity has to be reduced once more to the p-th.

4 Numerical verification

The practical validity of the parameter settings (20) was verified with the W3 [3] module of MAFIA [2], a numerical field analysis tool which solves the complete Maxwell equations in frequency–domain. For all simulations the same excitation current was used. The induced
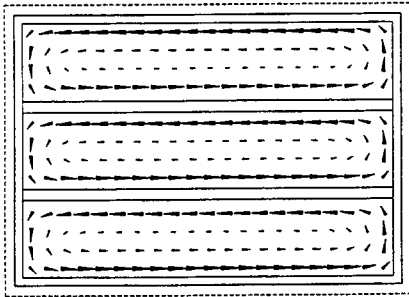
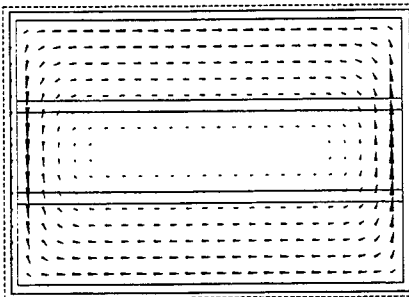Figure 4: Imaginary part of eddy current distribution in a laminated core

Figure 5: Imaginary part of eddy current distribution in an equivalent homogeneous core

Table 1:

δ	$\frac{\mathrm{Re}(V_{\mathrm{hom}}-V_{\mathrm{lam}})}{\mathrm{Re}(V_{\mathrm{lam}})}$ / %	$\frac{\mathrm{Im}(V_{\mathrm{hom}}-V_{\mathrm{lam}})}{\mathrm{Im}(V_{\mathrm{lam}})}$ / %
d	0.06	0.17
$\frac{d}{2}$	0.04	0.18
$\frac{d}{4}$	-0.20	0.17

Table 2:

p	$\frac{\mathrm{Re}(V_{\mathrm{hom}}-V_{\mathrm{lam}})}{\mathrm{Re}(V_{\mathrm{lam}})}$ / %	$\frac{\mathrm{Im}(V_{\mathrm{hom}}-V_{\mathrm{lam}})}{\mathrm{Im}(V_{\mathrm{lam}})}$ / %
3	0.20	0.21
4	0.00	0.19
5	-0.27	0.2

Further, it was verified for different total thicknesses b. The relative differences are shown in Tab. 3. The other parameters are the same as above.

Table 3:

b/mm	$\frac{\mathrm{Re}(V_{\mathrm{hom}}-V_{\mathrm{lam}})}{\mathrm{Re}(V_{\mathrm{lam}})}$ / %	$\frac{\mathrm{Im}(V_{\mathrm{hom}}-V_{\mathrm{lam}})}{\mathrm{Im}(V_{\mathrm{lam}})}$ / %
69	0.04	0.18
85	0.16	0.20
100	0.20	0.21

voltages of the laminated and the equivalent homogeneous core are compared for different skin depths δ. Tab. 1 shows the relative difference between the two models. The geometry and constitutive parameters are: $a = 0.1\,\mathrm{m}$, $b = 0.069\,\mathrm{m}$, $d = 0.021\,\mathrm{m}$, $p = 3$, $\mu_r = 500$, $\kappa = 10^6\,\mathrm{S/m}$. The same mesh was used for each of the two calculations to be compared, in order to avoid numerical differences.

The parameter settings (20) were also verified for different numbers of sheets p. The result is shown in Tab. 2 for a total thickness $b = 0.1\,\mathrm{m}$, an air gap of 3 mm and a skin depth of $\delta = d/2$. The other geometry and constitutive parameters are the same as above.

The second parameter setting (21) was verified for one example and showed exactly the same magnetomotive force than the simulation with the first parameter setting (20).

The choice of model parameters (20) was also applied to an example where the premises for the derivation are strongly violated. A core was used where the width a is periodically widening and narrowing in z-direction (see Fig. 6). The x,y-geometry is the same as in Fig. 1 The other geometry and constitutive parameters are: $b = 0.069\,\mathrm{m}$, $d = 0.021\,\mathrm{m}$, $p = 3$,

$\mu_r = 500$, $\kappa = 10^6\,\text{S/m}$. The simulation was restricted to the range between the two thick lines. There the boundary condition $H_t = 0$ was applied. This geometry is still easy enough to simulate also the laminated core.
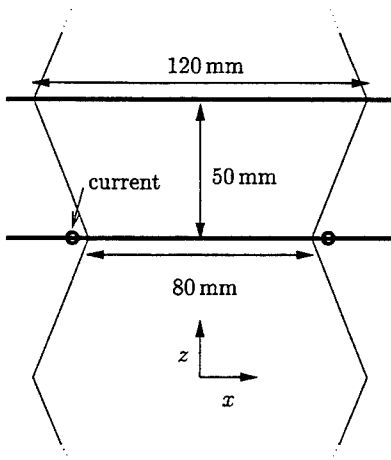
Figure 6: Geometry of example where premises for derivation are strongly violated

Table 4:

δ	$\frac{\text{Re}(V_{\text{hom}}-V_{\text{lam}})}{\text{Re}(V_{\text{lam}})}$ / %	$\frac{\text{Im}(V_{\text{hom}}-V_{\text{lam}})}{\text{Im}(V_{\text{lam}})}$ / %
d	-11.07	0.15
$\frac{d}{2}$	-10.25	0.16
$\frac{d}{4}$	-9.07	0.14

Since the analytical 2D-solution is independent of μ_{hx}, μ_{hy} and κ_{hz}, it does not provide any values for these. There are good reasons to set $\mu_{hx} = \mu_{hz}$ and $\mu_{hy} = \mu$, but κ_{hz} remains undetermined. For this simulation, $\kappa_{hz} = \kappa_{hx}$ was taken.

The results are shown in Tab. 4. The relative differences in the imaginary parts of the voltages are negligible, since it is mainly influenced by the equivalent permeability. The real parts of the voltages, representing the eddy current losses show a relative difference of about 10 %. So even though the premises are more strongly violated than in many practical applications, the proposed simulation model yields useful results.

5 Conclusion

Replacing a laminated iron core by an equivalent homogeneous core with anisotropic constitutive parameters reduces the computational effort for eddy current simulations significantly. The presented simulation model has some important advantages. First, it is independent of the width a, which is good for varying cross-sections. Then, the parameter setting is valid for the whole frequency range (as long as we can neglect wave propagation). Finally, it is also independent of the frequency, which is a strong advantage for time–domain simulations.

References

[1] P. Hahne, R. Dietz, B. Rieth, T. Weiland: *Determination of Anisotropic Equivalent Conductivity of Laminated Cores for Numerical Computation*, IEEE Transactions on Magnetics, Vol. 32, No. 2, May 1996, p. 1184–1187

[2] T. Weiland: A Discretisation Method for the Solution of Maxwell's Equations for Six-Component Fields, AEÜ 31 (1977), p.116-120

[3] P. Hahne, T. Weiland: *3D Eddy Current Computation in the Frequency Domain Regarding the Displacement Current*, IEEE Transactions on Magnetics, Vol. 28, No. 2, March 1992, p. 1801-1804

Barring Characteristic of an Ion Shutter

Berndt M. Cramer, Dieter A. Mlynski

Institut für Theoretische Elektrotechnik und Messtechnik,
Universität Karlsruhe
Kaiserstr. 12, D-76128 Karlsruhe, Germany
E-mail: cramer@tem.etec.uni-karlsruhe.de

Abstract

Ion shutters commonly have dissatisfying barring characteristics. Especially an ion shutter used in ambient air has considerable zero offsets in the ion current, which is very deranging if the current signal has a small amplitude at the outset. The aim of our work is to predict the current offset and to present a powerful tool which allows to optimize the geometry of the ion shutter interactively. The tool is not limited to ion mobility spectrometry but it will be described with it.

KEYWORDS: Ion mobility spectrometer, ion shutter, geometry optimization, cross field dependence.

1 Introduction

Ion mobility spectrometry (IMS) is a technique for the detection of trace gases in ambient air. The heart of an IMS cell is illustrated in figure 1. The ion shutter divides the cell into two contiguous
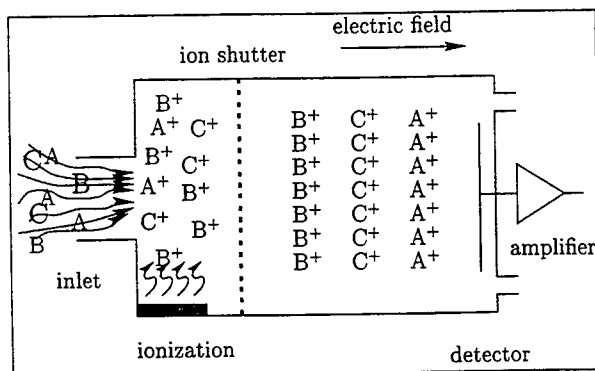
Figure 1: Basic structure of an ion mobility spectrometer

tubes: on the left the reaction tube where the ionization takes place and on the right the drift

tube. The shutter grid normally annihilates the ions at the end of the reaction tube. The shutter consists of thin wires. It is periodically opened to let a quantity of ions drift down the drift tube. The arriving ions are converted to the signal current by the detector. An amplifier produces an equivalent signal voltage. The time passed from the opening of the shutter until the center of the pulse arrives at the detector is called drift time. It is inversely proportional to the ion mobility which is an attribute that allows to discriminate the different sorts of ions.

The amplitude of the signal contains the information of quantity (of trace gas). The signal is made up of Gaussian peaks and has a considerable offset which is caused by the incomplete annihilation of the ions by the shutter [1, 2].

In a simple model one can determine the paths of ions, following the gradient of the potential. However this leads to no offset current in the detector signal and the cutoff voltage would depend on the strength of geometry. If we neglect the Maxwell distribution of the velocities within a gas we can give an estimation of the maximum of the grid voltage at which no ions can pass through:

$$\Delta V < 2bE_{\text{drift}}$$

ΔV is the voltage between two adjacent grid wires. E_{drift} is the strength of the electric drift field and b is the thickness of the grid. With this model no cutoff voltage can be found. A reasonable model must take into account the distribution of velocity .

2 Strategy

To obtain the characteristic of the shutter we proceed in three main steps:

1. With the commercial finite volume integration program MAFIA [3] the field calculation is performed. MAFIA has no limitation in mesh points. The geometry data is changed easily which is important for the study of the influence of the geometry on the characteristic of the shutter.

2. The field data taken from MAFIA are post-processed for the following particle simulation.

3. Afterwards the particle simulation is started. The number of annihilation of ions is counted separately for any material. Any particle path can be traced.

The modular structure allows us to compare different strategies.

3 Field Calculation

We perform the field calculation using the measurements shown in figure 2. In a resistant layer encasing the drift tube is a constant current. Therefore boundary condition curlE = 0 at the
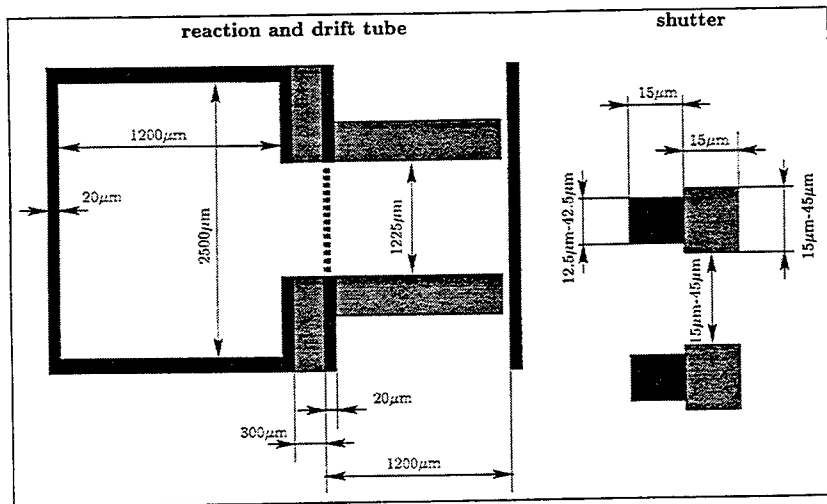
Figure 2: Measurements for field calculation

tube wall enforces steady tangential component of the electric field. It keeps the inner field nearly homogeneous. Particularly the inhomogeneity in the electrode direction can be neglected.
The different dimensions of the shutter grid (μm) and the reaction tube (cm) requires already 150,000 mesh points.
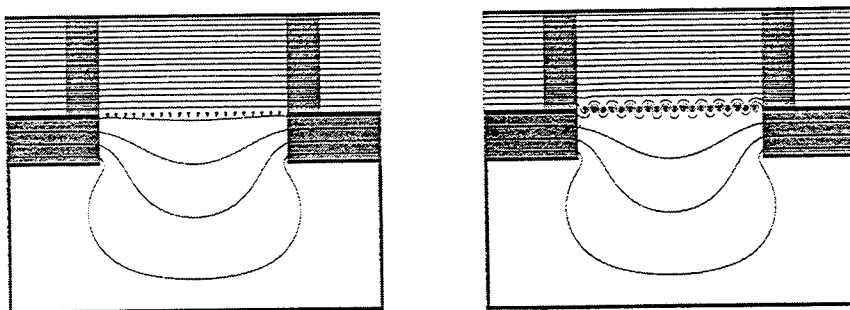
Figure 3: Contour plot of the IMS at 0 and $\pm$30 Volts, respectively

The field calculation is done on a DEC Alpha 200 workstation, 166 MHz, 128 MByte RAM. Depending on the required accuracy the computation time is about half an hour. We compute the field distribution varying the grid voltage from 0 Volt to $\pm$ 30 Volts in steps of 2.5 Volts.
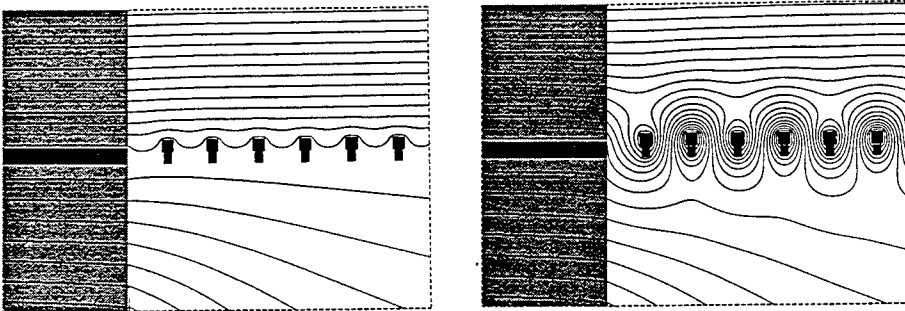
Figure 4: Detailed Contour plot of shutter grid at 0 and ±30 Volts, respectively
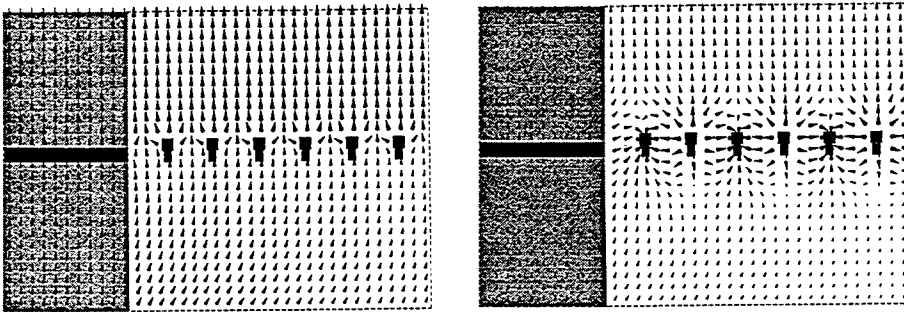
Figure 5: Detailed Field plot of the IMS, of shutter grid at 0 and ±30 Volts, respectively

The voltage is understood as difference between the potential of the grid wire and the potential corresponding to the location. The results are shown in figures 3, 4, 5. The gray parts symbolize the insulation and the drift tube walls ($\varepsilon_r = 5.1$). Figure 4 is a detailed contour plot at the fit of the tubes and figure 5 shows the electric field vectors at the same location.

4 Particle Simulation

The simulation starts by emitting a given amount of ions from an ion source in the reaction tube near the shutter by so-called "source materials". We restrict the simulation area to a small region around the shutter (shown in fig. 6) in order to limit the computation time.

The advanced model uses statistic distribution of the following variables in order to form a rea-
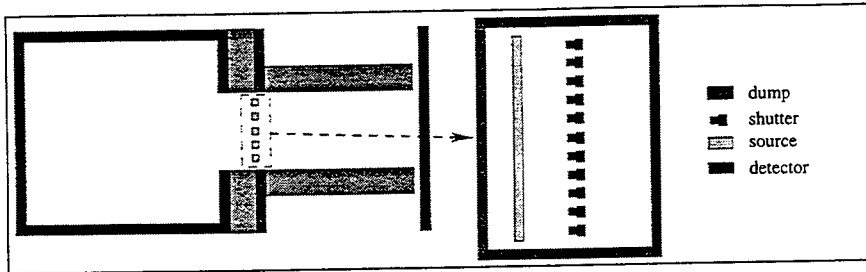
Figure 6: Geometric model used for particle simulation

sonable model:

- the velocity of the ions (Maxwell distribution),
- the initial direction of the molecules (homogeneous distribution),
- the distance between two collisions (free path).
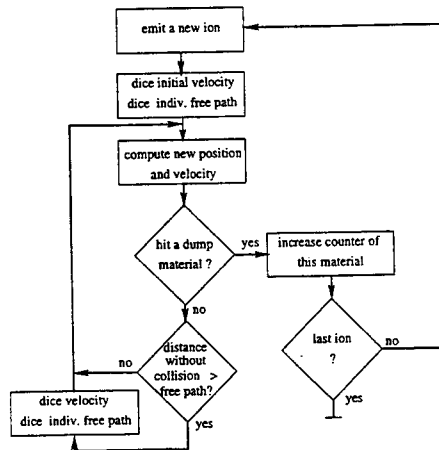
Figure 7: Model used for particle simulation

This enables us to calculate the paths of the ions considering the statistic distribution. An ion having hit the wall or shutter, so-called "dump materials", is treated like a neutral gas molecule thereafter. The number of ions hitting the wall is registered for every dump material of the device (detector, shutter and tube walls). Otherwise the computation follows the flow chart in figure 7.

5 Results

The following table shows some parts of our results of the simulation. The source emitted 300,000 ions. The potential difference of the drift field is 1200 Volts.

	measurements of shutter (see fig. 2)			
	15/45μm	.	30/30μm	
ΔV in V	detector annihilation rate in %	shutter annihilation rate in %	detector annihilation rate in %	shutter annihilation rate in %
0.0	44.89	55.10	28.97	61.12
2.5	37.77	62.20	19.77	80.22
5.0	27.22	72.77	6.24	93.75
7.5	12.32	87.67	1.32	98.66
10.0	1.43	98.56	0.38	99.60
12.5	0.00	99.99	0.00	99.99
15.0	0.09	99.90	0.12	99.88
20.0	0.02	99.97	0.06	99.94
25.0	0.02	99.98	0.04	99.96

ΔV is the difference between a shutter wire and the potential corresponding to the location of the shutter in the drift field. The minimal difference between the sum of the annihilation rates for the shutter and the detector and 100% makes the rate of ions annihilated by the tube walls. As expected the grid with the higher space filling has a lower pass through.

We found a minimum of ions passing through the shutter unexpectedly not at the end of the voltage range but at 12.5 Volts. Our results confirm to experimental results measured by the industrial partner *Daimler-Benz R&D* in Munich/Germany.

Figure 8 shows the paths traced by the program. The edges are a result of a new dice of velocity and direction.

direction of drift   direction of drift
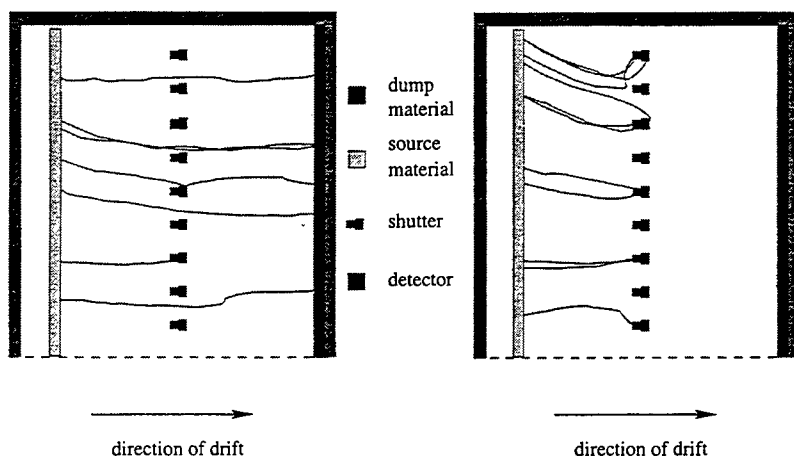
Figure 8: Paths of ions at 0V and 30V, respectively

6   Conclusion

We have presented a new simulation strategy which allows the computation of paths, gain of ions and forecasts of the barring characteristics of the ion shutter. Thus it is possible to optimize the geometry and the voltage amplitudes of the ion shutter grid before manufacturing. The software interfacing MAFIA compatible data format replaces time and money consuming series of prototypes.

The presented tool is a part of a comprehensive simulation tool for the complete ion mobility spectrometer, computing paths and gain of ions from their generation to their annihilation on the detector or as a loss at the tube walls.

References

[1] Joseph E. Roehl. Environmental and Process Applications for Ion Mobility Spectrometry. *APPLIED SPECTROSCOPY REVIEWS*, 26(1,2):1–57, 1991.

[2] R. Wernlund E. Mason. *Plasma Chromatography*. Plenum Press, 1984.

[3] T. Weiland. *MAFIA*. The MAFIA Collaboration, Darmstadt, 1994.

STABILITY ANALYSIS OF RE-ENTRANT MULTI-TURN TOROIDAL/HELICAL ELECTRON ORBITS IN STRONG-FOCUSING ALTERNATING-GRADIENT MAGNETIC FIELDS.

Ross A. Speciale

Redondo Beach, California

polytope@msn.com

A new, rather revolutionary type of High Power Microwave (HPM) Source, presently under development, synergistically combines the basic principles of the Relativistic Klystron Amplifier (RKA) with those of Electron Storage Rings [1].

This new type of electron device simultaneously performs the functions of a High Power Microwave Amplifier, and of a Frequency Multiplier, by circulating a sharply-bunched Intense Relativistic Electron Beam (IREB) along a re-entrant, multi-turn, toroidal/helical orbit, each orbit turn being separately guided and strongly-focused by an Alternating-Gradient (AG) magnetic field (Figure 1).

The new High Power Microwave Amplifier attains very high efficiency, by performing 100 % beam-energy recovery after microwave-power extraction, is suited to high duty-cycle applications, and exhibits high spectral purity, because of the well-known phase-stability of the electron orbital motion in storage rings.

A guiding magnetic field has been designed that admits a specified, re-entrant, multi-turn, toroidal/helical electron *"equilibrium-orbit"*, defined by the parametric equation :

$$r(\varphi,\theta) = x(\varphi,\theta) \cdot i + y(\varphi,\theta) \cdot j + z(\varphi,\theta) \cdot k \qquad (1)$$

where φ is the azimuth angle around the torus axis, θ is the helical *"wrapping angle"* around the *"body"* of the torus, and the three Cartesian components of the position-vector r are given by :

$$x = (R + r\cos\theta)\cos\varphi \qquad (2)$$

$$y = (R + r\cos\theta)\sin\varphi \qquad (3)$$

$$z = r\sin\theta \qquad (4)$$

while the linear relation between the angles φ, and θ is determined by the integer number n of re-entrant turns :

$$\theta = \frac{n-1}{n} \varphi \qquad\qquad (5)$$

The integer n in (5) is the *minimum* number of turns around the torus axis that brings the re-entrant, multi-turn equilibrium orbit to close on itself, while it is $0 \le \varphi \le 2\,n\,\pi$.

The stability of the *actual* electron motion, in the vicinity of the equilibrium orbit, is being analyzed in a moving, Cartesian reference frame that follows the *"equilibrium-electrons"*, by simultaneously rotating around the torus *axis* , and around its *"body"*. This rotating, right-handed, Cartesian reference frame has its Z-axis tangent to the toroidal/helical equilibrium orbit and oriented in the direction of electron motion, while the X-axis is directed outward of the torus, along its minor radius r.

A relativistically-covariant Hamiltonian formulation of the electronic oscillatory motion [2 , 3], about the equilibrium orbit in the directions of the three axes of the rotating reference frame, is being developed assuming the presence of an appropriate azimuthally periodic strong-focusing magnetic field, with a gradient that alternates, around the torus, in the directions of both the X, and Y axes of the moving reference frame.

This relativistically-covariant formulation involve the time and space coordinates in a completely symmetric way, so that any of them can be selected as the independent variable.

In a time-independent magnetic field the analysis is considerably simplified by selecting the azimuth angle φ (around the torus axis) as the independent variable of the motion.

REFERENCES.

[1] Speciale R. A. ,"High Power Microwave Amplification by High-Intensity Relativistic Electron-Beam Storage Rings," Proceedings of the 12th Review of Progress in Applied Computational Electromagnetics, Monterey, California, March 18-22, 1996, pages 464-468.

[2] Jackson J. D. ,"Classical Electrodynamics," Second Edition, Chapter 12, pages 571-613, John Wiley & Sons, Inc. , New York, N. Y. .

[3] Goldstein H. ,"Classical Mechanics," Second Edition, Chapters 7, 8, 9, and 11, Addison-Wesley Publishing Company, Inc. , Reading, Massachusetts, 1980.

3D PLOT OF THE TOROIDAL–HELICAL ORBITS

X-AXIS

Y-AXIS

Z-AXIS
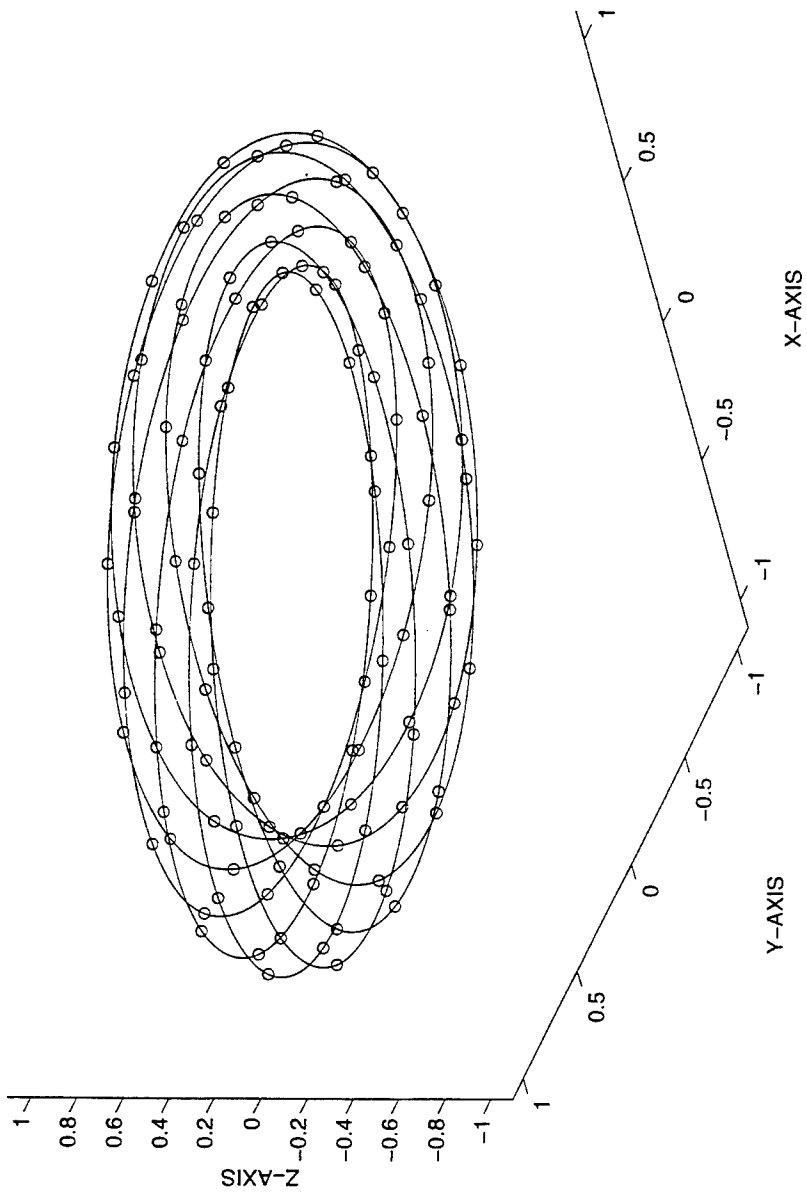
SESSION 10:

FINITE ELEMENT
ANALYSIS

Chairs: J. Brauer and Z. Cendes

557

FINITE-ELEMENT AND METHOD-OF-MOMENTS ANALYSES
OF AN ULTRAWIDE-BANDWIDTH TEM HORN

M.H. Vogel
Ansoft Corporation
Four Station Square - Suite 660
Pittsburgh, PA 15219
e-mail vogel@ansoft.com

1. Introduction

Many applications require radiation of a very short, ultrawide-bandwidth pulse of electromagnetic energy out to large distances. These applications include radar target detection in a cluttered environment, such as targets close to the sea surface or hidden by foliage, and radar target identification by means of high resolution, for targets such as military vehicles or buried objects. Short pulses for which the ratio between the highest and the lowest frequencies in the spectrum, at the -3 dB points, are of the order of 100:1 without dispersion are often desirable. To radiate such an ultra-wide-bandwidth pulse, a TEM horn can be used.

Since a TEM horn can, for the lowest frequencies, be modeled as a transmission line, it presents an open circuit for the low-frequency part of the pulse [1]. As a result, a large part of the pulse energy may be reflected towards the source and may damage it. A remedy is to connect a resistive termination to the horn, so that it will no longer act as an open circuit a low frequencies. The shape of this termination is important, as it significantly affects low-frequency performance [2]. It is possible, by careful design, to double the low-frequency radiation in the forward direction and cancel it in the backward direction.

In section 2 of this paper, the design of the low-frequency compensation is presented. As we were concentrating on the lowest frequencies, a method-of-moments code for electrostatics was used. In section 3, results of NEC-2 simulations for low and intermediate frequencies are discussed. With NEC-2, antenna patterns could be obtained successfully. However, the antenna impedance, an important parameter in any antenna design, could not be obtained for the low frequencies, while intermediate-frequency results were questionable. As is outlined in section 4, however, with Ansoft's finite-element code High-Frequency Structure Simulator (HFSS) the author has been able to obtain the desired data.

2. Design of the low-frequency compensation

For low frequencies (wavelength much larger than antenna dimensions), the TEM horn will have poor impedance matching to the transmission line. As a consequence, most of the power will be reflected toward the source and may damage it. Further, the radiation pattern of a TEM horn will be similar to that of a small dipole: a doughnut-shaped pattern, in which the horn radiates just as much power backwards and sideward as it does in the forward direction. In order to eliminate reflections back into the source, a resistive termination can be added to the horn. This termination should close the

current loop and provide a matched load to the transmission line. The shape of the resistive termination is important, as it significantly affects the low-frequency radiation pattern. A current loop adds, for low frequencies, a magnetic dipole moment $\underline{m}$ to the existing electric dipole moment $\underline{p}$. When the magnitudes are matched, such that $|\underline{m}|=c|\underline{p}|$, the antenna will have a cardioid antenna pattern in the $\underline{p}\times\underline{m}$ direction and no radiation in the $-\underline{p}\times\underline{m}$ direction. Of course, the loop should be designed in such a way that the cardioid beam points in the forward direction and that the radiation in the backward direction is zero. Fig. 2.1 depicts a basic design that, when the dimensions are chosen properly, will achieve the following objectives:

- Matched impedance for low frequencies
- Good directivity for low frequencies
- Large radiation bandwidth
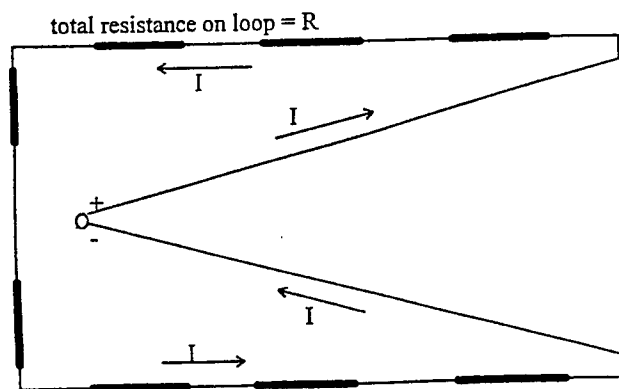
Fig. 2.1. Basic design of a TEM horn with low-frequency compensation

The actual low-frequency compensation was designed with the Method of Moments for electrostatic fields, as explained by Harrington [3]. First, the shape of the structure and the distribution of the resistors were specified. Then, given the voltage distribution, the charge distribution was obtained with the Method of Moments. From this, the electric dipole moment can be calculated. The magnetic dipole moment follows from the current and the loop area. In an iterative procedure, the shape of the structure and the distribution of the resistors were varied until the matching condition had been satisfied. A more detailed description of the method and of various designs is presented in [4].The final design is depicted in Figure 2.2. It is a design with a finite ground plane instead of a complete horn, as this is the kind of antenna that was to be built after the analysis.

top view   side view
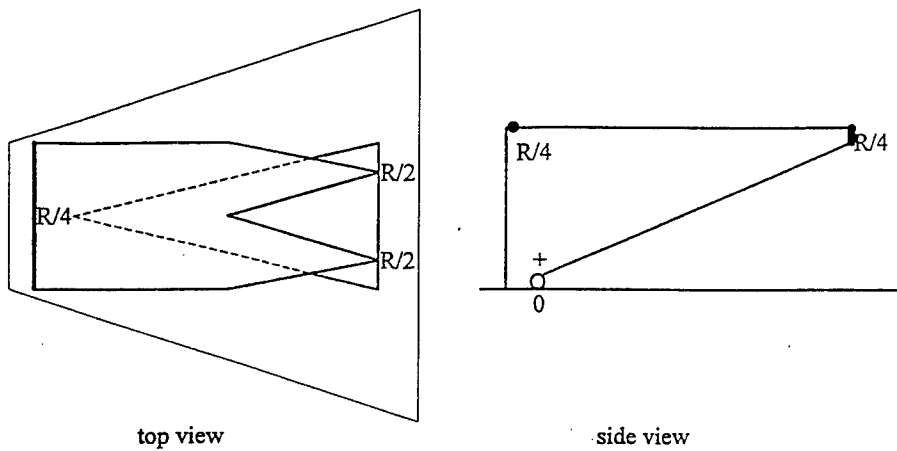
Fig. 2.2. The final design

In this final design, the dimensions are as follows: The aperture is 50 cm high and 50 cm wide. The distance from the apex to the aperture is 137 cm. The ground plane extends 175 cm in front of the apex and has a maximum width of 150 cm. The compensating loop runs 52.5 cm above the ground plane and 10 cm behind the apex. The value of R is 240 Ohm. The antenna pattern at 5 MHz, calculated by Ansoft HFSS (to be discussed in section 4) is shown in Figure 2.3.
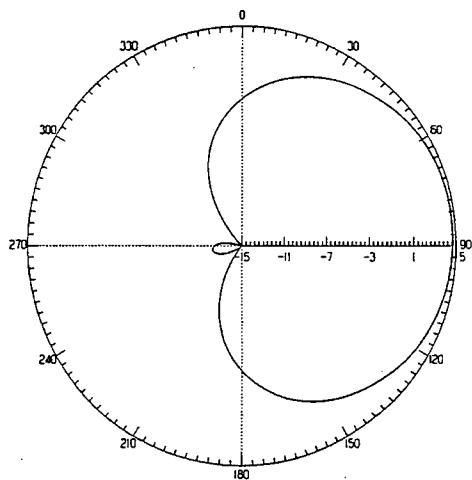
Fig. 2.3. Antennapattern at 5 MHz for the horn with low-frequency compensation

560

The final design could just as well be constructed with one or two wires and an appropriate resistor distribution. The reason for the present, more complicated design is the following: Fields traveling in the region between the antenna plate and the loop will, in this design, be traveling in a structure that looks like a *receiving* TEM horn with a matched load. Hence, they will be absorbed by the load instead of radiating in unwanted directions. This improves the antenna directivity.

3. NEC-2 results

Having obtained a design that meets the requirements in the low-frequency limit, it is desirable to investigate its behaviour in the intermediate-frequency region. In this case, the intermediate-frequency region is considered to range roughly from 15 MHz to 600 MHz. At the low end, the antenna size is about one-tenth of a wavelength, and the front-to-back ratio, defined as the ratio of the powers in the forward and backward directions, is better than 10 dB. At the high end, the aperture is one wavelength high and wide, and the antenna pattern is showing clear high-frequency characteristics: a forward pointing beam with the sidelobes more than 10 dB down.

The antenna with the compensating loop has been modeled in NEC-2 with a wire mesh. The guidelines described by Moore and Pizer [5] for constructing a wire mesh have been taken into account. For the lower frequencies, the number of segments was about 550, for the higher frequencies is was about 2200. Because of symmetry, only half of the antenna needed to be modeled. Computation times on a Sun Sparc-2 workstation were a few minutes per frequency point for the coarser mesh and a few hours per frequency point for the finer mesh. The largest job needed 50 Mbyte of RAM. The front-to-back ratio as a function of frequency, calculated with NEC-2, is presented in figure 3.1. A more elaborate presentation of the NEC-2 results can be found in [6].
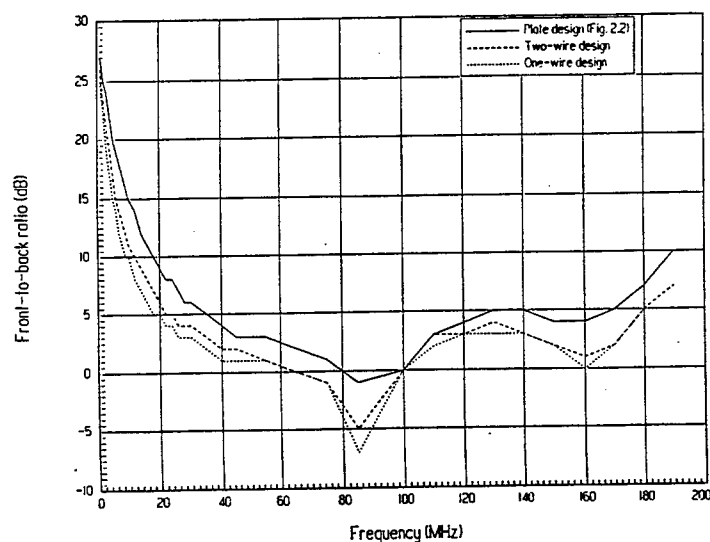
Fig. 3.1.   Front-to-back ratio as a function of frequency of the TEM horn with the loop

As is pointed out by Moore and Pizer [5], the values calculated by NEC-2 for the individual currents in the wire segments cannot be trusted. Sometimes loop currents are observed that have no physical meaning. Therefore, NEC-2 near-field results can be meaningless, while far-field results are still okay, because the errors tend to integrate out. As a consequence, antenna patterns computed by NEC-2 are likely to be accurate. Two patterns will be presented in the next section, together with finite-element results. The antenna impedance from NEC-2, however, can be very inaccurate. In principle, the antenna impedance can be calculated from the transmission line impedance and the S parameter. As currents in individual segments, as calculated by NEC, including the segments in the source region, can be very inaccurate, the S parameter cannot be determined. The inaccuracies in individual currents have indeed been observed, especially for frequencies below 45 MHz.

4. Ansoft HFSS results

The TEM horn, with and without low-frequency computation, has been modeled with Ansoft's finite-element software package HFSS. Thin metal plates have been modeled as two-dimensional objects, so that the entire structure can be meshed more efficiently. In HFSS, the radiation boundary, or absorbing boundary, can be placed at only a fourth of a wavelength from the antenna, and can be conforming to the antenna shape. This is an enormous advantage over finite-element packages in which the radiation boundary has to be spherical or more than a quarter wavelength away from the antenna. The mesh generator generates the mesh without user interference, and refines the mesh iteratively in regions where this is necessary. This is determined by the software itself by evaluating the field solutions that are obtained. The user can set a maximum number of iterations and a convergence criterion for the S matrix. When the solution has reached the desired accuracy, HFSS can perform a fast frequency sweep over a user-specified frequency range. This fast frequency sweep is based on a reduced-order pole-zero model, and can provide approximate solutions for a wide range of frequencies without having to solve the problem for each desired frequency point. Depending on the problem at hand, the fast frequency sweep easily reduces the computation time by an order of magnitude or more.

In order to check results from HFSS, front-to-back ratios and antenna patterns as calculated by HFSS have been compared to those calculated by NEC. The agreement is good. Figure 4.1 shows the pattern at 45 MHz; Figure 4.2 shows the pattern at 110 MHz. Note that these patterns are very different from both the behaviour at the low-frequency end and that at the high-frequency end.

From a calculated field solution, HFSS also determines the S matrix, which in this case is just one parameter. From the fields in the driving transmission line, HFSS calculates the transmission-line impedance. From these two quantities, the antenna input impedance is determined. Results are presented in Figures 4.3 and 4.4.

Note that the S parameter at the lowest frequencies is one for the horn without compensation while it is close to zero for the horn with compensation. This arises from the fact that in the horn without compensation all of the low-frequency power is reflected towards the source, while in the horn with compensation it is not reflected at all, but mostly absorbed by the resistors. What is not absorbed by the resistors is radiated in the forward direction, as shown in Fig. 2.3. The impedance of the horn with compensation is 120 Ohms, which means it is perfectly matched to the transmission line, while the impedance of the horn without compensation is extremely high, reflecting the fact that the horn provides an open end to the transmission line. In fact, this open end is a capacitance.
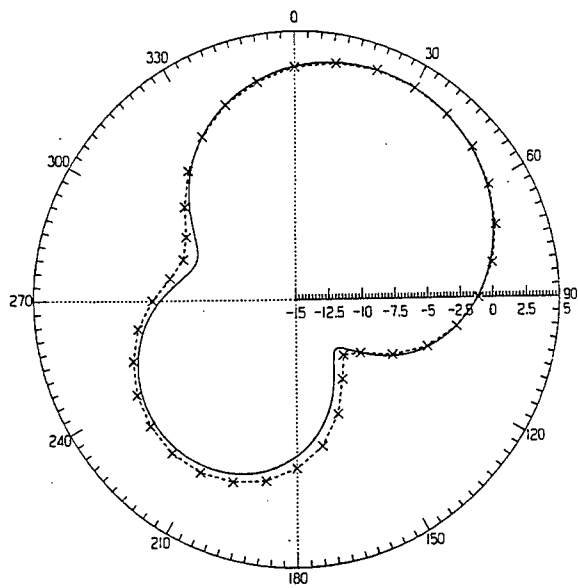
Fig. 4.1. Antenna pattern at 45 MHz. Solid line: HFSS, dotted line: NEC
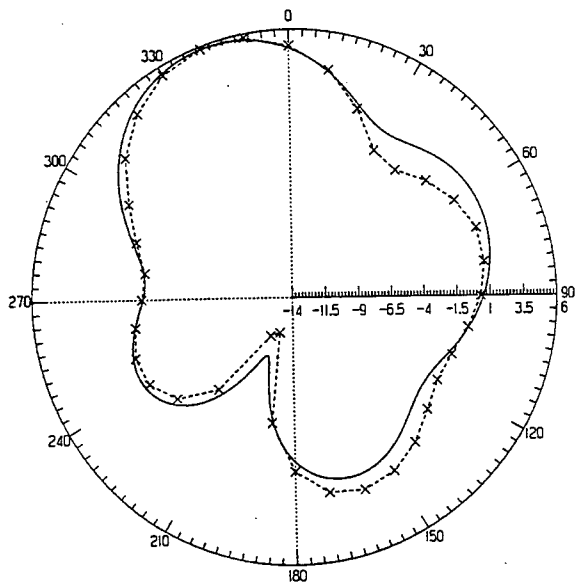

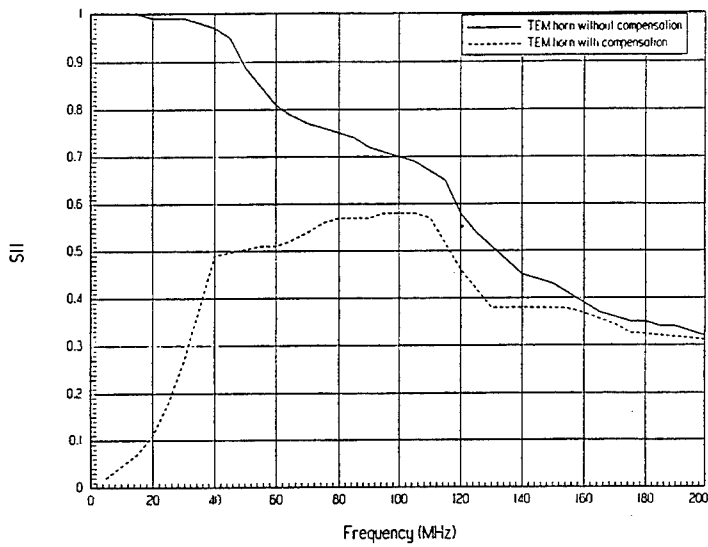Fig. 4.2. Antenna pattern at 110 MHz. Solid line: HFSS, dotted line: NEC

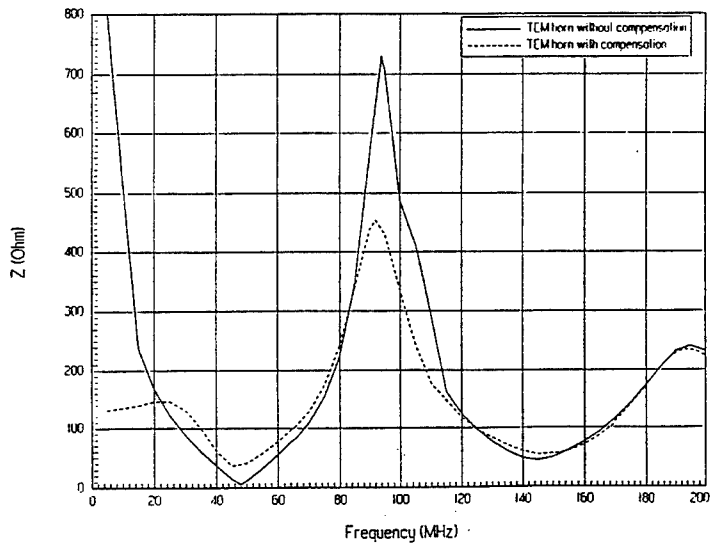Fig. 4.3. S parameters for the horn with and without compensation

Fig. 4.4. Input impedances of the horn with and without compensation

With increasing frequency, the S parameters of the horn with and without compensation approach each other, and above 110 MHz they both decrease, reflecting the fact that for higher frequencies both horns become good radiators, and the presence of the compensation does not make much difference anymore. As an example of the results above 200 MHz, in the frequency range from 400 to 600 MHz the S parameter for the antenna with compensation decreases monotonically from 0.20 to 0.11.

For both horns , we notice minima in Z at 48 and 144 MHz, and a peak at 96 MHz. At the minima, the field that is reflected back into the transmission line has reversed its phase relative to the driving field at the antenna apex, and the antenna partly behaves as a short with low impedance. At the peak, the field that is reflected has the same phase as the driving field at the antenna apex, and the antenna partly behaves as an open circuit. Note that the horn with compensation has a better-behaved impedance, i.e. the oscillations are smaller. With increasing frequency, the maxima and minima become less pronounced, as the antenna radiates a larger fraction of the input power. For example, the impedance of the horn with compensation has a maximum of 179 Ohms at 430 MHz and a minumum of 84 Ohms at 483 MHz. The next oscillation shows a smaller maximum of 158 Ohms at 537 MHz and a larger minimum of 98 Ohms at 591 MHz. At higher frequencies, this oscillation is expected to become a smaller oscillation around an impedance that is very close to the transmission-line impedance. Note that the maxima and minima are spaced by 48 to 53 MHz. A frequency of 50 MHz corresponds to a free-space wavelength of 6.0 m. A quarter wavelength is 1.50 m for this frequency. This is close to the length of the antenna plate, which is 1.46 m.

It is expected that the Ansoft HFSS results for the antenna impedance will soon be compared to measurement results produced by the US Air Force Phillips Laboratory at Kirtland Air Force Base, New Mexico, where this antenna has been built.

Finally, the typical computation time and memory requirement for this kind of simulation are as follows. With 21000 tetrahedra, the CPU time for the solution process is just under 8 hours on an HP 9000 workstation. During the computation, HFSS uses 200 Mb of RAM and 500 Mb of disk space. In these simulations, the symmetry of the antenna has not been used to reduce the number of elements.

References

[1] E.G. Farr and C.E. Baum, "A Simple Model of Small-Angle TEM Horns", US Air Force Phillips Laboratory Sensor and Simulation Note 340, May 1992.
[2] C.E. Baum, "Low-Frequency Compensated TEM Horn", US Air Force Phillips Laboratory Sensor and Simulation Note 377, January 1995.
[3] R.F. Harrington, "Field Computation by Moment Methods", Chapter 2, Krieger Publishing Company, 1982, ISBN 0-89874-465-2.
[4] M.H. Vogel, "Design of the Low-Frequency Compensation of an Extreme-Bandwidth TEM Horn and Lens IRA", US Air Force Phillips Laboratory Sensor and Simulation Note 391, April 1996.
[5] J. Moore and R. Pizer, "Moment Methods in Electromagnetics", John Wiley and Sons, 1986, ISBN 0-471-90414-7.
[6] M.H. Vogel, "Intermediate-Frequency Behaviour of an Extreme-Bandwidth TEM Horn and Lens IRA", US Air Force Phillips Laboratory Transient Radiating Antenna Memos, Memo 3, August 1996.

A Modified Mei Method for Solving Scattering Problems with the Finite Element Method

Yun Li and Zoltan J. Cendes

Department of Electrical and Computer Engineering
Carnegie Mellon University
Pittsburgh, PA 15213
and
Ansoft Corporation
Pittsburgh, PA 15219

Abstract

A new absorbing boundary condition(ABC) is developed that allows the boundary to be very close to the scatterer. The boundary condition is a modification of the Mei method enabling it to be applied to the finite element method using variational principles. It is very efficient since it retains the sparsity of the finite element matrix equation. The procedure is applied to a number of scattering problems and the results compared with that of the pure moment method and the hybrid moment finite element method, and with that obtained by using modal expansion ABC's. We show that the solutions obtained by using the modified Mei method are very accurate even when the boundary is close to the scatterer and are better than the solutions obtained by modal expansion ABC's.

I. Introduction

To solve electromagnetic scattering problems with the finite difference or the finite element method, the solution region must be truncated to a finite size. An artificial boundary condition that models the behavior of the field extending to infinity is placed on the outer boundary of this finite region. This artificial boundary condition is sometimes an absorbing boundary condition or ABC [1]-[5]. When this procedure is correctly applied, the solution inside the truncated region is the same as if the entire problem were solved, except that it is directly computed only inside the truncated region. In effect, one has taken a picture of fields around the scatterer; for this reason, the artificial boundary is sometimes called a picture frame boundary [6].

Although many procedures exist for introducing absorbing boundary conditions on the picture frame boundary, most of these give poor results if the boundary is close to the scatterer. Prouty, Mei, Schwarz and Pous have recently introduced a new method called the Measured Equation of Invariance or the Mei method [7] that allows the boundary to be placed very close to the scatterer. The results obtained by Mei method are very close to the results obtained by using exact methods. It is also very efficient since it maintains the sparsity of the resulting matrix equation.

The Mei procedure is specifically designed to work with the finite difference method. In this paper, this procedure is modified to work with the finite element method. Since the finite element method allows irregular boundaries to be modeled more easily than does the finite difference method, the modified Mei method present here provides more flexibility for modeling complicated geometries than does the original Mei approach.

The results presented here are compared with results obtained by using the moment method and the hybrid moment - finite element method, and with results obtained by using modal expansion absorbing boundary conditions [8].

II. Formulation

II.1   The Mei Method

This paper considers the solution of the wave equation

$$\nabla^2\Phi + k^2\Phi = 0 \qquad \text{in } \Omega \qquad (1)$$

where Ω is a two dimensional, unbounded region and Φ represents E_z for *TM* waves and H_z for *TE* waves. In the finite difference method, equation (1) is replaced by a matrix equation for point values of the field Φ on a finite difference grid. The basic idea of the Mei method is to assume that a linear relationship exits between the field values at nearby nodes on a finite difference grid

$$\sum_{i=1}^{n} c_i \cdot \Phi = 0 \tag{2}$$

By specifying n linearly independent but otherwise arbitrary solutions to the original problem, the coefficients c_i are determined. These coefficients may then be used to solve the scattering problem for any excitation.

In the Mei method, a basis of solutions for (1) is provided by assigning the current on the surface of the scatterer Γ' to be a set of independent functions. For example, as indicated in Figure 1 we may assign the current on the surface of an arbitrary cylinder as the sequence

$$J_m(t) = \left\{ \sin\left(\frac{2\pi m t}{T}\right) and/or \cos\left(\frac{2\pi m t}{T}\right) \right\} \tag{3}$$

where t is the parametric coordinate around the boundary Γ' and T is the total distance around the cylinder. The field at node n produced by the current $J_m(t)$ is given by the integral

$$\Phi_{mn} = \oint_{\Gamma} G(t,t') J_m(t') dt' \tag{4}$$

where $G(t,t')$ is the appropriate Green's function. Equation (4) is used in combination with equation (2) to generate an n by n system of equations for the coefficients c_i.

In the finite element method, equation (1) is replaced by the variational principle

$$F(\Phi) = -\int_{\Omega} \nabla \Phi \cdot \nabla \Phi \, d\Omega + k^2 \int_{\Omega} \Phi \, d\Omega + \int_{\Gamma} \Phi \frac{\partial \Phi}{\partial n} d\Gamma \tag{5}$$

where (5) over an open region, we need to find the relationship between the field Φ and its normal derivative $\partial \Phi / \partial n$.

By analogy with the Mei method, we assume that linear relationship exists between the normal derivative of the field at a node and the nearby nodes

$$\frac{\partial \Phi}{\partial n} = \sum_i c_i \Phi_i \tag{6}$$

Given the current distribution J_m, it is straightforward to compute Φ and $\partial \Phi / \partial n$ at node n

$$\Phi_{mn} = \Phi|_n$$

$$= \oint G(t_n, t') J_m(t') dt' \tag{7}$$

$$M_{mn} = \left.\frac{\partial \Phi}{\partial n}\right|_n$$

$$= \oint \frac{\partial G(t_n,t')}{\partial n} J_m(t')dt' \tag{8}$$

The implementation described here uses second order finite elements to approximate the field. As explained below, four points are used to approximate the derivative in equation (6). The locations of these points are indicated in Figure 2. For example, at node 2 the derivative of the field is expressed as

$$\left.\frac{\partial \Phi}{\partial n}\right|_2 = c_1 \Phi\big|_1 + c_2 \Phi\big|_2 + c_3 \Phi\big|_3 + c_4 \Phi\big|_4 \tag{9}$$

where i, $i=1, 2,...4$ are the field values evaluated at node i in Figure 2. Similar equations apply at the other nodes. Using four different metrons in equation (9) results in a matrix equation

$$c_1 \Phi_{11} + c_2 \Phi_{12} + c_3 \Phi_{13} + c_4 \Phi_{14} = M_{12}$$
$$c_1 \Phi_{21} + c_2 \Phi_{22} + c_3 \Phi_{23} + c_4 \Phi_{24} = M_{22} \tag{10}$$
$$c_1 \Phi_{31} + c_2 \Phi_{32} + c_3 \Phi_{33} + c_4 \Phi_{34} = M_{32}$$
$$c_1 \Phi_{41} + c_2 \Phi_{42} + c_3 \Phi_{43} + c_4 \Phi_{44} = M_{42}$$

which may be used to solve for the coefficients c_i, i=1,...,4. This procedure is repeated for each boundary segment. Hence, each boundary point has a unique set of coefficients c_i, i=1,2,...,4.

II.2 Evaluating the Derivatives

The derivative values M_{mn} are evaluated separately for *TM* and *TE* waves. Let (x,y) be a point on the boundary and (x',y') be a point on the scatterer surface, as shown in Figure 1.

For *TM* waves, $G(t,t') = -\frac{k\eta}{4}H_0^{(2)}(k|r-r'|)$. It follows that

$$\Phi_{mn} = -\frac{k\eta}{4}\oint_\Gamma H_0^{(2)}(k|r-r'|)J_m(t')dt' \tag{11}$$

where

$$|r - r'| = \sqrt{(x - x')^2 + (y - y')^2} \qquad (12)$$

The normal derivative of Φ is given by

$$M_{mn} = \frac{\partial \Phi}{\partial n}$$

$$= \oint \frac{\partial G(t,t')}{\partial n} J_m(t')dt'$$

$$= \oint_{\Gamma} - \frac{k\eta}{4} \frac{\partial H_0^{(2)}(k|r - r'|)}{\partial n} J_m(t')dt' \qquad (13)$$

We have that

$$\frac{\partial H_0^{(2)}(k|r - r'|)}{\partial n} = - kH_1^{(2)}(k|r - r'|)\frac{\partial |r - r'|}{\partial n} \qquad (14)$$

and

$$\frac{\partial |r - r'|}{\partial n} = \nabla(|r - r'|) \cdot n \qquad (15)$$

$$= \left(\frac{\partial |r - r'|}{\partial x} e_x + \frac{\partial |r - r'|}{\partial y} e_y\right) \cdot (\cos v e_x + \sin v e_y) \qquad (16)$$

where e_x and e_y are the unit vectors in the x and y directions respectively.
Thus, we have

$$\frac{\partial H_0^{(2)}(k|r - r'|)}{\partial n} = - kH_1^{(2)}(k\sqrt{(x - x')^2 + (y - y')^2})\frac{(x - x')\cos v + (y - y')\sin v}{\sqrt{(x - x')^2 + (y - y')^2}} \qquad (17)$$

where v is defined in Figure 1.

For *TE* waves, the field is represented by

$$\Phi = u_z \cdot \nabla \times \oint_{\Gamma} G(t,t')J(t')dt' \qquad (18)$$

$$\Phi = \oint_{\Gamma} J(t')\left(\frac{\partial G}{\partial x}\frac{\partial y'}{\partial t} - \frac{\partial G}{\partial y}\frac{\partial x'}{\partial t}\right)dt' \qquad (19)$$

where $G(t,t') = \frac{1}{4j} H_0^{(2)}(k|r - r'|)$. After some algebra, we obtain

$$\Phi = -\frac{k}{4j}\sum_{l_i}\int_{t_{i-1}}^{t_i} J(t')H_1 \frac{(x-x')\cos(\theta_i) - (y-y')\sin(\theta_i)}{\sqrt{(x-x')^2 + (y-y')^2}}dt' \tag{20}$$

$$\frac{\partial\Phi}{\partial n} = -\frac{k}{4j}\sum_{l_i}\int_{t_{i-1}}^{t_i} J(t')\partial\left[H_1 \frac{(x-x')\cos(\theta_i) - (y-y')\sin(\theta_i)}{\sqrt{(x-x')^2 + (y-y')^2}}\right]/\partial n\, dt' \tag{21}$$

Φ_{mn} and M_{mn} are computed by using (20) and (21) for *TE* waves and (11) and (13) for *TM* waves.

II.3 Finite Element Approximation

As mentioned previously, second order finite elements are used to approximate the field and its derivative. As indicated in Figure 2, the field derivative on a line segment is written

$$\frac{\partial\Phi}{\partial n} = \left.\frac{\partial\Phi}{\partial n}\right|_1 \alpha_1 + \left.\frac{\partial\Phi}{\partial n}\right|_2 \alpha_2 + \left.\frac{\partial\Phi}{\partial n}\right|_3 \alpha_3 \tag{22}$$

where α_1, α_2 and α_3 are the weighting functions

$$\begin{aligned}
\alpha_1 &= 2\zeta_0(\zeta_0 - 0.5) \\
\alpha_2 &= 4\zeta_0\zeta_1 \\
\alpha_3 &= 2\zeta_1(\zeta_1 - 0.5)
\end{aligned} \tag{23}$$

and ζ_i are homogeneous coordinates. Now write the nodal derivatives as

$$\begin{bmatrix} \partial\Phi/\partial n|_1 \\ \partial\Phi/\partial n|_2 \\ \partial\Phi/\partial n|_3 \end{bmatrix} = \begin{bmatrix} c_{11} & c_{21} & c_{31} & c_{41} \\ c_{12} & c_{22} & c_{32} & c_{42} \\ c_{13} & c_{23} & c_{33} & c_{43} \end{bmatrix}\begin{bmatrix} \Phi_1 \\ \Phi_2 \\ \Phi_3 \\ \Phi_4 \end{bmatrix} = [c]\begin{bmatrix} \Phi_1 \\ \Phi_2 \\ \Phi_3 \\ \Phi_4 \end{bmatrix} \tag{24}$$

The boundary integral in equation (5) thus becomes

$$\oint_\Gamma \Phi \frac{\partial \Phi}{\partial n} d\Gamma = \sum_i \int_{li} (\Phi_1 \alpha_1 + \Phi_2 \alpha_2 + \Phi_3 \alpha_3)\left(\frac{\partial \Phi}{\partial n}\bigg|_1 \alpha_1 + \frac{\partial \Phi}{\partial n}\bigg|_2 \alpha_2 + \frac{\partial \Phi}{\partial n}\bigg|_3 \alpha_3\right) dl_i$$

$$= \sum_i \begin{bmatrix} \Phi_1 & \Phi_2 & \Phi_3 \end{bmatrix} [A][C] \begin{bmatrix} \Phi_1 \\ \Phi_2 \\ \Phi_3 \\ \Phi_4 \end{bmatrix} \tag{25}$$

where

$$[A] = \begin{bmatrix} 4 & 2 & -1 \\ 2 & 16 & 2 \\ -1 & 2 & 4 \end{bmatrix} \tag{26}$$

and [C] is given in equation (26). This contribution must be added to the finite element matrices produced by the first two terms in equation (5) to model open boundaries. We note that the resulting matrix contribution is not symmetric because [C] matrix in general is not symmetric.

III. Numerical Examples and Discussion

To demonstrate the accuracy of the proposed modified MEI method, we first solve for the induced electric current on a square cylinder impinged on by a plane wave. The square cylinder has side length 4 and is depicted in Figure 3. The modified MEI boundary condition is applied only a couple layers away from the cylinder. From Figures 4 and 5, one can see that the results obtained by modified MEI agrees well with the hybrid MOM/FEM technique for both TE and TM cases. Here, we consider hybrid MOM/FEM as numerically "exact" since the radiation boundary condition is exactly embedded in the Green's Function. It is interesting to note that modified MEI produces more accurate results than the modal expansion ABC like many other ABC's in the literature must be applied at certain distance away from the scatter in order to maintain the accuracy. As the original MEI method proposed in [7], the modified MEI has no such restriction which makes the method efficient.

The second example is scattering by a pentagon shown in Figure 6. Figures 7 and 8 compare the induced electric currents on the object obtained by various techniques. Once again, the agreement between modified MEI and the hybrid MOM/FEM is very god, while modal expansion ABC produces less accurate results. The modified MEI method seems to

have no difficulty to produce correct results even at corners where the current varies rapidly.

The third example is a circular cylinder with an open slit. The plane wave incidents perpendicular on the slit. Figures 9 and 10 present the contours of E_z for TM case obtain by modified MEI and modal expansion ABC. In this case, the agreement is very good because the exterior boundary is sufficiently far away from the scatterer.

The above three examples demonstrate that the modified MEI method is able to generate accurate results even when the boundary condition is applied on a boundary only a couple of layers away from the scatterer. Hence, one could conclude that the modified MEI is more computational efficient than other absorbing boundary conditions such as the modal expansion ABC. Unfortunately, the answer is no longer as simple if one also considers the cost of generating the numerical absorbing boundary condition and solving the non-symmetric resulting matrix. However, we believe the modified MEI is still very competitive if the computational domain can be significantly reduced compared with other ABC's.

One factor of uncertainty in applying MEI method is the choice of metrons. In the above examples, we experimented with several different metrons of the type given in equation (3) and found the results to be insensitive to the choice of metrons. However, we did not attempt in this work to thoroughly investigate the choice of metrons on the accuracy of the solutions. There are reports in the literature that the demonstrate the choice of metrons could have some adverse effect on the accuracy of the solution. This remains to be research issue in the future.

Finally, we demonstrate in the following two examples that the modified MEI method does not yield correct results if it is applied on a concave boundary. In contrast, the modified MEI boundary condition has always been applied on a convex artificial boundary in the above examples. Figure 11 defines the geometry of an arbitrary concave scatterer. The incoming wave incidents from the left. Figure 12 shows the current densities on the scatterer obtained by using modified MEI applied on a concave artificial boundary. We see that the results do not agree well with the results obtained by the method of moments which is used as a reference for comparison. Most errors occur in the region where the artificial boundary is concave. Figure 13 shows the current density on the same scatterer due to the same plane wave except that the modified MEI is applied on a convex artificial boundary. In this case, the agreement is much better.

To further demonstrate the point, we examine another concave geometry shown in Figure 14. Figures 15 and 16 show the induced current density on the scatterer obtained by modified MEI method applied either on a concave (Figure 15) or on a convex (Figure 16) artificial boundary. As in the previous cases, quite inaccurate results are produced in the region where the artificial boundary is concave.

IV. Conclusion

The MEI absorbing boundary condition has been modified for use with the finite element method. The original implementation of the MEI method employed the finite difference method and replaced the field in the open region by a linear combination of point values of the interior field. In the modified approach, the derivative of the field on the absorbing boundary is replaced by a linear combination of interior field point values. Using the derivative of the field itself is preferred with finite element method because this term is contained in the natural boundary condition of this method.

The modified MEI method gives excellent results for conducting scatterers even if the picture frame boundary is placed very close to the scatterer, for example when the boundary is only one or two elements away from the scatterer. However, the method does not appear to work with concave boundaries. Further work is required to extend the modified MEI approach to these situations.

References

[1] A. Bayliss and E. Turkel, "Boundary conditions for the numerical solution of elliptic equations in exterior regions," SIAM J. *Appl. Math.*, vol. 42, n. 2., pp. 430-451, Apr. 1982.

[2] B. Engquist and A. Majda, "Radiation boundary conditions for the number simulation waves," *Math. Comp.*, vol. 31, no. 139, pp. 629-651, July 1977.

[3] Robert L. Higdon, "Absorbing boundary conditions for difference approximations to the multi-dimensional wave equations, "*Math. Comput.*, vol. 47, no. 176, pp. 437-459, Oct. 1986.

[4] Omar M. Ramahi, Ahmed Khebir, and Raj Mittra, "Numerically derived absorbing boundary condition for the solution of open region scattering problems," *IEEE Trans. Antennas Propag.*, vol. 39, no. 3, pp. 350-353, March 1991.

[5] Gregory A. Kriegsmann, Allen Taflove, and Korada R. Umashankar, "A new formulation of electromagnetic wave scattering using an on-surface radiation boundary condition approach," *IEEE Trans. Antennas Propag.*, vol. AP-35, no. 2., Feb. 1987.

[6] P. Silvester and M.S. Hsieh, "Finite-element solution of 2-dimensional exterior field problems," *Proc. IEEE,* vol. 118, pp. 1743-1747, Dec. 1971.

[7] M.D. Prouty, K.K. MEI, S.E. Schwarz and R. Pous, "A·new approach to quasi-static analysis with application to microstrip," *IEEE Microwave Guided wave Lett.*, vol. 3, no. 9, pp. 302-304, Sept. 1993.

[8] Y. Li and Z. J. Csendes, "Modal Expansion Absorbing Boundary Conditions for Two-Dimensional Electromagnetic Scattering," going to be published in *IEEE Trans. Magnetics*, March, 1993.

[9] X. Yuan, "Electromagnetic scattering from inhomogeneous dielectrics and perfect conductors by hybrid moment and finite element method," private communication.
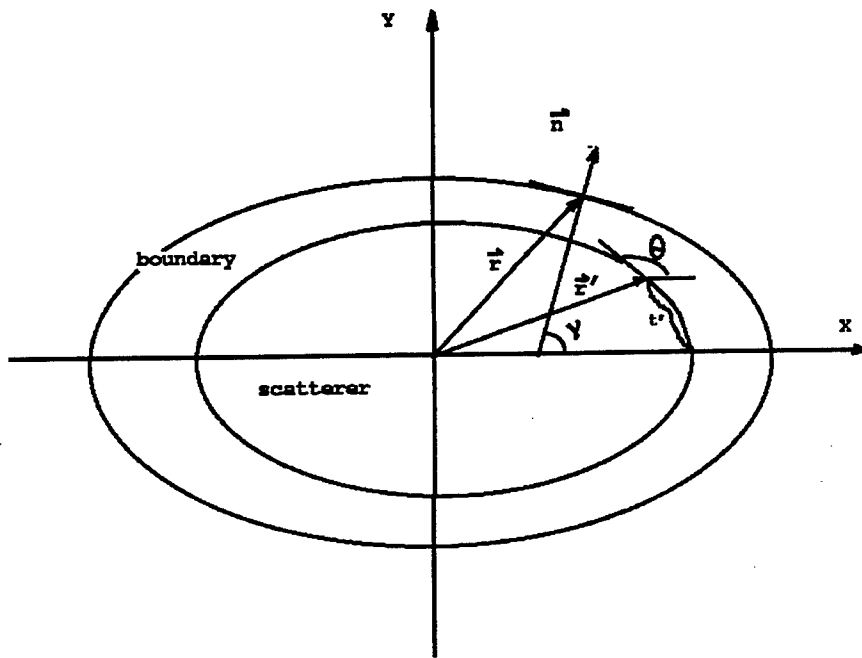
Figure 1: The coordinates used to define the two dimensional scatterering problem.
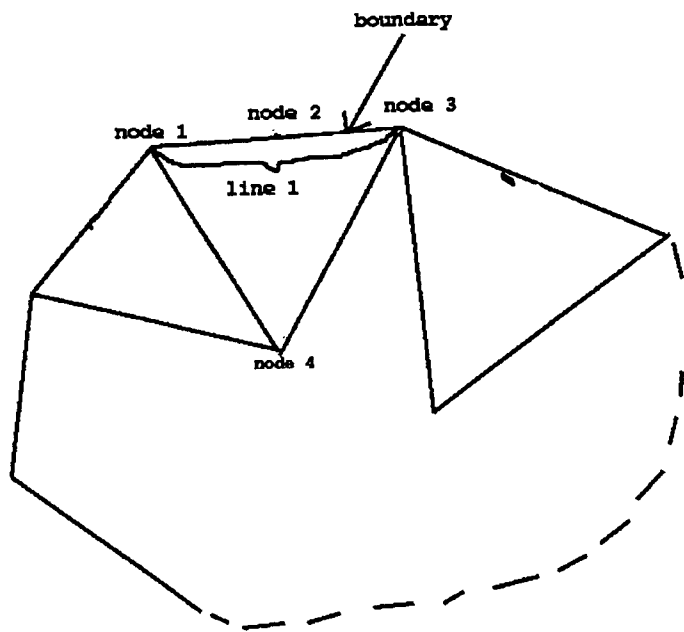
Figure 2: Node positions used in the element on the boundary.
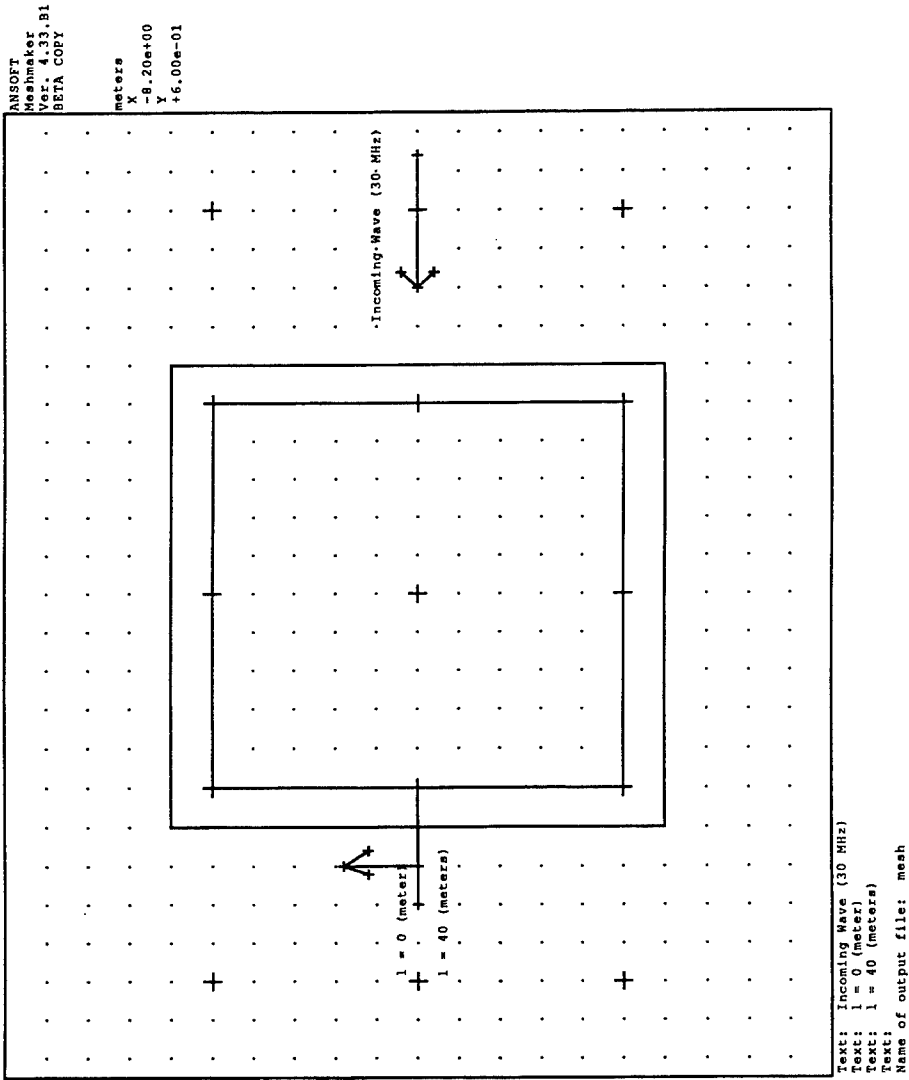
Figure 3: Geometry used to compute the scattered field from a square perfect conducting cylinder.
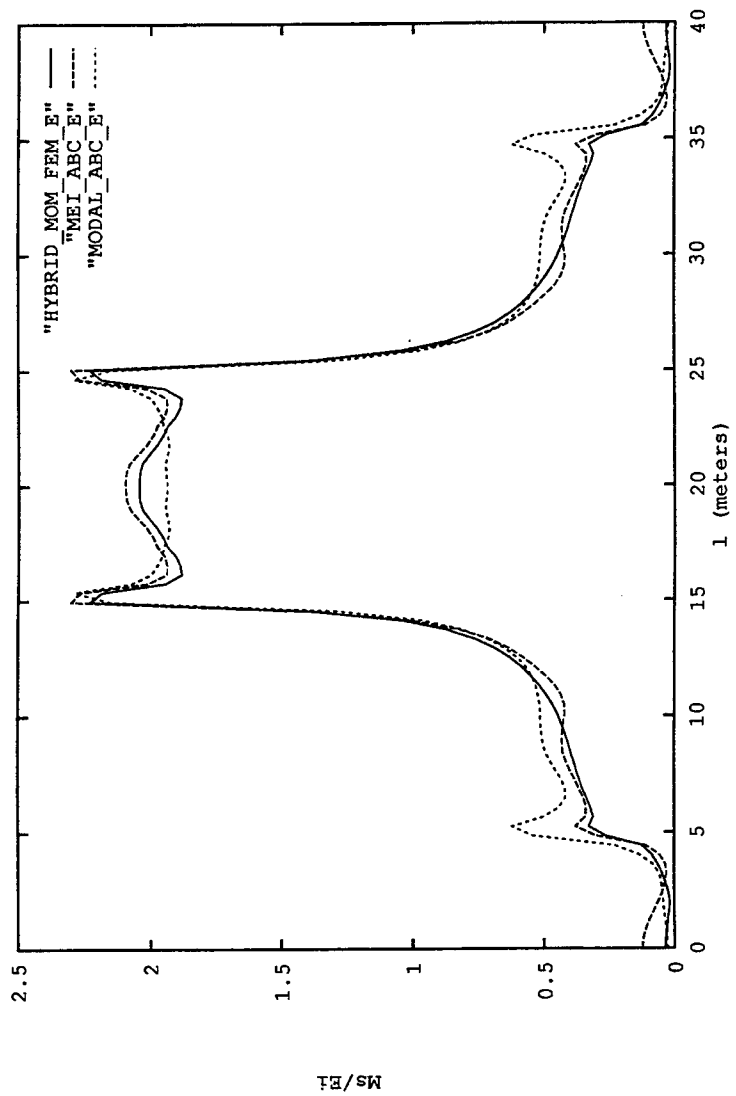
Figure 4: A comparison of the surface current densities on a square conducting cylinder for a TM wave obtained by using the hybrid moment and finite element method, the modified Mei method and modal expansion ABC's.
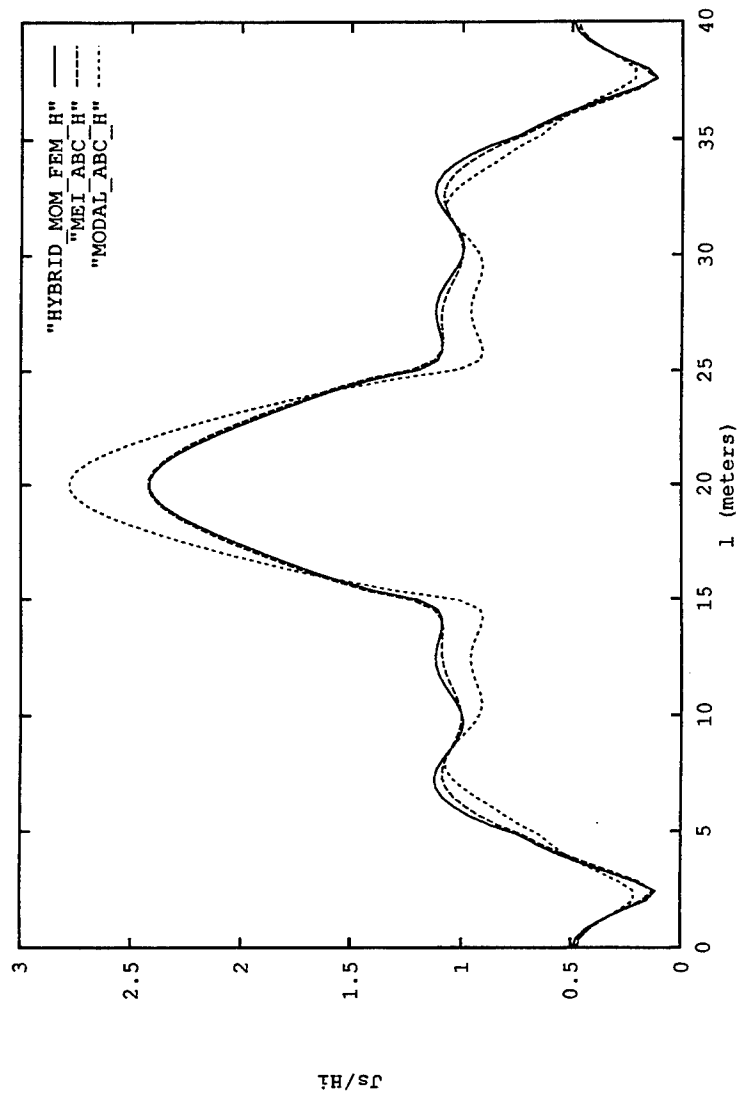
Figure 5: A comparison of the surface current densities on a square conducting cylinder for a TE wave obtained by using the hybrid moment and finite element method, the modified Mei method and modal expansion ABC's.

Figure 6: Geometry used to compute the scattered field from a pentagon-shaped perfect conducting cylinder.
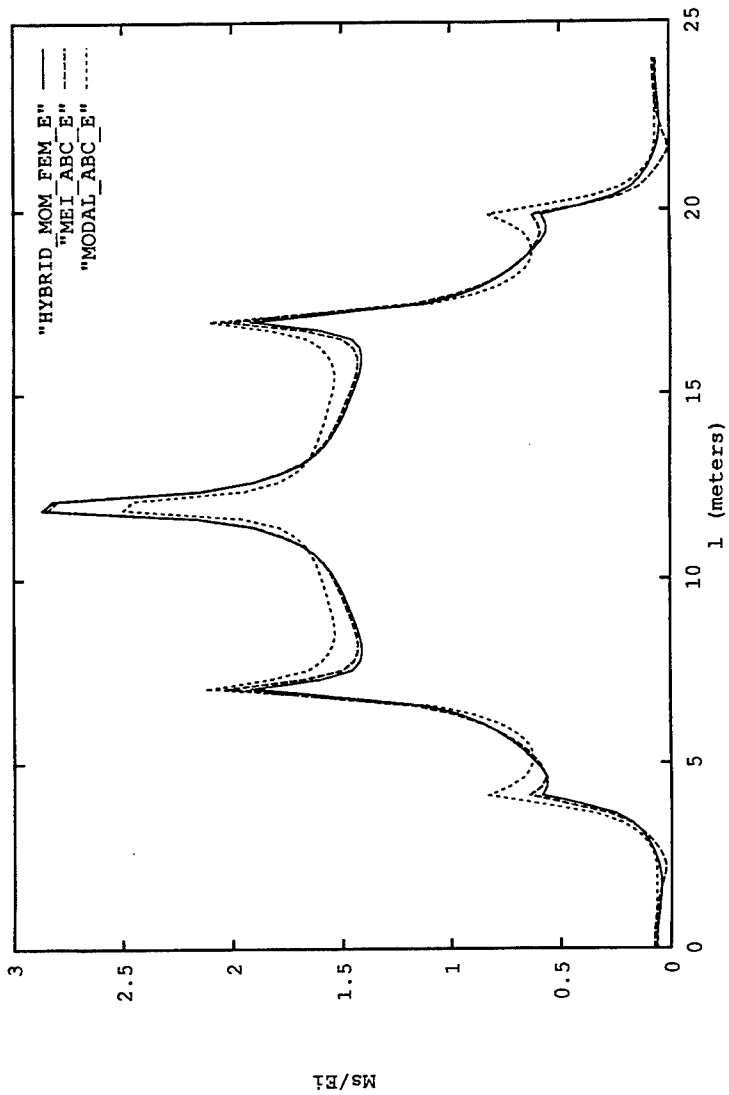
Figure 7: A comparison of the surface current densities on a pentagon-shaped conducting cylinder for a TM wave obtained by using the hybrid moment and finite element method, the modified Mei method and modal expansion ABC's.
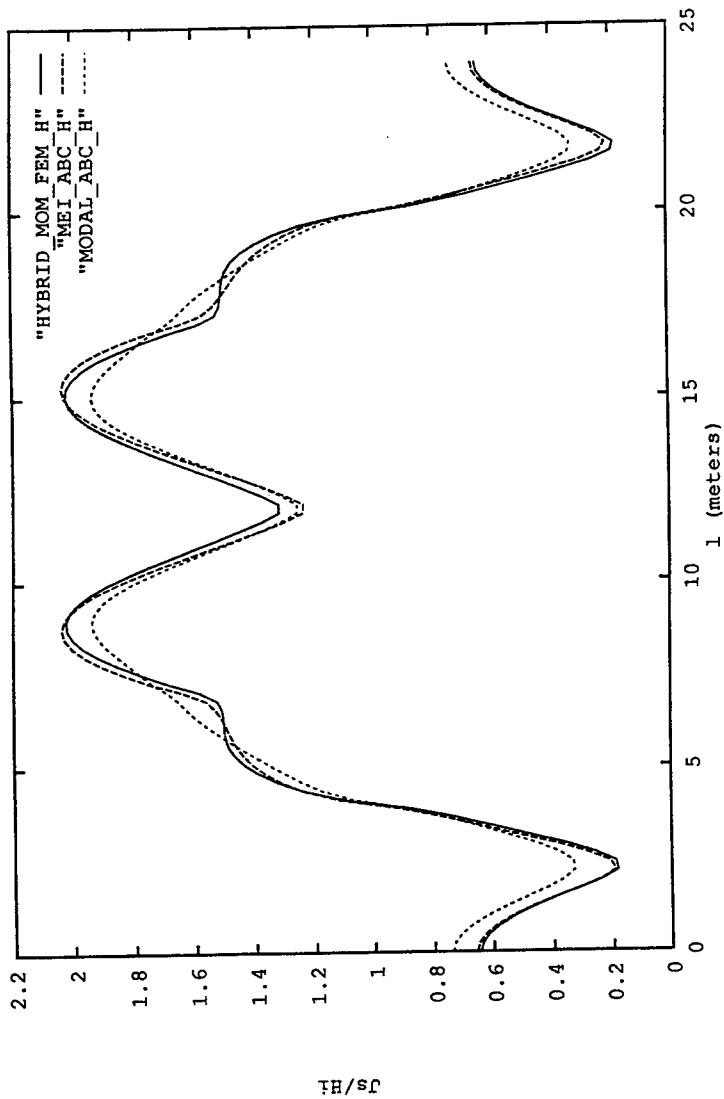
Figure 8: A comparison of the surface current densities on a pentagon-shaped conducting cylinder for a TE wave obtained by using the hybrid moment and finite element method, the modified Mei method and modal expansion ABC's.

ANSOFT
Antenna
Ver. 4.33

(null)meters
X -4.99e+00
Y -5.53e+00
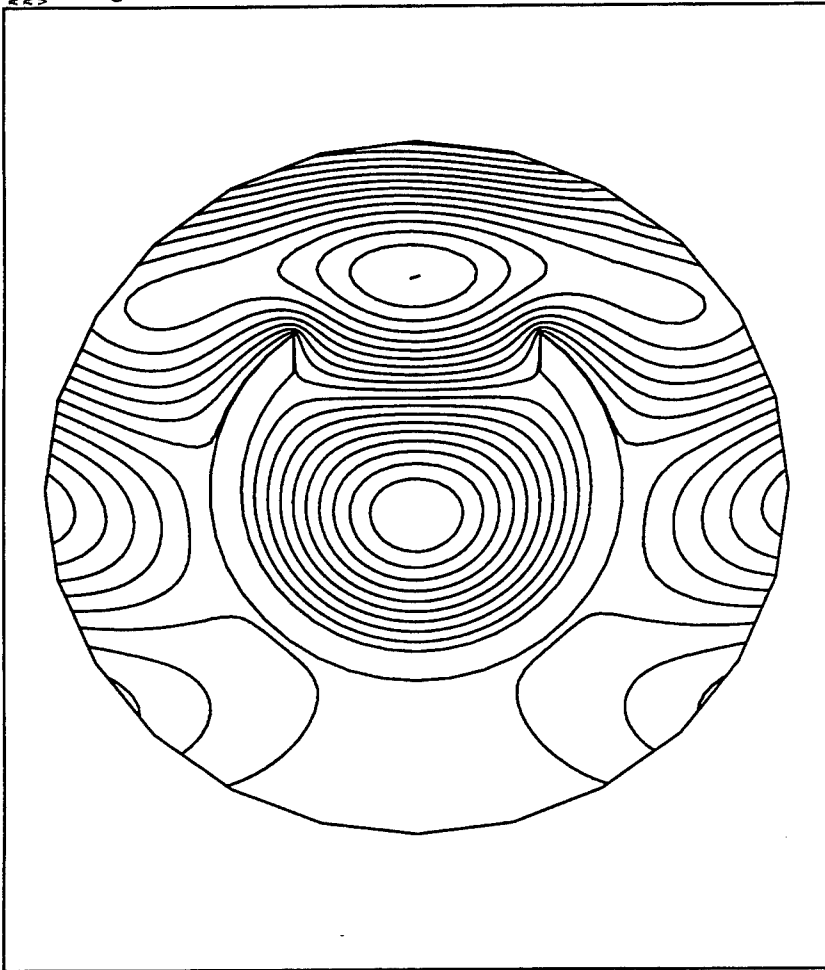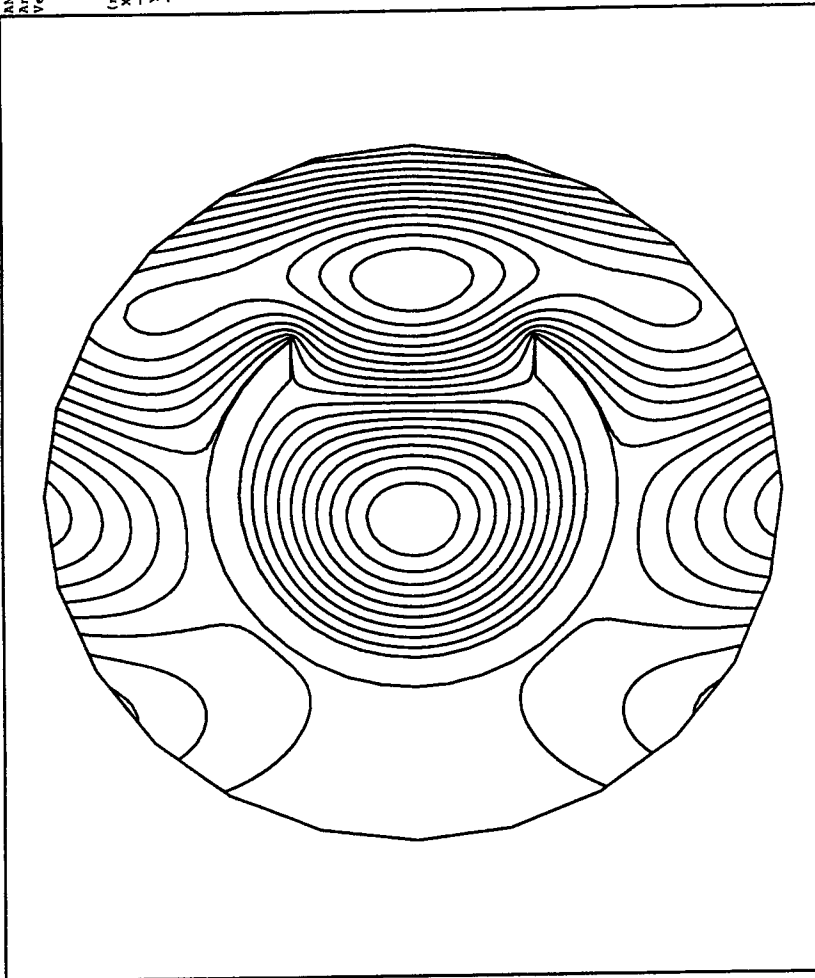
Min(-2.15e+00)
Divisons(20)
Plot Quality : Good , Fair
or Poor - [Good]
Name of output file: Concave_Mei

Figure 9: Contours of constant E_z for a perfect conductor having a concave shape using the modified Mei method.

Figure 10: Contours of constant E_z for a perfect conductor having a concave shape using the modal expansion ABC.
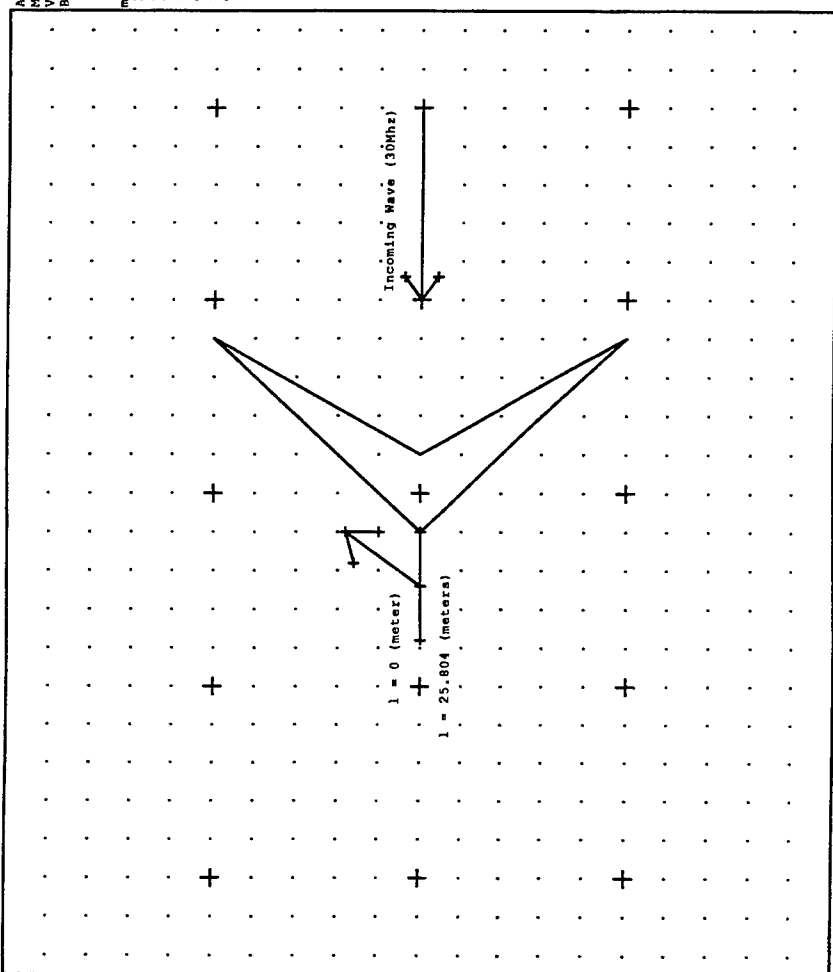
Figure 11: Geometry used to compute the scattered field from a concave perfect conducting cylinder.
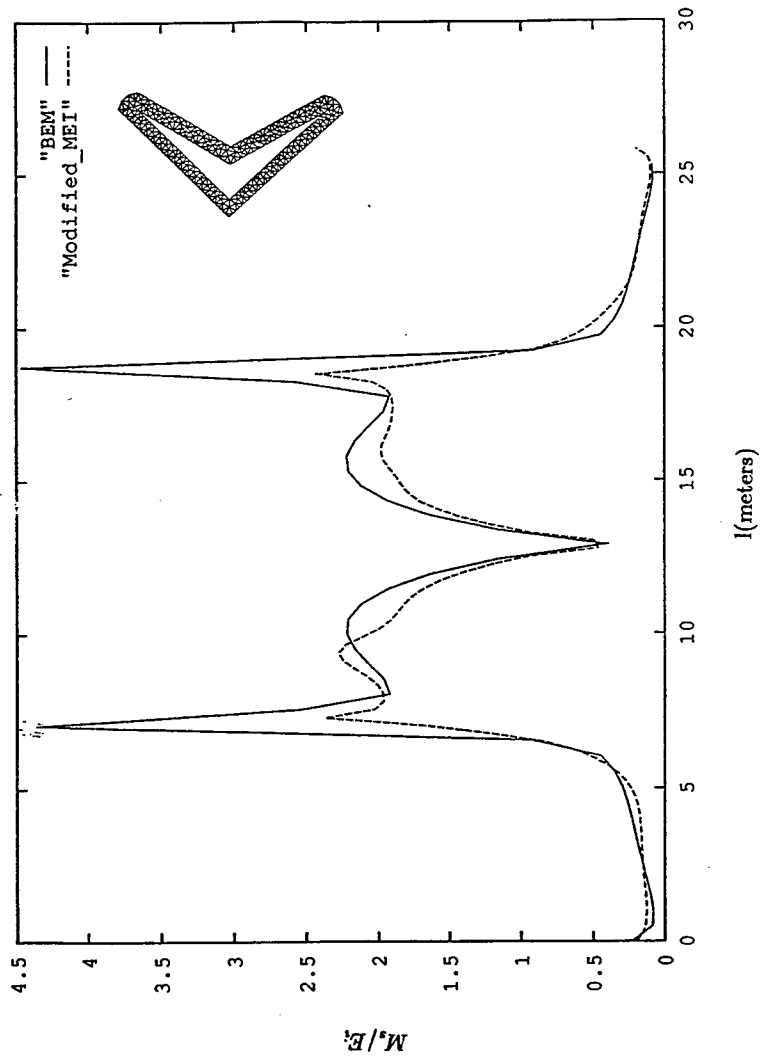
Figure 12: The current density for a TM wave on the concave perfect conductor with the modified Mei method and with the boundary element method using a concave outer boundary.
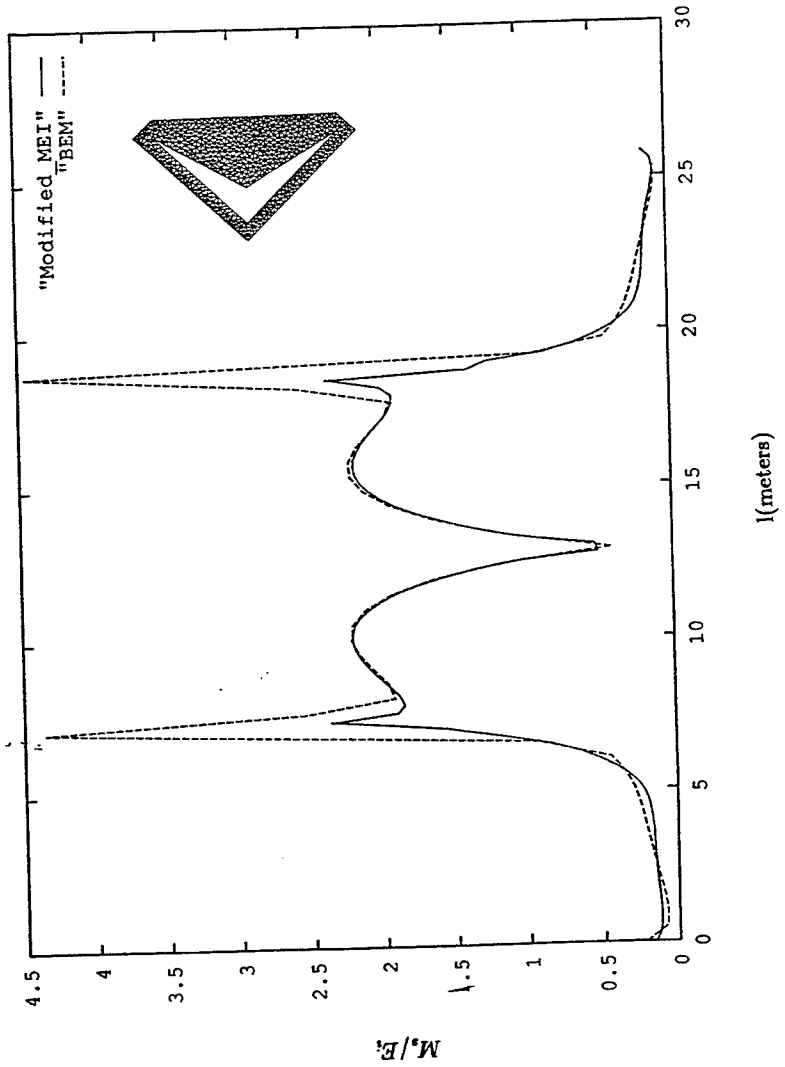
Figure 13: The current density for a TM wave on the concave perfect conductor with the modified Mei method and with the boundary element method using a convex outer boundary.
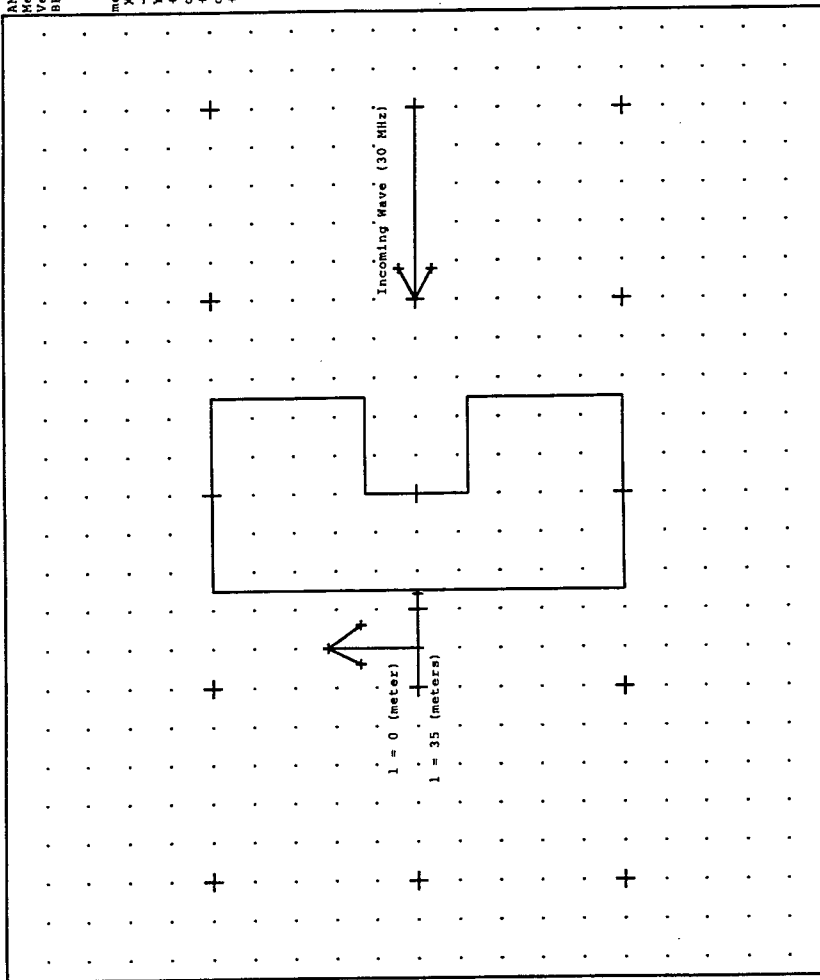
Figure 14: Geometry used to compute the scattered field from a concave perfect conducting cylinder.
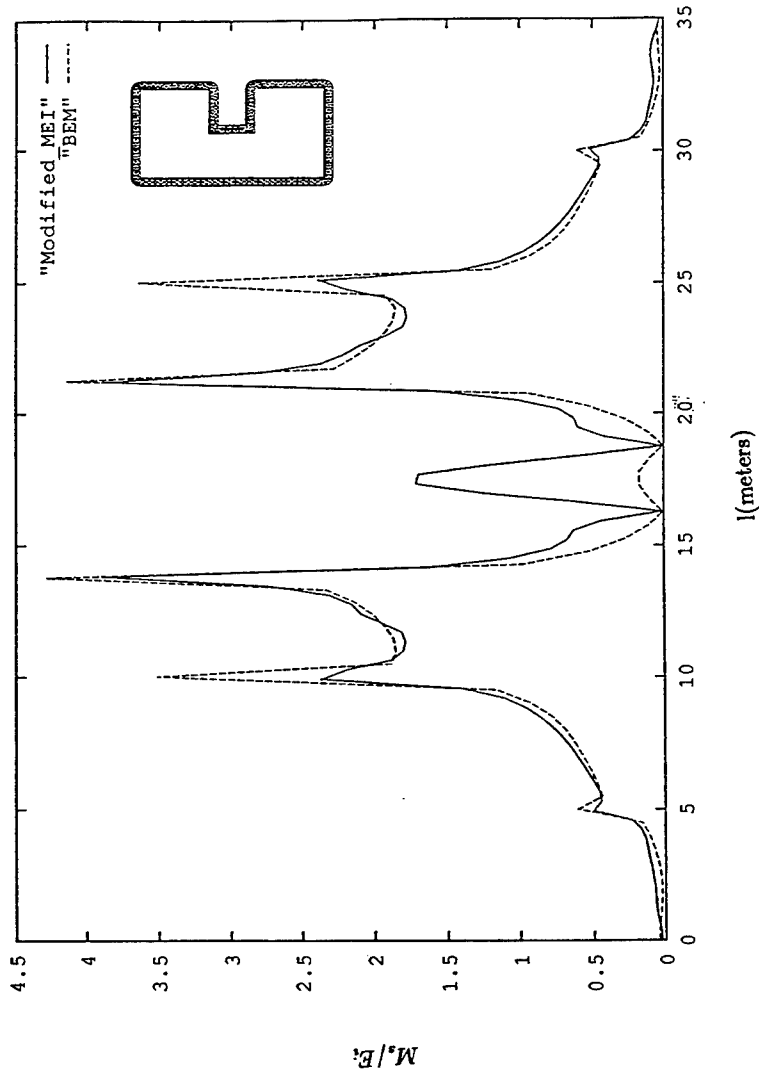
Figure 15: The current density for a TM wave on the concave perfect conductor with the modified Mei method and with the boundary element method using a concave outer boundary.
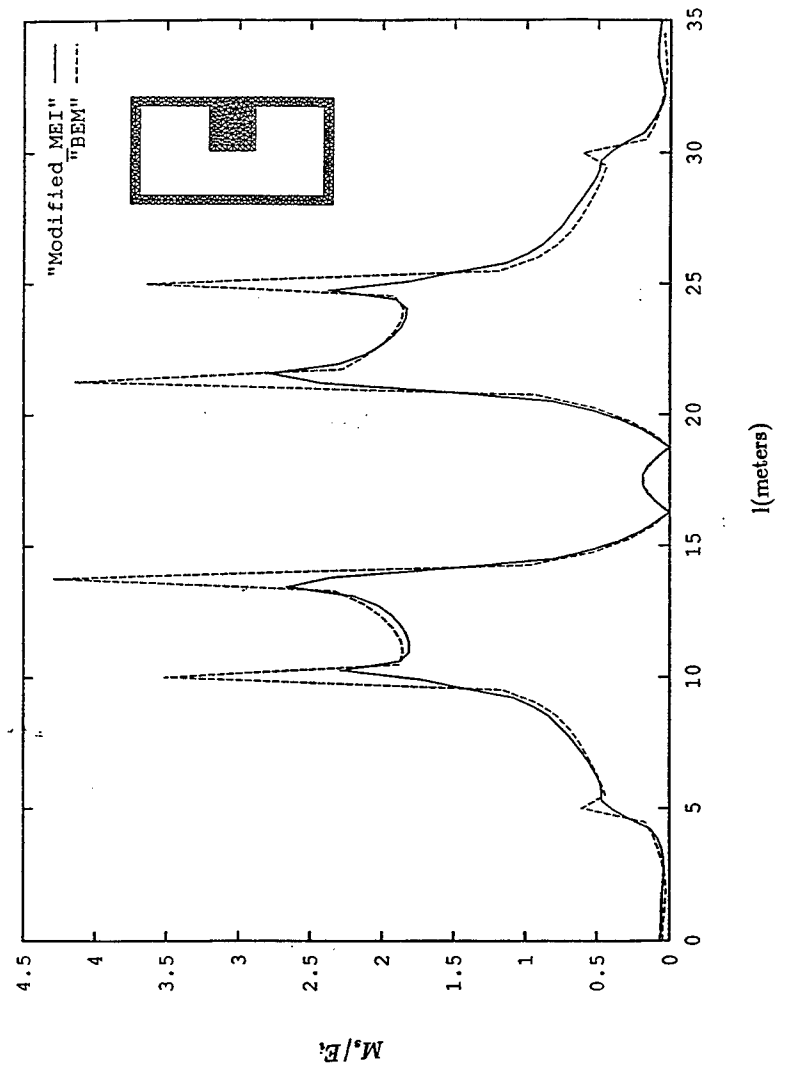
Figure 16: The current density for a TM wave on the concave perfect conductor with the modified Mei method and with the boundary element method using a concave outer boundary.

Investigation of the Limitations of Perfectly-Matched Absorber Boundaries in Antenna Applications

J. F. DeFord
Ansoft Corporation
4300 W. Brown Deer Rd., Suite 300, Milwaukee, WI 53223
Phone: (414) 357-0328 FAX: (414) 357-0347 e-mail: deford@ansoft.com

Abstract

Perfectly-matched absorber (PMA) boundary conditions have been shown to provide excellent absorption properties over a wide range of incident angles and frequencies. When meshed such that the element thickness increases rapidly with depth in the layer, PMA can yield better than −60dB reflection coefficients over a 3:1 range of normal wavenumber with only 3 finite-element layers. PMA can also be designed to attenuate evanescent modes that contact the boundary.

In this paper it will be shown that the unique properties of PMA allow it to be used very close to radiating structures. For example, tests on a simple 1/4λ monopole over a ground plane show that accurate input admittances over a 2 octave frequency range can be obtained with PMA starting just .03λ from the wire. Similar accuracies have been obtained for open-ended waveguides radiating in free space with the PMA at just .02λ from the aperture.

Introduction

Perfectly-matched layers using Maxwellian materials[1] are used as absorbing boundary conditions in radiation problems. A PMA is a layer composed of an orthotropic material that has the following properties:

$$\epsilon_r = \begin{bmatrix} \epsilon_1 & 0 & 0 \\ 0 & \epsilon_1 & 0 \\ 0 & 0 & \epsilon_2 \end{bmatrix}, \quad \mu_r = \begin{bmatrix} \mu_1 & 0 & 0 \\ 0 & \mu_1 & 0 \\ 0 & 0 & \mu_2 \end{bmatrix}, \tag{1}$$

where $\epsilon_1/\epsilon_i = \mu_1/\mu_i = \epsilon_i/\epsilon_2 = \mu_i/\mu_2 \equiv \kappa$, with ϵ_i and μ_i the permittivity and permeability of the media abutting the PMA, respectively. A PMA layer can theoretically absorb all polarizations of incident plane waves even with very large angles of incidence. PMA layers can also damp evanescent modes, and so may be used quite close to radiating structures or in situations where the propagating mode is traveling parallel to the boundary.

Proper design of the mesh in a PMA is important to achieving optimum properties while keeping computation costs to a minimum. A highly efficient mesh in a PMA has thin elements near the boundary, with geometrically increasing element thickness away from the boundary inside the layer. The meshing formulation for the results included in this paper is presented in Ref. [2].

Monopole Problem

A monopole over a ground plane was used to investigate the limitations of PMA for antenna analysis. The geometry is shown in Fig. 1a. The monopole is formed from the center conductor of

a coaxial feed line that connects from below the ground plane. The wire is 7.5 cm in length, including a spherical end-cap, and is resonant at about 900 MHz. The wire has a thickness of .2106 cm, and the feed coax is air-filled with a characteristic impedance of 67Ω. All conductors are assumed perfectly conducting. Two planes of symmetry are used to reduce the computation time. This device was studied using FDTD in a paper by Maloney, et al.[3], and the measurements referenced in that paper performed by Cooper[4] are reproduced here for comparison.

Several different cases were considered. In the first set of runs, the radiation boundary is cylindrical and each analysis was done with a different cylinder radius (Fig. 1b). The radii ranged from .24λ down to .03λ (wavelength at 900MHz). Note that although the results become much better as the radius of the radiation enclosure is increased to 1/4λ, there remains significant error between measured and calculated results (Fig. 2b).

In the second set of analyses, the radiation enclosure was a rectangular box (Fig. 1c). As with the cylindrical enclosure, runs were made for a range of box dimensions. Results for these calculations are shown in Fig. 2a.

In all cases, the PMA layer was three elements thick, with the first element having a thickness of 1.25 cm, the second element 2.5 cm, and the third element 7.5 cm.
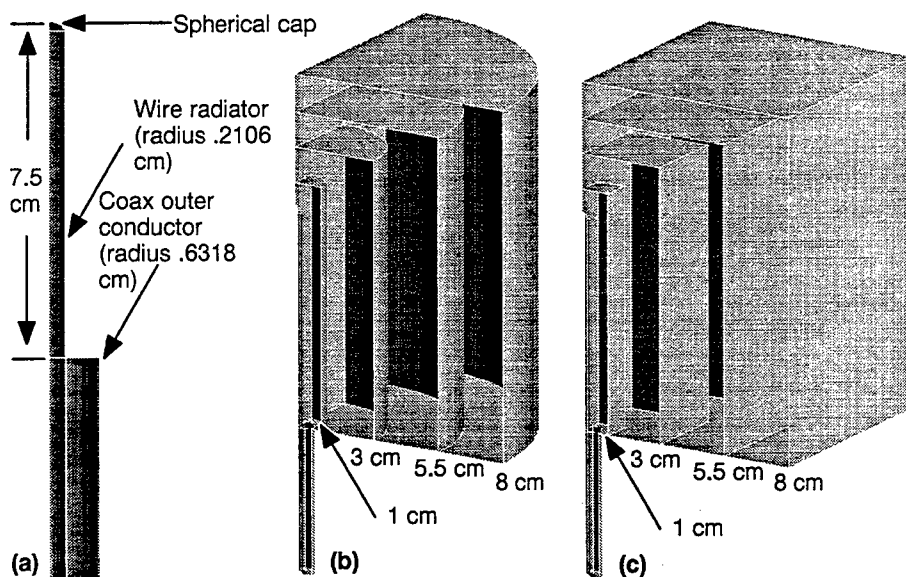

Figure 1: Geometries for test cases. (a) Radiator is a wire monopole above a ground plane with a spherical end-cap. The metal is perfectly conducting, and the feed coax is 67Ω. (b) Cylindrical radiation boundaries. (c) Rectangular radiation boundaries. Each boundary location is a distinct case.
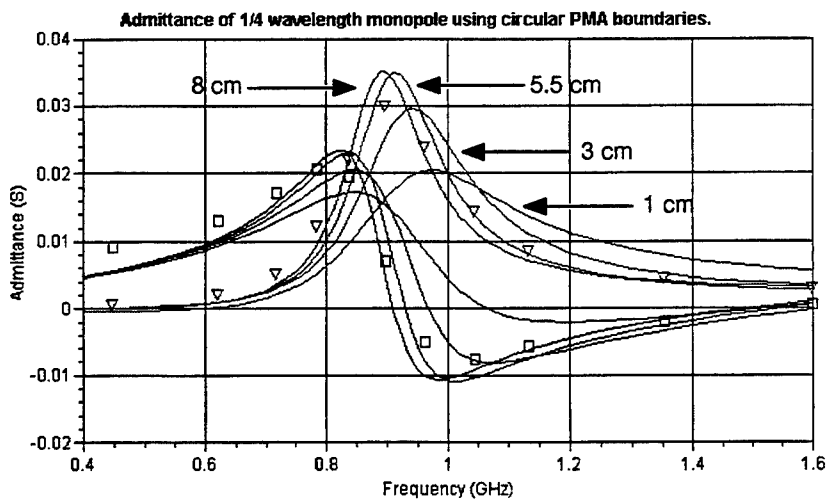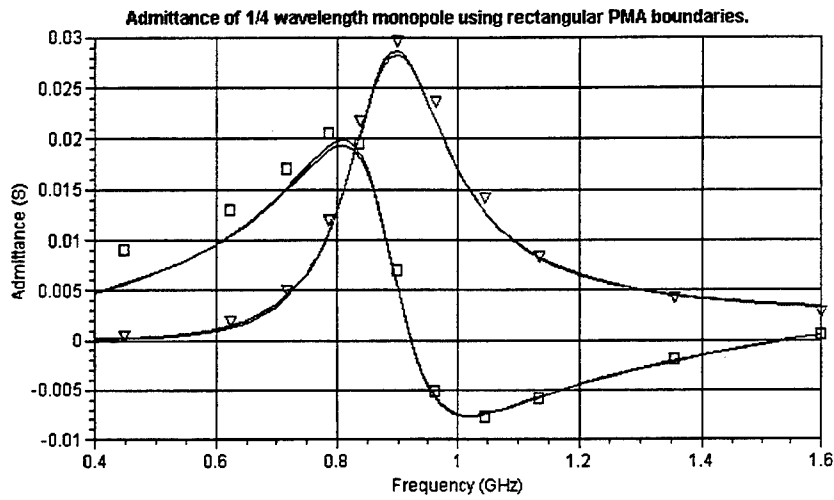
(a)

(b)

Figure 2: Admittance of 7.5 cm monopole over broad frequency range for two cases (a)
PMA on rectangular boundary, and (b) PMA on cylindrical boundary. Measured values are
indicated by triangles and boxes

As opposed to the previous case, a rectangular boundary provides solutions that are very close to the measured data even when the radiation enclosure is extremely close to the wire radiator. In fact, the results for .24λ box and .03λ box very nearly overlay each other.

Circular Patch Antenna

Characterization of a circular patch has been carried out by Aberle [5], and ref. [2] discusses the calculation of terminal characteristics using the finite-element method with PMA on a *spherical* boundary above the patch. In this paper the calculation was redone using PMA on a rectangular boundary as shown in Fig. 3.
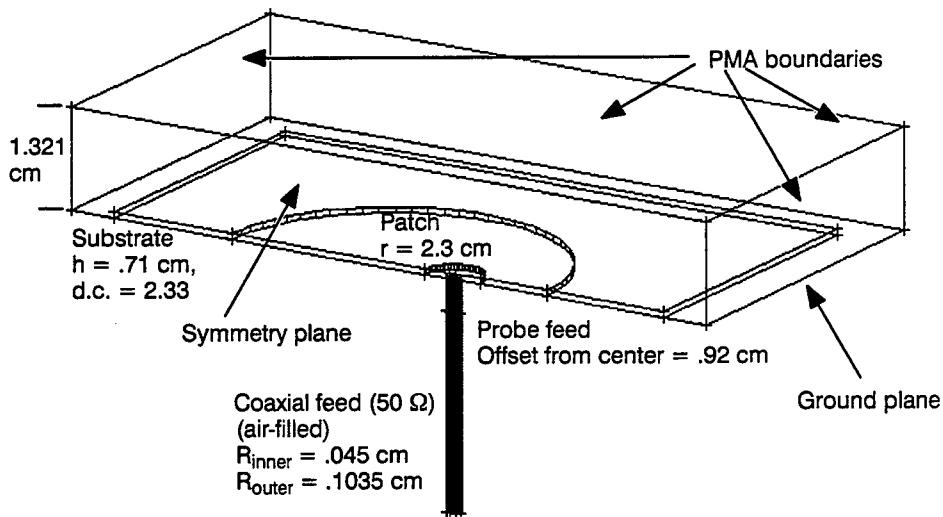
Figure 3: Patch model geometry. The substrate is terminated prior to meeting the PMA boundary as required by MicroWaveLab for rectangular boundaries, with negligible effect on the results.

Results for the circular patch are shown in Fig. 4. The experimental and MoM values are circled, and the finite-element results are shown as lines. The rectangular PMA results are closer to the experiment than the spherical PMA. In addition to the former curve being closer to the measurements, it also shows better agreement with the measured resonant frequency (rotation of curve is less for rectangular PMA). At resonance, the PMA surface is just 1/10λ from the top of the patch.

Conclusions

Perfectly-matched absorbers have been shown to be effective as radiation boundary conditions over a wide range of plane-wave incident angles and frequencies. In this paper it has been dem-

onstrated that in some cases the PMA surface may be brought very close to the radiator and still effectively simulate an "open" boundary. For example, placing the PMA surface only a few hundredths of a wavelength from a wire radiator yields accurate results for input admittance of the antenna.
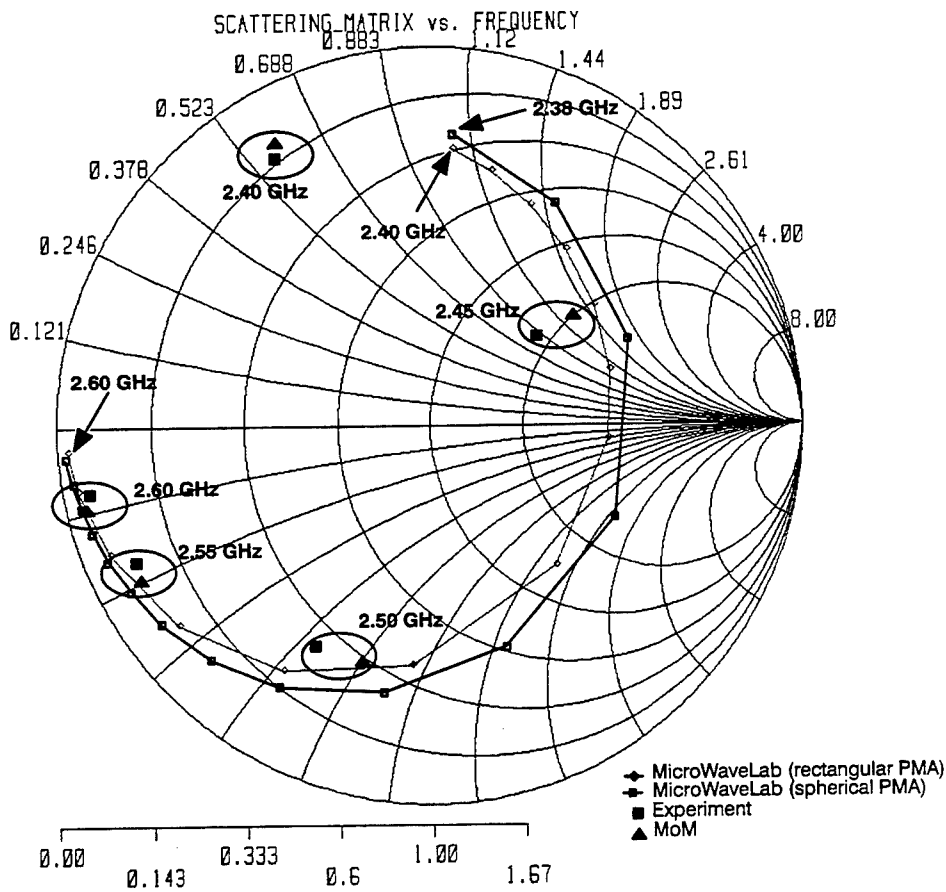

Figure 4: Results for circular patch. Experimental and MoM results taken from Aberle [5]. Spherical PMA result presented in reference [2].

References

[1]   D. M. Kingsland, Z. S. Sacks, and J. F. Lee, "Perfectly matched anisotropic absorbers for finite element applications in electromagnetics," *ACES Conference Proceedings*, Mar. 20–25, 1995, pp. 490–497.

[2]   J. F. DeFord and G. C. Lizalek, "Use of perfectly-matched absorber boundaries in the finite-element analysis of patch antennas," *ACES Conference Proceedings*, Mar. 18–22, 1996, pp. 1190–1195.

[3]   J. G. Maloney, G. S. Smith, and W. R. Scott, Jr., "Accurate computation of the radiation from simple antennas using the finite-difference time-domain method," *IEEE Trans. Ant. Prop.*, **38**, July, 1990, pp. 1059–1068.

[4]   L. J. Cooper, *Monopole Antennas on Electrically Thick Conducting Cylinders*, Ph. D. dissertation, Harvard Univ., Cambridge, MA, Mar. 1975.

[5]   J. T. Aberle, *Analysis of Probe-Fed Circular Microstrip Antennas*, Ph.D. Dissertation, University of Massachusetts, Electrical and Computer Engineering Dept. (1989).

The Spectral Lanczos Decomposition Method for Solving Axisymmetric Low-Frequency Electromagnetic Diffusion by the Finite-Element Method

Mohammad Zunoubi, Jian-Ming Jin, and Weng C. Chew
Center for Computational Electromagnetics
Department of Electrical and Computer Engineering
The University of Illinois at Urbana-Champaign
Urbana, IL 61801-2991
zunoubi@sunchew.ece.uiuc.edu

Dave Kennedy
Mobil R & D Corporation
13777 Midway Road
Dallas, TX 75381-90047

Abstract

A new explicit axisymmetric solver for the diffusion of electromagnetic fields in an inhomogeneous medium is described. The proposed method is based on the Krylov subspace (Lanczos) approximation of the solution in frequency domain. The finite-element method (FEM) is employed to discretize Maxwell's equations. It is shown that the SLDM is extremely fast. Furthermore, the electromagnetic fields at many frequencies can be evaluated by performing the SLDM iteration only once. Analysis of a practical geophysical problem is also included.

1 Introduction

A very common problem encountered in electromagnetic exploration is the efficient computation of the electromagnetic fields excited by a low-frequency harmonic source where the effect of displacement currents may be neglected. Traditional modeling procedures for Maxwell's equations suggest obtaining solutions independently for every frequency [1]. This has been proven to be extremely time consuming for multi-frequency simulations. Recently, Druskin and Knizhnerman [1] have introduced a new technique called the Spectral Lanczos Decomposition Method (SLDM), which is capable of solving Maxwell's equations for many frequencies in a negligible amount of extra computing time compared to one frequency. The method has been applied to solve for electromagnetic fields discretized by the finite difference method.

When Maxwell's equations are discretized by either the finite element or the finite difference method, the resulting equation may be formed into a matrix equation

$$Ax - i\omega Cx = b \tag{1}$$

where A and C are typically real square matrices, x is the unknown vector, and b is the excitation vector. This matrix equation can be modified as

$$A'x - i\omega I x = b' \tag{2}$$

where I is the identity matrix. Eq. (2) can be solved by SLDM which is based on approximations in a global Krylov subspace to the product of a matrix and a vector using the Lanczos method.

In this work, the finite element method (FEM) is employed to discretize Maxwell's equations in a low-frequency regime for axisymmetric problems. SLDM is then applied to the resulting matrix equation to solve for the electromagnetic fields for multiple frequencies. The formulation is done for the magnetic field intensity $\mathbf{H}$ while the electric field formulation follows the same procedure.

2 Finite-Element Formulation

In a low-frequency regime, where the effect of displacement currents can be neglected, Maxwell's equations are written as

$$\nabla \times \mathbf{H} = \sigma\mathbf{E} + \mathbf{J}, \qquad \nabla \times \mathbf{E} = -j\omega\mu\mathbf{H}, \tag{3}$$

which can be solved for either the electric field intensity $\mathbf{E}$ or the magnetic field intensity $\mathbf{H}$. If Eq. (3) is solved for the $\mathbf{H}$-field, we obtain

$$\nabla \times \left(\frac{1}{\sigma}\nabla \times \mathbf{H}\right) + j\omega\mu\mathbf{H} = \nabla \times \left(\frac{\mathbf{J}}{\sigma}\right). \tag{4}$$

Assuming a TM excitation in cylindrical coordinates where the only non-zero components of the fields are H_ϕ, E_ρ, and E_z, we can write [2]

$$\hat{\phi} \cdot \nabla \times \left(\frac{1}{\sigma}\nabla \times H_\phi\hat{\phi}\right) + j\omega\mu H_\phi = M_\phi, \tag{5}$$

where M_ϕ is the magnetic current density defined as

$$M_\phi = -\hat{\phi} \cdot \nabla \times \left(\frac{\mathbf{J}}{\sigma}\right) = \frac{\partial}{\partial\rho}\left(\frac{J_z}{\sigma}\right) - \frac{\partial}{\partial z}\left(\frac{J_\rho}{\sigma}\right), \tag{6}$$

which for a toroidal coil can be written as

$$M_\phi = -j\omega\mu I N_T \pi r_s^2 \frac{\delta(\rho - r_s)}{2\pi\rho}\delta(z - z_o), \tag{7}$$

where I is the current, N_T is the total number of turns and r_s is the radius of the toroidal coil in the ρz plane and is assumed to be small.

It is shown that Eq. (5) can be expressed as [3]

$$-\frac{\partial}{\partial\rho}\left[\frac{1}{\rho\sigma}\frac{\partial(\rho H_\phi)}{\partial\rho}\right] - \frac{\partial}{\partial z}\left[\frac{1}{\rho\sigma}\frac{\partial(\rho H_\phi)}{\partial z}\right] + \frac{j\omega\mu}{\rho}(\rho H_\phi) = M_\phi. \tag{8}$$

If we let $\rho H_\phi = \Phi$, $x = \rho$, $y = z$, $\alpha_x = \alpha_y = 1/\rho\sigma$, $j\omega\mu/\rho = \beta$, and $M_\phi = f$, Eq. (8) becomes

$$-\frac{\partial}{\partial x}\left(\alpha_x\frac{\partial \Phi}{\partial x}\right) - \frac{\partial}{\partial y}\left(\alpha_y\frac{\partial \Phi}{\partial y}\right) + \beta\Phi = f, \tag{9}$$

which is the standard form of a two-dimensional Helmholtz equation and its solution is equivalent to minimizing the functional

$$F(\Phi) = \frac{1}{2}\iint_S\left[\alpha_x\left(\frac{\partial \Phi}{\partial x}\right)^2 + \alpha_y\left(\frac{\partial \Phi}{\partial y}\right)^2 + \beta\Phi^2\right]dS - \iint_S f\Phi dS. \tag{10}$$

The boundary condition along the z-axis is

$$\frac{\partial \Phi}{\partial \rho} = 0 \quad \text{at } \rho = 0, \tag{11}$$

which is satisfied automatically as the natural boundary condition. For simplicity, we choose the outer boundaries sufficiently far from the source so that the field satisfies the boundary condition

$$\Phi = 0, \tag{12}$$

which is imposed in the minimization of $F(\Phi)$.

Next, we employ the finite-element technique to discretize Eq. (10) using linear triangular elements which would result in a matrix equation of the form

$$(C + \beta T)\Phi = b, \tag{13}$$

where C and T are called the *stiffness* and *mass* matrix, respectively. The matrix equation (13) may then be solved by employing SLDM which is discussed next.

3 Spectral Lanczos Decomposition Method

The electromagnetic simulation problems in frequency and time domains can be considered as particular cases of a more general problem of solving the following matrix equation [1]

$$u = f(A)b, \tag{14}$$

where A is an $n \times n$ symmetric matrix, f is a function defined on the spectral interval of A, and b is a vector in $\Re^n$. SLDM estimates the solution of Eq. (14) by first applying m steps of the Lanczos algorithm for approximate computation of eigenvalues and eigenvectors of matrix A. Accordingly, in the Krylov subspace, the basis $q_1, q_2, \ldots, q_m$ are generated by the *Gram-Schmidt* orthogonalization of vectors $b, Ab, \ldots, A^{m-1}b$ by the following recurrence formula

$$\beta_i q_{i+1} = r_{i+1} = Aq_i - \beta_{i-1}q_{i-1} - \alpha_i q_i,$$
$$\alpha_i - q_i^* Aq_i, \ \beta_i = \| r_{i+1} \|, \ i = 1, 2, \ldots, m \tag{15}$$

with $\beta_0 q_0 = 0$, $q_1 = b \parallel b \parallel$, and $\beta_i \geq 0$. Having evaluated α and β terms for m steps, a tridiagonal matrix H is formed with eigenvalues θ_i, $\theta_i < \theta_{i+1}$ and normalized eigenvectors $S_i = $

$(S_{1i}, \ldots, S_{mi})^*, i = 1, 2, \ldots, m$. Next, we define $e_1 = (1, 0, 0, \ldots, 0)^*$ as the first unit m vector, a matrix Q of basis vectors q_i as $Q = [q_1| q_2|, \ldots, |q_m]$, and vectors $y_i = QS_i$. Matrix H is referred to as the Ritz approximation of matrix A and (θ_i, y_i) are the approximate eigenvalues and eigenvectors of A that would be obtained if the Ritz method was applied to K^m [1].

In view of the definition of Q and the orthonormality of matrix $[S_1|S_2|, \ldots, |S_m]$, we can write

$$b = \| b \| q_1 = \| b \| Qe_1 = \| b \| Q \sum_{i=1}^{m} S_{1i}S_i = \| b \| \sum_{i=1}^{m} S_{1i}y_i, \tag{16}$$

which would result in an approximate solution of the matrix equation (14) as

$$u_m = \| b \| \sum_{i=1}^{m} S_{i1} f(\theta_i) y_i = \| b \| Q f(H) e_1, \tag{17}$$

which is a valid approximation of the unknown vector u, since the spectrum of matrix H is contained in the spectral segment of matrix A.

The main arithmetic work in SLDM is to obtain matrices Q and H. However, the dimension of the Krylov subspace m necessary to reach convergence is typically much smaller than the dimension of matrix A, n [1]. For approximate computations of the eigenvalues and eigenvectors of matrix A, the PWK and inverse iteration algorithms are implemented. With the above algorithms used to compute the eigenpairs of matrix A, only $O(m^2)$ operations are required. Additionally, it is not necessary to recompute Q and H matrices for multi-frequency simulations. Only the matrix functional $f(H)$ of Eq. (17) needs to be computed for various frequencies. This proves to be the most attractive feature of SLDM.

In order to solve Eq. (13) for either the electric field or the magnetic field by SLDM, this equation must be converted to a form

$$(A + j\omega I) x = u, \tag{18}$$

with I being the identity matrix. Therefore, matrix T of Eq. (13) is first converted to a diagonal matrix by the lumping procedure to yield

$$(C + \beta D) \Phi = b \tag{19}$$

which can be written as

$$\left(D^{-1/2}CD^{-1/2} + \beta I\right) \Phi' = D^{-1/2}b, \tag{20}$$

or

$$(A' + \beta I) \Phi' = b'. \tag{21}$$

with $D^{1/2}\Phi = \Phi'$. We approximate the solution to the matrix equation (21) by

$$\Phi' \approx \Phi'_m = \sum_{i=1}^{m} C_i q_i = QC, \qquad C = (c_1, \ldots, c_m)^*. \tag{22}$$

It is shown that Eq. (22) can be expressed as [1]

$$\Phi'_m = Q (H + \beta I)^{-1} \| b' \| e_1, \tag{23}$$

or

$$\Phi'_m = \| b' \| Q \sum_{i=1}^{m} S_{1i} S_i (\theta_i + \beta)^{-1}. \tag{24}$$

It is evident that SLDM allows one to obtain solutions of the electric and magnetic fields for multi-frequency simulations by forming Q and H matrices only once while recomputing the matrix functional $(H + \beta I)^{-1}$ at each frequency. This fact is further verified in the next section.

4 Results

To verify the formulation presented in this work, a practical geophysical problem is analyzed. The geometry considered here is a vertical borehole penetrating horizontal layered beds [2]. For the TM excitation, we model a toroidal antenna. The unknown field is evaluated by SLDM and the field contour lines are plotted. The inhomogeneity of the media is introduced by modeling multi-layers of various electrical conductivity σ. The computations are performed on a *DEC Alpha Workstation* computer with a throughput of 44 *MFlops*.

The problem configuration considered in this work is illustrated in Figure 1. The geometry dimension is 18 m × 18 m and it is subdivided into 101 segments on both ρ and z directions. The dimensions are given in terms of the number of segments. The magnetic current source M_ϕ is applied at $(\rho, z) = (60,3)$. The magnetic field intensity H_ϕ is evaluated throughout the region due to the magnetic current density M_ϕ in a frequency range of 100-900 KHz with an increment of 50 KHz. SLDM is employed to solve for the field at the lowest frequency of interest at 100 KHz. Exploiting axisymmetry, the total number of unknowns is 10,102. The number of iterations required to reach convergence is 191 SLDM steps. However, the same H and Q matrices are used to evaluate the results at higher frequencies by only recomputing the matrix functional of Eq. (24) at each single frequency. The total amount of computing time is approximately 24.7 seconds when computing the fields for the whole frequency range while the CPU time for the fields computation at the frequency of 100 KHz is 22.5 seconds. Therefore, only an additional 2.2 seconds is needed to obtain results for the remaining 16 frequencies. The ρH_ϕ contour lines are plotted at a frequency of 100 KHz in Figure 2. For low frequencies, these contour lines are also the electric field lines. To illustrate the effectiveness of SLDM further, the geometrical size of Figure 1 is extended from $18m \times 18m$ to $70m \times 70m$ with the number of unknowns growing from 10,102 to 90,302. The CPU time is illustrated in Figure 3. As can be seen from this figure, the maximum CPU is only 69 seconds for approximately 10^5 unknowns.

5 Conclusion

SLDM is successfully applied to the solution of the axisymmetric Maxwell's equations in a low-frequency regime when the finite-element method is employed to discretize Maxwell's equations. By considering a practical geophysical problem, the effectiveness of SLDM is demonstrated. It is shown that SLDM is not only fast, but also is capable of providing the solutions at multi frequencies by performing the SLDM iteration only for the lowest frequency of interest.

References

[1] V. Druskin and L. Knizhnerman, "Spectral Approach to Solving Three-Dimensional Maxwell's Diffusion Equations in the Time and Frequency Domainms," *Radio Science*, vol. 29, no. 4, pp. 937-953, August 1994.

[2] J. R. Lovell, *Finite Element Methods in Resistivity Logging*, Schlumberger Technology Corporation, Ridgefield, CT, 1993.

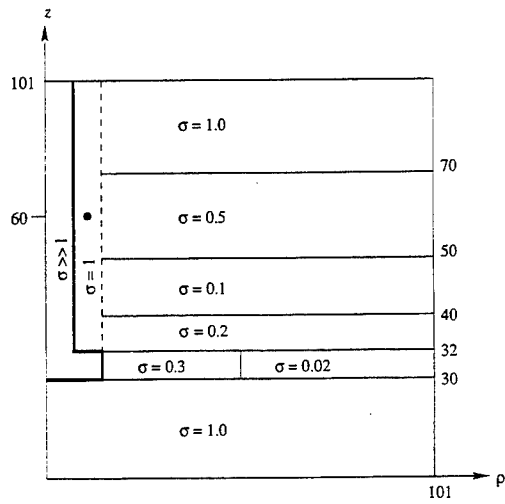[3] J. Jin, *The Finite Element Method in Electromagnetics*, John Wiley & Sons, New York, NY, 1993.

Figure 1: The problem geometry for the vertical borehole penetrating horizontal layered beds.
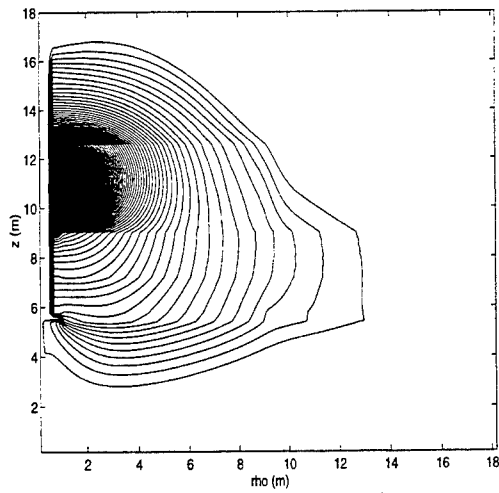
Figure 2: ρH_ϕ contour lines induced by a toroidal coil on a drill-stem in an inhomogeneous horizontal layered bed at 100 KHz.
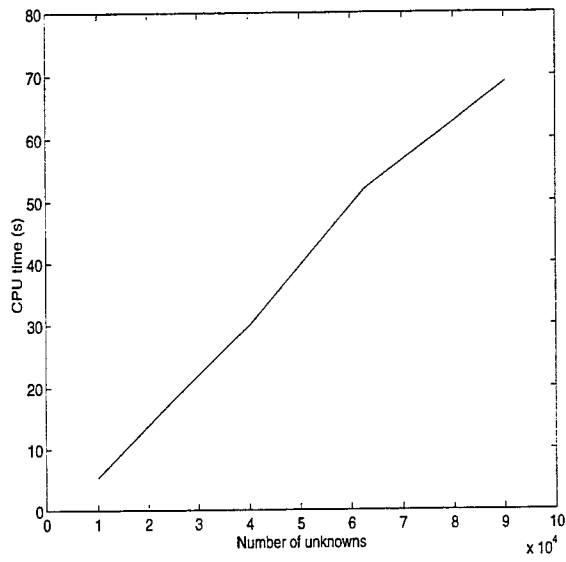
Figure 3: CPU time versus the number of unknowns for the magnetic field simulation at a frequency of 400 KHz.

Duality between finite elements
and Hodge operator in three dimensions.

Armel de La BOURDONNAYE, Stéphanie LALA
INRIA Sophia-Antipolis, BP 93, 06 902 Sophia-Antipolis Cedex (France).
E-mail : Armel.De_la_Bourdonnaye@sophia.inria.fr, Stephanie.Lala@sophia.inria.fr
Tel: (33) 4-93-65-79-00, Fax: (33) 4-93-65-77-40

1   Presentation

The partial differential equations modeling physical phenomena can be studied by two different ways at least. On one hand the analyst's point of view emphasises on properties of existence, uniqueness, maximum principle... On the other hand the geometric point of view, stresses on global behavior, invariance... Up to now, almost all discretizations of these equations are based on classical analysis point of view. Since, the micro-local analysis begins to be considered for several hyperbolic problems. However the differential geometry is not yet taken into account. J.C. Nedelec [1] introduced it for finite elements adapted to the electromagnetism. It is a generalization of the mixed finite elements introduced by P.A. Raviart and J.M. Thomas for the dimension two [2]. This work is formalized by A. Bossavit [3], which proves that they are discrete differential forms : the Whitney's elements [4]. So we can use this formalism on these elements. This is what we will present in our paper, with an application to the Maxwell system in dimension three.

In electromagnetism, one problem is the conservation of the properties of divergence for electric and magnetic fields. The divergence conditions (Gauss laws) and the charge's conservation are redundant in the continuous model with the Maxwell system, if the initial conditions satisfy them. Numerically they are not implemented and can not be preserved in time by the scheme, excepted for some schemes with orthogonal grid. This non conservation may introduce non-physical effects in the numerical simulations.

For instance, for wave propagation in a neutral plasmas, the preservation's these equations is essential. Indeed, their non-conservation may lead to a heating of the plasma and additional charges completely artificially.

In a first part, we will briefly, present the different ways used for trying to preserve Gauss laws. Then we will expose a new method for solving the time-domain Maxwell equations in three dimensions and preserving the divergence, which is based on differential geometry.

2   Survey of existing methods

Several methods exist for solving the time-domain Maxwell equations in three dimensions, which try to preserve the divergence laws. When they use finite differences, they are based on the Yee's scheme [5]. But they more generally use finite volumes with a constant time-step [6],[7], or a variable one [8]. An other method to have an acceptable conservation of the Gauss laws is to use a penalization with finite volumes [9]. But the divergence are not exactly conserved but only with the same order as the scheme for structured or unstructured meshes.

So when we want to apply them to the plasma for the charged particles transport, they add artificial charges. However numerical models try to solve this problem [10].

We can use a method of finite volumes coupled with finite elements for unstructured meshes for solving Maxwell system. The finite volumes are, in dimension 2, the polygons whose the edges are the bisectors of the triangle's edges. The Vlasov equation is satisfied if we consider the gauss law $divD = \rho$ as a constraint and we introduce a potential for the correction of the electric field [11],[12]. So we have two orthogonal meshes, but constructions of them are difficult for complex geometry and are not well controled, in particular in the neighborhood of the domain's frontier.

We can also try to extend a method using Hood-Taylor finite elements with an arbitrary triangulation of the

domain. Introduction of Lagrange's multipliers associated to constraints is needed [13],[14]. But this method can not be applied to Maxwell-Vlasov system : as the dimension of the phase-space is six, the number of degrees of freedom is too big.

We can have a particle in cell approach; a moderated number of degrees of freedom is needed for this method. The distribution function of the particles is approached by a linear combination of Dirac's masses in the phase-space [15]. The boundary needs a particular treatment [16], [17]. This method may to be coupled with finite volumes or elements. But algorithms must be developed for coupling particle-method with unstructured-grid schemes.

As the resolution of the complete Maxwell-Vlasov system is very expensive in computational time, an other way of doing is to use an approximated model. This is the case in particular for the transport of intense beams of charge's particles, where we use a paraxial approach model, which is more simple than the Maxwell-Vlasov system [18]. The paraxial model has to be coupled with the complete system to simulate a complete apparatus with transport and injection.

A geometrical approach is possible too, and this is our choice. We will present how we can solve Maxwell system in time domain in three dimension, if we consider variables as differential forms [19].

3   Description of the method based on the differential geometry

3.1   Discrete differential geometry

On a manifold X of dimension n, a differential p-form on X is a p-linear alternate form.

If X is $I\!R^3$ and u a vector field, in each point M of X, the linear application $\alpha \longmapsto u(M).\alpha$ is a 1-form, the bilinear application $\alpha, \beta \longmapsto |u(M), \alpha, \beta|$ is a 2-form.

And when u is a function, in each point M, $u(M)$ is a 0-form and the trilinear application $\alpha, \beta, \gamma \longmapsto u(M)|\alpha, \beta, \gamma|$ is a 3-form.

These forms have classical operators like multiplication, integration but they can also be differentiated thanks to the exterior differentiation d which satisfies $\int_S {}^{p+1}(d\ {}^p f) = \int_{\partial S} {}^p f$ and $d \circ d = 0$. This operator transforms a p-form to a (p+1)-form.

If $X = I\!R^3$, d coincides with $\bigtriangledown$ for a 0-form, with *curl* for a 1-form and with *div* for a 2-form.

It is possible to transform a p-form on a (n-p)-form thanks the Hodge operator denoted by $\star$.

It satisfies $\star \circ \star = (-1)^{p(n-p)} Id$. In particular, when n is odd (it's the case when $X=I\!R^3$) one has : $\star \circ \star = Id$.

3.2   Whitney finite elements

Now we recall some well-known facts on Whitney finite elements which are well adapted for the discretization of the differential geometry.

Let's consider a mesh of n-simplexes in $I\!R^n$. We denote by s_i the vertices of the mesh and by p_i the P_1-Lagrange basis functions associated to these points. Furthermore we denote by $\{i_1, ..., i_p\}$ the p-simplex convex hull of the points $s_{i_1}, ..., s_{i_p}$. In each n-simplex we have $p_i = \lambda_i$ where λ_i is the barycentric coordinate to s_i in the simplex under consideration. Functions p_i are used as basis functions to discretize 0-forms. We have $\int_{s_j} p_i = \delta_i^j$.

For *1*-forms, we look for basis functions integrable along the edges of the mesh. In a n-simplex, we define the function associated to the edge $\{i, j\}$ by : $p_{ij}^1 = \lambda_i d\lambda_j - \lambda_j d\lambda_i$.

In the same manner, for *(p-1)*-forms, in a n-simplex, we have basis functions defined by :
$p_{i_1 i_2 \cdots i_p}^{p-1} = \sum_{\sigma \in S[1:p]} \epsilon(\sigma) \lambda_{i_{\sigma(1)}} d\lambda_{i_{\sigma(2)}} \wedge \cdots \wedge \lambda_{i_{\sigma(p)}}$ where $S[I]$ is the set of permutations of the discrete set I. One can verify that $\int_{\{j_1 \cdots j_p\}} p_{i_1 i_2 \cdots i_p}^{p-1} = \delta_{j_1}^{i_1} \cdots \delta_{j_p}^{i_p}$. And so, for the p-form basis functions, the degrees of freedom are their integrals on the p-simplexes of the mesh.

So when we distretize differential geometry formalism on a three-dimensional mesh of tetrahedra with Whitney finite elements we obtain that :

- a 0-form is discretized by P1-Lagrange functions; the degrees of freedom are associated to the vertices of the mesh.

- a 1-form is discretized by H-curl elements, which satisfy the continuity of the tangential trace across faces.
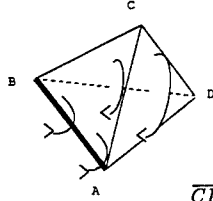
For example, for the edge $[AB]$, the basis function associated is $\dfrac{\overrightarrow{CD} \wedge \overrightarrow{CX}}{6V}$: the circulation along edge $[AB]$ is unitary and null along the others.

- a 2-form is discretized by H-div elements, which satisfy the continuity of the normal trace across faces.
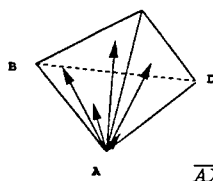
For example for the face $[BCD]$, the basis function associated is $\dfrac{\overrightarrow{AX}}{3V}$: the flux across face BCD is unitary and null across the others.

- a 3-form is discretized by P0-Lagrange functions; the degrees of freedom are the integrals on tetrahedra.

The discretization of the differentiation operator d is obtained thanks to the relation $\int_C df = \int_{\partial C} f$.

So when f is a 0-form, d satisfies $\int_{[AB]} grad \, {}^0f.\tau = {}^0f(B) - {}^0f(A)$. For a 1-form $\int_\phi curl \, {}^1f.n = \int_{\partial \phi} {}^1f.\tau$, and for a 2-form $\int_v div \, {}^2f = \int_{\partial v} {}^2f.n$.

We can see that we apply twice d to a 1-form, each edge contributes twice but with opposite signs. So $d \circ d = 0$ exactly.
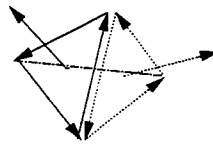
For the discretization of the Hodge operator, we use the fact that $\int \star^2f^1a = \left\langle {}^2f, {}^1a \right\rangle$, $\forall \; {}^1a$ a 1-form. As $\star$ ${}^2f$ is a $(3 - 2 = 1)$-form, we can decompose it on the discrete basis $\left({}^1a_i \right)$ of the 1-forms : $\star \, {}^2f = \sum_i \alpha_i \, {}^1a_i$. So $\alpha = (\alpha_i)_i$ satisfies $M\alpha = \left(\left\langle {}^2f, a_i \right\rangle \right)_i$ where M is the mass matrix of the 1-forms. This matrix will be inversed at each time step. We can not use an associated mass-lumped matrix [20] : the coefficient associated to an edge on a tetrahedron is proportional to the scalar product of the normal vectors of the faces opposite to this edge. So, if the mesh is too regular, contributions of all tetrahedra containing the same edge, can cancel.

3.3 Numerical scheme

Maxwell system : $\begin{cases} \dfrac{\partial B}{\partial t} + curlE = 0 & E \text{ is a 1-form, } B \text{ a 2-form} \\ \dfrac{\partial D}{\partial t} - curlH = J & H \text{ is a 1-form, } D \text{ and } J \text{ 2-forms} \\ divD = \rho & \rho \text{ is a 3-form} \\ divB = 0 \end{cases}$

We also need material constitutive laws : $D = \varepsilon E$, $B = \mu H$. For the transformation of a 1-form $(E$ or $H)$ to a 2-form $(D$ or $B)$, we need the Hodge operator $\star$. Maxwell system can be written as :

$$\begin{cases} \frac{\partial^2 B}{\partial t} + d\,^1E = 0 \\ \frac{\partial^2 D}{\partial t} - d\,^1H = {}^2J \\ d\,^2D = {}^3\rho \\ d\,^2B = 0 \end{cases} \qquad\qquad \begin{array}{l} {}^2D = \varepsilon \star {}^1E \\ {}^2B = \mu \star {}^1H \end{array}$$

For the implementation, we choose the leap-frog scheme, writing :

$$B^{n+\frac{1}{2}} = B^{n-\frac{1}{2}} - \Delta t dE^n \qquad\qquad D^{n+1} = D^n + \Delta t dH^{n+\frac{1}{2}} + \Delta t J^{n+\frac{1}{2}} \ .$$

Classically, one writes the scheme on (B,E) : $\quad B^{n+\frac{1}{2}} = B^{n-\frac{1}{2}} - \Delta t dE^n \qquad E^{n+1} = E^n + \Delta t \frac{\star d\star}{\varepsilon\mu} B^{n+\frac{1}{2}} + \Delta t \star J^{n+\frac{1}{2}}$
In this case, dD needs the operator $d \star \star d \star$. Now $\star\star$ is not exact numerically, because the matrix associated to $\star$ is inversed thanks to the conjugate gradient. On the other hand, with (B,D), we have that $dd = 0$ exactly, so we prefer to write the scheme on (B,D) :

$$B^{n+\frac{1}{2}} = B^{n-\frac{1}{2}} - \Delta t \frac{d\star}{\varepsilon} D^n \qquad\qquad D^{n+1} = D^n + \Delta t \frac{d\star}{\mu} B^{n+\frac{1}{2}} + \Delta t J^{n+\frac{1}{2}} \ .$$

Now, we will prove that Gauss laws are numerically exactly conserved. We suppose that $dB^{n-\frac{1}{2}} = 0$. So
$dB^{n+\frac{1}{2}} = dB^{n-\frac{1}{2}} - d\Delta t \frac{d\star}{\varepsilon} D^n = 0 - \frac{\Delta t}{\varepsilon} dd \star D^n = 0$

We suppose that $dD^n = \rho^n$ and $dJ^{n+\frac{1}{2}} = \frac{\rho^{n+1} - \rho^n}{\Delta t}$.

So $dD^{n+1} = dD^n - d\Delta t \frac{d\star}{\mu} B^{n+\frac{1}{2}} + d\Delta t J^{n+\frac{1}{2}} = \rho^n - \frac{\Delta t}{\mu} dd \star B^{n+\frac{1}{2}} + \Delta t dJ^{n+\frac{1}{2}} = \rho^n + \Delta t dJ^{n+\frac{1}{2}} = \rho^{n+1}$

As divergence laws are satisfied by initial conditions, and the electric charge conservation law is true at every time $n\Delta t$, we have the proposition :

$$dB^{\frac{1}{2}} = 0 \Rightarrow dB^{n+\frac{1}{2}} = 0 \ \forall n.$$
$$dD^0 = \rho^0 \ \text{ and } \ dJ^{n+\frac{1}{2}} = \frac{\rho^{n+1} - \rho^n}{\Delta t} \ \forall n \Rightarrow dD^n = \rho^n \ \forall n.$$

As we use a leap-frog scheme, our scheme is 2nd order accurate in time. d is exact; however it is 1st order accurate in space. That is because Hodge operator is discretized by $\int \star^2 f^1 a = \langle {}^2 f, {}^1 a \rangle$, and the inner product of their projections on the space of the 1-forms is an approximation of order 1 of their inner product, and the discretization of a form is also in order 1.

For the study of condition of the stability we write the scheme with matrix form :

If $V^n = \begin{pmatrix} B^{n-\frac{1}{2}} \\ D^n \end{pmatrix}$, $V^{n+1} = \begin{pmatrix} I & -\Delta t \frac{d\star}{\varepsilon} \\ \Delta t \frac{d\star}{\mu} & I - \Delta t^2 \frac{d\star}{\mu}\frac{d\star}{\varepsilon} \end{pmatrix} V^n = A V^n.$

We denote by (e_n, λ_n) eigenvalues of the previous matrix. So the associated matrix is $\begin{pmatrix} I & \Delta t \\ -\Delta t \lambda_n & I - \Delta t^2 \lambda_n \end{pmatrix}$.
The product of the eigenvalues is 1; for stability, we need them to be of modulus 1.
This leads to the condition CFL $(\Delta t^2)\, max(\lambda_n) \le 4$.
In practice, with c=1, we have : $\frac{\Delta t}{\Delta x} \le 0.2$.

Our scheme does not conserve the classical energy, $\int_V (D^n.E^n + B^n.H^n)$ at the time steps $n\Delta t$, because B and H are not known at the time $n\Delta t$. But if we use that $B^n \approx B^{n-\frac{1}{2}} + \frac{\Delta t}{2}\frac{\partial B}{\partial t} = B^{n-\frac{1}{2}} - \frac{\Delta t}{2} dE^n$. as $H^n = \star B^n$,
$H^n \approx H^{n-\frac{1}{2}} - \frac{\Delta t}{2} \star dE^n$, one has $B^n.H^n \approx B^{n-\frac{1}{2}}.H^{n-\frac{1}{2}} - \frac{\Delta t}{2} dE^n.H^{n-\frac{1}{2}} - \frac{\Delta t}{2} \star dE^n.B^{n-\frac{1}{2}}$, so
$B^n.H^n \approx B^{n-\frac{1}{2}}.H^{n-\frac{1}{2}} - \Delta t dE^n.H^{n-\frac{1}{2}}$. If we replace the approximation of $B.H$, $B^n.H^n$, by the previous approximation, we obtain that the energy $\mathcal{E}^n = \int_V D^n.E^n + B^{n-\frac{1}{2}}.H^{n-\frac{1}{2}} - \Delta t dH^{n-\frac{1}{2}} E^n$ approximates the continuous energy, and that this scheme preserves exactly the energy $\mathcal{E}^n$.

3.4 Numerical results

We have implemented the previous scheme in C_{++}. We test it with the mode (1,1,1) of a cubic cavity, with a metallic boundary condition. We can prove that the metallic condition, $E \times n = 0$, is equivalent to implement a

zero-coefficient to every basis function associated with an edge of the boundary. So, just a simplification of the mass matrix is need. If we look at a cut of the cube after several periods, we see that the general shape is conserved.
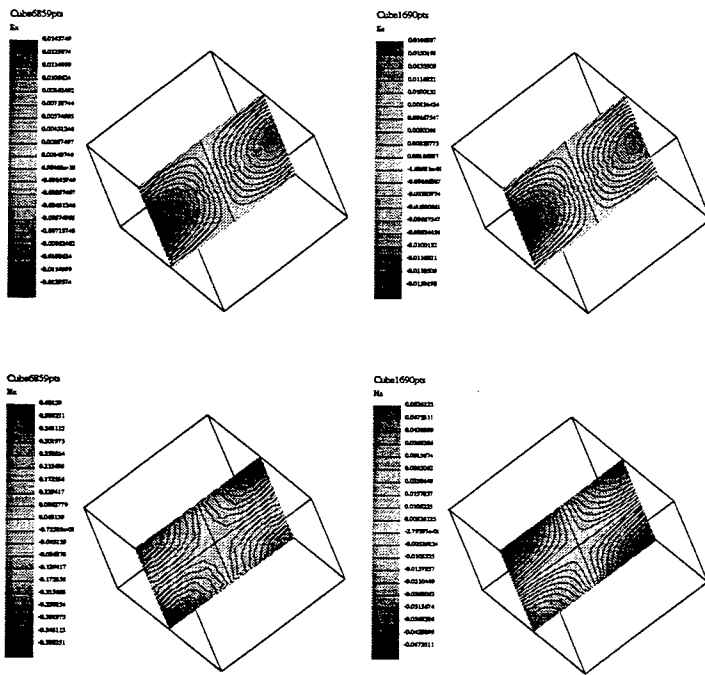

(left : Hodge solution - right : Exact solution)

With the following figure, we can see that the evolution in time at a given point gives more information. We have used a small mesh with 1000 points, and a bigger one with 6859 points. These two meshes are in fact accumulation of small cubes, each one cut in the same way in six tetrahedra. As our scheme is first order accurate, we have dissipation. It depends of the position of the point in the cube. We also have a phase shift of few percents, which is independent of the position.
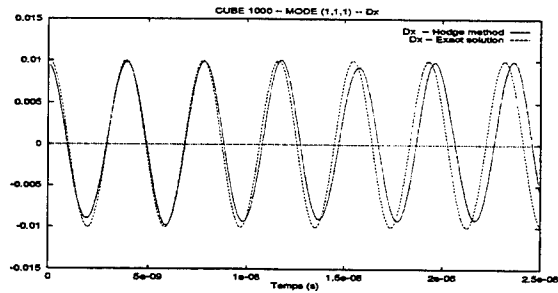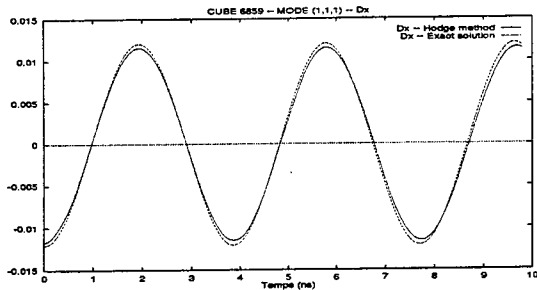
When we use a mesh made with Voronoi algorithm we obtain better results.
Nevertheless our goal was to make a method which preserves exactly divergence laws. It is reached. Whatever
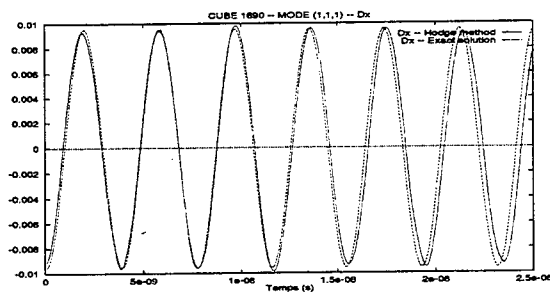
mesh we use, we obtain that the divergence of the magnetic field is in order of 10^{-17} : the computer precision. We have compared it with results obtained by the method developed in [7].
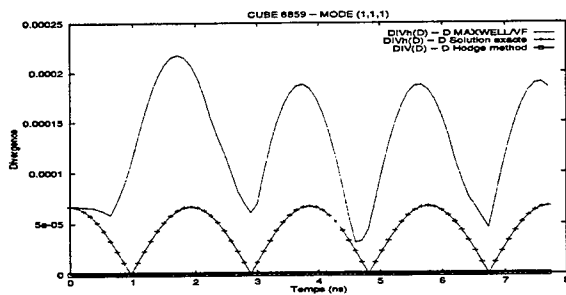
4   Conclusion

By using the differential geometry of the Maxwell system to discretize it, we have obtained a scheme which correctly simulates the electromagnetic field propagation and satisfied exactly to Gauss laws. Presented results are not excellent because the scheme we use is just first order accurate in space. They can improved thanks to an improvement of the accuracy of the space discretization.

Nevertheless our main goal is attained: If the divergence laws $divB = 0$ and $divD = \rho$ are satisfied by the initial conditions, and $dJ^{n+\frac{1}{2}} = \dfrac{\rho^{n+1} - \rho^n}{\Delta t}$ $\forall n$, then the divergences are conserved. Now we will develop others 3D

numerical simulations concerning wave propagation in non-cubic cavities and scattering problems.

References

[1] J. C. Nedelec, Mixed Finite Elements in $I\!R^3$, Numer. Math. **35**, 315–341 (1980).

[2] P. A. Raviart and J. M. Thomas, A mixed finite element method for 2nd order elliptic problems, Lecture Notes in Mathematics **606** (1977).

[3] A. Bossavit, *Méthodes numériques en électromagnétisme*, CEA-EDF INRIA, Eyrolles, 1991.

[4] A. Bossavit, Un nouveau point de vue sur les éléments mixtes, MATAPLI **20**, 23–35 (1989).

[5] K. S. Yee, Numerical Solution of Initial Boundary Value Problems Involving Maxwell's Equations in Isotropic Media, IEEE Trans. Antennas and Propagation **14**(3), 302–307 (1966).

[6] R. W. Noack and D. A. Anderson, Time Domain Solutions of Maxwell's Equations using a Finite Volume Formulation, AIAA J. **0451** (1992).

[7] J. P. Cioni, L. Fezoui, and D. Issautier, High order upwind schemes for solving time-domain Maxwell equations, La Recherche Aérospatiale **5**, 319–328 (1994).

[8] J. S. Shang, A Fractional-Step Method for Solving 3-D Time Domain Maxwell Equations, AIAA J. **0461** (1993).

[9] S. Depeyre and D. Issautier, A new constrained formulation of the Maxwell system, accepted for publication in Math. Model. and Num. Anal. (1997).

[10] P. A. Raviart, Modèles numériques en transport de particules chargées. in *Optimisation et Contrôle, Hommage à Jean Céa*, pages 217–232. Sophia Antipolis, Apr. 8-10 1992.

[11] F. Hermelin, Triangulation automatique d'un polyèdre en dimension N. RAIRO Anal. Numér. **16**, 211–242 (1982).

[12] R. A. Nicolaides, Direct discretization of planar div-curl problems, ICASE **89-76** (1989).

[13] E. Heintze, *Résolution des équations de Mazell tridimensionnelles instationnaires par une méthode d'éléments finis conformes*, PhD thesis, Paris, 1992.

[14] F. Assous, P. Degond, E. Heintze, P. A. Raviart, and J. Segre, On a finite element method for solving the three dimensional Maxwell equations, J. Comput. Phys. **109** (1993).

[15] P. A. Raviart, An analysis of particle methods, Lecture Notes in Mathematics **1127**, 243–324 (1985).

[16] P. Degond, S. Jaffard, F. Poupaud, and P. A. Raviart, The Child Langmuir law for cylindrically or spherically symmetric solutions of the Vlasov-Poisson equations. Part I : Statement for the problem and basic estimates, Math. Meth. Appl. Sc. **19**, 287–312 (1996).

[17] P. Degond, S. Jaffard, F. Poupaud, and P. A. Raviart, The Child Langmuir law for cylindrically or spherically symmetric solutions of the Vlasov-Poisson equations. Part II : Analysis of the reduced problem and determination on child langmuir current, Math. Meth. Appl. Sc. **19**, 313–340 (1996).

[18] P. Degond and P. A. Raviart, On the paraxial approximation of the stationnary Vlasov-Maxwell system, Centre de Mathématiques Appliquées, X, 1993.

[19] A. de La Bourdonnaye, Géométrie différentielle et éléments finis : l'exemple de l'électromagnétisme. CERMICS, ENPC-INRIA, Aug. 1995.

[20] Y. Haugazeau and P. Lacoste, Lumped of the Mass Matrix for 1st-Order Mixed Finite Elements of H(curl), Mathematical and Numerical aspects of wave propagation (1993).

A GENERALIZED METHOD FOR INCLUDING TWO PORT NETWORKS IN MICROWAVE CIRCUITS USING THE FINITE ELEMENT METHOD

Eray Yasan, Jong-Gwan Yook and Linda P. Katehi
Radiation Laboratory
Dept. of Electrical Engineering and Computer Sci.
The University of Michigan, Ann Arbor, MI 48109-2122, U.S.A.
Tel: 313-764-0502, Fax: 313-747-2106, Email: eray@engin.umich.edu

Abstract

This paper discusses the methodologies required to introduce basic passive elements into a FEM modelled microstrip circuit. Three different approaches have been investigated and are presented herein. The first two methods use the basic principles of circuit theory, while the third employs the so called zeroth order approximation or volume current method. The first of EM-circuit methods uses the voltage-current relations applying at the passive elements in the circuit. This is done through the impedance of that element and requires a modification of the functional of the FEM equations. The second method uses the S-parameters of the passive elements to provide the required circuit relation. By using these methods the effect of the presence of the passive elements on the microstrip circuit can be observed.

1 Introduction

The Finite Element Method (FEM) has been established during the past ten years as an accurate and versatile frequency-domain technique for passive circuit problems. Despite the capability of the technique to treat a broad variety of circuit geometries, it has been limited to only distributed elements that are mostly passive and linear. To be able to make the technique applicable to more complete microwave and millimeter wave circuits, its capability needs to be extended to handle passive and active elements. Some studies about these issues have been made by using different techniques such as FDTD, TLM and FEM [1]-[5]. The techniques presented herein are divided into circuit element methods and volume current methods. In the following, a short description of each technique is given.

1.1 Circuit Method # 1

This method uses circuit concepts such as the current-voltage $(I - V)$ relations through the nodes connected to the element[6]. From circuit theory the following relations for the resistor, capacitor and inductor hold respectively

$$V = RI \qquad V = j\omega L I \qquad I = j\omega C V. \tag{1}$$

In terms of field quantities the voltage and current are expressed in the following way

$$V = \int \mathbf{E} \cdot d\mathbf{l} \tag{2}$$

$$I = \oint_c \mathbf{H} \cdot d\mathbf{l} \tag{3}$$

where the integral is evaluated along the element for the voltage and around the element for the current flowing through the nodal points. Since tetrahedral based FEM is used throughout the analysis, lumped elements are located along the edges of the tetrahedrons.

1.2 Circuit Method # 2

In the second circuit method, S-parameters of the lumped elements are known and given to the system a priori. In order to use $(I - V)$ relations, S-parameters are converted to Z-parameters. Referring to Fig.1, the following relations hold

$$V_1 = Z_{11}I_1 + Z_{12}I_2 \tag{4}$$

$$V_2 = Z_{21}I_1 + Z_{22}I_2 \tag{5}$$

In the microstrip case V_1 is the voltage between the signal line and the ground. If this is a symmetric microwave circuit, then V_1 is equal to V_2. I_1 and I_2 are the currents flowing through the conductors towards the element as shown in Fig. 1. In terms of field expressions V_1 and V_2 are the line integrals of electric fields evaluated through the edges from conductors to the ground. I_1 and I_2 are the closed line integrals of magnetic fields around the conductors.

1.3 Volume Current Method

The third method [7] uses the relation

$$\mathbf{J}_i = \sigma \mathbf{E} \tag{6}$$

in order to account for the lumped elements' contribution by introducing fictitious conductivity regions in the volume. The conductivity σ in these regions is given by

$$\sigma = l/(Z_L s) \tag{7}$$

where Z_L, s and l represent load impedance in ohms(Ω), cross-sectional area and length of the load respectively.
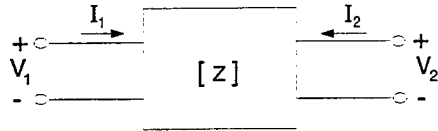
Figure 1: Two port network with Z parameters

2   FEM Formulation

Starting with Maxwell's equations, the following wave equation is weighted according to Galerkin's method and discretized

$$\nabla \times \nabla \times \mathbf{E} - \omega^2 \mu \epsilon \mathbf{E} = -j\omega\mu \mathbf{J}_i \tag{8}$$

where $\mathbf{J}_i$ is the impressed current source. Discretization is done in a conventional way using tetrahedral elements. The following weak form of Maxwell's equations is obtained

$$\int\int\int_v [(\nabla \times \mathbf{E}) \cdot (\nabla \times \mathbf{P}) - \omega^2 \mu \epsilon \mathbf{E} \cdot \mathbf{P}] dv = \oint_s j\omega\mu (\mathbf{H} \times \mathbf{P}) \cdot \hat{\mathbf{n}} ds - \int\int\int_v j\omega\mu \mathbf{P} \cdot \mathbf{J}_i dv \ . \tag{9}$$

Expanding the electric field as a summation of linear basis functions and choosing the weighting function as the same edge basis function give

$$\mathbf{E} = \sum_{i=1}^{6} a_i \mathbf{W}_i \tag{10}$$

$$\mathbf{P} = \mathbf{W}_j \ , \ j = 1, ..., 6 \tag{11}$$

where a_i are the unknowns to be determined, and $\mathbf{W}$'s are the first order edge based Whitney functions. For the circuit method #1 the first term on the right hand side of the FEM equation (9) is expressed in such a way that the effect of the lumped element is included. The resulting term in the FEM equations becomes

$$\frac{-j\omega\mu}{Z_L} \oint_s [\mathbf{e}_{12} \cdot \mathbf{E}\delta(\mathbf{r} - \mathbf{r}_o)][\int_1^2 \mathbf{E} \cdot d\mathbf{l}] ds \tag{12}$$

where $\mathbf{e}_{12}$ is the unit vector pointing from node 1 to node 2 along which the element is placed and Z_L is the load impedance.

According to the circuit method #2, having additional set of equations from $I - V$ relations enables us to write another matrix equation having N unknowns not necessarily being equal to the number of additional equations. By careful examination, elimination of some of the

615

unknowns, especially through the edges along which the element is located, by use of these equations decreases the size of the original FEM matrix. This matrix equation is solved using iterative matrix-solving algorithms.

The third method uses the second term on the right hand side of the FEM equation (9) in order to introduce the effect of the lumped element to the equations. The term takes the form

$$\frac{-j\omega\mu l^2}{Z_L} \int \int \int_v \mathbf{E} \cdot \mathbf{E} dv \ . \tag{13}$$

Similar to the first method, this term only contributes to the diagonal elements in the FEM matrix. The most efficient way to solve these matrix equations is found to be the Pre-Conditioned Conjugate Orthogonal Conjugate Gradient (COCG) Method.

3 Results

A shielded symmetric two port microstrip structure shown in Fig. 2 was examined. Using circuit method # 1 and volume current method, the case of 100Ω between the lines was studied. The S parameters obtained out of these two methods are shown in Fig. 3. For S_{11} the results agreed with theoritical ones ($|S_{11}| = |S_{22}| = -6.02\text{dB}$) quite reasonably but for S_{12} they are degraded in the high frequency region. This might arise because of circuit discontinuity at the element and also insufficient discretization. For circuit method # 2, the same geometry with a PEC wire is used in place of the resistor(Fig. 4). The results are shown in Fig. 5 and are in good agreement with the regular FEM results.

A variety of results involving complex arrangement of passive elements will be presented and discussed at the conference.

4 Conclusions

Three different approaches have been proposed and applied to the shielded two port microstrip geometry. These approaches can be applied to similar geometries which include inductors and capacitors as well. Generalization of these approaches might lead us to analyze structures having active lumped elements and to utilize harmonic balance technique with FEM.

References

[1] T. Shibata and H. Kimura,"Computer-aided engineering for microwave and millimeter-wave circuits using the FDTD technique of field simulations,"Int. Journal of Microwave and

Millimeter-Wave Computer-Aided Engineering, Vol.3, No. 3 pp. 238-250, 1993.

[2] V.A. Thomas, M.E. Jones,M. Piket-May, A. Taflove and E. Harrigan,"The use of SPICE lumped circuits as sub-grid models for FDTD analysis," IEEE Microwave Guided Wave Ltters,vol. 4, pp. 141-143, May 1994.

[3] A. Jahnsen and V. Hansen,"Spectral analysis of multiport microstrip circuit with active and passive lumped elements,"EMC, p. 1053,1990.

[4] R.H. Voelker and R. Lomax, "A Finite Difference Transmission Line Matrix method incorporating a nonlinear device model," IEEE Trans. Microwave Theory Tech., vol.38, March 1990,pp.302-312.

[5] K. Guillouard, M.-F. Wong, V. Fouad Hanna, J. Citerne, "A new global Finite Element analysis of microwave circuits including lumped elements," Digest of the 1996 IEEE Microwave Theory Tech. Symposium,vol. 1.

[6] E. Yasan , J.-G. Yook and L. Katehi, "Modeling the interface between fields and devices using the Finite Element Method," Digest of 1996 Progress In Electromagnetic Research Symposium (PIERS).

[7] Jong-Gwan Yook, "Electromagnetic modeling of high-speed high frequency interconnects," PhD Thesis,The University of Michigan 1996.
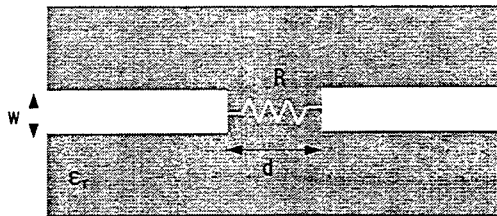
Figure 2: Shielded microstrip circuit with $Z_o = 50\Omega$, $\epsilon_r = 10.5$ w= $0.34mm$ $R = 100\Omega$ h=0.38mm
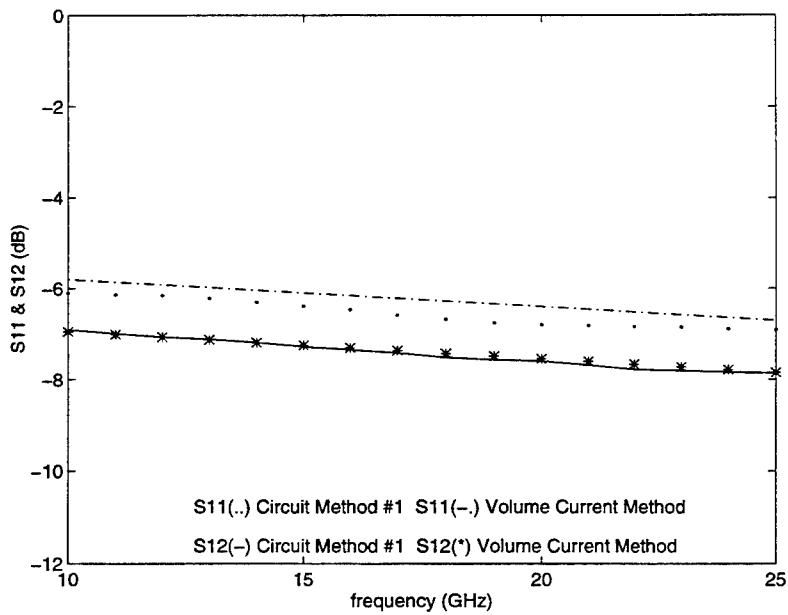
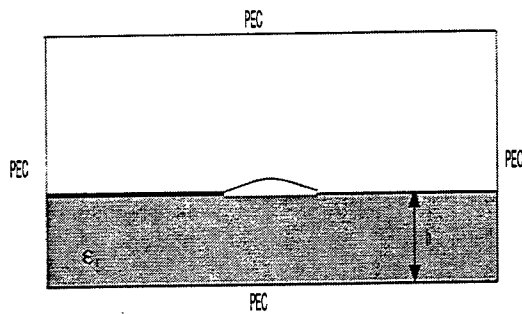Figure 3: S-parameters of the shielded microstrip circuit with a resistor

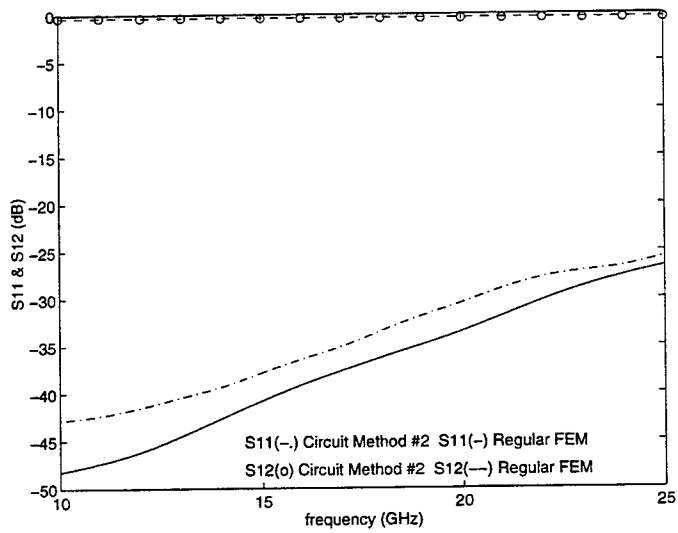Figure 4: Shielded microstrip circuit with a PEC wire between the conductors

Figure 5: S-parameters of the shielded microstrip circuit with a PEC wire

619

Projecting Between Complementary
Vector Basis Functions

J. Scott Savage and Andrew F. Peterson
School of Electrical and Computer Engineering
Georgia Institute of Technology
Atlanta, GA 30332-0250

I. INTRODUCTION

Vector basis functions for representing electromagnetic fields and currents have recently gained popularity in finite element and moment method algorithms [1,2]. Vector functions are naturally suited for modeling vector quantities in both 2–D and 3–D applications. Nedelec has defined a general class of vector functions which reside on simplices: triangles in 2–D, tetrahedra in 3–D [3]. These function sets can be decomposed into two categories: curl–conforming functions and divergence–conforming functions [4]. Curl–conforming vector functions exhibit tangential vector field continuity and, thus, have a finite curl. Divergence–conforming functions exhibit normal vector field continuity and have a finite divergence.

In a particular computational model, the unknown quantity and the governing equations dictate the choice between curl and divergence conforming vector functions. For example, the electric field integral equation for conductors, in which the surface current is the unknown vector quantity, contains terms involving the divergence of the basis functions, but no terms involving the curl. Therefore, divergence conforming functions are the natural choice to represent the current. Similarly, in a finite element analysis where the electric or magnetic field is the unknown vector quantity, the vector Helmholtz equation contains terms involving the curl of the basis functions, but no terms involving the divergence. In this case, curl-conforming basis functions are well suited to represent the field. Table 1 identifies which vector basis function set is typically chosen to approximate a field with the various properties shown.

Table 1		
Field to Represent	**J**	**E, H**
Continuity Requirement	Normal	Tangential
Derivatives appearing in the Governing Equations	$\nabla \bullet$	$\nabla \times$
Basis Function Choice	Divergence Conforming	Curl Conforming

One drawback to both types of Nedelec basis functions is that the complementary vector derivative operation is not well defined. Divergence–conforming basis functions have singular curl, while curl–conforming basis functions have singular divergence. There are several numerical formulations in which computing both the curl and the divergence of the vector basis functions is required. For example, integral equation formulations for scattering often use divergence–conforming functions to represent surface currents. However, the combined field integral equation requires both divergence and curl operations. The singular curl of divergence–conforming basis functions is problematic. Similarly, vector finite element algorithms usually use curl–conforming basis functions. However, higher-order radiation boundary conditions applied within these formulations require divergence computations, which are not directly possible using curl–conforming functions. To use Nedelec's vector basis functions in these examples, a method of computing the problematical derivatives is needed.

The proposed method of computing these terms uses a projection between the complementary basis function sets. To compute the incompatible derivatives, project one type of basis function onto the other, compute the required derivatives using the conforming basis function set, and then project back to the original basis set.

This paper develops a projection which is exact for constant vector fields and which retains the curl and divergence of the vector fields through the projection. Examples of projecting vector functions will be presented which demonstrate the capabilities of the projection. In addition, computations similar to those in the radiation boundary condition will be given to validate the projection.

II. Basis Function Projection

Curl–conforming vector basis functions may be used to approximate a vector field, $\overline{\mathbf{A}}$. At this point, no restrictions are made on the behavior or dimension of $\overline{\mathbf{A}}$. The basis function representation is expressed by

$$\overline{\mathbf{A}} \cong \sum_{i=1}^{N} \alpha_i \overline{\mathbf{T}}_i \tag{1}$$

where N is the total number of basis functions and α_i is the coefficient of the *i-th* curl–conforming basis function, $\overline{\mathbf{T}}_i$. The number of basis functions depends on the mesh used to discretize the domain of the vector field. Since Nedelec's basis functions are interpolatory, the curl–conforming coefficients may be obtained by directly sampling tangential components of the vector field.

Simultaneously, divergence–conforming basis functions may be used to represent the same vector field

$$\overline{\mathbf{A}} \cong \sum_{j=1}^{N} \beta_j \overline{\mathbf{S}}_j \tag{2}$$

where β_j is the coefficient of the *j-th* divergence–conforming basis function, $\overline{\mathbf{S}}_j$. The total number of divergence conforming functions is the same as the total number of curl conforming functions when equivalent order basis functions are used on the same mesh. The divergence–conforming coefficients may be obtained by sampling the normal components of the vector field.

The goal of this research is to find a projection between these complementary basis sets which will preserve information pertaining to the curl and divergence of the original vector field. The forward and backward projections will be represented mathematically by the matrices, **P** and **Q**. It is necessary that these matrices preserve as much information about the original vector field as possible. In other words, if α is chosen so that (1) is a good approximation, then $\beta = \mathbf{P}\alpha$ should produce a good approximation in Eqn. (2).

III. Conformal Vector Basis Functions

Nedelec's conformal vector functions developed in [4] are mixed order functions and are interpolatory in nature. The lowest order curl–conforming functions are often called constant tangential, linear normal (CT/LN) functions due to the behavior of fields along cell boundaries. There

is one CT/LN function associated with each edge of a finite element mesh. This association means that the field representation interpolates to the coefficient of the CT/LN function on that edge. The equivalent divergence–comforming functions are often called constant normal, linear tangential (CN/LT) functions, and are also associated with mesh edges. Higher–order Nedelec functions interpolate to edges, as well as faces and tetrahedra in the finite element mesh. For a given order, curl–conforming functions are distributed on the mesh identically to divergence–comforming functions, with identical interpolation points. In other words, $\overline{T}_i$ has the same domain and the same interpolation location as $\overline{S}_i$. This is the key property which allows a projection between the complementary basis functions.

To illustrate this point, consider the two connected triangular cells in a 2–D mesh shown in Fig. 1. The curl–conforming function on the common edge is shown in Fig. 1(a). This lowest order CT/LN function interpolates at the midpoint of each edge. In Fig. 1(b), the divergence–comforming function associated with the common edge is shown. Each row in the projection matrix of one basis set onto another is accomplished by sampling a single basis function of one type with each basis function of the complementary type.

Fig. 1(a) illustrates that each curl–conforming function has a possible normal component only on the five edges of its two cell domain. The same is true for divergence–comforming functions. Therefore, the projection matrices for low–order elements will be sparse: only 5 non–zero entries per row. After projecting, the single basis function in Fig. 1(a) will be represented by five divergence–comforming functions shown in Fig. 2(a). Likewise, the basis function in Fig. 1(b) will project onto the five curl–conforming functions in Fig. 2(b). The projection spreads the influence of one function into neighboring cells.

Mathematically, the projection matrices, **P** and **Q**, may be formed by

$$P_{ij} = \hat{t}_i \cdot \overline{S}_j \Big|_{m_i} \tag{3}$$

$$Q_{ij} = \hat{n}_i \cdot \overline{T}_j \Big|_{m_i} \tag{4}$$

where $\hat{n}_i$ and $\hat{t}_i$ are the unit normal and unit tangential vectors at the midpoint of the *i-th* edge, m_i. Fig. 3 shows the orientation and locations of the vectors in (3) and (4).

IV. Sample Projections

To analyze the accuracy of the projection proposed above, a sample 2–D mesh was constructed. Next, a constant vector field was sampled at the midpoints of each edge to obtain the curl–conforming coefficients, α, and the divergence–conforming coefficients, β. The projection matrices were then formed using (3) and (4), and it was verified that $\beta = P\alpha$ and $\alpha = Q\beta$. Since both CT/LN and CN/LT functions exactly model constant fields, this example demonstrates that the projection is exact for constant fields. Fig. 4 illustrates the representation of a constant vector field.

Next, the polynomial vector field

$$\overline{A} = \frac{x^2}{4}\hat{x} + \frac{xy}{2}\hat{y} \qquad (5)$$

was sampled with both basis function sets to obtain α and β. Fig. 5(a) shows this field after sampling with curl–conforming functions. Close inspection of this field representation reveals the tangential continuity property of curl–conforming functions which allows curl operations. However, the normal component discontinuities evident in Fig. 5(a) reveal the difficulty computing the divergence of this field representation. Fig 5(b) shows the divergence–conforming representation of the field after the projection, i.e. using $P\alpha$. This field representation has normal continuity which allows divergence operations. The β coefficients obtained from direct sampling of (5) differ from $P\alpha$ by less than a few percent. Furthermore, the divergence of the $P\alpha$ representation closely approximates the divergence of the original vector field.

V. References

[1]   J. S. Savage and A. F. Peterson, "Higher-order vector finite elements for tetrahedral cells," *IEEE Trans. Microwave Theory Tech.*, vol. 44, pp. 874–879, June 1996.

[2]   S. M. Rao, D. R. Wilton, and A. W. Glisson, "Electromagnetic scattering by surfaces of arbitrary shape," *IEEE Trans. Antennas and Propagation*, vol. 30, pp. 409–418, 1982.

[3]   J. C. Nedelec, "Mixed finite elements in R3," *Numer. Math.*, vol. 35, pp. 315–341, 1980.

[4]   R. D. Graglia, D. R. Wilton, and A. F. Peterson, "Higher order interpolatory vector bases for computational electromagnetics," *IEEE Trans. Antennas and Propagation*, 1997 (to appear).
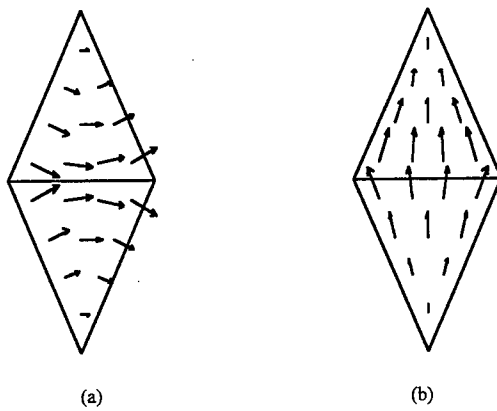
Figure 1. (a) A CT/LN curl–conforming element. (b) A CN/LT divergence–conforming element
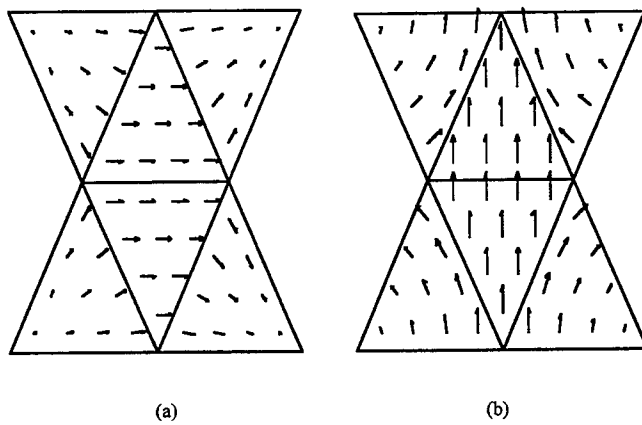

Figure 2. (a) A CT/LN element projected onto divergence–conforming functions. (b) A CN/LT element projected onto curl–conforming functions.
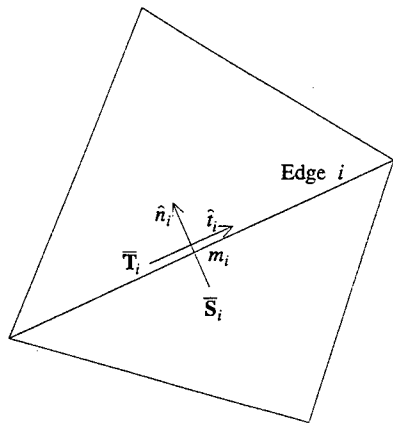
Figure 3. An edge of the finite element mesh demonstrating the orientation of the basis functions and component vectors.
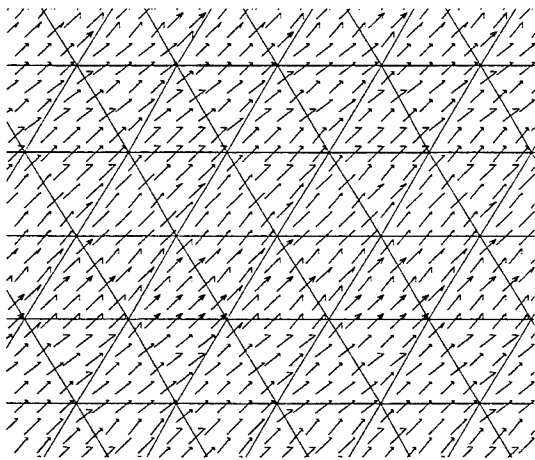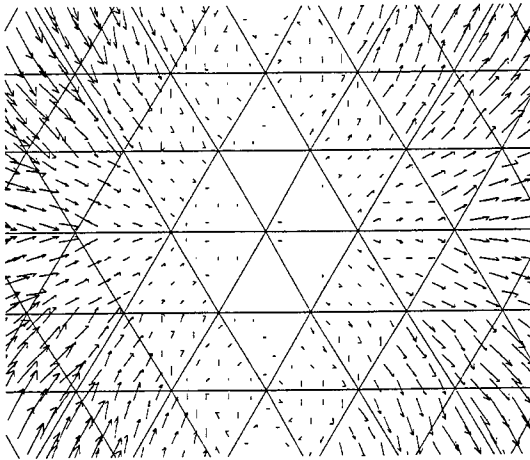

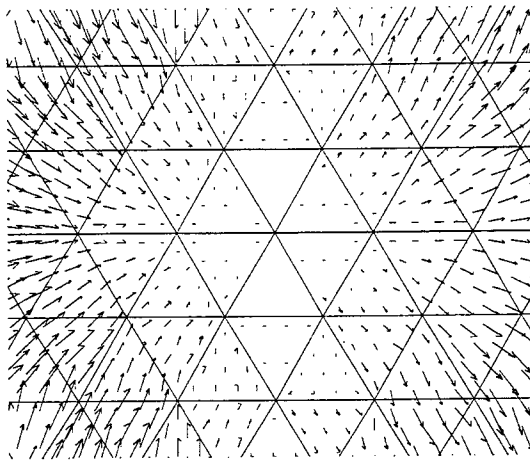Figure 4. The constant vector field, $\hat{x} + \hat{y}$ sampled by either curl–conforming or divergence–conforming functions gives an exact field representation. Also, the projections preserve a constant field.

Figure 5. Two representations of a quadratic vector field: (a) the CT/LN curl–conforming representation and (b) the CN/LT divergence–conforming representation projected from (a).

ADVANCES IN TRANSMISSION LINE MATRIX (TLM) MODELING I

Chairs: W. Hoefer and F. German

Modelling of Ferrite Tiles as Frequency Dependent Boundaries in General Time-Domain TLM Schemes

V. Trenkic, J. Paul, I. Argyri and C. Christopoulos

Numerical Modelling Group

Department of Electrical and Electronic Engineering

University of Nottingham

University Park, Nottingham NG7 2RD, United Kingdom

Tel: (44) 1159 515-563, Fax: -616, E-mail: vmt@eee.nott.ac.uk

Abstract

Numerical modelling of frequency dependent boundary conditions, such as ferrite tiles, using the time-domain transmission-line modelling (TLM) method is discussed. A previous formulation of frequency dependent ferrite tile boundaries in terms of second-order digital filters is extended so that it can be applied in a graded TLM mesh and more general TLM schemes where the characteristic impedance of link lines may differ from the intrinsic impedance of free space. A mathematical analysis is performed to ensure that the proposed model is unconditionally stable. The model is implemented and validated using different TLM schemes and different mesh gradings. Simulation results showing the electric field response in a typical screened room configuration are presented to demonstrate the effectiveness of the method.

1 Introduction

It has been long established that the application of ferrites as homogeneous single layer absorbers is effective for the frequency range of 20 MHz to 2 GHz. This feature makes ferrite tiles the standard absorbing material (RAM) for lining anechoic chambers used for electromagnetic compatibility (EMC) measurements and testing [1]–[4]. The factors that determine a ferrite tile's absorbing characteristics are its geometry, in particular its thickness, and its intrinsic electromagnetic parameters. The relative permittivity (ε_r) of ferrite materials is assumed real and constant for the frequency range of interest. The relative permeability (μ_r) of ferrite materials is a function of frequency and a first order Laplace function provides a good approximation over the frequency range [2]:

$$\mu_r(s) = 1 + \frac{\mu_{r0} - 1}{1 + \frac{s}{\omega_r}} \tag{1}$$

where μ_{r0} is the dc permeability of the material, $\omega_r = 2\pi f_r$ is the angular frequency at which the real and imaginary parts of the susceptibility are equal in magnitude (the Debye frequency) and s is the complex frequency. The frequency response is obtained by the substitution $s = j\omega$.
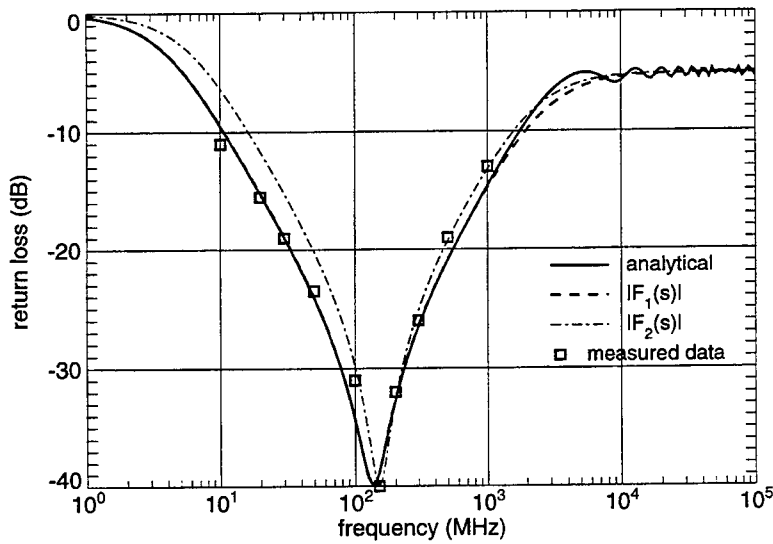
Figure 1: Return loss of a flat ferrite tile

The reflection coefficient Γ of a flat tile with thickness Δ with a perfect electric conductor (PEC) backed rear face can be determined from transmission-line theory [4]:

$$\Gamma(s) = \frac{\Gamma_f(s) - \exp(-2\gamma(s)\Delta)}{1 - \Gamma_f(s)\exp(-2\gamma(s)\Delta)} \qquad (2)$$

where $\Gamma_f(s)$ describes the reflectivity of the front face of the tile and $\gamma(s)$ is the propagation constant of the tile. These are defined as:

$$\Gamma_f(s) = \frac{\sqrt{\mu_r(s)} - \sqrt{\varepsilon_r}}{\sqrt{\mu_r(s)} + \sqrt{\varepsilon_r}} \qquad\qquad \gamma(s) = s\sqrt{\mu_0\mu_r(s)\varepsilon_0\varepsilon_r} \qquad (3)$$

The expressions (1)–(3) show that the reflectivity of the ferrite tile is a function of the complex frequency. The analytical return loss, defined as $20\log|\Gamma(s)|$ (dB), for a typical flat tile of depth $\Delta = 6.3$mm, $\varepsilon_r = 12$, $\mu_{r0} = 1051$ and $f_r = 7.06$MHz, is calculated using (1)–(3) and plotted in Figure 1 (solid line).

Based on the observation that the tile reflectivity can be approximated with a second order band-reject filter, the basic scheme for description of a ferrite tile boundary condition in the Transmission Line Modelling (TLM) method [5] was established in Reference [3]. This ferrite tile model [3, 4] was developed for application to the basic 12-port TLM symmetrical condensed node (SCN), but cannot be applied to a graded mesh or for advanced nodes. The graded mesh, which contains cells of different aspect ratios, is used to represent smaller features in an otherwise large modelling space (e.g. a screened

room) in order to minimize the computational memory and run-time demands. To further reduce the computational effort, advanced TLM schemes, such as the hybrid [6], supercondensed [7] and other schemes derivable from the General Symmetrical Condensed Node (GSCN) [8], have been recently introduced. In these nodes, the characteristic impedance of the link lines is in general different from the intrinsic impedance of free space. Hence, pulses travelling along the link lines connecting to the boundary encounter a different reflection coefficient than that described by equation (2) thus requiring an extension to the original approach [3, 4]. The generalization of the existing ferrite tile formulation for TLM is the main topic of this paper.

2 Approximations to the Ferrite Tile Reflectivity Function

As shown in [3], the ferrite tile reflectivity can be approximated with a second order transfer function:

$$F(s) = -\left[\frac{s^2 + 2s\zeta\omega_n + \omega_n^2}{k(s+d)}\right] \tag{4}$$

where $\omega_n = 2\pi f_n$ is the undamped natural frequency (i.e. the frequency of the reflection coefficient minimum), ζ is the damping ratio, d is the pole frequency and k is the parameter chosen to give $F(0) = -1$. The filter characteristics are obtained from the reflection coefficient magnitudes of $\rho_{\min}$ given at ω_n and ρ_u given at the highest frequency of interest, $\omega_u = 2\pi f_u$. This transfer function is unbounded as $s \to \infty$ and will become unstable with high-frequency excitation. In TLM, the highest frequency excited is dependent on the type of the excitation as well as on the time step. Hence, when modelling ferrite tiles with transfer function (4) the parameters of the mesh and the excitation must be chosen so as not to excite angular frequencies greater than k. This condition poses serious restrictions when modelling fine meshes which have small time steps.

As shown in [4], to provide a bounded infinite frequency response, another pole is incorporated into (4):

$$F(s) = -\rho_h\left[\frac{s^2 + 2s\zeta\omega_n + \omega_n^2}{(s+d)(s+e)}\right] \tag{5}$$

Assuming a wide separation between the poles and zeros in the complex plane, and taking e and d as real positive numbers, the following approximations are valid:

$$d^2 << \omega_n^2, \qquad e^2 >> \omega_n^2, \qquad \omega_u^2 >> \omega_n^2 \tag{6}$$

At dc ($s \to 0$) physical arguments require that the reflection coefficient tends to -1, therefore:

$$\lim_{s \to 0} F(s) = -\frac{\rho_h \omega_n^2}{de} = -1 \tag{7}$$

In the Fourier domain ($s = j\omega$), and taking into account the approximations (6), it also follows:

$$|F(j\omega_n)| = \rho_{\min} \approx \frac{2\rho_h \zeta \omega_n}{e} \tag{8}$$

$$|F(j\omega_u)| = \rho_u \approx \frac{\rho_h \omega_u}{\sqrt{\omega_u^2 + e^2}} \tag{9}$$

632

The high frequency pole e is determined from (9) as:

$$e = \omega_u \sqrt{\left(\frac{\rho_h}{\rho_u}\right)^2 - 1} \tag{10}$$

while from (7) and (8) it follows:

$$d = \frac{\rho_h \omega_n^2}{e} \tag{11}$$

$$\zeta = \frac{e \rho_{\min}}{2 \omega_n \rho_h} \tag{12}$$

Therefore, from (10)–(12), the poles e and d and the damping factor ζ can be obtained from ω_n, ω_u, $\rho_{\min}$, ρ_u and ρ_h, which are given by the analytical solution of (2) or from the measured data. Note that for $s \to \infty$ we have

$$\lim_{s \to \infty} F(s) = -\rho_h \tag{13}$$

hence, ρ_h represents the amplitude of the reflection coefficient at infinite frequency. By studying equations (1)–(3) and the analytical plot in Figure 1, we can see that at high frequencies, the reflection coefficient Γ oscillates around $\rho_h = (1 - \sqrt{\varepsilon_r})/(1 + \sqrt{\varepsilon_r})$ due to the layer effect of the tile.

For the typical ferrite, with $\varepsilon_r = 12$, we find $\rho_h = 0.552$. Also, it can be found from the analytical expression plotted in Figure 1 that the reflection minimum of $\rho_{\min} = 0.01$ occurs at $f_n = 135\text{MHz}$, while at $f_u = 1\text{GHz}$, $\rho_u = 0.1862$. Using these values in (10)–(12) and (5), we obtain the transfer function $F_1(s)$ which is plotted in Figure 1 using broken lines. It can be seen from the figure that $F_1(s)$ is indistinguishable from the analytical reflectivity up to 1GHz. The measured data [3] for this tile is also plotted in Figure 1, using box symbols. As can be seen, a close fit has been obtained between the measured data and the filter approximation $F_1(s)$, although a slight discrepancy is noted around the reflection minimum. This is due to the fact that expression (1) is only an approximation to the true permeability function and due to the error margin of the measured data. Another second-order approximation, $F_2(s)$, used in references [3, 4], plotted in Figure 1 using dot-dash lines, takes $f_n = 150\text{MHz}$ in order to fit the measured data values around the reflection minimum. However, this advantage is offset by a larger deviation from the measured data in the frequency range below 100MHz, as seen from the figure.

A better fit to the measured data can be achieved by the use of higher-order filters which require the expense of extra storage and run-time. Design of such higher-order filters is currently being investigated for application to grid tiles. These tiles have a reflectivity which cannot be described very accurately using the second-order approximation [3, 4], considered here.

3 Application to the General TLM Schemes

Following the principles described in [4], the continuous function $F(s)$ is approximated with a discrete function $H(Z)$ (where Z is the time shift operator) compatible with the sampled nature of the TLM paradigm. However, function $F(s)$ can only be used to find $H(Z)$ in TLM models using a uniform mesh (i.e. cubic cells) and with impedance of link lines equal to that of free-space. For general cases, an additional transformation of $F(s)$ is required as described below.

For a plane wave propagating in the i-direction in free-space, with transverse field components E_j and H_k, (where $i, j, k \in \{x, y, z\}$ and $i, j \neq k$) the total capacitance C_j and the total inductance L_k, of the block of space modelled by the TLM cell, are:

$$C_j = \varepsilon_0 \frac{\Delta i \Delta k}{\Delta j} \qquad L_k = \mu_0 \frac{\Delta i \Delta j}{\Delta k}$$

The intrinsic impedance of the medium seen by such a wave is defined by

$$Z_{ij}^m = \sqrt{\frac{L_k}{C_j}} = \sqrt{\frac{\mu_0}{\varepsilon_0}} \frac{\Delta j}{\Delta k} = Z_0 \frac{\Delta j}{\Delta k}$$

and the termination resistance $R_{ij}(s)$, required to give the desired reflection coefficient $F(s)$, is obtained from

$$F(s) = \frac{R_{ij}(s) - Z_{ij}^m}{R_{ij}(s) + Z_{ij}^m}$$

to give

$$R_{ij}(s) = Z_{ij}^m \frac{1 + F(s)}{1 - F(s)}$$

The i-directed, j-polarized link line reflection coefficient, $\rho_{ij}(s)$, is then found by terminating the line of characteristic impedance Z_{ij} with this same resistance:

$$\rho_{ij}(s) = \frac{R_{ij}(s) - Z_{ij}}{R_{ij}(s) + Z_{ij}} = \frac{[1 + F(s)] - \alpha[1 - F(s)]}{[1 + F(s)] + \alpha[1 - F(s)]} \tag{14}$$

where $\alpha = Z_{ij}/Z_{ij}^m$. Therefore, the reflection coefficient of a link line of general impedance Z_{ij} is given by the function $\rho_{ij}(s)$ which is equal to $F(s)$ only when $\alpha = 1$, that is when $\Delta j = \Delta k$ and $Z_{ij} = Z_0$. So for the general case, the transfer function $\rho_{ij}(s)$ is dependent on the polarization and characteristic impedance of the link line.

Inserting (5) into (14) and making use of (11) and (12) we obtain:

$$\rho_{ij}(s) = -\frac{A_1 s^2 + B_1 s + C}{A_2 s^2 + B_2 s + C} = -\frac{A_1}{A_2} \frac{(s - z_1)(s - z_2)}{(s - p_1)(s - p_2)} \tag{15}$$

with

$$A_{1,2} = \alpha(1 + \rho_h) \mp (1 - \rho_h) \tag{16}$$

$$B_{1,2} = \alpha[d + e(1 + \rho_{\min})] \mp [d + e(1 - \rho_{\min})] \tag{17}$$

$$C = 2\alpha \rho_h \omega_n^2 \tag{18}$$

The revised poles and zeros are obtained from the solution of the quadratics:

$$z_{1,2} = \frac{-B_1 \pm \sqrt{B_1^2 - 4A_1 C}}{2A_1}$$

$$p_{1,2} = \frac{-B_2 \pm \sqrt{B_2^2 - 4A_2 C}}{2A_2}$$

The stability condition for $\rho_{ij}(s)$ requires that real parts of the poles are always negative, $\mathcal{R}(p_{1,2}) < 0$, which is satisfied if A_2, B_2 and C are positive, as verified in (16)–(18).

The continuous function $\rho_{ij}(s)$ is converted to the discrete time function, with the time step T, using the transformations $s \rightarrow Z$, $z_{1,2} \rightarrow \exp(z_{1,2}T)$ and $p_{1,2} \rightarrow \exp(p_{1,2}T)$ to give:

$$H(Z) = \frac{b_0 + Z^{-1}b_1 + Z^{-2}b_2}{1 - Z^{-1}a_1 - Z^{-2}a_2}$$

where coefficients a_1, a_2, b_1 and b_2 are:

$$a_1 = \exp(p_1T) + \exp(p_2T) \qquad a_2 = -\exp(p_1T + p_2T)$$
$$b_1 = -b_0(\exp(z_1T) + \exp(z_2T)) \qquad b_2 = b_0 \exp(z_1T + z_2T)$$

while b_0 is determined from the impulse invariant condition applied at dc:

$$\lim_{s \to 0} \rho_{ij}(s) = \lim_{Z \to 1} H(Z) = -1$$

The implementation of this second-order digital filter in TLM is described in [3, 4]. Following a schematic of the second-order digital filter section [3, 4], a voltage pulse $_nV^r$ reflected from the boundary at the time step n is efficiently calculated from the incident pulse $_nV^i$ and two other quantities, $_{n-1}V_0$ and $_{n-2}V_0$, saved from the two previous time steps, using the following algorithm:

$$_nV_0 \quad \leftarrow \quad _nV^i + a_1\,_{n-1}V_0 + a_2\,_{n-2}V_0$$
$$_nV^r \quad \leftarrow \quad b_0\,_nV_0 + b_1\,_{n-1}V_0 + b_2\,_{n-2}V_0$$

This procedure requires storage and update of $_{n-1}V_0$ and $_{n-2}V_0$ for each link line adjacent to the ferrite tile boundary.

4   Validation and Simulation Results

Using the formulation established in the previous section, we have implemented the ferrite tile boundary conditions into a general TLM solver. The validation of the new algorithm was performed by simulating return loss of the flat ferrite tile using different TLM schemes and using nodes with different aspect ratios. The results were then compared with those obtained by a uniform mesh SCN and with the analytic plot of the transfer function. The simulated return loss is calculated from

$$20 \log \left| \frac{E_1(f) - E_0(f)}{E_0(f)} \right|$$

where $E_1(f)$ and $E_0(f)$ are the frequency response of total electric field with and without the presence of the ferrite tile boundary, respectively. In the latter case, unbounded space was simulated by means of simple matching boundary condition [7]. As an example, simulation results of the return loss of a plane wave travelling along the x direction, using SCN with $\Delta l = 2.5$cm, HSCN with $\Delta x = 5$cm and $\Delta y = \Delta z = 2.5$cm, and SSCN with $\Delta x = 2.5$cm, $\Delta y = 5$cm and $\Delta z = 1.5$cm are compared in Figure 2. Excellent agreement between the results can be noted from the figure. The small differences are
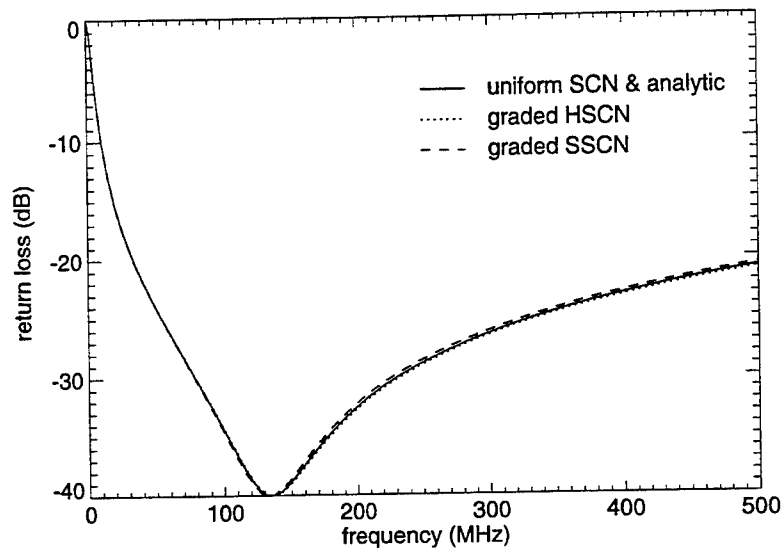
Figure 2: Simulation of the return loss

due to different dispersion properties of the nodes and due to the simulation error of matched boundaries for graded nodes.

Figure 3 shows the electric field impulse response of a typical screened room (7.2m × 3.6m × 2.4m) with various linings and using identical excitations. The solid line (PEC room) shows the resonant modes of an untiled room. The short-dash line shows the response of the room fully lined with tiles and indicates the damping which can be achieved using ferrite tiles. It is often not economically viable to completely line a large room with tiles, but it is possible to damp a room effectively by placing tiles at the positions of the magnetic field maxima. The long-dash line shows the room response with 120cm width crosses on all walls. As can be seen, the room with crosses provides similar damping to the fully lined room with approximately half the number of tiles.

5 Conclusions

A generalization of the modelling of frequency dependent ferrite tile boundary conditions using time-domain TLM was presented. A general second-order transfer function, which takes into account different node gradings and arbitrary link line characteristic impedance, was developed and implemented using digital filter methods. The presented formulation was shown to be unconditionally stable. The simulation results using different TLM condensed nodes indicated good agreement with the analytical and measured data.
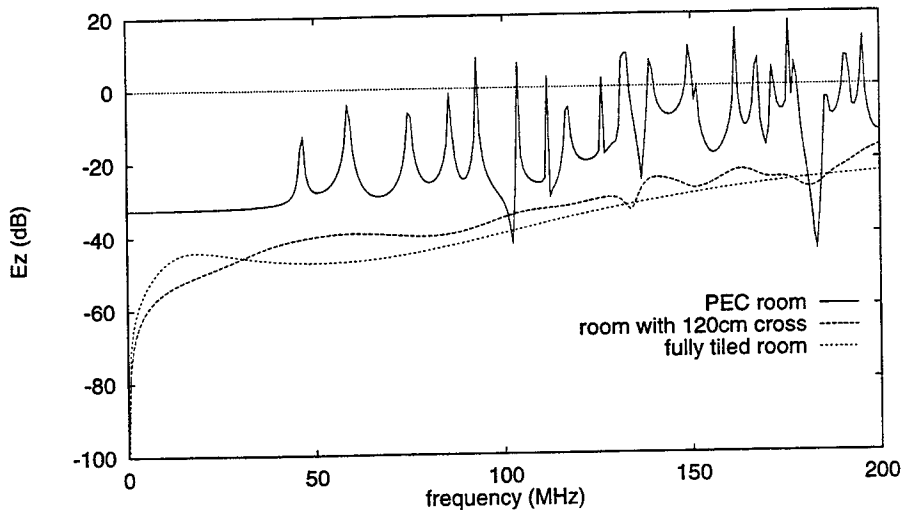
Figure 3: Electric field response in a screened room

References

[1] C. Christopoulos. *Principles and Techniques of Electromagnetic Compatibility*. CRC Press, 1995.

[2] J. F. Dawson. Improved magnetic loss for TLM. *Electronics Letters*, 29(5):467–478, March 1993.

[3] J. F. Dawson. Representing ferrite absorbing tiles as frequency dependent boundaries in TLM. *Electronics Letters*, 29(9):791–792, April 1993.

[4] J. F. Dawson, J. Ahmadi, and A. C. Marvin. Modelling the damping of screened room resonances by ferrite tiles using frequency dependent boundaries in TLM. In *2nd Intl. Conf. Comp. Electromagn.*, pp. 271–274, Nottingham, UK, April 1994. IEE Conf. Publ. 384.

[5] C. Christopoulos. *The Transmission-Line Modelling (TLM) Method*. IEEE Press, 1995.

[6] R. A. Scaramuzza and A. J. Lowery. Hybrid symmetrical condensed node for TLM method. *Electronics Letters*, 26(23):1947–1949, Nov. 1990.

[7] V. Trenkic, C. Christopoulos, and T. M. Benson. Theory of the symmetrical super-condensed node for the TLM method. *IEEE Trans. Microwave Theory Tech.*, 43(6):1342–1348, June 1995.

[8] V. Trenkic, C. Christopoulos, and T. M. Benson. Development of a general symmetrical condensed node for the TLM method. To appear in *IEEE Trans. Microwave Theory Tech.*, 44(12/1), December 1996.

THE USE OF SOURCES FOR TLM MODELING OF COMPLEX MATERIALS

J. Represa, A. C. L. Cabeceira and I. Barba.
Dept. Electricidad y Electrónica. Facultad de Ciencias.
Universidad de Valladolid. 47071 Valladolid. Spain.

Abstract. The transmission line matrix method (TLM) is a numerical technique in the time domain for solving electromagnetic problems which, since its establishment in 1970 by P. B. Johns, has shown its power and versatility. It has been, and still is, a wide field of research, allowing the method to treat more and more general problems. One of the points of recent interest lies on the modeling of material media with complex electromagnetic properties. In this paper we present some extensions for the treatment of frequency dispersive media and anisotropic media, starting from the description of the properties of such media in the TLM network through additional voltage sources which accounts for the part of the behavior not included in the classic TLM algorithm.

1.- INTRODUCTION.

In the last few years, there is a remarkable effort to enlarge the TLM capabilities for the analysis of media with complex characteristics [2]. This is the case of frequency dispersive media [15-19,26] and anisotropic media [6-9,24,25]. In the first case, the usual description of such a material is presented in the frequency domain, so it is not possible a direct inclusion of its behavior in the TLM algorithm, being a time domain method. For the second case, the tensorial description of the media, which produces a coupling between the field components, makes difficult to include it in the TLM mesh, strongly dependent on the synchronism and the geometry of the basic network.

Nevertheless, TLM is a flexible tool and, in many cases, allows the modeling through additional circuit elements in the basic node. This is the case of [16]where nonlinear and dispersive media can be modeled by the inclusion of nonlinear loads connected to 2D nodes. On the other hand, relevant ideas developed for other time-domain techniques, such as FDTD [10-14], can be modified and applied successfully to the TLM method.

In this work, we concentrate on the modeling of anisotropic and dispersive media using additional voltage sources in the basic node, which accounts for the properties of the media not described in the basic network. The starting point, in every case, is to discretize the field equations (i.e. Maxwell equations or wave equation) for a field component of interest, then we include the time domain description of the media properties and finally, we compare with the equations modeled by TLM. The terms in the field equations having not an analogy in the TLM equations are included through a voltage source in each node on the media, and are updated each time iteration. For the dispersive case, in which the response depends on the previous instants, it implies the summation of the responses from the first time step. So, a very high CPU time and memory storage will be needed. Fortunately, the techniques for recursive convolution [21-23] can, in most cases, simplify and reduce this task.

For the anisotropic case, considering the general non-dispersive case of non-diagonal anisotropy over the axis of the mesh, there is no need of storing the response on the previous time steps, but to describe the different properties of the medium along the axis. This is achieved through meshes with different admittances in each direction and voltage sources accounting for the cross-coupling of the field components.

2.- ANISOTROPIC MEDIA. 2D MODELING.

The modeling of anisotropic non-dispersive media in TLM has been done, in the case where the medium is described by a diagonal tensor [2,4-9] on the TLM mesh axis, with the addition of stubs, associated to the principal values of the tensor. It is possible to model it with a variable mesh or through the interconnection of different lines (i.e. different characteristic admittance for each arm on the node). For the general case of non-diagonal tensors, we write down a field equation for a component affected by the medium properties: i.e. if we deal with TE modes, the wave equation for H_z is:

$$\varepsilon_{xx}\frac{\partial^2 H_z}{\partial x^2}+\varepsilon_{yy}\frac{\partial^2 H_z}{\partial y^2}+2\varepsilon_{xy}\frac{\partial^2 H_z}{\partial x\partial y}=\mu_0\varepsilon_0\left(\varepsilon_{xx}\varepsilon_{yy}-\varepsilon_{xy}^2\right)\frac{\partial^2 H_z}{\partial t^2} \tag{1}$$

which can be discretized in finite differences as:

$$
\begin{aligned}
_{k+1}H_z(i,j) &= \frac{\varepsilon_{xx}}{2\left(\varepsilon_{xx}\varepsilon_{yy} - \varepsilon_{xy}^2\right)}\left[_kH_z(i+1,j) + _kH_z(i-1,j) + \frac{\varepsilon_{yy}}{\varepsilon_{xx}}\,_kH_z(i,j+1) + \frac{\varepsilon_{yy}}{\varepsilon_{xx}}\,_kH_z(i,j-1) \right. \\
&\left. + 2\left(2\left(\varepsilon_{yy} - \frac{\varepsilon_{xy}^2}{\varepsilon_{xx}}\right) - \left(1 + \frac{\varepsilon_{yy}}{\varepsilon_{xx}}\right)\right)_kH_z(i,j) \right] - _{k-1}H_z(i,j) + \frac{\varepsilon_{xy}}{2\left(\varepsilon_{xx}\varepsilon_{yy} - \varepsilon_{xy}^2\right)}\Delta_{xy}^2\,_kH_z(i,j)
\end{aligned}
\tag{2}
$$

here, Δ_{xy}^2 represents the discrete cross-derivative. Let us consider the basic node as a shunt-node with characteristic admittances Y_x, Y_y, permittivity stub Y_o and a series source V_s. The total potential V_z, equivalent to H_z, modeled by this node is:

$$
_{k+1}V_z(i,j) = \frac{2}{2(Y_x + Y_y) + Y_0}\left[Y_y\,_kV_z(i,j-1) + Y_x\,_kV_z(i-1,j) + Y_y\,_kV_z(i,j+1) + Y_x\,_kV_z(i+1,j)\right] - \\
- _{k-1}V_z(i,j) + _{k+1}V_s(i,j) - _{k-1}V_s(i,j)
\tag{3}
$$

If we compare it to (2), after normalization relative to Y_x (i.e. $Y_x=1$, $Y_y=\varepsilon_{xx}/\varepsilon_{yy}$), then:

$$
Y_0 = 2\left(2\left(\varepsilon_{yy} - \frac{\varepsilon_{xy}^2}{\varepsilon_{xx}}\right) - \left(1 + \frac{\varepsilon_{yy}}{\varepsilon_{xx}}\right)\right)
\tag{4}
$$

where it can be seen that (4) reduces to the diagonal case if $\varepsilon_{xy}=0$, and to the isotropic case if $\varepsilon_{xx}=\varepsilon_{yy}$. Furthermore, V_s must verify:

$$
_{k+1}V_s(i,j) = _{k-1}V_s(i,j) + \frac{\varepsilon_{xy}}{\varepsilon_{xx}\varepsilon_{yy} - \varepsilon_{xy}^2}\Delta_{xy}^2\,_kV_z(i,j)
\tag{5}
$$

where it must be pointed out that Δ_{xy}^2 is computed with centered differences except for the cases of nodes adjacent to the boundaries of the structure, where advanced or retarded differences have to be used [24].

The case of non-homogeneous media only requires to pay attention to the reflection coefficients on the interfaces, the propagation velocities being correctly implemented due to the presence of the stubs. For this case, we include reflection coefficients as:

$$
r_{xz} = \frac{1}{\varepsilon_{xx} - \frac{\varepsilon_{xy}^2}{\varepsilon_{yy}}} \qquad\qquad r_{yz} = \frac{1}{\varepsilon_{yy} - \frac{\varepsilon_{xy}^2}{\varepsilon_{xx}}}
\tag{6}
$$

for interfaces on XZ and YZ planes respectively.

3.- ANISOTROPIC MEDIA. 3D MODELING.

Anisotropic medium has been modeled in 3D for the cases of diagonal tensors and even general non-diagonal cases. We propose a way based on HSCN nodes [1,3], for it has the advantages of unequal arms and source ports. Now we start from Maxwell curl equations, i.e:

$$
\frac{\partial H_z}{\partial y} - \frac{\partial H_y}{\partial z} = \varepsilon_{xx}\frac{\partial E_x}{\partial t} + \varepsilon_{xy}\frac{\partial E_y}{\partial t} + \varepsilon_{xz}\frac{\partial E_z}{\partial t}
\tag{7}
$$

and similar expressions for the other components. The diagonal terms ε_{xx}, ε_{yy} and ε_{zz}, can be accounted adding permittivity stubs.

The required capacitance is $C_x=\varepsilon_{xx}.\Delta y\Delta z/\Delta x$ then leading to a stub admittance of:

$$\hat{Y}_x^s = 4\left[\varepsilon_{xx}\frac{\Delta y\Delta z}{\Delta x\Delta L} - \frac{\Delta L\left((\Delta y)^2 + (\Delta z)^2\right)}{2\mu_r \Delta x\Delta y\Delta z}\right]$$ (8)

and similar expressions for y and z.

If we introduce additional sources through ports 16, 17 and 18 as incident voltages $V_{16}^i=V_{sx}$, and equivalent sources for V_{17}^i and V_{18}^i, then, we can write, for instance, for the shunt connection on the plane YZ [1]:

$$I_1 + I_2 + I_9 + I_{12} + I_{13} = C_x\frac{\partial\left(V_x - V_{sx}\right)}{\partial t}$$ (9)

which models the equation (7) if we choose :

$$V_{sx} = V_{16}^i = -\frac{1}{\varepsilon_{xx}}\left(\varepsilon_{xy}V_y + \varepsilon_{xz}V_z\right)$$ (10)

The same treatment can be done for V_{sy} and V_{sz}.

3.1.- Boundaries in 3D.

As long as the permittivity depends on the direction of the fields, the absorbing boundaries must be treated carefully. Consider, for instance, the line #9 with x-polarization and y-propagation. The space impedance is [24]:

$$Z = \sqrt{\frac{L_y}{C_x}} = Z_0\sqrt{\frac{\mu_r}{\varepsilon_{xx}}}\frac{\Delta y}{\Delta x}$$ (11)

and $Z_y=Z_0.\Delta y\Delta z/\Delta L\Delta x$, so the reflection coefficient for an absorbing boundary will be:

$$\rho_9^{abs} = \frac{Z - Z_y}{Z + Z_y} = \frac{\Delta L - \sqrt{\mu_r\varepsilon_{xx}}\Delta z}{\Delta L + \sqrt{\mu_r\varepsilon_{xx}}\Delta z}$$ (12)

For oblique incidence, we can improve the boundary condition using, for an incidence angle of Φ, $Z_x=Z_0/\cos\Phi$, and similar expressions for Z_y, Z_z.

4.- DISPERSIVE MEDIA.

For a dispersive, linear medium, we must express the relationship between the field vectors, say **D** and **E** for the dielectric case, in time domain through the causality principle. This means a convolution integral as:

$$\mathbf{D}(t) = \varepsilon_0\left[\varepsilon_\infty\mathbf{E}(t) + \left(\varepsilon_s - \varepsilon_\infty\right)\int_0^\infty\mathbf{E}(t - \tau)g(\tau)d\tau\right]$$ (13)

where ε_s, ε_∞ are the static and the high frequency permittivities, respectively, and $g(\tau)$ the response function. Taking into account that it is the temporal part of the response the most relevant in the behavior of the medium, we discretice it, denoting only the time dependence:

$$_kD = \varepsilon_0\left[\varepsilon_{\infty k}E + \sum_{n=0}^{k-1}\chi_n{}_{k-n}E\right]$$ (14)

where we have used the definition of a generalized electrical susceptibility as [11]:

$$\chi_n = \int_{n\Delta t}^{(n+1)\Delta t} (\chi_s - \chi_\infty) g(\tau) d\tau \tag{15}$$

4.1.- 2D models.

Starting from the curl Maxwell equations, we can write a finite difference equation relating D and E components and, with the use of (14) a equation for each component of E as:

$$_{k+1}E(i,j) = \frac{2}{4+Y_0} \left\{ \begin{array}{c} _kE(i+1,j)+_kE(i-1,j)+_kE(i,j+1)+_kE(i,j-1) \\ +Y_0\,_kE(i,j)-\dfrac{4+Y_0}{2}\,_{k-1}E(i,j) \\ -\chi_0\left[4_kE(i,j)-2\,_{k-1}E(i,j)\right] \\ -2\sum_{n=0}^{k-1}\,_{k-n}E(i,j)\left[\chi_{n+1}+\chi_{n-1}-2\chi_n\right] \end{array} \right\} \tag{16}$$

where $Y_0=4(\varepsilon_\infty+\chi_0-1)$. If we compare it with the total transversal voltage equation in TLM for a shunt stubbed node, with a series source V_s [15]:

$$_{k+1}V_z(i,j) = \frac{2}{4+Y_0} \left\{ \begin{array}{c} _kV_z(i-1,j)+_kV_z(i+1,j)+_kV_z(i,j-1)+_kV_z(i,j+1) \\ +Y_0\,_kV_z(i,j)-\dfrac{4+Y_0}{2}\,_{k-1}V_z(i,j) \\ +_{k+1}V_s(i,j)-_{k-1}V_s(i,j) \end{array} \right\} \tag{17}$$

and we compare it to the field equation, then we conclude that the value of the stub is $Y_0=4(\varepsilon_r-1)$ and the source must verify:

$$_{k+1}V_s(i,j) = _{k-1}V_s(i,j) - \frac{4}{4+Y_0} \left\{ \begin{array}{c} \chi_0\left\{2_kV_z(i,j)-_{k-1}V_z(i,j)\right\} \\ +\sum_{n=0}^{k-1}\,_{k-n}V_z(i,j)\left(\chi_{n+1}+\chi_{n-1}-2\chi_n\right) \end{array} \right\} \tag{18}$$

thus giving us an iterative way of computing the source starting from the previous values. The modeling is completed with the calculation of χ_n, which depends on the behavior of the medium.

4.1.1.- Debye media.

In this case, the frequency domain electric susceptibility is

$$\chi^* = \chi_\infty + \frac{\chi_s - \chi_\infty}{1+j\omega\tau} \tag{19}$$

τ being the relaxation time. So, $\chi_n=(\chi_s-\chi_\infty)e^{-n\Delta t/\tau 0}(1-e^{-\Delta t/\tau 0})$ where a $\Delta t \ll \tau$ discretization is required. It can be easily seen that, for this case, χ_n can be computed recursively, as long as $\chi_n = e^{-\Delta t/\tau 0}\chi_{n-1}$. If we call

$$_k\text{Sum}(i,j) = \sum_{n=0}^{k-1}\,_{k-n}V_z(i,j)\left(\chi_{n+1}+\chi_{n-1}-2\chi_n\right) \tag{20}$$

then:

$$_{k+1}V_s(i,j) = _{k-1}V_s(i,j) - \frac{4}{4+Y_0}\left\{\chi_0\left[2_kV_z(i,j)-_{k-1}V_z(i,j)\right]+_k\text{Sum}(i,j)\right\} \tag{21}$$

641

4.1.2.- Lorentz media (2nd order). [11-13]

Now, the electric susceptibility is:

$$\chi^* = \chi_\infty + \frac{(\chi_s - \chi_\infty)\omega_0^2}{\omega_0^2 - \omega^2 + j2\delta_0\omega} \tag{22}$$

with δ_o damping factor and ω_o resonance frequency. This leads to a expression for χ_n as:

$$\chi_n = \frac{\chi_s - \chi_\infty}{\beta} e^{-n\delta_0 \Delta t} \left\{ \begin{array}{l} \sin(n\beta\Delta t)\left[\delta_0 - e^{-\delta_0\Delta t}\left(\delta_0 \cos(\beta\Delta t) - \beta\sin(\beta\Delta t)\right)\right] \\ + \cos(n\beta\Delta t)\left[\beta - e^{-\delta_0\Delta t}\left(\delta_0\sin(\beta\Delta t) + \beta\cos(\beta\Delta t)\right)\right] \end{array} \right\} \tag{23}$$

with $\beta = (\omega_0^2 - \delta_0^2)^{1/2}$. Now we cannot directly compute it in a recursive way, but we can perform the summation only until n=N, not until (k-1), for high values of k. This means that the time response of the dielectric its affected only by the very late values of the electric field, and we can neglect the early ones. With a complex definition of the electric susceptibility as:

$$\chi_n^* = \frac{\chi_s - \chi_\infty}{\beta}\left(A_1 + jA_2\right)e^{-(\delta_0 + j\beta)n\Delta t} \tag{24}$$

where:

$$\begin{array}{l} A_1 = \delta_0 - e^{-\delta_0\Delta t}\left(\delta_0 \cos(\beta\Delta t) - \beta\sin(\beta\Delta t)\right) \\ A_2 = \beta - e^{-\delta_0\Delta t}\left(\delta_0\sin(\beta\Delta t) + \beta\cos(\beta\Delta t)\right) \end{array} \tag{25}$$

we can write now χ_n^* in a recursive way as $\chi_n^* = e^{-(\delta_0 + j\beta\Delta t)}\chi_{n-1}^*$. then taking the real part of it. Now :

$$_k\text{Sum}(i, j) = e^{-(\delta_0 + j\beta)\Delta t}\left\{ _{k-1}\text{Sum}(i, j) + \left(e^{-(\delta_0 + j\beta)\Delta t} + e^{(\delta_0 + j\beta)\Delta t} - 2\right)\frac{\chi_s - \chi_\infty}{\beta}\left(A_1 + jA_2\right)_{k-1}V_y(i, j)\right\} \tag{26}$$

if we use constant recursive convolution. (CRC). Also, we can use trapezoidal recursive convolution (TRC) [21-23].

4.1.3.- Cold plasmas. [5,14,27]

For this case. the frequency domain susceptibility is [14]:

$$\chi^* = \frac{\omega_p^2}{\omega(j\omega_c - \omega)} \tag{27}$$

with ω_p plasma frequency, ω_c collisions frequency. For the corresponding time domain expression, (27) presents a singular point at $\omega=0$, then not allowing a causal expression for $\chi(\tau)$. Nevertheless. contouring this singularity, we can obtain:

$$\chi(\tau) = \frac{\omega_p^2}{\omega_c}\left\{1 - e^{-\omega_c\tau}\right\}U(\tau) \tag{28}$$

with $U(\tau)=1$ if $\tau>0$ and 0 elsewhere. Now, for χ_n:

$$\chi_n = \frac{\omega_p^2}{\omega_c}\Delta t - \left(\frac{\omega_p}{\omega_c}\right)^2\left\{1 - e^{-\omega_c\Delta t}\right\}e^{-n\omega_c\Delta t} \tag{29}$$

642

which can be computed with constant recursive convolution, as:

$$_k\text{Sum}(i,j) = e^{-\omega_c\Delta t}\left\{_{k-1}\text{Sum}(i,j) - \left(\frac{\omega_p}{\omega_c}\right)^2\left(1 - e^{-\omega_c\Delta t}\right)\left\{e^{-\omega_c\Delta t} + e^{\omega_c\Delta t} - 2\right\}_{k-1}V(i,j)\right\}$$ (30)

4.1.4.- Fourth order media.

In this case, we choose a representation as two 2nd order Lorentz resonances with frequencies ω_1 and ω_2, damping factors δ_1 and δ_2 and weights p_1 and p_2, as [12]:

$$\chi^* = \chi_\infty + (\chi_s - \chi_\infty)\left[\frac{p_1\omega_1^2}{\omega_1^2 - \omega^2 + j2\delta_1\omega} + \frac{p_2\omega_2^2}{\omega_2^2 - \omega^2 + j2\delta_2\omega}\right]$$ (31)

and now it is easy to obtain $\chi_n = p_1\chi_{n1} + p_2\chi_{n2}$, χ_{n1}, χ_{n2} being the susceptibilities associated with each 2nd order Lorentz mechanism. The recursive technique is then identical to the 2nd order case and we can write $_k\text{Sum}(i,j) = p_1 \, _k\text{Sum}_1(i,j) + p_2 \, _k\text{Sum}_2(i,j)$ each corresponding to the 2nd order case.

4.1.5.- Distributed relaxation times.

This case corresponds to Debye relaxation mechanisms with distributed relaxation times given by a function $y(\tau)$ as:

$$\chi^* - \chi_\infty = \int_0^\infty \frac{y(\tau)d\tau}{1 + j\omega\tau}$$ (32)

where different models for $y(\tau)$ exists, each trying to adjust a realistic response of a wide variety of media. We choose the Cole-Davidson model, giving a distribution of growing importance as the frequency decreases from a value $1/\tau_0$:

$$y(\tau) = \frac{\sin(\alpha\pi)}{\pi}\left(\frac{\tau}{\tau_0 - \tau}\right)^\alpha, \quad \tau \leq \tau_0$$
$$y(\tau) = 0, \quad \tau > \tau_0$$ (33)

The frequency domain susceptibility is now:

$$\chi^* = \chi_\infty + \frac{\chi_s - \chi_\infty}{\left(1 + j\omega\tau_0\right)^\alpha}$$ (34)

and the time domain susceptibility:

$$\chi(\tau) = \frac{\left(\chi_s - \chi_\infty\right)\tau^{\alpha-1}e^{-\tau/\tau_0}}{\Gamma(\alpha)\tau_0^\alpha}$$ (35)

Unfortunately, (35) does not allow to compute the integral in a closed form, so we approximate χ_n as:

$$\chi_n \cong \chi(n\Delta t)\Delta t \quad \text{or, alternatively} \quad \chi_n \cong \chi\left(\left(n + \frac{1}{2}\right)\Delta t\right)\Delta t$$ (36)

4.2.- 3D models.

The main part of the 3D modeling is almost solved, because the behavior of the dielectric is described in time domain through a convolution integral of its frequency domain expression. We only need to model the introduction of the corresponding sources in a 3D node. If we choose, as in the anisotropic case, a HSCN node [1], with equal

characteristic admittances for each direction, and we add voltage sources V_{sx}, V_{sy}, V_{sz} through ports 16, 17 and 18, then for V_x we can write, for each point (i,j,l):

$$_kV_x = \frac{2}{4+\hat{Y}_x^s}\left\{{_kV_1^i}+{_kV_2^i}+{_kV_9^i}+{_kV_{12}^i}+Y_s\;{_kV_{13}^i}\right\}+\frac{1}{4+\hat{Y}_x^s}{_kV_s} \tag{37}$$

as a function of incident potentials, where the charge conservation has been used at the node, and similar expressions for V_{sy}, V_{sz}. Now, we must find the source definition. To do this, we use the Maxwell curl equation for D_x:

$$\frac{\partial D_x}{\partial t} = \frac{\partial H_z}{\partial y} - \frac{\partial H_y}{\partial z} \tag{38}$$

The finite difference form of the HSCN mesh equations can be expressed as [20]:

$$\frac{-\hat{Y}_x}{Z_0}\left[{_kV_1^r}(i,j,l)-{_{k+1}V_1^i}(i,j,l)\right]={_{k+1/2}I_{z12}}(i,j-1,l)$$

$$\frac{\hat{Y}_x}{Z_0}\left[{_kV_2^r}(i,j,l)-{_{k+1}V_2^i}(i,j,l)\right]={_{k+1/2}I_{y9}}(i,j,l-1)$$

$$\frac{-\hat{Y}_x}{Z_0}\left[{_kV_9^r}(i,j,l)-{_{k+1}V_9^i}(i,j,l)\right]={_{k+1/2}I_{y9}}(i,j,l) \tag{39}$$

$$\frac{-\hat{Y}_x}{Z_0}\left[{_kV_{12}^r}(i,j,l)-{_{k+1}V_{12}^i}(i,j,l)\right]={_{k+1/2}I_{z12}}(i,j,l)$$

then, the total value of V_x is:

$$_{k+1}V_x(i,j,l)={_kV_x}(i,j,l)+\frac{1}{4+\hat{Y}_x^s}\left\{{_{k+1}V_{sx}}(i,j,l+{_kV_{sx}}(i,j,l)\right\}$$

$$+\frac{2Z_0}{4+\hat{Y}_x^s}\left\{{_{k+1/2}I_{z12}}(i,j-1,l)-{_{k+1/2}I_{z12}}(i,j,l)-{_{k+1/2}I_{y9}}(i,j,l-1)+{_{k+1/2}I_{y9}}(i,j,l)\right\} \tag{40}$$

If we compare it with the discretized field equation for E_x (using Yee's algorithm) we obtain, for the constant convolution case:

$$_{k+1}V_s = -{_kV_s} - \frac{\chi_0\left(4+\hat{Y}_x^s\right)}{\varepsilon_\infty+\chi_0}{_kV_x} - \frac{4+\hat{Y}_x^s}{\varepsilon_\infty+\chi_0}\sum_{n=0}^{k-1}{_{k-n}V_x}\left(\chi_{n+1}-\chi_n\right) \tag{41}$$

for each point (i,j,l) and similar expression for TC. The other sources V_{sy} and V_{sz} are computed in the same way.

5.- RESULTS.

We present some of the results obtained with the proposed algorithms., For the dispersive case we have computed reflection coefficients versus frequency for a plane wave inciding on a vacuum-medium interface, except for the case of cold plasma, where the transmission coefficient through the plasma is calculated. They are presented in figures 1 to 5 and compared to analytical results. For the anisotropic case, cut-off frquencies of rectangular cross-section waveguides are computed and compared with finite element method calculations. They are presented in tables I and II.

REFERENCES.

1.- C. Christopoulos. The transmission line modeling method. Oxford University Press / IEEE Press. New York. 1995.

2.- L. de Menezes and W. J. R. Hoefer. Modeling of general constitutive relationships in TLM. IEEE Trans. on MTT. MTT-44, 6, pp. 854-861. Jun. 1996.

3.- P. Berini and K. Wu. A pair of hybrid symmetrical condensed TLM nodes. IEEE Microwave and Guided Wave Letters. vol. 4, 7, pp. 244-246. Jul. 1994.

4.- J. Huang and K. Wu. Towards a generalized TLM algorithm for solving arbitrary reciprocal and nonreciprocal planar structures. IEEE Trans on MTT. MTT-44, 8, pp.1508-1511. Aug. 1996.

5.- T. Kashiwa, N. Yoshida and Y. Fukai. Transient analysis of a magnetized plasma in three dimensional space. IEEE Trans. on AP. AP-36, 8, pp. 1096-1105, Aug. 1988.

6.- J. Huang and K. Wu. A unified TLM model for wave propagation of electrical and optical structures considering permittivity and permeability tensors. IEEE Trans on MTT. MTT-43,10, pp. 2472-2477. Oct. 1995.

7.- G. E. Mariki and C. Yeh. Dynamic three-dimensional TLM analysis of microstriplines on anisotropic substrate. IEEE Trans. on MTT. MTT-33, 9, pp. 789-799. Sept. 1985.

8.- L. de Menezes and W. J. R. Hoefer. Modeling anisotropic dispersive materials in TLM. 1st. International Workshop on TLM modeling. University of Victoria. pp. 91-94. Aug. 1995.

9.- C. Bulutay and S. Prasad. Analysis of millimeter waveguides on anisotropic substrates using the three-dimensional transmission-line matrix method. IEEE Trans. on MTT. MTT-41, 6/7, pp.1119-1125. Jun/Jul. 1993.

10.- O. P. Gandhi, B. Gao and J. Chen. A frequency dependent finite difference time domain formulation for general dispersive media. IEEE Trans. on MTT. MTT- 41, 4, pp. 658-664. Apr. 1993.

11.- R. Luebbers, F. P. Hunsberger, K. S. Kunz, R. B. Standler and M. Schneider. A frequency dependent finite difference time domain formulation for dispersive materials. IEEE Trans. on EMC. EMC-32, 3, pp. 222-227. Aug. 1990.

12.- R. J. Luebbers and F. Hunsberger. FDTD for Nth-order dispersive media. IEEE Trans. on AP. AP-40, 11, pp. 1297-1301. Nov. 1992.

13.- R. Luebbers, D. Steich and K. Kunz. FDTD calculation of scattering from frequency dependent materials. IEEE Trans. on AP. AP-41, 9, pp. 1249-1257. Sep. 1993.

14.- R. J. Luebbers, F. Hunsberger and K. S. Kunz. A frequency dependent finite difference time domain formulation for transient propagation in plasma. IEEE Trans. on AP. AP- 39, 1, pp. 29-34. Jan. 1991.

15.- I. Barba, A.C. L. Cabeceira, J. Represa, M. Panizo and C. Pereira. Modeling dispersive dielectrics for the 2D-TLM method. IEEE Microwave and guided wave letters. Vol. 6, 4, pp. 174-176. Apr. 1996.

16.- L. De Menezes and W. J. R. Hoefer. Modeling nonlinear dispersive media in 2D-TLM. 19941st. Int. Workshop on TLM modeling.

17.- M. Ney. Dispersive boundaries and media in TLM. 1st. Int. Workshop on TLM modeling. pp. 81-87. 1995.

18.- I. Salama, W. Su and M. Riad. Modeling of frequency dependent material parameters using TLM. 1st. Int. Workshop on TLM modeling. pp. 95- 98. 1995.

19.- L. De Menezes and W. J. R. Hoefer. Modeling frequency dependent dielectrics in TLM. IEEE&AP Symp. Pp. 1140-1143. 1994.

20.- R. Voelker and R. Lomax. A finite difference transmission line matrix method incorporating a nonlinear device model. IEEE Trans. MTT. MTT-38, 3, pp. 302-311. Mar 1990.

21.- J. L. Young. Propagation in linear dispersive media: finite difference time domain methodologies. IEEE Trans. On AP. AP-43, 4, pp.422-426. Apr.1995.

22.- D. F. Kelley and R. J. Luebbers. Piecewise linear recursive convolution for dispersive media using FDTD. IEEE Trans. On AP. AP-44, 6, pp. 792-797. Jun. 1996.

23.- R. Siushansian and J. LoVetri. A comparison of numerical techniques for modeling electromagnetic dispersive media. IEEE Microwave and guided wave letters. Vol. 5, 12, pp. 426-428. Dec. 1995.

24.- A. C. L. Cabeceira. Modeling anisotropic media for TLM method. Ph. D. Thesis dissertation. University of Valladolid. Dec. 1996.

25.- A. C. L. Cabeceira, I. Barba, F. Ndagijimana, P. Saguet and J. Represa. Simulation des milieux anisotropes avec TLM-2D. XXV URSI General Assembly. BP52. Lille. 1996.

26.- I. Barba, A. C. L. Cabeceira, M. Panizo and J. Represa. Modeling Lorentz dielectrics in TLM method. XXV URSI General Assembly. BP42. Lille. 1996.

27.- R. M. Joseph, S. C. Hagness and A. Taflove. Direct time integration of Maxwell's equations in linear dispersive media with absortion for scattering and propagation of femtoseconds electromagnetic pulses. Optic Letters, Vol. 16, 18, Sep. 15. 1991
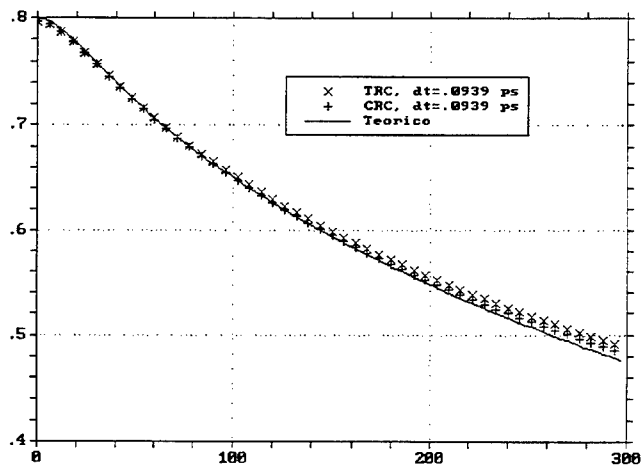
Fig. 1.- Reflection coefficient on a vacuum/water interface. 3D simulation. Discretization 5x5x990 (100 vacuum, 890 water). $\varepsilon_s=81$, $\varepsilon_\infty=1.8$, $\tau_0=9.4$ ps. 2000 time iterations, $\Delta t=.0939$ ps.
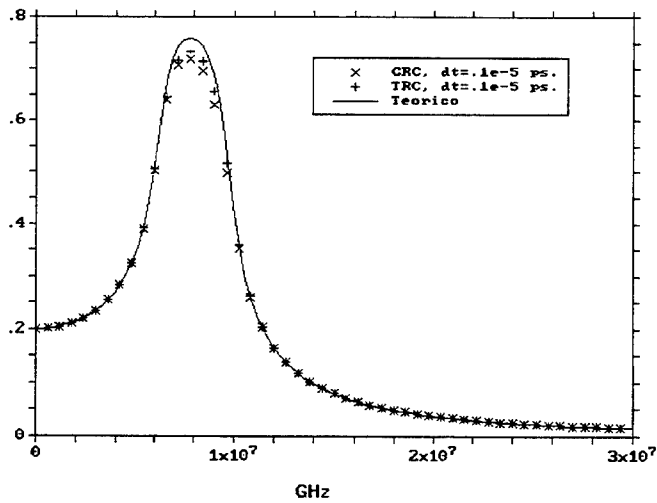

Fig 2.- Reflection coefficient on a vacuum/Lorentz medium interface. 3D simulation. Discretization 5x5x990 (100 vacuum, 890 Lorentz medium). $\varepsilon_s=2.25$, $\varepsilon_\infty=1.0$, $\omega_0=4*10^{16}$ rad/s and $\delta_0=0.28*10^{16}$ s^{-1}. 2000 time iterations. $\Delta t=10^{-18}$ s.
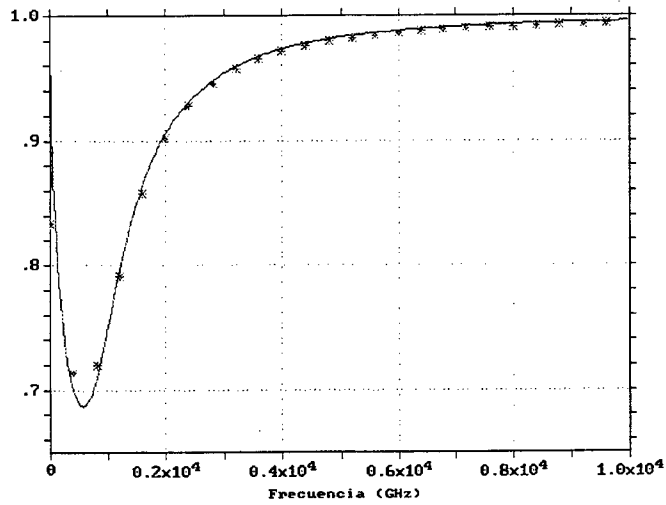
Fig. 3.- Transmission coefficient through a cold plasma at a distance $1000\Delta l=4.2*10^{-5}$ m. 2D simulation. Discretization 10000x2. $\omega_p=\omega_c=1000$ GHz. 1500 time iterations. $\Delta t=10^{-16}$ s.
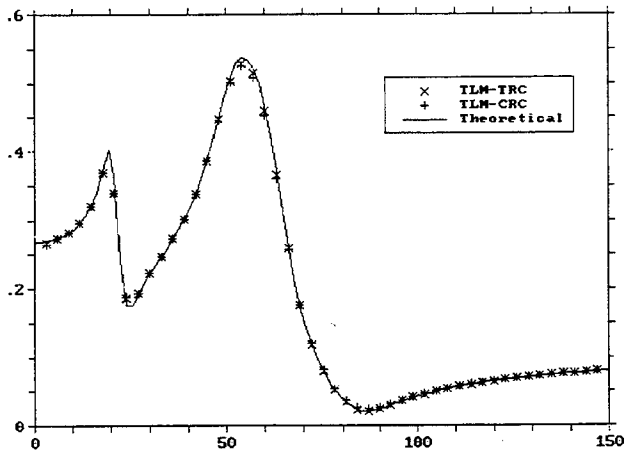
Fig. 4.- Reflection coefficient on a vacuum/4th order medium interface. 2D simulation. Discretization 2000x2. (100 vacuum, 1900 medium). $\omega_1=20$ GHz, $\delta_1=1.26*10^{10}$ s^{-1}, $p_1 = 0.4$, $\omega_2 = 50$ GHz, $\delta_2=3.14159*10^{10}$ s^{-1}, $p_2= 0.6$, $\varepsilon_s=3$, $\varepsilon_\infty=1.5$. 4000 time iterations, $\Delta t=10^{-13}$ s.
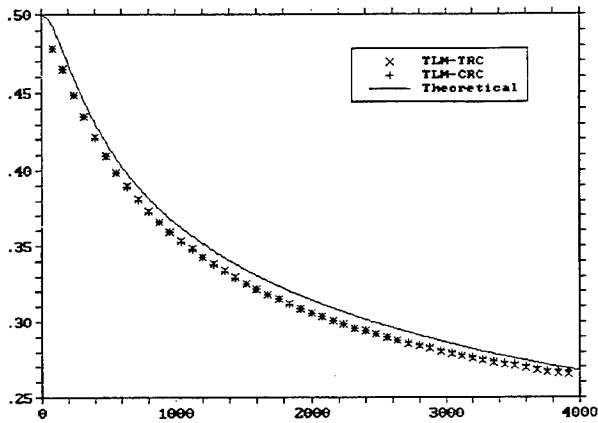
Fig. 5.- Reflection coefficient on a vacuum/Cole-Davidson medium interface. 2D simulation. Discretization 1000x2. (100 vacuum, 900 medium). $\varepsilon_s=9$, $\varepsilon_\infty=1.5$. $\tau_0=1$ ps. $\alpha=0.5$. 800 time iterations. $\Delta t=.01$ ps.

Table I. Cut-off frequencies of a half-filled (YZ interface) ($\varepsilon_{xx}=4.53$, $\varepsilon_{yy}=5.03$, $\varepsilon_{xy}=0.14$) rectangular, cross-section 16x10 mm waveguide. $\Delta l=1$mm.

Mode	FEM (GHz)	TLM-2D ($\pm$ 0'01 GHz)	Error (%)
1°	5'14	5'15	0'19
2°	8'01	8'00	0'12
3°	12'05	11'87	1'49

Table II. Cut-off frequencies of a full-filled ($\varepsilon_{xx}=4.53$, $\varepsilon_{yy}=5.03$, $\varepsilon_{zz}=1$, $\varepsilon_{xy}=0.14$, $\varepsilon_{xz}=\varepsilon_{yz}=0$) rectangular 16x10x5 mm waveguide. (Z propagation). $\Delta l=1$mm.

Mode	FEM (GHz)	TLM-2D ($\pm$ 0'01 GHz)	TLM-3D ($\pm$ 0'01 GHz)	Error (%) FEM	Error (%) TLM-2D
1°	4'18	4'17	4'19	0'24	0'48
2°	7'05	7'03	7'12	0'99	1'28
3°	8'19	8'13	7'99	2'44	1'72

ELECTROMAGNETIC FIELDS GENERATED BY CURRENT TRANSIENTS ON PROTECTION STRUCTURES USING TLM - A FD-TD COMPARISON

Caixeta, G. P. - M.Sc. and Pissolato J. - Ph.D.

State University of Campinas - DSCE/FEEC
13081-970, Campinas, S.P., Brazil
Fax: (55-19) 239-1395
E-mail: geraldo@dsce.fee.unicamp.br

1.   Abstract

This paper presents the simulation results of current transients in a Lighting Protection Structure against Lightning (LPS) in a building and solves the Electromagnetic Fields (EMF) generated in this interior.

For the current transients, the numerical technique TLM (Transmission Line Modeling) was used and each piecewise for the protection structure was considered as a transmission line with frequency dependent parameters – R (Ω), L (H), C (C) and G (S) – for each lumped element.

The TLM and FD-TD techniques were used for the computation of the Electromagnetic Field generated. The results presented by each technique were compared.

2.   Introduction

We know electromagnetic interference is generated in electronics equipment or circuits installed in the interior of a building when the lightning strikes an LPS [1]. This paper presents software whose principal aim is determine the intensity of an electromagnetic field generated in the interior of an LPS in time domain.

The structure, as shown in Figure 1, where a source of current with a double exponential waveform is linked to a point on the top of this LPS, was considered. A ground system was included in this work composed of four points, 3 meters long and interconnected by cable. With this model, we can solve the current

transients in structures using the TLM method with lumped parameters along a line and at time domain [2].

With these results of current transients, it was possible to determine the EMF generated at any point in the interior of an LPS, considering each line of this LPS as an antenna and using TLM and FD-TD techniques for comparison [3].

The results showed good agreement for each method and they also show the advantages and disadvantages of each one.
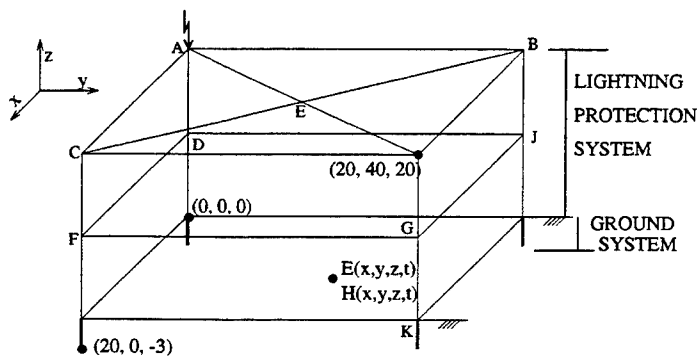
Figure 1: Lightning Protection System.

3. Lightning Protection System Model

A protection system is made of a set of conductors to drag down to earth the lightning current, avoiding in this way a damage to the building. Thus, it is made of a mesh that covers the structure (Figure 1). Each conductor of this mesh can be modeled as a transmission line. The terminations of each transmission line may be another conductor, the earth, the grounding system or the lightning channel. This structure is linked to the grounding system that is considered as a connection of transmission lines with a width of 3 meters.

The results of the current transient were obtained applying TLM technique and the parameters of that LPS from reference [4].

4. Electromagnetic Field Calculation

4.1. The FD-TD model - or hybrid model

The electric and magnetic fields are obtained considering the conductors made of infinitesimal linear antennas with a current i(t) in it (obtained by TLM - one-dimensional). Each of these segments are dz_o long (Figure 1). Using the Maxwell equations and the magnetic potential vector, the electrical potential is derived from electric and magnetic fields. This potential has three components: the static component (E_s), the radiated component (E_r), and the induced component (E_i). The equation is integrated along the transmission line to calculate the total field [3].

The electric and magnetic fields are expressed in terms of the current as a function of position and time, making possible a straightforward application of this technique to arbitrary current distributions.

This method apply the FD-TD (to calculate the fields) with TLM in one dimension (to obtain the current and voltage transients): so, we will call it of **hybrid model.**

4.2. The TLM model

As described above, the voltage transient at LPS is obtained applying TLM (one-dimensional) at each of the conductor and latter, each of those segments dz_o is considered as a source of voltage (boundary condition) and then is applied TLM all over space on interior of the structure [3].

5. Results

In Figure 1 a building with its protection system is shown. With the above described model and applying a source discharge on a structure (at point A(0;0;20)), the transients are analyzed. The source considered here is a bi-exponential waveform given by [5] and presented on Figure 2a.

The protection system has the dimensions of 20x40x20 m^3. As described above, the parameters of that LPS were obtained from [1].

Some of the current distribution on the structure's cables can be seen in Figure 2b. It is clear that the current at vertical cables is greater then that of horizontal cables. From these currents the electric and magnetic fields were then

a) Source connected at point A(0;0;20) in LPS.   b) Current transient at half of the cables AB, AD and AE in LPS.
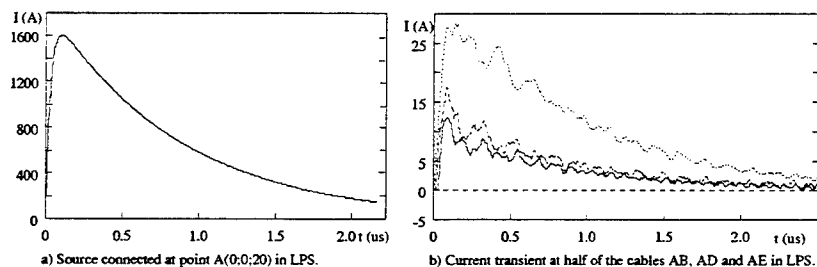
Figure 2: Source and current transient at LPS.

obtained using the FD-TD technique [3]. Figures 3-5 show the graphics of the fields at point $P(10;30;5)$ – inside the structure.

The graphics shows several cases to be analyzed.

The Figure 3 show those components of the electric field discussed above. In this Figure, the static field component is greater than the induced and radiated (both multiplied by 3 in it Figure). Those components of the fields is not possible by TLM technique itself.

The Figure 4 show the electric field simulated by two models described above and it is in good agreement. The hybrid model shows less scattering than TLM model.

Finally, the Figure 5 show the magnetic field simulated too by two models and it is in good agreement.

The hybrid model described here, showed advantages, as for about eleven times faster than TLM mode in computing program and the scattering problems not so accentuated. The hybrid model is more flexible to calculate the electromagnetic fields at any point of cartesian coordinate.

6. Conclusions

The computer program developed based on the described models is a useful tool for electrical engineers. With this simulator the protection systems can be better designed and the distribution of electrical systems inside the building optimised.

The results showed good agreement for each method and they also show the
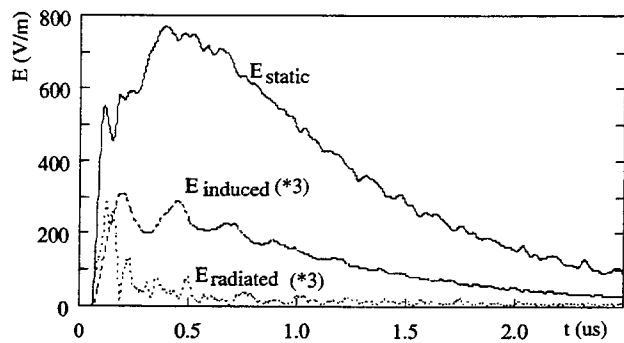
Figure 3: Electric fields components: static, induced and radiated - simulated by hybrid model at point P(10;30;5).
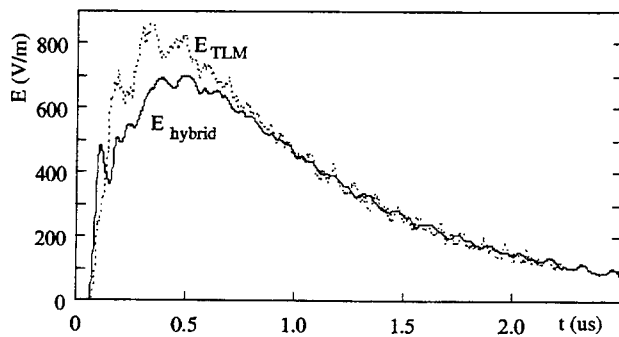
Figure 4: Electric field simulated by TLM and Hybrid model at point P(10;30;5).
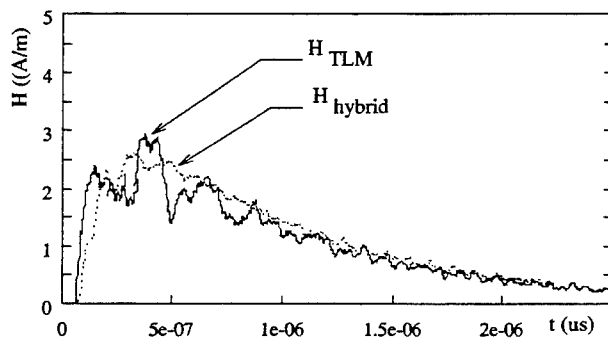
Figure 5: Magnetic field simulated by TLM and Hybrid model.

advantages of the hybrid model.

References

[1] Mattos, M.A.F. and Caixeta, G.P.; *Lightning Induced Current on a Building Wiring System* Int. Conf. on Lightning Protection - ICLP, Germany, Sep. 1992.

[2] Christopoulos C.; *The Transmission-Line Modeling Method - TLM* The IEEE/OUP Series on Electromagnetic Wave Theory, 1995.

[3] Thomas, David W.P.; Christopoulos, C. and Pereira, Elisete T.; *Calculation of Radiated Electromagnetic Fields from Cables Using Time-Domain Simulation* IEEE Trans. EMC, Vol. 36, No. 3, pp. 201-205, Aug. 1994.

[4] Mattos, M.A.F. and Christopoulos C.; *A Model of the Lightning Channel, Including Corona, and Prediction of the Generated Electromagnetic Fields* Journal Phys. D. 23, pp. 40-46, 1990.

[5] Christopoulos C.; *Propagation of Surges Above the Corona Threshold on a Line With a Lossy Earth Return.* COMPEL, Vol.4, No.2, 91-102, 1985.

Towards a TLM description of an open-boundary condition

Donard de Cogan (ddc@sys.uea.ac.uk)
School of Information Systems, University of East Anglia, Norwich NR4 7TJ (UK)

Zhizhang Chen (chenz@tuns.ca)
Dept. of Electrical Engineering, Technical University of Nova Scotia, Halifax, Canada B3J 2X4

Introduction

Electromagnetic and acoustic modellers frequently have to deal with scattering problems which are open or unbounded. In order to maintain the computational load within reasonable limits many modelling techniques require that some form of artificial boundary must be invoked. This should provide a perfect match between the immediate problem space and its surrounds. In the transmission line matrix (TLM) technique this might be approached by means of a reflectionless ($\rho = 0$) boundary description. However, it is well known that this is not appropriate over a wide range of frequencies and angles of incidence. To overcome this difficulty a number of options have been investigated and the current status has been reviewed by Chen [1]. The Discrete Green's Function (Johns Matrix) [2] stores the response at the boundary nodes due to all the region beyond the boundary. A variant of this technique has also been proposed for heat-flow modelling in open-boundary problems [3]. Eswarrappa et al [4] have used a technique whereby the region outside the immediate problem space becomes progressively lossy. By far the most popular approach to perfect matched load (pml) boundary modelling is to use either the Higdon [5] or Berenger [6] boundaries. These are essentially finite difference descriptions which are bolted onto the periphery of a TLM model. Although they work effectively, they largely ignore the intuitive essence of TLM as promoted by Johns himself. The nearest approach to this philosophy is the method used in acoustic propagation by O Connor [7]. This assumes that a proportion of every impulse is absorbed (in a method which is not specified) at every node within a boundary layer at every iteration. This has also been used in diffusion modelling. Johns was particularly admiring of an early treatment of the recombination of charge carriers in semiconductors [8]. The carriers scattered from a node were assumed to undergo a first order annihilation process during transit along the link transmission lines. A network description of this process was subsequently provided by Al-Zeben et al.[9]. In this paper we attempt to provide a similar physical basis for perfectly matched layers by constructing a network of broad-band absorbing TLM nodes.

In two- or three-dimensional TLM treatments bulk properties such as excitation or absorption can be applied at intervals kΔt (k = 1,2,3. . .) at the centre of each relevant node. Alternatively, a set of equivalent conditions which result in the same nodal outcome can be applied at intervals (k+1/2)Δt on the link-lines which interconnect adjacent nodes. This latter approach permits us to develop a one-dimensional network description which results in a perfect matched load node. This will now be outlined in an evolutionary format which describes the basic approach, the experiments which were undertaken and the latest results.

A TLM matched boundary

The inclusion of a shunt resistor, r, will provide absorption in a one-dimensional TLM shunt node. The phase shift can be compensated by means of series resistors, R. The network, which is shown in figure 1 is matched to the adjacent lossless lines when

$$\left[\frac{1}{r} + \frac{1}{R+Z}\right]^{-1} + R = Z \qquad (1)$$

So long as the node is symmetrical then it provides a match for pulse flow in both directions. This node is very similar to that found in diffusion (e.g. diffusion/recombination of minority carriers in a semiconductor [9]) and like such nodes there will be severe dispersion.
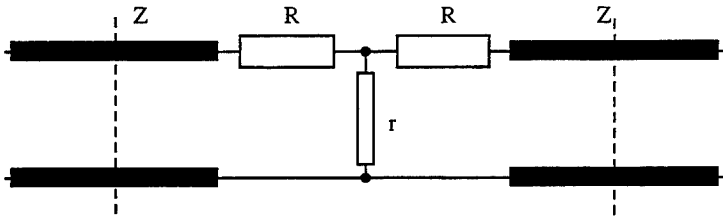
Figure 1 A diffusion node with a shunt loss

Dispersion of an impulse can be inhibited if the network is adapted so that it fulfils the Heaviside condition for a distortionless line. For a line with inductance, L, capacitance, C, resistance, 2R and conductance, G the condition is

$$\frac{L}{C} = \frac{2R}{G} \qquad (2)$$

For the node in figure 1 with a characteristic impedance, Z and conductance, G = 1/r this yields

$$Z^2 = 2R\, r \qquad (3)$$

With normalised characteristic impedance the conditions for distortionless matching (eqns (1) and (3)) give non-negative solutions

$$R = -r + \sqrt{r^2 + 1} \quad \text{(matching)}$$
$$\qquad (4)$$
$$R = \frac{1}{2r} \text{ (distortionless)}$$

Sadly these two expressions for R do not coincide for any value of R < ∞ so that as it stands it is not possible to achieve distortionless matching.

This situation can be radically altered by the inclusion of an open circuit half-length (capacitive) stub transmission line which is placed at the node centre as shown in figure 2.
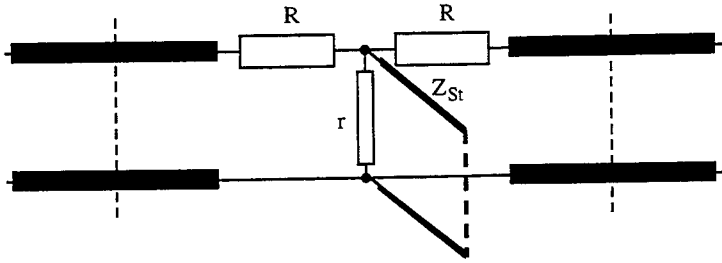
Figure 2 Lossy diffusion node with capacitive stub

The inclusion of the stub means that the total capacitance of the node is increased and the Heaviside condition (assuming normalised impedances) now becomes

$$\left[\frac{Z_{St}}{Z_{St} + 1}\right]^2 = 2R\,r \tag{5}$$

The equivalent expression for the matching condition is

$$R = \frac{-r\,Z_{St} + \sqrt{r^2\,Z_{St}^2 + Z_{St}^2 + 2\,r\,Z_{St} + r^2}}{r + Z_{St}} \tag{6}$$

These equations are plotted in figure 3 for the case where $Z_{St} = 2$ and confirms that there is a point of coincidence which can be determined iteratively as $r = 0.28432$.
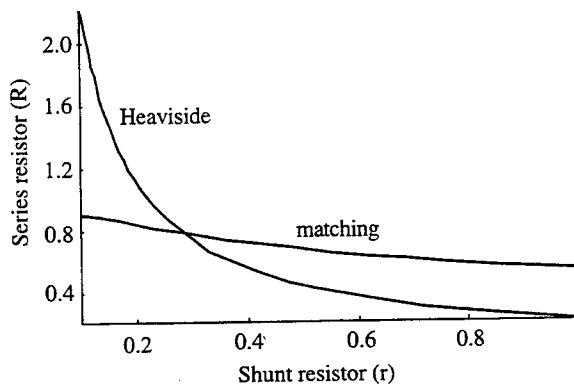
Figure 3 Plots of the matching and distortionless dependence of R as a function of r for a node with a capacitive stub $Z_{St} = 2$.

Experiments and Results

A set of experiments were carried out using a one-dimensional TLM model comprising 199 lossless nodes connected to a set of 51 identical lossy nodes whose parameters were determined so as to ensure distortionless matching for a given value of stub impedance. An excitation was applied at node 150. This comprised a Gaussian impulse moving to the right whose magnitude at the k-th iteration was given by

$$k^s V_R(150) = 1000 \exp(-(k-10)^2/\zeta) \qquad (7)$$

Initially, ζ was set to 10.

The algorithm was prepared using Matlab and run for sufficient iterations to permit the pulse to penetrate the interface. The nature of the reflected and transmitted pulses was then investigated. Using the case of $Z_{St} = 2$ it was noted that there was total absorption of the pulse within the boundary. However, a Gaussian return pulse with a peak magnitude of 15.6 was observed. Further experiments confirmed that this is due to the impulse response of the stub itself; indeed if the capacitive stub were to be replaced by an infinite line of impedance Z_{St}, then there was no return signal, regardless of the magnitude of the stub. Although this might be a useful way of providing absorption paths in a TLM formulation it was felt to be contrary to the spirit of the exercise. However, it would be quite reasonable to adjust the size of the stub so as to minimise the return signal and this formed the basis of further experiments.

At this stage the test mesh was reduced in size to 80 nodes with the transition from lossless to 'pml' at node 75. The Gaussian excitation moving from left to right was applied at node 40. These changes speeded up the calculations and had no effects upon the previous results.
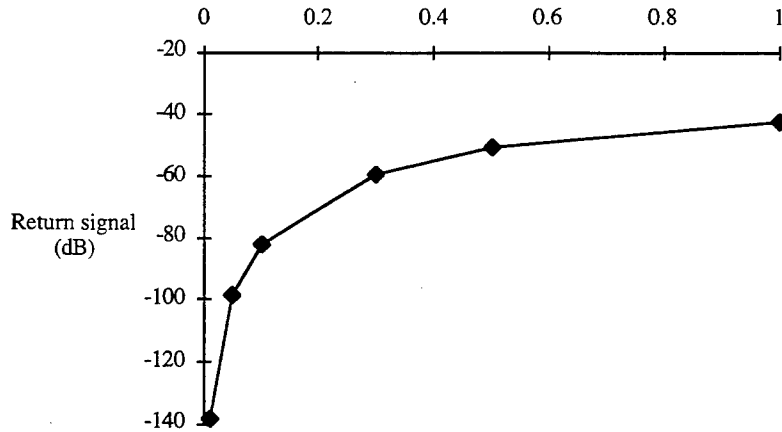
Figure 4 The return signal as a function of stub impedance for small values of impedance. The horizontal axis is stub impedance in the range $Z_{St} = 0 - 1$.

A set of experiments was then undertaken to determine the influence of Z_{St} on the magnitude of the return signal. The results are summarised in table I where the return signal is expressed in dB (defined as

$$\text{Return (dB)} = 20 \log_{10}\left[\frac{\text{peak return}}{\text{peak input}}\right] \qquad (8)$$

The results are shown in figures 4 and 5. It can be seen that the return signal is very small at very small values of Z_{St} and then tends towards a maximum value at before decreasing slowly for larger stubs.
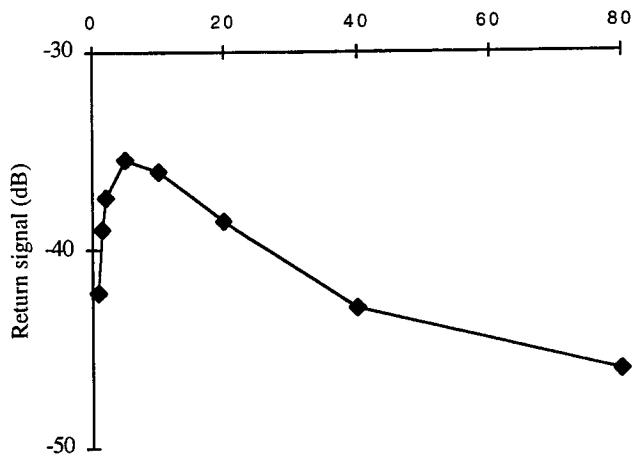

Figure 5 The return signal as a function of stub impedance for large values of impedance (x-axis). The return signal corresponding to Z_{St} = 200 and 1000 are -51.2dB and -62.8dB respectively.

During these investigations there was no evidence of dispersion, but an initial test with a rectangular impulse showed considerable ringing on the leading and trailing edges. Accordingly, the constant ζ in the Gaussian excitation (eqn 7) was progressively reduced so as to increase the band-width. At $\zeta = 5$ there was no observable effect. $\zeta = 3$ showed tiny ripples trailing from the return signal which became larger at $\zeta = 2$ and very significant at $\zeta = 1$. It was also noted that these effects became more significant at the extreme values of stub impedance (i.e. very large or very small). However, this has yet to be investigated in detail.

This work was followed by an investigation of the number of nodes which are required to ensure that a complete absorption of the signal has occurred. Our initial study has been limited to the low values of stub impedance. The Matlab output can be used to predict the contents of all 'pml' nodes and our criterion of effective absorption was when the potential at a node was less than 10^{-7} times the peak input. These results are shown in Table I.

Table I

Stub impedance	Min. node number
0.5	5
0.1	4
0.05	3

Conclusions

This work has demonstrated that it is possible to develop a TLM description for a perfect-matched load boundary node. There are frequency limitations and these have yet to be investigated in greater detail. We have concentrated on the conditions which minimise the magnitude of the signal which is returned to the lossless mesh from the capacitive stubs in the 'pml' and it is quite clear that there is much work which has still to be done and many promising avenues remain to be examined. Inductive stubs could be incorporated in such a way as to cancel the return from the capacitive stub.

Within a two or three-dimensional algorithm our 'pml' node would be treated as a sub-circuit which would be located at each of the interfaces between nodes within the absorbing boundary region of space.

We believe that the technique of finding values of absorbing and phase matching components which fulfil both line matching and distortionless conditions can be extended to graded meshes, but at first sight the algebra appears to be non-trivial.

References

1. Z. Chen, *Modelling of absorbing boundary conditions with TLM.* Proc. First International Workshop on Transmission Line Matrix (TLM) Modelling - Theory and Applications, Victoria (BC), August 1-3 1995, pp 63 - 72

2. W.J.R. Hoefer, *The discrete time domain Green's function or Johns Matrix - A new powerful concept in transmission line modelling.* International Journal of Numerical Modelling 2 (1989) 215-225.

3. D. de Cogan and P. Enders, *Discrete Green's functions and hybrid modelling of thermal and particle diffusion.* International Journal of Numerical Modelling, 7 (1994) 407 - 418

4. E. Eswarrappa, G. Costache and W.J.R. Hoefer, *TLM modelling of dispersive wide-band absorbing boundaries with time-domain diakoptics for S-parameter extraction.* IEEE Trans. on Microwave Theory and Techniques **MTT-38** (1990) 379-385

5. R.L. Higdon, *Numerical absorbing boundary conditions for the wave equation.* Math. Comp. **49** (1987) 65 - 91

6. J.P. Berenger, *A perfectly matched layer for the absorption of electromagnetic waves.* J. Comp. Phys. **114** (1994) 185-200

7. W. O' Connor (to be published)

8. D. de Cogan and M. Henini, *Transmission line Matrix (TLM): A novel technique for modelling reaction kinetics.* J. Chem. Soc. Faraday Transactions II **83** (1987) 843-855

9. M.Y. Al-Zeben, A.H.M. Saleh and M.A. Al-Omar, *TLM modelling of diffusion, drift and recombination of charge carriers in semiconductors.* International Journal of Numerical Modelling **5** (1992) 219 - 225

A Modified 3D-TLM Variable Node for the Berenger's Perfectly Matched Layer implementation

J.L. Dubard, D. Pompei
Electronic, Antenna and Telecommunication laboratory
Nice-Sophia Antipolis University , CNRS
250, rue Albert Einstein, 06560 Valbonne, France.
tel (33) 04 92 94 28 00 ; fax : (33) 04 92 94 28 12
e mail : pompei@alto.unice.fr

Abstract - A modified TLM symmetrical condensed node is proposed which allows a direct implementation of Berenger's PML in variable mesh 3D-TLM method. The new scattering matrix is given and several tests are performed to set the optimal characteristics of Berenger's PML in TLM simulations.

I. INTRODUCTION

Berenger's Perfectly Matched Layer (PML) with the FDTD method provides 40dB more accurate absorbing boundary conditions than currently exist. Then it was recently implemented in 2D-TLM [1], using an interface between the FDTD and the TLM network. We propose here a modified symmetrical condensed node (modified SCN) which allows a direct implementation of Berenger's PML in variable mesh 3D-TLM method. Then usual and PML media can be simulate at once allowing easier implementation on parallel computers as the Connection Machine 5. A parametric study of PML layers in TLM simulations is also proposed.

II. THEORY

In the PML medium, each electromagnetic field is split into two sub components and the six Maxwell equations are replaced by twelve equations [2] with use of anisotropic electric and magnetic conductivities. We have designed a modified TLM SCN by using centered differencing and averaging of these twelve PML equations as described in [3] by H.Jin and R. Vahldieck. The node is made of a transmission line network with 24 branches. The 12 main branches are identical to those of the usual SCN. 6 open stubs and 6 short stubs are necessary to transform the 12 sub components of the electromagnetic field at the node center (i,j,k) and time step $(n-1/2)\Delta t$ or $(n+1/2)\Delta t$ into respectively incident V_i or reflected V_r voltage impulses on the stubs at time step $n\Delta t$ as follows.

$$_{n \mp 1/2} E_{xy}(i, j, k) = 2\, _n V_{13}^{i,r}/_u \,, \quad _{n \mp 1/2} E_{xz}(i, j, k) = 2\, _n V_{14}^{i,r}/_u$$

$$_{n \mp 1/2} E_{yx}(i, j, k) = 2\, _n V_{15}^{i,r}/_v \,, \quad _{n \mp 1/2} E_{yz}(i, j, k) = 2\, _n V_{16}^{i,r}/_v$$

$$_{n \mp 1/2} E_{zx}(i, j, k) = 2\, _n V_{17}^{i,r}/_w \,, \quad _{n \mp 1/2} E_{zy}(i, j, k) = 2\, _n V_{18}^{i,r}/_w$$

$$(1)$$

$$_{n \mp 1/2} H_{xy}(i, j, k) = \pm 2\, _n V_{19}^{i,r}/(z_x u) \,, \quad _{n \mp 1/2} H_{xz}(i, j, k) = \pm 2\, _n V_{20}^{i,r}/(z_x u)$$

$$_{n \mp 1/2} H_{yx}(i, j, k) = \pm 2\, _n V_{21}^{i,r}/(z_y v) \,, \quad _{n \mp 1/2} H_{yz}(i, j, k) = \pm 2\, _n V_{22}^{i,r}/(z_y v)$$

$$_{n \mp 1/2} H_{zx}(i, j, k) = \pm 2\, _n V_{23}^{i,r}/(z_z w) \,, \quad _{n \mp 1/2} H_{zy}(i, j, k) = \pm 2\, _n V_{24}^{i,r}/(z_z w)$$

u, v, w are the cell sizes along the x, y, z directions, the time step is $\Delta t = \Delta l / 2c$ with Δl being the smallest cell size and c the wave velocity in free space. The open and short stubs are characterised by normalised characteristic admittances Y and impedances Z identical to those of the classical variable mesh SCN. The 24 reflected voltage impulses are deduced from the 24 incident impulses using the scattering matrix shown in figure 1. The matrix elements are given as follows:

$$a = \frac{2}{Y + ge_\alpha + 4} - \frac{2}{Z + gm_\alpha + 4} \qquad b = \frac{2}{Y + ge_\beta + 4}$$

$$c = \frac{2}{Y + ge_\alpha + 4} + \frac{2}{Z + gm_\alpha + 4} - 1 \qquad d = \frac{2}{Z + gm_\gamma + 4}$$

$$e = \frac{2(Y+2)}{Y + ge_\alpha + 4} - 2b \qquad f = (Y+2)b - \frac{4}{Y + ge_\alpha + 4}$$

$$g = \frac{2(Z+2)}{Z(Z + gm_\alpha + 4)} - \frac{2d}{Z} \qquad h = \frac{(Z+2)d}{(Z)} - \frac{4}{Z(Z + gm_\alpha + 4)} \qquad (2)$$

$$i = \frac{2}{Y + ge_\alpha + 4} \qquad j = (Y+2)i - 1 \qquad k = -2i \qquad l = (Y+2)b - 1$$

$$m = -2b \qquad n = \frac{2Z}{Z + gm_\alpha + 4} \qquad o = \frac{(Z+2)n}{Z} - 1$$

$$p = \frac{2n}{Z} \qquad q = (Z+2)d - 1 \qquad r = 2d$$

where Y, Z, ge_α, ge_β, gm_α and gm_γ take a subscript appropriate to the corresponding stub. For example,

$$S_{8,4} = c = \frac{2}{Y_y + ge_{yz} + 4} + \frac{2}{Z_x + gm_{xz} + 4} - 1 \qquad (3)$$

The normalised conductances ge and resistances gm of the lossy stubs, simulating the anisotropic electric σ and magnetic σ^* conductivities, are given by (with Zo the characteristic impedance of the free space)

$$ge_{xy} = \sigma_y Z_o \frac{vw}{u}, \ldots, ge_{yz} = \sigma_z Z_o \frac{uw}{v}, \ldots, ge_{zx} = \sigma_x Z_o \frac{uv}{w}$$
$$ge_{xz} = \sigma_z Z_o \frac{vw}{u}, \ldots, ge_{yx} = \sigma_x Z_o \frac{uw}{v}, \ldots, ge_{zy} = \sigma_y Z_o \frac{uv}{w}$$

$$(4)$$

$$gm_{xy} = \sigma_y^* Z_o^{-1} \frac{vw}{u}, \ldots, gm_{yz} = \sigma_z^* Z_o^{-1} \frac{uw}{v}, \ldots, gm_{zx} = \sigma_x^* Z_o^{-1} \frac{uv}{w}$$
$$gm_{xz} = \sigma_z^* Z_o^{-1} \frac{vw}{u}, \ldots, gm_{yx} = \sigma_x^* Z_o^{-1} \frac{uw}{v}, \ldots, gm_{zy} = \sigma_y^* Z_o^{-1} \frac{uv}{w}$$

	1	2	3	4	5	6	7	8	9	10	11	12	13	14	15	16	17	18	19	20	21	22	23	24
α	y	z	x	z	y	x	y	z	z	x	x	y	y	y	x	x	x	x	y	y	x	x	x	x
β	y	z	x	z	y	x	y	z	z	x	x	y	z	z	z	z	y	y						
γ	y	z	x	z	y	x	y	z	z	x	x	y							z	z	z	z	y	y
o/c Stubs	x	x	y	y	z	z	z	y	x	z	y	x	x	x	y	y	z	z						
s/c Stubs	z	y	z	x	x	y	x	x	y	y	z	z							x	x	y	y	z	z
Vinc	1	2	3	4	5	6	7	8	9	10	11	12	13	14	15	16	17	18	19	20	21	22	23	24
Vref 1	a	b	d						b		-d	c	e	f									g	h
Vref 2	b	a				d			c	-d		b	e	f							-g	-h		
Vref 3	d		a	b			b		c	-d			e	f									-g	-h
Vref 4			b	a	d		-d	c			b		e	f					g	h				
Vref 5				d	a	b	c	-d		b					e	f			-g	-h				
Vref 6		d			b	a	b		-d	c					e	f					g	h		
Vref 7			-d	c	b	a	d		b						e	f	g	h						
Vref 8			b	c	-d		d	a			b				e	f			-g	-h				
Vref 9	b	c				-d			a	d		b	e	f							g	h		
Vref 10		-d			b	c	b		d	a					e	f			-g	-h				
Vref 11	-d		c	b			b				a	d	e	f									g	h
Vref 12	c	b	-d						b		d	a	e	f									-g	-h
Vref 13	i										i	j	k											
Vref 14		i							i				m	l										
Vref 15			i						i						j	k								
Vref 16			i				i								m	l								
Vref 17				i					i								j	k						
Vref 18				i	i												m	l						
Vref 19				-n		n													-o	p				
Vref 20			n				-n												r	-q				
Vref 21						n			-n												-o	p		
Vref 22		-n							n												r	-q		
Vref 23			-n								n												-o	p
Vref 24	n											-n											r	-q

Figure 1 : The new PML-TLM matrix

III. NUMERICAL RESULTS

To valid the modified SCN, we have first considered a simple point source radiating in a free space simulated by 51x51x51 cells. The methodology is similar to that used in [4]. Ez at the center of the test domain is excited with a smooth compact pulse and the response at time step 100 is observed along the line (iΔl,1,1) where i=1 to 51. This response is compared to a reference solution obtained with a large domain of 151x151x151 cells by computing the local error :

$$\text{error}\,(i) = \left| E_z\,(i,\,1,\,1) - E_{z\,\text{ref}}\,(i,\,1,\,1) \right|$$
$$\text{for}\quad i = 1\ \text{to}\ 51 \qquad (5)$$

The test domain is surrounded by various PML layers characterised by the thickness N (cells number in the layer), the conductivity σ and σ^* profile and the theoritical reflection factor R. We have observed that the efficiency of the PML increases when the thickness grows up. Figure 2 shows that PML layers with 16 cells, parabolic profile of order 2 and $R=10^{-2}$ provide 60dB more accurate solution than matched terminations. The performances are improved by using geometric progression for the conductivity profile. We can obtain 100dB more accurate solution than matched terminations with an optimal geometric ratio of 2,15. These results are independant of the choice of R if $R \geq 10^{-4}$. However, reducing R increases the local error and may give instabilities.
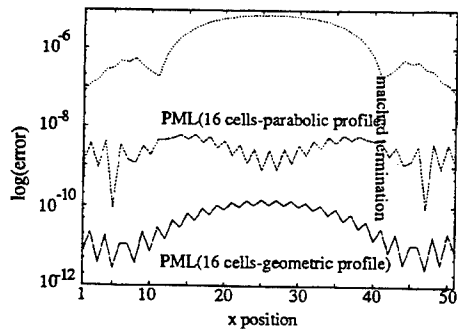
| Figure 2 : Local error for various absorbing boundary conditions | Figure 3 : Field temporal evolution for various PML thickness |
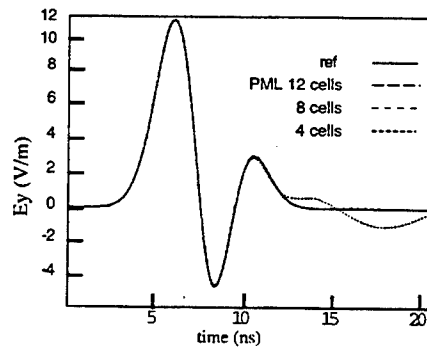
Performing the test studied by Berenger [5], all the results are confirmed. We have considered the Ez field radiated at point (2,12,2) by a dipole located at (2,2,2) in a domain of 14x14x14 cells. The excitation signal is gaussian and the response is compared to a reference solution obtained with a large domain of 150x150x150 cells. We have plotted in figure 3 the field temporal evolutions obtained for PML layers with various thickness, geometric profile (optimal ratio=2,15) and $R=10^{-2}$. The result with a 12 cells PML layer is very close to the reference solution while oscillations appear for a 4 and 8 cells PML layer. In figure 4, we give the field spectral density, for the same cases. The temporal disagreements induce important oscillations in the low frequency domain. They seem to be caused by evanescent waves which cannot be absorbed by PML layers, especially for low frequencies. Then, the efficiency of the PML layer is sensitive to the choice of the electric conductivity σ_0 in the interface vacuum-PML medium which depends on the layer thickness and on R. As observed by Berenger in
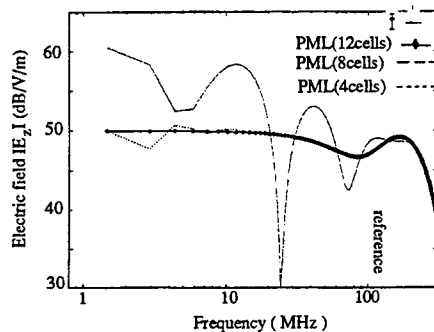
Figure 4 : power spectral density for various PML thickness.

FDTD simulations, the frequency domain of validity for PML layers in TLM simulation is given by (6).

$$f > fc = \frac{\sigma_o}{2\pi\varepsilon_o} \qquad (6)$$

IV. CONCLUSION

A new general variable mesh SCN was derived for direct implementation of Berenger's PML in 3D-TLM simulation. Numerical experiments have proved the validity of the modified SCN and the ability to absorb outgoing waves. A parametric study have allowed the determination of the optimal PML characteristics and the validity frequency domain. Current works are made to avoid instabilities for improving performances of PML in TLM method.

V. ACKNOWLEDGMENT

Computational ressources were supported by the Connection Machine 5 of the Centre National de Calcul Parallele en Sciences de la Terre, Paris, France.

VI. REFERENCES

[1]   Eswarappa, C., Hoefer, W.J.R. : 'Implementation of Berenger absorbing boundary conditions in TLM by interfacing FDTD perfectly matched layers', *Electronics Letters*, 1995, vol. 31, n°15, pp. 1264-1266.

[2]   Berenger, J.P. : 'A perfectly matched layer for the absorption of electromagnetic waves', *J. Computational Physics*, 1994, vol. 114, n°2, pp. 185-200.

[3]   Jin, H., Vahldieck, R. : 'Direct Derivations of TLM symmetrical condensed node and hybrid symmetrical condensed node from Maxwell's equations using centered differencing and averaging', *IEEE Transactions on Microwave Theory and Tchniques*, 1994, vol. 42, n°12, pp. 2554-2561.

[4]   Katz, D.S., Thiele, E.T., Taflove, A. : 'Validation and extension to three dimensions of the Berenger PML absorbing boundary conditions for FD-TD meshes', *IEEE Microwave and Guided Wave Letters*, 1994, vol. 4, n°8, pp. 268-270.

[5]   Berenger, J.P. : "Couches absorbantes parfaitement adaptées pour la simulation en espace libre". JINA, Nov

Electromagnetic Field Computations by a Generalized Network Formulation

L. B. Felsen[1], M. Mongiardo[2], P. Russer[3]

[1] Department of Aerospace and Mechanical Engineering and Department of Electrical
and Computer Engineering, Boston University, 110 Cummington Street, Boston, Ma 02215, U.S.A
[2] Istituto di Elettronica, Università di Perugia, I-06100 Perugia, Italy.
[3] Lehrstuhl für Hochfrequenztechnik, Technische Universität München, Arcisstr. 21,
D-80333 München 2, Germany, phone +49(0)89/21058390, fax +49(0)89/21053365

Abstract

Field computations in complex geometrical environments require simultaneous use of various analytic and numerical techniques. In the approach pursued here, the overall spatial domain is partitioned into subdomains which can be treated by available methods for electromagnetic field computation. The field solutions in the various subdomains are matched across the interfaces between adjacent subregions. To implement this strategy, a generalized network formulation is derived systematically from problem-matched alternative representations of the dyadic Green's functions for each subdomain. The algorithm architecture is presented in terms of a compact operator format that highlights the underlying principles. A simple example of a waveguide circuit is introduced to illustrate relevant concepts.

1 Introduction

Electromagnetic field computations in complex structures are required in a variety of scenarios dealing either with natural environments or with man–made devices. To attack such problems systematically, it is advantageous to parametrize the "complexity" of the overall domain in terms of interactions between simpler tractable subdomains. A general architecture has been proposed elsewhere [1], and it is specialized here to a class of problems concerned with microwave components and devices. For such applications, much work has been done on relating the field problem to sophisticated analytically and computationally based network models, which are summarized below.

In the past few years the advantages of dealing with complex structures by hybrid methods of analysis have become apparent. As a result, several approaches have been proposed, e. g. [2],[3],[4] to cite just a few, which combine different numerical methodologies such as finite differences techniques, TLM and integral-equation-based methods. Moreover, also apparent has been the necessity of overcoming some limitations of classical modal techniques by developing new approaches as described e. g. in [5], where a three–dimensional modal approach has been pursued based on the admittance representation, or in [6], where a full wave method of analysis has been applied also to metallic regions. In addition, important in the practical design of microwave components are efficiency considerations, which are closely linked to the appropriate choice of the Green's functions, as demonstrated in [7].
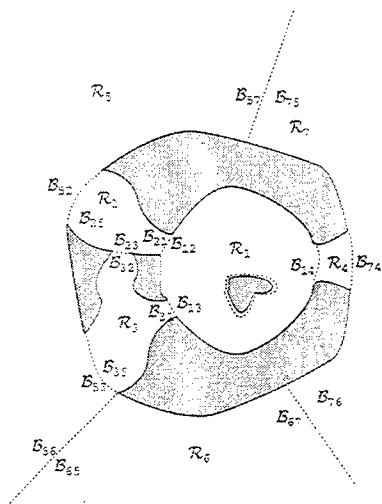
Figure 1: Segmentation of the space into different regions denoted by $\mathcal{R}_\ell$ separated by boundaries $\mathcal{B}_{\ell k}$ (dashed curves); in this notation the first index refers to the region and the second index refers to the boundary with adjacent regions. The shadowed regions are either p.e.c. or p.m.c.

The above approaches, and the pertaining alternative Green's functions representations, have been implemented in an empirical way, mainly on a case by case basis. The purpose of the contribution here is to present a systematic approach to dealing with complex systems, starting with alternative Green's function representations [8, Secs. 2.3, 2.6 and 3.3c] which guide the construction of hybrid analytic and numerical methods. Thus, the message we attempt to convey in this paper is twofold:

1. to introduce a generalized problem-matched approach to field problems which greatly enlarges the arsenal of alternatives, and

2. to show how each alternative impacts the network formulation as well as numerical strategies.

To make these points succintly without undue complication through details we use compact operator notation and illustrate only the general *concepts*; this is done in order to grant a bird's eye view of the totality. The details become evident when we treat particular problem geometries.

2   Method of Analysis

We start with subdividing the complex system into a number of subdomains (clusters), see Fig. 1, which may be of different types, and which are joined together across interfaces

mapping representations on one side into those on the other side. The electromagnetic field transmission through each subdomain is completely characterized by the relations between the tangential field components (TFCs) on its boundary. The TFCs are subdivided into independent and dependent TFCs: we may use, for example, on part of the boundary the electric TFC as the independent field component and the magnetic TFC as the dependent TFC; on other parts of the boundary we can make the opposite choice. We may also choose linear combinations of the electric and of the rotated magnetic TFC; such linear combinations may represent waves incident into the subdomain and scattered from the subdomain, and will be called tangential wavefields in the following. The representations of the total electromagnetic field may be analytic, with basis functions that satisfy the relevant field equations in the subdomain, or they may be numerical grids for direct computation of the fields. In particular, the overall space $\mathcal{R}$ is divided into $\mathcal{N}_R$ subdomains $\mathcal{R}_\ell$, $\ell = 1 \ldots \mathcal{N}_R$, (Fig. 1); two subdomains $\mathcal{R}_\ell$ and $\mathcal{R}_k$ are connected across the interface $\mathcal{B}_{\ell k}$, whose subscripts are ordered so that the first index identifies the region of interest and the second index identifies the exterior region. Whenever some portion is an open structure embedded in unbounded space, this surrounding space may also be treated as a region, e.g. regions, $\mathcal{R}_5$, $\mathcal{R}_6$ and $\mathcal{R}_7$ in Fig. 1. Each region $\mathcal{R}_\ell$ is enclosed by the boundary

$$\mathcal{B}_\ell = \sum_k^{K_\ell} \mathcal{B}_{\ell k}. \tag{1}$$

When parts of a boundary $\mathcal{B}_\ell$ are impenetrable (i.e., perfect electric or magnetic conductors), the access to neighbouring subdomains is granted via apertures (ports) $\mathcal{B}_{\ell k}$ as in Fig. 1, and the subdomains are closed regions. This special case of the more general problem, which is of interest expecially for multiport waveguide and cavity systems, is the focus of the present paper. In Fig. 1, the impenetrable portions are shown shaded and they are omitted from the sum in eq. 1; the number of apertures (ports) on the boundary of region $\mathcal{R}_\ell$ is denoted by K_ℓ. Two adjacent boundaries $\mathcal{B}_{\ell k}$ and $\mathcal{B}_{k\ell}$ belonging to $\mathcal{R}_\ell$ and $\mathcal{R}_k$, respectively, enclose a volume of zero measure and thereby form an interface. We also introduce the normal vectors $\mathbf{n}_{\ell k}$ on the boundaries $\mathcal{B}_{\ell k}$ directed toward the exterior of $\mathcal{R}_\ell$. For a subdomain whose entire boundary is penetrable, the access "port" is that entire boundary. This is depicted by the separate "obstacle" in the interior of $\mathcal{R}$; for simplicity the obstacle shall be regarded as perfectly conducting but this restriction can readily be removed.

On each boundary $\mathcal{B}_{\ell k}$, as seen from $\mathcal{R}_\ell$, we shall *specify independent exciting fields* and then *determine* via the corresponding Green's function representations the resulting *dependent* fields generated at $\mathcal{B}_{\ell k}$ through interaction with the interior of $\mathcal{R}_\ell$. The resulting electromagnetic description of each subdomain has an analog in network theory where it is customary to describe a multiport network in terms of the relationship between dependent and independent quantities. For example, by choosing the currents as independent variables and the voltages as dependent variables, an impedance description of the network is obtained.

In the operator notation we denote by $(\mathbf{F})_i$ and $(\mathbf{F})_d$ the state vectors containing all of the independent and dependent electromagnetic field quantities, respectively, of our complex system. The relation between dependent and independent state vectors is expressed by a suitable operator $\hat{O}$ as

$$(\mathbf{F})_d = \hat{O}\left\{(\mathbf{F})_i\right\} \tag{2}$$

The operator takes different forms depending on the complexity of the subdomains and their analytic representability. Whenever feasible and convenient, field representations in a subdomain are based on the dyadic Green's functions for that region. The choice of these Green's functions impacts in a significant manner the "efficiency" (i.e. rapidity of convergence) of the resulting formulation. Alternative Green's function representations differ from one another by the choice of boundary conditions on the interconnects between adjacent subdomains. These boundary conditions, in turn, govern the field decomposition into oscillatory constituents, traveling wave constituents or hybrid combinations of both, which should be chosen so as to provide a good, i.e. well convergent, match to the phenomenology in different portions of the subdomain interior.

Different subdomains are then connected according to their topology, and so as to satisfy continuity of the transverse field at the boundaries. By noting that each interface has two "sides", here denoted by the superscripts α and β, we may subdivide the state vectors as

$$(\mathbf{F})_d = \begin{pmatrix} \mathbf{F}^\alpha \\ \mathbf{F}^\beta \end{pmatrix}_d, \quad (\mathbf{F})_i = \begin{pmatrix} \mathbf{F}^\alpha \\ \mathbf{F}^\beta \end{pmatrix}_i \tag{3}$$

Knowledge of the dependent and independent field quantities on each side of the boundaries provides the transverse electromagnetic field quantities, $\mathbf{E}_t, \mathbf{H}_t$, on the boundaries. These relations can be expressed by using the operators $\hat{C}^\alpha$ and $\hat{C}^\beta$,

$$\hat{C}^\alpha \begin{pmatrix} (\mathbf{F}^\alpha)_i \\ (\mathbf{F}^\alpha)_d \end{pmatrix} = \begin{pmatrix} \mathbf{E}_t \\ \mathbf{H}_t \end{pmatrix}, \quad \hat{C}^\beta \begin{pmatrix} (\mathbf{F}^\beta)_i \\ (\mathbf{F}^\beta)_d \end{pmatrix} = \begin{pmatrix} \mathbf{E}_t \\ \mathbf{H}_t \end{pmatrix} \tag{4}$$

thereby describing compactly the continuity of the transverse components of the electromagnetic field on the interfaces as

$$\hat{C}^\alpha \begin{pmatrix} (\mathbf{F}^\alpha)_i \\ (\mathbf{F}^\alpha)_d \end{pmatrix} = \hat{C}^\beta \begin{pmatrix} (\mathbf{F}^\beta)_i \\ (\mathbf{F}^\beta)_d \end{pmatrix} \tag{5}$$

The topological relationships in the field equations (2) and (5) provide the reduction to the multiport and connection network descriptions, respectively, in network theory. The actual multiport and connection networks corresponding to the complex field problem are obtained from the latter equations via moment method discretization.

3 An example

3.1 Statement of the problem

In this section we illustrate application of the above theory on a simple example: a practical waveguide circuit, with cross-section shown in Fig. 2. For ease of manufacturing, since a milling technique is assumed, the waveguide component is constructed by inserting suitable stubs, represented by subregions $\mathcal{R}_2$, $\mathcal{R}_3$ etc. in Fig. 2, along the main waveguide. This motivates the subdivision of our structure into one main subregion, i.e. subregion $\mathcal{R}_1$ in Fig. 2 with boundaries at $\mathcal{B}_{10}$ and $\mathcal{B}_{20}$, and several other subregions corresponding to the stubs. Efficient characterization of region $\mathcal{R}_1$ depends on a suitable choice of the independent and dependent field quantities and on the appropriate Green's function expansion. Section 3.2 illustrates how to choose the independent field quantities in a convenient manner.
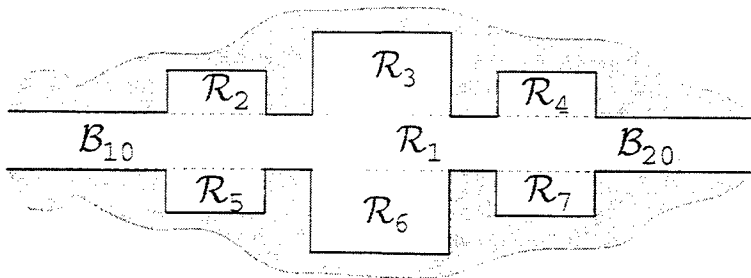
Figure 2: Cross-section of a waveguide circuit, showing subdivision into different subregions. In this model, for ease of manufacturing, the height/width of the guide is left unchanged and stubs are generated by milling techniques, thereby suggesting the choice of the above subdivisions. Evaluation of the network elements is efficiently accomplished by choosing appropriate Green's function representations. The latter choice depends on the problem parameters (i.e. relative distances between stubs, waveguide height/width etc.).
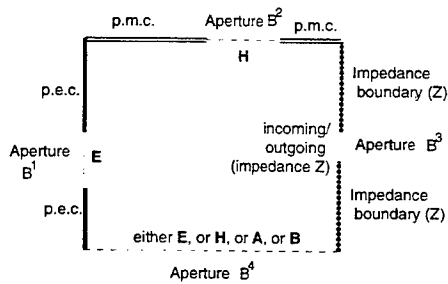
Figure 3: A region $\mathcal{R}$ is connected to other regions through apertures, and bounded by perfect electric conductors (p.e.c.), perfect magnetic conductors (p.m.c.) and impedance impedance boundaries. The boundary conditions on the coordinate surfaces determine the choice of the **independent wavefields**. The latter are also identified in the figure. Here **E** and **H** refer to standing wave representations, whereas **A** and **B** refer to incoming and outgoing traveling waves, respectively. Note that when an aperture covers an entire boundary segment, like B^4, the **independent wavefield** may be chosen as desired.

3.2 Choice of problem-matched independent field quantities

In circuit theory, it is customary to use either standing wave voltages and currents or incoming and outgoing traveling waves, but not both in hybrid combinations. However, in field problems, the choice of the **independent wavefields** may be adapted to the ambient boundary conditions, i.e. to the pattern of p.e.c., p.m.c., impedance conditions etc. specified on the boundary of our region.

To illustrate these considerations let us refer to the region depicted in Fig. 3. Note that in order to compute the field produced by one of the **independent sources**, *all the other independent sources must be set to zero*. This fact has direct impact on the boundary conditions. For example, to compute the field produced by the independent magnetic field source **H** in aperture B^2 on the p.m.c., we have to set to zero the electric field on aperture B^1 and the incoming (or outgoing) wave on aperture B^3. However, imposing a zero tangential electric field is equivalent to imposing the presence of a p.e.c.; also, a zero incoming wave is equivalent to a boundary impedance Z. It is readily observed that the above choice of **independent wavefields** leads to homogeneous boundary conditions and, therefore, to the direct availability of the problem-matched Green's function. On aperture B^4, one may exercise alternative options in the choice of the independent wavefield.

3.3 Application to the waveguide circuit

Applying the observations made in connection with Fig. 3 to the waveguide circuit in Fig. 2 it is seen that electric fields are a convenient choice for the independent field quantities on boundaries between subregion $\mathcal{R}_1$ and the subregions occupied by the stubs. However, at the input-output ports (i.e. at ports corresponding to boundaries B_{10} and B_{20}) it is customary to use a scattering wave representation. It is thus apparent that subregion $\mathcal{R}_1$ is conveniently described by taking as independent quantities the electric fields at the boundaries between $\mathcal{R}_1$ and the stubs, and the incident waves at the input-output ports, i.e. on boundaries B_{10} and B_{20}.

As a numerical example we consider a nine stub waveguide phase shifter: Fig. 4 shows measured and computed return loss and phase shift obtained by using alternative Green's function expansions.

4 Conclusions

A systematic and comprehensive approach for electromagnetic field computations in complex structures has been outlined. Subdivision of the problem space into subdomains allows the simultaneous use of analytic methods in some subdomains and numerical methods in other subdomains. When using analytic methods, alternative Green's function representations provide the arsenal for efficient computations. Different field representations used in adjacent subdomains are matched at the boundaries by using suitable connection networks directly obtained from the field problem.
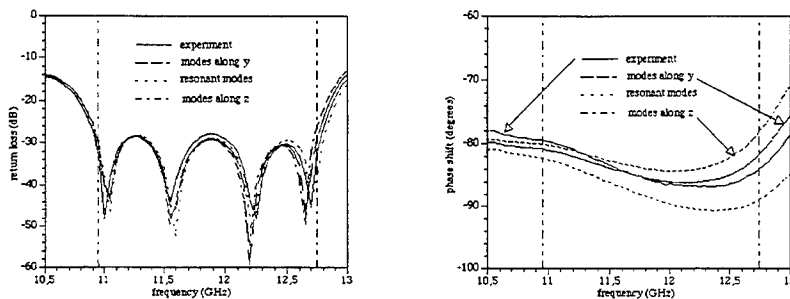
Figure 4: Return loss and phase shift of a waveguide phase shifter with nine stubs which has been analyzed by using the network approach [7]. Measured data have been compared with theoretical results obtained by using alternative Green's function expansions.

Reference

[1] L. B. Felsen, "An architecture for wave interaction with complex environments: Fields, networks, interface mappings and computations," *presented at the First Annual Symposium of Radio Science in Israel, Tel Aviv, Israel,* Dec. 1996.

[2] M. Mongiardo and R. Sorrentino, "Efficient and versatile analysis of microwave structures by combined mode matching and finite difference methods," *IEEE Microwave Guided Wave Lett.,* vol. 3, pp. 241–243, Aug. 1993.

[3] M. Sohby, E. A. Hosny, P. Russer, B. Isele, and C. Christopoulos, "Interfacing the transmission line method (tlm) and state–space technique to analyse general non linear structures," *Proc. 2nd Int. Conf. Comp. Electromagnetics, Nottingham,* pp. 299–302, 1994.

[4] M. Righi, W. J. R. Hoefer, M. Mongiardo, and R. Sorrentino, "Efficient TLM diakoptics for separable structures," *IEEE Trans. Microwave Theory Tech.,* vol. 43, pp. 854–859, Apr. 1995.

[5] F. Alessandri, G. Baini, M. Mongiardo, and R. Sorrentino, "A 3-D mode matching technique for the efficient analysis of coplanar MMIC discontinuities with finite metallization thickness," *IEEE Trans. Microwave Theory Tech.,* vol. 41, pp. 1625–1629, Sept. 1993.

[6] R. Schmidt and P. Russer, "Modeling of cascaded coplanar waveguide discontinuities by the mode–matching approach," *IEEE Trans. Microwave Theory Tech.,* vol. 43, pp. 2910–2917, Dec. 1995.

[7] F. Alessandri, M. Mongiardo, and R. Sorrentino, "A technique for the full-wave automatic synthesis of waveguide components: Application to fixed phase shifters," *IEEE Trans. Microwave Theory Tech.,* vol. 40, pp. 1484–1495, July 1992.

[8] L. B. Felsen and N. Marcuvitz, *Radiation and Scattering of Waves.* Englewood Cliffs, NJ: Prentice Hall, 1973.

A Comparative Study of Dispersion Errors and Performance of Absorbing Boundary Conditions in SCN-TLM and FDTD

L. De Menezes, C. Eswarappa and W. J. R. Hoefer

NSERC/MPR Teltech Research Chair in RF Engineering, Department of Electrical and Computer Engineering, University of Victoria, Victoria, B.C., CANADA V8W 3P6

Abstract

In this paper, a comparative study of dispersion errors and performance of Higdon's absorbing boundary conditions (ABCs) in Symmetrical Condensed Node Transmission Line Matrix (SCN-TLM) and Finite Difference Time-Domain (FDTD) methods is described. We have computed the dispersion errors of the SCN-TLM and FDTD methods in free space and in rectangular waveguide structures numerically as well as analytically. In both the cases, the dispersion error in SCN-TLM is less than that of the FDTD method, as expected from dispersion analysis. Moreover, for TE_{10} mode of propagation in rectangular waveguide structures, the dispersion error in SCN-TLM is constant with frequency and is equal to the minimum value obtained with the FDTD method. Hence, this error could be systematically corrected in SCN-TLM. We also observed that accurate extraction of the propagation constants demands very good absorbing boundary conditions, otherwise the inaccuracies of the order of three percent are easily obtained. Furthermore, it has been observed that a one-way equation ABC applied directly to the SCN-TLM voltage impulses absorbs better than the same ABC applied to the FDTD field values. The improvements in return loss are of the order of 20 dB. Also, the performance of an ABC in SCN-TLM is not very sensitive to the choice of the incidence angles, and broadband absorption can be obtained with a rough choice of incidence angles.

1. Introduction

The Transmission Line Matrix (TLM) [1] and Finite-Difference Time-Domain (FDTD) [2] methods are suitable for time-domain simulation of complex guiding and radiating structures. The TLM method is based on transmission line analogy whereas FDTD is a mathematical discretization model. Each method has its own advantages and disadvantages. The reported major advantages of the SCN-TLM [3] method are less propagation or dispersion error [4], more accurate description of boundaries (due to denser spatial field sampling), unconditional stability, better performance of one-way equation absorbing boundaries, while the disadvantages are the existence of spurious modes (observed rarely in practical simulations) and extra effort needed when deriving the equivalent transmission line network models (ex., Berenger's PML [5]). The major advantages of the FDTD are lesser computer memory storage and updating time per node and ease of implementation, while the main disadvantage is that it is only conditionally stable and the stability of the algorithm is more prone to absorbing boundary errors [6]. The major errors affecting the time-domain numerical techniques are the dispersion error, coarseness error, discretization error and absorbing boundary error. In this paper, the dispersion and absorbing boundary errors have been further studied in detail under identical conditions such as identical time step, mesh size, excitation, etc. The physical origin of the coarseness and dispersion errors in TLM is described in [7] where the difference equations of the TLM method are solved analytically.

2. Dispersion Error

We have studied the dispersion errors of FDTD and SCN-TLM in case of free space, waveguide transmission lines and waveguide cavities using the analytical dispersion equations as well as the numerical simulations.

a) Dispersion of FDTD and SCN-TLM in Free Space

The dispersion relationship of FDTD [8] is:

$$(c\frac{\Delta t}{\Delta l})^2 \sin^2(\frac{\omega\Delta t}{2}[\frac{\Delta l}{c\Delta t}]) = \sin^2(\frac{k_x\Delta l}{2}) + \sin^2(\frac{k_y\Delta l}{2}) + \sin^2(\frac{k_z\Delta l}{2}) \qquad (1)$$

The dispersion relationship of SCN-TLM [9] is:

$$\cos\omega\Delta t = \frac{1}{2}(\cos k_x\Delta l\cos k_y\Delta l + \cos k_x\Delta l\cos k_z\Delta l + \cos k_y\Delta l\cos k_z\Delta l - 1) \qquad (2)$$

The above equations (1) and (2) are used to plot the worst case dispersion errors, i.e, in the main diagonal direction (111) for SCN-TLM and the axial direction (100) for FDTD, in Fig. 1 below. We can see that the dispersion error of the SCN-TLM mesh is always smaller than that of the FDTD mesh, and the convergence is second-order as expected.
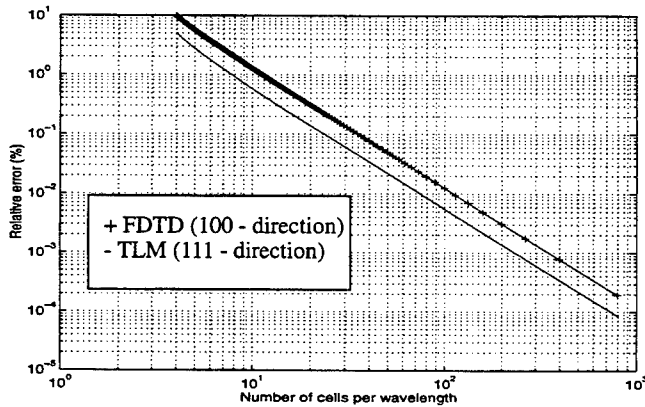
Fig. 1: Dispersion errors of FDTD and SCN-TLM meshes in free space
Note that the error decreases as Δl^2 (second order accuracy).

b) Dispersion of FDTD and SCN-TLM in Rectangular Waveguide Models

We will consider a rectangular waveguide of width a and height b, discretized with N cells across the width and M cells across the height. The propagation constant k_z of the waveguide that would be obtained with the FDTD and SCN-TLM can be obtained by substituting for k_x and k_y of waveguides in equations (1) and (2):
The propagation constant calculated using FDTD is:

$$k_z = \frac{2}{\Delta l}\text{asin}\left[\sqrt{(c\frac{\Delta t}{\Delta l})^2 \sin^2(\frac{\omega\Delta t}{2}[\frac{\Delta l}{c\Delta t}]) - (\sin^2(\frac{n\pi}{2N}) + \sin^2(\frac{m\pi}{2M}))}\right] \qquad (3)$$

674

The propagation constant calculated using TLM is:

$$k_z = \frac{1}{\Delta l} \text{acos} \left[\frac{2\cos\omega\Delta t - \cos\frac{n\pi}{2N}\cos\frac{m\pi}{2M} + 1}{\cos\frac{n\pi}{2N} + \cos\frac{m\pi}{2M}} \right] \tag{4}$$

where n varies from 1 to N-1 and m varies from 0 to M-1.

The analytically exact value of the propagation constant is:

$$k_z = \sqrt{(\frac{n\pi}{a})^2 + (\frac{m\pi}{b})^2 - (\frac{\omega}{c})^2} \tag{5}$$

where $n = 1,2,...$ and $m = 0,1,2....$

For a WR28 waveguide with 10 cells across the width of the waveguide, the numerically simulated and the analytical values (obtained with (3) and (4)) of the propagation constant errors are plotted in Fig. 2. The propagation constant error is defined as

Propagation constant error $= \dfrac{\beta_e - \beta_{s,d}}{\beta_e} \times 100$

where β_e is the exact propagation constant, β_s is the numerically simulated propagation constant and β_d is the propagation constant computed analytically for the discrete scheme.

We can see that for the TE_{10}-mode in waveguides, the dispersion error in FDTD is very high near cutoff (about -3 percent), decreases to a minimum of -0.415 percent at 30 GHz (corresponding to the incidence angle of 45 degrees), and then increases again to larger than -2 percent as the frequency increases. But the dispersion error in SCN-TLM is constant with frequency and is equal to -0.415 percent, the minimum value obtained with the FDTD method. We also observed that accurate extraction of the propagation constants demands very good absorbing boundary conditions, otherwise the inaccuracies of the order of three percent are easily obtained. Higdon's second-order absorbing boundaries were used in the simulations. In the case of SCN-TLM, the simulated propagation constant values were obtained for the whole frequency range with only one simulation (with incidence angles of 30 and 45 degrees), while in the case of FDTD several simulations had to be performed with different sets of incidence angles to extract the values of the propagation constants accurately.

c) Dispersion of FDTD and SCN-TLM in Waveguide Cavity Models

Consider a waveguide cavity of width a, height b and depth c, discretized with N cells across the width, M cells across the height, and L cells across the depth.

The resonant frequencies that would be obtained with a FDTD mesh can be calculated using the following equation:

$$\omega = \frac{2c}{\Delta l} \text{asin} \left[\left[\frac{\Delta l}{c\Delta t} \right] \sqrt{(\sin^2(\frac{n\pi}{2N}) + \sin^2(\frac{m\pi}{2M}) + \sin^2(\frac{l\pi}{2L}))} \right] \tag{6}$$

The resonant frequencies that would be obtained with a SCN-TLM mesh can be calculated using the following equation:
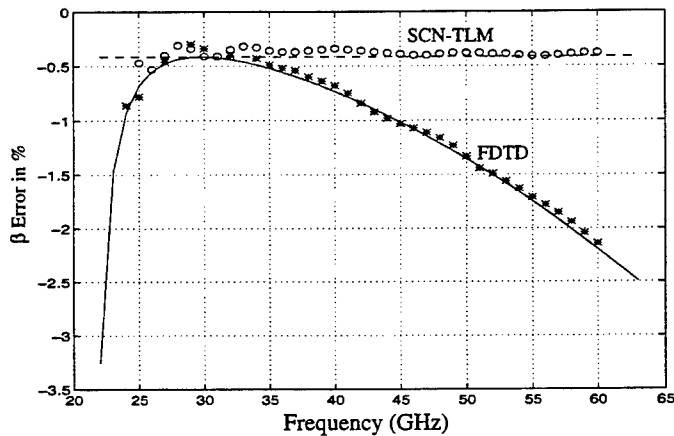
Fig. 2: Propagation constant (β) errors for FDTD and SCN-TLM solutions of the dominant mode in a WR 28 waveguide. No. of cells across the width of the waveguide = 10
— FDTD analytical, * FDTD Simulated, --- TLM Analytical, o TLM Simulated

$$\omega = \frac{1}{\Delta t}\text{acos}\left[\frac{1}{2}\left(\cos k_x\Delta l\cos k_y\Delta l + \cos k_x\Delta l\cos k_z\Delta l + \cos k_y\Delta l\cos k_z\Delta l - 1\right)\right]$$ (7)

The analytically exact value of the resonant frequency is:

$$\omega = c\sqrt{\left(\frac{n\pi}{a}\right)^2 + \left(\frac{m\pi}{b}\right)^2 + \left(\frac{l\pi}{c}\right)^2}$$ (8)

where n varies from 1 to N-1, m varies from 0 to M-1, and l varies from 1 to L-1. In Table 1, the exact and the analytical resonant frequencies (computed using (6) and (7)) of the first ten modes in a cubical waveguide cavity for the SCN-TLM and FDTD methods are compared.

3. Performance of One Way Equation Absorbing Boundaries

Good quality ABCs are very important for simulating open surfaces in radiating and scattering problems, and dispersive matched loads for extraction of scattering parameters. In our earlier work [6], we found that Higdon's one-way equation absorbing boundaries perform better in two-dimensional shunt TLM than in two-dimensional FDTD. The absorbing boundaries when implemented directly for the TLM voltage impulses gave about 20 dB better return loss than the same absorbing boundary conditions applied to the electric fields in FDTD. In this paper, we have extended this work to three-dimensional SCN-TLM and FDTD. We have studied the absorption properties of Higdon's second-order absorbing boundaries [10] by applying them at the two ends of a WR 28 rectangular waveguide section. The mesh size was (60x10). The space resolution and time step were 0.7112 mm and 1.185 ps, respectively. The dominant TE_{10} mode in the waveguide was excited. Cosine modulated Gaussian temporal variation was used to make sure that only the frequencies of interest were excited. The electric field values were sampled along the propagation direction and Fourier transformed to obtain the minimum and maximum field values at each

Mode	Exact	Analytical TLM (N=10)	Analytical FDTD (N=10)	Analytical TLM (N=20)	Analytical FDTD (N=20)
110	4.44288	4.43371	4.43371	4.44059	4.44059
111	5.44398	5.41838	5.43576	5.43576	5.43999
120	7.02480	7.00148	6.96224	7.01904	7.00926
121	7.69530	7.64577	7.64742	7.68331	7.68341
220	8.8857	8.81142	8.81141	8.86740	8.86742
221	9.4247	9.31444	9.36885	9.39852	9.41099
130	9.9345	9.89714	9.69848	9.92536	9.87616
222	10.8867	10.68130	10.83670	10.83680	10.8715
230	11.3272	10.59460	11.12650	11.29470	11.2779
231	11.7548	11.57110	11.58170	11.71180	11.7122

Table 1: Resonant frequencies (Ka) of a cubical waveguide cavity computed using analytical equations (6) and (7) and the exact formula (8):

frequency. The magnitude of reflections obtained as (VSWR-1)/(VSWR+1) are plotted in Fig. 3. We can see that the reflections obtained for the ABC applied to the SCN-TLM voltage impulses are lower by about 20 dB when compared to the same ABC applied to FDTD. This good absorption in SCN-TLM is due to the fact that as the voltage impulses contain both electric and magnetic fields, it is equivalent to applying ABC to both electric and magnetic fields simultaneously. It should be noted here that the superior performance of the absorbing boundaries in the two-dimensional shunt TLM has also been independently observed by Giannopoulos and Tealby [11].

4. Conclusions

The dispersion errors of SCN-TLM and FDTD in free space and waveguide structures have been studied. Our study confirms that the dispersion error in SCN-TLM is less than that of the FDTD method. The surprising fact is that the dispersion error in SCN-TLM is virtually constant with frequency for TE_{10} mode of propagation in rectangular waveguide structures. This constant is equal to the minimum value of the dispersion obtained with the FDTD method.

The performance of Higdon's ABCs in SCN-TLM and FDTD under identical conditions has been studied. ABCs applied directly to the SCN-TLM voltage impulses absorb better than those applied to the FDTD fields. Also the choice in incidence angles in the design of ABCs is not critical in SCN-TLM. These features of SCN-TLM offer a definite advantage over the FDTD method.

Acknowledgments
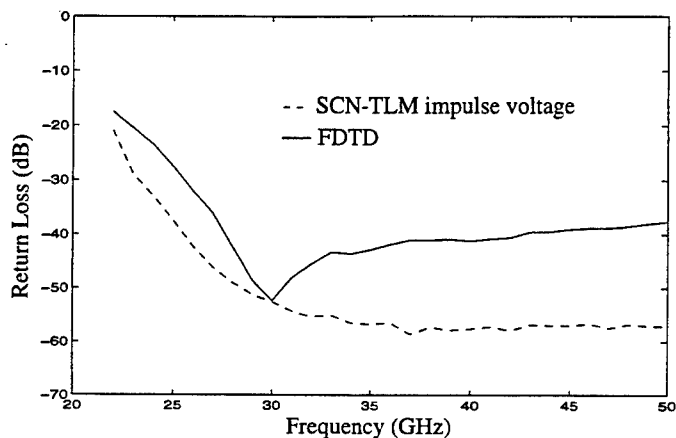
Fig. 3: Return loss of Higdon's second-order absorbing boundary conditions in a WR28 waveguide ($\theta_1 = 30^0$, $\theta_2 = 45^0$)

References

1] W. J. R. Hoefer, "The Transmission Line Matrix (TLM) Method", in T. Itoh: *Numerical Techniques for Microwave and Millimeter Wave Passive Structures*, John Wiley & Sons, New York.

[2] K.S. Yee, "Numerical Solution of Initial Boundary Value Problems Involving Maxwell's Equations", *IEEE Trans. Antennas and Propagation*, vol. 14, no.3, pp. 302-307, May 1966.

[3] P. B. Johns, "Symmetrical Condensed Node for the TLM method", *IEEE Trans. Microwave Theory Tech.*, vol. MTT-35, no. 4, pp. 370-377, April 1987.

[4] F.J. German, J.A. Svigelj and R. Mittra, "A Numerical Comparison of Dispersion in Irregularly Graded TLM and FDTD Meshes", *12th Annual Review of Progress in Applied Computational Electromagnetics* Digest, pp. 270-278, March 18-22, 1996, Monterey, CA.

[5] N. Pena and M.M. Ney, "A New TLM Node for Berenger's Perfectly Matched Layer", *IEEE Microwave and Guided Wave Letters*, vol. 6, no. 11, pp. 410-412, November 1996.

[6] C. Eswarappa and W.J.R. Hoefer, "A Comparative Performance Study of Absorbing Boundary Conditions in TLM and FDTD", *12th Annual Review of Progress in Applied Computational Electromagnetics* Digest, pp. 302-309, March 18-22, 1996, Monterey, CA.

[7] L. R. A. X. de Menezes and W. J. R. Hoefer, "Accuracy of TLM Solutions of Maxwell's Equations", *IEEE Trans. Microwave Theory Tech.*, vol. 44, no. 12, pp. 2512-2518, Dec. 1996.

[8] K.S. Kunz and R.J. Luebbers, "The finite difference time domain method for electromagnetics", CRC Press, 1993.

[9] M. Krumpholz and P. Russer, "On the dispersion of TLM and FDTD," *IEEE Trans. Microwave Theory Tech.*, vol. 42, pp. 1275-1279, July 1994.

[10] C. Eswarappa and W.J.R. Hoefer, "One-Way Equation Absorbing Boundary Conditions for 3-D TLM Analysis of Planar and Quasi-planar Structures", *IEEE Trans. Microwave Theory Techniques*, vol. 42, no. 9, pp. 1669-1677, Sep. 1994.

[11] A. Giannopoulos and J.M. Tealby, "Comparison of performance of absorbing boundary conditions in TLM and FDTD", *Electronics Letters*, 14th Sept. 1995, vol. 31, no. 9, pp. 1639-1640.

ANALYSIS OF PLANAR STRUCTURE ON GENERAL ANISOTROPIC MATERIAL: UNIFIED TLM MODEL IN FREQUENCY- AND TIME-DOMAIN AND EXPERIMENTAL VERIFICATION

Ke WU*, Qi ZHANG#, Jifu HUANG&

Poly-Grames Research Center
Dept. de génie électrique et de génie informatique, École Polytechnique
C. P. 6079, Succ. Centre-Ville, Montréal, Canada H3C 3A7

*On leave from the above institution and currently with
Department of Electronic Engineering, City University of Hong Kong
Tat Chee Avenue, Kowloon, Hong Kong

#Nortel Inc., Ottawa, Canada

&Harris-Farinon, Montreal, Canada

ABSTRACT

This paper presents a unified frequency- and time-domain analysis of planar structure printed on generalized anisotropic medium under the TLM formalism. Two- and three-dimensional arbitrary wave propagations are effectively modeled that account for complex electromagnetic effects of both permittivity and permeability tensors. Computational issues and technical merits are presented and discussed for the frequency and time domain solutions. Numerical examples are shown for two orthogonally-oriented microstrip line resonators deposited on a r-cut sapphire substrate. Experimental prototypes are made and comparison between the theoretical and measurement results indicates that the proposed simulation strategy is adequate for application and design of integrated circuits involving complex anisotropic materials.

INTRODUCTION

Modeling and analysis of guided-wave propagation for complex structures involving generalized anisotropic media have been a research subject of interest since decades [1-8]. These studies are directed to the aim at exploring certain unparalleled electrical properties suitable for design of microwave and millimeter-wave integrated circuits. In spite of a number of interesting aspects known

for these complex materials, there has been a limited design information available now on this subject. Apart from many other reasons, modeling techniques become much more involved with bi-isotropic and/or bi-anisotropic formulations that are usually coupled to each other. Although some analytical methods were reported and applied to the analysis of regular structures under some strict conditions related to material parameter and geometrical topology, there are limited techniques available which can handle generalized guided-wave structure including discontinuities under a unified algorithm. Therefore, a unified framework is essential for exploring new features of these complex structure which should be able to deal with the modeling, analysis, and circuit design aspects.

The transmission line matrix (TLM) method was first proposed by P. B. Johns for the analysis of electromagnetic structure [9]. The theoretical foundation of this technique is the well-known concept of modeling field space by lumped network [10, 11], where the network is constructed to imitate the wave propagation and the Maxwell's equation is satisfied in an intrinsic way. With a distributed parameter transmission-line network model, the wave propagation space is represented by a mesh of transmission lines. In this case, electric and magnetic fields are equivalent to modal voltages and currents defined on the network. A number of TLM algorithms have been developed in both time- and frequency-domains [12-15] whose major advantages for the application of planar structures involving anisotropic materials will be briefly presented in the paper. The recent proposal for a unified TLM model was proposed for handling wave propagation in electrical and optical structures considering arbitrary permittivity and permeability tensors [16]. This model is extended into the time domain which is also a subject of the present work. Therefore, a unified frequency- and time-domain TLM algorithm is developed to tackle these complex problems. To verify our numerical results, experimental prototypes are fabricated and comparison between the theoretical prediction and measurement results is made to show the suitability of this unified technique for application to modeling, design and analysis of high-frequency planar circuits involving general anisotropic materials.

UNIFIED TLM MODEL IN FREQUENCY- AND TIME-DOMAIN

The development of a unified TLM model in the frequency- and time-domain is actually the search for a generalized TLM node in the frequency- and time-domain. The framework of development such a node is similar to that of the conventional SCN except that the anisotropic parameters are involved in the formulation. Starting from the Maxwell's equation, the field components can be defined in the discrete space domain. In our algorithm, tensors characterizing material electric and magnetic properties are expressed under the Cartesian coordinate in the form of

$$\bar{\varepsilon} = \varepsilon_0 \begin{pmatrix} \varepsilon_{xx} & \varepsilon_{xy} & \varepsilon_{xz} \\ \varepsilon_{yx} & \varepsilon_{yy} & \varepsilon_{yz} \\ \varepsilon_{zx} & \varepsilon_{zy} & \varepsilon_{zz} \end{pmatrix}, \quad \bar{\mu} = \mu_0 \begin{pmatrix} \mu_{xx} & \mu_{xy} & \mu_{xz} \\ \mu_{yx} & \mu_{yy} & \mu_{yz} \\ \mu_{zx} & \mu_{zy} & \mu_{zz} \end{pmatrix} \tag{1}$$

$\bar{\varepsilon}$ and $\bar{\mu}$ are the permittivity tensor and permeability tensor of the medium, respectively. To obtain a standard TLM formulation using the SCN [17] (see Fig. 1), an equality is established that relates network voltages and currents to the electric and magnetic fields. Subsequently, a set of coupled nodal

voltage and current differential equations for a single node. A central finite-difference is used at the center of the SCN in the network model of TLM such that a set of voltage and current components are obtained at the boundary planes of the node. Each pair of voltage and current variables consists of a polarized planar wave. Thereafter, the voltage and current variables are adequately transformed at the nodal boundary planes into relevant incident and reflected waves [16, 17]. After some manipulation, a relationship can be set up to interrelate the equivalent voltage and current variables to the corresponding incident voltages as described in a matrix equation.

The immediate step now is to make appropriate averaging of the relevant nodal voltages and currents at the center of the node. It yields six pairs of hybrid equations that interrelate reflected and incident voltages [16, 17]. As such, a full 12×12 nodal scattering matrix that completely describes the scattering property of the TLM node. Furthermore, the matrix consists of a number of explicit elements which are convenient for the numerical implementation.

In characterizing planar structures having electric and magnetic tensors, the time-domain model presents the following major advantages: (a) nonlinear effects can be incorporated in the algorithm; (b) multiport structures can easily be simulated; (c) wideband modeling can be done in a single step; and (d) required computer resource is linearly proportional to the number of node involved in the simulation. On the other hand, the frequency-domain model presents a number of advantages which are found to be complementary to the time-domain model. They can be summarized as follows: (a) fast steady-state solution is obtained without iterative process; (b) the dispersion and truncation errors can be minimized; (c) frequency-dependent anisotropic materials can be easily introduced in the model; and (d) absorbing boundary can be simulated in a very precise manner. Therefore, the appropriate combination of the frequency- and time-model will generate an efficient algorithm which can find application in modeling different guided-wave structures.

NUMERICAL AND EXPERIMENTAL RESULTS

To verify our unified frequency- and time-domain model, a set of experimental prototypes are fabricated in the laboratory with a r-cut Sapphire substrate having a thickness of 10 mil as shown in Fig. 2. Details are presented in [16] in connection with the electrical parameter of the r-cut substrate. In our experiments, two sets of planar line resonators as shown in Fig. 3 are made which are placed in $0°$ (or x-oriented) and $90°$ (or y-oriented) orientations, respectively. This orthogonal arrangement is made such that the anisotropic effect can be visualized in the numerical and experimental results (see Fig. 5) since identical circuit dimensions are selected. In addition, two sets of patch resonators are also simulated to showcase our unified model, as plotted in Fig. 4. The ohmic loss is not considered in modeling of these examples.

It can be seen that anisotropic effects are clearly indicated in both models. Compared to the experimental results, it is found that the frequency domain results are more accurate than its time domain counterpart. This can be explained that the dispersion and discretization errors can be minimized in the frequency domain. This is in particular significant in the case of handling a planar structure because the modeling of field singularity is closely related to the solution accuracy for which

the frequency domain is easier. In modeling the patch resonators for the two orthogonal orientations, it is observed that the anisotropic effect is much more pronounced in the frequency domain solution.

REFERENCES

[1]   N. Enghera and P. Pelet, "Modes in chirowaveguides," *Opt. Lett.*, vol. 14, pp. 593-595, 1989.

[2]   J. M. Svedin, "Propagation analysis of chirowaveguides using the finite-element method. " *IEEE Trans. Microwave Theory Tech.*, vol. MTT-38, pp. 1488-1496, Oct. 1990.

[3]   C. M. Krowne, "Nonreciprocal electromagnetic properties of composite chiral-ferrite media," *IEE Proceedings-H*, vol. 140, pp. 242-248, June 1993.

[4]   M. I. Saadoun and N. Enghera, "Theoretical study of variation of propagation constant in a cylindrical waveguide due to chirality: chiro-phase shifting," *IEEE Trans. Microwave Theory Tech.*, vol. MTT-42, pp. 1690-1694, Sept. 1994.

[5]   W. Yin, W. Wang and P. Li, "Guided electromagnetic waves in gyrotropic chirowaveguidess," *IEEE Trans. Microwave Theory Tech.*, vol. MTT-42, pp. 2156-2163, Nov. 1994.

[6]   P. K. Koivisto and J. Sten, "Quasi-static image method applied to bi-isotropic microstrip geometry," *IEEE Trans. Microwave Theory Tech.*, vol. MTT-43, pp. 169-175, Jan. 1995.

[7]   F. Olyslager, E. Laermans and D. Zutter, "Rigorous quasi-TEM analysis of multiconductor transmission lines in bi-isotropic media — Part I: Theoretical analysis for general inhomogeneous media and generalization to bi-anisotropic media; Part II: Numerical solution for layered media," *IEEE Trans. Microwave Theory Tech.*, vol. MTT-43, pp. 1409-1423, 1995.

[8]   M. Norgren and S. He, "Reconstruction of the constitutive parameters for an Ω material in a rectangular waveguide," *IEEE Trans. Microwave Theory Tech.*, vol. MTT-43, pp. 1315-1321, 1995.

[9]   P. B. John, and R. L. Beurle, "Numerical solution of 2-dimensional scattering problems using a transmission-line matrix," *Proc. IEE*, 118, (9), pp. 1203-1208, 1971.

[10]   J. R. Whinnery and S. Ramo, "A new approach to the solution of high frequency field problems," *Proc. IRE*, 32, pp. 284-288, 1944.

[11]   W. J. R. Hoefer, "The transmission-line matrix method - theory and applications," *IEEE Trans. Microwave Theory Tech.*, vol. MTT-33, pp. 882-893, 1985.

[12]   H. Jin, and R. Vahldieck, "The frequency domain transmission line matrix method - a new concept," *IEEE Trans. Microwave Theory Tech.*, vol. MTT-40, pp. 2207-2218, 1992.

[13]   C. Christopoulos, *The Transmission-Line Matrix (TLM) Method*, Series on Electromagnetic Wave Theory, IEEE/OUP Press, 1995.

[14]   Q. Zhang, and W. J. R. Hoefer, "Characteristics of new 3D distributed node TLM mesh with arbitrary aspect ratio," in *IEEE MTT-S Int. Microwave Symp. Dig.*, pp. 369-371, 1994.

[15]   P. Berini and K. Wu, "A new frequency-domain symmetrical condensed TLM node," *IEEE Microwave and Guided-Wave Lett.*, vol. 4, pp. 180-182, June 1994.

[16]   J. Huang and K. Wu, "A unified TLM model for wave propagation of electrical and optical structures considering permittivity and permeability tensors," *IEEE Trans. Microwave Theory Tech.*, vol. MTT-43, pp. 2472-2477, Oct. 1995.

[17]   P. B. Johns, "A symmetrical condensed node for the TLM method," *IEEE Trans. Microwave Theory Tech.*, vol. MTT-35, pp. 370-377, Apr. 1987.
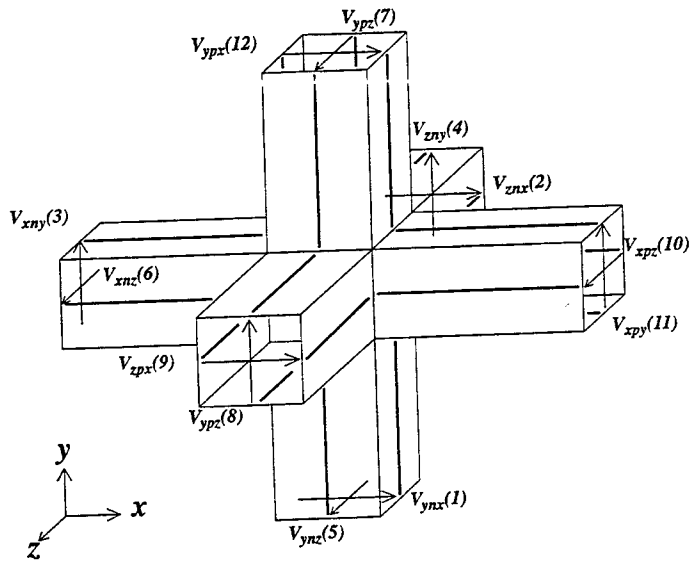
Fig. 1 Three dimensional condensed node
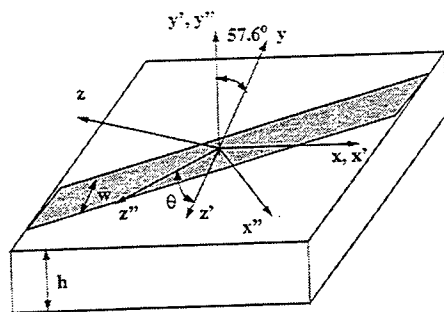
Fig. 2 Arbitrarily oriented r-cut sapphire-based microstrip
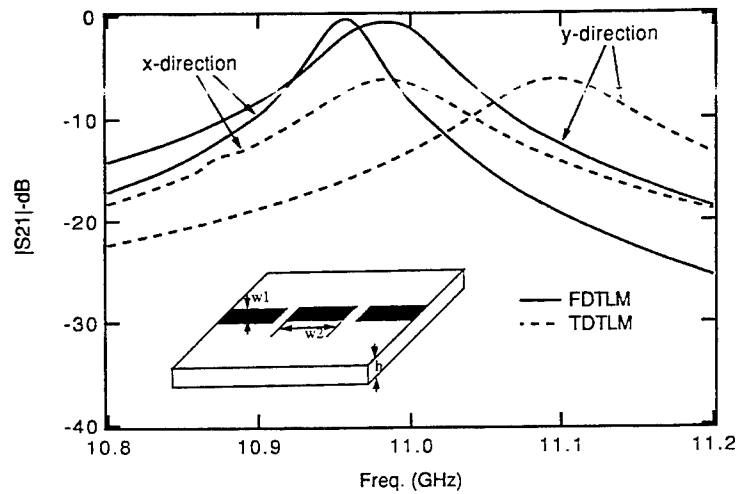
Fig. 3 Insertion loss of the structure printed on r-cut sapphire.
(h=0.254, w1=0.24, w2=5.0, gap=0.0254 mm)
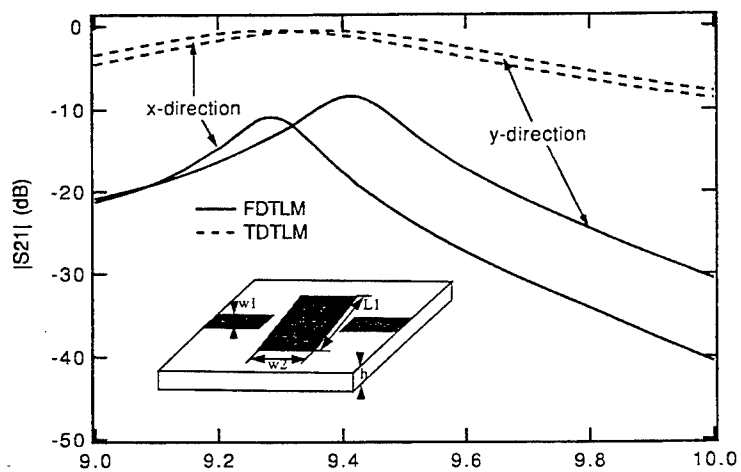
Fig. 4 Insertion loss of the structure printed on r-cut sapphire.
(h=0.254, w1=0.24, w2 = l1 = 5.0, gap = 0.0254 mm)
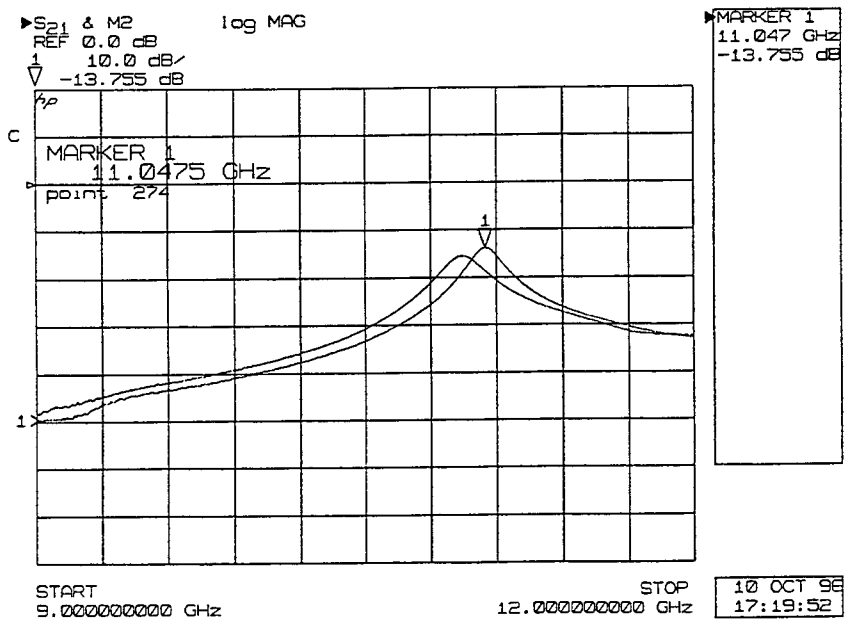
Fig. 5 Experimental results for two identical line resonator prototypes which are placed in 0 and 90 degree orientations, respectively.

A digital filter technique for electromagnetic modelling of thin composite layers in TLM

J. A. Cole, J. F. Dawson, S. J. Porter

Department of Electronics, University of York, England

Abstract

The paper describes a method for designing recursive filters for frequency dependent boundary conditions in the TLM method using frequency domain data. The approach described here allows the development of boundary conditions representing thin inhomogeneous composite materials where an analytical approach is excessively complex.

1 Introduction

The Transmission Line Matrix (TLM) method has been used to model enclosures whose walls are composed of material which is strongly conducting. Typically energy penetration into such enclosures is via apertures and cabling: the walls can be considered to be approximated by perfect conductors. As such the walls are often incorporated using a boundary between nodes in the TLM mesh. The effects of the walls are modelled using frequency-independent reflection coefficients, typically of value -1: there is no transmission allowed. This has proved to be successful where the dominant energy penetration mechanism is via apertures.

In the case where the enclosure walls are composed of thin sheets of a moderately conducting material (for example, materials with conductivities in the range of $1\,\text{kS/m}$ to $30\,\text{kS/m}$), and where the energy penetration mechanism is not dominantly through apertures and cabling, the use of a fixed reflection coefficient and zero transmission coefficient is inadequate. In this case, it is necessary to use boundaries with frequency dependent reflection and transmission coefficients.

Direct incorporation of the walls within the normal TLM mesh is possible, but requires a prohibitively small grid size.

1.1 Thin Layer Models

Various methods for circumventing this problem have been tried. Mallik and Loller [1] present a method using a parallel combination of resistors to represent the frequency dependent reflection and transmission properties of thin sheets of conducting materials. This becomes computationally inefficient when many layers of resistance are required to model the composite structure.

Since the lateral propagation in such materials is negligible, the efficiency of the computation can be increased if only propagation through the layer is considered. Johns et al [2] have proposed such a method using lossy, loaded transmission lines later improved by Trenkic [3].

Fuchs [4] has succeeded in demonstrating a full analytical, time-domain solution to the transmission through thin, homogeneous, isotropic conducting layers. The authors have also presented an approximate solution [5] in series form using a filter design of the type proposed in this paper.

Other thin layer models have been derived for the Finite Difference Time-Domain method. A vast majority of this work is concerned with perfect conductors or infinitely thin sheets. Other methods such as those described by Maloney [6] primarily consider the modelling of thin conducting sheets of relatively low conductivity. They do not take into account the decay of fields propagating through a conductor which is many skin-depths thick.

1.2 New thin layer model

The implementation described here is designed in the frequency domain using discrete time recursive digital filters. It is applicable to composite materials with complex internal structures that cannot be solved by analytical means. The filter algorithm can be determined from measured, frequency-domain data. This paper describes the design of the filter algorithms from measured or computed data.

2 Use of digital filters as frequency dependent boundaries in TLM

This section reviews the operation of recursive digital filters and their application as frequency dependent boundaries in TLM.

2.1 Digital filters

Digital filters are the embodiment of a set of difference equations in a sampled data system. Figure 1 shows one way of implementing a digital filter of order N, where the order N is the greater of the orders N_b and N_a. The unit time delay is represented by the boxes marked Z^{-1}, the triangles labelled a_n or b_n are coefficient multipliers, and the circles containing a plus sign are adders (with a minus sign on an input denoting subtraction).
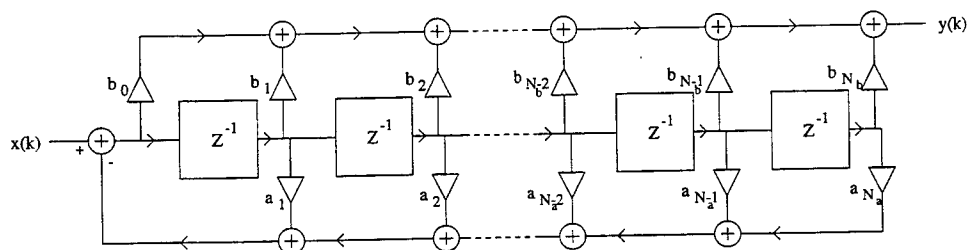
Figure 1: Structure of an Nth order recursive digital filter

The transfer function of the filter is often described as a ratio of polynomials in Z^{-1}. This can be used to determine the time response of the filter, by means of Z-transforms, or the frequency

response of the filter by letting $Z = exp(j\omega T_s)$ where ω is the angular frequency and T_s is the sampling period. For Figure 1 the transfer function in Z^{-1} is:

$$H(Z) = \frac{b_0 + Z^{-1}b_1 + Z^{-2}b_2 + \cdots Z^{-(N_b-2)}b_{N_b-2} + Z^{-(N_b-1)}b_{N_b-1} + Z^{-N_b}b_{N_b}}{1 + Z^{-1}a_1 + Z^{-2}a_2 + \cdots Z^{-(N_a-2)}a_{N_a-2} + Z^{-(N_a-1)}a_{N_a-1} + Z^{-N_a}a_{N_a}} \tag{1}$$

Using the structure of Figure 1 can cause numerical problems. In practice filters are often implemented as a cascade of second order sections which gives improved numerical accuracy. In order for the filter to be stable the poles of Equation 1 (zeros of the denominator) must lie inside the unit circle on the Z-plane.

2.2 Realisation of TLM boundary

The digital filter as described above has a single input and a single output. A boundary in TLM is defined by reflection and transmission in two directions and each with two polarisations. For each boundary element, four filters must be used for transmission and four for reflection. Often the number of filters can be reduced: e.g. to model ferrite tiles [7], used as radio absorptive material against a metal backing, only the reflection coefficients for one direction and two polarisations are required.

3 The Wiener-Hopf algorithm applied to recursive design

Here the design of a least-mean-squares 'best-fit' filter using measurement or simulation data is described. The method is based on a novel application of the Wiener-Hopf equation for signal estimators as described in [8, pp250-264]. The same method is also described by Levy [9] and used in the Matlab 'Signal processing toolbox' [10] routines 'invfreqz' and 'invfreqs'.

If we rewrite Equation 1 as:

$$H(Z) = \frac{B(Z)}{1 + A(Z)} \tag{2}$$

and assume we wish to choose the coefficients of $A(Z)$ and $B(Z)$ so that $H(Z)$ is the best fit to the function $G(Z)$. The error in the fit, in the frequency domain is given by:

$$\epsilon'(j\omega) = S(j\omega) \left\{ \frac{B(j\omega)}{1 + A(j\omega)} - G(j\omega) \right\} \tag{3}$$

where $\epsilon'(j\omega)$ is the error, $G(j\omega)$ is the desired frequency response and $H(j\omega)$ is the frequency response of the filter calculated by substituting $Z = exp(j\omega T_s)$ in $H(Z)$. $S(j\omega)$ is a weighting function which can be chosen to make the problem more sensitive to errors at particular frequencies.

In principle the mean squared error $\overline{|\epsilon|^2}$ can be calculated and minimised over the desired frequency range. However H has very non-linear dependence on the coefficients of A and is difficult to minimise. Widrow and Stearns [8, pp250-264] suggest an alternative formulation which overcomes this problem. If we multiply both sides of Equation 3 by $(1 + A(j\omega))$ we get:

$$\epsilon(j\omega) = (1 + A(j\omega))\epsilon'(j\omega) = -S(j\omega)G(j\omega) - S(j\omega)G(j\omega)A(j\omega) + S(j\omega)B(j\omega) \tag{4}$$

The new error ϵ is dependent upon A but minimising $\overline{|\epsilon|^2}$ also minimises $\overline{|\epsilon'|^2}$.

If we make $[\epsilon]$ a column vector of K samples of the error at discrete frequencies ω_k, Equation 4 can be written as:

$$[\epsilon] = [D] - [X][W] \tag{5}$$

where $[D]$ is the vector containing the product $-s_k g_k$:

$$[D] = [-s_1 g_1, -s_2 g_2, \cdots, -s_K g_K]^T \tag{6}$$

$[X]$ is the matrix combining the products $s_k g_k e^{-n_a j \omega_k T_s}$, $n_a = 1, \ldots N_a$ and $-s_k e^{-n_b j \omega_k T_s}$, $n_b = 0, \ldots N_b$ which multiply the coefficients a_{n_a} and b_{n_b} of the filter:

$$[X] = \begin{bmatrix} s_1 g_1 e^{-j\omega_1 T_s} & s_1 g_1 e^{-2j\omega_1 T_s} & \cdots & s_1 g_1 e^{-N_a j\omega_1 T_s} & -s_1 & -s_1 e^{-j\omega_1 T_s} \cdots & -s_1 e^{-N_b j\omega_1 T_s} \\ s_2 g_2 e^{-j\omega_2 T_s} & s_2 g_2 e^{-2j\omega_2 T_s} & \cdots & s_2 g_2 e^{-N_a j\omega_2 T_s} & -s_2 & -s_2 e^{-j\omega_2 T_s} \cdots & -s_2 e^{-N_b j\omega_2 T_s} \\ s_3 g_3 e^{-j\omega_3 T_s} & s_3 g_3 e^{-2j\omega_3 T_s} & \cdots & s_3 g_3 e^{-N_a j\omega_3 T_s} & -s_3 & -s_3 e^{-j\omega_3 T_s} \cdots & -s_3 e^{-N_b j\omega_3 T_s} \\ \vdots & \ddots & & & & & \vdots \\ s_K g_K e^{-j\omega_K T_s} & s_K g_K e^{-2j\omega_K T_s} & \cdots & s_K g_K e^{-N_a j\omega_K T_s} & -s_K & -s_K e^{-j\omega_K T_s} \cdots & -s_K e^{-N_b j\omega_K T_s} \end{bmatrix} \tag{7}$$

$[W]$ is the vector containing the (unknown) filter coefficients a_{n_a} and b_{n_b}:

$$[W] = [a_1, a_2, \cdots, a_{N_a}, b_0, b_1, \cdots, b_{N_b}]^T \tag{8}$$

If $\Re(x)$ denotes the real part of x, $[Q]^T$ is the transpose of $[Q]$ and $[Q]^*$ is the conjugate transpose of $[Q]$, the mean squared error is:

$$\overline{|\epsilon|^2} = \frac{1}{K} \Re \left\{ [\epsilon]^* [\epsilon] \right\} = \frac{1}{K} \Re \left\{ [D]^* [D] + [W]^T [X]^* [X][W] - 2[D][X]^*[W] \right\} \tag{9}$$

If we let $[R] = \Re \left\{ [X]^*[X] \right\}$ and $P = \Re \left\{ [X]^*[D] \right\}$ then

$$\overline{|\epsilon|^2} = \frac{1}{K} \left\{ [D]^*[D] + [W]^T [R][W] - 2[P]^T[W] \right\} \tag{10}$$

In order to determine the minimum mean squared error we can differentiate Equation 10 with respect to the coefficient vector, $[W]$, and equate to zero:

$$\frac{\partial \overline{|\epsilon|^2}}{\partial [W]} = \frac{1}{K} \left\{ 2[R][W] - 2[P] \right\} = 0 \tag{11}$$

This is a system of linear equations which can be solved by matrix inversion to give the filter coefficients:

$$[W] = [R]^{-1}[P] \tag{12}$$

Thus it is possible to design a filter to give a least-mean-squares fit to measured or computed data for a thin layer.

This technique has two potential problems:

1. The filter design is not necessarily stable.

2. The required filter order is also unknown.

The next section shows results of using the method to design filters to match reflection and transmission coefficients.

4 Results

4.1 Perforated screen

Here the transmission coefficient of a perforated screen was simulated using a fine grid TLM model (0.1 mm) and the resulting frequency domain data used to design a transmission filter for use as a boundary in a larger mesh (10 cm). A set of 50 data points were used to represent the frequency domain data (ie. $K = 50$). Filters of increasing order were designed and the mean squared error for a range is tabulated in Table 1 below.

Poles	Zeros	Mean squared error	Note
2	2	0.00049888	
8	4	0.00024546	
9	9	0.00016312	
10	10	0.00011883	Unstable

Table 1: Mean squared error for a range of 'perforated screen' filter designs

The weighting function $S = 1/|G|$ was used so that the relative error tended to be the same at all frequency points. Filters of order 10 and above were unstable and therefore not used.
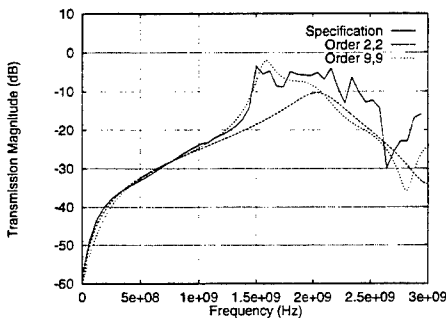
Figure 2: Frequency response of transmission through a perforated screen (Specification) and filter designs of order 2 and 9.
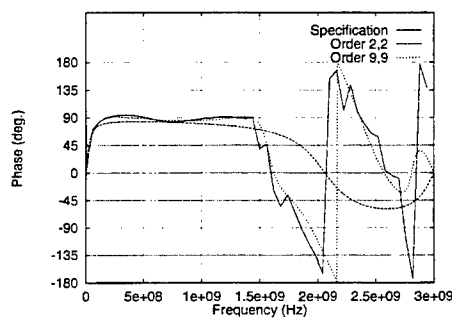
Figure 3: Phase response of transmission through a perforated screen (Specification) and filter designs of order 2 and 9.

Figures 2 and 3 show the magnitude and phase response of the filters of order 2 and 9 with the original specified response. Figures 4 and 5 show the error in magnitude and phase response of the filters as a function of frequency. The frequency range extends to half the sampling frequency of the 10 cm mesh, however results from TLM would normally only be used for one tenth of this range. It can be seen that both filters have better accuracy in the low frequency range, this is probably due to the difficulty of controlling the frequency response near the upper limit in digital filters.
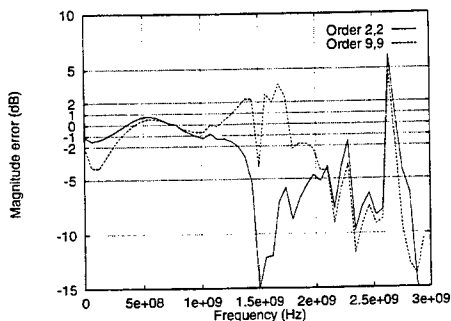
Figure 4: Magnitude error for 'perforated screen' filter designs of order 2 and 9.
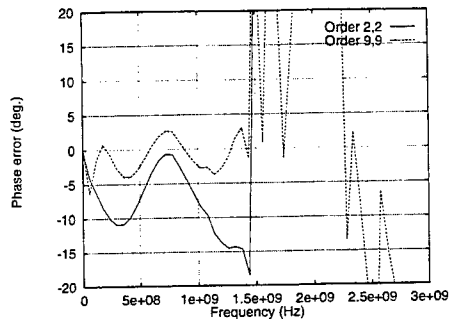
Figure 5: Phase error for 'perforated screen' filter designs of order 2 and 9.

4.2 Ferrite tile

The reflection coefficient of a ferrite tile was computed with TLM using a 1.05 mm grid using the technique in [11]. The Wiener-Hopf design technique was then used to compute the filter design suitable for use in a TLM model with 10 cm grid. This was also compared with the 2nd order approximation described in [12]. A set of 200 data points were used to represent the frequency domain data (ie. $K = 200$). Filters of order 3 or less produced unsatisfactory results. The first design to produce an acceptable approximation to the desired frequency response was of order 4. It was however unstable. The filter was stabilised by removing the unstable pole and nearby zero, or alternatively by simply moving the unstable pole inside the unit circle such that its effect on the magnitude response was unchanged. The mean squared error for a number of designs is shown below in Table 2 below. Filters 1–3 have $S = 1/|G|$ however it was noticed that the zero

No.	Poles	Zeros	Mean squared error	Note
1	4	4	0.00024291	Unstable $S = 1/G$
2	3	3	0.0023514	By removing pole and zero outside unit circle from 1
3	3	3	0.013959	By stabilising polynomial of 1
4	4	4	0.00030563	Unstable (changed S)
5	3	3	0.0024013	By removing pole and zero outside unit circle from 4

Table 2: Mean squared error for a range of 'ferrite tile' filter designs

frequency gain of the filter had a large error. For filters 4 and 5 the zero frequency weighting was increased by a factor of 10 which reduced the zero frequency error for a small increase in overall error (comparing filter 5 with filter 2). This demonstrated the importance of the weighting function in controlling the overall error.

Figures 6 and 7 show the frequency and phase response of the two 3rd order filters compared with the specified frequency response and the result of the 2nd order approximation of [12]. The responses of the two 3rd order filters are almost indistinguishable at this resolution. It can be seen that the Wiener-Hopf design is slightly more accurate than the 2nd order approximation at higher

frequencies. However phase information is required for the Wiener-Hopf design which must be measured or determined by simulation whilst the 2nd order approximation can be computed from the magnitude of the tile's reflection coefficient only.
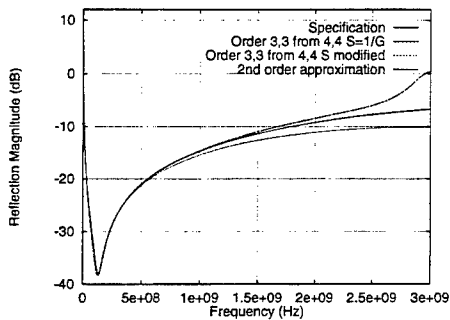
Figure 6: Frequency response of reflection from a ferrite tile absorber (Specification) and filter designs of order 2 and 3.
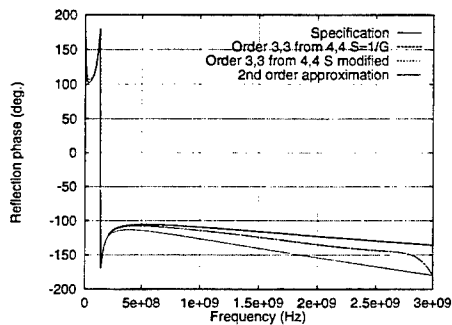
Figure 7: Phase response of reflection from a ferrite tile absorber (Specification) and filter designs of order 2 and 3.

Figures 8 and 9 show the error in the magnitude and phase response of the 3rd-order filters as a function of frequency.
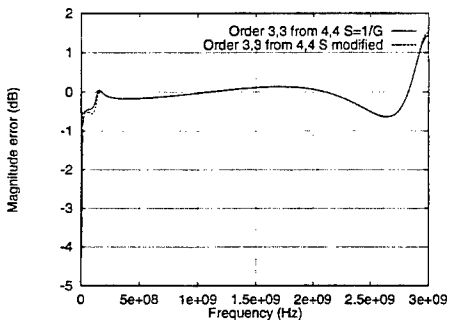
Figure 8: Magnitude error for the 'ferrite tile' filter designs of order 3.
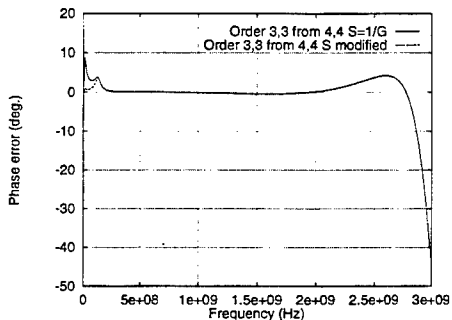
Figure 9: Phase error for the 'ferrite tile' filter designs of order 3.

5   Conclusions

The Wiener-Hopf algorithm allows frequency dependent boundary conditions to be designed from measured or computed frequency response (phase and magnitude). However the order of the filter must be determined experimentally and sometimes manual interaction is required to stabilise the filter.

The algorithm will find application in the modelling of thin lossy layers, such as composite materials, where the transmission and reflection coefficients can be measured or computed in the frequency domain.

Acknowledgments

References

[1] A. Mallik and C. P. Loller. The modelling of EM leakage into advanced composite enclosures using the TLM technique. *International Journal of Numerical Modelling, Electronic Networks, Devices and Fields*, 2(4):241–248, 1989.

[2] D.P. Johns, J. Wlodarczyk, and A. Mallik. New TLM models for thin structures. In *IEE Proc. International Conference on Computation in Electromagnetics*, pages 335–338, 1991.

[3] V. Trenkic, A. P. Duffy, T. M. Benson, and C. Christopoulos. Numerical simulation of penetration and coupling using the TLM method. In *EMC'94 Roma*, pages 321–326, 13–16 September 1994.

[4] Ch. Fuchs and A. J. Schwab. Efficient computation of 3D shielding enclosures in time domain with TLM. In *COST 243 Workshop, Numerical Methods and their Applications, Hamburg*, June 1995.

[5] J. A. Cole, J. F. Dawson, and S. J. Porter. Efficient modelling of thin conducting sheets within the TLM method. In *IEE 3rd Int. Conference on Computation in Electromagnetics*, Bath, 10–12 April 1996.

[6] J.G. Maloney and G.S. Smith. A comparison of methods for modelling electrically thin dielectric and conducting sheets in the finite-difference time-domain (FDTD) method. *IEEE Transactions on Antennas and Propagation*, pages 690–694, 1993.

[7] J.F. Dawson. Representing ferrite absorbing tiles as frequency dependent boundaries in TLM. *Electronics Letters*, 29(9):791–792, 1993.

[8] B Widrow and S. D. Stearns. *Adaptive signal processing*. Prentice-Hall, 1985. ISBN 0-13-004029-01.

[9] E. C. Levy. Complex curve fitting. *IRE Trans. on Automatic Control*, AC-4:37–44, 1959.

[10] T. P. Krauss, L. Shure, and J. N. Little. *Signal processing toolbox for use with Matlab*. The Mathworks Inc., 1994.

[11] J.F. Dawson. Improved magnetic loss for TLM. *Electronics Letters*, 29(5):467–468, 1993.

[12] J.F. Dawson, J. Ahmadi, and A. C. Marvin. Modelling the damping of screened room resonances by ferrite tiles using frequency dependent boundaries in TLM. In *IEE 2nd Int. Conf. on Computation in Electromagnetics*, pages 271–274, 1994.

HYBRID TECHNIQUES
FOR LARGE
BODY PROBLEMS

Chairs: D. Pflug and R. Burkholder

Hybrid MoM/SBR Method to Compute Scattering from a Slot Array Antenna in a Complex Geometry

Andrew D. Greenwood
Rome Laboratory and University of Illinois
Center for Computational Electromagnetics
Urbana, Illinois 61801

Jianming Jin
University of Illinois
Center for Computational Electromagnetics
Urbana, Illinois 61801

1 Introduction

The presence of a slotted waveguide array antenna on a radar target may have a significant contribution to the overall radar cross-section (RCS) of the target. Therefore, the computation of the RCS should include the scattering from the slot array. Recently, a method of moments (MoM) procedure has been introduced to compute the scattering from a cylindrically conformal slotted-waveguide array antenna [1, 2]. However, this procedure does not take into account the geometry in which the slot array is located. If the slot array is located in a complex, three dimensional (3-D) geometry, the MoM cannot efficiently account for the effect of the geometry. A more efficient method to compute the scattering from a large, 3-D body is the high frequency shooting and bouncing ray (SBR) method. However, this method cannot accurately account for the slots, each of which is typically smaller than an electromagnetic wavelength in size. In this paper, the MoM computation of the scattering from a slot array is hybridized with the SBR method to compute the electromagnetic scattering from a large, 3-D target which includes a slot array antenna.

The basis of the hybrid method is the field equivalence principle, which allows the scattering geometry to be decomposed into separate regions. The MoM is applied to the slotted waveguides, while the SBR method is applied to the region outside the waveguides, which includes the complex, 3-D target. By using the hybrid method, the scattering from a large, 3-D target, which includes a slotted-waveguide array antenna, can be efficiently and accurately computed.

The remainder of this paper is divided into five sections. Section 2 describes the formulation of the problem, including the use of the MoM, the use of the SBR method, and techniques to decouple the computations of the two methods. Section 3 describes briefly how the method has been tested, and Section 4 gives some numerical results which show the capability of the method. The results in Section 4 also demonstrate the need to include the slot array in scattering computations. Finally, Section 5 gives a brief conclusion.

2 Formulation

Consider the example target shown in Figure 1a. The target is complex and 3-D, and it includes a slotted waveguide array antenna on its surface. The slotted waveguide array antenna may be planar, or it may conform to the surface of a cylinder. The first step to compute the scattering from this target is to analyze the slotted waveguides using the MoM. Then, the scattering from the target with the slot

(a) Large target   (b) Local slot geometry
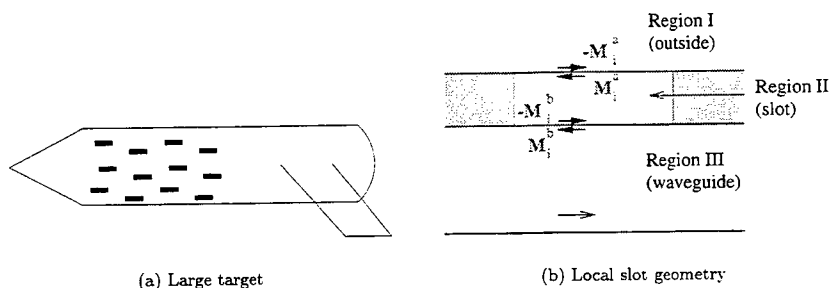
Figure 1: Example of a complex, 3-D target with a slot array antenna and the local slot geometry.

apertures covered by perfect electric conductor (PEC) is computed using the SBR method. During the SBR calculation, the incident field on the slot array antenna is computed and stored. This incident field is combined with the MoM analysis to find an equivalent magnetic current on the outer aperture of each slot. Finally, the radiation of these equivalent magnetic currents in the presence of the complex, 3-D target is computed using the reciprocity theorem. This result is added to the previously computed SBR scattering result.

2.1 Use of MoM

The first step in the formulation of the problem is to analyze the slotted waveguides using the MoM. There are two main steps in the application of the MoM. First, the problem must be described in terms of an integral equation. Then, the integral equation is discretized to find a numerical solution. The steps are outlined here, and more detail is given in [1,2].

To derive the integral equation, the apertures of each slot are first covered with PEC, and equivalent magnetic currents over each aperture are introduced. Figure 1b depicts the situation for the ith slot. The region outside of the antenna is denoted Region I, the region inside the slot is Region II, and the region outside of the slot but inside the waveguide is Region III. An equivalent magnetic current M_i^a is introduced on the inside of the outer slot aperture (between Regions I and II), and the equivalent current M_i^b is introduced on the waveguide side of the inner aperture (between Regions II and III). Because the electric field must be continuous across each aperture, $-M_i^a$ must be introduced on the outside of the outer aperture, and $-M_i^b$ must be introduced on the slot side of the inner aperture. Note that when the analysis is complete, $-M_i^a$ are the currents that radiate in the presence of the complex, 3-D body as discussed above.

To derive the integral equation, the continuity of the tangential magnetic field across each aperture is enforced. Denoting the tangential magnetic field in Region III on the ith slot aperture due to the magnetic current on the jth aperture as $\mathbf{H}_{\tau i}^{III}(M_j^b)$, the following must hold on each inner aperture:

$$\sum_j \mathbf{H}_{\tau i}^{III}(M_j^b) + \mathbf{H}_{\tau i}^{II}(M_i^b) - \mathbf{H}_{\tau i}^{II}(M_i^a) = 0. \tag{1}$$

Further, denoting the tangential incident field on the ith slot aperture as $\mathbf{H}_{\tau i}^{SBR}$,

$$\sum_j \mathbf{H}_{\tau i}^{I}(M_j^a) + \mathbf{H}_{\tau i}^{II}(M_i^a) - \mathbf{H}_{\tau i}^{II}(M_i^b) = \mathbf{H}_{\tau i}^{SBR} \tag{2}$$

697

must hold on each outer slot aperture. Note that the incident fields are calculated using the SBR method, and the magnetic field due to a magnetic current is found from

$$\mathbf{H}^{\alpha}(\mathbf{M}) = \iint_{S} \overline{\overline{G}}^{\alpha}(\mathbf{r}, \mathbf{r}') \cdot \mathbf{M}(\mathbf{r}') dS' \tag{3}$$

where α is I, II, or III, depending on the region of interest, $\overline{\overline{G}}^{\alpha}(\mathbf{r}, \mathbf{r}')$ is the magnetic source-magnetic field dyadic Green's function in the appropriate region, and $\mathbf{r}$ corresponds to the point at which the magnetic field is to be evaluated. Combining Equations 1, 2, and 3 gives an integral equation for the magnetic currents.

The second main step in application of the MoM is to discretize the integral equation to find a numerical solution for the currents. To accomplish this step, the currents are expanded in terms of sinusoidal basis functions. Defining $\hat{\xi}$ to be the direction parallel to the lengths of the slots and using a local coordinate system in which $\xi_j = 0$ at one end of the jth slot, the current on the jth slot aperture is expanded as

$$\mathbf{M}_j^{\beta} = \hat{\xi} \sum_{q=1}^{N} V_{qj}^{\beta} \sin\left(\frac{q\pi}{L_j} \xi_j\right) \tag{4}$$

where N is the number of terms in the expansion, and β represents a for the current on the outer aperture or b for the current on the inner aperture. Equation 4 is valid for points on the jth slot aperture: for points outside of the aperture, the expansion is defined to be zero. Assuming the width of a slot is much less than its length, the $\hat{\xi}$ component of the current is the only component of interest.

Substituting the expansion given in Equation 4 into the integral equation allows the integral equation to be converted to a matrix equation which can be solved numerically. For the more details about solving the integral equation, the reader is referred to [1, 2]. However, one important step that should be mentioned here is the derivation of the dyadic Green's functions for the various regions. The Green's functions given in [1, 2] for Regions II and III are applicable to the present problem. For Region I, the dyadic Green's function can be written as

$$\overline{\overline{G}}^{I}(\mathbf{r}, \mathbf{r}') = \overline{\overline{G}}^{cyl}(\mathbf{r}, \mathbf{r}') + \overline{\overline{G}}^{diff}(\mathbf{r}, \mathbf{r}'). \tag{5}$$

The Green's function given in [1, 2] for the exterior region corresponds to $\overline{\overline{G}}^{cyl}(\mathbf{r}, \mathbf{r}')$, and $\overline{\overline{G}}^{diff}(\mathbf{r}, \mathbf{r}')$ is a perturbation term due to diffraction and reflection by the complex target in which the slot array is embedded. Neglecting $\overline{\overline{G}}^{diff}(\mathbf{r}, \mathbf{r}')$ neglects fields which are scattered by the slots, diffracted or reflected by the large body back to the slots, and scattered by the slots again [3]. These fields are usually an insignificant part of the scattering, and this term is neglected in the computations. Thus, the Green's function given in [1, 2] for Region I is used for the present problem.

2.2   Use of SBR

As previously mentioned, the MoM is used to analyze the slot array antenna while the SBR method is used for the remainder of the problem. Thus, there are three main tasks to be accomplished by the SBR method: to compute the scattering from the complex, 3-D target, to compute the incident magnetic fields on the slot apertures, and to compute the radiation of the equivalent currents on the slot apertures in the presence of the complex, 3-D target. In all of these cases, the slot apertures are covered with PEC.

In the SBR method, a dense grid of rays, corresponding to a plane wave, is launched toward the target, and each ray is traced as it bounces around the target. The bounces are governed by Geometrical

Optics (GO), and as each ray leaves the target, its contribution to the scattering is computed by a Physical Optics (PO) integration. If more accuracy is desired, the first order edge diffracted terms are computed using the Geometrical Theory of Diffraction (GTD) and added to the result [3–6]. For the present problem, this SBR procedure is followed to compute the scattering from the complex, 3-D target with the slot apertures closed by PEC. The SBR procedure is implemented using the XPATCH software package [4,5].

The incident magnetic field on the slot apertures is computed using SBR at the same time the scattering from the complex, 3-D target is computed. While tracing the rays to find the scattering, some rays will hit on or near a slot aperture. The field contributions from each of these rays are combined with appropriate phase shifts to find the incident magnetic field on each slot aperture. The incident magnetic fields on the slot apertures are used by the MoM to compute the equivalent magnetic currents on the apertures.

The remaining step in the problem is to compute the radiation of the magnetic currents in the presence of the large body. The SBR method together with the reciprocity theorem is employed for this task [3,6]. Consider an infinitesimal dipole placed at the scattering observation point. If the target containing the slot array is in the far field of the dipole, the dipole launches a plane wave toward this target. Recall that for the SBR method, the grid of rays launched toward the target corresponds to a plane wave. Note also that the reciprocity theorem states

$$\iiint_V \mathbf{E}^{Slot} \cdot \mathbf{J} dV = \iint_S \mathbf{H}_\tau^{SBR} \cdot \mathbf{M}^a \tag{6}$$

where $\mathbf{H}_\tau^{SBR}$ is the incident field on the slot apertures due to the dipole at the scattering observation point, $\mathbf{M}^a$ is the current on the outer slot apertures, which is found using the MoM. $\mathbf{E}^{Slot}$ is the radiation due to $-\mathbf{M}^a$, and $\mathbf{J}$ is the dipole current. Thus, if the dipole current ($\mathbf{J}$) is appropriately chosen and monostatic scattering is being computed, all components to find $\mathbf{E}^{Slot}$ using reciprocity are computed already. If bistatic scattering results are desired, $\mathbf{H}_\tau^{SBR}$ resulting from a dipole at the scattering observation point must be computed first, then $\mathbf{E}^{Slot}$ can be computed.

2.3 Decoupling the MoM from the SBR Method

As they are presented in Section 2.1, the MoM computations are coupled to the SBR method computations. This is due to the fact that the incident magnetic field on the slot apertures, which is computed using the SBR method, is required for the MoM computations. To avoid having to repeat the MoM computations in order to analyze the scattering from many different incidence angles, it is desirable to decouple the computations of the two methods. There are two ways of doing this. The first method preserves the coupling interactions between different slots; the second involves an approximation which neglects the coupling between different slots to achieve lower computational complexity.

To decouple the MoM computations from the SBR computations while preserving the coupling between the various slots, the incident magnetic field on the slot apertures can be expanded in terms of basis functions. Assuming that the width of a slot is much less than its length, the component of the incident magnetic field along the length of a slot is the only component of interest. A convenient basis set is the set of pulse basis functions, where the ith basis function is defined to be one on the ith slot aperture and zero elsewhere. There will be n basis functions in the set, where n is the number of slots in the array. The magnetic currents on each slot aperture are then computed with the incident field on the slot array set equal to each of the n basis functions in turn. A matrix-vector multiply is then carried out during the SBR computations. This matrix-vector multiply converts the incident magnetic fields on the slot apertures to the equivalent currents on the apertures.
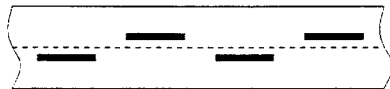
Figure 2: Configuration of the slots on the surface of a waveguide.

The second method of decoupling the MoM computations from the SBR computations neglects the coupling between the individual slots. One slot on the slot array is chosen, and it is assumed that this slot is the only slot present. The MoM computation is carried out with a magnetic field of unit amplitude on this slot, and the result is a magnetic current for the slot. It is then assumed that all of the slots in the array are equivalent; the magnetic current on each slot is set equal to the magnetic field on that slot times the single magnetic current which is computed by the MoM. This approximation reduces the computational complexity and the sizes of data files. However, it does not produce accurate results when the frequency is near the working frequency of the slot array. This is demonstrated in Section 4.

3 Testing

Before using any new numerical technique, the technique should be tested against existing techniques to ensure its validity. The validity of the MoM computation involving the coupling between the different slots in the array is validated by comparison with previous MoM and finite element method (FEM) techniques [2,7]. The SBR method is also validated through extensive, previous testing [4,5]. The hybrid technique is validated by comparison with a previous hybrid method to compute the scattering from complex targets with cracks and cavities on their surfaces [3]. This is accomplished by considering a waveguide with a single slot on its surface. The slotted waveguide is placed an a large plate, and the problem is modeled both with the hybrid MoM/SBR method discussed in this paper and with the hybrid FEM/SBR method presented in [3]. The two solutions show good agreement.

4 Numerical Examples

To show the validity and utility of the proposed technique. several numerical results are presented. For all of the numerical examples, the slot array contains 16 waveguides with 16 slots on each waveguide, and the array is designed to radiate at 9.1 GHz. In addition. the following parameters apply to all of the examples presented: the upper waveguide wall in which the slots are cut is 0.08 cm thick, the waveguides are separated by walls 0.1cm thick, each slot is 1.6 cm long and 0.16 cm wide, and the slots are positioned on the waveguide surface as shown in Figure 2, where the offset of each slot from the center of the waveguide is 0.15 cm. Unless otherwise noted, the coupling between individual slots in the array is included in the results.

The first example is a planar slot array which is in a simple ground plane geometry. The waveguides are 2.230 cm wide by 1.016 cm high, the slot centers are 2.444 cm apart, and the first and last slots centers are 1.222 cm from the ends of the waveguides. Thus, the entire slot array and the ground plate are 37.3 cm wide by 39.1 cm long. In Figure 3, the radar cross-section (RCS) of the plate with the slots is superimposed on the scattering from the plate alone. The scattering frequency is 9.1 GHz, which is the working frequency of the slot array. Figure 3 shows results in both the H-plane and the E-plane and for waveguides which are terminated both with matched loads and with short circuits. For some incidence angles, the slot array has a dominant effect on the scattering.

(a) *H*-plane, matched waveguide loads

(b) *E*-plane, matched waveguide loads

(c) *H*-plane, short-circuit waveguide loads

(d) *E*-plane, short-circuit waveguide loads
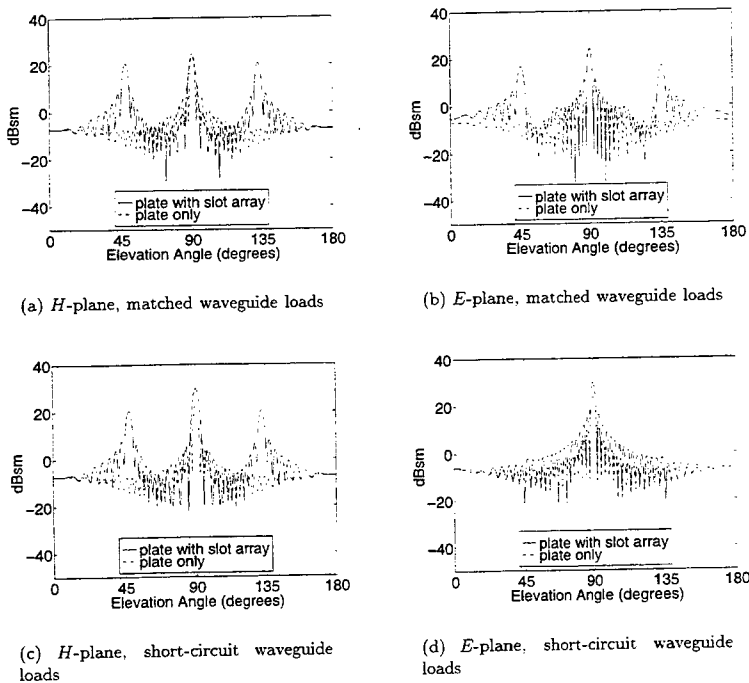
Figure 3: RCS of a planar slot array on a ground plate at 9.1 GHz, the working frequency of the slot array.

The second example is a slot array on a cylinder with a nose cone. The radius of the cylinder is 16.096 cm, and the length without the nose cone is 100 cm. The nose cone is 30 cm long. The waveguide cross-sections are sectoral in shape and are 1.016 cm thick. Along the slotted surface, the waveguides are 2.230 cm wide. The slots are 2.573 cm apart, and the first and last slots are 1.287 cm from the ends of the waveguides. The entire slot array is 37.3 cm along the circumference of the cylinder and 41.2 cm along the axis of the cylinder. In Figure 4, the *H*-plane RCS of the cylinder alone and the RCS of the cylinder with the slot array are compared. Again, the scattering frequency is 9.1 GHz, the working frequency of the slot array, and again, there are scattering directions for which the slot array dominates the return.

The next example is intended to show the effect of the uncoupled slot approximation which was discussed in Section 2.3. Figure 5 shows the RCS of the same geometry considered in the second example, but as a function of frequency. The incident direction is 40° in the *H*-plane. The RCS computed considering the coupling between individual slots is plotted with the RCS computed by neglecting the slot coupling. The approximation neglecting slot coupling is reasonably accurate away from the working frequency of the slot array antenna, but there is significant error near the working frequency. Thus, this approximation must be applied with care.

(a) Matched waveguide loads   (b) Short-circuit waveguide loads
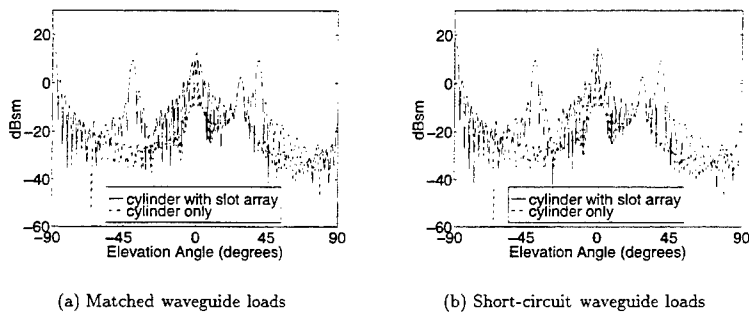
Figure 4: RCS of a conformal slot array on a cylinder with a nose cone at 9.1 GHz, the working frequency of the slot array.

(a) Matched waveguide loads   (b) Short-circuit waveguide loads
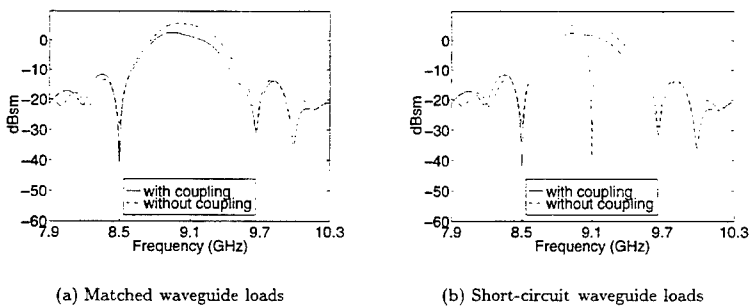
Figure 5: RCS of a conformal slot array on a cylinder with a nose cone. The scattering is computed with and without including the coupling between individual slots. Near the working frequency of the slot array (9.1 GHz), the slot coupling must be included.

The final example shows the usefulness of the method. The slot array antenna from the first example is mounted on the belly of an f309 aircraft, with the lengths of the slots perpendicular the the length of the aircraft body (see Figure 6a). Figure 6b shows the VV-polarized range profile of the airplane both with and without the slot array. The range profile is the time domain response to an incident sinc pulse. The sinc pulse in this example has a center frequency of 10 GHz and a bandwidth of 2 GHz, and the slot array has matched waveguide loads. The slot scattering dominates the range profile.

5   Conclusion

A hybrid MoM/SBR method is developed to compute the scattering from a complex, 3-D target with a slotted waveguide array antenna. Because the target is large and 3-D, the MoM alone cannot efficiently compute the scattering, and because the slots on the waveguides are small features, the SBR method alone is not accurate. The hybrid method combines the two individual methods in such a manner that
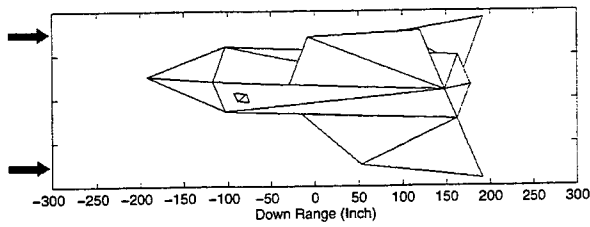
(a) f309 with slot array
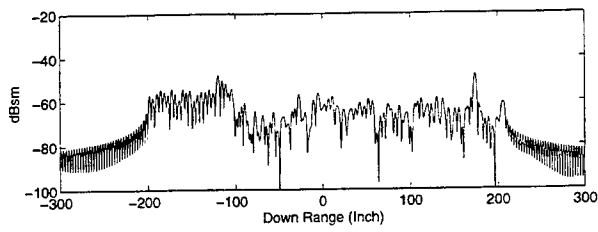
(b) Range profile without slot array.
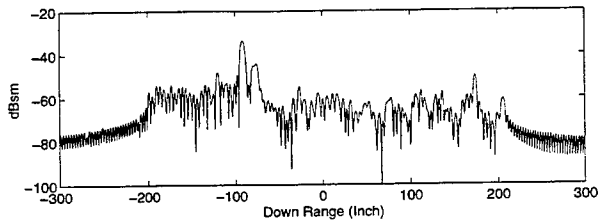
(c) Range profile with slot array.

Figure 6: Range profile of an f309, VV-polarization, 10 GHz center frequency, 2 GHz bandwidth. The slot array has matched waveguide loads.

the scattering can be efficiently and accurately computed. In the hybrid method, the MoM is used to model the details of the slot array, and the SBR method is used to model the electromagnetic interactions with the large, complex target. The method is validated by comparison to previously published methods. Numerical examples show the need to include a slot array model when computing the scattering from a complex target with a slotted waveguide array. The examples also illustrate the capability of the method.

References

[1] G. Fan and J. M. Jin, "Scattering from a cylindrically conformal slotted-waveguide array antenna," *IEEE Antennas and Propagation Society International Symposium Digest*, pp. 1394–1397, 1996.

[2] G. X. Fan and J. M. Jin, "Scattering from a cylindrically conformal slotted-waveguide array antenna," Submitted to *IEEE Trans. Antennas Propagat.*, 1996.

[3] J. M. Jin, S. S. Ni, and S. W. Lee, "Hybridization of SBR and FEM for scattering by large bodies with cracks and cavities," *IEEE Trans. Antennas Propagat.*, vol. 43, no. 10, pp. 1130–1139, Oct. 1995.

[4] S. W. Lee, D. J. Andersh, D. D. Reeves, S. K. Jeng, H. Ling, Y. Chu, D. P. Sullivan, and C. L. Yu, "User manual for xpatch," DEMACO, Inc., Champaign, IL, 1993.

[5] D.J. Andersh, M. Hazlett, S. W. Lee, D. D. Reeves, D. P. Sullivan, and Y. Chu, "Xpatch: A high-frequency electromagnetic-scattering prediction code and environment for complex three-dimensional objects," *IEEE Antennas Propagat. Mag.*, vol. 36, no. 1, pp. 65–69, Feb. 1994.

[6] A. D. Greenwood, S. S. Ni, J. M. Jin, and S. W. Lee, "Hybrid FEM/SBR method to compute the radiation pattern from a microstrip patch antenna in a complex geometry," *Microwave and Optical Technology Letters*, vol. 13, no. 2, pp. 84–87, Oct. 1996.

[7] J. Chen and J. M. Jin, "Electromagnetic scattering from slot antennas on waveguides with arbitrary terminations," *Microwave and Optical Technology Letters*, vol. 10, no. 5, pp. 286–291, Dec. 1995.

Use of Near-Field Predictions in the Hybrid Approach
J.L. Karty, J.M. Putman, J.M. Roedder
McDonnell Douglas Corporation
Mail Code S0642263
PO Box 516
St. Louis, MO 63166
and
C.L. Yu
Naval Air Warfare Center Weapons Division
Pt. Mugu, CA 93042

Abstract

Recent advances in applying the Galerkin form of the method of moments (MM) theory to arbitrary 3-D objects have resulted in the accurate prediction of radar cross section (RCS) from fighter-sized aircraft up to several hundred MHz. To increase the frequency coverage of the technique, hybrid formulations combining high frequency physical optics (PO) currents with the numerical algorithms have been implemented. This formulation is based on derivatives of the CARLOS-3D and CADDSCAT codes developed at McDonnell Douglas Aerospace (MDA). Various partitioning and decomposition strategies suggest that in order to maximize computational efficiency achievable with this hybrid formulation, physical optics is used on portions of the body with large radius-of-curvature, while MM is used to calculate the currents on more complex portions of the geometry.

Some components may be subject to near-field illumination from other portions of the body. These areas may be analyzed with a near-field version of CADDSCAT and the resulting currents used as input to CARLOS-3D to calculate RCS. This scheme is also applicable to the calculation of near-field scattering for far- or near-field incidence on the aircraft as might be useful for missile fuzing problems.

Demonstration of this hybrid technique is dependent on accurate calculation of CADDSCAT currents in the near-field. Enhancements to CADDSCAT allowing near-field prediction of monostatic or bistatic physical optics, edge diffraction, and multiple bounce effects are described and results compared to test data. Analytic issues are outlined for future investigations using these near-field results as input to the CARLOS-3D algorithms.

1. Introduction

The synergism of high and low frequency codes naturally led MDA to the development of hybrid approaches. In this paper, hybrid refers to the merger of method of moments (MM) and physical optics (PO) techniques. A hierarchy of hybridization effects have been identified. In the simplest scheme, the decomposition strategy that maximizes computational efficiency uses physical optics on the large radius-of-curvature portions of the body while MM is used to calculate the currents of other portions. This is suitable to a low level of interactions. No secondary illumination or multibounce is taken into account (section II). A second level hybridization is identified which takes into account interactions. Near field illumination of parts of the body becomes an important contributor (section III).

2. First Order Hybridization

An example of first order hybridization is the specialized gap/crack analysis of CADDSCAT. Detailed local analysis with MM is incorporated from the CARLOS code. This first level hybrid feature has been used to model surface details due to cracks and gaps arising from equipment access panels. Discontinuities from repair of damaged areas of the control surfaces on the F/A 18 and other aircraft can also be analyzed in this fashion. A workstation version of this basic type of hybridization combining the CADDSCAT and CARLOS codes has been tested and prototyped. Figure 1 shows application of this approach for a narrow gap embedded in an almond-shaped fixture. The high frequency contributions computed by CADDSCAT are combined with MM based CARLOS calculations. The CARLOS based approach is used for highly irregular gaps associated with aircraft access panels. An aircraft such as the F-15 or F/A 18 has well over a hundred of these.
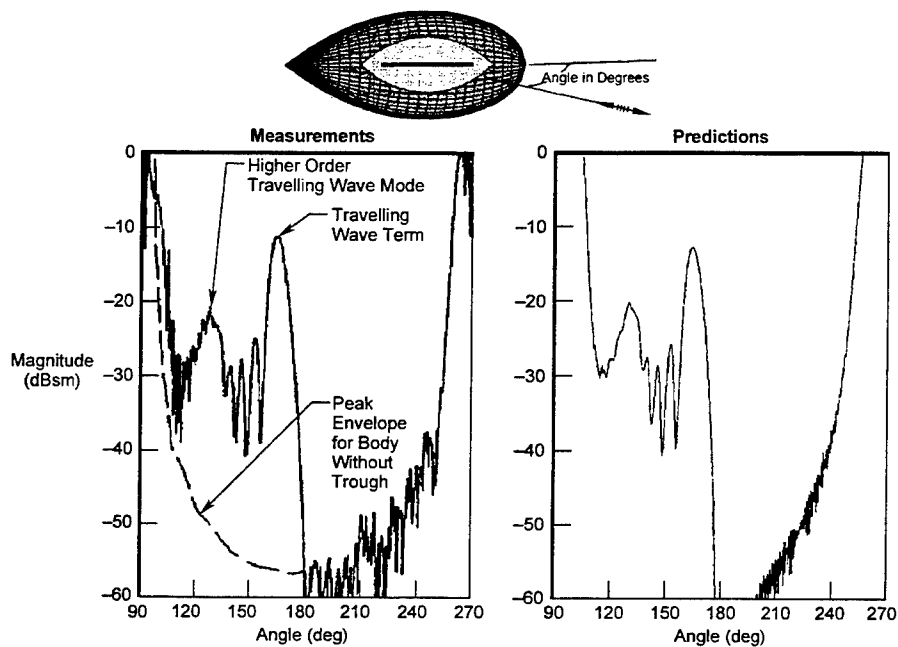
Figure 1. CADDSCAT/CARLOS RCS Predictions and Measurements for an Almond With Rectangular Trough at 12 GHz (.20 Wavelength Wide, .85 Wavelength Deep) – Type I Hybrid

3. Second Order Hybridization

This formulation is appropriate when the interactions between the asymptotic and non-asymptotic regions such as nearby apertures or radiating structures are strongly coupled. Fields computed from the asymptotic region modify the effective source for the MM region (i.e., right hand side of the MM system of equations). A case where this 3D hybrid MM/PO solution technique is demonstrated is shown in Figure 2. A multi-level unknown ordering scheme is used to specify the MM and PO regions of a surface. The MM currents are computed using roof top expansion representation of the currents. Figure 2 shows the vertical polarization results for a curved kite shaped fixture which is approximately 5 wavelengths long. In the hybrid MM/PO solution, the PO currents span the curved top with the MM currents spanning the top edges and the flat bottom. The hybrid method uses two-thirds as many unknowns as the full MM solution but is still capable of predicting the traveling wave return which a PO based formulation alone cannot.
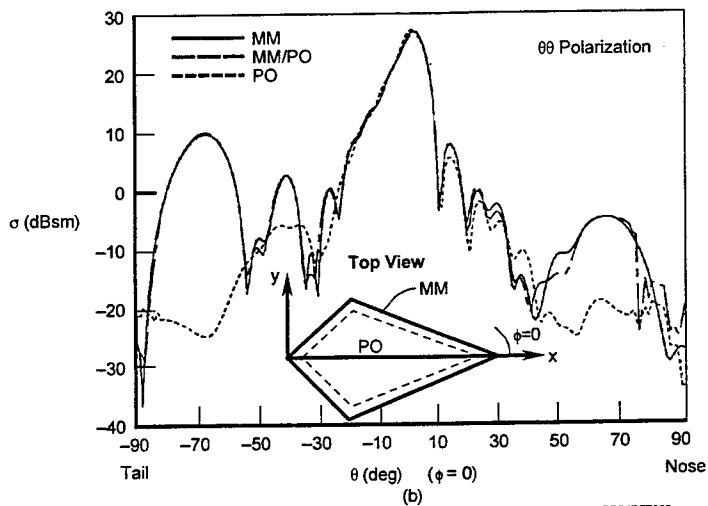
**Figure 2. Monostatic Scattering of a 3-D Kite. The Bottom of the Kite Lies in the xy Plane.
Nose and Tail Illuminations are at θ=±90°, as Indicated in the Figure.
The Angular Cut Is in the xy Plane Over the Top of the Body**

Figure 3 considers a case where the gap of Figure 1 is in an area of secondary illumination on the F-15. In this case a representation for the currents taking secondary illumination into account is needed. These can be obtained from a near field calculation. This more accurately reflects the actual currents. If the near field illuminated surfaces still have a large radii of curvature, CADDSCAT can continue to be used to calculate the RCS. If there are complex surface gaps or cracks, then the secondarily illuminated incidence currents calculated on this portion of the body can be used as input to the CARLOS impedance matrix. In this sense, the accurate calculation of the CADDSCAT currents in the near field are needed as input to the CARLOS code as discussed next.
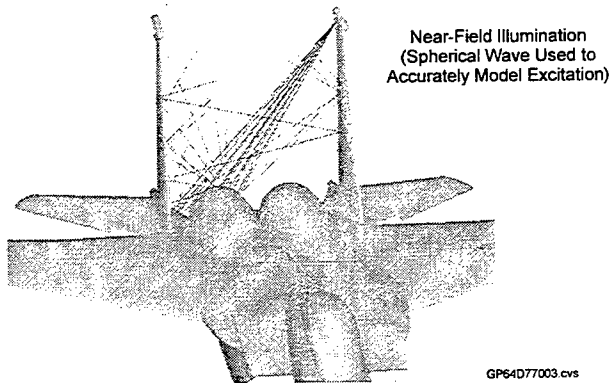
Figure 3. Schematic of Secondary Near-Field Illumination

4. Near Field Capability of CADDSCAT and Validations

In the near zone calculations with CADDSCAT, the spherical nature of the incident and scattered waves are taken into account. The implementation includes PO, Ufimtsev's physical theory of diffraction (PTD) for edges, multibounce effects, and provides both bistatic and monostatic RCS. RAM coatings are an option. Results of near field calculations in CADDSCAT follow. Figure 4 illustrates a bistatic case of a fixed illuminator in the far field and a moving receiver in the near field. Both PO and edge diffraction are necessary here in the CADDSCAT calculations to achieve excellent agreement with the CARLOS (MM) code.

GP64D77004.cvs
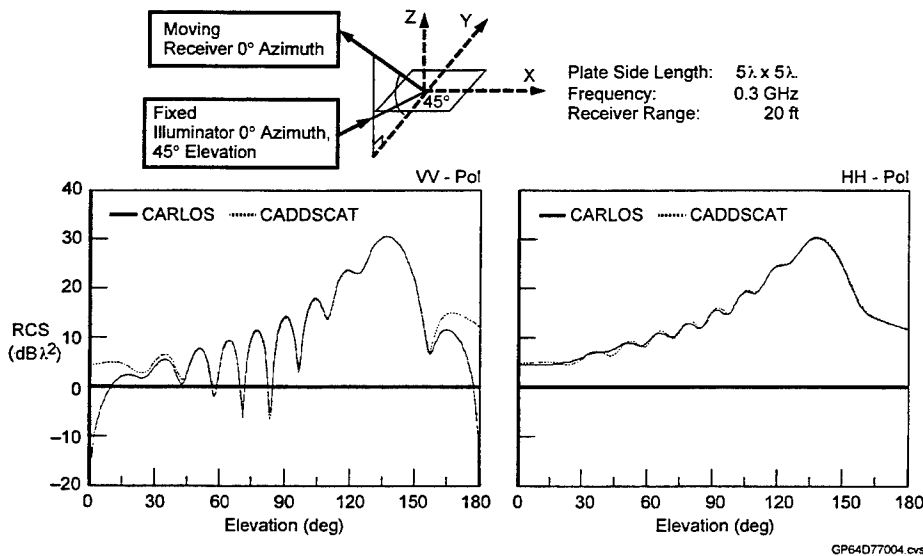
Figure 4. Bistatic RCS of 5λ Square Plate in the Near-Field: Elevation Sweep

Figure 5 summarizes the approach for CADDSCAT with a near field source and receiver for a generic multiple bounce geometry. There are three steps to the calculation of radar cross section from such a geometry. The first is the ray initiation. In far field plane wave incidence case, rays are uniformly spaced and sent out in a dense pack, all parallel to each other. In the near field case, the waves are modeled with spherical spreading, similar to the Generalized Ray Expansion pioneered by OSU for cavity analysis (Ref 1). In the next step, for the interim bounces the rays are tracked according to conventional Fresnel reflection for both metal and treated surfaces. Divergence effects of curved surfaces are accurately analyzed. Finally, for near field scattering, the Kirchhoff integral is evaluated with the generalized Green's function instead of the asymptotic form.

We have validated this three step process using test data (Ref 2). As can be seen for the dihedral geometry in Figure 6, there is very good correlation with test data. We have also run the CARLOS code for the same geometry. Note that the results for CARLOS and CADDSCAT are in excellent agreement. The slight discrepancy with test data is due to experimental uncertainties such as the exact dihedral angle. (This geometry is particularly sensitive to the dihedral angle.)

708

1. *Ray Initiation*
   Waves Modeled With Spherical
   Spreading as With Generalized Ray
   Expansion Without Far Field-Weighted
   Amplitude and Phase

2. *Interim Bouncing*
   Tracked According to Conventional
   Fresnel Reflections (Metal and Treated)

   Surface S'

3. *Near Field RCS Integral*
   Kirchhoff Integral Evaluated With
   General Green Function Instead
   of Asymptotic Form

$$G(\vec{r},\vec{r}') \rightarrow \frac{1}{4\pi} \frac{e^{jkr}}{r} e^{-j\vec{k}\cdot\vec{r}'}$$

$$\vec{E}_s(\vec{r}) \rightarrow \frac{e^{jkr}}{r} \vec{F}(\vec{k},\vec{k}_0)$$

GP64D77005.cvs

**Figure 5. CADDSCAT Near-Field Multiple Bounce Capability:
Near-Field Source/Near-Field Receiver Case**
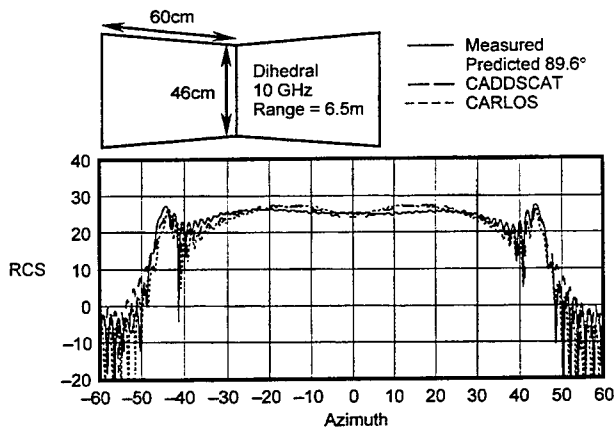
Test Data: "Near-Field to Far-Field Transformation of RCS Data,"
Mensa and Vaccaro, Nov 1995
GP64D77006.cvs

**Figure 6. Near-Field Analysis: Comparison of Test Data With CADDSCAT
and CARLOS Results**

We also tested far field data for asymptotic convergence of the near field integral. According to the $2d^2/\lambda$ criteria, a range of less than 158 ft is in the near field. Results (not shown) comparing the CADDSCAT far field calculation with the near field calculations at a range of 500 ft essentially overlay for both polarizations. Test data is also in excellent agreement with this solution.

A comparison of far-to-near field has also been made in Figure 7. The consequences of wavefront curvature are that the near field magnitude of the central lobe is depressed and specular peaks are broadened and depressed. Note that for agreement with this test data geometry, CADDSCAT's near field prediction of PO, edge diffraction and multiple bounce effects are all important. Clearly, the inclusion of near field incidence in secondarily illuminated parts of the body is a consideration in hybridization schemes.

Test Data: "Near-Field to Far-Field Transformation of RCS Data,"
Mensa and Vaccaro, Nov 1995
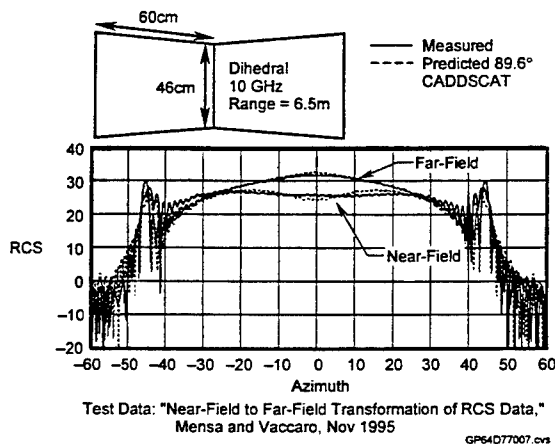
Figure 7. Validation of CADDSCAT Near-Field Multiple Bounce Capability

5. Synthesis of CADDSCAT Near Field Results for CARLOS Scattering Calculations

The hybrid formulation here is current based and builds upon a previous investigation (Ref. 3). In this earlier work, the optic-derived current used for hybridization was standard physical optics. The algorithm was developed with sufficient generality that the earlier formalism applies here as well. Here we synopsize the key operations of this formulation.

Using the notation of Ref. 3, the general governing equation known as the electric field integral equation (EFIE) for perfectly electrically conducting surfaces (PEC) is:

$$\left. \overline{E}^s \right|_{tan} = -\left. \overline{E}^i \right|_{tan} = -L\overline{J}$$

(1)

where

$$L\overline{J} = jk\eta \int_s \left(\overline{J} + \frac{1}{k^2} \nabla\nabla' \cdot \overline{J} \right) \Phi \, ds' \quad \text{and} \quad \Phi = \frac{e^{-jkr}}{4\pi R}$$

with R being the distance from the source to the field point, ∇ the surface gradient on the body with respect to the unprimed variables, $k = \frac{2\pi}{\lambda}$ and $\eta = \sqrt{\frac{\mu}{\epsilon}}$.

We have chosen the PEC case for clarity of discussion. The method easily extends to surfaces which are coated. For normal scattering problems, the incident field $\overline{E}^i$ is a known quantity with induced current $\overline{J}$ being the unknown. If we consider partitioning the domain into two regions we obtain formally:

$$L \, \overline{J}_{MM} = \left. \overline{E}^i \right|_{tan} - L\overline{J}_{PO}$$

(2)

In Ref. 3, the MM representation was used on all parts of the surfaces of a body for which no optic-derived asymptotic forms are available, such as most edges and surface details. The asymptotic region covers the remainder of the body. We now consider the $\bar{J}_{PO}$ of equation (2) to include portions of secondary illumination. This equation gets transformed into:

$$\mathcal{L}^{MM,MM} I_{MM} = \mathcal{E}^i - \mathcal{L}^{MM,PO} I_{PO} \tag{3}$$

with $\bar{J}_{MM}$ expanded into basis functions of coefficients I_{MM} and $\bar{J}_{PO}$ expanded with basis functions of coefficients I_{PO}. $\mathcal{L}^{MM,MM}$ is the Galerkin matrix operator which results from testing unknown currents, defined as

$$\mathcal{L}_{kl}^{MM,MM} = \left\langle \hat{f}_k^{MM}, L\left(\hat{f}_l^{MM}\right) \right\rangle \tag{4}$$

where $\hat{f}_k^{MM}$ and $\hat{f}_l^{MM}$ are expansion functions on the MM part of the surface. Respectively, $\mathcal{L}_{kl}^{MM,\ PO}$ is defined with

$$\mathcal{L}_{kl}^{MM,PO} = \left\langle \hat{f}_k^{MM}, L\left(\hat{f}_l^{PO}\right) \right\rangle. \tag{5}$$

In equation (3), the right hand side denotes the Galerkin transformed effective illuminating field, i.e., consisting of the incident electric field plane wave and near field contributions of the PO region. I^{PO} could be either the far field currents or currents calculated from near field incidence (sources) as in Figure 3.

CADDSCAT's near field calculations are necessary for consideration of accurate analysis of currents to be used as hybrid inputs to CARLOS-3D. The CADDSCAT near field results are also applicable to near field fuzing problems as shown in Figure 8. For an engagement such as shown, calculation of currents in the near field is necessary for modeling warhead detonation.
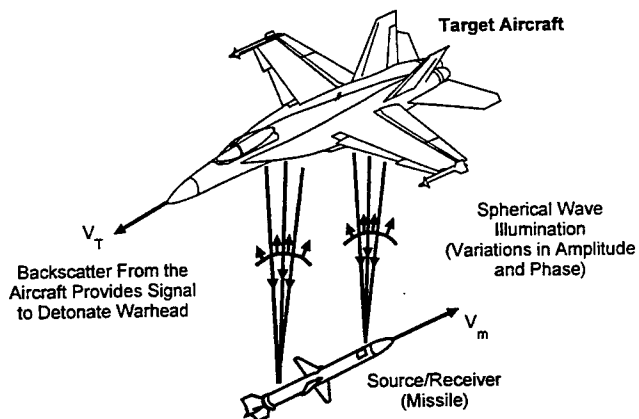
Figure 8. CADDSCAT Near-Field RCS Predictions Used for End-Game Scenario

6. Summary

Two levels of hybridization have been discussed. In the second, accurate consideration of effects of secondary illumination are critical for successful hybridization. These effects require near field incidence and scattering calculations which are available with the MDA CADDSCAT code.

References

[1] P.H. Pathak and R.J. Burkholder, "High-frequency electromagnetic scattering by open-ended waveguide cavities", Radio Science, Vol. 26, No. 1, pp. 211-218, Jan-Feb. 1991.

[2] D.L. Mensa and K. Vaccaro, "Near-Field to Far-Field Transformation of RCS Data", presented at the 17th Annual Meeting and Symposium, Antenna Measurement Techniques Assocation, NASA Langley Research Center, November 1995, Williamsburg, VA, pp. 155-161.

[3] L.N. Medgyesi-Mitschang and J.M. Putman, "Hybrid Formulation for Arbitrary 3-D Bodies", presented at the 10th Annual Review of Progress in Applied Computational Electromagnetics, March 1994, Monterey, CA, Vol II, pp. 267-274.

A Hybrid Surface Integral Equation and Partial Differential Equation Method

J.M. Putnam, M.R. Axe and D.S. Wang
McDonnell Douglas Corporation
Mail Code: S064-2263
P.O. Box 516
St. Louis, MO 63166

1. Introduction

Much work has been done in the last 15 years in hybrid formulations and their efficacy has been demonstrated in a number of applications. In this paper we will present an approach which combines surface integral equation (SIE) formulations and partial differential equation (PDE) formulations together. The SIE approach encompasses a novel generalization of the usual method of moments (MM) with arbitrary boundary conditions. The PDE formulation spans the internal, penetrable regions of a scatterer. These regions may be anisotropic in both permittivity and permeability. The particular PDE approach chosen here is a finite volume frequency domain (FVFD) method, and is based upon a computational fluid dynamics (CFD) code implementation of Maxwell's equations. This is demonstrably more robust than conventional finite difference methods. The SIE formulation spans the external surfaces of the target effectively providing truncation of the PDE computational domain.

The SIE formulation is discretized and solved with the MM implementation from the CARLOS code. The PDE formulation used for the interior penetrable regions of a scatterer, is solved as a FVFD problem using a direct solver implementation of the CFDMAXES code. Both codes are MDA proprietary RCS codes for solving 2D and 3D problems. They are generalizations of the earlier developed EMCC codes CARLOS-3D [1] and CFDMAXES (pseudo-time formulation) [2]. In this hybrid formulation, the exterior MM and interior PDE computational domains are rigorously coupled. Numerical solution of the hybrid problem can be carried out in a number of ways. Depending on the extent of the penetrable region, a solution may be obtained by a serial cascaded decomposition of the interior and exterior solution domains or direct computation of both. For maximum versatility we have implemented both.

Results are presented validating this method in both two and three dimensions. Various isotropic and anisotropic test cases are shown for a variety of different geometries. The ability to efficiently model inhomogeneous media is also demonstrated. The results presented are compared to other methods.

2. MM Formulation for a Partially Coated Body

In this section the method of moments solution based on a surface integral equation formulation for a partially coated body is outlined to define the notation that will be used subsequently for the hybrid formulation. The notation here follows that of [1 and 3] and applies to both 2D and 3D geometries. Refering to Figure 1, the Stratton-Chu equations for the total electric and magnetic fields in region 1 are given by

$$\theta_1(\bar{r})\bar{E}_1(\bar{r}) = \bar{E}^{inc}(\bar{r}) - L_1\bar{J}^+(\bar{r}) + K_1\bar{M}^+(\bar{r}) \qquad \theta_1(\bar{r})\bar{H}_1(\bar{r}) = \bar{H}^{inc}(\bar{r}) - K_1\bar{J}^+(\bar{r}) - \frac{1}{\eta_1^2}L_1\bar{M}^+(\bar{r}) \qquad (1)$$

where J^+ and M^+ are the equivalent currents on the surfaces bounding region 1. For region 2 the total fields are given by

$$\theta_2(\bar{r})\bar{E}_2(\bar{r}) = -L_2\bar{J}^-(\bar{r}) + K_2\bar{M}^-(\bar{r}) \qquad \theta_2(\bar{r})\bar{H}_2(\bar{r}) = -K_2\bar{J}^-(\bar{r}) - \frac{1}{\eta_2^2}L_2\bar{M}^-(\bar{r}) \qquad (2)$$

Similarly, J^- and M^- are the currents on the surfaces bounding region 2. The integro-differential operators are defined as

$$L_i\bar{X}(\bar{r}) = \int_{\partial R_i}\left(j\omega\mu_i\bar{X}(\bar{r}') + \frac{j}{\omega\varepsilon_i}\nabla\nabla'\cdot\bar{X}(\bar{r}')\right)\Phi_i(\bar{r}-\bar{r}')ds' \qquad K_i\bar{X}(\bar{r}) = \int_{\partial R_i}\bar{X}(\bar{r}')\times\nabla\Phi_i(\bar{r}-\bar{r}')ds' \qquad (3)$$

Specializing these equations for the geometry and currents in Figure 1, and applying the tangential field boundary conditions on the conducting surfaces and the dielectric boundary, we obtain four field equations (two EFIE and two PMCHW)

$$0 = \left\{L_2(\bar{J}_2 - \bar{J}_3) + K_2\bar{M}_3\right\}\Big|_{\tan S_2} \qquad \bar{E}^i\Big|_{\tan S_1} = \left\{L_1(\bar{J}_1 + \bar{J}_3) - K_1\bar{M}_3\right\}\Big|_{\tan S_1} \qquad (4)$$

$$\bar{E}^i\Big|_{\tan S_1} = \left\{L_1\bar{J}_1 + (L_1 + L_2)\bar{J}_3 - L_2\bar{J}_2 - (K_1 + K_2)\bar{M}_3\right\}\Big|_{\tan S_1} \qquad (5)$$

$$\left. \vec{H}^i \right|_{\tan S_3} = \left\{ K_1 \vec{J}_1 + \left(K_1 + K_2 \right) \vec{J}_3 - K_2 \vec{J}_2 + \left(\frac{1}{\eta_1^2} L_1 + \frac{1}{\eta_2^2} L_2 \right) \vec{M}_3 \right\} \Bigg|_{\tan S_3} \tag{6}$$

Applying the MM technique to these four equations transforms the integral operators L and K into matrix operators $\mathcal{L}$ and $\mathcal{K}$, and results in the matrix equation

$$\begin{bmatrix} \mathcal{L}_{22}(R_2) & 0 & -\mathcal{L}_{23}(R_2) & \mathcal{K}_{23}(R_2) \\ 0 & \mathcal{L}_{11}(R_1) & \mathcal{L}_{13}(R_1) & -\mathcal{K}_{13}(R_1) \\ -\mathcal{L}_{32}(R_2) & \mathcal{L}_{31}(R_1) & \mathcal{L}_{33}(R_1) + \mathcal{L}_{33}(R_2) & -\mathcal{K}_{33}(R_1) - \mathcal{K}_{33}(R_2) \\ -\mathcal{K}_{32}(R_2) & \mathcal{K}_{31}(R_1) & \mathcal{K}_{33}(R_1) + \mathcal{K}_{33}(R_2) & \frac{1}{\eta_1^2}\mathcal{L}_{33}(R_1) + \frac{1}{\eta_2^2}\mathcal{L}_{33}(R_2) \end{bmatrix} \begin{bmatrix} J_2 \\ J_1 \\ J_3 \\ M_3 \end{bmatrix} = \begin{bmatrix} 0 \\ \mathcal{E}_1 \\ \mathcal{E}_3 \\ \mathcal{H}_3 \end{bmatrix} \tag{7}$$

The subscripts specify the test and source surface numbers, and R_i defines the region where the Green's function is defined. Explicit expressions for $\mathcal{L}$ and $\mathcal{K}$ can be given once a geometry type is specified (i.e., 2D or 3D), and the basis and testing functions are defined. In the present implementation, we use Galerkin testing with overlapping triangle basis functions for 2D geometries, and basis functions defined on a quadrilateral mesh for 3D geometries. A quadrilateral mesh is used for 3D in order to simplify the subsequent coupling of the exterior MM formulation and the interior PDE formulation which uses a structured interior mesh.
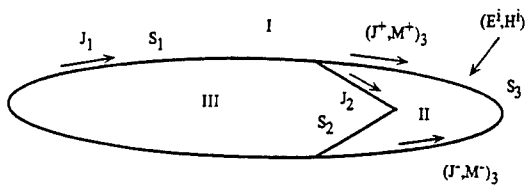
Figure 1. Geometry for a Partially Coated Scatterer. (Region III is PEC)
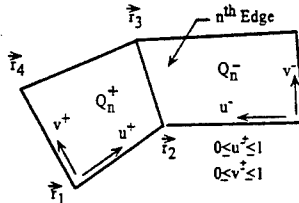
Figure 2. Linear Quad Expansion Function Definitions and Coordinates.

For a quadrilateral mesh, we define basis functions in a manner analogous to the Rao-Wilton-Glisson basis functions on a triangular mesh. Refering to Figure 2, the basis function for the n-th edge is defined as

$$\vec{f}_n(u,v) = \begin{cases} \dfrac{l_n u}{\sqrt{g(u,v)}} \vec{u}, & \vec{r} \in Q_n^+ \\[2mm] -\dfrac{l_n u}{\sqrt{g(u,v)}} \vec{u}, & \vec{r} \in Q_n^- \\[2mm] 0, & otherwise \end{cases} \quad \text{where}$$

$$\vec{r}(u,v) = \vec{r}_1 + u(\vec{r}_2 - \vec{r}_1) + v(\vec{r}_4 - \vec{r}_1) + uv(\vec{r}_1 - \vec{r}_2 + \vec{r}_3 - \vec{r}_4)$$

$$\vec{u} = \frac{\partial \vec{r}}{\partial u} = (\vec{r}_2 - \vec{r}_1) + v(\vec{r}_1 - \vec{r}_2 + \vec{r}_3 - \vec{r}_4) \tag{8}$$

$$\sqrt{g(u,v)} = \|\vec{u} \times \vec{v}\| \quad \text{and} \quad \iint ds = \iint \sqrt{g(u,v)}\, du\, dv$$

The divergence of the basis function is given by

$$\nabla \cdot \vec{f}_n(u,v) = \begin{cases} \dfrac{1}{\sqrt{g(u,v)}} \vec{u}, & \vec{r} \in Q_n^+ \\[2mm] -\dfrac{1}{\sqrt{g(u,v)}} \vec{u}, & \vec{r} \in Q_n^- \\[2mm] 0, & otherwise \end{cases} \tag{9}$$

3. Interior CFD Based Formulation

In this section we describe the adaptation of the CFDMAXES code to a matrix based fully implicit formulation. This work builds in part on an earlier non-matrix based explicit pseudo-time implementation of CFDMAXES. We chose to implement a finite volume frequency domain (FVFD) method for penetrable interiors of a scatterer. Our approach is based on extensive fundamental developments arising from computational fluid dynamics (CFD) research. The power of

this multi-disciplinary approach is that the highly refined algorithms and tools of CFD under this approach can be transferred directly to the CEM arena. A PDE formulation for penetrable regions, solved with CFD based methods, is often superior to integral equation volume formulations solved by the MM technique. Our approach is generalized to handle anisotropic materials in the penetrable region. The formulation is in the frequency domain so that it can be coupled to the SIE formulation solved with the generalized MM approach.

The analysis begins with Maxwell's curl equations, written in symmetric form in terms of the electric and magnetic currents, $\vec{J}$ and $\vec{M}$, respectively

$$\frac{\partial \vec{D}}{\partial t} - \nabla \times \vec{H} = -\vec{J} \qquad\qquad \frac{\partial \vec{B}}{\partial t} + \nabla \times \vec{E} = -\vec{M} \tag{10}$$

where $\vec{D}$ is the electric field displacement, $\vec{B}$ is the magnetic field induction, and $\vec{E}$ and $\vec{H}$ are the electric and magnetic field intensities, respectively. The electric field displacement and magnetic field induction are related to the electric and magnetic field intensities through the permittivity, ε, and the permeability, μ, as follows, $\vec{D} = \varepsilon \vec{E}$, and $\vec{B} = \mu \vec{H}$. Using the theory of equivalent currents, the electric and magnetic current densities can be related to the electric and magnetic field intensities as $\vec{J} = \hat{n} \times \vec{H}$, and $\vec{M} = -\hat{n} \times \vec{E}$. Since, the governing equations are linear, the assumption that the incident field is time harmonic with a frequency ω, results in the total field also being harmonic with frequency ω. Thus, the Maxwell curl equations are recast as a set of coupled steady state complex equations, $j\omega\varepsilon\vec{E} - \nabla \times \vec{H} = -\vec{J}$ and $j\omega\mu\vec{H} + \nabla \times \vec{E} = -\vec{M}$. Next these equations are recast in conservation law form. Then they are transformed to curvilinear coordinates (ξ, η, ζ) and combined into a single system of six equations with six unknowns as

$$j\omega J \begin{pmatrix} \varepsilon\vec{E} \\ \mu\vec{H} \end{pmatrix} + \frac{\partial}{\partial \xi}\begin{pmatrix} -\bar{\xi} \times \vec{H} \\ \bar{\xi} \times \vec{E} \end{pmatrix} + \frac{\partial}{\partial \eta}\begin{pmatrix} -\bar{\eta} \times \vec{H} \\ \bar{\eta} \times \vec{E} \end{pmatrix} + \frac{\partial}{\partial \zeta}\begin{pmatrix} -\bar{\zeta} \times \vec{H} \\ \bar{\zeta} \times \vec{E} \end{pmatrix} = \begin{pmatrix} -\vec{J} \\ -\vec{M} \end{pmatrix} \tag{11}$$

where J is the Jacobian of the transformation. This system is solved using the CFD based methods as outlined below.

To solve equation (11) the computational domain is discretized by dividing it into hexahedral cells. The discretization procedure for this equation follows the method of lines in decoupling the approximation of the spatial (the curl terms) and temporal terms (the $j\omega$ terms). Physically, the curl terms can be viewed as the flux of the electric and magnetic fields. A system of ordinary differential equations is obtained by applying this equation to each of the hexahedral cells separately. Let the values of the unknown quantities associated with each cell be denoted by i, j, k. These can be regarded as values at each cell center or the average value for each cell. Thus explicitly for each cell, equation (2) takes the form

$$j\omega J_{i,j,k}\begin{pmatrix} \varepsilon\vec{E} \\ \mu\vec{H} \end{pmatrix}_{i,j,k} + \begin{pmatrix} -\bar{\xi} \times \vec{H} \\ \bar{\xi} \times \vec{E} \end{pmatrix}_{i+\frac{1}{2},j,k} - \begin{pmatrix} -\bar{\xi} \times \vec{H} \\ \bar{\xi} \times \vec{E} \end{pmatrix}_{i-\frac{1}{2},j,k}$$
$$+ \begin{pmatrix} -\bar{\eta} \times \vec{H} \\ \bar{\eta} \times \vec{E} \end{pmatrix}_{i,j+\frac{1}{2},k} - \begin{pmatrix} -\bar{\eta} \times \vec{H} \\ \bar{\eta} \times \vec{E} \end{pmatrix}_{i,j-\frac{1}{2},k} + \begin{pmatrix} -\bar{\zeta} \times \vec{H} \\ \bar{\zeta} \times \vec{E} \end{pmatrix}_{i,j,k+\frac{1}{2}} - \begin{pmatrix} -\bar{\zeta} \times \vec{H} \\ \bar{\zeta} \times \vec{E} \end{pmatrix}_{i,j,k-\frac{1}{2}} = \begin{pmatrix} -\vec{J} \\ -\vec{M} \end{pmatrix}_{i,j,k} \tag{12}$$

The i, j, k subscripted terms are evaluated at the center of each cell. The $i \pm 1/2$, $j \pm 1/2$, or $k \pm 1/2$ subscripted terms are evaluated at the center of each cell face. Field values for the cell faces are created by averaging the two adjoining cell centered values. The Jacobian of the Cartesian to curvilinear coordinate transformation, $J_{i,j,k}$, is equivalent to the hexahedral cell volume. The ξ, η, ζ terms in equation (12) are the normal vectors to the six faces of a cell. The magnitude of these normal vectors are equal to the cell's facial area. The direction of the unit normal is in the direction of the positive curvilinear axis.

For the subsequent development it is advantageous to write equation (12) as $\left[j\omega J_{i,j,k} + \Im_{i,j,k}(\ ) \right]\tilde{Q}_{i,j,k} = \tilde{J}_{i,j,k}$ or for compact notational purposes in matrix form as $[A]Q = h$, where the bracked terms are the A matrix that comprises the temporal or $j\omega$ terms and the curl or flux terms. $\Im(\ )$ is the flux terms operator, Q is a column vector that represents the unknown, $\vec{E}$ and $\vec{H}$ fields, and h is a column vector that represents the right hand side currents from the exterior domain. The ordering of unknowns within A and Q have the following sequence:

715

$$\left(\left(\left(\left(\left[E_x, E_y, E_z, H_x, H_y, H_z\right]_{i,j,k,iz}, i=1, n_i\right), j=1, n_j\right), k=1, n_k\right), iz=1, n_{nz}\right) \tag{13}$$

where n_i is the number of cells in the i-direction, n_j is the number of cells in the j-direction, n_k is the number of cells in the k-direction, and n_{nz} is the number of zones. The A matrix is of order $6m$, where $m=n_i \times n_j \times n_k \times n_{nz}$.

To model the electromagnetic fields interior to a penetrable region, a series of boundary conditions must be considered to produce a bounded domain. The boundary conditions implemented in this formulation of CFDMAXES are perfectly conducting surfaces, zonal, dielectric interface, geometric symmetry and interface to method of moments. These boundary conditions are handled as boundary groups. Each boundary group is a particular boundary condition type.

For a perfectly conducting surface we use the boundary conditions, $\hat{n} \times \bar{E}_{wall} = 0$ and $\hat{n} \times \bar{H}_{Wall} = \hat{n} \times \bar{H}_{Neighbor}$, where E and H are the total field values, and $\hat{n}$ is the unit normal vector to the conducting surface. These equations imply that the tangential electric field at the wall is zero and that the tangential magnetic field at the wall is equivalent to that of the neighboring cell.

The generation of structured curvilinear or body fitted grids about geometrically complex structures is facilitated by a zonal gridding strategy. Dividing the computational domain into a multi-zone framework allows for the independent treatment of geometrically complex internal/external structures. Radar absorbing structures (RAS) and radar absorbing material (RAM) with many material layers require a zonal gridding strategy to handle the varying grid density requirements that the layer's material properties dictate. In this work zone-to-zone communication is provided through a bookeeping system of overlapping ghost cells. The i, j, k indices for each zone varies as follows:

$$i = 0,1,2,3,....,i_{max-1}, i_{max} \qquad j = 0,1,2,3,....,j_{max-1}, j_{max} \qquad k = 0,1,2,3,....,k_{max-1}, k_{max} \tag{14}$$

where the 0 and max indices represent the fictitious or ghost cell layer that surrounds the real cells in the interior of the zone. Each ghost cell overlaps an interior cell and acts as a place holder during the initial phase of the matrix fill. In the second phase of the matrix fill the flux terms associated with the fictious ghost cells are matched with their corresponding real cell. This boundary condition allows ghost cells in the i, j and k directions to overlap any $i, j,$ or k direction interior cells. Our method allows exact 1-to-1, 2-to-1, or 4-to-1 point matching along the zonal boundary.

In general, a scatterer may consist of layered material media with variations in material properties (ε and μ) from layer to layer. The incident and scattered fields must satisfy the appropriate boundary conditions on the surface of the scatterer that for a layered media scatterer includes all material interfaces. Since in this algorithm material properties within a cells are uniform, all material interfaces are at cell boundaries. A difference in the material properties from cell to cell causes a discontinuity. We use a 1-D characteristic based boundary condition to model these dielectric discontinuities. As discussed previously, equation (12) can be solved numerically and $\bar{E}$ and $\bar{H}$ can be found once the fluxes through the cell walls are computed. The cell wall fluxes are obtained by computing the tangential fields on the walls of the cells. This is done by applying characteristic theory. Consider the local unit normal, $\hat{n}$, to the dielectric discontinuity. The boundary condition then becomes

$$\bar{E}_D = \frac{\left[\bar{E}^+(\varepsilon\mu)^+ + \hat{n} \times \bar{H}^+\right] + \left[\bar{E}^-(\varepsilon\mu)^- - \hat{n} \times \bar{H}^-\right]}{(\varepsilon\mu)^- + (\varepsilon\mu)^+} \qquad \bar{H}_D = \frac{\left[\bar{H}^-(\varepsilon\mu)^- + \hat{n} \times \bar{E}^-\right] + \left[\bar{H}^+(\varepsilon\mu)^+ - \hat{n} \times \bar{E}^+\right]}{(\varepsilon\mu)^- + (\varepsilon\mu)^+} \tag{15}$$

where $\bar{H}^-, \bar{H}^-, \bar{E}^+, \bar{E}^-$ are the cell centered electromagnetic field values of the cells on the "+" and "-" side of the dielectric boundary. $(\varepsilon\mu)^-, (\varepsilon\mu)^+$ are the associated material properties of the cells on either side of the dielectric boundary condition, and $\bar{H}_D, \bar{E}_D$ are the values of the fields at the dielectric boundary's cell face.

Our approach for modeling anisotropic media generalizes the method for modeling isotropic material [4]. Equation (11) can be recast into an equivalent form exhibiting an explicit dependence of the fluxes on the solution vector, by writing $\bar{E} = \bar{\bar{\varepsilon}}^{-1}\bar{D}$ and $\bar{H} = \bar{\bar{\mu}}^{-1}\bar{B}$, where $\bar{\bar{\varepsilon}}$ and $\bar{\bar{\mu}}$ are the tensor forms of the permittivity and permeability, then the derivative terms in equation (11) take the form, as shown for the ξ-direction derivative

$$\frac{\partial}{\partial\xi}\begin{pmatrix} \bar{\xi} \times \bar{E} \\ -\bar{\xi} \times \bar{H} \end{pmatrix} = \frac{\partial}{\partial\xi}\left(\begin{bmatrix} 0 & \bar{\xi} \times \bar{\bar{\varepsilon}}^{-1} \\ -\bar{\xi} \times \bar{\bar{\mu}}^{-1} & 0 \end{bmatrix} Q\right) = \frac{\partial}{\partial\xi}(AQ) \tag{16}$$

where the positional dependence of $\overline{\overline{\varepsilon}}$ and $\overline{\overline{\mu}}$ are accounted for in the 6×6 Jacobian matrix A. As with the isotropic case we solve the one-dimensional Riemann problem separately for each coordinate direction. The method of characteristics relies on finding the eigenvalues and eigenvectors of the Jacobian matrix A. The solution vectors as well as the interface fluxes are subsequently expanded in the six dimensional space spanned by the eigenvectors of A.

The MM interface boundary condition is defined in terms of equivalent currents which supply the electric and magnetic field components for the CFD cell faces that compose the interface boundary. Thus the boundary condition becomes, $\vec{E}_B = \vec{E}_N$ and $\vec{H}_B = \vec{H}_N$, where $\vec{H}_B, \vec{E}_B$ are the electromagnetic field values at the MM/CFD boundary and $\vec{H}_N, \vec{E}_N$ are the values at the neighboring interior cell. In the framework of CFDMAXES, the field values supplied by the MM techniques is treated as a flux along the faces of the boundary cells.

4. Hybrid MM/CFD Formulation

In this section we summarize the hybrid coupling of the SIE formulation for the exterior of the scatterer with a PDE time harmonic formulation for the interior penetrable regions of the scatterer. The computer implementation of this approach involves the coupling of the MM and PDE developments, discussed in Sections 2 and 3.

Fundamental to a hybrid formulation is the decomposition of the problem into regions where different analysis techniques are used. In this case the decomposition is into an interior and exterior one. The interior region may consist of several subregions, not necessarily contiguous. To simplify the following discussion, we omit this generalization, however, the implementing software allows such generality. The electromagnetic fields obtained from the MM (exterior) and FVFD (interior) solutions are matched rigorously at the boundary of the regions. (See the MM interface boundary condition definition in Section 3.) The details of the solution process for each of the regions are described next.

To clarify this development it is convenient to introduce a generic scatterer, that is part conducting and part penetrable as is depicted in Figure 1. The case of a totally coated scatterer is a subcase of the former. For ease of illustration, the geometry in Figure 1 depicted as 2D, however, the present formulation applies equally well to arbitrary 3D cases. The exterior and interior regions are denoted as regions 1 and 2, respectively. The equivalent surface currents associated with the various surfaces bounding the regions are shown.

The time harmonic interior PDE formulation can be written in matrix form as (Section 3):

$$AQ = h \tag{17}$$

where the column vector Q represents the cell centered E and H fields for the interior region. Each cell in the interior mesh has six field components; $E_x, E_y, E_z, H_x, H_y, H_z$. The unknowns and equations in (17) can be reordered so that the interior cells which border the coupling surface S_3 are grouped first. With this reordering, the matrix equation (17) can be written in partitioned form as:

$$A\begin{bmatrix} E_3^- \\ H_3^- \\ E_i \\ H_i \end{bmatrix} = \begin{bmatrix} J_3^- \\ M_3^- \\ 0 \\ 0 \end{bmatrix} \tag{18}$$

where the vectors J_3^- and M_3^- represent the source currents (fluxes) on S_3 for the interior problem. The vectors E_3^- and H_3^- are the cell centered fields for the cells which border the coupling surface S_3, and E_i and H_i are the remaining interior cell centered fields. Note, the number of terms in each of E_3^-, H_3^-, J_3^-, and M_3^- is 3 times the number of cells which border surface S_3. In the following, we will assume that equations (17 and 18) have the same ordering, and we will use both notations at times for describing the interior problem. For the exterior problem, referring to Figure 1, the total fields in the free space region R_1 are given by equation (1), and can be written explicitly as:

$$\theta(\vec{r})\vec{E}_1 = \vec{E}^{inc}(\vec{r}) - L_1[\vec{J}_1 + \vec{J}_3](\vec{r}) + K_1\vec{M}_3(\vec{r}) \qquad \theta(\vec{r})\vec{H}_1 = \vec{H}^{inc}(\vec{r}) - K_1[\vec{J}_1 + \vec{J}_3](\vec{r}) + \frac{1}{\eta_1^2}L_1\vec{M}_3(\vec{r}) \tag{19}$$

Applying the Galerkin method of moments to the E-field equation on surface 1, we obtain the matrix equation

$$\mathcal{L}_{11}J_1 + \mathcal{L}_{13}J_3 - \mathcal{K}_{13}M_3 = \mathcal{E}_1 \tag{20}$$

which is the second row of the matrix equation (7) of Section 1. On the MM/PDE coupling surface, S_3, we have

$$\left\{ L_1\left(\bar{J}_1 + \bar{J}_3^+\right) - K_1\bar{M}_3^+ + \frac{\bar{E}_3^+}{2} \right\}_{\tan} = \bar{E}_{\tan}^{inc} \qquad \left\{ K_1\left(\bar{J}_1 + \bar{J}_3^+\right) + \frac{1}{\eta_1^2}L_1\bar{M}_3^+ + \frac{\bar{H}_3^+}{2} \right\}_{\tan} = \bar{H}_{\tan}^{inc} \tag{21}$$

In order to couple to the interior problem, we enforce continuity of the tangential E and H fields across S_3 by substituting $\bar{E}_3^-|_{\tan}$ and $\bar{H}_3^-|_{\tan}$ for $\bar{E}_3^+|_{\tan}$ and $\bar{H}_3^+|_{\tan}$, respectively. These fields are represented by the interior PDE unknowns in Q which border S_3. Applying the Galerkin MM to equation (21), we obtain (note that H-field equation is multiplied by η_0)

$$\mathcal{L}_{31}J_1 + \mathcal{L}_{33}J_3 - \mathcal{K}_{33}M_3 + \tilde{B}E_3^- = \mathcal{E}_3 \qquad \mathcal{K}_{31}J_1 + \mathcal{K}_{33}J_3 + \frac{\varepsilon_1}{\mu_1}\mathcal{L}_{33}M_3 + \tilde{B}H_3^- = \mathcal{H}_3 \tag{22}$$

The matrix $\tilde{B}$, which results from testing the fields on surface S_3, is sparse since each exterior MM testing function only interacts with the interior cells which are contained within the support of the testing function. The three MM matrix equations (20 and 22), in terms of the exterior MM unknowns J_1, J_3, and M_3, and the interior PDE unknowns E_3^-, H_3^-, E_i, and H_i can be written as

$$\begin{bmatrix} \mathcal{L}_{11} & \mathcal{L}_{13} & -\mathcal{K}_{13} & 0 & 0 & 0 & 0 \\ \mathcal{L}_{31} & \mathcal{L}_{33} & -\mathcal{K}_{33} & \tilde{B} & 0 & 0 & 0 \\ \mathcal{K}_{31} & \mathcal{K}_{33} & \frac{\varepsilon_1}{\mu_1}\mathcal{L}_{33} & 0 & \tilde{B} & 0 & 0 \end{bmatrix} \begin{bmatrix} J_1 \\ J_3 \\ M_3 \\ E_3^- \\ H_3^- \\ E_i \\ H_i \end{bmatrix} = \begin{bmatrix} \mathcal{E}_1 \\ \mathcal{E}_3 \\ \mathcal{H}_3 \end{bmatrix} \tag{23}$$

Note, we have omitted the region numbers from the Galerkin MM operators since they only apply to the exterior free-space region. For convenience, we will write equation (23) as

$$ZI + BQ = V \tag{24}$$

where $I = \begin{bmatrix} J_1 \\ J_3 \\ M_3 \end{bmatrix}$ are the MM exterior unknowns, $Q = \begin{bmatrix} E_3^- \\ H_3^- \\ E_i \\ H_i \end{bmatrix}$ are the PDE interior unknowns, and $V = \begin{bmatrix} \mathcal{E}_1 \\ \mathcal{E}_3 \\ \mathcal{H}_3 \end{bmatrix}$ are the tested exterior incident fields.

Note that in equation (24), the MM matrix Z is dense, the coupling matrix B is sparse, and we have fewer equations than unknowns. In order to obtain a determined system of equations, we will relate the interior problem source terms in equation (18) to the exterior MM unknowns in equation (23). This results in a sparse transformation matrix $\tilde{T}$ which relates the MM unknowns J_3 and M_3 to the PDE sources J_3^- and M_3^- (i.e. $\tilde{T}J_3 = J_3^-$ and $\tilde{T}M_3 = M_3^-$). Equation (18) can now be rewritten as

$$A \begin{bmatrix} E_3^- \\ H_3^- \\ E_i \\ H_i \end{bmatrix} = \begin{bmatrix} \tilde{T}J_3^- \\ \tilde{T}M_3^- \\ 0 \\ 0 \end{bmatrix} \tag{25}$$

For convenience, we will write this equation as $AQ = h = -TI$ or equivalently

$$AQ + TI = 0 \tag{26}$$

718

The MM/PDE coupled system of equations (24 and 26) is thus given by

$$\begin{bmatrix} A & T \\ B & Z \end{bmatrix} \begin{bmatrix} Q \\ I \end{bmatrix} = \begin{bmatrix} 0 \\ V \end{bmatrix} \tag{27}$$

where the matrices A, T, and B are sparse, and Z is dense. Note, this equation is valid for either 2D or 3D geometries. The explicit forms of the matrix elements depends on the geometry type, basis functions, etc. Note, MM/FEM solutions also result in this same matrix form. This matrix equation can be solved for both the interior and exterior unknowns, or if only the MM exterior unknowns are required, the following reduced matrix equation can be used to solve for I

$$[Z - BA^{-1}T]I = V \tag{28}$$

5. Results

The results presented here include two- and three- dimensional (2D and 3D) cases. Results for the hybrid code are compared to MM results. For all these cases CFD was used to model the interior and MM for the exterior. Figures 3-5 show bistatic RCS (dB/λ) results for both TE and TM polarization for 2D circular cylinder cases. The direction of incidence is θ=0°. Figure 3 is for a perfectly electrically conducting (PEC) case, where the air coating is ring shaped,
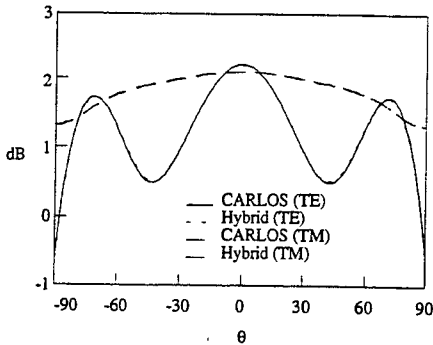
Figure 3. 2D PEC circular cylinder,1λ diameter with 0.0375λ air coating.
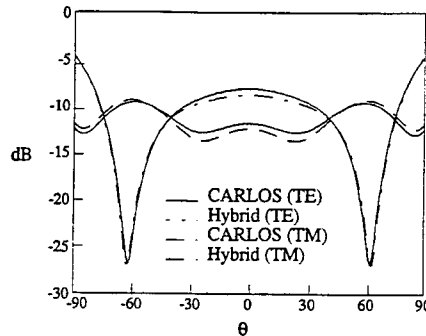
Figure 4. 2D lossy (ε=2-j0.4) circular cylinder, 1λ diameter
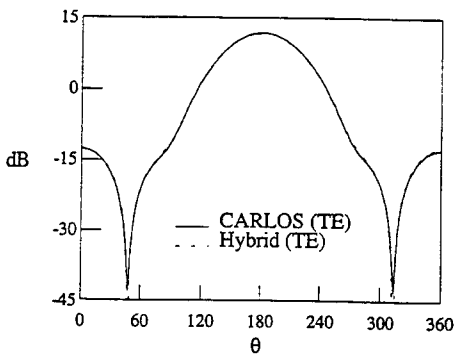
Figure 5. 2D anisotropic circular cylinder, 0.5λ diameter. Material properties are μ_{zz}=2, ε_{xx}=1, ε_{yy}=4 [5].
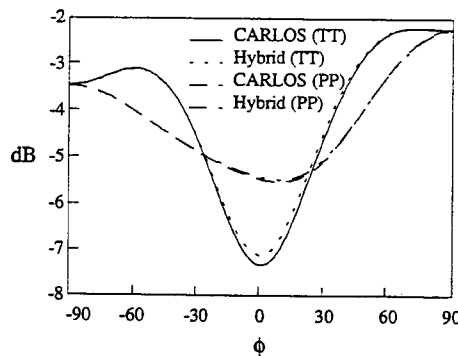
Figure 6. 3D cubic duct (1/4λ on a side), filled with ε=4 material.

with 160×6 quadrilateral cells. Figures 4 is a homogeneous lossy case, while Figure 5 is a lossless anisotropic case. The

719

mesh for Figure 4 is 120×24 and for Figure 5 the mesh is 80×14, with both arranged in a polar topology. All three problems are meshed with even spacing in the circumferential direction, and in the radial direction with a gradually finer spacing towards the CFD/MM boundary.

Figures 6-8 are 3D cavity cases and show the monostatic RCS in dB/λ^2. Each case consists of a box shaped cavity with an opening at one end (ϕ=90°), PEC walls for the other five faces and a homogeneous dielectric material filled interior. Figures 6 and 7 have been run both with and without geometric symmetry and as either as a single problem or as a serial cascaded decomposition of the interior. The interior mesh for the full geometry for Figures 6 and 8 was a 10×10× 14 hexahedral cell mesh, and for Figure 7 a 10×10×44 cell mesh. TT signifies $\theta\theta$ polarization and PP is for $\phi\phi$ polarization.
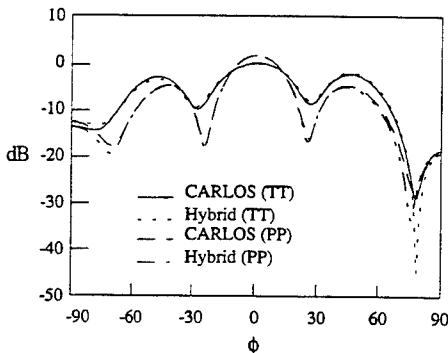
Figure 7. 3D rectangular duct ($1\lambda \times 1/4\lambda \times 1/4\lambda$), filled with ε=2 material.
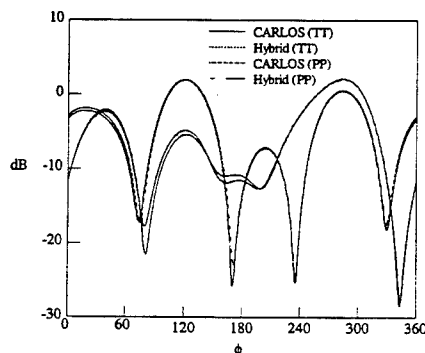
Figure 8. 3D wedged shaped duct ($1/2\lambda \times 1/2\lambda$ base, $1/2\lambda \times 1/4\lambda$ top, $1/4\lambda$ height, 45° slanted aperture), filled with ε=2-j0.4 material.

6. Conclusions

We have presented a hybrid formulation which couples an interior PDE solution with an exterior MM solution for truncation of the computational domain. We have shown both 2D and 3D results validating the approach. The interior solution is based upon well developed CFD methods for solving PDEs. The numerical implementation is robust. It allows both 2D and 3D solutions, uses geometric symmetry, zonal decomposition of the interior domain, and is applicable to all of the standard MM boundary conditions for the exterior problem. Solutions can be based on a total solution approach, or a cascaded solution approach which eliminates the interior problem from the solution.

7. References

[1]   J. M. Putnam, L. N. Medgyesi-Mitschang, and M. B. Gedera, CARLOS-3D: Three-Dimensional Method of Moments Code, Vols. I & II, McDonnell Douglas Aerospace Report, 10 December 1992.

[2]   R. Agarwal, D.S. Wang, M. Axe, "A Hybrid Method of Moments and Computational Fluid Dynamics Method for Computational Electromagnetics", Dec 1994, NASA Ames Report.

[3]   J. M. Putnam and L. N. Medgyesi-Mitschang, "Combined Field Integral Equation Formulation for Inhomogeneous Two- and Three-Dimensional Bodies: The Junction Problem", IEEE Trans. Antenna Propagat., AP-39(5), pp. 667-672, 1991.

[4]   E. Bleszynski, M. Bleszynski, and W. Hall, "Characteristic Theory and Maxwell's Equations in Anisotropic Media", unpublished paper.

[5]   J. Cesar Monzon, Nickander J. Damaskos, "Two-Dimensional Scattering by a Homogeneous Anisotropic Rod", IEEE Trans. Antenna Propagat., AP-34(10), pp. 1243-1246, 1986, Figure 3b.

Improved Hybrid Finite Element-Integral Equation Methods

S. Bindiganavale, J. Gong, Y. Erdemli and J. Volakis
Radiation Laboratory
Department of Electrical Engineering and Computer Science
The University of Michigan
Ann Arbor, MI 48109-2122

Abstract

Hybrid finite element - boundary integral methods are quite attractive because they combine the rigor of integral equation mesh truncation and the adaptability of the finite element method for modeling dielectric and inhomogeneous volumes. However, for arbitrary geometries, boundary integral truncations lead to much larger CPU requirements and memory. Also, being a frequency domain method, the finite element method may not be attractive for generating broadband data sets. In this paper, we present two improvements to the hybrid finite element - boundary integral method aimed at improving its memory and CPU efficiency in generating single frequency and broadband data. In terms of CPU efficiency, a hybridization of the finite element method with a windowed version of the fast multipole method will be discussed which provides for a good compromise between speed and accuracy. Results will be given for scattering applications of the hybrid method. Asymptotic waveform evaluation is a frequency extrapolation approach and allows for the prediction of broadband responses using a few data points generated from the full wave analysis. In the paper, we will demonstrate the efficiency afforded by this technique when applied to circuit analysis using the finite element method.

1 Introduction

The finite element-boundary integral (FE-BI) method has been quite popular and extensively applied to many scattering and radiation problems. The method [1] combines the geometrical adaptability and material generality of the FEM with the rigorous boundary integral (BI) for truncating the mesh. Nevertheless, although "exact", the FE-BI leads to a partly full and partly sparse system which is computationally intensive for large boundary integrals. When the boundary is rectangular or circular, the FFT can be used to reduce the memory and CPU requirements down to $N \log N$ [1][2]. However, in general, the boundary integral is not convolutional and in that case the CPU requirements will be $O(N_b^2)$, where N_b denotes the unknowns on the boundary. The application of the fast multipole method (FMM) enables the computation of the boundary matrix-vector product using $O(N_b^{1.5})$ operations per iteration [3]. Multilevel schemes can also be employed to reduce the operation count down to $O(N_b^{1.33})$ [4]. In this paper, we apply three different versions of the FMM to reduce the storage and computational requirements of the boundary integral when the latter is used to terminate the finite element mesh. By virtue of its low operation count, the application of the FMM results in substantial speed-up of the boundary integral portion of the code independent of the boundary shape. Each version of the FMM is associated with inherent approximations and a goal of this paper is the evaluation of these approaches in terms of CPU requirements and accuracy.

The method of Asymptotic Waveform Evaluation (AWE) provides a reduced-order model of a linear system and has already been successfully used in VLSI and circuit analysis to approximate the transfer function associated with a given set of ports/variables in circuit networks [5](this also contains extensive references on the method and its application). The basic idea of the method is

to develop an approximate transfer function of a given linear system from a limited set of spectral solutions. Typically, a Padè expansion of the transfer function is postulated whose coefficients are then determined by matching the Padè representation to the available spectral solutions of the complete system. In this paper we investigate the suitability of the AWE method for approximating the response of a given parameter in full wave simulations of radiation or scattering problems in electromagnetics. Of particular interest is the use of AWE for evaluating the input impedance of the antenna over a given bandwidth from a knowledge of the full wave solution at a few (even a single) frequency points. Also, the method can be used to fill–in a backscattering pattern with respect to frequency using a few data samples of that pattern. We describe the application of the AWE to a FEM system. At the conference, we will describe its application to a hybrid FE-BI system.

2 Formulation

2.1 Application of the FMM to hybrid FE-BI systems

As an illustration of the proposed application of the FMM to hybrid FE-BI systems we consider the scattering by a cavity-backed groove. The FE-BI formulation for this problem was already outlined in [2] and results in the system

$$
\begin{bmatrix} [A_{Int}] & [A_x] \\ [A_x^T] & [B] \end{bmatrix} \left\{ \begin{array}{c} \{\phi\} \\ \{\psi\} \end{array} \right\} = \left\{ \begin{array}{c} 0 \\ \{\phi_{inc}\} \end{array} \right\} \tag{1}
$$

For H_z-incidence, the vector $\{\phi\}$ represents the magnetic field at the nodes within the groove and on the boundary whereas $\{\psi\}$ is proportional to the magnetic current (or tangential electric field) on the boundary cells. By virtue of the finite element method, the matrices $[A_{Int}]$ and $[A_x]$ are sparse and thus the corresponding matrix-vector products are implemented using $O(N)$ operations. However $[B]$ is a full sub-matrix and thus $O(N_b^2)$ operations are needed to perform the product $[B]\{\psi\}$ with N_b denoting the number of nodes on the cavity aperture. Consequently, in an iterative solution, this matrix-vector product becomes the computational bottleneck. To reduce the operation count we can employ the FMM procedure for implementing the products $[B]\{\psi\}$. We thus examine three versions of the FMM to accelerate the boundary integral matrix-vector product computation. Specifically, the exact FMM [6], a windowed FMM [7] and an approximate FMM [8] are examined. The theory of the FMM has been described in the previously mentioned references and in this paper we focus on their implementation and performance in a hybrid environment and on clearly describing how their reduced operation count is achieved. For the system (1) the pertinent matrix vector product $[B]\{\psi\}$ is obtained from the discretization of the integral equation (for TE incidence)

$$
2H_z^i - \frac{1}{2} \int_\Gamma \psi(\overline{\rho'}) H_0^{(2)} (k_0 |\overline{\rho} - \overline{\rho'}|)\, dl' = H_z^{FEM} \qquad \overline{\rho}, \overline{\rho'} \ \epsilon \ \Gamma \tag{2}
$$

where H_z^i denotes the incident field on the aperture Γ and H_z^{FEM} is the magnetic field in the FEM domain evaluated just below the aperture. Since

$$
H_z^s = -\frac{1}{2} \int_\Gamma \psi(\overline{\rho'}) H_0^{(2)} (k_0 |\overline{\rho} - \overline{\rho'}|)\, dl' \qquad \overline{\rho}, \overline{\rho'} \ \epsilon \ \Gamma \tag{3}
$$

is the scattered field it follows that $\psi = k_0 Y_0 M_z = k_0 Y_0 E_x$ and E_x is the x-component of the electric field on the aperture. It is readily identified that (2) enforces continuity of the magnetic field across the aperture (i.e. across the interior FEM domain and the exterior region). The continuity of the corresponding tangential electric field components is enforced by choosing the excitation of the FEM

domain to be the negative of the magnetic current across the aperture just below Γ as described in [2].

The FMM achieves its reduced operation count by expanding the Green's function to decouple the source and test elements, then grouping the elements which are electrically far apart and finally interacting their weighted contributions. The computation of matrix-vector product during the execution of the boundary integral is indicated in Figure 1. The sequence of operations comprises of aggregating the radiation of each individual source element into a group (aggregation), translating the radiation to a test group center (translation), and then redistributing to the individual elements in the test group (disaggregation).

In the exact FMM, the translation operation between groups assumes isotropic radiation. However, it is suggestive that the groups would interact strongly along the line joining them and less so in other directions. Indeed, it was shown in [7] that the translation operator could be contemplated as composed of a geometrical optics (GO) term (along the line joining the source and test group) and two diffraction terms associated with the shadow boundaries of the GO term. This high frequency model enables the identification of a lit region even for groups which are not widely separated and achievement of a reduced operation count (see Figure 2) by eliminating the translations in the dark region.

The approximate FMM also referred to as the Fast Far Field Algorithm (FAFFA) makes use of the far-zone expansion of the Green's function and is thus more approximate than the other two techniques. The technique by which it achieves a reduced operation count is shown in Figure 3.

2.2 AWE

To describe the basic idea of AWE in conjunction with the FEM, we begin by first expanding the solution $\{X\}$ of the FEM system in a Taylor series about k_0 as

$$\{X\} = \{X_0\} + (k - k_0)\{X_1\} + (k - k_0)^2\{X_2\} + \dots$$
$$+ (k - k_0)^l\{X_l\} + \mathcal{O}\left\{(k - k_0)^{l+1}\right\} \tag{4}$$

where $\{X_0\}$ is the solution of the original FEM system corresponding to the wavenumber k_0. After some manipulations, we find that

$$
\begin{aligned}
\{X_0\} &= k_0 \bar{A}_0^{-1}\{f_1\} \\
\{X_1\} &= \bar{A}_0^{-1}[\{f_1\} - A_1\{X_0\} - 2k_0 A_2\{X_0\}] \\
\{X_2\} &= -\bar{A}_0^{-1}[A_1\{X_1\} + A_2(\{X_0\} + 2k_0\{X_1\})] \\
\dots &= \dots\dots \\
\{X_l\} &= -\bar{A}_0^{-1}[A_1\{X_{l-1}\} + A_2(\{X_{l-2}\} + 2k_0\{X_{l-1}\})]
\end{aligned} \tag{5}
$$

with

$$\bar{A}_0 = A_0 + k_0 A_1 + k_0^2 A_2 \tag{6}$$

where A_i denote the usual sparse matrices.

Expressions (5) are referred to as the system moments whereas (6) is the system at the prescribed wavenumber (k_0). Although an explicit inversion of A_0^{-1} may be needed as indicated in (5), this inversion is used repeatedly and can thus be stored out-of-core for the implementation of AWE. Also, given that for input impedance computations we are typically interested in the field value at one location of the computational domain, only a single entry of $\{X_l(k)\}$ need be considered, say (the pth entry) $X_l^p(k)$. The above moments can then be reduced to scalar form and the expansions (5) become
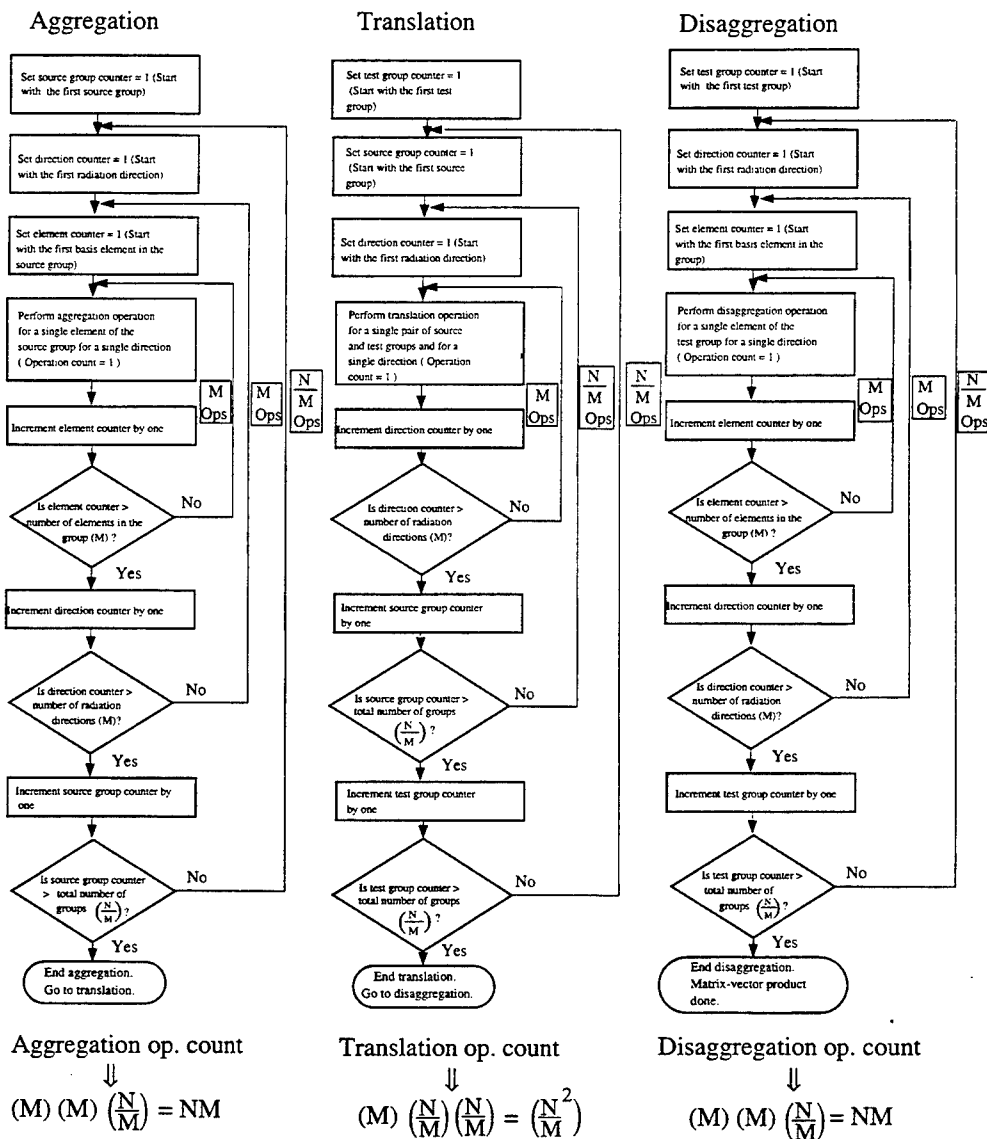
Figure 1: Sequence of operations to be performed in the Exact FMM

Translation op. count

$$\Downarrow$$

$$\left(\frac{N}{M}\right)\left(\frac{N}{M}\right) = \left(\frac{N^2}{M^2}\right)$$

Total op. count

$$(M+1)\left(\frac{N}{M}\right)\left(\frac{N}{M}\right) + \left(\frac{N}{M}\right)(M)\left(\frac{N}{M}\right)$$

$$= \left(\frac{N^2}{M}\right) + \left(\frac{N^2}{M^2}\right) + \left(\frac{N^2}{M}\right)$$

$$\Downarrow \qquad\quad \Downarrow \qquad\quad \Downarrow$$

Aggregation Translation Disaggregation
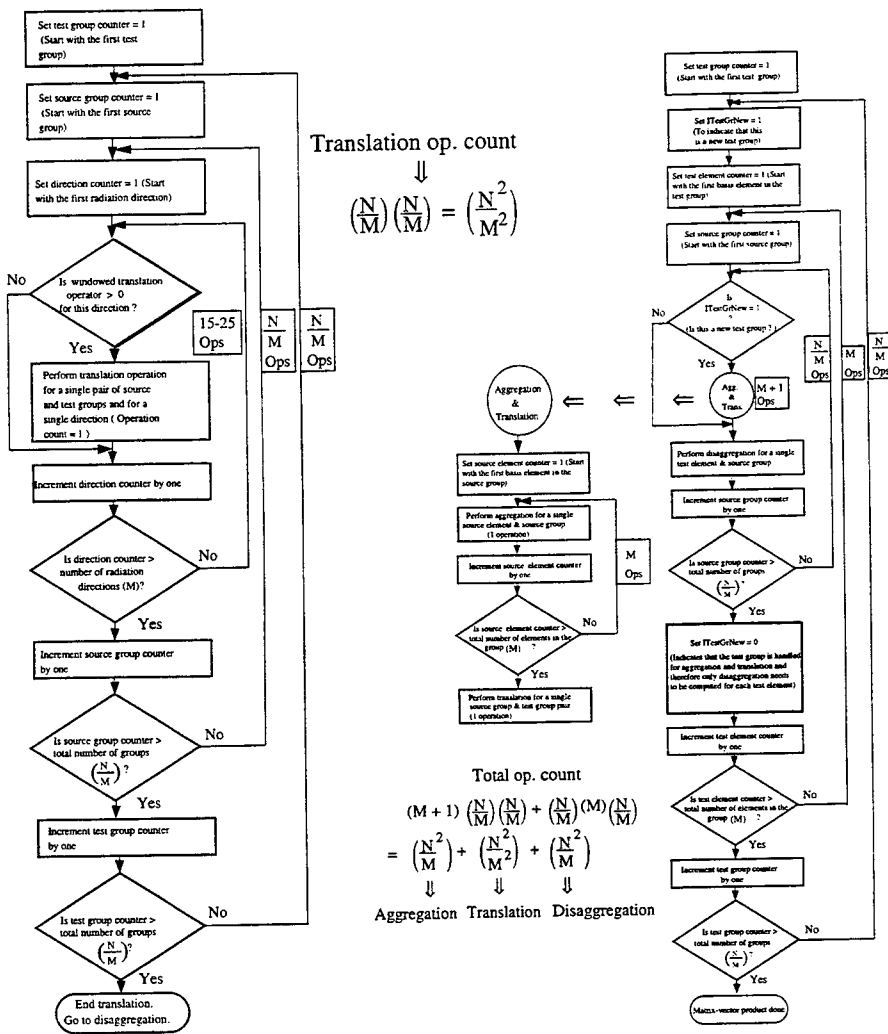
Figure 2: Translation flow of the WFMM Figure 3: Flow of the Approximate FMM

a scalar representation of $X_i^p(k)$ about the corresponding solution at k_0. To yield a more convergent expression, we can instead revert to a Padè expansion which is a conventional rational function.

For a hybrid finite element – boundary integral system, the implementation of AWE is more in-

volved because the fully populated boundary integral submatrix of the system has a more complex dependence on frequency. In this case we may instead approximate the full submatrix with a spectral expansion of the exponential boundary integral kernel to facilitate the extraction of the system moments. This approach does increase the complexity in implementing AWE. However, AWE still remains far more efficient in terms of CPU requirements when compared to the conventional approach of repeating the system solution at each frequency.

3 Results

3.1 FE-FMM

A computer code based on the above FMM formulations and utilizing the conjugate gradient solver was implemented and executed on a HP 9000/750 workstation with a peak flop rate of 23.7 MFLOPS. Table 1 compares the execution time and RMS error [9] of the standard FE-BI to the FE-Exact FMM, FE-FAFFA and the FE-Windowed FMM (FE-WFMM) for rectangular grooves of widths 25λ, 35λ and 50λ. The depth of the groove was 0.35λ with a material filling of $\epsilon_r = 4$ and $\mu_r=1$ and was illuminated at normal incidence. The data reveal that the FE-FMM^{Exact} offers almost a 50% savings in execution time with almost no compromise in accuracy. While the FE-FAFFA is the fastest of the three algorithms, the RMS error was substantially higher (>1 dB). If the maximum tolerable RMS error is set at 1 dB[1][9], the FE-Windowed FMM is the most attractive option since it meets the error criterion and is only slightly slower than the FE-FAFFA. Of interest is the comparison of the residual error as a function of the number of iterations in the CG solver. Such a comparison is shown in Figure 4 and is seen that the curves for the FE-BI and the FE-FMM^{Exact} overlap to graphical accuracy whereas the FE-WFMM shows a very small deviation from the exact result. Thus, the hybridization of the FMM does not have any adverse effect on the condition of the FE-BI system.

Groove Width	Total Unknowns	BI Unknowns	CPU Time for BI (Minutes,seconds)			
			FE-BI (CG)	FE-FAFFA	FE-FMM^{Exact}	FE-WFMM
25λ	2631	375	(8,48)	(3,26)	(5,25)	(4,13)
35λ	3681	525	(16,34)	(5,55)	(10,31)	(7,22)
50λ	5256	750	(45,1)	(14,31)	(26,18)	(16,10)

	RMS error (dB)		
Groove Width	FE-FAFFA	FE-FMM^{Exact}	FE-WFMM
25λ	1.12	0.0752	0.6218
35λ	1.2	0.1058	0.721
50λ	1.36	0.1123	0.843

Table 1: CPU Times and RMS error of the hybrid algorithms

3.2 AWE

As an application of AWE to a full wave electromagnetic simulation, we consider the evaluation of the input impedance for a microstrip stub shielded in a metallic rectangular cavity as shown in figure

---

[1]To our experience, this error criterion gives a calculated pattern that is visually in excellent agreement with the exact. Typically, a 3 dB error criterion can lead to large deviations between calculated and exact data
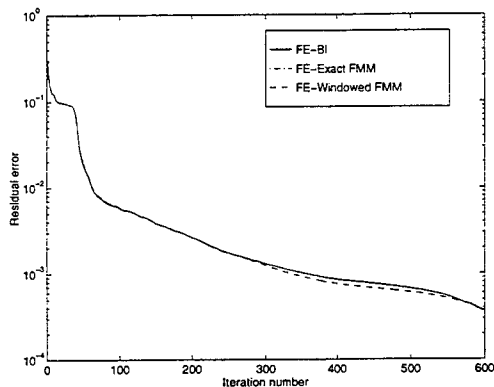
Figure 4: Convergence curves for the hybrid algorithms for the groove of width 25λ

5(a). The stub's input impedance is a strong function of frequency from 1–3 GHz and this example is therefore a good demonstration of AWE's capability.

The shielded cavity is $2.38cm \times 6.00cm \times 1.06cm$ in size and the microstrip stub resides on a $0.35cm$ thick substrate having a dielectric constant of 3.2. The stub is $0.79cm$ wide and $\lambda/2$ long at 1.785 GHz and we note that the back wall of the cavity is terminated by a metal-backed artificial absorber having relative constants of $\epsilon_r = (3.2, -3.2)$ and $\mu_r = (1.0, -1.0)$.

As a reference solution, the frequency response of the shielded stub was first computed from 1 to 3 GHz at 40 MHz intervals (50 points) using a full wave finite element solution. To demonstrate the efficacy and accuracy of AWE we chose a single input impedance solution at 1.78 GHz in conjunction with the 4th order and 8th order AWE to approximate the system response. Clearly the chosen number of poles or order of the expansion leads to different accuracies. As seen in Figure 5(b), the 4th order AWE representation is in agreement with the real and reactive parts of the reference input impedance solution over a 56% and 33% bandwidth, respectively. Surprisingly, the 8th order AWE representation recovers the reference solution over the entire 1-3 GHz band for both the real and reactive parts of the impedance. However, the CPU requirements for the 4th and 8th order approximations are nearly the same except for a few more matrix–vector products needed for the higher order expansion. The number of these operations are of the same order as that of the AWE expansion and are much smaller than the size of the original numerical system.

We conclude that the AWE representation is an extremely useful addition to electromagnetic simulation codes and packages for computing wideband frequency responses using only a few samples of the system solution.

References

[1] J.L. Volakis, J. Gong, and A. Alexanian. A finite element boundary integral method for antenna RCS analysis. *Electromagnetics*, 14(1):83–85, 1994.
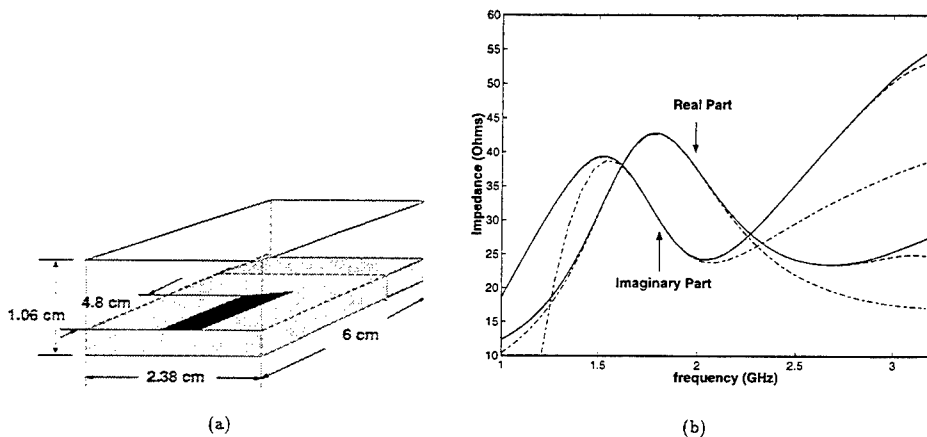
Figure 5: (a) Illustration of the shielded microstrip stub excited with a current probe (b) Real and imaginary parts of input impedance computations based upon the 4th and 8th order AWE implementations using a single point expansion at 1.78 GHz. Solid lines: exact reference data; Dashed lines: 8th order AWE results; Dash-doted lines: 4th order AWE results.

[2] J.-M. Jin and J.L. Volakis. TE scattering by a inhomogeneously filled aperture in a thick conducting plane. *IEE Proc., Part H*, 137:153–159, 1990.

[3] S. S. Bindiganavale and J. L. Volakis. A hybrid FEM-FMM technique for electromagnetic scattering. *IEEE Trans. Antennas and Propagat.*, 45(1):180–181, January 1997.

[4] N. Lu and J. M. Jin. Application of the fast multipole method to finite element-boundary integral solution of scattering problems. *IEEE Trans. Antennas and Propagat.*, 44(6):781–786, 1996.

[5] J. Gong and J.L. Volakis. AWE implementation for electromagnetic FEM analysis. *Electronics Letters*, 32(24):2216–2217, 1996.

[6] V. Rokhlin. Rapid solution of integral equations of scattering theory in two dimensions. *J. Comput. Phys.*, 86(2):414–439, 1990.

[7] R.J. Burkholder and D.H. Kwon. High-frequency asymptotic acceleration of the fast multipole method. *Radio Science*, 31(5), Sept-Oct 1996.

[8] C.C. Lu and W.C. Chew. Fast far field approximation for calculating the RCS of large objects. *Micro. Opt. Tech. Lett.*, 8(5):238–241, April 1995.

[9] S. S. Bindiganavale and J. L. Volakis. Guidelines for using the fast multipole method to calculate the RCS of large objects. *Micro. Opt. Tech. Lett.*, 11(4):190–194, March 1996.

A Hybrid Approach for Simulation of Log Periodic Antennas on an Aircraft

Brian E. Gray and Jacob J. Kim

Texas Instruments Incorporated
2501 West University Drive, MS 8019
McKinney, Texas 75070

Abstract

Antenna system performance is largely dependent upon resulting antenna radiation patterns. For this reason, the design of airborne antenna systems requires radiation analysis of antennas on an aircraft structure. However, it is a difficult task to predict the radiation patterns of practical antennas/arrays mounted on an airframe due to the limitations of current analysis techniques. Thus, a hybrid approach has been investigated to simulate complex antennas mounted on an aircraft utilizing both low and high frequency analysis techniques. This paper describes an efficient computer simulation of log periodic slot arrays when the arrays are mounted on a large curved surface such as an aircraft fuselage or wing. The approach utilizes both low and high frequency techniques but does not require modification of existing prediction codes.

Introduction

In recent years, many computer codes based on low frequency numerical techniques (i.e. MoM, FEM, FDTD, etc.) have been developed to predict the radiation characteristics of various antenna types. However, application of these methods is limited to antennas on a planar surface due to the large electrical size of realistic aircraft models. The Airborne Antenna Radiation Pattern (AIRCRAFT) code[1], which is based on the Uniform Geometrical Theory of Diffraction (UTD), has been widely used for predicting the radiation patterns of antennas mounted on a curved surface. The method takes into account creeping wave scattering in shadow regions and scattering by other aircraft structures. The antenna models used as sources for predicting radiation patterns with the AIRCRAFT code, however, are limited to a few basic antenna types due to the numerical techniques involved. This limitation means one can not directly model complex antenna shapes, such as log-periodic antennas, using the AIRCRAFT code. For this reason, a new simulation approach is investigated which utilizes equivalent sources to approximate the actual current distribution on the antenna for use as input to the AIRCRAFT code.

A wing mounted log periodic slot array (LPSA) operating from 2 to 18 GHz (9:1 bandwidth) is considered for analysis. Initially, a log-periodic dipole array

(LPDA) is analyzed, later being converted to an equivalent log periodic slot array using duality. As frequency varies over the given range, the current distribution on the arms of the antenna changes significantly. Low-frequency numerical techniques (i.e. MoM, FEM, FDTD) allow for analysis of these current distributions for the antenna on a planar surface. Once the current distribution of the antenna is analyzed at a particular frequency, the NEC/Basic Scattering Code (NEC/BSC) [2] is used to determine the equivalent source types for the AIRCRAFT code. The equivalent current sources and a computer generated aircraft geometry are then used by the AIRCRAFT code to predict the resulting radiation patterns. These patterns include the effects of creeping wave scattering in the shadow region as well as scattering from complex aircraft structures. A block diagram of the complete simulation process is illustrated in Figure 1. The methods used have been verified with both measurements and other numerical solutions.

Figure 1: Process for airborne LP slot array analysis .
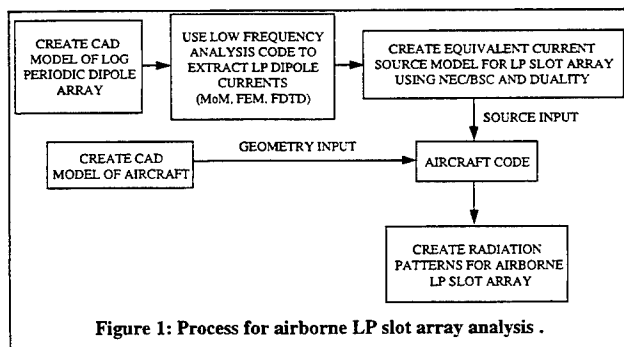
Computation of LP Antenna Currents

Figure 2: A LPDA designed to operate from 2 to 18 GHz.
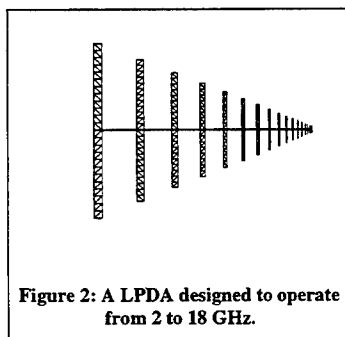
Figure 2 illustrates an example of a planar LPDA with 17 radiating elements designed for operation from 2 to 18 GHz. As a first step in the modeling process, the current distributions on the arms of the antenna are calculated using low frequency MoM codes [3,4]. The geometry is discretized as shown, allowing the relative current distribution in the center of each arm of the antenna to be easily computed. Since the current distributions vary with frequency, separate distributions must be

computed for each frequency. Figure 3 illustrates the calculated principal plane antenna patterns at 2 GHz using a MoM code and current maximum on each of the arms of the antenna. Upon inspection of Figure 3, it is seen that elements 13 through 16 (element 17 being the largest) are the active elements of the antenna since these elements are supporting the most current. Figure 4 illustrates the current distributions for each element of the antenna versus element length.
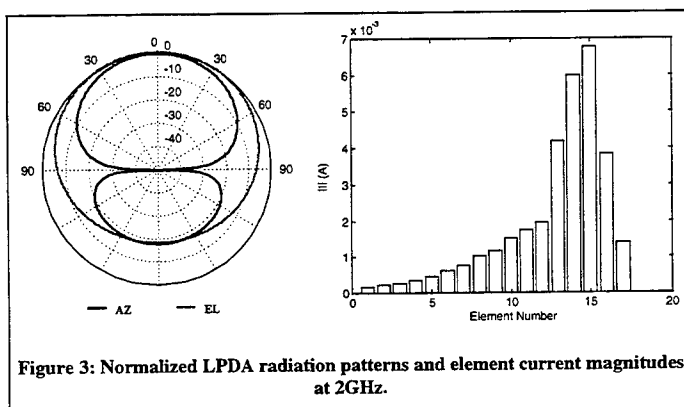
Figure 3: Normalized LPDA radiation patterns and element current magnitudes at 2GHz.

Equivalent Source Determination Using the NEC/BSC

Once current distributions are generated, the NEC/BSC is used to determine an equivalent source representation of the LPSA for use with the AIRCRAFT Code. Note that the LP dipole current (electric current) is used to determine the LP slot aperture current (magnetic current) by duality. The cosinusoidal behavior of the current on the active elements of the antenna allows for close approximation by the equivalent source representation of the NEC/BSC. Figure 5 illustrates a comparison of radiation patterns obtained from the MoM versus those obtained from the equivalent source model of the NEC/BSC at frequencies of 2, 10 and 18 GHz. The comparisons show that the patterns are not sensitive to small variations of the current in the apertures. Since the NEC/BSC is closely related to the AIRCRAFT Code, the equivalent current sources from the NEC/BSC may be used directly by the AIRCRAFT Code.

Application of the AIRCRAFT Code

For the purposes discussed here, the antenna is placed on the bottom of the wing of an aircraft. This is accomplished by modeling the wing as a composite

ellipsoid, with the fuselage approximated using flat triangular plates. Figure 6 illustrates a computer model of an aircraft with the antenna mounted on the wing. Figure 7 compares AIRCRAFT code predictions with measurements at a frequency of 2 GHz for a LPSA mounted in both inboard and outboard positions of the wing. The comparisons show close agreement in the angular section of interest. Note that measured data was taken for the LPSA on a full scale model aircraft whereas the computer aircraft model did not include aft aircraft and wing sections. Thus, one can not expect good agreement in the aft directions.

Conclusions

An efficient computer simulation technique has been developed for radiation analysis of practical antennas mounted on a large aircraft structure. The simulation technique utilizes low frequency analysis techniques for the antenna simulation, and high frequency techniques for modeling of equivalent sources. In addition, the technique includes scattering/creeping wave effects from aircraft structures. Extensive measurements have been taken to verify the accuracy of the hybrid simulation technique. All comparisons demonstrate close agreement between predictions and measurements in angular sections of interest. In this study, the technique was applied to a log periodic slot array mounted on the wing of an aircraft. However, the technique is also applicable to many other complex airborne antenna types. This technique can be used to determine optimum locations for complex airborne antennas as well as to evaluate the overall installed performance of practical antenna systems.

Acknowledgments

References

[1] W. D. Burnside, J. J. Kim, B. Grandchamp, R. G. Rojas, P. Law, "Airborne Antenna Radiation Pattern Code Users' Manual," Technical Report 716199-4, The Ohio State University ElectroScience Laboratory, Department of Electrical Engineering, September 1985.

[2] R.J. Marhefka, and J.W. Silvestro, "Near-Zone Basic Scattering Code User's Manual with Space Station Applications," Technical Report 716199-13, The Ohio State University ElectroScience Laboratory, Department of Electrical Engineering, March 1989.

[3] W. A. Johnson, D. R. Wilton, R. M. Sharpe, "PATCH Code Users' Manual", SAND87-2991, Sandia National Laboratories Technical Report, Albuquerque, New Mexico, May 1988.

[4] G. J. Burke, A. J. Pogio, "Numerical Electromagnetics Code (NEC) Method of Moments", Technical Document 116, Volume 2, Lawrence Livermore Laboratory, January 1981.
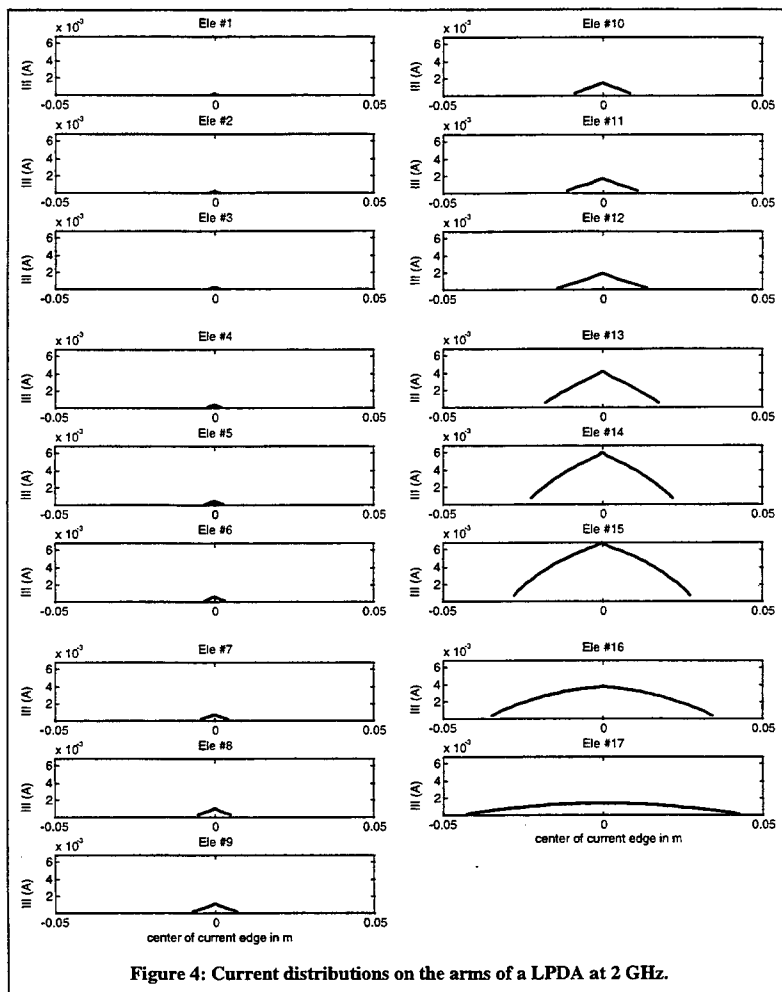
Figure 4: Current distributions on the arms of a LPDA at 2 GHz.

Figure 5: Comparison of normalized radiation patterns obtained from PATCH and NEC/BSC at 2, 10, and 18 GHz.

Figure 6: Computer representation of aircraft fuselage used to locate and create triangular PEC plate definitions.

Figure 7: Normalized measured VS calculated azimuth scans with LPSA on bottom of wing, vertical polarization, 2 GHz.
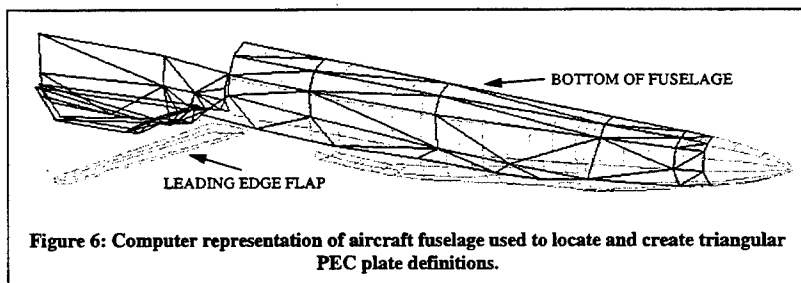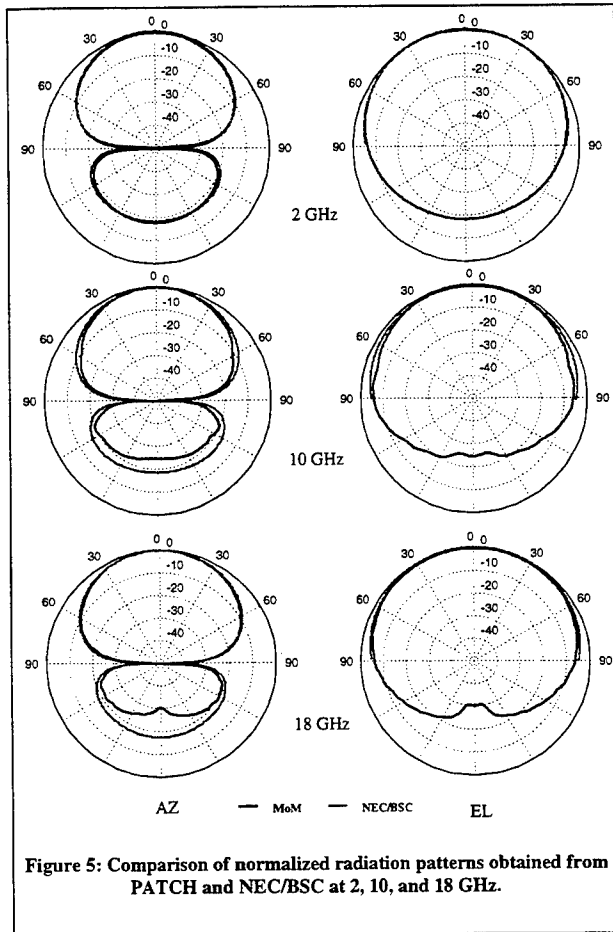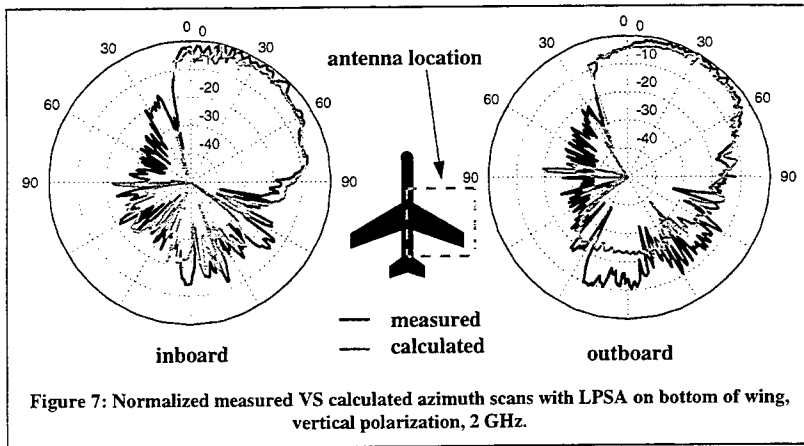
Duct RCS Computation Using a Hybrid Finite Element Integral Equation Approach

Y. C. Ma
Richard McClary
Maurice Sancer
George Antilla

Northrop Grumman Corporation
Military Aircraft Systems Division
Pico Rivera, California

Abstract

Several choices and issues related to the RCS computation of a duct are presented. In all cases the duct is embedded in a ground plane and the first choice is whether to model some of the exterior of the duct or to consider it flush with the ground plane. The latter choice was made. The next choice is which hybrid formulation to use for the interior of the duct. The case where the interior of the duct has a non-metallic liner is considered. For this situation the entire interior can be modeled with finite elements, or only the interior of the liner can be modeled with finite elements and then integral equations defined on the outer surface of the liner are necessary.

These two choices are discussed relative to two issues. The first is how readily can a code be written that allows the duct to be computed a segment at a time, and then have these analyses combined for the entire duct computation. The second issue related to this choice is the present and future availability of sparse and dense solvers. Running time, scaling information, and storage requirements are presented for existing and developing solvers that bear on this formulation decision.

It is recognized that for obtaining accurate RCS for electrically large $(\gg 10\lambda)$ ducts, a higher order field expansion may be required, but for purposes of discussing duct solution approaches, the first order expansions are assumed for simplicity.

I. Introduction

The discussion of this problem will be based on providing operation counts and memory requirements for alternative frequency domain approaches to compute duct RCS. In all cases, the duct will be considered to be embedded in a ground plane. Our SWITCH code can accommodate a very general duct with very general treatments; however, the operation count will be presented for a duct that has a square opening and a rectangular profile. The duct will be gridded with hexahedral elements and for this discussion, first order field expansions are assumed so that each element edge corresponds to one field unknown. The number of edges on each side of the square opening is N_{edg} and the depth of the duct requires $10N_{edg}$ edges.

Two basic formulations are compared without using the connection procedure. One considers that the entire interior duct is gridded with finite elements and this would permit a very general liner treatment. The other considers the duct to be perfectly conducting and a pure moment formulation is considered. In both cases the duct opening is treated with a moment formulation. Using standard solvers, the hybrid

finite element formulation which can compute the general liner case uses less computational resources than the perfectly conducting moment formulation.

The same kind of comparison is presented for two additional situations. One is the introduction of advanced iterative solvers and the other is the use of a connection procedure. The connection procedure is based on computing relevant quantities for the duct, one section at a time, and then combing results to compute the total duct RCS.

II. USD Solver

Recently, Professor Duc Nguyen of Old Dominion University has developed a mixed Sparse-Dense symmetrical-unsymmetrical equation solver (USD) for the SWITCH code. This solver is tailored to the matrix form generated by the hybrid finite element boundary integral formulation in SWITCH. In this section we will discuss how to connect the SWITCH code to the sparse portion of the solver and to apply it to predict the RCS of a duct embedded in an infinite ground plane. The connection procedure for ducts will be discussed.

The USD solver assumes the sparse sub-matrix is symmetric. To satisfy this requirement we have to assume the dielectric material is isotropic (or symmetric tensor anisotropic), but it can be inhomogeneous. The sparse solver of USD corresponds to solving the following finite element equation portion of SWITCH.

$$\mu_r^{-1} \iiint_V \left(\nabla \times \vec{E} \right) \cdot \left(\nabla \times \vec{W} \right) ds - k_0^2 \varepsilon_r \iiint_V \vec{E} \cdot \vec{W} ds = j k_0 \iint_S \vec{W} \cdot \left(\hat{n} \times \vec{H} \right) ds \tag{1}$$

Due to the isotropy of the dielectric material, μ_r and ε_r are scalars. Equation (1) leads to a system of N_e equations for N_e unknown amplitudes of the electric field $\vec{E}$. The solution of this system of equations leads to a relationship of the $\vec{E}$ field in terms of the surface $\vec{H}$ field. Let N_{hs} be the number of unknown amplitudes of the surface magnetic field at the duct aperture opening, equation (1) can be expressed in matrix form

$$A_{11} E = A_{12} H_s \tag{2}$$

In equation (2) A_{11} is a sparse symmetric matrix of $N_e * N_e$. If an edge is shared by at most 4 elements, then the number of non-zero elements per row is at most 33 independent of the problem size. A_{12} is a sparse non-square matrix of $N_e * N_{hs}$. Let $N_e = N_{ei} + N_{es}$, where N_{ei} is the number of unknown amplitudes of the interior electric field and N_{es} is the number of unknown amplitudes of the surface electric field (E_s), $N_{es} \leq N_{hs}$. The solution of (2) leads to a matrix relationship between the surface electric field and the surface magnetic field;

$$E_s = CR \, H_s \tag{3}$$

where CR is the computed relationship matrix of $N_{es} * N_{hs}$. It be should mentioned that even though CR is a much smaller matrix than A_{11} and A_{12}, the matrix A_{11} must be inverted in order to obtain the CR matrix.

Here, it is worth discussing the symmetric sparse equation solver developed by professor Nguyen and NASA Langley. A procedure similar to the Choleski factorization of a symmetric positive-definite

matrix has been developed for the factorization of a general symmetric matrix. After factorization the matrix A_{11} becomes

$$A_{11} = LDL^T \tag{4}$$

where L is a lower triangular matrix with unit value on the diagonal and L^T is the transpose of L and is an upper triangular matrix. D is a diagonal matrix. The number of arithmetic operations for the factorization of matrix A_{11} in equation (4) depends on the sparsity and the location of the non-zero elements of matrix A_{11} and it is difficult to quantify the number of operations in terms of the matrix size N_e. In general, the lower triangular matrix L is still sparse, but has more non-zero elements than matrix A_{11}. The additional non-zero matrix elements in L (which are zero in matrix A_{11}) are named "fill-in" terms. The reordering algorithms in the USD solver such as the modified minimum degree (MMD) or the nested dissection (ND) are to minimize the fill-in terms in L. Assuming the number of non-zero terms in L is 20 times the number of non-zero elements in A_{11} (based on experience), the number of arithmetic operations in factoring A_{11} is approximately (best guess based on conversations with Duc Nguyen)

$$N_{Fac} \sim 6000 N_e^{3/2} \tag{5}$$

With the same assumption of fill-in terms, the number of arithmetic operations to solve N_e unknown amplitudes for $\vec{E}$ in terms of N_s unknown amplitudes for $\vec{H}$ will be

$$N_{sol} \sim 680 N_e N_{hs} \tag{6}$$

The above procedure only leads to the CR matrix relating the aperture opening $\vec{E}$ field in terms of the aperture $\vec{H}$ field. An integral equation must be applied at the opening and its surroundings to solve for the surface $\vec{H}$ field in terms of the incident excitations.

Let us compare the USD sparse solver with the MOM based on purely integral equation approach. For the best scenario for the pure MOM approach we further assume the duct is metallic. For simplicity, consider a rectangular duct with N_{edg} edges in the x and in the y direction and $10 N_{edg}$ edges in the Z direction and Z=0 is the location of the infinite ground plane. The total number of patches for the MOM approach is $N_P^{MOM} = 41 N_{edg}^2 + N_{edg}^2$, and the total number of H unknowns is $N_h^{MOM} \sim 84 N_{edg}^2$ and the E unknowns is $N_e^{MOM} \sim 2 N_{edg}^2$. It leads to a dense matrix $86 N_{edg}^2$ by $86 N_{edg}^2$. If Gaussian elimination is applied to factor this matrix the number of arithmetic operations is about

$$N_{Fac}^{MOM} = \frac{1}{3} \left(86 N_{edg}^2 \right)^3 \approx 200000 * N_{edg}^6 \tag{7}$$

Since $N_{edg} \gg 1$, the solve time is much less than the factor time and will be ignored.

For the USD solver, the total number of $\vec{E}$ field unknowns is $30N_{edg}^3$ (ignoring unknowns set to 0 on metal surface) and the total number of aperture $\vec{H}$ unknowns is $2N_{edg}^2$. The number of arithmetic operations to factor the sparse matrix A_{11} is given in equation 5.

$$N_{Fac}^{USD} \sim 6000\left(30N_{edg}^3\right)^{\frac{3}{2}} \sim 10^6 N_{edg}^{4.5} \tag{8}$$

The number of arithmetic operations to solve the sparse matrix A_{11} with $2N_{edg}^2$ right-hand sides, using equation (6) is

$$N_{sol}^{USD} \sim 680 \cdot 30N_{edg}^3 \cdot 2N_{edg}^2 \sim 4*10^4 N_{edg}^5 \tag{9}$$

The total number of arithmetic operations for the USD solver to generate the CR matrix is

$$N^{USD} \sim 10^6 N_{edg}^{4.5} + 4*10^4 N_{edg}^5 \tag{10}$$

The number of arithmetic operations to substitute the CR matrix into the surface integral equation of the SWITCH code is

$$N_{sub} = \left(2N_{edg}^2\right)^3 = 8N_{edg}^6 \tag{11}$$

due to a matrix multiply. The number of arithmetic operations to factor the surface integral equation of SWITCH is $\approx \frac{1}{3}*8N_{edg}^6$. The total number of operations for the USD solver is

$$N_T^{USD} \approx 10^6 N_{edg}^{4.5} + 4*10^4 N_{edg}^5 + 11N_{edg}^6 \tag{12}$$

A practical problem of interest might be $N_{edg} = 100$. This problem corresponds to 30 million unknowns for SWITCH and corresponds to 860,000 unknowns for the MOM approach. The total number of arithmetic operations for the MOM approach is $2*10^{17}$ operations. For the USD solver it is $1.4*10^{15}$. The USD solver for the SWITCH code is 140 times faster than the Gaussian elimination method for the MOM approach even though the SWITCH code has many more unknowns than the MOM approach. The larger the problem size, i.e., the larger the N_{edg}, the faster the USD solver since the coefficient in front of N_{edg}^6 is much smaller for the USD solver than the Gaussian elimination for the MOM approach.

III. Dense Iterative Solver Approach

Advanced dense iterative solvers such as INTEL's Turbo Solver and Elegant Mathematic's LRA-CDENSE scale like the rank of the matrix to a power p where $p \le 2$. After descretization the moment equation at the mouth of the duct has the form

$$AE_s + BH_s = S \tag{13}$$

where A and B are dense square matrices and S is a source term constructed from the incident field. If (3) were substituted into (13) and the system was solved using LUD then the operation count would be as follows. The total number of unknowns is $4N_{edg}^2$. The substitution of (3) into (13) would be $0\left(N_{edg}^6\right)$. After the substitution into (13) we would have a square system of rank $2N_{edg}^2$ and the LUD solution would require $0\left(N_{edg}^6\right)$ operations.

If instead, (3) and (13) were solved simultaneously without substituting (3) into (13), and a dense iterative solver having an operation count corresponding to the square of the rank of the dense system, then the final operation count would be $0\left(N_{edg}^4\right)$.

The constants associated with these order arguments are complicated to obtain. The key question is when will the computer time be less than that for LUD. On a two processor CRAY C90 at the cross over is at approximately 15,000 unknowns. We expect the Turbo Solver will cross over a useful small number.

IV. Connection Procedure

The connection procedure was introduced by Wang and Ling[1] for a pure integral equation approach. The hybrid finite element integral equation approach to the connection procedure was introduced by us[2]. The idea is that the duct is divided into sections and selected quantities are computed for each section. The section specific quantities are then connected to compute the RCS of the entire duct.

If the connection procedure is applied to the USD solver, the number of arithmetic operations can be reduced. Assuming for the same duct geometry mentioned before and the connection procedure is applied 10 times. Each segment of the connection procedure requires the inversion of a sparse matrix of $3*10^6$ rank. The number of operations to factor this matrix is

$$N_{Facb}^{USD} \sim 6000 * \left(3*10^6\right)^{\frac{3}{2}} = 3*10^{13} \tag{14}$$

The solve time increases since the number of right-hand sides is $4 * N_{edg}^2$. The total solve time per connection procedure is

$$N_{solb}^{USD} = 680 * 3*10^6 * 4*10^4 = 8*10^{13} \tag{15}$$

In addition, there are additional operations due to the CR matrix substitution. The number of operations per substitution is

$$N_{sub}^{USD} = \left(2*10^4\right)^3 = 8*10^{12} \tag{16}$$

The total number of operations per connection scheme is approximately $1.2*10^{14}$. Since the connection procedure has to be applied 10 times, the total connection procedure is only a little faster than the one-step procedure which requires $1.4*10^{15}$ operations. It is conceivable however, that as the problem size gets bigger, the connection procedure will be faster than the one-step procedure. If the same connection procedure is applied to the pure MOM formulation, the number of unknowns per connection procedure

is $1.2*10^5$. The number of operations to factor the matrix is $N_{Facb}^{MOM} = \frac{1}{3}*\left(1.2*10^5\right)^3 = 5.76*10^{14}$. The number of operations to solve the matrix with 40,000 right-hand sides is

$$N_{solb}^{MOM} = \left(1.2*10^5\right)^2 * 40000 = 5.76*10^{14} \tag{17}$$

The CR matrix substitution requires $\left(2*10^4\right)^3 = 8*10^{12}$ substitutions. The total number of operations per connection scheme is $N^{MOM} = 1.16*10^{15}$. Since the connection scheme will be applied 10 times, the total of operations is $\approx 1.16*10^{16}$ which is still a factor of almost 10 slower than the USD solver.

The above comparisons are based on a metallic duct. For a RAM coated duct the number of operations based on SWITCH and the USD solver remains the same whereas the number of operations for the MOM approach will increase rapidly.

References

1. Wang, T.M. and Ling, H. (1991) Electromagnetic scattering from three-dimensional cavities via a connection scheme, I.E.E.E. Trans. Antennas Propagat. 39, 1505-1513.

2. Sancer, M.E., Antilla, G.G., Ma, Y.C., and McClary, R.L. (1997) Computational electromagnetics for radar cross section application (to be published by Kluiver academic publishers) presented at the 1996 CASE/LaRC workshop on computational electromagnetics.

Validation Studies of the GEMACS Computational Electromagnetics Code Using Measurement Data From the Transformable Scale Aircraft-Like Model (TSAM)

Donald R. Pflug and Timothy W. Blocher
Rome Laboratory/ERST
525 Brooks Road
Rome, NY 13441-4505
(315)330-4290
pflugd@rl.af.mil

INTRODUCTION

In order to determine accurately the radar cross section (RCS) of a modern high performance aircraft or the electromagnetic performance of antennas mounted on complex platforms, computational electromagnetics (CEM) tools of exceptional capability and speed are required. To obtain the computational accuracy for such CEM problems necessitates using a detailed geometry (usually CAD based) of the platform and/or antennas together with those equations and solvers which capture all the relevant physics and permit the timely determination of the CEM solution. CEM simulations computable in reasonable times require not only fast solution algorithms but also high performance workstations and, increasingly, massively parallel computing platforms. These requirements, taken together, have made CEM code validation much more difficult. Errors in system geometry, CEM equations or computational algorithms can be strongly dependent on each other and hard to determine. The situation is complicated further due to the complexity of CEM codes designed to treat real world problems. Such problems require large hybrid CEM codes that combine several CEM techniques. Validation of such codes is extremely difficult because the locations of errors in the code are extremely difficult to determine. These difficulties increase as CEM codes are modified periodically over their lifecycle and the algorithms upgraded. Such errors may not be under the control of or even known by the analyst.

During the past two years Rome Laboratory, Rome NY, has constructed a unique all metal test article, the Transformable Scale Aircraft-Like Model (TSAM) to obtain measured antenna pattern and isolation data to support the validation of large complex CEM codes. TSAM is a 1/20 scale model of a wide-bodied aircraft with simplified platform geometry on which are mounted six monopole antennas. The uniqueness of TSAM is in its changeable configuration and use of geometrically simple modular components. All components and antennas are removable allowing TSAM complexity to be modified incrementally. As platform complexity changes, computed results should track the measured results. The canonical component geometry (flat plates and elliptic/circular cylinders) minimizes geometry modeling error. Differences between measurement and simulation then are due to algorithm errors once measurement error is taken into account. Validation of algorithms within complex CEM codes using measurements on a variety of platform configurations allows the measurements to target errors in the CEM code more precisely.

This paper will report and discuss a series of validation measurements made on TSAM at Rome Laboratory in the 4-8 GHz. range involving seven different TSAM configurations. The measurements are being used to perform validation studies using the Rome Laboratory CEM program GEMACS (General Electromagnetic Model for the Analysis of Complex Systems) [1] as a testbed. Several deeply buried problems have been identified in GEMACS using TSAM data and a set of code fixes were developed. Two validation studies using selected TSAM measurements to validate parts of GEMACS will be discussed as examples of more precise uses of measurements in CEM code validation.

TRANSFORMABLE SCALE AIRCRAFT-LIKE MODEL (TSAM)

The Transformable Scale Aircraft-Like Model (TSAM) is a novel test article of variable configuration designed and constructed by Rome Laboratory, Rome NY for validating modern complex CEM codes. The TSAM design was chosen to represent approximately a 1/20 scale model wide bodied aircraft having a simplified structural geometry composed of canonical shapes. The full-up TSAM together with the disassembled component parts are shown below in Figure 1. The fuselage and engine nacelles are capped cylinders while the wings, stabilizers and pylons are flat plates. The reason for choosing the TSAM structural geometry simplicity is that it is meant to be a duplicate in both form and substance of the model in the CEM computer code. Code validation using TSAM measurements can then focus on the CEM algorithms since the geometry error is insignificant. A unique feature of TSAM is that the structural configuration is "transformable" by which is meant that major structural components can be removed or replaced at will. By correlating changes in the EM fields that couple between TSAM antennas or that are radiated or scattered from TSAM with the changes in TSAM configuration, the effects of structural complexity can be assessed and CEM code validation becomes more thorough and focused. If the computed EM properties do not track the measured properties as the TSAM configuration is changed, there are errors likely located within the CEM code modules associated with the configuration changes.
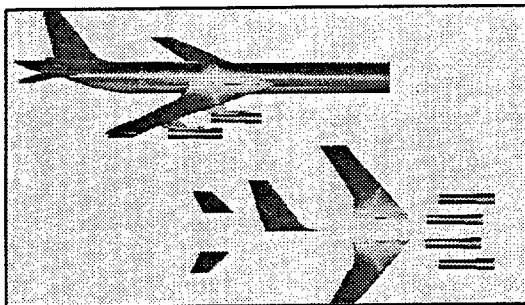
Figure 1. TSAM Assembled and with Removable Components

The TSAM structure is excited by six thin wire monopole antennas located at various points on the fuselage. A set of principal plane antenna patterns were measured for each monopole for seven different TSAM configurations in the 4-8 GHz frequency range. In addition antenna-to-antenna

coupling data was measured for all antenna pairs for the same set of TSAM configurations over the same frequency range. Because of the thin wire nature of the antennas and their small physical size (15 mm. long), the antenna locations on TSAM only are shown schematically below in Figure 2.
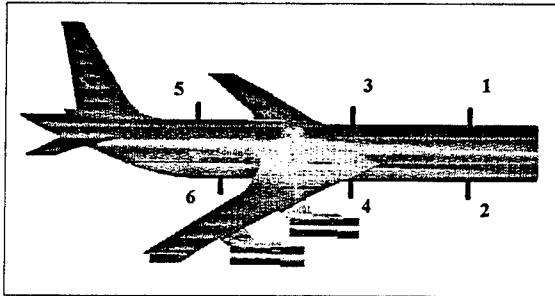
Figure 2. Monopole Antenna Locations on TSAM

All antenna radiation patterns and antenna-to-antenna coupling measurements were performed in the large anechoic chamber located in the Rome Laboratory Electromagnetic Environmental Effects Research Center. These data have been finalized and a final report detailing the complete TSAM measurement program and listing all measured antenna pattern and isolation data is in final preparation [2]. A new in-house program is currently underway at Rome Laboratory to begin using these data to perform validation studies on the Rome Laboratory GEMACS hybrid CEM code.

GEMACS

In this section a brief overview is given of those features and characteristics of GEMACS that are pertinent to validation studies using TSAM measured data. GEMACS is a frequency domain CEM code that uses the Method of Moments (MoM) and GTD/UTD high frequency asymptotic methods to analyze external EM problems, such as antenna-to-antenna coupling and the radiated or scattered fields from a complex platform, and uses finite difference techniques to analyze internal problems such as fields inside an enclosure and external-to-internal coupling. A hybrid solution is rigorously formulated in terms of admittance matrices characterizing all apertures in the platform through which electromagnetic energy can couple. All apertures are specified within the GEMACS code and their aperture admittances computed to permit a simultaneous solution of the external and internal problems simultaneously.

The current version of GEMACS runs to nearly 100K lines of code and includes graphics support as well as a graphical user interface (GUI) to facilitate platform and data input as well as display of the computed results. GEMACS has evolved over nearly 25 years and has been modified and upgraded many times. Validation studies have been performed on GEMACS using both measurements and computed results from other CEM codes but always for GEMACS considered as a single module. When disagreements between measurements and computation have arisen, it usually has been possible

to find the errors which manifest themselves in an obvious way. However, determining the origins of errors in GEMACS that give rise to "smaller" disagreements between computed and measured data has proved to be elusive. For these reasons GEMACS was deemed to be a good candidate CEM code to initiate validation tests using the TSAM data. An additional benefit is that GEMACS represents the surface geometry of the platform in terms of a set of cylinders and infinitely thin plates that are joined together to form an approximate platform computer model. Since the TSAM geometry is configured using a set of thin plates and cylinders for simplicity, the geometry modeling error is minimal between TSAM and the GEMACS computer model.

VALIDATION TEST CASES FOR GEMACS USING TSAM DATA

Two validation test cases will be described in this section as examples of how TSAM measured data can be used to pinpoint subtle problems in CEM codes that probably would not be found by the usual validation methods. During the construction of TSAM, some of the antennas inadvertently were mounted slightly off of the center line of the TSAM fuselage (butt line = 0). Although viewed initially as a problem, it was realized that this asymmetrical mounting of the TSAM antennas was an advantage since it would break the antenna symmetry of the problem slightly. When the GEMACS simulations were run with the above-mentioned antenna asymmetry present in the GEMACS data, it was found that GEMACS would assume that the bottom MoM wire segment of each off-center antenna was not connected to the GEMACS elliptic cylinder fuselage. This result was contrary to the GEMACS documentation and previous experience. The only way to ensure attachment was to place these segments along the one of the elliptic axes. The cause of this error was identified in the GEMACS code and corrected allowing wire segments to attach to arbitrary locations on cylinders as intended.
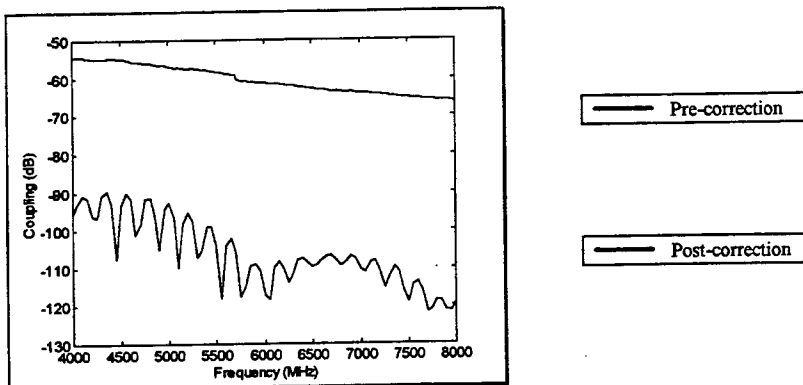
Figure 3. Coupling of Antenna 4 to Antenna 3 Before and After Blockage Correction (Configuration 2)

Several antenna isolation studies were performed using GEMACS computed antenna-to-antenna coupling data. During the studies, it was noted that the coupling between TSAM antenna 3 (top center) and antenna 4 (bottom center) was identical for both configuration 1 (antennas with fuselage only) and configuration 2 (antennas and fuselage with wings). These results were clearly in

error since the presence of the wings in configuration 2 should have created a blockage for the creeping wave. Upon investigation, it was discovered that, while GEMACS recognized the wings as being attached geometrically to the fuselage, GEMACS was not recognizing the wing plates as being a blockage to creeping waves. The results of this correction are shown above in Figure 3 and show a significant drop in coupling as expected.
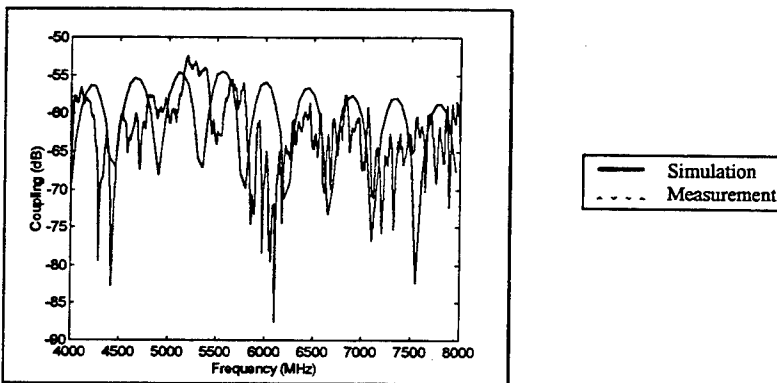
Figure 4. Antenna 3 to Antenna 4 coupling: GEMACS vs. TSAM Measurements (Configuration 7)

As a demonstration of these corrections and of a recently completed parallel processing version of GEMACS [3], a computation of the antenna-to-antenna coupling between antenna 3 and antenna 4 for configuration 7 (full configuration) was performed using the Rome Laboratory Intel Paragon. This computation utilized both the GTD/UTD and MoM modules of GEMACS, however, at this time only the GTD module had been parallelized. Using 128 nodes of the Paragon to compute 80 frequencies for each of the 5 receive antennas required 10 hours. The same simulation on a Sun SPARC 2 would have required 48 days. The simulation results are compared with measurements in Figure 3 and show generally good agreement.

CONCLUSION AND DISCUSSION

This paper has described the use of measured data from the TSAM test article at Rome Laboratory to perform initial validation studies using the Rome laboratory CEM code GEMACS as part of a recently initiated in-house validation program. Two initial validation studies on GEMACS were described concerning antenna placement with respect to the center line of the GEMACS model of TSAM and the antenna-to-antenna coupling algorithms within the code. These two validation studies uncovered two subtle problems within GEMACS. The first problem was that all antennas mounted on the GEMACS geometry model were treated in the code as being unattached if they were mounted asymmetrically with respect to the platform axis despite the intent of the code and the statements in the code documentation. This problem probably originated as a result of code modification over the years. In the second problem the antenna-to-antenna coupling algorithm in GEMACS did not recognize the platform wings as being attached to the cylindrical fuselage despite the fact that in the geometric model the wings were recognized as being attached. The effect manifested itself by allowing the creeping

wave between antennas to couple even though the wings would block the wave. The problem in the code was located, although deeply buried, and fixed. It is to be emphasized that the comparison of computed GEMACS results to measured TSAM data was key in identifying the code bugs in a timely manner. More extensive validation studies of GEMACS are now in progress and future plans envision performing similar studies on the Finite Element/APATCH hybrid code recently developed under a continuing Rome Laboratory contract [4]. In addition additional measurements on TSAM are planned and a new generation TSAM test article is being designed for future construction.

REFERENCES

1. E. L. Coffey III and D. L. Kadlee, *General Electromagnetic Model for the Analysis of Complex Systems (GEMACS), Version 5.0*, Advanced Electromagnetics, RADC-TR-90-360, Volumes I, II, III, December 1990.

2. *Transformable Scale Aircraft-Like Model (TSAM) Antenna Measurement Program*, RL/ERS-96-027, Volumes 1-3, Rome Research Corporation, in Preparation.

3. Developed by the Ultra Corporation under RL SBIR phase II contract F30602-95-C-0221.

4. Developed by Mission Research Corporation, DEMACO Corporation and the University of Michigan under RL SBIR phase II contract F30602-93-C-0036.

A Combination of Current– and Ray–Based Techniques for the Efficient Analysis of Electrically Large Scattering Problems

U. Jakobus and F. M. Landstorfer

Institut für Hochfrequenztechnik. University of Stuttgart,
Pfaffenwaldring 47. D-70550 Stuttgart. Germany

Abstract

We extend the current–based method of moments/physical optics hybrid method by the ray–based diffraction theory (UTD). In this paper emphasis is placed on the general methodology of the new hybrid formulation as well as on some details concerning the coupling between the different regions. Special care is taken when electromagnetic sources are located close to the UTD–region or even directly on its surface. An example is given which shows the accuracy of the hybrid approach and the achievable reduction in memory and computation time.

1 Introduction

Problems concerning radiation and scattering with perfectly conducting bodies are frequently analyzed by the method of moments (MoM). This method is a current–based technique, since in the first step the unknown currents are solved for, and only in the second step the electromagnetic fields are computed. For high frequency problems, however, the MoM suffers from the fact that its memory requirement grows proportional to f^4 (f is the frequency) and, depending on the algorithm used to solve the system of linear equations, the CPU time is proportional to $f^{4..6}$.

The authors of this contribution have already proposed a current–based hybrid method combining the MoM with Physical Optics (PO) [1, 2] or other asymptotic current representations [3, 4], e.g. Fock currents. In the asymptotic limit, both memory and CPU time of this hybrid method show a f^2 dependency, which represents a major computational advantage as compared to the conventional MoM.

However, for very large geometries (in terms of wavelengths), this dependency proportional to f^2 may still be too high. In this case a combination of the current–based MoM/PO with ray–based techniques such as UTD (uniform theory of diffraction) might be a possible solution, since for the UTD formulation memory and CPU time requirement are essentially frequency independent, i.e. proportional to f^0.

Combinations of the MoM with diffraction theory have already been presented by several authors (e.g. Refs. [5, 6, 7, 8]), and an implementation is also available with the computer code GEMACS [9]. The advantage of our proposal is, however, that we plan to use not only MoM/UTD but also asymptotic currents (e.g. PO, Fock), thus yielding a far more flexible computational tool as will be described in Section 2.

Since the PO/MoM hybrid method has already been presented in detail in the literature (e.g. Ref. [1]), this paper concentrates on the extension by the UTD. Some of the details concerning the addition of the UTD to the already existing PO/MoM hybrid approach are outlined in Section 3.

2 Description of the hybrid method combining MoM, PO and UTD
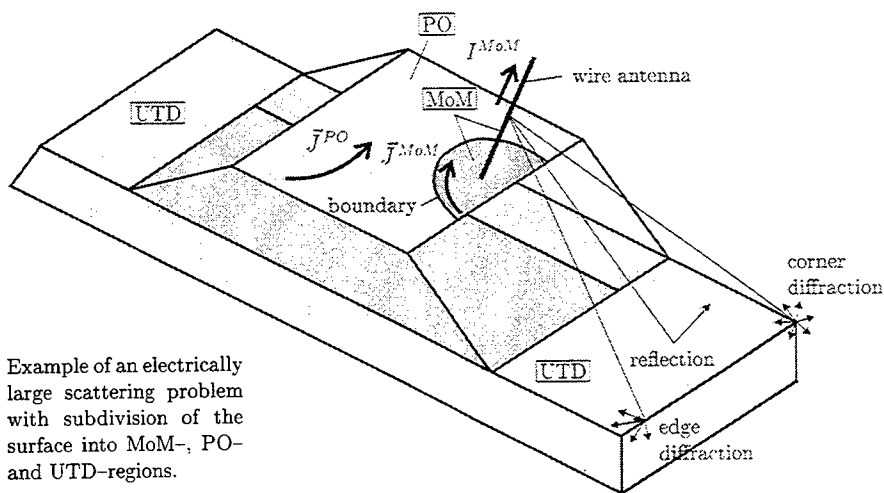
Fig. 1: Example of an electrically large scattering problem with subdivision of the surface into MoM-, PO- and UTD-regions.

An example for a general, three-dimensional scattering body consisting of perfectly conducting metallic surfaces and wires is depicted in Fig. 1. This model of a mobile communications antenna radiating in the GHz range and mounted on top of a car shall serve as an example to explain the general methodology of the proposed hybrid method.

We have defined several regions in Fig. 1. The electric line current I along the wire antenna is calculated by the MoM since no asymptotic high frequency expressions exist for currents on electrically thin wires. Hence, this line current is denoted as I^{MoM}.

If one is interested in accurate values of the input impedance of the antenna, it is usually necessary to model the area close to the feeding zone of the antenna also very accurately, i.e. this region should also be treated by the MoM. In our example in Fig. 1 the dark area around the antenna base with the surface current density $\vec{J}^{MoM}$ also represents part of the MoM-region.

The line labeled "boundary" in Fig. 1 separates this MoM–region from the remaining surface of the roof of the car. As mentioned in the introduction, we have already implemented a hybrid method combining the MoM with asymptotic current expressions such as PO or Fock currents. The advantage of such a current–based approximation is, that a continuous current flow can be modeled across the boundary, see for instance Fig. 2 in Ref. [10]. Therefore we suggest to use the PO approximation $\vec{J}^{PO}$ for the remaining part of the roof, possibly with correction terms based on fringe currents to take the effect of the edges into account [1].

The extension of the already existing MoM/PO hybrid method by the UTD is proposed in this paper for electrically large scatterers. The main reason for this is the CPU–time dependency, see the discussion in the introduction. Therefore all remaining surfaces of the car (e.g. hood, fenders and trunk) are assigned to the UTD–region. We now have to take effects such as reflection, edge and corner diffraction into account, where the sources are current elements radiating in the MoM– or PO–region. Some of the resulting rays are depicted in Fig. 1 for illustration.

In the remaining part of the paper, we will concentrate on the implementation of the coupling between the MoM– and the UTD–region. The coupling between the PO– and the UTD–region has not been implemented yet. We do not expect any difficulties for a geometry as shown in Fig. 1 where there is no direct boundary between these two regions. However, it remains a challenging task to solve the problem when the current–based PO and the ray–based UTD shall be applied to two adjacent regions with a common boundary.

3   Implementation of the coupling between MoM and UTD

The hybrid method has been implemented in such a way that the coupling between the UTD– and the MoM–region is fully taken into account, i.e. the currents in the MoM–region will change when for instance the position of some structures in the UTD–region is modified.

In the MoM–region we may have metallic wires and surfaces. The wires are subdivided into electrically small wire segments and we use triangular basis functions for the line current I^{MoM}.
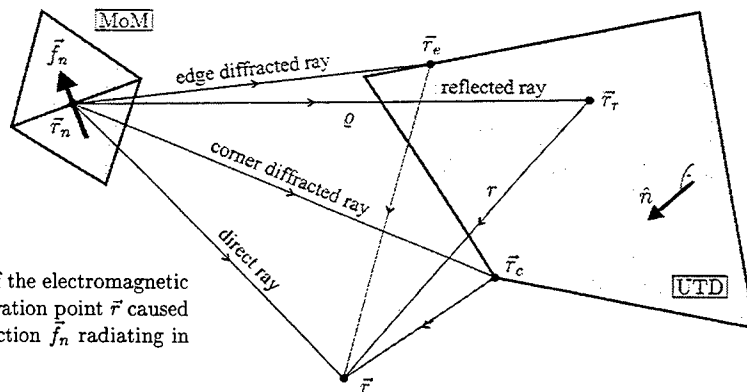
Fig. 2: Determination of the electromagnetic field at an observation point $\vec{r}$ caused by one basis function $\vec{f}_n$ radiating in the MoM–region.

Metallic surfaces are subdivided into triangular patches and the vectorial rooftop basis functions $\vec{f}_n$ according to Rao, Wilton and Glisson [11] are applied. In Fig. 2 we have symbolically depicted two adjacent triangular patches in the MoM–region and the basis function $\vec{f}_n$ defined on these two triangles. If we now want to calculate the electromagnetic field strength radiated by this basis function in free space (i.e. no UTD–region present) at an arbitrary observation point $\vec{r}$, then we apply the usual equations. e.g. for the electric field strength

$$\vec{E}(\vec{r}) = \vec{\mathcal{E}}\left\{\vec{f}_n\right\}(\vec{r}) = -\frac{j}{4\pi\varepsilon\omega} \vec{\nabla} \iint\limits_{A'} (\vec{\nabla}'_A \cdot \vec{f}_n(\vec{r}')) \cdot \frac{e^{-j\beta|\vec{r}-\vec{r}'|}}{|\vec{r}-\vec{r}'|} dA'$$

$$-j\omega\frac{\mu}{4\pi} \iint\limits_{A'} \vec{f}_n(\vec{r}') \cdot \frac{e^{-j\beta|\vec{r}-\vec{r}'|}}{|\vec{r}-\vec{r}'|} dA'. \tag{1}$$

The surface of the two triangles represents the domain of integration A', and $\beta = \frac{2\pi}{\lambda}$ denotes the wavenumber. As an abbreviation we have introduced the operator notation $\vec{\mathcal{E}}\left\{\vec{f}_n\right\}(\vec{r})$ which shall in the following always represent the electric field strength at the location $\vec{r}$ radiated by the basis function $\vec{f}_n$ and calculated by means of the exact relation (1) in free space.

If we now face a situation as depicted in Fig. 2 where the basis function $\vec{f}_n$ radiates in the presence of other structures representing the UTD–region, then the total field strength at the observation point $\vec{r}$ is the superposition of different ray contributions. We consider direct, reflected, edge and corner diffracted rays (UTD according to Refs. [12, 13]) as well as multiple reflections or combinations of multiple reflections and diffractions. But currently we do not take creeping waves on curved surfaces into account, therefore the formulation is limited to geometries in the UTD–region composed of flat polygonal plates or wedges.

The total electric field strength at the observation point $\vec{r}$ in Fig. 2 is given by

$$\vec{E}(\vec{r}) = \delta \cdot \vec{\mathcal{E}}\left\{\vec{f}_n\right\}(\vec{r}) + \vec{E}^{UTD}. \tag{2}$$

The first term corresponds to the direct ray. i.e. we calculate the scattered field with the exact equation (1), but we have to introduce a coefficient δ in order to account for shadowing effects of the direct ray with δ being zero or one. The second term $\vec{E}^{UTD}$ represents the sum of all the other ray contributions mentioned above.

Expression (2) for the total field is used not only when we calculate the radiated near- and far-fields, but also when constraining the boundary condition $\vec{E}_{tan} = 0$ on the perfectly conducting surfaces in the MoM–region leading to an integral equation, so that the coupling between the MoM– and UTD–region is considered when the currents in the MoM–region are solved for.

Since in some cases the basis function $\vec{f}_n$ in the MoM–region might be quite close in space to the UTD–region, the classical reflection of a spherical wavefront at a flat plate based on Geometrical Optics (GO) given by

$$\vec{E}_r^{UTD}(\vec{r}) = \vec{\mathcal{E}}\left\{\vec{f}_n\right\}(\vec{r}_r) \cdot \vec{\vec{R}} \cdot \frac{\varrho}{r+\varrho} \cdot e^{-j\beta r} \tag{3}$$

must be replaced by the mirror principle. In eqn. (3) $\vec{r}_r$ denotes the reflection point on the reflecting surface, see Fig. 2. $\vec{\vec{R}}$ is the dyadic reflection coefficient and the two distances ϱ and r

are defined according to Fig. 2. In the near–field of the radiating basis function $\vec{f}_n$ we also have higher order terms present which decay proportional to $(r + \varrho)^{-2}$ or $(r + \varrho)^{-3}$, i.e. faster than the factor $(r + \varrho)^{-1}$ in eqn. (3) allows.

Therefore, we have replaced the classical GO reflection according to eqn. (3) by the mirror principle

$$\vec{E}_r^{UTD}(\vec{r}) = \left(2\,\hat{n}\hat{n} - \vec{\vec{I}} \right) \cdot \vec{\mathcal{E}} \left\{ \vec{f}_n \right\} (\vec{r}^*) \tag{4}$$

with the unit dyad $\vec{\vec{I}}$ and the mirrored observation point $\vec{r}^* = \vec{r} - 2 \cdot [\hat{n} \cdot (\vec{r} - \vec{r}_r)] \cdot \hat{n}$. The unit vector $\hat{n}$ denotes the surface normal, see Fig. 2. As opposed to eqn. (3), where the scattered field $\vec{\mathcal{E}} \left\{ \vec{f}_n \right\} (\vec{r}_r)$ has been computed with the aid of eqn. (1) at the reflection point $\vec{r}_r$, i.e. at a distance ϱ to the source, in eqn. (4) we now compute the field at $\vec{r}^*$ with the correct distance $\varrho + r$, so that the higher order terms are accurately taken into account.

In eqn. (4) the field strength radiated by the basis function $\vec{f}_n$ is required at location $\vec{r}^*$. For the diffraction we require the field at the diffraction points $\vec{r}_e$ or $\vec{r}_c$, respectively, see Fig. 2. It should be noted, that in each of these cases we calculate the field strength in an exact manner directly with eqn. (1), i.e. we avoid the introduction of equivalent point sources as is done for instance in Ref. [8]. Only for ray–tracing purposes we do assume that the basis function $\vec{f}_n$ behaves like a point source located at the center of the edge $\vec{r}_n$ between the two triangles.

The example given below in Section 4 demonstrates, that the replacement of eqn. (3) by eqn. (4) is an absolute necessity when the basis function in the MoM–region is close to the UTD–region. Only one drawback results from this replacement: At the reflection shadow boundary the GO field has a discontinuity, which is removed by the edge diffracted contribution. This is only exact for the classical GO (3), however if we use eqn. (4) instead, there remains a very small discontinuity, which is, however, tolerable in most cases, see the example below.

For quite a number of geometrical structures it is necessary to model wire elements which are attached to surfaces. One possibility with a MoM–region around the antenna base has already been suggested in Fig. 1. But it is also possible to attach the wire antenna, which is always part of the MoM–region, directly to the UTD–region as indicated in Fig. 3. In this case the distance between MoM– and UTD–region is even zero, but due to the modified treatment of reflections by the mirror principle in eqn. (4) this does not pose any problem as long as there remains a certain distance to the edges of the plate (diffraction).

Fig. 3: Attachment of a wire to a surface.

The only modification necessary is the following: Metallic wires are subdivided into electrically small segments and we apply overlapping triangular basis functions g_n along the wire surface. These basis functions always force the current to be zero at the wire ends. Hence we have to introduce a new basis function at the attachment point, which is simply defined as half of a regular basis function g_n, see the dark shaded triangle depicted at the lower antenna end in Fig. 3.

4 Example

Fig. 4: $\frac{\lambda}{2}$–dipole antenna located in front of a reflecting plate.

A simple example is depicted in Fig. 4. A $\frac{\lambda}{2}$–dipole antenna is located at a distance d in front of a square reflecting plate with a side length of 2λ. This example demonstrates the application of the hybrid method, where the current along the wire antenna is calculated by means of the MoM. and the influence of the square plate is accounted for by PO or UTD. For the purpose of comparison, a calculation based on an application of the MoM alone has also been carried out (reference solution).

Fig. 5 shows the variation of the real and imaginary part, respectively, of the input impedance Z of the dipole antenna as a function of its normalized distance $\frac{d}{\lambda}$ to the reflecting plate. The solid line represents the reference solution based on an application of the conventional MoM to the entire structure. i.e. dipole antenna and plate. The dashed curve is the result of the MoM/PO hybrid method, and the dotted and dash–dotted lines depict the impedance resulting from the MoM/UTD hybrid formulation with the reflection treated by eqns. (3) and (4). respectively. It is obvious that for distances of about $d < 0.5\lambda$ the application of the classical GO according to eqn. (3) leads to quite inaccurate results (dotted curve), while the other three methods are in excellent agreement even for very small distances d.

The horizontal radiation pattern for a distance of $d = \frac{3}{4}\lambda$ is depicted in Fig. 6. Again we can observe an excellent agreement between the results of the two hybrid methods and the reference solution.

The MoM/UTD hybrid solution in Fig. 6 is based on eqn. (4). It has already been mentioned in Section 3 that replacing eqn. (3) by eqn. (4) leads to small discontinuities at the reflection shadow boundaries. Here for this example the reflection shadow boundaries can be found at $\varphi = 216.9°$ and $\varphi = 323.1°$. These locations are indicated in Fig. 6 by two small circles, but the discontinuities of the dash–dotted curve are so small that they are hardly visible.

	convent. MoM	hybrid MoM/PO	hybrid MoM/UTD
memory (KByte)	2604	585	15
CPU–time (sec)	79	47	19

TABLE 1: Memory and CPU–time for the example of a dipole antenna in front of a reflecting plate.

Table 1 compares memory requirement and CPU time on a PC for the three formulations. The superiority of the two proposed hybrid approaches becomes obvious, even for this example with a relatively small (in terms of wavelength) scatterer.
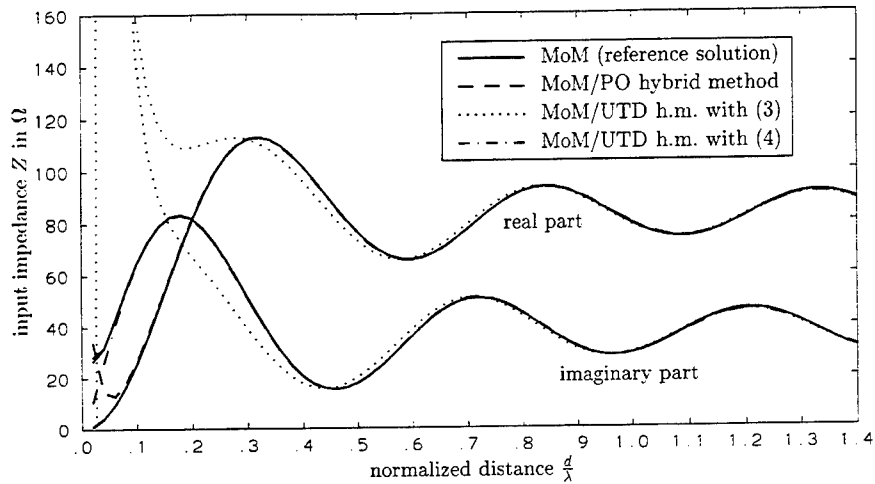
Fig. 5: Input impedance Z of the dipole antenna in front of a square plate as a function of the normalized distance $\frac{d}{\lambda}$.
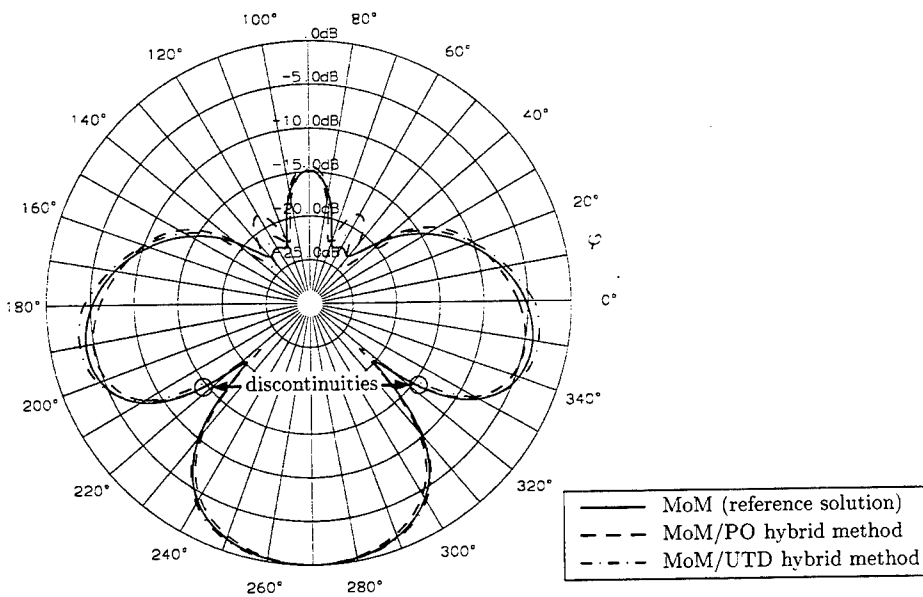
Fig. 6: Horizontal radiation pattern in the plane $\vartheta = 90°$ for a distance $d = \frac{3}{4}\lambda$.

5 Conclusions

We have presented the idea of a hybrid method combining MoM, PO and UTD. Even though the coupling between PO und UTD has not been implemented yet, the MoM/PO and MoM/UTD combinations already result in very useful formulations as confirmed by an example.

References

[1] U. Jakobus and F. M. Landstorfer, "Improved PO–MM hybrid formulation for scattering from three-dimensional perfectly conducting bodies of arbitrary shape," *IEEE Transactions on Antennas and Propagation*, vol. 43, pp. 162–169, Feb. 1995.

[2] U. Jakobus and F. M. Landstorfer, "Current–based hybrid moment method analysis of electromagnetic radiation and scattering problems," *ACES Journal*, vol. 10, pp. 38–46, Nov. 1995. Special Issue on Advances In the Application of the Method of Moments to Electromagnetic Radiation and Scattering Problems.

[3] U. Jakobus and F. M. Landstorfer, "Improvement of the PO–MoM hybrid method by accounting for effects of perfectly conducting wedges," *IEEE Transactions on Antennas and Propagation*, vol. 43, pp. 1123–1129, Oct. 1995.

[4] U. Jakobus and F. M. Landstorfer, "Hybrid MM–PO–Fock analysis of monopole antennas mounted on curved convex bodies," in *Conference Proceedings of the 12th Annual Review of Progress in Applied Computational Electromagnetics, Monterey*, pp. 101–108, Mar. 1996.

[5] G. A. Thiele and T. H. Newhouse, "A hybrid technique for combining moment methods with the geometrical theory of diffraction," *IEEE Transactions on Antennas and Propagation*, vol. 23, pp. 62–69, Jan. 1975.

[6] W. D. Burnside, C. L. Yu, and R. J. Marhefka, "A technique to combine the geometrical theory of diffraction and the moment method," *IEEE Transactions on Antennas and Propagation*, vol. 23, pp. 551–558, July 1975.

[7] E. P. Ekelman and G. A. Thiele, "A hybrid technique for combining the moment method treatment of wire antennas with the GTD for curved surfaces," *IEEE Transactions on Antennas and Propagation*, vol. 28, pp. 831–839, Nov. 1980.

[8] H.-F. Harms and K.-H. Gonschorek, "The use of point sources to rebuild piecewise linear current basic functions in the combination of MOM and UTD," in *URSI International Symposium on Electromagnetic Theory, St. Petersburg*, pp. 289–291, May 1995.

[9] D. L. Kadlec and E. L. Coffey, "General electromagnetics model for the analysis of complex systems (GEMACS)," tech. rep., Rome Air Development Center, Sept. 1983.

[10] U. Jakobus and F. J. C. Meyer, "A hybrid physical optics/method of moments numerical technique: Theory, investigation and application," in *IEEE AFRICON'96, 4th Africon Conference in Africa, Stellenbosch*, pp. 282–287, Sept. 1996.

[11] S. M. Rao, D. R. Wilton, and A. W. Glisson, "Electromagnetic scattering by surfaces of arbitrary shape," *IEEE Transactions on Antennas and Propagation*, vol. 30, pp. 409–418, May 1982.

[12] R. G. Kouyoumjian and P. H. Pathak, "A uniform geometrical theory of diffraction for an edge in a perfectly conducting surface," *Proceedings of the IEEE*, vol. 62, pp. 1448–1461, Nov. 1974.

[13] F. A. Sitka, W. D. Burnside, T.-T. Chu, and L. Peters, "First-order equivalent current and corner diffraction scattering from flat plate structures," *IEEE Transactions on Antennas and Propagation*, vol. 31, pp. 584–589, July 1983.

Field Computation for Large Dielectric Bodies by the PPP Method

M. S. Abrishamian, N. J. McEwan and R. A. Sadeghzadeh
Department of Electronics and Electrical Engineering
University of Bradford, UK

1-Introduction

The PPP method [1], [2] is a novel numerical technique for electromagnetic scattering problems. For modern computers with generous memory capacity, it is claimed to run substantially faster than a moment method. It can also if needed be run at low speed with extremely low memory requirements. However, following an initial exposition of the technique [1] very little further work based on it appears to have been reported, whether by its originators or others. The purpose of the present paper is to present some new results showing the method's successes and limitations for electrically larger bodies than previously treated.

2-Outline of the Method

As originally expounded in [1] and [2], the PPP method increases the constitutive parameters of the scatterer in small steps from $\sigma = 0.$, $\varepsilon_r = 1.0$ to their actual value. At each stage the field exciting the scatterer is approximated by the value obtained in the previous step, and the first step corresponds to the Born approximation. At the end of computation, and possibly at intermediate stages, iteration may also be performed with constant values of the parameters [1]. It is noted in [1] that stability may be improved by removing the self or diagonal terms from the coupling matrix.

The simplest way of performing the described PPP procedure is to approximate the domain of the body by means of N small homogeneous cubes, and to assume the complex polarisation vector P to be constant in every cube. We thus obtain the following iteration scheme:

$$P_j^{(1)} = \varepsilon_0 \Delta \chi_e E_0 \qquad j=1,2,...,N \qquad (1)$$

$$P_j^{(k)} = \frac{\varepsilon_0 k \Delta \chi_e}{1 - \varepsilon_0 k \Delta \chi_e a_{self}} \left[E_0 + \sum_{i=1, i \neq j}^{N} (E_d)_{ji}^{(k-1)} \right] \qquad (2)$$

where

$$E_d^{(k-1)} = \frac{1}{\varepsilon_0}\left(\int_v \rho^{(k-1)} G(R) r_0 dv + \int_v \sigma^{(k-1)} G(R) r_0 \right)$$

(3)

$$-j\omega \mu_0 \int_v J^{(k-1)} g(R) dv$$

and $r_0 = R/R$, k=2,3,...,n. The volume and surface charge densities $\rho^{(k-1)}$, $\sigma^{(k-1)}$ are computed by means of $\sigma^{(k-1)} = P^{(k-1)}.n$, $\rho^{(k-1)} = -\Delta.P^{(k-1)}$, respectively, and the total current density is given by $J^{(k-1)} = j\omega P^{(k-1)}$, and g(R) and G(R) can be computed by $g(R) = \dfrac{e^{-j\beta R}}{4\pi R}$, $G(R) = -\dfrac{dg(R)}{dR} = \dfrac{1+j\beta R}{R} g(R)$. In these equations β is the free-space phase coefficient, $\beta = \omega\sqrt{(\varepsilon_0 \mu_0)} = 2\pi/\lambda$. In this model the charges are represented by surface charges over the sides of the small cubes. The electric field due to the equivalent source is evaluated as described in [1].

3-Test Problem

The PPP method has been evaluated for a problem for which a reliable solution can be obtained by an alternative method, namely a half-wavelength dipole antenna placed near a dielectric sphere. The current distribution in the antenna is assumed to be sinusoidal and to be unaffected by the sphere, with unit rms. current at its centre. As obtained previously [5], the problem can be solved analytically by spherical wave expansion(generalised Mie method). The co-ordinate system has the sphere centre at x=y=z=0; the antenna is parallel to the z axis and its centre lies on the positive x axis at 3 cm from the surface of the sphere. Comparison is made on the basis of the far-field radiation pattern of the whole structure in the x-y plane, and of the rms. total electric field intensity inside the scatterers. We use a sphere which is formed from many cubes, as shown in Figure (1). In this way we can compare our PPP results with Mie method results.

4-Numerical Results

Fortunately the results are found to be in excellent agreement provided the dielectric electrical parameters are not too large. The number of iterations depends on the size and electrical parameters of the dielectric (σ,ω). We have used these empirical equations

$$T_g = \left| \varepsilon_r - \frac{(j\sigma)}{(\omega \varepsilon_0)} \right|$$

(4)

$$D = \frac{R_s}{9 T_g}$$

(5)

$$NIT = \frac{30 R_s T_g}{\lambda} \qquad (6)$$

where T_g is the electrical parameter of the sphere, R_s the radius of the sphere, D the side of each discrete cube and NIT the number of iterations. Five final additional iterations with constant permittivity were performed in order to improve the accuracy of calculation by allowing the field to "catch up". For frequency 1.GHz, and a dielectric sphere of 3λ diameter, the Figure (2) shows there is near perfect agreement between Mie(analytical method) and PPP numerical method. We also calculated the perturbation in input impedance of the thin half-wave dipole antenna as shown in Figure (4).

5-Comparison with the MoM

For comparison of MoM and PPP methods from the viewpoint of time and memory, we choose a sphere with the parameters: Radius=5.cm, permittivity $\varepsilon = 3.$, conductivity $\sigma = 0.0$ and number of cells=485 so that the side of each cubic cell is $d = \frac{\lambda}{30}$. We use the MoM formulation of [4] with Gaussian elimination method for solution of the MoM matrix without using any symmetry. The comparison is shown in table[1]. The calculation was ran on a SUN SPARC SERVER 20/712 computer system.

6-Convergence Properties

The conditions for the PPP method to converge have not been clearly defined by the method's originators. The method has the same convergence properties as solving the general equation:

$$X = AX + B \qquad (7)$$

by the iteration scheme:

$$X_n = A X_{n-1} + B \qquad (8)$$

which is equivalent to:

$$(I - A)^{-1} = \sum_{k=0}^{\infty} A^k \qquad (9)$$

It is readily shown that series (9) is convergent if the largest eigenvalue of the operator A has modulus less than unity. This clearly sets an upper limit on the permittivity and the electrical size of the scatterer.

If operator A has eigenvalue unity, which must happen at a complex value of the frequency, the Equation (7) has a non-zero solution for B=0, corresponding to an unforced resonance of the scatterer. For a large permittivity scatterer, this will imply that an eigenvalue of modulus near unity occurs at a neighbouring real value of frequency. It therefore appears that the method is fundamentally limited by keeping the calculation frequency below the first natural resonance of the scatterer.

It can be shown that the convergence situation can be improved somewhat by subtracting a multiple of the unit matrix from operator A, and inserting a suitable scalar response coefficient in the equation. As seen in Equation (2), the removal of the self coupling, as proposed in [1], is the special case of this which sets the diagonal elements of A to zero. A slightly better value may be found by examining the spectrum of the operator A.

7-Conclusion

The PPP method can be programmed in two versions: with low memory and time consuming, or fast running with high memory requirement. Unfortunately, two limitations on the PPP method have been discovered in the present work: the size and the permittivity of dielectric body. For an electrical size (diameter) of 3λ, we can only use ε_r up to 1.50. As the size reduces, the larger values of ε_r can also be used. However, within those limitations, the method has high computational efficiency.

8-References

[1] B. D. Popovic, B. M. Notaros, ``PPP method for analysis of electromagnetic fields in inhomogeneous media'', IEE proc. S-H, Vol. 140, Feb. 1993.

[2] B. D. Popovic, B. M. Notaros, ``The PPP-method for analysis of electromagnetic fields in the presence of dielectric bodies'', Proc.7th ICAP, York, IEE conf. publ.No. 333, pp. 946-949,1991.

[3] J. A. Stratton, Electromagnetic Theory, McGraw-Hill, New York, USA, 1941.

[4] D. E. Livesay, K. M. Chen, ``Electromagnetic fields induced inside arbitrarily shaped biological bodies'', IEEE Trans. Micro. Theo. Tech., Vol. MTT-22, No. 12, pp. 1273-1280, Dec. 1974.

[5] R. A. Sadeghzadeh N. J. McEwan and M. S. Abrishamian, ``Improved modelling of head antenna interaction using spherical wave expansions'', 2nd Int. Conf. on Computation in Electromagnetic, Nottingham, U.K., 12th-16th April, IEE Conf. Publ. 384, pp. 95-98, 1994.

[6] D. S. Jones, 1986, Acoustic and Electromagnetic Waves, Clarendon Press, Oxford.
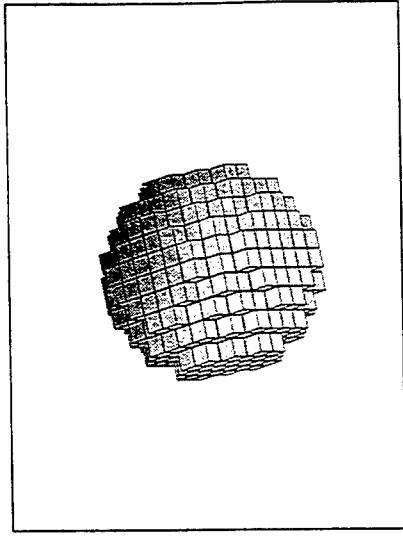
Figure 1: Spherical dielectric formed from many cubes
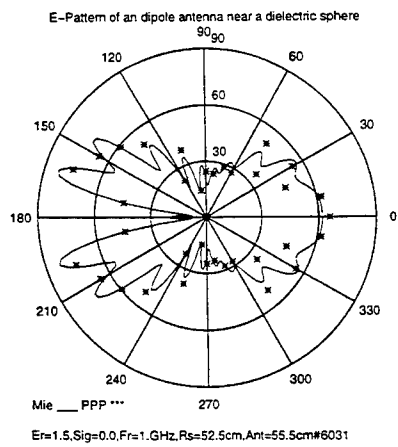
Figure 2: E-pattern of a thin dipole antenna near a dielectric sphere
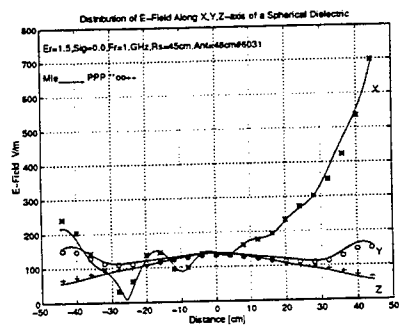
Figure 3: Distribution of E-field along three main axis inside a dielectric sphere
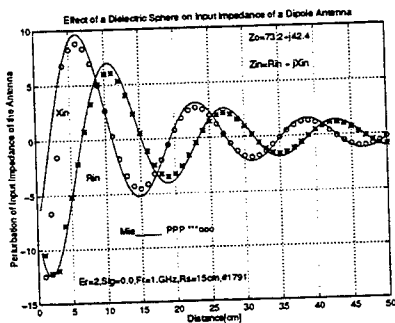
Figure 4: Perturbation of input impedance of a thin $\lambda/2$ dipole antenna

Table 1: Comparison of MoM and PPP Method

Method	MoM	PPP
Time (real)	1:14:07.7	1:42.3
Time (user)	1:12:19.3	1:37.8
Time (sys)	4.5	0.2
Memory	17.5M	3.3M
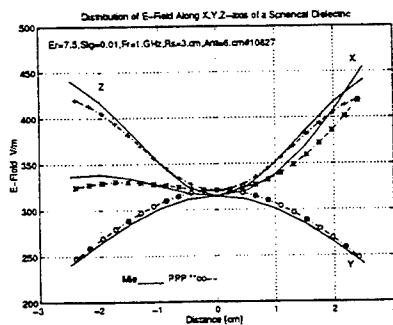
Figure 5: Distribution of E-field along three main axis inside a dielectric sphere